Transactions of the ASME®

Journal of Heat Transfer

Published Quarterly by The American Society of Mechanical Engineers

VOLUME 118 • NUMBER 2 • MAY 1996

Transactions of the ASME, Journal of Heat Transfer (ISSN 0022-1481) is published quarterly (Feb., May, Aug., Nov.) for $210.00 per year by The American Society of Mechanical Engineers, 345 East 47th Street, New York, NY 10017. Second class postage paid at New York, NY and additional mailing offices. POSTMASTER: Send address changes to Transactions of the ASME, Journal of Heat Transfer, c/o THE AMERICAN SOCIETY OF MECHANICAL ENGINEERS, 22 Law Drive, Box 2300, Fairfield, NJ 07007-2300.
CHANGES OF ADDRESS must be received at Society headquarters seven weeks before they are to be effective. Please send old label and new address. **PRICES:** To members, $40.00, annually: to nonmembers, $210.00. Add $30.00 for postage to countries outside the United States and Canada.

TECHNICAL PAPERS

(Contents continued)

Boiling and Two-Phase Heat Transfer

Transport in Porous Media

Heat Transfer in Manufacturing

TECHNICAL NOTES

ANNOUNCEMENTS

Thermal Conduction in Nonhomogeneous CVD Diamond Layers in Electronic Microstructures

K. E. Goodson
Mechanical Engineering Department,
Stanford University,
Stanford, CA 94305-3030

Chemical-vapor-deposited diamond layers of thickness between 0.1 and 5 μm have the potential to improve conduction cooling in electronic microstructures. However, thermal conduction in these layers is strongly impeded by phonon scattering on defects, whose concentrations can be highly nonhomogeneous, and on layer boundaries. By assuming that defects are concentrated near grain boundaries, this work relates the internal phonon scattering rate to the local characteristic grain dimension and to the dimensionless grain-boundary scattering strength, a parameter defined here that varies little within a given layer. Solutions to the Peierls–Boltzmann phonon transport equation for conduction along and normal to layers account for the nonhomogeneous internal scattering rate. Predictions for conduction along and normal to layers as thin as 0.2 μm agree well with room-temperature data. This research helps optimize diamond layer thicknesses for specific microstructures, such as silicon-on-diamond (SOD) circuits.

1 Introduction

At room temperature, chemical-vapor-deposited (CVD) diamond can be both an excellent thermal conductor and an electrical insulator, making it ideal for passive use in electronic microstructures. The benefit is greatest if diamond can be brought within micrometers of active regions, typically made of silicon or gallium arsenide (Goodson, 1995). The small separation allows the diamond to reduce the problem of local hotspots with micrometer-scale dimensions, which degrade the performance and reliability of electronic systems. One example is a high-power-density laser-diode array based on a novel composite diamond/gallium-arsenide substrate (Goodson et al., 1995c). Another example is a silicon-on-diamond (SOD) circuit in which a thin diamond layer separates active silicon regions from the substrate (Ravi and Landstrass, 1989). SOD circuits are a novel form of silicon-on-insulator (SOI) technology, which improve the speed and voltage-blocking capability of devices through the use of a buried insulating layer. The use of diamond as the buried insulating layer offers the promise of avoiding the thermal resistance due to conventional buried insulators, such as silicon dioxide (Goodson et al., 1995a). Temperature fields in SOD circuits are strongly influenced by conduction along and normal to diamond layers thinner than 5 μm.

The deposition of thin diamond layers on silicon yields a highly imperfect and nonhomogeneous material, particularly near the interface. This is evident in the grain structure, which is shown in the cross-sectional micrograph in Fig. 1 and approximately depicted in Fig. 2. The nucleation of diamond on a silicon substrate results in very small grains near the interface (e.g., Stoner et al., 1992). The scattering rate of phonons, which are responsible for heat conduction in diamond, is strongly influenced by the local grain size. However, the relationship between the phonon scattering rate and the grain size has not been rigorously determined. In thin layers, heat conduction is influenced by the strong nonhomogeneity of the phonon scattering rate, which results from the varying grain size, and by phonon scattering on the layer boundaries. Predictions require solutions to the phonon transport equation in nonhomogeneous layers, which are not available.

Previous data demonstrated the strong dependence of the local thermal conductivity along diamond layers on the coordinate z in Fig. 2 (Graebner et al., 1992a, b; Käding et al., 1993, 1994). The room-temperature conductivity varies from approximately 2000 W m^{-1} K^{-1} for values of z greater than about 150 μm, to values below the conductivity of silicon, 150 W m^{-1} K^{-1}, for values of z less than about 5 μm. Recent work measured the effective thermal conductivities normal to thinner layers, obtaining values between 12 and 75 W m^{-1} K^{-1} for layers of thickness 0.2 and 2.6 μm, respectively (Goodson et al., 1995b). Previous analysis solved the transient equation of phonon radiative transfer for conduction normal to diamond layers using the homogeneous phonon-scattering parameters of nearly perfect crystals (Joshi and Majumdar, 1993). There is a need to solve the transport equation considering the nonhomogeneous, highly imperfect conditions in contemporary layers of thickness less than a few micrometers.

This work develops a theory for the dependence of the local phonon scattering rate in diamond layers on the local characteristic dimension of grains, d_G. The phonon transport equation is integrated for the case of conduction along a layer with a nonhomogeneous phonon mean free path, yielding the effective thermal conductivity as a function of layer thickness, temperature, and parameters describing the grain structure. An approximate solution to the transport equation for the case of conduction normal to a nonhomogeneous layer is also given. Predictions for conduction along and normal to diamond layers as thin as 0.2 μm are compared with experimental data. This work is of interest to researchers fitting the temperature-dependent conductivity in diamond polycrystals, who lack a precise treatment of the scattering rate due to grain boundaries. This research helps quantify the benefit of using passive diamond layers in electronic microstructures, which is governed by the ability of the layers to conduct heat from active semiconducting regions.

Contributed by the Heat Transfer Division and presented at the Fourth ASME/JSME Thermal Engineering Joint Conference, Maui, Hawaii, March 19–24, 1995. Manuscript received by the Heat Transfer Division February 1995; revision received December 1995. Keywords: Conduction, Electronic Equipment. Associate Technical Editor: R. Viskanta.

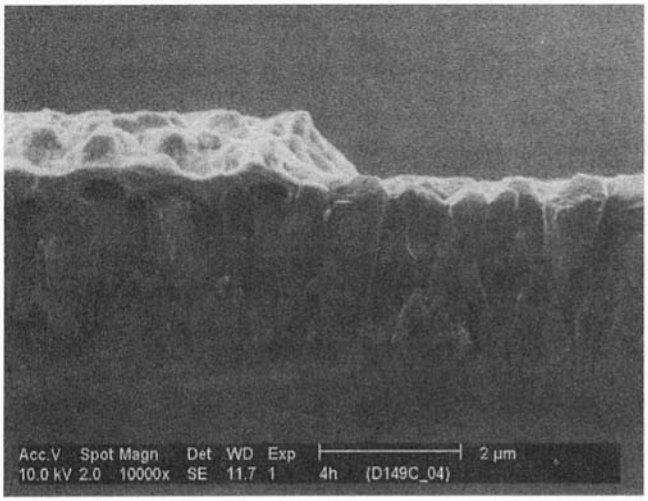

Fig. 1 Cross-sectional scanning electron microscopy image of a partially metallized diamond layer on silicon. The diamond layer thickness is 2.6 μm and the metallization is gold with a titanium adhesion layer. This structure was used by Goodson et al. (1995b) to measure the thermal resistance for conduction normal to the diamond layer into the silicon.

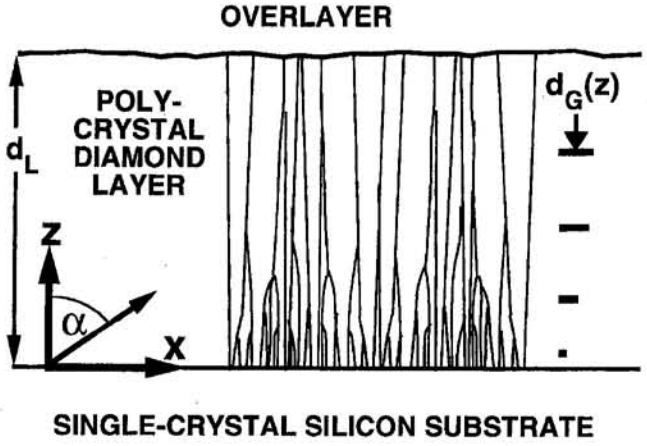

Fig. 2 Grain structure in CVD diamond layers

2 Grain Boundaries and the Local Phonon Scattering Rate

Phonon thermal conduction in diamond layers can be described using a phonon relaxation time, τ (e.g., Graebner, 1993). The total phonon scattering rate, $1/\tau$, is given by

$$[\tau(z, \omega, T)]^{-1} = [\tau_U(\omega, T)]^{-1} + [\tau_D(z, \omega)]^{-1} \quad (1)$$

The terms in Eq. (1) depend on the phonon angular frequency, ω, the temperature, T, and the position in the layer with respect to the substrate on which it was deposited, z. The first term on the right is due to phonon–phonon Umklapp scattering. The second term on the right is the phonon scattering rate due to defects, which is strongly influenced by the grain structure. The grain structure is described by the characteristic grain dimension, $d_G(z)$, which is defined as the average distance between intersections of grain boundaries with a reference line placed on a top-view electron micrograph of a layer of thickness z.

Scattering on diamond grain boundaries is at the root of a puzzle. Diamond layers with columnar grains have higher room-temperature thermal conductivities in the z direction, i.e., parallel to grain boundaries, than in the x direction (e.g., Graebner, 1993), suggesting that scattering on grain boundaries is important. But the importance of scattering on grain boundaries is questionable, due to the lack of an appropriate signature in the measured temperature dependence of the low-temperature thermal conductivity (e.g., Morelli et al., 1993). At tempera-

Nomenclature

A_U = fitting parameter, relaxation time for scattering on phonons, $s^{-1}\ K^{-3}$
B_U = fitting parameter, relaxation time for scattering on phonons, K
C_V = phonon specific heat per unit volume, $J\ m^{-3}\ K^{-1}$
D_{RC} = diameter of extended defects, m
d_D = maximum separation of defective region from grain boundaries, m
d_G = characteristic grain dimension, m
$d_{G,n}$ = distance between consecutive grains along phonon trajectory line, m
d_L = layer thickness, m
F_A, F_B = parameters in integrand, m
h_P = Planck's constant divided by $2\pi = 1.05 \times 10^{-34}$ J s
I_{GB} = distribution function for relating d_G and B_V, m^{-1}
J = total number of types of defects
j = integer denoting defect type
k_B = Boltzmann constant = $1.38 \times 10^{-23}\ J\ K^{-1}$
m, n = integers used in summation
N_0 = equilibrium phonon distribution function
N_X = phonon transport parameter, defined in Eq. (18), m^{-1}
$n_{GB,j}$ = number of defects of type j per unit grain-boundary area, m^{-2}
p = probability for transmission through grain boundary without scattering
q_a = heat flux along layer, $W\ m^{-2}$
q_{BULK} = heat flux in a homogeneous bulk medium, $W\ m^{-2}$
S_{A1}, S_{A2}, S_{B1}, S_{B2}, = parameters for integrand, Eqs. (24)–(26)
T = temperature, K
v_s = average phonon velocity, $m\ s^{-1}$
x, y = coordinates along layer, m
z = coordinate normal to layer, m
z_1 = coordinate of step nonhomogeneity, m
z_E = acoustic depth, defined in Eq. (17)
α = angular coordinate, see Fig. 3
β = angular coordinate, see Fig. 3
η = grain-boundary scattering strength, defined by Eq. (3)
Λ = phonon mean free path = $\nu_s\tau$, m
Λ_{AV} = average phonon mean free path, defined in Eq. (29), m
Λ_{GB} = phonon mean free path, grain boundaries, m
Λ_Z = linear slope of phonon mean free path with increasing z
Λ_0 = minimum phonon mean free path, m
Λ_1, Λ_2 = phonon mean free paths for step nonhomogeneity, m
μ = cos (α_P)
σ_j = phonon-scattering cross section of defects of type j, m^2
τ = phonon relaxation time = Λ/ν_s, s
τ_{GB} = phonon relaxation time, defects concentrated at grain boundaries, s
τ_D = phonon relaxation time, defects, s
τ_U = phonon relaxation time, Umklapp processes, s
ω = phonon angular frequency, rad s^{-1}

tures above a few degrees Kelvin, the rate of phonon scattering on distinct grain boundaries, which is independent of the phonon frequency, is much smaller than the rate of scattering on other types of defects, e.g., impurities, which depends strongly on the phonon frequency.

An explanation is suggested by the electron micrographs of Heatherington et al. (1990), which show a high concentration of defects within about 2000 Å of grain boundaries. Scattering on defects concentrated at grain boundaries yields anisotropy in layers with columnar grains and has the phonon frequency dependence needed to explain low-temperature conductivity data. Goodson et al. (1994b) used this assumption to relate the effective thermal conductivity along layers to d_G, yielding predictions in reasonable agreement with data for which the local value of d_G is known. This work assumes that in layers of thickness less than a few micrometers, the small grain dimension causes phonon scattering on defects near grain boundaries to dominate over scattering on defects within grains. This allows $1/\tau_D$ in Eq. (1) to be replaced by $1/\tau_{GB}$, which is the scattering rate due to grain boundaries. This work also assumes that $1/\tau_D$ can be treated as homogeneous within a given plane z in solving the phonon transport equation, even though the scattering rate must be higher near grain boundaries. This yields accurate predictions of the heat flux as long as (a) the characteristic length scale of the medium in which transport is analyzed is large compared to d_G and (b) the geometry is such that energy must travel through many grain boundaries, both of which are satisfied here.

This analysis uses two different approximations to relate $1/\tau_{GB}$ to d_G. The first, approximation A, distributes the defects contributed by grain boundaries homogeneously within the plane z. The second, approximation B, assumes that the defects contributed by a grain boundary are located within a distinct distance from grain boundaries, d_D, that is finite but much smaller than d_G. For case B, the scattering rate due to grain boundaries is analyzed considering ballistic phonon transport between boundaries, at which phonons have a probability for transmission without scattering. For both cases, the total scattering rate is calculated using Eq. (1) with the expression for the scattering rate due to grain boundaries derived in the following subsections. Approximation A is most appropriate for $d_G \sim d_D$ and approximation B is most appropriate for $d_G \gg d_D$. The electron micrographs of Heatherington et al. (1990) indicate that $d_D \sim 2000$ Å for grains with $d_G \sim 1$ μm. Since grain dimensions in diamond layers vary between a few tens of nanometers to several tens of micrometers depending on the coordinate z, both approximations are of practical importance.

2.1 Approximation A: Lateral-Homogeneous Distribution of Defects Related to Grain Boundaries. Because grain-boundary scattering is considered geometrically in this work, it is helpful to define a mean free path for scattering on grain boundaries $\Lambda_{GB} = \tau_{GB} v_s$, where $v_s = 1.32 \times 10^4$ m s^{-1} is the average phonon velocity in diamond. Given approximation A, the inverse of the mean free path can be expanded using

$$[\Lambda_{GB}(z, \omega)]^{-1} = B_V(z)\eta(z, \omega) \quad (2)$$

where B_V is the grain-boundary area per unit volume. The scattering rate determined using Eq. (2) can be applied directly in Eq. (1). The dimensionless *grain-boundary scattering strength* is defined here,

$$\eta(z, \omega) = \sum_{j=1}^{J} \sigma_j(\omega) n_{GB,j}(z) \quad (3)$$

where σ is the scattering cross section of defects of type j for phonons of frequency ω. The concentration of defects of type j is the product of the number density of those defects per unit grain-boundary area, $n_{GB,j}$, and B_V. Section 2.2 shows that η is simply related to the probability for phonon transmission through a grain boundary without scattering.

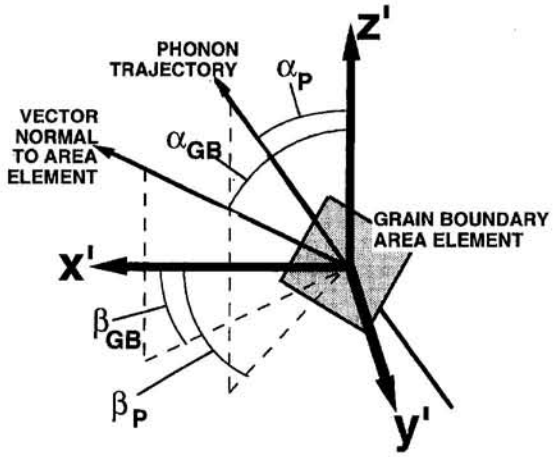

Fig. 3 Angles describing a phonon trajectory and a differential grain-boundary area element

This work derives the relationship between B_V and d_G by assuming that d_G is independent of the direction of the reference line within a given x-y plane. This is not strictly correct for nearly heteroepitaxial layers, which have a large fraction of grain boundaries oriented in the crystallographic directions of the underlying silicon substrates (e.g., Rösler et al., 1993). But the oriented grains prevail only for relatively large values of z, so the present approach is still appropriate. The angles α_{GB} and β_{GB} of the area-element normal vector and a set of relative rectangular coordinates are defined in Fig. 3. The grain-boundary area per unit volume is

$$B_V(z) = 4 \int_0^{\pi} \int_0^{\pi/2} \frac{I_{GB}(z, \alpha_{GB}, \beta_{GB})}{\sin(\alpha_{GB}) \cos(\beta_{GB})} d\beta_{GB} d\alpha_{GB} \quad (4)$$

where $I_{GB}(\alpha_{GB}, \beta_{GB}) d\alpha_{GB} d\beta_{GB}$ is the number of intersections per unit length of grains of angles α_{GB} and β_{GB} with the x' axis, which serves here as the reference line for the measurement of d_G. The denominator of the integrand in Eq. (4) accounts for the increased contribution of grain-boundary area per unit volume by area elements with normal vectors not parallel to the reference line.

If the grain structure is random, then I_{GB} is

$$I_{GB}(z, \alpha_{GB}, \beta_{GB}) = [\sin(\alpha_{GB})][\sin(\alpha_{GB})|\cos(\beta_{GB})|]\left[\frac{1}{2\pi d_{GB}(z)}\right] \quad (5)$$

The first term in brackets accounts for the fraction of grain-boundary area elements in the $x'-y'$ plane having angle α_{GB}, which decreases to zero with α_{GB}. The second term in brackets accounts for the diminished profiles presented by grain-boundary area elements whose normal vectors are not parallel to the reference line. In layers with *columnar* grain structure, grain boundaries are predominantly parallel to the z axis but have intersections with $x'-y'$ planes that are randomly oriented. For this case, I_{GB} is

$$I_{GB}(z, \alpha_{GB}, \beta_{GB}) = \left[\delta\left(\alpha_{GB} - \frac{\pi}{2} + \Delta\alpha\right) + \delta\left(\alpha_{GB} - \frac{\pi}{2} - \Delta\alpha\right)\right]$$

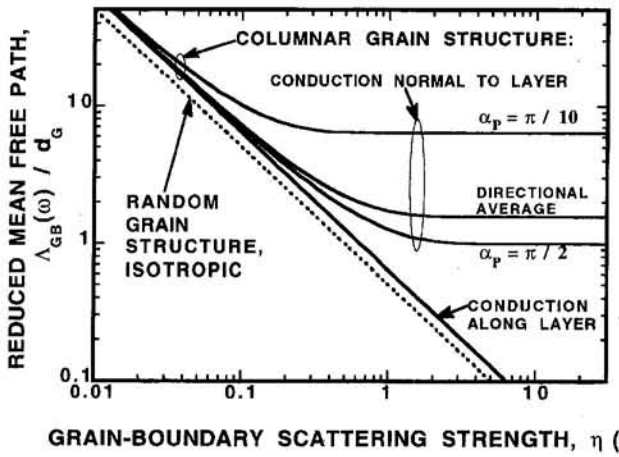

Fig. 4 Phonon mean free path limited by scattering due to grain boundaries

$$\times [|\cos(\beta_{GB})|]\left[\frac{1}{8d_G(z)}\right];$$

$$\sin(\Delta\alpha) = \frac{1}{2}\frac{d}{dz}[d_G(z)] \quad (6)$$

The use of delta functions assumes that grain boundaries have exactly the slope that accommodates the change of d_G with respect to z. Combining Eqs. (2), (4), and (5) yields

$$\frac{\Lambda_{GB}(z,\omega)}{d_G(z)} = \frac{1}{2\eta(z,\omega)} \quad (7)$$

for random grains and

$$\frac{\Lambda_{GB}(z,\omega)}{d_G(z)} = \frac{2}{\pi\eta(z,\omega)}\left[1 + \left(\frac{1}{2}\frac{d}{dz}[d_G(z)]\right)^2\right]^{-1/2} \quad (8)$$

for columnar grains. The term in brackets in Eq. (8) is usually very near to unity.

The mean free paths for random and columnar grains are plotted in Fig. 4. Practical layers have grain structures between these two extremes. The difference between the two results becomes clear when considering the contribution of each grain boundary to B_V within a cylindrical differential volume element centered about the reference line used to measure d_G. Each intersection of the reference line with the boundary of a columnar grain contributes less to B_V than an intersection with a typical randomly oriented grain boundary.

2.2 Approximation B: Concentration at Grain Boundaries of Defects Related to Grain Boundaries. If d_G is considerably larger than d_D, then approximation A is poorly suited. The error is greatest if the geometry makes it unnecessary for phonons to travel through grain boundaries, which is the case for conduction normal to a layer with a perfect columnar grain structure. Equations (7) and (8) predict that the phonon mean free path, and therefore the thermal conductance for heat transport normal to the layer, can be made arbitrarily small by increasing the grain-boundary scattering strength, η. But if defects related to grain boundaries are restricted to a region near grain boundaries of thickness much less than d_G, then a very large η can at most reduce Λ_{GB} to the order of d_G.

The phonon mean free path to be used for conduction normal to layers with columnar grains is obtained here using approximation B, which assumes that d_D is much smaller than d_G. The probability of phonon transmission through a grain boundary without scattering, p, decreases exponentially with the ratio of the path length of the phonon through the defective region, which for phonons with normal incidence is $2d_D$, to the phonon mean free path in the defective regions, which is $2d_D/\eta$. This yields

$$p[\eta(z,\omega), \alpha_P - \alpha_{GB}, \beta_P - \beta_{GB}] = \exp\left[\frac{-\eta(z,\omega)}{|\cos(\alpha_P - \alpha_{GB})\cos(\beta_P - \beta_{GB})|}\right] \quad (9)$$

where the angles α_P and β_P are those of the phonon trajectory shown in Fig. 3. The mean free path of a group of phonons launched with a given trajectory is

$$\Lambda_{GB} = d_{G,0} + \sum_{n=1}^{\infty} d_{G,n} \prod_{m=1}^{n} p\left[\eta, \alpha_P - \frac{\pi}{2}, \beta_P - \beta_{GB,m}\right] \quad (10)$$

The integer subscripts label the grain boundaries intersected by the phonon trajectory line. The angle $\beta_{GB,m}$ is for the area element of the grain boundary m at the intersection of the trajectory line. The length $d_{G,n}$ is the distance along the trajectory line between grain boundaries n and $n+1$. To obtain an approximate result in closed form, *all* grain-boundary area elements intersected by the phonon trajectory line are assumed to have the same angle β_{GB} and all $d_{G,n}$ are all assumed to be $d_G/\sin(\alpha_P)$. Equation (10) reduces to

$$\frac{\Lambda_{GB}(z,\alpha_P,\omega)[\sin(\alpha_P)]}{d_G(z)} = \left[1 + \frac{1}{\exp\left[\frac{\pi}{2}\frac{\eta(z,\omega)}{\sin(\alpha_P)}\right] - 1}\right] \quad (11)$$

The coefficient in the exponential function, $\pi/2$, is determined by requiring that approximations A and B yield the same mean free path when $\eta/\sin(\alpha_P)$ is much smaller than unity. In this limit, phonons travel through many grains and the distinction between the two approximations is unimportant. For solutions to the phonon transport equation that assume an isotropic phonon mean free path, it is useful to average Eq. (11) over the solid hemisphere. Numerical integration yields a result within 3 percent of

$$\frac{\Lambda_{GB}(z,\omega)}{d_G(z)} = \frac{\pi}{2}\left[1 + \frac{1}{\exp\left[\left(\frac{\pi}{2}\right)^2\eta(z,\omega)\right] - 1}\right] \quad (12)$$

Figure 4 shows that Eqs. (11) and (12), which are appropriate for columnar grains, yield longer mean free paths than the results for randomly oriented grains for large η.

2.3 Parameter Values for CVD Diamond. The results derived in Sections 2.1 and 2.2 apply to polycrystalline layers. The results are applied to CVD diamond layers using the phonon-scattering parameters of Graebner (1993) and Goodson et al. (1994b). The first term on the right of Eq. (1) is

$$[\tau_U(x_\omega, T)]^{-1} = A_U(x_\omega)^2 T^3 \exp\left(\frac{-B_U}{T}\right) \quad (13)$$

where $A_U = 640\ \mathrm{s}^{-1}\ \mathrm{K}^{-3}$ and $B_U = 470$ K. The dimensionless phonon frequency is $x_\omega = h_P\omega/(k_B T)$, where h_P is Planck's constant divided by 2π and k_B is the Boltzmann constant. Imperfections are considered using

$$\sigma_1(x_\omega T) = \frac{V_0^2 x_\omega^4 T^4}{4\pi v_s^4}\left(\frac{k_B}{h_P}\right)^4 \quad (14)$$

for point defects, where $V_0 = 5.68 \times 10^{-30}$ m^3, and

$$\sigma_2(x_\omega T) = \frac{\pi D_{RC}^6}{4v_s^4}\left(\frac{k_B}{h_P}\right)^4 (x_\omega T)^4 \quad \text{for} \quad x_\omega T < \frac{h_P v_s}{k_B D_{RC}}$$

$$= \frac{\pi (D_{RC})^2}{4} \quad \text{for} \quad x_\omega T \geq \frac{h_P v_s}{k_B D_{RC}} \tag{15}$$

for extended defects, e.g., groups of point defects or small regions with amorphous microstructure. These cross sections vary with phonon angular frequency but not with temperature, so the independent variable is denoted as the product $x_\omega T$. This work uses the values fitted by Goodson et al. (1994b) for the diameter of extended defects, $D_{RC} = 1.4 \times 10^{-9}$ m, and for the number densities of defects per unit grain boundary area, $n_{GB,1} = 2.2 \times 10^{20}$ m^{-2} and $n_{GB,2} = 1.5 \times 10^{18}$ m^{-2}.

These scattering cross sections do not explicitly account for normal phonon–phonon scattering processes. While normal phonon–phonon scattering does not contribute directly to the thermal resistance, it increases the coupling between phonon scattering at high frequencies and phonons at low frequencies, which effectively increases the resistance. This could be most significant at low temperatures, where normal processes become more important compared to Umklapp processes. The scattering cross sections used here were fitted to thermal conductivity data for thick diamond layers over a large regime of temperatures (Graebner, 1993), and therefore implicitly account for normal processes. A small error may result in the present study of thin layers due to the impact of nonhomogeneity and boundary scattering on the influence of normal processes.

3 Solutions to the Phonon Transport Equation for Nonhomogeneous Layers

The scattering mechanisms discussed in Section 2 govern phonon transport *within* diamond layers. For layers that are sufficiently thin, phonon scattering on the layer boundaries can also be important (e.g., Flik et al., 1992). This necessitates solving the phonon transport equation of Peierls (1955) based on the Boltzmann equation, whose boundary conditions describe the interaction of phonons with the interfaces of a layer. To accommodate the phonon mean free path developed in Section 2, the collision integral in the Peierls–Boltzmann equation must be simplified using the relaxation-time approximation. If the medium is isotropic and the differences between phonon polarizations are neglected, the steady-state form of this equation for the two-dimensional geometry in Fig. 2 reduces to

$$\sin(\alpha_P)\cos(\beta_P)\frac{\partial N(x, z, \omega, \alpha_P, \beta_P)}{\partial x} + \cos(\alpha_P)\frac{\partial N(x, z, \omega, \alpha_P, \beta_P)}{\partial z} = \frac{N_0(\omega, T(x, z)) - N(x, z, \omega, \alpha_P, \beta_P)}{\Lambda(z, \omega, T)} \tag{16}$$

where N is the local phonon distribution function and N_0 is the local equilibrium distribution function. An approximate solution approach is to enforce energy conservation within each energy level (e.g., Brewster, 1992), which in this case is distinguished by the phonon angular frequency, ω. This can lead to inaccurate predictions of phonon distribution functions, but it is expected to yield good predictions of the total phonon heat flux. When this method is used, Eq. (16) differs only by a constant of multiplication from the equation of phonon radiative transfer derived by Majumdar (1993). It is useful to define the dimensionless *acoustic depth*

$$z_E(z, \omega, T) = \int_0^z \frac{dz'}{\Lambda(z, \omega, T)} \tag{17}$$

3.1 Transport Along a Layer. Transport in the x direction is due to the following condition:

$$\frac{\partial N_0(\omega, T)}{\partial x} = \frac{\partial N_0(\omega, T)}{\partial T}\frac{\partial T}{\partial x} = N_X \tag{18}$$

where N_X is defined here. For conduction along layers it helps to integrate the Eq. (16) along a line of sight. The position along this line is z_E/μ, where $\mu = \cos(\alpha_P)$. For phonons with $\mu > 0$, i.e., that travel upward in Fig. 2, the integration yields

$$N(z_E, x_0) = N_0[x(z_E' = 0)]\exp\left(-\frac{z_E}{\mu}\right) + \int_0^{z_E} N_0[x(z_E')]\exp\left(\frac{z_E' - z_E}{\mu}\right)\frac{dz_E'}{\mu} \tag{19}$$

where

$$N_0[x(z_E')] = N_0(x_0) - N_X[z(z_E) - z(z_E')]\tan(\alpha_P)\cos(\beta_P) \tag{20}$$

The heat flux is an integral involving the distribution function over all frequencies. The challenge for a nonhomogeneous medium arises due to the nested integral, whose evaluation must carefully consider the variation of the free path in the medium. This work chooses two forms for $\Lambda(z)$ that allow the heat flux to be evaluated analytically:

Linear Nonhomogeneity:

$$\Lambda(z, \omega, T) = \Lambda_0(\omega, T) + z\Lambda_Z(\omega, T) \tag{21}$$

Step Nonhomogeneity:

$$\Lambda(z, \omega, T) = \Lambda_1(\omega, T), \; 0 \leq z < z_1 \qquad = \Lambda_2(\omega, T), \; z_1 \leq z < d_L \tag{22}$$

where x_ω is the dimensionless phonon frequency defined in Section 2.3. For the calculations presented in Section 4, a linear dependence is used, as in Eq. (21). This gradual growth is consistent with micrographs of the layers whose transport properties are predicted in the present study. Conduction in some diamond layers may be better modeled using the step change, due to a highly disordered near-interfacial region beneath a region of relatively large grains.

The heat flux for both cases reduces to

$$q_a(x_\omega) = -\frac{dT}{dx}C_V(x_\omega, T)\frac{v_s}{4d_L} \times \int_0^{d_L}\int_0^{\pi/2} \sin^2(\alpha_P)\tan(\alpha_P)[F_A + F_B]d\alpha_P dz \tag{23}$$

where d_L is the layer thickness. The specific heat function C_V is from the theory of Debye (Berman, 1976). For linear nonhomogeneity, the parameters F_A and F_B are

$$F_A = z(S_{A1} + S_{A2} - S_{A1}S_{A2}) - \frac{zS_{A1} - \left(\frac{\Lambda_0}{\Lambda_Z}\right)S_{A2}}{\mu\Lambda_z + 1} \tag{24}$$

$$F_B = z(S_{B1} + S_{B2} - S_{B1}S_{B2}) - \frac{zS_{B1} - \left(\frac{\Lambda_0}{\Lambda_Z} + d_L\right)S_{B2}}{1 - \mu\Lambda_Z} \tag{25}$$

where

$$S_{A1} = \left(\frac{\Lambda_0}{z\Lambda_Z} + 1\right); \quad S_{A2} = \left(\frac{z\Lambda_Z}{\Lambda_0} + 1\right)^{-1/\mu\Lambda_z}$$

$$S_{B1} = \left(1 - \frac{\Lambda_0}{z\Lambda_Z} - \frac{d}{z}\right); \quad S_{B2} = \left(1 - \frac{z\Lambda_Z}{\Lambda_0 + d\Lambda_Z}\right)^{1/\mu\Lambda_z} \tag{26}$$

For the step nonhomogeneity,

$$F_A = \mu\Lambda_1\left[1 - \exp\left(\frac{-z}{\mu\Lambda_1}\right)\right] \quad \text{for} \quad 0 \le z \le z_1$$

$$= \mu\Lambda_2 + z\exp\left[\frac{z_1\left(1 - \frac{\Lambda_2}{\Lambda_1}\right) - z}{\mu\Lambda_2}\right] + \exp\left[\frac{z_1 - z}{\mu\Lambda_2}\right] \times\left[(z + \mu\Lambda_1)\left(1 - \exp\left(\frac{-z_1}{\mu\Lambda_1}\right)\right) - z - \mu\Lambda_2\right]$$

$$\text{for} \quad z_1 \le z \le d_L \tag{27}$$

$$F_B = \mu\Lambda_2\left[1 - \exp\left(\frac{-z}{\mu\Lambda_2}\right)\right] \quad \text{for} \quad 0 \le z \le d_L - z_1$$

$$= \mu\Lambda_1 + z\exp\left[\frac{(d_L - z_1)\left(1 - \frac{\Lambda_1}{\Lambda_2}\right) - z}{\mu\Lambda_1}\right] + \exp\left[\frac{d_L - z_1 - z}{\mu\Lambda_1}\right] \times\left[(z + \mu\Lambda_2)\left(1 - \exp\left(\frac{z_1 - d_L}{\mu\Lambda_2}\right)\right) - z - \mu\Lambda_1\right]$$

$$\text{for} \quad d_L - z_1 < z \le d_L \tag{28}$$

It is useful to compare the heat flux calculated here to that along a very thick homogeneous layer, which has a mean free path that is equal to the average of that in the thin diamond layer,

$$q_{\text{BULK}}(x_\omega) = -\frac{dT}{dx}\frac{1}{3}C_V(x_\omega, T)\frac{v_s}{d_L}\int_0^{d_L}\Lambda(z, x_\omega)dz$$

$$= -\frac{dT}{dx}\frac{1}{3}C_V(x_\omega, T)v_s\Lambda_{AV}(x_\omega) \tag{29}$$

Figure 5 contrasts the ratio of Eqs. (23) and (29) to the solution to the transport equation for a homogeneous medium, which was provided by Fuchs (1938) and Sondheimer (1952). Although these authors actually solved the equation to determine the impact of electron-boundary scattering on the electrical conductivity, the mathematics is completely analogous. When the linear form applies, the average heat flux along the layer can be estimated within 15 percent using the solution of Fuchs (1938) and Sondheimer (1952) and Λ_{AV}. Nonhomogeneity reduces the heat flux along a layer. Conduction in regions with a relatively long mean free path is more strongly impeded by the boundaries than in a homogeneous layer with the same average mean free path, which prevents the heat flux in these regions from completely balancing the low heat flux in regions with a relatively short mean free path. This is most clearly evidenced

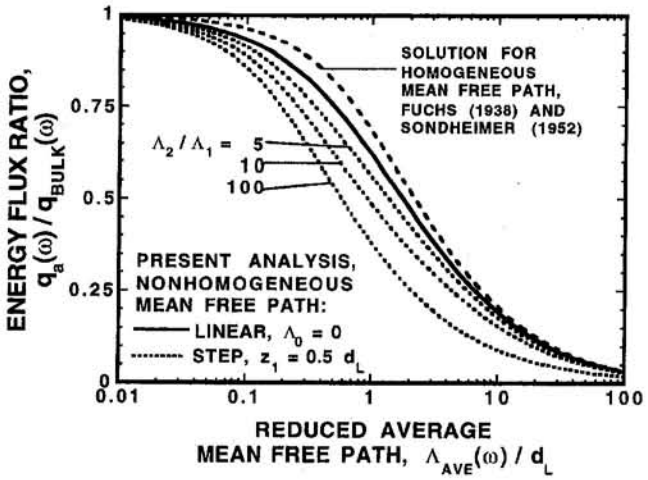

Fig. 5 Reduction of heat flux along a thin layer due to boundary scattering considering a nonhomogeneous mean free path. The bulk heat flux is that for an infinite medium with mean free path equal to the spatially averaged value in the layer.

by the step model, which yields predictions that differ substantially from the homogeneous case.

The effective thermal conductivity along the layer is

$$k_{a,eff} = -\left(\frac{dT}{dx}\right)^{-1}\int_0^{\theta/T} q_a(x_\omega)dx_\omega \tag{30}$$

where $\theta = 2032$ K is the Debye temperature of diamond.

3.2 Transport Normal to a Layer. The solution to Eq. (16) for conduction normal to a layer is discussed in textbooks for photon transport normal to a gray medium with gray, diffuse boundaries (e.g., Brewster, 1992). The exact solution for the heat flux cannot be written explicitly. But the solution obtained using the diffusion approximation and a slip boundary condition is simple and agrees within a few percent of the exact result. Chen and Tien (1993) used the approximate result to derive the effective thermal conductivity for conduction normal to homogeneous layers. This expression yields predictions that agree with thermal-resistance data for conduction normal to thin amorphous silicon-dioxide layers at low temperatures (Goodson et al., 1994a). For a nonhomogeneous medium,

$$\frac{1}{R_T} = \frac{k_{n,eff}}{d_L} = \frac{v_s}{3}\int_0^{\theta/T}\frac{C_V(x_\omega, T)dx_\omega}{d_E(x_\omega, T) + \frac{4}{3}\left(\frac{1}{\alpha_0} + \frac{1}{\alpha_1} - 1\right)} \tag{31}$$

where the dimensionless effective layer thickness d_E is calculated using $z = d_L$ in Eq. (17). The transmission coefficients for phonons into the bounding media, α_0 and α_1, are calculated using the diffuse mismatch theory of Swartz and Pohl (1989).

This study neglects lateral variation of the phonon scattering rate, which yields a thermal resistance that is homogeneous in the $x-y$ plane. In practical layers, the thermal resistance may vary significantly in the $x-y$ plane due to the higher scattering rate near grain boundaries. Since the resistance is dominated by the regions with smallest grains, nonuniformity would be observable using experimental techniques with resolution finer than d_{G0}. Section 4 compares the thermal resistance predictions with data from a laser-reflectance technique with resolution limited by diffraction to roughly 1 μm. Since d_{G0} is of the order of 20–50 nm for the layers interrogated here, the comparison is appropriate.

4 Results and Discussion

Figure 6 plots the effective conductivity along layers as a function of the layer thickness at temperatures of 300 and 77 K. The calculations are performed using two different linear slopes relating the grain dimension to z. The data in the figure are for layers in which the reported grain dimension at a given thickness is approximately equal to that used in the calculations. Graebner et al. (1992b) measured the conductivity along several thin layers of varying thickness grown under different conditions. The two layers studied here were grown at nearly the same rate and had almost the same ratios of $d_G(d_L)/d_L$. In order to plot the data in Fig. 6, these two layers are both assumed to have the same linear dependence of d_G on z. The intercept grain dimension, 0.2 μm, is chosen for consistency with the other grain-dimension function, which was provided by Plamann et al. (1994) for their layers. While both sets of layers were fabricated using a similar microwave-plasma assisted technique, the process of Plamann et al. (1994) yielded a microstructure with finer grains. The agreement between the predictions and data at room temperature is achieved using no fitting parameters. The grain-boundary scattering strength η used here was determined during a prior research project by fitting the conductivity of diamond layers thicker than 50 μm (Goodson et al., 1994b). This lends support to the assumption that η is independent of z.

Figure 6 shows the importance of obtaining a rapid increase of grain dimension with the layer thickness. The conductivity of layers with larger grains increases far more rapidly with increasing z, which can allow a total required conductance along a layer to be achieved using less diamond. The conductivities predicted in Fig. 6 are much less than that of high-quality thick CVD diamond layers at both 77 K and 300 K, which exceeds 2000 W m^{-1} K^{-1}. The reduction is most severe at cryogenic temperatures. At 77 K the phonon mean free path is limited by scattering on grain and layer boundaries and the phonon specific heat is much less than that at room temperature. This causes the conductivities at 77 K of the diamond layers to be more than an order of magnitude less than those at room temperature, although the bulk conductivity has the opposite behavior.

For conduction normal to diamond layers, the grain size at the interface is very important. Figure 7 predicts the thermal resistance using a relationship between d_G and z that is based on top-view electron micrographs of layers experimentally investigated by Goodson et al. (1995b), one of which is shown in Fig. 1. The data agree well with the predictions if a random grain structure is assumed and the diamond grain dimension

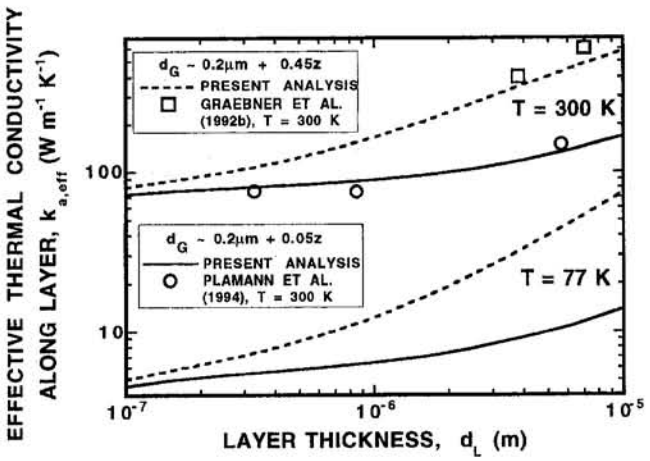

Fig. 6 Effective conductivity along thin nonhomogeneous diamond layers considering two relationships between the grain size and thickness. The data are for layers whose reported grain dimensions for a given thickness are the same as those used in the respective calculations.

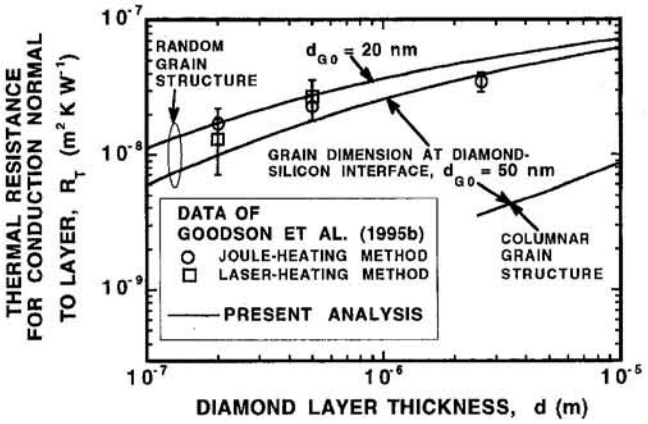

Fig. 7 Thermal resistance for conduction normal to thin metallized diamond layers on silicon

near the interface is assumed to be between 20 and 50 nm. These assumptions are consistent with top-view micrograph of the layers in the study, although the grain structure of the thickest layer appeared to be at least partially columnar. A columnar grain structure improves conduction in the direction normal to the layer compared to that for a random grain structure, as shown in the predictions in Fig. 7. This may explain the overprediction of the data for the thickest layer by the analysis that assumes randomly oriented grains.

The scattering theory in Section 2 can be applied independently of the solution to the transport equation to estimate the local conductivity in layers of thickness greater than 1 μm at room temperature as a function of the grain dimension d_G. Using approximation A with Eqs. (29) and (30), the diamond conductivity at 300 K is fit within 6 percent by

$$k(d_G) = (2169 \text{ W m}^{-1} \text{ K}^{-1})\left[1 - \frac{6.785 \times 10^{-6} \text{ m}}{d_G + 6.785 \times 10^{-6} \text{ m}}\right] \tag{31}$$

5 Conclusions

This research uses phonon transport theory to relate the conductivity of thin diamond layers to the size and orientation of their grains. The agreement between predictions and data lend support to the hypothesis that defects concentrated near grain boundaries limit the mean free path of phonons in thin diamond layers. Future deposition research must target the most rapid increase in grain dimension with thickness during layer growth. The different mean-free-path expressions derived here for conduction along and normal to layers with columnar grains should be used to model the anisotropy measured in thick diamond layers (Graebner, 1993).

This work shows that contemporary layers have the potential to provide electrical insulation without the problematic thermal resistance resulting from conventional dielectrics, e.g., amorphous silicon dioxide. A major task required to realize this potential is to minimize the thermal boundary resistances between diamond and neighboring materials, which can result due to disordered interfacial layers or to incomplete contact.

Acknowledgments

The author is grateful to O. W. Käding of Stanford University for helpful comments and to M. N. Touzelbaev of Stanford University for general comments and fitting Eq. (31).

References

Annamalai, N. K., Sawyer, J., Karulkar, P., Masyara, W., and Landstrass, M., 1993, "Silicon-on-Diamond Field-Effect Devices," *Proceedings of the 3rd*

IUMRS International Conference on Advanced Materials, Tokyo, Japan, Aug. 31–Sept. 4.

Berman, R., 1976, *Thermal Conduction in Solids,* Oxford University Press, Oxford, United Kingdom, p. 23.

Brewster, M. Q., 1992, *Thermal Radiative Transfer and Properties,* Wiley, New York, Chap. 11, p. 232.

Chen, G., and Tien, C. L., 1993, "Thermal Conductivity of Quantum-Well Structures," *J. Thermophysics and Heat Transfer,* Vol. 7, pp. 311–318.

Flik, M. I., Choi, B. I., and Goodson, K. E., 1992, "Heat Transfer Regimes in Microstructures," ASME JOURNAL OF HEAT TRANSFER, Vol. 114, pp. 666–674.

Fuchs, K., 1938, "The Conductivity of Thin Metallic Films According to the Electron Theory of Metals," *Proc. Cambridge Phil. Soc.,* Vol. 34, pp. 100–108.

Goodson, K. E., Flik, M. I., Su, L. T., and Antoniadis, D. A., 1994a, "Prediction and Measurement of the Thermal Conductivity of Amorphous Dielectric Layers," ASME JOURNAL OF HEAT TRANSFER, Vol. 116, pp. 317–324.

Goodson, K. E., Käding, O. W., and Zachai, R., 1994b, "Thermal Resistances at the Boundaries of CVD Diamond Layers in Electronic Systems," presented at the ASME Winter Annual Meeting, Chicago, IL, Nov. 11–18.

Goodson, K. E., 1995, "Impact of CVD Diamond Layers on the Thermal Engineering of Electronic Systems," *Annual Review of Heat Transfer,* Vol. VI, Begell House, New York, pp. 323–353.

Goodson, K. E., Flik, M. I., Su, L. T., and Antoniadis, D. A., 1995a, "Prediction and Measurement of Temperature Fields in Silicon-on-Insulator Electronic Circuits," ASME JOURNAL OF HEAT TRANSFER, Vol. 117, pp. 574–581.

Goodson, K. E., Käding, O. W., Rösler, M., and Zachai, R., 1995b, "Experimental Investigation of Thermal Conduction Normal to Diamond-Silicon Boundaries," *J. Appl. Phys.,* Vol. 77, pp. 1385–1392.

Goodson, K. E., Kurabayashi, K., and Pease, R. F. W., 1995c, "Improved Heat Sinking for Laser-Diode Arrays Using Microchannels in CVD Diamond," *Proceedings of the ASME National Heat Transfer Conference,* Portland, OR, Aug. 5–9, S. S. Sadhal et al., eds., Vol. 3, pp. 187–192.

Graebner, J. E., Jin, S., Kammlott, G. W., Herb, J. A., and Gardinier, C. F., 1992a, "Unusually High Thermal Conductivity in Diamond Films," *Appl. Phys. Lett.,* Vol. 60, pp. 1576–1578.

Graebner, J. E., Mucha, J. A., Seibles, L., and Kammlott, G. W., 1992b, "The Thermal Conductivity of Chemical-Vapor-Deposited Diamond Films on Silicon," *J. Appl. Phys.,* Vol. 71, pp. 3143–3146.

Graebner, J. E., 1993, "Thermal Conductivity of CVD Diamond: Techniques and Results," *Diamond Films and Technology,* Vol. 3, pp. 77–130.

Heatherington, A. V., Wort, C. J. H., and Southworth, P., 1990, "Crystalline Perfection of Chemical Vapor Deposited Diamond Films," *J. Materials Research,* Vol. 5, pp. 1591–1594.

Joshi, A. A., and Majumdar, A., 1993, "Transient Ballistic and Diffusive Phonon Heat Transport in Thin Films," *J. Appl. Phys.,* Vol. 74, pp. 31–39.

Käding, O. W., Matthias, E., Zachai, R., Füßer, H. J., and Münziger, P., 1993, "Thermal Diffusivities of Thin Diamond Films on Silicon," *Diamond and Related Materials,* Vol. 2, pp. 1185–1190.

Käding, O. W., Rösler, M., Zachai, R., and Füßer, H.-J., 1994, "Lateral Thermal Diffusivity of Epitaxial Diamond Films," *Diamond and Related Materials,* Vol. 3, pp. 1175–1182.

Majumdar, A., 1993, "Microscale Heat Conduction in Dielectric Thin Films," ASME JOURNAL OF HEAT TRANSFER, Vol. 115, p. 7.

Morelli, D. T., Uher, C., and Robinson, C. J., 1993, "Transmission of Phonons Through Grain Boundaries in Diamond Films," *Appl. Phys. Lett.,* Vol. 62, pp. 1085–1087.

Peierls, R. E., 1955, *Quantum Theory of Solids,* Oxford University Press, New York, Chaps. 1 and 2.

Plamann, K., Fournier, D., Anger, E., and Gicquel, A., 1994, "Photothermal Examination of the Heat Diffusion Inhomogeneity in Diamond Films of Submicron Thickness," *Diamond and Related Materials,* Vol. 3, pp. 752–756.

Ravi, K. V., and Landstrass, M. I., 1989, "Silicon on Insulator Technology Using CVD Diamond," *Proceedings of the First International Symposium on Diamond and Diamond-Like Films,* J. P. Dismukes et al., eds., The Electrochemical Society, Pennington, NJ, pp. 24–37.

Rösler, M., Zachai, R., Füßer, H.-J., Jiang, X., and Klages, C.-P., 1993, "Structural Properties of Heteroepitaxial Diamond on Silicon," *Proceedings of the 2nd International Conference on the Applications of Diamond Films and Related Materials,* M. Yoshikawa et al., eds., MYU Press, Tokyo, Japan, pp. 691–696.

Sondheimer, E. H., 1952, "The Mean Free Path of Electrons in Metals," *Advances in Physics,* Vol. 1, pp. 1–42.

Stoner, B. R., Ma, G.-H. M., Wolter, S. D., and Glass, J. T., 1992, "Characterization of Bias-Enhanced Nucleation of Diamond on Silicon by in Vacuo Surface Analysis and Transmission Electron Microscopy," *Phys. Rev. B,* Vol. 45, pp. 11067–11084.

Swartz, E. T., and Pohl, R. O., 1989, "Thermal Boundary Resistance," *Rev. Mod. Phys.,* Vol. 61, pp. 605–668.

Elements of a General Correlation for Turbulent Heat Transfer

P. K. Maciejewski
Mechanical Engineering Department,
University of Pittsburgh,
Pittsburgh, PA 15261

A. M. Anderson
Department of Mechanical Engineering,
Union College,
Schenectady, NY 12308

Typically, heat transfer researchers present results in the form of an empirically based relationship between a length-based Nusselt number, a length-based Reynolds number, and a fluid Prandtl number. This approach has resulted in a multitude of heat transfer correlations, each tied to a specific geometry type. Two recent studies have contributed key ideas that support the development of a more general correlation for turbulent heat transfer that is based on local parameters. Maciejewski and Moffat (1992a, b) found that wall heat transfer rates scale with streamwise turbulent velocity fluctuations and Anderson and Moffat (1992a, b) found that the adiabatic temperature rise is the driving potential for heat transfer. Using these two concepts and a novel approach to dimensional analysis, the present authors have formulated a general correlation for turbulent heat transfer. This correlation predicts wall heat flux as a function of the turbulent velocity fluctuations, the adiabatic temperature rise, and the fluid properties (density, specific heat, thermal conductivity, and viscosity). The correlation applies to both internal and external flows and is tested in air, water, and FC77. The correlation predicts local values of surface heat flux to within ± 12.0 percent at 95 percent confidence.

Introduction

Historically, correlations constructed for turbulent heat transfer in incompressible flows have been specific to flow geometry, thermal boundary conditions, and fluid properties. Heat transfer results are typically cast in the form $\mathrm{Nu} = f(\mathrm{Re}, \mathrm{Pr})$ for a given geometry. As a consequence, existing empirical knowledge in turbulent heat transfer is represented by a somewhat disparate collection of case-specific correlations. The aim of this paper is to present a new analysis of some recently published data, which suggests that turbulent heat transfer in incompressible flows may be represented in a single, general correlation.

The hope of constructing a general correlation for turbulent heat transfer rests on the possibility that surface convective heat transfer rates in turbulent flows can be characterized in purely local terms, i.e., that the surface heat flux may be correlated in terms of a set of variables defined near the point at which the heat transfer occurs, irrespective of the global geometry of the flow. This possibility may be linked to a series of questions. Is there a local measure of the flow field turbulence that serves as a proxy for the entire velocity field? Is there a local driving potential (temperature difference) for heat transfer which accounts for the effects of upstream thermal boundary conditions? Can a correlation for turbulent heat transfer be constructed in the absence of any variable representing the global geometry of the flow? The possibility of constructing a general correlation for turbulent heat transfer may require an affirmative answer to each of these questions.

Two recent studies guide the present analysis, each contributing an insight to the problem of constructing a general correlation for turbulent heat transfer. The first of these studies, Maciejewski and Moffat (1992a, b) [see also Maciejewski and Moffat (1989, 1990) on this point], provides the insight that the local value of the surface heat flux may be directly determined by the maximum local value of the turbulent velocity fluctuations, $u'_{\max}$. If this proves to be correct, then perhaps a general correlation for turbulent heat transfer need only include this single variable representing the influence of the velocity field on surface heat flux. The second of these studies, Anderson and Moffat (1992a, b) [see also Moffat and Anderson (1991) on this point], provides the insight that the local driving potential for heat transfer, which accounts for the effects of upstream thermal boundary conditions, is the difference between the actual local surface temperature, T_s, and the local adiabatic surface temperature, T_{ad}, where T_{ad} is the temperature that would be present in the absence of local surface heat transfer. Furthermore, local surface heat flux is expected to be directly proportional to ΔT_{ad}. While the studies of both Maciejewski and Moffat (1992a, b) and Anderson and Moffat (1992a, b) have been conducted in air, they represent what would be considered two different types of turbulent flow situations: The former study is an investigation of external, boundary layer heat transfer in the presence of very high levels of free-stream turbulence, and the latter study is an investigation of heat transfer in an internal flow with roughness elements (i.e., in a geometry typical of electronics cooling applications).

The present study seeks a general correlation for turbulent heat transfer, which represents the heat transfer data of both Maciejewski and Moffat (1992a, b) and Anderson and Moffat (1992a, b, 1990), as well as the turbulent boundary layer heat transfer data of Hollingsworth and Moffat (1989) (a study conducted in water on both flat and concave surfaces), and the channel flow data of Garimella and Schlitz (1992) (a study conducted in FC77). The final correlation will account for the effects of turbulence, upstream thermal boundary conditions, and fluid properties.

General Formulation

The studies selected consist of the external flow studies of Maciejewski and Moffat (1992a, b) and Hollingsworth and Moffat (1989) and the internal flow studies of Anderson and Moffat (1992a, b, 1990) and Garimella and Schlitz (1992). These five studies were chosen because (1) they represent heat transfer data from a diverse set of turbulent flows, and (2) these studies either include measurements or allow assessments of local surface heat flux and the variables that hypothetically

Contributed by the Heat Transfer Division for publication in the JOURNAL OF HEAT TRANSFER. Manuscript received by the Heat Transfer Division August 1995; revision received February 1996. Keywords: Forced Convection, Turbulence. Associate Technical Editor: A. Lavine.

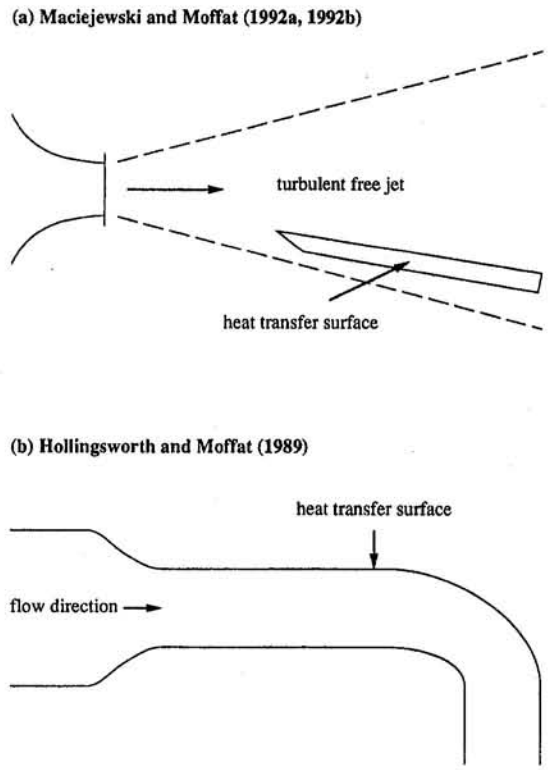

Fig. 1 Schematic of Maciejewski and Moffat (1992a, b) and Hollingsworth and Moffat (1989)

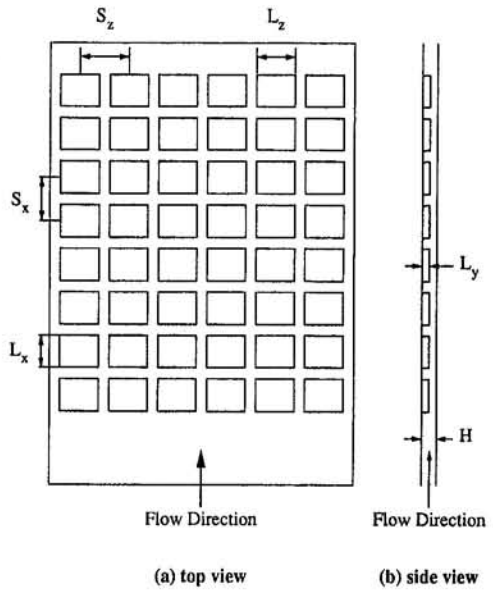

Fig. 2 Schematic of internal channel flows (see Table 1)

determine the value of local surface heat flux. Figures 1 and 2 and Table 1 display the diversity of the experimental facilities associated with the studies considered. Taken together, these five studies incorporate five geometries (including both external, boundary layer flows and internal, electronics cooling flows) and three fluids (air, water, and FC77).

The data of Maciejewski and Moffat (1992a, b) and Hollingsworth and Moffat (1989) will be collectively designated "external flow data." The study of Maciejewski and Moffat (1992a, b), a study of boundary layer heat transfer in the presence of very high levels of free-stream turbulence (i.e., local free-stream turbulence levels between 20 and 60 percent of the local free-stream mean velocity), represented schematically in Fig. 1(*a*), was conducted in air on a flat heat transfer surface placed in the margin of a turbulent free-jet. The study of Hollingsworth and Moffat (1989), a study of boundary layer heat transfer in the absence of free-stream turbulence, represented in Fig. 1(*b*), was conducted on both flat and concave heat transfer surfaces placed in a water channel. For the data of Hollingsworth and Moffat (1989), the maximum local value of the turbulent fluctuations, u'_{max}, is estimated from the data of Johnson and Johnston (1989), which includes a parallel study of the velocity boundary layer performed in the same facility used by Hollingsworth and Moffat (1989).

The data of Anderson and Moffat (1992a, b), Anderson and Moffat (1990), and Garimella and Schlitz (1992) will be collectively designated "internal flow data." The studies of Anderson and Moffat (1992a, b, 1990), studies in air, and Garimella and Schlitz (1992) [see also Schlitz (1992)], a study in FC77, were conducted in rectangular channels with roughness elements on one wall, as represented in Fig. 2. The values for the geometric parameters for each of these studies are provided in

Nomenclature

A = correlation constant, external flow
$a1$ = exponent on $\Pi_{1,\infty}$, external flow
$a2$ = exponent on Π_2, external flow
B = correlation constant, internal flow
$b1$ = exponent on Π_1, internal flow
$b2$ = exponent on $\Pi_{2,\Delta P}$, internal flow
$b3$ = exponent on Π_3, internal flow
C = correlation constant, general correlation
C_p = specific heat
H = channel height, internal flow
h = heat transfer coefficient
k = thermal conductivity
k_B = Boltzmann constant = 1.38×10^{-23} J/K
L_x = module length
L_y = module height
L_z = module width
$L^* = (\rho C_p)^{-1/3}$
m = exponent on Π_2, general correlation
n = exponent on Π_3, general correlation
Nu = Nusselt number
Pr = Prandtl number
q''_w = wall heat flux
Re = Reynolds number
S_x = module streamwise spacing
S_z = module spanwise spacing
T = temperature
u' = root-mean-square streamwise turbulent velocity fluctuation
$U' = u'_{max}/u'_{max,\Delta P}$
$U^* = k/(\rho C_p)^{2/3}$
U = mean channel velocity
x = coordinate in flow direction
ΔP = pressure drop per row
$\Theta = \Delta T_{ad}/\Delta T_\infty$
μ = viscosity
Π_0 = nondimensional surface heat flux
Π_1 = nondimensional temperature difference
Π_2 = nondimensional turbulent fluctuation
Π_3 = nondimensional viscosity
π_0 = nondimensional heat transfer coefficient
π_1 = reciprocal of nondimensional viscosity
π_2 = nondimensional ratio of viscosity and thermal conductivity
ρ = density

Subscripts

ad = adiabatic
f = film
max = maximum
s = surface
∞ = free stream

Table 1 (all dimensions in cm)

Study	L_x	L_z	S_x	S_z	H	L_y
Anderson and Moffat (1992a, 1992b)	3.75	4.65	5.02	5.92	1.42-4.37	0.95
Anderson and Moffat (1990)	1.27	1.27	3.81	3.81	2.86-5.84	1.27
Garimella and Schlitz (1992)	1.02	1.02	1.60	1.60	0.2	0.064
Wirtz and Chen (1992)	3.60	3.60	3.60	3.60	1.8	0.60

Table 1. Although the geometries associated with this set of studies in channels with roughness elements may be characterized by a common set of variables, within this common geometric description the studies themselves are quite diverse. The study of Anderson and Moffat (1992a, b) employs a dense array of flat elements, the study of Anderson and Moffat (1990) employs a sparse array of cubical elements, and the study of Garimella and Schlitz (1992) employs an array of extremely flat elements.

It is presumed that the surface heat flux, q''_w, can be represented as a function of the maximum local value of the turbulent fluctuations, $u'_{\max}$, the local value of the difference between the surface temperature and the adiabatic surface temperature, ΔT_{ad}, and the fluid density, ρ, specific heat, C_p, thermal conductivity, k, and viscosity, μ. The relation between these variables can be expressed as follows:

$$q''_w = f(u'_{\max}, \Delta T_{ad}, \rho, C_p, k, \mu) \tag{1}$$

Each of these variables has either been measured or can be estimated for each of the five studies considered.

Following Panton (1984), Callen (1985), and others, it is presumed that temperature and energy are dimensionally equivalent. (In this system, ΔT is expressed in J, C_p is expressed in kg^{-1}, and k is expressed in $m^{-1}\ s^{-1}$. The Boltzmann constant, $k_B = 1.38 \times 10^{-23}$ J/K, is used to convert Kelvins to Joules for the purpose of evaluating ΔT, C_p and k.) The relation between the variables can be expressed nondimensionally as follows:

$$\Pi_0 = f(\Pi_1, \Pi_2, \Pi_3) \tag{2}$$

where

$$\Pi_0 \equiv q''_w/\rho U^{*3}$$

$$\Pi_1 \equiv C_p(T_s - T_{ad})/U^{*2}$$

$$\Pi_2 \equiv u'_{\max}/U^*$$

$$\Pi_3 \equiv \mu C_p/k$$

and

$$U^* \equiv k/(\rho C_p)^{2/3}$$

In this formulation, Π_0 may be interpreted as the nondimensional surface heat flux, Π_1 as the nondimensional driving potential for heat transfer (temperature difference), Π_2 as the nondimensional level of the turbulent fluctuations, and Π_3 as the nondimensional fluid viscosity (also recognized as Prandtl number). The variables ρ, C_p, and k serve as the basis variables for this nondimensionalization. The combination $U^* \equiv k/(\rho C_p)^{2/3}$ is a fluid property, which has the dimension of velocity. Fluid properties are evaluated at the film temperature, $T_f = (T_s + T_\infty)/2$.

It is anticipated that the relation between the nondimensional variables can be expressed in a simple product, power-law form:

$$\Pi_0 = C\Pi_1\Pi_2^m\Pi_3^n \tag{3}$$

where the coefficient C and the exponents m and n will be estimated from the data. The anticipated linear relation between Π_0 and Π_1 reflects the conjecture that q''_w is directly proportional to ΔT_{ad}.

Ideally, each of the five data sets would allow direct assessments of Π_0, Π_1, Π_2, and Π_3, but unfortunately this is not the case: The external, boundary layer heat transfer data do not include measured values of ΔT_{ad}, and the internal, electronics cooling data do not include measured values of $u'_{\max}$. As a result of this deficiency, the model parameters of Eq. (3) will be estimated by isolating the external flow data to determine m, isolating the internal flow data to determine n (and to confirm that the exponent on Π_1 is 1), and making reasonable assumptions about ΔT_{ad} for the external flow data and about $u'_{\max}$ for the internal flow data to determine C.

Analysis of the External Flow Data

For the data of Maciejewski and Moffat (1992a, b) and Hollingsworth and Moffat (1989), the relation between the surface to adiabatic wall temperature difference, ΔT_{ad}, and the surface to free-stream fluid temperature difference, ΔT_∞, can be expressed as follows:

$$\Theta \equiv (T_s - T_{ad})/(T_s - T_\infty) \equiv \Delta T_{ad}/\Delta T_\infty$$

Π_1 can then be expressed by

$$\Pi_1 = \Pi_{1,\infty}\Theta$$

where $\Pi_{1,\infty}$ is based on ΔT_∞. The general correlation of Eq. (3) is then

$$\Pi_0 = C\Pi_1\Pi_2^m\Pi_3^n = C(\Pi_{1,\infty}\Theta)\Pi_2^m\Pi_3^n \tag{4}$$

For the external flow data, the values of $\Pi_{1,\infty}$ and Π_3 are highly correlated, which precludes any meaningful estimation of the dependence of Π_0 on Π_3. However, Π_0 can be adequately modeled for the external flow data by a correlation of the following form:

$$\Pi_0 = A\Pi_{1,\infty}^{a1}\Pi_2^{a2} \tag{5}$$

The relation between the two correlations given in Eqs. (4) and (5) results in:

$$\Theta = (A/C)\Pi_{1,\infty}^{(a1-1)}\Pi_2^{(a2-m)}\Pi_3^{-n} \tag{6}$$

This relation for Θ may be interpreted as the form of the empirical relation between ΔT_∞ and ΔT_{ad} for the external flow data. Since $u'_{\max}$ has been directly measured for the external flows, the model parameter $a2$ in Eq. (5) will be taken as an estimate of m, the exponent on Π_2 in Eq. (3).

The parameters A, $a1$, and $a2$ of Eq. (5) can be estimated directly from the data of Maciejewski and Moffat (1992a, b) and Hollingsworth and Moffat (1989). A regression of these external flow data yields:

$$\Pi_0 = 3.78 \times 10^{-4}\Pi_{1,\infty}^{0.728}\Pi_2^{5/6} \tag{7}$$

The model parameter $a2$ is estimated at 0.828 ± 0.080 at 95 percent confidence, permitting the conjecture that the value of m is 5/6. Figure 3 displays the agreement between this correlation, represented by the solid line, and the data. The pair of dashed lines in Fig. 3, located 13.7 percent above and below the correlation line, represents a 95 percent confidence interval for values of Π_0 predicted with this correlation. The limits of measurement uncertainty displayed for each datum in Fig. 3 represent 95 percent confidence intervals.

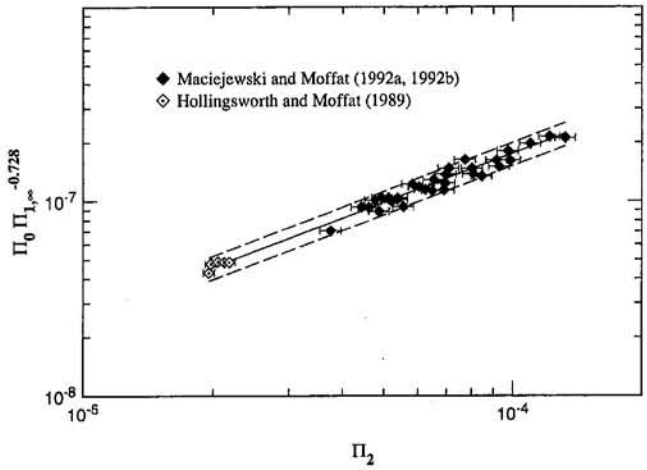

Fig. 3 $\Pi_0 \Pi_{1,\infty}^{-a1}$ versus Π_2 for external flow

Analysis of the Internal Flow Data

For the data of Anderson and Moffat (1992a, b), Anderson and Moffat (1990), and Garimella and Schlitz (1992), the maximum level of the turbulent fluctuations in the fully developed region can be estimated in terms of the channel pressure drop by means of the method presented by Anderson and Moffat (1992b):

$$u'_{\max,\Delta P} = (3/2)^{-1/2} [U\Delta P(H - L_y)/\rho L_x]^{1/3} \quad (8)$$

This result estimates the maximum possible level of u' within the channel, not the actual level of $u'_{\max}$. The relation between $u'_{\max,\Delta P}$ and the actual value of $u'_{\max}$ can be expressed as follows:

$$U' \equiv u'_{\max}/u'_{\max,\Delta P}$$

Π_2 can then be expressed by

$$\Pi_2 = \Pi_{2,\Delta P} U'$$

where $\Pi_{2,\Delta P}$ is based on $u'_{\max,\Delta P}$. The general correlation of Eq. (3) is then

$$\Pi_0 = C\Pi_1 \Pi_2^m \Pi_3^n = C\Pi_1 (\Pi_{2,\Delta P} U')^m \Pi_3^n \quad (9)$$

Π_0 can be adequately modeled for the internal flow data by a correlation of the following form:

$$\Pi_0 = B\Pi_1^{b1} \Pi_{2,\Delta P}^{b2} \Pi_3^{b3} \quad (10)$$

The relation between the two correlations given in Eqs. (9) and (10) results in:

$$U' = \{(B/C)\Pi_1^{(b1-1)} \Pi_3^{(b3-n)}\}^{1/m} \Pi_{2,\Delta P}^{(b2/m-1)} \quad (11)$$

This relation for U' may be interpreted as the form of the empirical relation between $u'_{\max,\Delta P}$ and $u'_{\max}$ for the internal flow data. Since ΔT_{ad} has been directly measured for the internal flows, the model parameter $b1$ in Eq. (10) is expected to have a value of 1. Since Π_3 is highly correlated with $\Pi_{1,\infty}$ for the external flow data, but not highly correlated with either Π_1 or $\Pi_{2,\Delta P}$ for the internal flow data, the model parameter $b3$ in Eq. (10) will be taken as an estimate of n, the exponent on Π_3 in Eq. (3).

The parameters B, $b1$, $b2$, and $b3$ can be estimated directly from the data of Anderson and Moffat (1992a, b, 1990) and Garimella and Schlitz (1992). A regression of these internal flow data yields:

$$\Pi_0 = 3.38 \times 10^{-3} \Pi_1^{1} \Pi_{2,\Delta P}^{0.748} \Pi_3^{-2/5} \quad (12)$$

The model parameter $b1$ is estimated at 1.000 ± 0.032 at 95 percent confidence, confirming the hypothesis that Π_0 is linear in Π_1. The model parameter $b3$ is estimated at -0.417 ± 0.096 at 95 percent confidence, permitting the conjecture that the value of n is $-2/5$. Figure 4 displays the agreement between this correlation, represented by the solid line, and the data. The pair of dashed lines in Fig. 4, located 10.6 percent above and below the correlation line, represents a 95 percent confidence interval for values of Π_0 predicted with this correlation. The limits of measurement uncertainty displayed for each datum in Fig. 4 represent 95 percent confidence intervals.

Estimation of the Model Coefficient

At this point in the analysis, the general correlation for turbulent heat transfer that is sought has the following form:

$$\Pi_0 = C\Pi_1 \Pi_2^{5/6} \Pi_3^{-2/5} \quad (13)$$

The coefficient C, which remains to be determined, is directly related to the factor Θ, which relates ΔT_∞ to ΔT_{ad} for the external flow data, and to the factor U', which relates $u'_{\max,\Delta P}$ to $u'_{\max}$ for the internal flow data. Indeed, specification of the model coefficient C will suffice to determine both the relation $\Theta = \Theta(C, n, A, a1; \Pi_{1,\infty}, \Pi_3)$ of Eq. (6) and the relation $U' = U'(C, m, B, b2; \Pi_{2,\Delta P})$ of Eq. (11). The aim is to select a value for C that produces physically meaningful estimates of Θ for the external flow data and physically meaningful estimates of U' for the internal flow data. This will be accomplished by choosing C in a manner that reconciles the empirically based relations for Θ and U' with (1) estimates of Θ derived from the data of Ames and Moffat (1990) for boundary layer flow in the presence of free-stream turbulence, and (2) estimates of U' derived from the data of Wirtz and Chen (1992) for turbulence in a channel flow with transverse ribs.

Ames and Moffat (1990) measure the decay of wall temperature on a flat surface in air in the presence of high levels of free-stream turbulence (i.e., local free-stream turbulence levels between 7 and 17 percent of the local free-stream mean velocity) following an initial length for which the surface is uniformly heated. Their data suggest that the ratio of ΔT_{ad} to ΔT_∞ for these circumstances falls between 0.33 and 0.40. Assuming that the data of Ames and Moffat (1990) provide a reasonable estimate for Θ for the data of Maciejewski and Moffat (1992a, b), the model coefficient C can be estimated from the data of Maciejewski and Moffat (1992a, b) using Eq. (6) as follows:

$$C = (A/\Theta)\Pi_{1,\infty}^{(a1-1)} \Pi_3^{-n} \quad (14)$$

where $n = -2/5$, $A = 3.78 \times 10^{-4}$, and $a1 = 0.728$. The value of $\Pi_{1,\infty}^{(a1-1)} \Pi_3^{-n}$ is nearly constant for their data. As the value of Θ is varied from 0.33 to 0.40, the value of C varies from 0.0102

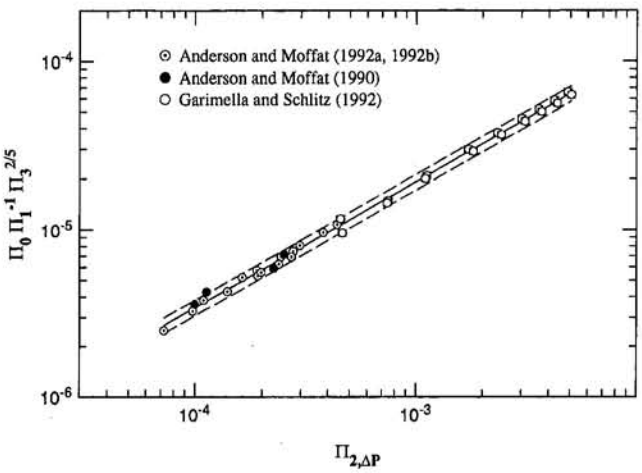

Fig. 4 $\Pi_0 \Pi_1^{-b1} \Pi_3^{-b3}$ versus $\Pi_{2,\Delta P}$ for internal flow

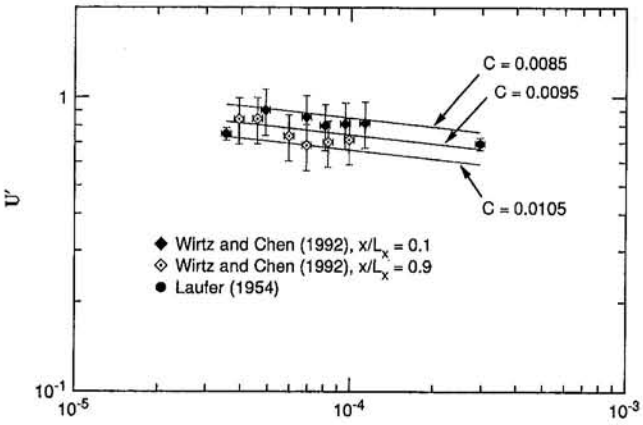

Fig. 5 Determination of C from U' using the data of Wirtz and Chen (1992)

to 0.0084. If the value of Θ is taken to be 0.365, then the value of C is estimated to be 0.0092.

Wirtz and Chen (1992) measure the level of turbulence at various locations in a rectangular channel with a series of rectangular transverse ribs located along one wall. [The geometry of the experiments of Wirtz and Chen (1992) can be expressed in terms of the geometric variables introduced in Fig. 2 and Table 1.] This study provides direct measurement of $u'_{\max}$ and allows direct assessment of $u'_{\max,\Delta P}$ and $\Pi_{2,\Delta P}$ for an internal flow geometry that is typical of electronics cooling applications. The model coefficient C can be estimated from the data of Wirtz and Chen (1992) using Eq. (11) as follows:

$$C = BU'^{-m}\Pi_{2,\Delta P}^{(b2-m)} \tag{15}$$

where $m = 5/6$, $B = 3.38 \times 10^{-3}$, and $b2 = 0.748$. Figure 5 displays the relation between U' and $\Pi_{2,\Delta P}$ for the data of Wirtz and Chen (1992) for each of their measurement stations and compares their data to the model in Eq. (11) for values of C equal to 0.0085, 0.0095, and 0.0105. The limits of measurement uncertainty displayed for each datum in Fig. 5 represent 95 percent confidence intervals. The data near the leading edge of each rib, measured at $x/L_x = 0.1$, suggest a value for C near 0.0088. The data near the trailing edge of each rib, measured at $x/L_x = 0.9$, suggest a value of C near 0.0098. Given that the location of the local value of the surface heat flux on the rib, which corresponds to the mean value of the surface heat flux for the entire rib, is expected to be closer to $x/L_x = 0.1$ than to $x/L_x = 0.9$, a value of C near 0.0092 may produce a typical value of U' along the surface of the rib. Two data points constructed from the smooth-wall pipe flow data of Laufer (1954) have also been included in Fig. 5 and are in agreement with the data of Wirtz and Chen (1992).

The estimate of C obtained from the data of Ames and Moffat (1990) and the estimate of C obtained independently from the data of Wirtz and Chen (1992) are consistent, $C \approx 0.0092$. Using $C = 0.0092$, $\Pi_{1,\infty}$ can be converted to Π_1 for the external flow data of Maciejewski and Moffat (1992a, b) and Hollingsworth and Moffat (1989) by means of the relation:

$$\Pi_1 = 0.041\Pi_{1,\infty}^{0.728}\Pi_3^{2/5} \tag{16}$$

For the internal flow data of Anderson and Moffat (1992a, b, 1990) and Garimella and Schlitz (1992), $\Pi_{2,\Delta P}$ can be converted to Π_2 by means of the relation:

$$\Pi_2 = 0.30\Pi_{2,\Delta P}^{0.898} \tag{17}$$

With the aid of Eqs. (16) and (17), Π_0, Π_1, Π_2 and Π_3 can be constructed for each of the five data sets.

A General Correlation for Turbulent Heat Transfer

A complete general correlation for turbulent heat transfer can now be given as follows:

$$\Pi_0 = 0.0092\Pi_1\Pi_2^{5/6}\Pi_3^{-2/5} \tag{18}$$

Figure 6 displays the agreement between this final correlation, represented by the solid line, and all of the heat transfer data under consideration. The pair of dashed lines in Fig. 6, located 12.0 percent above and below the correlation line, represents a 95 percent confidence interval for values of Π_0 predicted with this correlation. The limits of measurement uncertainty displayed for each datum in Fig. 6 represent 95 percent confidence intervals.

Given that q''_w is linear in ΔT_{ad}, and given a means to estimate both ΔT_{ad} and $u'_{\max}$, an alternative general correlation for turbulent heat transfer can be constructed. Dimensionally, the problem is recast as follows:

$$h_{ad} = f(u'_{\max}, \rho, C_p, k, \mu) \tag{19}$$

where

$$h_{ad} = q''_w/\Delta T_{ad}$$

There are now only three nondimensional variables to be constructed. One possible nondimensionalization is as follows:

$$\pi_0 = f(\pi_1, \pi_2) \tag{20}$$

where

$$\pi_0 \equiv \Pi_0/(\Pi_1\Pi_2) \equiv h_{ad}/\rho C_p u'_{\max}$$

$$\pi_1 \equiv \Pi_2/\Pi_3 \equiv \rho u'_{\max} L^*/\mu$$

$$\pi_2 \equiv \Pi_3 \equiv \mu C_p/k$$

and

$$L^* \equiv (\rho C_p)^{-1/3}$$

In this formulation, π_0 may be interpreted as the nondimensional heat transfer coefficient (perhaps analogous to Stanton number), π_1 as the reciprocal of the nondimensional fluid viscosity (perhaps analogous to Reynolds number), and π_2 as the reciprocal of the ratio of the nondimensional fluid thermal conductivity and the nondimensional fluid viscosity (also recognized as Prandtl number). The variables ρ, C_p, and $u'_{\max}$ serve as the basis variables for the purpose of this nondimensionalization. L^* serves as a reference length.

Re-expressing the previously derived general correlation for turbulent heat transfer in terms of this alternative set of nondimensional variables results in the following correlation:

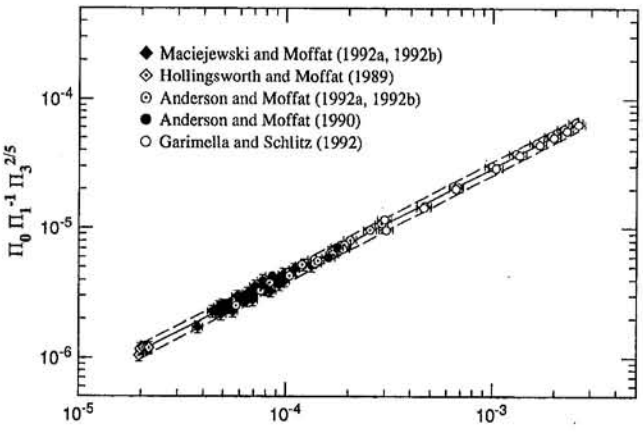

Fig. 6 General correlation (Π_0, Π_1, Π_2, Π_3)

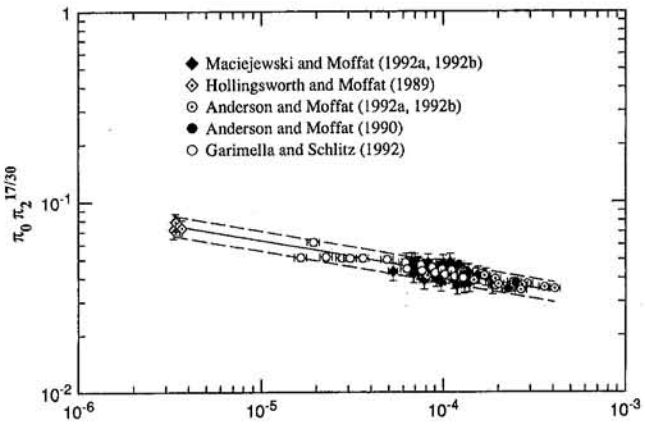

Fig. 7 Alternate formulation of general correlation (π_0, π_1, π_2)

$$\pi_0 = 0.0092\pi_1^{-1/6}\pi_2^{-17/30} \tag{21}$$

Figure 7 displays the agreement between this alternative form of the general correlation for turbulent heat transfer, represented by the solid line, and all the heat transfer data presently under consideration. The pair of dashed lines in Fig. 7, located 12.0 percent above and below the correlation line, represents a 95 percent confidence interval for values of π_0 predicted with this correlation. The limits of measurement uncertainty displayed for each datum in Fig. 7 represent 95 percent confidence intervals.

Discussion

This paper demonstrates that heat transfer data taken from a set of diverse experiments in turbulent flows can be accurately represented by a single, simple correlation. Information from the velocity field is carried into the correlation by means of a single measure of the local turbulence field, u'_{max}, information from the upstream temperature boundary condition is carried into the correlation by means of ΔT_{ad}, and information pertaining to the properties of the fluid is carried into the correlation by means of ρ, C_p, k, and μ. This set of variables is sufficient to determine q''_w for the set of experiments considered.

Noticeably absent from the correlation is any variable directly representing the geometry of the flow field. Indeed, the absence of geometry-specific variables makes a general correlation for turbulent heat transfer possible. It may reasonably be asserted that the geometry of the flow contributes to the determination of u'_{max} and ΔT_{ad}.

Although this paper presents a method for estimating ΔT_{ad} for the studies considered that investigate boundary layers and a method for estimating u'_{max} for the studies considered that investigate channels with roughness elements, it by no means resolves the ambiguities in defining and determining ΔT_{ad} for continuous surfaces and in defining and determining u'_{max} for finite and perhaps complex regions of a flow field near heated elements. The path to a general correlation for turbulent heat transfer would have been more direct if existing studies in turbulent heat transfer had provided unambiguous, measured determinations of both u'_{max} and ΔT_{ad}. There remains a need for measurement techniques and/or methods of assessment for each of these quantities.

The present analysis adopts the proposition that the local value of the surface heat flux is determined by some measure of the maximum local value of the turbulent velocity fluctuations and employs a measure associated with the streamwise component of the turbulent fluctuations, u'_{max}. Antonia et al. (1988) establish the presence of a strong correlation between streamwise velocity fluctuations and fluid temperature fluctuations in the near-wall region of a turbulent boundary layer, a connection that may ultimately justify the use of u'_{max} for predicting local surface heat flux. At the same time, it is plausible that u'_{max} serves as a surrogate for a more appropriate measure of the maximum local value of the turbulent velocity fluctuations, perhaps one defined in terms of the component of the turbulent fluctuations normal to the surface or in terms of the turbulence kinetic energy. It is also plausible that the structure of near-wall turbulence makes the choice among these alternative measures a matter of indifference and convenience.

The particular and perhaps peculiar set of nondimensional variables adopted by the present analysis rests on the presumption that units of energy and units of temperature are dimensionally equivalent, contrary to the position typically adopted by heat transfer texts. Discussions on this point originate in an exchange between Rayleigh (1915a, b) and Riabouchinsky (1915) in which Riabouchinsky challenges Rayleigh's assumption that temperature is a primary dimension and asserts that the dimension of temperature can be expressed in terms of the dimensions of mass, length, and time. Conceding the point to Riabouchinsky, texts devoted to dimensional analysis either require (Sedov, 1959) or accept (Bridgman, 1931) the dimensional equivalence of energy and temperature. In the absence of the presumption that energy and temperature are dimensionally equivalent, an evaluation of the present data forces one to adopt at least one of the following positions: (1) q''_w is not linear in ΔT_{ad}, (2) q''_w is linear in u'_{max} (i.e., π_0 depends only on π_2), or (3) some variable or variables, most likely some geometric variable or variables, are missing from the general characterization of the problem. Alternative (1) is theoretically unsatisfying, alternative (2) is empirically inadequate, and alternative (3) undermines the entire project of seeking a general correlation for turbulent heat transfer. Adopting the perspective that energy and temperature are dimensionally equivalent, contrary to texts in heat transfer but consistent with texts in dimensional analysis, allows one to reject each of these positions and construct a theoretically satisfying, empirically adequate, geometry-independent correlation for the present data.

The correlation's claim to generality rests on the diversity of the experiments considered and the simplicity of the result. Figure 8 documents the domain of the data considered in the present study, mapped in terms of π_1 and π_2. The limits of measurement uncertainty displayed for each datum in Fig. 8 represent 95 percent confidence intervals. This domain covers two orders of magnitude in π_1 and one and one-half orders of magnitude in π_2. While caution advises that the correlation should be restricted to this domain, the limits of its usefulness remain to be determined.

Conclusion

Heat transfer data from the diverse set of experiments in turbulent flows given by Maciejewski and Moffat (1992a, b),

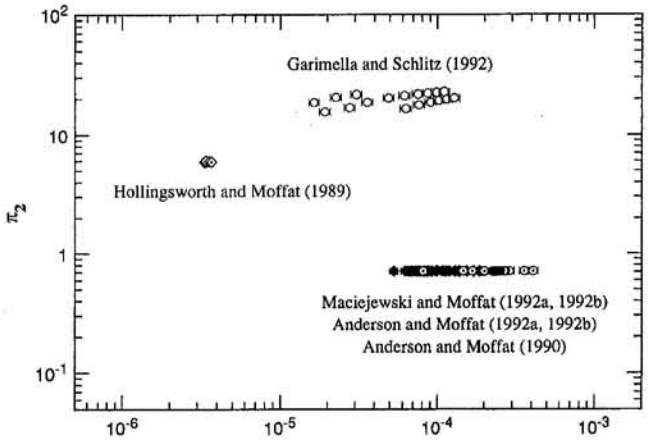

Fig. 8 Domain map, π_2 versus π_1

Hollingsworth and Moffat (1989), Anderson and Moffat (1992a, b, 1990), and Garimella and Schlitz (1992) can be accurately represented by a single correlation expressed in terms of q''_w, u'_{max}, ΔT_{ad}, ρ, C_p, k, and μ. The success of the resulting correlation may be attributed, at least in part, to the adoption of the position that temperature and energy are dimensionally equivalent.

Acknowledgments

Dr. Paul K. Maciejewski's efforts on this project have been supported by NSF CTS 92-10215. The authors acknowledge the work of Dr. Robert J. Moffat, who directed many of the studies that made this finding possible. The authors thank Dr. Suresh V. Garimella for providing access to his original data.

References

Ames, F. E., and Moffat, R. J., 1990, "Heat Transfer With High Intensity Large Scale Turbulence: The Flate Plate Turbulent Boundary Layer and the Cylindrical Stagnation Point," Rept. No. HMT-44, Department of Mechanical Engineering, Stanford University, Stanford, CA.

Anderson, A. M., and Moffat, R. J., 1990, "Convective Heat Transfer From Arrays of Modules With Non-uniform Heating: Experiments and Models," Rept. No. HMT-43, Department of Mechanical Engineering, Stanford University, Stanford, CA.

Anderson, A. M., and Moffat, R. J., 1992a, "The Adiabatic Heat Transfer Coefficient and the Superposition Kernel Function: Part 1—Data for Arrays of Flat Packs for Different Flow Conditions," ASME *Journal of Electronic Packaging,* Vol. 114, p 14–21.

Anderson, A. M., and Moffat, R. J., 1992b, "The Adiabatic Heat Transfer Coefficient and the Superposition Kernel Function: Part 2—Modeling Flat Pack Data as a Function of Channel Turbulence," ASME *Journal of Electronic Packaging,* Vol. 114, p 22–28.

Antonia, R. A., Krishnamoorthy, L. V., and Fulachier, L., 1988, "Correlation Between the Longitudinal Velocity Fluctuation and Temperature Fluctuation in the Near-Wall Region of a Turbulent Boundary Layer," *Int. J. Heat Mass Transfer,* Vol. 31, No. 4, pp. 723–730.

Bridgman, P. W., 1931, *Dimensional Analysis,* Yale University Press, New Haven, CT.

Callen, H. B., 1985, *Thermodynamics and an Introduction to Thermostatistics, Second Edition,* Wiley, New York.

Garimella, S. V., and Schlitz, D. J., 1992, "Enhanced Internal Cooling of Turbine Blades Using Large Scale Roughness Elements," *Fundamentals and Applied Heat Transfer Research for Gas Turbine Engines,* ASME HTD-Vol. 226, pp. 9–15.

Hollingsworth, D. K., and Moffat, R. J., 1989, "Measurement and Prediction of the Turbulent Thermal Boundary Layer in Water on Flat and Concave Surfaces," Rept. No. HMT-41, Department of Mechanical Engineering, Stanford University, Stanford, CA.

Johnson, P. L., and Johnston, J. P., 1989, "The Effects of Grid Generated Turbulence on Flat and Concave Turbulent Boundary Layers," Rept. No. MD-53, Department of Mechanical Engineering, Stanford University, Stanford, CA.

Laufer, J., 1954, "The Structure of Turbulence in Fully Developed Pipe Flow," NACA Tech. Rept. No. 1174.

Maciejewski, P. K., and Moffat, R. J., 1989, "Heat Transfer With Very High Free Stream Turbulence," Rept. No. HMT-42, Department of Mechanical Engineering, Stanford University, Stanford, CA.

Maciejewski, P. K., and Moffat, R. J., 1990, "A Correlation for Boundary Layer Heat Transfer Accounting for Free Stream Turbulence," *Heat Transfer 1990,* Vol. 3, Hemisphere Pub. Corp., pp. 303–308.

Maciejewski, P. K., and Moffat, R. J., 1992a, "Heat Transfer With Very High Free Stream Turbulence: Part I—Experimental Data," ASME JOURNAL OF HEAT TRANSFER, Vol. 114, No. 4, pp. 827–833.

Maciejewski, P. K., and Moffat, R. J., 1992b, "Heat Transfer With Very High Free Stream Turbulence: Part II—Analysis of Results," ASME JOURNAL OF HEAT TRANSFER, Vol. 114, No. 4, pp. 834–839.

Moffat, R. J., and Anderson, A. M., 1991, "Applying Heat Transfer Coefficient Data to Electronics Cooling," ASME JOURNAL OF HEAT TRANSFER, Vol. 112, pp. 882–890.

Panton, R. L., 1984, *Incompressible Flow,* Wiley, New York.

Rayleigh, L., 1915a, b, "The Principle of Similitude," *Nature,* Vol. 95, pp. 66–68, p. 644.

Riabouchinsky, L., 1915, "The Principle of Similitude," *Nature,* Vol. 95, p. 591.

Schlitz, D. J., 1992, "Localized Enhancement of Heat Transfer From an Array of Heat Sources in Forced Convection," MS Thesis, Department of Mechanical Engineering, University of Wisconsin—Milwaukee.

Sedov, L. I., 1959, *Similarity and Dimensional Methods in Mechanics,* Academic Press, New York.

Wirtz, R. A., and Chen, W., 1992, "Laminar-Transitional Convection From Repeated Ribs in a Channel," ASME *Journal of Electronic Packaging,* Vol. 114, p 29–34.

The Effect of Placing Vortex Generators Above Ribs in Ribbed Ducts on the Flow, Flow Temperature, and Heat Transfer Behavior

T. A. Myrum

S. Acharya

S. Sinha

X. Qui

Mechanical Engineering Department,
Louisiana State University,
Baton Rouge, LA 70803

Flow temperature and laser-Doppler velocity measurements are presented to understand better the flow and heat transfer behavior resulting from the placement of vortex generators above the first and fifth ribs in a ribbed duct air flow (Re = 3450) and as a benchmark for comparing model predictions. Because the generator–rib spacing, at the smallest spacing (s/h = 0.25), was too small for the flow to pass through it, the generator–rib pair functioned as a single element with an increased effective height, comprising the rib height, the generator–rib space, and the generator proper, which resulted in a downstream shift in the flow reattachment and peak Nusselt number locations. At s/h = 0.75, the flow expanded as it passed through the generator–rib space. Dictated by the upstream flow conditions, the expansion resulted in a vertical downward flow behind the first generator–rib configuration and no vertical downward flow behind the fifth. The vertical downward flow compensated for generator-induced reductions in the near-wall streamwise velocities behind the first generator–rib configuration, resulting in increased local Nusselt numbers, whereas the generator-induced reductions in the streamwise velocities in the absence of the vertical downward flow gave way to reduced Nusselt numbers behind the fifth generator–rib configuration.

Introduction

Recently considerable attention has been focused on increasing the heat transfer in ribbed ducts. Hung and Lin (1992) positioned a two-dimensional turbulence promoter on the vertical wall opposite a heated wall containing an array of two-dimensional rectangular rib elements and found that it improved the heat transfer characteristics in the duct and reduced the occurrence of hot spots. Myrum et al. (1991, 1992) examined the effect of placing a vortex generator (circular rod) above or just downstream of a two-dimensional rib and found that at transitional duct Reynolds numbers (3300), the generator resulted in average Nusselt number increases of up to 30 percent. Myrum et al. (1993) later placed vortex generators (circular rods) immediately above or just downstream of several rib elements in a fully ribbed duct. They found that for generator diameters equal to the rib element height and rib pitches of 38.4 and 19.2 rib heights, the entropy generation per unit duct length (a thermodynamically based measure of the heat transfer augmentation, including the heat transfer and pressure drop) could be reduced (implying heat transfer enhancement) by as much as 27 and 9 percent, respectively. Eibeck and Garimella (1991) examined the effect of protruding vortex generators (half-delta wings placed at a 20-deg angle of attack to the flow) on the heat transfer from an array of discrete heated elements. A peak enhancement of 40 percent occurred in the second row of elements.

Measurements of the turbulent heat transport in a boundary layer with a protruding vortex generator by Wroblewski and Eibeck (1991) demonstrated that the vortex interaction with the turbulent boundary layer enhanced the heat transfer to a greater extent than the momentum transport. Thomas (1965, 1966) and Karniadakis et al. (1988) showed that for laminar flow, circular wires placed above a smooth horizontal surface resulted in a premature transition to turbulence, causing increased heat and mass transfer rates.

The main objectives of the present investigation are: (1) to obtain flow temperature results and laser-Doppler flow results (streamwise and cross-stream velocities, streamwise turbulence intensities, and turbulent shear stresses) in order to explain the flow and heat transfer behavior resulting from the placement of vortex generators (cylindrical rods) immediately above the ribs (see Fig. 1) and (2) to provide temperature data and flow data for a complex flow for the purpose of developing and validating a computational model.

For purposes of this study, vortex generators were placed at 0.25 ($s/h = 0.25$) and 0.75 ($s/h = 0.75$) rib heights above the first and fifth ribs in a ribbed duct (see Fig. 1). The generator diameter was one half the rib height; the rib pitch was 19.2 rib heights; and the duct Reynolds number was 3450. This Reynolds number is at the lower end of the spectrum for gas turbine blade cooling channels, as evidenced from the parameters reported in several papers pertinent to gas turbine blade cooling (Parsons et al., 1995, Re = 2500–25,000; Liou and Hwang, 1992, Re = 5000–50,000). Such flows can also be encountered in internally ribbed heat exchanger passages (Mills, 1995; Chang and Mills, 1993, Re = 5200–41,800). Regarding the rib pitch studied in this paper, it is at the upper end of the range routinely encountered in the cooling passages of gas turbine blades and in heat exchangers. Mills (1995), for heat exchanger applications, gives a common p/h between 6.3 and 20, putting the $p/h = 19.2$ of this study at the upper end of the range. Moreover, Sparrow and Tao (1983) found that p/h values as large as 36.6 resulted in enhancements of up to 60 percent.

Contributed by the Heat Transfer Division for publication in the JOURNAL OF HEAT TRANSFER. Manuscript received by the Heat Transfer Division July 1994; revision received February 1996. Keywords: Augmentation and Enhancement, Forced Convection, Turbulence. Associate Technical Editor: T. W. Simon.

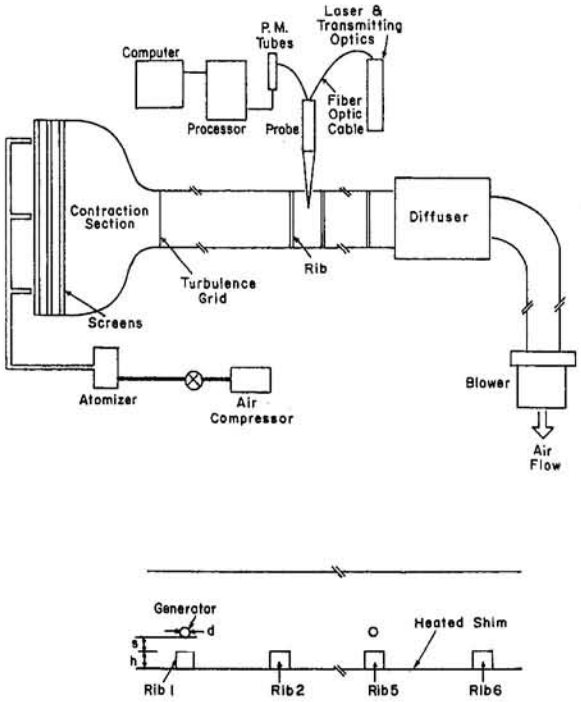

Fig. 1 Experimental setup

Indeed, these authors found that the $p/h = 19.2$ ribbing resulted in a 73 percent increase in the average Nusselt number above the smooth duct result, which is quite effective. There are also several papers pertaining to blade cooling that report results with $p/h = 20$ (see Zhang et al. 1994, $p/h = 8–30$; Han et al., 1988, $p/h = 10–20$; Liou et al., 1993, $p/h = 7–20$; Liou and Hwang, 1992, $p/h = 10–20$).

The heat transfer experiments were conducted in an insulated, asymmetrically heated, 99.8-cm-long, 30.5-cm-wide, 6.10-cm-high test section located after a 40-hydraulic-diameter-long flow-development section. A constant heat flux was simulated along the bottom wall of the test section by dissipating direct current in a 0.025-mm-thick stainless steel shim. Chromel-constantan thermocouples (0.076 mm diameter), spot welded to the underside of the shim along the centerline, were used to measure the local shim temperatures. Thermocouples positioned at off-centerline locations confirmed that the spanwise temperature variation was within ± 0.1°C, which is the uncertainty of the temperature measurements. The maximum effect of the heating current on the measured thermocouple voltage was also less than 0.1°C. To minimize buoyancy effects, the power supplied to the shim was set to give $Gr_H/(Re_H)^2 < 0.10$, where Gr_H and Re_H are the duct height based Grashof and Reynolds numbers, respectively, and Gr_H is based on the maximum shim-to-inlet temperature difference.

Local Nusselt number results for the heated wall of the test section were determined from the local convective heat flux $q''_c(x)$ and involved subtracting local conduction and radiation heat losses from the local electric heat flux generation (measured to within 2.0 percent), which was determined from measurements of the current (measured to within 0.1 percent) supplied to the shim and the temperature-dependent electrical resistivity of the shim (measured to within 1.8 percent). A finite-difference procedure was used to compute the conduction heat losses to within 8 percent. Temperatures measured to within ± 0.12°C along the inner surfaces of the side walls and the top wall were used as boundary conditions in the heat conduction code and were the dominant sources of uncertainty in the conduction loss. Local radiation losses were estimated to within 15 percent (Kline and McClintock, 1953) using $\epsilon = 0.20 \pm 0.03$ for the shim and $\epsilon = 0.9 \pm 0.1$ for the plexiglass top wall and side walls. The emissivity uncertainties were the dominant sources of uncertainty in the computed radiation loss. The conduction and radiation losses were each 18 percent of the local electric heat flux generation.

Flow temperature measurements were obtained to within ± 0.4°C, ± 10 percent of the minimum shim-to-bulk temperature difference, by traversing a 0.076-mm-chromel-constantan thermocouple across the flow cross section. Measurements were obtained at 1.1, 7.5, 12.3, 14.7, and 17.1 rib heights downstream of the ribs or generator–rib pairs of interest.

Figure 1 depicts the setup used for the laser-Doppler flow measurements. This duct duplicates that for heat transfer measurements, with no heating. Air was drawn into the development duct through a 5.25:1 contraction section containing a honeycomb baffle and four screens. All of the flow measurements were performed using a conventional two-color DANTEC fiber-optic LDV system operating in the back-scatter mode. Each measurement consisted of 2000 samples recorded at a sampling rate ranging from 25 samples/s in the near-wall recirculating region to 1500 samples/s at the edge of the shear layer. It was

Nomenclature

A = cross-sectional area = (186 ± 2 cm^2)[2]
c_p = constant pressure specific heat of air
d = diameter of cylindrical vortex generator = (3.2 mm)
D_h = hydraulic diameter = (10.2 ± 0.1 cm)[2]
h = rib height = (6.4 mm)
k = air thermal conductivity at T_{in}
$k(x)$ = air thermal conductivity at $(T_w(x) + T_b(x))/2$
$\dot{m}$ = mass flow rate (uncertainty ± 2.0 percent)[2]
Nu = local Nusselt number = $q''c(x)D_h/((T_w(x) - T_b(x)))k(x))$ (uncertainty ± 3.5 percent)[2]
Q = electrical power supplied to the heated shim
$q''c(x)$ = convective heat flux corrected for radiation and conduction losses (uncertainty ± 4.6 percent)[2]
Re = Reynolds number = (U_oD_h/υ) (uncertainty ± 2.4 percent)[2]
s = generator–rib spacing
T = flow temperature (measured to within ± 0.10°C)
$T_b(x)$ = local bulk temperature = $((w/\dot{m}c_p)\int_o^x q''c(x)dx + T_{in})$ (uncertainty ± 0.16°C)[2]
T_{in} = inlet bulk temperature (measured to ± 0.12°C)[2]
$T_w(x)$ = local bottom wall temperature (measured to ± 0.12°C)[2]
u, u' = mean and fluctuating streamwise velocities
U_0 = average duct velocity = $(\dot{m}/\rho A)$ (uncertainty ± 2.2 percent)[2]
υ = mean cross-stream velocity
x = streamwise (axial coordinate)
x' = interrib coordinate (measured from the downstream face of the first rib in each interrib space)
y = cross-stream coordinate (measured from the bottom wall)

[2] Uncertainties are discussed by Myrum et al. (1993).

found that varying the sample size from 2000 to 10,000 yielded less than a 1 percent change in the mean and rms values. As recommended by Driver and Seegmiller (1982, 1985), the mean velocities and Reynolds stresses were obtained by ensemble averaging without bias correction. Uncertainties were calculated to a 95 percent confidence level (Kline and McClintock, 1953; Rood and Telionis, 1991); they were ±3.5 percent and ±3 percent for the mean u and v velocities and ± 5 percent for the streamwise turbulence intensity, and ± 8 percent for the turbulent shear stress.

Before presenting the results, it is worthwhile discussing the velocity profile (not presented) at the inlet to the test section. The inlet flow was a developing, transitional flow. Moreover, the streamwise turbulence intensity at this point ranged from zero at the wall to about 7 percent away from the wall. The cross-stream velocities and turbulence intensities were effectively negligible. It was also found that the leading rib was completely immersed in the boundary layer.

Heat Transfer Results

Figure 2 is taken from Myrum et al. (1993). The black squares on the abscissa represent rib elements, while the open symbols immediately above the first and fifth ribs depict the vortex generators. The arrowheads on the abscissa in the first, second, and fifth interrib spaces have been included for reference purposes, and correspond to the $x'/h = 7.5$, 12.3, 14.7, and 17.1 and represent the flow and flow temperature measurement locations. Each data point in the figure corresponds to a thermocouple location on the shim.

Figure 3 shows that in the first interrib space, the wall temperatures—represented by the first symbol on the right for each data set—are higher for $s/h = 0.25$ than for the baseline and $s/h = 0.75$ up to 14.7 rib heights, where they are the same. Since for a uniform wall heat flux, the higher the wall temperature, the lower the corresponding local Nusselt number; this echoes the Nu behavior at the flow temperature measurement locations represented by arrowheads in Fig. 2. Moreover, it is seen that the flow temperatures and the thermal shear layer thickness for $s/h = 0.25$ exceed those for the baseline and $s/h = 0.75$ cases up to 17.1 rib heights, where the flow temperatures for all three cases coincide. This suggests weaker flow and poorer mixing between the core and near-wall flows in the first interrib space up to $x'/h \leq 17.1$ for the $s/h = 0.25$ case. The corresponding lower Nu values for $s/h = 0.25$ in Fig. 2, corresponding to the first four arrowheads, are consistent with this observation.

A comparison between the wall temperatures for $s/h = 0.75$ to those of the baseline demonstrates that the main difference

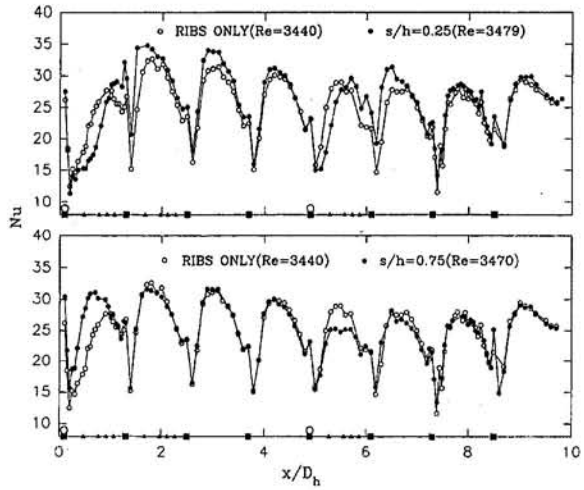

Fig. 2 Effect of vortex generators on the local Nusselt number

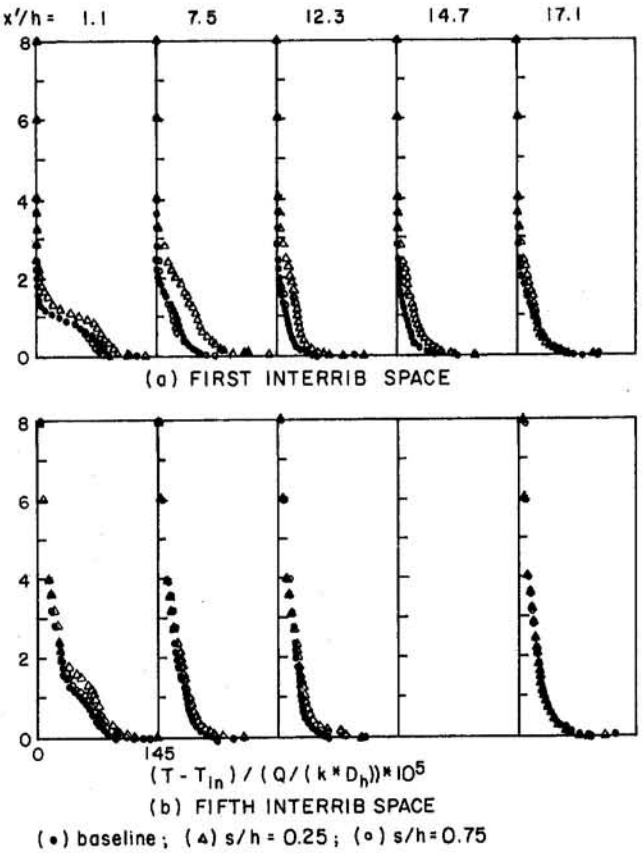

Fig. 3 Flow temperatures in the first and the fifth interrib spaces

between the $s/h = 0.75$ and baseline profiles is confined to the extreme near-wall region, where the wall temperature for $s/h = 0.75$ is less than that for the baseline up to $x'/h = 12.3$. This translates to the higher Nusselt numbers for $s/h = 0.75$ relative to the baseline in Fig. 2.

Downstream, in the fifth interrib space, all three flow temperature profiles are nearly the same away from the wall, except at $x'/h = 1.1$ where the flow temperatures for the $s/h = 0.25$ case are somewhat higher.

Flow Results

The objective of the ensuing discussion of the flow results will be to get a better idea of how the generators, positioned at the two spacings of interest, above the first and fifth ribs impact the basic flow structure in a ribbed duct. Wherever possible, the flow results will be linked to the local Nusselt number behavior of Fig. 2 and the flow temperature behavior of Fig. 3.

Mean Streamwise Velocities. Figure 4(*a*) presents the mean streamwise velocities in the first interrib space. The near-zero velocities up to $y/h = 1.75$ for the $s/h = 0.25$ flow at $x'/h = 1.1$ and 3.1 demonstrate that the generator–rib spacing ($1.0 < y/h < 1.25$) is too small for the flow to pass through. This confirms the speculations made by Myrum et al. (1991, 1992, 1993) that at this spacing, the generator–rib pair functions as a single element with an effective height (rib height plus the rib–generator space thickness plus the generator diameter) that is 1.75 times that of the rib itself. Since increasing the effective height retards the downstream evolution of the flow, resulting in the downstream migration of the reattachment point, this explains the downstream shift in the Nu distribution behind the first rib relative to the baseline distribution. Also noteworthy is the fact that the near-wall velocities move from a negative orientation at 12.3 rib heights to a positive one at 14.7 rib

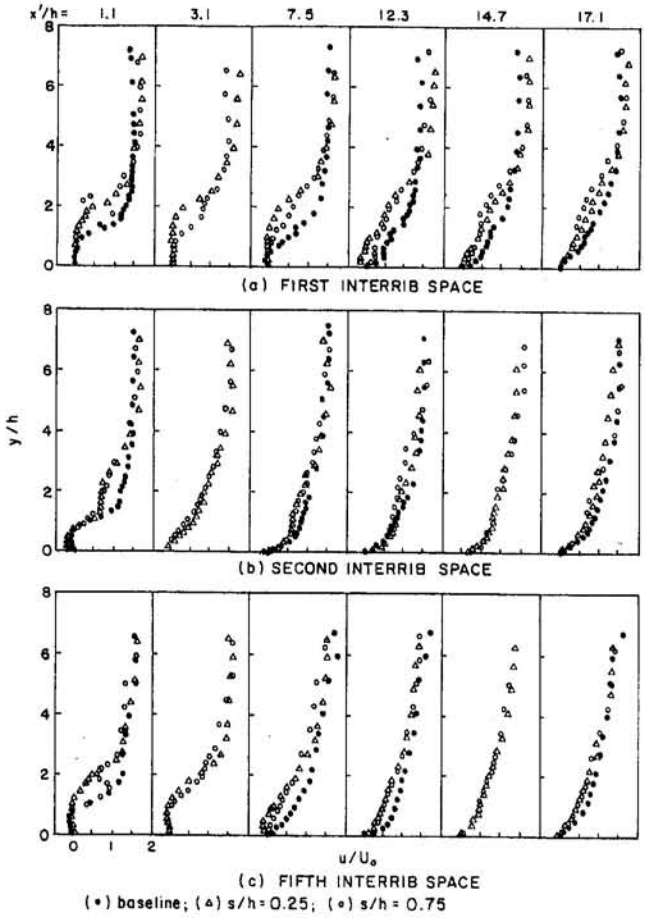

Fig. 4 Mean streamwise velocities in the first, second, and fifth interrib spaces

heights, suggesting flow reattachment in this region. On the other hand, the near-wall velocities go from negative to positive for the baseline between 7.5 and 12.3 rib heights, confirming the downstream migration of the reattachment point with the vortex generator at $s/h = 0.25$.

The effect of moving the generator up to $s/h = 0.75$ is most notable immediately behind the first rib at $x'/h = 1.1$. Figure $4(a)$ shows that the velocity parallels the baseline up to the upper extreme of the generator–rib space ($y/h = 1.75$). Beyond this point, because of the presence of the generator, the velocity decays to nearly zero behind the generator ($1.75 \leq y/h \leq 2.25$) and exhibits a wakelike profile. Further increases in y/h above the generator show that the velocity increases to a uniform value that is roughly equal to that of the other two flows. It is seen, in contrast to the baseline and $s/h = 0.25$ flows, that negative time-averaged streamwise velocities behind the first rib are confined to a much smaller region very close to the lower wall.

Turning to the second interrib space, Fig. $4(b)$ shows that the $s/h = 0.25$ and 0.75 profiles are virtually similar to each other, with both exhibiting a velocity deficit, relative to the baseline, at $x'/h = 1.1$ and y/h at and above one rib height. This deficit persists up to at least 7.5 rib heights downstream. However, compared to the flows in the first interrib space, the mean streamwise velocity profiles for the vortex-generator cases appeared to have recovered and are quite similar to each other in the second space. It should be noticed that the baseline flow reattaches upstream of that in the first interrib space. This can be seen by noting a slightly negative near-wall velocity at $x'/h = 7.5$ in the first interrib space, while no such behavior is observed at $x'/h = 7.5$, or downstream, in the second space. Indeed, Fig. 2 shows that the peak Nu location in the second space has migrated upstream relative to that in the first space. Moreover, for $s/h = 0.25$, the only location where a negative velocity is witnessed is at $x'/h = 1.1$, compared to $x'/h = 12.3$ for the first interrib space, confirming the upstream migration of the Nu peak in the second interrib space relative to the first for this flow.

Figure $4(c)$ exhibits velocity trends at $x'/h = 1.1$ in the fifth interrib space that are quite similar to their counterparts in the first interrib space, which is not too surprising since the respective geometric conditions above the leading rib of the space are duplicated for the respective cases (i.e., no generator, a generator at $s/h = 0.25$, and a generator at $s/h = 0.75$). As the $s/h = 0.25$ and 0.75 flows evolve with increasing x'/h, it is observed that this evolution is much more rapid than in the first interrib space, and the two profiles are quite similar by $x/h = 3.1$. Note that flow reattachment for both s/h cases appears to be between 7.5 and 12.3 rib heights in the fifth interrib space while this flow reattaches between 12.3 and 14.7 rib heights in the first interrib space. It is also interesting to note that the baseline profiles have essentially the same shape as those in the second interrib space, suggesting only minor periodic hydrodynamic flow development between the two locations.

Mean Cross-Stream Velocities. Mean cross-stream velocity trends in the first interrib space are portrayed in Fig. $5(a)$. For the baseline flow, the near-wall v-velocities change from a positive to a negative value somewhere between $x'/h = 7.5$ and 12.3, indicative of flow reattachment in this region. Meanwhile, for the $s/h = 0.25$ flow, the persistence of positive velocities at the wall at $x'/h = 12.3$ indicates flow reattachment between $x'/h = 12.3$ and 14.7. At 17.1 rib heights, the baseline flow is directed upward, as indicated by the positive velocities near the wall, and is in preparation for the flow moving over

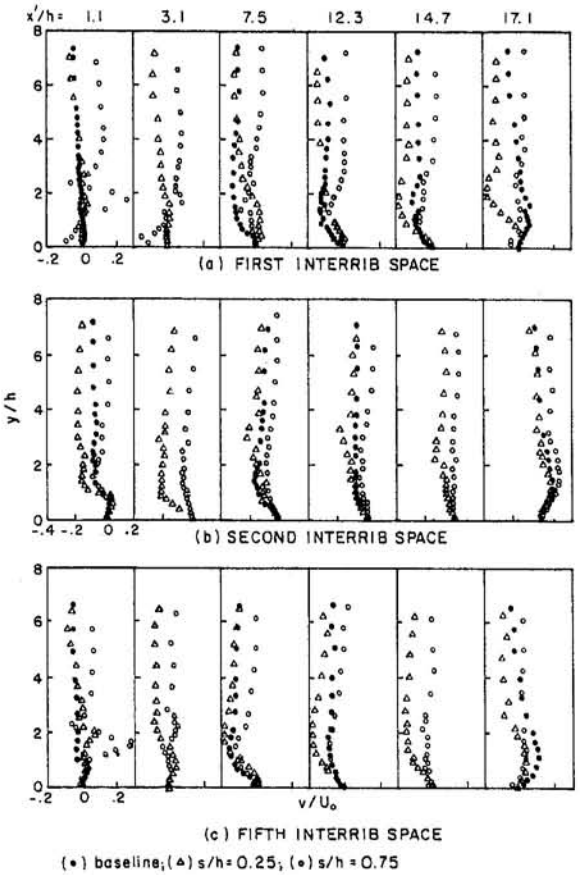

Fig. 5 Mean cross-stream velocities in the first, second, and fifth interrib spaces

the second rib. On the other hand, the negative velocities close to the wall at $x'/h = 17.1$ for $s/h = 0.25$ indicate that the flow is still moving downward this close to the second rib. This is due to the downstream shift of the flow caused by the larger effective height. At $x'/h = 1.1$ both the baseline and $s/h = 0.25$ velocities are uniform and near zero.

It is seen that for $s/h = 0.25$, the v velocity remains close to zero—for y/h values up to two—all the way to $x'/h = 7.5$. Coupling this fact with the fact that the streamwise velocities (see Fig. 4(a)) are nearly zero for y/h up to 1.75 and $x'/h = 7.5$ suggests a region of nearly "dead" air. Note that at $x'/h = 7.5$, the baseline streamwise (Fig. 4(a)) and cross-stream velocities are considerably greater than the s/h velocities for $y/h < 2$. This explains why at $x'/h = 7.5$, the flow temperatures in Fig. 3(a) are considerably greater for the $s/h = 0.25$ flow than those of the baseline.

Continuing with the first interrib results, it is seen that for $s/h = 0.75$, the v velocity increases—in the negative sense—at $x'/h = 1.1$ from $y/h = 1.0$, where it is zero, toward the wall. This observation, together with the fact that Fig. 4(a) shows the corresponding streamwise velocity to be virtually zero, indicates that the flow is moving vertically downward here. It is seen for $y/h < 1.0$ that this is also true at $x'/h = 3.1$. Note that this is not the case for the baseline flow at $x'/h = 1.1$ nor the $s/h = 0.25$ flow for $x'/h = 1.1$ and 3.1, where the respective flows (both u and v) are virtually stagnant. This explains why the wall temperature at $x'/h = 1.1$ in Fig. 3(a) is smaller for the $s/h = 0.75$ flow than those for the baseline and $s/h = 0.25$ flows, resulting in larger Nu values in this region (see Fig. 2) than those for the baseline or $s/h = 0.25$ flows.

Returning to $x'/h = 1.1$, it is seen that the v velocity increases from zero with increasing y/h for the $s/h = 0.75$ flow until $y/h = 1.75$, the upper extent of the generator–rib space. Further increases in y/h, in the region behind the generator, result in a decrease in v up to $y/h = 2.25$, the upper reach of the generator, where v is slightly negative. Above the generator, the velocity increases to a uniform, positive value.

The foregoing observations of the streamwise (Fig. 4(a)) and cross-stream (Fig. 5(a)) velocity behavior of the $s/h = 0.75$ flow at $x'/h = 1.1$ suggest the following scenario: After the flow passes through the generator–rib space (an asymmetric flow passage), where the flow is undoubtedly in the streamwise direction, it expands in the cross-stream direction, giving rise to positive and negative v velocities. Since the presence of rib shelters the region behind the rib from the oncoming flow, it is speculated that the expanding flow moves vertically downward into the wall. This is ultimately responsible for the reduced wall temperatures and increased Nu values for $s/h = 0.75$ at $x'/h = 1.1$.

Further examination of the v velocities for $y/h < 1.0$ shows that the $s/h = 0.75$ flow velocity becomes uniform at a near-zero value at $x'/h = 7.5$. At 12.3 rib heights downstream, it becomes negative, with the negative values persisting down to the wall. Figure 2 shows that the peak Nu value occurs between $x'/h = 7.5$ and 12.3.

Figure 5(b) shows that the v velocities for all three flow configurations are negative from $y/h = 1.0$ to $y/h = 7.0$ for $x'/h = 1.1$ in the second interrib space, with largest negative velocities belonging to the $s/h = 0.25$ flow. At $x'/h = 3.1$ the negative v velocities for $s/h = 0.25$ and 0.75 persist all the way down to the wall. Again, the negative velocities, including those near the wall are greater for the $x'/h = 0.25$ flow. This explains the upstream shift and increase in the peak Nu value for $s/h = 0.25$ compared to that for $s/h = 0.75$ portrayed for the second interrib space in Fig. 2. (The increased negative v values for $s/h = 0.25$ are believed to be a carryover from the large negative v values just upstream of the second rib at $x'/h = 17.1$ in the first interrib space.) Moreover, the fact that the near-wall negative velocities persist at 7.5 rib heights indicates that all three flows are reattached by this location, which is in agreement with the fact that Fig. 2 shows the peak Nu value occurring at or before 7.5 rib heights in the second interrib space for all three cases.

A comparison of the v-velocity behavior in the first interrib space (Fig. 5(a)) to that in the second interrib space (Fig. 5(b)) will now be made to gain insights into the rather different Nu behavior in the respective interrib spaces for the respective baseline and $s/h = 0.25$ flows, as shown in Fig. 2. It is seen that near-wall negative velocities for the baseline and $s/h = 0.25$ flows occur as early as $x'/h = 7.5$ in the second interrib space, but they do not appear until 12.3 rib heights in the first interrib space. In that these negative velocities suggest the vicinity of reattachment, this agrees with the fact that the baseline and $s/h = 0.25$ peak Nu locations are shifted upstream in the second interrib space relative to the first.

The cross-stream velocities in the fifth interrib space are displayed in Fig. 5(c). It is seen that the baseline profiles exhibit nearly the same behavior as those in the second interrib space. Similar to the cross-stream velocity behavior in the first interrib space, the cross-stream velocity profiles for the $s/h = 0.25$ and 0.75 flows are different from each other at each streamwise measuring location. On the other hand, unlike the velocity behavior in the first interrib space, the near-wall velocities for the $s/h = 0.75$ flow at $x'/h = 1.1$ and 3.1 are nearly zero instead of negative. The fact that both the near-wall streamwise (Fig. 4(c)) and cross-stream velocities are close to zero at $x'/h = 1.1$ and 3.1 in the fifth interrib space suggests that the $s/h = 0.75$ flow is rather weak here. Recall that in this region of the first interrib space, the flow moved vertically downward toward the wall. It was speculated that the vertically downward flow resulted from the expansion of the flow as it passed through the generator–rib space. The same situation occurs at the fifth rib: the flow must expand as it passes through the space; however, the v-velocity directed toward the wall is rather weak. Since the only difference between the first and fifth ribs is the state of the oncoming flow, it is believed that this difference is responsible for the departure of the v-velocity behavior behind the first and fifth ribs. Indeed, in the region spanning the generator–rib space, the streamwise velocity ranges from 0.75 to 1.25 U_o upstream of the first rib, whereas it ranges from about 0.5 to 0.75 U_o upstream of the fifth rib.

Above $y/h = 1.0$, at $x'/h = 1.1$ and 3.1, the v-velocity behavior for $s/h = 0.75$ is quite similar to that in the first interrib space. Moreover, for $x'/h > 3.1$, the $s/h = 0.75$ profiles are similar to those in the first interrib space.

For the $s/h = 0.25$ flow, the most dramatic departure from the first interrib space behavior occurs at $x'/h = 17.1$, where the rather large near-wall negative velocities of the first space are replaced by positive values.

The streamwise and cross-stream velocity behavior discussed in the foregoing can be linked to the Nu behavior for the baseline and $s/h = 0.75$ flows, in the first and fifth interrib spaces as follows: As seen in Figs. 4(a, b), the presence of the generator leads to a reduction in the streamwise velocities near the wall in both the first and fifth interrib spaces at $x'/h = 7.5$ and 12.3. Consequently, a Nu reduction is expected. However, in the first interrib spaces the reduced streamwise velocity appears to be more than compensated for by the negative velocities near the wall at $x'/h = 1.1$ and 3.1, as shown in Fig. 5(a), causing both an upstream shift and an increase in the peak Nu value. As just pointed out, there are no such negative velocities in the fifth interrib space, apparently resulting in the Nu decrease observed in Fig. 2.

Turbulent Stresses. Streamwise turbulence intensity results are presented in Figs. 6(a–c). Figure 6(a) shows that the near-wall intensities at $x'/h = 1.1$ and 3.1 for the $s/h = 0.75$ flow are considerably greater than for the other two flows. The increased turbulence levels are due to the vertical downward flow in this region for this flow. In the fifth interrib space, at $x'/h = 1.1$ and 3.1, the elevated near-wall turbulence levels for

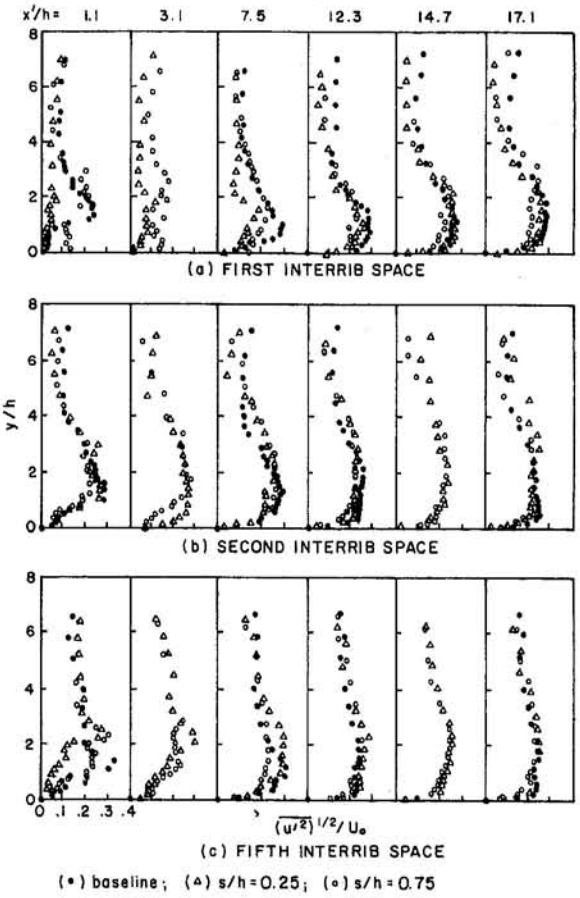

Fig. 6 Streamwise turbulence intensities in the first, second, and fifth interrib spaces

$s/h = 0.75$ do not exist, owing to the absence of the vertical downward flow behind the fifth rib. Another noteworthy feature, displayed in Fig. 6(b), is that the near-wall turbulence levels for the $s/h = 0.25$ flow at $x'/h = 3.1$ behind the second rib are larger than those for $s/h = 0.75$. This is most likely caused by the large v velocity observed here for the $s/h = 0.25$ flow. The increased mixing associated with elevated turbulence levels, which result from the relatively large negative v velocities, indeed contribute to the increased Nu values behind the first and second ribs for the $s/h = 0.75$ and 0.25 flows, respectively.

The correlation between the mean flow field and the observed Nusselt number behavior has already been described. In examining the relationship between Nu and the streamwise turbulence intensity, the interdependance of the measured hydrodynamic parameters should be kept in mind. In the first interrib space, the $s/h = 0.75$ streamwise turbulence levels are highest at $x'/h = 1.1$ and 3.1, and the Nu values reflect this trend. At $x'/h = 14.7$ and 17.1 the largest Nu values are for $s/h = 0.25$ and, as explained earlier, are due to the delayed reattachment for this case. In the second interrib space, the streamwise turbulence levels for $s/h = 0.25$ are marginally higher, and the same behavior is noted in the Nu profiles. In the fifth interrib module, for $x'/h \geq 3.1$, the streamwise turbulence levels for $s/h = 0.75$ are clearly the smallest, and so are the Nu values.

Figures 7(a–c) present the turbulent shear stress results. In view of the fact that the generator–rib element for the $s/h = 0.25$ case functions as a single rib with an increased effective height, Fig. 7(a) shows the retarded streamwise development of the turbulent shear stress for this case relative to that of the baseline case in the first interrib space. On the other hand, the turbulent shear stress distribution for $s/h = 0.75$ remains quite uniform at a near-zero value over a rather large portion of the interrib space, with the notable exception being behind the generator at $x'/h = 1.1$ and 3.1. It is noteworthy that for $s/h = 0.25$, where the rib generator acts as an effectively larger rib, the shear stress profile does eventually recover to that of the baseline rib-only profile. For $s/h = 0.75$, where the generator wake is significant, this recovery does not recurr.

In Fig. 7(b), the turbulent shear stress profiles for all three flows depict a rather normal flow development in the second interrib space that is accelerated relative to that in the first. It is clear from this figure that for the $s/h = 0.75$ flow the generator wake effect, so dominant in the first interrib space, quickly disappears, and by $x'/h = 12.3$, all three profiles are similar. Between x'/h of 1.1 and 7.5, the $s/h = 0.25$ shear stress values are larger and appear to correlate with the corresponding Nu values in Fig. 2.

Figure 7(c) shows that the turbulent shear profiles for the baseline case in the fifth interrib space are nearly the same as those in the second. For the $s/h = 0.25$ case, it is seen that the turbulent shear stress profiles behind the respective generator–rib pairs in the fifth interrib space are quite different from those in the first interrib space. It is seen that the $s/h = 0.25$ profiles are no longer uniform as in the first interrib space: Noteworthy are the high turbulent stress levels at $x'/h = 1.1$ to 7.5 that are nearly zero in the first interrib space. While the $s/h = 0.75$ case qualitatively shows the same behavior as in the first interrib space, the levels are higher, and the profile rapidly recovers to the rib-only profile.

The link between the turbulent shear stress behavior and the local Nu appears to be more tenuous than the previously described correlations between Nu, u'^2, and the mean flow field.

Conclusions

Flow temperature measurements and laser-Doppler flow measurements were presented in order to understand better the effect

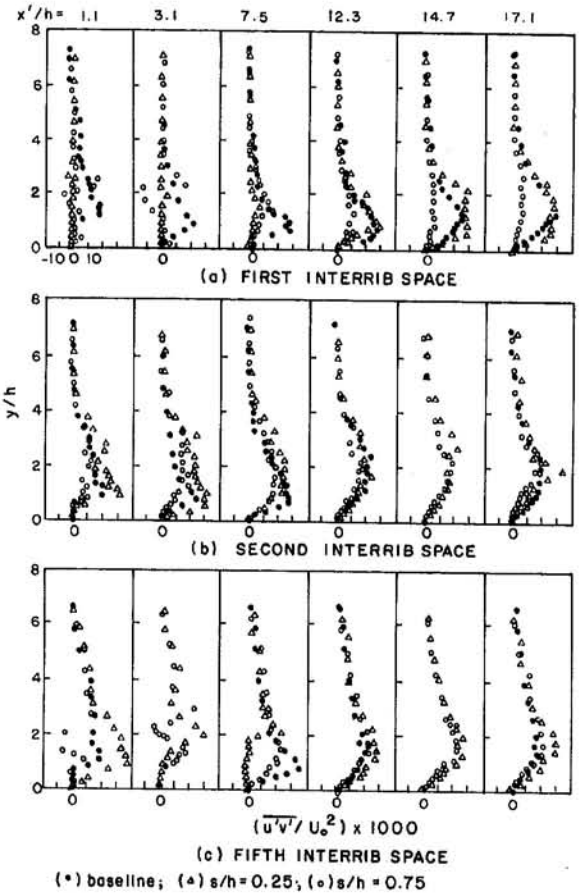

Fig. 7 Turbulent shear stresses in the first, second, and fifth interrib spaces

of placing vortex generators (cylindrical rods in this case) directly above selected rib elements (the first and fifth) on the flow and heat transfer in a ribbed duct flow, with Re = 3450. Moreover, the results are intended as a baseline for validating computational models.

At the smallest generator–rib spacing ($s/h = 0.25$), because the generator-rib space was too small for flow to pass through it, the generator–rib pairs functioned as a single entity with an increased effective height, comprising the rib, the generator–rib space, and the generator proper. This resulted in a downstream shift in both the reattachment and the peak Nusselt number locations in the interrib spaces immediately behind the generator–rib pairs, especially in the first interrib space. In fact, the reattachment location in the first interrib space was so close to the adjacent downstream rib that the resulting negative cross-stream flow carried over into the second interrib space, causing increased streamwise turbulence levels, an upstream shift in the flow reattachment and peak Nusselt number locations, and an increased peak Nusselt number in the second interrib space.

At the larger spacing ($s/h = 0.75$), the flow was capable of passing through the generator–rib space. As it exited the space, the flow expanded in the cross-stream direction. In the first interrib space, the flow expansion gave rise to a vertical downward flow behind the rib that was directed toward the wall. This flow brought the cool upstream flow into the vicinity of the wall, causing a reduced wall temperature and, owing to the uniform wall heat flux, increased Nusselt numbers. Further, the vertical downward flow resulted in increased streamwise turbulence intensities. In the fifth interrib space, although the flow had to expand as it exited the generator–rib space, no vertical downward flow was observed, owing to the different flow conditions upstream of the respective (first and fifth) generator–rib pairs. Moreover, it was observed that the presence of the generator reduced the near-wall streamwise velocities in both the first and fifth interrib spaces. In the fifth space, the reduced velocity resulted in the degradation of the local Nusselt numbers, whereas in the first interrib space, it was speculated that the vertical downward flow more than compensated for the reduction in the streamwise velocity.

Acknowledgments

This research was supported by the Gas Research Institute under contract number GRI 5090-260-1961. Their support is gratefully acknowledged.

References

Acharya, S., Dutta, S., Myrum, T. A., and Baker, R. S., 1993, "Periodically Developed Flow and Heat Transfer in a Ribbed Duct," *Int. J. Heat Mass Transfer*, Vol. 36, pp. 2069–2082.

Chang, B. H., and Mills, A. F., 1993, "Turbulent Flow in a Channel With Transverse Rib Heat Transfer Augmentation," *Int. J. Heat Mass Transfer*, Vol. 36, pp. 1459–1469.

Driver, D. M., and Seegmiller, H. L., 1982, "Features of a Reattaching Shear Layer Subject to Adverse Pressure Gradient," Paper No. AIAA-82-1029.

Driver, D. M., and Seegmiller, H. L., 1985, "Features of a Reattaching Turbulent Shear Layer in Divergent Channel Flow," *AIAA J.*, Vol. 23, pp. 163–171.

Eibeck, P. A., and Garimella, S. V., 1991, "Enhancement of Single Phase Convective Heat Transfer From Protruding Elements Using Vortex Generators," *Int. J. Heat Mass Transfer*, Vol. 34, pp. 2431–2433.

Han, J. C., Chandra, P. R., and Lau, S. C., 1988, "Local Heat/Mass Transfer Distributions Around 180 Degree Turns in Two-Pass Smooth and Rib-Roughened Channels," ASME JOURNAL OF HEAT TRANSFER, Vol. 110, pp. 91–98.

Hung, Y. H., and Lin, H. H., 1992, "An Effective Installation of Turbulence Promotors for Heat Transfer Augmentation in a Vertical Rib-Heated Channel," *Int. J. Heat Mass Transfer*, Vol. 35, pp. 29–42.

Karniadakis, G. E., Mikic, B. B., and Patera, A. T., 1988, "Minimum-Dissipation Transport Enhancement by Flow Destabilization: Reynolds Analogy Revisited," *J. Fluid Mech.*, Vol. 192, pp. 365–391.

Kline, S. J., and McClintock, F. A., 1953, "Estimating Uncertainty in Single-Sample Experiments," *Mech. Engng.*, Vol. 75, Jan., pp. 3–8.

Liou, T., and Hwang, J., 1992, "Developing Heat Transfer and Friction in a Ribbed Rectangular Duct With Flow Separation at Inlet," ASME JOURNAL OF HEAT TRANSFER, Vol. 114, pp. 565–573.

Liou, T., Hwang, J., and Chen, S., 1993, "Simulation and Measurement of Enhanced Turbulent Heat Transfer in a Channel With Periodic Ribs on One Principal Wall," *Int. J. Heat Mass Transfer*, Vol. 36, pp. 507–517.

Mills, A. F., 1995, *Basic Heat and Mass Transfer*, Irwin, Chicago, IL.

Myrum, T. A., Acharya, S., Inamdar, S., and Mehrotra, A., 1991, "Vortex Generator Induced Heat Transfer Augmentation Past a Rib in a Heated Duct Air Flow," *Convective Heat Transfer and Transport Processes*, ASME HTD-Vol. 168, pp. 61–67.

Myrum, T. A., Acharya, S., Inamdar, S., and Mehrotra, A., 1992, "Vortex Generator Induced Heat Transfer Augmentation in a Heated Duct Air Flow," ASME JOURNAL OF HEAT TRANSFER, Vol. 114, pp. 280–284.

Myrum, T. A., Qui, X., and Acharya, S., 1993, "Heat Transfer Enhancement in a Ribbed Duct Using Vortex Generators," *Int. J. Heat Mass Transfer*, Vol. 36, pp. 3497–3508.

Parsons, J. A., Han, J. C., and Zhang, Y., 1995, "Effect of Model Orientation and Wall Heating Conduction on Local Heat Transfer in a Rotating Two-Pass Square Channel With Rib Turbulators," *Int. J. Heat Mass Transfer*, Vol. 38, pp. 1151–1159.

Rood, E. P., and Telionis, D. P., 1991, "Journal of Fluids Engineering Policy on Reporting Uncertainties in Experimental Measurements and Results," ASME *Journal of Fluids Engineering*, Vol. 113, pp. 313–314.

Sparrow, E. M., and Tao, W. Q., 1983, "Enhanced Heat Transfer in a Flat Rectangular Duct With Streamwise-Periodic Disturbances at One Principal Wall," ASME JOURNAL OF HEAT TRANSFER, Vol. 105, pp. 851–861.

Thomas, D. G., 1965, "Forced Convection Mass Transfer: Part II. Effect of Wires Located Near the Edge of the Laminar Boundary Layer on the Rate of Forced Convection From a Flat Plate," *AIChE J.*, Vol. 11, pp. 848–852.

Thomas, D. G., 1966, "Forced Convection Mass Transfer: Part III. Increased Mass Transfer From a Flat Plate Caused by the Wake From Cylinders Located Near the Edge of the Boundary Layer," *AIChE J.*, Vol. 12, pp. 124–130.

Wroblewski, D. E., and Eibeck, P. A., 1991, "Measurements of the Turbulent Heat Transport in a Boundary Layer With an Embedded Streamwise Vortex," *Int. J. Heat Mass Transfer*, Vol. 34, pp. 1617–1631.

Zhang, Y. M., Gu, W. Z., and Han, J. C., 1994, "Heat Transfer and Friction in Rectangular Channels With Ribbed or Ribbed-Grooved Walls," ASME JOURNAL OF HEAT TRANSFER, Vol. 116, pp. 58–65.

Conjugate Heat Transfer From a Single Surface-Mounted Block to Forced Convective Air Flow in a Channel

W. Nakayama
Professor,
Department of Mechanical & Intelligent Systems Engineering,
Tokyo Institute of Technology,
2-12-1 Oh-Okayama, Meguro-ku,
Tokyo 152, Japan
Fellow ASME

S.-H. Park
Lecturer,
Department of Mechanical Engineering,
Kum-Oh National University of Technology,
188 Shinpyung-Dong, Kumi,
Kyungbuk 730-701, Korea

Conjugate heat transfer from a surface-mounted block ($31 \times 31 \times 7$ mm^3) to forced convective air flow (1–7 m/s) in a parallel-plate channel was studied experimentally and analytically. Particular attention was directed to the heat flow from the block to the floor through the block support, which was eventually transferred to the air flow over the floor. The concepts of adiabatic wall temperature (T_{ad}) and adiabatic heat transfer coefficient (h_{ad}) were employed to account for the effect of thermal wake shed from the block on the heat transfer from the floor. The experimental data of T_{ad} and h_{ad} were used in setting the boundary condition for the numerical analysis of heat conduction in the floor. The accuracy of the numerical predictions of the thermal conductances for different heat flow paths was proven experimentally. The heat conduction analysis code was then used to find the heat transfer capability of various block-support/floor combinations.

Introduction

In industrial equipment we find a number of circumstances where the conductive–convective conjugate mode plays important roles in the heat transfer from functional or structural members. Conjugate heat transfer in microelectronic equipment, in particular, is becoming increasingly important in thermal management of components. Due to the progress of circuit integration the heat dissipation is concentrated in fewer components, while the system volume shrinks, thereby reducing the space for coolant flows. In order to lower the level of heat flux on the component surface, we will have to count more on the heat spreader function of the substrate supporting the components.

The present study was conducted using a model where the essential physics of conjugate heat transfer in microelectronic and other industrial equipment is produced in a fundamental way. Figure 1 depicts a situation under investigation, where a heat-dissipating block (simulated module) is mounted on the floor of a parallel-plate channel, and cooled by forced convection of air. The heat from the block (Q) finds its way to the air through two paths, one from the block surface directly to the air (direct heat transfer, Q_A) and the other leading from the block to the floor (substrate) by way of a block support, then, to the air (Q_B). Our attention is focused on the heat transfer from the block and the upper surface of the floor, so that the lower side of the floor is made adiabatic. The heat transfer process is complex, in particular, on the floor area near the block. The flow is three dimensional around the block, producing a complex distribution of heat transfer coefficient on the floor. Besides, heat flow components Q_A and Q_B are coupled. That is, the air mass warmed up by Q_A (thermal wake) blankets the floor area, thus affecting heat flow Q_B. In many cases of industrial equipment design the total heat dissipation from the block (Q) is specified, and the designer's task is to estimate the block temperature T_M, or determine the required coolant velocity and temperature to hold T_M below an acceptable level. The design analysis necessarily involves the estimation of how Q is partitioned into Q_A and Q_B, for which the existing literature provide little information. The purpose of the present study is to establish a methodology by which we generate handy estimates of conjugate heat transfer. The present paper illustrates a path toward such a goal on the synthesis of physical modeling, experiments, and numerical analysis.

In recent years conjugate heat transfer in microelectronic equipment has received considerable attention from heat transfer researchers. A brief review of the previous literature is presented below. Due to space limitation, only those works on forced convective conjugate heat transfer will be included.

Ramadhyani et al. (1985) and Sugavanam et al. (1994) reported the results of numerical analysis on conjugate heat transfer from two-dimensional flush-mounted heat sources to laminar flow in the channel. They show that the heat transfer is enhanced by the extended surface effect of the substrate. Incropera et al. (1986) and Ortega et al. (1994) used two-dimensional flush-mounted heat sources in their experimental investigations. The data were obtained mainly in turbulent flows, and exhibit relatively small effects of substrate conduction in enhancing heat transfer. This was corroborated by the numerical analysis also reported by Incropera et al. (1986). The function of the substrate as a heat spreader extending from the embedded heat source(s) was the subject of analyses by Culham and Yovanovich (1987), Lall et al. (1994), Godfrey et al. (1990), and Ortega et al. (1993). Heat conduction problems with uniform heat transfer coefficients were solved, or the problem was simplified by assuming a uniform coolant flow (Ortega et al., 1993). Heat transfer from two-dimensional block arrays mounted on the substrate has been the subject of numerical investigations. The assumption of fully developed flow on repeated blocks, coupled with the periodic condition in the cross-stream direction, allows analysis on a zone confined in one pitch of the block placement (Webb and Ramadhyani, 1985; Kim and Anand, 1994a, b; Nigen and Amon, 1994; Kim and Anand, 1995). In this situation, the role of substrate conduction is to direct a large fraction of heat generation from the heat source across the substrate thickness and to the lower side of the substrate where the surface is free of blocks. In cases where a finite number of blocks are mounted on the substrate, there

Contributed by the Heat Transfer Division for publication in the JOURNAL OF HEAT TRANSFER. Manuscript received by the Heat Transfer Division March 1995; revision received November 1995. Keywords: Conjugate Heat Transfer, Electronic Equipment, Forced Convection. Associate Technical Editor: R. Viskanta.

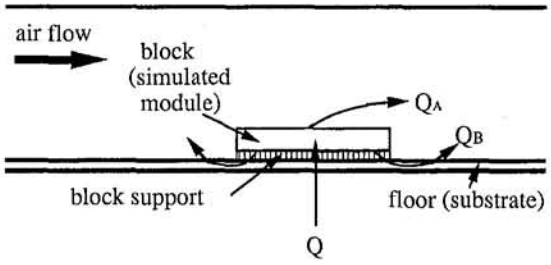

Fig. 1 Heat transfer paths from a surface-mounted block to air flow

are additional heat transfer paths provided by the portions of the substrate extending upstream and downstream of the block array (Davalath and Bayazitoglu, 1987; Zebib and Wo, 1989; Kim and Anand, 1994a, b; Choi et al., 1994; Kim et al., 1994).

Numerical studies on heat transfer from three-dimensional modules are relatively scarce; Asako and Faghri (1989), Shaw et al. (1991), Faghri and Asako (1992), and Rosten and Viswanath (1994). These studies were focused on direct heat transfer component (Q_A), and conjugate heat transfer was not the focus of investigation.

Equally scarce is the literature reporting the experimental data of conjugate heat transfer from surface-mounted blocks. Most of the previous experimental investigations were focused on direct heat transfer component (Q_A). Citing only those reports on heat transfer from a single block, we find the data for a two-dimensional block in Kang and Jaluria (1989), Kang et al. (1990), and Igarashi and Takasaki (1990), and those for a three-dimensional block in Ashiwake et al. (1983), Roeller et al. (1991), and Chyu and Natarajan (1991). To the authors' knowledge, the only report that emphasizes the importance of conjugate heat transfer from a three-dimensional surface-mounted module is Graham and Witzman (1988). It was pointed out that, in many designs, 40 to 60 percent of the total heat load would be dissipated through the substrate into the air stream. The semi-empirical analysis was attempted; however, the details of flow and the thermal wake effects were not taken into consideration.

The present study distinguishes itself from the previous investigations in the following respects. First, a significant part of our attention is set on the heat transfer from the floor area near the surface-mounted block. Second, several different experiments and the numerical analysis of heat transfer in and from the substrate (channel floor) constitute a synthetic set of research programs, each designed to make specific contributions to the development of a prediction method of conjugate heat transfer.

Experimental Programs

Several experimental programs were executed to obtain fundamental data to be used later in conjunction with the numerical analysis of heat conduction in the floor (substrate). The first subsection describes the geometric and operative parameters that were fixed throughout different experiments. The second and the third subsections describe the measurements of fundamental data required later in the numerical analysis. The final subsection describes the experiment performed using different block support designs. All data were collected after having confirmed the steady state of the experimental system.

Invariant Part of the Apparatus. A block was placed on the floor of a parallel-plate channel, and cooled by air drawn from the room by a suction blower. The overall dimensions of the block and the channel were unchanged throughout different experiments. The block has a geometry of square flat package; its area projected on the channel floor is 31×31 mm^2, and its total height from the floor surface is 7 mm. The channel is 20 mm high and 320 mm wide, so that its hydraulic diameter (D_h) is 37.7 mm. The block was placed on the centerline of the channel, setting its leading edge at a distance of 120 mm from the channel inlet, and leaving another 500-mm-long floor section between the rear edge of the block and the channel exit.

The flow rate of air, measured by an orifice flow meter installed between the channel exit and the suction blower, was changed in a few steps by restricting the exit area of the blower. The average air velocity (V) at a cross section free of the block was changed in a range from 1 to 7 m/s; this is the range most commonly found in real equipment. The corresponding channel Reynolds number ($\mathrm{Re} = VD_h/\nu$) was 2200–16,000. Due precautions were exercised to realize smooth transition of the cross section throughout the duct system; they were the attachment of a bell mouth at the channel inlet, the installation of a transition duct connecting the channel exit to a circular pipe, and the provision of a sufficiently long running distance (1140 mm) upstream and downstream of the metering orifice. The uniformity of velocity distribution and the low level of turbulence at the channel inlet were confirmed using a hot-wire probe. Although the channel Re was in a range indicative of transitional to turbulent flow regimes, the flow approaching the block was of laminar boundary layer type, and showed the sign of transition to turbulence at a certain downstream location near and after the block. This was confirmed introducing smoke streaks in the flow, and also inserting the hot-wire probe in the channel. Further details of the flow will be reported elsewhere due to space limitation. The uncertainty in the measurement of air flow rate was estimated as 1.6 percent of the specified value.

Nomenclature

A_M = external surface area of copper piece in block, m^2
D_h = hydraulic diameter of channel, m
F = thermal wake function [Eq. (1)], K/W
h_{ad} = adiabatic heat transfer coefficient [Eq. (2)], W/m^2 K
h_M = heat transfer coefficient on block surface, W/m^2 K
L = side length of block, m
Nu_M = Nusselt number for direct heat transfer
Q = net heat dissipation from block = $Q_p - Q_l$, W
Q_A = direct heat transfer from block to air, W
Q_B = heat transfer from block to floor, W
Q_l = heat flow through power leads, W
Q_p = power input to block, W
q = heat flux, W/m^2
R_c = thermal resistance of block support, K/W
Re = channel Reynolds number
T_{ad} = adiabatic wall temperature, °C
T_s = surface temperature of floor, °C
T_M = block (simulated module) temperature, °C
T_0 = air temperature at channel inlet, °C
ΔT = temperature difference between block and room air, K
t_F = floor thickness, mm
U = overall thermal conductance, W/K
U_A = thermal conductance for direct heat transfer, W/K
U_{BB} = thermal conductance for conjugate heat transfer, W/K
V = mean air velocity in channel, m/s
x = longitudinal coordinate
y = cross-stream coordinate
λ = thermal conductivity of air, W/m K
λ_F = thermal conductivity of floor, W/m K
ν = kinematic viscosity of air, m^2/s

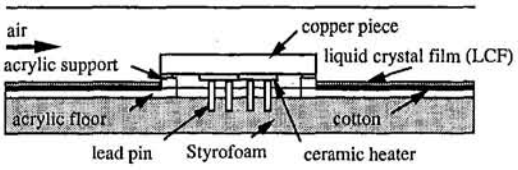

(a) Heated Block/Adiabatic Floor(HB/AF)

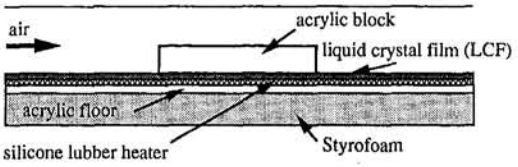

(b) Adiabatic Block/Heated Floor(AB/HF)

Fig. 2 Longitudinal cross sections of the test assembly

The whole duct system was constructed using transparent acrylic materials. Another structural feature common to all the experiments was the thermal insulation applied to the bottom side of the channel. The channel floor has a double-deck structure, and the space between the floor plate and the bottom plate was filled with 10-mm-thick Styrofoam. The thermal resistance for a heat flow path leading from the upper floor plate, across the Styrofoam, down to the constrained air space between the bottom plate and the supporting table was estimated as 1 K/W per unit floor area (1 m^2). Compared to this value, the order of thermal resistance on the floor surface facing the forced convective air flow in the channel was estimated to be very low, 2.5–5 percent of the resistance for heat loss from the bottom.

Heated Block on Adiabatic Floor (HB/AF) Arrangement. A simulated module (block) in this experiment consists of a copper piece having an area 31 × 31 mm^2 and thickness 4 mm, and four ceramic heaters bonded by solder to the lower face of the copper piece. The channel floor is a 1-mm-thick acrylic plate, a portion of which under the block was cut out for access of power leads to the electric heaters. The block is supported on the edge of this opening by a 3-mm-high acrylic support, which was designed to impose a large thermal resistance (496 K/W) between the block and the floor. Figure 2(a) shows the longitudinal cross section of this arrangement.

The purpose of this experiment was to measure the direct heat transfer from the block (Q_A), and find the adiabatic wall temperature on the floor (T_{ad}). The latter was measured by means of a liquid crystal film (LCF) laid on the floor. The adiabatic condition on the floor was already realized to a sufficient degree by the use of an acrylic plate for the floor; however, this was further enhanced by inserting a 0.2-mm-thick cotton cloth between the LCF and the floor. For the concept and the usage of T_{ad} the reader is referred to Anderson (1994), Ortega et al. (1993), and Moffat and Ortega (1988). The concept has been most frequently applied to heat transfer from block arrays (Arvizu and Moffat, 1982; Ashiwake et al., 1983; Wirtz and Dykshoorn, 1984; Nakayama et al., 1988; Sridhar et al., 1990). The LCF contains cholesteric-type crystal in microcapsules, and changes its color in a temperature range 32.3–39.6°C from brown, red, green, blue, to dark blue. The clearest detection of color change can be made at the red/green and green/blue boundaries at 33.7°C and 37°C (±0.3°C), respectively. Photographs were taken from above the transparent ceiling of the channel, and isotherms were drawn by the experimenter (S.-H. Park). This method was rather primitive compared to a more sophisticated technique using digital imaging (Hollingsworth et al., 1989; Ortega et al., 1993). However, considerable effort was waged to secure the measurement accuracy. For calibration, a piece of LCF was bonded to the top surface of the block, the block temperature was monitored at five locations by thermocouples confirming the isothermal state of the block, pictures were taken under the lighting condition of the experiment, and developed and printed under a strictly regulated condition. The templates thus produced were used to determine isotherms on pictures of the LCF on the floor. The uncertainty of the floor temperature measurement by LCF was estimated as ±0.3 K, and the spatial resolution of color boundaries on LCF was within 1 mm. This accuracy is comparable to that achieved by a more thorough calibration technique reported by Farina et al. (1994).

The block was kept in a nearly isothermal state throughout the experiment. This was confirmed by the readings of five thermocouples (0.2-mm-dia copper-constantan), one embedded at the center of the top surface of the copper piece, and four others between the copper piece and the ceramic heaters. Their readings agreed within ±0.5 K. Another indicator of the isothermal state is the Biot number defined in terms of the length scale of the copper piece and the heat transfer coefficient on the block surface. When the former is set as 15.5 mm (half length of the copper piece) and the latter as 20 W/m^2 K, the Biot number is 8×10^{-4}.

In this experiment the heat conduction from the block to the floor was effectively suppressed by the means described above. There was, however, a need to elaborate on the determination of direct heat flow rate Q_A. The use of a small three-dimensional heat source like the present one inevitably requires the attention on the heat flow through the power leads to the room air below the channel. Unlike two-dimensional heater construction, the size of the power leads becomes comparable to the size of the heater. (The diameter of the lead is a design item to be optimized; thin leads generate heat, while thick leads increase the heat flow through them.) Since the leads are good thermal conductors, and extend to the room-temperature environment, the measurement of heat flow through them (Q_l) has to be an integral part of the experiment. The need of this elaboration has not necessarily been emphasized in the previous literature. In the present study calibration experiments were conducted to determine the thermal resistance on the power leads (R_l). The value of R_l was 32 K/W with an uncertainty bound of ±0.2 K/W. Details of the derivation of these values have to be spared due to space limitation. The heat flow Q_A was determined from $Q_A = Q_p - Q_l = Q - R_l\Delta T$, where Q_p is the total power input to the heater, and ΔT is the temperature difference between the block and the room air. The uncertainty in the measurement of Q_p, bound by the accuracy in the measurement of electrical resistance of the heaters and the resolution of the voltmeter, was estimated as 0.7 percent of the measured value. The temperatures of the block and the room air were measured to the accuracy of ±0.3 K. These uncertainty components result in the cumulative rms uncertainty in the estimation of Q_A which amounts to 1.3 percent of the measured value. Hence, Q_A was determined accurately, although Q_l amounted to 8–17 percent of Q_p. In subsequent sections the net power generation of the block ($Q_p - Q_l$) will be denoted as Q, which is equal to Q_A only on the HB/AF arrangement.

Experimental data of T_{ad} were reduced to the following form, which we will call the thermal wake function,

$$F = \frac{T_{ad} - T_0}{Q_A} \tag{1}$$

where T_0 is the air temperature at the channel inlet, which was measured by a thermocouple suspended at the inlet. Keeping the air flow at a given flow rate, Q_p was changed in several steps to shift the color boundaries over the floor area, and iso-F contours were superposed in a single figure.

Adiabatic Block on Heated Floor (AB/HF) Arrangement. A plastic block was mounted on a uniform-heat-flux floor. Figure 2(b) shows the longitudinal cross section of this arrange-

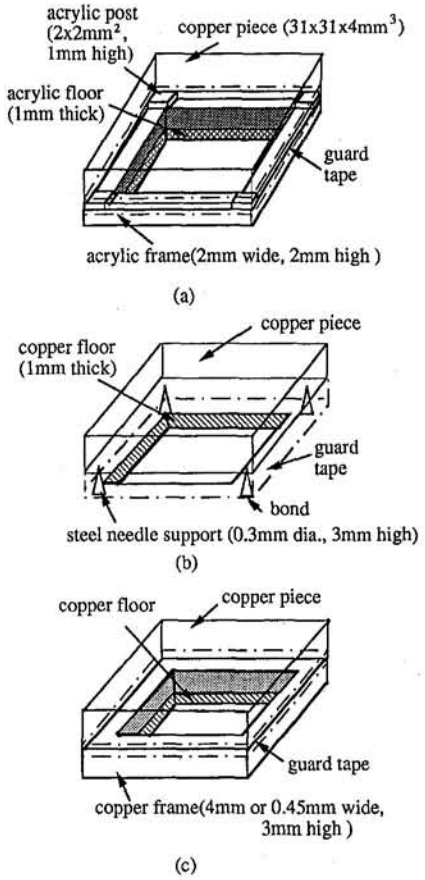

Fig. 3 Block supports

ment. The uniform heat flux condition was created by a rubber heater having dimensions 0.3 mm (thickness) × 225 mm (width) × 285 mm (length). The leading edge of the rubber heater is at 40 mm from the upstream edge of the channel's straight section and 50 mm from the front face of the block. The heating elements are find Nichrome wires densely embedded in the plastic matrix, having a total electrical resistance of 21.8 Ω. The rubber heater is overlaid by a LCF, which has the same characteristics as described above for the HB/AF arrangement. The purpose of this experiment was to measure the adiabatic heat transfer coefficient on the floor,

$$h_{ad} = \frac{q}{T_s - T_{ad}} \tag{2}$$

where q is the surface heat flux, and T_s is the surface temperature, which was determined from the pictures of LCF as described in the previous subsection. The adiabatic temperature T_{ad} in Eq. (2) was set equal to T_0 (air inlet temperature), on the understanding that the effect of thermal wake generated by the floor itself was included in h_{ad}. Namely, the term "thermal wake" is reserved only for that from the block, and in this experiment it was absent. It was confirmed by the temperature measurement on the block that the plastic block actually served as an adiabatic body.

The heat flux (q) was determined by dividing the power input to the rubber heater by the area of the heater. The thickness of the laminate composed of the heater and the LCF is 0.6 mm, sufficiently small compared to the length scale for a significant variation of heat transfer coefficient to occur. Besides, the heat flow to the bottom of the channel was reduced to a negligible level as described in the previous section. All those factors combined contribute to the realization of a uniform heat flux condition on the floor. The uncertainty in the measurement of h_{ad} was maximum in a region close to the block where the heat transfer coefficient varied in a short distance, and was estimated as 12 percent of the measured value. In order to determine h_{ad} over the whole area of LCF for a specified air velocity, the location of color-change boundaries had to be shifted by changing the heat flux on the floor.

Within this experimental program supplementary runs were executed, removing the block from the channel. The local heat transfer coefficient thus obtained was later used in the numerical analysis, and applied to the floor area outside the zone of influence of the block. Near the leading edge of the heater, the heat transfer coefficient agreed well with the existing correlation for laminar boundary layer heat transfer on a uniform heat flux plate with an unheated length (Incropera and De Witt, 1981). Toward the trailing edge of the heater, the heat transfer coefficient approached that predicted by the well-established correlation for fully turbulent heat transfer in the channel. The results served to confirm the accuracy of the present measurement of heat transfer coefficient.

Different Block Supports on Copper Floor. A heater block was mounted on a copper floor or an acrylic floor using different block supports. The block has the same construction as the one used in the HB/AF experiment. The copper floor was 1 mm thick, with its lower side thermally insulated as described in the previous subsection. This experimental program had two objectives: (1) find the effect of thermal resistance of the block support on the thermal conductance between the block and the cooling air, and (2) provide the benchmark data to be compared with the numerical prediction. The use of copper as the floor material maximizes the heat spreading function of the floor.

Figure 3 shows three designs of the block support. All designs have the height of 3 mm, so that the total height of the block was unchanged at 7 mm. The one shown in Fig. 3(a) has a layered structure composed of a 2-mm-thick and 2-mm-wide acrylic frame and four acrylic posts attached on the corners. Each post has an area 2 × 2 mm² and a height 1 mm. In Fig. 3(b) four steel needles, each 3 mm high and having a base diameter of 0.3 mm, are erected to support the copper piece on the corners. Figure 3(c) shows a 3-mm-thick copper frame interfacing both the copper piece and the floor. This has two subdesigns where the width of the frame is different, one being 0.45 mm, and the other 4 mm. In all support constructions adhesive was used to bond the components. A guard tape wrapping the sides of the block support sealed any gap left between the copper piece and the floor, while due to its thin thickness (35 μm) the tape had a negligible contribution to heat conduction.

Table 1 shows the thermal resistances of the block support and the identification numbers of the experiments in Roman letters. As indicated in Table 1, the support of Fig. 3(a) was used to mount the copper piece on the acrylic floor, the assembly identified as the HB/AF arrangement in the previous subsection. The thermal resistances of the block supports (Rc) were computed, some by applying the simple Fourier formula, while others by using the finite difference analysis code. Details of the derivation have to be spared.

Table 1 Combinations of block support and floor material (identified by Roman figures), and thermal resistances (R_c) of the supports estimated by computation

support	acrylic	steel needle	copper	copper
Rc [K/W]	496	210	0.14	0.015
copper floor	—	I	II	III
acrylic floor	IV	—	—	—

Comparison of the data obtained by experiments I and IV provided information about how effectively the heat flow to the floor (Q_B) was reduced to a negligible level. The data, reduced to the thermal conductance U_A ($\equiv Q/(T_M - T_0)$), differ by no more than 2 percent throughout the velocity range studied. This agreement is considered as indicating a high confidence level in the measurement of U_A. A formula is fitted to the data of direct heat transfer as

$$\mathrm{Nu}_M = 1.78\ \mathrm{Re}^{0.43} \tag{3}$$

where $\mathrm{Nu}_M = h_M L/\lambda$, $h_M = U_A/A_M$, A_M = external surface area of the copper piece, L = side length of the block, λ = thermal conductivity of air. The equation is valid for $2200 \leq \mathrm{Re} \leq 16{,}000$. There are a few different length scales in the system, so that the use of D_h is among different options to define Reynolds number. Several investigators proposed correlations for direct heat transfer: Ashiwake et al. (1983), Chang et al. (1987), Roeller et al. (1991). The exponents of Re in those correlations are all similar, 0.43 or a little less. However, when applied to the present block dimensions, those correlations produced predictions that differ among them and underpredict the present data by 25 percent at best (Ashiwake et al., 1983). This indicates the need for more work to derive a correlation of wide applicability even for the direct heat transfer from the block.

Equation (3) now provides a means to separate Q_A from Q and derive Q_B from the data of the experiments II and III. Namely, Q_B is computed from $Q_B = Q - Q_A$. The data were further reduced to the thermal conductance, which accounts for the heat transfer from the floor surface,

$$U_{BB} = \frac{1}{\dfrac{1}{U - U_A} - R_c} \tag{4}$$

where U is the overall thermal conductance: $U = Q/(T_M - T_0)$. Assumed in this induction of Q_B and U_{BB} is that the thermal wake originating from the floor does not seriously modify Q_A.

The isothermal state of the block on the copper supports was confirmed by computing the Biot number defined in terms of an equivalent heat transfer coefficient at the contact between the block's periphery and the support, the half length of the block, and the thermal conductivity of copper. The equivalent heat transfer coefficient was computed by dividing a typical value of U_{BB} by the contact area, which was 231 W/m^{2}K. The Biot number was computed as 0.009.

Additional instrumentation was provided to measure temperature distributions of the copper floor. Thermocouples (0.2-mm-dia copper-constantan) were imbedded in the copper floor from the lower side. In total 85 junctions were located, the closest placement pitch being set at 1 mm. The readings of the thermocouples on the centerline of the channel will be compared later with the numerical predictions of the floor temperature. The use of thermocouples in place of LCF was dictated by the following requirements. First, the benchmark data had to be obtained keeping Q at a specified value. For a fixed Q, only a few color-change boundaries are available on LCF. Second, high heat spreader capability of the copper floor made the floor temperature below the lowest color-change (red/green) temperature (33.7°C) of LCF.

Experimental Results and Numerical Predictions

The experimental programs described in the previous section produced two groups of data of different usage. Those in the first group served to formulate the boundary condition for the numerical analysis of heat conduction in the floor. The second group provided the benchmarks against which the numerical predictions were compared.

Thermal Wake Function, F. Figure 4 shows the iso-F contours on the channel floor: Fig. 4(a) for V = 1 m/s, and (b) for V = 7 m/s. Each figure is composed superposing F-contours obtained at three different values of Q_A (2.7, 4.8, 6.9 W). It is shown that the adiabatic temperature decreases rapidly with increasing distance from the block.

Adiabatic Heat Transfer Coefficient, h_{ad}. Figure 5 shows the iso-h contours on the channel floor: Fig. 5(a) for V = 1 m/s, and (b) for V = 7 m/s. Each figure is composed superposing iso-h contours obtained at several different levels of surface heat flux on the floor (0.039, 0.047, 0.055, 0.062 W/cm^2). The h-contours apparently coincide with the development of the horseshoe vortex around the block. Also shown in Fig. 5 are the lines that show the heat transfer coefficients on the floor in the absence of the block. In some of the experimental runs with the block-mounted floor, the color-change boundaries were observed also on the area outside the zone of influence of the block. They extended laterally across the stream, and merged with the horseshoe contours near the block. Based on this observation, in the numerical analysis, those horizontal iso-h lines were extended to the periphery of the horseshoe contours, as indicated by the broken lines in Fig. 5.

Numerical Solution of Heat Transfer Equation. A two-dimensional finite difference equation (of the standard scheme found in any heat transfer textbook) is solved to determine temperature distributions over the floor. The analysis was applied to the case of a copper floor to compare the predictions with the experimental data. The negligence of temperature variation across the thickness of the floor is justified on the ground that the Biot number based on the floor thickness is of the order of 10^{-5}–10^{-4}. The coordinates are x, extending in the streamwise direction from the leading edge of the block, and y, extending in the cross-stream direction from the centerline of the channel. The area of analysis is bound by -120 mm $\leq x \leq 420$ mm and $0 \leq y \leq 160$ mm. The discretization is made finer near the block, minimum 1 mm × 1 mm, and coarser in the far field, maximum 30 mm × 25 mm. The node population is 43 along the x axis and 18 along the y axis. Finer discretizations could be employed, however, the spatial resolution of F and h_{ad}, estimated as 1 mm as noted previously, made the adoption of finer meshes less meaningful. The data of F and h_{ad} were used to define the boundary condition, as follows.

We write $T_0 = 0$ for convenience, and assume that the air velocity V is specified. For the purpose of illustration, we set Q_A = 1 W. Then, F gives directly the adiabatic temperature T_{ad}. Using this T_{ad}, and the data of h_{ad}, we write a heat balance equation for the surface element $\Delta x \Delta y$ using Eq. (2). Meanwhile, Q_A sets the block temperature T_M through Eq. (3). This T_M and the thermal resistance of the block support, R_c, are used to write a heat balance equation for the surface element under the block support. The finite difference equation was integrated by iteration until the convergence criterion based on the energy conservation, less than 2 percent of discrepancy in global energy conservation, was satisfied. Using the solution for the floor temperature, we compute the heat flow rate from the block to the floor (Q_B). Using the sum, $Q = Q_A + Q_B$, and T_M, we find the overall thermal resistance (U), and that for the conjugate heat transfer from the floor (U_{BB}) from Eq. (4). U_A in Eq. (4) is already computed when T_M is found from Eq. (3). Where Q is specified, its division into Q_A and Q_B can be computed using U_A and U_{BB} determined by the procedure as described above. The assumption made about the value of Q_A (1 W) in the above explanation is not substantial, because the heat transfer system considered in the analysis is a linear system; hence, the solution can be scaled by any factor.

Comparison of Numerical Predictions With the Experimental Data. The numerical analysis was performed assuming the different block supports on a 1-mm-thick copper floor.

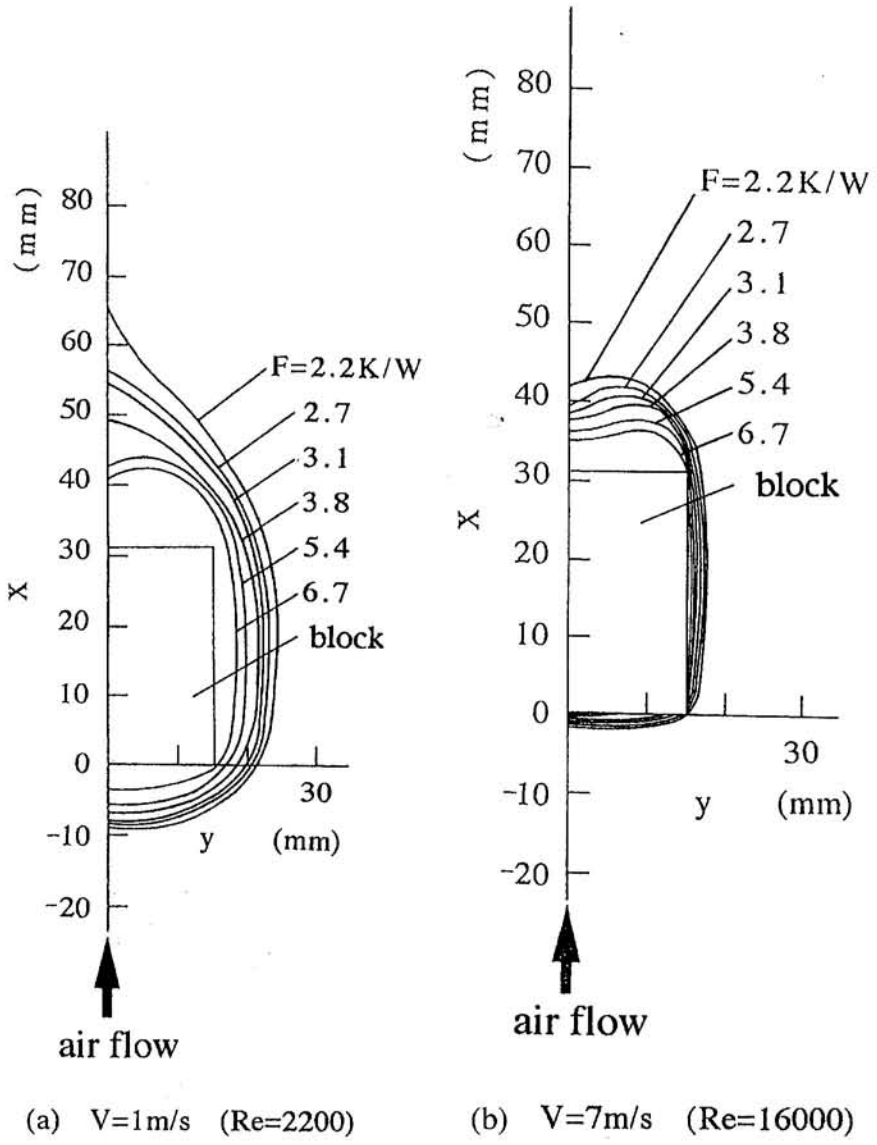

Fig. 4 Thermal wake function *F* on the floor

The designs of the supports and their thermal resistances are shown in Fig. 3 and Table 1, respectively.

Figure 6 shows the comparison between the predicted wall temperature distributions on the centerline of the floor and the experimental data, for the case of R_c = 0.015 K/W and Q = 3.6 W. The experimental data for V = 1 m/s are overpredicted in the area downstream of the block by about 0.5 K at maximum; otherwise, excellent agreement is obtained. The effect of air velocity on the temperature distribution is reproduced with a good accuracy by the numerical analysis.

Figure 7 shows the comparison between the predictions for R_c = 0.015 K/W and 210 K/W and the experimental data. The fixed parameters are V = 1 m/s and Q = 3.6 W. Again, good agreement is observed. As noted previously, the combination of the needle supports (R_c = 210 K/W) and the copper floor produced the experimental data of U_A almost coinciding with those obtained using the acrylic support and the acrylic floor, implying that the heat flow from the block to the floor was effectively cut off in those experiments. Therefore, the creation of a floor temperature distribution in the case of R_c = 210 K/W is attributed to the redistribution of heat flow between the air and the floor. That is, there is a heat flow from the high-temperature air near the block to the floor; the heat spreads by conduction through the floor, and eventually returns to cooler air. (The redistribution heat flow rate is small compared to other heat flow components, in particular in cases of good block/floor thermal bonding. This justifies our assumption that T_{ad} is not seriously modified on the conductive floor.)

Figure 8 shows the comparison between the predicted conductance U_{BB} and the experimental data. The experiments were conducted changing the power input to the block in two steps, 1.6 W and 3.6 W. The data of U_{BB} thus obtained differed by only a negligibly small margin, so that the data for a given set of R_c and V were overlapped in each data symbol in Fig. 8. The predictions and the data agree within 10 percent. It is interesting to note that U_{BB} depends on R_c. This is a manifestation of the fact that a larger R_c increases the fraction Q_A/Q, which leads to higher T_{ad} and increases the impedance to Q_B.

Effects of Thermal Properties of the Block Support and the Floor. Once verified by the benchmark test in the previous subsection, the numerical analysis code now provides a means to survey the effects of thermal properties of the block support and the floor.

Figure 9 shows the predictions of U_{BB} for the case of V = 1 m/s. In the two-dimensional heat conduction equation the thermal conductivity of the floor (λ_F) is coupled with the floor thickness (t_F), forming a parameter $\lambda_F t_F$. To facilitate a quick look at the

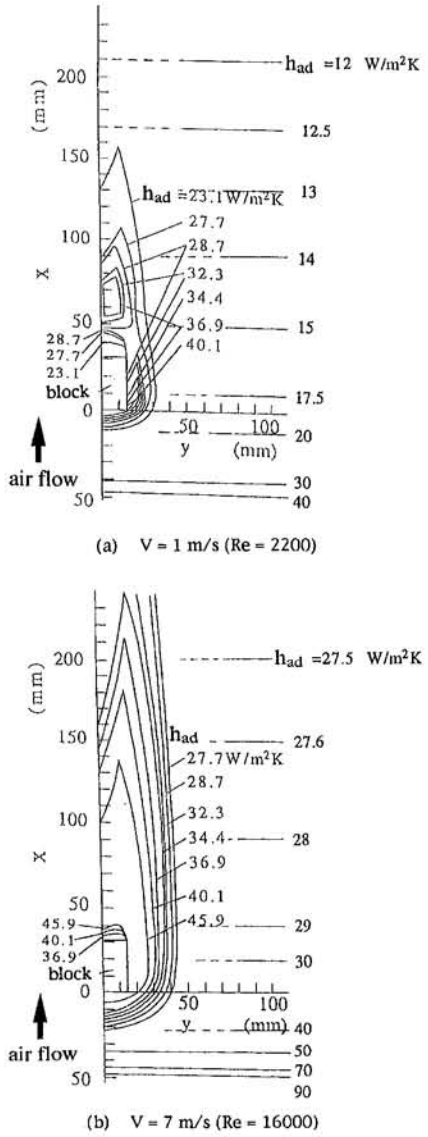

Fig. 5 Adiabatic heat transfer h_{ad} coefficient on the floor

results the product $\lambda_F t_F$ is shown in the dimension of (W · mm/m · K), (mm) for t_F and (W/m · K) for λ_F. Figure 9 shows U_{BB} versus R_c for four different values of $\lambda_F t_F$. The plots are logarithmic, so that the actual values of U_{BB} for different $\lambda_F t_F$

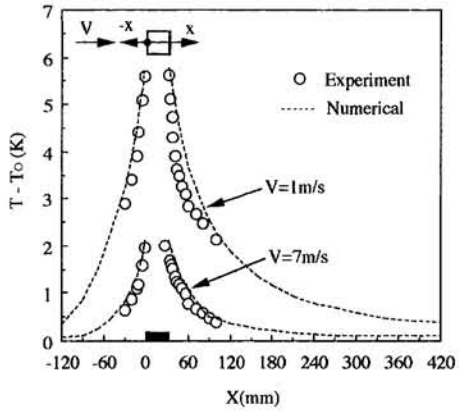

Fig. 6 Comparison of temperature distributions on the centerline of the floor (copper floor, R_c = 0.015 K/W, Q = 3.6 W)

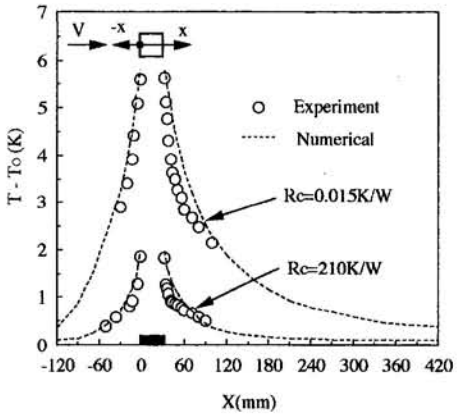

Fig. 7 Comparison of temperature distributions on the centerline of the floor (copper floor, V = 1 m/s, Q = 3.6 W)

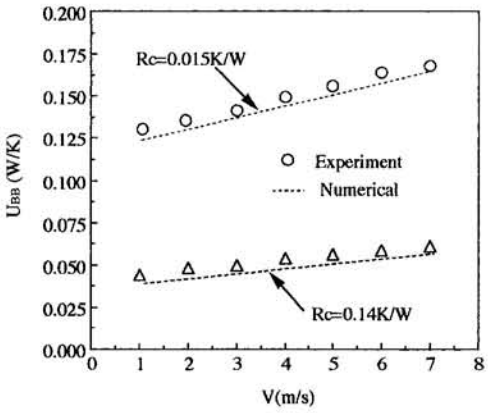

Fig. 8 Thermal conductance U_{BB} versus air velocity V

approach one another with increasing R_c. This is a manifestation of the decreasing role of conjugate heat transfer from the floor. It should also be noted that the inverse of U_{BB}, that is the thermal resistance on the conjugate heat transfer path, is larger than R_c by an order of magnitude. This results from large thermal resistance to convective heat transfer on the floor surface, in particular, at the air velocity of V = 1 m/s. Since U_{BB} is a governing parameter in the determination of Q_B, a high level of accuracy in the estimation of R_c is not required for the prediction of conjugate heat transfer. The slope of the curves in Fig. 9 also indicates a relative insensitivity of heat transfer predictions to the accuracy of R_c estimation.

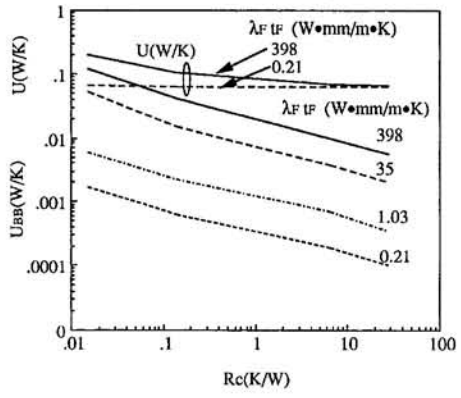

Fig. 9 Relationships among U, U_{BB}, R_c, and $\lambda_F t_F$ for V = 1 m/s (Re = 2200)

Included in Fig. 9 is a curve of the overall thermal conductance U for the cases of $\lambda_F t_F = 398$ and 0.21 W · mm/m · K. The sensitivity of U to R_c is less than that of U_{BB}; however, its real sensitivity is somehow obscured in the logarithmic plot.

Finally, a numerical example will be used to discuss cooling of an electronic module by the present mode of conjugate heat transfer. A possible maximum value of the overall thermal conductance with $V = 1$ m/s is $U = 0.185$ W/K. Where the allowable temperature difference between the module and the inlet air is 40 K, the total heat dissipation from the module can be $Q = 7.4$ W. This level of cooling capability is normally provided by a 10-mm-high heat sink and a relatively high air velocity in the range 4–5 m/s. The cooling-by-floor technique is suited where the system needs to have a flat profile and low-speed air flow. To achieve effective designs, good thermal bonding between the module and the substrate, high thermal conductivity of the substrate, and clearing one side of the substrate of other components by removing them to the bottom side of the substrate need to be realized. Some of those measures have already being made available in the industry, although more work is needed to make the cooling-by-floor technique truly effective.

Conclusions

Conjugate heat transfer from a block on the floor of a parallel-plate channel was studied experimentally and analytically. The dimensions of the block ($31 \times 31 \times 7$ mm^3) and the range of air velocity (1–7 m/s) were set referring to those of practical interest. Particular attention was directed to the heat transfer from the floor area near the block, where the three-dimensional development of air flow produces complex distributions of heat transfer coefficient and air temperature. The conclusions and remarks are summarized as follows.

1 The concepts of adiabatic wall temperature (T_{ad}) and adiabatic heat transfer coefficient (h_{ad}) were employed to account for the effect of thermal wake shed from the block on the heat transfer from the floor. The information about T_{ad} and h_{ad} was obtained experimentally. Alternatively, they may be found by three-dimensional numerical simulations of air flow and heat transfer assuming a situation corresponding to the present experimental one. Once T_{ad} and h_{ad} are found by either experimental or numerical means, they can be used repeatedly to compute temperature and heat flux distributions on floors of different materials.

2 The thermal resistance of the block support (R_c) is another important parameter that controls the conjugate heat transfer from the floor. The numerical analysis produced predictions that agreed well with the experimental data obtained using different block supports. A large thermal resistance of the order of a few hundreds K/W on the block support proved effective to reduce the heat flow from the block to the floor to a negligibly low level, thereby facilitating the measurement of direct heat transfer from the block to the air flow over it. A good thermal bonding between the block and the floor, with R_c of the order of 0.01 K/W, and a high thermal conductance of the floor, of that of a 1-mm-thick copper plate, maximizes the contribution of conjugate heat transfer (Q_B) to the total heat dissipation (Q), raising the ratio Q_B/Q to more than 0.5.

References

Anderson, A. M., 1994, "Decoupling of Convective and Conductive Heat Transfer Using the Adiabatic Heat Transfer Coefficient," ASME *Journal of Electronic Packaging,* Vol. 116, pp. 310–316.

Arvizu, D. C., and Moffat, R. J., 1982, "The Use of Superposition in Calculating Cooling Requirements for Circuit Board Mounted Electronic Components," *Electron. Components Conference,* Vol. 32, pp. 133–134.

Asako, Y., and Faghri, M., 1989, "Three-Dimensional Heat Transfer Analysis of Arrays of Heated Square Blocks," *International Journal of Heat and Mass Transfer,* Vol. 32, No. 2, pp. 395–405.

Ashiwake, N., Nakayama, W., Daikoku, T., and Kobayashi, F., 1983, "Forced Convective Heat Transfer From LSI Packages in an Air-Cooled Wiring Board Array," *Heat Transfer in Electronic Equipment—1983,* ASME HTD-Vol. 28, pp. 35–42.

Chang, M. J., Shyu, R. J., and Fang, L. J., 1987, "An Experimental Study of Heat Transfer From Surface Mounted Components to a Channel Airflow," ASME Paper No. 87-HT-75.

Choi, C. Y., Kim, S. J., and Ortega, A., 1994, "Effects of Substrate Conductivity on Cooling of Electronic Components," ASME *Journal of Electronic Packaging,* Vol. 116, pp. 198–205.

Chyu, M. K., and Natarajan, V., 1991, "Local Heat/Mass Transfer Distributions on the Surface of a Wall-Mounted Cube," ASME JOURNAL OF HEAT TRANSFER, Vol. 113, pp. 851–857.

Culham, J. R., and Yovanovich, M. M., 1987, "Non-iterative Technique for Computing Temperature Distributions in Flat Plates With Distributed Heat Sources and Convective Cooling," *Proc. ASME/JSME Thermal Engineering Joint Conference,* Vol. 3, pp. 403–409.

Davalath, J., and Bayazitoglu, Y., 1987, "Forced Convection Cooling Across Rectangular Blocks," ASME JOURNAL OF HEAT TRANSFER, Vol. 109, pp. 321–328.

Faghri, M., and Asako, Y., 1992, "Prediction of Turbulent Three-Dimensional Heat Transfer of Heated Blocks Using Low-Reynolds Number Two-Equation Model," *Topics in Heat Transfer,* Vol. 1, ASME HTD-Vol. 206-1, pp. 39–45.

Farina, D. J., Hacker, J. M., Moffat, R. J., and Eaton, J. K., 1994, "Illuminant Invariant Calibration of Thermochromic Liquid Crystals," *Experimental Thermal and Fluid Science,* Vol. 9, No. 1, pp. 1–12.

Godfrey, W. M., Taghavi, K., Cremers, C. J., and Menguc, M. P., 1990, "Interactive Thermal Modeling of Electronic Circuit Boards," *Thermal Modeling and Design of Electronic Systems and Devices,* ASME HTD-Vol. 153, pp. 65–71.

Graham, K., and Witzman, S., 1988, "Analytical Correlation of Thermal Design of Electronic Packages," *Cooling Technology for Electronic Equipment,* W. Aung, ed., Hemisphere Publishing Corporation, New York, pp. 249–264.

Hollingsworth, D. K., Boehman, A. L., Smith, E. G., and Moffat, R. J., 1989, "Measurement of Temperature and Heat Transfer Coefficient Distributions in a Complex Flow Using Liquid Crystal Thermography and True-Color Image Processing," *Collected Papers in Heat Transfer 1989,* ASME HTD-Vol. 123, pp. 35–42.

Igarashi, T., and Takasaki, H., 1990, "Enhancement of Heat Transfer Around a Rectangular Cylinder in a Flat Plate Boundary Layer," *Transactions of the Japan Society of Mechanical Engineers,* Vol. 56, No. 531, pp. 227–234.

Incropera, F. P., and De Witt, D. P., 1981, *Fundamentals of Heat and Mass Transfer,* Wiley, New York, pp. 399–400.

Incropera, F. P., Kerby, J. S., Moffatt, D. F., and Ramadhyani, S., 1986, "Convection Heat Transfer From Discrete Heat Sources in a Rectangular Channel," *International Journal of Heat and Mass Transfer,* Vol. 29, pp. 1051–1058.

Kang, B. H., and Jaluria, Y., 1989, "Mixed Convection Transport From a Protruding Heat Source Module on a Vertical Surface," *AIAA Journal of Thermophysics,* Vol. 4, pp. 384–390.

Kang, B. H., Jaluria, Y., and Tewari, S. S., 1990, "Mixed Convection Transport From an Isolated Heat Source Module on a Horizontal Plate," ASME JOURNAL OF HEAT TRANSFER, Vol. 112, pp. 653–661.

Kim, S. H., and Anand, A. K., 1994a, "Laminar Developing Flow and Heat Transfer Between a Series of Parallel Plates With Surface-Mounted Discrete Heat Sources," *International Journal of Heat and Mass Transfer,* Vol. 37, pp. 2231–2244.

Kim, S. H., and Anand, A. K., 1994b, "Turbulent Heat Transfer Between a Series of Parallel Plates With Surface-Mounted Discrete Heat Sources," ASME JOURNAL OF HEAT TRANSFER, Vol. 116, pp. 577–587.

Kim, S. H., Sung, H. J., and Hyun, J. M., 1994, "Mixed Convection From Multiple-Layered Boards With Cross-Streamwise Periodic Boundary Conditions," *International Journal of Heat and Mass Transfer,* Vol. 35, pp. 2941–2952.

Kim, S. H., and Anand, A. K., 1995, "Laminar Heat Transfer Between a Series of Parallel Plates With Surface-Mounted Discrete Heat Sources," ASME *Journal of Electronic Packaging,* Vol. 117, pp. 52–62.

Lall, B. S., Ortega, A., and Kabir, H., 1994, "Thermal Design Rules for Electronic Components on Conducting Boards in Passively Cooled Enclosures," *Proc. Intersociety Conference on Thermal Phenomena in Electronic Systems (I-THERM IV),* Washington, DC, pp. 50–61.

Moffat, R. J., and Ortega, A., 1988, "Direct Air-Cooling of Electronic Components," *Advances in Thermal Modeling of Electronic Components and Systems,* A. Bar-Cohen and A. D. Kraus, eds., Hemisphere Publishing Corporation, New York, Vol. 1, Chap. 3, pp. 129–282.

Nakayama, W., Matsushima, H., and Goel, P., 1988, "Forced Convective Heat Transfer From Arrays of Finned Packages," *Cooling Technology for Electronic Equipment,* W. Aung, ed., Hemisphere Publishing Corporation, New York, pp. 195–210.

Nigen, J. S., and Amon, C. H., 1994, "Time-Dependent Conjugate Heat Transfer Characteristics of Self-Sustained Oscillatory Flows in a Grooved Channel," ASME *Journal of Fluids Engineering,* Vol. 116, pp. 499–507.

Ortega, A., Ramanathan, S., Chicci, J. D., and Prince, J. L., 1993, "Thermal Wake Models for Forced Air Cooling of Electronic Components," *Proc. 9th IEEE SEMI-THERM Symposium,* pp. 63–74.

Ortega, A., Wirth, U. S., and Kim, S. J., 1994, "Conjugate Forced Convection From a Discrete Heat Source on a Plane Conducting Surface: A Benchmark Experiment," *Heat Transfer in Electronic Systems,* ASME HTD-Vol. 292, pp. 25–36.

Ramadhyani, S., Moffatt, D. F., and Incropera, F. P., 1985, "Conjugate Heat Transfer From Small Isothermal Heat Sources Embedded in a Large Substrate," *International Journal of Heat and Mass Transfer,* Vol. 28, pp. 1945–1952.

Roeller, P. T., Stevens, J., and Webb, B. W., 1991, "Heat Transfer and Turbulent Flow Characteristics of Isolated Three-Dimensional Protrusions in Channels," ASME JOURNAL OF HEAT TRANSFER, Vol. 113, pp. 597–603.

Rosten, H. I., and Viswanath, R., 1994, "Thermal Modeling of the Pentium™ Processor Package," presented at the IEEE Electronic Component Technology Conference (ECTC), Washington, DC, May.

Shaw, H.-J., Chen, W.-L., and Chen, C.-K., 1991, "Study on the Laminar Mixed Convective Heat Transfer in Three-Dimensional Channel With a Thermal Source," ASME *Journal of Electronic Packaging,* Vol. 113, pp. 40–49.

Sridhar, S., Faghri, M., Lessmann, R. C., and Schmidt, R., 1990, "Heat Transfer Behavior Including Thermal Wake Effects in Forced Air Cooling of Arrays of Rectangular Blocks," *Thermal Modeling and Design of Electronic Systems and Devices,* ASME HTD-Vol. 153, pp. 15–26.

Sugavanam, R., Ortega, A., and Choi, C. Y., 1994, "A Numerical Investigation of Conjugate Heat Transfer From a Flush Heat Source on a Conductive Board in Laminar Channel Flow," *Proc. Intersociety Conference on Thermal Phenomena in Electronic Systems (I-THERM IV),* Washington, DC, pp. 62–72.

Webb, B. W., and Ramadhyani, S., 1985, "Conjugate Heat Transfer in a Channel With Staggered Ribs," *International Journal of Heat and Mass Transfer,* Vol. 28, pp. 1679–1687.

Wirtz, R. A., and Dykshoorn, P., 1984, "Heat Transfer From Arrays of Flat Packs in a Channel Flow," *Proc. 4th International Electronic Packaging Conference,* pp. 318–326.

Zebib, A., and Wo, Y. K., 1989, "A Two-Dimensional Conjugate Heat Transfer Model for Forced Air Cooling of an Electronic Device," ASME *Journal of Electronic Packaging,* Vol. 111, pp. 41–45.

A. S. Wood

G. E. Tupholme

M. I. H. Bhatti[1]

Department of Mathematics,
University of Bradford,
Bradford, West Yorkshire BD7 1DP,
United Kingdom

P. J. Heggs
Department of Chemical Engineering,
UMIST,
P.O. Box 88,
Manchester M60 1QD, United Kingdom

Performance Indicators for Steady-State Heat Transfer Through Fin Assemblies

A comparative study is presented of several models describing steady-state heat flow through an assembly consisting of a primary surface (wall) and attached extended surface (fin). Attention is focused on the validity of four performance indicators. The work shows that the augmentation factor is the only indicator capable of correctly predicting the behavioral trends of the rate of heat flow through the assembly as the influencing physical parameters are varied.

1 Introduction

The benefit sought in the use of a heat transfer assembly is to facilitate the design of smaller heat exchangers, in which the higher capital cost of the extended surface configuration is offset against a smaller shell, or to minimize weight and volume constraints for automobiles and offshore applications. To determine whether a particular configuration is satisfying the objective of enhancing the heat flow, a number of quantitative measures of performance have been suggested.

A well-defined performance indicator should reflect the quality of performance. For individual fins there are two commonly used measures of performance: the fin efficiency (Harper and Brown, 1992; Gardner, 1945) and fin effectiveness (Gardner, 1942; Kern and Kraus, 1972; Incropera and DeWitt, 1990). Unfortunately Harper and Brown (1922) used the term "effectiveness" to describe what is now known as "efficiency." Both measures result from analyzing a decoupled mathematical description of the heat flow from the source to the sink. In practice they reflect the relative amount of heat flow through the fin and are based on the assumption of a one-dimensional analysis. To estimate the total heat flow across an assembly, either the efficiency or the effectiveness can be combined with the heat flow from those parts of the primary surface that are not supplemented by the extended surface. A sum of resistances approach is then used and the rate of heat flow is obtained from the formula

$$\text{Rate} = \frac{\text{Driving force}}{\text{Total resistance}}. \tag{1}$$

More recently, two further performance indicators have been proposed for the assessment of assemblies: the augmentation factor (Heggs and Stones, 1980) and the enhancement factor (Manzoor et al., 1983). These are obtained from a mathematical representation of the complete assembly. The enhancement factor incorporates the fin spacing whereas the augmentation factor depends upon the geometry of the entire assembly and its associated thermal properties.

It is the purpose here to extend the study of Wood et al. (1995) to include both a quantitative and a qualitative assessment of the four performance indicators with respect to the heat flow through the entire fin assembly. The effectiveness and efficiency do not take into account the effects of the primary surface, the enhancement factor does include the effect of fin spacing, but only the augmentation factor is based on the complete assembly. Such a comparison has not been published previously.

The present investigation is illustrated using the assembly shown in Fig. 1. Wood et al. (1995) focused on temperature profiles and heat transfer rates and established that it is feasible to allow heat flow from the fin tip (diabatic condition) rather than the unrealistic perfectly insulated fin tip (adiabatic condition). Further, to predict the operation of assemblies, the use of isolated fins was shown to be totally inappropriate when evaluating heat transfer rates. Previous discussions (Manzoor et al., 1983; Manzoor, 1984) suggest that the conclusions presented in this paper are equally applicable to fins of other geometries, such as those having triangular cross sections, annular fins, and pin fins.

2 Model Descriptions

Consider the steady-state heat flow through a heat exchanger consisting of a plane wall with an attached rectangular fin, both of uniform cross-sectional area as discussed by Stones (1980), and shown in Fig. 1(*a*). It is assumed that most conductive heat flow takes place in a direction perpendicular to the wall surface $X = 0$ (Fig. 1(*b*)). The temperature distributions in the wall and fin are governed by

$$\frac{d^2T_w}{dX^2} = 0, \quad 0 \le X \le D, \tag{2}$$

$$W\lambda_f \frac{d^2T_f}{dX^2} - 2\alpha_a(T_f - T_a) = 0, \quad D \le X \le D + H, \tag{3}$$

subject to convective and conductive boundary conditions describing heat transfer from all the exposed surfaces and from the interface of the wall and fin. The fin tip, at $X = D + H$, has a diabatic surface heat transfer condition. Mathematically the appropriate surface and wall-fin interface conditions are described by the following equations:

$$\alpha_b(T_b - T_w) = -\lambda_w \frac{dT_w}{dX}, \quad \text{at} \quad X = 0, \tag{4}$$

$$T_w = T_f, \; -\lambda_w P \frac{dT_w}{dX} = \alpha_a S(T_w - T_a) - \lambda_f W \frac{dT_f}{dX}, \quad \text{at} \quad X = D, \tag{5}$$

[1] On leave from CASPAM, Bahauddin Zakariya University, Multan, Pakistan; now deceased.

Contributed by the Heat Transfer Division for publication in the JOURNAL OF HEAT TRANSFER. Manuscript received by the Heat Transfer Division June 1995; revision received November 1995. Keywords: Augmentation and Enhancement, Finned Surfaces, Heat Exchangers. Associate Technical Editor: T. J. Rabas.

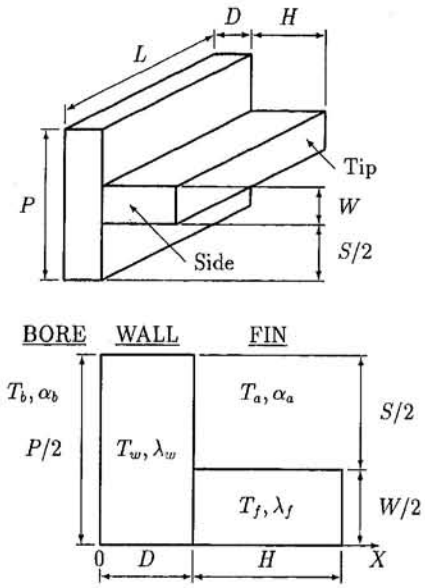

Fig. 1 (*a*) Wall and extended surface and (*b*) one-dimensional domain

$$-\lambda_f \frac{dT_f}{dX} = \alpha_a(T_f - T_a), \quad \text{at} \quad X = D + H. \tag{6}$$

It is convenient to use certain dimensionless parameters to express the assembly's characteristics. These are the Biot numbers

$$\mathrm{Bi}_{11} = \frac{\alpha_b P}{\lambda_w}, \quad \mathrm{Bi}_{21} = \frac{\alpha_a P}{\lambda_w}, \quad \mathrm{Bi}_{22} = \frac{\alpha_a P}{\lambda_f}, \tag{7}$$

where $P = W + S$ is the *fin pitch,* and the aspect ratios

$$l = \frac{L}{P}, \quad \nu = \frac{H}{P}, \quad \gamma = \frac{S}{P}, \quad \delta = \frac{D}{P} \tag{8}$$

for the fin length, fin height, fin spacing, and wall thickness, respectively. The pitch is the appropriate scaling length used for assemblies, because it defines the number of fins per unit length of the wall. This permits the effect of varying S (or W) with P fixed to be studied. Introducing the scaling $x = X/P$ and the normalized dimensionless temperatures

$$\theta_w = \frac{T_w - T_a}{T_b - T_a}, \quad \theta_f = \frac{T_f - T_a}{T_b - T_a} \tag{9}$$

a nondimensional heat transfer model is then given by

$$\frac{d^2\theta_w}{dx^2} = 0, \quad 0 \le x \le \delta, \tag{10}$$

$$\frac{d^2\theta_f}{dx^2} - \frac{2\,\mathrm{Bi}_{22}}{1-\gamma}\theta_f = 0, \quad \delta \le x \le \delta + \nu, \tag{11}$$

$$\mathrm{Bi}_{11}(1 - \theta_w) = -\frac{d\theta_w}{dx}, \quad \text{at} \quad x = 0, \tag{12}$$

$$\theta_w = \theta_f, \; -\Lambda \frac{d\theta_w}{dx} = \mathrm{Bi}_{22}\gamma\theta_w - (1-\gamma)\frac{d\theta_f}{dx}, \quad \text{at} \quad x = \delta, \tag{13}$$

$$-\frac{d\theta_f}{dx} = \mathrm{Bi}_{22}\theta_f, \quad \text{at} \quad x = \delta + \nu, \tag{14}$$

where $\Lambda = \lambda_w/\lambda_f$. It is assumed here that the ratio l is sufficiently large for the heat loss from the side faces to be ignored.

The analytic solutions of Eqs. (10)–(14) can be written as

$$\theta_w = ax + b, \tag{15}$$

$$\theta_f = ce^{\mu x} + de^{-\mu x}, \tag{16}$$

where the constants a, b, c, and d are given by

$$a = \frac{(1-\gamma)\mu\xi_\phi - \mathrm{Bi}_{22}\gamma}{\Lambda - [(1-\gamma)\mu\xi_\phi - \mathrm{Bi}_{22}\gamma]\psi}, \quad b = 1 + \frac{a}{\mathrm{Bi}_{11}},$$

$$c = \frac{(1 + a\psi)e^{-\mu\delta}}{1 + \phi e^{2\mu\nu}}, \quad d = \phi e^{2\mu(\delta+\nu)}c, \tag{17}$$

and

$$\mu^2 = \frac{2\,\mathrm{Bi}_{22}}{1-\gamma}, \quad \phi = \frac{\mu + \mathrm{Bi}_{22}}{\mu - \mathrm{Bi}_{22}},$$

$$\xi_\phi = \frac{1 - \phi e^{2\mu\nu}}{1 + \phi e^{2\mu\nu}}, \quad \psi = \delta + \frac{1}{\mathrm{Bi}_{11}}. \tag{18}$$

It is important to note that ξ_ϕ is a grouping common to all four performance indicators.

Fin Effectiveness. The fin heat transfer rate, $\dot{Q}_f$, is the quantity of heat flowing through the fin, from the primary surface, and must pass through its base:

$$\dot{Q}_f = -\lambda_f A_{\text{base}} \left.\frac{dT_f}{dX}\right|_{X=D}, \tag{19}$$

where $A_{\text{base}} = WL$ is the base area of the fin. The fin effectiveness, ζ_f, is defined as

$$\zeta_f = \frac{\text{Fin heat transfer rate}}{\text{Heat transfer rate without fin}} = \left.\frac{\dot{Q}_f}{\alpha_a A_{\text{base}}(T_f - T_a)}\right|_{X=D}, \tag{20}$$

and measures the additional heat flow through a surface region of the wall whose area is equal to that of the base of the fin

Nomenclature

AUG = augmentation factor
Bi_{11}, Bi_{21}, Bi_{22} = Biot numbers; see Eq. (7)
D = wall thickness, m
H = fin height, m
L = fin length, m
l = fin length aspect ratio
P = fin pitch $W + S$, m
$\dot{Q}$ = heat transfer rate, W
S = interfin spacing, m
T = temperature, °C
W = fin thickness, m
X = distance, m
x = dimensionless distance
α = surface heat transfer coefficient, W/m² K
γ = fin spacing aspect ratio
δ = wall thickness aspect ratio
ϵ = enhancement factor
ζ = fin effectiveness
η = fin efficiency
θ = dimensionless temperature
λ = thermal conductivity, W/m K
μ = constant; $\mu^2 = 2\mathrm{Bi}_{22}$
ν = fin height aspect ratio
ξ_ϕ = constant, see Eq. (18)
ϕ = constant, see Eq. (18)
ψ = constant, see Eq. (18)
Ω = thermal resistance, K/W

Subscripts

a = air (sink-side)
b = bore (source-side)
f = fin
w = wall

and whose temperature is equal to the base temperature of the (isolated) fin. It then follows from Eqs. (9), (16), (19), and (20) that

$$\zeta_f = -\frac{\mu\xi_\phi}{\mathrm{Bi}_{22}} = \frac{\mu}{\mathrm{Bi}_{22}} \frac{\mu \tanh \mu\nu + \mathrm{Bi}_{22}}{\mathrm{Bi}_{22}\mu + \mathrm{Bi}_{22} \tanh \mu\nu} \tag{21}$$

which is recognized as being the effectiveness for an isolated diabatic fin (Gardner, 1942). This validates the previous assertion that ζ_f does *not* include wall effects. The ratio γ is involved via μ and represents the effect of varying the fin thickness W (for fixed pitch P).

Fin Efficiency. A further measure of fin performance is the fin efficiency, η_f, which is defined as (Harper and Brown, 1922; Gardner, 1945)

$$\eta_f = \frac{\text{Heat dissipated by fin}}{\text{Heat dissipated by fin at base temperature}} = \left.\frac{\dot{Q}_f}{\alpha_a A_{\mathrm{sur}}(T_f - T_a)}\right|_{X=D}. \tag{22}$$

$A_{\mathrm{sur}} = (2H + W)L$ is the total surface area of the diabatic fin contributing toward convective heat transfer. Using Eqs. (9), (16), (19), and (22) we find that

$$\eta_f = -\frac{\mu\xi_\phi}{\mu^2\nu + \mathrm{Bi}_{22}} = \left(\frac{1-\gamma}{2\nu + 1 - \gamma}\right)\zeta_f. \tag{23}$$

It is clear from Eq. (23) that η_f is related to the fin characteristics only, with no reference to any wall effects. ξ_ϕ can be thought of as a "scaling" factor. For an adiabatic tip condition the terms Bi_{22} in the expression for ϕ are absent. The term μ remains since it describes the heat loss from the upper and lower faces of the fin. In this case $\phi = 1$ and so $\xi_\phi \to \xi_1 = (1 - e^{2\mu\nu})/(1 + e^{2\mu\nu})$. The ratio ξ_ϕ/ξ_1 expresses the importance of considering a diabatic tip in place of an adiabatic tip. If the ratio is close to unity then there is little to be gained by modeling a diabatic tip. If, however, the ratio is much greater than unity, then the diabatic tip will play a significant role in the transfer of heat and must be incorporated into the model to avoid misleading results.

The ratio

$$\frac{\zeta_f}{\eta_f} = \frac{2\nu + 1 - \gamma}{1 - \gamma} \tag{24}$$

increases indefinitely as H (or ν) increases, for fixed width W (or γ) $-$ P is fixed. In this case $\nu \to \infty$, $\xi_\phi \to -1$ and the effectiveness asymptotes to the value $\sqrt{2/((1-\gamma)\mathrm{Bi}_{22})}$ whereas the efficiency reduces to zero.

Augmentation Factor. Both the effectiveness and efficiency are defined for an isolated fin, yet implicit in the use of extended surfaces is a *primary* surface, the wall. It is desirable to have indicators that measure changes in heat transfer when a fin is attached to a wall. One such practical indicator of an assembly's performance is the augmentation factor (Heggs and Stones, 1980), which measures the increase in heat flow obtained by attaching fins to a wall. Equivalently, it can be described as the potential reduction in size of a heat exchanger when combined with the fin assembly under investigation. It is defined as

$$\mathrm{AUG} = \frac{\text{Heat flow between fluids separated by finned primary surface}}{\text{Heat flow between fluids separated by unfinned primary surface}} = \frac{\dot{Q}_{w+f}}{\dot{Q}_w} = \frac{\Omega_w}{\Omega_{w+f}}, \tag{25}$$

at *steady state* and accounts for the presence of the unfinned primary surface on the sink side *and* the physical characteristics of the primary surface (depth, conductivity, etc.). $\dot{Q}_w$ and $\dot{Q}_{w+f}$ are the heat transfer rates through an isolated primary surface and through an assembly, respectively, and Ω_w and Ω_{w+f} are the corresponding total thermal resistances. $\dot{Q}$ and Ω are related through Eq. (1).

A convenient way to quantify the augmentation factor is to consider an equivalent electrical circuit whose resistances are the thermal resistances of the conducting body. For heat transfer through a medium of thickness Δx and cross-sectional area A, perpendicular to the direction of heat flow, the conductive resistance is $\Delta x/\lambda A$, and the surface convection resistance is $1/\alpha A$. The total heat transfer rate between two fluids at temperatures T_b and T_a is then given by Eq. (1) as the driving force, $T_b - T_a$, divided by the total thermal resistance.

The assembly's thermal resistance is obtained by the above sum of resistances approach, applied to Fig. 1, and is given by

$$\Omega_{w+f} = \frac{1}{\alpha_b PL} + \frac{D}{\lambda_w PL} + \frac{1}{\alpha_a SL + \alpha_a \eta_f A_{\mathrm{sur}}}. \tag{26}$$

The thermal resistance of the wall is

$$\Omega_w = \frac{1}{\alpha_b PL} + \frac{D}{\lambda_w PL} + \frac{1}{\alpha_a PL}. \tag{27}$$

Substitution of these expressions into Eq. (25) yields the formula

$$\mathrm{AUG} = \left[\frac{1}{\mathrm{Bi}_{11}} + \delta + \frac{1}{\mathrm{Bi}_{21}}\right] \Bigg/ \left[\frac{1}{\mathrm{Bi}_{11}} + \delta + \frac{1}{\mathrm{Bi}_{21}}\left(\frac{1}{\gamma - \frac{2}{\mu}\xi_\phi}\right)\right]. \tag{28}$$

Enhancement Factor. The term enclosed in parentheses in Eq. (28) was described by Manzoor et al. (1983) as the enhancement factor, ϵ_f, and is the component of the augmentation factor that solely contains the fin characteristics, including the fin spacing. Whereas AUG is concerned with the heat transfer of an *assembly*, ϵ_f can only quantify the effects upon the assembly's heat transfer rate of varying the fin parameters alone. It is found that

$$\epsilon_f = \frac{1}{\gamma - \frac{2}{\mu}\xi_\phi} = \frac{1}{\gamma + (1-\gamma)\zeta_f} = \frac{1}{\gamma + (2\nu + 1 - \gamma)\eta_f}. \tag{29}$$

3 Results and Discussion

The results of various illustrative simulations are presented in this section with attention focused on a comparison of the behavior of the four performance indicators. Dimensional data given by Stones (1980), which are typical of mild steel double-pipe heat exchangers with longitudinal fins, are used: D = 0.00368 m, H = 0.0127 m, W = 0.00089 m, L = 24 m, S = 0.00539 m, and $\lambda_w = \lambda_f$ = 45 W/m K. The heat transfer coefficients are α_b = 1343 W/m^2 K and α_a = 533 W/m^2 K and the external temperatures are taken to be T_b = 121°C and T_a = 26°C. The use of a model based on Cartesian coordinates is justified in this case, because the thickness of the pipe is small in comparison to the inside radius.

Table 1 Values of performance indicators for isolated fins and fin assemblies

	Isolated Fin		Fin Assembly	
	Ad.	Diab.	Ad.	Diab.
ζ_f	13.344	13.401	13.344	13.401
η_f	0.468	0.454	0.468	0.454
AUG			1.791	1.794
ϵ_f			0.364	0.363
$\dot{Q}_{w+f}$ (kW)	2.292	2.294	9.490	9.503
$\dot{Q}_f$ (kW)	2.292	2.294	6.528	6.545

Table 1 shows the values of the performance indicators for an assembly of mild steel components with a diabatic and an adiabatic tip, and also for isolated fins for comparison. The analytical results for these can be deduced from the work of Wood et al. (1995). All four indicators distinguish between adiabatic cases and diabatic cases. When an adiabatic tip is replaced by a diabatic tip the fin efficiency, η_f, and enhancement factor, ϵ_f, both decrease while the effectiveness, ζ_f, and augmentation factor, AUG, both increase. The increase in AUG occurs because the thermal resistance of the assembly is reduced by the addition of the convective surface area of the tip, leading to an increase in the assembly's heat transfer rate. Equation (29) implies the consequent decrease in the enhancement factor. The effectiveness, ζ_f, rises solely as a result of the increased fin heat transfer rate, $\dot{Q}_f$ (see Eq. (20)), whereas the efficiency, η_f, decreases due to an enhanced maximum heat transfer rate (see the denominator of Eq. (22)). Thus the desirable effect of a higher total heat transfer rate with a diabatic condition ($\dot{Q}_{w+f}$ in Table 1) is correctly indicated by the increases in ζ_f and AUG but would be vetoed if either η_f or ϵ_f was the arbiter of the assembly's performance. Further, although the trends of ζ_f and AUG are similar, it is the value of AUG that provides an *absolute* measure of the improvement in attaching a fin, while ζ_f is only a *relative* measure. When dimension changes are investigated, clear distinctions between ζ_f and AUG become apparent.

Table 2 shows the effect that altering the fin material has on the effectiveness, efficiency, and enhancement factor, for the diabatic situation. The values shown hold no matter what wall dimensions or thermal properties are used. The thermal conductivities used, in W/m K, are 385 (copper), 201 (aluminium), 110 (brass), 45 (mild steel), and 16 (stainless steel). Both the effectiveness ζ_f and efficiency η_f decrease as λ_f is reduced as a result of a reduced fin heat transfer rate. The enhancement factor ϵ_f increases with decreasing λ_f, which is a counterproductive indication. This indicates that the fin is providing a greater proportion of the heat flow in a trend of diminishing total heat transfer.

Table 3 shows the effect that different wall-fin material combinations have on the augmentation factor. A scaled augmentation factor is used, normalized with respect to that of a mild steel assembly. Clearly, the augmentation factor is affected by changes in the wall parameters. It is, however, the fin that exerts

Table 2 Effect of fin material (thermal conductivity λ_f) on fin performance

Material	ζ_f	η_f	ϵ_f
Copper	25.182	0.853	0.226
Aluminium	22.349	0.757	0.248
Brass	18.932	0.641	0.282
Mild Steel	13.402	0.454	0.363
Stainless Steel	8.201	0.278	0.495

Table 3 Effect of assembly material combination on augmentation factor, normalized to a mild steel assembly

FIN / WALL	C	A	B	MS	SS
Copper (C)	1.25	1.20	1.14	1.02	0.87
Aluminium (A)	1.24	1.20	1.14	1.02	0.87
Brass (B)	1.23	1.19	1.13	1.02	0.87
Mild Steel (MS)	1.21	1.17	1.11	1.00	0.86
Stainless Steel (SS)	1.14	1.10	1.06	0.96	0.84

the most significant influence on AUG. In the case of a reduced wall conductivity, AUG behaves according to

$$\frac{\lambda_w c_1 + \delta}{\lambda_w (c_1 + c_2) + \delta}, \tag{30}$$

where $c_1 = 1/\alpha_b P + 1/\alpha_a P$ and $c_2 = (\epsilon_f - 1)/\alpha_a P$ are constants, which are independent of λ_w and $c_1 + c_2 > 0$. If $c_2 < 0$, then the thermal resistance of the wall decreases more rapidly than the thermal resistance of the assembly, hence reducing the augmentation factor. This effect occurs if $\eta_f > 1/(2\nu + 1)$, which is the case for most fin sizes. The AUG-λ_f dependence is more complicated since η_f is dependent upon λ_f; see Eqs. (25), (26), (27), and (28).

Figures 2–8 illustrate the effects on the performance indicators and heat transfer rates caused by variations in each of the parameters of the complete assembly. A more concise summary of how the performance indicators reflect the quality of performance, that is overall heat flow through the assembly, is given in Table 4.

Height ν (or H). Both ζ_f and AUG increase with ν while η_f and ϵ_f both decrease (see Fig. 2). The behavior of ζ_f and AUG is similar with both variables correctly describing the trend of increasing total heat flow $\dot{Q}_{w+f}$ (see Table 4) and asymptoting as ν approaches 3 (for these data). The asymptotic behavior indicates that the heat transfer rates are saturated. The efficiency η_f follows a significant downward trend as ν increases indicating that, pro rata, an increasing fin surface area results in a diminishing increase in heat transfer. The reason is that by increasing ν (or H) we are not increasing the area of the base of the fin, A_{base}, through which all heat flowing through the fin must pass. Any increase in $\dot{Q}_f$ is due solely to a modified fin base temperature T_{base}, which manifests itself in Eq. (19).

Spacing γ (or S) or Fin Thickness (W). When assessing the effect of the fin spacing (see Fig. 3) on the characteristics of the assembly, it is important to be aware exactly what length parameters are being varied. Varying γ by simply altering S will also change the *pitch* $P = W + S$. In this case the total sink side area of the primary surface being serviced by the fin is also changing. Thus, it is important to maintain a fixed pitch.

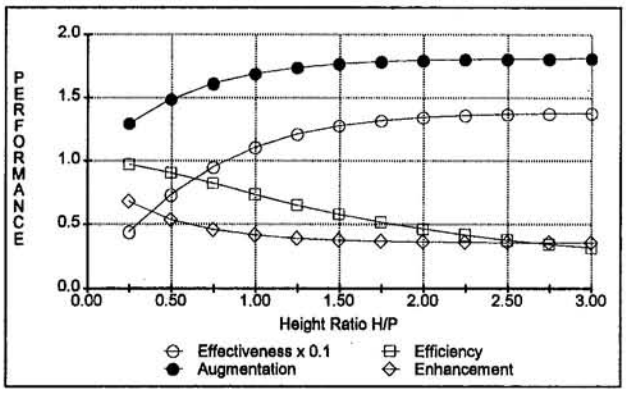

Fig. 2 Fin performance as a function of fin height ν

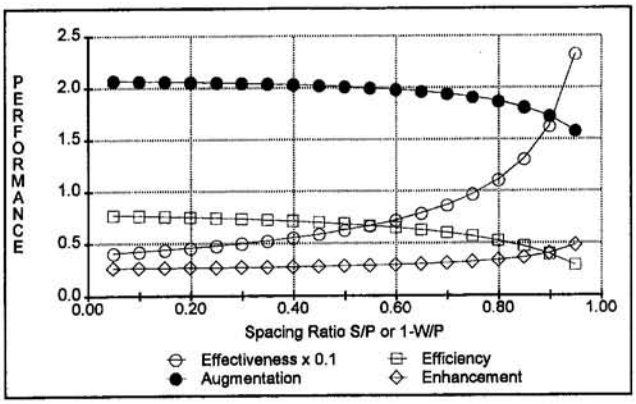

Fig. 3 Fin performance as a function of fin spacing γ for fixed pitch P

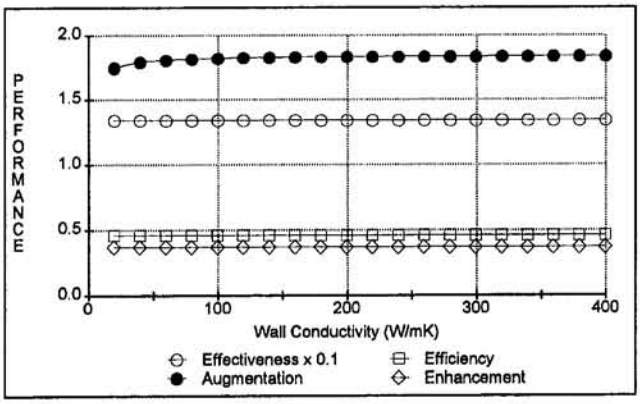

Fig. 5 Fin performance as a function of wall conductivity λ_w

Hence changing γ will also indicate the effects of changing W for a fixed pitch, i.e., $W = P - S$. At this point it must be stressed that the effectiveness and efficiency, shown on Fig. 3, are not changing in response to the varying spacing—this would contradict the assertion that these indicators depend solely upon fin properties. Their variation results from the fact that for a fixed pitch then changing the spacing S automatically alters the fin thickness W.

When $\gamma = 0$ there is no spacing (and so the model in this paper is inappropriate). When $\gamma = 1$ there is no fin, $W = 0$. It is therefore assumed that $0 < \gamma < 1$. As γ increases (increasing S for fixed pitch) so the total heat flow through the assembly decreases (see Table 4), which is correctly described by both the augmentation factor and the efficiency. This reflects the fact that the decrease in the sink side convective thermal resistance of the wall is more than offset by the increasing conductive thermal resistance of the fin (because of a decreasing cross-sectional area). Both effectiveness and enhancement increase, which simply reflects the fact that for increased spacing (decreased fin width) the temperature drop along the fin is reduced.

Wall Thickness δ (or D). Figure 4 illustrates the behavior of the performance indicators as the wall thickness is altered. It is manifestly evident that all the indicators remain constant with the exception of the augmentation factor. In other words it is only AUG that describes the behavior of the complete assembly. Naturally we would expect AUG to decrease as D increases since then the thermal resistance of the wall is increasing. For a fixed driving force, $T_b - T_a$, the total heat transfer rate is then decreasing (see Table 4), which is correctly described by AUG.

Thermal Conductivity. Figures 5 and 6 show the assembly's response to different material thermal conductivities in the wall and fin, respectively. The trends are entirely predictable. Increasing the wall conductivity λ_w increases the total heat flow $\dot{Q}_{w+f}$ and hence the fin heat transfer rate $\dot{Q}_f$, since the percentage of heat flowing through the fin will remain constant. This increase is only reflected by the augmentation factor (see Fig. 5), all other indicators remaining constant. The asymptotic nature of the augmentation curve simply indicates that as the wall conductivity is increased sufficiently, the convective thermal resistances of both the source and sink sides become the rate limiting factors.

The trend of increasing heat flow is also illustrated in Fig. 6 as the fin thermal conductivity λ_f increases. Once again we are reducing the overall thermal resistance of the assembly, which must increase the heat transfer rate. This trend is reflected by all indicators except the enhancement, which is simply stating that incremental changes in conductivity for an increasingly thermally conductive material will have a decreasing relative effect on the system. This can also be observed in the asymptotic nature of the augmentation curve for these particular system dimensions.

Surface Heat Transfer Coefficient. Figures 7 and 8 illustrate the dependence of the performance indicators upon the surface heat transfer coefficients α_a and α_b.

Considering first α_a, Fig. 7 shows that AUG is monotonically decreasing toward unity as α_a increases, which indicates a diminishing increase in heat transfer rate $\dot{Q}_{w+f}$. As α_a is decreased below the lower "reference" value 533 W/m^2 K, so AUG rapidly increases (roughly in line with α_a^{-1}). In this case the controlling (dominant) resistance to the flow of heat occurs at the sink side of the heat transfer assembly and adding fins will have a significant effect on the heat transfer rate, as is clearly described by AUG. The message is "put fins where the resistance is highest." While the efficiency and effectiveness also

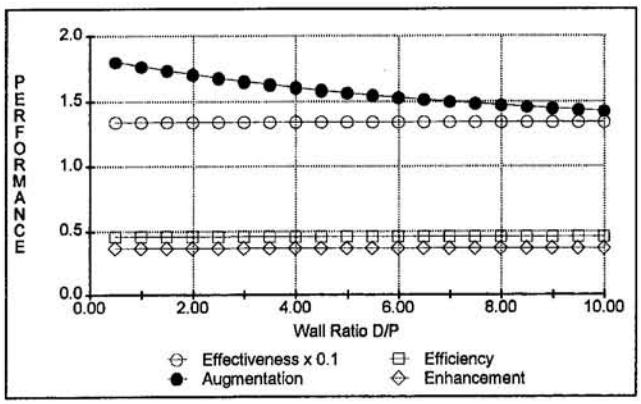

Fig. 4 Fin performance as a function of wall thickness δ

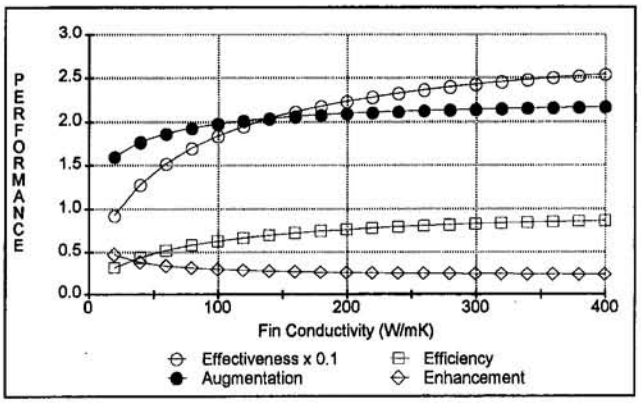

Fig. 6 Fin performance as a function of fin conductivity λ_f

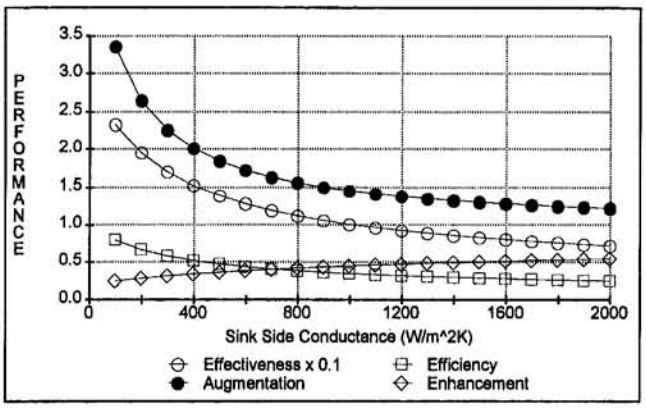

Fig. 7 Fin performance as a function of sink side surface heat transfer α_a

Table 4 Performance indicator trends as functions of primary assembly influencing variables, for fixed pitch P; arrows in boxes denote correctly predicted trends

Trend of	on increasing							
	H	W	S	D	λ_w	λ_f	α_b	α_a
$\dot{Q}_{w+f}$	↑	↑	↓	↓	↑	↑	↑	↑
$\dot{Q}_f$	↑	↑	↓	↓	↑	↑	↑	↑↓
$\dot{Q}_w$	-	-	-	↓	↑	-	↑	↑
ζ_f	[↑]	↓	↑	-	-	[↑]	-	↓
η_f	↓	[↑]	[↓]	-	-	[↑]	-	↓
AUG	[↑]	[↑]	[↓]	[↓]	[↑]	[↑]	[↑]	↓
ϵ_f	↓	↓	↑	-	-	↓	-	[↑]
B_{11}					↓	-	↑	-
B_{21}					↓	-	-	↑
B_{22}					-	↓	-	↑

indicate similar conclusions, the enhancement is obviously a poor measure of performance, exhibiting a decreasing trend (as α_a decreases), which could be erroneously interpreted as a decreasing assembly performance.

The most striking observation to be made from Fig. 8 is that changes in the source side heat transfer coefficient α_b are only reflected by AUG. The other three indicators remain fixed. Clearly, changing α_b *will* alter the significance of adding one or more fins to a heat transfer assembly, yet the traditional indicators of efficiency and effectiveness do not address this fact, a defect shared by the enhancement. As α_b decreases, so AUG decreases, which indicates that the source side thermal resistance is becoming dominant. In this case the addition of fins to the sink side will not tackle the region of highest resistance and, consequently, will not substantially enhance the heat transfer rate, a fact that is mirrored precisely by AUG. As α_b increases significantly above the upper "reference" value of 1343 W/m^2 K so AUG increases. In this case the sink side resistance starts to dominate the source side resistance and so the benefit of adding fins to the sink side is increased significantly.

We conclude with a note concerning the column headed α_a in Table 4. As the sink side surface conductance increases, the augmentation factor decreases monotonically. This might be rather misleading in that the total heat transfer rate, $\dot{Q}_{w+f}$, is increasing. From Fig. 9 it is clear that the wall heat transfer rate, $\dot{Q}_w$, increases with α_a and AUG is simply the ratio $\dot{Q}_{w+f}/\dot{Q}_w$. Increasing α_a will always *increase* the heat flow rate through a wall or assembly since a component of the total thermal resistance is being decreased. AUG is a measure of the *improvement* afforded to the heat transfer properties of a primary surface by the addition of a fin. For large values of α_a the behavior of AUG is simply stating that there will be a diminishing increase in $\dot{Q}$ since the sink side thermal resistance will no longer be the controlling factor.

4 Conclusions

The results presented in the previous section have illustrated the differences between the four performance indicators ζ_f, η_f, AUG, and ϵ_f. In particular this assessment has confirmed the preconceived notion that the effectiveness and efficiency take no account of primary surface effects, with the exception of the spacing S, which is intrinsically linked to the fin width W, and the augmentation factor takes account of wall *and* fin effects, through both dimensional and material property changes.

For the primary parameters investigated, namely the dimensions H, S (or W), and D, the material properties λ_w and λ_f, and the ambient parameters α_b and α_a, only the augmentation factor correctly describes the behavior of the heat transfer rates. Table 4 summarizes the results. AUG allows a definitive measure of assembly performance and a genuine comparison between competing fin specifications. Manufacturers have implicitly been using this idea for some time in their characterization data for fins. The usual data supplied are ratios of $\dot{Q}$. Since AUG is simply a ratio of $\dot{Q}$ values, then listing values of the augmentation factor provides the same information. The added advantage is that AUG is a scaling factor and so can be used to compare, at a glance, the relative merits of a selection of fin assemblies.

Acknowledgments

M. I. H. Bhatti was funded through an Overseas Development Administration link project between the University of Bradford

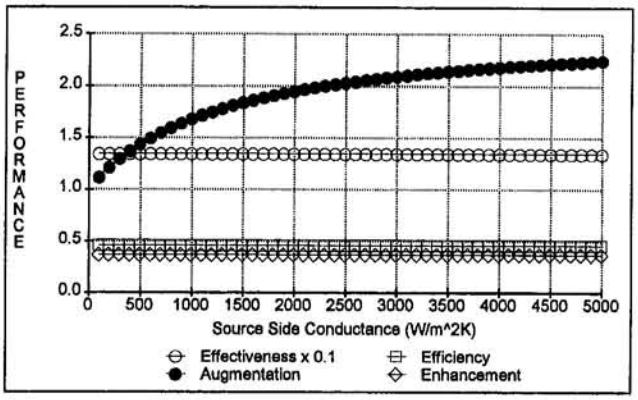

Fig. 8 Fin performance as a function of source side surface heat transfer α_b

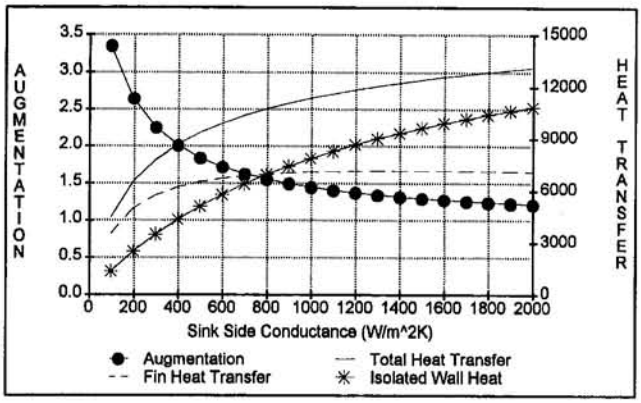

Fig. 9 Assembly performance and constituent heat transfer rates as functions of sink side surface heat transfer α_a

and Bahauddin Zakariya University, Multan, Pakistan. Sadly he and most of his family were tragically killed in a recent automobile accident in Pakistan while the manuscript of this paper was in preparation.

References

Gardner, K. A., 1942, "Heat Exchanger Tube Sheet Temperatures," *Refiner Nat. Gas. Manu.*, Vol. 21, pp. 71–77.

Gardner, K. A., 1945, "Efficiency of Extended Surface," ASME JOURNAL OF HEAT TRANSFER, Vol. 67, pp. 621–631.

Harper, D. R., and Brown, W. B., 1922, "Mathematical Equations for Heat Conduction in the Fins of Air-Cooled Engines," NACA Report No. 158.

Heggs, P. J., and Stones, P. R., 1980, "Improved Design Methods for Finned Tube Heat Exchangers," *Trans. IChemE*, Vol. 58, pp. 147–154.

Incropera, F. P., and DeWitt, D. P., 1990, *Fundamentals of Heat and Mass Transfer*, 3rd ed., Wiley, New York.

Kern, D. Q., and Kraus, A. D., 1972, *Extended Surface Heat Transfer*, McGraw-Hill, New York.

Manzoor, M., Ingham, D. B., and Heggs, P. J., 1983, "The One-Dimensional Analysis of Fin Assembly Heat Transfer," ASME JOURNAL OF HEAT TRANSFER, Vol. 105, pp. 646–651.

Manzoor, M., 1984, *Heat Flow Through Extended Surface Heat Exchangers*, Lecture notes in Engineering, Springer-Verlag, Berlin.

Stones, P. R., 1980, "Effects of Dimensions on the Heat Flowrate Through Extended Surfaces," Ph.D. Thesis, Univ. Leeds, United Kingdom.

Wood, A. S., Tupholme, G. E., Bhatti, M. I. H., and Heggs, P. J., 1995, "Steady-State Heat Transfer Through Extended Plane Surfaces," *Int. Comms. Heat Mass Transfer*, Vol. 22, pp. 99–109.

S. P. Kearney
Graduate Research Assistant.
Student Mem. ASME

A. M. Jacobi
Assistant Professor of Mechanical Engineering,
Assoc. Mem. ASME

Department of Mechanical and Industrial Engineering,
University of Illinois at Urbana–Champaign,
Urbana, IL 61801

Local Convective Behavior and Fin Efficiency in Shallow Banks of In-Line and Staggered, Annularly Finned Tubes

Local mass transfer data for high-profile fins in the second row of in-line and staggered, circular-finned tubes are presented for Reynolds numbers from 5000 to 28,000 based on hydraulic diameter and velocity at the minimum flow area. The data, obtained using an optical adaptation of the naphthalene sublimation technique, show that local variations in heat transfer do not cause significant fin efficiency deviations from the analytical solution of Gardner (contrary to earlier reports). Average heat transfer and pressure drop data indicate that the thermal performance of the in-line arrangement is comparable to the staggered configuration.

Introduction

Because of its relative simplicity, maturity, and wide applicability, the circular-finned tube is of special interest as a heat exchanger geometry. Notwithstanding extensive research, aspects of the local flow and heat transfer in this geometry remain unclear. A complete understanding of local transport and its relation to fin efficiency and overall bundle performance could lead to more efficient heat exchanger designs; furthermore, understanding local effects in this relatively simple geometry may cultivate a clearer understanding of flow and heat transfer in more complex heat exchanger passages.

Local heat transfer from a circular-finned tube in a simulated bank of staggered tubes was studied by Neal and Hitchcock (1966). Using thermocouples on the fin surface, they found that local Nu variations resulted in roughly a 16 percent decrease in fin efficiency from the constant Nusselt number case. Unfortunately, conventional thermocouples disturb the flow and heat transfer, and only limited spatial resolution can be obtained with this method. Zukauskas et al. (1966) used a point-heating method to study local heat transfer on circular fins, but this method imposes unrealistic thermal boundary conditions (see Stasiulevicius and Skrinska, 1988; Hu and Jacobi, 1993). Krückels and Kottke (1970) used a mass transfer method to provide high-resolution local data for a single finned tube in crossflow. They reported convection coefficients that differ by roughly 100 percent from a similar heat transfer study (see results of Legkiy et al., 1974); the reason for the disagreement is unclear. Local heat transfer for a single row of finned tubes was studied by Hu and Jacobi (1993) using the nonintrusive naphthalene sublimation technique. They provided a detailed description of flow and heat transfer interactions for Reynolds numbers from 3300 to 12,000, as summarized in Fig. 1. Hu and Jacobi also reported that variations in the local Nusselt number decreased the fin efficiency.

The average (overall) performance of circular-finned tubes in deep bundles has been studied extensively, and thorough reviews of the topic are available (see Webb, 1980; Nir, 1991); several articles closely related to the current research have appeared. From experiments with staggered finned-tube banks, Briggs and Young (1963) developed a widely used heat transfer correlation, valid for Re_d from 1100 to 1800, where Re_d is the Reynolds number based on bare tube diameter and velocity at the minimum free flow area. A study by Schmidt (1988) considered staggered- and in-line-tube arrangements with Re_d from 1000 to 40,000. Zukauskas (1988) presented Nusselt number and friction factor correlations valid for staggered-tube arrangements with Re_d from 20,000 to 1.3×10^6. Their correlations account for the effects of fin height, fin spacing, and tube pitch. Zukauskas and co-workers (1966) used their overall heat transfer measurements to infer that local variations in heat transfer decreased the fin efficiency.

Shallow bundles of circular tubes, with five or fewer tube rows, have been studied by Goldschmidt and co-workers. They considered a two-row in-line-tube arrangement and provided heat transfer and friction factor correlations valid for Reynolds numbers from 160 to 1600 (Idem et al., 1987, 1990). Sparrow and Samie (1985) compared the performance of two-row, in-line, and staggered banks of annularly finned tubes, reporting the effects of longitudinal and transverse tube spacing for Re_d from 7500 to 32,000 based on approach velocity. A study of bundle-depth effects on heat transfer performance was presented by Yudin et al. (1988) for Re_d from 1000 to 20,000. The overall heat transfer was found to decrease with bundle depth for in-line-tube arrangements and increase with depth for staggered-tube arrangements. These results were recently confirmed in a study of bundle arrangement effects reported by Kuntysh and Stenin (1993). Based on row-by-row measurements in a four-row bundle, they found that an arrangement somewhere between staggered and in-line provided the highest heat transfer rate. Unfortunately, since fin efficiency was not considered in their study, it is difficult to compare their results to correlations from the literature.

In this article we will describe an optical adaptation of the naphthalene sublimation technique that provides mass transfer measurements with a very high spatial resolution. This method was used to obtain local mass transfer data for circular-finned tubes in staggered and in-line two-row bundles over a Reynolds number range from 5000 to 28,000 ($2(10^4) < Re_d < 1.2(10^5)$). These local data are used in conjunction with the single-row results of Hu and Jacobi (1993) to develop a complete picture of the local Nusselt number distribution in the first two rows of in-line and staggered bundles. After presenting the local measurements, we will use the data to assess the impact of flow and heat transfer interactions on fin efficiency and bundle performance. Spatially averaged heat transfer results will be

Contributed by the Heat Transfer Division for publication in the JOURNAL OF HEAT TRANSFER. Manuscript received by the Heat Transfer Division August 1995; revision received February 1996. Keywords: Finned Surfaces, Measurement Techniques, Heat Exchangers. Associate Technical Editor: S. H. Chan.

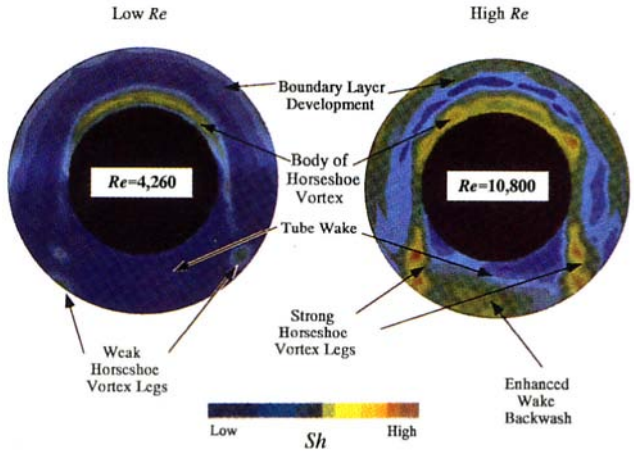

Fig. 1 Typical Sherwood number distributions for the first row of an annularly finned tube bank for high (Re > 8800) and low Reynolds numbers. The influence of local flow structures is shown (Hu and Jacobi, 1993).

presented along with pressure drop data, and correlations for the Nusselt number and the Euler number will be presented. By comparing the results of this research to previous work, the effects of fin height and tube arrangement on bundle performance will be clarified, and contradictions with earlier reports of fin efficiency impact will be resolved.

Experimental Method

Description of the Apparatus. Mass transfer experiments were conducted in an open-loop wind tunnel; a detailed description of this apparatus has been provided by Kearney (1995) and Kearney and Jacobi (1995). Laboratory air entered the wind tunnel through screens and a honeycomb flow straightener with a 2.16 by 2.16 m cross section. Downstream of the inlet, the air flowed through a smooth 32:1 area contraction into a test section with a 381 by 381 mm cross section. From the test section, the flow passed through a diffuser to a 15 kW blower and was finally discharged through a long duct. Baseline measurements at the test section inlet indicated that the approach velocity profile was flat to within 5 percent, and the free-stream turbulence intensity was below 1 percent for approach velocities between 1 and 25 m/s.

The model heat exchanger, illustrated in Fig. 2, was constructed using aluminum tubes with an outside diameter, d_t, of 38.1 mm. The fins were 1.02 mm thick and had an outside diameter, d_f, of 76.2 mm; they were glued to the tubes at a fin pitch of 139 fins per meter. These circular-finned tubes were assembled in a staggered or in-line two-row bundle and placed in the test section as shown in Fig. 2. For both the staggered and in-line configurations, the transverse tube spacing, S_T, was 76.2 mm. The longitudinal tube spacing, S_L, was 76.2 mm for the in-line bundle and 66.0 mm for the staggered tube bank.

A single naphthalene fin, located in the center of a finned tube in the middle of the second row, served as a test specimen, and the other fins and tubes provided proper flow conditions. Several experiments with two neighboring naphthalene fins were conducted,[1] and the mass transfer results always agreed with the single-fin measurements to within the experimental uncertainty. This result implies that the local mass transfer was unaffected by mass transfer from neighboring fins in this Reynolds number range, and it justifies the use of a single test specimen for each experiment (see Kearney, 1995, for a full description of these auxiliary experiments).

Temperatures were recorded upstream of the finned tube bank and near the surface of the naphthalene fin using calibrated platinum RTDs; the measurement uncertainty was less than 0.1°C. Free-stream velocity was measured using an ANSI/ASHRAE pitot-static tube and an electronic manometer (0 to 500 Pa, ±0.12 Pa). Static pressure drop across the core was determined using a calibrated differential pressure transducer (0 to 1250 Pa, ±21 Pa). Pressure drop and temperature data were recorded at 333 Hz and averaged over the period of an experiment.

[1] We are indebted to Professor Mitrovic, Universität Stuttgart, for raising this issue in a personal correspondence in 1993.

Nomenclature

A = total heat transfer surface area
A_c = minimum free flow area of heat exchanger core
A_f = fin surface area
A_t = bare tube surface area
d_f = fin diameter
d_H = hydraulic diameter
d_t = bare tube diameter
D_{na} = binary diffusion coefficient for naphthalene in air
Eu = Euler number = $\Delta P/\rho_{a,w}U_c^2$
f = Fanning friction factor
h = heat transfer coefficient
h_m = mass transfer coefficient
I_n = modified Bessel function of the first kind of order n
k = thermal conductivity
K_n = modified Bessel function of the second kind of order n
Le = Lewis number = Pr/Sc
m = mass, square root of the fin parameter
m^2 = fin parameter = $2hr_b^2/k_f\delta$
Nu = Nusselt number
P = pressure
Pr = Prandtl number
q = heat flux
Q = heat transfer rate
r = radial coordinate
R = ratio of fin diameter to bare tube diameter = d_F/d_T
Re = Reynolds number = $U_c d_H/\nu$
s = fin spacing
S_L = longitudinal tube spacing
S_T = transverse tube spacing
Sc = Schmidt number
Sh = Sherwood number
T = temperature
t = time
U_c = velocity at minimum free flow area
$(\bar{\ })$ = surface-averaged quantity
δ = fin thickness
δ_{sh} = local sublimation depth
Δ = indicates change of a quantity during the experiment
η_f = fin efficiency
η_o = overall surface efficiency
θ = dimensionless temperature = $(T - T_\infty)/(T_b - T_\infty)$
ν = kinematic viscosity
$\rho_{n,v}$ = density of saturated naphthalene vapor
$\rho_{n,s}$ = density of solid naphthalene
$\rho_{a,w}$ = density of air and water vapor mixture
ϕ = angular coordinate (zero in the direction of the approach flow)

Subscripts

b = fin base
d = based on the tube diameter
f = fin
ft = fin and tube
G = Gardner value, uniform over the fin surface
t = tube
∞ = free-stream quantity

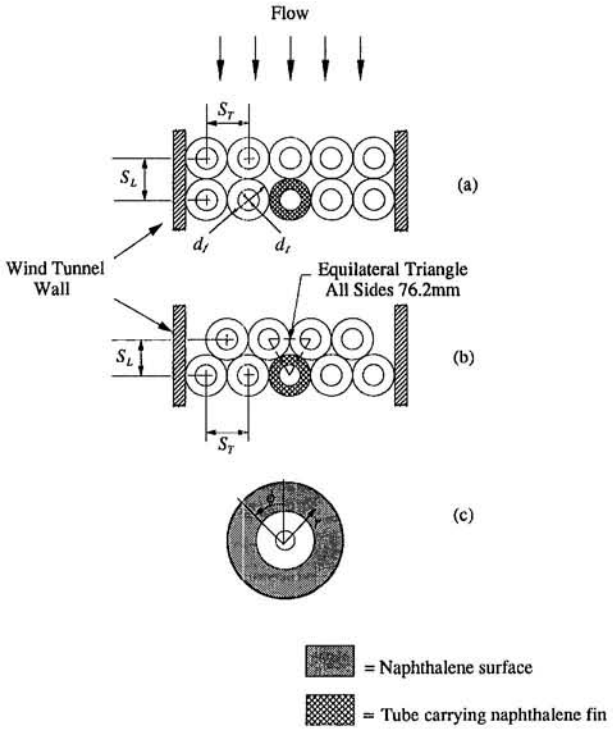

Fig. 2 A schematic of the finned tube heat exchangers studied. The flow is from top to bottom and the naphthalene test fin is placed at the center of the middle tube in the second row (shown cross hatched) for both (*a*) the in-line configuration, and (*b*) the staggered configuration. The fin carrying the naphthalene test specimen with the polar coordinate directions is shown in (*c*).

Optical Adaptation of the Naphthalene Sublimation Technique. The conventional naphthalene sublimation technique is well established, and excellent reviews of the experimental method are available (Souza Mendes, 1991; Goldstein and Cho, 1995). Hu and Jacobi (1993) used the method to study circular-finned tubes, and in the current research we adopted their approach with modifications to allow for the optical measurement of naphthalene surface contours.

In a conventional naphthalene sublimation experiment, the test specimen is weighed and its surface contour is measured by a mechanical device (typically an LVDT). After the initial measurement, the specimen is exposed to a prescribed convective environment for a measured period of time, and the weight and surface contour measurements are repeated. These measurements allow a determination of the local mass transfer coefficient and the overall mass transfer rate. Unfortunately, the spatial resolution on the fin surface (in (r, ϕ); see Fig. 2) is limited by the mechanical measurement of the surface contours. In addition to this spatial limitation, mechanical devices can deform the naphthalene surface during measurement.

In this research, naphthalene sublimation depths were measured using the laser triangulation technique. A coherent light source, provided by a laser diode, is focused onto the naphthalene surface and partially reflected back as shown in Fig. 3. The receiving-optics lens focuses the reflected light onto a photodetector or CCD array. Reflections from different heights on the naphthalene surface strike the photodetector at different locations, as shown in the figure. The location of the reflected light on the photodetector is easily determined from the photodetector output. By calibrating the change in location on the photodetector, Δx, to the change in height, Δz, the naphthalene surface profile can be measured. In laser triangulation, the reflecting surface can be diffuse and need not be parallel to the reference surface used in calibration. The receiving lens is designed to treat the reflection as a point source, and one only needs to measure the location of this point source along the known axis of the emitted beam. A more complete description of the geometric aspects of laser triangulation has been given by Jalkio et al. (1985).

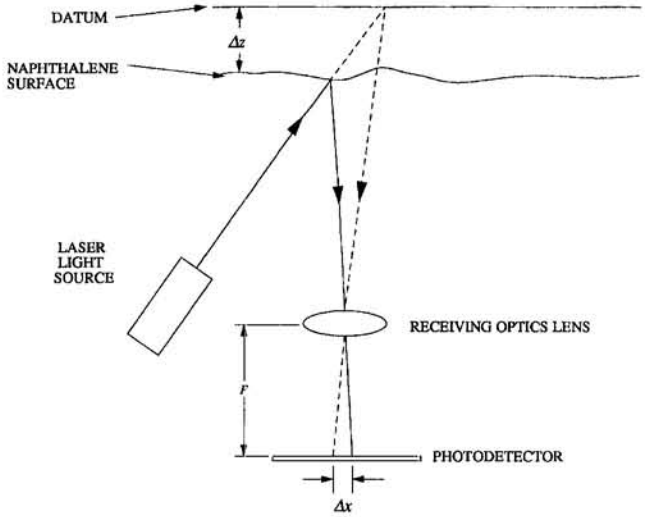

Fig. 3 Schematic explanation of the laser triangulation technique used to optically determine naphthalene surface contours (after Jalkio et al., 1985)

A sketch of the laser triangulation system hardware is provided in Fig. 4. System components include the sensor (probe), vibration isolation table, two translation stages (providing 88.9 mm translation in the plane of the naphthalene specimen), stepper motors, a micrometer (to position the probe normal to the naphthalene surface, 2.5 μm/div), a 254 mm $\times$ 254 mm measurement platform, and a computer with appropriate interface cards for sensor and stage controls. The probe contains the laser and the photodetector. The naphthalene specimen rests on

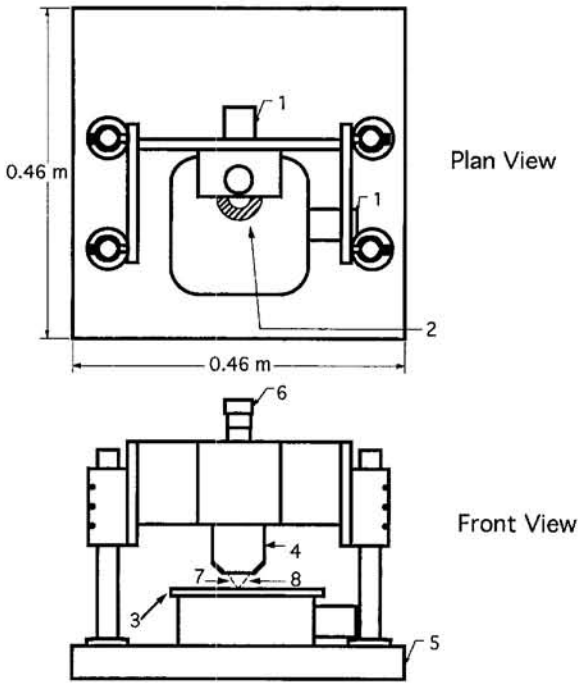

Fig. 4 Schematic of the laser profilometry system: (1) stepper motors, (2) naphthalene specimen, (3) positioning table, (4) sensor (containing laser light source and photodetector), (5) vibration isolation table, (6) probe-positioning micrometer, (7) source laser beam, (8) reflected laser beam

the positioning table and the probe remains stationary (approximately 20 mm above the specimen) while the stepper motors control the (r, ϕ) position of the naphthalene specimen. The laser spot size is 10.2 μm, and the resolution of the linear encoders that control translation is 1 μm. This provides the capability to measure local sublimation depths with a resolution as fine as the laser spot size.

Application of laser triangulation to naphthalene sublimation experiments requires special attention to noise reduction. Because the naphthalene surface may vary from opaque and milky white in appearance to semi-transparent, surface variability and possible multiple reflections from planes beneath the naphthalene surface complicate the application of optical methods. These difficulties can be surmounted by seeding the naphthalene specimen with a dye that strongly absorbs light at the laser wavelength and thereby reduces false reflections from planes beneath the surface. An iodine-based dye with an absorption peak at 750 nm was added to the liquid naphthalene in a concentration of about 10^{-3} gmol/liter during the fabrication process (see Kearney and Jacobi, 1995, for details). Any effect on the thermophysical properties of the naphthalene was assumed to be negligible. This assumption was confirmed by conducting experiments using specimens with and without the laser dye; the surface average Sherwood number results agreed to within the experimental uncertainty.

It is useful to compare the conventional and optical methods of surface contour measurement. Sublimation depths measured in a contact measurement apparatus can be obtained to within ± 0.15 μm at a rate of 2000 measurements per hour (Goldstein and Cho, 1995). The sublimation depth uncertainty using the optical method was ± 6 μm and the sampling rate was higher than 14,000 points per hour. The $2 - \sigma$ measurement uncertainty reported by Goldstein and Cho (1995) was based on contact measurements from a nonsubliming surface, and it is unclear that this uncertainty is applicable to a naphthalene surface that may deform under the contact. Nevertheless, contact measurement methods can probably provide four to five times lower uncertainty in sublimation depth than optical methods. However, if the increased Sherwood number uncertainty of the optical method is acceptable, the order of magnitude increase in spatial resolution due to higher sampling rates and the small laser spot size might make the optical approach attractive.

In addition, it should be noted that the main source of error in the optical implementation described above is thought to be thermal drift associated with heat transfer from stepper motors to the aluminum components of the translation table. Fabricating translation table stages from other metals might significantly reduce the uncertainty in sublimation depth associated with the optical method. In the experiments reported here, care was taken to ensure that the laser triangulation measurements were conducted in a controlled environment after a sufficient warm-up period (typically 5 hours). This enabled the conductive environment in the base of the measurement system to reach a quasi-steady state and eliminated any error associated with the initial warm-up of the system.

Experiment Procedure Details. Before a wind tunnel exposure, naphthalene surface contours were measured on a grid that consisted of 31 evenly spaced radii at angular increments of 4 deg. This resulted in a total of 2790 local measurement sites on the naphthalene-covered surface area of 3301 mm^2. The time that the naphthalene specimen was exposed to natural convection in room air during contour measurement was recorded and, following this measurement, the test fin was transported in a special container saturated with naphthalene to the wind tunnel test section.

The specimen was weighed with a precision balance (0–200 g, ± 0.0001 g), mounted in the model heat exchanger, and exposed to forced convection in the wind tunnel. During the test, barometric pressure (± 0.5 mmHg) and relative humidity ($\pm$ 2 percent) were recorded along with wind tunnel temperatures (± 0.1°C). These data were used to calculate the air density and thermophysical properties of naphthalene. After 30 to 50 minutes, the test was stopped and the naphthalene fin was reweighed, placed in the special container, and transported back to the optical measurement table where two more contour measurements were performed. The first two sets of contour data were subtracted to obtain raw sublimation depths, and the third set of sublimation data was used to correct for natural sublimation using the methods described by Hu and Jacobi (1993) and Goldstein and Cho (1995).

Data Reduction and Interpretation. The Reynolds number was based on the maximum free flow velocity and the hydraulic diameter per Kays and London (1984). Local mass transfer coefficients, h_m, were computed from the measured sublimation depth, δ_{sb}, and the exposure time, Δt, using the following expression:

$$h_m = \frac{\rho_{n,s}\delta_{sb}}{\rho_{n,v}\Delta t} \tag{1}$$

The density of solid naphthalene, $\rho_{n,s}$ was taken to be 1162.0 kg/m^3 (Kudchadker et al., 1978). The vapor density of saturated naphthalene, $\rho_{n,v}$ was calculated based on ideal gas behavior and the vapor pressure expression given by Ambrose et al. (1975).

Calculating the binary diffusion coefficient as recommended by Cho et al. (1992), the local mass transfer coefficients were then used to determine the local Sherwood numbers,

$$\mathrm{Sh} = \frac{h_m d_H}{D_{na}} \tag{2}$$

A common hydraulic diameter (d_H = 9.16 mm, the value for the in-line bank) was used for both bundle configurations so that the Sherwood numbers could be compared directly.

Area-averaged mass transfer coefficients were computed using the fin weight measurements and

$$\overline{h_m} = \frac{\Delta m}{A_f \rho_{n,v} \Delta t} \tag{3}$$

Integrating the local data provided a redundant check for the area-averaged mass transfer results. This integration was performed using the following approximation, where h_j is the mass transfer coefficient for a point measurement on the surface, ΔA_j is the area element associated with the point measurement, and N is the total number of point measurements:

$$\overline{h_m} = \frac{1}{A_f}\int_{A_f} h(r, \phi)dA \approx \frac{1}{A_f}\sum_{j=1}^{N} h_j \Delta A_j \tag{4}$$

and

$$\overline{\mathrm{Sh}} = \frac{\overline{h_m} d_H}{D_{na}} \tag{5}$$

The average Sherwood numbers obtained from Eqs. (3) and (4) usually did not differ by more than the experimental uncertainty, and they differed by less than 10 percent for all of the data reported.

To compute composite Nusselt numbers for a two-row bundle, average Sherwood number data were recorded in a single-row tube bank and for the second row in staggered and in-line tube banks. Applying the heat and mass analogy to each measurement, as given in Eq. (6), the Nusselt number behavior for each tube row was obtained. Power law curve fits to the Nusselt number were then combined on an area-averaged basis to develop overall bundle correlations.

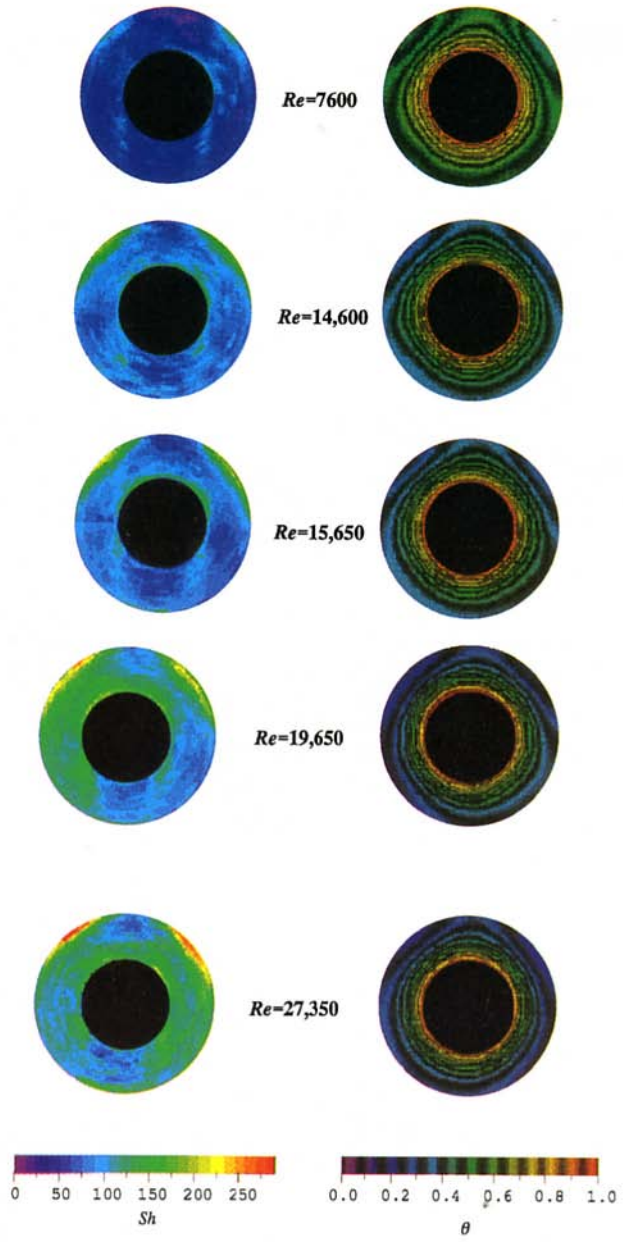

Fig. 5 Local Sherwood numbers and dimensionless temperature profiles for annular fins in the second row of an in-line tube banks, shown for Re = 7600, 14,600, 14,650, 19,650, and 27,350. The flow is from top to bottom. Sh varies from 0 (violet) to 290 (red) and θ varies from 0 to 1 with a similar, but banded, color scheme.

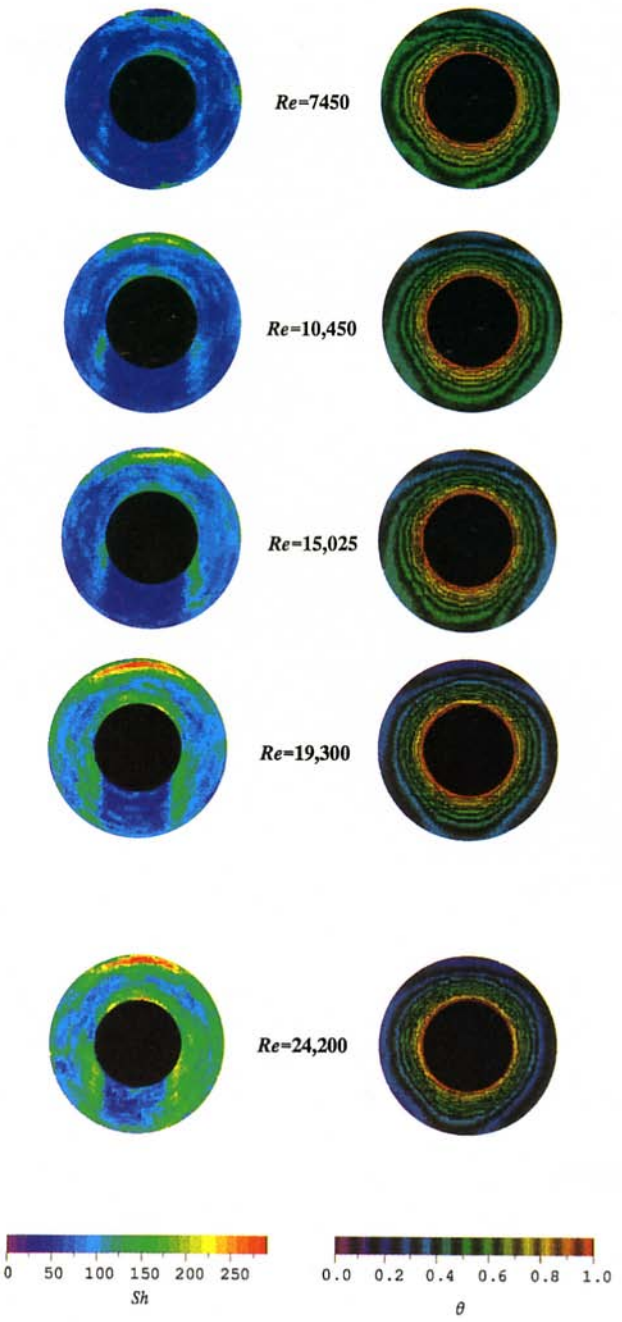

Fig. 6 Local Sherwood numbers and dimensionless temperature profiles for annular fins in the second row of a staggered tube bank, shown for Re = 7450, 10,450, 15,025, 19,300, and 24,200. The flow is from top to bottom. Sh varies from 0 (violet) to 290 (red) and θ varies from 0 to 1 with a similar, but banded, color scheme.

$$\overline{\mathrm{Nu}} = \overline{\mathrm{Sh}} \cdot \mathrm{Le}^{1/3} \tag{6}$$

The Lewis number was computed per the correlation of Cho et al. (1992). This method is justified by noting that Sparrow and Samie (1985) observed that the average heat transfer coefficient for finned tubes in the first row is relatively insensitive to the presence of downstream rows. In addition, experiments were conducted with a naphthalene fin in the first row of a two-row staggered bundle and the average Sherwood number was in good agreement with results obtained for a single row of tubes (differing by no more than the uncertainty).

The Euler number was determined from pressure drop measurements assuming a constant property flow:

$$\mathrm{Eu} = \frac{\Delta P}{\rho_{a,w} U_c^2} = \frac{f}{2}\left(\frac{A}{A_c}\right) \tag{7}$$

Using the method of Kline and McClintock (1953), the typical uncertainty in Re was found to be ±1 percent; the uncertainty in $\overline{\mathrm{Sh}}$ was ±4.3 percent, and the uncertainty in Eu was found to be less than ±5 percent for most of the experiments reported here. The uncertainty in local Sherwood number, Sh, depended strongly on the local sublimation depth and, therefore, varied over the fin surface. In regions of high mass transfer (where $\delta_{sb} \approx 100$ μm) the Sh uncertainty was estimated to be ±7 percent; in regions of lower sublimation depths ($\delta_{sb} \approx 30$ μm) the uncertainty was about ±20 percent. Using the mean sublimation depth, averaged over all experiments, the mean uncertainty in local Sh was found to be ±10 percent. The average sublimation depth in this study is about 8 percent of the fin thickness and about 1.3 percent of the fin spacing.

Fin efficiencies were determined by solving the heat conduction equation within the fin using a standard second-order finite difference technique. This solution was undertaken by assuming the fin material to homogeneous and isotropic, and by neglecting conduction normal to the fin surface (the thin-fin approximation). The fin root was assumed to be isothermal, and the fin tip was assumed to be adiabatic. Convection from the surface of the fin was modeled using the measured Sh data and $Nu = Sh \cdot Le^{1/3}$. This procedure follows Hu and Jacobi (1993) (except as discussed later), and it yields the true fin efficiency, η_f, from the temperature solution and the following relation:

$$\eta_f = \frac{\int_{A_f} h(r, \phi)\theta(r, \phi)dA}{\int_{A_f} h(r, \phi)dA} \approx \frac{\sum_{i=1}^{N} h_i\theta_i\Delta A_i}{\sum_{i=1}^{N} h_i\Delta A_i} \quad (8)$$

The usual design procedure invokes the assumption that the Nusselt number is uniform over the fin surface. Under these conditions, the well-known solution of Gardner (1945) results,

$$\eta_G(\bar{m}, R) = \frac{2}{\bar{m}(R^2 - 1)} \frac{I_1(\bar{m}R)K_1(\bar{m}) - K_1(\bar{m}R)I_1(\bar{m})}{I_0(\bar{m})K_1(\bar{m}R) + K_0(\bar{m})I_1(\bar{m}R)} \quad (9)$$

The numerical errors associated with the solution of the heat equation and the numerical evaluation of Eqs. (8) and (9) were estimated to be less than 0.5 percent (Kearney, 1995).

Results and Discussion

Local Mass Transfer. Local Sherwood numbers and dimensionless temperature distributions for annular fins in the second row of in-line and staggered arrays are shown in Figs. 5 and 6, respectively. The plots of local Sherwood number show the effects of several flow structures on local heat transfer, particularly flow impingement regions, boundary layer development, horseshoe vortices, and tube wakes.

For tubes in the in-line configuration, the flow impinges on the second row fin tips near 20 deg $\leq |\phi| \leq$ 90 deg (see Fig. 5). The local mass transfer is high at these locations and decreases in the flow direction due to the developing boundary layer. Between these impingement regions and away from the fin root, the local mass transfer is relatively low due to the wake of the upstream tube. Near the fin root for 0 deg $\leq |\phi| \leq$ 90 deg, the local mass transfer is enhanced by a horseshoe vortex system of the type described by Baker (1979) and Hu and Jacobi (1993). The separated boundary layer rolls up into a system of vortices upstream of the fin-tube junction, forming the "body" of the vortex. The vortices are advected around the tube and downstream, forming the "legs" of the vortex in the characteristic horseshoe pattern. Adjacent to the legs of the horseshoe vortex, directly behind the tube, a wake is formed and the local mass transfer is lower in this region.

For the staggered-tube arrangement, the local Sherwood number distribution exhibits similar types of localized flow structure, but at different locations on the fin surface. The flow impinges on the second row at the fin tip where 0 deg $\leq |\phi| \leq$ 20 deg, and local enhancement due to a newly developing boundary layer is evident. The wake from the upstream tubes influences the lateral fin tip region where 20 deg $\leq |\phi| \leq$ 90 deg and lower mass transfer rates result. Both the in-line and staggered tubes in the second row exhibit a wake region behind the tubes, similar to that observed in the first row (see Fig. 1).

The impact of the horseshoe vortex is apparently more pronounced for the staggered case, as evidenced by higher mass transfer enhancement associated with the legs of the vortex. The staggered arrangement presents a situation in which the tubes in the second row are outside the wakes of the tubes in the first row. Therefore, in the staggered arrangement, a higher-momentum boundary layer separates at the fin-tube junction to form the horseshoe vortex system. This vortex is strong enough to propagate downstream enhancing the heat transfer. In the in-line arrangement, the boundary layer upstream of the second-row tubes is influenced by the wakes of the first-row tubes. The result is a horseshoe vortex system with less impact on the local heat transfer. This effect is especially observable at higher Reynolds numbers.

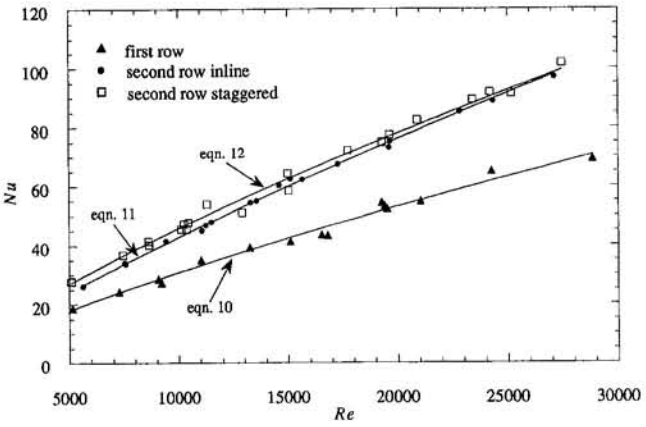

Fig. 7 Surface-averaged Nusselt numbers for banks of in-line and staggered, annularly finned tubes. Row-by-row data are presented for the first and second rows. Power-law correlations are plotted (Pr = 0.7) for the first row, the second row in-line, and the second row staggered.

Average Heat Transfer and Pressure Drop. Average Nusselt number (Pr = 0.7) data for the first and second rows of the in-line and staggered configurations are presented in Fig. 7, along with the correlations given below:

$$\overline{Nu} = 0.0265\ Re^{0.780}\ Pr^{1/3} \quad \text{(row 1)} \quad (10)$$

$$\overline{Nu} = 0.0233\ Re^{0.829}\ Pr^{1/3} \quad \text{(row 2 in-line)} \quad (11)$$

$$\overline{Nu} = 0.0451\ Re^{0.765}\ Pr^{1/3} \quad \text{(row 2 staggered)} \quad (12)$$

These row-by-row data indicate that the heat transfer coefficient for the first row of tubes is lower than for the second row. For the in-line array, the first-row Nusselt number was 34 to 45 percent lower than the second-row Nusselt number, and the difference increased with Reynolds number. The staggered arrangement exhibited a first-row Nusselt number that was about 45 percent lower over the entire range of Reynolds numbers. These findings are in qualitative agreement with those of Sparrow and Samie (1985) who found the second-row Nusselt number to be a maximum of 35 percent higher than the first row for in-line arrangements and 45 percent higher for staggered arrangements (for Reynolds numbers slightly below the range of the present work).

The following bundle correlations were obtained from Eqs. (10) – (12) and are plotted in Figs. 8 and 9 for the in-line and staggered arrangements, respectively:

$$\overline{Nu} = 0.0242\ Re^{0.809}\ Pr^{1/3} \quad \text{(in-line)} \quad (13)$$

$$\overline{Nu} = 0.0357\ Re^{0.771}\ Pr^{1/3} \quad \text{(staggered)} \quad (14)$$

At a Reynolds number of 5000, the average Nusselt number for the staggered bundle is 7 percent higher than for the in-line configuration. At Re = 10,000, the difference is less than the experimental uncertainty, with the performance of the two bundles becoming closer with increasing Reynolds number. This result suggests that the heat transfer performance of the two configurations is essentially equal over a broad range of Reynolds number.

Comparisons of Eqs. (13) and (14) to existing correlations for in-line and staggered tube banks are also provided in Figs. 8 and 9. To account for the effects of shallow bundles, the

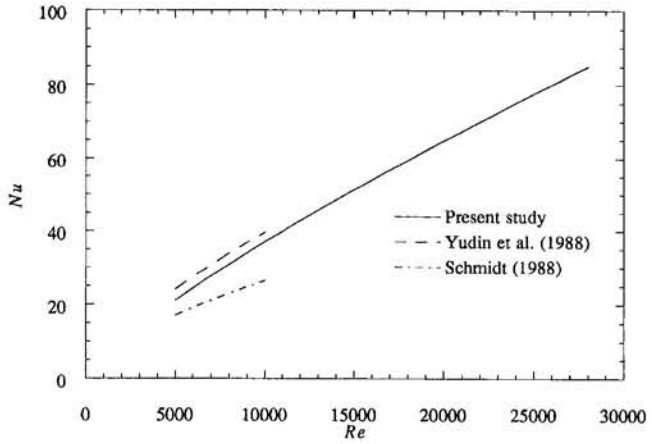

Fig. 8 A comparison of the in-line-bundle design correlation from the present study (Eq. (13)) to previous expressions from the literature. The shallow bundle correction factors of Yudin et al. (1988) have been applied to the correlations from the literature.

correction factors of Yudin et al. (1988) were applied to the existing deep bundle correlations (this correction amounted to multiplying the in-line correlations by 1.3 and the staggered correlations by 0.9).

For the in-line configuration (Fig. 8), no correlation was found that covered the entire Reynolds number range of the current study. The equations of Yudin et al. (1988) and Schmidt (1988) are plotted with Eq. (13) in Fig. 8, where it is seen that, for $Re \leq 10{,}000$ the Yudin correlation overpredicts our results by 7 to 14 percent. The Schmidt correlation underpredicts by 17 to 26.5 percent. It is interesting to observe that the Yudin correlations, from which the shallow bundle corrections were taken, predict in-line-bank Nusselt numbers 30 to 35 percent lower than for the staggered arrangement.

For staggered tubes (Fig. 9), the corrected correlation of Zukauskas (1988) compared favorably to Eq. (14) over the entire Reynolds number range, differing from the current study by no more than 6.5 percent. The Zukauskas correlation was the only staggered-bundle correlation found that was valid over the entire Reynolds number range of interest. Below $Re = 8000$, Eq. (14) is within 7.3 percent of the well-known Briggs and Young (1963) correlation. Equations due to Yudin et al. (1988) and Schmidt (1988) did not compare as favorably, differing by as much as 50 and 30 percent respectively, below $Re = 10{,}000$.

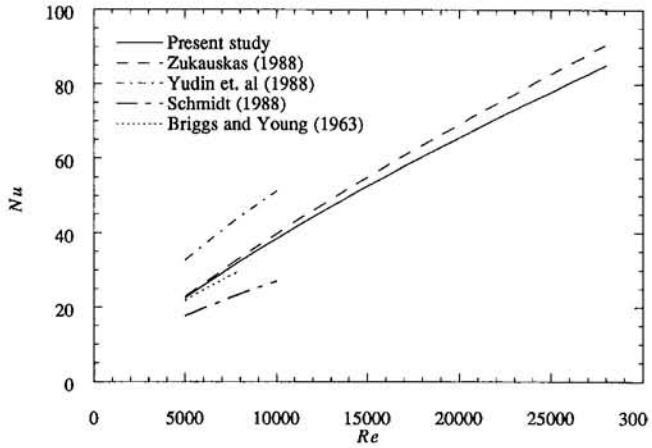

Fig. 9 A comparison of the staggered-bundle design correlation from the present study (Eq. (14)) to previous expressions from the literature. The shallow bundle correction factors of Yudin et al. (1988) have been applied to the correlations from the literature.

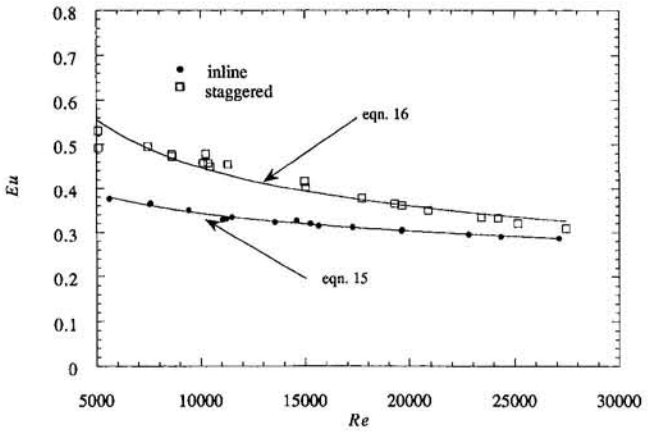

Fig. 10 Euler numbers for two-row banks of in-line and staggered, annularly finned tubes

The results from the second row were obtained without upstream heating (no naphthalene specimens were in the first row). The thermal boundary layer or wake from an upstream row might affect the details of the downstream fin heat transfer; however, we believe the basic flow and heat transfer interactions will remain unchanged. Furthermore, the effect on averaged results (overall performance predictions) appears to be very small. The overall bundle performance results of this study show good agreement with results from other studies of fully heated bundles (see Figs. 8 and 9). The approach taken in this study assumes that the interrow temperature distribution is uniform; this assumption is valid for high-Reynolds-number, well mixed, flows. At lower Reynolds numbers the effects of upstream heating may be more important.

Pressure drop data, in the form of Euler numbers, are plotted along with power law correlations in Fig. 10. These correlations are

$$Eu = 1.78\ Re^{-0.178} \quad \text{(in-line)} \tag{15}$$

$$Eu = 8.17\ Re^{-0.315} \quad \text{(staggered)} \tag{16}$$

The Euler numbers associated with the staggered configuration were 12 to 44 percent higher than for the in-line arrangement. This result is in reasonable agreement with the observations of Sparrow and Samie (1985) in which two-row banks of staggered tubes exhibited roughly a 50 percent higher pressure drop for Reynolds numbers slightly below the lower limit of those considered in the present work. A performance evaluation criterion, $Nu/Eu^{1/3}$, was computed from Eqs. (13)–(16), and it is shown in Fig. 11. The in-line performance is 4 to 5 percent higher than the staggered configuration; however, the uncertainty in these numbers is 7 to 8 percent. Therefore, on the basis of this comparison, we may conclude that for this geometry (tube diameter, fin diameter, fin spacing, etc.) the two bundles offer essentially equal performance over the range of Reynolds numbers studied. This result is contrary to the conventional design wisdom that staggered configurations outperform in-line arrangements. The results of the present study can be explained by noting that: (*i*) most of the existing correlations are for deep bundles (6 or more rows); and (*ii*) the fins used in this study were of relatively high profile ($R = 2$) when compared to many of those used in the previous studies.

The relationship between bundle arrangement, fin height, and heat transfer can be clarified by considering the bulk flow patterns through low- and high-finned bundles, as shown schematically in Fig. 12. For a low-finned bank the tube wakes influence a relatively large part of the finned area. The effect is more profound for in-line arrangements, and it explains the common conclusion that staggered arrangements have superior heat

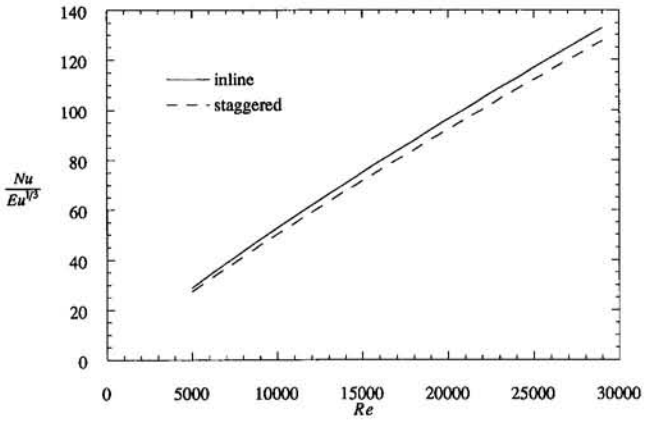

Fig. 11 A performance comparison, $Nu/Eu^{1/3}$ versus Reynolds number, for the in-line and staggered annularly finned tube banks

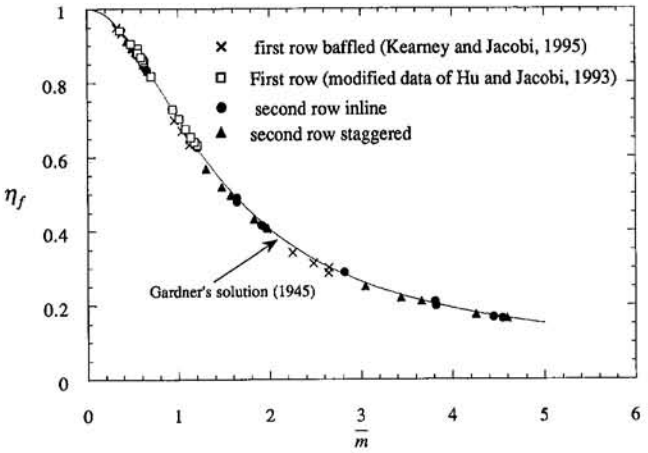

Fig. 13 True fin efficiencies plotted versus the square root of the fin parameter. The solid line is the analytical solution of Gardner (1945), and data based on studies of local fin heat transfer from four different situations are presented. The results indicate that Gardner's solution is accurate over a broad range of fin efficiencies.

transfer performance. However, as the fin height increases (see Fig. 12) the role of the tube wake becomes less important. For very high fins ($R \gg 1$), the bulk flow patterns become indistinguishable for the in-line and staggered arrangements because the tube wakes close before the flow reaches the next tube row. Therefore, we expect fewer differences between the in-line and staggered bundles with increasing fin height. Our high-fin data reflect this trend when compared to studies with lower fins.

The local mass transfer results from this study provide further insights (see Figs. 5 and 6). Although the details depend on the arrangement and Reynolds number, the most important flow features are the tube wakes, boundary layer development, and the horseshoe vortex. For in-line-tube arrangements, the heat transfer is significantly influenced by flow impingement and boundary layer development, and these flow features have a broad spatial distribution on the lateral portions of the fin. In staggered-tube arrangements, the horseshoe vortex has a more significant effect, but its influence is confined to the area near the root and the rearward portions of the fin. Therefore, low fins are preferred in staggered arrangements because the horseshoe vortex is localized near the fin root and a high fin has "wasted" area. High fins are preferred for in-line arrangements, where increased area can exploit the boundary layer development effects on the lateral regions of the fin. High fins in an in-line arrangement can approach the staggered arrangement heat transfer performance with a lower pressure drop.

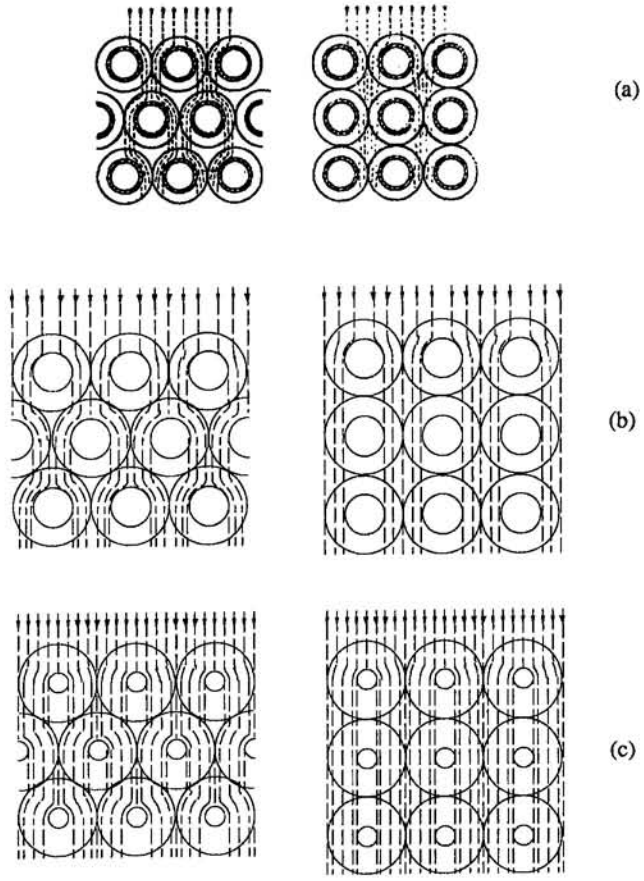

Fig. 12 Bulk flow patterns through banks of low- and high-finned tubes; (*a*) a typical low fin array (Brauer, 1964), (*b*) fins of the type used in the present study, with $R = 2$, and (*c*) even higher fins with $R = 4$

Fin Efficiency. A plot of fin efficiency, η_f, versus $\bar{m}$ is shown in Fig. 13, where values of η_f are obtained from four sources: (*i*) Gardner's analytical solution, (*ii*) data for the second row of in-line and staggered banks from the present study, (*iii*) results for fins in a single-row tube bank with wake reducing baffles (Kearney and Jacobi, 1995), and (*iv*) data for the first row of tubes, due to Hu and Jacobi (1993) (corrected as described later). The analytical solution provides an excellent approximation of the true fin efficiency over a broad range of the fin parameter. Considering all four sets of fin data, the mean deviation from the analytical prediction is 1.7 percent, the rms deviation is 1.3 percent, and 88 percent of the deviations are less than 3.5 percent.

The fin efficiency results of the present study are contrary to the previous work of Hu and Jacobi (1993) and Zukauskas et al. (1966), both of which indicated that the Gardner solution significantly overestimates the true fin efficiency for low efficiency fins. However, the differences in these conclusions can be explained, and we believe that local variations in h do not have a significant impact on fin efficiency for the annular fin geometry.

Hu and Jacobi used geometrically identical fins and the same technique that was used in the present study to determine true fin efficiencies. Unfortunately, in calculating fin efficiencies from the local data, they used a Lewis number of unity. The correct value of Le $\approx$ 0.3 was used in computing the surface average coefficient for the Gardner solution. This error caused the true fin efficiency to be underestimated, and the effect was magnified as η_f became smaller. We have corrected this mistake and present the reduced data of Hu (1992) in Fig. 13.

The finned tubes used by Zukauskas et al. were not geometrically identical to those used in the present study, so the local Nusselt number distributions may differ. Nevertheless, the data of Fig. 13 give the true fin efficiency for four different local Nusselt number distributions and all four give results in excellent agreement with Gardner's solution. Therefore, we conclude that the true fin efficiency of circular fins is relatively insensitive to this distribution. So, why did Zukauskas and his co-workers find significant deviations from the Gardner efficiency?

By measuring the total finned-tube heat transfer rate, the free-stream temperature, and fin base temperature, Zukauskas et al. determined the $\bar{h}\eta_o$ product using

$$\bar{h}\eta_o = \frac{Q_{ft}}{A_{ft}(T_b - T_\infty)} \tag{17}$$

where

$$\bar{h}\eta_o = \bar{h}\left\{1 - \frac{A_f}{A_{ft}}(1 - \eta_f)\right\} \tag{18}$$

The heat transfer coefficient was found from Newton's law of cooling, written as

$$\bar{h} = \frac{Q_{ft}}{A_{ft}(T_m - T_\infty)} \tag{19}$$

with an effective surface temperature, T_m defined as

$$T_m = \frac{1}{A_{ft}}\int_{A_{ft}} T(r, \phi)dA_{ft} \tag{20}$$

With the $\bar{h}\eta_o$ product and $\bar{h}$ independently determined by Eqs. (17) and (19), respectively, Zukauskas et al. solved Eq. (18) to find their "true" fin efficiency.

Unfortunately, the effective surface temperature defined in Eq. (20) is inconsistent with the definition of the heat transfer coefficient as it is used in the fin efficiency (see Eq. (8)). A proof is provided in the appendix. The local fin surface temperature and the local heat transfer rate must be known to calculate the true fin efficiency. Zukauskas et al. did not make measurements that would provide this information.

Summary and Conclusion

An optical adaptation of the naphthalene sublimation technique was described. This new approach for measuring sublimation depths offers an order of magnitude increase in spatial resolution but, in the implementation described, the uncertainty in local Sherwood number is higher than can be achieved using mechanical profilometry. The average local Sherwood number uncertainty using laser profilometry was ±10 percent. The local uncertainty is a function of the local sublimation depth, and experiments require a compromise between local uncertainty and geometric distortion of the specimen. Therefore, Sherwood number uncertainties depend on the particular experimental geometry of interest. If the Sherwood number uncertainty is acceptable, the increased spatial resolution of laser profilometry makes optical methods for measuring sublimation depths attractive.

Local transport behavior in the second row of a finned tube bundle is influenced by flow impingement, boundary layer development, tube wakes (including those from upstream tubes), and a horseshoe vortex system. The spatial distribution of these flow features depends on the tube arrangement and relative fin height. Local mass transfer results were used to infer local heat transfer coefficients, and these data were in turn used in a numerical solution of the heat equation to determine the true fin efficiency. The results show that local variations in the heat transfer coefficient do not significantly affect the fin efficiency. This conclusion is contradictory to previous reports (Hu and Jacobi, 1993; Zukauskas et al., 1966), and a detailed discussion of the disagreement is provided—we believe the earlier studies to be incorrect.

The effects of bundle arrangement and fin height on local and average heat transfer performance are coupled. Low-finned tubes may perform better in a staggered arrangement, but the heat transfer performance of high-finned tubes is not as sensitive to bundle arrangement in the Reynolds number range studied. In-line arrangements can operate with a lower pressure-drop penalty, and by considering a standard performance evaluation criterion, the thermal performance of in-line, high-finned tubes was found to be comparable to the staggered arrangement.

References

Ambrose, D., Lawrenson, I. J., and Sprake, C. H. S., 1975, "The Vapor Pressure of Naphthalene," *Journal of Chemical Thermodynamics,* Vol. 7, pp. 1173–1176.

Baker, C. J., 1979, "The Laminar Horseshoe Vortex," *J. Fluid Mech.,* Vol. 95, pp. 347–367.

Brauer, H., 1964, "Compact Heat Exchangers," *Chem. Process Eng. (London),* pp. 451–460.

Briggs, D. E., and Young, E. H., 1963, "Convection Heat Transfer and Pressure Drop of Air Flowing Across Triangular Pitch Banks of Finned Tubes," *Chem Eng. Prog. Symp. Ser.,* Vol. 59, No. 41, pp. 1–10.

Cho, K., Irvine, T. F., and Karni, J., 1992, "Measurement of the Diffusion Coefficient of Naphthalene Into Air," *Int. J. Heat Mass Transfer,* Vol. 35, No. 4, pp. 957–966.

Gardner, K. A., 1945, "Efficiency of Extended Surfaces," *Trans. ASME,* Vol. 67, pp. 621–631.

Goldstein, R. J., and Cho, H. H., 1995, "A Review of Mass Transfer Measurements Using Naphthalene Sublimation," *Exp. Thermal Fluid Sci.,* Vol. 10, pp. 416–434.

Hu, X., 1992, "Local Heat and Mass Transfer Characteristics of Circular-Finned Tubes," M. S. Thesis, The Johns Hopkins University, Baltimore.

Hu, X., and Jacobi, A. M., 1993, "Local Heat Transfer Behavior and Its Impact on a Single Row, Annularly Finned Tube Heat Exchanger," ASME JOURNAL OF HEAT TRANSFER, Vol. 115, pp. 66–74.

Idem, S. A., Jung, C., Gonzalez, G. J., and Goldschmidt, V. W., 1987, "Performance of Air-to-Water Copper Finned-Tube Heat Exchangers at Moderately Low Air-Side Reynolds Numbers, Including Effects of Baffles," *Int. J. Heat Mass Transfer,* Vol. 30, pp. 1733–1741.

Idem, S. A., Jacobi, A. M., and Goldschmidt, V. W., 1990, "Heat Transfer Characterization of a Finned-Tube Heat Exchanger (With and Without Condensation)," ASME JOURNAL OF HEAT TRANSFER, Vol. 112, pp. 64–70.

Jalkio, J. A., Kim, R. C., and Case, S. K., 1985, "Three Dimensional Inspection Using Multistripe Structured Light," *Optical Engineering,* Vol. 24, No. 6, pp. 966–974.

Kays, W. M., and London, A. L., 1984, *Compact Heat Exchangers,* 3rd ed., McGraw-Hill, New York.

Kearney, S. P., and Jacobi, A. M., 1995, "Effects of Gull-Wing Baffles on the Performance of a Single-Row, Annularly Finned Tube Heat Exchanger," *Int. J. HVAC&R Research,* Vol. 1 (4), pp. 257–272.

Kearney, S. P., 1995, "Local and Average Heat Transfer and Pressure Drop Characteristics of Annularly Finned Tube Heat Exchangers," M. S. Thesis, University of Illinois at Urbana–Champaign, Urbana, IL.

Kline, S. J., and McClintock, F. A., 1953, "Describing Uncertainties in Single Sample Experiments," *Mechanical Engineering,* Vol. 75, pp. 3–8.

Krückels, W., and Kottke, V., 1970, "Untersuchung uber die Verteilung des Warmeubergangs an Rippen und Rippenrohr-Modellen," *Chemie. Ing. Tech.,* Vol. 42, pp. 355–362.

Kudchadker, A. P., Kudchadker, S. A., and Wilhoit, R. C., 1978, *Naphthalene,* American Petroleum Institute, Washington, DC.

Kuntysh, V. B., and Stenin, N. N., 1993, "Heat Transfer and Pressure Drop in Cross Flow Through Mixed In-Line-Staggered Finned Tube Bundles," *Thermal Engineering,* Vol. 40, No. 2, pp. 126–129.

Legkiy, V. M., Pavlenko, V. P., Makarov, A. S., and Zheludov, Y. A. S., 1974, "Investigation of Local Heat Transfer in a Tube With Annular Fins in Transverse Air Flow," *Heat Transfer—Soviet Research,* Vol. 6, No. 6, pp. 101–107.

Neal, S. B. H. C., and Hitchcock, J. A., 1966, "A Study of the Heat Transfer Processes in Banks of Finned Tubes in Cross Flow, Using a Large Scale Model Technique," *Proc. Third International Heat Transfer Conference,* Chicago, Vol. 3, pp. 290–298.

Nir, A., 1991, "Heat Transfer and Friction Factor Correlations for Crossflow Over Staggered Finned Tube Banks," *Heat Transfer Engineering,* Vol. 12, No. 1, pp. 43–58.

Schmidt, Th., 1988, in: *Heat Transfer of Finned Tube Bundles in Crossflow,* A. Zukauskas, and G. Hewitt, eds., p. 172, Hemisphere Publishing, Washington, DC.

Souza Mendes, P. R., 1991, "The Naphthalene Sublimation Technique," *Exp. Thermal Fluid Sci.,* Vol. 4, pp. 510–523.

Sparrow, E. M., and Samie, F., 1985, "Heat Transfer and Pressure Drop Results for One and Two-Row Arrays of Finned Tubes," *Int. J. Heat Mass Transfer,* Vol. 28, No. 12, pp. 2247–2259.

Stasiulevicius, J., and Skrinska, A., 1988, *Heat Transfer of Finned Tube Bundles in Crossflow,* Hemisphere Publishing, Washington, DC.

Webb, R. L., 1980, "Air-Side Heat Transfer in Finned Tube Heat Exchangers," *Heat Transfer Eng.,* Vol. 1, No. 3, pp. 33–49.

Yudin, V. F., and Tochtarova, L. S., Lokshin, V. A., and Tulin, S. N., 1988, in: *Heat Transfer of Finned Tube Bundles in Crossflow,* A. Zukauskas and G. Hewitt, eds., p. 173, Hemisphere Publishing, Washington, DC.

Zukauskas, A., Stasiulevicius, J., and Skrinska, A., 1966, "Experimental Investigation of Efficiency of Heat Transfer of a Tube With Spiral Fins in Cross-flow," *Proc. Third International Heat Transfer Conference,* Chicago, Vol. 3, pp. 299–305.

Zukauskas, A., 1988, in: *Heat Transfer of Finned Tube Bundles in Crossflow,* A. Zukauskas and G. Hewitt, eds., p. 173, Hemisphere Publishing, Washington, DC.

APPENDIX

Zukauskas' effective temperature, given by Eq. (20), only provides the correct mean surface temperature for cases of a constant heat transfer coefficient on the fin surface. To demonstrate that this assertion is true, consider integrating a local application of Newton's law of cooling over the entire finned-tube surface to obtain the total finned-tube heat transfer rate:

$$Q_{ft} = \int_{A_{ft}} h\{T(r, \phi) - T_\infty\} dA_{ft} \qquad \text{(A-1)}$$

For a constant heat transfer coefficient, we may bring h outside of the integral and, upon rearranging, Eq. (A-1) can be written as follows:

$$h = \bar{h} = \frac{Q_{ft}}{A_{ft}\left(\frac{1}{A_{ft}}\int_{A_{ft}} T(r, \phi) dA_{ft} - T_\infty\right)} \qquad \text{(A-2)}$$

Comparing Eqs. (A-2), (19), and (20), it is apparent that Zukauskas' definition for the mean temperature tacitly assumes that h is constant on the fin surface.

To develop an expression for the correct mean temperature for cases where h varies on the fin surface, we must first recognize that the following definition of a mean convective heat transfer coefficient must be used if Eq. (18) is employed:

$$\bar{h} = \frac{1}{A_{ft}}\int_{A_{ft}} h(r, \phi) dA_{ft} \qquad \text{(A-3)}$$

Rewriting Eq. (19) we have

$$T_m = T_\infty + \frac{Q_{ft}}{A_{ft}\bar{h}}$$

Substituting Eq. (A-3) and rearranging with Newton's law of cooling, we obtain

$$T_m = T_\infty + \frac{Q_{ft}}{\int_{A_{ft}} \frac{q}{T(r, \phi) - T_\infty} dA_{ft}} \qquad \text{(A-4)}$$

Equation (A-4) shows that experimental determination of the correct mean surface temperature requires heat flux (or local h) data. Since Zukauskas did not make these measurements, it is impossible to use his surface-averaged data to obtain true fin efficiencies.

Effect of Film Hole Row Location on Film Effectiveness on a Gas Turbine Blade

H. Wanda Jiang[1]
Research Assistant.

J.-C. Han
HTRI Professor.
Fellow ASME

Turbine Heat Transfer Laboratory,
Department of Mechanical Engineering,
Texas A&M University,
College Station, TX 77843-3123

Experiments were performed to study the effect of film hole row location on local film effectiveness distribution of a turbine blade model with air or CO_2 film injection. Tests were performed on a five-blade linear cascade at the chord Reynolds number of 3.0×10^5 at the cascade inlet. A combination of turbulence grid and unsteady wake was used to create a higher free-stream turbulence level. The test blade had three rows of film holes in the leading edge region and two rows each on the pressure and suction surfaces. Film hole row locations were set by leaving the film holes at that row location open and covering the remaining rows. In addition, the additive nature of film cooling on the turbine blade model was examined by comparing the measured film effectiveness with the predicted effectiveness from the superposition method. Results show that injection from a different film hole row location provides a different effectiveness distribution on pressure and suction surfaces depending on local mainstream velocity and blade curvature. In most cases, the superposition method holds downstream of the last film hole row.

Introduction

A continuing trend toward higher gas turbine inlet temperatures has resulted in improved gas turbine performance and higher heat loads on turbine blades. Therefore, sophisticated turbine blade cooling techniques must be employed to maintain the blade under the allowable metallurgical temperature limit. Mainstream turbulence generated by combustor and unsteady wakes shed by upstream stationary vanes may have an adverse impact on film cooling performance. This study focuses on the effect of film hole row location on local film effectiveness distribution for a turbine rotating blade model with air or CO_2 film injection, under high mainstream turbulence conditions.

Nirmalan and Hylton (1990) reported an experimental study of turbine vane heat transfer with leading edge and downstream film cooling. Camci and Arts (1990) investigated convective heat transfer around a film-cooled gas turbine blade. Abhari and Epstein (1994) studied heat transfer on a film-cooled blade with time-resolved measurements under simulated engine conditions in a blowdown facility. Ito et al. (1978) and Haas et al. (1992) studied the effect of injectant density on film effectiveness of a gas turbine blade under low mainstream turbulence and no wake conditions. They reported that at blowing ratios higher than 0.5, a higher density injectant produces higher film effectiveness, whereas this behavior reverses at the low blowing ratio of 0.5. Takeishi et al. (1992) compared the film effectiveness values for a stationary cascade less than 4 percent mainstream turbulence intensity and a rotor blade using the heat–mass transfer analogy. They reported that in the leading edge region and suction surface, film effectiveness values for cascade and rotor blade match well, whereas on the pressure surface, the cascade values are higher.

Ou et al. (1994) and Mehendale et al. (1994a) studied the effects of incident unsteady wake conditions and injectant density on blade heat transfer coefficient and film effectiveness from a linear turbine blade cascade. They reported that an increase in unsteady wake strength causes an increase in heat transfer coefficient and a decrease in film effectiveness. They also reported that higher density injectant provides better film effectiveness at higher blowing ratios. Mehendale et al. (1994b) studied the effect of varying free-stream turbulence on heat transfer coefficient and film effectiveness of a film cooled turbine blade. Mehendale et al. (1996) studied the effect of film injection location on heat transfer coefficient distributions on a turbine blade. They observed that film injection promotes an earlier transition and the onset of transition depends on the film injection location. Ekkad et al. (1996) studied the combined effect of upstream unsteady wake and free-stream turbulence on heat transfer coefficient and film effectiveness of a film cooled turbine blade.

This study is a continuation of Mehendale et al. (1996) and focuses on the effect of film injection location on local film effectiveness distribution on a turbine blade model for two mainstream turbulence conditions ($\bar{T}u$ = 0.75 percent and $\bar{T}u$ = 16.4 percent) with air or CO_2 film injection ($D.R.$ = 0.97 or 1.48). The effects of four different film injection locations were investigated: (1) film injection through three film hole rows in the leading edge region, called leading edge injection in this paper, (2) film injection through only one film hole row each on the pressure and suction surfaces (X/C = −0.13 and 0.18), called second row injection in this paper, (3) film injection through only one film hole row each on the pressure and suction surfaces (X/C = −0.2 and 0.41), called third-row injection in this paper, and (4) film injection at all of the above-mentioned film hole row locations, called all-holes-open injection in this paper.

The objectives of this study are to: (1) determine the changes in film effectiveness for different film injection locations, (2) investigate the combined effect of upstream unsteady wake and free-stream turbulence, blowing ratio, and injectant-to-mainstream density ratio on blade film effectiveness distribution for leading edge injection and second row injection only, and (3) examine the additive nature of film cooling on both pressure and suction surfaces.

Test Apparatus and Instrumentation

Figure 1 is a top view of the test section (Han et al., 1993). The test apparatus consisted of a low-speed, low-turbulence, suction-type wind tunnel with an inlet nozzle, a turbulence grid,

[1] Current Address: Applied Materials, Santa Clara, CA 95054.

Contributed by the Heat Transfer Division for publication in the JOURNAL OF HEAT TRANSFER. Manuscript received by the Heat Transfer Division August 1994; revision received February 1996. Keywords: Jets, Turbines, Turbulence. Associate Technical Editor: T. W. Simon.

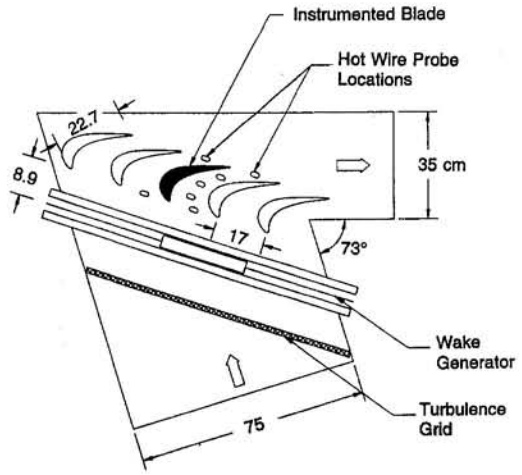

Fig. 1 Top view of the linear cascade, wake generator, and turbulence grid

a spoked-wheel-type wake generator, a linear turbine blade cascade with an instrumented blade at its center, and a blower. The blade and cascade configurations produced similar velocity ratio distributions as a typical advanced high-pressure turbine blade row. The relative flow angles were 35 and −72.49 deg, respectively, at the blade inlet and exit. A five-times scaled-up model simulated the engine Reynolds number. The cascade had five blades (each with 22.68 cm chord length and 25.2 cm radial span), all made from high-quality model wood. Blades were spaced 17.01 cm apart at the cascade inlet. Only the center blade had film holes and was instrumented with heater foils and thermocouples.

Combustor turbulence was simulated by a square mesh, square bar, biplanar turbulence grid, which generated free-stream turbulence. The turbulence grid had 0.5 cm square bars spaced 1.9 cm apart in both the horizontal and vertical directions. The turbulence grid was located 30 cm ($x/b = 63$) upstream of the cascade leading edge. The turbulence intensity and the integral length scale at the cascade inlet were estimated to be 5.7 percent and 1.1 cm, respectively.

Unsteady wake, shed by the trailing edge of an upstream blade, was simulated using the spoked-wheel-type wake generator (32 rods, each 0.63 cm in diameter, Han et al., 1993). The wake generator shaft was positioned 20 cm below the bottom wall of the wind tunnel. Wake Strouhal number was set by controlling motor speed and measuring the wake generator rotation speed with a digital photo tachometer.

Slots were machined in the top wall of the wind tunnel to insert flow measurement probes. Hot-wire probes inserted through slots near the cascade entrance measured oncoming flow velocity, turbulent fluctuations, and to check flow periodicity between adjacent flow passages (Han et al., 1993). Exit flow velocity was measured through slots near the cascade exit. Instantaneous velocity fluctuations at locations in the flow passages were measured through remaining slots. A calibrated single hot wire, connected to a four-channel TSI IFA 100 hot-wire anemometer, was used to measure instantaneous velocity profiles. The anemometer signal (digitized by a Data Translation DT 2831-G A/D board connected to a PC) was also connected to a spectrum analyzer for displaying instantaneous velocity profile and frequency distribution.

Figure 2 illustrates a schematic of the top view of the test blade (Ou et al., 1994). Cavity 1 supplied three rows of film holes—one near the leading edge, and one each on the pressure and suction surfaces. Cavity 2 supplied one row each on the pressure and suction surfaces. Cavities 3 and 4 supplied one row of film holes on the pressure and suction surfaces, respectively. Depending on its location, each row had 8 to 10 film holes between 30 and 70 percent of the blade span. Details of the film hole configuration (streamwise location, diameter, length, spanwise spacing, and compound angle) for this $5X$ model blade are presented by Ou et al. (1994). Each cavity was connected with an individually controllable injectant (air or CO_2) supply. Stainless steel foil strips (25.4 cm long × 1.8 cm wide × 0.00378 cm thick) were cemented vertically on the test blade, except in the film hole regions where there was no foil. Two layers of cellophane tape were used in these film hole regions to make the surface level with the rest of the test surface. Holes were cut in the tape to match the holes in the blade. The foil strips were separated by 0.8 mm gaps filled with wood putty and made flush with the foil surface. All foil strips were connected in series by copper bus bars. When heated electrically, the foil strips provided constant wall heat flux boundary condition. Thirty-six gage copper constantan thermocouples were cemented on the undersides of the foil strips. There were nine rows of thermocouples on the pressure surface and thirteen rows on the suction surface. Each row had four thermocouples (two along adjacent hole centerlines and two along centerlines between adjacent holes) in the radial midspan region. Thermocouples mounted in the injection cavities measured the injectant

Nomenclature

b = turbulence grid bar width
C = blade chord length, straight distance between leading and trailing
d = wake generator rod diameter
D = film hole diameter
$D.R.$ = density ratio (injectant to mainstream) = ρ_s/ρ_∞
h = local heat transfer coefficient
I = momentum flux ratio (injectant to mainstream) = $(\rho V^2)_s/(\rho V^2)_\infty$
k = local air thermal conductivity
K = acceleration parameter = $\nu/V^2 \cdot dV/dX$
M = blowing ratio (injectant to mainstream mass flux ratio) = $(\rho V)_s/(\rho V)_\infty$
n = number of rods in the wake generator
N = wake generator rotation speed, rpm
P = film hole pitch
q''_{cond} = local conduction heat loss flux
$q''_{\text{cond},g}$ = local conduction heat gain flux
q''_{rad} = local radiation heat loss flux
r_m = distance between the wake generator shaft center and the cascade midspan
Re = cascade inlet Reynolds number based on the blade chord = $V_1 C/\nu$
S = wake Strouhal number = $2\pi Ndn/(60V_1)$
T_{aw} = local adiabatic wall temperature
T_s = injection flow temperature within injection cavity
Tu = mean turbulence intensity
T_w = local wall temperature
T_∞ = mainstream temperature at cascade inlet
U_r = rotational velocity at the cascade midspan
V = local mainstream velocity around the blade
V_1 = mean mainstream velocity at cascade inlet
V_2 = mean mainstream velocity at the cascade exit
x = distance between turbulence grid and cascade leading edge
X = streamwise distance from stagnation along blade suction surface (+) or pressure surface (−)
η = local film effectiveness
$\bar{\eta}$ = spanwise-averaged film effectiveness
ν = kinematic viscosity

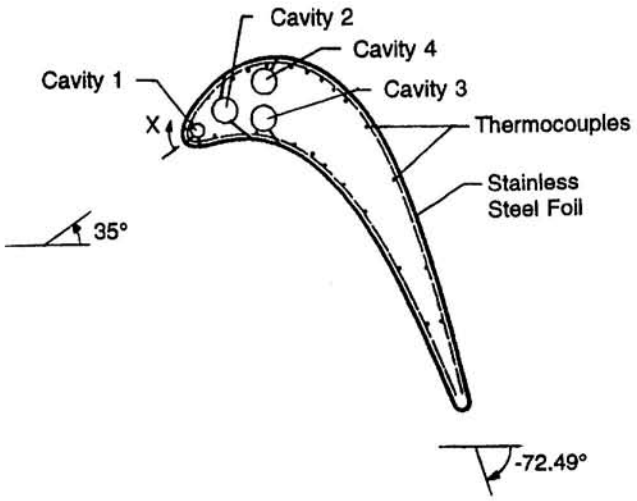

Film Hole Row Location	P/D	Axial Angle	Radial Angle	Tangential Angle
Cavity 1: All Three	7.31	90°	27°	–
Cavity 2: Pressure Side	6.79	–	32°	55°
Cavity 2: Suction Side	4.13	–	90°	45°
Cavity 3: Pressure Side	5.00	–	35°	50°
Cavity 4: Suction Side	5.71	–	90°	30°

Fig. 2 Schematic of test blade with film holes

flow temperatures just before injection. All thermocouples were connected to a 100-channel FLUKE 2285B datalogger interfaced with a PC. A multimeter and a current clamp measured the input voltage and line current for the test blade.

Test Conditions and Data Analysis

All tests were done at the chord Reynolds number (Re) of 3×10^5 at the cascade inlet (or 7.5×10^5 at cascade exit). The corresponding cascade inlet and outlet velocities were 21 and 52 m/s.

Two turbulence conditions at the cascade inlet were studied: (1) the low-turbulence condition ($\bar{T}u$ = 0.75 percent) where the turbulence grid and all rods from the wake generator were removed, and (2) the high turbulence condition ($\bar{T}u$ = 16.4 percent), where the turbulence grid is 30 cm (x/b = 63) upstream of the cascade leading edge and the wake generator rotates at N = 287 rpm, which corresponds to the wake Strouhal number S = 0.3 and the flow coefficient $V_t/U_r = dn/r_m$S = 1.9. The phase-averaged (or ensemble-averaged) method was used to obtain the time-dependent periodic velocity and time-dependent turbulence intensity. For this study, a mean turbulence intensity ($\bar{T}u$) is used to find the turbulence level of the combined grid turbulence and unsteady wake flow. The mean turbulence intensity is the mean value of the phase-averaged turbulence intensity over one period of unsteady flow, described in detail by Zhang and Han (1995).

The injectant mass flux rate for a given row of injection holes was determined from the chosen blowing ratio and the local mainstream velocity at that location (as measured with a pressure tap instrumented blade; Han et al., 1993). Tests were conducted at the blowing ratios of 0.5, 1.0, and 1.5. Air ($D.R.$ = 0.97) or CO_2 ($D.R.$ = 1.48) was the injectant used to study injectant-to-mainstream density ratio effect. Film injection, through the desired film hole rows, was achieved by sealing film holes at other locations and making the surface flush with the rest of the blade surface. Note that the mean value of the blowing ratio for the leading edge injection, the second row, and the third row injection are the same. However, the blowing ratio from each film hole row in the leading edge region may not be uniform. Also, the blowing ratios from the pressure and suction side film holes of the second row injection are different because both share the same injection cavity.

During film effectiveness tests, the mainstream temperature at the cascade inlet (T_∞) was at ambient conditions and the injectant temperature within the injection cavity (T_s) was at 50°C. As described by Mehendale et al. (1994a), local film effectiveness was calculated from

$$\eta = \frac{T_{aw} - T_\infty}{T_s - T_\infty} = \frac{T_w - T_\infty}{T_s - T_\infty} + \frac{(q''_{\text{cond}} + q''_{\text{rad}}) - q''_{\text{cond},g}}{h(T_s - T_\infty)} \quad (1)$$

where h is the local heat transfer coefficient evaluated from corresponding heat transfer tests, described later, under the same film injection test conditions. Heat loss tests were performed to estimate total local heat loss. The second term of Eq. (1) represents a corrective film effectiveness term to compensate for heat loss/gain during the experiments. This corrective term contributes less than 10 percent of the film effectiveness value. Four local film effectiveness values calculated from four local wall temperatures at a given streamwise location were algebraically averaged to obtain the spanwise-averaged film effectiveness ($\bar{\eta}$) at that location. The local heat transfer coefficient (h) in Eq. (1) was obtained from heat transfer tests. The results for heat transfer coefficient distributions are presented by Mehendale et al. (1996). Since the heat transfer coefficients are measured at the same location as the film effectiveness, this study uses the results from Mehendale et al. (1996) in the correction term (second term in Eq. (1)). The flow conditions are the same for both studies.

An uncertainty analysis was carried out using Kline and McClintock's method (1953). The wall-to-mainstream temperature difference mainly influenced the uncertainty in the film effectiveness. The uncertainty in film effectiveness for increasing X/C increases because the wall-to-mainstream temperature difference decreases. According to Omega Engineering Inc., the uncertainty for a 36-gage copper-constantan thermocouple bead is about ±0.2°C. In general, the uncertainty of the wall-to-mainstream temperature difference is less than 6 percent for those locations where the film effectiveness are greater than 0.1. Therefore, the uncertainty in the film effectiveness measurement is estimated to be less than 7.4 percent. However, the uncertainty in film effectiveness can be greater than 7.4 percent for those locations where the values are less than 0.1.

Results and Discussion

Ou et al. (1994) described the velocity profiles in the radial direction at the inlet and outlet of the passages adjacent to the instrumented blade. Results show that the inlet and outlet velocity profiles in the flow paths are essentially uniform in the midspan region. In addition, the flow direction at the inlet and outlet of both flow paths was uniform. Thus, the film effectiveness values are free from the top and bottom wall boundary layer effects. An identical profile blade with static pressure taps was used to measure local mainstream velocity around the blade (Han et al., 1993). Han et al. (1993) presented the local-to-exit velocity ratio (V/V_2) distributions for several upstream turbulence conditions. The results show that unsteady wake or free-stream turbulence may not change the mean (time-averaged) velocity near the blade surface. Figure 3 shows the local-to-exit velocity ratio and calculated acceleration parameter (K) for $\bar{T}u$ = 0.7 percent. These pressure gradients strongly affect the boundary layer transition and blade heat transfer. The velocity on the suction surface accelerates to about X/C = 0.6 and then decelerates until the exit. However, the velocity decelerates to about X/C = −0.2 on the pressure side and then accelerates.

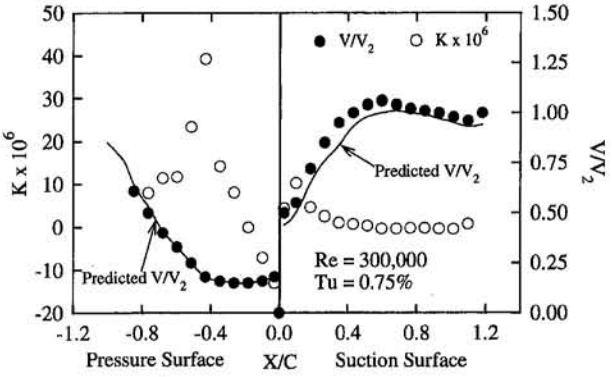

Fig. 3 Velocity distribution and calculated acceleration parameter for $\bar{T}u$ = 0.75 percent

Figure 4 illustrates the effect of blowing ratio on spanwise-averaged film effectiveness distribution for film injection through leading edge film holes (Cavity 1). The effect of density ratio with air or CO_2 injection is also studied under free-stream turbulence intensities of $\bar{T}u$ = 0.75 percent and 16.4 percent. At either free-stream turbulence ($\bar{T}u$ = 0.75 or 16.4 percent), for air or CO_2 injectant at all blowing ratio, film effectiveness on both suction and pressure surfaces decreases downstream of the film injection holes due to injectant dilution. Generally, film effectiveness increases with an increase in blowing ratio except downstream on the pressure surface. This may be because of the low injectant mass coming out of the film holes in the leading edge region at low blowing ratios. Film effectiveness is low for leading edge injection with the maximum value of 0.2 achieved immediately downstream of the film hole by CO_2 injection at the blowing ratio of 1.5. Note that no data are taken within the leading edge film hole region.

For $\bar{T}u$ = 0.75 percent, film effectiveness with air injection is higher than for CO_2 injection except that the difference diminishes far downstream on the pressure surface at lower blowing ratios (M = 0.5, 1.0). This may be because the heat capacity of CO_2 is 10 percent lower than that for air. It is well known that a lower heat capacity injectant implies a lower film effectiveness at the same conditions. However, CO_2 injection provides higher film effectiveness than air close to the film holes at a higher blowing ratio (M = 1.5), whereas film effectiveness with air injection is higher than with CO_2 injection far downstream. This may be because the jet lift-off effect for air injection is stronger than for CO_2 injection close to the film holes at higher blowing ratios (M = 1.5).

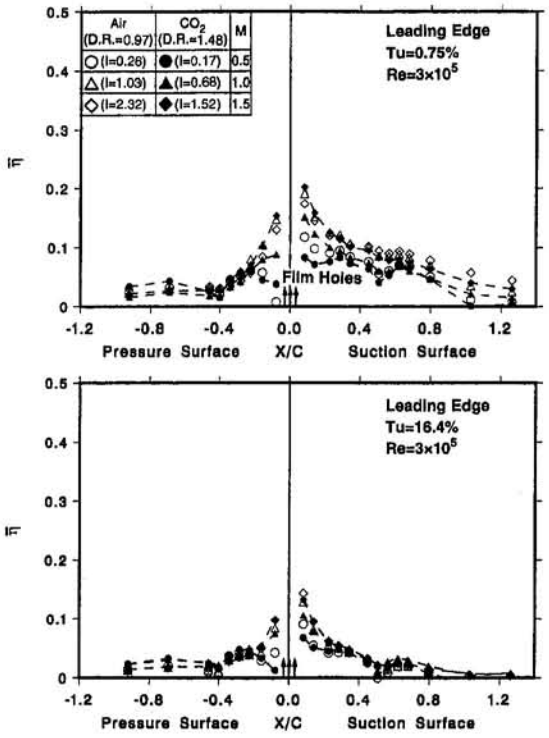

Fig. 4 Effect of air or CO_2 injection from the leading edge on $\bar{\eta}$ distribution at $\bar{T}u$ = 0.75 and 16.4 percent

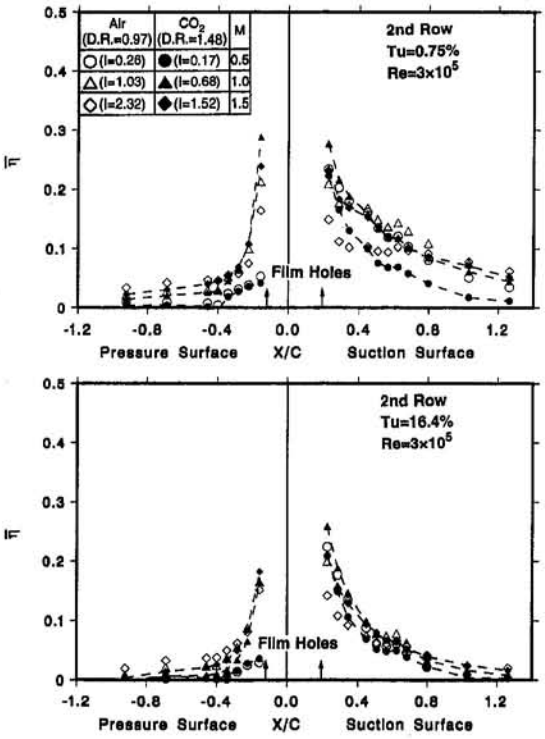

Fig. 5 Effect of air or CO_2 injection from the second row on $\bar{\eta}$ distribution at $\bar{T}u$ = 0.75 and 16.4 percent

For $\bar{T}u$ = 16.4 percent, an increase in blowing ratio increases film effectiveness for both injectants on both pressure and suction surfaces. The effect diminishes far downstream of injection. The effectiveness is lower for this case when compared with a low $\bar{T}u$ = 0.75 percent. This is because the unsteady high-turbulence mainstream flow interacts with the injectant and disrupts the film coverage, which causes lower film effectiveness. Previous studies (Mehendale et al., 1994a; Ekkad et al., 1996) have shown that the unsteady high turbulence flow causes lower film effectiveness on both pressure and suction surfaces.

Figure 5 shows the effect of blowing ratio on spanwise-averaged film effectiveness distribution for film injection through the second rows of film holes on the pressure and suction surfaces (Cavity 2, X/C = −0.12 and X/C = 0.19). The effect of density ratio with air or CO_2 injection is also studied under free-stream turbulence intensities of $\bar{T}u$ = 0.75 and 16.4 percent. Overall, film effectiveness on both the suction and pressure surfaces decreases downstream of the film injection holes due to injection dilution for both injectants at all blowing ratios. Film effectiveness on the pressure surface drops faster than on the suction surface. This may be caused by the higher local mainstream velocity on the suction surface at the second row injection location, which is about three times higher than on the pressure surface. Since the same cavity provides the injectant to both the pressure and suction surfaces, less injectant could be coming out of the pressure side holes than the suction side holes due to the mainstream velocity difference.

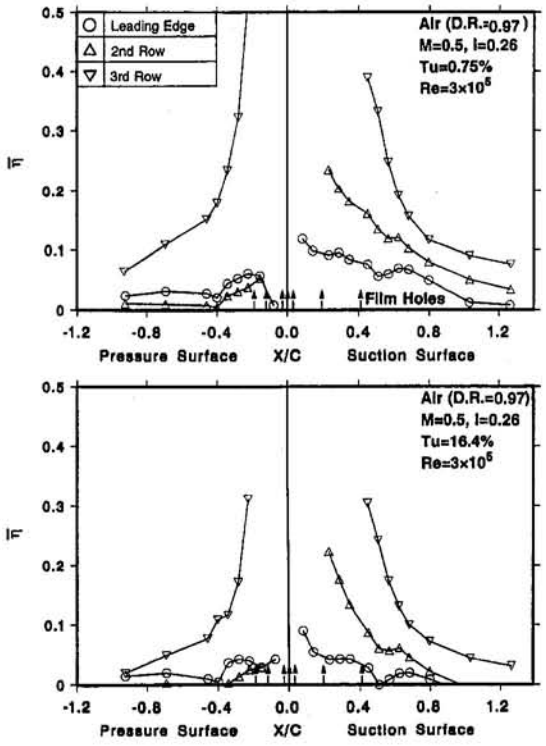

Fig. 6 Effect of film hole row location with air injection on $\bar{\eta}$ distribution at $M = 0.5$ for $\bar{T}u = 0.75$ and 16.4 percent

Lastly, CO_2 injection provides higher film effectiveness closer to film holes than air injection. However, air provides higher effectiveness far downstream. This may be due to the difference in jet momentum and heat capacity of the injectants. CO_2 injection at $M = 1.0$ produces the highest $\bar{\eta}$ near the film holes on the suction surface. However, the highest $\bar{\eta}$ near the film holes on the pressure surface is for air injection at $M = 0.5$. The injectant jets seldom lift off from the surface for CO_2 injection due to the higher density producing higher effectiveness at higher blowing ratios ($M = 1.0, 1.5$). However, since CO_2 jet momentum is small and has a lower heat capacity, air produces better film effectiveness than CO_2 at a lower blowing ratio of 0.5. In the second row injection case, the highest film effectiveness, about 0.3, is obtained for CO_2 injection at the blowing ratio of 1.0.

At a higher free-stream turbulence, the effect of blowing and density ratios on the film effectiveness is similar to that in the low turbulence intensity case. As mentioned earlier, film effectiveness at $\bar{T}u = 16.4$ percent is lower than that at $\bar{T}u = 0.75$ percent due to the disruption of the film layer by the unsteady high turbulence. Film effectiveness decreases downstream of injection faster for $\bar{T}u = 16.4$ percent than for $\bar{T}u = 0.75$ percent for both injectants. Also, the differences in film effectiveness produced by the two injectants on the suction surface diminish at the high turbulence condition.

Figure 6 depicts the effect of film hole row location on spanwise-averaged film effectiveness for air injection at the blowing ratio of $M = 0.5$ under free-stream turbulence intensities of 0.75 and 16.4 percent. Results from Ou and Han (1994) for air injection through the third row film holes on the pressure and suction surfaces (Cavities 3, $X/C = -0.2$ and cavity 4, $X/C = 0.41$) are shown for comparison. As shown, film effectiveness decreases downstream of the film holes for each injection location case (only leading edge injection, second row injection, and third row injection). At $\bar{T}u = 0.75$ percent on the suction surfaces, injections through the third row, the second row, and the leading edge row of film holes provides effectiveness in a decreasing order. Possible factors for this behavior (although blowing and density ratios and, thus, the momentum flux ratio remain the same) are the local mainstream velocity, the blade curvature, and the compound angle of the film holes (Figs. 2 and 3) in the injection location. The local mainstream velocity increases from location to location (Fig. 3) for each injection location going from leading edge to second row to third row. Injection at a location with higher local mainstream velocity has higher mass flux and, therefore, has more film coverage over the surface. In addition, due to the curvature, the injectant from the third row film holes can easily attach to the surface to provide better film coverage when compared with the leading edge injection. Here, the third row injection provides the highest film effectiveness of 0.4. However, the second row injection on the pressure side provides the lowest film effectiveness. As explained earlier, this may be due to the low injectant mass coming out of the film holes on the pressure side. Similar trends are also observed for air injection at the blowing ratios of 1.0 and 1.5 (not shown here).

At the higher mainstream turbulence intensity of $\bar{T}u = 16.4$ percent, the effect of film hole row location on film effectiveness is the same as for the lower mainstream turbulence case. However, as mentioned earlier, film effectiveness values are lower since the highly turbulent unsteady flow disrupts the film coverage.

Figure 7 displays the effect of film hole row location on spanwise-averaged film effectiveness, for CO_2 injection at the blowing ratio of $M = 1.5$, and at the turbulence intensities of $\bar{T}u = 0.75$ and 16.4 percent. Results from Ou and Han (1994) for CO_2 injection through the third-row film holes on the pressure and suction surfaces (Cavities 3 and 4) are shown for comparison. The effects of film hole row location and turbulence intensity on local spanwise-averaged film effectiveness are similar to those for air injection. However, the third row holes provide only a slightly higher effectiveness compared to second row holes on the suction side and the second row injection on the pressure side has a higher film effectiveness (instead of lower for the case of air injection in Fig. 6) than the leading

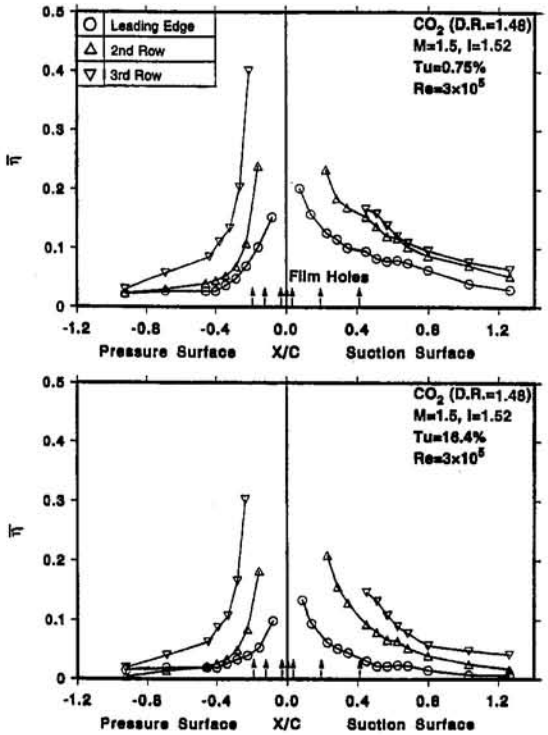

Fig. 7 Effect of film hole row location with CO_2 injection on $\bar{\eta}$ distribution at $M = 1.5$ for $\bar{T}u = 0.75$ and 16.4 percent

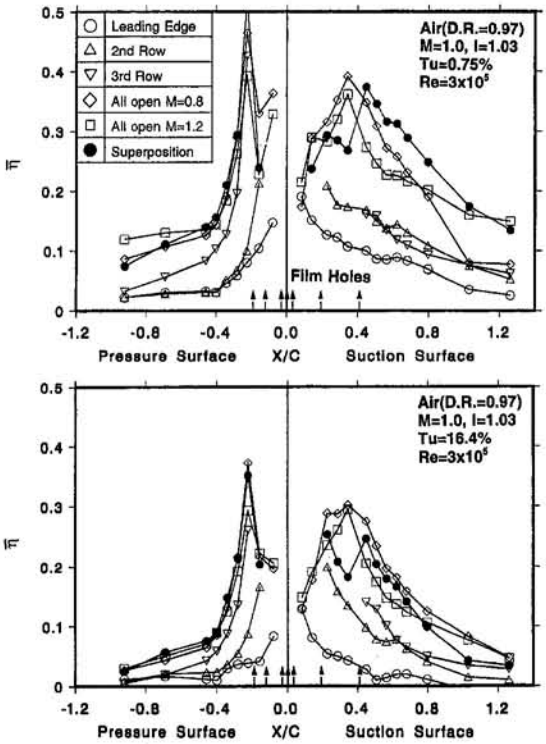

Fig. 8 The additive nature of film cooling with air injection at $M = 1.0$ for $\bar{T}u = 0.75$ and 16.4 percent

edge injection. This may be caused by different injectant densities.

Muska et al. (1976) applied a method of superposition to predict the cumulative effect of film cooling from multiple injection rows. Sellers (1963) first demonstrated this method for injection from multiple slots. The superposition method for multiple row injection proposes that the overall film effectiveness from a group of rows of holes can be calculated from data or correlations for injection one row at a time. The single rows of holes in this study are the leading edge film holes, the second rows of film holes, and the third rows of film holes, each of which individually produces a film effectiveness of η_1, η_2, and η_3, respectively. The predicted overall film effectiveness η was calculated based on the superposition model as follows:

$$\eta = \eta_1 + \eta_2(1 - \eta_1) + \eta_3(1 - \eta_1)(1 - \eta_2) \qquad (2)$$

Figure 8 compares the predicted overall film effectiveness for air injection on both the pressure and suction surfaces from the leading edge, second row, and the third rows of film holes with the measured data for the all-holes-open case, at the blowing ratio of 1.0 and at the mainstream turbulence intensities of 0.75 and 16.4 percent. Results from Ou and Han (1994) for air injection through the third row film holes on the pressure and suction surfaces (Cavities 3 and 4) and from Ekkad et al. (1996) for air injection ($M = 0.8$ and 1.2) through all rows of film holes are shown for comparison. On both the pressure and suction surfaces, at a mainstream turbulence intensity of $\bar{T}u = 0.75$ percent or $\bar{T}u = 16.4$ percent, the additive nature is not evident in the region between the second and third film hole rows. This is because the injectant-mainstream interaction gives rise to a three-dimensional flow in this injection hole region. Another reason may be due to different compound angles for each film row location (Fig. 2). However, favorable agreement is observed between the predicted and measured film effectiveness downstream of the third row injection region where a two-dimensional boundary layer develops. One exception is the case of film injection on the suction surface at the turbulence intensity of $\bar{T}u = 0.75$ percent, where the superposition model overpredicted the all-holes-open film effectiveness.

Figure 9 shows a trend, consistent with air injection, for CO_2 injection at the blowing ratio of 1.0 at the turbulence intensities of 0.75 and 16.4 percent.

Similar results are also evident for air and CO_2 injection at the blowing ratios of 0.5 and 1.5, at the turbulence intensity of 0.75 and 16.4 percent (not shown). The additive nature of film cooling on the turbine blade model agrees with Takeishi et al. (1992), who reported that the superposition film cooling model does not hold between the film hole rows. However, far downstream, a two-dimensional boundary layer develops. Note that the superposition method was developed for multiple rows of film holes with the same injection angles on a flat surface.

Concluding Remarks

The effect of film hole row location on film effectiveness distributions was investigated on a model turbine blade, with air ($D.R. = 0.97$) or CO_2 ($D.R. = 1.48$) film injection, in a linear cascade. Tests were performed at the chord Reynolds number of 3.0×10^5 at the cascade inlet (or 7.5×10^5 at the cascade exit), at free-stream turbulence intensities of 0.75 and 16.4 percent at the cascade inlet, and at blowing ratios of 0.5, 1.0, and 1.5. The main findings were:

1 Film effectiveness is low and increases with an increase in blowing ratio for leading edge injection. CO_2 injection produces higher effectiveness closer to the film holes but air injection produces higher values far downstream.

2 Film effectiveness drops faster on the pressure side than on the suction side for the second row injection. CO_2 injection produces higher effectiveness than air near the film holes but lower effectiveness far downstream. The highest effectiveness is produced near film holes by CO_2 injection at $M = 1.0$.

3 An increase in mainstream turbulence intensity reduces film effectiveness over the entire blade surface for all cases of film hole row location, both density ratio injectants, and at all blowing ratios.

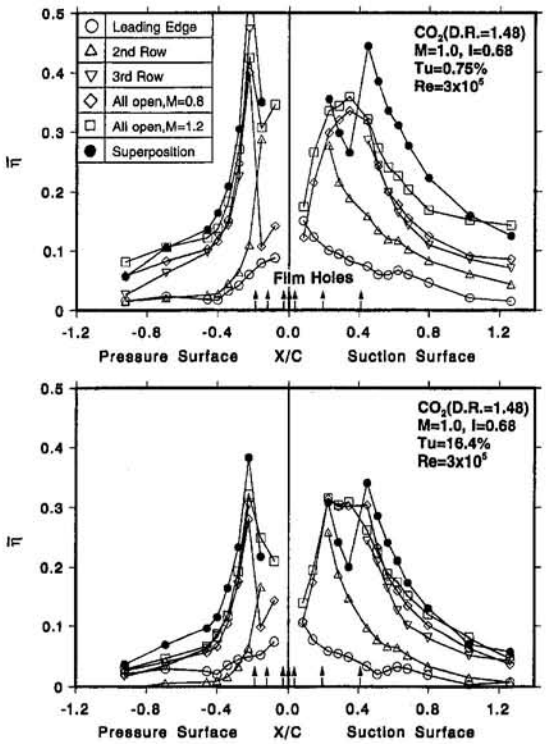

Fig. 9 The additive nature of film cooling with CO_2 injection at $M = 1.0$ for $\bar{T}u = 0.75$ and 16.4 percent

4 Film effectiveness values for injection through the third rows, the second rows, or leading edge are in decreasing order for both injectants on both the pressure and suction surfaces. However, second row injection on the pressure side has the lowest effectiveness at $M = 0.5$.

5 For both air or CO_2 injection at $\overline{Tu} = 0.75$ percent and $Tu = 16.4$ percent, the superposition method holds downstream of the third film hole row on both the pressure and suction surfaces (except on the suction surface at $\overline{Tu} = 0.75$ percent). However, it tends to underpredict the film effectiveness in the region between the second and third film hole rows.

Acknowledgments

The project was sponsored by the Texas Higher Education Coordinating Board—Advanced Technology Program under Grant #999903-104. The authors would like to thank Dr. Anant Mehendale and Dr. Srinath Ekkad, of Texas A&M University, for their assistance and comments.

References

Abhari, R. S., and Epstein, A. H., 1994, "An Experimental Study of Film Cooling in a Rotating Transonic Turbine," ASME *Journal of Turbomachinery,* Vol. 116, pp. 63–70.

Camci, C., and Arts, T., 1990, "An Experimental Convective Heat Transfer Investigation Around a Film-Cooled Gas Turbine Blade," ASME *Journal of Turbomachinery,* Vol. 112, pp. 497–503.

Ekkad, S. V., Mehendale, A. B., and Han, J. C., 1996, "Combined Effect of Grid Turbulence and Unsteady Wake on Film Effectiveness and Heat Transfer Coefficient of a Gas Turbine Blade With Air and CO_2 Film Injection," ASME *Journal of Turbomachinery,* in press.

Haas, W., Rodi, W., and Schönung, B., 1992, "The Influence of Density Difference Between Hot and Coolant Gas on Film Cooling by a Row of Holes: Predictions and Experiments," ASME *Journal of Turbomachinery,* Vol. 114, pp. 747–755.

Han, J. C., Zhang, L., and Ou, S., 1993, "Influence of Unsteady Wake on Heat Transfer Coefficient From a Gas Turbine Blade," ASME JOURNAL OF HEAT TRANSFER, Vol. 115, pp. 904–911.

Ito, S., Goldstein, R. J., and Eckert, E. R. G., 1978, "Film Cooling of a Gas Turbine Blade," ASME *Journal of Engineering for Power,* Vol. 100, pp. 476–481.

Kline, S. J., and McClintock, F. A., 1953, "Describing Uncertainties in Single-Sample Experiments," *Mechanical Engineering,* Vol. 75, Jan., pp. 3–8.

Mehendale, A. B., Han, J. C., Ou, S., and Lee, C. P., 1994a, "Unsteady Wake Over a Linear Turbine Blade Cascade With Air and CO_2 Film Injection: Part II—Effect on Film Effectiveness and Heat Transfer Distributions," ASME *Journal of Turbomachinery,* Vol. 116, pp. 730–737.

Mehendale, A. B., Ekkad, S. V., Han, J. C., 1994b, "Mainstream Turbulence Effect on Film Effectiveness and Heat Transfer Coefficient of a Gas Turbine Blade With Air and CO_2 Film Injection," *International Journal of Heat and Mass Transfer,* Vol. 37, pp. 2707–2714.

Mehendale, A. B., Jiang, H. W., Ekkad, S. V., and Han, J. C., 1996, "Effect of Film Injection Location on Local Heat Transfer Coefficient on a Gas Turbine Blade," *International Journal of Rotating Machinery,* in press.

Muska, J. F., Fish, R. W., and Suo, M., 1976, "The Additive Nature of Film Cooling From Rows of Holes," ASME *Journal of Engineering for Power,* Vol. 98, pp. 457–467.

Nirmalan, V., and Hylton, L. O., 1990, "An Experimental Study of Turbine Vane Heat Transfer With Leading Edge and Downstream Film Cooling," ASME *Journal of Turbomachinery,* Vol. 112, pp. 477–487.

Ou, S., and Han, J. C., 1994, "Unsteady Wake Effect on Film Effectiveness and Heat Transfer Coefficient From a Turbine Blade With One Row of Air and CO_2 Film Injection," ASME JOURNAL OF HEAT TRANSFER, Vol. 116, pp. 921–928.

Ou, S., Han, J. C., Mehendale, A. B., and Lee, C. P., 1994, "Unsteady Wake Over a Linear Turbine Blade Cascade With Air and CO_2 Film Injection: Part I—Effect on Heat Transfer Coefficients," ASME *Journal of Turbomachinery,* Vol. 116, pp. 721–729.

Sellers, J. P., 1963, "Gaseous Film Cooling With Multiple Injection Stations," *AIAA Journal,* Vol. 1, pp. 2154–2156.

Takeishi, K., Aoki, S., Sato, T., and Tsukagoshi, K., 1992, "Film Cooling on a Gas Turbine Rotor Blade," ASME *Journal of Turbomachinery,* Vol. 114, pp. 828–834.

Zhang, L., and Han, J. C., 1995, "Combined Effect of Free-Stream Turbulence and Unsteady Wake on Heat Transfer Coefficient From a Gas Turbine Blade," ASME JOURNAL OF HEAT TRANSFER, Vol. 117, pp. 296–302.

Local, Instantaneous Heat Transfer Coefficients for Jet Impingement on a Phase Change Surface

A. P. Bhansali
Post-doctoral Research Fellow,
Department of Mechanical Engineering
and Material Sciences,
Rice University,
Houston, TX 77251
Assoc. Mem. ASME

W. Z. Black
Regents Professor,
George W. Woodruff School of
Mechanical Engineering,
Georgia Institute of Technology,
Atlanta, GA 30332-0405
Fellow ASME

The local variation in the heat transfer coefficient for an axisymmetric, turbulent, submerged liquid jet impinging on a nonuniform boundary of a phase-change material is measured with an ultrasonic measurement technique. The time required for an acoustic wave to traverse the phase-change material is measured with an ultrasonic transducer and the time data are converted into local thickness profiles of the phase-change material via knowledge of the longitudinal acoustic velocity in the material. An energy balance at the melt interface between the impinging jet and the phase-change material is used in conjunction with the local thickness profile data to determine the local variation in the heat transfer coefficient. The phase-change material is originally flat, but its shape changes with time as the heated jet melts a complex shape into its surface. The heat transfer rate over the surface of the melting interface is shown to vary with time as a result of the changing shape of the phase change material. A deep cavity is melted into the solid at the stagnation point and secondary cavities are melted into the interface for certain jet flow rates and surface spacings between the jet nozzle and the melt interface. When secondary cavities are produced, secondary peaks in the local heat transfer coefficient are observed. The heat transfer data are formulated into two Nusselt number correlations that are functions of the dimensionless time, dimensionless radius, dimensionless jet-to-surface spacing, and jet Reynolds number. One correlation is formulated for all locations along the surface of the phase-change material except the stagnation point, and a second correlation is valid at the stagnation point.

Introduction

The phenomenon of jet impingement on a phase-change surface can occur in numerous applications, such as in the mining and excavating industries where high-pressure jets are often used for cutting and wielding of frozen media (Yen and Zehnder, 1973). Yen (1974) described the application of a bubble-induced subsurface warm water jet to de-ice frozen structures in cold regions operations. Epstein et al. (1980) investigated the simultaneous freezing of a molten jet and melting of a subcooled impingement surface, which is a situation that is prevalent in fast reactor safety research. Stefanick (1988) used a nonacoustic method to locate stationary nuclear submarines in the Arctic regions by detecting the condenser discharge water where it contacts the glacial ice. Chatwani et al. (1991) recently documented a new type of steel scrap furnace that involves a jet of combustible gases that impinges onto submerged solid scrap.

The literature on jet impingement heat transfer is typically divided into two categories: submerged jet impingement and free jet impingement. The major distinguishing feature between the two is that the densities of the jet fluid and of the surrounding medium are nearly the same for the submerged case, while for free jet impingement, the densities of the jet fluid and the ambient fluid are drastically different. Womac et al. (1993) have documented the differences in heat transfer characteristics between the two cases using various liquids and this issue will therefore not be discussed here. While most of the previous work to date on jet impingement heat transfer has focused on either free liquid jets in air or submerged gas jets, the emphasis of this paper is on a submerged water jet issuing into stagnant, ambient water.

The existing literature reveals numerous studies in which heat transfer coefficients have been experimentally measured for jet impingement on normal, stationary surfaces (Brdlik and Savin, 1965; Donaldson et al., 1971; Metzger et al., 1974; Giralt et al., 1977; Kiper, 1984), but few studies have been carried out in which a jet impacts a phase-change material in which a concave surface changes shape during the process. In an attempt to study an economic means for tunneling, Yen and Zehnder (1973) experimentally investigated the melting of an ice block subject to a highly pressurized, turbulent, axisymmetric, submerged impinging jet. By correlating weight loss data recorded by a load cell as a function of time, average Nusselt number relations were derived as a function of jet discharge temperature. Gilpin (1973–74) experimentally measured the thawing of high-ice-content soils by investigating the impingement of a turbulent, axisymmetric, unsubmerged high-pressure water jet, and he observed that the melt rate of the ice was linearly dependent on the jet temperature. Average Nusselt number correlations were developed as a function of a modified Reynolds number, which was dependent on the pressure of the jet at the nozzle discharge. Lipsett and Gilpin (1978) studied an axisymmetric unsubmerged water jet impinging on a melting surface by using a finite element method to solve the conservation equations. However, they investigated jet Reynolds numbers only in the laminar flow regime. They obtained expressions for the local Nusselt number as a function of the Reynolds number and the radial distance from the stagnation point for various Stefan numbers. However, when they solved the equations in

Contributed by the Heat Transfer Division for publication in the JOURNAL OF HEAT TRANSFER. Manuscript received by the Heat Transfer Division November 1994; revision received February 1996. Keywords: Jets, Moving Boundaries, Phase-Change Phenomena. Associate Technical Editor: B. W. Webb.

the free region, they ignored any curvature effects of the ice and they assumed that the ice maintained its initially flat profile.

Jusionis (1970) was one of the first to develop heat transfer correlations for jet impingement on a curved surface in his study on stagnation-point cooling on the leading edge of supersonic vehicles. Both local and average Nusselt number correlations were determined for gas impingement on a concave surface as a function of angular displacement from the stagnation point along a surface, nozzle-to-surface (stagnation point) spacing, and jet discharge temperature. He concluded that nozzle-to-surface spacing for a jet impinging on a concave surface has less effect on the heat transfer rate than it does for a flat plate. Dyban and Mazur (1970) investigated turbulent gas impingement on a narrow parabolic shaped concave enclosure. The angle of attack of the nozzle with respect to the surface was varied and Nusselt number correlations were obtained as a function of angular distance from the effective stagnation point. They noted marked differences in the distribution of the local heat transfer coefficients in comparison to the flat plate case. More recently, Hrycak (1982) completed a study of gas impingement on a hemispherical plate. Both local and average Nusselt number correlations were developed and they were found to vary with angular coordinate, nozzle-to-plate spacing, Reynolds number, Prandtl number, and nozzle diameter.

In this study, the local, convective heat transfer coefficients are determined for the situation that results when a forced, turbulent, submerged water jet impinges normally on a horizontal sheet of ice that is initially flat. As the heated, axisymmetric jet flows over the impingement surface of the ice, the ice melts and the shape of the surface changes and the flow pattern over the interface changes from a normal stagnation point flow to flow over a concave surface, producing variations in the local heat transfer coefficient with respect to time. An energy balance on the phase-change surface produces an expression for the local heat transfer coefficient as a function of interfacial velocity and slope of the ice/water interface. Values for these two quantities are determined through measurements of the interface profile that are obtained with a dual element high-frequency ultrasonic transducer. The distinguishing feature of the work presented in this paper from previous jet impingement heat transfer studies is the incorporation of (1) a melting interface, (2) a nonuniform impingement surface, and (3) the time-dependent nature of the flow pattern and heat transfer. The resulting Nusselt number correlations for all locations along the ice surface, including the stagnation point, are the first reported for jet impingement that includes phase change for the given conditions of the jet.

Experimental Procedure

A schematic of the ice/water melt interface is shown in Fig. 1. An energy balance at the solid/liquid interface yields the well-known expression (Özişik, 1980)

$$\rho_s h_{sf} v_n = k_s \frac{\partial T_s}{\partial n} - h(r, t)(T_j - T_m) \tag{1}$$

where the latent heat term on the left side is balanced by the difference between the conductive heat transfer through the ice and the convective heat transfer in the liquid. The variable, n, represents the coordinate direction that is normal to the interface into the liquid and v_n is the velocity of the interface along n. A more convenient form of Eq. (1) expressed in cylindrical coordinates is (see appendix for the derivation)

$$\rho_s h_{sf} \frac{\partial \eta(r, t)}{\partial t} = k_s \frac{\partial T_s}{\partial z}\left[\left(\frac{\partial \eta(r, t)}{\partial r}\right)^2 + 1\right] - h(r, t)(T_j - T_m)\left[\left(\frac{\partial \eta(r, t)}{\partial r}\right)^2 + 1\right]^{0.5} \tag{2}$$

where the term $\partial\eta(r, t)/\partial r$ represents the local, instantaneous slope or curvature of the ice interface and $\partial\eta(r, t)/\partial t$ represents the velocity of the interface in the axial (z) direction.

Equation (2) can be simplified by recognizing that the conductive term is negligible in comparison to the convective and latent terms. A computer model was developed to estimate the magnitude of the each of the three terms. The computer model was capable of simultaneously evaluating both the position of the moving interface and the temperature distribution within the solid by solving the two-dimensional, transient energy equation in the solid. The model utilized a line iterative front tracking scheme with a method-of-lines finite differences discretization that employed an invariant embedding solution technique simi-

Nomenclature

c_L = longitudinal speed of sound, m/s
d = diameter, mm
$f^j(r)$ = polynomial expression of the thickness profile for each traverse
F = variable defining the surface of the interface (Appendix A)
g = gravitational acceleration, m^2/s
$h(r, t)$, h = local heat transfer coefficient, W/m^2-K
h_{sf} = latent heat of fusion, J/kg
H = initial thickness of ice sheet, mm
k = thermal conductivity, W/m-K
n = direction normal to the interface
$\bar{n}$ = unit normal in the n direction
Nu = Nusselt number = $h(r, t)d_j/k_j$
r = radial coordinate
Δr = radial distance between measurement points, mm
Re_d = Reynolds number based on jet diameter = $v_j d_j/\nu_j$
Ste = Stefan number
t = time, s or min
t^* = dimensionless time = $v_j t/d_j$
t_f = time-of-flight of sound wave through the ice, μs
Δt = elapsed time between given traverse and $t = 0$, s
T = temperature, K
u = uncertainties in various independent parameters (Eqs. (11)–(15))
v = velocity, m/s
z = axial coordinate
Z = distance between nozzle and ice, mm
$\eta(r, t)$, η = instantaneous location of interface in coordinate system shown in Fig. 1, mm
$\Delta\eta(r, t)$ = difference in ice thickness between measurements, mm
ν = kinematic viscosity, m^2/s
ρ = density, kg/m^3

Subscripts

beg = centerline measurement
i = radial location of interest
j = jet discharge
m = melt
n = direction normal to the interface
o = stagnation condition
s = solid phase
t = control tank
w = supply water

Superscripts

j = current time step
0 = time zero

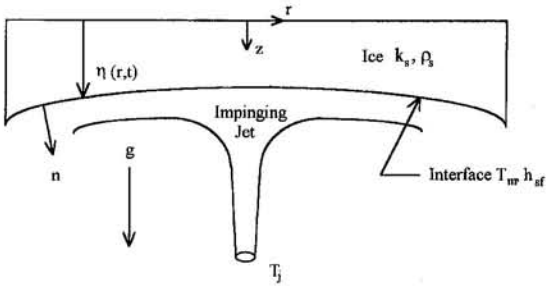

Fig. 1 Schematic of solid/liquid melt interface

lar to the method developed by Meyer (1978, 1981). The accuracy of the model was found to be excellent when compared to other models that can be used to solve moving boundary problems, such as standard finite difference, finite element, and enthalpy methods. Details of the formulation and results of the numerical solution are given by Bhansali (1994). A conservative estimate of the heat transfer coefficient was used in the simulation for a variety of initial ice temperatures ranging between −2°C and −20°C. A conservatively low value for the heat transfer coefficient was chosen in order to provide the maximum possible error when the conductive term was neglected. Typical dimensions of the ice used in the experiment ranged from an initial thickness between 89 mm and 114 mm (nearly 3.5 and 4.5 in.) with a diameter of approximately 0.495 m (19.5 in.). The results of these simulations are shown in Fig. 2. They indicate that the conductive term constituted a maximum of only 7 percent of the total heat transfer at the interface after one minute of elapsed time assuming that the initial temperature of the ice was no lower than −10°C. Therefore, as long as measurements taken at times less than about one minute were eliminated, Eq. (2) could be simplified and rearranged such that the local instantaneous heat transfer coefficient could be estimated by

$$h(r, t) = -\frac{\rho_s h_{sf} \dfrac{\partial \eta(r, t)}{\partial t}}{(T_j - T_m)\left[\left(\dfrac{\partial \eta(r, t)}{\partial r}\right)^2 + 1\right]^{0.5}} \quad (3)$$

The initial ice temperatures in the experiments varied between −5°C and −9°C. Since the value for the heat transfer coefficient used in the computer model was much less than the experimentally measured values, the error due to neglecting the conductive term is actually less than that predicted by the model. Since the density, ρ_s, the latent heat of fusion of the ice, h_{sf}, and the temperature difference between the jet and the melting ice ($T_j - T_m$) are known constants, the convective heat transfer coefficient can be determined once the velocity of the melt interface, $\partial\eta(r, t)/\partial t$ and the slope of the ice/water interface, $\partial\eta(r, t)/\partial r$ are measured.

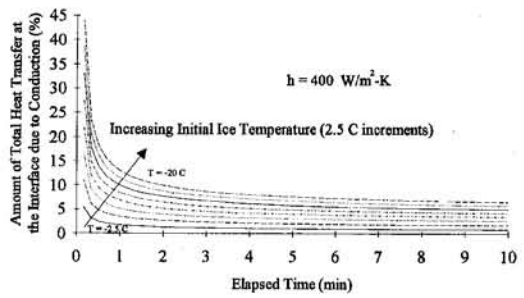

Fig. 2 Conductive heat transfer at the melt interface as a function of time

A schematic of the experimental apparatus used to measure the melt velocity and slope of the ice/water interface is shown in Fig. 3. A fractional horsepower single-speed, centrifugal pump was used to deliver water from a supply tank that was maintained at a constant temperature, T_w = 30°C. The jet water temperature was also monitored and maintained the same as T_w while the volumetric flow rate of the jet was measured with a standard rotameter. The control tank had a diameter of 0.546 m (21.5 in.) and it contained the ambient water. The diameter of the nozzle in the bottom of the control tank was 15.2 mm (0.6 in.). Thermocouples were placed along the inner wall of the control tank to monitor the temperature of the ambient water, T_t, which was initially 19°C. The ambient fluid temperature was subject to a possible rise during the course of a given experiment, but the temperature rise did not exceed 0.8°C during the course of any experiment. The fact that the temperature rise was minimal can be attributed to the fact that cold water was continually being "injected" into the jet boundary layer as a result of the melting. All temperatures were monitored with standard type *T* thermocouples. After exiting the nozzle, the jet was directed vertically upward in the form of a heated water jet that impinged on the under side of the ice sheet. A drain line connected to the bottom of the control tank allowed the water level in the tank to be maintained at a constant height and it therefore was used to prevent any vertical motion of the ice during each experiment.

Each sheet of ice had an initial diameter of approximately 0.495 m (19.5 in.) and ranged in initial thickness, H, between 89 mm and 114 mm (3.5 in. and 4.5 in.). Deaerated water was frozen in the form of large blocks and the ice sheets were cut from these blocks. The ice sheets were placed in an insulation sleeve to prevent heated water from contacting the edge of the ice sheet and also to minimize radial melting. The sleeve was constructed from a closed-cell polyethylene foam. The sleeve was 25.4 mm (1 in.) thick and had a 25.4 mm (1 in.) lip on the bottom that protruded radially inward and rigidly held the ice in place. Once the ice sheets were positioned in the insulation

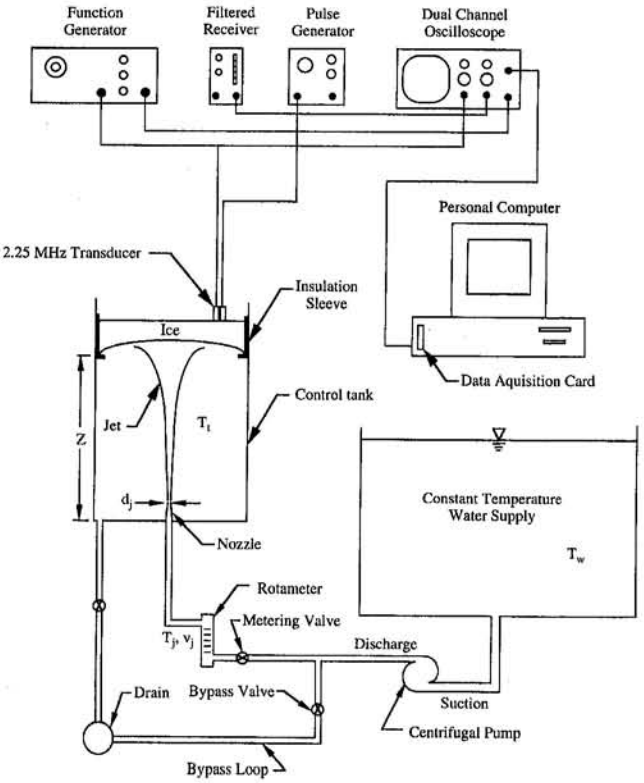

Fig. 3 Experimental model

sleeve, they were then placed into the control tank that had been filled with ambient water to the required elevation. Any air that remained between the bottom surface of the ice and the ambient water level was then removed before the experiment was initiated.

Since the instantaneous, local measurement of the thickness of ice was needed to determine the convective heat transfer coefficient, it was necessary to process and measure the time of transit of the reflected wave from the melting interface of the ice layer. Time-of-flight measurements were performed with a dual element 2.25 MHz ultrasonic transducer as shown in Fig. 3. An electronic signal generator produced the acoustic wave, a couplant was used between the transducer and the medium to transfer the input energy into the specimen, and a receiving transducer collected the acoustic wave upon reflection at the ice/water interface. A gated input signal in the form of a sine wave was produced by a function generator that was pulsed with a pulse generator. A wide-band ultrasonic receiver amplifier was used to eliminate low-frequency noise between 0.5 and 4.0 MHz. A dual channel digital oscilloscope was used to display the incident input and reflected signals. An interface board with a data transfer rate of 1 megabyte/s was installed on a PC-compatible computer to allow communication between the oscilloscope and the computer. More details of the acoustic apparatus are given by Bhansali et al. (1996).

Once the acoustic wave encountered the ice/water interface, it was reflected back toward the top surface of the ice, displayed on the oscilloscope, and eventually downloaded onto the hard drive of the computer in a data file. Each measurement or data point consisted of a time-averaged value of 256 readings, which were sampled by the oscilloscope. There were a total of 1147 data points in all of the experiments combined. The thickness of the ice, $\eta(r, t)$, was then calculated based on the measured time of flight, t_f, and a knowledge of the longitudinal acoustic velocity in ice by using the following equation:

$$\eta(r, t) \approx \frac{c_L t_f}{2} \tag{4}$$

A single traverse of the ice consisted of scanning the top surface and collecting time-of-flight measurements at 12.7 mm ($\frac{1}{2}$ in.) increments from the centerline to the outer edge of the ice. The elapsed time between two adjacent radial locations across the ice surface ranged between five and seven seconds. During the course of a single experiment, prior to the center of the ice melting through, four to six traverses were completed across the surface of ice.

Equation (3) signifies that the heat transfer coefficient depends upon the curvature at the interface and the melt rate of the interface because both of these parameters were dependent on the radial location. Thickness measurements on the ice indicated that the melt rate at each radial location was approximately constant over the majority of a 13 minute duration of a typical experiment with a slight deviation in the linear behavior near the end of the experiment (see Fig. 4). Since the velocity varied in this manner at all radial locations, the velocity of the interface could be approximated, in conjunction with Eq. (4), as

$$\frac{\partial \eta(r, t)}{\partial t} \approx \frac{\Delta \eta_i^j}{\Delta t_i} = \frac{\eta_i^j - \eta_i^0}{\Delta t_i} = \frac{c_L(t_{f_i}^j - t_{f_i}^0)}{2\Delta t_i} \tag{5}$$

where the superscript j represents data collected during the current traverse, the superscript 0 represents data at time, $t = 0$, and the subscript i denotes a specific radial location.

The approximation of the slope, $\partial \eta(r, t)/\partial r$, in Eq. (3) was based on a least-squares regression analysis of the thickness profile data for each traverse. Although the thickness data at each radial location for each traverse were not obtained simultaneously, the data could be extrapolated back to the time at which the centerline measurement was made because the melt

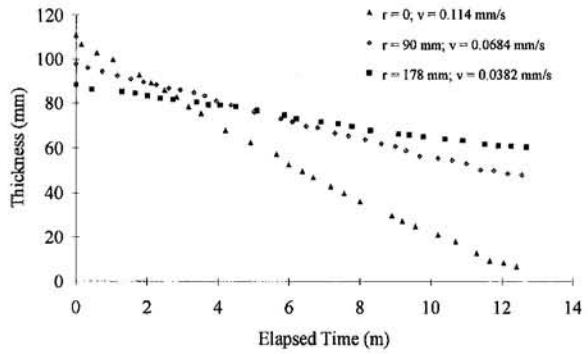

Fig. 4 Representative variation in ice thickness as a function of time, $Re_d = 9220$, $Z/d_j = 15$

rate at each radial location was found to be constant. The regression yielded a polynomial expression at each traverse for the thickness as a function of radial distance from the stagnation point. This expression could then be differentiated and evaluated at discrete radial locations to give the required slope

$$\frac{\partial \eta(r, t)}{\partial r} \approx \frac{d}{dr} f^j(r)\big|_{t_{\text{beg}}} \tag{6}$$

where $f^j(r)$ is the polynomial expression and t_{beg} is the time at which the centerline measurement was made for each traverse.

Uncertainty Analysis

Since this paper describes a new experimental methodology for evaluating heat transfer coefficients, it is important that the uncertainty analysis be presented in some detail. Equation (3) reflects the dependency of local heat transfer coefficient on thermal properties, h_{sf} and ρ_s, as well as on other measured quantities, $(T_j - T_m)$, $\partial \eta(r, t)/\partial t$, and $\partial \eta(r, t)/\partial r$. Since the errors in each of the variables are random, they can be combined in the quadrature such that the uncertainty in the heat transfer coefficient can be represented as (Taylor, 1982)

$$u_h = \left\{ \left(\frac{\partial h}{\partial \rho_s} u_{\rho_s} \right)^2 + \left(\frac{\partial h}{\partial h_{sf}} u_{h_{sf}} \right)^2 + \left(\frac{\partial h}{\partial (T_j - T_m)} u_{(T_j - T_m)} \right)^2 + \left(\frac{\partial h}{\partial (\partial \eta/\partial t)} u_{\partial \eta/\partial t} \right)^2 + \left(\frac{\partial h}{\partial (\partial \eta/\partial r)} u_{\partial \eta/\partial r} \right)^2 \right\}^{0.5} \tag{7}$$

Ideally, each individual experiment should be repeated sufficient times that the reliability of the results could be assured by using multiple-sample statistical methods. However, repetition was not feasible in this study and hence, each data point obtained in this study was a result of a single-sample estimate. Hence, the standard procedure for evaluating u_h could not be applied. However, Kline and McClintock (1953) developed a methodology that has been used as the standard (by AIAA) for evaluating uncertainty in single-sample experiments.

The ability to evaluate the uncertainty in the heat transfer coefficient lies in the ability to determine the uncertainty in each of the independent variables, as shown in Eq. (7). Keenan (1970), Hobbs (1974), and Eisenberg and Kauzmann (1969) have documented values of the latent heat of fusion of water at atmospheric pressure to be within 0.11 percent of each other so the uncertainty in the latent heat of fusion was assumed to be negligible in this study. The density of ice at the fusion temperature is also well documented (Lonsdale, 1958; Ginnings and Corruccini, 1947) and this value was used in Eq. (3). However, since the initial ice temperature was as low as −9°C, the maximum possible uncertainty in the density was determined to be 2.3 kg/m^3. Standard copper-constantan type-T ther-

mocouples were used in the experiment to measure relative temperatures, and as specified by the manufacturer, the maximum uncertainty in measuring these temperatures was 1.21°C. The digital thermometer used in the apparatus was calibrated over the range of temperatures experienced in any given experiment and its uncertainty was found to be negligible in comparison to the uncertainty associated with the thermocouple.

By inspection of Eqs. (4) and (5), it can be seen that the evaluation of the uncertainty in the melt velocity, $\partial\eta(r, t)/\partial t$ is dependent on the individual uncertainties of the acoustic velocity, the time of flight, t_f, and the time elapsed up to the current traverse, Δt, and can be expressed as (Taylor, 1982)

$$\frac{u_{(\partial\eta/\partial t)}}{|(\partial\eta/\partial t)|} = \left\{\left(\frac{u_{c_L}}{c_L}\right)^2 + 2\left(\frac{u_{t_f}}{t_f}\right)^2 + \left(\frac{u_{\Delta t}}{\Delta t}\right)^2\right\}^{0.5} \quad (8)$$

While the acoustic velocity, and therefore its uncertainty, both vary with the type of ice and its crystalline structure, Hobbs (1974) has documented that only one type of ice, hexagonal type Ih, is possible for water frozen at atmospheric pressure above −80°C. The ice used in this study was well within this regime and the value of the acoustic velocity used in this study was the average of the values obtained at the melt temperature from various references (Kaye and Laby, 1973; Krautkramer and Krautkramer, 1990; Hobbs, 1985, 1974; Smith and Kishoni, 1986). Hansman and Kirby's (1985) study further verified that the acoustic velocity in ice was insensitive to the type of ice, either glazed, rimed, or crystalline. The maximum uncertainty in the acoustic velocity was then determined to be the maximum variance between any two of the values from the cited references. The dependence of c_L on temperature over the range of ice temperatures experienced in this study was negligible. The uncertainty in t_f was specified by the manufacturer of the transducer to be 0.0195 ms while the uncertainty in Δt was negligible compared to the uncertainty in c_L and t_f.

The uncertainty in the curvature was more involved since there were three possible sources of error: (1) uncertainty in the thickness measurements (time-of-flight readings), (2) uncertainty in the radial location at which the transducer was positioned, and (3) uncertainty in the regression analysis. Since no analytical expression for the uncertainty in the curvature was attainable, a Monte Carlo simulation technique was performed for each traverse of each experiment to determine the maximum uncertainty in the slope (Scott, 1995). Having determined the uncertainty in each of the independent variables, Eq. (7) was then used to evaluate the maximum uncertainty in the heat transfer coefficient, which was determined to be 128 W/m^2-K. All the individual uncertainties used in this study were within the 95 percent confidence interval.

Results

Experiments were performed for jet Reynolds number in the turbulent regime between 6150 and 15,370. Since the average heat transfer coefficients have been shown to be independent for $Z/d_j < 7$ (Sitharamayya and Raju, 1969; Rao and Trass, 1964), the majority of the experiments were performed at values of Z/d_j outside this range. Values of Z/d_j were varied between 5.8 and 20. The characteristic temperature difference employed in the definition of the heat transfer coefficient in this study was the one utilized in most jet impingement studies: that is, the difference between the jet discharge temperature and the impingement surface temperature, $(T_j - T_m)$. Even though the ambient temperature of the water in the tank was not regulated, it remained practically constant during all experiments and therefore the use of $(T_j - T_m)$ as the temperature difference in the definition of the heat transfer coefficient was reasonable.

The general trends in the data suggest that the melt rate and hence, the magnitude of the local heat transfer coefficient, increased as the flow rate was increased and/or the nozzle-to-ice height was decreased. The local heat transfer coefficient was found to have a relatively weak dependence on the nozzle-to-ice height except in the region close to the stagnation point. The heat transfer coefficient at each radial location was also found to decrease with respect to time due primarily to two factors: (1) an increase in the curvature close to the centerline with respect to time, which leads to a general decrease in liquid velocity over the surface of the ice, and (2) an accumulation of a stagnant water layer underneath the ice that serves as a thermal resistance to heat transfer.

The shape of the surface of the ice can significantly affect the value of the local heat transfer coefficient. Figures 5(a, b) represent the local variation in the heat transfer coefficient corresponding to the ice thickness profiles shown in Figs. 6(a, b) respectively. In the case of the larger Reynolds number, the presence of a steep cavity begins to appear in the third and fourth traverses, which inhibited the spreading of the jet across the surface of the ice, reducing the heat transfer process at the stagnation point and causing a rapid decline in the local transfer coefficient in the radial direction.

Figures 6(a, b) show the radial variation in the thickness profiles for extreme cases. Figure 6(a) represents a test that was performed at the lowest Re_d and highest Z/d_j while Fig. 6(b) represents a case that was performed at the highest Re_d and lowest value Z/d_j. By inspection of Fig. 6(a), it can be seen that a slightly sloping profile exists along the ice/water interface for the small Reynolds numbers and large nozzle-to-ice spacings while Fig. 6(b) shows that the profile of the interface can have a more complex shape for the other extreme case. For the data represented by the conditions Re_d = 15,370 and Z/d_j = 5.8, the jet bored a somewhat narrow, steep cavity into the ice that was centered at the stagnation point. The steep curvature of the cavity deflected the jet downward, inhibiting flow in the radial direction. In addition, the water was sufficiently cooled while in contact with the ice in the cavity so that the buoyancy of the heated jet was reduced. When the temperature of the water in the jet

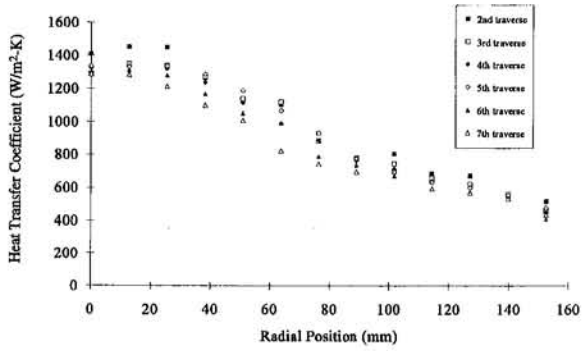

Fig. 5(a) Radial variation in the heat transfer coefficients, Re_d = 6150, Z/d_j = 15

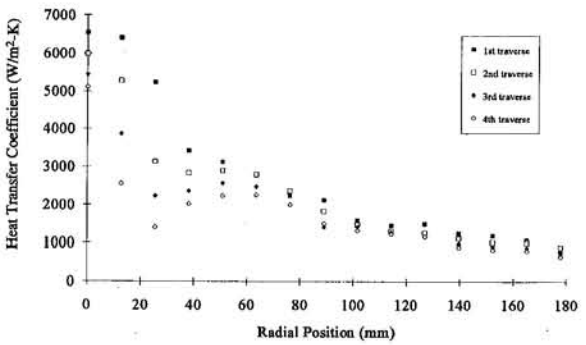

Fig. 5(b) Radial variation in the heat transfer coefficients, Re_d = 15370, Z/d_j = 5.8

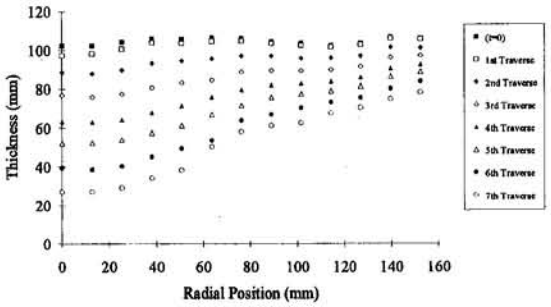

Fig. 6(*a*) Thickness profiles, Re_d = 6150, Z/d_j = 15

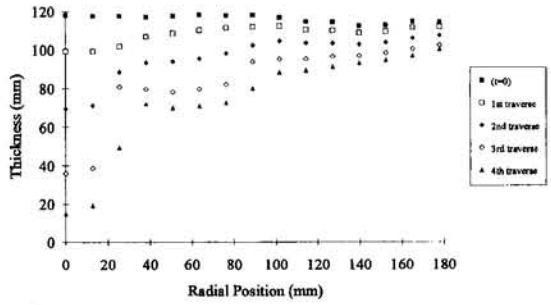

Fig. 6(*b*) Thickness profiles, Re_d = 15,370, Z/d_j = 5.8

dropped below the temperature of the ambient fluid, it entrained surrounding fluid and created a secondary circulation cell, shown schematically in Fig. 7. The occurrence of the secondary cell tended to produce a second shallow cavity in the ice farther away from the stagnation point. When this flow phenomenon occurred, an annular lip of ice remained between the deep central cavity and the shallow secondary cavity near the outer edge of the ice sample. This type of ice surface profile can be seen in the data illustrated in Fig. 6(*b*), especially during the third and fourth traverses of the ice.

Heat Transfer Coefficients. The shape that the ice attained as it was melted by the jet played a large role in determining the local heat transfer coefficients. In particular, a secondary peak in the local heat transfer coefficient can result that is solely dependent on the curvature along the interface. Martin (1977) also documented secondary peaks in the heat transfer coefficient for the case of submerged impingement on a normal, flat surface, but he attributed these peaks to transition from the laminar to turbulent flow regimes in the wall jet region that is radially displaced from the stagnation point. Although previous studies have considered jet impingement on nonuniform surfaces, the issue of heat transfer on a melting concave surface that continually changes shape has not been addressed.

For low Re_d and large values of Z/d_j, the local heat transfer coefficients were found to decrease gradually from the stagnation point, while at higher values of Re_d and lower values of Z/d_j, the trend in the local heat transfer coefficients reflected the more complex shape of the ice surface. Typical results are shown in Figs. 8(*a*, *b*). In Fig. 8(*a*), the low mass flow rate jet separated far from the surface of the ice created a gradual decrease in the heat transfer coefficient from the stagnation point. In Fig. 8(*b*), the results clearly reflect the occurrence of the ridge formed between the two cavities and the appearance of a local minima in the heat transfer coefficient at the location of the ridge. The variation in heat transfer coefficient becomes more severe as time progresses and as the depth of the two cavities increases.

Figure 8(*a*) shows local heat transfer data during the first traverse for a fixed ice spacing and different jet Reynolds numbers. The results show the decline in values for increasing radial distances from the stagnation point and the decrease in local values as the Reynolds number decreases. The data in Fig. 8(*b*) show the variation in heat transfer coefficient for a fixed value of jet Reynolds number during the initial traverse. The heat transfer coefficient has a relatively weak dependence on the separation distance between the jet and the surface of the ice except for the region close to the stagnation point. The data for $Z/d_j = 5.8$ show the large increase in the stagnation point heat transfer that occurs early in the melting process. The high heat transfer at the jet centerline decreases rapidly as the jet begins to bore a steep cavity into the ice. The presence of the cavity inhibits flow across the surface of the ice and the heat transfer process at the stagnation point becomes less efficient.

Nusselt Number Correlations. In order to formulate the measured heat transfer coefficient data into a dimensionless correlation, a dimensional analysis was performed on the data. The analysis produced the following nondimensional relation:

$$\mathrm{Nu} = \frac{hd_j}{k_w} = f\left(\frac{v_j t}{d_j}, \frac{v_j d_j}{\upsilon_j}, \frac{Z}{d_j}, \frac{r}{d_j}\right) = f\left(t^*, \mathrm{Re}_d, \frac{Z}{d_j}, \frac{r}{d_j}\right) \quad (9)$$

Typically of phase-change problems involving melting or solidi-

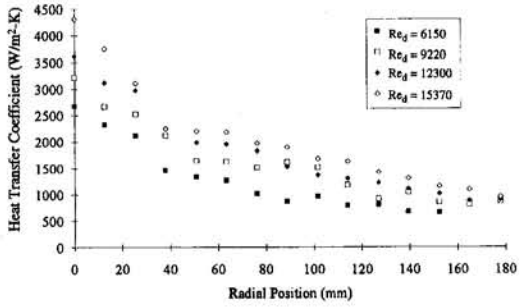

Fig. 8(*a*) Radial variation in the heat transfer coefficients, the initial traverse, Z/d_j = 15

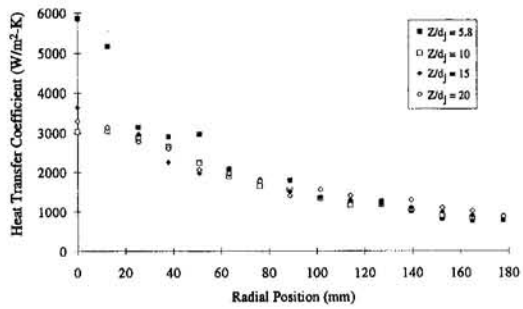

Fig. 8(*b*) Radial variation in the heat transfer coefficients for the initial traverse, Re_d = 12,300

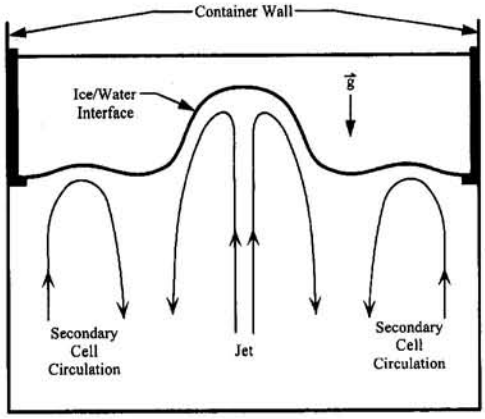

Fig. 7 Schematic of secondary flow cells

fication, a Stefan number would normally be included in the analysis. However, since all experiments were performed at Ste = 0.18, it was unnecessary to include the Stefan number in the formulation.

Before determining the precise functionality in Eq. (9), the data points for all the experimental runs, excluding the stagnation point data, were divided into two regimes: one regime for $r/d_j \leq 4.2$ and the other regime for $r/d_j > 4.2$. A regression analysis was then performed on the data using the SAS statistical software package. Both linear (power-law) and nonlinear regression models were considered. Four nonlinear models were developed that included as many as 12 parameters (Emanuel and Barcenas, 1994). However, the linear model gave more accurate results with a lower value of the mean square error. The resulting correlating equations for the two regimes were determined to be:

$$\mathrm{Nu} = 0.315\ \mathrm{Re}_d^{0.776}\ t^{*\,-0.147}(Z/d_j)^{-0.235}(r/d_j)^{-0.325} \qquad \frac{r}{d_j} \leq 4.2 \quad (10a)$$

$$\mathrm{Nu} = 0.091\ \mathrm{Re}_d^{0.886}\ t^{*\,-0.101}(r/d_j)^{-0.845} \qquad \frac{r}{d_j} > 4.2 \quad (10b)$$

for $6 \times 10^3 \leq \mathrm{Re}_d \leq 1.6 \times 10^4$, $5 \leq Z/d_j \leq 20$, Pr ≈ 5, and Ste = 0.18. The results of the regression analysis indicate that the heat transfer coefficient is relatively independent of Z/d_j for $r/d_j > 4.2$ (in the developed wall jet region). This phenomenon was also observed by Stevens and Webb (1989), Vallis et al. (1978), and Ma et al. (1988). Inspection of the results from the regression analysis also suggests that more scatter in the data exists in the regime $r/d_j \leq 4.2$ than in the regime $r/d_j > 4.2$ as shown in Fig. 9. This observation can be explained because the data in the regime $r/d_j \leq 4.2$ include the majority of the points measured in the region in which steep slopes and secondary cavities in the ice occurred and these factors were known to produce the greatest uncertainty when acoustically measuring the local ice thickness.

The stagnation point Nusselt number necessitated a separate correlation solely due to the independence of the Nusselt number on r/d_j at the stagnation point. A linear regression was performed on the stagnation point data and it yielded the following expression for the stagnation point Nusselt number:

$$\mathrm{Nu}_o = 0.210\ \mathrm{Re}_d^{0.934}\ t^{*\,-0.173}(Z/d_j)^{-0.551} \quad (11)$$

Figure 10 shows the correlation between the curve given by Eq. (11) and the measured stagnation point heat transfer coefficients.

The accuracy of the Nusselt number correlations is the lowest in the regime $r/d_j \leq 4.2$ governed by Eq. (10a). The reduced accuracy is expected because local minima and secondary peaks in the local heat transfer coefficient occur in this regime. Hence, the Nusselt number correlation frequently overpredicts the heat transfer in this regime. However, 91 percent of all data points in this regime predicted by the correlations falls within 25 percent of the measured values while 96 percent of the points in the regime, $r/d_j > 4.2$, and 94 percent of the stagnation point data fall within 25 percent of the measured values. The mean square errors associated with the regression were determined to be 0.031, 0.021, and 0.014 for the $r/d_j \leq 4.2$ regime, $r/d_j > 4.2$ regime, and the stagnation point, respectively.

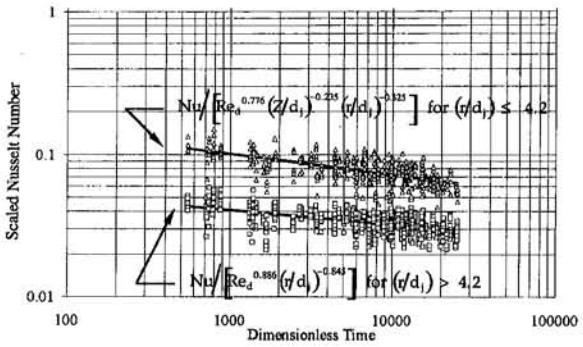

Fig. 9 Scaled Nusselt number correlation

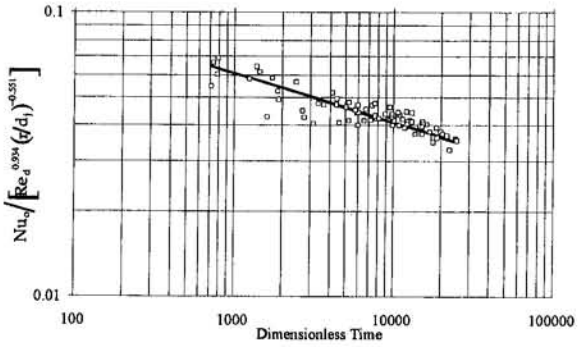

Fig. 10 Scaled Nusselt number correlation at stagnation point

Concluding Remarks

An ultrasonic technique was designed and utilized to measure radial variations in the heat transfer coefficient for a turbulent, submerged, liquid jet impinging vertically on a horizontal surface of a sheet of ice. Local Nusselt number correlations were developed for a range of turbulent Reynolds number and various nozzle-to-ice spacings for a constant-diameter jet. Separate Nusselt number correlations were obtained for the stagnation point and for the local, instantaneous heat transfer coefficient at radial positions excluding the stagnation point. This study is the first instance in which jet impingement heat transfer coefficients were measured on a surface that continually changed shape during the process. The results show that secondary flow cells developed on the ice/water interface for low nozzle-to-ice distances and high jet Reynolds numbers. These cells caused irregular shapes to be formed on the ice/water interface and they played a large role in determining the magnitude of the local heat transfer coefficients. The boundary between the two counterrotating cells formed a ridge in the ice that was a location of low melt rates and corresponded to a location of low heat transfer coefficients.

Acknowledgments

We would like to express gratitude to the Georgia Power Company for funding this work. We would also like to extend our appreciation to Sally Sellers and Nick Francis for their assistance in the data acquisition.

References

Bhansali, A. P., 1994, PhD Thesis, Georgia Institute of Technology, Atlanta, GA.

Bhansali, A. P., Black, W. Z., and Jarzynski, J., 1996, "Ultrasonic Measurement of Convective Heat Transfer Coefficients on a Non-uniform Melt Layer," *Review of Scientific Instruments,* Vol. 67, pp. 1577–1585.

Brdlik, P. M., and Savin, V. K., 1965, "Heat Transfer Between an Axisymmetric Jet and a Plate Normal to the Flow," *Journal of Engineering Physics,* Vol. 8, pp. 91–98.

Chatwani, A. U., Goldfarb, V., and Woodroffe, J., 1991, "Heat Transfer Issues in a Slagbath Heated by an Impinging Combustion Jet," *Heat Transfer in Metals and Containerless Processing and Manufacturing,* ASME HTD-Vol. 162, pp. 57–66.

Donaldson, C. D., Snedeker, R. S., and Margolis, D. P., 1971, "A Study of Free Jet Impingement: Pt. 2: Free Jet Turbulent Structure and Impingement Heat Transfer," *Journal of Fluid Mechanics,* Vol. 45, Pt. 3, pp. 477–512.

Dyban, Y. P., and Mazur, A. I., 1970, "Heat Transfer From a Flat Air Jet Flowing Into a Concave Surface," *Heat Transfer—Soviet Research,* Vol. 2, No. 3, pp. 15–20.

Eisenberg, D., and Kauzmann, W., 1969, *The Structure and Properties of Water,* Oxford University Press, New York, p. 100.

Emanuel, K., and Barcenas, C., 1994, private communication.

Epstein, M., et al., 1980, "Simultaneous Melting and Freezing in the Impingement Region of a Liquid Jet," *American Institute of Chemical Engineers,* Vol. 26, No. 5, pp. 743–751.

Gilpin, R. R., 1973–74, "The Ablation of Ice by a Water Jet," *Transactions of the Canadian Society of Mechanical Engineering,* Vol. 2, No. 2, pp. 91–96.

Ginnings, D. C., and Corruccini, R. J., 1947, "An Improved Ice Calorimeter—the Determination of Its Calibration Factor and the Density of Ice at 0°C," *Journal of Research,* National Bureau of Standards, Vol. 38, pp. 583–602.

Giralt, F., Chia, C., and Trass, O., 1977, "Characterization of the Impingement Region in an Axisymmetric Turbulent Jet," *Industrial Engineering Chemistry, Fundamentals,* Vol. 16, No. 1, pp. 21–27.

Hansman, R. J., Jr. and Kirby, M. S., 1985, "Measurement of Ice Accretion Using Ultrasonic Pulse-Echo Techniques," *Journal of Aircraft,* Vol. 22, No. 6, pp. 530–534.

Hobbs, P. V., 1974, *Ice Physics,* Clarendon Press, Oxford, pp. 257; 1; 361.

Hrycak, P., 1982, "Heat Transfer and Flow Characteristics of Jets Impinging on a Concave Hemispherical Plate," *Proceedings of the 7th International Heat Transfer Conference,* Vol. 3, pp. 357–362.

Jusionis, V. J., 1970, "Heat Transfer From Impinging Gas Jets on an Enclosed Concave Surface," *Journal of Aircraft,* Vol. 7, No. 1, pp. 87–88.

Kaye, G. W. C., and Laby, T. H., 1973, *Tables of Physical and Chemical Constants,* 14th ed., Longman Group Limited, London, p. 68.

Keenan, J. H., 1970, *Thermodynamics,* Wiley, New York, p. 45.

Kiper, A. M., 1984, "Impinging Water Jet Cooling of VLSI Circuits," *International Communications in Heat and Mass Transfer,* Vol. 11, pp. 517–526.

Kline, S. J., and McClintock, F. A., 1953, "Describing Uncertainties in Single-Sample Experiments," *Mechanical Engineering,* Jan., pp. 3–8.

Krautkramer, J., and Krautkramer, H., 1990, *Ultrasonic Testing of Materials,* 4th ed., Springer-Verlag, Berlin, p. 620.

Lipsett, A. W., and Gilpin, R. R., 1978, "Laminar Jet Impingement Heat Transfer Including the Effects of Melting," *International Journal of Heat and Mass Transfer,* Vol. 21, pp. 25–33.

Lonsdale, K., 1958, "The Structure of Ice," *Proceedings of the Royal Society A,* Vol. 247, pp. 424–434.

Ma, C. F., Tian, Y. Q., Sun, H., Lei, D. H., and Bergles, A. E., 1988, "Local Characteristics of Heat Transfer From a Small Heater to an Impinging Round Jet of Liquid of Larger Pr Number," presented at the International Symposium on Heat Transfer Enhancement and Energy Conservation, People's Republic of China.

Martin, H., 1977, "Heat and Mass Transfer Between Impinging Gas Jets and Solid Surfaces," *Advances in Heat Transfer,* Vol. 13, pp. 1–60.

Metzger, D. E., Cummings, K. N., and Ruby, W. A., 1974, "Effects of Prandtl Number on Heat Transfer Characteristics of Impinging Liquid Jets," *Proceedings of the International Heat Transfer Conference,* Vol. II, pp. 20–24.

Meyer, G. H., 1978, "Direct and Iterative One-Dimensional Front Tracking Methods for the Two-Dimensional Stefan Problem," *Numerical Heat Transfer,* Vol. 1, pp. 3511–364.

Meyer, G. H., 1981, "The Method of Straight Lines and Invariant Imbedding for Elliptic and Parabolic Free Boundary Problems," *Society for Industrial and Applied Mathematics, Journal of Numerical Analysis,* Vol. 18, No. 1, pp. 150–164.

Özişik, M. N., 1980, *Heat Conduction,* Wiley, New York, p. 403.

Rao, V. V., and Trass, O., 1964, "Mass Transfer From a Flat Surface to an Impinging Turbulent Jet," *The Canadian Journal of Chemical Engineering,* pp. 95–99.

Scott, D., 1995, private communication, Rice University, Houston, TX.

Sitharamayya, S., and Raju, S. K., 1969, "Heat Transfer Between an Axisymmetric Jet and a Plate Held Normal to the Flow," *The Canadian Journal of Chemical Engineering,* Vol. 47, pp. 365–368.

Smith, A. C., and Kishoni, D., 1986, "Measurement of the Speed of Sound in Ice," *American Institute of Aeronautics and Astronautics Journal,* Technical Notes, Vol. 24, No. 10, pp. 1713–1715.

Stefanick, T., 1988, "The Nonacoustic Detection of Submarines," *Scientific American,* Vol. 258, No. 3, pp. 41–47.

Stevens, J., and Webb, B. W., 1989, "Local Heat Transfer Coefficients Under an Axisymmetric, Single-Phase Liquid Jet," ASME HTD-Vol. 111, pp. 113–119.

Taylor, J. R., 1982, *An Introduction to Error Analysis,* University Science Books, Mill Valley, CA, pp. 73; 57.

Vallis, E. A., Patrick, M. A., and Wragg, A. A., 1978, "Radial Distribution of Convective Heat Transfer Coefficient Between an Axisymmetric Turbulent Jet and a Flat Plate Held Normal to the Flow," *Proceedings of the 6th International Heat Transfer Conference,* Vol. 5, pp. 297–303.

Womac, D. J., Ramadhyani, S., and Incropera, F. P., 1993, "Correlating Equations for Impingement Cooling of Small Heat Sources With Single Circular Liquid Jets," ASME JOURNAL OF HEAT TRANSFER, Vol. 115, pp. 106–115.

Yen, Y. C., and Zehnder, A., 1973, "Melting Heat Transfer With a Water Jet," *International Journal of Heat and Mass Transfer,* Vol. 16, pp. 219–23.

Yen, Y.-C., 1974, "Heat Transfer Characteristics of a Bubble-Induced Water Jet Impinging on an Ice Surface," *International Journal of Heat and Mass Transfer,* Vol. 18, pp. 917–926.

APPENDIX

The well-known energy balance at the interface (Fig. 2) is expressed by

$$\rho_s h_{sf} v_n = k_s \frac{\partial T_s}{\partial n} - h(T_j - T_m) \tag{A1}$$

This energy balance is valid along the surface in a cylindrical frame of reference for an axisymmetric case:

$$F(r, z, t) = 0 \tag{A2}$$

Since both F and the temperature along the interface are constant, then

$$\vec{n} = \frac{\nabla F}{|\nabla F|} = \frac{\nabla T_s}{|\nabla T_s|} \quad \text{where} \quad \nabla = \frac{\partial}{\partial r}\vec{e}_r + \frac{\partial}{\partial z}\vec{e}_z \tag{A3}$$

and the temperature gradient and the interface velocity normal to the interface are written as

$$\frac{\partial T_s}{\partial n} = \nabla T_s \cdot \vec{n} = \frac{\nabla T_s \cdot \nabla F}{|\nabla F|} \tag{A4}$$

$$v_n = \nabla \vec{v} \cdot \vec{n} = \frac{\vec{v} \cdot \nabla F}{|\nabla F|} \tag{A5}$$

where $\vec{v} = \dot{r}\vec{e}_r + \dot{z}\vec{e}_z$. The dot terms represent derivatives with respect to time.

Evaluating the total derivative of Eq. (A2) and rearranging terms produces the relation

$$\frac{\partial F}{\partial t} = -\frac{\partial F}{\partial r}\dot{r} - \frac{\partial F}{\partial z}\dot{z} \tag{A6}$$

Then utilizing Eq. (A6)

$$\vec{v} \cdot \nabla F = (\dot{r}\vec{e}_r + \dot{z}\vec{e}_z) \cdot \left(\frac{\partial F}{\partial r}\vec{e}_r + \frac{\partial F}{\partial z}\vec{e}_z\right)$$

$$= \dot{r}\frac{\partial F}{\partial r} + \dot{z}\frac{\partial F}{\partial z} = -\frac{\partial F}{\partial t} \tag{A7}$$

Introducing Eq. (A7) into Eq. (A5) yields

$$v_n = -\frac{\partial F/\partial t}{|\nabla F|} \tag{A8}$$

Substituting of Eqs. (A4) and (A8) into Eq. (A1) allows the energy balance to be represented by:

$$\rho_s h_{sf} \frac{(-\partial F/\partial t)}{|\nabla F|} = k_s \frac{\nabla T_s \cdot \nabla F}{|\nabla F|} - h(T_j - T_m) \tag{A9}$$

Defining

$$F(r, z, t) \equiv z - \eta(r, t) \tag{A10}$$

and evaluating its partial derivatives with respect to variables r and z allows $|\nabla F|$ to be written as

$$|\nabla F| = \left|\frac{\partial F}{\partial r}\vec{e}_r + \frac{\partial F}{\partial z}\vec{e}_z\right|$$

$$= \left[\left(\frac{\partial F}{\partial r}\right)^2 + \left(\frac{\partial F}{\partial z}\right)^2\right]^{0.5} = \sqrt{\left(\frac{\partial \eta}{\partial r}\right)^2 + 1} \tag{A11}$$

By inspection of Eq. (A3), it is obvious that

$$\frac{\partial T_s}{\partial r}\vec{e}_r + \frac{\partial T_s}{\partial z}\vec{e}_z = \beta\left(\frac{\partial F}{\partial r}\vec{e}_r + \frac{\partial F}{\partial z}\vec{e}_z\right) \tag{A12}$$

where β is a scalar coefficient given by $\beta = \partial T_s/\partial F$. Then from Eq. (A12)

$$\frac{\partial T_s}{\partial r} = \frac{\partial T_s}{\partial F}\frac{\partial F}{\partial r} \tag{A13a}$$

$$\frac{\partial T_s}{\partial z} = \frac{\partial T_s}{\partial F}\frac{\partial F}{\partial z} \tag{A13b}$$

Solving Eq. (A13b) for $\partial T_s/\partial F$ and substituting into Eq. (A13a) yields

$$\frac{\partial T_s}{\partial r} = \frac{\partial T_s}{\partial z}\frac{\partial z}{\partial F}\frac{\partial F}{\partial r} \tag{A14}$$

Then

$$\nabla T_s \cdot \nabla F = \frac{\partial T_s}{\partial r}\frac{\partial F}{\partial r} + \frac{\partial T_s}{\partial z}\frac{\partial F}{\partial z} = \frac{\partial T_s}{\partial z}\left[\frac{\partial z}{\partial F}\left(\frac{\partial F}{\partial r}\right)^2 + \frac{\partial F}{\partial z}\right]$$

$$= \frac{\partial T_s}{\partial z}\left[\left(\frac{\partial \eta}{\partial r}\right)^2 + 1\right] \tag{A15}$$

Substituting Eqs. (A11) and (A15) into Eq. (A9) and recognizing that $\partial F/\partial t = -\partial \eta/\partial t$ from Eq. (A10) gives the energy balance in its desired form:

$$\rho_s h_{sf}\frac{\partial \eta}{\partial t} = k_s\frac{\partial T_s}{\partial z}\left[\left(\frac{\partial \eta}{\partial r}\right)^2 + 1\right] - \left[\left(\frac{\partial \eta}{\partial r}\right)^2 + 1\right]^{0.5} h(T_j - T_m) \tag{A16}$$

Experimental and Theoretical Studies of Mist Jet Impingement Cooling

K. M. Graham

S. Ramadhyani

Heat Transfer Laboratory,
School of Mechanical Engineering,
Purdue University,
West Lafayette, IN 47907

Experimental data and analytical predictions for air/liquid mist jet cooling of small heat sources are presented. The mist jet was created using a coaxial jet atomizer, with a liquid jet of diameter 190 μm located on the axis of an annular air jet of diameter 2 mm. The impingement surface was a square of side 6.35 mm. Experimental data were obtained with mists of both methanol and water. Surface-averaged heat fluxes as high as 60 W/cm² could be dissipated with the methanol/air mist while maintaining the target surface below 70°C. With the water/air mist, a heat flux of 60 W/cm² could be dissipated with the target surface at 80°C. Major trends in the data and model predictions have been explained in terms of the underlying hydrodynamic and heat transfer phenomena.

Introduction

The impingement of a gas/liquid mist on a surface is an effective way of dissipating high heat fluxes from the surface. Several studies of mist impingement, in which surface temperatures exceeded the normal boiling temperature of the liquid, can be found in the literature (e.g., Ohkubo and Nishio, 1989; Koria and Datta, 1992). However, studies of mist impingement on surfaces at temperatures lower than the normal boiling temperature of the liquid are more sparse, and the literature to date does not lead to a thorough understanding of the phenomena involved. The present work is an attempt to redress this situation by obtaining experimental data with two different liquids—water and methanol—and developing a simple analytical model to predict the results. Although the work is part of an ongoing effort to develop new schemes for cooling high-power microelectronic chips, the results of this investigation may find applications in other technological areas as well.

A brief review of the available literature will provide a rationale for the present study. Siwon and Wisniewski (1986) modeled mist impingement by assuming the entire impingement surface was covered with a thin laminar liquid film, that the film was undisturbed by impinging droplets, that no evaporation occurred from the liquid film surface, that no heat transfer occurred from the film surface to the gas jet, and that droplets entered the film only in the impingement region. They did not attempt to verify their model through a quantitative comparison with experimental data. Hatta et al. (1991) numerically investigated a laminar mist jet impinging on a surface. Their numerical scheme involved tracking the trajectories of small groups of particles through the computational domain. A serious deficiency of their model is that heat absorption due to evaporation of the particles was neglected. Ma and Tian (1990) experimentally measured impingement heat transfer in a water–nitrogen mist. They measured a heat flux of 280 W/cm² at a low surface temperature of 58°C and a water-to-nitrogen mass flow ratio of 4.3. They did not explain the mechanisms behind their extraordinarily high heat fluxes.

Pais et al. (1992) investigated surface roughness effects in an air–water mist impingement scheme. Their experiment was mostly concerned with nucleation and boiling of the thin film on the surface, but some data were given for temperatures in the range of 80 to 100°C for water. For a water-to-air mass flow ratio of 2.09, with an air flow rate of 0.16 liters per second, the heat flux at 80°C was 200 W/cm². Sehmbey et al. (1992), a few months later, reported experimental results with essentially the same apparatus. For a water-to-air mass flow ratio of 1.49, and air flow rate of 0.16 liters per second, the heat flux at 80°C was about 100 W/cm², a value that is substantially lower than in their previous study. The large difference in heat flux between the two studies was not discussed in the latter study.

Siwon (1993) measured the thickness of the film that is formed when a mist impinges on a flat surface. In the impingement region, films from 10 to 30 μm thick were measured, and thicknesses as high as 50 μm were noted further out. No heat transfer measurements were reported in that study.

In summary, it appears that there is a very limited knowledge base on mist jet impingement cooling of surfaces for situations in which the surface temperature is below the boiling point of the liquid. Only a few experimental studies have been reported, and differences in the results reported by different investigators are irreconcilably large. Attempts to model the situations analytically have also been limited, and few comparisons between model predictions and experimental data have been provided.

The present paper reports a combined experimental and analytical study of gas/liquid mist jet impingement cooling. Experiments were conducted with air/water and air/methanol mist jets with varying air velocities and liquid mass flow rates. A simple analytical model was developed to predict the liquid film thickness and the heat transfer rate. Although the model is a great simplification of the physical situation, its predictions are in very good agreement with the air/methanol data and tolerable agreement with the air/water data.

Figure 1(*a*) is a schematic of the gas/liquid mist jet investigated in this study. The mist is formed by an annular air jet atomizing a liquid jet located in its core. The mist impinges on the surface, where the droplets form a thin film. There are three different components of the overall heat transfer: an evaporative component at the air/liquid interface; a convective component at the air/liquid interface due to the air flow over the surface of the heated liquid film; and a component due to the sensible heating of the liquid in the film as it flows from the stagnation point toward the edge of the heater.

Experimental Apparatus and Procedures

The experimental apparatus consisted of an atomizing nozzle, an air flow system, a liquid flow system, a power supply, a heater module, and a data acquisition unit. The atomizing nozzle

Contributed by the Heat Transfer Division for publication in the JOURNAL OF HEAT TRANSFER. Manuscript received by the Heat Transfer Division January 1995; revision received February 1996. Keywords: Evaporation, Sprays/Droplets, Thin Film Flow. Associate Technical Editor: A. Faghri.

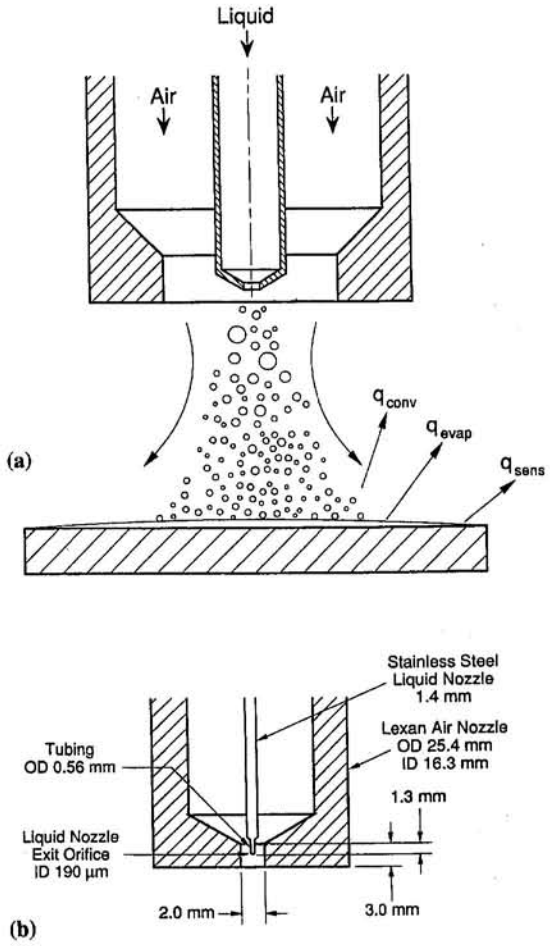

Fig. 1 Schematic of (*a*) gas/liquid mist jet and (*b*) atomizing nozzle

is depicted schematically in Fig. 1(*b*). Air flowing through the annular contraction efficiently atomized the liquid jet positioned at its core. The air nozzle was constructed from Lexan, and its exit section had a diameter of 2 mm and a length of 3 mm. The liquid nozzle was constructed of stainless steel hypodermic tubing. Its exit section had an inside diameter of 190 μm and an outside diameter of 1.4 mm. As shown in Fig. 1(*b*), the liquid nozzle overlapped the air nozzle exit length by 1.3 mm. The exit plane of the air nozzle was positioned 10.9 mm above the horizontal heater surface. The heater and the mist nozzle were mounted within a test chamber with appropriate ports for inflow and outflow.

The air flow system consisted of a vacuum pump, a condenser, and a rotameter. The vacuum pump pulled air from the room into the test chamber through the air nozzle. Only a slight reduction in the pressure of the test chamber (5000 Pa, maximum) was needed to produce the desired air flow through the nozzle. The air exiting the test chamber was passed through a condenser, to remove any evaporated liquid, and a rotameter, to measure the air flow rate. The relationship between the measured air flow rate and the velocity of the air jet was established in preliminary tests where the actual air jet velocity was measured with a pitot tube and curve fit against the air flow rate. The pressure inside the test chamber was monitored with a calibrated vacuum gage, and the ambient temperature was monitored with a thermocouple placed near the air nozzle inlet. For experiments with water/air mists, the dew point temperature of the ambient air was measured with a calibrated chilled-mirror hygrometer.

The liquid flow system consisted of a compressed nitrogen cylinder, a pressure tank, regulating valves, filters, and a pressure transducer. Liquid inside the pressure tank was forced by the compressed nitrogen to flow through the filter and liquid nozzle before being atomized by the coaxial air jet. The pressure upstream of the liquid nozzle was measured with a calibrated pressure transducer. The liquid was always injected at the ambient temperature. The liquid flow rate was determined by using a calibration of the liquid orifice flow rate as a function of the difference in pressure between the upstream measuring location

Nomenclature

A_{ring} = top area of a control volume ring
A = area of heater
C = constant in velocity profile
C_f = skin friction coefficient
c_p = specific heat
D = air nozzle diameter
D_{ab} = mass diffusivity
H_{in} = enthalpy flow into a control volume associated with flowing liquid
H_{out} = enthalpy flow out of a control volume associated with flowing liquid
h = heat transfer coefficient
h_{fg} = latent heat of vaporization
hg = enthalpy of saturated vapor
h_m = mass transfer coefficient
k = thermal conductivity
$\dot{M}_{evap}$ = liquid mass evaporating from a control volume
$\dot{M}_{in}$ = liquid mass flowing radially into a control volume
$\dot{M}_{out}$ = liquid mass flowing radially out of a control volume
$\dot{M}_{spray}$ = liquid mass flow due to impinging spray
$\dot{M}_{liq}$ = total liquid mass supplied
$\dot{m}''(r)$ = spray mass flux distribution
Nu_D = local Nusselt number = hD/k_a
Nu_0 = stagnation point Nusselt number
Pr = Prandtl number
Q_{cond} = heat conduction into control volume from heater
Q_{conv} = heat convected away from control volume by air flow
Q_{evap} = heat dissipated by evaporation
q'' = local heat flux
$\bar{q}''$ = surface-average heat flux
R_{conv} = convective resistance
R_{cond} = conductive resistance
Re_D = Reynolds number based on jet velocity and air nozzle diameter
r_{in} = radius from stagnation point to first face of control volume
r_{out} = radius from stagnation point to second face of control volume
r = radius from stagnation point
S = distance from air nozzle face to heater surface
T_s = temperature of heater surface
T_δ = temperature at the surface of the liquid film
T_{amb} = ambient temperature
T_m = mean temperature of liquid in a control volume
V_j = air jet velocity
$V(z)$ = velocity of the flowing film
x = serial number of a control volume
z = perpendicular distance from heater surface
δ = thickness of the liquid film
μ = dynamic viscosity
ν = kinematic viscosity
ρ = density
τ_f = shear stress imparted on liquid film surface by flowing air
τ_s = shear stress in liquid film at heater surface

Subscripts

a = air
l = liquid
x = for control volume x

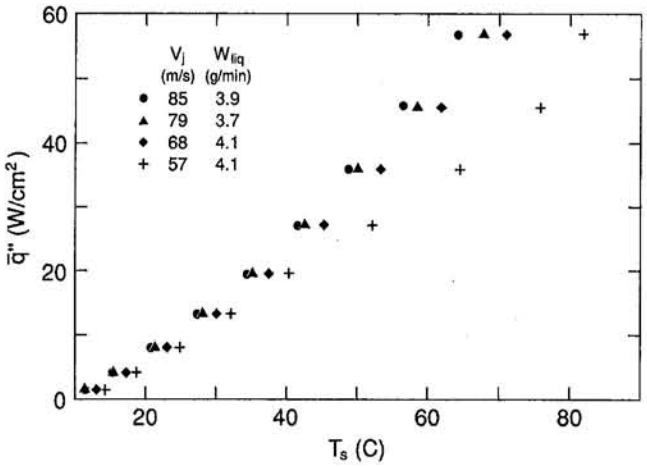

Fig. 2 Variation of surface heat flux as a function of surface temperature at various air exit velocities for air/methanol mist jet; T_{amb} = 22.6°C

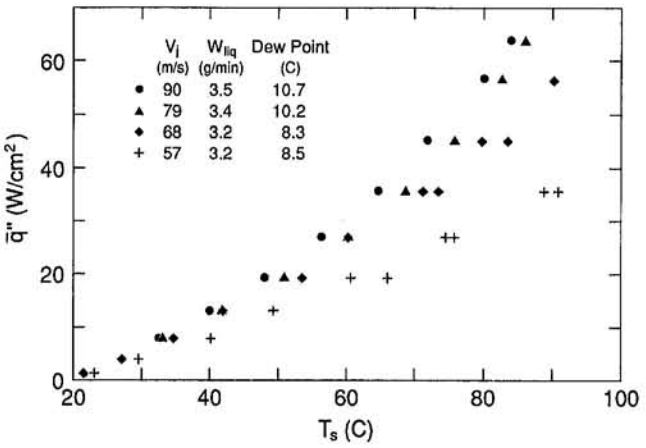

Fig. 3 Variation of surface-average heat flux as a function of surface temperature at various air velocities for air/water mist; T_{amb} = 22.6°C

and the test chamber. The orifice calibration was checked at the beginning of each data run to ensure accurate flow measurements.

The heater module consisted of a 6.35 mm cube of oxygen-free copper flush-mounted in a Lexan heater support. A resistance heater was bonded to the back of the copper block, and its front surface temperature was registered by two calibrated copper-constantan thermocouples routed through small holes in the body of the block. Power was supplied to the heater with a DC power supply.

During a typical experimental run, the air and liquid flow rates were held constant and the heater power was incremented upward. Data were taken only when steady-state conditions were reached after incrementing the power. The surface temperature, T_s, was taken to be the arithmetic average of the temperatures indicated by the thermocouples. The two thermocouples were usually in agreement within a few tenths of a degree Celsius. The surface-average heat flux, $\bar{q}''$, was determined from:

$$\bar{q}'' = \frac{Q}{A} \tag{1}$$

where Q is the power supplied to the resistance heater, and A is the surface area of the copper exposed to the impinging mist. A numerical model of the heater block and the Lexan support structure (Graham, 1994) indicated that the heat losses through the sides and the back of the copper block were less than 2.5 percent. This loss was considered to be negligible, and all the supplied power was assumed to be conducted through the copper block to the surface.

Droplet size and velocity measurements were taken with a Phase-Doppler Particle Analyzer (PDPA) and a Malvern drop sizing system. Results of these measurements indicate that the droplets ranged in size from 3 μm to 400 μm at a distance of 10.9 mm downstream from the nozzle exit, with a typical Sauter mean diameter of 100 μm for the water sprays and 40 μm for the methanol sprays (Graham, 1994). Radial distributions of the liquid volume flux were also obtained, and were later used as an input to the analytical model, in the form of spray mass flux distributions.

Experimental Results

Figure 2 shows the dependence of surface heat dissipation on surface temperature for various air jet velocities with an air/methanol mist jet. For a given air exit velocity, higher values of heat dissipation are achieved with higher surface temperatures. In addition, an increase in the air velocity at any given surface temperature results in a higher heat dissipation. Due to the limitations of the power supply employed in these experiments, data were not taken at temperatures higher than those plotted; however, at a moderate surface temperature of 60°C, a heat flux of approximately 50 W/cm² was achieved.

Figure 3 presents the dependence of surface heat flux on surface temperature for various air jet velocities with an air/water mist. The trends of increasing surface heat dissipation with increasing surface temperature and air jet velocity are again noted. At a surface temperature of 60°C, heat fluxes on the order of 30 W/cm² are noted, a significant drop from the 50 W/cm² found for an air/methanol mist jet. The lower heat fluxes observed with water are mainly due to its lower saturation vapor pressure, which results in a lower evaporation rate.

Figure 4 presents the dependence of surface heat flux on surface temperature at various liquid mass flow rates for an air/water mist jet. The data do not reveal a clear trend in the heat flux as the liquid mass flow is increased. The lack of a clear trend may be due to a trade-off between competing influences on the heat transfer rate. An increase in the liquid flow rate results in a thicker film, which, in turn, acts to decrease evaporative and convective heat transfer by increasing the conductive resistance of the film. However, an increase in liquid flow also results in an increase in convective heat transfer to the liquid (heat transfer from the surface to the liquid itself) since more liquid is supplied.

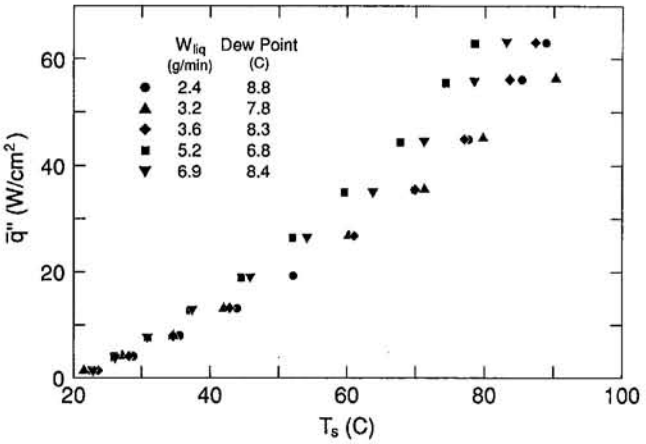

Fig. 4 Variation of surface-average heat flux with surface temperature for various liquid flow rates with air/water mist; T_{amb} = 23.5°C; V_j = 68 m/s

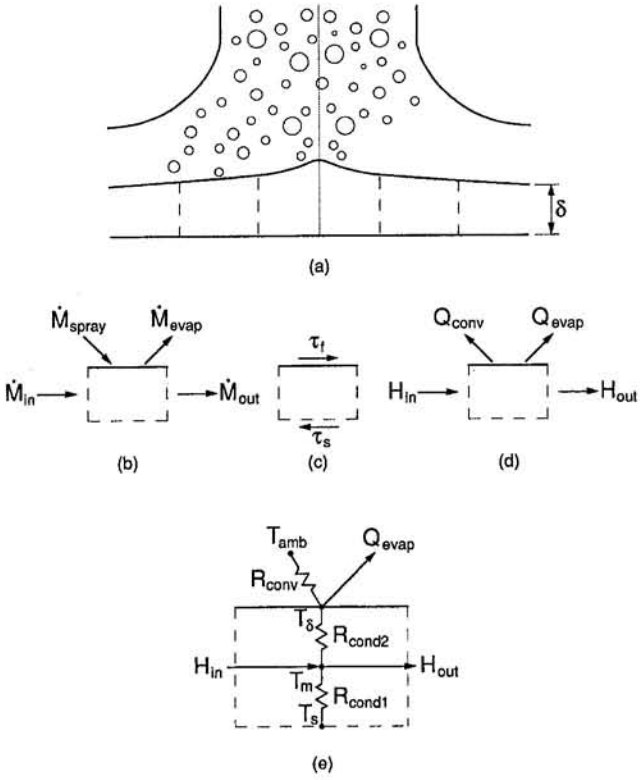

Fig. 5 Details of control volume used for analytical model: (*a*) schematic of control volume; (*b*) mass flows; (*c*) shear stresses; (*d*) heat transfer components; (*e*) resistance network

Multiple tests were conducted with both the air/methanol and the air/water mists to assess the repeatability of the measurements. While excellent repeatability was obtained with the air/methanol tests, small but significant run-to-run differences were observed with the air/water mists. The data scatter was found to increase as the temperature of the heater surface increased. At a representative surface temperature of 80°C and an air jet velocity of 68 m/s, run-to-run variations of up to 5 W/cm^2 in the average heat flux were observed for the air–water mists.

A systematic analysis of the uncertainties in the primary measurements, and the cumulative uncertainties in the reported quantities, was conducted by the procedure described by Kline and McClintock (1953). As detailed by Graham (1994), these uncertainties were estimated to be as follows: $\dot{M}_{liq}$, ±0.2 g/min; $\bar{q}''$, ±2.5 W/cm^2 for air/methanol mists and ±5 W/cm^2 for air/water mists; V_j, ±0.7 m/s; T_s, ±0.5°C; T_{amb}, ±0.5°C.

Analytical Model

An analytical model of the air/liquid mist jet was developed in order to investigate the magnitudes of the different components of heat transfer. Figure 5(*a*) is a schematic representation of the impinging mist with a control volume to facilitate the analysis. The liquid droplets impinge on the surface and join the liquid film, the thickness of which need not be constant. The top surface of the control volume is coincident with the top edge of the liquid film, and the bottom surface is defined by the heated copper surface. Since the system is assumed to be axisymmetric, the indicated control volume is a ring that intersects the plane of the paper at the two cross sections shown. Since the actual heater surface is not circular but square, the axisymmetric model represents an approximation. In the model, the heater is taken to be a circular surface of the same area as the actual heater.

Hydrodynamics. Figure 5(*b*) specifies the mass flows in and out of the control volume. A mass balance on the control volume yields:

$$\dot{M}_{spray,x} + \dot{M}_{in,x} = \dot{M}_{evap,x} + \dot{M}_{out,x} \tag{2}$$

$\dot{M}_{spray,x}$ is known from the drop velocity and size distribution data, and $\dot{M}_{evap,x}$ is determined from the heat transfer model. $\dot{M}_{in,x}$ and $\dot{M}_{out,x}$ are computed by assuming a linear velocity distribution through the thickness of the liquid film:

$$V_x(z) = C_x \cdot z \tag{3}$$

where C_x is a different constant for each control volume and z is the vertical distance from the surface of the heater. Then,

$$\dot{M}_{in,x} = \int_{A_{in,x}} \rho_{x-1} \cdot V_{x-1} \cdot dA = \pi \cdot \rho_{x-1} \cdot C_{x-1} \cdot r_{in} \cdot \delta_{x-1}^2 \tag{4}$$

$$\dot{M}_{out,x} = \int_{A_{out,x}} \rho_x \cdot V_x \cdot dA = \pi \cdot \rho_x \cdot C_x \cdot r_{out} \cdot \delta_x^2 \tag{5}$$

Figure 5(*c*) depicts the shear stresses acting on the control volume, with τ_s representing the shear at the heated surface, and τ_f representing the shear at the film surface due to the flowing air. A momentum balance can then be written:

$$\int_{A_{out,x}} \rho V^2 \cdot dA - \int_{A_{in,x}} \rho V^2 \cdot dA = (\tau_{f,x} - \tau_{s,x}) A_{ring,x} - \pi (r_{out} + r_{in}) \delta_x (p_{out} - p_{in}) \tag{6}$$

The terms on the left side are momentum fluxes, $A_{ring,x}$ is the top area of the control volume, and the last term is the contribution from the radial pressure gradient produced by the impinging jet. The shear stress, $\tau_{s,x}$, is computed from the linear velocity profile, as:

$$\tau_{s,x} = \mu_x \frac{dV}{dz} = \mu_x \cdot C_x \tag{7}$$

The radial pressure gradient is significant only in the vicinity of the stagnation point. There, the gas flow is likely to be laminarized by the favorable pressure gradient, and the shear stress it exerts on the liquid film, τ_f, can be approximated as the shear of a laminar gas jet impinging on a solid surface. White (1991) presents a solution for axisymmetric stagnation flows that results in an expression for the skin friction coefficient, C_f:

$$C_f = \frac{2 \cdot \tau_f}{\rho_a \cdot V_j^2} = \frac{2.624}{\sqrt{\mathrm{Re}_D}} \frac{r}{D} \tag{8}$$

The analysis presented by White (1991) is valid for the impingement region of a laminar air jet. In the wall-jet region, where the boundary layer is likely to be turbulent, Poreh et al. (1967) provide a correlation for the shear stress, which is valid to a lower limit of $r/S = 0.3$. The correlation, after some simplification and re-arranging, may be expressed as:

$$C_f = 0.3219 \cdot \frac{D^2}{r^2} \cdot \mathrm{Re}_D^{-0.3} \cdot (S/r)^{0.3} \tag{9}$$

To make the solution in the turbulent boundary layer region (Eq. (9)) meet with the solution in the laminar boundary layer region (Eq. (8)), the correlation of Poreh et al. (1967) was extended to a lower limit of $r/S = 0.2$. With the shear stress given by Eqs. (8) and (9), the linear velocity profile given by Eq. (3), and the radial pressure gradient in the stagnation zone given by White's solution, Eqs. (2) and (6) can be solved simultaneously for the values of the film thickness, δ_x, and the constant C_x, provided that the values corresponding to the previous control volume (subscript $x - 1$) have been determined.

The spray volume flux distribution data obtained with the PDPA system were used to evaluate $\dot{M}_{\text{spray},x}$ for each control volume by multiplying the mass flux at the radial location x by the area of the control volume ring, $A_{\text{ring},x}$. A typical curve fit for $\dot{m}''(r)$ corresponding to an air/methanol mist with $V_j = 90$ m/s and a liquid mass flow rate of 3.7 g/min is:

$$\dot{m}''(r) = 7.967 - 3.740 \times 10^3 r + 2.002 \times 10^5 r^2 + 6.585 \times 10^7 r^3 \quad (10)$$

with $\dot{m}''$ measured in kg/m^2 s and r measured in meters.

Heat Transfer. Figure 5(d) depicts the different components of heat transfer from a surface with elevated temperature T_s. Heat is transferred into the liquid film from the surface, where it is dissipated in one of three ways: (1) evaporation (Q_{evap}), (2) convection to the flowing air (Q_{conv}), and (3) increasing the bulk temperature of the liquid. The bulk liquid temperature increase is associated with a change in the enthalpy of the flowing liquid from where it enters (H_{in}) to where it leaves (H_{out}) the control volume. An energy balance can be written as:

$$Q_{\text{cond},x} = Q_{\text{conv},x} + Q_{\text{evap},x} + (H_{\text{out},x} - H_{\text{in},x}) \quad (11)$$

where Q_{cond} is the amount of heat conducted into the control volume from the heated surface. Modeling of the heat transfer situation is facilitated by a resistance network, which is shown on the control volume in Fig. 5(e).

The convective resistance is given by:

$$R_{\text{conv},x} = \frac{1}{h_x \cdot A_{\text{ring},x}} \quad (12)$$

where h_x is the local heat transfer coefficient of the air jet. The local heat transfer coefficient is determined from the local Nusselt number, which is obtained from a correlation adapted from Ma et al. (1988):

$$(r/D < 2) \quad \frac{\text{Nu}_D}{\text{Nu}_0} = (r/D)^{-0.5} \tanh^{0.5}(0.88 \cdot r/D) \quad (13)$$

$$(r/D \geq 2) \quad \frac{\text{Nu}_D}{\text{Nu}_0} = 0.348 \cdot \text{Re}_D^{(n-0.5)} \cdot (r/D)^{-1.25} \quad (14)$$

where n is a function presented graphically by Ma et al. It was fit with the following lines:

$$r/D < 2.8 \quad n = 0.55 + 0.181(r/D - 2)$$

$$r/D \geq 2.8 \quad n = 0.695 \quad (15)$$

The stagnation point Nusselt number, Nu_0, was calculated as:

$$\text{Nu}_0 = \text{Re}_D^{0.5} \cdot \text{Pr}^{0.4} \quad (16)$$

The determination of this local Nusselt number profile and stagnation point Nusselt number correlation are further detailed by Graham (1994).

The evaporative heat transfer, $Q_{\text{evap},x}$, can be evaluated from the expression

$$Q_{\text{evap},x} = h_{m,x} \cdot hg_x \cdot (\rho_{s,\delta,x} - \rho_{s,\text{air}}) \cdot A_{\text{ring},x} \quad (17)$$

where $h_{m,x}$ is the mass transfer coefficient, hg_x is the enthalpy of the saturated vapor at the surface of the liquid, $\rho_{s,\delta,x}$ is the saturated vapor density at $T_{\delta,x}$, and $\rho_{s,\text{air}}$ is the vapor density in the air (due to relative humidity). The mass transfer coefficient, $h_{m,x}$, can be determined once h_x is known, from the heat and mass transfer analogy (Incropera and DeWitt, 1990):

$$h_{m,x} = \frac{h_x}{c_{p,a} \cdot \rho_a} \cdot (D_{ab} \cdot \text{Pr}_a / \nu_a)^{0.666} \quad (18)$$

The enthalpy of the saturated vapor, hg, is computed from the expression:

$$hg_x = h_{fg} + c_{p,l} \cdot (T_{\delta,x} - T_{\text{amb}}) \quad (19)$$

The saturated vapor density of water contained in the air, $\rho_{s,\text{air}}$ is calculated from knowledge of the dewpoint temperature using the ideal gas equation. The value of $\rho_{s,\text{air}}$ is zero for liquids other than water.

The enthalpy flows, $H_{\text{in},x}$ and $H_{\text{out},x}$ are calculated from

$$H_{\text{in},x} = \dot{M}_{\text{in},x} \cdot c_{p,l} \cdot (T_{m,x-1} - T_{\text{amb}}) \quad (20)$$

$$H_{\text{out},x} = \dot{M}_{\text{out},x} \cdot c_{p,l} \cdot (T_{m,x} - T_{\text{amb}}) \quad (21)$$

The two mass flow rates, $\dot{M}_{\text{in},x}$ and $\dot{M}_{\text{out},x}$, are given by Eqs. (4) and (5). The enthalpy flows calculated in Eqs. (20) and (21) use T_{amb} as the zero point (H is zero when $T_m = T_{\text{amb}}$), so that the impinging spray droplets (which are at T_{amb}) contribute nothing to the enthalpy balance. The conduction resistances, $R_{\text{cond1},x}$ and $R_{\text{cond2},x}$, are given by

$$R_{\text{cond},x} = \frac{\delta_x}{2 \cdot A_{\text{ring},x} \cdot k_l} \quad (22)$$

where k_l is the thermal conductivity of the liquid.

Referring back to Fig. 5(e), it is apparent that two energy balances must be solved, one at node $T_{m,x}$ and one at node $T_{\delta,x}$:

$$\frac{T_s - T_{m,x}}{R_{\text{cond1},x}} + H_{\text{in},x} = \frac{T_{m,x} - T_{\delta,x}}{R_{\text{cond2},x}} + H_{\text{out},x} \quad (23)$$

$$\frac{T_{m,x} - T_{\delta,x}}{R_{\text{cond2},x}} = \frac{T_{\delta,x} - T_{\text{amb}}}{R_{\text{conv},x}} + Q_{\text{evap},x} \quad (24)$$

Equations (23) and (24) can be solved simultaneously for $T_{m,x}$ and $T_{\delta,x}$. Once the values of $T_{m,x}$ and $T_{\delta,x}$ are known, the total heat dissipated from that control volume can be calculated. This analysis limits the range of liquid flows that can be modeled. Under very low flow rates, it is possible that all of the liquid in a control volume will evaporate, causing the film thickness, δ, to be zero. The associated conductive resistance, $R_{\text{cond},x}$, will also be zero, which causes terms in Eqs. (23) and (24) to become undefined. Flow rates investigated in the present study were always sufficient to prevent this local dryout. An iterative procedure is employed in the analytical model, as liquid and air properties change with temperature and the nodal temperatures are the unknowns. The first control volume is located near the stagnation point, and the solution then proceeds in a step-by-step march in the radial direction.

Analytical Model Predictions

Figure 6 is a comparison of predicted surface-averaged heat fluxes with experimentally measured data for various surface temperatures, using an air/methanol mist. It is apparent that the model predicts the data quite well, with a maximum deviation of 2.4 W/cm^2 (4.2 percent) at 64°C for the 85 m/s jet, and 1.9 W/cm^2 (3.4 percent) for the 68 m/s jet. The good agreement between the predictions and the data provides some confidence in the validity of this simple analytical model. Figure 7 is a breakdown of the different heat transfer components for the 85 m/s mist jet, as predicted by the model. The evaporative component of heat transfer is by far the largest, and accounts for 74 percent of the total heat flux at a temperature of 60°C (air convection accounts for 4 percent, and the enthalpy flows account for 22 percent). At heater surface temperatures below T_{amb}, the impinging mist is warmer than the liquid film, and therefore transfers heat to it. As a result, the convective and enthalpy-flow components of heat transfer actually subtract

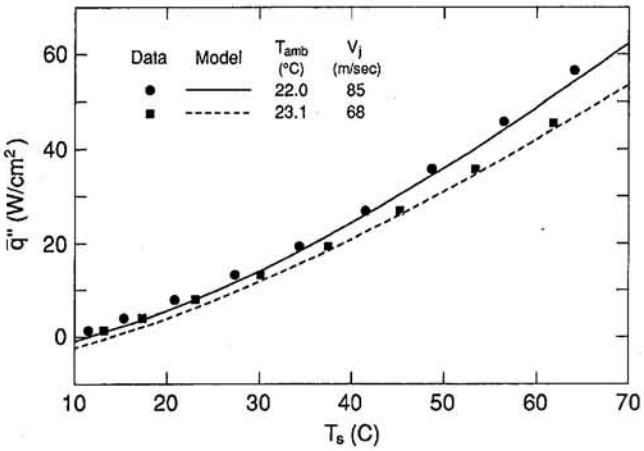

Fig. 6 Comparison of predicted average heat flux with data for air/methanol mist; $\dot{M}_{liq}$ = 4 g/min

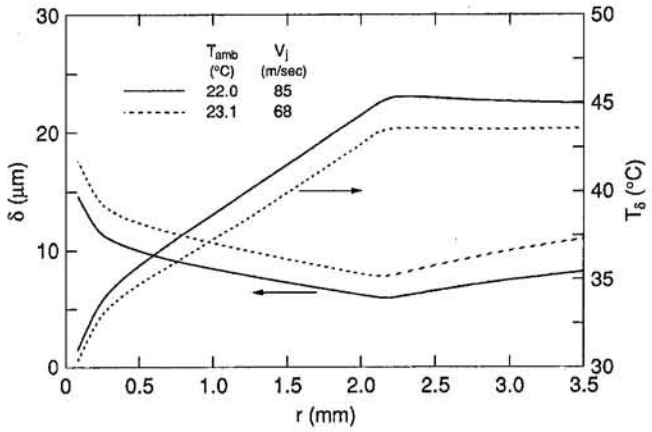

Fig. 8 Model predictions of film thickness and film surface temperature for air/methanol mist; $\dot{M}_{liq}$ = 4 g/min; T_s = 60°C

from the evaporative heat flux at low temperatures. The heat transfer component breakdown for the 68 m/s mist jet at 60°C is 69 percent due to evaporation, 4 percent due to air convection, and 27 percent due to the enthalpy increase of the liquid.

Figure 8 shows model predictions of the film thickness, δ, and film surface temperature, T_δ, as a function of the radial distance along the heater surface at a heater surface temperature of 60°C. The film is thickest near the jet stagnation point, where the impinging liquid mass flux is the highest and the shear stress at the film surface (due to the flowing air stream) is the lowest. The film thickness then decreases radially as the shear stress increases and the mass flux decreases, until a radius of approximately 2.2 mm, where the shear stress again starts to decrease. The sharp change in the slope of the curve around r = 2.2 mm is a result of switching from the impingement-zone skin friction correlation to the wall-jet skin friction correlation.

Yang et al. (1992) have presented experimental measurements of film thickness that suggest that the film is flat to within 1 μm, while the present model predicts variations of about 3 μm. However, the air and water flow rates in their study were much higher, resulting in a mean film thickness of about 150 μm compared to 10 μm in the present study. Yang et al. did not report spray mass flux distributions in their paper. Consequently, their results cannot be used as an independent test of the present model.

The lowest film surface temperature is encountered at the stagnation point, where the film is the thickest and is composed entirely of liquid impinging at T_{amb}. The temperature then increases, as the film thickness decreases, until a radius of approximately 2.2 mm, where it starts to decrease again. It is evident from this figure that δ and T_δ are coupled: As δ increases, T_δ decreases, and vice versa. The film is thinner for the higher air velocity case, and the temperature at its surface is correspondingly higher.

The predictions displayed in Fig. 8 reveal that the increased evaporative component of heat transfer for the higher velocity case is due to an increase in the saturated vapor density of the liquid (which increases with temperature) as well as the enhancement of heat and mass transfer coefficients. The variations in the predicted local heat flux for the two air/methanol mist jets, which are presented in Fig. 9, may also be interpreted in the light of Fig. 8. The initial rapid increase in the local heat flux is consistent with the rapid decrease in δ. The subsequent plateau in the curve is due to a slower decline in δ combined with a decline in the convection coefficient. The rapid decrease in q'' beyond r = 2.2 mm is due to the increase in δ combined with a decrease in the convection coefficient, h.

The analytical model was also used to predict surface heat fluxes for an air/water mist, but the results were much less encouraging, and Fig. 10 presents a comparison of the model predictions with data. The model overpredicted the data by as much as 50 percent at a surface temperature of 84°C for the 90 m/s air jet, and 70 percent at a surface temperature of 83°C for the 68 m/s air jet. The reasons for the large difference between the data and predictions are, at the moment, uncertain. It is tentatively suggested that part of the difference can be attributed

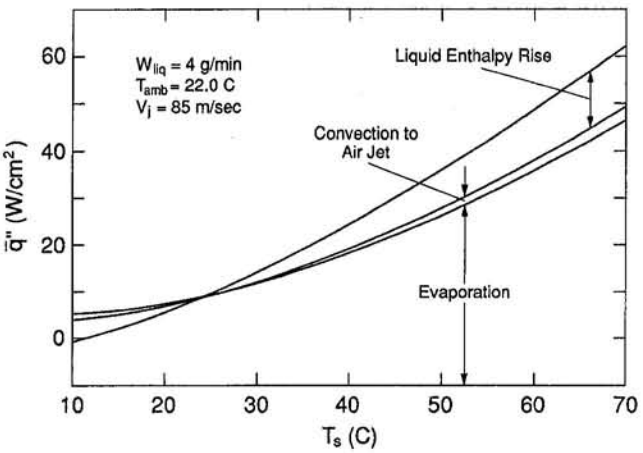

Fig. 7 Model predictions of heat transfer components for air/methanol mist; $\dot{M}_{liq}$ = 4 g/min; T_{amb} = 22.0°C; V_j = 85 m/s

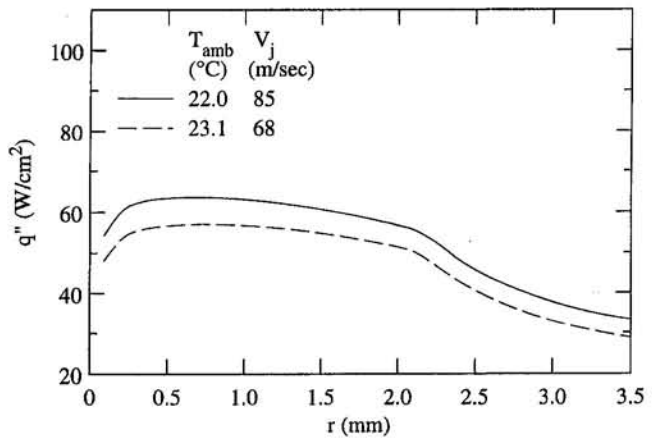

Fig. 9 Model predictions of local heat flux from the surface of the heater for air/methanol mist; $\dot{M}_{liq}$ = 4 g/min; T_s = 60°C

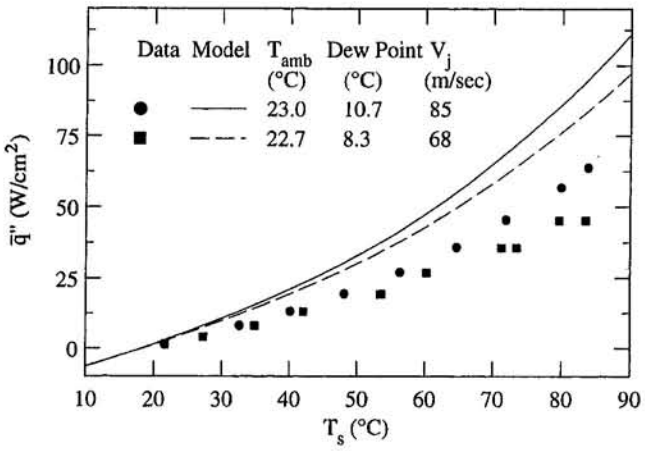

Fig. 10 Comparison of predicted average heat flux with data for air/water mist; $\dot{M}_{liq}$ = 3.5 g/min

to surface tension effects, which were completely neglected in the analysis. The surface tension of water is approximately 3.5 times larger than the surface tension of methanol, and may contribute significantly to increasing the film thickness. Efforts to resolve the discrepancy will be undertaken as part of a follow-up study.

A comparison of air/water mist impingement data reported by various investigators is presented by Graham (1994). The heat fluxes are found to vary by about an order of magnitude, with the present data lying at the low end of the range.

Summary

Experimental data have been presented for heat transfer from a small square heat source, 6.35 mm on a side, cooled by circular impinging mist jets of air/water and air/methanol. Heat fluxes as high as 60 W/cm^2 could be dissipated with both combinations, the resulting surface temperature being around 70°C for the air/methanol mist and around 80°C for the air/water mist. A relatively simple analytical model has been developed to gain insights on the heat transfer and fluid flow phenomena associated with this problem. For the air/methanol mist, model predictions of the surface-averaged heat flux were found to be in very good agreement with experimental data. For the air/water mist, model predictions were only qualitatively in agreement with the data. The model was able to quantify the relative magnitudes of the various heat transfer mechanisms and reveal that, at low liquid flow rates, the dominant mechanism is evaporation at the surface of the liquid film.

References

Graham, K. M., 1994, "Experimental and Analytical Investigation of Gas/Liquid Jet Impingement Cooling of Small Heat Sources," M.S.M.E. Thesis, Purdue University, West Lafayette, IN.

Hatta, N., Fujimoto, H., and Ishii, R., 1991, "Numerical Analysis of a Gas--Particle Subsonic Jet Impinging on a Flat Plate," *ISIJ International,* Vol. 31, No. 4, pp. 342–349.

Incropera, F. P., and DeWitt, D. P., 1990, *Fundamentals of Heat and Mass Transfer,* 3rd ed., Wiley, New York.

Kline, S. J., and McClintock, F. A., 1953, "Describing Uncertainties in Single-Sample Experiments," *Mechanical Engineering,* Vol. 75, Jan., pp. 3–8.

Koria, S. C., and Datta, I., 1992, "Studies on the Behavior of Mist Jet and Its Cooling Capacity of Hot Steel Surface," *Steel Research,* Vol. 63, pp. 19–26.

Ma, C. F., Tian, Y. Q., Sun, H., Lei, D. H., and Bergles, A. E., 1988, "Local Characteristics of Heat Transfer From a Small Heater to an Impinging Round Jet of Liquid of Larger Pr Number," *Proceedings of the International Symposium on Heat Transfer Enhancement and Energy Conservation,* Canton, China.

Ma, C. F., and Tian, Y. Q., 1990, "Experimental Investigation on Two-Phase Two-Component Jet Impingement Heat Transfer From Simulated Microelectronic Heat Sources," *International Communications in Heat and Mass Transfer,* Vol. 17, pp. 399–408.

Ohkubo, H., and Nishio, S., 1989, "Study on Accurate Prediction of Mist Cooling Characteristics (Part I, Effects of Surface Roughness)," *Heat Transfer—Japanese Research,* Vol. 18, pp. 43–50.

Pais, M. R., Chow, L. C., and Mahefkey, E. T., 1992, "Surface Roughness and Its Effects on the Heat Transfer Mechanism in Spray Cooling," ASME JOURNAL OF HEAT TRANSFER, Vol. 114, pp. 211–219.

Poreh, M., Tsuei, Y. G., and Cermak, J. E., 1967, "Investigation of a Turbulent Radial Wall Jet," *Journal of Applied Mechanics,* Vol. 34, No. 2, pp. 457–463.

Sehmbey, M. S., Pais, M. R., and Chow, L. C., 1992, "Effect of Surface Material Properties and Surface Characteristics in Evaporative Spray Cooling," *Journal of Thermophysics and Heat Transfer,* Vol. 6, No. 3, pp. 505–512.

Siwon, B., and Wisniewski, M., 1986, "Heat Transfer by Directing Gas-Liquid Spray Perpendicularly on a Flat Surface," *Heat Transfer 1986: Proceedings of the Eighth International Heat Transfer Conference,* San Francisco, C. L. Tien, ed., pp. 1237–1242.

Siwon, B., 1993, "Experimental Investigations of the Liquid Film by a Gas-Liquid Spray Jet Impinging Onto a Flat Surface," *International Communications in Heat and Mass Transfer,* Vol. 20, pp. 665–674.

White, F. M., 1991, *Viscous Fluid Flow,* McGraw-Hill, New York, pp. 156–159.

Yang, J., Chow, L. C., Pais, M. R., and Ito, A., 1992, "Liquid Film Thickness and Topography Determination Using Fresnel Diffraction and Holography," *Experimental Heat Transfer,* Vol. 5, pp. 239–252.

Effects of Variable Properties and Viscous Dissipation During Optical Fiber Drawing

S. H.-K. Lee
Assistant Professor,
Department of Mechanical Engineering,
The Hong Kong University of
Science & Technology,
Clear Water Bay, Kowloon, Hong Kong
Assoc. Mem. ASME

Y. Jaluria
Distinguished Professor,
Department of Mechanical &
Aerospace Engineering,
Rutgers, The State University of
New Jersey,
New Brunswick, NJ 08855
Fellow ASME

The axisymmetric free-surface flow and thermal transport of fused silica during optical fiber drawing was considered with variable properties, prescribed heat flux, and neck shape. Experimental data from previous researchers were adapted or used as the basis for assumptions in order to enable a realistic analysis. The main objectives were to model the neck-down process in order to clarify the effects of the variable properties and the associated viscous dissipation. Due to the large changes in dimension and viscosity, this system poses severe nonlinearities, and a new solution algorithm was necessarily developed. Validation was achieved and several important results were obtained. Among these, it was shown that the viscous dissipation has considerable impact on the fiber temperature due to its localization to a small volume near the fiber section. Also, it was shown that a variable viscosity generated vorticity, which was localized to the region where the preform radius undergoes large changes.

1 Introduction

During the drawing of an optical fiber, a preform glass rod is pulled while it is heated to an elevated temperature. As the fused silica flows, the diameter changes by two orders of magnitude over a mere distance of 10 cm. Simultaneously the physical properties, and in particular the viscosity, will undergo changes of several orders of magnitude over this distance. For the viscosity, the change of roughly seven orders of magnitude is expected to produce significant viscous heating. Together, these variations should significantly affect the thermal transport during the drawing operation, the subsequent geometric and optical quality of the fiber, and the implicit signal loss characteristics.

There has been limited amount of work done in this area (cf. Paek and Runk, 1978; Homsy and Walker, 1979; Sayles, 1982; Vasilijev et al., 1989; Myers, 1989). For brevity, only a sketch of the past work will be presented here. Interested readers are referred to Lee (1993) for a more comprehensive review. By and large, most of the previous researchers have made varying assumptions on the impact of the variable properties and the resulting viscous heating. These assumptions were usually inconsistent with each other, and seemed to be based more on convenience. For example, Sayles (1982) chose a viscosity that varied as $1/T$ instead of $\exp(1/T)$, which accordingly was due to convergence difficulties. Likewise, others have chosen one-dimensional analyses, which greatly simplified the computations and reduced the nonlinearity from the viscous heating. Indeed, the difficulty in obtaining a converged solution may be the reason why none have properly accounted for the viscous dissipation, although some have explained its neglect by pointing out that the heat generated is minimal compared to that from the furnace. It will be shown here that while this explanation is correct, the viscous heating is localized and consequently has a substantial impact on the temperature profile.

It is clearly of academic and practical interest to systematically clarify the extent and impact of the variable properties, and of the related viscous dissipation. The motivation is not only to increase the understanding of the underlying physics, but also to clearly identify important properties both for proper inclusions in future models, and for determining the areas in which the need for improved experimental data is the greatest. In addition, some of the properties, such as the surface tension, can be manipulated using different dopants. Thus, it is important to grasp its extent and impact.

The properties being studied are the viscosity, surface tension, thermal conductivity, and specific heat. These are all taken here to be temperature dependent, while the density is assumed to be constant at 2200 kg/m^3 since it varies minimally over the temperature range of 300–2000 K. This configuration poses some unique difficulties, since not only does the physical geometry undergo drastic changes, but also the viscosity and viscous dissipation. The combined effect is a nonlinear system with significant convergence difficulties. That is, a small temperature fluctuation can cause velocity changes, which, in turn, amplify the temperature fluctuations through the viscous dissipation. Thus, besides clarifying the roles of the variable properties and viscous dissipation, one additional contribution of this work is the development of an algorithm for the solution of systems with viscous heating and exponential viscosity dependence.

2 Analysis

To achieve a realistic study, data were taken from the literature whenever possible. The justification of these data is presented in detail in the appendix. The temperature dependence of the thermal conductivity, surface tension, specific heat, and viscosity were all taken from either Fleming (1964) or Myers (1989), and whenever possible, cross checked against each other. In addition, the geometric configuration, as given in the appendix, was taken from Paek and Runk (1978). This is shown in Fig. 1, where the free surface of the preform exchanges heat through convection and an incoming heat flux. In an actual drawing operation, this incoming heat flux results from the radiative exchange with the furnace, while the necking profile is the result of the local force balance along the free surface. However since both of these computations are quite complex, they were subjects of separate studies (Lee and Jaluria, 1995a; Choudhury et al., 1995). For the present work, the heat flux and the neck profile are prescribed, as shown in Fig. 2 and discussed in greater detail in the appendix.

2.1 Governing Equations. The laminar free-surface flow of fused silica with a prescribed neck shape and variable properties was considered, and the silica, as discussed in the appendix,

Contributed by the Heat Transfer Division for publication in the JOURNAL OF HEAT TRANSFER. Manuscript received by the Heat Transfer Division August 1995; revision received February 1996. Keywords: Materials Processing and Manufacturing Process, Numerical Methods, High-Temperature Phenomena. Associate Technical Editor: J. R. Howell.

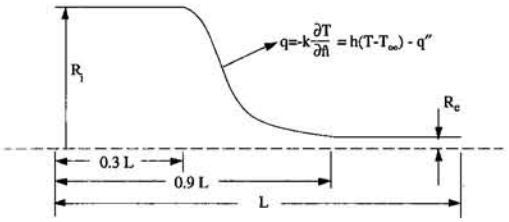

Fig. 1 Geometric configuration of the present study

was modeled as a Newtonian fluid. Using Landau's transformation (1950), the necking geometry was mapped into a rectangular domain, and the time-dependent energy equation as well as the $\Psi-\Omega$ equations were transformed and solved on a nonuniform grid (Lee and Jaluria, 1995b). Including the effect of viscous dissipation and variable properties, these equations are given in terms of the transformed coordinates, η and β, as:

$$\frac{\partial T^*}{\partial t^*} + \frac{v_i R_i}{R}\frac{\partial}{\partial \eta}(\eta u^* T^*) + \frac{v_i R_i}{L}\frac{\partial}{\partial \beta}(v^* T^*) - \eta\frac{v_i R_i}{R}\frac{dR}{dz}\frac{\partial}{\partial \eta}(v^* T^*) = \frac{1}{\rho c_p}\left[\frac{R_i}{\eta R^2}\frac{\partial}{\partial \eta}\left(k\eta\frac{\partial T^*}{\partial \eta}\right) + \frac{R_i}{L^2}\frac{\partial}{\partial \beta}\left(k\frac{\partial T^*}{\partial \beta}\right) - \frac{\eta R_i}{L}\frac{\partial}{\partial \beta}\left(\frac{k}{R}\frac{dR}{dz}\frac{\partial T^*}{\partial \eta}\right) - \frac{\eta R_i}{RL}\frac{dR}{dz}\frac{\partial}{\partial \eta}\left(k\frac{\partial T^*}{\partial \beta}\right) + \frac{\eta R_i}{R^2}\left(\frac{dR}{dz}\right)^2\frac{\partial}{\partial \eta}\left(k\eta\frac{\partial T^*}{\partial \eta}\right)\right] + \frac{R_i \Phi}{c_p T_m} \quad (1a)$$

The last term in Eq. (1*a*) represents the viscous dissipation, and is detailed below as:

$$\Phi = 2\nu v_i^2\left[\frac{1}{R^2}\left(\frac{\partial u^*}{\partial \eta}\right)^2 + \left(\frac{1}{L}\frac{\partial v^*}{\partial \beta} - \frac{\eta}{R}\frac{dR}{dz}\frac{\partial v^*}{\partial \eta}\right)^2 + \left(\frac{u^*}{\eta R}\right)^2 + \frac{1}{2}\left(\frac{1}{L}\frac{\partial u^*}{\partial \beta} - \frac{\eta}{R}\frac{dR}{dz}\frac{\partial u^*}{\partial \eta} + \frac{1}{R}\frac{\partial v^*}{\partial \eta}\right)^2\right] \quad (1b)$$

Similarly, the streamfunction and vorticity equations are given as:

$$\left(\frac{R_i}{R}\right)^3\frac{\partial}{\partial \eta}\left(\frac{1}{\eta}\frac{\partial \Psi}{\partial \eta}\right) + \left(\frac{R_i}{R}\right)^3\left(\frac{dR}{dz}\right)^2\eta\frac{\partial^2 \Psi}{\partial \eta^2} + \left[2\left(\frac{dR}{dz}\right)^2\left(\frac{R_i}{R}\right)^3 - \frac{R_i^3}{R^2}\frac{d^2R}{dz^2}\right]\frac{\partial \Psi}{\partial \eta} - \frac{2R_i^3}{R^2 L}\frac{dR}{dz}\frac{\partial^2 \Psi}{\partial \eta \partial \beta} + \frac{R_i^3}{RL^2}\frac{1}{\eta}\frac{\partial^2 \Psi}{\partial \beta^2} = -\Omega \quad (2)$$

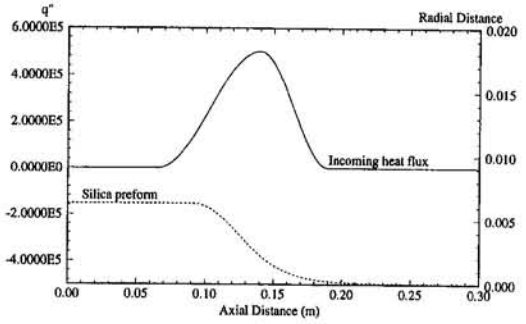

Fig. 2 Axial variation of the heat flux and necking profile used in this study, both of which were based on the experimental data of Paek and Runk (1978)

$$\left(\frac{v_i R_i}{R}\right)\frac{\partial}{\partial \eta}(u^*\Omega) - \frac{dR}{dz}\left(\frac{v_i R_i}{R}\right)\eta\frac{\partial}{\partial \eta}(v^*\Omega) + \left(\frac{v_i R_i}{L}\right)\frac{\partial}{\partial \beta}(v^*\Omega) = \nu\left[\frac{R_i}{R^2}\frac{\partial}{\partial \eta}\left(\frac{1}{\eta}\frac{\partial}{\partial \eta}(\eta\Omega)\right) + \left(\frac{\eta}{R}\right)^2\left(\frac{dR}{dz}\right)^2 R_i\frac{\partial^2 \Omega}{\partial \eta^2} - \frac{2\eta R_i}{RL}\frac{dR}{dz}\frac{\partial^2 \Omega}{\partial \eta \partial \beta} - \frac{\eta R_i}{R}\left(\frac{d^2R}{dz^2} - \frac{2}{R}\left(\frac{dR}{dz}\right)^2\right)\frac{\partial \Omega}{\partial \eta} + \frac{R_i}{L^2}\frac{\partial^2 \Omega}{\partial \beta^2}\right] + \frac{R_i^2}{v_i}S_\nu \quad (3a)$$

The last term in Eq. (3*a*), S_v, represents the source term due to variable viscosity and is given by:

$$S_\nu = \frac{\partial \nu}{\partial z}\left[2\frac{\partial^2 u}{\partial r^2} + 2\frac{\partial^2 u}{\partial z^2} + \frac{2}{r}\frac{\partial u}{\partial r} - \frac{2u}{r^2}\right] - \frac{\partial \nu}{\partial r}\left[2\frac{\partial^2 v}{\partial r^2} + 2\frac{\partial^2 v}{\partial z^2} + \frac{1}{r}\left(\frac{\partial v}{\partial r} + \frac{\partial u}{\partial z}\right)\right] + \left(\frac{\partial^2 \nu}{\partial z^2} - \frac{\partial^2 \nu}{\partial r^2}\right)\left[\frac{\partial u}{\partial z} + \frac{\partial v}{\partial r}\right] + \frac{\partial^2 \nu}{\partial r \partial z}\left[2\frac{\partial u}{\partial r} - 2\frac{\partial v}{\partial z}\right] \quad (3b)$$

Note that each term within Eq. (3*b*) can be expressed in terms of u^*, v^*, and the transformed coordinates, η and β, as outlined by Lee (1993).

2.2 Boundary Conditions. At the inlet, the preform enters with a uniform velocity and loses heat to the ambient through convection. Dropping the asterisks for convenience, this is given below as:

Nomenclature

a = absorption coefficient
Br = Brayton number = Ec Pr/2
h = heat transfer coefficient = 200 W/m^2
L = length of furnace and preform = 0.3 m
n = index of refraction
$\hat{n}$, $\hat{t}$ = outward normal and tangential vectors
q'' = heat flux, W/m^2
T^* = temperature scaled by $T_m = T/T_m$
t^* = time divided by inlet radius = t/R_i
u^*, v^* = radial and axial velocity scaled by inlet velocity
γ = viscosity variation parameter
η, β = transformed coordinates = r/R, z/L
μ, ν = dynamic and kinematic viscosity
ξ = surface tension
ψ, Ψ = streamfunction; $\Psi = \psi/R_i^2 v_i$
ω, Ω = vorticity; $\Omega = \omega R_i/v_i$

Subscripts

1, 2 = locations where neck begins and ends
∞ = ambient temperature = 300 K
c, s = center and surface values
i, e = inlet and exit values
m = softening point of fused silica, taken to be 1900 K

$$\Psi(\eta{:}0,\ 1) = \frac{\eta^2}{2}, \quad \Omega = 0, \quad \frac{\partial T}{\partial \beta} = \frac{hL}{K}(T_{z=0} - T_\infty) \quad (4a)$$

At the end of the neck region, the fiber also attains uniform velocity, and thus a developed condition is imposed for the stream function and vorticity. However, due to the presence of viscous dissipation, the temperature at the exit may not necessarily attain a developed condition. Therefore, a zero diffusion condition is prescribed instead, which is consistent with the large local Pe number at the exit. These are given below as:

$$\frac{\partial \Psi}{\partial \beta} = \frac{\partial \Omega}{\partial \beta} = \frac{\partial^2 T}{\partial \beta^2} = 0 \quad (4b)$$

Also, recognizing symmetry at the center, the boundary conditions become:

$$\Psi = 0, \quad \Omega = 0, \quad \frac{\partial T}{\partial \eta} = 0 \quad (4c)$$

Finally, there exists a surface tension and a heat flux condition at the free surface, which have been shown to take on the following forms (Lee, 1993):

$$\Psi = \frac{1}{2}, \quad \Omega = \frac{-R_i}{\mu v_i}\frac{\partial \xi}{\partial \hat{t}}, \quad -k\frac{\partial T}{\partial \hat{n}} = h(T_s - T_\infty) - q'' \quad (4d)$$

The heat flux condition in Eq. $(4d)$ assumes a heat flux, q'', from the furnace, which in a later study serves as a coupling point with the radiative analysis. Due to the unstable nature of this system, it was extremely crucial that the approximation of the heat flux condition be at least second-order accurate. Thus, the computation for the normal temperature gradient along an arbitrary surface required greater consideration (Lee, 1993).

2.3 Method of Solution. One of the keys to solving this system is the proper capturing of the large gradients, since it has been observed that minor temperature fluctuations can trigger divergence through the combined effects of the exponentially dependent viscosity and the viscous dissipation. Fortunately, the regions of large gradients can be deduced from the physics of the problem. Thus, they were successfully resolved using a custom-designed nonuniform grid in conjunction with a newly derived finite differencing scheme, which was nominally second-order accurate (Lee and Jaluria, 1995b). In addition, since the diameter changes by two orders of magnitude, a hybrid scheme was used to approximate the changing advection terms of the energy equation.

Another source of instability was the viscosity range, which, depending on the temperature range, can be as high as 50 orders of magnitude. Depending on the memory size, computer zero corresponded to roughly 10^{-20}. Therefore, artifacts and instability were generated from the multiplication of computer zero with a viscosity value of 10^{50} (at $T \approx 312$ K). To avoid this, an upper limit of 5×10^7 was imposed on the viscosity, with the resulting viscosity range reduced to 7 orders of magnitude. This limit was varied in order to determine its effect. There was no appreciable effect, as this value was chosen to correspond to the region far upstream of the necking region where the temperature of roughly 1472 K is considerably below the softening temperature, T_m, of 1900 K. As there was no deformation upstream of the necking region, the effect of changing the limit was transparent.

Generally, a steady-state solution required solving the pseudo-transient form of the $\Psi-\Omega$ equations. However, this encountered considerable difficulties due to the large variation in the viscosity (7 orders of magnitude) and the associated time step (14 orders of magnitude). An entirely different approach was developed by realizing that the entire system is driven by the heat exchange, and thus the most relevant is the energy equation. Therefore the energy equation was used to lead the transient calculation, and at each time step, the properties were re-evaluated and the velocity was updated by iterating once the steady-state form of the $\Psi-\Omega$ equations. Using the new velocity, the temperature equation marched another time step and the entire process was repeated until convergence was achieved. The solution was then verified to be independent of user-prescribed parameters. Of particular emphasis was independence from the grid (so long as it was sufficiently fine to capture the viscosity gradients), and the viscosity limit.

Two convergence criteria were concurrently used. In one, the maximum difference between two successive iterations of T, Ψ, and Ω in the entire computational domain reached a constant value (Lee and Jaluria, 1995b). This ensured that a small difference reflects a steady-state value and not merely an effect brought on by an excessively small time step. Depending on the variable, this value was usually found to be around 10^{-10}. In the second criterion, the computation continued until the residuals of the energy, stream function, and the vorticity equations reached a constant value. Generally, these values were also found to be smaller than 10^{-10}.

3 Results and Discussion

Results for the free-surface transport of a Newtonian fluid with variable properties, viscous dissipation, and a prescribed neck shape were obtained. As discussed in the appendix, the neck shape is part of the solution to the problem, and the presumption of a neck shape may induce unrealistic artifacts. Despite attempts to be consistent with experimental measurements (Paek and Runk, 1978; Fleming, 1964; Myers, 1989), some caution is still required in extracting and interpreting the results obtained here. As mentioned earlier, the main goal of this study is systematically to clarify the roles of each variable property and the associated viscous dissipation. To achieve this, results were first obtained with all the properties being temperature dependent (fully variable case), since they provide an overall perspective, and the general trends that can be expected in the actual necking region of an optical fiber. Results were then obtained by systematically allowing each property to be temperature dependent while keeping all the other properties constant. Thus the effect of each variable property was interpreted by appropriately contrasting the results.

3.1 Validation. Due to the lack of similar studies, validation through direct comparisons is difficult. Instead, the computational scheme was verified through physical consistencies and comparisons with a degenerate case of duct flows with a variable property fluid. These comparisons are presented below, and, in general, close agreements have been obtained. The discussions on physical consistencies are presented in the relevant sections where the results appear.

The results for the thermally developing flow of a variable viscosity liquid in a tube with a step change in wall temperature are presented in Figs. 3 and 4. Consistent with Yang's (1962) definition, $\gamma < 0$ denotes a heating liquid where the viscosity decreases with increasing temperature, $\gamma > 0$ denotes a cooling liquid where the viscosity increases with decreasing temperature, and $\gamma = 0$ denotes a constant-viscosity liquid. As expected, the results, as shown in Fig. $3(a)$ show that the axial velocity profiles for a constant-viscosity liquid are unaffected by the sudden change in wall temperature. However, for cooling liquids (Fig. $3(b)$), the axial velocity profiles, at successive axial locations, show the velocity at the center increases in the axial direction. This is due to the increase in viscosity near the cooling wall, which retards the flow near the wall, and thus increases the flow at the center. The opposite effect is observed for a heating liquid, where the decrease in viscosity near the heating wall causes an increase in the flow near the wall and a subsequent decrease in the velocity at the center. This is shown in Fig. $3(c)$ by the axial velocity profiles at successive axial locations. As expected, the local Nusselt number in Fig. $3(d)$ re-

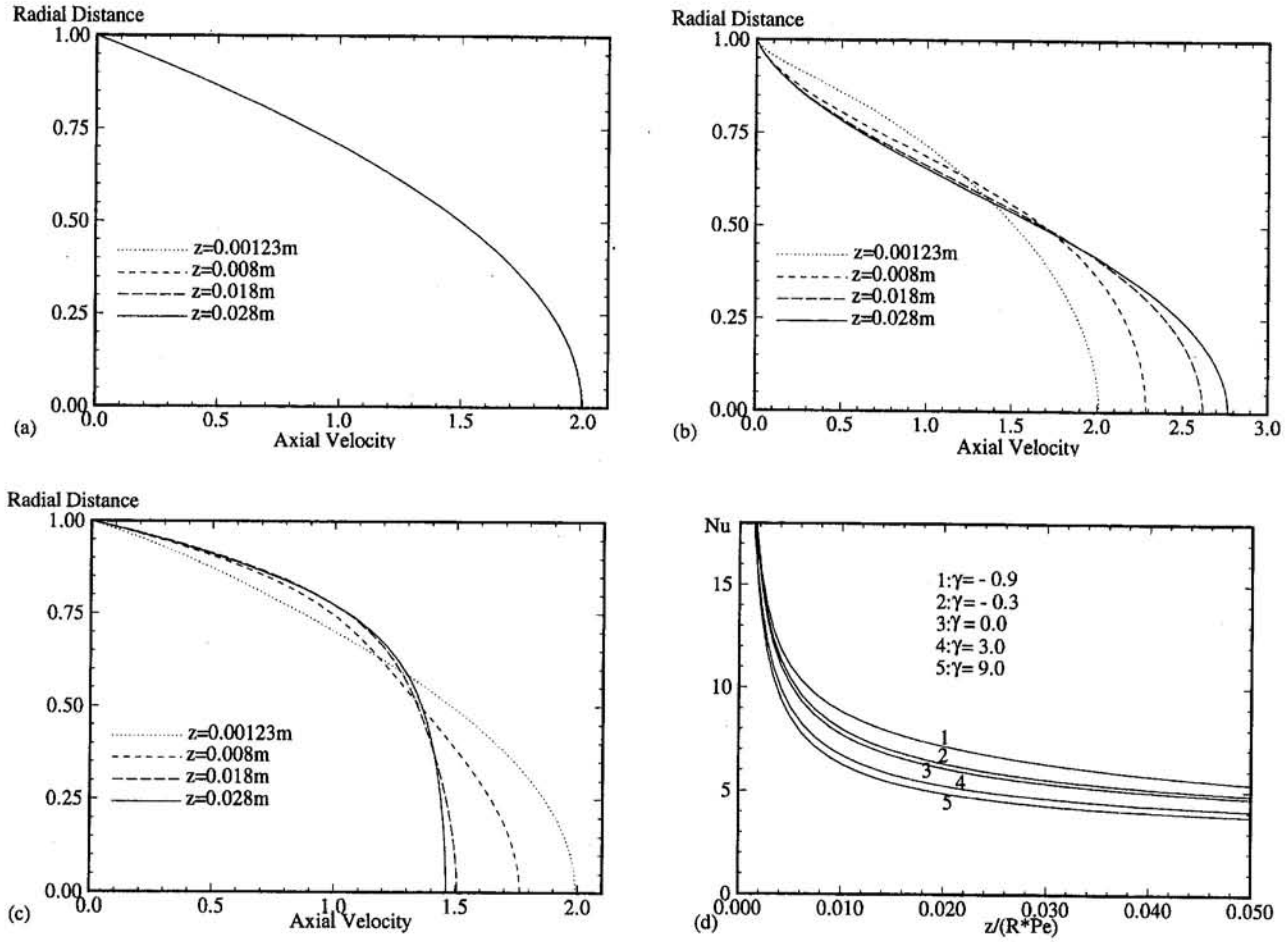

Fig. 3 Results for flow in a tube with a step change in wall temperature of a fluid with (*a*) $\gamma = 0$, (*b*) $\gamma > 0$, (*c*) $\gamma < 0$, (*d*) different viscosity dependence

flects the same general trends, where it increases with decreasing viscosity. All the results shown in Fig. 3 are consistent with physical expectations. As further verification, the Nusselt number profiles of Fig. 3(*d*) are compared against the corresponding results of Yang (1962). This is shown in Fig. 4, where the present computed profiles compare favorably with the approximate solutions obtained by Yang (1962). The lower values of Yang's Nusselt number are consistent with the neglecting of axial conduction in his study.

The effects of viscous dissipation on the thermally developing flow in a tube with a step change in wall temperature are separately considered in Fig. 5, where in Figs. 5(*a*, *b*), the temperatures near the wall were found to be higher with viscous dissipation than without. This is again consistent with expectations, as are the results shown in Fig. 5(*c*) where the local Nusselt number was higher for a larger viscous dissipative effect. Comparisons were also made against available results. As shown in Fig. 6(*a*), excellent agreement was obtained against the numerical results of Krishnan and Sastri (1978), where the minor discrepancy is most likely due to errors incurred during the manual extractions from their semi-log graph. Comparisons were also made against the numerical results of Lawal and Mujumdar (1989), as well as the analytical results of Ou and Cheng (1973), which the former had tabulated for comparison purposes. Figure 6(*b*) shows this comparison, where the considerable discrepancy between the results of Ou and Cheng (1973) and Lawal and Mujumdar (1989) were deemed to be acceptable to the latter authors. Considerably better agreement is achieved with the present results, where the minor discrepancy can be attributed to Ou and Cheng's (1973) early truncation of their series solution and Lawal and Mujumdar's (1989) neglect of axial diffusion. As a final check, the asymptotic Nusselt number is shown in Fig. 6(*b*) to be 9.6, which is in exact agreement with the results of Lin et al. (1983).

3.2 Overall Perspective. Figure 7 shows the results for the case where all the properties are temperature dependent, in addition to the presence of viscous dissipation. As noted earlier, the results for this case are of interest since they would provide an overall view of the expected trends in the drawing of optical fibers. Figures 7(*a*) and 7(*d*) show the contours of the streamfunction and temperature, where in the former, the streamlines were seen to bend with the prescribed neck shape, while in the latter, the temperature were seen to exhibit a large degree of uniformity in the radial direction. Both of these are expected characteristics. However, the contour plot of the vorticity (Fig. 7(*b*)) showed that it was confined to the region where the fiber radius is changing. The reason for this can be seen in Eq. (3*b*) where a nonzero source term exists for regions with nonzero radial velocity or velocity gradients. This is previously unknown and is noteworthy since it indicates that any material distribution that may occur would also be confined to this region. Also, it is interesting to note the localization of the viscous dissipation, which was also previously unknown. This is shown for the first time in Fig. 7(*c*), where the region immediately upstream of where the neck terminates experienced the most significant viscous heating.

3.3 Effect of Viscous Dissipation. As mentioned earlier, the role of viscous dissipation needs to be clarified. Indeed, it is not uncommon for studies to ignore the viscous heating based

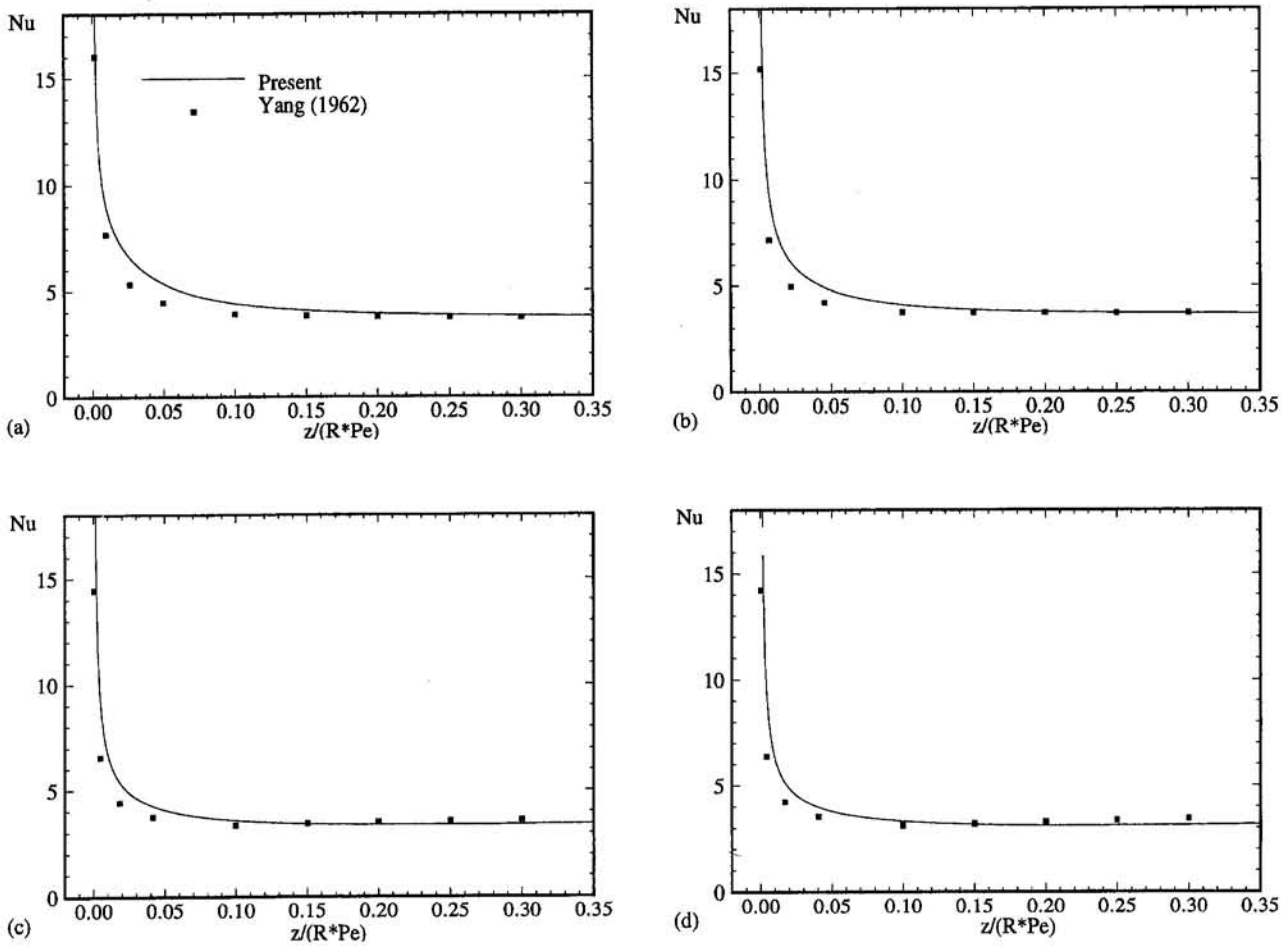

Fig. 4 Comparisons of the Nusselt number for the flow of a variable viscosity fluid in a duct with corresponding values of (*a*) $\gamma = -0.9$, (*b*) $\gamma = -0.3$, (*c*) $\gamma = 3.0$, and (*d*) $\gamma = 9.0$

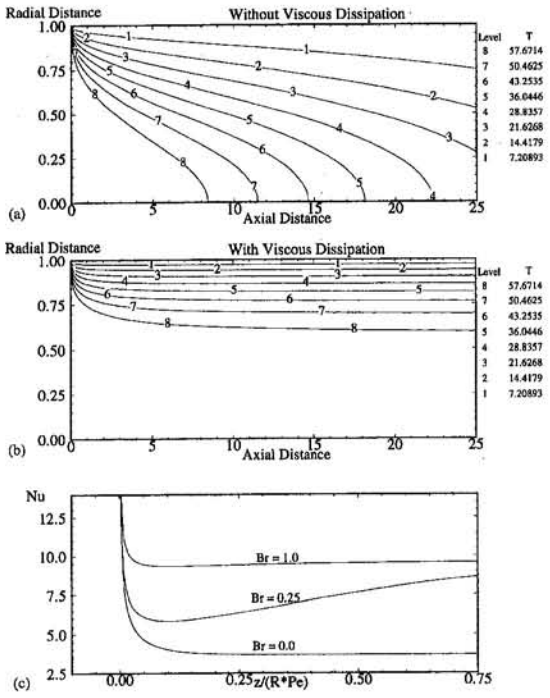

Fig. 5 (*a*, *b*) Temperature profiles for flows with and without viscous dissipation and (*c*) the local Nusselt number for various values of Br

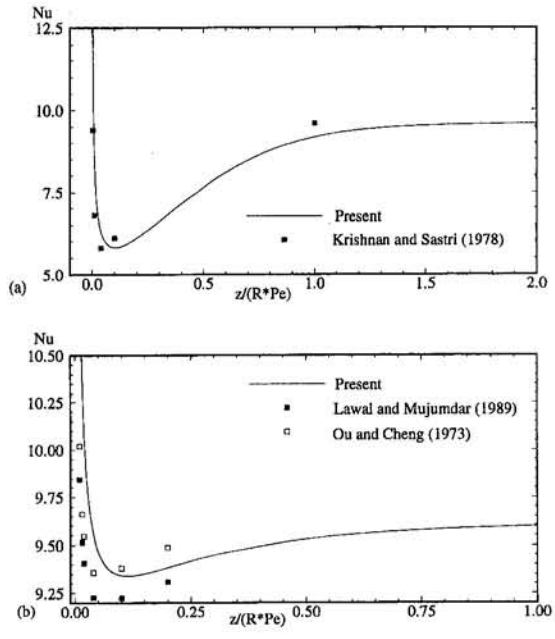

Fig. 6 Comparisons of the local Nusselt number for flows with (*a*) Br = 0.25 and (*b*) Br = 1.0

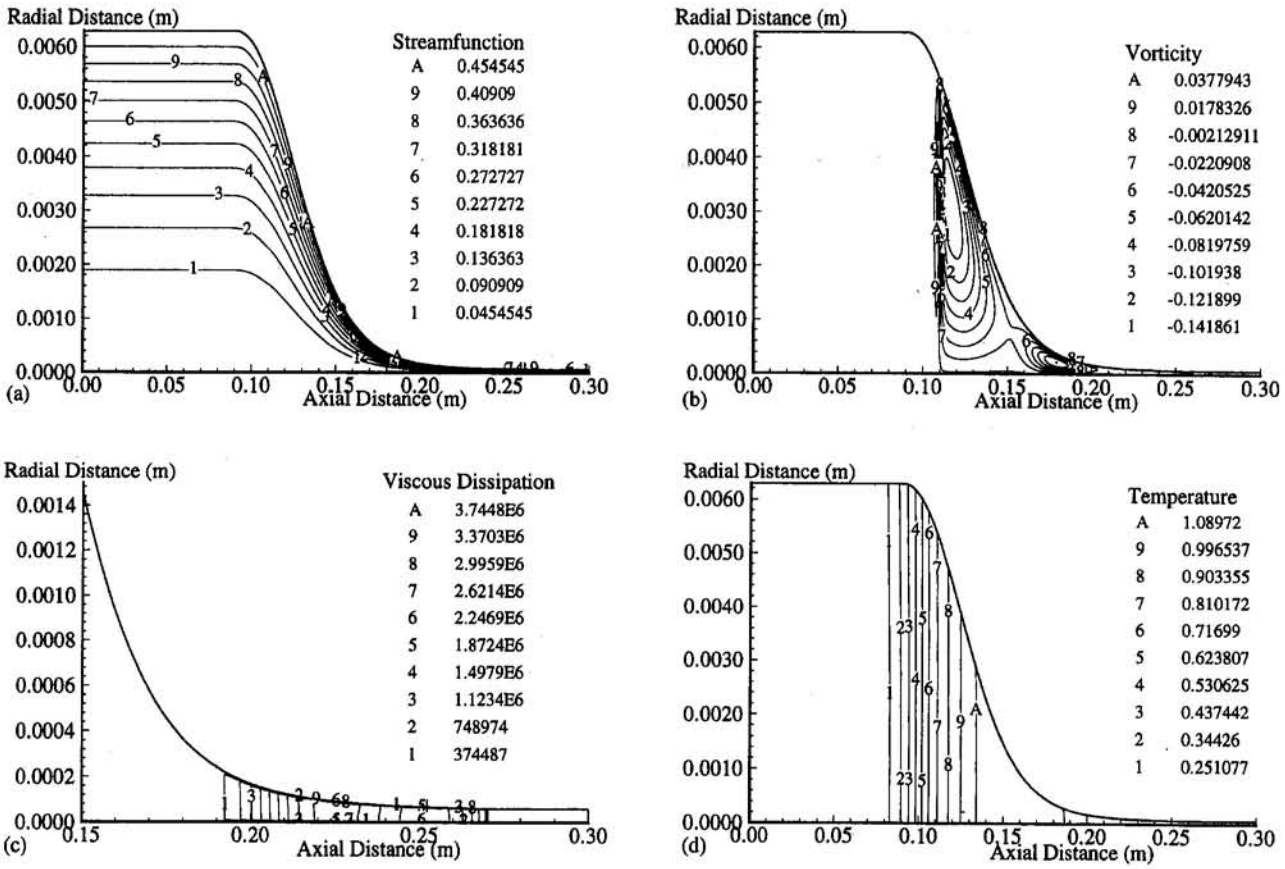

Fig. 7 Results for the fully variable case in terms of contours of (*a*) streamfunction, (*b*) vorticity, (*c*) viscous dissipation function, and (*d*) temperature

on the argument that it is negligible relative to the heat received from the furnace. To investigate this more closely, results are obtained for cases with and without viscous dissipation. However, since the viscous heating is sensitive to the viscosity and thus the local temperature, the comparisons must be made for both cases where all the properties are variable and held constant. Therefore altogether, the four cases studied were: constant properties with viscous dissipation, constant properties without viscous dissipation, variable properties with viscous dissipation, and variable properties without viscous dissipation.

Previously it was shown in Fig. 7(*c*) that the viscous dissipation is localized to a small volume upstream of the fiber section. The implications are that not only will the power density be large, but also the small surface area will limit the influence of the convective and radiative exchange. Thus, contrary to the common assumption, the effect of viscous dissipation may be considerable. As shown in Fig. 8, this was indeed the case,

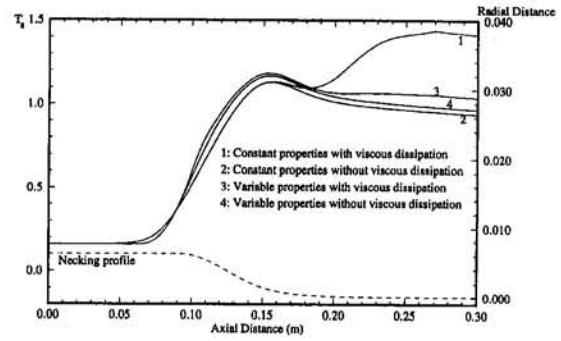

Fig. 8 Effect of viscous dissipation on the surface temperature

where the localized heating can be seen to have a large impact on the exit temperature, regardless of whether the properties were variable or held constant. Of course, when the properties were held constant, the viscosity at the exit was higher and thus, the consequent effect of viscous dissipation was more pronounced. The difference was more subtle (~190 K) when the properties are allowed to vary with temperature, but nonetheless important since the implication on the viscosity, the force balance, the neck shape, and the resulting transport is much more substantial (Choudhury et al., 1995).

3.4 Effect of Variable Properties. In this section, results are analyzed in detail to study the effects of each variable property. In general, three types of plot are presented. These are the axial variation of the surface temperature, the temperature lag, and the velocity lag (the last two are herein defined to be the difference between the surface and center values, divided by the center value). In each of these plots, comparisons were made between cases with and without allowing the property in question to vary with temperature. Where the property was not allow to vary with temperature, the value evaluated at T_m was used instead. Usually only one property is allow to vary in each case, since this would enable a clearer interpretation of the results. Also, all the studies presented include viscous dissipation effects. This is consistent with the fact that unlike properties that may be altered by different dopants, viscous dissipation is always present.

According to Eq. (4*d*), a variable surface tension can produce vorticity along the surface and thus impact the flow (Levich and Krylov, 1969). Specifically, the vorticity is equal to the quotient of the tangential variation in the surface tension and the local viscosity. Thus, there exists a possibility for the creation of considerable vorticity if a very high surface tension gradient co-existed with a very low viscosity. However, due to

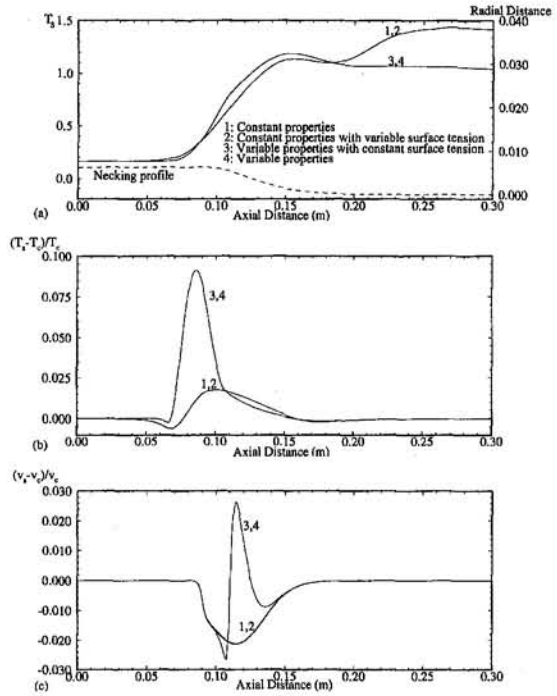

Fig. 9 Results illustrating the effect of surface tension on (*a*) the surface temperature, (*b*) temperature lag, and (*c*) velocity lag

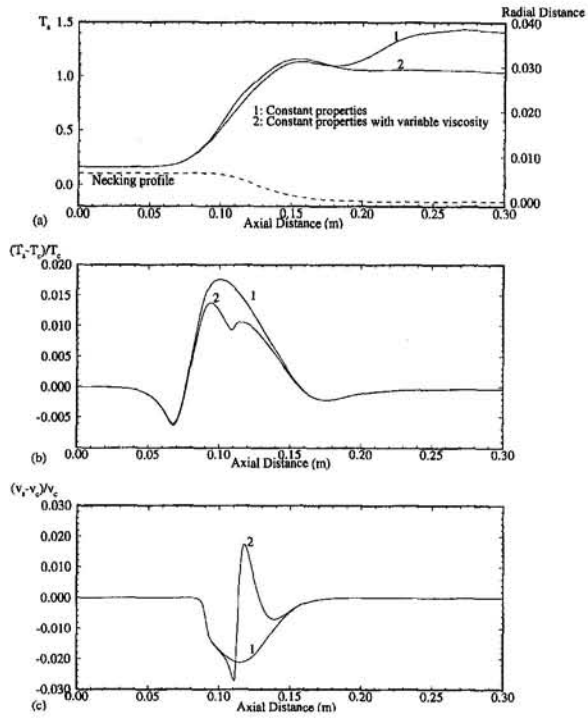

Fig. 10 Effect of variable viscosity on (*a*) surface temperature, (*b*) temperature lag, and (*c*) velocity lag

the large viscosity of fused silica and its weak surface tension dependence on temperature, this would require either a very high surface temperature, or a very high tangential temperature gradient. Therefore, it is of interest to investigate whether such conditions exist in a realistic situation. As shown in Fig. 9, these conditions did not exist since allowing the surface tension to vary with temperature produced negligible difference in the surface temperature, temperature lag, or velocity lag. It should be noted here that since the effect of surface tension can be magnified by a sufficiently low viscosity, comparisons were made both with the remaining properties variable (cases 3 and 4) and held constant (cases 1 and 2).

The effect of variable viscosity was considered next. As seen in Fig. $10(a)$, flows with a temperature-dependent viscosity attained a lower temperature at the exit than that for the case where the viscosity is evaluated at T_m. This is due to the fact that near the exit where the viscous heating was shown to be significant, the variable viscosity case allowed for a lower viscosity and thus a lower viscous dissipation. The presence of variable viscosity seems to also impact the flow within the necking region. This is evident by the differences in the temperature lag profiles shown in Fig. $10(b)$. It is also evident from the velocity lag profiles of Fig. $10(c)$, where the variable viscosity case produced a surface velocity larger than the center velocity, with the maximum difference being about 1.5 percent. This behavior is of particular importance since it could alter the material and impurity distribution within the neck region. As shown in Eq. $(3b)$, this is apparently due to the vorticity generated by the viscosity generated by the viscosity gradients, and was also previously observed in Fig. $7(b)$.

The effects of variable thermal properties, such as specific heat and thermal conductivity, are fairly straightforward and, in many cases, the basic trends can be deduced from physical intuition. Nonetheless for the sake of completeness and for checking the validity of the scheme, quantitative numerical results were obtained. Shown in Figs. 11 and 12 are the respective results for variable conductivity and specific heat, where each is contrasted with results obtained by assuming constant thermal properties with values proportional to that evaluated at T_m. Thus, for the variable thermal conductivity case, the three constant cases are denoted as $k1$, $k2$, and $k3$ where each corresponds to $k(T_m)$, $2k(T_m)$, and $4k(T_m)$, respectively. Similarly for c_p, the three constant cases are denoted c_p1, c_p2, and c_p3, which correspond to $c_p(T_m)$, $2c_p(T_m)$, and $4c_p(T_m)$, respectively. The results were generally consistent with expectations. That is, surfaces with larger thermal conductivities (Fig. $11(a)$) or lower specific heat (Fig. $12(a)$), heated and cooled faster, which is certainly consistent with the effect of a larger thermal diffusivity. Most importantly, the changing thermal diffusivity also tended to produce significant effect on the temperature lags (or gradients), which as shown in Figs. $11(b)$ and $12(b)$, cannot be reproduced by assuming constant properties.

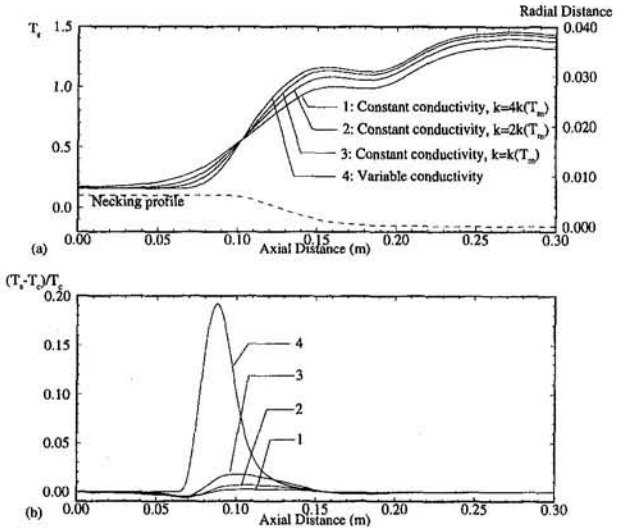

Fig. 11 Effect of variable thermal conductivity on (*a*) surface temperature and (*b*) temperature lag

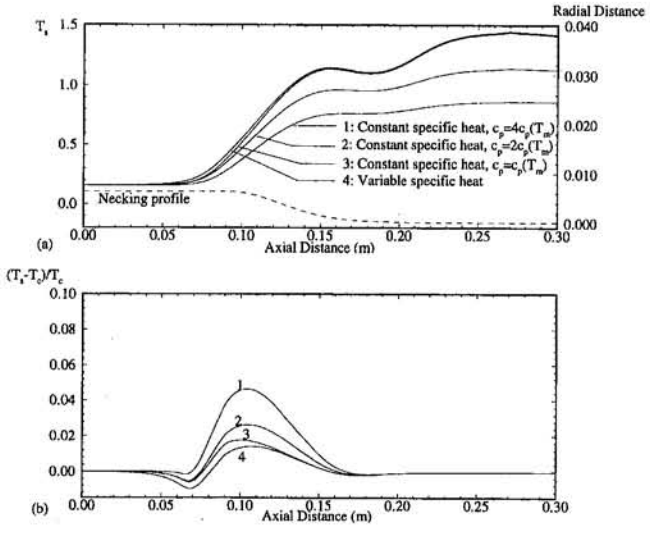

Fig. 12 Effect of variable specific heat on (*a*) surface temperature and (*b*) temperature lag

4 Conclusions

The free-surface flow and thermal transport of fused silica with variable properties, prescribed heat flux, and neck shape was considered. Experimental data from previous researchers were adapted or used as basis for assumptions in order to enable a realistic analysis. The main objectives were to investigate the effects of the variable properties and the associated viscous dissipation. A new solution algorithm was developed in order to overcome the difficulties posed by the large geometric variation and viscosity range as well as the coupling between the viscous dissipation and the exponentially dependent viscosity.

Validation was achieved through physical consistency and comparisons with results on duct flow with variable properties. Several new results were obtained. First, it was shown that although the viscous heating may be small relative to the heat from the furnace, it has considerable impact on the exit temperature due to its localization to a small volume near the fiber section. Second, it was shown that variable surface tension has negligible effect on the transport unless materials properties changed dramatically. In addition, it was shown that the effect of variable viscosity is to produce vorticity, but only in the neck-down region where the preform radius undergo changes. This may have implication on materials and defects redistribution, although the current velocity lag is small. Finally, the effect of variable thermal diffusivity seems to be only relevant in determining the radial temperature gradient, although this could have important implications since this may affect optical defects (Lee, 1993).

5 Acknowledgments

The authors wish to acknowledge the financial support by the National Science Foundation under grant No. DDM-92-13458 and the computational resource provided by the Pittsburgh Supercomputing Center, under grant No. CTS930050P.

References

Choudhury, S. R., Jaluria, Y., and Lee, S. H.-K., 1995, "Generation of Neck-Down Profile for Furnace Drawing of Optical Fiber," ASME HTD-Vol. 306, pp. 23–32.

Fleming, J. D., 1964, *Fused Silica Manual,* Final Report for The U. S. Atomic Energy Commission, Oak Ridge, Tennessee, Project No. B-153.

Homsy, G. M., and Walker, K., 1979, "Heat Transfer in Laser Drawing of Optical Fibres," *Glass Technology,* Vol. 20, No. 1, pp. 20–26.

Krishnan, K. N., and Sastri, V. M. K., 1978, "Numerical Solution of Thermal Entry Length Problem With Variable Viscosities and Viscous Dissipation," *Wärme- und Stoffübertragung,* Vol. 11, pp. 73–79.

Landau, H. G., 1950, "Heat Conduction in a Melting Solid," *Applied Math Quarterly,* Vol. 8, pp. 81–94.

Lawal, A., and Mujumdar, A. S., 1989, "Viscous Dissipation Effects on Thermal Entrance Heat Transfer to Power-Law Fluids in Arbitrary Cross-Sectional Ducts," *The Chemical Engineering Journal,* Vol. 41, pp. 57–66.

Lee, S. H.-K., 1993, "Numerical Investigation on the Neck-Down Region of a Furnace-Drawn Optical Fiber," Ph.D. Dissertation, Rutgers University, New Brunswick, NJ.

Lee, S. H.-K., and Jaluria, Y., 1995a, "The Effects of Geometry and Temperature Variations on the Radiative Transport During Optical Fiber Drawing," *Journal of Materials Processing and Manufacturing Science,* Vol. 3, No. 4, pp. 317–331.

Lee, S. H.-K., and Jaluria, Y., 1995b, "The Effects of Streamwise Convergence in Radius on the Laminar Forced Convection in Axisymmetric Ducts," *Numerical Heat Transfer,* Part A, Vol. 28, No. 1, pp. 19–38.

Levich, V. G., and Krylov, V. S., 1969, "Surface-Tension Driven Phenomena," *Annual Review of Fluid Mechanics,* Vol. 1, pp. 293–316.

Lin, T. F., Hawks, K. H., and Leidenfrost, W., 1983, "Analysis of Viscous Dissipation Effect on Thermal Entrance Heat Transfer in Laminar Pipe Flows With Convective Boundary Conditions," *Wärme- und Stoffübertragung,* Vol. 17, pp. 97–105.

Myers, M. R., 1989, "A Model for Unsteady Analysis of Preform Drawing," *AIChE Journal,* Vol. 35, No. 4, pp. 592–602.

Ou, J. W., and Cheng, K. C., 1973, "Viscous Dissipation Effects on Thermal Entrance Region Heat Transfer in Pipes With Uniform Wall Heat Flux," *Appl. Sci. Res.,* Vol. 28, pp. 289–301.

Paek, U. C., and Runk, R. B., 1978, "Physical Behavior of the Neck-Down Region During Furnace Drawing of Silica Fibers," *Journal of Applied Physics,* Vol. 49, pp. 4417–4422.

Patankar, S. V., 1980, *Numerical Heat Transfer and Fluid Flow,* Hemisphere, New York.

Roache, P. J., 1985, *Computational Fluid Dynamics,* Hermosa Publishers, Albuquerque, NM.

Sayles, R., 1982, "A Finite Element Analysis of the Upper Jet Region of a Fiber Drawing Flow Field," Ph.D. Dissertation, Brown University, Providence, RI.

Uhlmann, D. R., and Kreidl, N. J., 1984, *Glass Science and Technology,* Academic Press, New York.

Vasilijev, V. N., Dulnev, G. N., and Naumchic, V. D., 1989, "The Flow of a Highly Viscous Liquid With a Free Surface," *Glass Technology,* Vol. 30, No. 2, pp. 83–90.

Yang, K. T., 1962, "Laminar Forced Convection of Liquids in Tubes With Variable Viscosity," ASME JOURNAL OF HEAT TRANSFER, Vol. 94, pp. 353–362.

APPENDIX

Configuration and Properties Dependence

The objective of this work was to illustrate clearly the role of each of the variable properties and the viscous dissipation. To achieve this purpose, it is necessary to use configurations and properties data as closely resembling reality as possible. Thus, the variations in the properties and viscous dissipation are viewed as perturbation about this state.

In general, very little information is available on the incident heat flux. Most, if not all, of the previous studies have tended to make arbitrary assumptions. Paek and Runk (1978) were probably one of the few teams who had tried to obtain some experimental basis for their heat flux profile. Through a combination of experiment and analyses, they deduced that the incident heat flux should exhibit a Gaussian profile with a maximum value of 500,000 W/m^2. It is based on these facts that the Gaussian-like profile was chosen in Eq. (A.1). The cosinusoidal form was used as it allowed more flexibility in varying the shape of the profile.

$$\text{For} \quad z < z_a = 0.065 \text{ m}: \quad q'' = 0$$

$$\text{At} \quad z = z_b = 0.14 \text{ m}: \quad q'' = q''_{\max}$$

$$\text{For} \quad z > z_c = 0.19 \text{ m}: \quad q'' = 0$$

$$\text{For} \quad z_a \le z \le z_b:$$

$$q'' = \frac{q''_{\max}}{2} \cos\left[\pi\left(\frac{z - z_a}{z_b - z_a} + 1\right)\right] + \frac{q''_{\max}}{2}$$

$$\text{For} \quad z_b \le z \le z_c:$$

$$q'' = \frac{q''_{\max}}{2} \cos\left[\pi\left(\frac{z - z_b}{z_c - z_b}\right)\right] + \frac{q''_{\max}}{2} \qquad \text{(A.1)}$$

The maximum value of this profile was not taken directly from Paek and Runk (1978), but was instead deduced based on physical arguments. That is, the resulting temperature of the fiber should increase monotonically to a maximum value and then decrease monotonically to a minimum value, larger than T_m. This is in order to ensure the continuous drawing of the fiber without breakage, and the lowest q''_{max} that satisfied this condition was coincidentally found to be identical to the findings of Paek and Runk (1978) to be 500,000 W/m^2. Clearly, this is not the most rigorous approach to determining the heat flux profile, but the present one should be reasonably realistic so to enable our studies on the effect of variable properties. A later study will be performed to determine the nature of this heat flux more exactly.

The neck shape used in this study was also chosen to correspond with the measurements of Paek and Runk (1978). Their data were presently curve-fitted with an eighth-order polynomial, which is given below:

$$\text{For} \quad z < z_1 = 0.09 \text{ m}: \quad R = R_i = 0.006288 \text{ m}$$

$$\text{For} \quad z > z_2 = 0.27 \text{ m}: \quad R = R_e = 0.000059 \text{ m}$$

For $z_1 \le z \le z_2$:

$$\begin{aligned}\log_{10} R = {} & -6.66531 \times 10^5 (z - (z_1 - 0.02))^8 \\ & + 1.5152 \times 10^6 (z - (z_1 - 0.02))^7 \\ & - 6.20906 \times 10^5 (z - (z_1 - 0.02))^6 \\ & + 1.56512 \times 10^4 (z - (z_1 - 0.02))^5 \\ & + 3.0826 \times 10^4 (z - (z_1 - 0.02))^4 \\ & - 4.71803 \times 10^3 (z - (z_1 - 0.02))^3 \\ & + 78.84 (z - (z_1 - 0.02))^2 \\ & + 1.57224 (z - (z_1 - 0.02)) - 2.231642 \end{aligned} \quad \text{(A.2)}$$

Clearly, this neck shape is part of the solution to the overall process, and its prescription is of concern. The best approach is to generate the neck shape as part of the solution, but several other key questions must be answered before such an attempt can be successful. Thus, the current study represents one such attempt to clarify the roles of each properties. For this study, the configuration of the system is based on the available experimental measurements, and thus the computations that follow should be realistic. However, in eliminating the viscous dissipation or varying the properties, the results may be less realistic as the neck shape may vary in response. Still, the general behavior of the results would enable the determination of their respective roles. For example, one of the findings of this study is that the variable viscosity impacted the flow through the generation of vorticity. It is unlikely that this mechanism would disappear if the shape were allowed to vary.

The material properties such as thermal conductivity, surface tension, specific heat, and viscosity were all taken to be temperature dependent. The thermal conductivity was obtained from Fleming (1964), whose data were presently curve-fitted with a third-order polynomial:

$$\text{For} \quad 310.78 \text{ K} \le T \le 1921.89 \text{ K}$$

$$\begin{aligned} k_c(T) = {} & -1.6874325 \times 10^{-11} \left(\frac{9T}{5} - 459.4\right)^3 \\ & + 4.7386566 \times 10^{-9} \left(\frac{9T}{5} - 459.4\right)^2 \\ & + 4.3111737 \times 10^{-4} \left(\frac{9T}{5} - 459.4\right) + 1.3424434 \end{aligned}$$

$$\text{For} \quad T < 310.78 \text{ K}: \; k_c = k_c(310.78)$$

$$\text{For} \quad T > 1921.89 \text{ K}: \; k_c = k_c(1921.89) \quad \text{(A.3}a\text{)}$$

This conductivity was then combined with a radiative component, which, following Myers' (1989) approach, was obtained by using Rosseland's assumption to approximate the radiative transport within. From Myers (1989), this radiative conductivity was computed as:

$$k_r = \frac{16n^2\sigma T^3}{3a} = \frac{16(1.42)^2 5.729 \times 10^{-8}}{3} \frac{T^3}{400}$$

$$= 1.5402607 \times 10^{-9} T^3 \quad \text{(A.3}b\text{)}$$

The temperature dependence of the surface tension, specific heat, and kinematic viscosity were also obtained by the present curve-fitting of Fleming's (1964) data:

$$\text{For} \quad T < T_m, \quad \xi = 0.17315$$

$$\text{For} \quad T \ge T_m, \quad \xi = 3.375 \times 10^{-5} T + 0.10902625 \quad \text{(A.4)}$$

$$\text{For} \quad 310.78 \text{ K} \le T \le 1699.67 \text{ K}$$

$$\begin{aligned} c_p(T) = {} & -1.9202379 \times 10^{-11} \left(\frac{9T}{5} - 459.4\right)^4 \\ & + 8.9608033 \times 10^{-8} \left(\frac{9T}{5} - 459.4\right)^3 \\ & - 2.0008399 \times 10^{-4} \left(\frac{9T}{5} - 459.4\right)^2 \\ & + 0.59235423 \left(\frac{9T}{5} - 459.4\right) + 6.2175046 \times 10^2 \end{aligned}$$

$$\text{For} \quad T < 310.78 \text{ K}: \; c_p = c_p(310.78)$$

$$\text{For} \quad T > 1699.67 \text{ K}: \; c_p = c_p(1699.67) \quad \text{(A.5)}$$

$$\nu(T) = 4545.45 \exp\left[32\left(\frac{T_m}{T} - 1\right)\right] \quad \text{(A.6)}$$

Equation (A.6) assumes that the entire fused silica behaves as a Newtonian fluid with the viscosity varying exponentially with the temperature. This is consistent with the noncrystalline structure of glass, where the apparently solid portion is a fluid with a large viscosity. This assumption essentially ignores any viscoelastic or non-Newtonian behavior of the silica, since in general, very little is known about the behavior of fused silica under this flow configuration. However, it is clear that any viscoelastic effect will be minimal as the drawing tension is only on the order of 0.1 N. In addition, it is widely accepted that at low rate of deformation, glass behaves as a Newtonian fluid (Uhlmann and Kreidl, 1984). While in the current system, the deformation may be high, its rate may not be high as the feeding rate is low. Also, while the final drawing velocity is large, most of the deformation occurs under a relatively low velocity condition.

Instability of Convection and Heat Transfer of High Prandtl Number Fluids in a Vertical Slot

Y. Y. Jin

C. F. Chen

Department of Aerospace and Mechanical Engineering, The University of Arizona, Tucson, AZ 85721

The stability of convective motion of high-Prandtl-number fluids, generated by a lateral temperature difference across a vertical slot with aspect ratio 15, is studied numerically. The Prandtl number range studied is from 50 to 2000. The nonlinear governing equations are solved by a finite difference method. The predicted flow patterns and critical values are in good agreement with the recent experimental results of Wakitani (1994). It is found that the vorticity distribution along the vertical centerline of the slot is a very sensitive indicator of the onset of multicellular flow. The critical Grashof number varies almost inversely with the Prandtl number; consequently, the critical Rayleigh number is essentially independent of the Prandtl number. Heat transfer results show good agreement with the experimentally correlated values, and they are independent of the Prandtl numbers and the flow patterns.

1 Introduction

Since the pioneering work by Batchelor (1954), thermal convection in a vertical slot due to lateral temperature gradient has been the subject of extensive research because of its important applications in engineering and geophysics. Summaries of research results can be found in the papers of Lee and Korpela (1983) and Wakitani (1994). In this paper, we study the transitional process from unicellular to multicellular convection in constant-property fluids of large Prandtl numbers (50–2000) by numerical simulation. Results of previous research work closely related to our problem are reviewed in the following.

Elder (1965) was the first to observe experimentally that the convection pattern within the slot changes from a unicellular flow at low Rayleigh numbers to a secondary flow pattern consisting of an array of cells at higher Rayleigh numbers. When the Rayleigh number is further increased, a tertiary flow pattern emerges in which small counterrotating cells are generated between the well-established secondary cells. For a silicone oil with Pr $\approx$ 1000 in a slot of aspect ratio 19, the critical Rayleigh number was found to be $3 \times 10^5 \pm 30$ percent. Elder defined the onset of secondary flow by the appearance of two convection cells in the slot, one large cell in the upper $\frac{3}{4}$ of the slot and a small cell below it. The onset of multicellular convection in the form of five cells of approximately equal wavelength occurred at a much higher Rayleigh number of 4.9×10^5. Vest and Arpaci (1969) performed experiments with a silicone oil (Pr = 900) in a slot of aspect ratio 20. They found the critical Rayleigh number to be $3.7 \times 10^5 \pm 10$ percent. Seki et al. (1978) used water, transformer oil (Pr = 480), and glycerine (Pr = 12,500) in their experiments in a slot of aspect ratio 15. They obtained heat transfer data over a large Rayleigh number range and clear streak photographs of the convection patterns that compare well with their numerical simulations. It was noted that the viscosities of all three fluids are temperature dependent. More recently, Wakitani (1994) carried out experiments with silicone oils (Pr = 50, 125, and 900) to examine the transition to secondary flow at aspect ratios of 10, 15, and 20. The results were compared with previous experimental results and the theoretical predictions of Bergholz (1978). For $A = 15$, the critical Rayleigh numbers were determined to be 6.0×10^5 and 5.5×10^5 for Pr = 50 and 125, respectively.

In addition to their experiments, Vest and Arpaci (1969) carried out a linear stability analysis for an infinite slot for both the conduction and the boundary layer regime in the slot. In the conduction regime, the temperature within the slot did not vary in the vertical direction. As the flow entered the boundary layer regime, a positive vertical temperature gradient was established, as predicted by Gill (1966). Elder's (1965) data showed that the vertical temperature gradient remained constant over a wide Rayleigh number range. In a stability analysis based on the flow in the boundary layer regime, a value of the temperature gradient must be assumed. Hart (1971) considered the stability of convection in a sloping, narrow tank both theoretically and experimentally for air and water. He noted that a term was inadvertently left out of the linearized energy equation of Vest and Arpaci (1969). The stability analysis was based on the boundary layer regime using the experimentally determined temperature gradient in the fluid along the tank. Reasonable agreement was obtained between experimental and theoretical results. Bergholz (1978) performed linear stability analysis on fluids with Prandtl numbers ranging from 0.73 to 1000. He found that instability can onset either in a travelling wave mode or a steady convection mode. But for fluids with Pr $\geq$ 50, the steady convection mode is the critical one for a specified range of stratification parameter γ.

Lee and Korpela (1983) studied the problem by numerical simulation. They integrated the nonlinear governing equations for a constant-property, Boussinesq fluid with Prandtl numbers ranging from 0 to 1000. By examining the streamline pattern and the isotherms, a critical Rayleigh number can be determined. For $A = 15$ and Pr = 1000, the critical Rayleigh number was found to be 4×10^5. Daniels (1985, 1987, 1989), in a series of papers, considered convection and its subsequent instability in a finite slot by asymptotic analysis. His results showed that, for large-Prandtl-number fluids in a slot of large aspect ratio, a universal neutral curve can be obtained. Instability of the steady convective mode occurs at the critical value of stratification parameter $\gamma_c = 6.30$. It was also shown that this result was in reasonable agreement with earlier experimental observations.

The objective of this paper is to use an accurate numerical scheme to study the transitional process from unicellular to multicellular flow in a heated slot. Specifically, we examine the onset of secondary flow in a constant-property, Boussinesq fluid

Contributed by the Heat Transfer Division for publication in the JOURNAL OF HEAT TRANSFER. Manuscript received by the Heat Transfer Division February 1995; revision received December 1995. Keywords: Flow Instability, Natural Convection, Numerical Methods. Associate Technical Editor: P. G. Simpkins.

of high Prandtl number in a slot of aspect ratio 15. The Prandtl number range considered is from 50 to 2000. The critical Grashof number and the stratification parameter at the onset of secondary flow are determined and compared with the experimental results of Wakitani (1994) and the computational results of Lee and Korpela (1983). Good agreement is obtained. The heat transfer results show good agreement with the experimentally correlated values of Seki et al. (1978).

2 Governing Equations and Numerical Algorithm

Consider a vertical slot of height H and width L, with two horizontal impermeable, rigid adiabatic walls. The left and right walls are maintained at uniform constant temperatures, T_h and T_c ($<T_h$), respectively. The temperature difference is assumed to be small enough that the Boussinesq approximation holds when a Newtonian fluid of density ρ, with constant kinematic viscosity ν and thermal diffusivity α, is contained in the cavity.

The governing equations can be put into nondimensional form by scaling the vertical coordinate by H, the horizontal coordinate by L, time by L^2/ν, temperature by $\Delta T = T_h - T_c$, velocity by $U = g\beta\Delta TL^2/\nu$, and pressure by ρU^2. Introducing the stream function ψ and the vorticity ω

$$u = \frac{1}{A}\frac{\partial \psi}{\partial y} \quad v = -\frac{\partial \psi}{\partial x} \tag{1}$$

$$\omega = \frac{\partial v}{\partial x} - \frac{1}{A}\frac{\partial u}{\partial y} \tag{2}$$

we obtain the nondimensional governing equations:

$$\frac{\partial \omega}{\partial t} = \frac{\mathrm{Gr}}{A}\left(-\frac{\partial \psi}{\partial y}\frac{\partial \omega}{\partial x} + \frac{\partial \psi}{\partial x}\frac{\partial \omega}{\partial y}\right) + \frac{\partial^2 \omega}{\partial x^2} + \frac{1}{A^2}\frac{\partial^2 \omega}{\partial y^2} + \frac{\partial \theta}{\partial x} \tag{3}$$

$$\frac{\partial^2 \psi}{\partial x^2} + \frac{1}{A^2}\frac{\partial^2 \psi}{\partial y^2} = -\omega \tag{4}$$

$$\frac{\partial \theta}{\partial t} = \frac{\mathrm{Gr}}{A}\left(-\frac{\partial \psi}{\partial y}\frac{\partial \theta}{\partial x} + \frac{\partial \psi}{\partial x}\frac{\partial \theta}{\partial y}\right) + \frac{1}{\mathrm{Pr}}\left(\frac{\partial^2 \theta}{\partial x^2} + \frac{1}{A^2}\frac{\partial^2 \theta}{\partial y^2}\right) \tag{5}$$

The boundary conditions are

$$x = 0 \quad \psi = \partial\psi/\partial x = 0 \quad \theta = 1 \tag{6}$$

$$x = 1 \quad \psi = \partial\psi/\partial x = 0 \quad \theta = 0 \tag{7}$$

$$y = 0 \quad \psi = \partial\psi/\partial y = 0 \quad \partial\theta/\partial y = 0 \tag{8}$$

$$y = 1 \quad \psi = \partial\psi/\partial y = 0 \quad \partial\theta/\partial y = 0 \tag{9}$$

A finite difference method is used to solve the above governing equations. In detail, we adopt the schemes by Lee and Korpela (1983) to discretize Eqs. (3) and (5), that is, the explicit scheme of Arakawa (1966) for the nonlinear terms, the DuFort–Frankel (1953) scheme for the diffusive terms, and the central difference scheme for the time derivatives. The Poisson Eq. (4) is solved by Alternating Direction Implicit (ADI) method (Roache, 1982), aided with the prediction method (Van Doormaal and Raithby, 1984), and Block Correction Technique (BCT) (Patankar, 1981). The boundary vorticity is determined by Thom's rule (Roache, 1982). Calculations for cases of the specific Prandtl number or aspect ratio are started from an initially motionless state. Calculations at higher Grashof numbers are then initiated from the results of low Grashof numbers.

Table 1 Grid convergence test for $A = 16$, Ra = 24,000, and Pr = 0.71; ψ is evaluated at the center of the slot, and ω at the midheight of the wall

Authors	$\lvert\psi\rvert \times 10^3$	$\omega \times 10^2$	Nu	grids
Present study	1.586	7.026	1.830	9 × 65
	1.370	5.564	1.893	17 × 129
	1.336	5.236	1.901	33 × 129
	1.317	5.159	1.903	33 × 257
	1.310	5.088	1.902	65 × 257
Le Quéré (1990)	1.316	5.080	1.901	32 × 150

3 Accuracy Assessment

The code based on the algorithm given above has been tested by calculating the natural convection of air in vertical slots with aspect ratio $A = 16$ and 20 and comparing the output with known results. The following are the test results:

1 $A = 16$. We compare our results with those of the two-cell solution at Ra = 24000 (Gr = 33803) calculated by Le Quéré (1990) using the Tau–Chebyshev algorithm. A grid convergence study is first carried out. The results at the sampling points are given in Table 1. It shows that spatially converged results can be obtained with increasing grid numbers even for the more sensitive quantity, the vorticity at the midheight of the left wall. Since only a small improvement is obtained when refining grids from 33 × 129 to 33 × 257, the grid number of 33 × 129 is usually adopted in the study. With this grid, the vorticity is within 3 percent of the results of Le Quéré. The streamline and isotherm distributions are shown in Fig. 1. They are in good agreement with those obtained by Le Quéré. As can be seen, the flow is characterized by a two-cell secondary flow pattern, and has a wavenumber approximately 1.60. This wavenumber agrees very well with Le Quéré, who obtained a wavenumber 1.59.

Nomenclature

A = aspect ratio = H/L
g = gravitational acceleration
Gr = Grashof number = $g\beta\Delta TL^3/\nu^2$
H = height of the slot
L = width of the slot
Nu = Nusselt number
Pr = Prandtl number = ν/α
Ra = Rayleigh number = $g\beta\Delta TL^3/\alpha\nu$
S = dimensionless vertical temperature gradient at the center = $\partial\theta/\partial y$
t = dimensionless time
T = temperature
x, y = dimensionless Cartesian coordinates
U = characteristic velocity = $g\beta\Delta TL^2/\nu$
u, v = dimensionless velocity components
α = thermal diffusivity
β = coefficient of volumetric expansion
γ = stratification parameter = $(0.25\ S\ \mathrm{Ra}/A)^{0.25}$
ΔT = temperature difference
θ = dimensionless temperature
ν = kinematic viscosity
ρ = density
ψ = stream function
ω = vorticity

Subscripts

c = cold wall or critical value
h = hot wall
L = local value

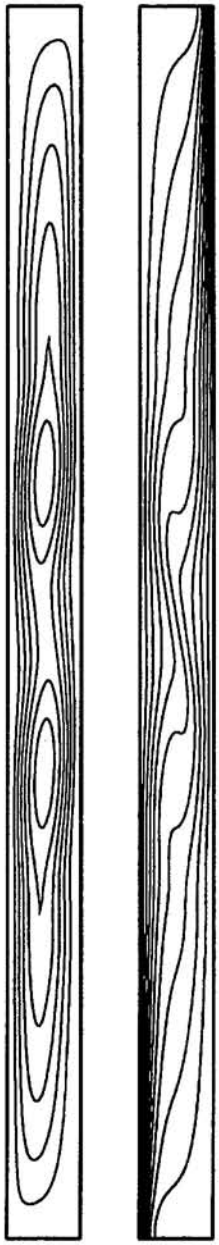

Fig. 1 Two-cell solution at Ra = 24,000 and Pr = 0.71: (*a*) streamfunction, $\psi = -3, -6, -9, -12, -15, -18 \times 10^{-4}$; (*b*) isotherm

2 $A = 20$. The second test is to determine the critical Grashof number by increasing Grashof number gradually. At Gr = 8800, only one large cell is observed. At Gr = 8900, very weak cells are observed in the cavity. Also, the horizontal velocity and temperature along the vertical plane show notable waviness indicating the onset of cellular flow. This value is in excellent agreement with that predicted by Lauriat and Desrayaud (1985), who obtained $Gr_c = 8900$.

4 Results and Discussion

4.1 Flow Development. The code is used to simulate the thermal convection in a vertical slot with $A = 15$, for which comparable, experimental results (Wakitani, 1994) are available. The chosen Prandtl numbers are 50, 125, 158, 405, 720, 1000, and 2000. The values 158, 405, and 720 correspond to 70, 80, and 90 percent glycerol in water, respectively. The onset of instabilities at these Prandtl numbers is determined.

For a high-Prandtl-number Boussinesq flow, the flow enters the transition and boundary layer regimes from the conduction regime as the Grashof number is increased with A fixed. The isotherms of these typical regimes corresponding to Gr = 50,500, and 5000 at Pr = 50 are shown in Fig. 2. As can be seen, in the conduction regime (Fig. 2(a)), convection is confined near the ends. The isotherms are almost vertical in the slot, i.e., heat transfer across the slot is conduction dominated. With increased Grashof number, a stable vertical temperature gradient develops in the core region of the flow (Fig. 2(b)), indicating the more significant role of the convection. Further increasing the Grashof number causes the flow to be confined to thin layers at the sidewalls, and the heat transfer to be primarily by convection (Fig. 2(c)). The horizontal temperature distributions at the midheight are shown in Fig. 3 at Gr = 50, 500, and 5000, respectively. The temperature gradient increases

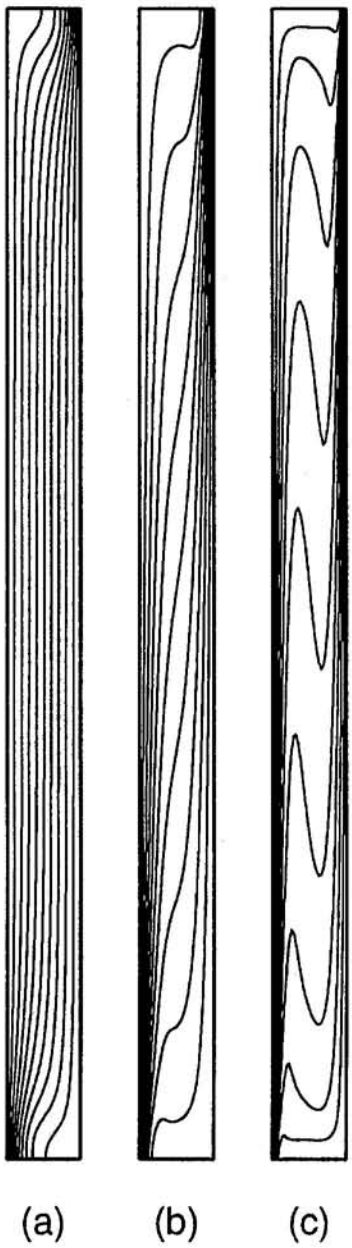

Fig. 2 Typical isotherms at Pr = 50: (*a*) Gr = 50, conduction regime; (*b*) 500, transition regime; (*c*) 5000, boundary layer regime

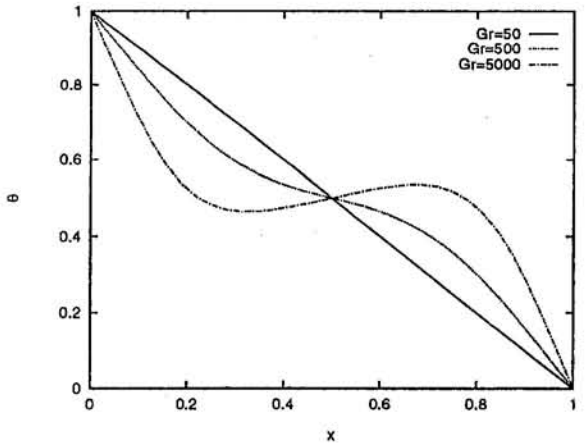

Fig. 3 The horizontal temperature distribution at the middle height

adjacent to the wall but decreases in the center region as the Grashof number increases. At still higher Grashof numbers, the horizontal temperature gradient becomes positive, as shown in the experiments of Wakitani (1994).

As the Grashof number is further increased, small cells rotating in the same direction as the original unicellular flow are observed in the center. These are commonly termed secondary cells and characterize the onset of instability. This typical development is illustrated in Fig. 4 for a fluid with Pr = 125. Note that to bring out the salient features of the flow changes in $\Delta\psi$ are not constant. The flow remains unicellular until Gr = 4400 (Fig. 4(a)), then instability develops and a four-cell secondary flow pattern with a wavelength $1.45L$ is found at Gr = 4500 (Fig. 4(b)). As the Grashof number is increased to 14,000, six well-developed secondary cells with an approximate wavelength of $2.25L$ are in the slot as shown in Fig. 4(c). Wakitani (1994) observed six secondary cells in his experiments when the Rayleigh number reached 7.49×10^5 (Gr = 5992). The corresponding experimental values of the wavelength, estimated from the flow patterns obtained by Wakitani, are $1.5L$ at Ra = 6.62×10^5 (Gr = 5296) and $2.21L$ at Ra = 1.8×10^6 (Gr = 14,400). The agreement is excellent. Actually, a smaller tertiary cell is sandwiched between two secondary cells in the center at Gr = 14,000 as shown in Fig. 4(c). Such tertiary cells were observed at Ra = 1.8×10^6 (Gr = 14,400) in Wakitani's experiment. The tertiary cell develops as the Grashof number is further increased. A well-developed tertiary flow pattern at Gr = 20,000 is shown in Fig. 4(d). The flow still shows six secondary cells; however, the cells at the ends become much weaker than those in the center. The wavelength is increased slightly to $2.35L$. The estimated wavelength from Wakitani's experimental flow pattern at Ra = 2.68×10^6 (Gr = 21,440) is $2.47L$. Comparing the cases shown in Fig. 4, we see that the flow in the end regions exhibits only slight variations as the Grashof numbers is increased. The corresponding isotherms, shown in Fig. 5, illustrate the boundary layer behavior before the onset of instability (Fig. 5(a)). As the Grashof number is increased, the isotherms show a strong convective motion in the central two cells (Fig. 5(b), 5(c), and 5(d)). When the tertiary cell develops, no notable variations in the isotherms are found. The isotherms at the end zones do not show much variation. This is in accordance with the flow at the ends as mentioned above.

The vorticity and temperature profiles along the vertical centerline, near the critical state and at one supercritical state, are shown in Fig. 6 for Pr = 125. It can be seen in Fig. 6(a) that the vorticity exhibits small variations even at the subcritical Gr = 4400, which corresponds to a single cellular flow in the slot (Fig. 4(a)). Such small variation in the vorticity just prior to the onset of instability is found in all of the cases studied. At the supercritical Gr = 4500, large variations develop. The four large modulations correspond to the four clearly established secondary cells (see Fig. 4(b)). It is evident that the vertical distribution of vorticity serves as an excellent indicator of the onset of instability, more sensitive than the streamline patterns. Small indentations are found in the positive peaks of vorticity when the tertiary flow is well developed (Gr = 20,000), which are indicative of the tertiary cells. It is interesting to note that this feature can be found in Fig. 3 of de Vahl Davis and Mallinson (1975) but it was not discussed by them. The vertical distribution of the horizontal velocity component and the stream function along the centerline are similarly modulated as the vorticity, but no small valleys are found at the locations of the tertiary cells.

The temperature profile, shown in Fig. 6(b), is quite smooth at Gr = 4400. At the onset of instability, near Gr = 4500, the temperature distribution is greatly altered by the multicellular convection, showing step changes between the cells. An unstable temperature gradient exists within each secondary cell, which disappears when the Grashof number is increased, resulting in better mixing. At Gr = 20,000, a small step change in temperature can be discerned at the locations of the tertiary cells. When the grid points in the vertical direction of the slot

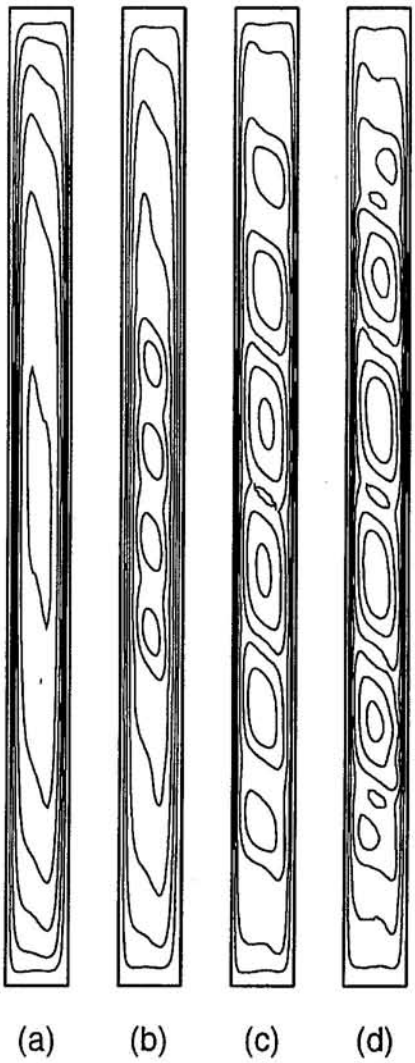

Fig. 4 Typical flow patterns at Pr = 125: (a) Gr = 4400, ψ = −4, −8, −12, −16, −20, −24 × 10^{-5}; (b) Gr = 4500, ψ = −5, −10, −15, −20, −24, −27 × 10^{-5}; (c) Gr = 14,000, ψ = −2, −4, −7, −10.4, −14, −19 × 10^{-5}; (d) Gr = 20,000, ψ = −2, −4, −5.8, −7.8, −11, −14 × 10^{-5}

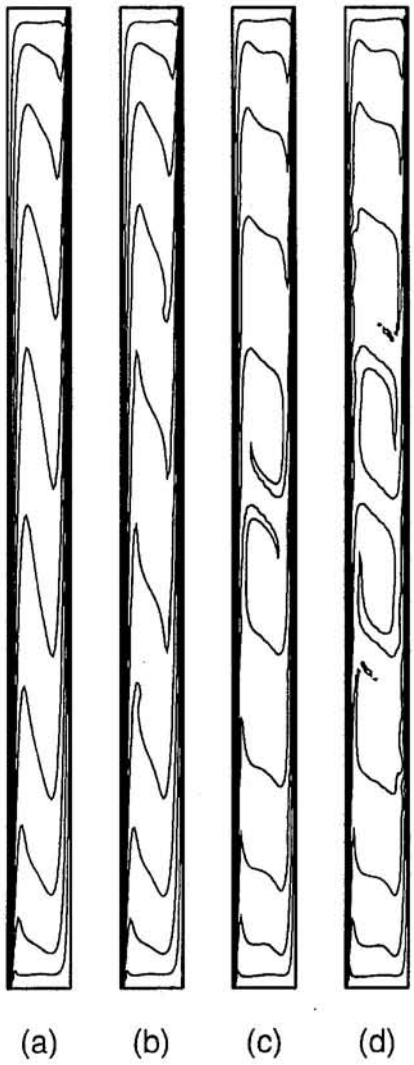

Fig. 5 Isotherms at Pr = 125: (*a*) Gr = 4400; (*b*) 4500; (*c*) 14,000; (*d*) 20,000

were increased to 257, the same salient features in the vertical profiles were obtained.

The results for Pr = 1000 are presented in Fig. 7 to illustrate the effect of large Prandtl number. Numerical calculations for this Prandtl number have been reported by de Vahl Davis and Mallinson (1975), and Lee and Korpela (1983). The latter gave results for $A = 15$ based on grid numbers 21×129. Our results are obtained based on grids of 33×129.

Figure 7 shows the typical flow patterns with increasing Grashof number. The flow in the slot is unicellular at Gr = 450 (Fig. 7(*a*)), although the horizontal velocity profile along the vertical centerline already shows some small waviness. With further increase in Grashof number, instability develops leading to a multicellular flow pattern at Gr = 500 (see Fig. 7(*b*)). This indicates $Gr_c = 450-500$, slightly greater than the numerical value given by Lee and Korpela, who obtained $Gr_c = 400$. This discrepancy is discussed in the next section. Further increase in the Grashof number strengthens the secondary flow, and at Gr = 2000, there is a small tertiary cell at the center of the slot as in the case of Pr = 125 at Gr = 14,000 (Fig. 4(*c*)). Well-developed tertiary cells are shown in Fig. 7(*d*) at Gr = 3000.

4.2 Critical Grashof Number. The critical Grashof numbers, Gr_c, for all the cases considered are presented in Table 2, together with the experimental results of Wakitani (1994) and the computational results of Lee and Korpela (1983). Also listed are the equivalent critical Rayleigh numbers, Ra_c, and the critical stratification parameter, γ_c. Our calculated results show excellent agreement with the experimental values of Wakitani at Pr = 50 and 125. At Pr = 1000, the value of Gr_c found by Lee and Korpela is ~15 percent lower than ours. We believe this is mainly due to the larger number of horizontal grid points we used (33) compared to Lee and Korpela (21). Table 1 shows that, as the grid points increase from 17×129 to 33×129, there is a decrease in the value of $|\psi|$. Since the cells are determined by the closed streamline surrounding the max $|\psi|$, instability as defined by us and by Lee and Korpela (1983) will appear first in the results from calculations made with less grid resolution. If we use the estimate of the boundary thickness suggested by Gill (1966), $\delta/L = 1.8(A/\mathrm{Ra})^{1/4}$, the boundary layer is resolved by 2.8 grid spacings in Lee and Korpela's calculations and by 4.5 grid spacings in our calculations. It is therefore reasonable to expect our results to be more accurate. Furthermore, in view of the excellent agreement between our results and those of Le Quéré (1990) and Lauriat and Desrayaud (1985), each using a computation scheme different from the present method, we are quite confident about the results presented here. For Pr = 50 and 1000, the values of Gr_c corresponding to our computed γ_c are approximately 7100 and 240, respectively, according to Bergholz's (1978) predictions. These values are approximately 50 percent less than the results obtained here.

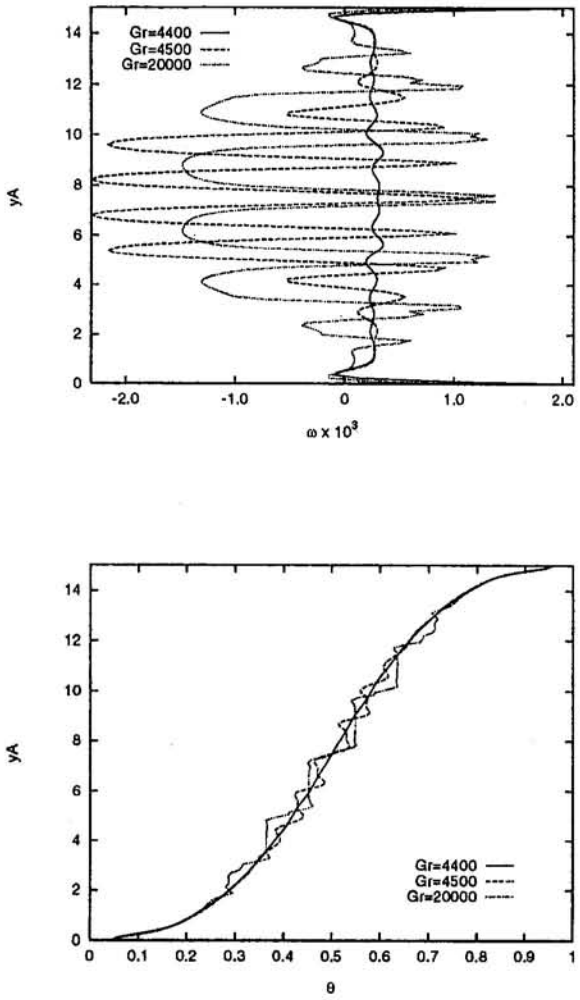

Fig. 6 Vorticity and temperature profiles along the vertical center line at Pr = 125 for Gr = 4400, 4500, and 20,000: (*a*) vorticity; (*b*) temperature

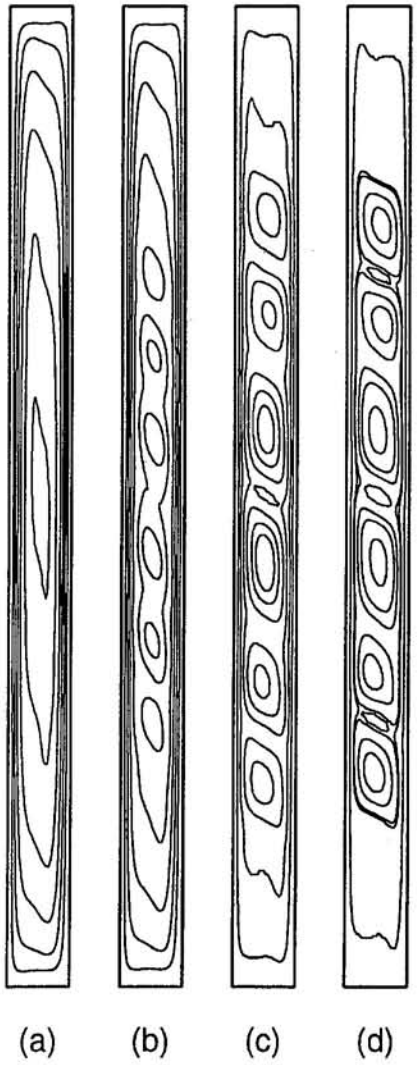

Fig. 7 Typical flow patterns at Pr = 1000: (*a*) Gr = 450, $\psi = -5, -10, -15, -20, -25, -28 \times 10^{-5}$; (*b*) Gr = 500, $\psi = -5, -10, -15, -20, -26, -29 \times 10^{-5}$; (*c*) Gr = 2000, $\psi = -3, -6, -9, -12, -15, -17 \times 10^{-5}$; (*d*) Gr = 3000, $\psi = -3, -6, -6.5, -9, -11, -14 \times 10^{-5}$

Table 2 Critical values at the onset of the secondary flow compared with available experimental and calculated results

Pr	Gr_c	$Ra_c \times 10^{-5}$	γ_c	authors
50	12000–13000	6.00–6.50	8.47	Present study
	12000	6.00	8.27	Wakitani (1994)
125	4400–4500	5.50–5.63	8.15	Present study
	4400	5.50	8.09	Wakitani (1994)
158	3300–3500	5.21–5.53	8.10	Present study
405	1200–1300	4.86–5.27	8.04	Present study
720	700–720	5.04–5.18	7.98	Present study
1000	450–500	4.50–5.00	7.81	Present study
	400	4.00	7.60	Lee and Korpela (1983)
2000	200–220	4.00–4.40	7.69	Present study

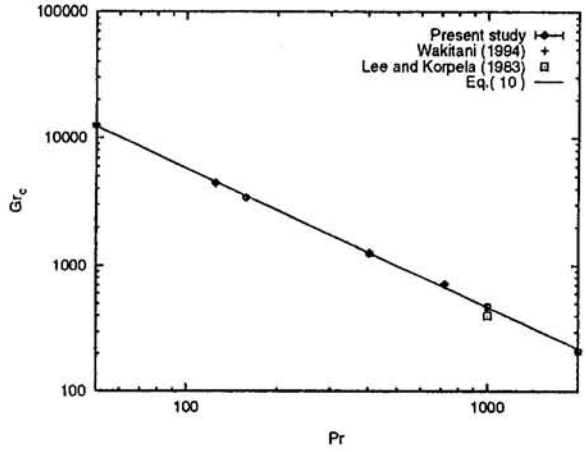

Fig. 8 Variation of the critical Grashof number with the Prandtl number

The nondimensional temperature gradient, S, evaluated near the center of the slot is essentially constant (=0.49) throughout the Prandtl number range. This compares favorably with the value of 0.468 obtained experimentally by Wakitani (1994). The critical stratification factor, γ_c, however, shows a slight decreasing trend with increasing Pr from 8.47 to 7.69; see Table 2. These values are 34 to 22 percent greater than the value predicted by Daniels (1989) of 6.3.

The variation of Gr_c with Pr is shown in Fig. 8, together with the results of Wakitani (1994) and Lee and Korpela (1983). The computed results suggest the following correlation:

$$Gr_c = 8.835 \times 10^5 \, Pr^{-1.092} \tag{10}$$

which is also shown in the same figure. From the definition of γ and with a constant S, $Gr_c = 8A\gamma^4 Pr^{-1}$. The slight decrease of γ with Pr as shown in Table 2 resulted in the $Pr^{-1.092}$ dependence of the critical Grashof number.

4.3 Heat Transfer Results. The local heat transfer rate along any vertical plane in the cavity is given by

$$Nu_L = -\frac{\partial \theta}{\partial x} + Pr\ Gr\ u\ \theta \tag{11}$$

The average heat transfer rate is calculated by Simpson's rule. A typical local heat transfer rate along the hot wall is shown in Fig. 9, for Pr = 125. The maximum value occurs near the bottom of the cavity, where the boundary layer flow begins. At Gr = 4500, the local Nusselt number still shows a smooth

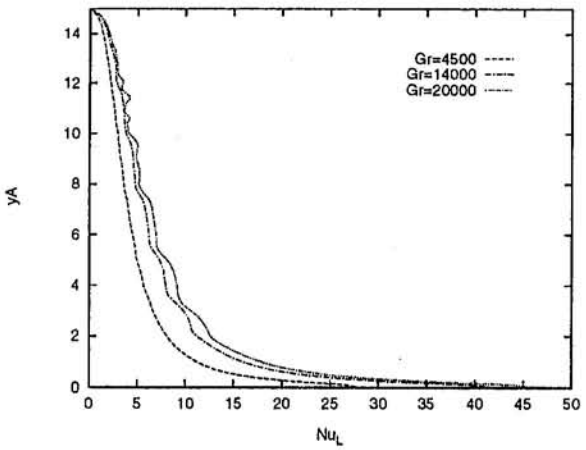

Fig. 9 The local Nusselt number along the hot wall at Pr = 125

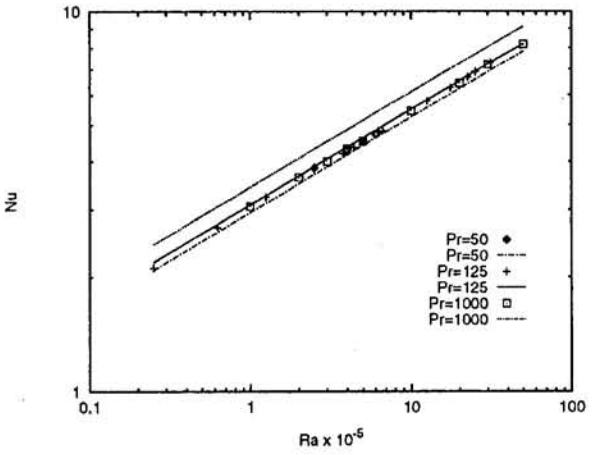

Fig. 10 Variation of the average Nusselt number with the Rayleigh number: Points are numerical results; lines are results of experimental correlations given by Seki et al. (1978)

variation although the instability has already occurred. As the Grashof number is increased to 14,000, modulations in Nu_L coinciding with the locations of the six cells (Fig. 4(c)) are noted. When the tertiary flow is well developed, the local Nusselt number does not exhibit any different features at the tertiary zone. This suggests that the small tertiary cells, confined in the center part as shown in Fig. 4(d), are very weak compared with the secondary cells. Its influence on the flow cannot penetrate the vigorous boundary layer flow. At Gr = 20,000, several small disturbances in Nu_L are found at the height approximately $yA = 11-12$ along the left wall. These are the result of the disturbances in the flow at that location reflected both in the streamlines, Fig. 4(d), and isotherms, Fig. 5(d). Similar disturbances at the lower right cold wall, however, have no effect on the heat transfer from the hot wall. It is expected that the disturbance will become stronger and destroy the secondary cells at the ends as the Grashof number is further increased.

The average heat transfer rate for Pr = 50, 125, and 1000 is shown in Fig. 10. All the calculated results are located on the line

$$\mathrm{Nu} = 0.1631\ \mathrm{Ra}^{0.2537} \qquad (12)$$

Our results show that the effect of the Prandtl number on the heat transfer rate can be neglected if the fluid has constant thermophysical properties. The results are slightly different from the experimental correlations obtained by Seki et al. (1978), which are also shown in Fig. 10 in chain-dot (Pr = 50), solid (Pr = 125), and dotted (Pr = 1000) lines for comparison. As we can see, the experimental results for Pr = 50 and 125 bracket the present numerical results. For Pr = 1000, the experimental results are quite a bit higher. This discrepancy can be attributed to the variable thermal physical properties of the fluids used in the experiments. Although the change in the flow pattern, from unicellular to multicellular flow, significantly influences the local heat transfer rate along the hot wall, it does not show any noticeable effect on the average heat transfer results for the Rayleigh number range studied. Similar results were obtained experimentally by Seki et al.

5 Conclusions

Instability of convection and heat transfer of high Prandtl number fluids in a vertical slot with $A = 15$ has been studied. The range of Prandtl numbers studied varies from 50 to 2000. The critical Grashof number and wavelength, and the subsequent development of the flow field at supercritical states, show good agreement with the available experimental results of Wakitani (1994). Along the vertical centerline the vorticity distribution is found to be a very sensitive indicator of onset of multicellular flow. At the onset of instability the nondimensional temperature gradient is approximately constant at 0.49 in all of the cases studied. The critical stratification parameter, for the cases considered, is found to be between 22 and 34 percent greater than that predicted by Daniels (1989). The critical Grashof number varies almost inversely with the Prandtl number. Consequently, the critical Rayleigh number decreases only slightly with the Prandtl number. Bergholz's (1978) predictions for the critical Grashof number, based on linear stability theory, are approximately 50 percent lower than the present results. The onset of the tertiary cellular flow is first observed in the center of the slot, and is well developed when the Rayleigh number reaches 3×10^6. Although the multicellular flow significantly affects the local heat transfer rate, it has little influence on the average value. Furthermore, the effect of the Prandtl number on the average heat transfer rate is negligible when the thermal physical properties are invariant.

Acknowledgments

The financial support of the NASA Microgravity Science and Application Division through grant NAG 3-1386 is gratefully acknowledged.

References

Arakawa, A., 1966, "Computational Design for Long-Term Numerical Integration of the Equations of Fluid Motion: Two Dimensional Incompressible Flow, Part I," *Journal of Computational Physics,* Vol. 1, pp. 119–143.

Batchelor, G. K., 1954, "Heat Transfer by Free Convection Across a Closed Cavity Between Vertical Boundaries at Different Temperatures," *Quarterly Journal of Applied Mathematics,* Vol. 12, pp. 209–233.

Bergholz, R. F., 1978, "Instability of Steady Natural Convection in a Vertical Fluid Layer," *Journal of Fluid Mechanics,* Vol. 84, pp. 743–768.

Daniels, P. G., 1985, "Transition to the Convective Regime in a Vertical Slot," *International Journal of Heat and Mass Transfer,* Vol. 28, pp. 2071–2077.

Daniels, P. G., 1987, "Convection in a Vertical Slot," *Journal of Fluid Mechanics,* Vol. 176, pp. 419–441.

Daniels, P. G., 1989, "Stationary Instability of the Convective Flow Between Differentially Heated Vertical Planes," *Journal of Fluid Mechanics,* Vol. 203, pp. 525–540.

de Vahl Davis, G., and Mallinson, G. D., 1975, "A Note on Natural Convection in a Vertical Slot," *Journal of Fluid Mechanics,* Vol. 72, pp. 87–93.

DuFort, E. C., and Frankel, S. P., 1953, "Stability Conditions in the Numerical Treatment of Parabolic Differential Equations," *Math. Tables and Aids to Computation,* Vol. 7, pp. 135–152.

Elder, J. W., 1965, "Laminar Free Convection in a Vertical Slot," *Journal of Fluid Mechanics,* Vol. 23, pp. 77–98.

Gill, A. E., 1966, "The Boundary-Layer Regime for Convection in a Rectangular Cavity," *Journal of Fluid Mechanics,* Vol. 26, pp. 515–536.

Hart, J. E., 1971, "Stability of the Flow in a Differentially Heated Box," *Journal of Fluid Mechanics,* Vol. 47, pp. 547–576.

Lauriat, G., and Desrayaud, G., 1985, "Natural Convection in Air-Filled Cavities of High Aspect Ratios: Discrepancies Between Experimental and Theoretical Results," ASME Paper No. 85-HT-37.

Le Quéré, P., 1990, "A Note on Multiple and Unsteady Solutions in Two-Dimensional Convection in a Tall Cavity," ASME JOURNAL OF HEAT TRANSFER, Vol. 112, pp. 965–974.

Lee, Y., and Korpela, A., 1983, "Multicellular Natural Convection in a Vertical Slot," *Journal of Fluid Mechanics,* Vol. 126, pp. 91–121.

Patankar, S. V., 1981, "A Calculation Procedure for Two-Dimensional Elliptic Situations," *Numerical Heat Transfer,* Vol. 4, pp. 409–425.

Roache, P. J., 1982, *Computational Fluid Dynamics,* Hermosa, Albuquerque, NM.

Seki, N., Fukusako, S., and Inaba, H., 1978, "Visual Observation of Natural Convective Flows in a Narrow Vertical Cavity," *Journal of Fluid Mechanics,* Vol. 84, pp. 695–704.

Van Doormaal, J. P., and Raithby, G. D., 1984, "Enhancement of the SIMPLE Method for Predicting Incompressible Fluid Flows," *Numerical Heat Transfer,* Vol. 7, pp. 147–163.

Vest, C. M., and Arpaci, V. S., 1969, "Stability of Natural Convection in a Vertical Slot," *Journal of Fluid Mechanics,* Vol. 36, pp. 1–15.

Wakitani, S., 1994, "Experiments on Convective Instability of Large Prandtl Number Fluids in a Vertical Slot," ASME JOURNAL OF HEAT TRANSFER, Vol. 116, pp. 120–126.

Steady Rayleigh–Bénard Convection in a Two-Layer System of Immiscible Liquids

A. Prakash[1]

J. N. Koster

University of Colorado,
Department of Aerospace
Engineering Sciences,
Boulder, CO 80309-0429

Two-dimensional thermal convection in a system of two immiscible liquids heated from below is studied experimentally and numerically. Convection in the two-layer system is characterized by two distinct coupling modes between the layers. They are mechanical coupling and thermal coupling. These two coupling modes are visualized experimentally and found to be in reasonable agreement with numerical simulations. When buoyancy forces in both layers are of similar strength, thermal coupling is preferred. The mechanical coupling mode dominates when the buoyancy forces are very different in both layers.

Introduction

Thermal convection is studied in a system of two immiscible liquid layers heated from below. Layered liquid systems are relevant for technological applications such as liquid encapsulated crystal growth techniques (Barocela and Jalilevand, 1987). They are also considered a model for convection in the Earth's mantle, where a seismic discontinuity resembles the interface of a fluid–fluid system (Richter and Johnson, 1974).

Zeren and Reynolds (1972) considered the linear stability of a two-layer system in an infinite horizontal domain heated from below. They include the influence of thermocapillary stresses at the interface, and assume that onset of convection occurs through a monotonic instability. Some discrepancies between the theoretical prediction and the experimentally detected onset of convection are reported. The discrepancy was attributed to interfacial contamination.

A Hopf bifurcation, or an oscillatory instability at onset, in the limit of negligible distortion of the interface was identified by Gershuni and Zhukhovitskii (1982). Renardy and Joseph (1985) provide a theoretical proof demonstrating that onset of convection can occur through an oscillatory instability if deformation of the interface is considered. Renardy and Joseph also point out that traveling waves on the interface of immiscible liquids may be relevant.

Honda (1982) performed marginal stability and finite amplitude analyses of layered convection. His analysis identifies three distinct modes of coupling between the liquid layers: thermal coupling, mechanical coupling, and a dragging mode of mechanical coupling. Thermal coupling is identified by corotating rolls, or same-sign vorticity, on both sides of the interface, i.e., a shear flow develops in a thin region along the interface. Mechanical (also termed viscous) coupling is identified by counterrotating rolls, or opposite sign vorticity, on the two sides of the interface, i.e., the local velocity vectors on either side of the interface point in the same direction. In the dragging mode, the unstable convecting layer drags a small region of fluid in the adjacent subcritical passive layer, where the flow is considered essentially stagnant. Honda concludes that when the difference between the upper and lower fluid properties is very small, thermal coupling is the preferred state. If one of the fluid layers is more unstable than the other, mechanical coupling or the dragging mode is the preferred state. Only mechanical coupling is observed in their finite amplitude calculations. They also conclude that heat transport is more efficient in thermal coupling mode than in mechanical coupling mode.

Cserepes and Rabinowicz (1985/86) performed a nonlinear finite amplitude analysis of bilayer convection in a system with a free upper surface. They conclude that mechanical coupling prevails when the viscosity ratio is of order one, and thermal coupling becomes predominant when the viscosity ratio is larger than 100. Although this appears to contradict Honda's conclusions, their results confirm that when driving forces for convection in the two layers are very different, the flow structure is dominated by mechanical coupling. This conclusion is in agreement with Honda (1982).

In an experimental study, Nataf et al. (1988) addressed the question: What is responsible for thermal coupling in layered convection? They observe a thermally coupled state of superposed cells. The observations contradict numerical simulations, which support a mechanically coupled state. The discrepancy is tentatively explained by "interfacial longitudinal viscosity" attributed to contamination of the interface. Although the interfacial tension at a liquid/liquid interface depends on the concentration of contaminants (Levich, 1962), there is no conclusive acceptance of *how* coupling between the layers is affected by such contaminants.

Rasenat et al. (1989) performed a parametric investigation of two-layer systems. In addition to the oscillatory instability due to perturbations of the interface, an oscillatory instability mechanism with cyclic switching between thermal and mechanical coupling was identified. The onset of oscillations is described as an intermediate state between the states of mechanical and thermal coupling. These parametric studies lead to the conclusion that thermally coupled or oscillatory motions can be expected only if the buoyancy forces, as measured by the Rayleigh numbers, in the two layers are not very different. Otherwise, convective flow in the subcritical layer will be mechanically driven by convection in the other layer, at least close to the onset of convection. This is also in support of Honda's (1982) findings. Rasenat et al. (1989) also performed experiments in two-layer systems using a shadowgraph technique. They observe mechanical coupling at onset, which eventually transitions to thermal coupling. The experiments are reported to be in good agreement with linear theory. They were unable to observe oscillations at the onset of convection.

The complete parameter space defining a two-layer system is very large. But, based on the above-cited investigations, it can be conjectured that the coupling mechanism depends on the viscosity ratio, and on the ratio of driving forces between the two liquids. In the following work the viscosity ratio is

[1] Currently at NASDA, Space Utilization Dept., Tsukuba City, Japan.

Contributed by the Heat Transfer Division for publication in the JOURNAL OF HEAT TRANSFER. Manuscript received by the Heat Transfer Division June 1995; revision received November 1995. Keywords: Enclosure Flows, Flow Instability, Flow Visualization. Associate Technical Editor: P. G. Simpkins.

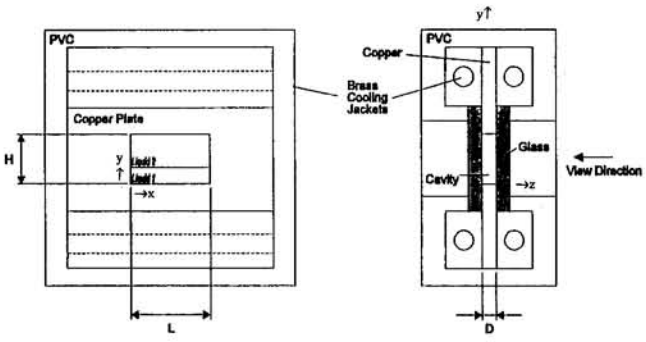

Fig. 1 Schematic of the test cell

prescribed, and we focus on the driving buoyancy force ratio. We present detailed experimental observations of the temperature field resulting from thermal convection in a two-layer system confined in a slender rectangular cavity heated from below. The observations are compared with two-dimensional numerical simulations.

Experimental Setup

The test cell configuration is shown in Fig. 1. The fluid test volume is a rectangular gap-type cavity with width (L) of 68 mm, height (H) of 56 mm, and depth (D) of 8 mm. The horizontal (top/bottom) and vertical side walls of the test volume are copper. Copper, with a thermal conductivity three orders of magnitude higher than both fluids, provides isothermal conditions at the top and bottom boundaries. It forces a linear temperature profile and imposes a perfectly conducting boundary condition along the vertical side walls. For flow visualization, the front and back walls are window glass. The thermal conductivity of "window" glass is 1.1 W/m/K, i.e., an order of magnitude larger than both liquids. Brass water jackets soldered to the horizontal walls provide isothermal conditions at the top and bottom horizontal boundaries, and generate the vertical temperature gradient. The test cell is thermally insulated with a pvc frame. The glass windows are covered with foam insulation, which is removed for visualization only.

An idealized two-dimensional flow in an area $L \times H$ (x–y coordinate) typically extends infinitely deep in the third direction (z). Such an idealization cannot be achieved experimentally, particularly in Rayleigh–Bénard convection. In a rectangular cavity with a large extension in the z direction, Rayleigh–Bénard convection takes the form of rolls, whose axes are aligned parallel to the shorter side walls of the cavity (Davis, 1967). A two-dimensional flow can be approximated experimentally by flow in a narrow gap between parallel plates (Koster and Müller, 1982). The no-slip conditions at the front/back glass surfaces impose a variation in the velocity and temperature fields along the z direction. This leads to a velocity profile along the z direction that is similar to a Poiseuille flow profile. A narrow vertical slot flow is considered the closest, although imperfect, experimental approach to a two-dimensional flow.

Temperature control in the test cell is achieved via constant temperature bath circulators. The circulators provide bath temperature control of ±0.05°C, and can be programmed to sustain temperature ramping at an electronic controller rate equivalent to 0.01°C/min. Temperature stability in the test cell is further improved by passing the coolant through insulated brass blocks ("thermal buffers") before entering the test cell. Temperature in the top and bottom copper blocks, and in the fluid, is measured with K-type thermocouples. Thermocouples in each of the copper blocks are placed within 2 mm of the copper–fluid interface. These thermocouples provide the measured ΔT across the test cell. An accuracy of ±0.05°C in the temperature difference measurement is achieved with good confidence.

Real-time holographic interferometry is used to obtain the temperature field. Details of a typical real-time holographic interferometry setup may be found from Koster (1983). Interferograms visualize the integral temperature field of the light path, and lines of constant color represent isotherms. Rising hot fluid shifts the isotherms upward while descending cold fluid shifts the isotherms downward. Interpretation of interferograms is described in detail by Farhadieh and Tankin (1974).

Experiments are performed in a two-layer system composed of 100 cSt silicone oil over ethylene glycol. Thermophysical properties for these liquids, and thermophysical property ratios for the combination are shown in Tables 1 and 2, respectively. This liquid combination is considered immiscible, as no diffusion in the form of Schlieren could be detected under monochromatic laser light in preliminary experiments performed in a test cell with a light integration length of 2.5 cm.

Temperature of the upper boundary is ramped electronically at a rate of −0.01°C/min while the bottom boundary is ramped at +0.01°C/min. The ramps are halted at specific temperature differences. At these ΔT plateaus, the liquid layers are allowed to reach thermal equilibrium over a time period that is larger than the thermal diffusion times for the two liquids. After stabilization, the isotherms are photographed and temperature data is acquired. The ramping process is then restarted to achieve a new ΔT plateau.

Numerical Simulation

Flow in the two-layer system is numerically simulated using the commercial finite-element computer code FIDAP. Simulation is restricted to a two-dimensional model. The governing Navier–Stokes equations and the energy equation are discretized using the finite element method. The pressure formulation is based on the penalty approach. The discretized system of nonlinear equations is integrated in time using a second-order implicit scheme, with a predictor step using the Adams–Bash-

Nomenclature

Bd_d = dynamic Bond number = $\rho\beta g h^2/\gamma$
C_p = specific heat
D = cavity horizontal depth
g = gravitational acceleration
h = individual layer height
H = cavity height
H_1 = layer aspect ratio = L/h
H_2 = layer aspect ratio = D/h
k = unit vector = k
L = cavity width
p = pressure
P = ratio of buoyancy driving forces
Pr = Prandtl number
Ra = Rayleigh number
t = time
T = temperature
$\mathbf{u}$ = velocity vector
β = thermal expansion
γ = interface tension gradient (with respect to temperature)
θ = nondimensional temperature
κ = thermal diffusivity
λ = thermal conductivity
μ = dynamic viscosity
ν = kinematic viscosity
ρ = density
τ = diffusion time = H^2/κ

Superscripts and Subscripts

b = bottom
B = ratio of properties = b/b (equals unity)
c = critical value
i = layer numbering (t/b or T/B)
t = top
T = ratio of properties = t/b

Table 1 Fluid properties

Fluids	Density ρ (g/cm^3)	Kinematic viscosity ν (cm^2/s)	Thermal conductivity λ (W/cm K)	Specific heat C_p (J/g-K)	Thermal diffusivity κ (cm^2/s)	Coeff. of Expansion β (1/K)	Surface tension σ (dy/cm)	Surface tension gradient γ (dy/cm/K)	Prandtl number Pr
Ethylene Glycol	1.11	0.154	$2.58\ 10^{-3}$	2.39	$9.67\ 10^{-4}$	$6.2\ 10^{-4}$	50.2	-0.089	159
Silicone oil SIO 100 cSt	0.964	1.00	$1.55\ 10^{-3}$	1.47	$1.09\ 10^{-3}$	$9.3\ 10^{-4}$	20.9	-0.068	917

forth formula, followed by a corrector step utilizing the trapezoid rule. The time increment between integration steps is variable. The variation is determined by controlling the local time truncation error. At each time step, the nonlinear system of equations is solved using a quasi-Newton scheme. For a complete description of the discretization procedure and the solution methods available with FIDAP, we refer to the FIDAP users' manual (1993).

The test cavity is discretized with a graded mesh of 51×71. This mesh was found to be optimal for convergence, constancy of maximum streamfunctions, and the limited computer resources. The pressure penalty parameter is set to 1.0×10^{-9}. At each time step, the nonlinear system is iteratively solved until the two convergence criteria for velocity norm and residue norm are satisfied. For details on these convergence criteria, we refer again to the FIDAP users' manual (1993). The convergence criteria for the residue and velocity norm are set to 1.0×10^{-5} and 1.0×10^{-5}, respectively. The solution procedure is initiated by first solving the system with a steady solution scheme, where the time variation term is neglected. This elementary solution is performed to obtain the conductive temperature profile in the fluids at a low driving temperature difference. The time integration is started with the steady solution as the initial condition. The initial time step is selected to be 2.0×10^{-5}. The time step is increased or decreased by the truncation error control as the solution progresses. The integration is performed for a minimum of 200 steps, or until a steady state is achieved. A steady state is identified when the variation of all norms between successive time steps is less than 1.0×10^{-3}.

The governing equations are solved in nondimensional form. The lower layer thermophysical properties are used to nondimensionalize the system. The height H of the cavity is used as the length scale, and the thermal diffusion time, τ, for the *lower* layer fluid is used as the time scale. Combining these two scales provides the velocity scale. The total temperature drop ΔT between the top and bottom boundaries is used as the temperature scale. Using these scales, the governing equations in each layer become:

$$\nabla \cdot \mathbf{u} = 0 \tag{1}$$

$$\rho^i C_p^i \left[\frac{\partial \theta}{\partial t} + \mathbf{u} \cdot \nabla\, \theta\right] = \lambda^i \nabla^2 \theta \tag{2}$$

$$\rho^i \left[\frac{\partial \mathbf{u}}{\partial t} + \mathbf{u} \cdot \nabla\, \mathbf{u}\right] = -\nabla p + \mu^i\, \mathrm{Pr} \nabla^2 \mathbf{u} + \rho^i \beta^i\, \mathrm{Ra}\, \mathrm{Pr} \theta\, \hat{k} \tag{3}$$

The two nondimensional numbers Ra and Pr refer to the Rayleigh number and the Prandtl number, respectively. These are defined in terms of the bottom layer thermophysical properties as follows:

$$\mathrm{Ra} = \frac{g \beta_b H^3 \Delta T}{\nu_b \kappa_b}; \quad \mathrm{Pr} = \frac{\nu_b}{\kappa_b} \tag{4}$$

Flow boundary conditions along the rigid wall are the no-slip conditions. The temperatures along the isothermal top and bottom walls are prescribed as $T_{\mathrm{top}} = -0.5$ and $T_{\mathrm{bot}} = 0.5$. The vertical side walls connecting the top and bottom boundaries are subjected to a linear temperature profile. At the interface, normal and shear stress balance conditions, along with the kinematic condition are prescribed (Prakash and Koster, 1994). Under the assumption of a nondeformable interface, these conditions reduce to a balance of shear stress. Continuity of velocity and temperature, and heat flux balance are also imposed.

To improve the convergence rate of the calculations, the Prandtl number for the lower layer is set to 50. The ratio of Prandtl numbers for the liquid combination is maintained. Although the lower Prandtl number may influence the critical Rayleigh number at onset of convection, the flow pattern and the temperature field are not expected to be significantly affected.

Because of the low interfacial tension gradient (with respect to temperature) between the selected liquids, and the relatively large layer heights used in the experiments, buoyancy-driven convection dominates over thermocapillary convection. The exact variation of the interfacial tension with temperature for this liquid combination is unknown. Based on the surface tension gradients for the two liquids, the order of magnitude of the interface tension gradient can be estimated by Antonow's rule to be of order 10^{-1} dynes/cm/K. This translates into a dynamic Bond number $\mathrm{Bd}_d \sim O(100)$ for each layer. Therefore, thermocapillary effects are considered to be negligible.

Linear Stability Theory

Before proceeding to the results, we review some pertinent results from linear stability theory. Our objective is to ascertain the influence of cavity geometry on the thermal stability of individual layers, particularly the influence of the narrow gap on onset of convection. For our investigation, the side walls can be considered to be perfectly conductive. This is justified by the high thermal conductivity of copper and glass side walls as compared to the thermal conductivities of the two fluids. We disregard the interface boundary in the two-layer system, and proceed instead with a rigid cavity model. This approximation will not alter conclusions regarding the influence of cavity geometry on the stability limit.

Convection in three-dimensional boxes with perfectly conductive side walls has been analyzed by Davis (1967), Catton (1970, 1972), and Kirchartz and Oertel (1988). They utilize the Galerkin method to determine the critical Rayleigh numbers for onset of convection. In selecting the trial functions for the Galerkin method, Davis and Catton have noted that any three-dimensional motion can be generated by superposing two-dimensional motions that individually satisfy continuity, if sufficient terms are included in the expansion. We utilize Catton's (1970) method to determine critical Rayleigh numbers for the geometries relevant to our experiments. To characterize the cavity, two aspect ratios are defined: ($H_1 = L/h$ and $H_2 = D/h$), where h is the layer height. To confirm our implementation of Catton's method, we have compared our results with those reported by Kirchartz and Oertel (1988), and found them to be in agreement. As noted by Kirchartz and Oertel, the critical values are somewhat smaller than the reported values of Catton or Davis. This is attributed to the higher number of trial functions used in the analysis. To interpret the numerical simulations

Table 2 Ratio of properties

Ratios	Density	Kinematic viscosity	Thermal conductivity	Specific heat	Thermal diffusivity	Coeff. of Expansion
SIO 100 cSt / Eth. Glycol	0.865	6.493	0.601	0.616	1.127	1.500

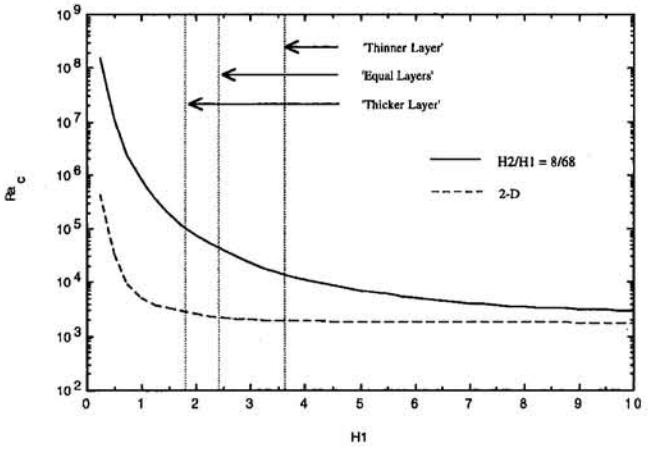

Fig. 2 Critical Rayleigh number versus cavity aspect ratio

we also considered the case of a two-dimensional cavity in the $x-y$ plane by only including trial functions corresponding to rolls with their axes aligned to the z direction, and by disregarding the z variation in the trial functions for velocity and temperature.

In Fig. 2, the calculated critical Rayleigh numbers for both the three-dimensional and the two-dimensional cases are plotted as a function of the aspect ratio H_1. The three-dimensional "single-layer cavity" cases of interest are represented by $H_2/H_1 = D/L$, a constant for the cavity.

Results

Three configurations of the silicone oil 100 cSt/ethylene glycol system are considered. These are: (i) the case where the lower layer is twice the height of the upper layer, (ii) the case with equal layer heights, and (iii) the case where the upper layer is twice the height of the lower layer. The dynamic viscosity ratio for the liquid system is $\mu^T = 5.6$.

To interpret experimental results, we introduce the parameter P, the ratio of individual layer Rayleigh numbers, as a measure of the relative strength of the buoyancy force in each layer:

$$\mathrm{Ra}_i = \frac{g\beta^i h_i^3 \Delta T_i}{\nu_i \kappa_i}; \quad i = b \text{ or } t \tag{5}$$

$$P = \frac{\mathrm{Ra}_t}{\mathrm{Ra}_b} = \frac{\beta^T (h^T)^4}{\nu^T \kappa^T \lambda^T} \tag{6}$$

The capitalized superscripts refer to the ratio of a thermophysical property with respect to the bottom layer property, i.e., $\beta^T = \beta_t/\beta_b$. The ratio of individual layer temperature differences is calculated from the conductive temperature profile:

$$\frac{\Delta T_t}{\Delta T_b} = \frac{h_t}{\lambda_t}\frac{\lambda_b}{h_b} = \frac{h^T}{\lambda^T} \tag{7}$$

These individual layer temperature differences are valid until onset of convection in any one of the layers. Beyond the onset of convection, the exact temperature difference across each layer is difficult to assess, and the interface temperature is no longer uniform. The ratio P is therefore independent of the overall vertical temperature difference.

The parameter P provides a measure of the relative strength of buoyancy forces in the two layers, as long as the critical Rayleigh numbers for the two layers are the same. This is the case for infinite layers with rigid top and bottom boundaries. However, for confined layers the critical Rayleigh numbers for the two layers are not the same. Therefore, to include the influence of the cavity geometry, a modified parameter $\bar{P}$ is introduced as follows:

$$\bar{P} = \frac{P}{(\mathrm{Ra}_t/\mathrm{Ra}_b)_c} \tag{8}$$

where P has been normalized by the ratio of individual layer critical Rayleigh numbers. In the case of equal layer heights, both parameters P and $\bar{P}$ are the same. The modified parameter $\bar{P}$ is also independent of the applied temperature difference. It is a function of the ratio of the layer heights, the ratios of thermophysical properties, and the cavity geometry. It should be noted that the ratio top/bottom in these definitions is quite arbitrary; the inverse ratio would be equally valid.

From the three configurations considered in the experiments, we obtain three single-layer cavity geometries. Parameters P and $\bar{P}$ for these geometries are tabulated in Table 3. The parameter $\bar{P}$ for the two-dimensional case, labeled $\bar{P}_{2\text{-D}}$, is also tabulated in Table 3. The two parameters $\bar{P}$ and $\bar{P}_{2\text{-D}}$ do not have the same value, except in the special case of equal layer heights. This is due to the fact that the ratio of individual layer critical Rayleigh numbers for the two-dimensional case is very different from that for the three-dimensional cavity case. As seen from Fig. 2, for the cavity case, the critical Rayleigh number for the "thinner layer" ($H_1 = 3.6$) is $\mathrm{Ra}_c = 1.4 \times 10^4$, and for the "thicker layer" ($H_1 = 1.8$) is $\mathrm{Ra}_c = 9.9 \times 10^4$, which is about seven times larger. For the two-dimensional case, the corresponding critical Rayleigh number values are $\mathrm{Ra}_c = 1.9 \times 10^3$ and $\mathrm{Ra}_c = 2.8 \times 10^3$, respectively; in other words the thicker layer Ra_c is about 1.5 times larger. In the case of equal layer heights ($H_1 = 2.4$), critical Rayleigh numbers for both layers are the same: for the cavity case, $\mathrm{Ra}_c = 4.1 \times 10^4$, and for the two-dimensional case, $\mathrm{Ra}_c = 2.2 \times 10^3$.

Defining an overall Rayleigh number for the entire two-layer system always leads to some ambiguity. The definition must be based on one or the other layer's thermophysical properties. Also, such a definition does not clearly show which of the layers will be more unstable. Therefore, the following results are presented in terms of the individual layer Rayleigh numbers normalized by their respective critical values, i.e., $(\mathrm{Ra}/\mathrm{Ra}_c)_b$ and $(\mathrm{Ra}/\mathrm{Ra}_c)_t$. As pointed out by Cserepes et al., these values provide "a rough measure of the instability of the two layers as if there were no coupling between them." It is again emphasized that these ratios are not independent. They are related through the parameter $\bar{P}$.

(i) Un-equal Layer Heights—Thicker Lower Layer. In this case, the lower layer height is twice that of the upper layer. The driving buoyancy force is much larger in the lower layer than in the upper layer, as indicated by the parameters $P = 0.02$ and $\bar{P} = 0.16$. Accordingly, convection develops first in the lower layer. This state is illustrated in the interferogram at $(\mathrm{Ra}/\mathrm{Ra}_c)_b = 2.0$, shown in Fig. 3$(a)$. The flow develops in the form of two counterrotating cells with upflow along the center. The upper layer remains in a passive conductive state as inferred from the nearly horizontal isotherms. Near the side walls, the equal spacing between isotherms indicates a linear temperature profile in the vertical side walls. Numerically calculated streamline and temperature contour plots at $(\mathrm{Ra}/\mathrm{Ra}_c)_b = 2.0$ are also shown in Fig. 3(a). Qualitatively the simulation reproduces a flow pattern that is very similar to the experimental

Table 3 Ratio of individual layer buoyancy forces as a function of layer height ratio

h_t/h_b	P	$\bar{P}$	$\bar{P}_{2\text{-D}}$	Coupling mode
0.5	0.02	0.16	0.03	mechanical
1.0	0.34	0.34	0.34	thermal ⇒ mechanical
2.0	5.5	0.75	3.77	thermal

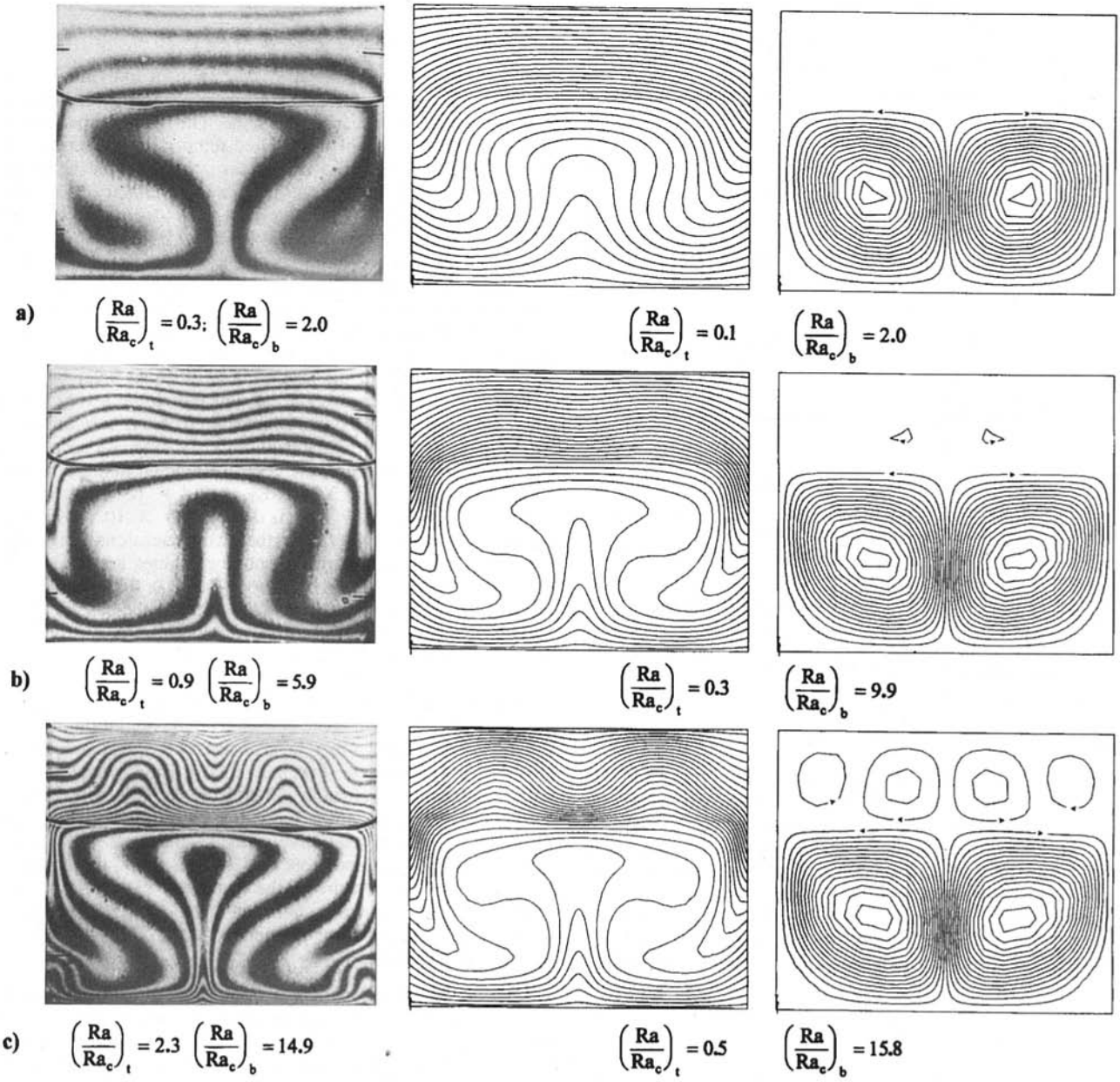

Fig. 3 Silicone oil 100 cSt over ethylene glycol: unequal layer heights—thicker lower layer: interferograms and numerical simulations (isotherms and streamfunction)

interferogram. The streamline plot shows the pertinent flow pattern: a double roll in the lower layer, and no flow in the upper layer.

An interferogram at a larger $(Ra/Ra_c)_b = 5.9$ is shown in Fig. 3(b). Convection in the lower layer has become stronger, though the flow retains its two-roll structure with upflow along the center. In the upper layer, weak convection has been initiated. In the numerical simulation, an increase in the Rayleigh number also leads to intensification of lower layer convection, and a destabilization of the upper layer. Although deformation of the isotherms is observed in the simulations at a Rayleigh number close to the experimental value given above, flow in the upper layer is very weak. At $(Ra/Ra_c)_b = 9.9$, recirculations in the upper layer are resolved, as can be seen in Fig. 3(b). The downflow along the center in the upper layer is aligned with the upflow in the lower layer, indicating mechanical coupling across the interface. This coupling mode suggests that flow in the upper layer is entrained by the lower layer flow, and that the stability limit of the upper layer has been exceeded. A further increase in the Rayleigh number leads to a significantly stronger flow structure (Fig. 3(c)), both in the experiments at $(Ra/Ra_c)_b = 14.9$, and in the simulations at $(Ra/Ra_c)_b = 15.8$. The upper layer develops a four-roll flow pattern, with stronger center rolls and weaker corner rolls. Thin interfacial shear rolls develop near the side walls in the upper layer. But these rolls can be visualized in the simulations only when the number of contour lines is increased substantially.

(*ii*) **Equal layer heights.** In this case, buoyancy driving forces in the two layers are comparable: $P = \bar{P} = 0.34$. Convection is initiated almost simultaneously in both layers. As seen in Fig. 4(a), convection in the bottom glycol layer is well established in the form of two counterrotating cells with upflow along the center $(Ra/Ra_c)_b = 2.9$. The upper oil layer exhibits weak convection, also in the form of two counterrotating cells with upflow along the center. This flow pattern, with aligned upflows in the two layers, is regarded a "thermally coupled" state. Streamline and isotherm contours from the numerical sim-

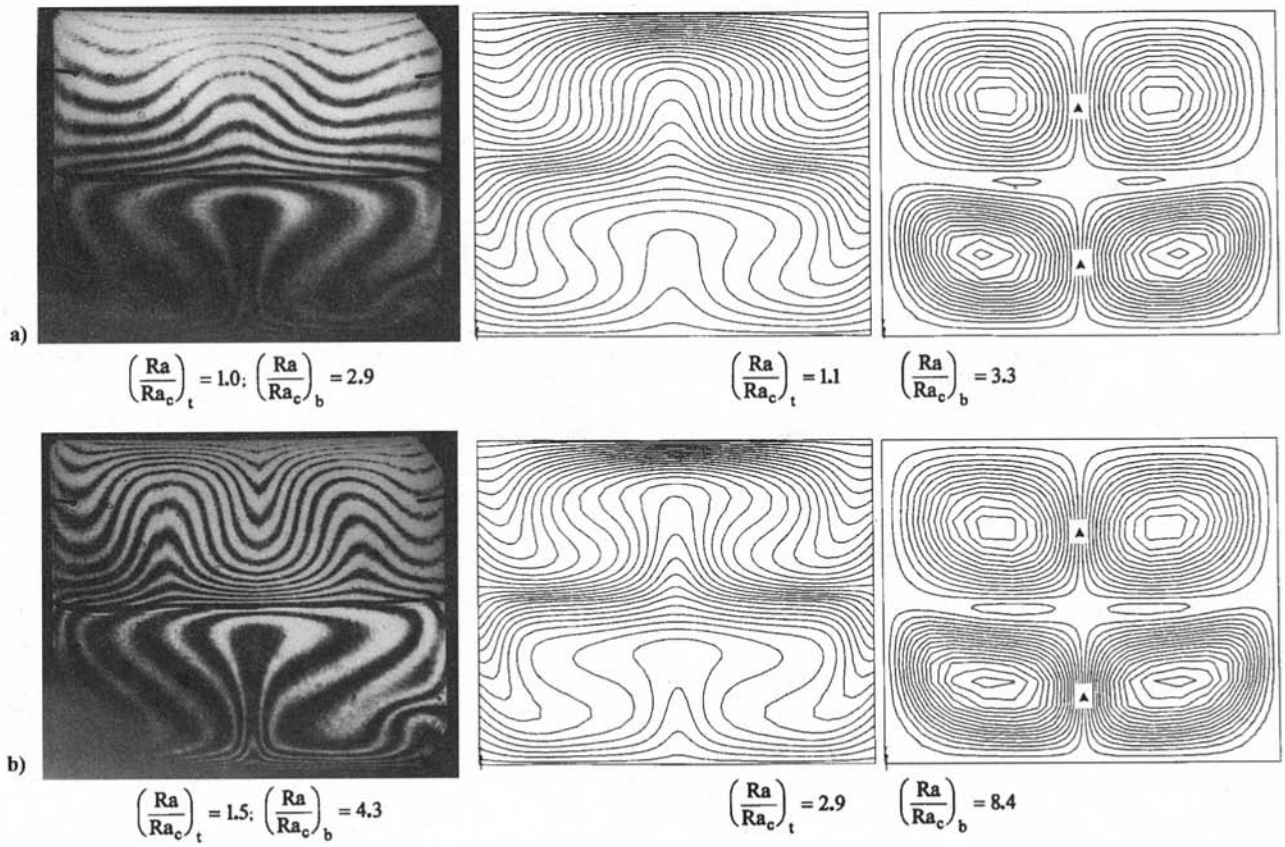

Fig. 4 Silicone oil 100 cSt over ethylene glycol: equal layer heights: interferograms and numerical simulations (isotherms and streamfunction)

ulation at $(Ra/Ra_c)_b = 3.3$ confirm the thermal coupling. To satisfy velocity continuity along the interface, very thin counterrotating rolls may have developed adjacent to the interface, or the interface may be immobile. These interfacial rolls will be too small to be detected experimentally. The thermal coupling mode will act across these interfacial cells, which serve to satisfy the continuity of velocity across the interface.

The interferogram in Fig. 4(*b*) $(Ra/Ra_c)_b = 4.3$, shows that convection in the lower layer has become much more vigorous as indicated by the higher number of fringes, and their changed deformation. Flow in the lower layer retains its pattern of two rolls with upflow along the center. Flow in the upper layer has changed to a four-roll pattern. The central downflow is now mechanically coupled to the lower layer. A numerical calculation at $(Ra/Ra_c)_b = 8.4$ shows that convection in the upper layer remains thermally coupled to the lower layer, with thin rolls developing along the interface. No transition to mechanical coupling is found. Why the transition to a four-roll pattern is not captured by the numerical simulation in the equal layer height case is elaborated in the discussion section.

(iii) Unequal Layer Heights—Thicker Upper Layer. Despite the large height of the oil layer, buoyancy forces in the two layers in this case are only nominally different, as indicated by the parameter $\bar{P} = 0.75$. In this case, the influence of the cavity, or the "gap" effect, is quite pronounced. While both parameters $P = 5.5$ and $\bar{P}_{2\text{-D}} = 3.8$ indicate that convection should be initiated in the upper layer, the modified parameter $\bar{P}$ indicates that the lower layer should be more unstable. Indeed, convection in the experiments starts in the lower layer, and not in the upper layer as shown in Fig. 5(*a*) at $(Ra/Ra_c)_b = 0.9$. Flow in the lower layer is comprised of four rolls, with a downflow at the center of the cavity. The upper layer is in a conductive state as inferred from the nearly horizontal isotherms. With a higher driving force, $(Ra/Ra_c)_b = 1.2$ (Fig. 5(*b*)), flow in the upper layer first assumes a two-roll pattern, and then transitions to a four-roll pattern (Fig. 5(*c*)) with downflow always in the center. This flow pattern reflects thermal coupling between the layers. Thermal coupling appears to destabilize the upper two-roll pattern.

While the experiments always produced thermally coupled flow, the numerical simulations always led to a mechanically coupled flow, as shown in Fig. 5(*d*). Application of strong local velocity perturbations in the simulations to force the flow to a stable thermally coupled flow were ineffectual. Unlike the experiments, and as predicted by the parameters P and $\bar{P}_{2\text{-D}}$, convection is initiated first in the upper oil layer. This flow entrains the thinner lower glycol layer, creating a mechanically coupled flow, which persists to high Rayleigh numbers.

Discussion of Results

The objective of this study is to understand the coupling physics at a liquid–liquid interface. As has been noted, the numerical solution and the experiments are not quantitatively comparable. The narrow-gap constraint of the experiment leads to a more restricted Poiseuille flow in the experimental cavity as compared with the two-dimensional solution. Therefore, the onset of convection and further points of bifurcation in the flow cannot be quantitatively compared with the calculations. Nevertheless, the two-dimensional character of the flow in the gap is clearly apparent in the experiments.

A mechanical coupling mode is observed experimentally and numerically in the case of a thicker lower layer, where driving forces for convection in the two layers are very different ($\bar{P} = 0.16$). Here, convection is initiated in the lower layer, while the upper layer remains in a passive conductive state. Flow in the convecting layer entrains the subcritical upper layer, thereby creating a weak flow in the layer [Honda's (1982) "dragging" mode]. With higher driving, the flow pattern in the passive

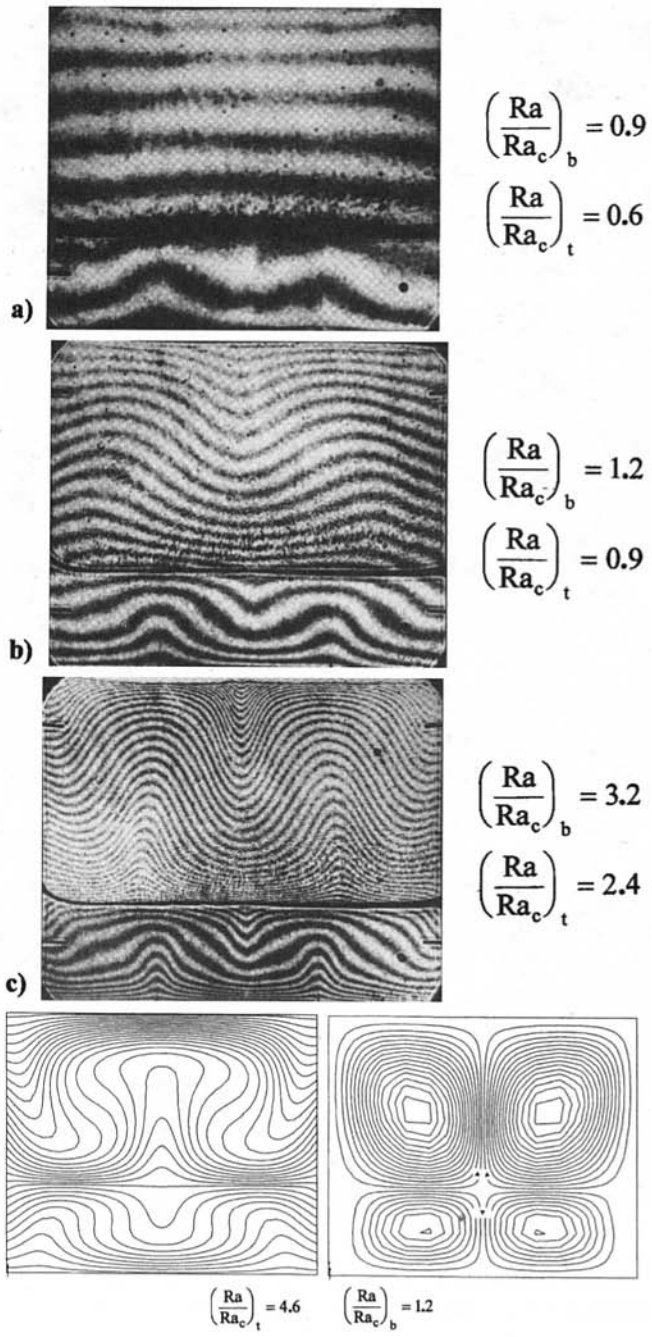

Fig. 5 Silicone oil 100 cSt over ethylene glycol: unequal layer heights—thicker upper layer; interferograms (*a*, *b*, *c*) and numerical simulation (*d*)

entrained layer remains unchanged until the layer becomes unstable. At this point, flow in the bulk of the upper layer is no longer entrained by the lower layer, and an independent, but coupled, flow pattern develops. Where necessary, interfacial rolls develop to satisfy continuity of velocity across the interface. This indicates that beyond the onset of convection the shear stresses imposed by the lower layer are not sufficient to impose a flow pattern in the entrained layer, as manifested by the appearance of a larger number of rolls in the thinner layer. In this case, where the driving force is much higher in one layer, agreement between experiments and numerical simulations is quite remarkable. The mechanically coupled flow did not transition to a thermally coupled state with increased driving.

A thermal coupling mode was observed in the case with equal layer heights ($\bar{P} = 0.34$), and in the case of a thinner lower layer ($\bar{P} = 0.75$). In both cases the driving forces for convection in the two layers are of comparable magnitude. This is consistent with Honda's (1982) marginal stability analysis. It is also consistent with the conclusion of Rasenat et al. (1989) that thermal coupling is the preferred mode when Rayleigh numbers in the two layers are nearly the same. The observed thermally coupled state at small Ra, and equal layer heights, is found to be in reasonable agreement with numerical simulations.

The transition from thermal to local mechanical coupling, observed in the equal layer height case, could not be reproduced in the numerical simulations. The restraining effect of the gap geometry is one plausible explanation for the transition from a thermal to a mechanically coupled state in the experiments. Comparatively, the glass walls restrain the Poiseuille flow in the higher viscosity oil layer more than in the thinner glycol layer. This is due to the larger contact surface between the thicker layer and the glass. Flow in the less viscous glycol layer, particularly the upflow along the center, creates high shear stresses along the interface. These shear stresses provide the necessary perturbation for the flow in the more viscous oil layer to transition to a four-roll structure. This establishes a pattern with local mechanical coupling. In the two-dimensional simulations, where flow in the layers is not restrained by glass walls, the thermally coupled flow structure established at the onset of convection remains locked in.

When driving forces in both layers are of comparable magnitude, i.e., $\bar{P} \sim 1$, the more "unstable" layer imposes a nonlinear temperature profile along the interface. This profile provides the perturbations for the onset of convection in the "stable" layer, which leads to thermally coupled flow.

In the case with a thicker upper layer, the effect of the cavity geometry on individual layer driving forces is very pronounced. In the experiments, where the driving forces are of comparable magnitude, $\bar{P} = 0.75$, coupling is predominantly thermal, and as expected, convection is initiated in the lower glycol layer. The layers are mechanically coupled in the two-dimensional simulations, where due to the absence of restraint provided by the glass walls, the corresponding ratio of the driving forces is higher: $\bar{P}_{2\text{-}D} = 3.8$. As has been noted, the inverse ratio of driving forces in the two-layer system is equally valid for the discussion of the coupling mechanism. The inverse ratio in this case is $(\bar{P}_{2\text{-}D})^{-1} = 0.26$. The contrast in driving forces in this case is not much different from the equal layer case where $\bar{P} = 0.34$, and the coupling at onset of convection is thermal. These results suggests a transition from thermal to mechanical coupling at $\bar{P} \cong 3$, or $\bar{P} \cong \frac{1}{3}$, with thermal coupling in the range $\frac{1}{3} \leq \bar{P} \leq 3$ and mechanical coupling outside.

The thermal coupling mode must either generate interfacial rolls to satisfy velocity continuity, or the interface must become immobile. This leads us to conclude that interface contamination is *not* the sole cause for thermally coupled flow. We observed local mechanical coupling with appearance of thin interfacial rolls (Fig. 3). Therefore, we are inclined to exclude the contamination option from our experiments.

Oscillatory convection at onset, as predicted by Rasenat et al. (1989), was not detected from the thermocouple signals, nor from visualizations. This may be due to pinning of the interface between the glass walls, which stabilizes the interface.

Conclusions

In contrast to single-layer Rayleigh–Bénard convection, a distinguishing feature of double-layer convection is the interface, across which fluid flow is coupled. Two different coupling mechanisms between the layers are possible: thermal coupling and mechanical coupling. Both states were observed. Another distinguishing feature of double-layer convection is the possibility of oscillatory motion at the onset of convection. This has been attributed to interfacial deformation and/or to an interme-

diate state between mechanical and thermal coupling at the onset of convection. Such oscillations were not observed.

When driving forces in both layers are similar ($\bar{P} \sim 1$), thermally coupled flow is observed. As the difference in buoyancy forces between the layers increases, the thermal coupling mode, which develops at the onset of convection, transitions to a mechanical coupling mode at higher Rayleigh numbers. When driving forces in the two layers are very different ($\bar{P} > 3$ or $\bar{P} < \frac{1}{3}$), mechanically coupled flow is observed. These results are applicable to a system with a dynamic viscosity ratio of 5.6. The findings are in general agreement with the theoretical results of Honda (1982) and Rasenat et al. (1989).

Onset of convection in one layer generates a temperature profile along the interface that provides the necessary perturbation for onset of convection in the adjacent layer, and the ensuing flow in the two layers to be thermally coupled. A thermally coupled flow either requires a small interfacial roll to satisfy continuity, or the interface to be immobile. In this sense, transfer of heat from one layer into the other generates thermal coupling, but the flow is still mechanically coupled along the interface.

Some disparities between experiments and two-dimensional simulations were observed. They are attributed, not to interfacial contamination, but to constraining effects of the gap geometry. The gap geometry modifies the critical driving force and the thermal boundary conditions for each layer. This modified critical driving force must be accounted for when comparing driving forces for convection in the different layers.

Acknowledgments

Support for this study from NASA under grant No. NAG3-1094 is gratefully acknowledged. Assistance provided by R. Harker, D. Fujita, and T. Tateyama during the experimental efforts is also gratefully acknowledged.

References

Barocela, E., and Jalilevand, A., 1987, "Liquid Encapsulated Float Zone Method for Microgravity Production of Gallium Arsenide," AIAA Paper No. 87-0390.

Catton, I., 1970, "Convection in a Closed Rectangular Region: The Onset of Motion," ASME JOURNAL OF HEAT TRANSFER, Vol. 92, pp. 186–188.

Catton, I., 1972, "Effect of Wall Conduction on the Stability of a Fluid in a Rectangular Region Heated From Below," ASME JOURNAL OF HEAT TRANSFER, Vol. 94, pp. 446–452.

Cserepes, L., and Rabinowicz, X. X., 1985/86, "Gravity and Convection in a Two-Layer Mantle," *Earth Plan. Sci. Lett.*, Vol. 76, pp. 193–207.

Davis, S. H., 1967, "Convection in a Box: Linear Theory," *J. Fluid Mech.*, Vol. 30, pp. 465–478.

Farhadieh, R., and Tankin, R. S., 1974, "Interferometric Study of Two-Dimensional Bénard Convection Cells," *J. Fluid Mech.*, Vol. 66, pp. 739–752.

Fluid Dynamics Analysis Package—Version 7.0, 1993, Users' Manual, Fluid Dynamics International, Evanston, IL.

Gershuni, G. Z., and Zhukhovitskii, E. M., 1982, "Monotonic and Oscillatory Instabilities of a Two Layer System of Immiscible Liquids Heated From Below," *Sov. Phys. Dokl.*, Vol. 27, pp. 531–533.

Honda, S., 1982, "Numerical Analysis of Layered Convection—Marginal Stability and Finite Amplitude Analyses," *Bull. Earthquake Res. Inst.*, Vol. 57, pp. 273–302.

Kirchartz, K. R., and Oertel, H., Jr., 1988, "Three-Dimensional Thermal Cellular Convection in Rectangular Boxes," *J. Fluid Mech.*, Vol. 192, pp. 249–286.

Koster, J. N., and Müller, U., 1982, "Free Convection in Vertical Gaps," *J. Fluid Mech.*, Vol. 125, pp. 429–451.

Koster, J. N., 1983, "Interferometric Investigation of Convection in Plexiglas Boxes," *Experiments in Fluids*, Vol. 1, pp. 121–128.

Levich, V. G., 1962, *Physicochemical Hydrodynamics*, Prentice-Hall.

Nataf, H. C., Moreno, S., and Cardin, Ph., 1988, "What is Responsible for Thermal Coupling in Layered Convection," *J. Phys. France*, Vol. 49, pp. 1707–1714.

Prakash, A., and Koster, J. N., 1994, "Convection in Multiple Layers of Immiscible Liquids in a Shallow Cavity—I, Steady Natural Convection," *Int. J. Multiphase Flow*, Vol. 20, No. 2, pp. 383–396.

Rasenat, S., Busse, F. H., and Rehberg, I., 1989, "A Theoretical and Experimental Study of Double-Layer Convection," *J. Fluid Mech.*, Vol. 199, pp. 519–540.

Renardy, Y., and Joseph, D. D., 1985, "Oscillatory Instability in a Bénard Problem of Two Fluids," *Phys. Fluids*, Vol. 28, pp. 788–793.

Richter, F. M., and Johnson, C. E., 1974, "Stability of a Chemically Layered Mantle," *J. Geophys. Res.*, Vol. 79–11, pp. 1635–1639.

Zeren, R. W., and Reynolds, W. C., 1972, "Thermal Instabilities in Two-Fluid Horizontal Layers," *J. Fluid Mech.*, Vol. 53, pp. 305–327.

The Temperature Rise at the Surface of a Liquid Layer Subject to a Concentrated Heat Source Placed Above the Layer

J. P. Burelbach

M. Epstein

M. G. Plys

Fauske & Associates, Inc.,
16W070 West 83rd Street,
Burr Ridge, IL 60521

A focused heat flux on the free surface of a liquid layer gives rise to combined thermocapillary and thermogravitational flow within the layer that dictates the magnitude of the temperature rise achieved at the surface. In the case of a high-boiling-point flammable liquid layer, this temperature rise determines the ignitability of the layer. An unconventional solution technique, which transforms the combined natural convection problem into a nonlinear conductionlike problem, is introduced to derive a convenient relationship between the heater power and size and the maximum liquid surface temperature. This expression depends on the layer thickness and fluid properties, but does not contain any adjustable (empirical) parameters. Experimental data are reported for dodecane layers between 2 and 7 mm thick for heat fluxes up to 63 kW m^{-2}. The data are well correlated by our analytical result.

Introduction

Consider a flammable liquid layer below its flash point temperature and subject to a focused heat source above the layer. Layer ignition becomes possible if the irradiation overwhelms the horizontally directed, thermogravitational and thermocapillary liquid convection and raises the liquid temperature above the flash point temperature. The motion induced in a liquid pool by concentrated heating from above has been the subject of several experimental studies (Murad et al., 1970; Ross et al., 1989; Ross, 1994). The observed flow field beneath a heated wire consists mainly of two counterrotating vortices, one on each side of the heat source. Detailed numerical analyses of transient heat transfer and hydrodynamics in a cylindrical enclosure filled with liquid and gas were conducted by Abramzon et al. (1987) and Schiller and Sirignano (1992a, b). In these studies the stratified gas and liquid system is heated by a fixed temperature hot-spot source. When thermogravitational effects are important, multiple vortices are predicted in the gas and liquid spaces. Other studies have attempted to correlate the maximum liquid temperature beneath a hot spot source to dominant physical parameters. In particular, Lai and Chai (1986) and Chan et al. (1988) have presented theoretical assessments of the induced surface temperature distributions in a layer or pool, while Kurosaki et al. (1989) reported experimental results for nonuniform radiative heating of silicone oil in a channel. Each of these studies considered downward heat losses but did not account for upward (convective) heat transfer off the unheated portions of the layer surface.

In the present study we are interested in determining the heat source power emission and size required to ignite residual organic solvent layers that may exist in storage tanks. In this application the substrate is treated as adiabatic and upward heat losses become important. As mentioned previously, ignition cannot occur if liquid-phase convection prevents the organic layer from exceeding the flash point temperature. Accordingly, we seek a heat transfer correlation that relates the maximum liquid surface temperature to the source power transmitted to the surface. The analytical method is verified experimentally using dodecane as a conservative (i.e., relatively volatile) representation of the aged solvent waste of interest in ongoing weapons site cleanup.

Theory

Figure 1 shows a sketch of a horizontal liquid layer and the liquid's flow due to the overhead heat source. The horizontal radial dimension of the layer is much larger than both its depth and the dimensions of the heat source. The heat source induces a negative horizontal temperature gradient within the liquid layer; that is, the temperature of the liquid decreases with distance from the source. Both thermogravitational and thermocapillary convection will occur under the action of the horizontal temperature gradient. Our goal is to correlate the maximum liquid temperature to the properties of the fluid layer and the size and strength of the heat source. An approximate theory of the combined thermogravitational and thermocapillary convection is introduced, which reduces the problem to the numerical solution of a single ordinary differential equation.

Physical Model, Governing Equations, and Approximate Technique. The discussion that follows is based on the momentum and energy conservation equations for laminar, axisymmetric, combined thermogravitational and thermocapillary convection in the liquid layer. The origin of the coordinate system (r, z) is placed at the surface of the organic layer just beneath the center of the heat source that transmits a heat flux q_0 to a circular region of the surface of radius r_0 (see Fig. 1). The horizontal liquid layer extends to infinity in the radial direction. The buoyancy-driven flow and thermal fields within the gas phase above the liquid layer are not modeled. Instead the liquid in the region $r_0 < r < r_\infty$ is assumed to lose heat to the gas at a rate given by Newton's law of cooling. The substrate that supports the liquid layer is assumed to be rigid and adiabatic. At steady state the source emission must equal the energy loss to the overlying gas.

The conservation equations for axisymmetric, laminar convection in the Boussinesq liquid are simplified based on the following assumptions:

1 The flow field consists of a single axisymmetric vortex. The layer is thin enough so that, instead of a boundary

Contributed by the Heat Transfer Division for publication in the JOURNAL OF HEAT TRANSFER. Manuscript received by the Heat Transfer Division August 1995; revision received November 1995. Keywords: Natural Convection, Thermocapillary Flows. Associate Technical Editor: T. Bergman.

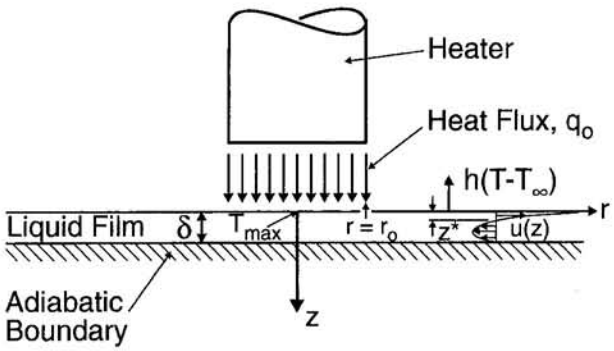

Fig. 1 Schematic diagram of physical model, indicating velocity profile in liquid layer and nomenclature

layer pattern, a nearly radial-parallel flow occurs within most of the flow field (vortex). The regions of flow reversal near $r = 0$ and r_∞ are ignored.

2 The layer depth is uniform and the liquid surface is flat.

3 Liquid-layer inertia is negligible relative to viscous effects.

4 Heat conduction in the radial direction is small compared to the vertical direction.

5 There are no surfactants present that can alter the surface tension or lead to the resistance of the free surface to thermocapillary motion (Keller and Bergman, 1990).

The momentum equations for liquid flow in the radial and downward directions become, respectively,

$$\frac{\partial P}{\partial r} = \mu \frac{\partial^2 u}{\partial z^2} \tag{1}$$

and

$$\frac{\partial P}{\partial z} = g\rho - g\rho\beta(T - T_{\text{ref}}) \tag{2}$$

and the energy equation is

$$u \frac{\partial T}{\partial r} = \alpha \frac{\partial^2 T}{\partial z^2} \tag{3}$$

while the condition for continuity is

$$\int_0^\delta u(z)dz = 0 \tag{4}$$

Since the surface tension of the liquid–gas interface decreases with increasing temperature, it produces a tangential surface stress, which is directed away from the heat source. Thus,

$$\mu \frac{\partial u}{\partial z} = \sigma' \frac{\partial T}{\partial r} \quad \text{at} \quad z = 0 \tag{5}$$

where σ' is assumed to be constant. The thermal boundary condition at $z = 0$ is

$$-k \frac{\partial T}{\partial z} = \begin{cases} q_0 & 0 < r < r_0 \\ h(T - T_\infty) & r_0 < r < r_\infty \end{cases} \tag{6}$$

and the remaining boundary conditions are

$$u = 0, \quad \frac{\partial T}{\partial z} = 0 \quad \text{at} \quad z = \delta \tag{7}$$

$$u \to 0, \quad T \to T_\infty \quad \text{as} \quad r \to r_\infty \tag{8}$$

$$u = 0 \quad \text{at} \quad r = 0 \tag{9}$$

The distance r_∞ is unknown and must be determined as part of the solution.

The model described above could, perhaps, be improved by introducing, say, a Gaussian distributed heat source rather than assuming that the heat source is uniform in the space $0 \le r \le r_0$ occupied by the heater. Moreover it could be argued that our choices of a constant heat transfer coefficient over the free surface outside the heated zone and a single, axisymmetric vortex are oversimplifications, considering the complex flow pattern created in the gas space by the outward thermocapillary flow at the liquid surface and the inward buoyancy-induced flow established by the heat source. However, as will be demonstrated later, the present model together with the assumptions of a local uniform heat source and constant h can adequately describe (or correlate) the temperature rise measurements at the liquid surface beneath the heat source. This tempers our concern about the validity of these assumptions.

Instead of attempting to solve the general problem as expressed by Eqs. (1)–(9), we first consider the following simpler combined thermocapillary/thermogravitational flow problem. The liquid velocity field obeys all the equations presented in the foregoing except for the boundary condition given by Eq. (6). In place of Eq. (6) we temporarily assume that $z = 0$

Nomenclature

A = integration constant in Eq. (10)
B = integration constant in Eq. (11)
Bi = Biot number = $h\delta/k$
Bo = Bond number = $g\beta\delta^2\rho/\sigma'$
C = integration constant in Eq. (15)
c_p = specific heat of the liquid
D = integration constant in Eq. (12)
g = gravitational acceleration
h = natural convection heat transfer coefficient
k = thermal conductivity of the liquid
k_e = effective conductivity transport coefficient
Ma = Marangoni number = $\sigma'\delta q_o/\mu\alpha h$
P = local pressure
q = heat flux transmitted radially through the liquid layer
q_0 = heat flux transmitted from the heater to the liquid layer
r = radial coordinate
r_0 = radius of heated zone
r_∞ = location far from heated zone at which $T = T_\infty$
T = temperature
$T(r, 0)$ = local temperature of the free surface (at $z = 0$)
$T_{\max}$ = maximum liquid temperature
T_{ref} = reference temperature in Boussinesq approximation
T_∞ = ambient temperature
u = velocity component in r direction
x = dimensionless radial coordinate = r/r_0
z = coordinate perpendicular to liquid surface
α = thermal diffusivity of liquid
β = expansion coefficient in Boussinesq approximation
δ = layer thickness (depth)
Δ = dimensionless layer thickness = δ/r_0
ΔT_s = maximum surface temperature difference = $T_{\max} - T_\infty$
θ = dimensionless temperature = $h(T - T_\infty)/q_0$
Λ = dimensionless parameter defined in Eq. (25)
μ = absolute viscosity of liquid
ν = kinematic viscosity of liquid = μ/ρ
ρ = density of liquid
σ = surface tension
σ' = absolute variation of σ with temperature = $d\sigma/dT$
Ω = dimensionless parameter defined in Eq. (25)

Subscripts

1 = under the heater (in the heated zone)
2 = outside the heated zone

is an adiabatic surface. Furthermore we assume that the temperature gradient $\partial T/\partial r$ is known and constant throughout the flow field. Once we make these assumptions, the radial extent of the flow field does not enter into the analysis and, as we shall see below, the solution of this problem with adiabatic horizontal surfaces yields a relationship between the radial heat flux transported through the convecting liquid and $\partial T/\partial r$. This relationship is then inserted into two local, liquid energy balance equations: one for the region beneath the heat source and one for the region outside the heat source. The solution of these equations yields the radial temperature profile over the entire flow field $0 < r < r_\infty$. In a sense our solution technique is an iterative one. A first approximation to the solution of the governing equations is obtained by suppressing heat exchange at the surface of the liquid layer. A second approximation is then obtained by allowing for surface heat transport. Obviously this iteration technique is not rigorous, and the fidelity of the method must be judged by comparison of the resulting heat transfer expression with experiment.

Flow and Energy Transport in a Horizontal Liquid Layer With Adiabatic Horizontal Surfaces and a Constant Radial Temperature Gradient. We begin by differentiating Eq. (1) with respect to z and Eq. (2) with respect to r and then eliminating P between these equations to obtain

$$\frac{d^3u}{dz^3} = -\frac{g\rho\beta}{\mu}\frac{dT}{dr} = A \tag{10}$$

The energy equation may be written as

$$\frac{1}{u}\frac{d^2T}{dz^2} = \frac{1}{\alpha}\frac{dT}{dr} = -B \tag{11}$$

From the capillary condition (5) the vertical velocity gradient at the free surface may be expressed as

$$\frac{du}{dz} = \frac{\sigma'}{\mu}\frac{dT}{dr} = -D \tag{12}$$

Integrating Eq. (10) and evaluating the integration constants using boundary conditions (7) and (12) and the continuity condition (4) leads to

$$u = A\left(\frac{1}{6}z^3 - \frac{3}{16}\delta z^2 + \frac{1}{48}\delta^3\right) + D\left(\frac{3}{4}\frac{z^2}{\delta} - z + \frac{\delta}{4}\right) \tag{13}$$

Substituting this expression into the energy equation (11) and integrating once gives

$$\frac{dT}{dz} = -AB\left(\frac{1}{24}z^4 - \frac{1}{16}\delta z^3 + \frac{1}{48}\delta^3 z\right) - BD\left(\frac{1}{4}\frac{z^3}{\delta} - \frac{1}{2}z^2 + \frac{1}{4}\delta z\right) \tag{14}$$

which satisfies the imposed conditions of adiabatic horizontal boundaries. Integrating Eq. (14) once more yields

$$T = -\frac{AB}{48}\left(\frac{2}{5}z^5 - \frac{3}{4}\delta z^4 + \frac{1}{2}\delta^3 z^2\right) - \frac{BD}{4}\left(\frac{1}{4}\frac{z^4}{\delta} - \frac{2}{3}z^3 + \frac{1}{2}\delta z^2\right) + C \tag{15}$$

Since we demand that there be no heat flow through the bounding horizontal surfaces, the net radial heat flux, q, is then determined from

$$q = \frac{1}{\delta}\int_0^\delta \rho c_p u T dz \tag{16}$$

Equations (13) and (15) are now substituted into Eq. (16). By virtue of the mass continuity condition all the resulting integral terms involving the unknown constant C in Eq. (15) are zero. Evaluating the nonzero integrals and combining like terms yields

$$\frac{q}{\rho c_p} = \frac{19A^2B\delta^8}{(10)(63)(48)^2} + \frac{ABD\delta^6}{(48)(120)} + \frac{BD^2\delta^4}{(48)(35)} \tag{17}$$

Finally, introducing the definitions for A, B, and D, Eq. (17) becomes

$$q = -k_e\left(\frac{dT}{dr}\right)^3 \tag{18}$$

where

$$k_e = \frac{\rho c_p(\sigma')^2\delta^4}{1680\alpha\mu^2}\left(1 + \frac{7}{24}\,\mathrm{Bo} + \frac{19}{864}\,\mathrm{Bo}^2\right) \tag{19}$$

Equation (18) may be regarded as a kind of nonlinear Fourier's law where k_e represents an effective conductivity (W m K^{-3}), which accounts for radial thermal advection due to both thermogravitational and thermocapillary forces.

It is recognized that, while Eq. (18) may accurately describe the local heat flow in regions where the flow pattern is characterized by parallel streamlines, it cannot be correct near $r = 0$ and as $r \to r_\infty$ where the flow reverses direction. However, Eq. (18) does at least exhibit the correct qualitative behavior in that $dT/dr \to 0$ and, therefore, $q \to 0$ in these limiting regions of the flow field. Since prediction of the radial temperature rise at the liquid surface beneath the heater rather than the flow field is our goal, we choose to ignore the zones of liquid flow reversal.

Radial Temperature Distribution and Correlation for T_{max}. We can now solve for the radial temperature distribution along the free surface of the liquid layer by relaxing our assumption that the surface is adiabatic and assuming that Eq. (18) can be applied locally. A thermal energy balance on a segment dr of the film exposed to the heat-source generated flux q_0 gives

$$\frac{1}{r}\frac{d}{dr}\left[r\left(\frac{dT_1}{dr}\right)^3\right] = -\frac{q_0}{\delta k_e} \quad 0 < r < r_0 \tag{20}$$

Another energy balance for a segment of the film outside the heated zone is

$$\frac{1}{r}\frac{d}{dr}\left[r\left(\frac{dT_2}{dr}\right)^3\right] = \frac{h}{\delta k_e}(T_2 - T_\infty) \quad r_0 < r < r_\infty \tag{21}$$

At $r = r_0$ we have the coupling conditions

$$T_1 = T_2, \quad \frac{dT_1}{dr} = \frac{dT_2}{dr} \tag{22}$$

The remaining boundary conditions are

$$T_1 = T_{max}, \quad \frac{dT_1}{dr} = 0 \quad \text{at} \quad r = 0 \tag{23}$$

$$T_2 \to T_\infty, \quad \frac{dT_2}{dr} \to 0 \quad \text{as} \quad r \to r_\infty \tag{24}$$

where T_{max} in Eq. (23) is an unknown quantity that we seek to

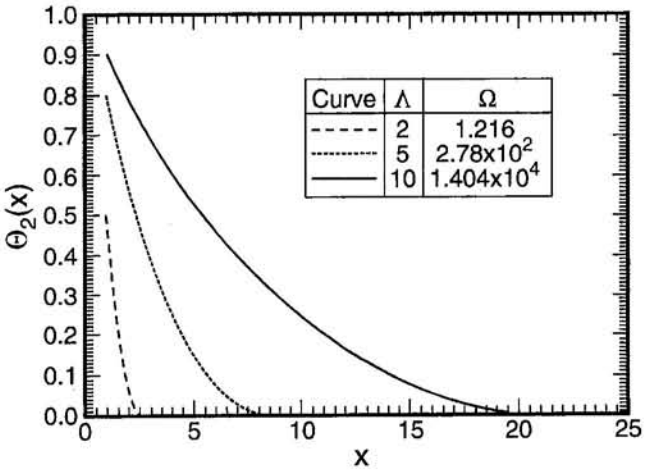

Fig. 2 Dimensionless radial temperature profiles in region external to heat impingement zone ($1 < x < \infty$); Λ or Ω as parameter; note that temperature profiles in heat impingement zone can be readily constructed from Eq. (31)

determine as part of the solution. At this stage it is convenient to treat T_{max} as a parameter whose value may be prescribed. It is recognized that, owing to the volumetric absorption of radiant energy and the possibility of a boundary-layer flow pattern beneath the heat source, it may be difficult to justify the use of Eq. (18) in the heated segment $0 < r < r_0$ (see Eq. (20)). It turns out, however, that we can eliminate Eq. (20) from this equation set, assume instead the constant temperature profile $T(r) = T_{max}$ in this segment, and still obtain the same theoretical result (see below).

The solution is facilitated by introducing the dimensionless quantities

$$x = \frac{r}{r_0}, \quad \theta_1 = \frac{T_1 - T_\infty}{T_{max} - T_\infty}, \quad \theta_2 = \frac{T_2 - T_\infty}{T_{max} - T_\infty}$$

$$\Lambda = \frac{4}{3}(T_{max} - T_\infty)\left(\frac{2k_e\delta}{q_0 r_0^4}\right)^{1/3}, \quad \Omega = \frac{k_e\delta(T_{max} - T_\infty)^2}{r_0^4 h} \tag{25}$$

Then the differential equations become

$$\frac{\Lambda^3}{x}\frac{d}{dx}\left[x\left(\frac{d\theta_1}{dx}\right)^3\right] = -2\left(\frac{4}{3}\right)^3 \quad 0 < x < 1.0 \tag{26}$$

$$\frac{\Omega}{x}\frac{d}{dx}\left[x\left(\frac{d\theta_2}{dx}\right)^3\right] = \theta_2 \quad 1.0 < x < x_\infty \tag{27}$$

and the boundary conditions are

$$\theta_1 = \theta_2, \quad \frac{d\theta_1}{dx} = \frac{d\theta_2}{dx} \quad \text{at} \quad x = 1.0 \tag{28}$$

$$\theta_1 = 1, \quad \frac{d\theta_1}{dx} = 0 \quad \text{at} \quad x = 0 \tag{29}$$

$$\theta_2 \to 0, \quad \frac{d\theta_2}{dx} \to 0 \quad \text{as} \quad x \to x_\infty \tag{30}$$

Equation (26) is solved in closed form subject to the conditions in Eq. (29), to give

$$\theta_1 = 1 - \frac{1}{\Lambda}x^{4/3} \tag{31}$$

Equation (27), however, is solved numerically using an available subroutine for integrating ordinary differential equations (Gear, 1971; Hindmarsh, 1972). For this purpose the boundary value problem represented by Eqs. (27), (28), and (30) is treated as an initial-value problem starting from $x = 1.0$ and integrating toward $x = x_\infty$. From Eqs. (28) and (31), the initial conditions are

$$\theta_2 = 1 - \frac{1}{\Lambda}, \quad \frac{d\theta_2}{dx} = -\frac{4}{3}\frac{1}{\Lambda} \tag{32}$$

Thus if Λ is specified, the initial conditions for Eq. (27) are known. The method of solution consists of guessing at the value of Ω in Eq. (27) and then systematically refining this guess so that the numerical solution satisfies the boundary conditions in Eq. (30). By assigning a sequence of values of Λ and solving the corresponding number of boundary value problems, the unique relationship between Λ and Ω is determined.

Plots of $\theta_2(x)$, based on solution of Eq. (27), are given in Fig. 2 for three values of Λ. The corresponding values of Ω are also shown. Note that the radial distance x over which the heat deposited in the liquid layer is removed by convection to the overlying ambient increases with increasing Λ or Ω. Also note from Fig. 2 that for $\Lambda = 10$ the radial extent of the cooling zone is about 20 times greater than the radius of the heated zone. The radial extent of the heater's zone of influence (i.e., the combined heating and cooling zones) is determined by generating numerous temperature profile curves of the type shown in Fig. 2. The functional relationship between x_∞ and Ω is well represented by

$$x_\infty = 1.93\Omega^{1/4} \tag{33}$$

The parameter Λ is plotted as a function of Ω in Fig. 3, where the dashed curves represent asymptotic limits. For sufficiently small values of Ω, i.e., in the high cooling-rate regime ($h \to \infty$), the parameter Λ is asymptotic to unity. In this limit all of the radial temperature decrease occurs in the heated zone ($0 < x < 1$), so that $\theta_1 = 0$ at $x = 1$ and it follows immediately that $\Lambda = 1.0$. A second asymptotic result occurs in the limit of large Ω (i.e., relatively small h). In this case the temperature decrease from T_{max} to T_∞ occurs outside the heated zone. The temperature of the liquid surface in the heated zone is uniform and $\theta_1 = 1.0$. This asymptotic curve for large Ω was obtained by replacing the first boundary condition in Eq. (32) by $\theta_2(1) = 1.0$ and solving Eq. (27) numerically as before.

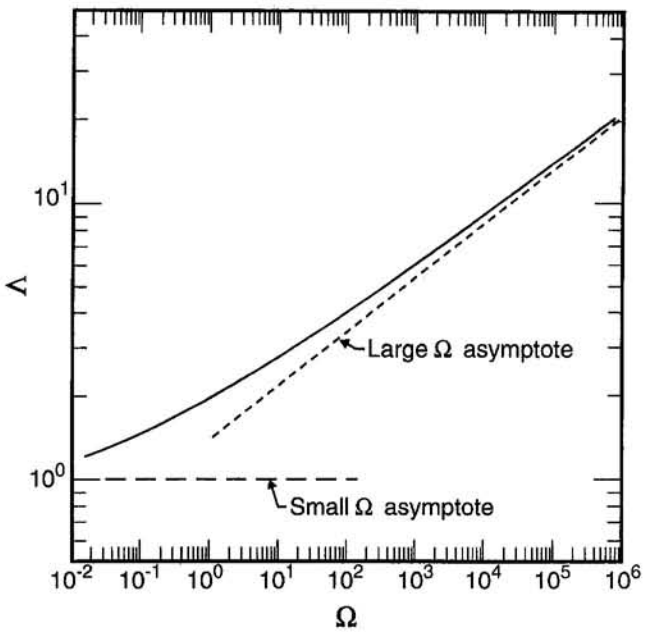

Fig. 3 Λ versus Ω function

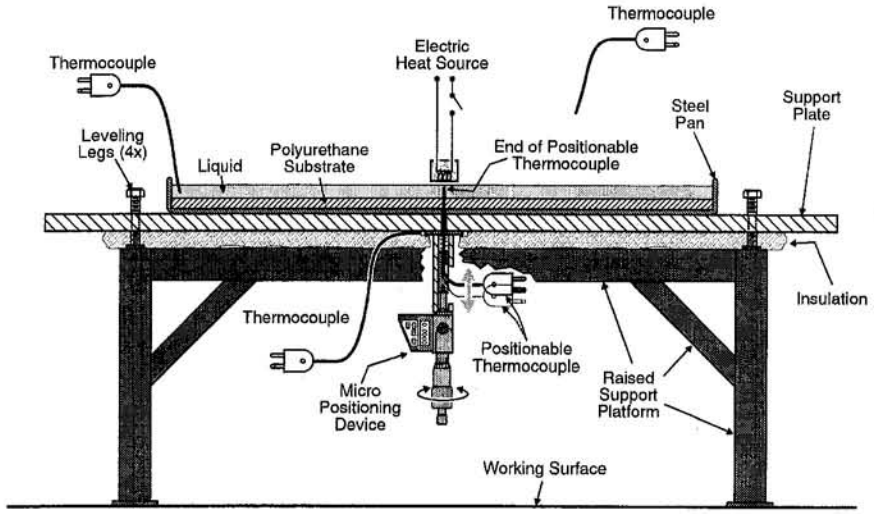

Fig. 4 Experimental apparatus

The parameter Ω is generally very large, but even at a reduced value of $\Omega = 10^3$ the asymptotic curve is only about 10 percent lower than the more complete solution. In view of the practical utility of the asymptotic solution for large Ω the following fit to that asymptotic curve is made to allow T_{max} to be readily calculable by hand:

$$\Lambda = 1.49\Omega^{0.191} \tag{34}$$

Introducing the physical variables of Eq. (25) into this relation and solving the result for $T_{max} - T_\infty$, we have

$$\frac{h(T_{max} - T_\infty)}{q_0} = 0.819 \left(\frac{r_0^4 h^3}{k_e \delta q_0^2}\right)^{0.231} \tag{35}$$

which is a readily applied expression for the maximum liquid layer temperature as a simple function of all pertinent parameters. When cast in terms of dimensionless parameters, Eq. (35) becomes

$$\theta_{max} = 4.55 \left[\frac{\mathrm{Bi}}{\Delta^4 \mathrm{Ma}^2 \left(1 + \frac{7}{24}\mathrm{Bo} + \frac{19}{864}\mathrm{Bo}^2\right)}\right]^{0.231} \tag{36}$$

Experiment

Apparatus. Figure 4 illustrates the apparatus. A 1.3-cm-thick circular slab of cast polyurethane ($k = 0.13$ W m^{-1} K^{-1}) serves as a solid substrate upon which the test liquid (dodecane) is placed. The polyurethane is glued into a 59-cm-dia galvanized steel pan, which, in turn, is glued to a 1.3-cm-thick aluminum plate. The pan height allows for layer depths up to 1 cm. The plate is supported on a square array of leveling screws, and the underside is insulated. A centrally located radiant heat source is suspended about 1 cm above the liquid.

Two different heaters are employed. A 1.3-cm-dia heating coil from a standard automobile cigarette lighter is used for the smallest source. A larger heater is similarly constructed from a coil of heater wire attached to a 5.9 cm diameter steel disk. Each heater is calibrated by measuring the heatup rate of a target dodecane sample for various electric power levels. Heater temperature measurements indicate that power calibration data are well represented by the Stefan–Boltzmann law applied to a gray body with emissivity between 0.8 and 0.9.

A movable temperature probe, centered beneath the overhead heater, provides for temperature measurements across the liquid layer and at the layer surface. The temperature probe is a type K chromel-alumel thermocouple (diameter 0.51 mm), which is translated vertically by means of a spring-loaded digital micrometer. To minimize disturbance of the layer, the probe enters the liquid from below by means of a sealed port in the substrate/pan/plate composite. This "TC probe" is also used to measure the layer thickness, defined as the difference between the micrometer readings when the probe first touches the free surface (from below) and when it is flush with the substrate. (The substrate itself is slightly convex such that the layer thickness increases by about 0.8 mm at a radial distance of 15 cm from the pan center.) Additional thermocouples are placed: (a) in the liquid layer near the pan wall, to measure the bulk temperature far from the heat source; (b) underneath the center of the aluminum plate, to confirm that heat conduction across the substrate/pan/plate composite is negligible; and (c) in the air space several inches above the liquid layer, but not close to the heater, to measure the ambient air temperature. The entire apparatus is enclosed in a hood to minimize air flow across the liquid surface.

Procedure. With a quiescent liquid layer in place, the TC probe is positioned so that its tip just contacts the layer free surface. This subjective indication is reproducible within ± 0.02 mm. Power is then supplied to the heater coil, which induces a temperature distribution in the liquid and surface traction away from the heated zone. The system is allowed to equilibrate so that the temperature reading at the layer surface is nearly constant. The liquid surface temperature measurement is not overly sensitive to thermocouple position, and typically is reproducible within ± 1°C at quasi-steady conditions.

Tests are performed in series using moderate steps in the heater power so as to minimize the equilibration time for each test. Such a series of tests usually lasts several hours. Evaporative layer thinning is negligible, based on isothermal thickness measurements taken before and after the test series. Local thermocapillary thinning of as much as 0.1 mm due to deformation of the free surface beneath the heat source is most pronounced for thin ($\sim$2 mm) dodecane layers. Thermal expansion of the substrate may also act to locally reduce the layer thickness, but this would amount to at most a 0.05 mm change in thickness, using an expansion coefficient of 1.6×10^{-4} K^{-1} and conservatively assuming an average 25°C heatup of the substrate beneath the heater.

An uncertainty analysis of the experimental measurements was performed by using the root-sum-square method (Kline and McClintock, 1953). The maximum error in measuring the layer thickness is estimated to be ± 0.05 mm, accounting for

uncertainty in both the substrate and free surface positions. Uncertainty in the effective heater power is estimated at ±10 percent based on scatter in the calibration data. Although temperature measurement error due to thermocouple calibration is within ±0.5°C, the uncertainty in the measured temperature difference, $\Delta T_s = T_{max} - T_\infty$, is estimated to be as much as ±2°C, or generally within ±10 percent, due to residual system unsteadiness and fluid instabilities. This is particularly the case for higher heat fluxes and thinner layers. The data and error limits are presented below in the dimensionless form of Eq. (35).

Results and Discussion

Experiments have been performed using dodecane layers with thicknesses ranging from 2 to 7 mm. Dodecane was chosen as the test fluid because it is a conservative (i.e., relatively volatile) representation of the NPH (normal paraffin hydrocarbon) found in some aged solvent waste tanks containing residual high-end organics that are of practical interest. It conforms to the model assumption that incident radiation is absorbed throughout the liquid layer (see Eq. (20)). Although organic layers in general must be about 15 mm thick before all the incident radiation is absorbed (Inamura et al., 1989) heater calibration did not suggest sensitivity to layer thickness for our tests. In most cases the liquid temperature far from the heat source (T_∞, near the side wall) remained close to the ambient gas temperature. The imposed horizontal surface temperature difference, ΔT_s, varied from 4°C to 33°C and the effective heat flux ranged up to 63 kW m^{-2}.

The results of the experiments may be examined to assess the usefulness of Eq. (35) for predicting the maximum liquid surface temperature. This requires an appropriate heat transfer coefficient h for heat loss from the liquid surface to the ambient air. Heat is carried away from the liquid surface both by thermal radiation and by natural convection. The flow pattern in the ambient air space above the liquid surface is obviously complex and the value of h and its variation with distance is difficult to predict. Accordingly, in keeping with our objective of developing a practical model, we assume a constant h whose value is based on thermal radiation and turbulent natural convection as predicted with standard correlations for a rigid horizontal surface facing upward (see, e.g., Bird et al., 1960; Gebhart et al., 1988). This approach results in $h = 10$ W m^{-2} K^{-1} for comparing theory with experiment. The effective heat transfer coefficient may be somewhat larger than this value (perhaps by as much as a factor of two for large ΔT_s; Epstein et al., 1995) due to the air/liquid counterflow induced by the radiant heater. Physical property data for dodecane are evaluated at 30°C, judged to be the best overall average "film temperature" for the temperature ranges encountered in the experimental program.

To show the degree of agreement with data all the temperature rise measurements for dodecane are plotted in Fig. 5 in the dimensionless form suggested by Eq. (35). Error bars reflect an uncertainty of up to 18 percent in the quantity $h(T_{max} - T_\infty)/q_0$ and up to 31 percent in the quantity $r_0^4 h^3/(k_e \delta q_0^2)$ for fixed h. The open circular data points represent experimental conditions for which the capillary/gravitational convection model does not formally apply because the assumptions of negligible radial momentum transport, radial conduction, or liquid inertia have been violated. The open square data points represent experimental conditions in which the radiant heater's zone of influence extends to the radial boundary of the organic layer. In other words, in these experiments the temperature of the liquid at the edge of the test pan remained above the ambient temperature and the boundary condition $T \to T_\infty$ as $r \to r_\infty$ was not satisfied. Despite these violations of our modeling assumptions, all the data are still reasonably well correlated by the model. Note that the data that lie well above the theoretical line in Fig. 5 correspond to small measured surface temperature increases

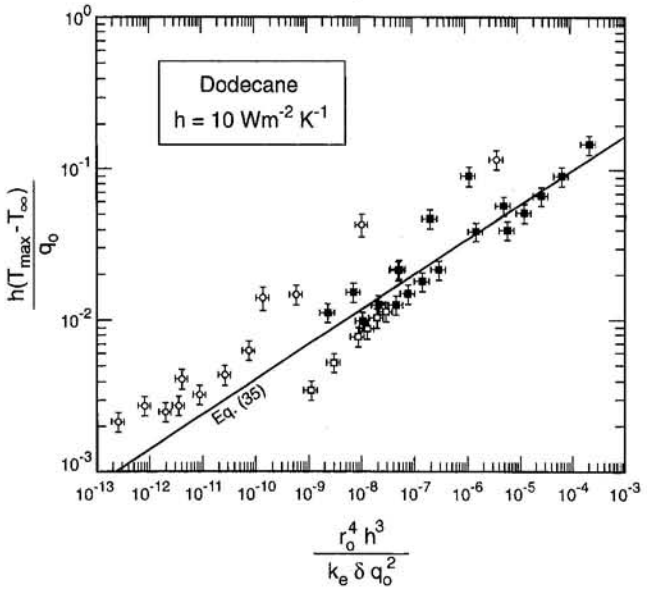

Fig. 5 Comparison of Eq. (35) with radiant-heating surface temperature rise data for dodecane

(low applied power and/or thick layers). Agreement between theory and measurements is best in the regime of practical interest of large temperature increases (thin layers). Better overall agreement could be demonstrated by assigning values of h somewhat less than 10 W m^{-2} K^{-1} for cases where ΔT_s is small and values of h somewhat greater than $h = 10$ W m^{-2} K^{-1} when ΔT_s is large. According to the theory presented here $T_{max} - T_\infty \sim h^{-0.31}$, so that moderate variations in the value of h result in only a small shift in the position of the data relative to the theoretical curve in Fig. 5.

It is obvious from Eq. (35) that T_{max} becomes unbounded as $\delta \to 0$. This result is a consequence of our assumption that the liquid layer is of uniform thickness. It is known that thermocapillary-driven flow causes the surface of the liquid layer under the heater to deform, and very thin fuel layers pull away from the heat source impingement zone (Torrance and Mahajan, 1975). A dry spot appears beneath the heat impingement zone because, for very thin layers, the thermocapillary force at the surface is strong enough to balance the gravitational force, which promotes fuel-layer spreading. A simple balance between these forces at the edge of a liquid layer that has withdrawn from the heat impingement zone provides the following condition on the liquid-layer thickness for dry spot formation (and nonignition):

$$\delta < \left[\frac{2\sigma'(T_{max} - T_\infty)}{\rho g}\right]^{1/2} \tag{37}$$

Setting $T_{max} - T_\infty = 35$°C, dry spot formation becomes possible in a dodecane layer if δ is less than about 1.0 mm. Indeed this phenomenon was observed during the radiant heating of a 2.0-mm layer of dodecane when the effective heat flux was increased to 35 kW m^{-2}; data for that δ were successfully collected only up to a heat flux of 23 kW m^{-2}.

In closing this section it is recognized that the above-described experiments and analysis have deliberately focused attention on the maximum temperature rise at a liquid surface subject to a concentrated heat source. However, in separate experimental work (Epstein et al., 1995) the surface temperature profile produced by a concentrated heat source in a channel flow environment was determined. The model presented here was found to be in good agreement with those measured profiles.

Conclusion

Experimental data for dodecane layers heated from above are well correlated by Eq. (35), which relates the liquid surface temperature beneath a radiant heat source of known dimensions to the fraction of source power transmitted to the liquid surface. This heat transfer correlation provides a practical criterion for flame spreading, in that ignition cannot occur if the predicted maximum surface temperature does not exceed the flashpoint temperature of the organic material.

References

Abramzon, B., Edwards, D. K., and Sirignano, W. A., 1987, "Transient, Stratified, Enclosed Gas and Liquid Behavior With Concentrated Heating From Above," *J. Thermophysics,* Vol. 1, pp. 355–364.

Bird, R. B., Stewart, W. E., and Lightfoot, E. N., 1960, *Transport Phenomena,* Wiley, New York.

Chan, C. L., Chen, M. M., and Mazumder, J., 1988, "Asymptotic Solution for Thermocapillary Flow at High and Low Prandtl Numbers Due to Concentrated Surface Heating," ASME JOURNAL OF HEAT TRANSFER, Vol. 110, pp. 140–146.

Epstein, M., Burelbach, J. P., and Plys, M. G., 1995, "Ignitability of Organic Solvent in Hanford Tank C-103 Following Interim Stabilization," Fauske & Associates, Inc. Report FAI/95-17, Feb.; also, "Surface Temperature Profiles Due to Radiant Heating in a Thermocapillary Channel Flow," in preparation.

Gear, C. W., 1971, *Numerical Initial Value Problems in Ordinary Differential Equations,* Prentice-Hall, Englewood Cliffs, NJ.

Gebhart, B., Jaluria, Y., Mahajan, R. L., and Sammaka, B., 1988, *Buoyancy-Induced Flows and Transport,* Hemisphere, New York.

Hindmarsh, A. C., 1972, "Linear Multistep Methods for Ordinary Differential Equations: Method Formulations, Stability, and the Methods of Nordsieck and Gear," Lawrence Livermore National Laboratory Report UCRL-51185, Rev. 1, March.

Inamura, T., Arai, M., Taghavi, K., and Saito, K., 1989, "A Simplified Model to Predict Boilover Time in Liquid Pool Fires," Spring Technical Meeting, Combustion Institute, Dearborn, MI, Apr. 30–May 2.

Keller, J. R., and Bergman, T. L., 1990, "Thermosolutal Inducement of No-Slip Free Surfaces in Combined Marangoni-Buoyancy Driven Cavity Flows," ASME JOURNAL OF HEAT TRANSFER, Vol. 112, pp. 363–369.

Kline, S. J., and McClintock, F. A., 1953, "Describing Uncertainties in Single-Sample Experiments," *Mech. Eng.,* Jan., pp. 3–8.

Kurosaki, Y., Satoh, I., Horiuchi, T., and Kashiwagi, T., 1989, "Effect of Marangoni Convection on the Temperature Profiles of a Free Surface Subject to Nonuniform Radiative Heating," *Experimental Thermal and Fluid Science,* Vol. 2, pp. 365–373.

Lai, C.-L., and Chai, A.-T., 1986, "Surface Temperature Distribution Along a Thin Liquid Layer Due to Thermocapillary Convection," *Acta Astronautica,* Vol. 3, No. 11/12, pp. 655–659.

Murad, R. J., Lamendola, J., Isoda, H., and Summerfield, M., 1970, "A Study of Some Factors Influencing the Ignition of a Liquid Fuel Pool," *Combustion and Flame,* Vol. 15, pp. 289–298.

Ross, H. D., Schiller, D. N., Disimile, P. J., and Sirignano, W. A., 1989, "Behavior in Normal and Reduced Gravity of an Enclosed, Liquid/Gas System With Nonuniform Heating From Above," AIAA Paper No. 89-0070; also, NASA TM-101471.

Ross, H. D., 1994, "Ignition of and Flame Spread Over Laboratory-Scale Pools of Pure Liquid Fuels," *Prog. Energy Combust. Sci.,* Vol. 20, pp. 17–63.

Schiller, D. N., and Sirignano, W. A., 1992a, "Buoyant-Thermocapillary Flow With Nonuniform Supra-Heating: I. Liquid-Phase Behavior," *J. Thermophysics and Heat Transfer,* Vol. 6, No. 1, pp. 105–113.

Schiller, D. N., and Sirignano, W. A., 1992b, "Buoyant-Thermocapillary Flow With Nonuniform Supra-Heating: II. Two-Phase Behavior," *J. Thermophysics and Heat Transfer,* Vol. 6, No. 1, pp. 113–120.

Torrance, K. E., and Mahajan, R. L., 1975, "Surface Tension Flows Induced by a Moving Thermal Source," *Combustion Sci. Technology,* Vol. 10, pp. 125–136.

Buoyancy and Property Variation Effects in Turbulent Mixed Convection of Water in Vertical Tubes

Y. Parlatan[1]

N. E. Todreas

M. J. Driscoll

Department of Nuclear Engineering,
Massachusetts Institute of Technology,
77 Massachusetts Avenue,
Cambridge, MA 02139

Friction factor and heat transfer coefficient behavior are investigated experimentally under mixed convection conditions in aiding and opposing transition and turbulent flow of water ($4000 < Re < 9000$ and $Bo < 1.3$). With increasing buoyancy influence, the friction factor increases by as much as 25 percent in aiding flow, while it decreases by as much as 25 percent in opposing flow ($Gr_{\Delta T} < 7 \cdot 10^6$). The effects of temperature-dependent viscosity variations are also included in the analysis ($0.5 < \mu_w/\mu_b < 1.0$). When they are taken into account, the increase in the friction factor due to buoyancy forces alone in upward flow becomes larger. The friction factor behavior is compared with previous studies in the literature. Our experimental data agree well with some of the previous experiments described in the literature. The heat transfer coefficient was also measured under the same experimental conditions; the heat transfer coefficient monotonically increases in opposing flow by as much as 40 percent, and first decreases by 50 percent and then recovers in aiding flow with increasing buoyancy influence.

1 Introduction

Mixed convection is a regime of heat transfer that occurs when the externally imposed axial pressure gradient is sufficiently low to render local buoyancy effects nonnegligible. In this mode of heat transfer, the flow field is significantly modified from that which would prevail under forced convection conditions. This modification is due to variations of gravitational body forces associated with the temperature gradient dependent density variations across the pipe. Mixed convection, both laminar and turbulent, has received increasing attention because it is encountered in many practical systems, including passive decay heat removal from nuclear power reactors, solar power development, and electronic device cooling. Since many of these systems have low coolant flow rates, they operate in laminar, transition, or low-Reynolds-number turbulence flow regimes.

The heat transfer coefficient in turbulent mixed convection has received considerably more attention than the friction factor for both aiding (heated upward or cooled downward) and opposing (heated downward or cooled upward) flows. The literature contains fairly accurate correlations describing the Nusselt number behavior; see Jackson et al. (1989) for a review. The majority of the experiments in the literature were performed using gases. In general, with increasing buoyancy influence the Nusselt number ratio increases in opposing flow, and first decreases and then recovers sharply in aiding flow. An explanation of the mechanism involved has been given by Hall and Jackson (1969). They suggested that the dominant factor was the modification of the shear stress distribution across the pipe, with a consequent change in turbulence production.

Investigations into the behavior of friction factor in mixed convection conditions are relatively scarce compared to those for the heat transfer. The difficulty in measuring the friction factor is probably the main reason for this scarcity since relatively large heat fluxes and/or high temperatures, and small friction pressure drops are usually involved. We have found several studies that involved experimental determination of friction factor behavior in either aiding or opposing mixed convection: Petukhov and Strigin (1968), Carr et al. (1973), Easby (1978), Polyakov and Shindin (1988), and Nakajima et al. (1980).

Carr et al. (1973), Polyakov and Shindin (1988), and Nakajima et al. (1980) measured the velocity profile using a hot-wire anemometer with air in uniformly heated upward flow. The friction factor was calculated from the wall shear stress, which was in turn calculated from the convective velocity gradient at specific axial positions. The uncertainty associated with the friction factor results was not reported in any of these studies. There was qualitative agreement between the results of the first two studies: The friction factor was found first to decrease and then to increase slightly with increasing relative buoyancy influence. However, the third study by Nakajima et al. was in disagreement with the first two: The friction factor was found to increase monotonically. The disagreement among these studies is probably due to the fact that the velocity measurements were not taken in the wall region ($y^+ \gtrsim 30$) in the first two experiments by Carr et al. and Polyakov and Shindin. This is apparent by comparing the results of these three experiments at the same Re and Gr number range, and which gave quite different results, as will be illustrated later.

Petukhov and Strigin (1968) measured the friction pressure drop with water in upward flow in a test section with a heated length of 80D (D = 49.66 mm). The flow was not developed at the inlet to the heated test section since it lacked a flow developing section. (A correction was reportedly introduced to take into account the pressure drop due to hydrodynamic development.) The range of the experiments included laminar as well as turbulent flow data ($300 \leq Re \leq 30{,}000$). The friction factor was found to increase monotonically with buoyancy influence. However, the experimental results reported in graphic form did not agree with the correlation offered in the same paper. Furthermore, Petukhov and Polyakov (1988) later

[1] Current address: Brookhaven National Laboratory, Building 475B, Upton, NY 11973.

Contributed by the Heat Transfer Division for publication in the JOURNAL OF HEAT TRANSFER. Manuscript received by the Heat Transfer Division April 1995; revision received February 1996. Keywords: Forced Convection, Mixed Convection, Natural Convection. Associate Technical Editor: Y. Jaluria.

reported a totally different behavior for the friction factor using the data of Polyakov and Shindin (1988).

Easby (1978) measured the friction factor and Nusselt number in his experiments with pressurized nitrogen in uniformly heated downward flow (L/D = 150 and D = 30 mm). The friction factor was determined from the manometer-measured total pressure drop, subtracting the gravitational pressure drop inside the pipe and along the manometer lines as well as the acceleration pressure drop between the inlet and exit. The bulk density was used in the approximate calculation of the acceleration pressure drop instead of the momentum density, an approximation that introduces negligible error, which we have also employed. The friction factor was found to decrease by as much as 20 percent with the buoyancy influence over the $\mathrm{Gr}_{\Delta T}/\mathrm{Re}^2$ range investigated:

$$\frac{f}{f_o} = 1.006 - 5.13\,\frac{\mathrm{Gr}_{\Delta T}}{\mathrm{Re}^2} \qquad (1)$$

The experimental data were taken in transition and turbulent flows: 2000 $\leq$ Re $\leq$ 10,000, and $\mathrm{Gr}_{\Delta T} \leq 10^6 (\mathrm{Gr}_{\Delta T}/\mathrm{Re}^2 \leq 0.04$ or Bo $\leq 0.55)$. The changes in the friction factor were attributed to distortion of the radial shear stress profile. The measurement errors were not reported, and the scatter of the data was about 20 percent.

Nakajima et al. (1980) carried out mixed convection experiments in upward flow between parallel plates. The wall temperatures were different and the bulk temperature was nearly uniform between inlet and exit. It was possible to obtain aiding and opposing flows simultaneously on the heated and cooled sides, respectively. The change in the friction factor was calculated from the measured velocity profile near the wall. The friction factor was found to decrease in opposing flow with increasing buoyancy influence.

Abdelmeguid and Spalding (1979) employed numerical methods to determine the friction factor in mixed convection. They predicted that the friction factor increases monotonically with increasing buoyancy influence in aiding flow, and decreases slightly in opposing flow (Re = 25,000 and $5 \times 10^7 < \mathrm{Gr}_q < 3 \times 10^{10}$). In general, the agreements between experimental and numerical studies as well as among the experimental studies themselves are not good in aiding flow. The results of the experimental studies in opposing flow by Easby (1978) and by Nakajima et al. (1980) agree qualitatively.

In this study, the results of our mixed convection experiments are presented, and compared with previous experiments in the literature. We also attempted to separate the effects of the viscosity changes from the density changes to determine the effects of buoyancy forces alone.

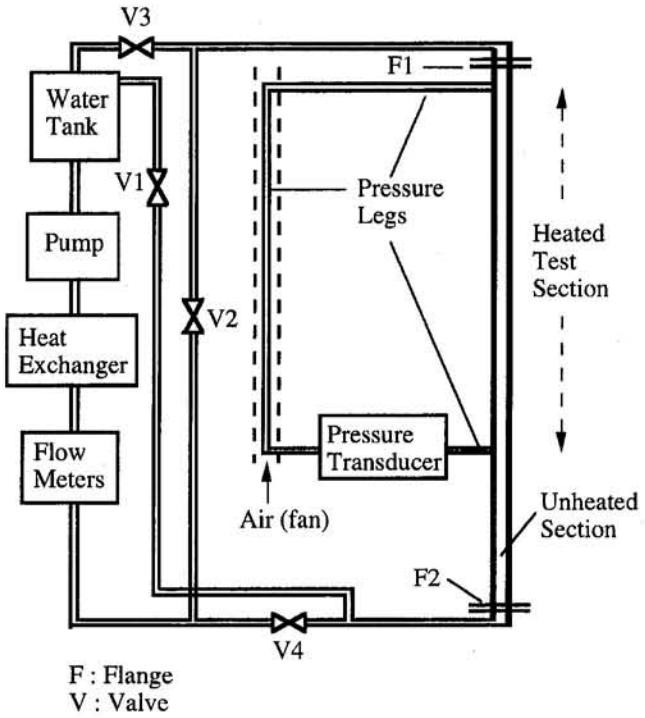

Fig. 1 Schematic of the experimental setup

2 Experimental Apparatus

Figure 1 shows a schematic of the experimental apparatus used to measure the friction factor and the Nusselt number in both aiding and opposing flows. The test section is a 3.50-m-long brass pipe of 26.64 mm ID and 3.38 mm wall thickness. The unheated flow development section is about 40D long, including a flow straightener in the upstream portion. The heated test section is about 80D long. Uniform heating is supplied by several glass-rope heaters wrapped around the pipe in a close spiral. Fiberglass thermal insulator jackets are used to cover the heaters to limit the heat loss to the environment.

Nomenclature

Bo = buoyancy number = $(8 \times 10^4 \cdot \mathrm{Gr}_q)/(\mathrm{Re}^{3.425}\,\mathrm{Pr}^{0.8})$
c_p = heat capacity
D = inside diameter of pipe
f = friction factor = $\Delta P_f \cdot 2D/\rho L V^2$ (Darcy factor)
f_o = isothermal friction factor in forced convection
g = gravitational acceleration
Gr_q = Grashof number = $\beta g q'' D^4/k\nu^2$
$\mathrm{Gr}_{\Delta T}$ = Grashof number = $\beta g(T_w - T_b)D^3/\nu^2$
k = thermal conductivity of fluid
L = test section length
Nu = Nusselt number = $q''D/k(T_w - T_b)$
$\mathrm{Nu}_{\mathrm{avg}}$ = pipe length averaged Nusselt number
Nu_o = Nusselt number in forced convection
P = pressure
ΔP = pressure drop
Pr = Prandtl number = ν/α
q'' = net wall heat flux
Q = volumetric flow rate
r = radial position
Re = Reynolds number = VD/ν
T = temperature
T_b = bulk temperature = $(\int_0^{D/2} 2\pi r \cdot v \cdot \mathrm{T} \cdot \mathrm{dr})/(\int_0^{D/2} 2\pi r \cdot v \cdot dr)$, assuming constant ρc_p
v = local axial velocity
V = bulk axial velocity
y^+ = dimensionless radial distance from the wall
α = thermal diffusivity
β = thermal expansion coefficient
ν = kinematic viscosity
ρ = density

Subscripts

a = acceleration
b = bulk averaged
e = test section exit
f = friction
FC = forced convection
g = gravitation
h = heat transfer coefficient = $q''/(T_w - T_b)$
i = test section inlet
ie = between test section inlet and exit
m = spatially averaged, e.g., $T_m = (\int_0^{D/2} 2\pi r \cdot T \cdot dr)/(\int_0^{D/2} 2\pi r \cdot dr)$
MC = mixed convection
pd = pressure transducer
pl = pressure leg(s)
vp = varying properties
w = wall

Deaerated water is supplied by a pump from a slightly pressurized helium–water tank. A constant temperature of about 30°C at the inlet is achieved by a heat exchanger, and the volumetric flow rate is measured by calibrated variable area flow meters placed in series. The same loop is used for both upward and downward flow configurations. The test section is inverted for downward flow measurements using two flanges: one near the inlet to the unheated test section and the other near the exit of the heated test section. Valves V1 and V2 are closed, and V3 and V4 are open in upward flow. The reverse is true for the valves in downward flow.

The bulk (mixing-cup) temperatures are obtained from thermocouples inserted inside the pipe at the inlet and exit of the heated section. A mixing element is used at the exit upstream of the thermocouple location. The wall temperature is measured by 13 thermocouples along the pipe (all thermocouples used in this experiment are of the copper-constantan type). Sheathed thermocouples are wrapped around the pipe inside a 2-mm-deep and wide groove and then welded to the pipe surface. With this configuration, it was possible to measure the temperature of the wall about 2 mm from the inside surface. The inside surface temperature is then calculated using the net heat flux through this wall thickness. The fluid temperatures are measured at five axial positions along the heated test section. Four thermocouples mounted at different radial positions on a small pin are inserted inside the pipe at each axial position to measure the temperature of the fluid across the turbulent core of the pipe. During the pressure drop measurements these thermocouples were temporarily removed, since they cause a small but nonnegligible pressure drop. We have visually inspected the inside surface of the pipe to confirm the absence of any protrusions that may affect the pressure reading or the pressure drop.

A differential pressure transducer calibrated against a manometer prior to data acquisition is used to measure pressure drop. Pressure legs, made of clear plastic (poly-flo) tubes, are used to connect the negative and positive sides of the pressure transducer to the inlet and exit of the heated portion of the test section, respectively. The pressure drop is measured along a heated length about 76D long. The pressure drop along the vertical section of the static pressure legs, $\Delta P_{g,pl}$, is calculated from the temperature of this section measured at several locations along the pressure leg. The temperature of the pressure leg is controlled, and a nearly uniform temperature is achieved by a heat exchanger placed around the pressure leg.

The ranges of parameters are as follows: $4100 < \mathrm{Re} < 9100$; $0.03 < \mathrm{Bo} < 1.3$; $3 \times 10^5 < \mathrm{Gr}_{\Delta T} < 7 \times 10^6$; $0.46 < \mu_w/\mu_b < 0.94$; $30°\mathrm{C} < T_b < 42°\mathrm{C}$; and $T_w < 88°\mathrm{C}$.

3 Data Reduction and Uncertainty Calculations

The friction pressure drop is calculated from the pressure differential measured by the pressure transducer, ΔP_{pd}, from the following equation:

$$\Delta P_{pd} = \Delta P_{f,ie} + \Delta P_{g,ie} + \Delta P_{a,ie} + \Delta P_{g,pl} \qquad (2)$$

where the first three pressure drop terms on the right-hand side are components of the total pressure drop inside the pipe and the fourth term is the pressure drop in the pressure leg. The friction pressure drop along the pipe, $\Delta P_{f,ie}$, is calculated from Eq. (2) by calculating the other three terms on the right-hand side. The following discussion summarizes the process.

For the acceleration pressure drop between the inlet and exit, one needs to know the momentum density, which requires the measurement of the velocity and temperature profiles at the inlet and exit. The acceleration pressure drop is two orders of magnitude smaller than the friction pressure drop. Hence, we have approximated the momentum density with the bulk density, which can be easily calculated by invoking an energy balance along the heated test section. That is

$$\Delta P_{a,ie} \approx (\rho V)^2 \left\{ \frac{1}{\rho_{be}} - \frac{1}{\rho_{bi}} \right\} \qquad (3)$$

To evaluate the gravitational pressure drop correctly along the heated section of the pipe, the spatially averaged fluid density must be known. The density evaluated at the bulk temperature, typically measured in experiments and calculated by lumped parameter analysis, differs from the density evaluated at the spatially averaged temperature. The fluid temperature across and along the pipe in the turbulent core region is measured at 20 positions (four thermocouples at five axial locations). The temperature drops sharply with the distance from the wall in the vicinity of the wall. The flow area between the closest temperature point (about 1 mm from the wall) and the wall is about 19 percent of the total area. For the wall region, a linear temperature profile was assumed between the closest temperature measurement point and the wall at the same axial position.

The gravitational pressure drop along the vertical sections of the pressure leg is calculated with a spatially averaged fluid density determined by interpolating the measured temperatures at five axial positions along the leg. The temperature of the leg is controlled by a heat exchanger to increase the accuracy of the pressure measurements by bringing the pressure drop near the maximum range of the transducer where the accuracy of the pressure transducer is higher.

The net total heat input was determined from the energy balance by measuring the bulk (mixed-cup) temperature increase along the heated section. The electrical power was also measured with a voltmeter. The heat loss from the system was about 5–15 percent of electrical power.

The Nusselt number was calculated from the following equation:

$$\mathrm{Nu}(z) = \frac{h(z)D}{k} = \frac{q''(z)D}{k\{T_w(z) - T_b(z)\}} \qquad (5)$$

where q'', T_w, and T_b are the net heat flux, wall, and bulk temperature as a function of axial position, respectively. The net heat flux and bulk temperature are determined from the energy balance and bulk temperature measurements, and the wall temperature was measured with 14 thermocouples soldered into the grooves prepared in the pipe wall.

The uncertainty associated with the friction factor and heat transfer coefficient is calculated from a statistical summation formula (Sirohi and Krishna, 1983). The dominant source of uncertainty in the friction factor is that associated with the gravitation pressure drop inside the pipe. The mean uncertainty values of the friction factor, Nu, and Bo numbers are 15, 8, and 15 percent, respectively. The corresponding maximum values are 23, 11, and 30 percent. Details of the uncertainty calculations can be found in Parlatan (1993).

4 Results and Discussion

(A) Experimental Results: Friction Factor. Figure 2 shows isothermal friction factor results of the current experiments in the same Reynolds number range. Our friction factor data fall randomly within ±10 percent of the Blasius correlation, $f_o = 0.3164 \cdot \mathrm{Re}^{-0.25}$ (Irvine and Karni, 1987).

Figure 3 shows friction factor results for both aiding and opposing turbulent mixed convection. The friction factor behavior, f/f_o, is plotted against relative buoyancy influence, in terms of the Bo number. Bo number and $\mathrm{Gr}_{\Delta T}/\mathrm{Re}^n\ \mathrm{Pr}^m$ are widely used in the literature to express the relative importance of buoyancy forces, where $1 < n < 2.7$ and $0 < m < 0.5$ (Jackson et al., 1989). Since $\mathrm{Gr}_{\Delta T} = \mathrm{Gr}_q/\mathrm{Nu}$, and assuming $\mathrm{Nu} \sim \mathrm{Re}^{0.8}\ \mathrm{Pr}^{0.4}$, the Bo number is equivalent to $\mathrm{Gr}_{\Delta T}/\mathrm{Re}^n\ \mathrm{Pr}^m$, where $n \sim 2.6$ and $m = 0.4$. The Bo number was originally developed by Hall and Jackson (1969) from considerations of modified

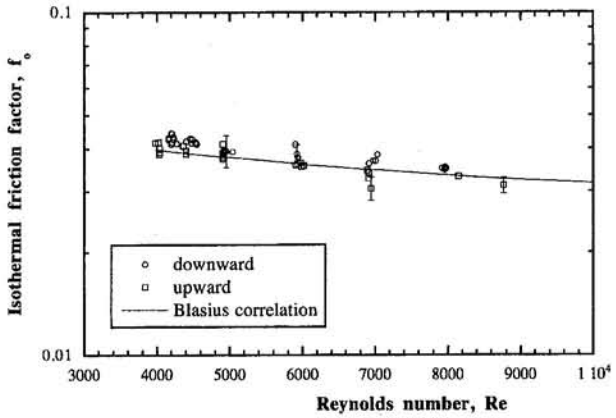

Fig. 2 Isothermal friction factor in current experiments

shear production of turbulent kinetic energy under mixed convection conditions. The Nusselt number behavior in mixed convection for gases from various sources was shown by Cotton and Jackson (1990) to be in good agreement when plotted in terms of the Bo number.

Experimental results of this study are also shown in Table 1. The physical properties are evaluated using the bulk temperature halfway between the inlet and exit of the heated test section. Since the physical properties evaluated at the local bulk temperature do not change significantly in our experiments, the dimensionless numbers evaluated at the axial midpoint adequately represent test section conditions.

The friction factor in aiding mixed convection remains nearly unchanged at low Bo numbers ($Bo < 0.1$). A 10 percent decrease in the friction factor is observed for $0.1 < Bo < 0.2$, and up to about 25 percent increase for $0.25 < Bo < 0.4$. The friction factor in opposing mixed convection, on the other hand, decreases monotonically by as much as 25 percent under similar buoyancy influence. Even though the deviation of f/f_o for individual data points is comparable to the error associated with it, the trend for the friction factor is clear for both aiding and opposing flows.

The behavior of friction factor in mixed convection can be explained by the modifications in the velocity profile near the pipe wall; an extended discussion can be found in Hall and Jackson (1969). In aiding flow, the flow direction and the buoyancy force near the wall are aligned and therefore the fluid is accelerated near the wall. However, the fluid near the center is decelerated, since the flow and buoyancy forces are in opposite directions. Consequently, the peak velocity shifts from the center toward a region near the wall and the velocity gradient in the vicinity of the wall becomes steeper, which increases the wall shear stress.

In opposing flow, the velocity decreases near the wall and increases near the center due to the buoyancy forces. The peak velocity is at the center, and its value is higher than that in forced convection at the same flow rate. Thus the velocity gradient near the wall becomes less steep, and the shear stress at the wall and friction factor decrease.

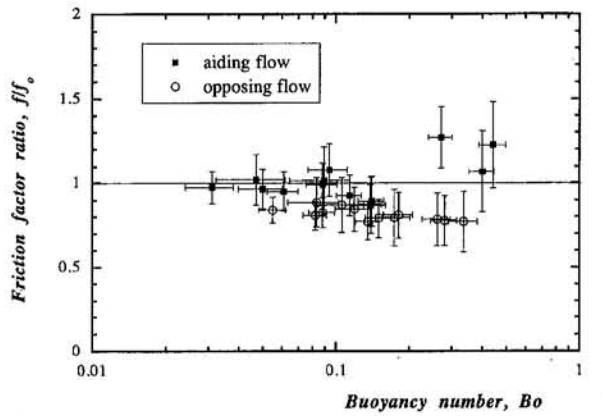

Fig. 3 Friction factor results in mixed convection

(B) Buoyancy Effects Versus Physical Property Effects: Friction Factor. The modifications in the friction factor and heat transfer coefficient in mixed convection are due to the combined effect of buoyancy forces as well as viscosity variations. Viscosity variations can be expressed in terms of dynamic viscosity ratio, μ_b/μ_w. The changes in the heat transfer and friction were often attributed only to buoyancy forces in the literature; see, for example, Carr et al. (1973), Easby (1978), Polyakov and Shindin (1988), and Nakajima et al. (1980). It is of interest to separate the effects of viscosity variations from the buoyancy forces.

There are several relations offered for the friction factor correction for viscosity variations in the literature (Kakaç, 1987, or Petukhov, 1970). Petukhov compiled data from several investigators and offered the following correlation for the friction factor in heated turbulent flow of liquids far from a supercritical state:

$$\frac{f_{vp}}{f_o} = \frac{1}{6}\left(7 - \frac{\mu_b}{\mu_w}\right) \tag{4}$$

where μ_b and μ_w are viscosities evaluated at the bulk (mixed-cup) and wall temperatures, respectively. To separate the effects of buoyancy forces from those of properties, we have calculated f_{vp}, which incorporates the effects of variable physical property variations from Eq. 4, but not those of buoyancy forces. The effect of viscosity variations decreases the friction factor in heated water flows regardless of the flow orientation: upward, downward, or horizontal. Since f_{vp} is always smaller than f_o (constant property friction factor), the ratio f/f_{vp} is greater than the ratio f/f_o. To quantify the effects of buoyancy forces alone, our experimentally measured f value is compared to the f_{vp} value. The increase in the friction factor becomes steeper in aiding flow, and the decrease in the friction factor shallower in opposing flow. Figure 4 shows this behavior. The increase in the friction factor due only to buoyancy forces increases with Bo number in upward flow, and it is as much as 50 percent higher near $Bo = 0.3$ than would be observed in a negligible buoyancy effect flow. In downward flow, f/f_{vp}, is about 5 percent greater than the ratio, f/f_o.

(C) Comparison With Previous Experiments: Friction Factor. A comparison of our results with the previous experimental and computational results in the literature is shown in Figs. 5(a, b). The literature contains two trends for the friction factor with increasing Bo number: an increasing trend (Nakajima, 1980; Abdelmeguid and Spalding, 1988), and a first decreasing then increasing trend (Carr et al., 1973; Polyakov and Shindin, 1988). Our results fall between these two trends. In downward flow, the friction factor decreases with increasing buoyancy influence, and our results agree qualitatively with those of Easby (1978), Nakajima et al. (1980), and Abdelmeguid and Spalding (1979). However, all our experimental results show a sharper decline than the Abdelmeguid and Spalding calculations.

All of the above-mentioned experiments have a flow development section prior to the heated section. However, flow continues to develop in the heated section. Since the measurement technique used by Carr et al., Nakajima et al., and Polyakov and Shindin allowed friction factor to be measured only at a fixed axial location (at $L/D = 100$, 110, and 53, respectively),

Table 1 Results of current experiment

Run No.	Re	$Gr_{\Delta T}$ x10^{-6}	Pr	Bo	f	$\frac{f}{f_o}$	$\frac{\mu_w}{\mu_b}$	$\frac{f_{vp}}{f_o}$	T_b °C	T_m °C	T_w °C	Nu_{av}	$\frac{Nu_{av}}{Nu_o}$
1 U	7513	4.730	4.97	0.138	0.0287	0.875	0.51	0.84	34.55	38.91	74.63	24.3	0.492
2 U	7391	2.110	5.06	0.114	0.0306	0.926	0.70	0.93	33.67	36.32	53.84	41.6	0.848
3 U	7200	0.988	5.22	0.061	0.0317	0.951	0.84	0.97	32.28	33.55	42.09	46.8	0.967
4 U	7031	0.474	5.36	0.031	0.0328	0.975	0.91	0.98	31.04	31.68	36.02	47.1	0.984
5 U	6069	0.538	5.38	0.050	0.0344	0.967	0.90	0.98	30.85	31.55	36.68	39.7	0.930
6 U	5012	0.653	5.40	0.094	0.0409	1.08	0.87	0.98	30.67	31.63	38.10	31.5	0.858
7 U	4163	1.080	5.36	0.151					31.07		42.26	16.6	0.527
8 U	4143	0.405	5.38	0.089	0.0408	1.014	0.92	0.98	30.82	31.49	35.49	24.8	0.800
9 U	4990	0.304	5.43	0.047	0.0388	1.020	0.94	0.99	30.44	30.84	33.85	33.8	0.925
10 U	5087	1.610	5.31	0.139	0.0328	0.869	0.75	0.94	31.44	33.61	47.77	20.1	0.544
11 U	4210	2.060	5.29	0.249					31.65		53.59	14.3	0.453
12 U	6218	1.050	5.24	0.088	0.0350	0.992	0.82	0.96	32.11	33.49	42.77	37.6	0.871
13 U	5268	3.130	5.10	0.227					33.29		61.50	17.8	0.474
14 U	4391	3.240	5.04	0.497					33.89		67.24	19.3	0.538
15 U	4578	4.620	4.82	0.771					36.01		78.06	28.1	0.833
16 U	5462	4.480	4.90	0.398	0.0394	1.068	0.47	0.82	35.23	37.50	79.09	22.7	0.595
17 U	6341	2.820	5.12	0.140	0.0312	0.893	0.65	0.91	33.15	35.94	58.30	24.0	0.551
18 U	6689	5.540	4.81	0.270	0.0436	1.271	0.46	0.81	36.04	40.25	81.36	24.8	0.556
19 U	4658	2.590	5.19	0.259					32.55		58.81	16.3	0.478
20 U	4837	3.540	4.97	0.441	0.0471	1.226	0.54	0.86	34.56	36.91	70.66	21.0	0.605
21 U	5220	6.930	4.55	0.920					38.77		87.29	27.8	0.772
22 D	5154	1.090	5.23	0.181	0.0325	0.81	0.82	0.96	32.13	33.35	42.85	40.2	1.085
23 D	5307	1.720	5.06	0.279	0.0309	0.776	0.76	0.95	33.68	35.48	48.99	42.0	1.114
24 D	5646	3.140	4.71	0.498					37.05		60.02	48.0	1.240
25 D	5956	4.950	4.43	0.730					40.05		70.69	52.1	1.312
26 D	5112	0.740	5.28	0.119	0.340	0.845	0.87	0.98	31.70	32.62	39.19	38.0	1.026
27 D	4653	0.815	5.19	0.174	0.0328	0.794	0.87	0.97	32.49	33.42	40.32	36.0	1.057
28 D	4366	0.812	5.29	0.204					31.63		39.93	34.5	1.058
29 D	4339	0.433	5.33	0.106	0.0367	0.871	0.92	0.98	31.30	31.95	35.92	32.3	0.993
30 D	4671	0.424	5.31	0.083	0.0366	0.886	0.92	0.99	31.50	32.05	35.82	34.2	0.992
31 D	4783	1.260	5.16	0.260	0.0321	0.783	0.81	0.96	32.74	34.14	44.67	38.1	1.092
32 D	4527	1.350	5.08	0.334	0.0321	0.771	0.80	0.96	33.54	34.97	45.78	37.4	1.128
33 D	4999	1.960	4.91	0.390					35.11		51.24	41.4	1.166
34 D	6333	1.530	5.13	0.150	0.0299	0.791	0.78	0.95	33.08	34.70	47.10	47.1	1.082
35 D	7357	1.370	5.18	0.088	0.0297	0.824	0.79	0.96	32.64	34.17	45.58	52.5	1.067
36 D	8468	1.250	5.15	0.055	0.0289	0.840	0.81	0.96	32.86	34.40	44.39	58.3	1.060
37 D	8640	1.900	5.03	0.082	0.0276	0.808	0.75	0.94	33.93	36.15	50.38	59.8	1.079
38 D	7582	2.140	5.00	0.135	0.0275	0.771	0.73	0.94	34.25	36.62	52.58	54.8	1.099
39 D	6606	2.470	4.89	0.234					35.35		55.25	50.7	1.142
40 D	5048	3.010	4.73	0.637					36.90		59.09	44.2	1.246
41 D	4868	3.890	4.67	0.756					37.50		60.13	43.8	1.278
42 D	7702	2.780	4.91	0.173					35.10		57.43	56.6	1.125
43 D	6710	3.190	4.80	0.302					36.21		60.52	52.8	1.181
44 D	5293	4.970	4.60	0.782					38.27		65.14	47.2	1.306
45 D	5020	4.140	4.51	0.983					39.23		66.18	46.9	1.349
46 D	8740	2.500	4.97	0.108					34.55		55.40	61.4	1.100
47 D	6993	4.340	4.57	0.390					38.50		67.51	55.8	1.225
48 D	7930	3.730	4.75	0.223					36.70		64.19	58.7	1.153
49 D	9059	3.410	4.77	0.139					36.51		61.89	63.7	1.123
50 D	5518	5.150	4.38	0.987					40.62		72.06	50.8	1.365
51 D	5251	5.600	4.28	1.273					41.79		73.48	50.4	1.420

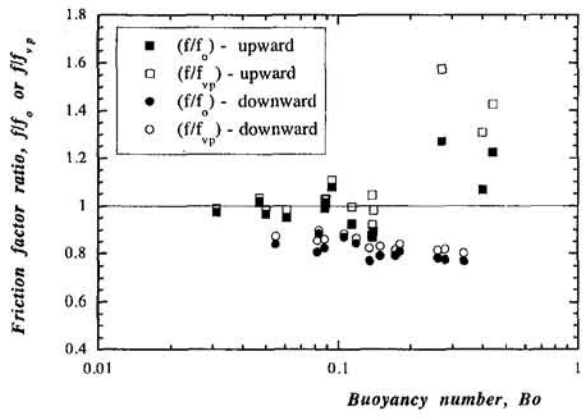

Fig. 4 Effects of variable physical properties and buoyancy forces

the comparison of their data with our average friction factor data over 0–80D in aiding flow becomes questionable if the flow developing effects cause a nonnegligible axial variation in the friction factor. In opposing flow, on the other hand, Easby measured the average friction factor over several intervals in the heated section. His results suggest that the friction factor does not have a length dependence.

The foregoing comparisons are based on the overall change in the friction factor; the effects of varying physical properties are not separated. A comparison of friction factor ratio solely due to buoyancy forces, f/f_{vp}, between our experiments and those in the literature would be more useful. For gases, the correlation, $f_{vp}/f_o = (T_w/T_b)^m$, is used to account for property variations (Perkins and Worsøe-Schmidt, 1965). However, the wall-to-bulk (absolute) temperature ratio was not available from Nakajima et al. (1980) and Polyakov and Shindin (1988). For Easby's data, f_{vp}/f_o is calculated from the above-mentioned correlation with $m = -0.264$. Carr et al. measured the wall temperature, and hence, we assume that the viscosity used in

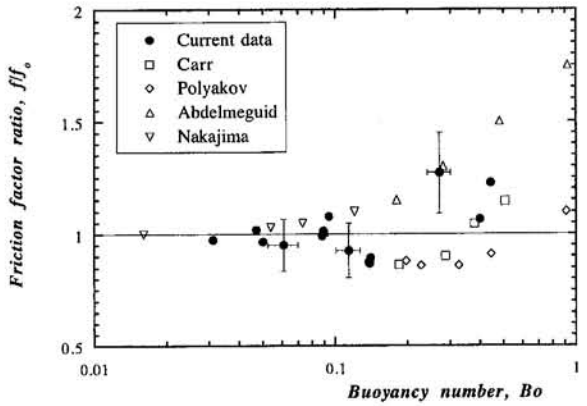

Fig. 5(*a*) Comparison of current experiment with previous work: friction factor in aiding flow

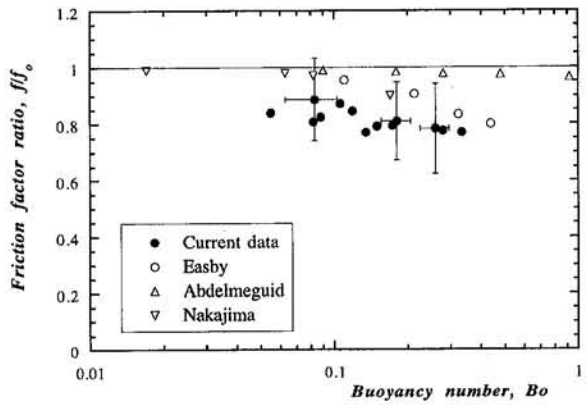

Fig. 5(*b*) Comparison of current experiment with previous work: friction factor in opposing flow

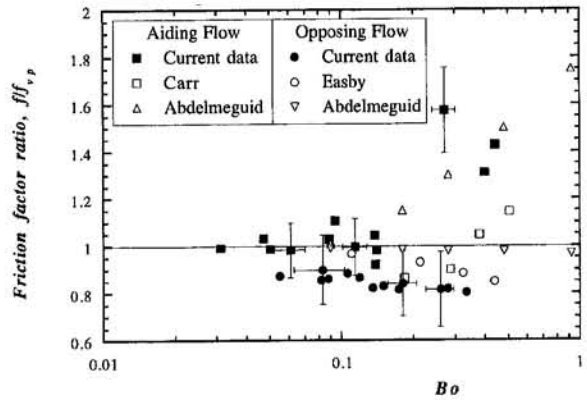

Fig. 5(*c*) Comparison of current experiment with previous work: buoyancy effects only

the friction factor calculation was evaluated at the wall temperature, and therefore, property variation effects were already accounted for in their data.

Figure 5(*c*) shows a comparison of our experimental f/f_{vp} results with these data. Our upward results lie again between the data of Carr et al. and Abdelmeguid and Spalding. However, when the property effects are accounted for, our data agree very well with the constant property results of Abdelmeguid and Spalding. In downward flow, the agreement between our data and that of Easby and Abdelmeguid and Spalding also improves slightly.

(D) Experimental Results and Comparison With Literature: Heat Transfer Coefficient. The heat transfer coefficient was found to be nearly uniform along the pipe in downward flow. However, four different heat transfer types were observed along the pipe in upward flow depending on the magnitude of the Bo number, which was nearly uniform along the tube: (1) No noticeable change in the heat transfer coefficient with axial position for Bo $<$ 0.125; (2) a substantial drop in the heat transfer coefficient without a recovery for 0.125 $<$ Bo $<$ 0.265; (3) a substantial drop in the heat transfer coefficient with a moderate recovery for 0.265 $<$ Bo $<$ 0.65; and (4) some drop in the heat transfer coefficient with a strong recovery for Bo $>$ 0.65. Figure 6 shows the heat transfer coefficient as a function of axial location for four cases with nearly the same Reynolds number. The Bo number was nearly uniform along the heated length in our experiments. The impairment in heat transfer coefficient, which corresponds to a local wall temperature peak, reaches a maximum due to thermal boundary layer development, and the location of this impairment moves upstream with increasing Bo. A Type 2 profile was observed in our experiments, probably due to the limited length-to-diameter ratio: For a longer tube, a recovery would be expected as in Type 3; see Fig. 6. The observed minimum values of heat transfer coefficient and their axial location in our experiment also agree well with the correlations proposed by Jackson et al. (1989).

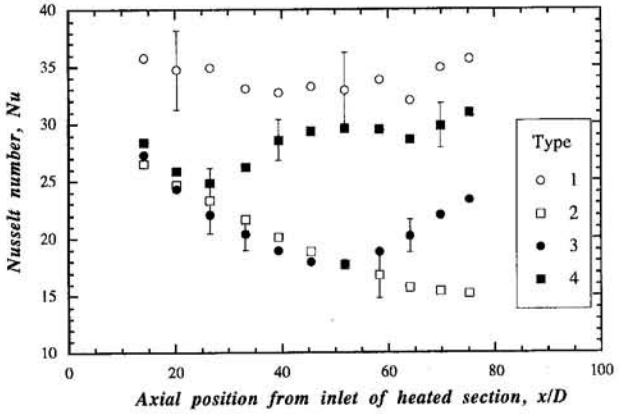

	Run No.	Bo_{av}	Re_{av}	Pr_{av}	Nu_{av}	Nu_{av}/Nu_o	Nu_{min}/Nu_{ave}
Type 1:	9U	0.05	5000	5.4	34	0.93	0.94
Type 2:	10U	0.14	5100	5.3	20	0.54	0.75
Type 3:	20U	0.44	4800	5.0	21	0.60	0.85
Type 4:	15U	0.77	4600	4.8	28	0.83	0.89

Fig. 6 Heat transfer coefficient results of current experiments in aiding flow

Average values of Nu number along the pipe were also calculated. The average Nu number monotonically increases with increasing Bo number in downward flow, and exhibits a sharp decrease at Bo of 0.1–0.2 for upward flow. The reduction in the Nusselt number is as large as 50 percent of Nu_o. After this minimum point, the average Nu number starts to increase again and recovers to Nu_o at about Bo $\geq$ 1, Fig. 7. Similar results were reported previously in the literature and comparisons with these results are also shown in this figure.

The main difference between this study and others in the literature is that we have used water (Pr = 3–5) and the others used air or other gases (Pr = 0.7). Jackson et al. (1990) have developed the following semi-empirical correlation based on experimental data as well as shear stress considerations:

$$\frac{Nu}{Nu_o} = \left\{1 \pm \frac{Bo}{(Nu/Nu_o)^2}\right\}^{0.46} \qquad (6)$$

where the + sign is for downward flow and the − sign is for upward flow. This equation is valid only near forced convection

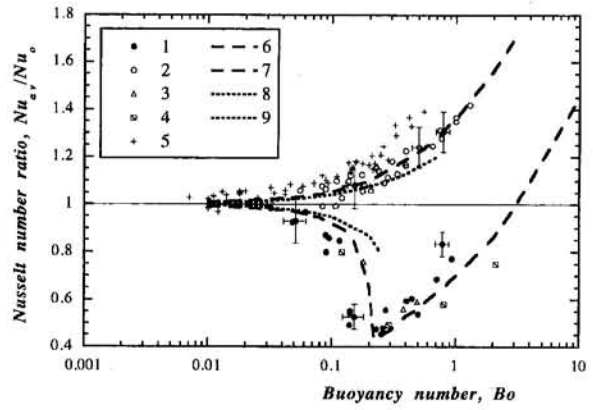

1: Current experiments in aiding flow (water)

2: Current experiments in opposing flow (water)

3: Carr et al's aiding flow experiments (air)

4: Steiner's aiding flow experiments (air)

5: Easby's opposing flow experiments (nitrogen)

6-7: Cotton et al. calculations in aiding and opposing flow (air)

8-9: Jackson's correlation in aiding and opposing flow

Fig. 7 Comparison of current experiment with previous work: heat transfer coefficient

conditions, and can not predict the minimum or the recovery of the heat transfer coefficient. Cotton and Jackson (1990) solved the governing mass, momentum, and energy equations using a low-turbulence $k-\epsilon$ model. The three experimental studies included in the comparison are those of Carr et al. (1973), Steiner (1971), and Easby (1978). The data of Carr et al. were taken at $z/D = 103$, Steiner's data at $z/D = 60$, and Easby's data at $z/D = 33$ to 167.

Our downward flow results agree well with the Jackson correlation and Cotton's numerical results, but are slightly lower than Easby's results. Our upward flow results, including the maximum impairment point of Bo $\sim$ 0.2, generally agree well with the others.

5 Conclusions

The friction factor and heat transfer coefficient behavior are experimentally determined in aiding and opposing turbulent mixed convection flow conditions for water in a vertical pipe in the following range: $4160 \le Re \le 9060$, $0.30 \le Gr_{\Delta T} \times 10^{-6} \le 6.93$, and $4.28 \le Pr \le 5.43$, or in terms of relative buoyancy influence, $0.03 \le Bo \le 1.27$. We have observed that:

1 The friction factor ratio, f/f_o, stays near unity near the forced convection regime. With increasing buoyancy influence, the friction factor increases by about 25 percent in upward flow, and decreases by about 25 percent in downward flow.

2 The combined effects of buoyancy forces and varying physical properties are analyzed. When the viscosity variations are taken into account, the friction factor increases at a faster rate in upward flow and decreases at a slower rate in downward flow than for the case when they are not taken into account.

3 Our experimental friction factor results are compared with previous experimental and numerical studies in the literature. There is poor agreement among previous studies. Our results agree well with some of the previous results.

4 We have observed that the average heat transfer coefficient decreases sharply with increasing buoyancy influence near Bo = 0.20 and then recovers in aiding flow. The heat transfer coefficient monotonically increases in opposing flow. Our heat transfer coefficient results with water agree well with the previous studies using gas.

References

Abdelmeguid, A. M., and Spalding, D. B., 1979, "Turbulent Flow and Heat Transfer in Pipes With Buoyancy Effects," *J Fluid Mech.*, Vol. 94, part 2, pp. 383–400.

Axcell, B. P., and Hall, W. B., 1978, "Mixed Convection to Air in a Vertical Pipe," *Proc. Int. Mass and Heat Transfer Conference*, Toronto, Canada, pp. 37–42.

Carr, A. D., Connor, M. A., and Buhr, H. O., 1973, "Velocity, Temperature and Turbulence Measurements in Air for Pipe Flow With Combined Free and Forced Convection," ASME JOURNAL OF HEAT TRANSFER, Vol. 95, pp. 445–452.

Cotton, M. A., and Jackson, J. D., 1990, "Vertical Tube Air Flows in the Turbulent Mixed Convection Regime Calculated Using a Low-Reynolds $k \sim \epsilon$ Model," *Int. J. Heat Mass Transfer*, Vol. 33, No. 2, pp. 275–286.

Easby, J. P., 1978, "The Effect of Buoyancy on Flow and Heat Transfer for a Gas Passing Down a Vertical Pipe at Low Turbulent Reynolds Numbers," *Int. J Heat Mass Transfer*, Vol. 21, pp. 791–801.

Hall, W. B., and Jackson, J. D., 1969, "Laminarization of a Turbulent Pipe Flow by Buoyancy Forces," ASME Paper No. 69-HT-55.

Irvine, T. F., and Karni, J., 1987, "Non-Newtonian Fluid Flow and Heat Transfer," in: *Handbook of Single-Phase Convective Heat Transfer*, S. Kakaç, R. K. Shah, and W. Aung, eds., Wiley, New York.

Jackson, J. D., Cotton, M. A., and Axcell, B. P., 1989, "Studies of Mixed Convection in Vertical Tubes," *Int. J. Heat Fluid Flow*, Vol. 10, pp. 2–15.

Jackson, J. D., et al., 1990, "Experimental and Computational Studies of Turbulent Forced and Mixed Convection Heat Transfer to Water in a Vertical Pipe," in: *Engineering Turbulence Modelling and Experiments*, W. Rodi and E. N. Ganic, eds., Elsevier Science Publishing Co., New York, pp. 809–818.

Kakaç, S., 1987, "The Effect of Temperature-Dependent Fluid Properties on Convective Heat Transfer," in: *Handbook of Single-Phase Convective Heat Transfer*, S. Kakaç, R. K. Shah, and W. Aung, eds., Wiley, New York.

Kays, W. M., and Perkins, H. C., 1973, "Forced Convection, Internal Flow in Ducts," in: *Handbook of Heat Transfer*, W. M. Rohsenow and J. P. Hartnett, eds., McGraw-Hill, New York.

Nakajima, M., et al., 1980, "Buoyancy Effects on Turbulent Transport in Combined Free and Forced Convection Between Vertical Parallel Plates," *Int. J. Heat Mass Transfer*, Vol. 23, pp. 1325–1336.

Parlatan, Y., 1993, "Friction Factor and Nusselt Number Behavior in Turbulent Mixed Convection in Vertical Pipes," Ph.D. thesis, Nuclear Engineering Department, Massachusetts Institute of Technology, Cambridge, MA.

Perkins, H. C., and Worsøe-Schmidt, 1965, "Turbulent Heat and Momentum Transfer for Gases in a Circular Tube at Wall to Bulk Temperature Ratios to Seven," *Int. J. Heat Mass Transfer*, Vol. 87, pp. 67–76.

Petukhov, B. S., and Strigin, B. K., 1968, "Experimental Investigation of Heat Transfer With Viscous-Inertial-Gravitational Flow of a Liquid in Vertical Tubes," *High Temperature*, Vol. 6, pp. 933–937.

Petukhov, B. S., 1970, "Heat Transfer and Friction Factor in Turbulent Pipe Flow With Variable Physical Properties," in: *Advances in Heat Transfer*, Vol. 6, Orlando, Academic Press, pp. 503–564.

Petukhov, B. S., and Polyakov, A. F., 1988, *Heat Transfer in Turbulent Mixed Convection*, Hemisphere Publishing Corporation, Washington, DC.

Polyakov, A. F., and Shindin, S. A., 1988, "Development of Turbulent Heat Transfer Over the Length of Vertical Tubes in the Presence of Mixed Air Convection," *Int. J. Heat Mass Transfer*, Vol. 31, pp. 987–992.

Sirohi, R. S., and Krishna, H. C. R., 1983, *Mechanical Measurements*, Wiley, New York.

Steiner, A. A., 1971, "On the Reverse Transition of a Turbulent Flow Under the Action of Buoyancy Forces," *J. Fluid Mechanics*, Vol. 47, pp. 503–512.

J. Zaworski

J. R. Welty

Department of Mechanical Engineering,
Oregon State University,
Corvallis, OR 97331

B. J. Palmer

M. K. Drost

Pacific Northwest Laboratory,[1]
Richland, WA 99352

Comparison of Experiment With Monte Carlo Simulations on a Reflective Gap Using a Detailed Surface Properties Model

The spatial distribution of light through a rectangular gap bounded by highly reflective, diffuse surfaces was measured and compared with the results of Monte Carlo simulations. Incorporating radiant properties for real surfaces into a Monte Carlo code was seen to be a significant problem; a number of techniques for accomplishing this are discussed. Independent results are reported for measured values of the bidirectional reflectance distribution function over incident polar angles from 0 to 90 deg for a semidiffuse surface treatment (Krylon™ flat white spray paint). The inclusion of this information into a Monte Carlo simulation yielded various levels of agreement with experimental results. The poorest agreement occurred when the incident radiation was at a grazing angle with respect to the surface and the reflectance was nearly specular.

1 Introduction

Radiative transfer between discrete surfaces is often treated using a diffuse gray approximation for surface properties. This removes the directional dependence of the reflectance and makes possible the development of analytical solutions for a wide range of problems. Unfortunately, the model of reflection as diffuse is not a particularly good approximation for most real surfaces. A modification to the diffuse-gray approximation is to replace real surface properties (which are generally neither specular nor diffuse but somewhere in between) with a combination of reflectances, one representing a purely diffuse component and the other representing a purely specular component (Modest, 1993). A difficulty with this model can be seen in Fig. 1, which shows the actual reflectance properties for a semi-diffuse surface. It is clear from this picture that application of the diffuse-specular model for incident polar angles of more than approximately 30 deg and less than approximately 80 deg will require some judgment to define what portion of the hemispheric reflectance is to be considered specular and what part diffuse. This approach also requires that the radiative transfer equation be modified to make use of separate diffuse and specular view factors. Although this model is an improvement over the diffuse-gray model, it still presents difficulties when dealing with properties that are dependent on the angle of incidence.

An alternative to the analytical approach, one for which the inclusion of surface property data is a reasonable proposition, is to use a Monte Carlo model. The specular-diffuse approximation, as well as more complicated surface property models, can easily be incorporated into a Monte Carlo algorithm. Toor and Viskanta have used Monte Carlo techniques to show that the radiative properties of simple systems can depend sensitively on the dependence of the reflectivity on the incident angle (Toor, 1967; Toor and Viskanta, 1968). This calculation would present almost insurmountable difficulties if attempted using an analytical approach. Numerous authors have described Monte Carlo codes that are good candidates for this type of problem (Palmer et al., 1995; Maltby and Burns, 1991; Burns and Pryor, 1989). For the numerical approach, bidirectional reflectance data can be tabulated on a discrete grid and then numerically inverted to prepare a look-up table for generating the correct distribution of postreflectance photon directions. The accuracy of this procedure depends on the density of points used to measure the bidirectional reflectance. Alternatively, the data can be modeled using an analytic form to describe the bidirectional reflectance as a function of incident angle.

Regardless of the model used to predict radiative transfer between surfaces, if detailed surface property data are to be used, they must first be available. In this paper, a single type of surface is considered. It is a semi-diffuse surface created by coating a smooth aluminum substrate with a flat white paint. The bidirectional reflectance distribution function (BRDF) of this surface was previously measured (Zaworski et al., 1993), and the results are used as input data for a Monte Carlo simulation. The data reduction required to prepare the BRDF data for use in a Monte Carlo code is described, and the resulting surface properties model is incorporated in a cell-to-cell transport Monte Carlo program. The program is then used to predict radiative transfer through a parallel-plate channel having the same surface treatment. Specific cases are selected to fully exercise the surface properties model; cases range from mostly specular reflection through the plates, to cases in which the reflection is mostly diffuse. The results predicted by the Monte Carlo model are confirmed through direct comparison with experimental findings.

2 The Problem Defined

The primary goal of this research was the validation of a surface properties model that includes the full bidirectional reflectance distribution function using a Monte Carlo algorithm. The Monte Carlo program was validated by direct comparison of the simulation output with experimental data for radiative transfer through a channel formed by parallel plates. As shown in Fig. 2, the problem was to predict the intensity $i_a(x)$ at the exit plane, given the intensity of a beam i_i directed through the entry plane to one of the two surfaces. The angle α describes the orientation of the incident beam with respect to the centerline and x is the position along the exit plane. The point $x = 0$ is located at the intersection of the centerline with the exit plane.

[1] Pacific Northwest Laboratory is operated for the U.S. Department of Energy by Battelle Memorial Institute under Contract No. DE-AC06-76RLO 1830.

Contributed by the Heat Transfer Division for publication in the JOURNAL OF HEAT TRANSFER. Manuscript received by the Heat Transfer Division August 1995; revision received January 1996. Keywords: Numerical Methods, Radiation, Radiation Interactions. Associate Technical Editor: M. Modest.

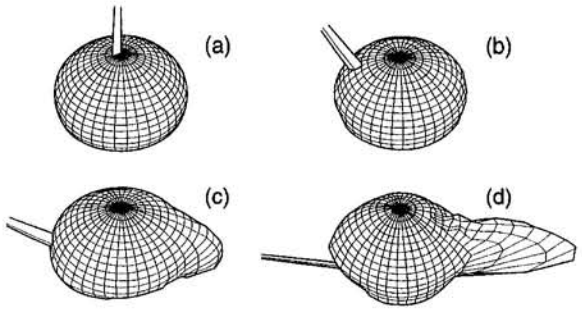

Fig. 1 Plots of log (BRDF) as a function of incident angle for a 632.5-nm source irradiating surface of flat white paint (Krylon™ No. 6502). The sharp feature in each plot is the incident beam. (*a*) $\theta_i = 0$ deg. (*b*) $\theta_i = 30$ deg. (*c*) $\theta_i = 60$ deg. (*d*) $\theta_i = 80$ deg.

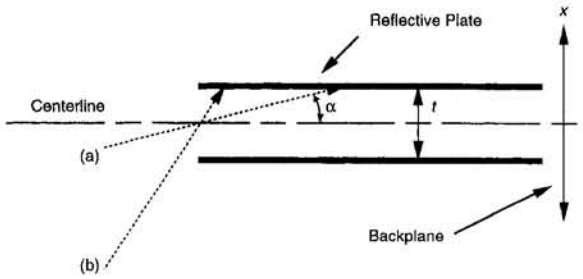

Fig. 2 Reflections through a channel for (*a*) small α and (*b*) large α

Depending on (1) the angle at which the incident beam strikes the plate and (2) the plate spacing, the nature of successive reflections through the channel can range from highly specular to highly diffuse.

The data of interest in this study were intensities at the exit plane of the channel as a function of exit plane position x, incident angle α, and plate spacing t. The full hemispherical intensity was measured at the exit plane along the line corresponding to the intersection of the backplane with the plane of incidence. The wavelength was held constant at 632.8 nm to match the data for which bidirectional surface properties were available. Temperatures were maintained near 20°C so that the only significant mechanism for radiative transfer was reflection. Polarization was not considered in this study (incident radiation was randomly polarized).

The surface used in the experimental effort is an aluminum substrate finished with 600-grit emery paper and then painted with three coats of Krylon™ spray paint No. 6502, Flat White. Bidirectional reflectance was measured for this material at a wavelength of 632.8 nm and with random incident beam polarization (Zaworski et al., 1993). The hemispherical reflectance varies slightly with incident polar angle but is generally in the range of 0.8. The bidirectional reflectance varies greatly with incident polar angle as shown in Fig. 1. A specular-like component starts to appear at an incident angle of approximately 45 deg and grows substantially as the angle increases. The bidirectional reflectance for this material is symmetric about the plane of incidence but is clearly a function of both the incident and reflected polar angles. Values of bidirectional reflectance average approximately 0.3 for the nearly diffuse cases of Fig. 1(*a*) and 1(*b*). For the strongly specular case shown in Fig. 1(*d*), the bidirectional reflectance varies from a low of 0.002 to a peak of 4.0. The uncertainty of these measurements is generally under 2 percent, with slightly higher values occurring at large incident polar angles.

3 The Monte Carlo Model

The Monte Carlo program used in this study, MCLITE, divides an array into rectangular computational cells where each cell contains one array element. The interaction of a photon with the element in a cell is predicted by geometric optics, and the location and characteristics of the photon as it exits the cell are calculated. This information is used to predict the photon entrance location for the next computational cell. The photon moves from cell to cell, interacting with array elements until it is absorbed or exits the array. The code calculates the location and angle of each photon exiting the array and the distribution of absorbed photons within the array. Cell-to-cell photon transport has proved to be an efficient method of modeling radiation heat transfer in arrays of discrete surfaces. A detailed description of cell-to-cell photon transport is presented by Palmer et al. (1995). Similar algorithms have been described by Maltby and Burns (1991). Only two cells were required for the simulations described here, with one cell containing a rectangular reflector element plus the gap space and the second cell containing a second rectangular reflector element that forms the other side of the gap. These were arranged to produce a gap with the same dimensions as the experimental system. The cells and reflector elements for the symmetric gap are shown in Fig. 3. The Monte Carlo Code treats the system as infinite in the direction normal to the plane of incidence.

Although the BRDF shown in Fig. 1 represents a large amount of data, it was still not sufficient to generate the postreflectance directions of the photon using a direct interpolation scheme. Because of this, a more approximate method was used. Extensive measurements were done to obtain the BRDF in the plane of incidence. The back-reflecting portion of the BRDF was assumed to be purely diffuse. By assuming that it is symmetric with respect to the azimuthal angle, the diffusely reflecting component can be extracted from the back-reflecting portion of the BRDF. From Fig. 1, it can be seen that this assumption is plausible. The specular component is obtained from the forward-reflecting portion of the BRDF by subtracting out the diffuse portion of the BRDF. This effectively means subtracting the back-reflecting portion of the BRDF from the

Nomenclature

A = absorptance
B = shifted Gaussian function
C = curve fit parameter (Gaussian amplitude)
e = energy parameter for tracking absorption
h = curve fit parameter (Gaussian shift)
i = intensity
P = Gaussian distribution function
R = hemispherical reflectance
t = plate spacing
x = position
y = random variable
α = angle of incident beam
γ = curve fit parameter (proportionality constant for Gaussian width)
θ = polar angle
ρ = reflectance
σ = curve fit parameter (Gaussian width)
ϕ = azimuthal angle

Superscripts

$'$ = quantity is defined only in the plane of incidence

Subscripts

D = diffuse
i = incident
r = reflected
S = specular

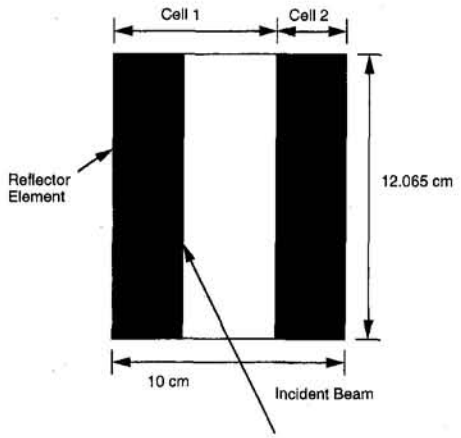

Fig. 3 Arrangement of cells used in Monte Carlo calculations for symmetric gap case

forward-reflecting portion. The width of the specular peak in the azimuthal direction is determined by some additional measurements of the BRDF, in which the polar angle is held fixed at the specular angle and the BRDF is measured as a function of the azimuthal angle. This information is then combined in an algorithm for generating postreflectance photon directions with approximately the same distribution as the BRDF.

Two coordinate systems are used to describe the behavior of the BRDF. The first, shown in Fig. 4(a), describes the BRDF in the plane of incidence and consists of the incident polar angle θ_i and the reflected polar angle θ_r'. The reflected polar angle θ_r' can take any value on the interval $[-\pi/2, \pi/2]$, the incident angle θ_i has values on $[0, \pi/2]$. The region $-\pi/2 \le \theta_r' < 0$ corresponds to forward reflection; the region $0 \le \theta_r' \le \pi/2$ corresponds to backward reflection. The second coordinate system, illustrated in Fig. 4(b), is a conventional spherical coordinate system, $(\theta_i, \theta_r, \phi_r)$ applied to both the incident and reflected beams. For both coordinate systems, θ_i is essentially the same. Because the surface is isotropic, only the azimuthal angle for the reflected beam needs to be specified and this is measured relative to the plane of incidence.

The majority of the data on the BRDF was originally available as a semi-regular grid of points in the (θ_i, θ_r') plane. The data contained gaps around the incident beam (points of the form (θ_i, θ_i)), and at extreme polar angles. The sampling of data was also more dense around regions of strong specular-like reflectance and sparse in regions of uniform reflectance. Linear interpolation was used to extend the data set around the incident beam and linear extrapolation was used to extend the data set to $\theta_i' = \pi/2$. The BRDF near $\theta_r = \pm\pi/2$ was assumed to vanish. This choice was supported by the behavior of the cosine distribution for a perfect diffuse reflector as well as the experimental data. Interpolation was also used to remap the BRDF to a uniform grid. Near the incident beam, the values of the reflectance are a smooth function of θ_i and interpolation is clearly appropriate. For the case $\theta_i' \to \pi/2$, the error associated with extrapolation is a function of the reflected angle; as the reflected angle approaches $\pi/2$, the error associated with extrapolation may be large.

Once the data are available on a uniform grid in the (θ_i, θ_r') plane, they must be put in a form that can be used in computations. For each incident angle the reflectance was separated into specular and diffused components. The portion of the BRDF in the interval $0 \le \theta_r' \le \pi/2$ (back reflectance) is taken to represent the diffuse component of the BRDF and is denoted $\rho_D'(\theta_r', \theta_i)$. The forward reflectance part of the BRDF is a combination of specular and diffuse reflectance. If the diffuse component of the BRDF is assumed to be azimuthally symmetric, then the specular component is defined as

$$\rho_S'(\theta_r', \theta_i) = \rho'(\theta_r', \theta_i) - \rho_D'(-\theta_r', \theta_i)$$

where $\rho'(\theta_r', \theta_i)$ is the total BRDF in the plane of incidence, and θ_r' is restricted to the interval $[-\pi/2, 0]$. If any values of $\rho_S'(\theta_r', \theta_i)$ turn out to be negative, they are set equal to zero. The reflectivities, $\rho_S'(\theta_r', \theta_i)$ and $\rho_D'(\theta_r', \theta_i)$, are only defined for θ_r' on the intervals $-\pi/2 \le \theta_r' < 0$ and $0 \le \theta_r' \le \pi/2$, respectively. For the polar coordinate system, θ_r is just defined on the interval $[0, \pi/2]$, so with a minor redefinition of ρ_S' and ρ_D', they can be written as functions of θ_r and θ_i instead of θ_r' and θ_i. Both ρ_S' and ρ_D' are now available on a uniformly spaced two-dimensional grid. For these calculations, each side of the grid was divided into 50 intervals, although the density of points in the original data set was considerably coarser.

Before the specular component of the reflectance distribution can be used, it is necessary to determine the behavior of the BRDF in the azimuthal direction. Measurements as a function of ϕ_r were obtained for a few values of θ_i with with θ_r held fixed at the specular angle $\theta_r = \theta_i$. The resulting curves are sharply peaked at $\phi_r = \pi$ and can be fit to a shifted Gaussian of the form

$$B_{\theta_i}(\phi_r) = Ce^{-(\phi_r - \pi)^2/2\sigma_\phi^2} + h$$

where C, σ_ϕ, and h are adjustable parameters. The dependence of σ_ϕ on the incident angle θ_i is taken as linear so that $\sigma_\phi(\theta_i) = \gamma(\theta_i - \pi/2)$. The value of γ is determined from a least-squares fit to the values of $\sigma_\phi(\theta_i)$. Once the width of the distribution in the azimuthal direction is known, the specular component of the reflectance can be written as

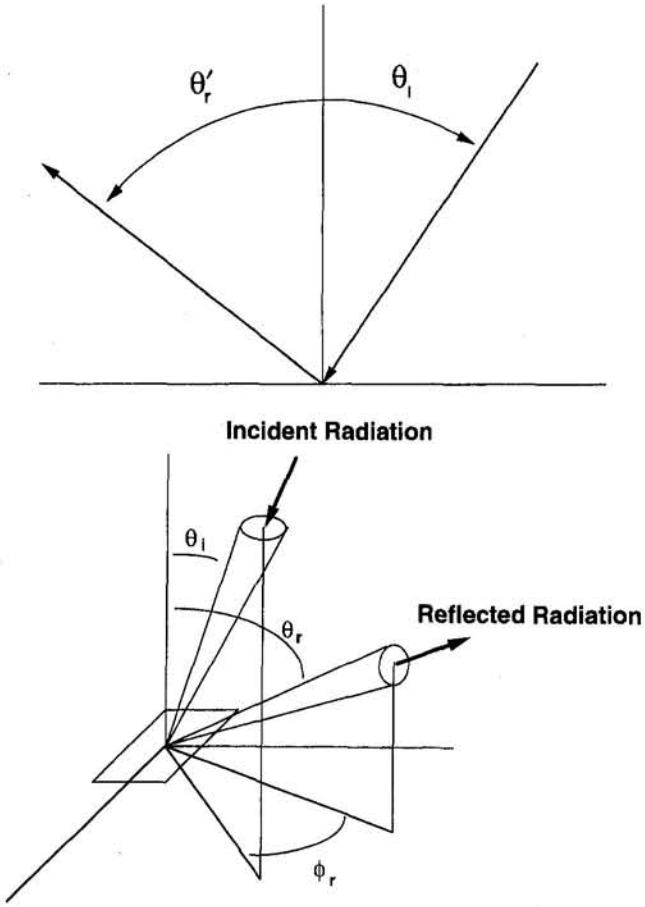

Fig. 4 Definition of angles for BRDF measurements: (a) definition of polar angles for incident and reflected beams in the plane of incidence; (b) definition of polar angle for incident beam and polar and azimuthal angles for reflected beam

$$\rho_S(\theta_r, \phi_r, \theta_i) = \rho'_S(\theta_r, \theta_i) e^{-(\phi_r - \pi)^2/2\sigma_\phi^2(\theta_i)}$$

The functions $\rho'_D(\theta_r, \theta_i)$ and $\rho_S(\theta_r, \phi_r, \theta_i)$ can now be used in Monte Carlo simulations. The total diffuse and specular reflectances are defined as

$$R_D(\theta_i) = 2\pi \int_0^{\pi/2} \rho'_D(\theta_r, \theta_i)\, d\cos\theta_r$$

$$R_S(\theta_i) = \int_0^{\pi/2} \rho'_S(\theta_r, \theta_i)\, d\cos\theta_r \int_0^{2\pi} e^{-(\phi_r - \pi)^2/2\sigma_\phi^2(\theta_i)} d\phi_r$$

$$\approx \sqrt{2\pi}\, \sigma_{\phi(\theta i)} \int_0^{\pi/2} \rho'_S(\theta_r, \theta_i) d\cos\theta_r$$

From the total diffuse and specular reflectances, the absorptance is defined to be

$$A(\theta_i) = 1 - R_D(\theta_i) - R_S(\theta_i)$$

If $A(\theta_i)$ turns out to be less than zero for any value of θ_i, then it is reset to zero.

Once the functions $A(\theta_i)$, $R_D(\theta_i)$, $R_S(\theta_i)$, and $\rho_D(\theta_i, \theta_r)$ have been calculated, it is possible to model photon collisions. As a first approximation, the following scheme was developed:

1 Each photon is assigned an "energy" parameter e_p that tracks the absorption of photons. At the beginning of each trajectory, e_p is set equal to one. Each particle in the Monte Carlo simulation can be thought of as representing a bundle of photons with the same energy and direction, e_p is the fraction of the original bundle that has not been absorbed.

2 Whenever a photon hits a surface with incident angle θ_i, the energy parameter is reduced by $e'_p = e_p(1 - A(\theta_i))$.

3 The photon is either specularly or diffusely reflected with the relative probabilities

$$R'_D(\theta_i) = \frac{R_D(\theta_i)}{R_D(\theta_i) + R_S(\theta_i)}$$

$$R'_S(\theta_i) = \frac{R_S(\theta_i)}{R_D(\theta_i) + R_S(\theta_i)}$$

The choice of specular or diffuse is made by generating a random number $0 \le y \le 1$. If $y < R'_D(\theta_i)$, then the photon is diffusely reflected; otherwise, it is specularly reflected.

$4(a)$ If the photon is diffusely reflected, the polar angle for the outgoing photon is generated by numerically inverting the distribution $\rho'_D(\theta_r, \theta_i)$ and the azimuthal angle is chosen by picking a random number in the interval $[0, 2\pi]$. The inverse of the distribution $\rho'_D(\theta_r, \theta_i)$ is calculated once at the beginning of the simulation and then stored for subsequent use as a lookup table (Press et al., 1992).

$4(b)$ If the photon is specularly reflected, the outgoing polar angle is chosen as $\theta_r = \theta_i$ and the azimuthal angle is set equal to $\phi_r = \pi$.

However, it was found that choosing the distribution of specularly reflected photons to be essentially a delta function gave very poor results, so the algorithm was modified to broaden the distribution of specular photons. The width of the specular peak in the θ_r direction can be calculated by fitting the θ_r dependence of $\rho(\theta_r, \theta_i)$ to the Gaussian form

$$B_{\theta_i}(\theta_r) = Ce^{-(\theta_r - \theta_i)^2/2\sigma_\theta^2} + h$$

for each value of θ_i. The fits give the Gaussian width σ_θ as a function of θ_i. The curve $\sigma_\theta(\theta_i)$ can be combined with $\sigma_\phi(\theta_i)$ (which is already known) to generate a specular reflection that has been slightly broadened in both the variables θ_r and ϕ_r. Step $4(b)$ was modified to the following:

$4(b)$ If the photon is specularly reflected, the outgoing angle is generated from the Gaussian distributions

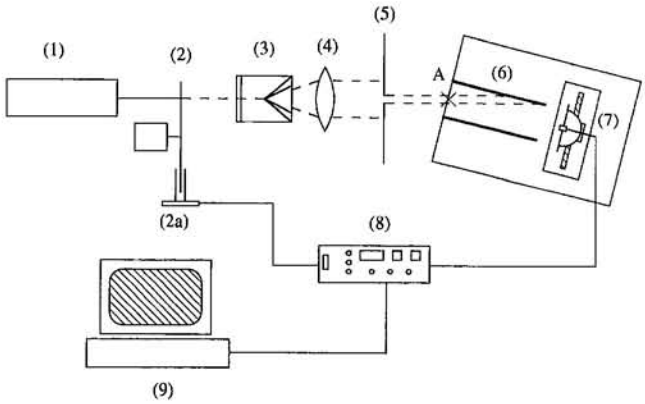

Fig. 5 Schematic of experimental apparatus: (1) He–Ne laser, (2) chopper with (2a) reference signal, (3) spatial filter, (4) collimating lens, (5) beam mask, (6) test channel mounted on a platform, which rotates about point A to vary the incident beam angle α, (7) sensor mounted on a platform which translates and rotates, (8) lock-in amplifier, (9) computer

$$P_\theta(\theta_r; \theta_i) \sim e^{-(\theta_r - \theta_i)^2/2\sigma_\theta^2(\theta_i)}$$

$$P_\phi(\phi_r; \theta_i) \sim e^{-(\phi_r - \pi)^2/2\sigma_\phi^2(\theta_i)}$$

The distributions are for θ_r and ϕ_r, but they both depend implicitly on θ_i. These distributions can be generated from a standard Gaussian random number generator (Press et al., 1992). Both ϕ_r and θ_r are picked directly from a Gaussian distribution. If the variable θ_r does not lie in the allowed range of values $[0, \pi/2]$, then θ_r is rejected and a new value is chosen.

4 Radiative Transfer Through Channel With Semi-diffuse Surfaces

Validation data were obtained using the apparatus indicated schematically in Fig. 5. A low-power 5 mW HeNe laser provided the incident beam. At the exit plane, intensity was measured as a function of position using a photodiode and sensitive voltmeter. The maximum uncertainty in these measurements was 10 percent for the lowest intensity values, and decreased with increasing intensity.

The cases presented include a variety of plate spacings and incident angles. Three plate spacings were investigated: case (a) was 40 mm, case (b) was 22 mm, and case (c) was 3 mm. For reasons associated with the experimental apparatus, the beam entered the channel at a line of symmetry for the 40 mm gap. (This line corresponds to the centerline in Fig. 2.) For narrower gaps, the entry point of the incident beam remained at the same location but the gap was reduced by moving only one side of the channel. Therefore, cases (b) and (c) were based on an asymmetric gap. The gap was 12.065 cm long and the height of the gap was sufficient that it could be treated as effectively infinite in the direction normal to the plane of incidence.

Figures 6 and 7 present a comparison between the experimentally determined distribution of light at the exit plane and the distribution calculated using the Monte Carlo code, MCLITE. Each Monte Carlo simulation consisted of 20 subruns consisting of 100,000 individual trajectories, for a total of 2 million trajectories per simulation. The statistics from the separate subruns were used to calculate the uncertainties to the 95 percent confidence levels in the simulated distributions. The uncertainties are included in each figure. The origin of the x axis is located at the intersection of the centerline with the backplane. The laser beam enters the gap at the point of intersection between the plane containing the front end of the gap and the centerline. Except for the case shown in Fig. $7(b)$, both the experimental and calculated distributions were normalized so that the maximum intensity was 1.0. For the wide gap array (Figs. $6(a)$ and

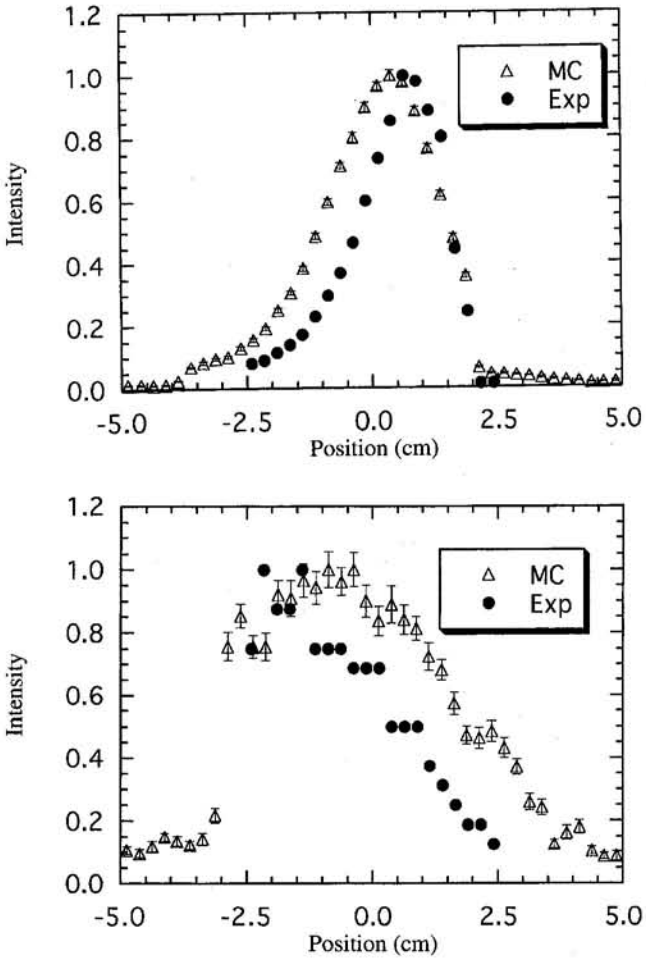

Fig. 6 Comparison of experimental transmission through a reflecting gap with Monte Carlo simulations. The gap spacing is 40 mm. The filled circles are the experimental values; the triangles are the results of the Monte Carlo simulations. The uncertainties at the 95 percent confidence level are shown for the Monte Carlo values. (*a*) Angle of incident radiation is 15 deg. (*b*) Angle of incident radiation is 30 deg.

6(*b*)), there is good agreement for the 15 and 30 deg incident angle cases, although the calculated distribution is slightly wider than the experimental distribution in both cases.

For the asymmetric gap (Fig. 7), the simulated results are generally in qualitative agreement with the experimental results. For the low incident angle case (Fig. 7(*a*)) both the simulation and the experiment show a single peak. However, the peak width for the experimental distribution is much narrower than that from the simulation. The experimental distribution for the 5 deg incident angle case (Fig. 7(*b*)) shows a single peak with rather broad wings. If the simulation curve is normalized at close to 40 percent of the height of the experimental curve, it does a good job of reproducing the broad wings but misses the narrow central peak. The 10 deg incident angle case (Fig. 7(*c*)) shows reasonable agreement between the experimental and the simulation based distributions. As in the symmetric gap case, the simulation distribution is slightly wider than the experimental distribution.

Overall, the simulations are in qualitative agreement with the experimental data, but the simulations consistently produce broader distributions. The worst agreement between simulation and experiment is for the low incident angle cases, which is not surprising because the BRDF must be obtained entirely by extrapolation for these angles. The differences between simulation and experiment can probably be attributed to the lack of precise information about the shape of the specular portion of the BRDF at low incident angles. The data reduction procedure assumes that the specular peak is Gaussian as a function of both azimuthal and polar angles, but this is only an approximation. As the incident angle approaches 0 deg, this must break down because the BRDF vanishes for outgoing photons parallel to the surface. Even for larger incident angles, the specular peak may contain broad wings that would be missed by the Gaussian profile.

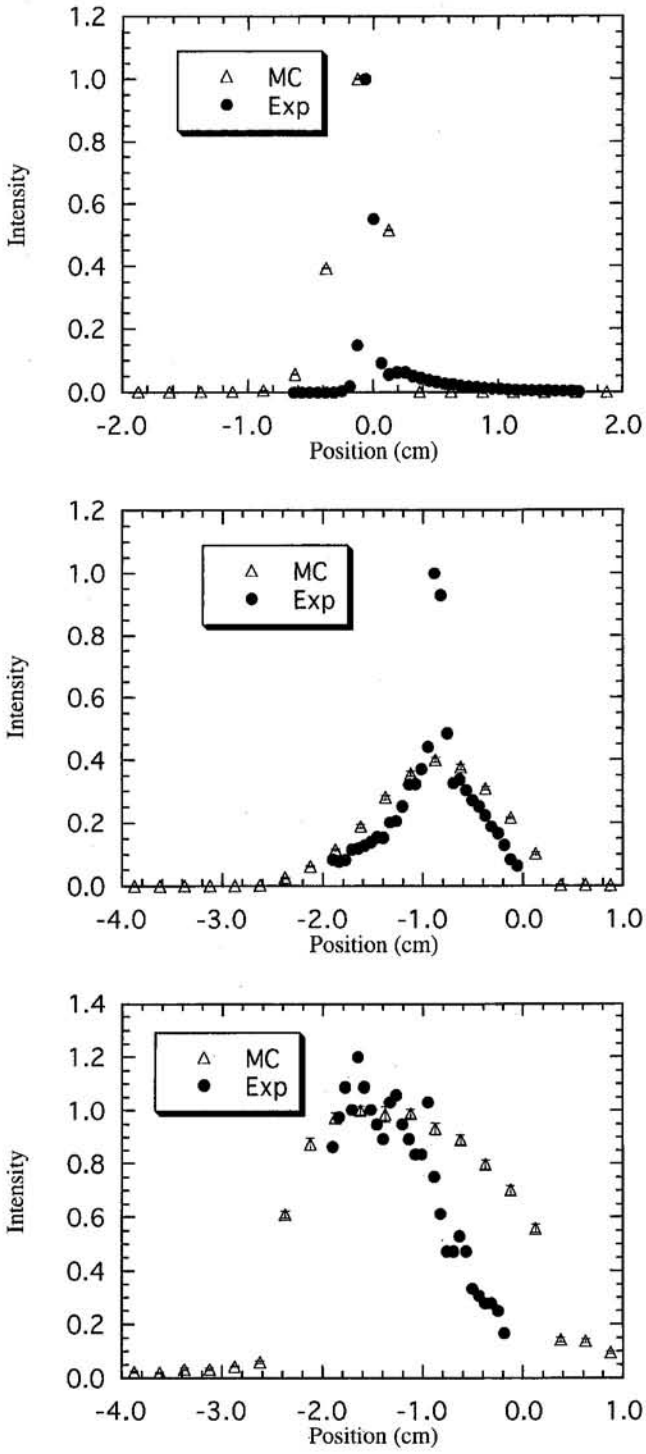

Fig. 7 Comparison of experimental transmission through a reflecting gap with Monte Carlo simulations. The gap spacing is 22 mm. The filled circles are the experimental values; the triangles are the results of the Monte Carlo simulations. (*a*) Angle of incident radiation is 2 deg. (*b*) Angle of incident radiation is 5 deg. (*c*) Angle of incident radiation is 10 deg.

5 Conclusions

A principal result of this work is that the inclusion of realistic surface properties in a Monte Carlo radiation simulation is not so simple an undertaking as one might believe a priori. When the surfaces in question display behavior that is not purely diffuse, then the problem of accounting for all of the functional variations in surface properties becomes formidable. It is also apparent that the assumption of diffuse-gray surfaces may yield results that are grossly in error. Some techniques for handling real surface properties have been attempted with reasonable success.

The Monte Carlo simulations successfully reproduced the experimental distribution of intensities in most cases for the simple gap geometry with diffuse reflecting surfaces. The only cases for which there were significant differences between the simulation and experiment were those in which the incident beam was at a low angle relative to the gap surfaces. Problems would be expected under these circumstances, because the BRDF in this region is obtained almost entirely by extrapolation.

The simulations also suggest that decomposing the reflectance into pure diffuse and specular components is not sufficient to model the properties of heat transfer systems accurately. Initial results using such a decomposition failed to match the experimental distributions. Only by broadening the specular peak was it possible to obtain satisfactory agreement with experimental results.

These results demonstrate the need for both accurate BRDF data, and a sophisticated model of those data. The experimental data on Krylon™ white paint shows clearly a requirement for data that increases both in accuracy and resolution with incident angle. In addition, accurate measurements of the total hemispherical reflectance should be made as a function of incident angle. This quantity represents the integral of the BRDF over both the polar and azimuthal angles. As such, it provides a useful check on the accuracy of the BRDF representation as well as a method for normalizing the data. This is particularly important if the BRDF is available only on a discrete, relatively sparse grid. The normalization provides a way of making sure that the overall reflectance of the BRDF is correct in any model that makes use of the data.

The challenge of accurately modeling BRDF data is seen for mostly diffusely reflecting surfaces. As shown for Krylon™ flat white paint, the BRDF becomes increasingly specular at low incident angles. The increase in specularity means that the BRDF begins to vary sharply as a function of the outgoing polar and azimuthal angles, a feature that is difficult to represent on a discrete grid of data points. Either the grid size for the data set must be decreased until the grid spacing is small relative to the scale of variations, or else large errors are introduced by inversion of the data grid into a form that can be used in a Monte Carlo simulation. The use of a fine grid for the BRDF rapidly becomes unattractive because of the large number of measurements required. This problem could be minimized if models that provided a good representation of the BRDF were available. Instead of doing hundreds, or possibly thousands of individual measurements, it would only be necessary to do enough to parameterize the model. Once the data are available in analytic form, the numerical problem of inverting the BRDF is straightforward.

Acknowledgments

The research reported in this paper was funded by the U.S. Department of Energy's Basic Energy Sciences Program. We would like to thank Dr. Oscar Manley of the Basic Energy Sciences Program for his support and guidance.

References

Burns, P. J., and Pryor, D. V., 1989, "Vector and Parallel Monte Carlo Radiative Heat Transfer Simulation," *Numerical Heat Transfer,* Vol. 16, pp. 97–124.

Haji-Sheikh, A., 1988, "Monte Carlo Methods," in: *Handbook of Numerical Heat Transfer,* Wiley Interscience, New York.

Maltby, J. D., and Burns, P. J., 1991, "Performance, Accuracy and Convergence in a Three-Dimensional Monte Carlo Radiative Heat Transfer Simulation," *Numerical Heat Transfer,* Vol. 19, pp. 191–209.

Modest, M. P., 1993, *Radiative Heat Transfer,* McGraw-Hill Inc., New York.

Palmer, B. J., Drost, M. K., and Welty, J. R., 1995, "Monte Carlo Simulation of Radiative Heat Transfer in Arrays of Fixed Discrete Surfaces Using Cell-to-Cell Photon Transport," *International Journal of Heat and Mass Transfer,* in press.

Press, W. H., Teukolsky, S. A., Vetterling, W. T., and Flannery, B. P., 1992, *Numerical Recipes,* Cambridge University Press, Cambridge, United Kingdom.

Siegel, R., and Howell, J. R., 1972, *Thermal Radiation Heat Transfer,* McGraw-Hill Inc., New York.

Toor, J. R., 1967, "Radiative Heat Transfer Analysis Among Surfaces Having Direction Dependent Properties by the Monte Carlo Method," M.S. Thesis, Purdue University, Lafayette, IN.

Toor, J. R., and Viskanta, R., 1968, "Radiative Heat Transfer Analysis Among Surfaces Having Direction Dependent Properties by the Monte Carlo Method," *International Journal of Heat and Mass Transfer,* Vol. 11, pp. 883–897.

Zaworski, J. R., Welty, J. R., and Drost, M. K., 1993, "Measurement Techniques for Bidirectional Reflectance of Engineering Materials," *Radiative Heat Transfer—Theory and Applications,* ASME HTD-Vol. 244.

Reordering the Absorption Coefficient Within the Wide Band for Predicting Gaseous Radiant Exchange

P. Y. C. Lee

K. G. T. Hollands

G. D. Raithby

Department of Mechanical Engineering,
University of Waterloo,
Waterloo, Ontario N2L 3G1 Canada

The "exact" calculation of the radiant transfer in gaseous enclosures has remained impractical for design; the highly complex nature of the absorption spectrum of the gases has meant that an inordinately large computational effort is required to effect an exact answer. In this paper we show how the complex absorption distribution for an isothermal gas can be replaced by a set of smooth curves. This procedure can be visualized as one of actually reordering the full complex absorption distribution within each vibration-rotation band, and then replacing it by a smooth curve. Such a smooth curve can then be readily approximated by a stepwise function, and radiant exchange calculations can be carried out at each step and then summed over all the steps to get the total exchange. This paper explains how the reordered curve can be obtained and gives some sample plots of the reordered absorption coefficient curve. Fitted functions for the rearranged curves have been provided, and some solutions to the radiant exchange problems are given and compared to line-by-line solutions. About 50 to 200 steps in the stepwise curve are found to be adequate in order to obtain an answer within a few percent of the exact answer.

Introduction

Calculating the radiant exchange in an enclosure containing a gas that has radiantly participating components, like CO_2 and H_2O, is made difficult by the complex spectral dependence of the absorption coefficient. These gases emit and absorb only inside certain bands (vibration-rotation bands), and inside each band, the spectral absorption coefficient a_η varies in a highly erratic way with the wavenumber η of the radiation. The complex nature of this dependence has made exact analysis impractical for engineering design. Yet the problem is of considerable practical importance. For example, the trend toward cleaner combustion in boilers, with fewer particulates in the combustion products, has meant that more and more of the radiant transfer is coming from gaseous (as opposed to particulate) radiation. Accurate predictions of radiant heat transfer through the atmosphere are also vitally needed. Consequently, the need for a precise and practical modeling capability—commensurate with the growing computational fluid dynamic capability for modeling the flow field—has become increasingly imperative.

The apparent impracticality, mentioned above, of obtaining an exact solution needs some explanation. In principle, centered at any wavenumber η there will always exist an interval $\delta\eta$ small enough that, inside that interval, a_η can be treated as constant. So, in principle, radiant exchange inside the interval can be calculated, by first solving the equation of transfer (the governing equation for radiative transfer) for the spectral intensity, and then calculating the total radiant exchange of interest, by means of integrating that spectral intensity over the relevant directions and volumes,[1] and then summing the result over all the various wavenumber intervals. In practice the needed interval $\delta\eta$ must be at least an order of magnitude less than the (wavenumber) scale of variation of a_η with η, which is of the order of 10^{-1} cm^{-1} or smaller. Since each of the vibration-rotation bands (of which there are typically 3) can typically extend over a wavenumber range of about 1000 cm^{-1}, the number of separate $\delta\eta$ intervals that must be solved for is of the order of 10^5 to 10^6. This is too large to make such "line-by-line" schemes practical, although they are useful for providing benchmark solutions.

For these reasons researchers have been developing simplified models for the gaseous interaction, which reduce the calculational effort, but at the expense of some rigor and accuracy. Howell (1988) has summarized some of the recent work. Suitable models for the integral, with respect to wavenumber η, of the spectral absorptance/emittance (i.e., of $1 - \exp(-a_\eta s)$), a function of path length s, are common and have been developed. Some examples are the Goody (1952) and Malkmus (1967) models, for the integral over a narrow interval (but one wide enough to contain very many $\delta\eta$'s), and the Edwards–Menard (1964), Morizumi (1970), Felske and Tien (1974), and Wang (1983) models, for the integral over an entire vibration–rotation band (i.e., the effective bandwidth $A_l(s)$). But, useful as these models are, they do not model a_η per se, and therefore their engineering application is restricted to certain classes of problems—e.g., to problems in which the gas is isothermal and the enclosure has a simple geometry and nonreflective walls.

One approach, sometimes called the weighted-sum-of-gray-gas (or WSGG) model and exemplified by the recent studies of Modest (1991), is conceptually to replace the real gas by a superposition of various hypothetical gas components, each with its own constant absorption coefficient. By choosing a set of weights (c_i) and absorption coefficients (a_i) of the various components, one can make the hypothetical gas behave somewhat like the real gas (at least so far as concerns the dependence of the absorptance/emittance on the path length s), with a

[1] This is not to minimize the problem of solving for the spectral intensity inside a wavenumber interval, even given that a_η is constant inside that interval. Because of the directional as well as spatial dependence of spectral intensity, a sophisticated directional and spatial discretization scheme and solver algorithm must be built up—preferably in a way that is compatible with the methods that are used simultaneously to solve the momentum and energy equations for the velocity and temperature fields. Raithby and Chui (1990), Fiveland (1984), and Mengüç and Viskanta (1985a), to name a few, have laid out some possible schemes.

Contributed by the Heat Transfer Division for publication in the JOURNAL OF HEAT TRANSFER. Manuscript received by the Heat Transfer Division February 1995; revision received November 1995. Keywords: Numerical Methods, Radiation, Radiation Interactions. Associate Technical Editor: B. W. Webb.

fidelity that increases as the number N of the components is increased. Modest (1991) determined a set of a_i's and c_i's for N up to about 5 by making a best fit to a band absorptance function. More recently, Denison and Webb (1993a, b) obtained the a_i's and c_i's for N up to 20 for H_2O gas. Since a_η is constant, the equation of transfer written for each component separately can be readily solved to obtain the total radiant transfer in each case, and the results summed. The assumption is that as N is allowed to approach infinity, the calculated radiant transfer will approach the true one.

An alternative approach uses the fact that, within a relatively wide spectral interval, the exchange depends only upon the fraction of the wavenumber interval that is associated with a small a_η interval around a particular value of a_η (Arking and Grossman, 1972). These fractions, as a function of a_η itself, constitute a distribution with a_η, and since a_η is sometimes called k, the result is called the *k-distribution* $f(k)$ or $f(a_\eta)$. The wavenumber interval over which this distribution is taken must be narrow enough that the black-body function is nearly constant over the interval. The $f(k)$ distribution has been worked out (Domoto, 1974) for the case where the interval is a narrow band inside a total vibration-rotation band, such as the narrow band modeled by Goody. Recently, Tang and Brewster (1994) applied the k-distribution method in the presence of particle scattering using Elsasser's narrow band model across the vibration-rotation band.

If the wavenumber interval is so wide that variations in the black-body function cannot be ignored, a similar approach can be developed; however, it is then necessary to deal with fractions of the *black-body energy* within the wavenumber interval, rather than the fraction of the interval itself (Hottel and Sarofim, 1967). Denison and Webb (1993a, b) developed this approach for the entire spectrum, and this forms the basis for obtaining the parameters a_i and c_i in their WSGG model. The distribution function can be obtained by doing a once-for-all line-by-line analysis of measured spectral plots of a_η like the HITRAN data base (Denison and Webb, 1993a, b), or by inferring the distribution function from accepted models for the dependence of the gas transmission on the path length s (Domoto, 1974).

Other approaches have been developed by Kim et al. (1991), Hartmann et al. (1984), Soufiani et al. (1985), and Koch et al. (1991). In all of these various models, however, the computational effort required to solve gaseous exchange problems is impractically large, even for the relatively simple parallel-plate geometry.

The approach described in the present paper is to actually reorder the full a_η curve for a band, replacing it by a smooth spectral curve. The shape of the spectral curve will be inferred from the dependence of the band's effective bandwidth $A_l(s)$ on path length s, for which there are a number of well-established models.

Given the smooth reordered curve of a_η versus η for the entire band, one can then discretize the total wavelength span into say N regions, and use a constant representative value of a_η in each region. As the number N becomes very large, the corresponding calculated radiant heat transfer rate will converge to the exact value. In this paper, we show that one can carry out a "once for all" reordering valid for all gases. Fitted functions for the reordered spectra are then provided so that future users of the method can obtain the reordered a_η spectrum without having to repeat the reordering process. Following an exposition of the reordering process, the paper provides an example application of the method to three simple problems, all of which involve an isothermal gas between infinite-parallel plates.

The broad goal of this work is to obtain a model capable of dealing with nonisothermal and/or nonhomogeneous gases, but the work presented in this paper is restricted to isothermal homogeneous gases, in order to lay the groundwork for the more general case. Our expectation is that, because the reordered spectrum is less dependent on gas temperature than those in some other models, the extension to the nonisothermal and/or nonhomogeneous gas should be more straightforward, although additional approximations will have to be invoked.

Reordering the Spectral Absorption Coefficient

Although the reordering method turns out to be mathematically similar to the k-distribution approach, there are important differences from a physical perspective. For example, in the k-distribution approach, the integrations are carried out over the relative frequency, whereas in the present reordering approach the traditional step of integrating over wavenumbers is maintained. This will mean that later allowance for the presence of soot and overlapping bands will be more straightforward. For these reasons, a physical picture for the reordering process is developed below.

For illustration, a particularly simple distribution of the spectral absorption coefficient a_η over one vibration-rotation band is shown in Fig. 1(a). A small section of the a_η curve is redrawn in Fig. 2(a), greatly expanded in the η direction. A narrow interval of width $\Delta a_{\eta,i}$ is drawn horizontally on the figure, and $a_{\eta,i}$ is located in the middle of the interval. The intersections of the boundaries of the interval with the a_η curve are then found. The first intersection with $\Delta a_{\eta,i}$ occurs over the wavelength interval $\Delta\eta_{i,1}$, the second over $\Delta\eta_{i,2}$, and so on. The total wavelength interval over which a_η lies within the $\Delta a_{\eta,i}$ region

Nomenclature

a_η = spectral absorption coefficient, cm^{-1}
a_ξ = reordered spectral absorption coefficient, cm^{-1}
a_ξ^* = dimensionless reordered spectral absorption coefficient
$A_l(s)$ = total band absorption (or effective bandwidth) for the lth vibration-rotation band, cm^{-1}
$A_l'(s)$ = derivative with respect to path length s of $A_l(s)$
$f(t)$ = inverse Laplace transform function
$F(t)$ = function in Eq. (8)
L = plate spacing, m
$\mathcal{L}$ = Laplace transform operator
s = pathlength, m or Laplace transform variable
T = temperature, K
α = integrated intensity of the vibration-rotation band, $cm^{-1}/(kg/m^2)$
β = line overlap parameter of the vibration-rotation band = $\pi(\gamma/d)$
ϵ = plate wall emissivity
η = wave number, cm^{-1}
θ = ln ξ^*
κ = second-order interpolation term in Eq. (15)
γ/d = line-width-to-spacing ratio of the vibration-rotation band
ρ = gas density, kg/m^3
σ = Stefan–Boltzmann constant, $W/m^2\ K^4$
τ = dimensionless pathlength = $(\alpha/\omega)\rho s$
ψ = $\log_{10}\beta$
ω = rotational bandwidth parameter of the vibration-rotation band, cm^{-1}
ξ = reordered wavenumber, cm^{-1}
ξ^* = dimensionless spectral distance from the band center = $2(\xi - \xi_c)/\omega$

Subscripts and Superscripts

c = band center
g = gas
l = integer specifying which vibration-rotation band is being considered; also lower limit
η = spectral quantity
ξ = reordered spectral quantity
$*$ = nondimensional quantity

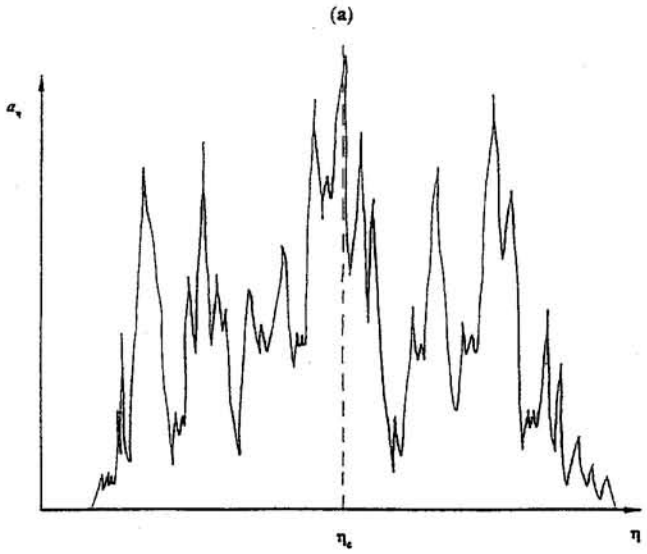

Fig. 1 A simple representation of a typical vibration-rotation band

is $\Delta\eta_{i,1} + \Delta\eta_{i,2} + \Delta\eta_{i,3} + \ldots = \Delta\eta_i$. Next the entire range of a_η for the given band is subdivided into similar intervals and from the intersections of each interval with the spectral curve, the wavenumber ranges $\Delta\eta_1$, $\Delta\eta_2$, ... can all be found in a similar manner to that just described for the ith interval. When these are added, as in Fig. 2(b), a stepwise reordered distribution is obtained.

As the widths of all intervals are made to approach zero, the curve approaches a smooth curve, as shown in Fig. 3(a). In drawing the smooth curve, the wavenumber has been replaced by a new variable ξ. This replacement recognizes that the numerical value of a_ξ at a given ξ does not correspond to the value of a_η (in Fig. 1, for example) at $\eta = \xi$.

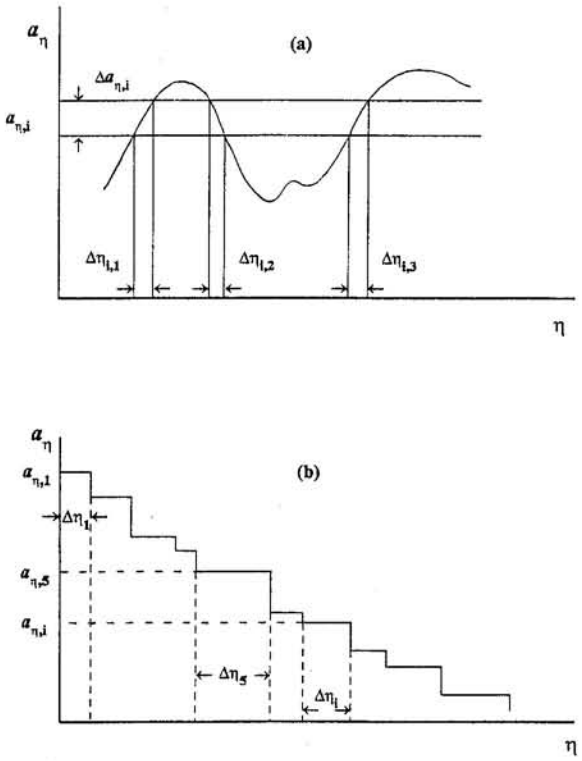

Fig. 2 (a) Small section of the actual a_η distribution; (b) stepwise reordered representation of a_η curve

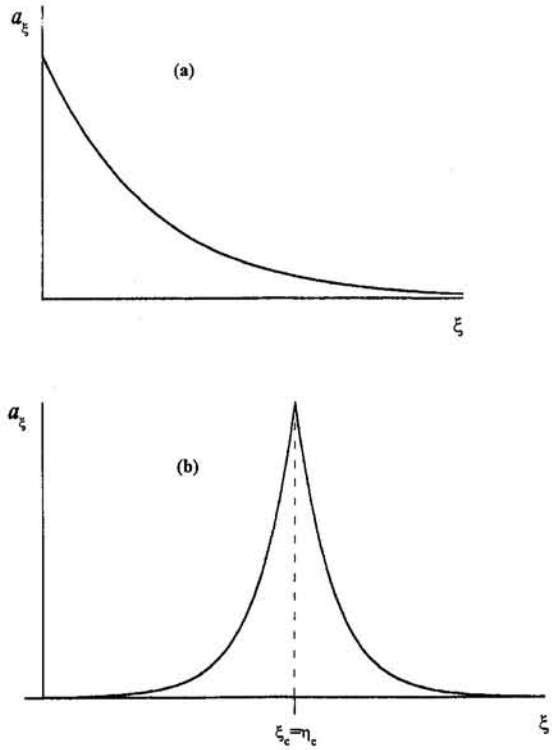

Fig. 3 Arbitrary smooth reordered representations of the actual distribution: (a) monotone decreasing function; (b) symmetric function

There is a degree of arbitrariness in drawing the a_ξ curves. Another alternative is, again, to number the $\Delta a_{\eta,i}$ intervals with $i = 1$ as the region associated with the highest a_η, and to plot the corresponding a_ξ at $\xi = \xi_c = \eta_c$. For the next lowest interval ($i = 2$) the $\Delta\eta_2$ interval is split into two equal parts and plotted respectively to the left and right of ξ_c. If this is then repeated for all $\Delta a_{\eta,i}$ bands, the resulting reordered distribution appears as in Fig. 3(b). This alternative gives a more realistic representation of the band and is suitable for the incorporation of a band overlap model.

Based on the method used to construct the reordered a_ξ distribution, the "area" under the smooth reordered absorption profile is equal to the "area" under the original absorption distribution for the same actual spectral region. This means that—if the black-body spectral intensity is constant over the spectral interval—the correct total emitted energy within the actual spectral interval over the entire band is equal to the emitted energy using the reordered data. We infer $a_\xi(\xi)$ from the existing knowledge of the effective bandwidth $A_l(s)$ and its dependence on the path length s.

The effective bandwidth, $A_l(s)$, of say the lth band is given by

$$A_l(s) = \int_{\Delta\eta_l} (1 - e^{-a_\eta s}) d\eta \tag{1}$$

where $\Delta\eta_l$ is the band interval. If $a_\xi(\xi)$ is the correct reordered distribution, then we must get the same result for $A_l(s)$ if we integrate over the reordered distribution. Thus,

$$A_l(s) = \int_{\Delta\xi_l} (1 - e^{-a_\xi s}) d\xi \tag{2}$$

where $\Delta\xi_l$ is the band width of the lth reordered band. Because of the symmetry about the band center $\xi_c = \eta_c$ (we choose the reordered profile shown in Fig. 3(b)), Eq. (2) can be written as

$$A_l(s) = 2\int_{\xi_{\min}}^{\xi_c} (1 - e^{-a_\xi s})d\xi \tag{3}$$

where $\xi_{\min}$ is some appropriately small lower bound for ξ (small enough for a_ξ to be essentially zero) in the lth band. Because, in the region of integration, a_ξ has been made a monotonic function of ξ, it is permissible to change the variable of integration from ξ to a_ξ. Noting that $a_\xi = 0$ when $\xi = \xi_{\min}$, we obtain

$$A_l(s) = \int_0^{a_{\xi_c}} (1 - e^{-a_\xi s})F(a_\xi)da_\xi \tag{4}$$

where $a_{\xi c}$ is the reordered absorption coefficient at the band center ξ_c, and

$$F(a_\xi) = 2\frac{d\xi}{da_\xi}. \tag{5}$$

Because $d\xi/da_\xi = 0$ for $a_\xi > a_{\xi,c}$, the upperlimit in the integral in Eq. (4) can be replaced by ∞. Therefore we can write

$$A_l(s) = \int_0^{\infty} (1 - e^{-a_\xi s})F(a_\xi)da_\xi. \tag{6}$$

If we assume that the function $A_l(s)$ is known, then Eq. (6) represents an integral equation in $F(a_\xi)$, which will have a unique solution. From this solution, $a_\xi(\xi)$ can be inferred by integrating Eq. (5).

Some simplification in the process of solving for $F(a_\xi)$ is achieved by first differentiating Eq. (6) with respect to path length s to yield

$$A_l'(s) = \int_0^{\infty} e^{-st} f(t)dt \tag{7}$$

where $A_l'(s) = dA_l(s)/ds$, a_ξ has been (temporarily) denoted by t, and

$$f(t) = tF(t). \tag{8}$$

It is now recognized that

$$f(t) = \mathcal{L}^{-1}\{A_l'(s)\} \tag{9}$$

where $\mathcal{L}$ is the Laplace transform operator, so finding $f(t)$ turns out to be tantamount to finding the inverse Laplace transform of $A_l'(s)$. From the Laplace transform theory (Churchill, 1972), there exists a unique solution $f(t)$ to Eq. (9). Having determined $f(t)$, by some appropriate inversion procedure, $a_\xi(\xi)$ can be determined by integrating the differential equation

$$\frac{da_\xi}{d\xi} = \frac{2a_\xi}{f(a_\xi)} \tag{10}$$

which follows from Eq. (5). The Laplace transform formalism was also used by Domoto (1974) to derive the a_ξ(or k)-distribution of a *narrow band* from the narrow-band *transmittance function.* We use it here to find the reordered distribution of an *entire* vibration-rotation band from derivative of the band's *absorptance function.*

For the function $A_l(s)$ we choose the Morizumi (1970) model. Given the proper parameters, this model is considered to be more accurate than the piecewise continuous functions generally used to represent the Edwards–Menard exponential wide band model, but it is much less used because it does not give an explicit equation for $A_l(s)$. On the other hand, after differentiating the Morizumi model of $A_l(s)$, with respect to s, one obtains an explicit equation for $A_l'(s)$. After carrying out the differentiation, substituting in the $A_l'(s)$ into Eq. (7), and dedimensionalizing the result, one obtains

$$\int_0^{\infty} e^{-\tau a_\xi^*} f^*(a_\xi^*)da_\xi^* = \frac{1}{\tau} - \left\{\left[\frac{1 + \tau/(2\beta)}{1 + \tau/\beta}\right] \times \left\{\frac{1}{\tau} - \frac{1}{\tau + 2\beta}\right\} \exp\left(-\frac{\tau}{\sqrt{1 + \tau/\beta}}\right)\right\} \tag{11}$$

where

$$a_\xi^* = \left(\frac{\omega}{\alpha}\right)\frac{1}{\rho}a_\xi \quad \text{and} \quad f^* = \frac{f}{\omega} \tag{12}$$

and band properties ω, α, ρ, and β are defined by Siegel and Howell (1992). The parameter β captures the pressure broadening effect referred to earlier. The problem of solving this integral equation for $f^*(a_\xi^*)$ is one of finding the inverse Laplace transform of the function of τ given on the left-hand side of Eq. (11); that is, τ represents the Laplace transform variable, usually denoted by s. (In fact, it is the dimensionless path length given by $\tau = \alpha\rho s/\omega$.) The quantity a_ξ^* is the variable normally denoted by t in the Laplace transform terminology. The dimensionless form of Eq. (10) is

$$f^*(a_\xi^*) = a_\xi^*\frac{d\xi^*}{da_\xi^*}$$

where $\xi^* = 2(\xi - \xi_c)/\omega$. After applying the boundary condition $a_\xi = \infty$ at $\xi = \eta_c$, this reduces to

$$\xi^* = \int_{a_\xi^*}^{\infty} \frac{f^*(a_\xi^*)}{a_\xi^*}da_\xi^* = \xi^*(a_\xi^*) \tag{13}$$

Equation (11) was solved for $f^*(a_\xi^*)$ using the numerical method of inverting the Laplace transform originally due to Dubner and Abate (1968), but later refined by Durbin (1973) and Honig and Hirdes (1984). The integral in Eq. (13) was then evaluated numerically, with the upper limit replaced by a large number (the result was essentially independent of that number, provided it was is sufficiently large). This procedure was repeated for various values of β of interest. The results are plotted in Fig. 4, in the more natural form $a_\xi^*(\xi^*)$ rather than $\xi^*(a_\xi^*)$.

These reordered results were checked by comparing the Morizumi function for $A_l(s)$ with the integral expression of Eq. (2) evaluated numerically from the reordered distribution. Excellent agreement (less than 0.1 percent difference) was found over a large range of path lengths between the reordered results and with the Morizumi function.

Functions to represent the de-dimensionalized reordered profile $a_\xi^* = a_\xi^*(\xi^*, \beta)$ shown in Fig. 4 were fitted once for all in order to permit a user to calculate the reordered spectra without having to resort to the numerical Laplace transform inversion procedure. The following functional form was chosen to fit the reordered spectrum:

$$a_\xi^* = \exp\left\{\frac{a + b\theta + c\theta^2 + d\theta^3 + e\theta^4 + f\theta^5}{1 + g\theta + h\theta^2 + i\theta^3 + j\theta^4 + k\theta^5}\right\};$$

$$\theta = \ln \xi^* \tag{14}$$

where a, b, c, d, e, f, g, h, i, j, and k are coefficients that depend upon β, and they are valid for values of θ within $-13.5 \le \theta \le 2.5$. There is no theoretical basis for this functional form; rather it was chosen for its ability to accurately represent the data. A summary of the coefficients for various values of $\psi = \log_{10}\beta$ is given in Table 1.

For values of $\psi = \log_{10}\beta$ that do not coincide with the listed values of ψ in Table 1, but fall between two adjacent values, ψ_j and ψ_{j+1}, a cubic spline interpolation scheme is used. (A linear interpolation scheme was found to lead to unacceptably

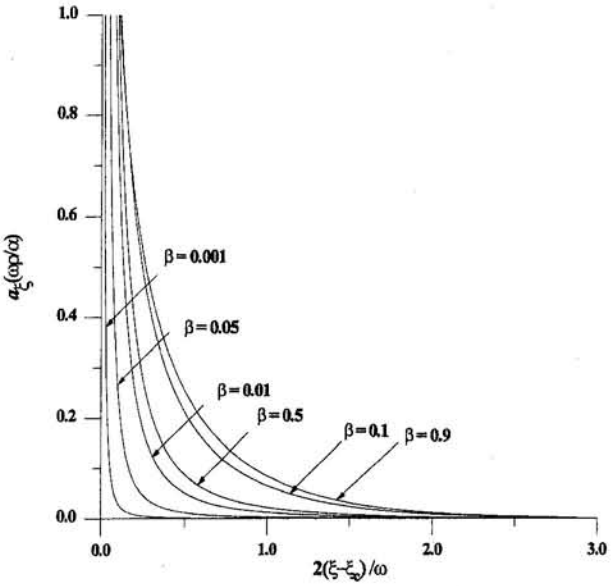

Fig. 4 Reordered nondimensional absorption coefficient distribution based on the Morizumi absorptance function

large errors.) The interpolation scheme described in the appendix generates the reordered distribution for any value of ψ (i.e., β) in the practical range of interest: $0.005 \leq \beta \leq 1$.

The fitted reordered results and the interpolated results based on the interpolation scheme of the appendix were checked by comparing the "exact" Morizumi function $A_f(s)$ with the integral expression of Eq. (2) evaluated numerically from the fitted reordered distributions. For any given specified values of β and τ presented, the maximum relative error between the exact and the fitted reordered results is about 2 percent.

Sample Problems Using the Reordered Distribution

The new model is now applied to three problems where the predictions can be compared to previous published results. In all three problems an isothermal gas is contained between black parallel plates at 0 K. All calculations were done using the finite-volume method (FVM) of Raithby and Chui (1990), extended to permit the medium to be treated as gray in narrow intervals (Lee et al., 1994). (The reordered distribution concept could equally well be applied in other discrete methods.) The FVM requires that the space be broken into discrete volumes (in this case, the gas slab is divided into layers) and that the direction be divided into discrete solid angles. The computations were performed on a SUN-SPARC IPX workstation (40 MHz SPARC IU and FPU rated at 4.2 MFLOPS and 25.0 SPECmarks).

In the first example, a gas having a single band was considered, and the pressure was chosen to be so high that the transfer occurs in the "weak-line" ($\beta \to \infty$) limit. This choice for β was made because of the availability of Modest's analytical solution (Modest 1992), based on Felske and Tien's band model (Felske and Tien, 1974). Since the Morizumi model and the Felske and Tien model reduce to the same result when $\beta \to \infty$, this comparison provides an evaluation of the discretization code rather than the modeling of the band structure. After some preliminary grid refinement studies, space and direction were divided into 20 layers and 20 solid angles, respectively. The number of spectral divisions was varied from 20 to 100. The wall fluxes evaluated using 100 spectral divisions were found to be only 0.4 percent different from the heat fluxes obtained using 50 spectral divisions, so 50 spectral divisions were fixed on for the comparisons. (Twenty spectral divisions, on the other hand, was found to be too course to give a reasonably accurate answer.) The nondimensional heat fluxes obtained (based on the band having a ω value corresponding to the 2.7 μm band of water vapor at 1000 K) are plotted as circles in Fig. 5; the curve is a plot of the analytical result. The present method agrees with analytical results to within a maximum relative error of 1.7 percent.

The second and third examples were chosen to match examples analyzed by Denison and Webb (1993a, b) using the line-by-line method. In the second (problem initially posed by Kim et al., 1991), pure water vapor at one atmosphere pressure and 1000 K was the gas, and all of its bands (rotational, 6.3 μm, 2.7 μm, 1.87 μm, and 1.38 μm) were considered, with L being either 10 cm or 100 cm. Volume and direction were discretized into 45 layers and 16 solid angles, respectively, and the number of spectral discretizations was 200 divisions for each band considered. As advised by Edwards and Balakrishnan (1973), the normally recommended values of α, ω, and β (Siegel and Howell, 1992; Modest, 1992) were adjusted according to a certain routine. (The normally recommended values are consistent only with the piecewise continuous fit of Edwards and Menard.) The adjusting routine corrects both α and ω by a factor (A/A_Q), this correction factor being a graphed function of β and τ, which makes it path length dependent. On the other hand, a universally constant value for A/A_Q of 1.2 may also be used with some success (Modak, 1979; Lee et al., 1994; Lee, 1995). For the major bands in the present problem, the values of β and τ all fell within the log-root region of Edwards and Balak-

Table 1 Constants for the fitted reordered absorption coefficient distribution given by Eq. (14), for $-2.5 \leq \log_{10}\beta \leq 0$

Coefficient	$\psi=\log_{10}\beta$										
	ψ_1=-2.5	ψ_2=-2.25	ψ_3=-2	ψ_4=-1.75	ψ_5=-1.5	ψ_6=-1.25	ψ_7=-1	ψ_8=-0.75	ψ_9=-0.5	ψ_{10}=-0.25	ψ_{11}=0
a	-6.98754	-6.41693	-5.97803	-5.47208	-4.91181	-4.36726	-3.974	-3.50335	-3.08529	-2.75864	-2.45351
b	-3.23214	-3.27462	-1.59172	-3.50185	-3.44405	-3.49680	-1.797	-1.63067	-1.44859	-1.26651	-0.28807
c	-0.80036	-0.86167	-0.11053	-0.93708	-0.98044	-1.05998	0	0	0	0	0.16831
d	-0.13066	-0.15358	-0.09045	-0.14765	-0.15789	-0.15925	0	0	0	0	-0.10754
e	-0.003939	-0.00484	-0.00503	-0.00450	-0.00495	-0.00502	0	0	0	0	-0.01036
f	0	0	0	0	0	0	0	0	0	0	-0.00026
g	0.060496	0.06850	-0.15429	0.10279	0.11474	0.15336	-0.026	-0.28301	-0.30348	-0.32217	-0.72571
h	-0.015268	-0.01230	-0.00645	-0.01573	-0.01749	-0.02905	0.0010	0.00044	-0.00051	-0.00149	0.2038
i	-0.011013	-0.01375	-0.01244	-0.01454	-0.01695	-0.01863	0	0	0	0	-0.01181
j	-0.000391	-0.00051	-0.00068	-0.00053	-0.00064	-0.00071	0	0	0	0	-0.00245
k	0	0	0	0	0	0	0	0	0	0	-0.00008

rishnan's graph, so the mean value of A/A_Q in this region, namely $A/A_Q = 1.26$, was used.

The negative of the divergence of the radiative heat flux vector, $-dq_r/dx$, obtained by this model is plotted as a function of nondimensional distance x/L across the layer in Figs. 6(*a*) and 6(*b*). Shown on the same graphs are the line-by-line solutions of Denison and Webb (1993a). The distribution of $-dq_r/dx$ for $L = 100$ cm agrees very closely with the results of Denison and Webb (1993a), and both methods gave a wall heat flux of $q_w = 28.7$ kW/m^2. For the plate spacing $L = 10$ cm, the present results are about 10 percent higher than the line-by-line results in the central region, and the predicted wall heat flux was 13.5 kW/m^2, which is 0.7 percent lower than the value of 13.6 obtained by Denison and Webb (1993a). Each prediction required about 300 CPU seconds on the SUN SPARC workstation.

In the third example, the gas, a mixture of 20 percent water vapor and 80 percent air, was at 1500 K and one atmosphere pressure, and the plate spacing L was 2 m. The computational grid had 20 layers, 20 directions, and 200 spectral divisions for each band of the five bands. The values of β and τ for the major bands were again found to fall within the log-root region of Edwards and Balakrishnan's graph, so a value of 1.26 for the correction factor A/A_Q was again used. Figure 6(*c*) compares the results with the line-by-line solutions of Denison and Webb (1993b). The plot of $-dq_r/dx$ agrees well with Denison and Webb's predictions, except near the walls where the present method gives a slightly higher divergence. The predicted wall heat flux q_w was calculated to be 75.3 kW/m^2, which was 6 percent higher than the value of 71.0 kW/m^2 predicted by Denison and Webb (1993b). The total CPU requirement for this example was about 200 seconds.

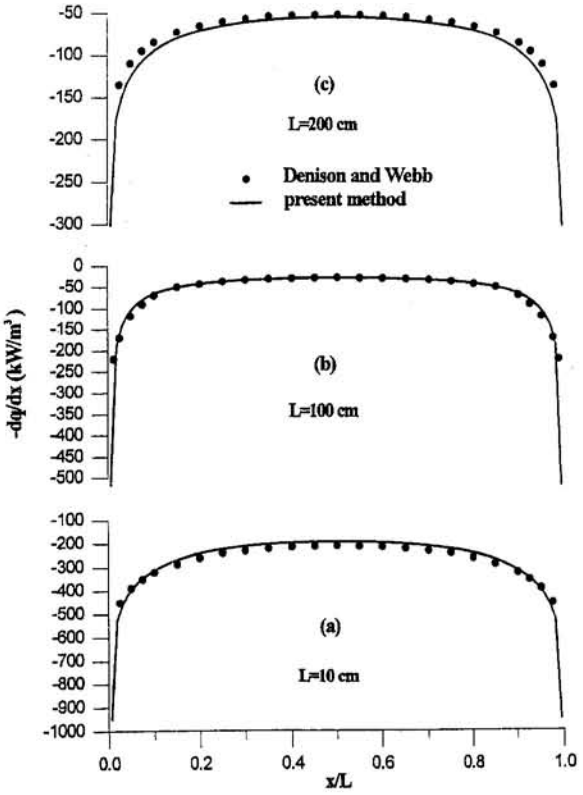

Fig. 6 Comparison of the present heat flux divergence results with the line-by-line solutions of Denison and Webb (1993a, b)

Concluding Remarks

A promising nongray gas model for predicting gaseous radiation calculations has been presented. The model resolves the complex line structure of the absorption coefficient for isothermal and homogeneous media and transforms it into a smooth reordered distribution. The reordered profile can then be approximated by a set of stepwise gray coefficients suitable for engineering radiant heat transfer application.

The Laplace inversion theory was used in the process to obtain the reordered spectral absorption coefficient distribution and the resulting reordered profiles were plotted. Fitted functions for the reordered absorption spectra for the practical range of β of interest were presented. The method was applied to simple examples and compared to line-by-line solutions for the wall heat fluxes and the radiative heat flux divergence.

It was found that 50 or more spectral divisions were required to model the complex band behavior adequately. With this spectral discretization, good agreement was observed with the benchmark solutions. Reasonable computational effort was required in the present numerical simulation.

Although the present method requires 50 to 200 solutions of the RTE, this is much more economical than a line-by-line solution. Still, the computation requirements for the current method are excessive for engineering application. The method does, however, provide a platform from which simplified models can be developed. In addition, it permits the effect of soot and an approximate treatment of band overlap to be included. It can also be used for gases where band parameters are available, even though line-by-line information is not available. Work is being done to extend the reordered distributions to handle nonisothermal and nonhomogeneous cases.

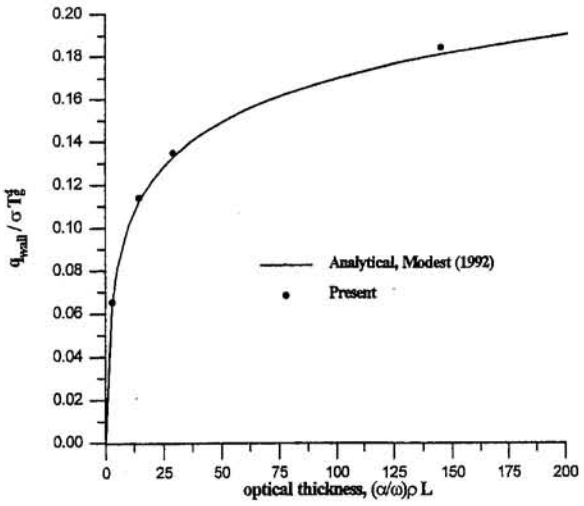

Fig. 5 Nondimensional radiative wall heat flux for the uniform temperature profile with varying optical thickness for the weal-line limit ($\beta \to \infty$)

Acknowledgments

This work was supported by a contract from CANMET, of the Energy Mines and Resources Department of Canada, with P. M. J. Hughes as Scientific Authority.

References

Arking, A., and Grossman, K., 1972, "The Influence of Line Shape and Band Structure on Temperatures in Planetary Atmospheres," *Journal of Atmospheric Science*, Vol. 29, pp. 937–949.

Churchill, R. V., 1972, *Operational Mathematics*, 3rd ed., McGraw-Hill, New York, pp. 7, 162–218.

Denison, M. K., and Webb, B. W., 1993a, "A Spectral Line-Based Weighted-Sum-of-Gray-Gases Model for Arbitrary RTE Solvers," ASME JOURNAL OF HEAT TRANSFER, Vol. 115, pp. 1004–1012.

Denison, M. K., and Webb, B. W., 1993b, "An Absorption-Line Blackbody Distribution Function for Efficient Calculation of Total Gas Radiative Transfer," *J. Quant. Spectrosc. Radiat. Transfer*, Vol. 50, No. 5, pp. 499–510.

Domoto, G. A., 1974, "Frequency Integration for Radiative Transfer Problems Involving Homogeneous Nongray Gases: The Inverse Transmission Function," *Journal of Quant. Spectrosc. Radiat. Transfer,* Vol. 14, pp. 935–942.

Dubner, H., and Abate, J., 1968, "Numerical Inversion of Laplace Transforms by Relating Them to the Finite Fourier Cosine Transform," *Journal of the Association for Computing Machinery,* Vol. 15, No. 1, pp. 115–123.

Durbin, F., 1973, "Numerical Inversion of Laplace Transforms: An Efficient Improvement to Dubner and Abate's Method," *The Computer Journal,* Vol. 17, No. 4, pp. 371–376.

Edwards, D. K., 1976, "Advances in Heat Transfer," T. F. Irvine and J. P. Hartnett, eds., Academic Press, New York, Vol. 12, pp. 115–193.

Edwards, D. K., and Menard, W. A., 1964, "Comparison of Models for Correlation of Total Band Absorption," *Applied Optics,* Vol. 3, No. 5, pp. 621–625.

Edwards, D. K., and Balakrishnan, A., 1973, "Thermal Radiation by Combustion Gases," *Int. J. Heat Mass Transfer,* Vol. 16, pp. 25–40.

Elsasser, W. M., 1938, "Mean Absorption and Equivalent Absorption Coefficients of a Band Spectrum," *Physical Review,* Vol. 54, pp. 126–129.

Felske, J. D., and Tien, C. L., 1974, "A Theoretical Closed Form Expression for the Total Band Absorptance of Infrared-Radiating Gases," ASME JOURNAL OF HEAT TRANSFER, Vol. 96, pp. 155–158.

Fiveland, W. A., 1984, "Discrete-Ordinate Solutions of the Radiative Transport Equation for Rectangular Enclosures," ASME JOURNAL OF HEAT TRANSFER, Vol. 106, pp. 699–706.

Flannery, B. P., Press, W. H., Teukolsky, S. A., and Vetterling, W. T., 1986, *Numerical Recipes,* 1st ed., Cambridge University Press, pp. 77–101.

Goody, R. M., 1952, "A Statistical Model for Water Vapour Absorption," *Quart. J. Royal Meteorol. Soc.,* Vol. 78, pp. 165–169.

Hartmann, J. M., Levi Di Leon, R., and Taine, J., 1984, "Line-by-Line and Narrow-Band Statistical Model Calculation for H_2O," *J. Quant. Spect. Radiat. Transfer,* Vol. 32, No. 2, pp. 119–127.

Honig, G., and Hirdes, U., 1984, "A Method for the Numerical Inversion of Laplace Transforms," *Journal of Computational and Applied Mathematics,* Vol. 10, pp. 113–132.

Hottel, H. C., and Sarofim, A. F., 1967, *Radiative Transfer,* McGraw-Hill, New York.

Howell, J. R., 1988, "Thermal Radiation in Participating Media: The Past, the Present, and Some Possible Futures," ASME JOURNAL OF HEAT TRANSFER, Vol. 110, pp. 1220–1226.

Kim, T. K., 1990, "Radiation and Combined Mode Heat Transfer Analyses in Absorbing, Emitting, and Mie-Anisotropic Scattering Media Using the S-N Discrete Ordinates Method," Ph.D. Thesis, University of Minnesota.

Kim, T. K., Menart, J. A., and Lee, H. S., 1991, "Non-gray Radiative Gas Analyses Using the S-N Discrete Ordinates Method," ASME JOURNAL OF HEAT TRANSFER, Vol. 113, pp. 946–952.

Koch, R., Wittig, S., and Noll, B., 1991, "The Harmonical Transmission Model: A New Approach to Multi-dimensional Radiative Transfer Calculation in Gases Under Consideration of Pressure Broadening," *Int. J. Heat Mass Transfer,* Vol. 34, No. 7, pp. 1871–1880.

Lee, P. Y. C., Raithby, G. D., and Hollands, K. G. T., 1994, "The 'Reordering' Concept of the Absorption Coefficient for Modelling Nongray Gases," *Radiation Heat Transfer: Current Research,* ASME HTD-Vol. 276, pp. 21–30.

Lee, P. Y. C., 1995, "Reordering the Absorption Coefficient Within the Wide Band for Predicting Gaseous Radiant Exchange," Ph.D. Thesis, Department of Mechanical Engineering, University of Waterloo, Waterloo, Canada.

Malkmus, W., 1967, "Random Lorentz Band Model With Exponential-Tailed S^{-1} Line Intensity Distribution Function," *Journal of the Optical Society of America,* Vol. 57, pp. 327–329.

Mengüç, M. P., and Viskanta, R., 1985a, "A Sensitivity Analysis for Radiative Heat Transfer in Pulverized Coal-Fired Furnaces," *Proc. ASME National Heat Transfer Conference,* ASME HTD-Vol. 45, pp. 221–229.

Modak, A. T., 1979, "Exponential Wide Band Parameters for the Pure Rotational Band of Water Vapour," *J. Quant. Spectrosc. Radiat. Transfer,* Vol. 21, pp. 131–142.

Modest, M. F., 1991, "The Weighted-Sum-of-Gray-Gases Model for Arbitrary Solution Methods in Radiative Transfer," ASME JOURNAL OF HEAT TRANSFER, Vol. 113, pp. 650–656.

Modest, M. F., 1992, *Radiative Heat Transfer,* McGraw-Hill, New York, Chap. 17, pp. 620–621.

Morizumi, S. J., 1970, "An Investigation of Infrared Radiation by Vibration-Rotation Bands of Molecular Gases," Ph.D. Thesis, University of California, Los Angeles.

Raithby, G. D., and Chui, E. H., 1990, "A Finite-Volume Method for Predicting Radiant Transfer in Enclosures With Participating Media," ASME JOURNAL OF HEAT TRANSFER, Vol. 112, pp. 415–423.

Siegel, R., and Howell, J. R., 1992, *Thermal Radiation Heat Transfer,* 3rd ed., Hemisphere Publishing, New York, Chap. 12, pp. 552–567.

Soufiani, A., Hartmann, J. M., and Taine, J., 1985, "Validity of Band-Model Calculations for CO_2 and H_2O Applied to Radiative Properties and Conductive Radiative Transfer," *J. Quant. Spect. Radiat. Transfer,* Vol. 33, No. 3, pp. 243–257.

Tang, K. C., and Brewster, M. Q., 1994, "*k*-Distribution Analysis of Gas Radiating With Nongray, Emitting, Absorbing, and Anisotropic Scattering Particles," ASME JOURNAL OF HEAT TRANSFER, Vol. 116, pp. 980–985.

Wang, W. C., 1983, "An Analytical Expression for the Total Band Absorptance of Infrared-Radiating Gases," *J. Quant. Spectrosc. Radiat. Transfer,* Vol. 29, No. 3, pp. 270–281.

APPENDIX

Interpolation Algorithm for a_ξ^*

The objective is to obtain a_ξ^* for a given θ (or ξ^*, since $\theta = \ln \xi^*$) using Eq. (14). The constants a to k in this equation depend on ψ (or β since $\psi = \log_{10}\beta$), and are tabulated in Table 1 for $\psi_1, \psi_2, \ldots, \psi_{11}$.

If the value ψ of interest corresponds to one of the tabulated values, the constants from the corresponding column in Table 1 are used in Eq. (14), and this equation is evaluated at the required θ.

If ψ does not correspond to one of the tabulated ψ's in Table 1, a_ξ^* is found from Eq. (14), at the required θ, for each ψ in Table 1. For $\psi_1, \psi_2, \ldots, \psi_{11}$, these values are denoted by $a_{\xi,1}^*, a_{\xi,2}^*, \ldots, a_{\xi,11}^*$. Now a spline interpolation (e.g., Flannery et al., 1986), uses these values to obtain a_ξ^* at the required ψ. For clarity, this interpolation algorithm is provided in detail.

The coefficients κ_j in the spline equation are given by

$$\kappa_{j-1} + 2\kappa_j + \kappa_{j+1} = 96(a_{\xi,j-1}^* - 2a_{\xi,j}^* + a_{\xi,j+1}^*), \quad \text{for} \quad j = 2, \ldots, 10 \qquad (15a)$$

$$\kappa_j = 0, \quad \text{for} \quad j = 1 \quad \text{and} \quad 11 \qquad (15b)$$

These equations are solved for κ_j ($j = 1, \ldots, 11$) using a tridiagonal solver. The interval in which ψ lies is, say, $\psi_i \le \psi \le \psi_{i+1}$ (e.g., if $\psi = -2.3$, $i = 1$; and if $\psi = -1.1$, $i = 6$). The desired a_ξ^* is found by evaluating the spline equation for this interval at ψ, as follows:

$$a_\xi^* = Aa_{\xi,i}^* + (1 - A)a_{\xi,i+1}^* + B\kappa_i + C\kappa_{i+1} \qquad (16)$$

where A, B, and C are given, respectively, by

$$A = \frac{1}{4}(\psi_{i+1} - \psi), \quad B = \frac{1}{96}(A^3 - A),$$

$$\text{and} \quad C = \frac{1}{96}(3A^2 - A^3 - 2A)$$

M. Cherkaoui

J.-L. Dufresne

Laboratoire de Météorologie Dynamique,
C.N.R.S.—Université Paris 6,
F-75252 Paris Cedex 05, France

R. Fournier[1]
LESETH,
Université Paul Sabatier,
F-31077 Toulouse Cedex, France

J.-Y. Grandpeix
LESETH,
Université Paul Sabatier,
F-31077 Toulouse Cedex, France;
also Laboratoire de Météorologie
Dynamique,
C.N.R.S.—Université Paris 6,
F-75252 Paris Cedex 05, France

A. Lahellec
Laboratoire de Météorologie Dynamique,
C.N.R.S.—Université Paris 6,
F-75252 Paris Cedex 05, France

Monte Carlo Simulation of Radiation in Gases With a Narrow-Band Model and a Net-Exchange Formulation

The Monte Carlo method is used for simulation of radiative heat transfers in nongray gases. The proposed procedure is based on a Net-Exchange Formulation (NEF). Such a formulation provides an efficient way of systematically fulfilling the reciprocity principle, which avoids some of the major problems usually associated with the Monte Carlo method: Numerical efficiency becomes independent of optical thickness, strongly nonuniform grid sizes can be used with no increase in computation time, and configurations with small temperature differences can be addressed with very good accuracy. The Exchange Monte Carlo Method (EMCM) is detailed for a one-dimensional slab with diffusely or specularly reflecting surfaces.

I Introduction

While the role of infrared exchanges in gases is well known for very large (atmospheric) or very hot (combustion) systems, its importance in small, nearly isothermal systems at moderate temperature is much less advertised. And yet, several experimental investigations concerning natural convection in dwelling rooms using various configurations including highly reflective walls seem to indicate a coupling between radiative processes and fluid flow (Yguel, 1988; Palenzuela, 1992; Fournier, 1994). Thus, the present study was devoted to the development of a sufficiently precise method for radiation exchange computations within nearly isothermal cavities at moderate temperature, filled with an air/water vapor/carbon dioxide mixture, and having possibly reflecting walls.

Numerical simulations of radiative heat transfer in gases originated mainly in meteorology and astrophysics research (Goody and Yung, 1989) as well as in engineering heat transfer research for high-temperature systems (Ludwig et al., 1973). These efforts concerned the development of gas radiation models and their implementation in complete radiation heat transfer simulations through the integration of the radiative transfer equation. Nowadays the use of "exact" line-by-line models remains unfeasible for complex systems; most authors make use of accurate band models like the narrow band statistical model (NBSM) proposed by Malkmus in 1967. This type of model leads to specific difficulties, when solving the radiative transfer equation, due to spectral correlations, within each band, between intensity and gas transmittance. We will not enter in a detailed description of this phenomenon which is extensively discussed in the literature. The main points are:

(*i*) whatever intrinsic precision band models may reach, final results can be very inaccurate if correlations are ignored;

(*ii*) specific solutions have been proposed for black wall enclosures (for example, Zhang et al., 1988) but the problem remains open when surface reflections occur (Menart et al., 1993; Menart and Lee, 1993).

One of the best available solutions to this complex problem seems to be the use of the Monte Carlo method (MCM). Some care is required for emission/absorption correlations but solutions are available (Modest, 1992). For details about the use of the MCM with a NBSM one may also refer to Cherkaoui et al. (1992) and Liu and Tiwari (1993, 1994). Two well-advertised disadvantages of the MCM are the difficulty in coping with strongly nonuniform grids and the drastic increase of computation times with increasing optical thickness (Howell, 1988; Siegel and Howell, 1992). A third difficulty appears, specific to nearly isothermal systems: Radiation energy balances are very small compared to emitted and absorbed energies; a 1 percent uncertainty on the computed absorbed and emitted energies may lead to more than 100 percent error on the radiation balance of a given cell. Such configurations would demand extremely accurate computations, that is to say extremely large numbers of rays to follow, and hence prohibitive computer run times. Many efforts are being made in trying to improve the MCM: biasing techniques (Martin and Pomraning, 1990), reverse MCM (Walters and Buckius, 1992), and hybrid methods (Vercammen and Froment, 1980; Farmer and Howell, 1994). These different approaches represent good tools for specific problems, but it can be a subtle task to choose among all available MCM improvements or to try to make use of several techniques simultaneously when required.

[1] Present address: Institute of Energy and Power Plant Technology, TH Darmstadt, 64287, Federal Republic of Germany.

Contributed by the Heat Transfer Division for publication in the JOURNAL OF HEAT TRANSFER. Manuscript received by the Heat Transfer Division April 1995; revision received January 1996. Keywords: Building, Numerical Methods, Radiation. Associate Technical Editor: M. F. Modest.

We started from the following statement: Most of the aforementioned difficulties seem to be related to the violation of the reciprocity principle (this is particularly obvious for the problem of strong grid size differences). We therefore aimed at the development of a MCM that would intrinsically fulfill this principle. The approach used is entirely based on the concept of radiative exchange. The analogy to the physical processes is kept but emission and absorption mechanisms are considered simultaneously. In the standard MCM, when a ray between two points A and B is defined, it is used for the transport of energy from A to B. In the present method, the same ray will be used for the radiative *exchange* between A and B. This means that radiative transports from A to B and from B to A are not dissociated. This is achieved through the development of the net-exchange formulation (NEF) described in Sec. II in the case of monodimensional configurations with black surfaces. Section III shows how the MCM can be efficiently applied on the basis of such a formulation. The extension to reflective surfaces and some validation tests are the subject of Sec. IV. Simulation results are presented in Sec. V.

II Net-Exchange Formulation (NEF)

The starting point is a formulation very similar to that proposed by Green (1967) for monochromatic radiative exchanges and extended by Joseph and Bursztyn (1976) for narrow-band models. These authors were concerned with the simulation of radiative heat transfers in stratified planetary atmospheres. The present formulation has some common features with the zone formulation (Hottel and Sarofim, 1967), the main difference being that the assumption of isothermal cells is dropped.

(a) Monochromatic Formulation. We consider here an infinite volume of gas at uniform pressure P confined between two parallel black plates. Plate 1 (at $S(1) = 0$ coordinate) is at temperature $\theta^s(1)$ and plate 2 ($S(2) = D$) is at temperature $\theta^s(2)$. As this configuration is one dimensional, we will only make use of fluxes and net fluxes per unit surface. The optical depth $\tau_\nu(x, x')$ between x and x' is defined as

$$\tau_\nu(x, x') = \left| \int_x^{x'} \frac{P_a(x'')}{P_0} k_\nu(x'') dx'' \right| \tag{1}$$

The net-exchange rate (NER) between two elementary gas layers at the x and x' coordinates is defined as the radiative flux emitted at x' and absorbed at x minus the radiative flux emitted at x and absorbed at x'. For a monochromatic radiation this NER can be written as (Green, 1967; Joseph and Bursztyn, 1976)

$$\frac{\partial^2 \psi_\nu^{gg}(x, x')}{\partial x \partial x'} = \pi[B_\nu(x') - B_\nu(x)] \left| \frac{\partial^2}{\partial x \partial x'} [\mathcal{T}_\nu(x, x')] \right| = -\frac{\partial^2 \psi_\nu^{gg}(x', x)}{\partial x' \partial x} \tag{2}$$

where $\mathcal{T}_\nu(x, x')$ is the monochromatic slab transmittance

$$\mathcal{T}_\nu(x, x') = 2 \int_0^1 \mu \exp(-\tau_\nu(x, x')/\mu) d\mu \tag{3}$$

Similar expressions can be derived for the NER between surface m and an elementary gas layer at x:

$$\frac{\partial \psi_\nu^{gs}(x, m)}{\partial x} = \pi[B_\nu^s(m) - B_\nu(x)] \left| \frac{\partial}{\partial x} [\mathcal{T}_\nu(S(m), x)] \right| = -\frac{\partial \psi_\nu^{sg}(m, x)}{\partial x} \tag{4}$$

Nomenclature

$\mathcal{A}$ = integral to estimate
B = black body intensity, W/($m^2 \cdot sr \cdot cm^{-1}$); $B(x)$ is the black body intensity at temperature $\theta(x)$, and $B^s(m)$ is the black body intensity for the surface temperature $\theta^s(m)$
D = distance between the two surfaces, m
$\mathcal{D}$ = integration spatial domain
$\bar{F}(\ )$ = narrow band average transmission function
k_ν = monochromatic absorption coefficient, m^{-1}
$\bar{k}$ = narrow band average absorption coefficient, m^{-1}
l = narrow band index
m = surface index
N = number of realizations
N_d = number of gas layers
N_b = number of narrow bands
$P_a(\ )$ = partial pressure of the gas absorber
P_0 = standard pressure = 1 atm
$\mathcal{P}(\ )$ = probability
$p(\ )$ = abscissa probability density function
$q(\ )$ = direction cosine probability density function
r = number of reflections
$S(\ )$ = surface abscissa, m
$\bar{T}(\ )$ = Malkmus transmission function
$\mathcal{T}$ = slab transmittance
u = effective path length, m
w, W = statistical weights
x, x' = coordinate
X_i = abscissa of separation between gas layers $(i-1)$ and (i), m
$\hat{X}_i$ = abscissa of layer (i) center, m
ΔX = gas layer thickness, m
$\Delta\nu$ = wavenumber interval, cm^{-1}
ν = wavenumber, cm^{-1}
ϵ = surface emissivity
ρ = surface reflectivity
μ = cosine of cone angle (measured from normal of surface)
Φ = shape parameter for the Malkmus model
$\psi(i, j)$ = energy net-exchange rate between (i) and (j), defined as the rate at which energy is emitted at (j) and absorbed at (i) minus the rate at which energy is emitted at (i) and absorbed at (j)
$\psi(i)$ = radiation budget of layer (i), W per unit of reference area, $W \cdot m^{-2}$
θ = temperature, K
τ_ν = monochromatic optical depth, m
γ = optical path index
χ_l = rough estimate of $\bar{\psi}_l$
ξ = overestimate of the truncation error
$\sigma(\ )$ = standard deviation

Superscripts

$\overline{(\ )}_l$ = average for narrow band l; l index is omitted when irrelevant
g = gas layers
gg = exchange between two gas layers
gs or sg = exchange between a gas layer and an opaque surface
s = opaque surface
ss = exchange between two opaque surfaces
$\hat{}$ = average according to the chosen pdf

Abbreviations

AMCM = Analogue Monte Carlo Method
EMCM = Exchange Monte Carlo Method
MCM = Monte Carlo Method
NEF = Net-Exchange Formulation
NER = Net-Exchange Rate
pdf = probability density function

and between the two surfaces

$$\psi_\nu^{ss}(1,2) = \pi[B_\nu^s(2) - B_\nu^s(1)]\mathcal{T}_\nu(S(1), S(2)) = -\psi_\nu^{ss}(2,1) \quad (5)$$

Local radiation balances may be expressed using partial exchanges. The resulting expression for the net inflow at x of monochromatic radiant energy per unit volume is:

$$\frac{\partial \psi_\nu^g(x)}{\partial x} = \int_0^D \frac{\partial^2 \psi_\nu^{gg}(x,x')}{\partial x \partial x'} dx' + \sum_{m=1}^{2} \frac{\partial \psi_\nu^{gs}(x,m)}{\partial x} \quad (6)$$

We shall use a term commonly used in the literature of atmospheric sciences: "radiation budget" is used instead of "radiation net flux" to avoid confusion between "net rates" and "net-exchange rates." Similarly, the surface radiation budget at $S(1)$ is:

$$\psi_\nu^s(1) = \int_0^D \frac{\partial \psi_\nu^{sg}(1,x)}{\partial x} dx + \psi_\nu^{ss}(1,2) \quad (7)$$

(b) Spectral Integration. The preceding expressions can be integrated over a spectral interval of width $\Delta\nu$. If the interval is narrow enough, the black body intensity can be assumed uniform. Integration of Eq. (2) gives, for instance,

$$\frac{\partial^2 \bar{\psi}^{gg}(x,x')}{\partial x \partial x'} = \frac{1}{\Delta\nu}\int_{\Delta\nu} \frac{\partial^2 \psi_\nu^{gg}(x,x')}{\partial x \partial x'} d\nu = \pi[\bar{B}(x') - \bar{B}(x)] \frac{1}{\Delta\nu}\left|\frac{\partial^2}{\partial x \partial x'}\left[\int_{\Delta\nu} \mathcal{T}_\nu(x,x')d\nu\right]\right| \quad (8)$$

Inverting the frequency and angular integration (see Eq. (3)) leads to the following expression:

$$\frac{\partial^2 \bar{\psi}^{gg}(x,x')}{\partial x \partial x'} = \pi[\bar{B}(x') - \bar{B}(x)]\left|\frac{\partial^2 \bar{\mathcal{T}}(x,x')}{\partial x \partial x'}\right| \quad (9)$$

with

$$\bar{\mathcal{T}}(x,x') = 2\int_0^1 \mu \bar{F}(x,x',\mu)d\mu \quad (10)$$

and

$$\bar{F}(x,x',\mu) = \frac{1}{\Delta\nu}\int_{\Delta\nu} \exp(-\tau_\nu(x,x')/\mu)d\nu \quad (11)$$

$\bar{\mathcal{T}}$ and $\bar{F}$ are respectively defined as the spectral average slab transmittance and the spectral average transmission function. Integration over the whole spectrum is obtained by adding the contributions of the N_b narrow bands:

$$\frac{\partial^2 \psi^{gg}(x,x')}{\partial x \partial x'} = \sum_{l=1}^{N_b} \frac{\partial^2 \bar{\psi}_l^{gg}(x,x')}{\partial x \partial x'} \Delta\nu_l \quad (12)$$

Averaging Eqs. (4) and (5) gives two very similar expressions for gas–surface and surface–surface exchanges. Up to this point, the only assumption made is the spectral independence of the black body intensity within a narrow band. It allows preserving the antisymmetry in (x, x') of the spectrally integrated NER. Various narrow-band models may be used to approximate the average transmission function. Considering the initial application field of the present work (building thermal analysis) the Malkmus NBSM was retained with the assumption of uniform gas radiative properties

$$\bar{F}(x,x',\mu) = \bar{T}(u(x,x',\mu)) \quad (13)$$

where u is the effective path length and $\bar{T}$ is the Malkmus transmission function

$$u(x,x',\mu) = \left|\int_x^{x'} \frac{P_a(x'')}{P_0\mu} dx''\right| \quad (14)$$

$$\bar{T}(u) = \exp\{-\Phi[(1 + 2\bar{k}u/\Phi)^{1/2} - 1]\} \quad (15)$$

(c) Discretization. The volume of gas is divided in N_d layers of thicknesses ΔX_i. We want to emphasize that the layers are not assumed isothermal; the internal temperature profiles are accounted for, without restriction. If we consider the ith gas layer, between the X_i and X_{i+1} abscissae, and the jth gas layer, between X_j and X_{j+1}, Eq. (9) can be integrated in x and x' to give the average NER between layers i and j:

$$\bar{\psi}^{gg}(i,j) = \int_{X_i}^{X_{i+1}} dx \int_{X_j}^{X_{j+1}} dx' \frac{\partial^2 \bar{\psi}^{gg}(x,x')}{\partial x \partial x'} = \int_{X_i}^{X_{i+1}} dx \int_{X_j}^{X_{j+1}} dx' \pi[\bar{B}(x') - \bar{B}(x)] \times \left|\frac{\partial^2}{\partial x \partial x'}[\bar{\mathcal{T}}(x,x')]\right| \quad (16)$$

Equivalent expressions can be derived for the NER $\bar{\psi}^{gs}(i,m)$ between layer i and surface m and $\bar{\psi}^{ss}(1,2)$ between surfaces 1 and 2. The average radiation budget for the ith layer is:

$$\bar{\psi}^g(i) = \sum_{j=1}^{N_d} \bar{\psi}^{gg}(i,j) + \sum_{m=1}^{2} \bar{\psi}^{gs}(i,m) \quad (17)$$

and for surface 1, it is expressed as

$$\bar{\psi}^s(1) = \sum_{i=1}^{N_d} \bar{\psi}^{sg}(1,i) + \bar{\psi}^{ss}(1,2) \quad (18)$$

III The Monte Carlo Numerical Scheme

Radiative transfer specialists commonly refer to the MCM as a method for numerical simulation of a stochastic process: by invoking a probabilistic model of the radiative exchange process and also applying Monte Carlo sampling techniques, it is possible to choose a semi-macroscopic approach, and avoid many of the difficulties inherent in the averaging process of the usual integral equation formulations (Howell, 1968). The aforementioned probabilistic model is usually designed in strict analogy with the physical processes of photon emission, transmission and absorption: We will refer to such methods as Analogue Monte Carlo Methods (AMCM).

The present approach is significantly different. We make use of the MCM for numerical computation of multidimensional integrals (Press et al., 1992). No physical probabilistic model is required. An integral formulation is chosen (NEF) and a statistical method (MCM) is used to compute integrals. A major feature of such a method is that the sampling laws could be chosen arbitrarily and do not have to match any physical property.

(a) Principle. The Monte Carlo procedure for numerical estimation of an integral $\mathcal{A} = \int_{\mathcal{D}} f(\vec{v})d\vec{v}$ is the following:

(*i*) A probability density function $p(\vec{v})$ is chosen arbitrarily on $\mathcal{D}$ with the only constraint that it must be nonzero on $\mathcal{D}$.

(*ii*) The associated weighting function is defined as

$$w(\vec{v}) = f(\vec{v})/p(\vec{v}) \quad (19)$$

(*iii*) N values of $\vec{v}$ are generated randomly according to $p(\vec{v})$ and for each value the corresponding weighting factor w is computed. The average value $\langle w\rangle_N$ and variance $\sigma_N^2(w)$ of these N realizations of the variable

$w(\vec{v})$ are then computed. $\langle w\rangle_N$ and $\sigma_N^2(w)$ themselves are random variables.

(iv) $\tilde{\mathcal{A}} = \langle w\rangle_N$ is an estimate of integral $\mathcal{A}$. The expectation of $\tilde{\mathcal{A}}$ is $\mathcal{A}$. An estimate of the standard deviation of $\tilde{\mathcal{A}}$ (henceforth named "statistical error") is $\tilde{\sigma}_N(\tilde{\mathcal{A}}) = N^{-0.5}\sigma_N(w)$.

When computing sums instead of integrals, the preceding procedure is valid if replacing pdf 's with discrete probabilities.

The key point of this method is the choice of probabilities and pdf. Again, this choice is a priori totally arbitrary. However, an improper choice of probabilities may lead, for a prescribed precision, to an extremely large sampling size. Obviously, the criterion is the variance of $w(\vec{v})$. Thus one should choose $p(\vec{v})$ such that the variations of $f(\vec{v})/p(\vec{v})$ are minimal, keeping in mind that the random generation according to $p(\vec{v})$ must be feasible and computationally efficient. Probabilities may also be chosen to match physical properties (like the Lambert law for surface emission angles). This may lead to an increase of computational costs but provides the developer with a useful physical insight into the numerical procedure.

(b) Probability Functions. The MCM is applied to compute the multidimensional integrals that appear in the NEF. In this formulation, independent expressions correspond to the NER for each pair of cells. It is therefore natural (although not necessary) to preserve this independence in the numerical scheme. We detail hereafter the probability functions retained for the MCM integration of the NER between two gas layers.

The total NER between the ith and the jth gas layers is defined from Eqs. (9), (12), and (16):

$$\psi^{gg}(i,j) = \sum_{l=1}^{N_b} \Delta\nu_l \int_{X_i}^{X_{i+1}} dx \int_{X_j}^{X_{j+1}} dx' \int_0^1 d\mu f^{gg}(l,x,x',\mu) \quad (20)$$

with

$$f^{gg}(l,x,x',\mu) = \pi[\overline{B}_l(x') - \overline{B}_l(x)]2\mu\left|\frac{\partial^2}{\partial x\partial x'}[\overline{T}_l(u(x,x',\mu))]\right| \quad (21)$$

Thus the total NER computation involves one discrete sum, one integral over angles, and two integrals over the x and x' coordinates. According to the general procedure presented in the preceding paragraph, we need to define probabilities for each of these quantities. The associated weighting function will then be (Eq. (19)):

$$w_{ij}^{gg}(l,x,x',\mu) = \frac{f^{gg}(l,x,x',\mu)}{\mathcal{P}(l)p_i(x)p_j(x')q(\mu)} \quad (22)$$

Uniform densities are used for positions within layers i and j and the pdf of the direction cosine μ corresponds to an isotropic emission (Table 1).

In order to determine discrete probabilities for spectral bands, we tried to estimate roughly the NER $\overline{\psi}_l^{gg}(i,j)$ between i and j on each band l. This renders it possible to favor bands on which most of the radiative exchanges occur. If the pdf chosen for x, x', and μ are meaningful, one can simply state that if $\bar{x}$, $\bar{x}'$, and $\bar{\mu}$ are the average values of x, x', and μ according to $p_i(x)$, $p_j(x')$, and $q(\mu)$, respectively, then a rough estimate $\chi_l^{gg}(i,j)$ of $\overline{\psi}_l^{gg}(i,j)$ is:

$$\chi_l^{gg}(i,j) = \frac{f^{gg}(l,\bar{x},\bar{x}',\bar{\mu})}{p_i(\bar{x})p_j(\bar{x}')q(\bar{\mu})} \quad (23)$$

Therefore the following probability is chosen for the lth spectral band:

$$\mathcal{P}(l) = \frac{|\chi_l|}{\sum_{k=1}^{N_b}|\chi_k|} \quad (24)$$

To avoid problems when $\theta(\bar{x}) = \theta(\bar{x}')$, the black body intensity differences that appears in Eq. (24) are replaced by their derivatives relative to temperature. Similar developments are required for gas–surface and surface–surface exchanges (Table 1).

It is worth mentioning that the distance traveled between emission and absorption points does not appear as a variable to be randomly generated. Two locations are generated independently within the two cells considered from which the "exchange distance" is simply computed.

(c) Implementation. The quantities to be numerically estimated are the NER for each pair of cells. The radiation budget of each cell is obtained by summing the NER between the cell considered and all other cells in the system (Eqs. (17, 18)). The code (see Fig. 1) contains therefore $(N_d + 2)(N_d + 1)/2$ independent Monte Carlo computations—the NER between a cell and itself being zero per definition.

The estimation of each $\psi(i,j)$ requires the Monte Carlo computation of an n-dimensional integral: $n = 4$ in case of two gas layers ($\vec{v} = (x, x', \mu, l)$), $n = 3$ in case of a gas layer and a surface ($\vec{v} = (x, \mu, l)$) and $n = 2$ in case of two surfaces ($\vec{v} = (\mu, l)$). The algorithm, following strictly the scheme detailed in Sec. III(a), involves: (i) random generation of N realizations of the vector $\vec{v}$ according to $p(x)$, $p(x')$, $q(\mu)$ and $\mathcal{P}(l)$ (see appendix), (ii) computation of the weighting function $w(\vec{v})$ (Eqs. (19) and (22)), (iii) storage of the sums of all w and w^2. Details are given in Fig. 1 for a two gas layer case.

Note that computing each NER separately allows specific optimization for each pair of cells. For instance, the statistical laws used for narrow-band sampling turn out to be quite different whether the two cells are geometrically far apart or nearly adjacent.

Many pseudo-random number generators may be used. As a matter of fact we did use five of them, from the very low grade RNDM (of the multiplicative congruent type) to the very high quality RANLUX ("subtract-with-borrow" algorithm modified according to Luscher, 1994), both implemented in the CERN program library (James, 1994). The results on which comparisons were made appeared compatible within statistical errors. This insensitivity is a strong argument for considering the present method as a good unbiased reference method.

IV One-Dimensional Slab With Reflective Surfaces

It is well known that narrow band models become difficult to handle (because of correlation effects) as soon as multiple reflections can play a significant part in the total heat transfer. As mentioned above, the NEF is not affected by correlation effects; therefore, the EMCM is quite efficient for such configurations. An outline of the method is presented, in the case of gas–surface exchanges with specular reflections. A detailed account is given in a forthcoming technical note (Cherkaoui, 1996).

(a) Formulation. The NER between gas layer i and surface m in a narrow band l can be split into an infinite sum of NER via 0, 1, 2 ... r, ... reflections:

$$\overline{\psi}_l^{gs}(i,m) = \sum_{r=0}^{\infty} \overline{\psi}_l^{gs}{}^*(i,m;r) \quad (25)$$

In the case of specular reflections, $\overline{\psi}^{gs}{}^*$ can be written as

$$\overline{\psi}_l^{gs}{}^*(i,m;r) = \int_{X_i}^{X_{i+1}} dx \int_0^1 d\mu\, h^{gs}(l,x,m,\mu,r) \quad (26)$$

Table 1 Function f to be integrated and chosen pdf for surface–surface, gas–surface and gas–gas radiation net exchanges with black surfaces

ψ	f	$p_i(x)$	$p_j(x')$	$q(\mu)$	$\mathcal{X}_l$
$\psi^{ss}(m,m')$	$f^{ss}(l,m,m',\mu)=\pi\left[\overline{B_l^s}(m')-\overline{B_l^s}(m)\right]\ 2\mu\ \overline{T}_l(u(S(m),S(m'),\mu))$	–	–	2μ	$\frac{f^{ss}(l,m,m',\tilde{\mu})}{q(\tilde{\mu})}$
$\psi^{gs}(i,m)$	$f^{gs}(l,x,m,\mu)=\pi\left[\overline{B_l^s}(m)-\overline{B_l}(x)\right]\ 2\mu\ \left\lvert\frac{\partial}{\partial x}\left[\overline{T}_l(u(x,S(m),\mu))\right]\right\rvert$	$\frac{1}{\Delta X_i}$	–	1	$\frac{f^{gs}(l,\tilde{x},m,\tilde{\mu})}{p_i(\tilde{x})\,q(\tilde{\mu})}$
$\psi^{gg}(i,j)$	$f^{gg}(l,x,x',\mu)=\pi\left[\overline{B_l}(x')-\overline{B_l}(x)\right]\ 2\mu\ \left\lvert\frac{\partial^2}{\partial x\partial x'}\left[\overline{T}_l(u(x,x',\mu))\right]\right\rvert$	$\frac{1}{\Delta X_i}$	$\frac{1}{\Delta X_j}$	1	$\frac{f^{gg}(l,\tilde{x},\tilde{x}',\tilde{\mu})}{p_i(\tilde{x})\,p_j(\tilde{x}')\,q(\tilde{\mu})}$

with

$$h^{gs}(l,x,m,\mu,r)=\pi\epsilon_m[\overline{B_l^s}(m)-\bar{B}(x)]2\mu R(r)\left|\frac{\partial}{\partial x}[\overline{T}_l(U(r))]\right| \quad (27)$$

where $R(r)$ is the product of the r surface reflectivity and $U(r)$ is the total effective path length.

Energy NER between surfaces
- computation of $\mathcal{X}_l^{ss}(1,2)$ for all the narrow-bands l
- M.C. computation of $\psi^{ss}(1,2)$ and its statistical error $\sigma(\psi^{ss}(1,2))$
- $\psi^{ss}(2,1)=-\psi^{ss}(1,2)$; $\sigma(\psi^{ss}(2,1))=\sigma(\psi^{ss}(1,2))$

Energy NER between gaz layers and surfaces
- loop on $i=1,N_d$
  - loop on $m=1,2$
    - computation of $\mathcal{X}_l^{gs}(i,m)$ for all the narrow-bands l
    - M.C. computation of $\psi^{gs}(i,m)$ and its statistical error $\sigma(\psi^{gs}(i,m))$
    - $\psi^{sg}(m,i)=-\psi^{gs}(i,m)$; $\sigma(\psi^{sg}(m,i))=\sigma(\psi^{gs}(i,m))$
  - end loop
- end loop

Energy NER between gaz layers
- loop on $i=1,N_d-1$
  - loop on $j=i+1,N_d$
    - computation of $\mathcal{X}_l^{gg}(i,j)$ for all the narrow-bands l
    - M.C. computation of $\psi^{gg}(i,j)$ and its statistical error $\sigma(\psi^{gg}(i,j))$
    - $\psi^{gg}(j,i)=-\psi^{gg}(i,j)$; $\sigma(\psi^{gg}(j,i))=\sigma(\psi^{gg}(i,j))$
  - end loop
- end loop

Radiative budgets
- loop on $m=1,2$
  - $\psi^s(m)=\sum_{m'=1}^{2}\psi^{ss}(m,m')+\sum_{i=1}^{N_d}\psi^{sg}(m,i)$
  - $\sigma(\psi^s(m))^2=\sum_{m'=1}^{2}\sigma(\psi^{ss}(m,m'))^2+\sum_{i=1}^{N_d}\sigma(\psi^{sg}(m,i))^2$
- end loop
- loop on $i=1,N_d$
  - $\psi^g(i)=\sum_{m=1}^{2}\psi^{gs}(i,m)+\sum_{j=1}^{N_d}\psi^{gg}(i,j)$
  - $\sigma(\psi^g(i))^2=\sum_{m=1}^{2}\sigma(\psi^{gs}(i,m))^2+\sum_{j=1}^{N_d}\sigma(\psi^{gg}(i,j))^2$
- end loop

M.C. computation of $\psi^{gg}(i,j)$ and its statistical error $\sigma(\psi^{gg}(i,j))$
- $\psi^{gg}(i,j)=0$; $\beta(i,j)=0$
- loop on e=1,N "loop on the N realizations"
  - random generation of x,x',μ,l (see appendix)
  - computation of $w_{ij}(l,x,x',\mu,)$ (equation (22))
  - $\psi^{gg}(i,j)=\psi^{gg}(i,j)+\frac{1}{N}.w_{ij}$
  - $\beta(i,j)=\beta(i,j)+\frac{1}{N}.[w_{ij}]^2$
- end loop
- $\sigma(\psi^{gg}(i,j))=\sqrt{\beta(i,j)-[\psi^{gg}(i,j)]^2}/\sqrt{N}$
- $\psi^{gg}(j,i)=-\psi^{gg}(i,j)$; $\sigma(\psi^{gg}(j,i))=\sigma(\psi^{gg}(i,j))$

Fig. 1 General EMCM algorithm and details for gas–gas NER computations

(b) Probability Functions and Implementation. The algorithm for the computation of radiative exchanges with reflecting surfaces is fairly similar to that presented in Section III for black surfaces. We again consider the NER separately for each pair of discretized elements. For a given pair we compute the NER without reflection and with more than one reflection separately. The term without reflection is computed with the algorithm presented for black surfaces; the only difference is that the surface emissivities need to be taken into account.

The term with more than one reflection is an infinite sum. Practically, the reflections are considered one after the other as for a ray tracking technique, and a truncation procedure is defined so that the computation is stopped as soon as further reflections do not participate significantly in the exchange. The overestimate ξ^{gs} of the truncation error after r_0 reflections is chosen such that

$$|\xi^{gs}(l,x,m,\mu,r_0)|\geq\left|\sum_{r=r_0+1}^{\infty}h^{gs}(l,x,m,\mu,r_0)\right| \quad (28)$$

Overestimation functions are proposed by Cherkaoui (1996). Probability functions are chosen as in the black body surfaces case, except for the narrow band probabilities: The NER rough estimate (Eq. (23)) is here replaced with

$$\chi_l^{gs}{}^*(i,m)=\frac{h^{gs}(l,\tilde{x},m,\tilde{\mu},1)+\xi^{gs}(l,\tilde{x},m,\tilde{\mu},1)}{p_i(\tilde{x})q(\tilde{\mu})} \quad (29)$$

which is the sum of the NER for one reflection and the truncation error overestimate for one reflection at $\mu=\tilde{\mu}$ and $x=\tilde{x}$. The resulting procedure is summarized hereafter:

(*i*) x, μ and l are generated randomly according to $p(x)$, $q(\mu)$, and $\mathcal{P}(l)$, respectively.

(*ii*) For each value of r, starting from $r=1$, we compute the truncation error $\xi^{gs}(l,x,m,\mu,r)$ and we keep the first value r_0 for which $\xi^{gs}(l,x,m,\mu,r_0)$ is lower than the required precision.

(*iii*) We then store the weighting factor w^{gs} associated with the first r_0 terms of h and the weighting factor W^{gs} associated with these first r_0 terms of h plus the truncation error:

$$w_{im}^{gs}(l,x,m,\mu,r_0)=\frac{\sum_{r=1}^{r_0}h^{gs}(l,x,m,\mu,r)}{\mathcal{P}(l)p_i(x)q(\mu)} \quad (30)$$

$$W_{im}^{gs}(l,x,m,\mu,r_0)=w_{im}^{gs}(l,x,m,\mu,r_0)+\frac{\xi^{gs}(l,\tilde{x},m,\tilde{\mu},r_0)}{\mathcal{P}(l)p_i(x)q(\mu)} \quad (31)$$

In this way the absolute value of the radiation budget ψ can be under and overestimated by using the average weights $\langle w\rangle$ and $\langle W\rangle$:

$$|\langle w\rangle|\leq|\psi|\leq|\langle W\rangle| \quad (32)$$

For pure diffusive surfaces, the same probabilities can be used, the only difference in the procedure being that the direction μ is not kept constant along the path. At each reflection a new value of μ is generated according to the Lambert angular distribution. The path-length $U(r)$ takes these various angles into account.

(c) Validation Tests. Most benchmark configurations for gas radiative transfer are in the high-temperature field. Table 2 contains results of high-precision EMCM simulations for configurations in which the gas is isothermal at $\theta = 1000$ K and is either pure carbon dioxide or pure water vapor at atmospheric pressure. In order to allow comparisons with published results, some simulations were held where only one spectral band is considered: the 3755 cm^{-1} band for water vapor (extending from 2875 cm^{-1} to 4250 cm^{-1}) and the 3715 cm^{-1} band for carbon dioxide (extending from 3275 cm^{-1} to 3875 cm^{-1}). Radiative band parameters are those published by Hartman et al. (1984), Soufiani et al. (1985), and Zhang et al. (1988). Our results are compatible (maximum 2 percent difference) with those published by Kim et al. (1991), Menart et al. (1993), Menart and Lee (1993) and Liu and Tiwari (1994).

Various internal consistency tests were also performed. The first one consists simply in the simultaneous development and intercomparison of two independent codes, one that corresponds exactly to the algorithm detailed in the present paper (Cherkaoui, 1993) and one that makes use of the same theoretical approach with a k-distribution method (Fournier, 1994). The second set of tests relates to the way reflections are handled. A double simulation is performed: one with two black surfaces, the other with a black surface facing a *specular* reflective surface (reflectivity ρ). It can be shown that, if the temperature is continuous at the gas/wall interface, the limit value of the volumetric radiation budget at the reflective wall is $1 + \rho$ times the radiation budget in the two black wall case. In the special case $\rho = 1$ that multiplication factor is equal to two as the gas sees the system twice, directly and through a "mirror" reflection. This property is verified within statistical errors in our computations. Finally, the numerical quality of the method was checked in numerous test runs with two highly reflective surfaces: Overestimation of the truncation error is confirmed and convergence achieved without any noticeable bias even for several hundred reflections.

V Results

The EMCM has been used for analysis of a wide range of nearly isothermal configurations with specular as well as diffuse surfaces (Cherkaoui, 1993). Figures 2 and 3 are meant to illustrate the gain over AMCM.

Table 2 Surface radiation budget at the walls and volumetric radiation budget at center for high temperature configurations ($\theta^g = 1000$ K, $\theta_1^s = \theta_2^s = \theta^s$)

Gaz	θ^s (K)	ϵ_1	ϵ_2	D (m)	$\psi^s(1)$ ($kW.m^{-2}$)	$\psi^s(2)$ ($kW.m^{-2}$)	volumetric radiative budget at center ($kW.m^{-3}$)
H_2O	0.	1.	1.	1.	28.094 ± 0.015	–	-23.17 ± 0.04
				0.5	24.26 ± 0.01	–	-50.07 ± 0.07
				0.1	14.417 ± 0.005	–	-219.6 ± 0.4
		0.1	1.	0.5	2.425 ± 0.004	28.00 ± 0.01	-34.40 ± 0.06
H_2O	500.	0.5	0.5	1.	4.700 ± 0.004	–	-4.917 ± 0.012
				10^{-1}	2.473 ± 0.002	–	-43.08 ± 0.08
($3755cm^{-1}$				10^{-2}	0.6594 ± 0.0004	–	-130.0 ± 0.2
bande		0.1	0.1	1.	1.160 ± 0.002	–	-1.410 ± 0.005
only)				10^{-1}	0.7755 ± 0.0007	–	-14.08 ± 0.04
				10^{-2}	0.3448 ± 0.0003	–	-68.17 ± 0.15
CO_2	500.	0.5	0.5	1.	1.709 ± 0.002	–	-1.278 ± 0.004
				10^{-1}	1.094 ± 0.001	–	-18.05 ± 0.04
($3715cm^{-1}$				10^{-2}	0.3379 ± 0.0002	–	-66.09 ± 0.11
bande		0.1	0.1	1.	1.278 ± 0.004	–	-0.3395 ± 0.0018
only)				10^{-1}	18.05 ± 0.04	–	-5.175 ± 0.017
				10^{-2}	66.09 ± 0.11	–	-31.48 ± 0.08

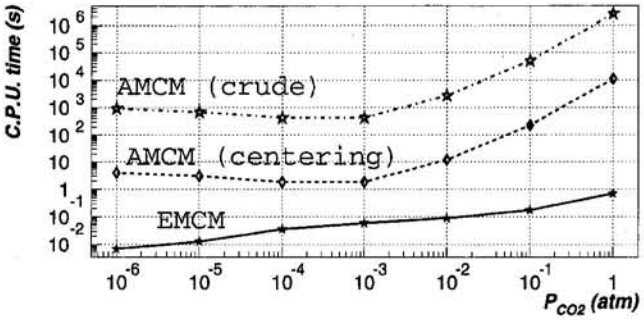

Fig. 2 CPU time (with RNDM as random generator, on a 40 MFlops workstation HP-735) versus carbon dioxide partial pressure for AMCM and EMCM. Bundle numbers are tuned to get a statistical error lower than 5 percent on radiation budgets 15 cm off the surfaces. Both surfaces are black ($\epsilon_1 = \epsilon_2 = 1$); temperature profile is linear from 295 K at $S(1) = 0$ to 305 K at $S(2) = 1$ m; the gas medium is regularly discretized into 10 layers.

1 Computations are a few orders of magnitude faster and numerical efficiency is little dependent on the system optical thickness: Figure 2 displays computation times for simulation of a one meter slab with black surfaces. The gas is at atmospheric pressure and consists of carbon dioxide mixed with a nonabsorbing gas composed of 79 percent nitrogen and 21 percent oxygen. The temperature profile is linear from the cold surface temperature ($\theta^s(1) = 295$ K at $S(1) = 0$) to the hot one ($\theta^s(2) = 305$ K at $S(2) = D = 1$ m). EMCM computation times are compared with those required by the AMCM code previously detailed by Cherkaoui et al. with and without centering. In this centering technique, computed fluxes are offset by corresponding fluxes in the isothermal case (Cherkaoui et al., 1992). The numbers of bundles are tuned in order to obtain a 5 percent precision: typically several hundreds per cell pair. These results confirm those of Liu and Tiwari (1994) illustrating the fact that the MCM can be computationally efficient for the simulation of gas radiative heat transfer. The EMCM allows us to go further in two ways: Computations are at least two orders of magnitude faster and the method remains operational for optically thick systems. Notice that the present approach accounts for nonuniform temperature profiles within each gas layer. Of course any further simplifying assumption (isothermal layers, uncorrelated reflections, . . .) would reduce the computational costs.

2 Strongly nonuniform discretizations introduce no specific convergence difficulties: Figure 3 displays volumetric radiation budgets in the pure carbon dioxide case with various surface emissivities. A strongly varied discretization is used in order to allow an accurate simulation of the large radiation budget gradients at the walls: 20 layers with sizes ranging from 5 mm to 10 cm and two zero thickness layers enabling the computation of the limit value of the radiation budget at the boundaries. These profiles are typical examples of convergence qualities that would not be achievable with a standard AMCM at acceptable computational costs.

Acknowledgments

We are grateful to Pr. J. Taine and A. Soufiani (EM2C laboratory, C.N.R.S./E.C.P.) for valuable discussions all during this work and for providing us with Narrow Band Model databases. We would like to thank L. Fairhead for English editing and R. "Ribs" Franchisseur for proficient true-hacker support. This work was sponsored by PIRSEM/CNRS, ADEME "Service Habitat et Tertiaire" and "Ministère de la Recherche et de la Technologie."

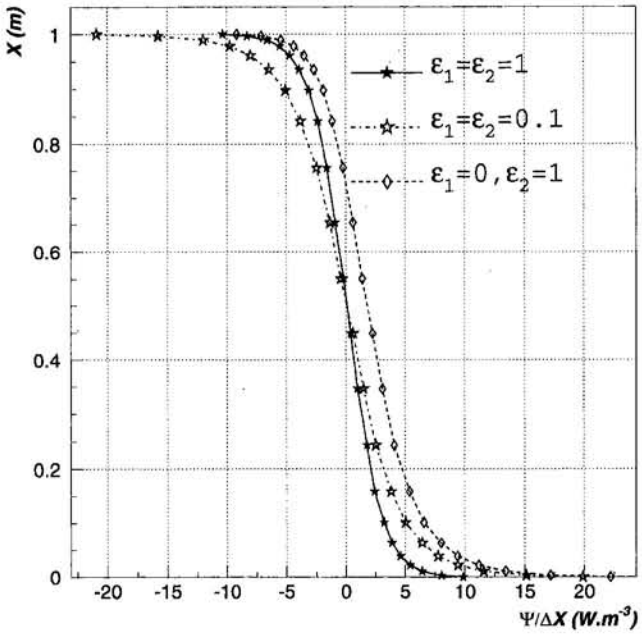

Fig. 3 Volumetric radiation budget for pure CO_2 (P_{CO_2} = 1 atm) with a linear temperature profile varying from 295 K at S(1) = 0 to 305 K at S(2) = 1 m. The diffuse surface emissivities are: $\epsilon_1 = \epsilon_2 = 1$; $\epsilon_1 = \epsilon_2 = 0.1$; $\epsilon_1 = 0$, $\epsilon_2 = 1$.

References

Cherkaoui, M., Dufresne, J. L., Fournier, R., Grandpeix, J. Y., Lahellec, A., and Palenzuela, D., 1992, "Two Procedures for Radiative Calculations With a Narrow-Band Statistical Model in a Volume of Gas at Room Temperature," *Proceedings of the 21st Eurotherm Seminar,* F. Allard, J. F. Sacadura, and M. Spiga, eds., EETI Paris, pp. 123–131.

Cherkaoui, M., 1993, "Modelisation et Etude de Sensibilite des Echanges Radiatifs et Conductifs Couples dans une Cavité Remplie d'Air Ambiant," Ph.D. dissertation, Université Paris XII, Paris, France.

Cherkaoui, M., Dufresne, J. L., Fournier, R., Grandpeix, J. Y., Lahellec, A., 1996, "Net Exchange Formulation for One Dimensional Configurations With Reflective Surfaces," submitted to ASME JOURNAL OF HEAT TRANSFER.

Farmer, J. T., and Howell, J. R., 1994, "Monte Carlo Algorithm for Predicting Radiative Heat Transport in Optically Thick Participating Media," *Proc. 10th International Heat Transfer Conference,* Vol. 2, G. F. Hewitt, ed., pp. 37–42.

Farmer, J. T., and Howell, J. R., 1994, "Hybrid Monte Carlo/Diffusion Methods for Enhanced Solution of Radiative Transfer in Optically Thick Nongray Media," ASME HTD-Vol. 276, pp. 203–212.

Fournier, R., 1994, "Rayonnement Thermique dans les Gaz: Analyse du Couplage avec la Convection Naturelle," Ph.D. dissertation, Université Paul Sabatier, Toulouse, France.

Goody, R. M., and Yung, Y. L., 1989, *Atmospheric Radiation,* 2nd ed., Oxford University Press, United Kingdom.

Green, J. S. A., 1967, "Division of Radiative Streams into Internal Transfer and Cooling to Space," *Quarterly Journal of the Royal Meteorological Society,* Vol. 93, pp. 371–372.

Hartmann, J. M., Levi Di Leon, R., and Taine, J., 1984, "Line-by-Line and Narrow-Band Statistical Model Calculations for H_2O," *Journal of Quantitative Spectroscopy and Radiative Transfer,* Vol. 32, No. 2, pp. 119–127.

Hottel, H. C., and Sarofim, A. F., 1967, *Radiative Transfer,* McGraw-Hill, New York.

Howell, J. R., 1968, "Application of Monte Carlo to Heat Transfer Problems," *Advances in Heat Transfer,* Vol. 5, T. F. Irvine and J. P. Hartnett, eds., pp. 1–54.

Howell, J. R., 1988, "Thermal Radiation in Participating Media: the Past, the Present and Some Possible Futures," ASME JOURNAL OF HEAT TRANSFER, Vol. 110, pp. 1220–1229.

James, F., 1994, "RANLUX: A Fortran Implementation of the High-Quality Pseudorandom Number Generator of Luscher," *Computer Phys. Commun.,* Vol. 79, pp. 111–114.

Joseph, J. M., and Bursztyn, R., 1976, "A Radiative Cooling Model in the Thermal Infrared for Application to Models of the General Circulation," *Journal of Applied Meteorology,* Vol. 15, pp. 319–325.

Kim, T. K., Menart, J. A., and Lee, H. S., 1991, "Nongray Radiative Gas Analyses Using the S-N Discrete Ordinates Method," ASME JOURNAL OF HEAT TRANSFER, Vol. 113, pp. 946–952.

Liu, J., and Tiwari, S. N., 1993, "Investigation of Two-Dimensional Radiation Using a Narrow Band Model and Monte Carlo Model," ASME HTD-Vol. 244, pp. 21–31.

Liu, J., and Tiwari, S. N., 1994, "Investigation of Radiative Transfer in Nongray Gases Using a Narrow Band Model and a Monte Carlo Simulation," ASME JOURNAL OF HEAT TRANSFER, Vol. 116, pp. 160–166.

Ludwig, C. B., Malkmus, W., Reardon, J. E., and Thompson, J. A. L., 1973, "Handbook of Infrared Radiation From Combustion Gases," NASA SP-3080.

Luscher, M., 1994, "A Portable High-Quality Random Number Generator for Lattice Field Theory Simulations," *Computer Phys. Commun.,* Vol. 79, pp. 100–110.

Malkmus, W., 1967, "Random Lorentz Band Model With Exponential-Tailed S-1 Line-Intensity Distribution Function," *Journal of the Optical Society of America,* Vol. 57, No. 3, pp. 323–329.

Martin, W. R., and Pomraning, G. C., 1990, "Monte Carlo Analysis of the Backscattering of Radiation From a Sphere to a Plane," *Journal of Quantitative Spectroscopy and Radiative Transfer,* Vol. 43, No. 2, pp. 115–126.

Menart, J. A., Lee, H. S., and Kim, T. K., 1993, "Discrete Ordinate Solutions of Nongray Radiative Transfer With Diffusely Reflecting Walls," ASME JOURNAL OF HEAT TRANSFER, Vol. 115, pp. 184–193.

Menart, J. A., and Lee, H. S., 1993, "Nongray Gas Analyses for Reflecting Walls Utilizing a Flux Technique," ASME JOURNAL OF HEAT TRANSFER, Vol. 115, pp. 645–652.

Modest, M. F., 1992, "The Monte Carlo Method Applied to Gases With Spectral Line Structures," *Numerical Heat Transfer,* Part B, Vol. 22, pp. 273–284.

Palenzuela, D., 1992, "Instabilités des Ecoulements de Convection Naturelle en Cavité. Introduction a l'Etude des Couplages Convection-Rayonnement," Ph.D. dissertation, Université Paul Sabatier, Toulouse, France.

Press, W. H., Flannery, B. P., Teukolsky, S. A., and Vetterling, W. T., 1992, *Numerical Recipes,* Cambridge University Press, New York.

Siegel, R., and Howell, J. R., 1992, *Thermal Radiation Heat Transfer,* 3rd ed., McGraw-Hill, New York.

Soufiani, A., Hartmann, J. M., and Taine, J., 1985, "Validity of Band-Model Calculations for CO_2 and H_2O Applied to Radiative Properties and Conductive-Radiative Transfer," *Journal of Quantitative Spectroscopy and Radiative Transfer,* Vol. 33, No. 3, pp. 243–257.

Vercammen, H. A. J., and Froment, G. F., 1980, "An Improved Zone Method Using Monte Carlo Techniques for the Simulation of Radiation in Industrial Furnaces," *International Journal of Heat and Mass Transfer,* Vol. 23, pp. 329–337.

Walters, D. V., and Buckius, R. O., 1992, "Rigorous Development for Radiation Heat Transfer in Nonhomogeneous Absorbing Emitting and Scattering Media," *International Journal of Heat and Mass Transfer,* Vol. 35, No. 12, pp. 3323–3333.

Yguel, F., 1988, "Etude de la Convection Naturelle Tridimensionnelle dans les Cavités Fermées de Grandes Dimensions," Ph.D. dissertation, Université de Poitiers, Poitiers, France.

Zhang, L., Soufiani, A., and Taine, J., 1988, "Spectral Correlated and Non-correlated Radiative Transfer in a Finite Axisymmetric System Containing an Absorbing and Emitting Real Gas-Particle Mixture," *International Journal of Heat and Mass Transfer,* Vol. 31, No. 11, pp. 2261–2272.

APPENDIX

Sampling Procedures

The cumulative distributions of the statistical laws introduced in the present text can be inverted analytically. Therefore, sampling procedures can be derived on the basis of the simple relation:

$$A = g^{-1}(R) \tag{33}$$

where R is a random variable distributed uniformly in the unit interval and g is the cumulative distribution function of the random variable A to be sampled. We give hereafter the corresponding relations for abscissae (x or x') and direction cosine (μ). Sampling of x (Table 1):

$$x = X_l + \Delta X_l R_x \tag{34}$$

Sampling of μ for isotropic angular distribution (Table 1):

$$\mu = R_\mu \tag{35}$$

Sampling of μ for Lambert angular distribution:

$$\mu = \sqrt{R_\mu} \tag{36}$$

For the random generation of a spectral band according to the set of discrete probabilities $\mathcal{P}(1)$, $\mathcal{P}(2)$ ... $\mathcal{P}(N_b)$, R_l is generated uniformly in the unit interval and l is chosen as the solution of the following double inequality:

$$\sum_{k=1}^{l-1} \mathcal{P}(k) < R_l \leq \sum_{k=1}^{l} \mathcal{P}(k) \tag{37}$$

Quartz-Fiber Thermal Insulation: Infrared Radiative Properties and Calculation of Radiative-Conductive Heat Transfer

L. A. Dombrovsky
The Scientific-Research Institute of Thermal Processes,
125438, Moscow, Russia

Calculations of absorption, transport scattering, and radiation diffusion coefficients for a highly porous material of quartz fibers are performed by use of rigorous scattering theory for arbitrarily oriented cylinders. New results concerning resonance absorption in the semitransparency region and intensive "scattering by absorption" at refractive index $n \approx 1$ in the opacity region are obtained. Numerical results for the radiation diffusion coefficient from a theoretical model without taking into account both dependent scattering and interference effects are in a good agreement with the experimental data for isotropic fibrous material of density 144 kg/m^3. Calculations allow us to give practical proposals to simplify the determination of optical properties of polydisperse material with randomly oriented fibers. Some results on the radiative–conductive heat transfer in the material considered are presented. The radiation transfer is described in the P_1 approximation. A two-band spectral model with bands corresponding to semitransparency and opacity regions is proposed. Applicability of a modified radiative conduction approximation both to transient and to steady-state calculations is discussed.

Introduction

To construct new highly porous fibrous materials for heat shielding, one needs effective methods of determining their spectral radiative properties. Experimental investigations in a wide spectral range at strong variations of the absorption coefficient are very difficult. For this reason, an appropriate theoretical description of the radiative properties is of great importance.

The traditional method of calculating the radiative properties for rarefied disperse systems of randomly placed spherical particles is based on the assumption of independent interaction of the radiation with individual particles. In this case, the particle properties may be calculated by the Mie theory following Bohren and Huffman (1983) when the radiative properties of the elementary volume are additive and do not depend on particle positions.

An analogous method is employed in theoretical models of the optical properties of highly porous fibrous materials. It is sufficient to remember the papers of Tong and Tien (1980, 1983), Houston and Korpela (1982), Wang and Tien (1983), Lee (1986, 1988, 1990a), and Jeandel et al. (1993). Dependent scattering and interference effects, which take place in dense regular structures (Lee, 1992b), are not taken into account. At the same time, applicability of the Mie theory and the radiation transfer theory for comparably dense fibrous materials is not obvious due to numerous contacts between fibers.

The main aim of this paper is to analyze the possibility for mathematical simulation of the radiative properties of quartz fibrous insulation in heat transfer problems by use of known methods. This question is of great importance both for the theory of radiation transfer in dense participating media and for a number of practical applications (Arduini and DePonte, 1987; Tien, 1988; Howell, 1988; Reiss, 1990). Analogous work has been done by Mathes et al. (1990) for the average integral extinction of evacuated glass fiber insulation of comparably high density (280 kg/m^3) and very thin fibers (fiber diameters 0.5–0.7 μm). The authors confirmed the accuracy of the Mie theory calculations. Now we present additional information on this subject for the spectral radiation diffusion coefficient of another polydisperse fibrous material.

A complete solution of the problem includes calculations of the combined heat transfer in the insulation layer as discussed, for example, by Alifanov et al. (1985). In present paper, we consider only the radiative–conductive heat transfer. The spectral radiation transfer is described by use of the well-known P_1 approximation of the spherical harmonics method. Applications of this technique to combined heat transfer calculations have been considered by Viskanta (1982).

Much computational time is needed to provide complete spectral heat transfer calculations for a polydisperse fibrous material. For this reason, considerable attention is given to different approximations both in radiative properties and in combined heat transfer calculations.

1 Mathematical Description

1.1 Radiative Properties. We use the analytical solution of the scattering problem for arbitrarily oriented infinite cylinders developed by Wait (1955). According to Bohren and Huffman (1983), the effect of finite fiber length is small at $l > 10r$. There are few papers dealing with calculations of optical properties of cylindrical particles at oblique radiation incidence: Lind and Greenberg (1966), Cooke and Kerker (1969), Kuo-Nan Liou (1972). The radiative properties of cylinders are more complex than those for spheres due to the dependence on the particle orientation and on the incident wave polarization. In this paper, we consider only the case of unpolarized radiation. The expressions for the efficiency factors of scattering Q_s and extinction $Q_t = Q_a + Q_s$ are well known. Analogous expressions for the transport efficiency factors Q_s^{tr}, Q_t^{tr} derived by Kolpakov et al. (1990) may be found also in paper by Dombrovsky (1994b). These values depend on the diffraction parameter x

Contributed by the Heat Transfer Division for publication in the JOURNAL OF HEAT TRANSFER. Manuscript received by the Heat Transfer Division December 1994; revision received January 1996. Keywords: Porous Media, Radiation Interactions, Thermophysical Properties. Associate Technical Editor: M. F. Modest.

$= 2\pi r/\lambda$, the angle of incidence α, and the complex index of refraction $m = n - i\kappa$.

The main difficulty in calculations of fiber radiative properties is the determination of the Bessel and Hankel functions by recurrence relations. The computational stability of direct run for cylinders at $|m|x \gg 1$ is not as good as that for spheres. Therefore, in contrast to the work by Lind and Greenberg (1966), we use the downward recurrence analogous to that for the normal incidence ($\alpha = 0$) in the monograph by Bohren and Huffman (1983). The computer code was verified by comparison with data by Lind and Greenberg (1966) at $m = 1.6$, $x < 5$ and with graphical form data by Swathi and Tong (1988) for metal fibers at x up to 1000.

Some variants of fiber orientation in materials have been first considered by Lee (1986, 1988). It was shown that one can use the following average values:

$$\{\bar{Q}_a, \bar{Q}_t^{tr}\} = \int_0^{\pi/2} \{Q_a, Q_t^{tr}\} \cos\alpha \cdot d\alpha \qquad (1)$$

$$\{\bar{Q}_a, \bar{Q}_t^{tr}\} = \int_0^{2\pi} \{Q_a(\alpha), Q_t^{tr}(\alpha)\} d\psi,$$

$$\alpha = |\arcsin(\sin\theta \cdot \cos\psi)| \qquad (2)$$

Equation (1) corresponds to the random orientation of fibers in space, Eq. (2) to that in parallel planes, when $\bar{Q}_a$, $\bar{Q}_t^{tr}$ depend on the angle of illumination θ. The corresponding coefficients for polydisperse material with the fiber size distribution $F(r)$ (at equal length of fibers) are:

$$\{\sigma_{a\lambda}, \sigma_\lambda^{tr}\} = \frac{2}{\pi}\frac{\rho}{\rho_f}\int_0^\infty \{Q_a, Q_t^{tr}\} rF(r)dr \Big/ \int_0^\infty r^2 F(r)dr \qquad (3)$$

where ρ_f, ρ are the densities of fibers and fibrous material.

1.2 Radiation Transfer. In the P_1 approximation, the radiation transfer problem for a plane-parallel layer is reduced to the following boundary-value problem for the spectral radiation energy density (Case and Zweifel, 1967):

$$-\frac{\partial}{\partial y}\left(D_\lambda \frac{\partial}{\partial y} I_{0\lambda}\right) + \sigma_{a\lambda} I_{0\lambda} = 4\pi\sigma_{a\lambda} B_\lambda(T)$$

$$y = 0, \quad D_\lambda \frac{\partial I_{0\lambda}}{\partial y} = \gamma_{w1}[I_{0\lambda} - 4\pi B_\lambda(T_{w1})]/2,$$

$$y = \delta, \quad D_\lambda \frac{\partial I_{0\lambda}}{\partial y} = \gamma_{w2}[4\pi B_\lambda(T_{w2}) - I_{0\lambda}]/2 \qquad (4)$$

where $\gamma_{w1} = \epsilon_{w1}/(2 - \epsilon_{w1})$, $\gamma_{w2} = \epsilon_{w2}/(2 - \epsilon_{w2})$, ϵ_{w1}, ϵ_{w2} are the spectral hemispherical emissivities of the walls. The spectral radiation flux is $q_\lambda = -D_\lambda \partial I_{0\lambda}/\partial y$.

In the case of the random orientation of fibers in planes $y =$ const, the coefficients in the radiation transfer equation depend on θ. By the usual transfer to the P_1 approximation, one can find the radiative diffusion coefficient is equal to $D_\lambda = 1/(3\bar{\sigma}_\lambda^{tr})$ and the absorption coefficient is $\bar{\sigma}_{a\lambda}$ instead of $\sigma_{a\lambda}$. The average values $\bar{\sigma}_{a\lambda}$, $\bar{\sigma}_\lambda^{tr}$ may be calculated analogous to Eq. (3) through the values

$$\bar{\bar{Q}}_a = \int_0^{\pi/2} \bar{Q}_a(\theta) \sin\theta \cdot d\theta,$$

$$\bar{\bar{Q}}_t^{tr} = 3\int_0^{\pi/2} \bar{Q}_t^{tr}(\theta) \sin\theta \cos^2\theta \cdot d\theta \qquad (5)$$

Note that $\bar{\bar{Q}}_s^{tr} = \bar{\bar{Q}}_t^{tr} - \bar{\bar{Q}}_a$, whereas $\bar{Q}_s^{tr} \neq \bar{Q}_t^{tr} - \bar{Q}_a$.

Although the linear (P_1) approximation of the radiation intensity angular dependence is crude (especially near to boundaries), an accuracy of the one-dimensional radiative flux calculations for homogeneous plane-parallel layer by use of P_1 is sufficiently high even in an anisotropically scattering medium at arbitrary optical thickness of the layer (Mengüç and Viskanta, 1983; Dombrovsky et al., 1991b). It should be mentioned that the relative error of the radiative flux determination by use of P_1 in the problem of the radiative equilibrium in gray optically thick isotropically scattering medium is evaluated as $0.0876/\tau$. At the same conditions, the anisotropy of scattering may be treated by the transport approximation and the radiation diffusion coefficient introduced above is applicable. The latter results have been developed by comparison with more accurate solutions by use of double spherical harmonics method (Dombrovsky, 1974).

The P_1 equations are identical to those of the diffusion approximation, which is commonly employed in experimental determination of the radiative diffusion coefficient (Moiseyev et al., 1990; Petrov, 1993). If one needs a comparison of the calculated and experimental data on this coefficient, it would be correct to use the common technique of combined heat transfer calculations and the inverse radiative transfer problem solution.

Nomenclature

B = Planck function for blackbody radiation
C = specific heat capacity
D = radiation diffusion coefficient
$F(r)$ = size distribution function
$i = \sqrt{-1}$
$I_{0\lambda}$ = cE_λ, where c is the velocity of light, E_λ is the radiation energy density
k = thermal conductivity
l = length of the fiber
m = complex index of refraction = $n - i\kappa$
n = index of refraction
P = porosity of the fibrous material = $1 - p$
q = specific heat flux
Q = cross section of scattering, absorption, or extinction
r = radius of fibers
t = time
T = absolute temperature; ΔT = temperature difference
y = coordinate across the insulation layer
x = size parameter (diffraction parameter) = $2\pi a/\lambda$
α = angle of radiation incidence on a single fiber
δ = thickness of thermal insulation layer
γ = part of fibers oriented parallel to heat flux
ϵ = emissivity or coefficient in two-band model
κ = index of absorption
λ = wavelength
η = coefficient in wavelength dependence of index of absorption
ρ = density
σ = Stefan–Boltzmann constant or radiative coefficients
θ = angle of radiation incidence on a layer of fibers
τ = optical thickness
ψ = azimuthal angle
ω = scattering albedo

Subscripts and Superscripts

a = absorption
eff = effective
f = property of the material of fibers
k = number of partial wave (in the Mie series)
λ = spectrally dependent
r = radiative
s = scattering
t = total (extinction)
tr = transport
w = wall
$*$ = peculiar value

1.3 Combined Heat Transfer. Following the traditional description of the heat transfer in fibrous insulations, reviewed by Arduini and DePonte (1987), we use the energy equation for combined heat transfer by conduction and radiation in a plane-parallel layer in the form:

$$\rho C \frac{\partial T}{\partial t} = \frac{\partial}{\partial y}\left(k \frac{\partial T}{\partial y}\right) + \int_0^\infty \bar{\sigma}_{a\lambda}[4\pi B_\lambda(T) - I_{0\lambda}]d\lambda \quad (6)$$

In the case of thermal contact of the material with the walls having temperatures T_{w1}, T_{w2}, the boundary conditions for Eq. (6) are very simple: $T = T_{w1}$ at $y = 0$, and $T = T_{w2}$ at $y = \delta$. When the main attention is focused on the steady-state thermal regime, the initial condition makes no difference. In this paper, we assume $T = T_{w1}$ at $t = 0$. To minimize an error of the P_1 we assume the walls are diffuse emitting and reflecting.

Specific heat flux due to conduction and radiation is

$$q = -k \frac{\partial T}{\partial y} + \int_0^\infty q_\lambda d\lambda \quad (7)$$

The thermal conductivity of a fibrous material may be evaluated by use of the following expression for open porous systems (Bankvall, 1973):

$$k = \gamma[P_1 k_g + (1 - P_1)k_f] + (1 - \gamma)k_f k_g/[P_2 k_f + (1 - P_2)k_g] \quad (8)$$

where k_g is the thermal conductivity of the gas between fibers, k_f is the conductivity of the fiber material, γ is the part of the fibers oriented parallel to the heat flux, P_1, P_2 are the porosity parameters. The total porosity of the material is $P = \gamma P_1 + (1 - \gamma)P_2$. We consider the material in vacuum. In this case, the effect of radiative properties on heat transfer is more pronounced. For approximate qualitative evaluation of the fiber conductivity effect, we assume that fibers are randomly placed and oriented in space: $\gamma = \frac{1}{3}$, $P_1 = P_2$; the thermal conductivity of the material is $k = pk_f/3$, where $p = 1 - P$.

The transient problem of the radiative–conductive heat transfer under consideration is solved by the decomposition method in much the same way as it was done by Dombrovsky et al. (1991a, 1993), and Dombrovsky (1994c).

2 Optical Constants Used in Calculations

The refractive index of fused silica at room temperature in the spectral range $0.21 \le \lambda \le 3.71$ mm was measured with high accuracy and it may be described by dispersion equation by Malitson (1965). Data reviewed by Petrov (1979) contain also a weak temperature dependence, which is not taken into account in this paper. The spectral absorption coefficient data for quartz glasses in the range from 0.2 to 5 μm at high temperatures have been also reviewed by Petrov (1979). The absorption index is usually less than 5×10^{-4}. As pointed by Kondratenko et al. (1991), small admixtures may have a considerable effect on this value. For this reason, calculations of the spectral absorption coefficient of quartz insulation in the semitransparency region are not representative. At the same time, the effect of small absorption on scattering by fibers is negligible.

The optical constants of quartz in the opacity region are presented in graphs by Banner et al. (1989). Ignoring the temperature dependence, we use the following approximation in the range from 7.6 to 12 μm:

$$\left.\begin{array}{ll} \lambda < 8, & \eta = (\lambda^2 + 20)/14 \\ 8 < \lambda < 9, & \eta = 6 + 0.6(\lambda - 8) \end{array}\right\},$$

$$n = \tfrac{65}{49}(\lambda - 8.3)^2 + 0.35$$

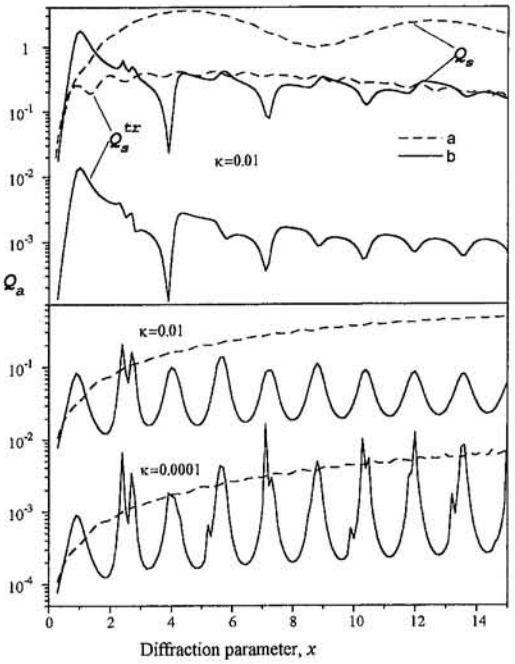

Fig. 1 Scattering and absorption of radiation by cylindrical particles with $n = 1.4$ at normal (a) and inclined incidence (b, $\alpha = 85$ deg)

$$\left.\begin{array}{ll} 9 < \lambda < 9.5, & n = 4(\lambda - 9) + 1 \\ 9.5 < \lambda < 10, & n = 3 - 0.8(\lambda - 9.5) \end{array}\right\},$$

$$\eta = 6.6 - 1.6(\lambda - 9)$$

$$\lambda > 10, \quad n = 2.6 - (\lambda - 10)/2,$$

$$\eta = 5 - 6(\lambda - 10)/25, \quad (9)$$

where $\eta = \log(4\pi\kappa/\lambda) + 6$. From here on λ is expressed in μm. At $\lambda < 7.6$ μm the dispersion equation of Malitson (1965) for $n(\lambda)$ is used and we assume $\kappa = 10^{-4}$, when Eqs. (9) give a smaller value. Note that $\kappa(\lambda)$ has a maximum at $\lambda = 9$ μm and there are two points in which $n = 1$: $\lambda = 7.6$ μm and 9 μm.

3 Calculations of Spectral Radiative Characteristics

3.1 Some Physical Results. To analyze some special features of quartz fiber properties in the semitransparency region, one can use the values $n = 1.4$, $\kappa \le 0.01$. At normal incidence there are no considerable differences between cylindrical and spherical particles considered by Dombrovsky (1990). The main qualitative results for large α are illustrated in Fig. 1: $Q_s^{tr} \ll Q_s$ due to high asymmetry of scattering, and there is a resonance absorption even at $\kappa = 0.01$. The resonance effect is more pronounced at smaller values of κ. Some results for $\alpha = 0$ in the spectral range including the opacity region are shown in Fig. 2(a). One can see intensive "scattering by absorption" at $\lambda = 9$ μm and maximum absorption near to 9.3 μm at $\kappa \approx 1$. For thin fibers ($r = 2$ μm), there is an additional strong maximum of scattering at $\lambda \approx 10$ μm corresponding to the main maximum of the function $Q_s^{tr}(x)$ at a high refractive index.

An example of calculation for monodisperse system of fibers with different orientations is given in Fig. 2(b). The values $\bar{\bar{Q}}_s^{tr}$ and $\bar{Q}_s^{tr}$ differ slightly from each other; the curves $\bar{\bar{Q}}_a(\lambda)$ and $\bar{Q}_a(\lambda)$ practically coincide. This result may be employed to simplify calculations for layered materials. It is of interest that the spectral curves are just similar to those for $\alpha = 0$. This may be explained by self-similar angular dependences of Q_a,

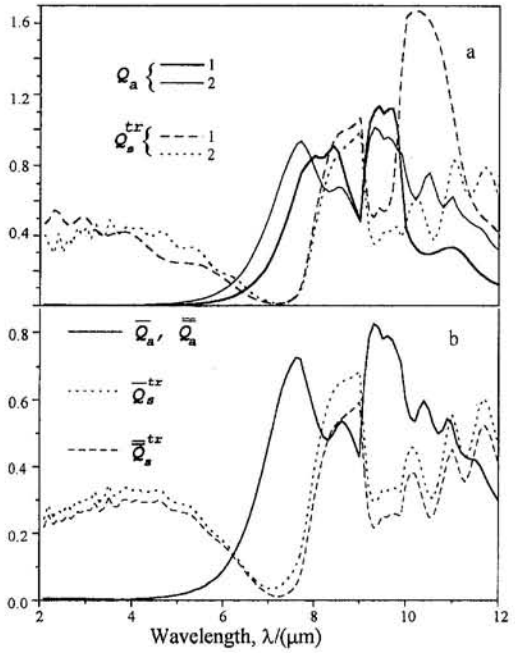

Fig. 2 Spectral properties of a single quartz fiber at normal incidence (*a*, 1—r = 2 μm, 2—5 μm) and average spectral properties of randomly oriented fibers (*b*, r = 5 μm)

Q_s^{tr}. If we suppose the cosine dependence, the coefficient $\pi/4$ appears in Eq. (1) instead of the integration. As a result, we obtain a simple way to evaluate the radiative properties of fibrous materials by use of the individual fiber properties at normal incidence. This conclusion does not refer to the absorption in the semitransparency region, in which resonance effects at oblique incidence are observed (Dombrovsky, 1994a). Fortunately, the resonance absorption is accompanied by relatively strong scattering and is not important in many problems.

One can simplify the calculations for materials with randomly oriented fibers by use of the coefficient $\pi/4$ mentioned above and numerical results for the normal incidence of the radiation on a single fiber. By analogy with spheres (Dombrovsky, 1976), the additional simplification may be reached by use of the monodisperse approximation with the equivalent fiber radius (Dombrovsky, 1994a, b). The corresponding savings in computer time are very significant.

3.2 Comparison With Experimental Data. The experimental determination of values $\sigma_{a\lambda}$, D_λ for highly porous isotropic quartz insulation with known fiber size distribution and the porosity 93.5 percent (the density is 144 kg/m^3) has been provided by Kondratenko et al. (1991) and are also presented by Moiseyev et al. (1992). The experimental method is based on the analytical solution in the diffusion approximation for the transmissivity of the cylindrical specimen. The mathematical treatment has been performed in some detail by Moiseyev et al. (1990). It was shown how to use measurements at collimated incident radiation to determine the required optical characteristics of the material. Measurements of the radiation diffusion coefficient for two sets of specimens of various orientations with respect to the material layer give the same values of D_λ with an accuracy of 0.5 percent. Size distribution of fibers presented by Kondratenko et al. (1991) (ten-interval histogram in the fiber diameter range 0–5 μm) makes it possible to calculate D_λ and compare it with the experimental values.

A comparison of calculations with these experimental data is presented in Fig. 3. The values of the absorption coefficient calculated at $\kappa = 10^{-4}$ are greater than those in the experiment. For this reason, the comparison of the values D_λ without any

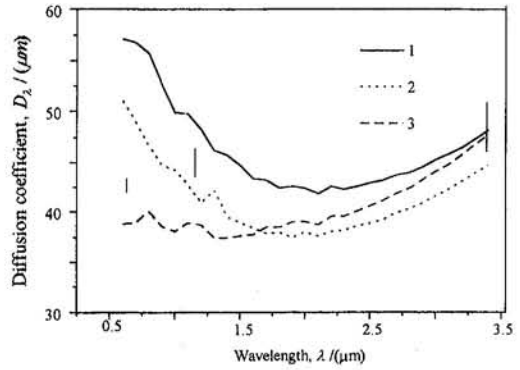

Fig. 3 Spectral radiation diffusion coefficient for fibrous insulation. Comparison with the experimental data by Kondratenko et al. (1991) (vertical line segments): 1, 2—calculations for fibrous disperse system (2—for 10 percent smaller fiber radius), 3—effect of small part (3 percent in mass) of monodisperse spherical particles.

selection of κ is quite correct. One can see that there is a good agreement between the calculations and the experiment in the infrared, the difference in the visible is about 20–30 percent. An error in the size distribution can not explain the difference at λ = 0.63 μm. Evaluations show that the effect of thin B_2O_3 shells on the fibers is negligible. The scattering by bends and seals of fibers as well as by a small amount of silica droplets (which are formed from thin fibers by preliminary thermal processing of the material) may be a cause of this disagreement. Indirect confirmation of this hypothesis is the more intensive scattering of the radiation by spherical particles of the same radius, which may be considered to simulate the real effect. One can assume that ~3 percent of the material mass is a monodisperse system of spherical particles of radius 0.5 μm. Numerical results for this model shown in Fig. 3 are close to the experimental values. Note that the collective effects (dependent scattering or interference) are not observed (at least in values of D_λ) for the material considered. It is of great interest to continue the investigation for more dense materials and in wide possible spectral range.

Some additional experimental data on the spectral properties of a fiberglass insulation of density 68 kg/m^3 in the semitransparency range $0.5 \le \lambda \le 5$ μm are given in a recent paper by Nicolau et al. (1994). A comparison of calculations of the optical thickness $\tau_\lambda = \sigma_\lambda^t \delta$ (δ = 4 mm is the sample thickness) for known fiber size distribution with the measurements is presented in Fig. 4. Two curves correspond to different approximations of the fiber radius distribution: continuous approximation with linear interpolation of tabulated data and discrete approximation with eight given values of fiber radius. In spite of consid-

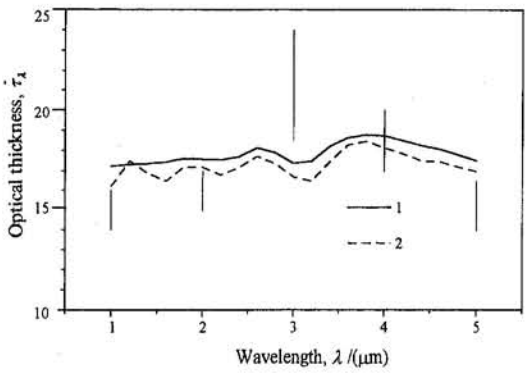

Fig. 4 Comparison of the calculated optical thickness of fiberglass insulation samples (1, 2) with the experimental data by Nicolau et al. (1994): 1—continuous fiber radius distribution, 2—discrete distribution

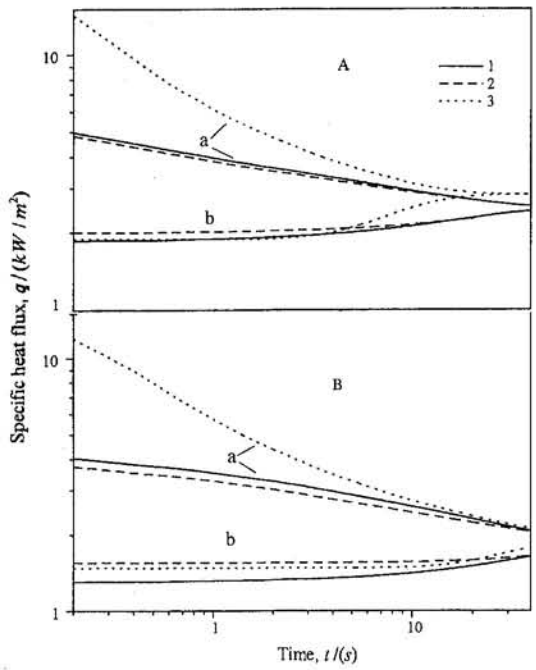

Fig. 5 Specific heat flux on hot (*a*) and cold (*b*) surfaces of the fibrous insulation layer: *A*—δ = 5, *B*—10 mm; 1, 2—P_1 approximation and two-band model (1—ϵ = 0.05, 2—$\epsilon \to 0$), 3—modified radiative conduction approximation

erable discrepancy at $\lambda = 4$ μm, there is a satisfactory agreement with the experimental data. It is difficult to expect a better accuracy of the calculations due to high sensitivity of the extinction coefficient to the fiber radius. The latter assertion was illustrated by Dombrovsky (1995a). It was shown that the computational prediction of the more practically important value of the spectral radiation diffusion coefficient is more reliable. An extended discussion of this problem is presented by Dombrovsky (1996).

In the opacity region, one can speak only about qualitative agreement of the calculated albedo $\omega_\lambda = \sigma_{s\lambda}^{tr}/\sigma^{tr}$ with the experimental data by Yeh and Roux (1988). Having no fiber size distribution, one cannot compare absolute values of the radiative characteristics.

4 Two-Band Model and Approximate Method of Heat Transfer Calculations

Besides the total calculation, we use the two-band approximate description of spectral properties, when the absorption coefficient and the transport scattering coefficient of a monodisperse fibrous material ($2 \le r \le 10$ μm) in the spectral range $2 \le \lambda \le 12$ μm are

$$\lambda < \lambda_*,\ \sigma_{s\lambda}^{tr} = 0.165p/r,\ \sigma_{a\lambda} = \epsilon\sigma_{s\lambda}^{tr};$$
$$\lambda > \lambda_*,\ \sigma_{s\lambda}^{tr} = \sigma_{a\lambda} = 0.33p/r \qquad (10)$$

For quartz fibers, one can use the value $\lambda_* = 6.5$ μm (Dombrovsky, 1994b). Calculations showed that small variations of λ_* in the limits from 6 to 7 μm are inessential and a satisfactory accuracy for the heat transfer calculations is obtained at ϵ = 0.05 (see also Dombrovsky, 1994c, d). The limiting volume of the paper does not allow us to give more detailed analysis of the accuracy of this model. It goes without saying that some more accurate approximations of the spectral radiative properties in a set of bands in more wide spectral range may be useful.

Transient heat transfer calculations up to the steady state are very complicated due to many times repeated calculations of the radiation transfer. For this reason, it is of interest to simplify the radiation transfer model. If we ignore a small error at ϵ = 0, as assumed by Dombrovsky (1994b), the spectral radiative flux in the semitransparency region may be obtained similar to that for the radiative equilibrium (Özişik, 1973; Dombrovsky, 1974):

$$q_\lambda = 2\pi[B_\lambda(T_{w1}) - B_\lambda(T_{w2})]/$$
$$[1/\gamma_{w1} + 1/\gamma_{w2} + \delta/(2D_\lambda)] \qquad (11)$$

At the same time, the modified radiative conduction approximation with the radiative conductivity, which differs from the usual one ($k_r = \frac{16}{3}\sigma T^3/\sigma_\lambda^{tr}$) by the coefficient

$$\zeta(\lambda_* T) = \frac{1}{4\sigma T^3}\int_{\lambda_*}^{\infty}\frac{\partial B_\lambda(T)}{\partial T}\,d\lambda < 1 \qquad (12)$$

may be used at $\lambda > \lambda_*$ instead of the complicated spectral calculations. This modification has been derived by Dombrovsky (1994b, c).

5 Heat Transfer Results

Figure 5 shows some representative dependences of the total heat flux on surfaces of a layer of the quartz fibrous insulation placed between two walls having different constant temperatures. Calculations were performed with the following parameters: T_{w1} = 600 K, $\Delta T_w = T_{w2} - T_{w1}$ = 100 K, $\epsilon_{w1} = \epsilon_{w2}$ = 0.8, ρ = 10 kg/m^3, r = 5 μm, k_f = 1.5 W/(m·K). An error of the limiting assumption $\epsilon \to 0$ is not large, especially at steady state (at equal heat fluxes on hot and cold surfaces of the insulation), due to small optical thickness with respect to absorption in the semitransparency region. When we use the modified radiative conduction approximation in the opacity region, the heat flux on the hot surface at the process beginning is not correct, but this effect decreases at steady state. It should be noted that the computational time is two orders of magnitude less than in spectral calculations.

Additional information on the accuracy of the two-band approximation discussed above is presented in Table 1 for the parameters of Fig. 5*A*. One can see that the approximation error is less than 10 percent (in heat flux value) and does not exceed the computational prediction error for the radiation diffusion coefficient.

Some results of calculations at steady state at the conditions cited above with variation of ρ, a, δ, and T_{w1} are presented in Fig. 6. Calculations were made using the modified radiative conduction approximation. Numerical data are interpreted in terms of the effective conductivity $k_{\text{eff}} = q\delta/\Delta T_w$. It is of interest that the dependences $k_{\text{eff}}(\rho)$ are nonmonotonic: There is a density of the fibrous material ρ_* corresponding to the best heat shielding. The effect of the fiber radius and the temperature on ρ_* may be evaluated from a comparison of the values k and k_r. It is easy to verify that $\rho_*^2 \sim T^3 r$. This relation is confirmed by direct calculations. Note that the concrete value of ρ_* is connected with the evaluation of k and depends on the orientation of the fibers and on thermal contact between them. The effective conductivity increases with increasing fiber radius. This effect is more pronounced at low density of the material. In

Table 1 Comparison of complete spectral calculation (*a*) with two-band calculations at λ_* = 6.5 μm (*b*) and 7 μm (*c*)

	$q, kW/m^2$					
	$y = \delta$			$y = 0$		
t, s	a	b	c	a	b	c
1	3.87	3.73	3.70	1.89	1.98	2.09
5	3.27	3.17	3.20	2.04	2.07	2.16
10	2.99	2.91	2.97	2.18	2.17	2.24
20	2.74	2.70	2.77	2.37	2.30	2.36

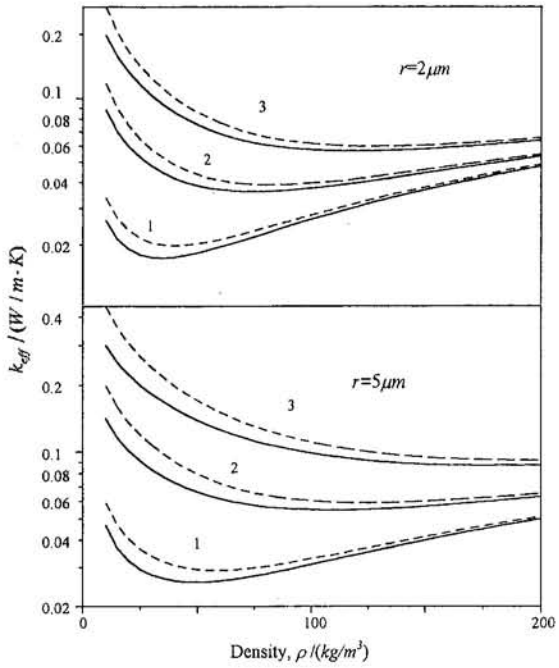

Fig. 6 Effective conductivity coefficient of monodisperse quartz fibrous material in vacuum at δ = 5 mm (solid lines) and 10 mm (dashed lines): 1—T_{w1} = 400, 2—600, 3—800 K (ΔT_w = 100 K, ϵ_w = 0.8)

other words, the thinner the fibers, the better the heat-shielding properties of the material. This conclusion is in good agreement with the known experimental data. Note that the accuracy of the computational results presented in Fig. 6 is mainly determined by the uncertainty of the fibrous material conductivity rather than by the errors in the radiation transfer calculation.

Conclusions

- Infrared radiative properties of quartz fibrous material with randomly oriented fibers are calculated by use of the scattering theory for infinite cylinders at oblique incidence of the radiation. A comparison of the calculated values of the radiation diffusion coefficient with the experimental data for fibrous quartz insulation of density 144 kg/m^3 in the semitransparency region shows that an insignificant discrepancy in the visible range may be explained by a small amount of admixed spherical particles and by analogous effect of bends and seals of fibers.
- Resonance properties of a single fiber analyzed in the paper may be of interest for regular structures but have no considerable effects on the radiative properties of the material containing randomly oriented polydisperse fibers. For this reason, one can use comparably simple approximate computational models without detail calculations of angular characteristics of a single particle.
- If we are interested only in steady-state heat transfer evaluations, a two-band spectral model with various approximate descriptions of the radiation transfer in each band may employed. Calculations of the transient radiative–conductive heat transfer in evacuated quartz fibrous insulation illustrate an error of the radiative conduction approximation. At the same time, it is shown that the modified radiative conduction approximation may be applicable in steady-state calculations.

References

Alifanov, O. M., Gerasimov, B. P., Elizarova, T. G., et al., 1985, "Mathematical Simulation of Combined Heat Transfer in Disperse Materials," *J. Engng Phys.*, Vol. 49, No. 5, pp. 781–791.

Arduini, M., and DePonte, F., 1987, "Combined Radiation and Conduction Heat Transfer in Insulating Materials," *High Temperatures—High Pressures*, Vol. 19, No. 3, pp. 237–249.

Bankvall, C., 1973, "Heat Transfer in Fibrous Materials," *J. Testing and Evaluation*, Vol. 1, No. 3, pp. 235–243.

Banner, D., Klarsfeld, S., and Langlais, C., 1989, "Temperature Dependence of the Optical Characteristics of Semitransparent Porous Media," *High Temperatures—High Pressures*, Vol. 21, No. 3, pp. 347–354.

Bohren, C. F., and Huffman, D. R., 1983, *Absorption and Scattering of Light by Small Particles*, Wiley, New York.

Case, K. M., and Zweifel, P. F., 1967, *Linear Transport Theory*, Univ. of Michigan, Addison-Wesley Publ. Co.

Cooke, D. D., and Kerker, M., 1969, "Light Scattering From Long Thin Glass Cylinders at Oblique Incidence," *J. Opt. Soc. Amer.*, Vol. 59, No. 1, pp. 43–48.

Dombrovsky, L. A., 1974, "Radiative Equilibrium in Plane-Parallel Layer of Absorbing and Scattering Medium," *Trans. USSR Acad. Sci., Fluid and Gas Mech.*, No. 4, pp. 183–186 [in Russian].

Dombrovsky, L. A., 1976, "Radiation of Isothermal Polydisperse Layer," *High Temperature*, Vol. 14, No. 4.

Dombrovsky, L. A., 1990, "Approximate Expressions for Calculation of the Main Radiative Properties of Spherical Particles in the Mie Scattering Region," *Teplofiz. Vysok. Temp.*, Vol. 28, No. 6, pp. 1242–1245 [in Russian].

Dombrovsky, L. A., Kolpakov, A. V., and Yukina, E. P., 1991a, "Calculation of Radiative-Conductive Heat Transfer in Thermal Processing of Synthetic Fibers," *Applied Problems of Aeromechanics and Space Physics*, Moscow, pp. 58–62 [in Russian].

Dombrovsky, L. A., Kolpakov, A. V., and Surzhikov, S. T., 1991b, "On Applicability of the Transport Approximation for Directional Radiation Transfer Calculations in Anisotropically Scattering Erosion Plume," *High Temperature*, Vol. 29, No. 6, pp. 954–960.

Dombrovsky, L. A., Yukina, E. P., Kolpakov, A. V., and Ivanov, V. A., 1993, "A Method of Thermal Destruction Calculation for Phenolic Carbon by Action of Intensive Infrared Radiation," *High Temperature*, Vol. 31, No. 4, pp. 619–625.

Dombrovsky, L. A., 1994a, "Quartz-Fiber Thermal Insulation: Calculation of Spectral Radiative Characteristics in the Infrared Region," *High Temperature*, Vol. 32, No. 2, pp. 197–203.

Dombrovsky, L. A., 1994b, "Calculation of Spectral Radiative Properties of Quartz Fibrous Insulation in the Infrared," *Proc. 10th Int. Heat Transfer Conf.*, Vol. 2, pp. 25–30.

Dombrovsky, L. A., 1994c, "Determination of Spectral Radiative Properties of Fiberglass Thermal Insulation From Steady-State Heat Flux Measurements," *Proc. 2nd Int. Conf. Identif. Dynam. Syst. and Inverse Problems*, St. Petersburg, Aug. 22–25, Vol. 2, pp. D-10-1–D-10-11 [in Russian].

Dombrovsky, L. A., 1994d, "Calculation of Radiative-Conductive Heat Transfer in Quartz Fibrous Insulation," *Proc. First Russ. Nat. Conf. on Heat and Mass Transfer*, Moscow, Nov. 21–25, pp. 91–96 [in Russian].

Dombrovsky, L. A., 1995a, "The Mie Theory Analysis of Comparably Dense Disperse Systems," *Proc. Intern. Symp. on Radiat. Heat Transfer*, Kuşadasi, Turkey, Aug. 13–18, pp. 156–158.

Dombrovsky, L. A., 1996, "Calculation of Infrared Radiative Properties of Isotropic Fiberglass Materials in the Semitransparency Region," *High Temperature*, Vol. 34, No. 1, pp. 156–158.

Houston, R. L., and Korpela, S. A., 1982, "Heat Transfer Through Fiberglass Insulation," *Proc. 7th Int. Heat Transfer Conf.*, Vol. 2, pp. 499–504.

Howell, J. R., 1988, "Thermal Radiation in Participating Media: The Past, the Present, and Some Possible Futures," ASME JOURNAL OF HEAT TRANSFER, Vol. 110, No. 4(B), pp. 1220–1229.

Jeandel, G., Boulet, P., and Morlot, G., 1993, "Radiative Transfer Through a Medium of Silica Fibers Oriented in Parallel Planes," *Int. J. Heat Mass Transfer*, Vol. 36, pp. 531–536.

Kolpakov, A. V., Dombrovsky, L. A., and Yukina, E. P., 1990, "Numerical Investigation of Light Scattering by Disperse Systems of Cylindrical Filaments," *Trans. XV Conf. Young Scient.*, Mosc. Inst. Phys. Engng, Moscow, Part 2 (Depon. VINITI, N 6175-B90, in Russian).

Kondratenko, A. V., Moiseyev, S. S., Petrov, V. A., and Stepanov, S. V., 1991, "Experimental Determination of Optical Properties of Fibrous Quartz Heat-Shielding Material," *High Temperature*, Vol. 29, No. 1, pp. 126–130.

Kuo-Nan Liou, 1972, "Electromagnetic Scattering by Arbitrarily Oriented Ice Cylinders," *Applied Optics*, Vol. 11, No. 3, pp. 667–674.

Lee, S. C., 1986, "Radiative Transfer Through a Fibrous Medium: Allowance for Fiber Orientation," *J. Quant. Spectr. Radiat. Transfer*, Vol. 36, No. 3, pp. 253–263.

Lee, S. C., 1988, "Radiation Heat-Transfer Model for Fibers Oriented Parallel to Diffuse Boundaries," *J. Thermophys. and Heat Transfer*, Vol. 2, No. 4, pp. 303–308.

Lee, S. C., 1990a, "Scattering Phase Function for Fibrous Media," *Int. J. Heat Mass Transfer*, Vol. 33, No. 10, pp. 2183–2190.

Lee, S. C., 1990b, "Dependent Scattering by Parallel Fibers: Effects of Multiple Scattering and Wave Interference," *J. Thermophys. and Heat Transfer*, Vol. 6, No. 4, p. 589.

Lind, A. C., and Greenberg, J. M., 1966, "Electromagnetic Scattering by Obliquely Oriented Cylinder," *J. Appl. Phys.*, Vol. 37, No. 8, pp. 3195–3203.

Mathes, R., Blumenberg, J., and Keller, K., 1990, "Radiative Heat Transfer in Insulations With Random Fibre Orientation," *Int. J. Heat Mass Transfer*, Vol. 33, No. 4, pp. 767–770.

Mengüç, M. P., and Viskanta, R., 1983, "Comparison of the Radiative Transfer Approximations for a Highly Forward Scattering Planar Medium," *J. Quant. Spectr. Radiat. Transfer*, Vol. 29, No. 5, pp. 381–392.

Malitson, I. H., 1965, "Interspecimen Comparison of the Refractive Index of Fused Silica," *J. Opt. Soc. Amer.*, Vol. 55, No. 10, pp. 1205–1209.

Moiseyev, S. S., Petrov, V. A., and Stepanov, S. V., 1990, "Measurement of the Optical Properties of Highly Scattering Ceramic Materials," *Int. J. Thermophysics*, Vol. 11, No. 3, pp. 587–596.

Moiseyev, S. S., Petrov, V. A., and Stepanov, S. V., 1992, "Optical Properties of High-Temperature Fibrous Silica Thermal Insulation," *High Temperature–High Pressure*, Vol. 24, No. 8, pp. 391–402.

Nicolau, V. P., Raynaud, M., and Sacadura, J. F., 1994, "Spectral Radiative Properties Identification of Fiber Insulating Materials," *Int. J. Heat Mass Transfer*, Vol. 37, Suppl. 1, pp. 311–324.

Özişik, M. H., 1973, *Radiative Transfer and Interactions With Conduction and Convection*, Wiley, New York.

Petrov, V. A., 1979, "Optical Properties of Silica Glasses at High Temperatures in the Semitransparent Region," *Rev. on Thermophys. Propert. of Subst.*, No. 3(17), pp. 30–72 [in Russian].

Petrov, V. A., 1993, "Optical and Thermophysical Properties of Semitransparent Materials in the Calculation of Combined Radiation–Conduction Heat Transfer," *Thermal Physics Reviews*, Harwood Acad. Publ., New York, Vol. 4, Pt. 5.

Reiss, H., 1990, "Radiative Transfer in Nontransparent Dispersed Media," *High Temperatures—High Pressures*, Vol. 22, No. 5, pp. 481–522.

Swathi, P. S., and Tong, T. W., 1988, "A New Algorithm for Computing the Scattering Coefficients of Highly Absorbing Cylinders," *J. Quant. Spectr. Radiat. Transfer*, Vol. 40, No. 4, pp. 525–530.

Tien, C. L., 1988, "Thermal Radiation in Packed and Fluidized Beds," ASME JOURNAL OF HEAT TRANSFER, Vol. 110, No. 4(B), pp. 1230–1242.

Tong, T. W., and Tien, C. L., 1980, "Analytical Model for Thermal Radiation in Fibrous Insulation," *J. Thermal Insulation*, Vol. 4, No. 7, pp. 27–44.

Tong, T. W., and Tien, C. L., 1983, "Radiative Heat Transfer in Fibrous Insulations. Part I: Analytical Study," ASME JOURNAL OF HEAT TRANSFER, Vol. 105, No. 1, pp. 70–75.

Viskanta, R., 1982, "Radiation Heat Transfer: Interaction With Conduction and Convection and Approximate Methods in Radiation," *Proc. 7th Heat Transfer Conf.*, Vol. 1, pp. 103–121.

Wait, J. R., 1955, "Scattering of a Plane Wave From a Circular Dielectric Cylinder at Oblique Incidence," *Canadian J. Phys.*, Vol. 33, No. 5, pp. 189–195.

Wang, K. Y., and Tien, C. L., 1983, "Radiative Heat Transfer Through Opacified Fibers and Powders," *J. Quant. Spectr. Radiat. Transfer*, Vol. 30, No. 3, pp. 213–223.

Yeh, H. Y., and Roux, J. A., 1988, "Spectral Radiative Properties of Fiberglass Insulation," *J. Thermophys. and Heat Transfer*, Vol. 2, No. 1, pp. 75–81.

Spectral Extinction Coefficients of Soot Aggregates From Turbulent Diffusion Flames

Ü. Ö. Köylü
Department of Chemical Engineering,
Yale University,
New Haven, CT 06520-8286

G. M. Faeth
Department of Aerospace Engineering,
The University of Michigan,
Ann Arbor, MI 48109-2118

The spectral extinction coefficients of soot aggregates were studied in the fuel-lean (overfire) region of buoyant turbulent diffusion flames. Extinction measurements were carried out in the wavelength region of 0.2–5.2 μm for flames fueled with acetylene, propylene, ethylene, and propane, burning in air. The present measurements were combined with earlier measurements of soot morphology and light scattering at 0.514 μm in order to evaluate the spectral soot refractive indices reported by Dalzell and Sarofim (1969), Lee and Tien (1981), and Chang and Charalampopoulos (1990). The specific extinction coefficients and emissivities were predicted based on Rayleigh–Debye–Gans theory for polydisperse fractal aggregates, which has been recently found to be the best approximation to treat optical cross sections of soot aggregates. The results indicated that available refractive indices of soot do not predict the spectral trends of present measurements in the ultraviolet and infrared regions. Soot complex refractive index was inferred to be $m = 1.54 + 0.48i$ at 0.514 μm, which is surprisingly in best agreement with the values reported by Dalzell and Sarofim (1969). Additionally, specific extinction coefficients of soot aggregates varied with wavelength as $\lambda^{-0.83}$ from the visible to the infrared. Finally, soot refractive indices were found to be relatively independent of fuel type for the visible and infrared spectral regions over the H/C ratio range of 0.08–0.22.

Introduction

Accurate knowledge of the spectral variation of the refractive indices of soot is necessary in order to estimate continuum radiation from luminous flames and to develop in situ optical techniques for measuring soot properties. However, there are fairly large variations among the soot refractive indices reported in the literature, implying uncertainties about which values should be used in a particular application; see, for example, Chang and Charalampopoulos (1990), Charalampopoulos (1992), Tien and Lee (1982), Viskanta and Mengüç (1987), and references cited therein for a complete discussion.

Some earlier determinations of soot refractive indices involved the use of ex-situ reflection methods involving compressed soot pellets sampled from flames; see Dalzell and Sarofim (1969), Felske et al. (1984), and references cited therein. These approaches were criticized, however, based on potential modification of soot properties by sampling and compression, as well as effects of surface roughness and voids on reflectance data that are difficult to evaluate (Felske et al., 1984; Tien and Lee, 1982; Charalampopoulos, 1992). Therefore, most recent work has employed in-situ measurements of scattering and extinction within both premixed and nonpremixed flames; see Habib and Vervisch (1988), Chang and Charalampopoulos (1990), Lee and Tien (1981), and Vaglieco et al. (1990). However, these determinations did not involve characterization of soot morphology and were analyzed using Mie theory whose accuracy to represent the optical cross sections of soot aggregates is questionable; see Dobbins and Megaridis (1991), Köylü and Faeth (1993, 1994a, b), Farias et al. (1995), and references cited therein. Additionally, there was always one more unknown than the measurements, so that a theoretical relationship between the real and imaginary parts of the refractive indices must be introduced, e.g., either the Drude–Lorentz dispersion model or the Kramers–Kronig relationships. Unfortunately, the Drude–Lorentz dispersion model requires constants that are not well known for soot and differ among the various investigations, while the Kramers–Kronig relationships require extinction data in the wavelength range of $0-\infty$, which is not feasible to obtain (Chang and Charalampopoulos, 1990; Felske and Ku, 1992; Lee and Tien, 1981). Moreover, results regarding the effects of fuel type (C/H ratio) on soot refractive indices are also contradictory. The early work of Dalzell and Sarofim (1969), and Lee and Tien (1981) suggested that soot refractive indices were weakly dependent on fuel type, although the specific findings of these studies were substantially different from each other in the visible. On the other hand, later work of Habib and Vervisch (1988), and Charalampopoulos et al. (1989) indicated significant effects of fuel type on soot refractive indices. However, Sivathanu et al. (1993) recently reported that their measurements were most consistent with the values reported by Dalzell and Sarofim (1969), while finding only a weak dependence of fuel type on soot refractive indices. Thus, the objective of the present study was to evaluate the capabilities of the soot refractive indices reported in the literature to treat the spectral extinction properties of soot aggregates, and to investigate the effect of fuel type on refractive indices.

Past work has provided information about soot morphology in the fuel-lean (overfire) region of buoyant turbulent diffusion flames for a variety of gaseous and liquid fuels burning in still air within the long residence time regime (Köylü and Faeth, 1992). In addition, angular scattering and extinction coefficients at 0.514 μm have been measured for the same conditions for flames fueled by the gaseous fuels (Köylü and Faeth, 1994a). Thus, the same conditions were adopted for the present study due to the well-characterized soot environment and the universality of overfire soot in the long residence time regime for a particular fuel. The present measurements included the extinction coefficients of soot in the wavelength region of 0.2–5.2 μm. Four gaseous hydrocarbon fuels—acetylene, propylene, ethylene and propane—were used to study the effect of fuel type (H/C ratio) on spectral refractive indices of soot. The

Contributed by the Heat Transfer Division for publication in the JOURNAL OF HEAT TRANSFER. Manuscript received by the Heat Transfer Division May 1995; revision received December 1995. Keywords: Combustion, Radiation, Thermophysical Properties. Associate Technical Editor: S. H. Chan.

spectral properties, e.g., specific extinction coefficients and emissivities, were predicted based on RDG theory for polydisperse fractal aggregates because this approach has been found to be the best approximation to represent the optical properties of soot aggregates (Köylü and Faeth, 1994a, b; Farias et al., 1995). The spectral soot refractive indices reported by Dalzell and Sarofim (1969), Lee and Tien (1981), and Chang and Charalampopoulos (1990) were chosen for comparison with the present measurements because they are frequently used in heat transfer and combustion studies and they also involve different experimental and data inversion methods.

The paper begins with description of experimental and theoretical methods. This is followed by results, considering earlier scattering measurements at 0.514 μm briefly, comparisons with different soot refractive indices in the literature, and the effect of fuel type on spectral refractive indices, in turn. An experimental correlation for the variation of specific extinction coefficients is also suggested.

Experimental Methods

The present test arrangement was the same as for the earlier light scattering measurements of Köylü and Faeth (1994a). The apparatus consisted of a 50-mm-dia water-cooled burner, which provided buoyant turbulent diffusion flames in the long residence time regime. The burner was located within a larger enclosure with a hood at the top and an adjustable exhaust system to remove the combustion products. The soot emitted from the flames was collected in a sampling duct with a 152-mm-dia exit at the top, which discharged into the main hood of the apparatus. The mixing within the duct was sufficient to yield homogeneous soot properties across the exit of the sampling duct where extinction measurements were carried out.

Three different light sources—a 30 W deuterium lamp (Oriel 6316), a 100 W QTH lamp (Oriel 6333), and a 100 W IR element (Oriel 6363)—were used in the wavelength regions 0.20–0.35, 0.35–2.0, and 2.0–5.2 μm, respectively. CaF_2 lenses were used for spatial filtering and collimating the incident light due to the wide range of wavelengths considered. The light was modulated by an enclosed chopper (Oriel 75155) before passing through the soot samples. Different interference filters were used in front of the detector to make measurements at the wavelength of interest. The reference (without soot) and transmitted (with soot) intensities were measured by a pyroelectric detector (Oriel 70841), which has a flat response in the wavelength range of 0.2–40 μm. The stability of the light sources was insured by measuring reference intensities before and after each test run at each wavelength. The detector output was stored on a computer, sampling at 400 Hz for 30 s for heavily sooting fuels (acetylene and propylene), while the sampling time was doubled to 60 s for lightly soothing fuels (ethylene and propylene) in order to increase signal-to-noise ratios. The results were averaged over three tests at each wavelength to achieve a repeatibility within 1 percent.

Experimental uncertainties of the extinction coefficients increased not only with decreasing tendency of the fuel to form soot but also with increasing wavelength, since they were inversely proportional to ln (I/I_o) and sampling times. Specifically, experimental uncertainties (95 percent confidence) were estimated to be generally less than 20 percent for acetylene and propylene, and less than 40 percent for ethylene and propane for present test conditions. It should be noted that the present measurements were also compared to the results of Köylü and Faeth (1994a) at the three laser wavelengths of 0.514, 0.633, and 1.152 μm to check current measurements independently.

Theoretical Methods

Radiative Properties of Polydisperse Soot Aggregates. The complete formulation of Rayleigh–Debye–Gans polydisperse fractal aggregate theory (RDG/PFA) as well as relevant references can be found in Köylü and Faeth (1994a, b). Briefly, assuming that the individual soot particles that combine to form aggregates satisfy Rayleigh approximation ($x_p \leq 0.3$), the various cross sections of an aggregate are expressed in terms of the morphology of the aggregate and the corresponding cross sections of primary particles within the RDG/FA approximation. The mean optical cross sections of populations of randomly oriented polydisperse aggregates are found by integrating over all aggregate sizes using the log-normal aggregate size distribution function. It should be mentioned that this formal integration is necessary, since no single parameter can represent the optical properties of polydisperse aggregates. The optical coefficients (the volumetric cross sections) are the products of the cross sections and the number density of aggregates, as follows:

$$K_j = n\overline{C_j}; \quad j = vv, s, a, e \tag{1}$$

Extinction coefficient is simply the sum of absorption and total scattering, i.e.,

$$K_e = K_a + K_s = K_a(1 + \rho_{sa}) \tag{2}$$

where

$$K_a = K_a^p = \frac{6\pi E(m)}{\lambda} f_v \tag{3}$$

Nomenclature

C = optical cross section
d_p = primary particle diameter
D_f = mass fractal dimension
$E(m)$ = refractive index function = Im $[(m^2 - 1)/(m^2 + 2)]$
f = scattering form factor = $f(qR_g)$
f_v = soot volume fraction
$F(m)$ = refractive index function = $|(m^2 - 1)/(m^2 + 2)|^2$
g = total scattering factor = $g(kR_g)$
i = $(-1)^{1/2}$
I = transmitted light intensity
I_o = reference light intensity
k = wave number = $2\pi/\lambda$
k_f = fractal prefactor
K = optical coefficient
m = refractive index of soot = $\eta + i\kappa$
n = number density of aggregates
N = number of primary particles in an aggregate
q = modulus of scattering vector = $2k \sin(\theta/2)$
R_g = radius of gyration of an aggregate
S = optical path length
x_p = optical size parameter of an individual particle = $\pi d_p/\lambda$
α = correlation constant, Eq. (11)
ϵ = emissivity of soot
η = real part of refractive index of soot
κ = imaginary part of refractive index of soot
λ = wavelength of radiation
θ = scattering angle
ρ_{sa} = ratio of total scattering to absorption cross section
Φ = phase function
Ω_o = single-scattering albedo

Subscripts

a = absorption
e = extinction
s = total scattering
vv = vertically polarized incident and scattered light

Superscripts

p = individual particle property
$\overline{\ }$ = mean value over a polydisperse aggregate population

and

$$\rho_{sa} = \rho_{sa}^{p} \frac{\overline{N^2 g}}{\bar{N}} \tag{4}$$

Therefore, the absorption coefficients of aggregates and the individual particles composing them are identical. Additionally, ρ_{sa} represents the effect of aggregation on total scattering and is related to albedo by $\rho_{sa} = \Omega_o/(1 - \Omega_o)$. The optical coefficients can be measured directly using light scattering and transmission measurements in a soot-containing environment. Specifically, the transmissivity, I/I_o, for a uniform path length of S is given as follows:

$$\frac{I}{I_0} = \exp(-K_e S) \tag{5}$$

where the quantity, $K_e S$, is called the optical thickness. The underlying requirement for the use of Eq. (5) is to have an optically thin medium, i.e., $K_e S \ll 1$. However, this condition can be relaxed somewhat as long as absorption is the dominant mechanism. In other words, the range of applicability of Eq. (5) is extended further as long as $K_s S \ll 1$ (Bohren and Huffman, 1983).

A useful quantity for radiative heat transfer calculations is the specific extinction coefficient, defined as the extinction coefficient per unit volume fraction of soot. By combining Eqs. (2)–(4), an explicit form for specific extinction coefficient is obtained as follows:

$$\frac{K_e}{f_v} = \frac{6\pi E(m)}{\lambda}\left[1 + \frac{2}{3}\frac{F(m)}{E(m)} x_p^3 \frac{\overline{N^2 g}}{\bar{N}}\right] \tag{6}$$

where $g = g(kR_g)$ is the total scattering factor. This implies that if the soot morphology is known, the right-hand side of Eq. (6) is only a function of the refractive indices. Thus, the specific extinction coefficient is a logical parameter for comparing refractive indices from different sources. The spectral emissivity can be expressed in terms of specific extinction coefficient as follows:

$$\epsilon_\lambda = 1 - \exp\left[-\left(\frac{K_e}{f_v}\right) f_v S\right] \tag{7}$$

Another important radiative property is the phase function (Siegel and Howell, 1981), which is given as follows within RDG/PFA theory:

$$\Phi(\theta) = \Phi^p(\theta)\left(\frac{\overline{N^2 f}}{\overline{N^2 g}}\right) \tag{8}$$

where $f = f(qR_g)$ represents the angular scattering form factor. This formulation implies that the radiative properties of aggregates are substantially different from those of individual particles.

Soot Refractive Indices. Among the mean radiative properties, only the albedo is independent of refractive indices, which are the fundamental quantities required for most practical optical property calculations. In particular, the values of $E(m)$ and the ratios of $F(m)/E(m)$ are needed for both spectral radiative properties and determinations of soot volume fractions; see Eqs. (6) and (7). Thus, the spectral variations of $E(m)$ and the ratio $F(m)/E(m)$ from different sources are illustrated in Fig. 1. Results in the figure are based on the measurements of Dalzell and Sarofim (1969), Lee and Tien (1981), and Chang and Charalampopoulos (1990). It is evident that there are significant differences for $E(m)$ and $F(m)/E(m)$ among these three studies, noting that other determinations in the literature would yield even wider variations (Charalampopoulos, 1992). $E(m)$ values

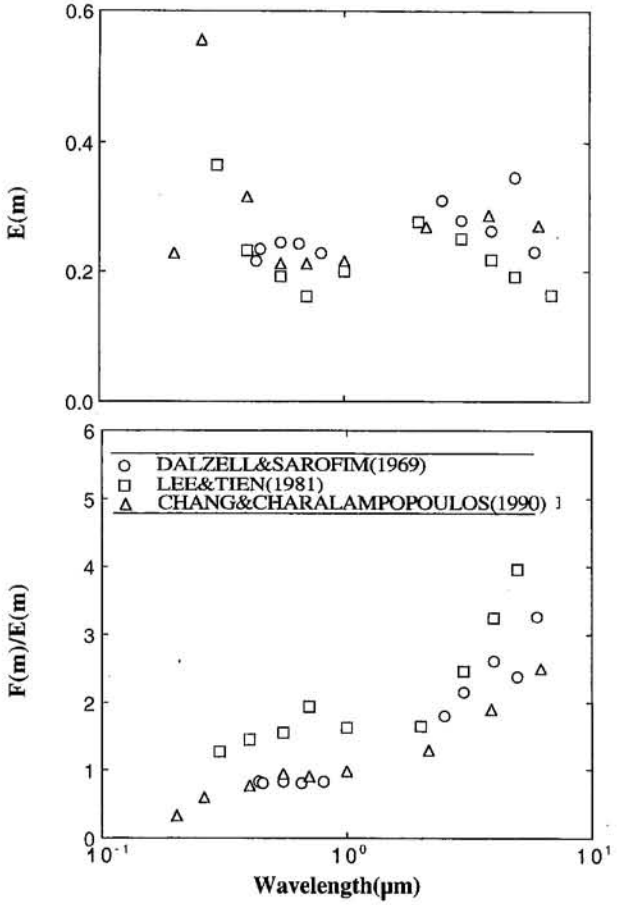

Fig. 1 $E(m)$ values and ratios of $F(m)/E(m)$ as a function of wavelength as determined by Dalzell and Sarofim (1969), Lee and Tien (1981), and Chang and Charalampopoulos (1990)

from the three investigations agree somewhat in the visible; however, there are up to 40 percent differences in the infrared and ultraviolet. Although, the values from Dalzell and Sarofim (1969), and Chang and Charalampopoulos (1990) yield very similar spectral variations of $E(m)$, Lee and Tien (1981) always give lower estimates. On the other hand, there is even less agreement about the ratios of $F(m)/E(m)$ among these three studies with up to 100 percent differences encountered in the infrared. The ratios of $F(m)/E(m)$ from Dalzell and Sarofim (1969), and Chang and Charalampopoulos (1990) agree well in the visible while the estimates from Lee and Tien (1981) are higher than the other two at all wavelengths. These differences among refractive indices result in corresponding uncertainties about radiative properties. Thus, use of refractive indices from a particular source can only be justified by the evidence that they treat measured spectral properties effectively, which was the main motivation for the present investigation.

Results and Discussion

Scattering at 0.514 μm. Measured phase function from the earlier scattering measurements, along with the predictions from the various approximate theories, are plotted as a function of scattering angle in Fig. 2. The measurements are for acetylene soot from the scattering measurements of Köylü and Faeth (1994a) at 0.514 μm, while the predictions are based on TEM characterization of soot morphology from Köylü and Faeth (1992). As can be seen from Fig. 2, soot aggregates scatter strongly in the forward direction; additionally, predictions of the RDG/PFA theory are in good agreement with measurements. However, neither Mie theory for an equivalent diameter nor the

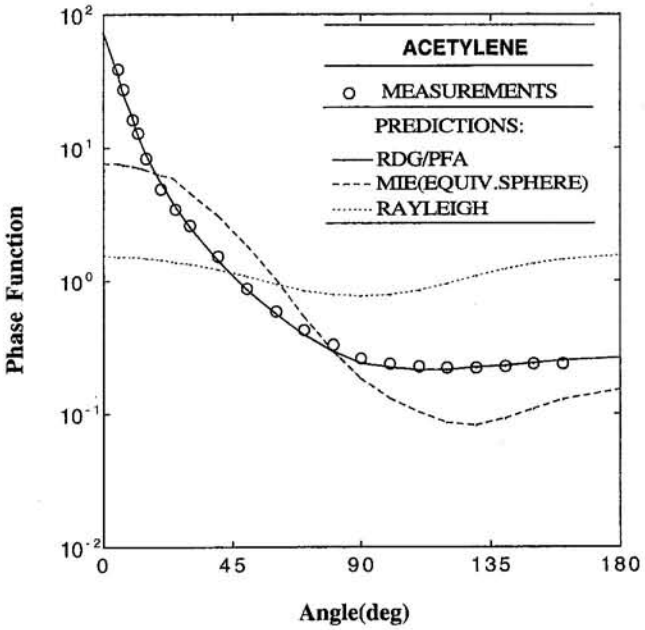

Fig. 2 Various theoretical predictions and measurements of phase function for soot aggregates in the overfire region of turbulent acetylene/air diffusion flame

Rayleigh approximation can predict the angular trends of phase function. These results suggest the importance of aggregate scattering and justifies the use of RDG/PFA theory to estimate spectral properties of soot.

Köylü and Faeth (1994a) reported a limited assessment of soot refractive indices at 0.514 μm based on RDG/PFA theory, which yielded the following relationship for large scattering angles corresponding to the power-law regime:

$$\frac{F(m)}{E(m)} = 4\pi \frac{(qd_p)^{D_f}}{k_f x_p^3} \frac{K_{vv}}{K_a} \tag{9}$$

However, this evaluation was based on an assumed value of fractal prefactor, k_f (appearing in the relationship $N = k_f(R_g/d_p)^{D_f}$ for fractal-like aggregates), and there were still some concerns about the reliability of RDG/FA theory. Later, Köylü et al. (1995) established a value of $k_f = 8.5 \pm 0.5$, independently from three-dimensional reconstructions of TEM images. Additionally, RDG/PFA theory was further evaluated both experimentally (Köylü and Faeth, 1994b) and computationally (Farias et al., 1995), finding satisfactory performance. Thus, it is appropriate to reconsider Eq. (9) in conjunction with the present study.

Using the earlier measurements of soot morphology and light scattering at 0.514 μm, together with values of $k_f = 8.5$ and $D_f = 1.8$, Eq. (9) yields $F(m)/E(m) = 0.78$ with a standard deviation of 0.09 over all the fuels. Since the range of $E(m)$ values from different sources are rather narrow compared to $F(m)$, a value of $E(m) = 0.23$ seems to be reasonable (see Fig. 1). This, together with measured value of $F(m)/E(m)$, yields a complex refractive index of $m = 1.54 + 0.48i$ at 0.514 μm, which is in reasonably good agreement with the measurements of Dalzell and Sarofim (1969) and Chang and Charalampopoulos (1990). However, the refractive indices at this wavelength given by Lee and Tien (1981) yield $F(m)/E(m) = 1.55$, which is almost 100 percent higher than the measured value.

Spectral Extinction Properties of Soot. Measured optical thicknesses, $K_e S$, in the wavelength range 0.2–5.2 μm, are illustrated in Fig. 3 for all the fuels considered during the present study. The strong gas absorption bands of H_2O at 2.7 μm, and CO_2 at 4.3 μm were avoided during the spectral measurements. The results yielded a maximum extinction coefficient in the ultraviolet region at a wavelength of approximately 0.25 μm for all fuels. Menna and D'Alessio (1982) and Chang and Charalampopoulos (1990) reported similar observations, which seem to be caused by a resonance of soot refractive indices at this wavelength range. In contrast, the behavior of spectral extinction coefficients in the infrared is monotonic, i.e., extinction coefficients decrease with increasing wavelength, as expected.

The present spectral measurements of extinction coefficients will now be used to assess existing refractive indices in the literature. Soot volume fractions are estimated using $m = 1.54 + 0.48i$ at 0.514 μm and applying Eq. (6) at the same wavelength. Knowing the volume fraction and the morphology of soot, then it is possible to evaluate Eq. (6) at each wavelength using refractive indices from different sources and to compare it with measurements. The resulting measured and predicted specific extinction coefficients are plotted as a function of wavelength in Fig. 4. The spectral measurements are for the overfire soot aggregates emitted from propane/air flame, while the predictions are based on RDG/PFA theory using the refractive indices of Dalzell and Sarofim (1969), Lee and Tien (1981), and Chang and Charalampopoulos (1990). The results indicate that the predictions of all three sources are in good agreement with measurements in the visible. However, this may be misleading for the values of Lee and Tien (1981), because it was previously shown that they overestimated scattering by almost 100 percent at 0.514 μm; therefore, the suitable extinction behavior is an artifact of their low values of $E(m)$ compensating for high ratios of $F(m)/E(m)$. Thus, only the refractive indices from Dalzell and Sarofim (1969), and Chang and Charalampopoulos (1990) seem to be acceptable in the visible.

The refractive indices from the three studies overestimate the observed extinction levels by up to a factor of three in the ultraviolet. However, the values from Chang and Charalampopoulos (1990) correctly predict the properties of the resonance of refractive indices near 0.25 μm. Although the measurements of Dalzell and Sarofim (1969), and Lee and Tien (1981) do not extend into this short wavelength region, their dispersion models fail to indicate the presence of the resonance phenomena, as quantified by Menna and D'Alessio (1982). In other

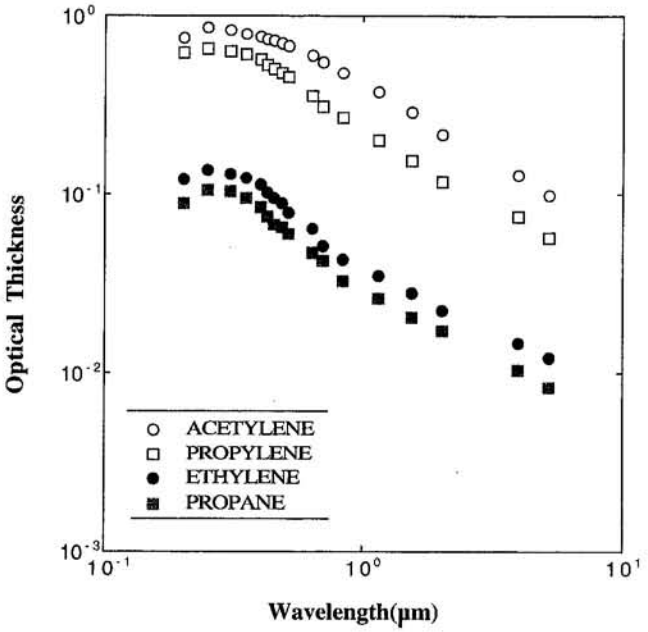

Fig. 3 Measurements of optical thickness as a function of wavelength for soot aggregates in the overfire region of turbulent hydrocarbon diffusion flames

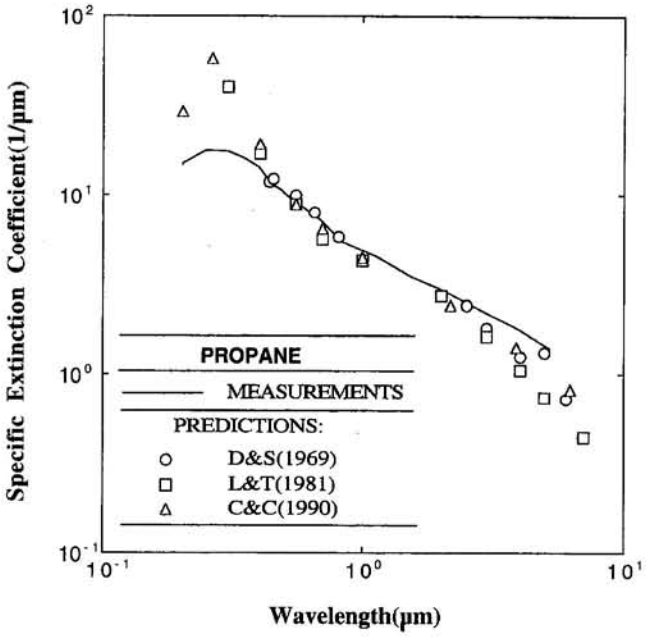

Fig. 4 Predictions of various refractive indices and measurements of spectral specific extinction coefficient of soot aggregates in the overfire region of turbulent propane/air diffusion flame

words, their extinction coefficient estimates would continue to increase with decreasing wavelength, with no peak in the UV. Thus, the magnitude as well as the trend of their refractive indices do not agree with present measurements. At this point, some of the overall poor agreement between predictions and measurements may be caused by the approximations of the RDG/PFA theory because optical size parameters become rather large in the region of the resonance. However, the mean individual particle diameter for propane soot is 30 nm, yielding $x_p = 0.38$ at 0.25 μm. Although this small deviation of individual particles from Rayleigh scattering behavior ($x_p \leq 0.3$) cannot be responsible for the significant differences between measurements and predictions at this wavelength, the performance of RDG/PFA theory in the ultraviolet region of the spectrum certainly merits additional study.

The refractive indices from the three sources yield predictions that begin to deviate from measurements as the wavelength increases from visible into the infrared. Although the values from Dalzell and Sarofim (1969) yield best agreement with measurements in this wavelength range, all three data sets underestimate the measurements of specific extinction coefficients. This is probably due to their low $E(m)$ values in the infrared, as will be demonstrated in the following by evaluating Eq. (6) at $\lambda_1 = 0.514$ μm and $\lambda_2 = 5.2$ μm, and taking the ratio:

$$\frac{E(\lambda_1)}{E(\lambda_2)} = \frac{\lambda_2}{\lambda_1}\frac{K_e(\lambda_2)}{K_e(\lambda_1)}[1 + \rho_{sa}(\lambda_1)] \qquad (10)$$

since the scattering is negligible at 5.2 μm, i.e., $\rho_{sa}(\lambda_2) \cong 0$. Noting that all the quantities on the right-hand side of Eq. (10) are known from the measurements, the ratios between $E(m)$ at 5.2 and 0.514 μm can be calculated. This yields $E(5.2\ \mu\text{m})/E(0.514\ \mu\text{m}) = 1.89$ with a standard deviation of 0.18 for all the fuels. This ratio is given by Dalzell and Sarofim (1969), Lee and Tien (1981), and Chang and Charalampopoulos (1990) as 1.38, 1.00, and 1.21, respectively. Thus, the closest agreement is obtained from the refractive indices of Dalzell and Sarofim (1969), underestimating the measured value by 27 percent. Nevertheless, the differences between predictions and measurements are typically 50–100 percent at long wavelengths. These results also suggest a value of $E(m) = 0.42$ at 5.2 μm, when $E(m)$ at 0.514 μm is taken to be 0.23.

The emissivities of the soot aggregates are illustrated as a function of wavelength for propylene in Fig. 5. Spectral emissivities are obtained from Eq. (7) using the measurements of specific extinction coefficients. Again, the predictions are based on the RDG/PFA theory with refractive indices from Dalzell and Sarofim (1969), Lee and Tien (1981), and Chang and Charalampopoulos (1990). Similar to the results for specific extinction coefficients, the predicted emissivities are overestimated in the UV and underestimated in the IR. On the other hand, measurements and predictions are in good agreement for visible wavelengths. Among the three, the refractive indices from Dalzell and Sarofim (1969) appear to be yielding best estimates of emissivities, followed by the results of Chang and Charalampopoulos (1990). It is a puzzling fact that not only this study but also other studies (Sivathanu et al., 1993; Choi et al., 1994; Dobbins et al., 1994) find that the refractive index data from the highly criticized ex-situ reflection measurements of Dalzell and Sarofim (1969) yield predictions that are in good agreement with the scattering/extinction/emission measurements in the visible and near-infrared portions of the spectrum. Why this is so is not clear and certainly merits further investigation. However, the overall differences between the measured and predicted spectral emissivities in the infrared may result in significant differences (20–40 percent) in the total emittance for typical flame temperatures. It should be mentioned that the results for other fuels were similar and will not be discussed here.

Experimental Correlation for Spectral Properties. As discussed in the introduction, it is well established that the Drude–Lorentz model is not only inappropriate for soot-like materials but also involves several unknown parameters. As a result, although it was desirable to obtain spectral refractive indices of soot, application of any dispersion model was avoided. On the other hand, several authors (see, for example, Siegel and Howell (1981), and Siddall and McGrath (1963)) have reported that the specific extinction coefficients of soot varied with wavelength according to:

$$K_e/f_v \propto \lambda^{-\alpha} \qquad (11)$$

The use of Eq. (11) is practical in radiative heat transfer calculations for soot, since the expression does not involve the compli-

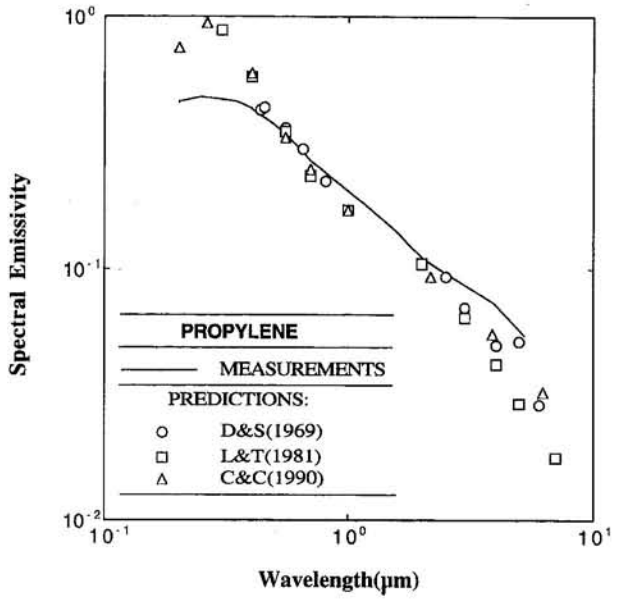

Fig. 5 Predictions of various refractive indices and measurements of emissivity of soot aggregates in the overfire region of turbulent propylene/air diffusion flame

cations of refractive indices. Thus, a similar correlation was sought for the present test conditions. The least-square fits of the measurements in the wavelength range of 0.514–5.2 μm yielded a value of $\alpha = 0.83$ with a standard deviation of 0.04 for the four fuels considered in this study. The values suggested by the refractive indices of Dalzell and Sarofim (1969), Lee and Tien (1981), and Chang and Charalampopoulos (1990) are in the range of 0.94–1.21, which are 13–47 percent higher than the present measurements. Additionally, the experimental correlation given above implies that $E(m)$ should increase slightly with increasing wavelength, i.e., $E(m) \propto \lambda^{0.17}$ in the infrared. This also suggests that the refractive indices of soot are weak functions of wavelength in this part of the spectrum. This behavior, however, differs from the behavior of available refractive indices in the infrared, as can be seen from Fig. 1, which shows a decrease (Dalzell and Sarofim, 1969; Lee and Tien, 1981), or almost no variation (Chang and Charalampopoulos, 1990) of $E(m)$ with increasing wavelength in the infrared.

Other evaluations of α directly from extinction measurements are available in the literature. Siddall and McGrath (1963) extensively studied the spectral behavior of several types of soot in the infrared portion, reporting $\alpha = 0.77–1.25$. However, most of their measurements involved optically thick conditions, where use of Eq. (5) is questionable, as discussed previously. Consistent with this observation, their measurements with avtur kerosine and amyl acetate soot had similar extinction levels to present study and yielded $\alpha = 0.77$ and 0.89, respectively. These values are in excellent agreement with the present measurements, which may imply that the results of the present study can be extended to other types of fuel. Additionally, their claim of variation of α with wavelength should be interpreted with great caution, since the method used to calculate α at each wavelength involved high experimental uncertainties due to taking successive logarithms. Thus, $\alpha = 0.83$ appears to be reasonable with a wavelength range from the visible to infrared.

Effect of Fuel Type on Soot Refractive Indices. Table 1 is a summary of soot refractive index properties found during the present study. The table includes $F(m)/E(m)$ at 0.514 μm, the ratios of the values of $E(m)$ at 5.2 μm and 0.514 μm, and the values of α, representing the spectral variation of refractive indices in the range of 0.514–5.2 μm. As can be seen from Eqs. (9), (10) and (11), these parameters are all obtained without using any assumptions including soot volume fraction. The changes in all three measurements with fuel type were within present experimental uncertainties, suggesting that the refractive indices of soot are relatively independent of fuel type from visible to infrared for the present test conditions. In view of similar observations of Sivathanu et al. (1993) for soot within laminar premixed flames, this weak dependence may apply to other flame environments, simplifying both in-situ soot volume fraction determinations and radiative heat transfer calculations.

Table 1

Fuel	F(0.514 μm)/E(0.514 μm)	E(5.2 μm)/E(0.514 μm)	α
Acetylene	0.66	2.07	0.84
Propylene	0.84	1.77	0.87
Ethylene	0.85	2.01	0.78
Propane	0.77	1.71	0.82
Mean (stand. dev.)	0.78 (0.09)	1.89 (0.18)	0.83 (0.04)

[a] Measurements involve overfire soot for buoyant turbulent diffusion flames burning in air for the designated fuel.

However, additional studies in various flames will be required in order to firmly establish the insensitivity of refractive indices to fuel type.

Conclusions

The spectral extinction coefficients of soot were measured in the wavelength region of 0.2–5.2 μm. Four hydrocarbon fuels were considered in order to vary H/C ratios in the range 0.08 to 0.22. Test conditions were limited to the fuel-lean (overfire) region of buoyant turbulent diffusion flames in the long residence time regime, where soot morphology, and soot scattering properties at 0.514 μm, were known from earlier work (Köylü and Faeth, 1992, 1994a). The results of the present measurements were combined with earlier findings in order to evaluate existing refractive indices in the literature. The major conclusions of the study are as follows:

1 The refractive indices determined by Dalzell and Sarofim (1969), and Chang and Charalampopoulos (1990) were in good agreement with present extinction and scattering measurements in the visible. The values from Lee and Tien (1981), however, gave less satisfactory results in the same wavelength region. Additionally, the present study suggests a complex refractive index of $m = 1.54 + 0.48i$ at 0.514 μm, which is in best agreement with the measurements of Dalzell and Sarofim (1969) at visible wavelengths.

2 The specific extinction coefficients of soot were found to vary with wavelength from visible to infrared according to $K_e/f_v \propto \lambda^{-\alpha}$, where $\alpha = 0.83 \pm 0.08$ for all the fuels considered in this investigation. The spectral refractive indices from Dalzell and Sarofim (1969), Lee and Tien (1981), and Chang and Charalampopoulos (1990) yielded values of α that are 13–47 percent higher than the measured value, which would result in an underestimation of total emittance up to 40 percent for typical flame temperatures.

3 The present spectral extinction measurements, together with previous scattering results, showed that the ratios of $F(m)/E(m)$ at 0.514 μm, the ratios of values of $E(m)$ at 5.2 μm and 0.514 μm, and the values of α, representing the spectral variation of refractive indices in the range of 0.514–5.2 μm did not change with fuel type within experimental uncertainties. All three measurements suggest that soot refractive indices are relatively independent of fuel type for the visible and infrared spectral ranges for the present test conditions.

Acknowledgments

This research was sponsored by the Building and Fire Research Laboratory of the National Institute of Standards and Technology, Grant No. 60NANB1D1175, with K. C. Smyth and H. R. Baum serving as Scientific Officers; and by NASA, Grant No. NAG3-1245, under the technical management of D. L. Urban of the Lewis Research Center. One of the authors (Ü. Ö. K.) would like to acknowledge the partial support by AFOSR, Grant No. 94-0143, with J. M. Tishkoff serving as Technical Monitor.

References

Bohren, C. F., and Huffman, D. R., 1983, *Absorption and Scattering of Light by Small Particles*, Wiley, New York, pp. 69–81.

Chang, H., and Charalampopoulos, T. T., 1990, "Determination of the Wavelength Dependence of Refractive Indices of Flame Soot," *Proc. R. Soc. London A*, Vol. 430, pp. 577–591.

Charalampopoulos, T. T., 1992, "Morphology and Dynamics of Agglomerated Particulates in Combustion Systems Using Light Scattering Techniques," *Prog. Energy Combust. Sci.*, Vol. 18, pp. 13–45.

Charalampopoulos, T. T., Chang, H., and Stagg, B. J., 1989, "The Effects of Temperature and Composition on the Complex Refractive Index of Flame Soot," *Fuel*, Vol. 68, pp. 1173–1179.

Choi, M. Y., Hamins, A., Mulholland, G. W., and Kashiwagi, T., 1994, "Simultaneous Optical Measurement of Soot Volume Fraction and Temperature in Premixed Flames," *Combust. Flame*, Vol. 99, pp. 174–186.

Dalzell, W. H., and Sarofim, A. F., 1969, "Optical Constants of Soot and Their Application to Heat Flux Calculations," ASME JOURNAL OF HEAT TRANSFER, Vol. 91, pp. 100–104.

Dobbins, R. A., and Megaridis, C. M., 1991, "Absorption and Scattering of Light by Polydisperse Aggregates," *Appl. Optics,* Vol. 30, pp. 4747–4754.

Dobbins, R. A., Mulholland, G. W., and Bryner, N. P., 1994, "Comparison of a Fractal Smoke Optics Model With Light Extinction Measurements," *Atmos. Environ.,* Vol. 28, pp. 889–897.

Farias, T. L., Carvalho, M. G., Köylü, Ü. Ö., and Faeth, G. M., 1995, "Computational Evaluation of Approximate Rayleigh-Debye-Gans/Fractal Aggregate Theory for the Absorption and Scattering Properties of Soot," ASME JOURNAL OF HEAT TRANSFER, Vol. 117, pp. 152–159.

Felske, J. D., and Ku, J. C., 1992, "A Technique for Determining the Spectral Refractive Indices, Size and Number Density of Soot Particles From Light Scattering and Spectral Extinction Measurements in Flames," *Combust. Flame,* Vol. 91, pp. 1–20.

Felske, J. D., Charalampopoulos, T. T., and Hura, H., 1984, "Determination of the Refractive Indices of Soot Particles From the Reflectivities of Compressed Soot Pellets," *Combust. Sci. Tech.,* Vol. 37, pp. 263–283.

Habib, Z. G., and Vervisch, P., 1988, "On the Refractive Index of Soot at Flame Temperature," *Combust. Sci. Tech.,* Vol. 59, pp. 261–274.

Köylü, Ü. Ö., and Faeth, G. M., 1992, "Structure of Overfire Soot in Buoyant Turbulent Diffusion Flames at Long Residence Times," *Combust. Flame,* Vol. 89, pp. 140–156.

Köylü, Ü. Ö., and Faeth, G. M., 1993, "Radiative Properties of Flame-Generated Soot," ASME JOURNAL OF HEAT TRANSFER, Vol. 115, pp. 409–417.

Köylü, Ü. Ö., and Faeth, G. M., 1994a, "Optical Properties of Overfire Soot in Buoyant Turbulent Diffusion Flames at Long Residence Times," ASME JOURNAL OF HEAT TRANSFER, Vol. 116, pp. 152–159.

Köylü, Ü. Ö., and Faeth, G. M., 1994b, "Optical Properties of Soot in Buoyant Laminar Diffusion Flames," ASME JOURNAL OF HEAT TRANSFER, Vol. 116, pp. 971–979.

Köylü, Ü. Ö., Faeth, G. M., Farias, T. L., and Carvalho, M. G., 1995, "Fractal and Projected Structure Properties of Soot Aggregates," *Combust. Flame,* Vol. 100, pp. 621–633.

Lee, S. C., and Tien, C. L., 1981, "Optical Constants of Soot in Hydrocarbon Flames," *Eighteenth Symposium (International) on Combustion,* The Combustion Institute, Pittsburgh, pp. 1159–1166.

Menna, P., and D'Alessio, A., 1982, "Light Scattering and Extinction Coefficients for Soot Forming Flames in the Wavelength Range From 200 nm to 600 nm," *Nineteenth Symposium (International) on Combustion,* The Combustion Institute, Pittsburgh, pp. 1421–1428.

Siddall, R. G., and McGrath, I. A., 1963, "The Emissivity of Luminous Flames," *Ninth Symposium (International) on Combustion,* The Combustion Institute, Pittsburgh, pp. 102–110.

Siegel, R., and Howell, J. R., 1981, *Thermal Radiation Heat Transfer,* Hemisphere, New York, pp. 658–669.

Sivathanu, Y. R., Gore, J. P., Janssen, J. M., and Senser, D. W., 1993, "A Study of In Situ Specific Absorption Coefficients of Soot Particles in Laminar Flat Flames," ASME JOURNAL OF HEAT TRANSFER, Vol. 115, pp. 653–658.

Tien, C. L., and Lee, S. C., 1982, "Flame Radiation," *Prog. Energy Combust. Sci.,* Vol. 8, pp. 41–59.

Vaglieco, B. M., Beretta, F., and D'Alessio, A., 1990, "In Situ Evaluation of the Soot Refractive Index in the UV-Visible from the Measurements of the Scattering and Extinction Coefficients in Rich Flames," *Combust. Flame,* Vol. 79, pp. 259–271.

Viskanta, R., and Mengüç, M. P., 1987, "Radiation Heat Transfer in Combustion Systems," *Prog. Energy Combust. Sci.,* Vol. 13, pp. 97–160.

Analytical Study of Critical Heat Flux in Two-Phase Thermosyphon: Relationship Between Maximum Falling Liquid Rate and Critical Heat Flux

M. Monde
Department of Mechanical Engineering,
Saga University,
1 Honjo Saga, Japan 840

An analytical study has been done on the critical heat flux of a two-phase thermosyphon, in which a liquid film and a vapor flow exist in a countercurrent annular flow. The CHF point on the thermosyphon is proved to correspond to a maximum falling liquid rate fed to the thermosyphon, which can be determined from three equations of momentum, its partial derivative with void fraction, and mass balance in the thermosyphon. This maximum point, furthermore, becomes identical to the point at which an envelope line generated from the momentum equation and its partial derivative intersects the mass balance line. The CHF calculated from the maximum liquid rate is found to be in fairly good agreement with the existing CHF data.

1 Introduction

Critical heat flux (CHF) phenomenon in a two-phase thermosyphon is very complicated and is usually considered as a kind of phenomenon closely related to "flooding" during countercurrent flow of vapor and liquid in a tube. As a result, most generalized correlations for CHF data have so far depended mainly on a flooding criterion.

According to a review on flooding (Bankoff and Lee, 1986), there are two different viewpoints: One (Imura et al., 1977; Tien et al., 1980) is that the flooding is thought to be caused by some kind of wave motion or instability, which appears on the gas–liquid interface, and another (Wallis, 1967; Bharathan et al., 1979; Taitel et al., 1982; Dobran, 1981) is that flooding is initiated by a limiting condition for the countercurrent flow as either liquid or gas flow rate is increased. If there are one-dimensional momentum equations for gas and liquid and these can be manipulated to give an equation, namely $F(j_L^*, j_G^*, \alpha) = 0$, the limiting condition is determined by an envelope, which is generated by eliminating α from $F(j_L^*, j_G^*, \alpha) = 0$ and its derivative with α, namely $G(j_L^*, j_G^*, \alpha) = \partial F(j_L^*, j_G^*, \alpha)/\partial\alpha = 0$.

$$F(j_L^*, j_G^*, \alpha) = 0 \tag{1}$$

$$G(j_L^*, j_G^*, \alpha) = \frac{\partial F(j_L^*, j_G^*, \alpha)}{\partial \alpha} = 0 \tag{2}$$

where j_L^* and j_G^* are nondimensional velocity of liquid and vapor, respectively, and the parameter α is void fraction. The envelope line gives the one-parameter family of curves in the (j_L^*, j_G^*) plane and is considered to be the locus of tangents to the operating lines in the (j_L^*, j_G^*) plane for constant void fraction and provides a limiting curve separating the operating region from an unattainable region for countercurrent flow. Another understanding of $\partial F/\partial\alpha = 0$ is an optimum force balance among external forces depending on j_L^*, j_G^* and α from a combination of j_L^*, j_G^*, and α that satisfies the momentum equation.

For the case of a two-phase thermosyphon, the continuity equation for two phases at any cross section in a tube becomes

$$\rho_L j_L = \rho_G j_G \quad \text{or} \quad \rho_L^{1/2} j_L^* = \rho_G^{1/2} j_G^* \tag{3}$$

It is clear that the point at which the line given by Eq. (3) intersects the envelope line corresponds to the limiting condition for the two-phase thermosyphon and thus controls the critical heat flux.

Katto and Watanabe (1992) analyzed the limiting conditions of steady-state countercurrent annular flow with interfacial friction, assuming a continuous change in the liquid film thickness along the tube wall, and predicted the critical heat flux of boiling in a vertical tube and an annulus with a saturated-liquid plenum at the top and a closed bottom end. More recently, Katto (1994) has refined the idea such that the condition that the void fraction, α (or δ/D) in Eq. (1) has an identical root for any constant j_L^*, to provide a curve on the (j_L^*, j_G^*) plane. Thus an intersectional point between the curve and Eq. (3) corresponds to the limiting condition for the thermosyphon, that is the critical heat flux. The analytical result computed in this way is reported to be in fairly good agreement with their CHF data in a two-phase thermosyphon. The Katto idea has merit in grasping the physical meanings of CHF, because if j_G^* increases beyond the identical root of α or δ/D, a real number for δ/D does not exist to satisfy Eq. (1).

More recently, Sudo (1994) has considered a limiting condition of falling liquid in countercurrent flow. The maximum falling liquid rate can be determined from the condition of $\partial j_L^*/\partial\delta = 0$ for constant j_G^* together with Eq. (1). Sudo proves by using a geometric relationship, $(1 - \sqrt{\alpha}) = 2\delta/D$, that the line derived in such a way becomes identical to the envelope line generated from Eqs. (1) and (2). The point at which the line determined by his method intersects the line of Eq. (3) is considered to give a CHF point in the thermosyphon. In addition, it is pointed out that the usage of $\partial j_L^*/\partial\delta = 0$ can reduce

Contributed by the Heat Transfer Division for publication in the JOURNAL OF HEAT TRANSFER. Manuscript received by the Heat Transfer Division April 1995; revision received December 1995. Keywords: Boiling, Heat Pipes and Thermosyphons, Phase-Change Phenomena. Associate Technical Editor: R. A. Nelson, Jr.

calculation time needed to obtain the envelope line compared with the procedure of getting it from Eqs. (1) and (2).

The present study shows that Katto's criterion is basically identical to Sudo's; a method is proposed to calculate the maximum rate of falling liquid easily in the countercurrent flow in the vertical tube by following their criterion. The maximum value derived thereby provides the critical heat flux in a two-phase thermosyphon. The predicted values are found to be in fairly good agreement with both the existing CHF data and the correlation of Imura et al. (1983). In addition, this criterion will be compared with the Helmholtz-based instability from which a maximum film thickness can be determined under a stable falling liquid.

2 Relationship Between Envelope Line and Maximum Falling Liquid

The momentum equation governing countercurrent flow in the channel can be generally given by a functional form such as Eq. (1). Taking into account a small change in void fraction α of Eq. (1), one can write the following relationship:

$$\frac{\partial F}{\partial j_G^*}\frac{\partial j_G^*}{\partial \alpha} + \frac{\partial F}{\partial j_L^*}\frac{\partial j_L^*}{\partial \alpha} + \frac{\partial F}{\partial \alpha} = 0 \tag{4}$$

Equation (4) shows that if

$$\partial j_G^*/\partial \alpha = \partial j_L^*/\partial \alpha = 0 \tag{5}$$

then Eq. (4) becomes Eq. (2). On the other hand, the fact that liquid film thickness, δ is a function of void fraction, $\alpha(2\delta/D = 1 - \sqrt{\alpha}$ and $\partial\delta/\partial\alpha = 0)$, shows that Eq. (5) is totally identical to the following expression:

$$\partial j_G^*/\partial \delta = \partial j_L^*/\partial \delta = 0 \tag{6}$$

Therefore, the ordinary method in which the envelope line is generated from Eqs. (1) and (2) can be concluded to be identical to one employed by Sudo (1994), which derives the envelope line using Eq. (1) and either Eq. (5) or Eq. (6) in place of Eq. (2). In addition, the envelope line determined thereby is understood to provide a maximum value of both j_L^* and j_G^* with respect to a change in α.

Meanwhile, Katto (1994) draws a $j_L^* - j_G^*$ curve using the condition that for a constant j_L^*, α in Eq. (1) becomes the identical root or does not exist as a real root, with an increase in j_G^*. It is mathematically concluded that his procedure just corresponds to Eq. (2). As the result, Katto's method is equivalent to Sudo's and both methods first draw the envelope line to give the limiting condition for countercurrent annular flow.

3 Application to CHF and Criterion of CHF Occurrence in the Thermosyphon

Equation (3) exists at any cross section in the two-phase thermosyphon. Substituting Eq. (3) into Eqs. (1) and (2), we can get the following equations:

$$F((\rho_G/\rho_L)^{1/2} j_G^*, j_G^*, \alpha) = 0 \tag{7}$$

$$\left(1 + \left(\frac{\rho_G}{\rho_L}\right)^{1/2}\right)\frac{\partial F}{\partial j_G^*}\frac{\partial j_G^*}{\partial \alpha} + \frac{\partial F}{\partial \alpha} = 0 \tag{8}$$

We assume that CHF takes place when mass flow rates for liquid and vapor at the entrance of the thermosyphon reach the maximum values, namely $\partial j_G^*/\partial\alpha = 0$. At the CHF point, Equation (8) becomes

$$\frac{\partial F((\rho_G/\rho_L)^{1/2} j_G^*, j_G^*, \alpha)}{\partial \alpha} = 0 \tag{9}$$

Equation (9) is the same as Eq. (2).

The maximum point of j_G^* and the α value at this point are calculated by simultaneously solving Eqs. (7) and (9). This method basically agrees with Katto's and Sudo's concepts, which require first obtaining the envelope and then looking for the intersection point between the envelope line and Eq. (3). On the other hand, this procedure provides the intersection point directly and also reduces the calculation time with higher accuracy than their techniques.

4 Calculation of CHF Value in Thermosyphon

4.1 Momentum Equations for Liquid and Vapor Flows. Liquid and vapor will be assumed to flow past each other in steady-state countercurrent flow in a pipe as shown in Fig. 1.

For the control volume I (total cross section) in a round pipe, the force balance is:

$$-\frac{dp}{dz}\frac{\pi D^2}{4} + \tau_w \pi D = [\rho_L(1-\alpha) + \rho_G\alpha]g\frac{\pi D^2}{4} \tag{10}$$

For the control volume II (see Fig. 2), which includes only the gas phase, one has:

$$-\frac{dp}{dz}\frac{\pi D^2}{4}\alpha - \tau_i \pi D\sqrt{\alpha} = \rho_G g\alpha\frac{\pi D^2}{4} \tag{11}$$

We can eliminate the pressure drop from Eqs. (10) and (11) and eventually we get:

Nomenclature

Bo = Bond number = $D^2 g(\rho_L - \rho_G)/\sigma$
Bo* = corrected Bond number = $[(D^2 g\rho_L)/\sigma]^{1/2}$
C_1 = constant = $(\rho_G/\rho_L)/(kC_w Bo/C_i^2)$
C_w = friction factor on the wall
C_i = friction factor on the interface
D = diameter of a heated tube
F = function derived by a manipulation from momentum equations
g = gravitational acceleration
H_{fg} = latent heat of evaporation
j_G = superficial velocity of vapor
j_L = superficial velocity of liquid
$j_G^* = j_G\rho_G^{1/2}/[g(\rho_L - \rho_G)D]^{1/2}$
$j_L^* = j_L\rho_L^{1/2}/[g(\rho_L - \rho_G)D]^{1/2}$
k = ratio = $\lambda_H/[4\pi\delta(1 + \rho_G/\rho_L)]$
L = length of the heated tube
q_{co} = critical heat flux for saturated boiling
$\mathrm{Re_L}$ = film Reynolds number = $4\rho_L u_L\delta/\mu_L = 4Lq/(H_{fg}\mu_L)$
$\mathrm{Re_G}$ = Reynolds number of vapor for relative velocities
u_L = liquid velocity = $j_L/(1-\alpha)$
u_G = vapor velocity = j_G/α
z = distance measured from the tube bottom
α = the void fraction of the gas
δ = liquid film thickness
λ = Helmholtz wavelength
μ_L = dynamic viscosity of saturated liquid
μ_G = dynamic viscosity of saturated vapor
ρ_L = density of saturated liquid
ρ_G = density of saturated vapor
σ = surface tension
τ_i = interfacial shear stress = $C_i\rho_G(u_G + u_L)^2/2) = C_i\rho_G j_G^2/(2\alpha^2)[1 + \alpha j_L/[(1-\alpha)j_G]]^2$
τ_w = wall shear stress = $C_w\rho_L u_L^2/2 = C_w\rho_L j_L^2/[2(1-\alpha)^2]$
$\Phi = (4L/D)(q_{co}/\rho_G H_{fg})/\sqrt[4]{\sigma g(\rho_L - \rho_G)/\rho_G^2}$
ϕ = parameter in Fig. 5 = $\dfrac{\alpha D/L}{32.0[1 + \alpha/(1-\alpha)(\rho_G/\rho_L)]}\mathrm{Re_G}$

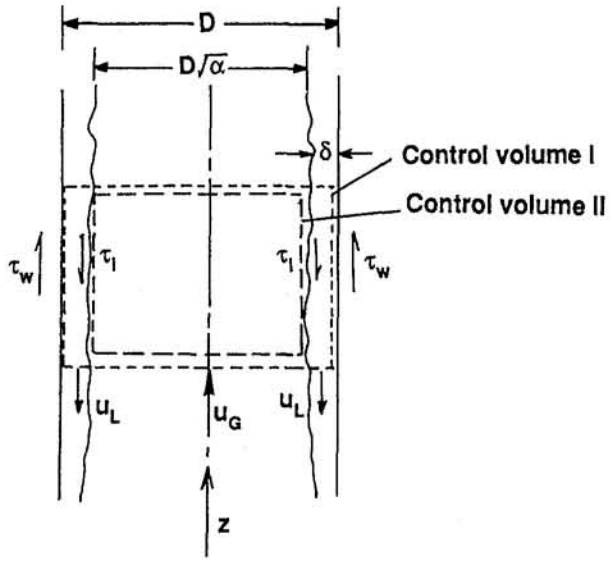

Fig. 1 Momentum balance for countercurrent annular flow

$$\frac{4\tau_w}{D} + \frac{4\tau_i}{D\sqrt{\alpha}} = (\rho_L - \rho_G)g(1-\alpha) \tag{12}$$

where the values of τ_w and τ_i in Eq. (12) can be evaluated by using the friction factors, C_w for the wall and C_i for the interface, which can be provided by the superficial velocities for liquid and vapor. Substituting these relations for τ_w and τ_i in to Eq. (12) and then rearranging it using nondimensional velocities of j_L^* and j_G^*, we can get the final equation as:

$$\frac{2C_i}{\alpha^{5/2}} j_G^{*2}\left(1 + \frac{\alpha}{1-\alpha}\left(\frac{\rho_G}{\rho_L}\right)^{1/2}\frac{j_L^*}{j_G^*}\right)^2 + \frac{2C_w}{(1-\alpha)^2} j_L^{*2} = 1-\alpha \tag{13}$$

Equation (13) is the same as one employed in a separate flow model (Sudo, 1994; Bharathan et al., 1979; Bharathan and Wallis, 1983; Richter, 1981).

Substitution of Eq. (3) into Eq. (13) gives the concrete functional form of Eq. (7) as:

$$F(j_G^*, \alpha) = \frac{2C_i}{\alpha^{5/2}} j_G^{*2}\left(1 + \frac{\alpha}{1-\alpha}\left(\frac{\rho_G}{\rho_L}\right)\right)^2 + \frac{2C_w}{(1-\alpha)^2}\frac{\rho_G}{\rho_L} j_G^{*2} - (1-\alpha) = 0 \tag{14}$$

The maximum value of j_G^* in Eq. (14) can be determined differentiating it as shown in Eq. (9).

In order to calculate the solution from Eqs. (9) and (14), one has to evaluate the friction factors C_i and C_w. These friction factors employed in the present analysis are handled in the following way. The empirical correlation for C_w is categorized into three regions depending on the film Reynolds number; the ones for laminar and turbulent flows are proposed by Wallis (1967), and the other one for transition region from laminar flow to turbulent flow is determined so as to connect the ones for both smooth regions. The equation for the transition region is prepared for this analysis. The other empirical correlation for C_i, similarly, is divided into four different equations depending on the Reynolds number of vapor; the one for laminar flow is proposed by Blangetti and Naushahi (1980), and for turbulent flow by Bharathan et al. (1979), and for the transition between laminar and turbulent flows, two equations to make the other two equations continuous are proposed by Katto and Watanabe (1992).

4.2 Analytical Result of CHF. The solutions of j_G^* and α are quickly calculated from Eqs. (9) and (14); both of these equations are relatively complicated functions of j_G^* and α. The calculation is iterated until convergence errors for j_G^* and α become less than 10^{-4}, except for a few cases where the convergence point appears near the transitional point of C_i and C_w and the convergence error only for j_G^* is relaxed up to 2×10^{-4}.

Figure 2 shows an example of j_G^* and α calculated for water, R22, and R113 from Eq. (14). The meaning of the k value and Eq. (23) in Fig. 2 will be described later. It is found from Fig. 2 that a maximum point of j_G^* exists in Eq. (14), which can be provided as the root of Eqs. (9) and (14). Table 1 gives the maximum value of j_G^* and the value of α and some values at the maximum point in a range in which some experiments have been so far done for CHF in two-phase thermosyphons.

Meanwhile, it may be of importance to briefly describe the physical meaning of $\partial F(j_G^*, \alpha)/\partial\alpha = 0$ and $\partial j_G^*/\partial\alpha = 0$. The first term in Eq. (14) related to the interface shear controls the flow condition at a void fraction beyond the point of $\partial F/\partial\alpha = 0$. Conversely below the point of $\partial F/\partial\alpha = 0$, the second term controls. As the result, the optimum balance between the wall and the interface shear forces on the curve of $F(j_G^*, \alpha) = 0$, can be considered to be reached at the maximum point of j_G^* from a possible combination of j_G^* and α. In other words, $\partial F(j_G^*, \alpha)/\partial\alpha = 0$ provides the optimum condition with respect to the void fraction.

Finally, the critical heat flux can be calculated from the maximum liquid flow rate through a simple energy balance, i.e., the heat input to the thermosyphon is consumed by the evaporation of liquid. The energy balance gives

$$\pi DLq = \frac{\pi}{4}(D^2 j_G)\rho_G H_{fg} \tag{15}$$

As the result, the CHF can be calculated through the maximum value of j_G^* as

$$q_{co} = \frac{D}{4L} H_{fg}\sqrt{\rho_G[g(\rho_L - \rho_G)D]}\, j_{G,\max}^* \tag{16}$$

In Fig. 3, the nondimensional parameter of CHF, Φ, which is widely used, is plotted against the density ratio ρ_L/ρ_G. For comparison, Fig. 3 includes the existing CHF data collected for a two-phase closed thermosyphon by Imura et al. (1983) and

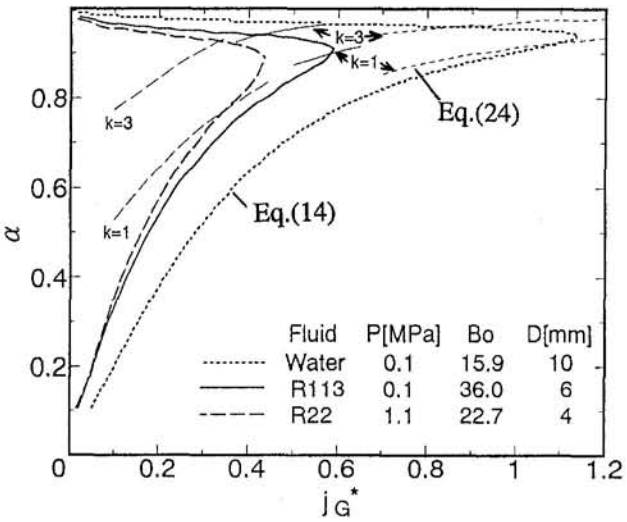

Fig. 2 α versus j_G^* curve

Table 1 Analytical range and related values

	D mm	P MPa	α	$j_{G,max}$*	C_i	C_w	Re_G	ϕ	Bo	k value	C_l	Constant Eq. (25)
Water	5	0.1	0.904 – 0.912	1.54 – 1.67	0.00596 – 0.00988	0.104 – 0.112	3670 – 3890	2.18 – 2.36	3.98	5.73 – 5.89	40.9 – 16.6	0.69 – 0.676
	7		0.921 – 0.925	1.30 – 1.38	0.00918 – 0.0124	0.0764 – 0.0809	5020 – 5240	2.17 – 2.30	7.80	5.17 – 5.27	22.5 – 13.3	0.685 – 0.675
	9		0.931 – 0.903	1.16 – 1.20	0.0120 – 0.0144	0.0612 – 0.0633	6380 – 6610	2.19 – 2.28	12.9	4.77 – 4.83	16.0 – 11.7	0.682 – 0.676
	11		0.938 – 0.939	1.06 – 1.08	0.0147 – 0.0162	0.0515 – 0.0524	7850 – 8000	2.22 – 2.27	19.3	4.47 – 4.50	12.6 – 10.7	0.679 – 0.676
R113	5	0.1	0.895 – 0.896	0.633 – 0.637	0.0563 – 0.0578	0.107	8040 – 8090	1.42	25.0	2.81 – 2.82	11.5 – 11.1	0.712 – 0.711
		0.3	0.890	0.502	0.087	0.0576	9860	1.19	31.7	2.48	8.77	0.719
		0.5	0.886	0.432	0.112	0.0452	11000	1.07	37.5	2.21	8.74	0.731
	7	0.1	0.910	0.562	0.0706	0.0736	11700	1.49	49.1	2.04	8.48	0.736
		0.3	0.902	0.467	0.0970	0.0400	15200	1.31	62.2	2.41	8.66	0.784
		0.5	0.897	0.409	0.119	0.0317	17400	1.20	73.5	2.09	8.18	0.797
	9	0.1	0.918	0.539	0.0739	0.0543	16300	1.62	81.1	1.88	8.21	0.803
		0.3	0.910	0.441	0.104	0.0312	21000	1.40	103	1.71	8.76	0.810
		0.5	0.904	0.390	0.125	0.0251	24300	1.29	122	2.21	7.64	0.811
	11	0.1	0.924	0.511	0.0792	0.0440	20900	1.70	121	1.90	7.99	0.825
		0.3	0.915	0.429	0.107	0.0256	27700	1.51	154	1.71	8.46	0.831
		0.5	0.909	0.374	0.131	0.0211	31700	1.37	182	1.56	8.86	0.834
R22	5	1.1	0.889	0.403	0.108	0.0291	11800	0.983	35.5	2.24	7.79	0.875
		1.7	0.879	0.336	0.137	0.0253	12500	0.876	46.3	1.89	7.43	0.889
		2.4	0.868	0.275	0.177	0.0234	12700	0.778	63.8	1.63	7.91	0.905
		3.1	0.852	0.224	0.236	0.0230	12000	0.693	91.8	1.43	7.86	0.922
	7	1.1	0.896	0.375	0.123	0.0216	18500	1.08	69.7	2.01	8.41	0.897
		1.7	0.885	0.307	0.163	0.0193	19200	0.947	90.8	1.71	7.52	0.907
		2.4	0.871	0.246	0.225	0.0183	19000	0.822	125	1.48	8.13	0.921
		3.1	0.853	0.197	0.317	0.0182	17500	0.721	180	1.30	7.79	0.935
	9	1.1	0.902	0.358	0.129	0.0176	26000	1.17	115	1.78	9.07	0.911
		1.7	0.892	0.291	0.171	0.0160	26900	1.02	150	1.53	7.38	0.916
		2.4	0.878	0.229	0.241	0.0154	26400	0.869	207	1.33	7.76	0.926
		3.1	0.861	0.178	0.359	0.0155	23600	0.739	298	1.17	7.02	0.938
	11	1.1	0.905	0.343	0.137	0.0152	33900	1.24	172	1.55	9.51	0.917
		1.7	0.895	0.276	0.187	0.0140	34700	1.07	224	1.34	7.03	0.919
		2.4	0.880	0.215	0.274	0.0136	33500	0.900	309	1.17	6.79	0.924
		3.1	0.860	0.164	0.427	0.0138	29400	0.754	444	1.04	5.65	0.933

The maximum points are calculated for seven different values of L/D= 5, 10, 30, 50, 100, 300, 500.
The change of values in each column is subject to the change in L/D.

their correlation (Eq. (17)) and the Tien and Chung (1979) correlation (Eq. (18)):

$$\Phi = 0.64\,(\rho_G/\rho_L)^{0.13} \tag{17}$$

$$\Phi = 3.2/\{1 + (\rho_G/\rho_L)^{1/4}\}^2 \tag{18}$$

Tien and Chung (1979) noticed that Eq. (18) with the constant value of 3.2, which is derived by putting $j_L = 0$ into the equation on the basis of the Kutateladze Stability Criterion (Pushkina and Sorokin, 1969), is in good agreement with the CHF data for $Bo^{1/2} > 30$ in a two-phase closed thermosyphon but is not applicable for the CHF data for $Bo^{1/2} < 10$. Therefore, they revised the constant 3.2 to connect the CHF to large Bo as well as small Bo, yielding Eq. (18).

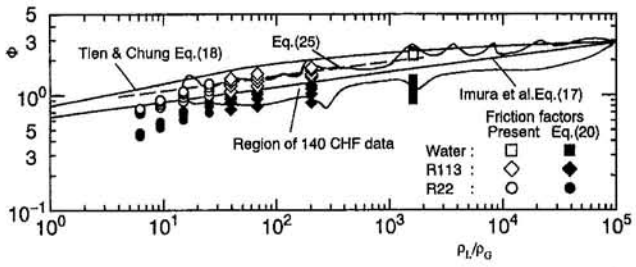

Fig. 3 Comparison of analytical and existing results

$$\Phi = \frac{3.2 \tanh (0.5\,Bo^{1/4})}{\{1 + (\rho_G/\rho_L)^{1/4}\}^2} \tag{19}$$

Tanh $(0.5\,Bo^{1/4})$ can be approximated within an error of ±10 percent by $0.474\,Bo^{1/8}$ for $1 < Bo < 500$.

Equation (19) in Fig. 3 used other friction factors employed by Sudo (1994), which will be described later. CHF data collected so far have been obtained for the range of Bond number, Bo = 10 to 500. Smirnov (1984) separately proposed Eq. (17) except that the constant is slightly changed from 0.64 to 0.65 and also the exponent from 0.13 to 0.1. The broken line in Fig. 3 is Eq. (24), which will be discussed in section 5.2.

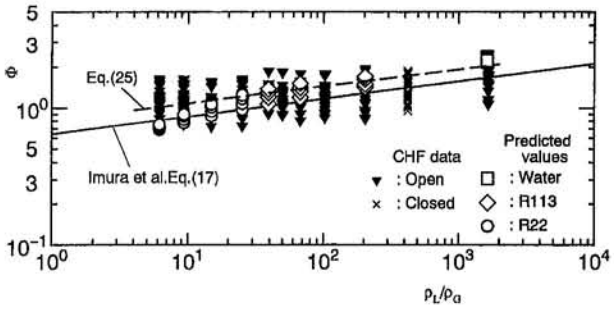

Fig. 4 Comparison of analytical values and CHF data

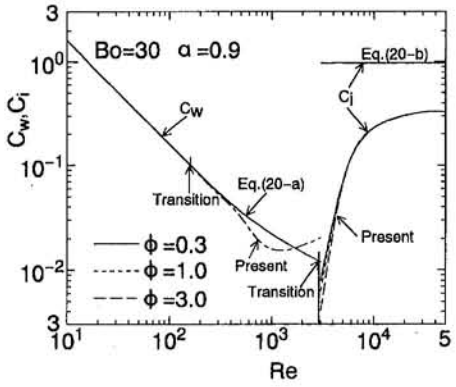

Fig. 5 Comparison of present and Sudo's friction factors

Figure 3 shows that the CHF values predicted from Eqs. (9) and (14) are in fairly good agreement with the existing CHF data as well as Eq. (17). In addition, the analytical result shows that the CHF tends to be proportional to $Bo^{1/8}$, which is similar to the dependence predicted by Eq. (19), while Imura et al. (1983) reported little effect of the Bond number on the CHF. A variation of this effect on CHF is only 1.63 ($=50^{1/8}$) times when Bond number changes from 10 to 500. Therefore, it may be difficult to distinguish this effect from uncertainties explicitly.

Figure 4 shows the CHF data measured for open and closed thermosyphons by Monde et al. (1992) and Monde (1995) plotted against the density ratio to compare them with the analytical result. Table 2 lists the statistical deviations when the analytical values are compared with Eq. (17) and CHF data.

Figure 4 and Table 2 show that the predicted values are in fairly good agreement with the CHF data.

4.3 Effect of Friction Factors on CHF. The friction factors of C_w and C_i needed to calculate j_G^* from Eqs. (9) and (14) influence the value of CHF. Therefore, their effects on CHF are compared by employing different expressions Eq. (20) for them, in accordance with the results of Sudo (1994).

For the liquid flow,

$$C_w = 16.0/\mathrm{Re_L} \quad (\mathrm{Re_L} \le 2000)$$
$$= 1.76 \times 10^{-10}\,\mathrm{Re_L^{2.32}} \quad (2000 \le \mathrm{Re_L} \le 4000)$$
$$= 0.314\,\mathrm{Re_L^{-1/4}} \quad (4000 \le \mathrm{Re_L}) \qquad (20a)$$

For the vapor flow,

$$C_i = 0.008 + m(2/D)^n$$
$$m = 0.3304\,(\mathrm{Bo}^*/2)^n \mathrm{Bo}^{*0.25}\,10^{9.07/\mathrm{Bo}^*}$$
$$n = 1.63 + 4.74/\mathrm{Bo}^* \qquad (20b)$$

For reference, Fig. 5 shows the difference among the employed factors in the range of the Reynolds number for liquid film and vapor where the solutions of Eqs. (9) and (14) exist.

The comparison of both results has already been shown in Fig. 4. Table 2 shows a comparison of the difference brought about by the different factors with Eq. (17). The comparison of the predicted CHF values and Eq. (17) as well as the existing CHF data (see Figs. 4 and 5) shows that the friction factors employed in the present analysis provide better results than those from Eq. (20). The reason is that Eq. (20) gives larger values of C_i than Eq. (15), that is the larger values of C_i increase the limitation of the falling liquid flow rate. However, the present procedure strongly supports the criterion that the occurrence of the CHF is restricted by the maximum rate of falling liquid, although the analytical values are influenced by the friction factors.

Table 2 Comparison of CHF measured and predicted

		Comparison of Eq.(17)			Comparison of Experimental data	
		Friction factors Present	Eq.(20)		Present Analysis	Eq.(17)
E_1		0.102	0.086		-0.018	0.094
E_2	Total	0.143	0.359	Total	0.231	0.199
E_3	(224)	0.165	0.543	(214)	0.281	0.241
E_1		0.260	-0.494		-0.040	0.239
E_2	Water	0.260	0.494	Water	0.145	0.239
E_3	(28)	0.261	0.546	(8)	0.176	0.275
E_1		0.169	-0.207		-0.177	0.092
E_2	R113	0.169	0.207	R113	0.230	0.168
E_3	(84)	0.183	0.253	(105)	0.283	0.211
E_1		0.013	0.440		0.149	0.102
E_2	R22	0.094	0.440	R22	0.237	0.233
E_3	(112)	0.110	0.467	(101)	0.279	0.268

The number of the parentheses is one of the referred data

Average error :$E_1 = \Sigma\,(1 - q_{cal}/q_{exp})/N$
Mean deviation :$E_2 = \Sigma\,|1 - q_{cal}/q_{exp}|/N$
Standard deviation :$E_3 = \sqrt{\Sigma\,(1 - q_{cal}/q_{exp})^2/N}$

5 Relationship Between Instability and Maximum Falling Liquid Concepts

Monde et al. (1993) previously analyzed the CHF in two-phase thermosyphons from the viewpoint that the critical heat flux takes place when the interface of the annular flow becomes unstable. The stable condition about a wavelength on the interface is specified from the Helmholtz instability as follows:

$$\lambda/[2\pi(1 + \rho_G/\rho_L)] \le \sigma/\rho_G(u_G + u_L)^2 \qquad (21)$$

In addition, an assumption was introduced that the wavelength is proportional to the film thickness because three unknowns, j_G, α (or δ), and λ, occur in Eqs. (14) and (21) so that one more independent equation was needed.

$$\lambda = k[4\pi\delta(1 + \rho_G/\rho_L)] \qquad (22)$$

Although the wavelength seems to be independent of the liquid film thickness, several researches (Anshus, 1972; Pierson and Whitaker, 1977; Imura et al., 1976; Richter, 1981; Moissis, 1963; Tippets, 1964) in work related to falling liquid film and flooding problems have discussed a relationship between the wavelength and the liquid film thickness.

5.1 Relationship Between the Wavelength and Liquid Film Thickness. The relationship between the wavelength and liquid film thickness has been studied experimentally and

theoretically when the liquid film falls down along a vertical plate and pipe. According to Anshus (1972) and Pierson and Whitaker (1977), the value of k in Eq. (22) is a function of two parameters, $\sigma(2\rho_L/(\mu_L^4 g))^{1/3}$ and the Reynolds number. The k value, for example, can be derived by reforming the equation proposed by Anshus (1972) using the film Reynolds number as follows:

$$k = 0.867(1 + \rho_G/\rho_L)^{-1}[\sigma(2\rho_L/(\mu_L^4 g))^{1/3}]^{4/11}\ \mathrm{Re}_L^{-1/3} \quad (23)$$

This correlation is found to be in good agreement with the relationship numerically predicted by Pierson and Whitaker (1977). The k values in Table 1 are calculated by using the values at the maximum point.

On the other hand, several studies about the flooding phenomenon in a countercurrent annular flow assume that the film thickness is proportional to the wavelength as indicated in Eq. (22). Richter (1981), for example, gave $k = 1$ as the limiting condition for the liquid film to be kept stable. The experiments of flooding in an air–water system (Imura et al., 1976; Moissis, 1963; Tippets 1964) show $k = 1 - 3$ ($\lambda/\delta = 10 - 40$) where the interface became unstable, although the value changes depending on the pipe diameter and the physical properties involved. It should be pointed out that in the experiment with the air–water system, mass flow rates of air and water are independently controlled so that the unstable situation happened at a relatively high velocity compared with that in the thermosyphon in which the vapor and liquid velocities are determined as a function of the heat input from the heat balance equation. In addition, the thickness of the liquid steadily decreases due to evaporation along the vertical wall. Taking such a difference into account, we guess that the k value becomes larger in the thermosyphon than that in the flooding experiment, since the relative velocity between the vapor and the liquid in the thermosyphon becomes rather small and thus a long wavelength can exist stably.

Eliminating λ from Eqs. (21) and (22) and normalizing it, we can get a final form for j_G^* and α as:

$$k\ \mathrm{Bo}\ j_G \le \frac{\alpha^2}{(1-\sqrt{\alpha})\left(1 + \dfrac{\alpha}{1-\alpha}\left(\dfrac{\rho_G}{\rho_L}\right)^2\right)} \quad (24)$$

Equation (24) specifies the regime of j_G^* and α where the vapor–liquid interface remains stable. Figure 2 shows the stable condition for different values of k and j_G^* and α curves derived from Eq. (14) on the $j_G^*-\alpha$ diagram. It is found from Fig. 2 that for the case of $k = 3$, the cross point appears before the maximum point is reached, while for $k = 1$, the cross point exceeds the maximum point. In other words, the unstable situation takes place before the maximum point is reached for $k = 1$, and beyond the maximum point for $k = 3$. This fact implies that if the k value could be measured in an experiment, the crossing point calculated from Eqs. (14) and (24) with Eq. (23) probably coincides with the maximum point.

5.2 CHF Due to Instability. Monde et al. (1993) derived the following expression predicting the CHF from Eqs. (14) and (24) for the case of δ/D ($=(1-\sqrt{\alpha})/2$) $\ll 1$, $u_L \ll u_G$, and $C_1 = (\rho_G/\rho_L)(kC_w\ \mathrm{Bo}/C_f^2) \gg 1$.

$$\Phi = [4/(C_w k^3\ \mathrm{Bo})]^{1/8}(\rho_L/\rho_G)^{1/8} \quad (25)$$

This expression is similar in functional form to Eq. (17) except for the constant including the Bond number, the k value, and the wall friction factor. The assumptions used to derive Eq. (25) are found to be reasonably satisfied from the values of the 4th and 12th columns in Table 1. Furthermore, the last column shows that the constant in Eq. (25) for the k value at the maximum point is in astonishingly good agreement with that in Eq. (17). Figures 4 and 5 show that the CHF value predicted by Eq. (25) is in better agreement with the existing CHF data than those calculated from Eqs. (9) and (14).

However, when two different methods to predict the CHF theoretically are compared, the way that the CHF takes place when the instability of wave is initiated has a weak point in determining the value of the unknown parameter, k, while the another way using Eqs. (9) and (14) has no ambiguity in calculating the maximum rate of falling liquid.

6 Conclusions

An analytical study has been made of critical heat flux of a two-phase thermosyphon, in which a liquid film and a vapor flow in a manner of countercurrent annular flow, leading to the following conclusions:

1. The procedures proposed from different points of view by Katto and Sudo are shown to be equivalent, by which the envelope line is first obtained to give the maximum falling liquid rate fed into the thermosyphon.
2. A method to obtain the maximum falling liquid rate directly from Eqs. (9) and (14) is developed.
3. The analytical value of CHF in the thermosyphon calculated from the maximum liquid rate is in fairly good agreement with the existing CHF data.

References

Anshus, B. E., 1972, "On the Asymptotic Solution to the Falling Film Stability Problem," *Ind. Eng. Chem. Fund.*, Vol. 11, pp. 502–508.

Bankoff, S. G., and Lee, S. C., 1986, "A Critical Review of the Flooding Literature," in: *Multi-phase Science and Technology*, G. F. Hewitt et al., eds., Vol. 2, Hemisphere, Washington, DC, pp. 95–180.

Bharathan, D., Wallis, G. B., and Richter, H. J., 1979, "Air-Water Countercurrent Annular Flow," EPRI Report NP-1165.

Bharathan, D., and Wallis, G. B., 1983, "Air-Water Countercurrent Annular Flow," *Int. J. Multiphase Flow*, Vol. 9, pp. 349–366.

Blangetti, F., and Naushahi, M., 1980, "Influence of Mass Transfer on the Momentum Transfer in Condensation and Evaporation Phenomena," *Int. J. Heat Mass Transfer*, Vol. 23, pp. 1694–1695.

Dobran, F., 1981, "Condensation Heat Transfer and Flooding in a Countercurrent Subcooled Liquid and Saturated Vapor Flow," *Thermal Hydraulics in Nuclear Research Technology Symposium*, K. H. Sun, S. C. Yao, P. Marinkovich, and V. K. Dhir, eds., ASME, HTD-Vol. 15.

Imura, H., Kusuda, H., and Funatsu, S., 1977, "Flooding Velocity in a Countercurrent Annular Two-Phase Flow," *Chemical Engineering Science*, Vol. 32, pp. 79–87.

Imura, H., Sasaguchi, K., Kozai, H., and Numata, S., 1983, "Critical Heat Flux in a Closed Two-Phase Thermosyphon," *Int. J. Heat Mass Transfer*, Vol. 26, pp. 1181–1188.

Katto, Y., and Watanabe, 1992, "An Analytical Study on Critical Heat Flux of Counterflow Boiling With a Closed Bottom," *Int. J. Heat Mass Transfer*, Vol. 35, pp. 3021–3028.

Katto, Y., 1994, "Limit Conditions of Steady-State Countercurrent Annular Flow and the Onset of Flooding, With Reference to the CHF of Boiling in a Bottom-Closed Vertical Tube," *Int. J. Multiphase Flow*, Vol. 20, No. 1, pp. 45–61.

Kusuda, H., and Imura., 1974, "Stability of Liquid Film in a Counter-current Annular Two-Phase Annular [in Japanese]," *Trans. JSME*, Vol. 40, pp. 1082–1088.

Lee, S. C., and Bankoff, S. G., 1983, "Stability of Steam–Water Countercurrent Flow in an Inclined Channel: Flooding," ASME JOURNAL OF HEAT TRANSFER, Vol. 105, pp. 713–718.

Moissis, R., 1963, "The Transition From Slug to Homogeneous Two-Phase Flows," ASME JOURNAL OF HEAT TRANSFER, Vol. 85, pp. 366–370.

Monde, M., Mihara, S., and Hashiguti, M., 1992, "Critical Heat Flux in an Open Two-Phase Thermosyphon," *Proc. 2nd JSME–KSME Thermal Engineering Conference*, Vol. 1, pp. 149–154.

Monde, M., Mihara, S., and Inoue, T., 1993, "An Analytical Study of Critical Heat Flux of a Two-Phase Thermosyphon [in Japanese]," *Trans. JSME*, Vol. 59, pp. 1258–1264.

Monde, M., 1995, Unpublished Data.

Pierson, F. W., and Whitaker, S., 1977, "Some Theoretical and Experimental Observations of the Wave Structure of Falling Liquid Films," *Ind. Eng. Chem. Fund.*, Vol. 16, pp. 401–408.

Pushkina, O. I., and Sorokin, Yu. L., 1969, "Breakdown of Liquid Film Motion in Vertical Tubes," *Heat Transfer—Soviet Research*, Vol. 1-5, pp. 56–64.

Richter, H., 1981, "Flooding in Tubes and Annuli," *Int. J. Multiphase Flow*, Vol. 7, pp. 647–658.

Smirnov, Ye. L., 1984, "Critical Heat Flux in Flooding in Vertical Channels," *Heat Transfer—Soviet Research*, Vol. 16-3, pp. 19–23.

Sudo, Y., 1994, "Analytical Study of Critical Heat Flux Under Countercurrent Flow Limitation in Vertical Channels [in Japanese]," *Trans. JSME,* Vol. 60, pp. 4222–4228.

Taitel, Y., Barnea, D., and Dukler, A. E., 1982, "A Fil Model for Prediction of Flooding and Flow Reversal for Gas-Liquid Flow in Vertical Tubes," *Int. J. Multiphase Flow,* Vol. 8, pp. 1–22.

Tien, C. L., 1977, "A Simple Analytical Model for Counter-current Flow Limiting Phenomena With Vapor Condensation," *Lett. Heat Mass Transfer,* Vol. 4, pp. 231–237.

Tien, C. L., and Chung, K. S., 1979, "Entrainment Limits in Heat Pipes," *AIAA J.,* Vol. 17, pp. 643–646.

Tien, C. L., Chung, K. S., and Liu, C. P., 1980, "Flooding in Two-Phase Countercurrent Flows," *Physicochem. Hydrodyn.,* Vol. 1, pp. 195–207.

Tippets, F. E., 1964, "Analysis of the Critical Heat-Flux Condition in High-Pressure Boiling Water Flows," ASME JOURNAL OF HEAT TRANSFER, Vol. 86, pp. 23–38.

Wallis, G. B., 1967, *One-Dimensional Two-Phase Flow,* McGraw-Hill, New York.

Determination of the Boiling Enhancement Mechanism Caused by Surfactant Addition to Water

C. N. Ammerman
Graduate Student.
Student Mem. ASME

S. M. You
Assistant Professor.
Mem. ASME

Department of Mechanical and Aerospace Engineering,
The University of Texas at Arlington,
Arlington, TX 76019

In the present investigation, boiling heat transfer coefficients are measured for an electrically heated 390-μm-dia, platinum wire immersed in saturated water, and in water mixed with three different concentrations of sodium dodecyl sulfate (an anionic surfactant). The addition of a surfactant to water is known to enhance boiling heat transfer. A recently developed photographic/laser-Doppler anemometry measurement technique is used to quantify the vapor volumetric flow rate departing from the wire during the boiling process. The volumetric flow rate data are used to calculate the latent heat and, indirectly, the convection heat transfer mechanisms that constitute the nucleate boiling heat flux. Comparisons are made to determine how the heat transfer mechanisms are affected by the surfactant addition, and thus, which mechanism promotes boiling enhancement. The present data are also compared with similar data taken for a 75-μm-dia wire immersed in saturated FC-72 (a highly wetting liquid) to provide increased insight into the nature of the boiling heat transfer mechanisms.

Introduction

In nucleate boiling, two different modes of heat dissipation are responsible for the total heat removal: latent heat and convection:

$$q_{\text{Tot}} = q_{LH} + q_{\text{CONV}} \quad (1)$$

Latent heat removal takes place when liquid vaporizes and leaves the surface. Convection, depending on the boiling regime and bulk fluid conditions, can be divided into microconvection, Marangoni flow, and natural convection. Microconvection heat transfer results from sensible energy being removed by entrainment of the superheated liquid in the departing bubble's wake. Marangoni flow is induced by the surface tension gradient that exists at the bubble's liquid/vapor interface while it is still attached to the heated surface. Natural convection occurs when sensible energy is removed from nonnucleating portions of the heated surface due to currents established by density gradients. Marangoni flow is usually only significant with subcooled or gas-saturated bulk fluids. Natural convection is important in the partially developed nucleate boiling regime (surface partially covered with active nucleation sites). Further understanding of these mechanisms is needed to enable the development of more accurate pool boiling heat transfer prediction models.

Previous investigators (McFadden and Grassmann, 1962; Rallis and Jawurek, 1964; Paul and Abdel-Khalik, 1983) have employed various photographic techniques to determine key boiling parameters such as bubble departure diameter, departure frequency, and nucleation site density. Several investigators have presented experimental results of these key boiling parameters and most have used them to calculate contributions to total heat flux from a heated surface. Despite their merits, however, the methods used by these investigators require the analysis of a large number of individual photographic frames at each heat flux.

Contributed by the Heat Transfer Division and presented at the ASME International Mechanical Engineering Congress and Exposition, San Francisco, California, November 12–17, 1995. Manuscript received by the Heat Transfer Division August 1995; revision received January 1996. Keywords: Boiling, Flow Visualization, Measurement Techniques. Associate Technical Editor: R. A. Nelson.

The present investigators recently developed a single-photo measurement technique (Ammerman et al., 1996) to enable rapid quantification of pool boiling heat transfer mechanisms. This measurement technique combines a single video image with laser-Doppler anemometry (LDA) bubble velocity data to determine the volumetric flow rate of vapor above a heated surface. The advantage of this over previous methods is that it requires the analysis, in many cases, of only a few photographs per heat flux. In addition, this technique evaluates bubbles departing from multiple cavities, instead of focusing on an isolated nucleation site.

Boiling Enhancement With Surfactants. The addition of surfactants to water has been known to reduce the surface tension and enhance the rate of boiling heat transfer. A reduction in interfacial tension decreases the pressure required within a vapor bubble, as indicated by the Young–Laplace equation (Carey, 1992). This decrease in vapor pressure translates into a corresponding decrease in heater surface temperature, resulting in boiling enhancement.

Frost and Kippenhan (1967) investigated forced convection boiling of subcooled water with varying concentrations of a surfactant ("Ultra Wet 60L") in an annular test section. They observed that addition of the surfactant enhanced the rate of heat transfer. They measured bubble growth and collapse rates with the aid of high-speed photography (7500 frames per second) to estimate the latent heat contribution to the total heat transfer. Their results showed that the latent heat component increased from approximately 50 to 80 percent of the total heat flux as the surface tension was reduced by 50 percent.

Tzan and Yang (1990) performed a detailed investigation of saturated nucleate boiling from an electrically heated, 3.35-mm-OD stainless steel tube immersed in saturated water with varying concentrations of an anionic surfactant (sodium dodecyl sulfate). Because the concentrations were low, addition of the surfactant to water caused no significant change in physical properties, except for the surface tension, which was greatly reduced. Their results showed dramatic increases in nucleate boiling heat transfer versus surface tension reduction.

Table 1 Property comparison between water and FC-72

Sat. Liquid Property (1 atm)	Water	FC-72	Ratio
Surface Tension (N/m)	0.0589	0.0083	7.07
Heat of Vaporization (kJ/kg)	2257	95.1	23.7
Thermal Conductivity (W/m°K)	0.680	0.054	12.6
Specific Heat (kJ/kg°C)	4.217	1.089	3.87
Thermal Diffusivity (m^2/s)	1.68×10^{-7}	3.10×10^{-8}	5.43
Prandtl Number	1.76	9.69	0.18
Liquid Density (kg/m^3)	958	1602	0.60
Vapor Density (kg/m^3)	0.596	13.07	0.045
Dynamic Viscosity (Ns/m^2)	2.79×10^{-4}	4.80×10^{-4}	0.58

Present Investigation. In the present investigation, the single-photo method is used to determine the boiling heat transfer mechanisms from a 390-μm-dia, platinum wire immersed in saturated water, and in saturated water with two different mass concentrations (500 and 1000 ppm) of sodium dodecyl sulfate (SDS). Comparisons are made to determine which heat transfer mechanisms are affected by the surfactant addition, and thus, which mechanisms promote boiling enhancement. The water data are also compared with data generated for a 2-cm-long, 75-μm-dia platinum wire immersed in saturated FC-72 (Ammerman et al., 1996). FC-72 is a highly wetting dielectric liquid with applications in immersion cooling of electronic equipment. Property data for both water and FC-72 are shown in Table 1, along with the water-to-FC-72 property ratio. Although the thermal transport properties of water are superior, FC-72 has very low surface tension. Therefore, because of their dissimilar properties, comparisons between water and FC-72 provide increased insight into the nature of boiling heat transfer mechanisms.

Experimental Apparatus and Procedure

The experimental setup for this study is shown in Fig. 1. The test section consisted of a 390-μm-dia wire heater, mounted between two copper terminals spaced 4 cm apart. The terminals were made from 3-cm sections of 6 gage (AWG) copper wire and were vertically oriented. The heater wire was soldered to the top end of each terminal. The heater was immersed in saturated water (at 1 atm), which was maintained at constant temperature with an isothermal oil bath. Voltage sensors and a power supply were connected to the heater via the copper terminals. The direct-current power supply was connected to the heater with two leads in parallel to divide the current. Each path contained a standard resistor, which was used to determine the current delivered to the wire heater. The standard resistors had resistances of 0.01 and 0.05 Ω, respectively, each with an accuracy of ± 0.75 percent. This equipment was interfaced via IEEE-488 cables and controlled by a 386 PC. Liquid temperatures were measured using copper-constantan thermocouples, which were calibrated with a precision thermometer. Since platinum has a repeatable temperature-versus-resistance relationship, the wire itself was used to measure heater temperature. The wire was calibrated prior to testing using a precision thermometer. The calibration was checked after the final test to ensure that the wire had not been damaged during testing.

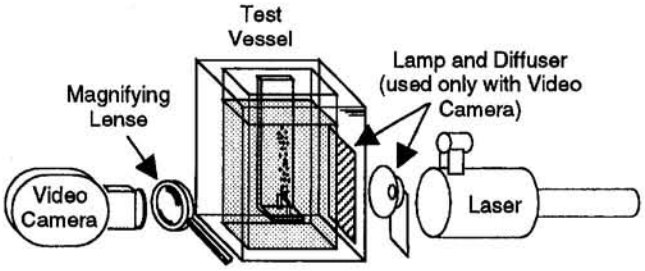

Fig. 1 Experimental setup

Video imaging equipment was used to capture single-frame images of vapor bubbles above the boiling wire. The camera's aperture was set to obtain a depth of field that ensured bubbles leaving the wire were in focus. The video image was magnified using a 30-cm-focal-length lens. High-intensity lamps filtered through a diffuser were used for background lighting. Video images of the 0 ppm data were synchronized and transferred to a 386 PC where they were digitized and analyzed by image-processing software. This software enabled rapid determination of vapor characteristics above the boiling wire including the number and sizes of bubbles. Video images for the SDS solutions were analyzed without the aid of the computer due to difficulties in image processing.

In addition to video photography, LDA measurement techniques were used to ascertain the bubble velocity as a function of height above the boiling wire. These LDA measurement techniques were previously applied by O'Connor et al. (1993) for the measurement of bubble velocity. The LDA equipment included a Dantec helium–neon (He–Ne) gas laser, 55X modular transmitting and receiving optics, a Bragg Cell (55X29) for beam frequency shift, and a flow-velocity-analyzer software/hardware package (FVA-58N20), which provided one-dimensional velocity measurements.

The constant-temperature bath was turned on and the test liquid was heated to saturation temperature. The test liquid was allowed to remain at saturation conditions for approximately 1 hour to attain steady-state conditions. Once steady state was achieved, the test was initiated. Video data were acquired first, followed by the acquisition of the LDA velocity data. Upon completion of each case, SDS was added to the test vessel to bring the concentration level up to that required for the next case. This was repeated until all cases had been run. Additional details on the experimental procedure can be obtained from Ammerman et al. (1996).

Experimental Results

Heat transfer coefficients for each of the solutions tested are shown in Fig. 2 versus heat flux. As was expected, the addition of the surfactant enhanced the boiling heat transfer from the

Nomenclature

D = diameter, mm
h_{fg} = latent heat of vaporization, kJ/kg
LDA = laser-Doppler anemometry
MA = measurement area
ppm = mass concentration in parts per million
q = heat flux, W/cm^2
V = volume, mm^3
$\dot{V}$ = volumetric flow rate, mm^3/s
x = width of measurement area, mm
y = vertical span of measurement area, mm
ρ = density, kg/m^3

Subscripts

b = property of bubble
CONV = convection component
g = property of vapor
i = property of ith bubble
LH = latent heat component

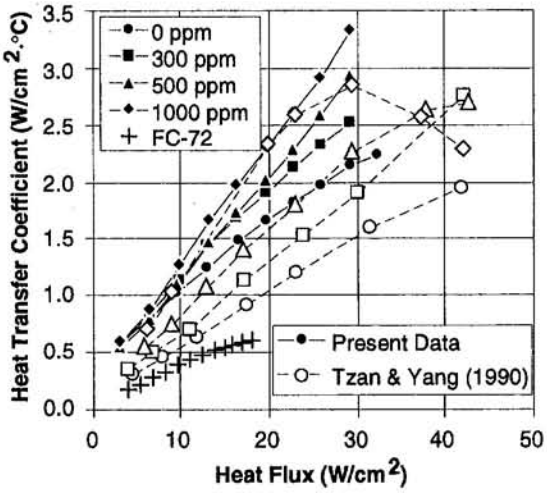

Fig. 2 Heat transfer coefficient

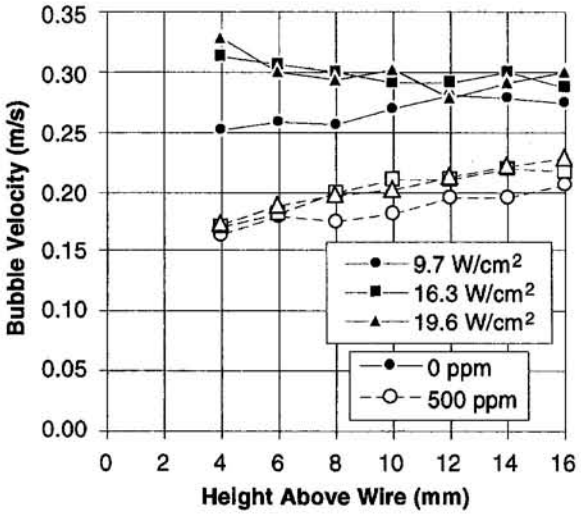

Fig. 4 Velocity versus height above wire

wire. Also included with the present data in Fig. 2 are the water/surfactant data of Tzan and Yang (1990), and the FC-72 data of Ammerman et al. (1996). The present test conditions were the same as those of Tzan and Yang except for the material and diameter of the heated cylinder. Tzan and Yang's stainless steel cylinder diameter was 8.6 times larger than the diameter of the present test section. The present 0 ppm results show a significant enhancement over Tzan and Yang's 0 ppm data. This enhancement is noticeable for the 300 and 500 ppm data as well; however, it tends to disappear at 1000 ppm. The heat transfer coefficients for the FC-72 data are much lower than those for water, emphasizing water's excellent thermal transport characteristics.

Samples of the photographic data analyzed for this study are shown in Fig. 3 at a heat flux of 16.3 W/cm^2. Video data were analyzed at 9.7, 16.3, and 19.6 W/cm^2. By inspection, the wire was determined to be in the fully developed nucleate boiling regime for all cases, with the possible exception of the 9.7 W/cm^2 data point for the 0 ppm case. The approximate magnification of the 0 ppm images was 5 times, and of all SDS-solution images was 10 times. (Figure 3(a) has been enlarged 2× to facilitate visual comparison with SDS-solution images.) For pure water, the average bubble size was observed to increase with increasing heat flux. This increase in size was also observed for the FC-72 data. However, for the SDS solutions, bubble size decreased with increasing heat flux. This size-versus-heat-flux behavior was also observed by Tzan and Yang (1990).

Bubble velocity measurements were recorded during testing using the LDA system. Since bubble velocity varies as a function of height above the wire, measurements were taken at several heights for each heat flux. A plot of bubble velocity versus height above the wire is shown in Fig. 4 for varying heat flux for both the 0 and 500 ppm cases. The 1000 ppm velocity data are not shown but are similar to those of the 500 ppm data.

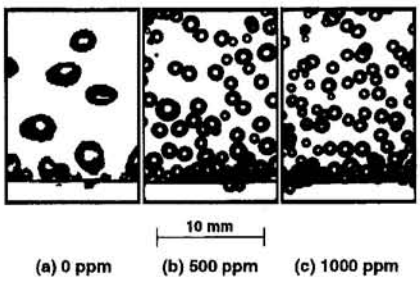

Fig. 3 Video data at 16.3 W/cm^2

Velocities for the SDS-solution cases were lower than for the 0 ppm case due to smaller bubble sizes. It is interesting to note that for pure water at the higher heat fluxes, the bubble velocity tended to decrease with increasing height. This may be due to meandering of bubbles where vertical velocity is traded for lateral velocity. Meandering would be less likely to occur within the SDS solutions due to the larger number of smaller bubbles leaving the wire. This higher departure frequency would result in a steady stream of liquid entrained within the bubble plume, thus reducing the drag force on a bubble and decreasing its tendency to meander.

Vapor Volumetric Flow Rate Measurement

Volumetric flow rate can be used to determine the latent heat flux component of heat dissipation from the heated surface with the following equation:

$$q_{LH} = \frac{\rho_g \dot{V}_g h_{fg}}{\pi D_{\text{wire}} x} \tag{2}$$

where ρ_g is the vapor density, h_{fg} is the latent heat of vaporization, and D_{wire} and x are the diameter and length of the heated wire, respectively. Subtracting latent heat from the total heat flux provides the remaining convection component.

The single-photo method is a rapid, straightforward means of measuring the volumetric flow rate of vapor, $\dot{V}_g$, leaving a heated wire. Individual bubble volumes are measured from a photo taken of the departing bubbles. These volumes are combined with vertical bubble velocities obtained with an LDA system, enabling the determination of the vapor volumetric flow rate. Depending on the heat flux and the type of liquid tested, the frame-to-frame volume uncertainty may be low enough to permit the use of a single photo at each heat flux. For the present study, five frames were analyzed for each heat flux to reduce uncertainty.

A rectangular measurement area (MA) was defined within each black-and-white photo to define a region wherein bubbles could be sized and counted. For the 0 ppm case, the MA was 12 mm high by 36 mm wide centered above the wire. The sides of the MA were set 2 mm inward from the ends of the heated wire to avoid possible effects of conduction heat loss to the posts. For the SDS-solution cases, the MA was 12 mm high by 18 mm wide, with each side set approximately 11 mm inward from the copper posts. For all cases, the lower edge of the MA was set 4 mm above the wire to ensure that bubbles would be detached before entering the area.

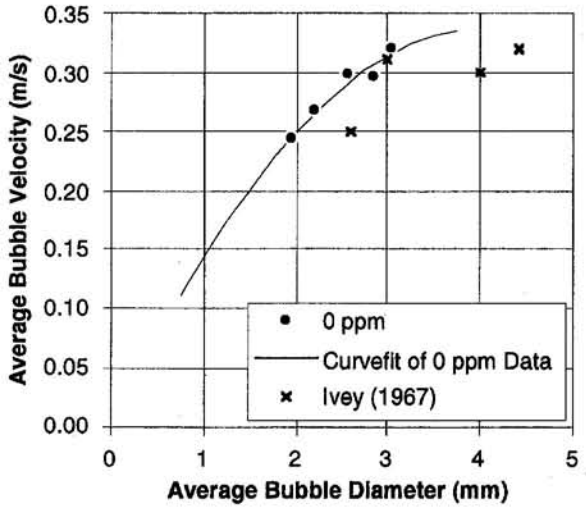

Fig. 5 Bubble velocity versus diameter

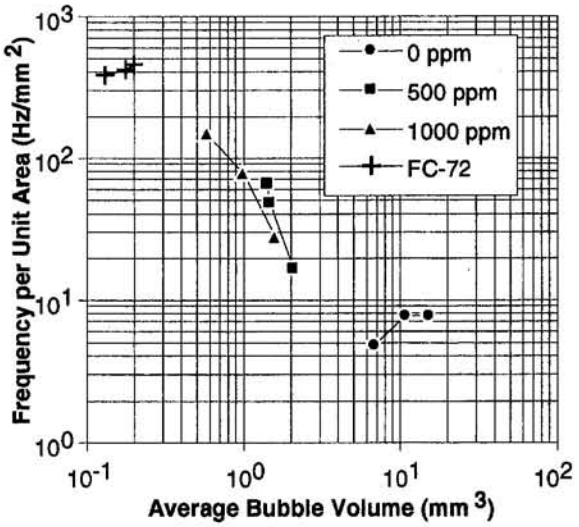

Fig. 7 Frequency per unit area versus bubble volume

Due to their irregular shape, bubbles for the 0 ppm case were sized on the computer with image processing tools. Bubble edges were defined by determining the difference between the gray level of the background versus the gray level of a bubble. While the shapes of the bubbles were slightly irregular, most bubbles appeared elliptical in two dimensions (Fig. 3(*a*)). This was due to the initially spherical bubble being flattened between the opposing buoyancy and drag forces. Based on this flattening phenomenon, the bubble volume was determined from the two-dimensional image. First, the image processor mathematically transformed the slightly irregular two-dimensional bubble shape into an equivalent-area, two-dimensional ellipse (semi-major and -minor axes of a and b, respectively) with identical second moments about the center of gravity. Then, based on the flattening phenomenon, the three-dimensional bubble was assumed to resemble an ellipsoid with semi-axes, a, a, and b, so that the bubble volume was calculated as

$$V_b = \tfrac{4}{3}\pi a^2 b \tag{3}$$

Finally, the spherical diameter was calculated based on an equivalent-volume sphere.

For the SDS-solution cases, image processing tools could not be used because bubble density within each frame was too great for the software to distinguish individual bubbles. However, since bubbles were nearly spherical, diameters were measured directly from enlargements of the photographs using a circle template. Overlapping of bubbles was not a concern since, in most instances, blocked areas were easily estimated. For the small number of bubbles in each case that happened to lie along the edge of the MA (boundary bubbles), only the portion within the MA was accounted for.

When each bubble's velocity is known, vapor volumetric flow rate can be computed for the length of wire examined as follows:

$$\dot{V}_g = \sum \frac{V_{b_i} u_{b_i}}{y} \tag{4}$$

where V_{b_i} and u_{b_i} are the volume and velocity of an individual bubble, respectively, and y is the vertical span of the MA.

Measuring individual bubble velocities during boiling was not possible; therefore, for the 0 ppm case, a velocity-versus-diameter trend was obtained by correlating average velocity versus heat flux with average diameter versus heat flux, as shown in Fig. 5. Velocity data taken by Ivey (1967) for bubble motion in boiling water from wires and cylinders are also displayed in Fig. 5 and show fairly good agreement in slope with the present data. The magnitudes of Ivey's velocity data appear

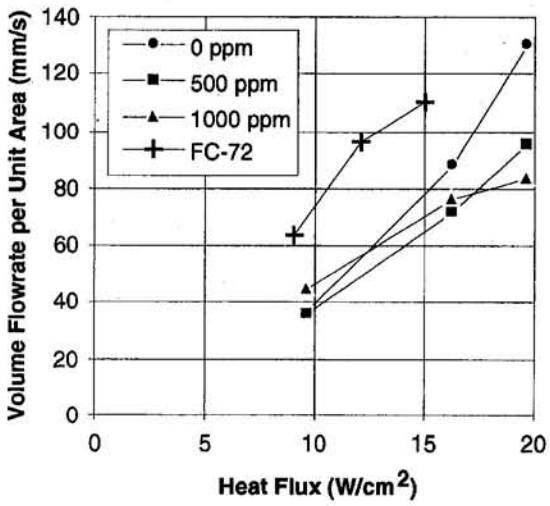

Fig. 6 Volume flow rate versus heat flux

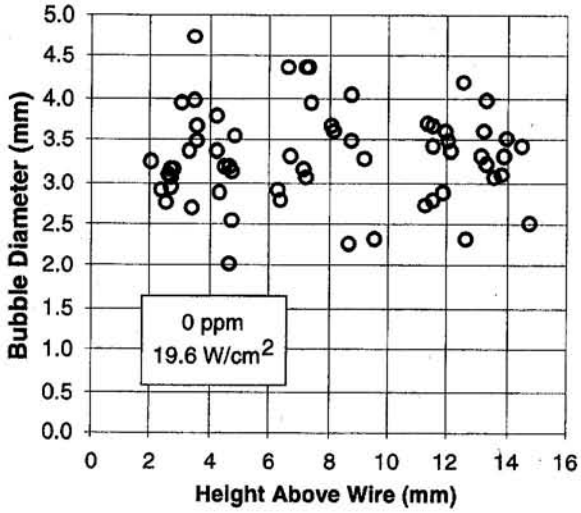

Fig. 8 Diameter versus height above wire

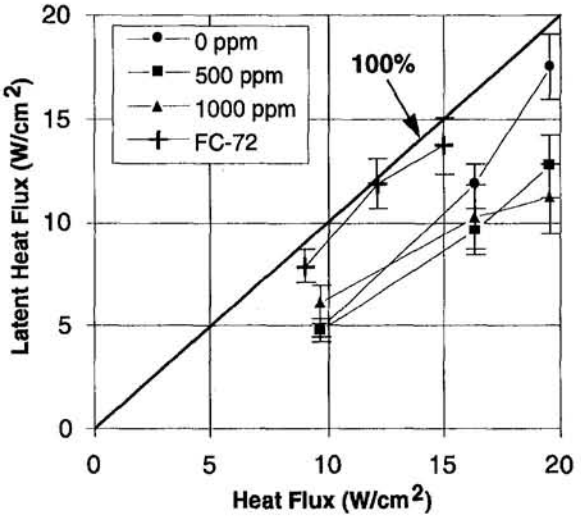

Fig. 9 Latent heat flux

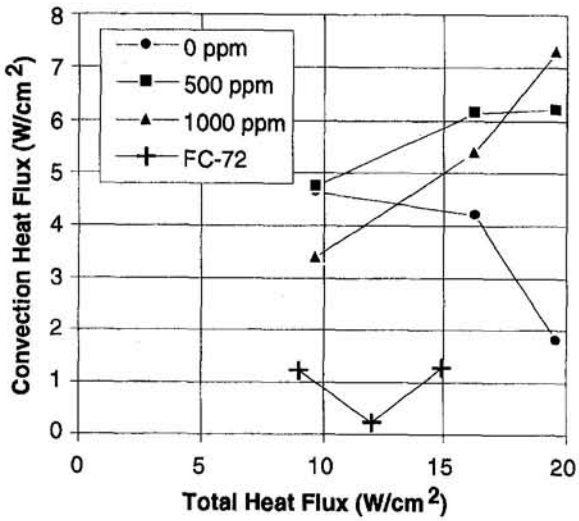

Fig. 10 Convection heat flux

slightly lower than those of the present data. A curvefit generated for the present velocity data is illustrated in Fig. 5 by the solid line. This curvefit was used to determine bubble velocity as a function of diameter for the 0 ppm case.

For the SDS-solution cases, velocities were much more uniform at a given height than for the pure water case. The standard deviations (as a percent of the mean) of the LDA-measured velocities for the surfactant cases were 50 percent lower than those of the 0 ppm case. This uniformity in velocity was due to the relatively high bubble frequency and increased bubble-induced liquid motion, as discussed previously. Therefore, for a given heat flux, the average bubble velocity within the MA was calculated by numerically integrating the LDA velocity-versus-height data and dividing by the total height. This average velocity was then used for each bubble within the MA.

Vapor volume flow rate was then computed using Eq. (4). Values of volume flow rate per unit wire area are plotted versus heat flux in Fig. 6 for both water and FC-72. The magnitude and slope of all water data sets are remarkably similar. The magnitude of the FC-72 data is approximately 70 percent greater than the water data. Volume flow rate is dependent on bubble departure frequency and average bubble volume. Figure 7 shows the relationship between the frequency per unit wire area and the average bubble volume. Even though the volume flow rate for each of the three water cases showed similar increases, their bubble generation characteristics were quite different. For pure water, the increase in volume flow rate versus heat flux was achieved by an increase in average bubble volume, with bubble frequency remaining fairly constant. For the SDS solutions, the increase in vapor generation was achieved by an increase in bubble frequency, with average bubble volume actually decreasing. For FC-72, the increase in volume flow rate was a result of both an increase in frequency and an increase in bubble volume.

Boiling Heat Transfer Mechanism Analysis

The results of the photographic and LDA investigations were used to determine the relative contributions of the latent heat and convection mechanisms that constituted the total heat dissipation above the wire. Because the lower edge of the MA was 4 mm above the wire (1.5 mm for FC-72), any evaporation that might have occurred between departure and the lower edge would be difficult to account for. However, evaporation within and just below the MA was not evident, as illustrated by the random scatter of bubble diameters versus height shown in Fig. 8. The data in this figure represent a compilation of bubble diameters from five different video images for the 0 ppm case at 19.6 W/cm^2. For this figure, the MA was extended downward to include bubbles that had just detached from the wire. Since negligible evaporation occurred within this region, the results from the following mechanism analysis apply to a region just above the heated surface.

Latent Heat. The latent heat flux was calculated using Eq. (2) with volume flow rate defined in Eq. (4). The vapor within the bubbles was assumed to be at saturation conditions. A plot of latent heat flux versus total heat flux is shown in Fig. 9 along with uncertainty ranges for each data point. This figure clearly shows that latent heat is an important heat removal mechanism for fully developed nucleate boiling. For most cases, especially at higher heat fluxes, latent heat is the dominant mechanism. In addition, latent heat for FC-72 is greater than for any of the water cases.

Convection. The convection heat flux was obtained by subtracting the latent heat flux term in Eq. (1) from the total heat flux. As mentioned in the introduction, the convection component may be composed of microconvection, Marangoni flow, and natural convection. Marangoni flow at saturated conditions is usually not significant and natural convection disappears in the fully developed nucleate boiling regime. Therefore, microconvection is the primary component.

The convection heat flux is shown in Fig. 10 versus total heat flux. For the 0 ppm case, the convection component continually decreased as heat flux increased; however, convection increased steadily with heat flux for both surfactant cases. Convection heat flux for FC-72 is low (as indicated by Fig. 9) and appears to fluctuate. This fluctuation results from the uncertainty in the latent heat data.

Uncertainty Analysis. Latent heat flux uncertainties for a 95 percent confidence level are shown in Table 2. For FC-72, the latent heat flux uncertainties are within ±10.1 percent. These

Table 2 Latent heat flux uncertainty estimates (95 percent confidence)

Heat Flux	0 ppm	500 ppm	1000 ppm
9.7 W/cm^2	±10.3%	±11.5%	±12.3%
16.3 W/cm^2	±9.5%	±12.1%	±13.5%
19.6 W/cm^2	±9.2%	±12.2%	±16.3%

Table 3 Diameter uncertainty estimates (95 percent confidence)

Heat Flux	0 ppm	500 ppm	1000 ppm
9.7 W/cm^2	±3.0%	±3.2%	±3.5%
16.3 W/cm^2	±2.8%	±3.6%	±4.2%
19.6 W/cm^2	±2.7%	±3.7%	±5.1%

uncertainties were calculated using the method of Kline and McClintock (1953). The uncertainty in latent heat flux was due to uncertainty in measurement of bubble diameter and velocity and MA height and width (see Eqs. (2) and (4)). Uncertainty estimates of bubble diameter measurements for the present data can be found in Table 3. For FC-72, diameter uncertainties were within ±3.1 percent. The main uncertainty in diameter measurement was due to difficulty in determining the edge of a bubble in the photographs. Uncertainty estimates of velocity for the present data are shown in Table 4. For FC-72, velocity uncertainty was ±5 percent. Velocity uncertainties were estimated based on the point-to-point fluctuations in the velocity versus height curve (Fig. 4). Uncertainties in MA height and width were estimated to be 2 percent.

Discussion

Figure 2 revealed that the addition of SDS to water enhanced boiling heat transfer. Tzan and Yang (1990) experimentally determined surface tension values for the SDS concentrations used in the present study. Heat transfer coefficients from the present study are plotted against those values of surface tension in Fig. 11. This figure indicates a clear trend in boiling enhancement versus surface tension reduction. At 16.3 and 19.6 W/cm^2, Figs. 9 and 10 indicate that this enhancement is due to an increase in convection with a corresponding decrease in latent heat. At 9.7 W/cm^2, however, the enhancement for the 1000 ppm case appears to be due to an increase in latent heat, as seen by Frost and Kippenhan (1967) and Ammerman et al. (1996). This apparent contradiction can be explained by examining the bubble nucleation dynamics. In the partially developed boiling region, a reduction in surface tension promotes nucleation by activating dormant cavities on the surface, thus increasing latent heat flux. In the fully developed region, the presence of the surfactant results in a decrease in bubble agglomeration at the surface and an increase in departure frequency. This increased frequency does not result in an increase in the latent heat flux component, however, because departure diameters are reduced. In addition, the increased frequency at a given site means less time for the superheated liquid layer to grow, resulting in a reduction in the average temperature within the layer. The effect of this temperature reduction is to inhibit boiling—ultimately trading latent heat for convection.

Figure 9 revealed that the latent heat was the largest component of the total heat flux for all cases examined. However, the relative magnitudes of the latent heat and convection components are approaching one another as the total heat flux decreases. At low enough heat fluxes, latent heat will disappear altogether leaving convection as the sole component. Figure 9 also showed that the latent heat flux for the FC-72 data was greater than for the water data. This latent heat difference is directly related to the vapor volumetric flow rate difference (Fig. 6) since the products of vapor density and latent heat of vaporization for the two fluids are similar.

Table 4 Velocity uncertainty estimates (95 percent confidence)

Heat Flux	0 ppm	500 ppm	1000 ppm
9.7 W/cm^2	±4.0%	±6.0%	±6.0%
16.3 W/cm^2	±3.5%	±5.0%	±5.0%
19.6 W/cm^2	±3.5%	±5.0%	±5.0%

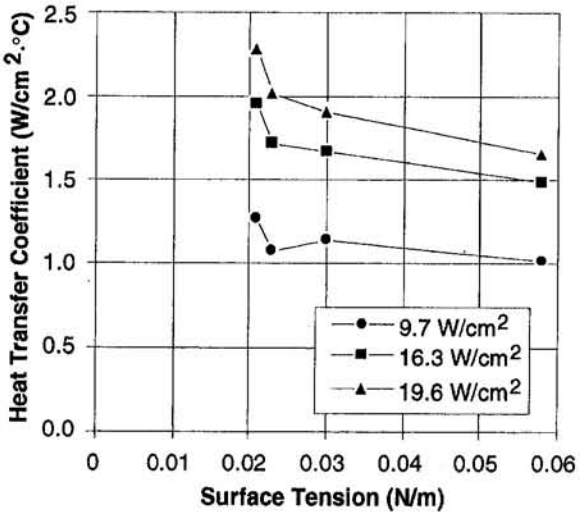

Fig. 11 Heat transfer coefficient versus surface tension

Conclusions

1 For a wire immersed in water, water with reduced surface tension due to surfactant addition, and FC-72, latent heat removal was the largest heat transfer mechanism under fully developed boiling conditions.

2 Addition of an anionic surfactant (sodium dodecyl sulfate) to water caused an increase in the convection component and a corresponding reduction in the latent heat component of the heat flux in the fully developed boiling region. The boiling enhancement of water due to the addition of a surfactant appears to be influenced by this relative change in heat flux components.

3 Vapor volume flow rate per unit wire area increased similarly versus heat flux for water, water with surfactant, and FC-72. The increase in vapor flow rate is due to an increase in average bubble volume for water, an increase in bubble frequency for water with surfactant, and an increase in both bubble volume and frequency for FC-72.

4 A recently developed measurement technique, which combines bubble volumes obtained from photographic images with LDA-measured bubble velocities, enables the determination of the vapor volume flow rate departing a heated wire immersed in a saturated liquid.

Acknowledgments

The authors would like to thank Mr. Y. S. Hong for technical support during testing and the Engineering Television Department at UTA for help in synchronization of the video data.

References

Ammerman, C. N., You, S. M., and Hong, Y. S., 1996, "Identification of Pool Boiling Heat Transfer Mechanisms From a Wire Immersed in FC-72 Using a Single-Photo/LDA Method," ASME JOURNAL OF HEAT TRANSFER, Vol. 118, pp. 117–123.

Carey, V. P., 1992, *Liquid--Vapor Phase-Change Phenomena*, Hemisphere Publishing Corporation, p. 34.

Frost, W., and Kippenhan, C. J., 1967, "Bubble Growth and Heat-Transfer Mechanisms in the Forced Convection Boiling of Water Containing a Surface Active Agent," *Int. J. Heat Mass Transfer,* Vol. 10, pp. 931–949.

Ivey, H. J., 1967, "Relationships Between Bubble Frequency, Departure Diameter and Rise Velocity in Nucleate Boiling," *Int. J. Heat Mass Transfer,* Vol. 10, pp. 1023–1040.

Kline, S. J., and McClintock, F. A., 1953, "Describing Uncertainties in Single-Sample Experiments," *Mechanical Engineering,* Vol. 75, Jan., pp. 3–8.

McFadden, P. W., and Grassmann, P., 1962, "The Relation Between Bubble Frequency and Diameter During Nucleate Pool Boiling," *Int. J. Heat Mass Transfer,* Vol. 5, pp. 169–173.

O'Connor, J. P., You, S. M., Hong, Y. S., and Haji-Sheikh, A., 1993, "Bubble Size, Velocity, and Frequency From a Wire Boiling in Saturated R-113," presented at the ASME 1993 Winter Annual Meeting, New Orleans, LA.

Paul, D. D., and Abdel-Khalik, S. I., 1983, "A Statistical Analysis of Saturated Nucleate Boiling Along a Heated Wire," *Int. J. Heat Mass Transfer,* Vol. 26, pp. 509–519.

Rallis, C. J., and Jawurek, H. H., 1964, "Latent Heat Transport in Saturated Nucleate Boiling," *Int. J. Heat Mass Transfer,* Vol. 7, pp. 1051–1068.

Tzan, Y. L., and Yang, Y. M., 1990, "Experimental Study of Surfactant Effects on Pool Boiling Heat Transfer," ASME JOURNAL OF HEAT TRANSFER, Vol. 112, pp. 207–212.

An Experimental Investigation of the Effects of Subcooling and Velocity on Boiling of Freon-113

L. Huang[1]
Research Assistant.

L. C. Witte
Professor.
Fellow ASME

Heat Transfer and Phase Change Laboratory,
Department of Mechanical Engineering,
University of Houston,
Houston, TX 77204-4792

Boiling heat transfer correlations were obtained for the maximum and minimum heat fluxes. Relationships among q_{min}/q_{max}, Weber number, and liquid Jakob number were obtained. Compelling evidence was found to indicate that significant cooling of the wake and/or the forward stagnation line can be caused by large-scale liquid–solid contacts while other parts of the surface experienced film boiling with little or no contact in the transition-film boiling regime. A criterion for large-scale liquid–solid contacts was developed. Another purpose of this study was to investigate whether a stable transition of boiling exists, i.e., if the ratio of the minimum and maximum heat fluxes approaches unity as liquid subcooling and velocity are increased. Extensive data using Freon-113 were taken, covering a wide range of fluid velocities (1.5 to 6.9 m/s) and liquid subcooling (29 to 100°C) at pressures ranging from 122 to 509 kPa. Cylindrical electric resistance heaters of two diameters, 6.35 mm and 4.29 mm, and made of Hastelloy-C and titanium, respectively, were used. The maximum q_{min}/q_{max} achievable with the apparatus was 0.9.

Introduction

Recent research in the field of boiling heat transfer has shown that liquid velocity and subcooling significantly affect boiling heat transfer. The minimum and maximum heat fluxes can be influenced by the liquid velocity and subcooling. It is suspected (Sankaran and Witte, 1990) that the ratio q_{min}/q_{max} would approach unity at sufficiently high liquid velocity and subcooling; this notion needs more investigation. If q_{min}/q_{max} were to be unity, then the unstable regime where q_w decreases with ΔT_{sat} could be avoided.

A previous study (Chang and Witte, 1990) showed that brief random small-scale contacts and longer large-scale contacts between the boiling liquid and heater surface occur in some portions of the film boiling regime. The vapor film may appear to be quite continuous to the naked eye, but the small contacts become longer and more numerous as the superheat approaches the minimum superheat. The liquid–solid contacts contribute to an increasingly efficient average heat transfer during film boiling, eventually leading to q_{min}. However, no investigation has been reported on liquid–solid contact during film boiling at the high liquid velocities and subcoolings covered in the present study.

The present study concentrated on the influence of liquid velocity and subcooling upon boiling heat transfer. Experiments were conducted on flow boiling of a highly subcooled liquid from a cylinder in crossflow, to see how the liquid velocity and subcooling influence nucleate boiling, the critical heat fluxes, and film boiling. The ultimate goal was to see if an entirely positive-sloped boiling curve can exist at sufficiently high liquid velocity and subcooling without the presence of a jump transition to film boiling. Experimental results showed strong evidence of significant liquid–solid contact well into the stable film boiling regime. This motivated the development of a simple criterion for the occurrence of liquid–solid contact in film boiling under such conditions.

Experimental Apparatus and Technique

The apparatus used to perform the experiments is shown in Fig. 1. A variable speed 450 gpm centrifugal pump was used to circulate the working fluid steadily in the closed loop. The flow passed through an expansion section, a honeycomb straightening section with screens on both ends, and a reducing nozzle to get a uniformly symmetric, fully developed low-turbulence flow before it entered the test section. A Dieterich Standard Diamond II 4-in. annubar flow sensor was used to measure the flow rates that were used to calculate flow velocities in the test section. The liquid in the loop was cooled by a water-cooled Filtrine POC-500 WC chiller with 16 kW cooling capacity. The liquid could be cooled to a temperature below 0°C. Therefore, liquid subcooling as high as 100°C for Freon-113 could be reached when the Freon pressure was high. A supply pump pumped the Freon from a storage tank into the main loop during the experiments, and the working fluid was returned to the storage tank, passing a half-opened valve on the top of the main loop. By setting the opening of the valve, a desired level of pressure could be maintained. The system pressure was measured with a pressure gauge and a pressure transducer as shown in Fig. 1. In this way, the desired liquid velocity, liquid subcooling, and pressure could be controlled at the test section.

The test section was made of aluminum with a cross-section of 63.5-mm by 63.5-mm. Two Plexiglas windows were installed at opposite sides of the test section for observation during the experiment. The heater was mounted horizontally across the test section with a leak-proof mounting configuration, as shown in Fig. 2.

Hastelloy-C tubes, of 6.35 mm diameter and 0.254 mm wall thickness, and titanium tubes, of 4.25 mm diameter and 0.25 mm wall thickness, were used as electric resistance heaters, inside which sintered lava cylinders were inserted as a heat insulator and rigid body for mounting thermocouples. The lava cylinder was grooved around the cylinder wall 45 deg apart, starting from the lower stagnation point, to position the thermocouples. Five 38-gage chromel-alumel with 0.5-mm-dia Inconel 600 sheathed thermocouples were cemented in the grooves using Omega CC high-temperature cement. To establish good thermal contact between the thermocouples and the heater wall, the lava insert was fitted snugly inside the tube after a thin coat of high temperature cement was applied. The thermocouples

[1] Current address: Research Engineer, Heat Transfer Research Inc., College Station, TX.

Contributed by the Heat Transfer Division for publication in the JOURNAL OF HEAT TRANSFER. Manuscript received by the Heat Transfer Division January 1995; revision received February 1996. Keywords: Boiling, Forced Convection, Thin Film Flow. Associate Technical Editor: V. K. Dhir.

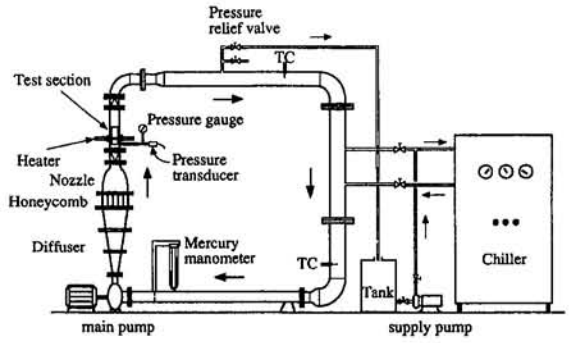

Fig. 1 Schematic diagram of the experimental apparatus

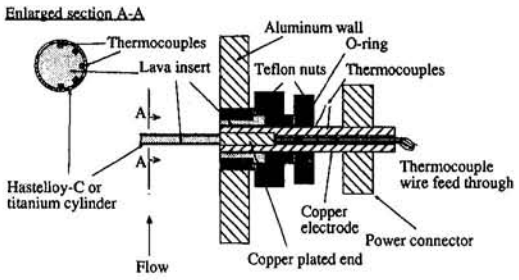

Fig. 2 Cross-sectional view of the heater section and the heater configuration

were located at the axial center of the heater, as shown in Fig. 2, to measure the azimuthal T_w distribution. Before the lava inserts were inserted into the tubes, both ends of the tubes were copper electroplated to a thickness of about 1 mm, with a length of 1.25 in. for Hastelloy-C tubes and 0.75 in. for titanium tubes, and machined to shrink fit to the copper electrodes, which were used to connect to the power supply. Two copper-constantan thermocouples on the copper electrode outside the test section wall were used to estimate the heat losses from the end of the heaters. Power was supplied to the heater by a Gulf Electroquip dc motor-generator set capable of providing up to 1500 amps at 45 volts of dc power.

For every flow boiling run, the heater surface was polished and cleaned with heavy-duty detergent, and then rinsed in water before it was carefully installed in the test section. The heater surface was smooth and lustrous. As an experiment progressed, the first set of data was read after the wall temperature readings became steady at a particular power setting. The power supplied to the heater was increased gradually after recording each set of data, moving from forced convection to nucleate boiling, then to film boiling at its burnout wall temperature. Then the power was decreased gradually, moving back from film boiling to nucleate boiling.

The experimental conditions for Freon-113 are shown in Table 1.

Table 1 Experimental conditions and results

Run #	Diameter mm	Material	Pressure kPa	Subcooling °C	Velocity m/s	q_{min} MW/m^2	q_{max} MW/m^2
1	6.35	Hastelloy-C	175.2	59.3	3.03		0.969
2			238.7	70.1	2.85		1.361
3			348.4	87.7	3.03	1.262	1.539
4			349.1	86.9	3.76	1.421	1.880
5			353.8	85.8	4.81	1.489	1.647
6			359.2	81.9	5.64	1.714	1.937
7			405.9	93.5	2.85	1.124	1.395
8			508.6	97.6	6.02	1.892	2.500
9			500.4	100.1	4.81	1.913	2.650
10			478.5	99.7	3.03	1.453	1.795
11			170.6	57.0	6.9		1.459
12			154.0	60.3	2.85	0.827	1.235
13			151.0	58.6	2.19	0.820	1.074
14			155.8	60.0	2.05	0.799	1.136
15			153.8	59.1	2.85	0.888	1.259
16			153.7	59.4	1.53		1.008
17			156.8	60.0	1.53		0.919
18			122.3	28.9	2.85	0.559	0.801
19	4.29	Titanium	247.8	65.0	3.03		1.218
20			245.7	73.4	3.03		1.223
21			239.5	67.6	6.23		1.985
22			245.3	56.7	6.23		2.449

Experimental Uncertainty

Experimental uncertainty was estimated according to the Kline–McClintock method (1953). It yielded maximum values of ±3.3 percent in heat flux, ±5 percent in critical heat fluxes, ±3.5°C or ±1 percent (whichever is greater) in heater surface temperature, ±2°C in saturation temperature, ±1.1°C in bulk temperature, ±3 percent in fluid velocity, and ±7 kPa in system pressure. Heat flux was calculated based on the area in contact with Freon and the measured power dissipation in the heater, less a small end-loss correction that was determined from temperature measurements made outside the test section. Uncertainty in the critical heat fluxes was higher because it involved

Nomenclature

D = diameter of cylinder heater, cm
h_{fg} = latent heat of vaporization, J/kg
Ja_l = liquid Jakob number = $c_{pl}\Delta T_{sub}/h_{fg}$
N^* = nondimensional group = $(\rho_l \mathrm{Ja}_l)/(\rho_v \mathrm{Pe}_l^{0.5})$
Pe = Peclet number = VD/α
q_w = wall heat flux, W/m^2
q^*_{min} = nondimensional minimum heat flux = $q_{min}/(\rho_v h_{fg} U_m)$
q^*_w = nondimensional wall heat flux = $q_w/(\rho_v h_{fg} V)$
Re = Reynolds number = VD/ν
V = liquid free-stream velocity in test section, m/s
w = width of the test section, m
We_v = Weber number based on vapor density and mean velocity = $D\rho_v U_m^2/\sigma$
ΔT_{sat} = vapor superheat = $T_w - T_{sat}$, °C
ΔT_{sub} = liquid subcooling = $T_s - T_\infty$, °C
α = thermal diffusivity, m^2/s
θ = azimuthal angle measured from forward stagnation point, deg
ν = kinematic viscosity, m^2/s
ρ = density, kg/m^3
σ = surface tension, N/m

Subscripts

l = liquid
min = minimum
max = maximum
s, sat = saturation
sub = subcooled
v = vapor
w = wall
∞ = bulk liquid

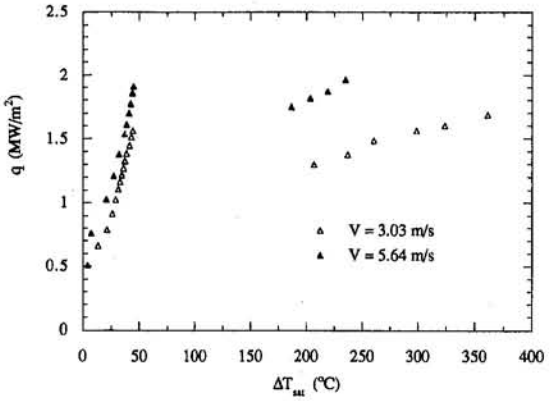

Fig. 3 Effect of fluid velocity on boiling curves at a fixed subcooling and pressure: Freon-113, ΔT_{sub} = 85 ± 4°C, p = 354 ± 7 kPa, D = 6.35 mm (Hastelloy-C), Runs 3 and 6

averaging the power levels just before and after the jump to film boiling, or back again. Temperature uncertainty included the effects of thermocouple calibration and data acquisition errors. The dominant factor was inherent inaccuracy in the thermocouple itself. The saturation temperature was found from a pressure measurement near the heater, thus its uncertainty depended essentially on the accuracy of the pressure.

While there was a temperature drop in the heater near its intersection with the test section wall, visual observations of boiling behavior showed that this occupied only a very small length, less than 5 mm, and that conditions could be considered uniform in the axial direction over most of the heated length. Based on the estimate of heat loss from the ends of the heater calculated from the temperature measurements outside the test section for the highest heat fluxes, a gradient of about 5°C/mm would occur along the heater near the point where it intersects the wall. Thus, a temperature drop of about 25°C at most could have occurred immediately adjacent to the wall. The middle portion of the heater, about 55 mm, could be considered to be under uniform heat flux and free of serious axial temperature gradients. Sankaran (1990) used a heater equipped with thermocouples located near the copper-plated electrodes as well as near the axial centerline for similar measurements in Freon-113. The thermocouples were about 1.27 cm from the copper-plated electrodes. Sankaran observed no appreciable difference in boiling behavior between the central thermocouples and the end thermocouples, thus in this family of heaters, those locations were omitted. The fact that the black deposit (to be discussed later) that formed over the wake portion of the heater was uniformly distributed down the axial length up to about 5 mm from the wall strengthens the conclusion of axial uniformity in temperature over most of the heater.

Heat Transfer Results and Discussion

Extensive data were taken for different test conditions. In total, 18 sets of runs were performed using Hastelloy-C heaters and four using titanium heaters as summarized in Table 1. Some heaters survived the jump to high T_w at q_{max}, and were returned to nucleate boiling, and some burned out at the maximum heat flux. All the titanium heaters burned out at q_{max}.

Figures 3 and 4 illustrate typical boiling curves, showing the effects of fluid velocity, liquid subcooling, and pressure. As expected, fluid velocity enhanced highly subcooled boiling heat transfer, as shown in Fig. 3, as it did in the case of very low subcooled boiling, as observed by Yilmaz and Westwater (1980) and Broussard and Westwater (1985). From Fig. 3, it can be seen that the entire boiling curve shifts up (i.e., q_w increases for a given ΔT_{sat}) as V increases from 3.03 m/s to 5.64 m/s. However, the curve shifts up much more in the film boiling regime. This figure also illustrates that both critical heat fluxes increase with V.

Figure 4 is typical of the influences of ΔT_{sub} and p on the boiling curves with V held constant. Figure 4 shows that ΔT_{sub} and p not only greatly enhance film boiling heat transfer, but also significantly enhance q_w in the nucleate boiling regime.

Critical Heat Flux Correlations. The relationship of the two critical heat fluxes, and their ratio, to fluid velocity and liquid subcooling is of great interest. The highest q_{max} reached in the present investigation was 2.65 MW/m^2 at a fluid velocity of 4.81 m/s and a ΔT_{sub} of 100.1°C, which was about 12 times the q_{max} in saturated pool boiling for Freon-113, reported by Elkassabgi and Lienhard (1988).

The mean cross-sectional velocity, U_m, which is defined as the volume flow rate divided by the mean flow area A_m, was used to correlate the critical heat fluxes, which accounts for the different heater diameters and different cross-sectional areas. The mean flow area A_m was defined as the ratio of the flow volume in the channel at the location of the heater to the heater diameter, following Vliet and Leppert (1961).

The nondimensional q_{max} was correlated using a multiple linear regression analysis with Weber number and liquid Jakob number as the nondimensional correlating groups. The result was

$$\frac{q_{max}}{\rho_v h_{fg} U_m} = 0.545\ \mathrm{We}_v^{-0.287} \left(\frac{\rho_l}{\rho_v}\mathrm{Ja}_l\right)^{0.046}. \quad (1)$$

While it is surprising that the dimensionless q_{max} is not a strong function of the dimensionless subcooling, Ja_l, the reason for it lies in the fact that a portion of the subcooling is produced by elevating the pressure of the Freon. Figures 3 and 4 show that q_{max} increases significantly with ΔT_{sub}, but the data sets were taken at different pressures. The nondimensionalizing factor $\rho_v h_{fg} U_m$ contains two factors that depend upon pressure: ρ_v, which increases virtually directly with p, and h_{fg}, which decreases with p at a much lower rate. The net effect is that the dimensionless q_{max} does not depend strongly on dimensionless subcooling because the changes in $\rho_v h_{fg}$ tend to mask the influence of subcooling. By ignoring the dependence upon Ja_l, the dimensionless q_{max} can be correlated as

$$\frac{q_{max}}{\rho_v h_{fg} U_m} = 0.679\ \mathrm{We}_v^{-0.30}, \quad (2)$$

as shown in Fig. 5. Sankaran and Witte's (1990) Freon-113 data are included, and fit the correlation well. Sankaran's data were obtained at near-atmospheric pressures, and for ΔT_{sub} from 41.4°C to 58.6°C. Run 18 was not included in Fig. 5 because it was the only data point collected at moderate subcooling.

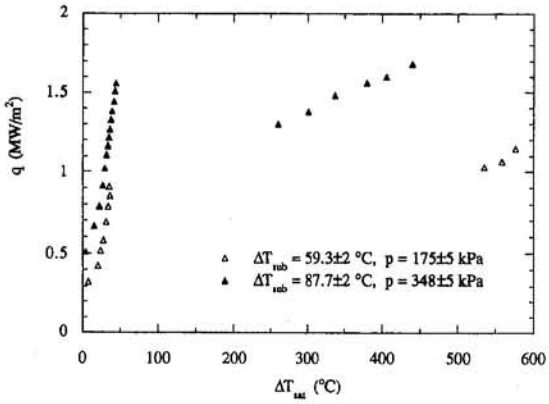

Fig. 4 Effect of subcooling and pressure on boiling curves: Freon-113, V = 3.03 m/s, D = 6.35 mm (Hastelloy-C), Runs 1 and 3

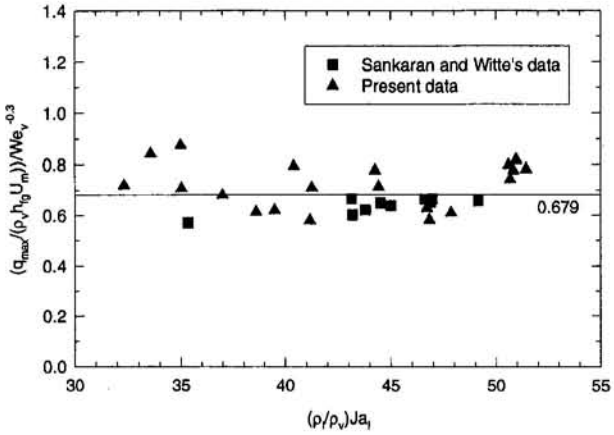

Fig. 5 Correlation of maximum nondimensional heat flux

Broussard and Westwater's correlation,

$$\frac{q_{\max}}{\rho_v h_{fg} U_m} = 0.412\ \mathrm{We}_v^{-0.329}, \tag{3}$$

is compared to the data in Fig. 6, along with Eq. (2). The average subcooling effect is contained in the lead constants for Eqs. (2) and (3). Thus the lead constant, 0.679, in Eq. (2) represents the average effect of subcooling between 41.4 and 100.1°C, as does the factor 0.412 in Eq. (3) for a subcooling of 4.5°C. Thus, it is expected that data for subcooling between these two levels would fall somewhere between the two correlations.

Equation (2) represents a Weber number range between 15 and 1090 for high subcooling. It can represent experimental data within a wide range of mean velocities (from 1.66 to 7.5 m/s) and pressures (from 151 to 509 kPa) for Freon-113 within −17 percent to +26 percent for liquid subcooling higher than 41.4°C.

By using the same set of dimensionless groups, $q_{\min}$ can be correlated by

$$\frac{q_{\min}}{\rho_v h_{fg} U_m} = 0.006\ \mathrm{We}_v^{-0.15} \left(\frac{\rho_l}{\rho_v}\,\mathrm{Ja}_l\right), \tag{4}$$

which shows that liquid subcooling (Ja_l) has a significant influence on $q_{\min}$, as does the mean velocity, U_m. Here $q_{\min}$ is proportional to the 0.70 power of mean velocity and to the 1.0 power of liquid subcooling. The present data, together with Sankaran and Witte's data, for $q_{\min}$ and the correlation, Eq. (4), are shown in Fig. 7. Equation (4) represents data to within −17 to +28 percent for mean velocities from 2.23 to 6.53 m/s and liquid subcooling from 28.9 to 100.1°C in the pressure range from 122.3 to 508.6 kPa for Freon-113.

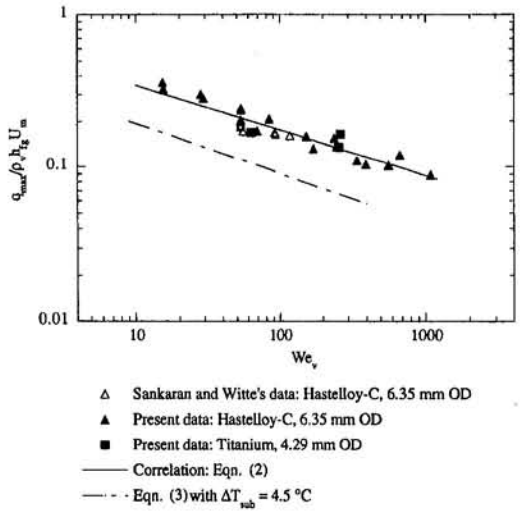

Fig. 6 Comparison of maximum nondimensional heat flux to the correlation of Broussard and Westwater: Freon-113 with ΔT_{sub} from 41.4 to 100.1°C, velocity from 1.53 to 6.9 m/s, and pressure from 151 to 509 kPa

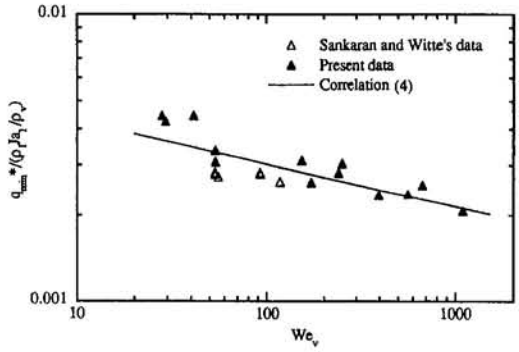

Fig. 7 Correlation of minimum heat flux: Freon-113, D = 6.35 mm (Hastelloy-C) with ΔT_{sub} from 29 to 100°C, velocity from 2.0 to 6.0 m/s, and pressure from 122 to 509 kPa

To get the dependence of the ratio of the two critical heat fluxes, $q_{\min}/q_{\max}$, with velocity and liquid subcooling, Eq. (4) was divided by Eq. (2), yielding

$$\frac{q_{\min}}{q_{\max}} = 0.00884\ \mathrm{We}_v^{0.15} \left(\frac{\rho_l}{\rho_v}\,\mathrm{Ja}_l\right). \tag{5}$$

Equation (5) is shown in Fig. 8; it is only valid in the range of the present experiment, i.e., We_v between 28 and 1090 and $(\rho_l/\rho_v)\mathrm{Ja}_l$ between 29 and 52. $q_{\min}/q_{\max}$ should be less than unity (or equal to unity, if such a condition exists). The highest $q_{\min}/q_{\max}$ reached in the present investigation was 0.9 at a mean velocity of 5.22 m/s with ΔT_{sub} = 86°C and p = 354 kPa.

Large-Scale Liquid–Solid Contacts in Film Boiling. T_w does not vary significantly with angular position at higher q_w in the film boiling regime, as shown in Fig. 9 for ΔT_{sat} greater than about 500°C. As q_w decreases however, T_w on the back of the heater becomes much lower compared to other portions of the heater. It is believed that this is caused by large-scale liquid–solid contacts on the wake side of the cylinder.

The situation where some portions on the heater have large-scale liquid–solid contacts at low T_w while others remain in pure film boiling with much higher T_w can be called "transition-film boiling," in accord with the description given by Witte

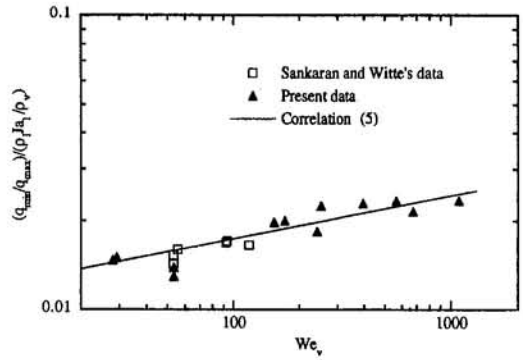

Fig. 8 The effect of Weber number on $q_{\min}/q_{\max}$: Freon-113, D = 6.35 mm (Hastelloy-C) with ΔT_{sub} from 29 to 100°C, velocity from 2.0 to 6.0 m/s, and pressure from 122 to 509 kPa

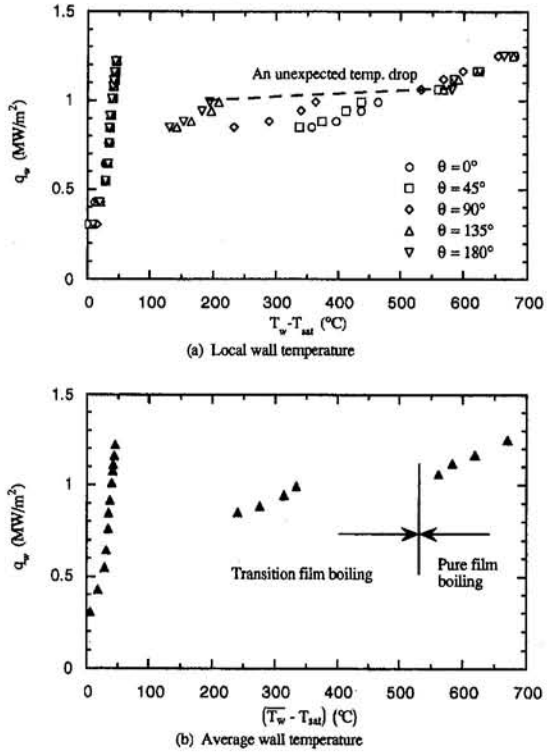

Fig. 9 Boiling curves showing the transition from pure film boiling to transition film boiling for Freon-113: V = 2.85 m/s, ΔT_{sub} = 59.1°C, p = 153.8 kPa, D = 6.35 mm (Hastelloy-C)

and Lienhard (1982). This is the nomenclature used in Fig. 9(b), in which heat fluxes were plotted in terms of a spatially averaged T_w. Figure 10(b) shows a similar plot for the higher velocity, higher subcooled data. From these figures, it can be seen that the boiling curves in the film boiling regime need not to be continuous and jumps from high T_w to lower T_w can occur as q_w is reduced.

Figure 9(a) shows that a large, unexpected drop in T_w occurred in film boiling as q_w was reduced. During the experiments, a dark area developed on the wake side of the heater; it became darker and darker, even as the power to the heater was being turned down. However, a vapor film could still be observed on other portions of the heater after the sudden drops in T_w, and T_w was still high enough to prevent the heater from returning to the nucleate boiling regime. T_w on the wake side of the heater was always lower than on other portions of the heater after T_w dropped as a result of a decrease in q_w. The highest temperature drop happened at θ = 180 deg, where a black deposit layer, having a width of about 5 mm and covering about 90 deg of included angle in the wake, was formed during the experiment. T_w at θ = 180 deg dropped from 642°C to 254°C when q_w decreased from 1.06 MW/m^2 to 0.99 MW/m^2 for the conditions shown in Fig. 9. When q_w was reduced to 0.80 MW/m^2 for conditions shown in Fig. 9 another drop in T_w occurred, which brought film boiling back to nucleate boiling.

Figure 10 shows no such discontinuity in film boiling. However, T_w on the wake side was always lower and a black deposit was found there as well, which suggests that the entire film boiling regime is in the transition-film boiling regime. This means that it is not necessary that the heater be in the pure film boiling regime, where T_w is usually very high, after the transition from nucleate boiling to film boiling. It can jump directly into the transition-film boiling regime from nucleate boiling. This leads to a lower T_w in the wake region compared to pure film boiling, caused by large-scale liquid–solid contacts.

A straight black line along the stagnation line of the heater was formed during some experimental runs, although the vapor film always appeared to the naked eye to be continuous on the front portion of the heater during these experiments. The line had a width of about 1 mm. In this case, T_w was lower at θ = 0 than on the sides and on the back side of the heater for cases where the deposit was not found on the wake side of the heater. If the black deposit was found on both the stagnation line and the wake side of the heater, T_w was higher on the sides of the heater.

The black deposit was chemically analyzed using a Siemens D5000 diffractometer. The deposit consisted mostly of nickel fluoride ($NiCl_2$), chromium nickel fluoride ($NiCrF_6$), and iron fluoride (FeF_2). These compounds resulted from chemical reaction of liquid Freon-113 with the heater material at elevated temperature. After the deposit was cleaned from the heater, the heater was no longer smooth, but slightly rough. This observation suggests significant liquid–solid contacts during film boiling at lower q_w. The fact that T_w was lower on the wake side of the heater during film boiling at relatively lower q_w was highly repeatable. Eleven data sets were taken that showed much lower T_w with the black deposit on the wake side of the heaters. Seven sets of data were taken that showed lower T_w and deposit lines on the front of the heaters. This suggested that frequent liquid–solid contacts occurred for highly subcooled film boiling before q_{min} was reached.

Large-scale liquid–solid contacts were also observed by Chang and Witte (1990). They measured the liquid–solid contacts for flow film boiling of subcooled Freon-11 over an electrically heated cylinder equipped with a surface microthermocouple probe. They detected very large temperature drops on the wake side of the heater, and a moderate temperature drop at θ = 90 deg. No large-scale contacts were detected at the stagnation point within their experimental range: liquid velocity from 0.7 to 1.7 m/s, and liquid subcooling from 2.8 to 6.7°C. The subcooling in the present experiments was an order of magnitude higher, accounting for contacts at the front stagnation point.

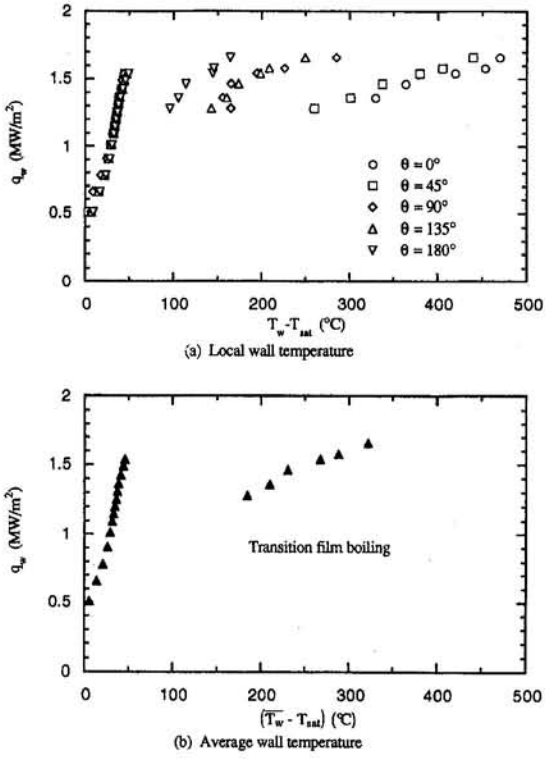

Fig. 10 Boiling curves showing transition film boiling with no pure film boiling for Freon-113: V = 3.03 m/s, ΔT_{sub} = 87.7°C, p = 348.4 kPa, D = 6.35 mm (Hastelloy-C)

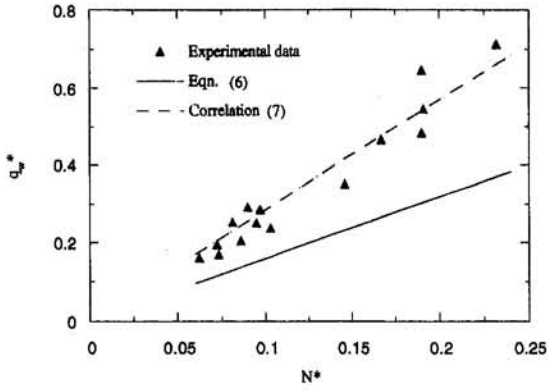

Fig. 11 Correlation for the lowest wall heat flux with no large-scale liquid–solid contact

In principle, a small disturbance of the liquid–vapor interface can result in momentary collapse of the vapor film when flow film boiling is unstable. The stability of flow film boiling depends on the interaction of the vapor film and the parameters that influence it. The likely condition for flow film boiling to become unstable seems to be one that leads to a thinner vapor film. Both fluid velocity and liquid subcooling have the effect of reducing the vapor film thickness. For example, the film thickness at the stagnation point for these heaters, predicted by an analytical model (Huang and Witte, 1995), is only about 0.015 mm for Freon-113 at $V = 3.03$ m/s and $\Delta T_{sub} = 100$°C at a q_w of 1.69 MW/m^2. At such a thin vapor film thickness, even very small oscillations of the liquid–vapor interface can induce the liquid to contact the heating surface.

However, large-scale liquid–solid contact does not necessarily mean the end of film boiling. If T_w is high enough that the vapor generation rate is sufficient to support the surrounding liquid on average, the vapor film can survive. For the case of flow film boiling in this study, large-scale liquid–solid contacts occurred only on some locations on the heating surface, like the front stagnation line and the wake side of the cylinder. The other portions of the heater remained in pure film boiling.

Criterion for Liquid–Solid Contact. The theoretical lower limit for a heater wall to sustain a vapor film is

$$q_w^* = 2\sqrt{\frac{2}{\pi}}N^* = 2\sqrt{\frac{2}{\pi}}\frac{\rho_l}{\rho_v}\mathrm{Ja}_l\mathrm{Re}_l^{-0.5}\mathrm{Pr}_l^{-0.5} \qquad (6)$$

(Huang and Witte, 1995). Equation (6) is based on the notion that the heat provided by the heater is just enough to heat the liquid to saturation and no vapor can be formed. q_w must be greater than the value calculated by using Eq. (6) to allow film boiling. q_{min} should also be greater than this value. Since it is more likely for liquid to contact the surface for a thinner film, it is assumed that these two nondimensional groups (q_w^* and N^*) relate to liquid–wall contact. With this idea, the data where T_w drops suddenly in the film boiling regime were extracted and plotted in Fig. 11, and compared to Eq. (6). The experimental data and Eq. (6) have similar tendencies, which encouraged a correlation of the data as

$$q_w^* = 2.85N^* = 2.85\frac{\rho_l}{\rho_v}\mathrm{Ja}_l\mathrm{Re}_l^{-0.5}\mathrm{Pr}_l^{-0.5}. \qquad (7)$$

Thus, if q_w is less than the value calculated by Eq. (7), the subcooled liquid will contact the heater surface.

Concluding Remarks

Based on the observations and data obtained from the present experimental investigation, the following summary and conclusions are made:

1 Fluid velocity enhances highly subcooled boiling heat transfer as it does in the case of saturated boiling. The enhancement is much more pronounced in the film boiling regime than in the nucleate boiling regime. Increased liquid subcooling and pressure also increase flow boiling heat transfer, especially in the film boiling regime.

2 Unexpected drops in T_w, up to 388°C, for a small decrease in q_w, were recorded in the film boiling regime for runs with low fluid velocities. These drops were caused by the transition from pure film boiling to transition-film boiling. This behavior occurred when large-scale liquid–solid contacts occurred on the wake side and/or on the front stagnation line of the heater. For those runs with higher fluid velocities, pure film boiling did not exist and no unexpected T_w drops were measured, which means that large-scale liquid–solid contacts can occur directly after the transition from nucleate boiling to film boiling. The entire film boiling regime is in the film-transition boiling regime at higher velocities and subcoolings. This results in a lower burnout T_w although q_{max} is higher.

3 Experimental data showed that the heat transfer on the downstream side of the cylinder contributed almost as much as that from the front part of the cylinder. The heat transfer in the wake cannot be neglected for high subcooling and high-flow-velocity film boiling.

4 A criterion for the lower limit of wall heat flux, Eq. (7), was developed from the experimental data to determine whether subcooled liquid will frequently contact the heater surface for a certain wall heat flux.

5 The ratio of q_{min} to q_{max} approached 90 percent for some of the high subcooling and velocity levels encountered in this study.

Acknowledgments

This work received support under a Texas Advanced Research Project, ARP-003652041.

References

Broussard, R. A., and Westwater, J. W., 1985, "Diameter and Velocity Effects for Cross-Flow Boiling," *AIAA Journal*, Vol. 23, pp. 1615–1620.

Chang, K. H., and Witte, L. C., 1990, "Liquid–Solid Contact During Flow Film Boiling of Subcooled Freon-11," ASME JOURNAL OF HEAT TRANSFER, Vol. 112, pp. 465–471.

Elkassabgi, Y., and Lienhard, J. H., 1988, "Influences of Subcooling on Burnout of Horizontal Cylindrical Heaters," ASME JOURNAL OF HEAT TRANSFER, Vol. 110, pp. 479–486.

Huang, L., 1994, "Subcooled Flow Boiling Across Horizontal Cylinders," Ph.D. Dissertation, University of Houston, Houston, TX.

Huang, L., and Witte, L. C., 1994, "Influences of Subcooling and Velocity on Boiling Heat Transfer Across Horizontal Cylinders," ASME HTD-Vol. 273, pp. 65–72.

Huang, L., and Witte, L. C., 1995, "Forced Convective Film Boiling Heat Transfer Across Horizontal Cylinders in Highly Subcooled Freon-113," *Proc. 4th ASME/JSME Thermal Engineering Joint Conference*, Vol. 2, pp. 315–322.

Kline, S. J., and McClintock, F. A., 1953, "Describing Uncertainties in Single-Sample Experiments," *Mechanical Engineering*, Jan., pp. 3–8.

Sankaran, S., and Witte, L. C., 1990, "Highly Subcooled Flow Boiling of Freon-113 Over Cylinders," ASME HTD-Vol. 136, pp. 29–34.

Sankaran, S., 1990, "Highly Subcooled Flow Boiling From a Cylinder in Cross-flow," Ph.D. Dissertation, University of Houston, Houston, TX.

Vliet, G. C., and Leppert, G., 1961, "Forced Convection Heat Transfer From an Isothermal Sphere to Water," ASME JOURNAL OF HEAT TRANSFER, Vol. 83, pp. 163–175.

Witte, L. C., and Lienhard, J. H., 1982, "On the Existence of Two 'Transition' Boiling Curves," *Int. J. Heat Mass Transfer*, Vol. 25, No. 6, pp. 771–780.

Yilmaz, S., and Westwater, J. W., 1980, "Effect of Velocity on Heat Transfer to Boiling Freon-113," ASME JOURNAL OF HEAT TRANSFER, Vol. 102, pp. 26–31.

R. C. Xin
Graduate Student.

A. Awwad
Graduate Student.

Z. F. Dong
Research Associate.

M. A. Ebadian
Fellow ASME

Hemispheric Center for
Environmental Technology,
Florida International University,
Miami, FL 33199

Heat Transfer of Air/Water Two-Phase Flow in Helicoidal Pipes

Heat transfer of air/water two-phase flow in helicoidal pipes is experimentally investigated in this study. Three test sections were tested in axially horizontal, vertical, and inclined orientations. It has been found that the ratio of the average heat transfer coefficient to that of the water flow is affected by the water flow rate along with the Lockhart–Martinelli parameter. For a fixed water flow rate, there is a maximum heat transfer coefficient as the air flow rate increases. The results indicate that tube diameter has a significant effect on the average heat transfer coefficient ratio. For large-tube-diameter coils, average heat transfer results vary for different orientations. For small-tube-diameter coils, orientation has an insignificant effect on the average heat transfer coefficient. Based on the experimental data, a set of correlations is proposed for the average heat transfer coefficient ratio versus the liquid superficial Reynolds number and Lockhart–Martinelli parameter.

Introduction

The prominent characteristics of high heat transfer efficiency and compact volume in helicoidal pipes make their use important to many engineering applications such as steam generators, chemical plants, nuclear reactors, and even medical equipment. In most applications, gas–liquid two-phase flow occurs inside the pipe. Pressure drop, void fraction, and flow patterns have been studied extensively for gas–liquid two-phase flow in curved and helicoidal pipes. Most of the frictional pressure drop data can be represented by the Lockhart–Martinelli correlation (Banerjee et al., 1969; Boyce et al., 1969). In the low flow rate range, the frictional pressure drop multipliers are also dependent on the liquid flow rate, in addition to the Lockhart–Martinelli parameter (Boyce et al., 1969; Awwad et al., 1995; Xin et al., 1996). Recently, Xin et al. (1996) proposed a correlation to account for the effect of liquid flow rate. It was noted that pressure drop multipliers are more significantly affected by liquid flow rate in horizontal coils than in vertical coils.

Only a few studies have dealt with two-phase heat transfer in helicoidal pipes. Among them, Owhadi et al. (1968) conducted experiments regarding forced convection boiling heat transfer in helicoidal pipes. Kozeki (1973) measured film thickness and the boiling heat transfer rate of two-phase annular flow in helicoidal pipes. It was found that the highest heat transfer coefficient appears at the outer side of the coil and the smallest at the inner side of the coil. The heat transfer coefficients at the upper and lower side fall between those two values. In the work by Crain and Bell (1973), forced convection heat transfer to a high-quality two-phase water/stream mixture in the helicoidal pipe was studied. In these three papers, the heat transfer coefficient was correlated as a function of the Lockhart–Martinelli parameter.

Some work on critical heat flux, characteristics of dryout, and the incipient point of boiling has been reported (Unal, 1978; Berthoud and Sreenivas, 1990; Jensen and Bergles, 1981). In the experiments of two-phase flow with phase change, the quality of the mixture changes along the pipe, so it is difficult to obtain fundamental information regarding flow and heat transfer characteristics at given gas and liquid flow rates. Nonetheless, the heat transfer of two-phase flow without phase change is also important in engineering (e.g., heating for the promotion of chemical reactions between gases and liquids, or removing the chemical reaction heat.) To the authors' knowledge, the study conducted by Watanabe et al. (1990) is the only investigation on heat transfer of two-phase flow in helicoidal pipes without phase change. The helicoidal pipes used by Watanabe et al. (1990) had a 10 mm inner diameter and coil diameters of 100 mm, 200 mm, and 400 mm. The coils were oriented vertically, horizontally, and inclined 45 deg from the vertical line. It was found that the local heat transfer coefficient for the horizontal coil varied in the coil circumferential direction, even at high air velocities. In addition, the average heat transfer coefficients were correlated using the Lockhart–Martinelli parameter in three regions for the vertical and horizontal coils.

The heat transfer characteristics of air/water two-phase flow in helicoidal pipe have not been verified for larger pipes, however. The effect of liquid flow rate on the relative heat transfer coefficient has not been carefully investigated. More information on wall temperature and the local heat transfer coefficient is needed to analyze the characteristics of the heat transfer inside helicoidal pipes. In this investigation, three coils with different pipe diameters, coil diameters, and pitches are tested to investigate the heat transfer characteristics of two-phase flow in vertical, horizontal, and inclined helicoidal pipes. Some correlations are suggested based on the experimental data.

Experimental System and Data Reduction

Experimental Apparatus. An experimental system was designed to conduct the two-phase flow and heat transfer experiments. A schematic representation of the flow loop is shown in Fig. 1. Details of this experimental system were described in our previous paper (Awwad et al., 1995). Some modifications were made to run the heat transfer experiments. A welding machine was used as a power source for heating. Another coil was connected to a chilled water line, which was placed into the water tank to remove the heat added to the water at the test section.

The test coils were constructed using 304 stainless-steel tubes. The geometry of the test coils is illustrated in Fig. 2. The tube inner diameter, coil diameter, and pitch were 22.9 mm, 259 mm, and 62.5 mm, respectively, for the first test section; 10.16 mm, 127 mm, and 76 mm for the second test section; and 10.16 mm, 381 mm, and 381 mm for the third test section. The turns of the test sections were 5, 10, and 3 for the first, second, and third test section, respectively. The test sections

Contributed by the Heat Transfer Division for publication in the JOURNAL OF HEAT TRANSFER. Manuscript received by the Heat Transfer Division June 1995; revision received February 1996. Keywords: Forced Convection, Heat Exchangers, Measurement Techniques. Associate Technical Editor: R. A. Nelson, Jr.

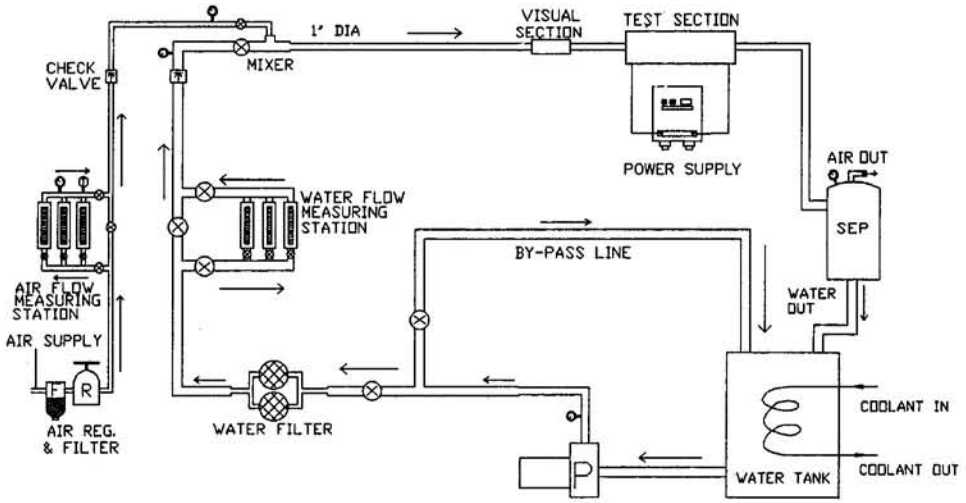

Fig. 1 Schematic representation of the experimental system

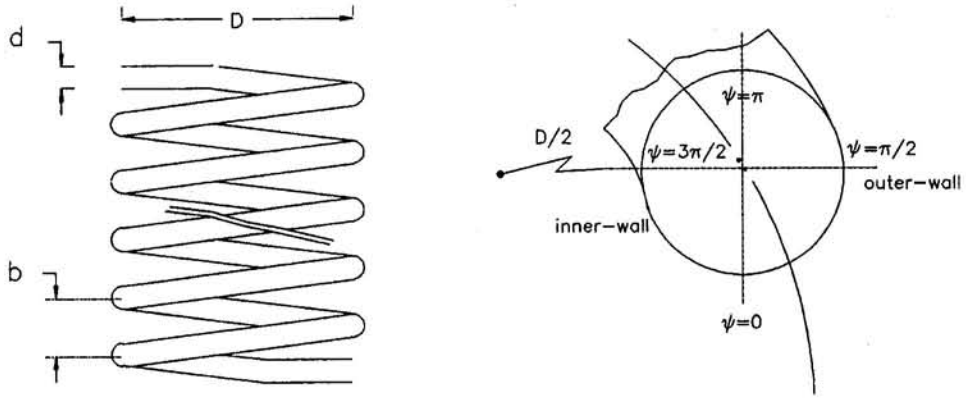

Fig. 2 Geometry of the test sections

were heated with direct current (DC) by the resistance of the tube wall. A voltmeter and an ammeter were used to measure the DC power. Also, the test sections were thermally insulated by wrapping them with several layers of fiberglass. Four (first coil) or two (second and third coils) thermocouples were installed on one cross section every quarter turn, except on the middle turn of each coil, where eight thermocouples were installed on one cross section every eighth circle. In this way, a total of 136, 144, and 88 thermocouples were installed on the first, second, and third test sections, respectively. These thermocouples were attached and electrically insulated on the pipe wall by Epoxy, which has high thermal conductivity and very high electrical resistance. Thus, the effect of heating current on the thermocouple readings was avoided. Inlet and outlet temperatures were measured using two sets of thermocouples with three thermocouples in each set.

Nomenclature

a = thermal diffusivity, m^2/s
b = pitch, m
C = correlating constant
d = tube diameter, m
D = coil diameter, m
dp/dz = pressure drop gradient, Pa/m
De = Dean number = $\mathrm{Re}(d/D)^{1/2}$
f = friction factor = $(dp/dz)d/(\frac{1}{2}\rho u^2)$
h = heat transfer coefficient, $W/(m^2°C)$
k = thermal conductivity, $W/(m°C)$
n = correlating constant
Nu = Nusselt number = hd/k
Pr = Prandtl number = $\mu/(a\rho)$
q = heat flux, W/m^2
Re = Reynolds number = $\rho ud/\mu$
r = pipe radius, m
T = temperature, °C
u = superficial velocity, m/s
X = Lockhart–Martinelli parameter, Eq. (3)
X_R = dimensionless parameter = $1/X$ or $(1/X)\,\mathrm{Re}^{0.667}/100$
z = axial location, m
Z = dimensionless axial location, Eq. (8)
ΔT = temperature difference, °C
θ = dimensionless temperature, Eq. (4)
μ = dynamic viscosity, kg/(m s)
ρ = density, kg/m^3
ψ = coordinate in the cross section of the pipe

Subscripts and Superscripts

b = fluid bulk
G = gas
i = inner surface
in = inlet
L = liquid
m = mean value
o = outer surface
out = outlet
TP = two-phase
w = wall
$\bar{}$ = average value

Before installation, all thermocouples were calibrated against a precision thermometer with an accuracy of ±0.1°C. After installing all thermocouples, the insulated test sections with thermocouples were calibrated again in situ at three fixed temperatures between 20° and 60°C. This was accomplished by passing preheated water at a high flow rate through the test section without heating. Under such conditions, readings of all wall temperatures and the inlet and outlet bulk temperatures should be consistent. The resulting differences among the thermocouple readings were less than 0.5°C.

The pressure drop across the test section and the pressure at the exit was measured by Rosemount pressure transducers to determine the average pressure in the test section for the purpose of selecting thermal properties. The entire output of the thermocouples and pressure transducer was automatically recorded by a Hewlett Packard (HP) data acquisition system, and the data were stored for reduction.

Experimental Procedure and Data Reduction. Preliminary experiments of single-phase flow heat transfer (air and water) were first conducted to verify the experimental system. The experimental data obtained agreed well with the available correlations (Manlapaz and Churchill, 1981; Gnielinski, 1986), exhibiting deviations of less than 12 percent.

The air/water two-phase flow investigation was performed for superficial air/water velocities in the ranges of 0.2–50 and 0.22–2.0 m/s, respectively. The heat balance was checked during each test run. A heat balance deviation of 10 percent was considered acceptable in most of the experiments, except for the cases of very high air flow and low water flow rates. In such cases, a portion of the water evaporates into the air flow as the fluid bulk temperature increases along the pipe. In these cases, the total heat input was used to determine the heat transfer coefficients.

In order to calculate the heat transfer coefficients, temperatures and heat flux values on the interior surface of the helicoidal pipe and the bulk temperature of the fluid were required. The temperature drop, ΔT_W, across the wall of the helicoidal pipe was calculated from the expression:

$$\Delta T_W = T_{WO} - T_{Wi} = \frac{\bar{q} r_i}{k_W}\left(\frac{r_i^2}{r_o^2 - r_i^2}\ln\frac{r_o}{r_i} - \frac{1}{2}\right) \quad (1)$$

where T_{w_o}, T_{w_i}, and $\bar{q}$ are the outer and inner surface temperatures of the pipe and the heat flux on the interior surface of the pipe, respectively; r_i and r_o are the inner and outer radii of the pipe; and k_W is the thermal conductivity of pipe. The local or mean heat transfer coefficients can be calculated by:

$$h = \frac{\bar{q}}{T_{w_i} - T_b} \quad \text{or} \quad \bar{h} = \frac{\bar{q}}{\Delta T_m} \quad (2)$$

It is assumed that T_b increases linearly in the flow direction. This assumption is appropriate to determine the heat transfer coefficient in the fully developed region. ΔT_m is the arithmetic mean value of the differences of wall temperatures and fluid bulk temperatures in the fully developed region.

The Lockhart–Martinelli approach (1949) was used to correlate the two-phase heat transfer coefficient data. The Lockhart–Martinelli parameter is defined as:

$$X^2 = \left(\frac{dp}{dz}\right)_L \Big/ \left(\frac{dp}{dz}\right)_G \quad (3)$$

where $(dp/dz)_L$ and $(dp/dz)_G$ are the pressure gradients of liquid and gas single-phase flow with the same flow rates as if they were to flow in the pipe individually. The relative heat transfer coefficient, defined as the ratio of the heat transfer coefficient for two-phase flow to that calculated as if only the liquid were flowing along the pipe, $\bar{h}_{TP}/h_L$, can be correlated in terms of the Lockhart–Martinelli parameter (X). The $(dp/dz)_L$ and $(dp/dz)_G$ in Eq. (3) are calculated from the friction factor equations provided by Manlapaz and Churchill (1981) for laminar flow and the equation developed by Ito (1959) for turbulent flow in helicoidal pipe.

Experimental Uncertainties. The quantities measured directly included the air and water flow rates, wall and fluid bulk temperatures, and the power input. The air and water flowmeters had an accuracy of ±2 percent. All the thermocouples were calibrated with an accuracy of ±0.1°C; thus, it was estimated that the uncertainty of the temperature difference was less than ±0.2°C. Considering the accuracy of the voltmeter, ammeter, and the heat balance data, the uncertainty of the heat flux calculation ($\delta q/q$) was estimated to be less than 5 percent. The accuracy of other quantities, such as geometric dimensions and thermal properties, were estimated to be 0.5 and 0.25 percent, respectively. Using the method recommended by Moffat (1988), an analysis of the uncertainties of X, Re, and $\bar{h}_{TP}/h_L$ was conducted throughout the experiments. It was estimated that the uncertainty of $\bar{h}_{TP}/h_L$ was 12 percent and the uncertainties of X and Re were about 9.2 and 2.5 percent, respectively.

Results and Discussion

In the following section, the experimental results are presented in terms of dimensionless temperature, θ, and the heat transfer coefficient ratio of the two-phase flow heat transfer coefficient to the heat transfer coefficient of water flow, h_{TP}/h_L, using the air and water flow Reynolds numbers, which are defined by using the superficial velocities of air and water, as parameters. The definition of the dimensionless temperature is as follows:

$$\theta = (T - T_{\text{in}})/(T_{\text{out}} - T_{\text{in}}) \quad (4)$$

where T_{in} and T_{out} are the inlet and outlet fluid bulk temperatures. The heat transfer coefficient of the water flow (h_L) is calculated from the equations provided by Manlapaz and Churchill (1981) for laminar flow and Gnielinski (1986) for turbulent flow, respectively:

$$\text{Nu} = \left\{\left[4.364 + \frac{4.636}{1 + 1342/(\text{De}^2\,\text{Pr}^2)}\right]^3 + 1.816\left(\frac{\text{De}}{1 + 1.15/\text{Pr}}\right)^{3/2}\right\}^{1/3} \quad (5)$$

$$\text{Nu} = \frac{(f/8)\,\text{Re}\,\text{Pr}}{1 + 12.7\sqrt{f/8}(\text{Pr}^{2/3} - 1)}\left(\frac{\text{Pr}}{\text{Pr}_W}\right)^{0.14} \quad (6)$$

In Eq. (6), the friction factor, f, is calculated by the equation

$$f = \left[\frac{0.3164}{\text{Re}^{0.25}} + 0.03\left(\frac{d}{D}\right)^{0.5}\right]\left(\frac{\mu_w}{\mu}\right)^{0.27} \quad (7)$$

where the Reynolds number is defined by the superficial velocity, which equals the volume flow rate divided by the tube cross section area.

The wall temperature distributions are presented in the form of θ versus dimensionless tube axial distance Z, which is defined as

$$Z = z/\pi D \quad (8)$$

The average heat transfer coefficient ratio is presented against the reciprocal of the Lockhart–Martinelli parameter ($1/X$).

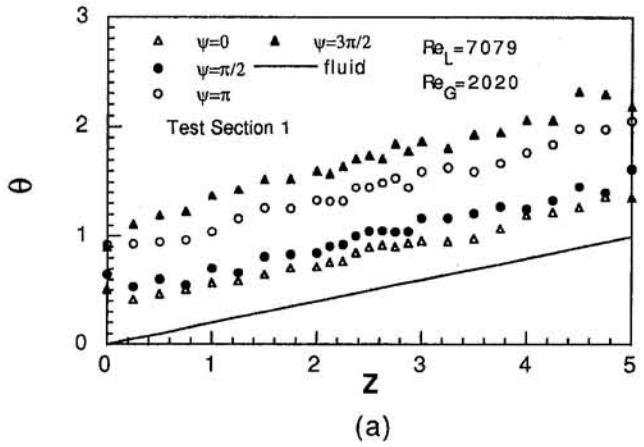

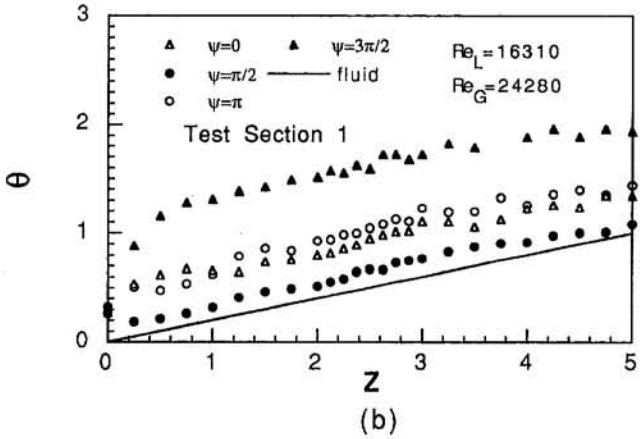

Fig. 3 Axial dimensionless temperature distribution in Test Section 1

Vertical Coils

Temperature Distribution. Dimensionless wall temperature distribution along the tube axial direction is shown in Fig. 3. For each case, the wall temperatures at different circumferential locations and the fluid bulk temperature are displayed for a specific combination of air and water flow Reynolds numbers (Re_L, Re_G). It can be observed that the temperature distribution at different circumferential locations becomes linear and parallel to the fluid bulk temperature distribution line after two turns for the first test section or earlier. For the low air flow rate, the air flows near the top of the cross section due to gravity; therefore, the temperatures at the outer part of the bottom of the tube cross section ($\psi = 0 \sim \pi/2$) are much lower than those at the inner part at the top ($\psi = \pi \sim 3\pi/2$), as shown in Fig. 3(a). For the very high air flow rate (Fig. 3(b)), the inertial force of the air flow overwhelms the force of gravity, and the temperature distribution becomes almost symmetric about the upper part and lower part of the tube cross section. The outer coil wall ($\psi = \pi/2$) and inner coil wall ($\psi = 3\pi/2$) have the lowest and highest temperature, respectively, over the tube cross section, and the temperatures at the top ($\psi = \pi$) and bottom ($\psi = 0$) are in between and near each other.

Local Heat Transfer Coefficient. The circumferential local heat transfer characteristics can be examined in detail from the peripheral local relative heat transfer coefficient distribution versus the circumferential angle, ψ, in the fully developed region. For a fixed water flow Reynolds number, the peripheral relative local heat transfer coefficient distributions for different air flow Reynolds numbers are shown in Fig. 4. For the low and medium air flow Reynolds numbers ($\mathrm{Re}_G < 5000$), the maximum heat transfer coefficient occurs at the outer bottom corner of the tube cross section ($\psi = \pi/4$) and the inner side of the coil is the lower heat transfer region ($\psi = \pi \sim 2\pi$). For a very high air flow Reynolds number ($\mathrm{Re}_G > 15{,}000$), the air flow inertial force and centrifugal force dominate the flow, and the circumferential heat transfer coefficient distribution becomes symmetric about the horizontal axis of the tube cross section. The inner and outer coil walls have the lowest and highest heat transfer coefficients, respectively. This can be explained by the film inversion at high air flow rate and low water flow rate. In such cases, the liquid film thickness in the inner wall region can be about four times that of the outer wall region (Banerjee et al., 1969). This phenomenon was also observed by Awwad et al. (1995) for horizontal helicoidal pipes with the same ranges of flow rates employed in the present experiments.

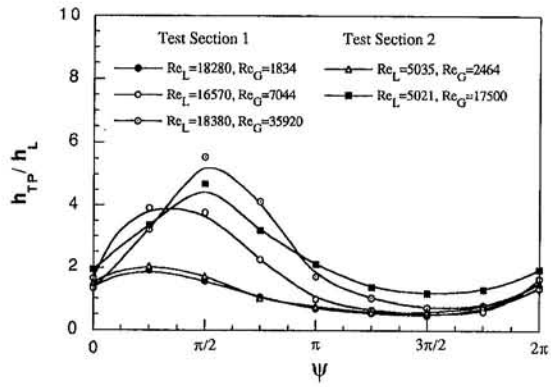

Fig. 4 Peripheral local relative heat transfer coefficient distribution of vertical coils

Average Heat Transfer Coefficient. Figure 5 shows the variation of the average value of $\bar{h}_{TP}/h_L$ versus the reciprocal of the Lockhart–Martinelli parameter ($1/X$). For all the coils, it can be observed that the average heat transfer coefficient ratio is not only a function of the Lockhart–Martinelli parameter but also dependent on the liquid flow Reynolds number. The dependence of the heat transfer coefficient ratio on the liquid flow Reynolds number is more significant for the large-tube-diameter coils (Test Section 1) than the small-tube-diameter coils (Test Section 2 and 3). For a fixed water flow Reynolds number,

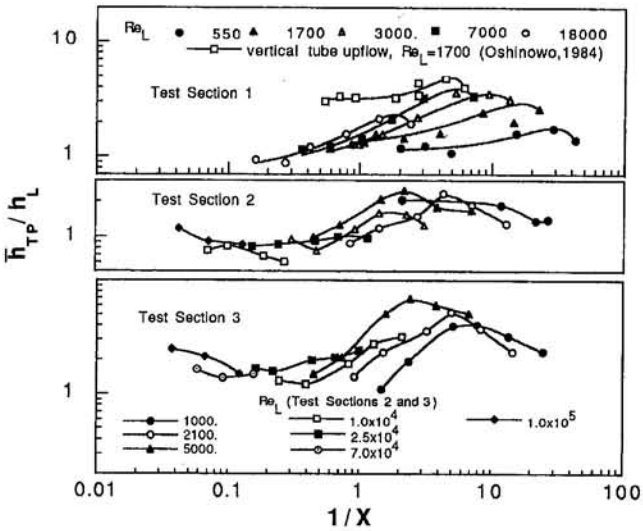

Fig. 5 The $\bar{h}_{TP}/h_L$ variation with $1/X$ of vertical coils

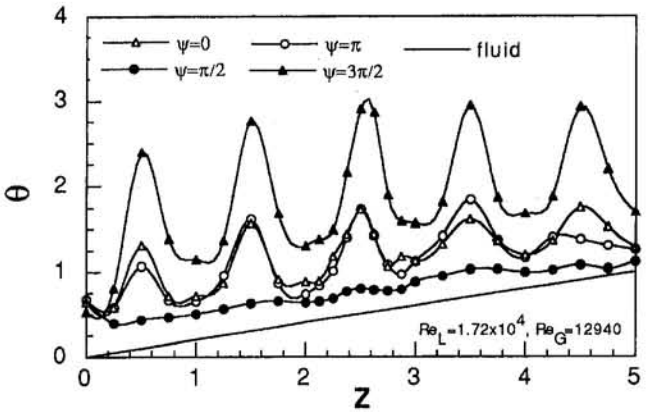

Fig. 6 Wall temperature distribution of Test Section 1 in horizontal orientation

the heat transfer coefficient ratio increases and subsequently decreases as the air flow rate increases. In other words, there is an optimum air flow rate that causes the heat transfer to be fully enhanced at a fixed water flow rate. The similar phenomenon also exits in the two-phase upflow in straight vertical pipe at a low water flow Reynolds number (Oshinowo et al., 1984), which is also shown in Fig. 5 for comparison. This phenomenon is even more obvious in the small-tube-diameter coils (Test Sections 2 and 3) than in the large-tube-diameter coil (Test Section 1). It is important to note that the introduction of very low air flow rates into the water flow can reduce the heat transfer coefficient, as indicated in this figure.

Horizontal and Inclined Coils. Two-phase flow in horizontal and inclined coils is very complicated, and the flow patterns in different cross sections vary (Awwad et al., 1995). In this experiment, the two-phase fluid mixture flows into the coils from the bottom of the coils, then moves up and down periodically through the coils. This flow characteristic causes the tube wall temperatures to fluctuate periodically along the tube axial direction, as shown in Fig. 6 for the low air flow Reynolds number. When the air flow rate is very high, the air flow inertial force overcomes the force of liquid gravity and makes the flow pattern uniform around the coil. Therefore, the wall temperature fluctuations vanish, and the wall temperatures at different circumferential locations become linear in the developed range. For the inclined coil (60 deg from horizontal), the wall temperatures also significantly fluctuate periodically along the flow direction.

Consequently, for horizontal and inclined coils, the peripheral local heat transfer coefficient ratio varies, as indicated in Fig. 7, as examples. It can be observed that the local heat transfer coefficient ratio distributions at both ends of one turn far downstream from the inlet (third turn of the first test section, sixth turn of the second test section) are almost identical. This implies that the distribution pattern is repeatable from one turn to another. Hence, the flow and heat transfer can be thought to be periodically fully developed. The distribution seen in Fig. 7(*b*) confirms that for a high air flow rate, the peripheral distributions at different locations along the flow are almost identical and symmetric.

The results of the average heat transfer coefficient ratio are displayed in Fig. 8 for Test Sections 1 (in horizontal and inclined), 2, and 3, respectively. The dependence of the heat transfer coefficient ratio on the liquid flow Reynolds number, in addition to the Lockhart–Martinelli parameter, is also true for the horizontal and inclined coils. As indicated in Fig. 8, the S-shaped variations of average heat transfer ratio with $1/X$ exist for most of the water flow Reynolds numbers. The same characteristic exists in two-phase downflow in vertical straight pipe (Oshinowo et al., 1984). Even though the local heat transfer characteristics are different, the same results for the average heat coefficient ratio have been obtained in both vertical and horizontal cases of the second and third test sections. Therefore, only the first test section was tested in inclined orientation.

Comparison and Correlations. From the results, it is found that heat transfer behavior is very different for large- and small-tube diameter coils. The results shown in Figs. 5 and 8(*a*) indicate that different orientations have different average heat transfer coefficient curves versus the reciprocal of the Lockhart–Martinelli parameter for the large-tube-diameter coil (Test Section 1). The following correlations were obtained for Test Section 1 in different orientations:

1 For vertical orientation,

$$\frac{\bar{h}_{TP}}{h_L} = 0.1646\ \mathrm{Re}_L^{0.254}\left(\frac{1}{X}\right)^{0.469} \times e^{[-0.0161(\ln(1/X))^2-0.0166(\ln(1/X))^3]} \quad (9)$$

$$0.1 < 1/X < 50,\ 550 < \mathrm{Re}_L < 18{,}000$$

2 For horizontal orientation,

$$\frac{\bar{h}_{TP}}{h_L} = 0.6235\ \mathrm{Re}_L^{0.231} X_R^{-1.335} e^{[0.842(\ln X_R)^2-0.1444(\ln X_R)^3]} \quad (10)$$

$$0.1 < 1/X < 40,\ 550 < \mathrm{Re}_L < 17{,}500$$

where $X_R = (1/X)*\mathrm{Re}_L^{0.667}/100$.

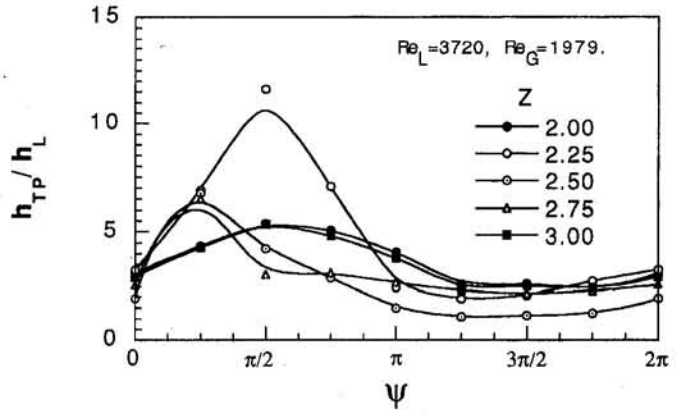

(a) Test Section 1

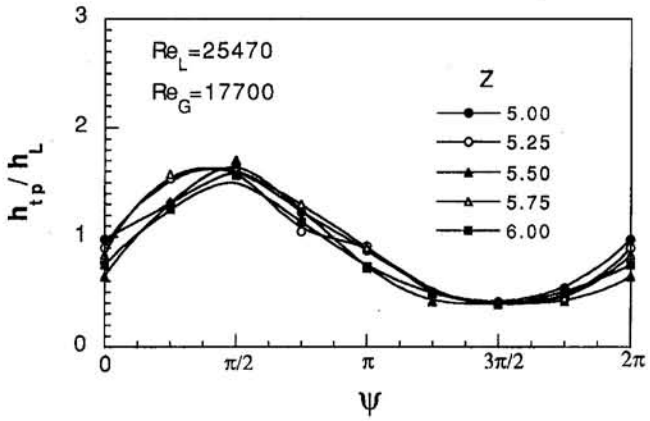

(b) Test Section 2

Fig. 7 Peripheral local relative heat transfer coefficient distribution of horizontal coils

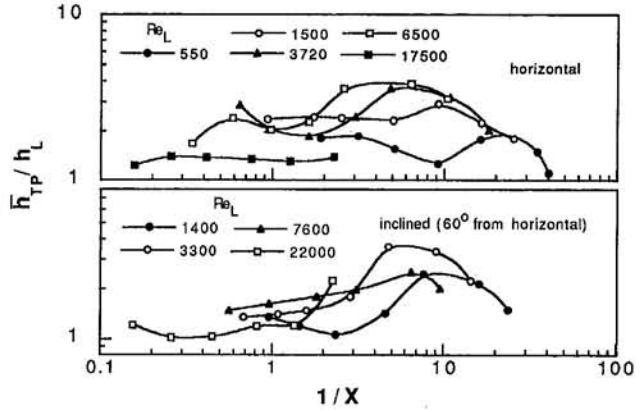

(a) Test Section 1

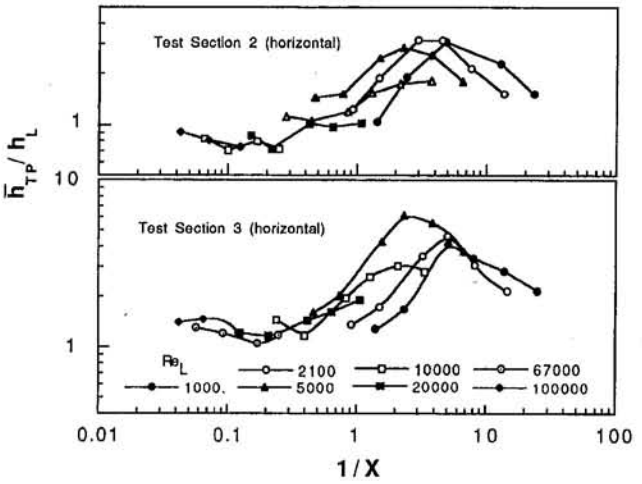

(b) Test Sections 2 and 3

Fig. 8 The $\bar{h}_{TP}/h_L$ variation with $1/X$ of horizontal and inclined coils

3 For inclined orientation (60 deg from the horizontal),

$$\frac{\bar{h}_{TP}}{h_L} = 0.953\ \mathrm{Re}_L^{0.0464}\left(\frac{1}{X}\right)^{0.193} \tag{11}$$

$$0.1 < 1/X < 25,\ 1400 < \mathrm{Re}_L < 22{,}000.$$

For the small-tube-diameter coils, it is found that the orientation has almost no effect on the average heat transfer coefficient. This conclusion leads to a single correlation for small-tube-diameter coils, as follows:

$$\frac{\bar{h}_{TP}}{h_L} = C\ \mathrm{Re}_L^{0.0403}\left(\frac{1}{X}\right)^{0.482} e^{1-0.0445(\ln(1/x))^3} \tag{12}$$

$$0.03 < 1/X < 30,\ 1000 < \mathrm{Re}_L < 1. \times 10^5$$

where $C = 0.887$ and 1.509 for the second and third test sections, respectively. The comparisons between the experimental data and the correlations are displayed in Figs. 9 and 10 for the large-tube-diameter coils and small-tube-diameter coils, respectively. In Fig. 9, n equals 0.254, 0.231, and 0.046 for vertical, horizontal, and inclined orientations, respectively. X_R takes the value of $1/X$ for vertical and inclined cases and $(1/X)\mathrm{Re}^{0.667}/100$ for the horizontal case. A fairly good agreement is obtained, except in Fig. 10 where the data vary by approximately a factor of four at $1/X = 2$. This variation can be explained by the fact that the heat transfer coefficient ratio is dependent on the liquid flow Reynolds number, in addition to the Lockhart–Martinelli

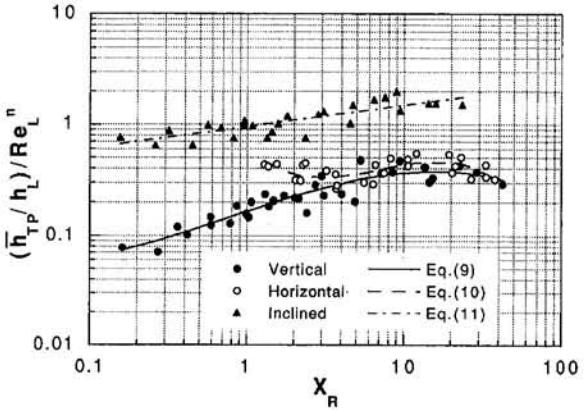

Fig. 9 Comparison of the experimental data with the correlations of Test Section 1

parameter (X). In general, this effect is not significant for small-tube-diameter coils, except the data near $1/X = 2$, where the liquid flow rate effect is very sensitive and cannot be represented by the term $\mathrm{Re}^{0.0403}$ in Eq. (12), which covers the whole data set.

Concluding Remarks

The heat transfer of air and water two-phase flow in helicoidal pipes has been experimentally investigated in the present study for three test sections in vertical, horizontal, and inclined orientations. The large-tube-diameter coil exhibits a different heat transfer behavior than the small-tube-diameter coils. The maximum heat transfer coefficient exists for a fixed water flow rate as the air flow rate changes. Orientation has a significant effect on heat transfer in the large-tube-diameter coil but has little effect in the case of the small-tube-diameter coil. For vertical coil, it has been found that fully developed flow and heat transfer are established after two turns. The tube wall temperatures vary periodically along the tube axial direction for the horizontal and inclined coils. An examination of the peripheral local heat transfer distributions around the coil indicates that flow and heat transfer can be thought of as periodically fully developed far downstream from the inlet. The average heat transfer coefficient results have been evaluated and presented for all the coils. The correlations of the average heat transfer coefficient ratio are proposed for the present experiment ranges.

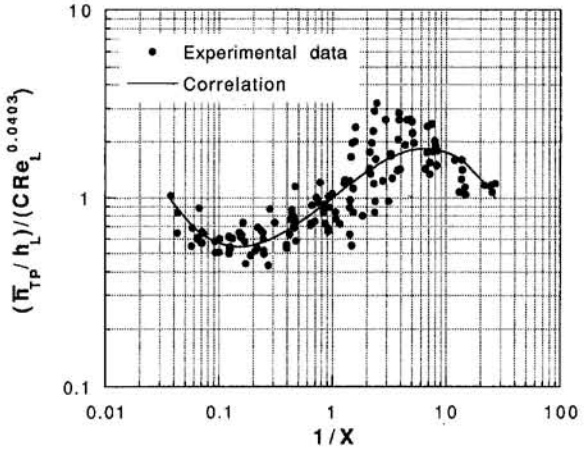

Fig. 10 Comparison of the experimental data with the correlations of Test Sections 2 and 3

References

Awwad, A., Xin, R. C., Dong, Z. F., and Ebadian, M. A., 1995, "Flow Pattern and Pressure Drop in Air–Water Two-Phase Flow in the Horizontal Helicoidal Pipe," ASME *Journal of Fluids Engineering,* Vol. 117, pp. 720–726.

Banerjee, S., Rhodes, E., and Scott, D. S., 1969, "Studies on Concurrent Gas–Liquid Flow in Helically Coiled Tubes, I—Flow Patterns, Pressure Drop and Holdup," *Candian J. of Chemical Engineering,* Vol. 47, pp. 445–453.

Berthoud, G., and Sreenivas, J., 1990, "Characterization of Dryout in Helical Coils," *Int. J. Heat Mass Transfer,* Vol. 33, No. 7, pp. 1451–1463.

Boyce, B. E., Collier, J. G., and Levy, J., 1969, "Hold-up and Pressure Drop Measurement: I. The Two-Phase Flow of Air–Water Mixture in Helical Coils," *Proc. Int. Symp. on Research in Concurrent Gas and Liquid Flow,* E. Rhodes and D. S. Scott, eds., Plenum Press, New York, pp. 203–231.

Crain, B., Jr., and Bell, K. J., 1973, "Forced Convection Heat Transfer to a Two-Phase Mixture of Water and Steam in a Helical Coil," *AIChE Symposium Series,* Vol. 69, No. 131, pp. 30–36.

Gnielinski, V., 1986, "Heat Transfer and Pressure Drop in Helically Heated Tubes," *Proc. 8th IHTC,* Vol. 3, pp. 2847–2853.

Ito, H., 1959, "Friction Factors for Turbulent Flow in Curved Pipes," ASME *Journal of Basic Engineering,* Vol. 81, pp. 123–124.

Jensen, M. K., and Bergles, A. E., 1981, "Critical Heat Flux in Helically Coiled Tubes," ASME JOURNAL OF HEAT TRANSFER, Vol. 103, pp. 660–666.

Kozeki, M., 1973, "Film Thickness and Flow Boiling for Two-Phase Annular Flow in the Helically Coiled Tube," *Proceedings of the International Meeting on Reactor Heat Transfer,* Karsruhe, Germany, Paper No. 16, pp. 351–372.

Lockhart, R. W., and Martinelli, R. C., 1949, "Proposed Correlation of Data for Isothermal Two-Phase Two-Component Flow in Pipes," *Chem. Engng. Prog.,* Vol. 45, pp. 39–48.

Manlapaz, R. L., and Churchill, S. W., 1981, "Fully Developed Laminar Convection From a Helical Coil," *Chem. Eng. Commun.,* Vol. 9, pp. 185–200.

Moffat, R. J., 1988, "Describing Uncertainties in Experimental Results," *Expl. Thermal Fluid Sci.,* Vol. 1, pp. 3–7.

Oshinowo, T., Betts, R. C., and Charles, M. E., 1984, "Heat Transfer in Cocurrent Vertical Two-Phase Flow," *Canadian J. of Chemical Engineering,* Vol. 62, pp. 194–198.

Owhadi, A., Bell, K. J., and Crain, B., Jr., 1968, "Forced Convection Boiling Inside Helically Coiled Tubes," *Int. J. Heat Mass Transfer,* Vol. 11, pp. 1779–1793.

Unal, H. C., 1978, "Determination of Void Fraction, Incipient Point of Boiling and Initial Point of Net Vapor Generation in Sodium-Heated Helically Coiled Steam Generator Tubes," ASME JOURNAL OF HEAT TRANSFER, Vol. 100, pp. 268–274.

Watanabe, O., Tajima, O., Shimoya, M., and Fujita, H., 1990, "Heat Transfer of a Gas and Liquid Two-Phase Flow in Helical Coiled Tubes," *Heat Transfer—Japanese Research,* Vol. 19, No. 5, pp. 492–506.

Xin, R. C., Awwad, A., Dong, Z. F., and Ebadian, M. A., 1996, "An Investigation and Comparative Study of the Pressure Drop in Air/Water Two-Phase Flow in Vertical Helicoidal Pipes," *Int. J. Heat Mass Transfer,* Vol. 39, No. 4, pp. 735–743.

An Experimental Study of Constant-Pressure Steam Injection and Transient Condensing Flow in an Air-Saturated Porous Medium

H. J. H. Brouwers
University of Twente,
Department of Civil Engineering & Management, P.O. Box 217,
7500 AE Enschede, The Netherlands

In this paper the unsteady process of constant pressure steam injection into an air-saturated porous medium is studied experimentally. To this end, vertical glass tubes are packed with dry quartz sand and injected with dry steam. The propagation of the steam front appears to be proportional to $\sqrt{t}$. It is observed that the water saturation is homogeneously distributed and remains below the irreducible water saturation. Furthermore, the theoretical model of Brouwers and Li (1994) of the process is applied to the experiments and extended to take wall effects into account. A comparison of the predicted front penetration and amount of condensed water with the experimental results yields fairly good agreement.

Introduction

Steam flow in porous media with heat transfer and condensation is encountered in many practical applications. Examples are steam injection enhanced oil recovery, geothermal energy production, drying processes, and cleaning contaminated soils.

Marx and Langenheim (1959) and Ramey (1959) were the first to model hot fluid injection into an oil reservoir. Mandl and Volek (1969) assessed the magnitude and importance of heat transfer ahead of the front and performed experiments. Based on the assumption of constant steam front velocity, Menegus and Udell (1985) and Stewart et al. (1989) also obtained an analytic expression, which agreed with their experiments. Morrison (1973) studied transient two-phase flow in porous media. Heat transfer ahead of the front was neglected and the governing equations were solved numerically. Based on a simple single-phase flow model, Brouwers and Li (1994) derived analytical expressions for transient condensing steam flow in a porous medium. Hanamura and Kaviany (1995) derived a constant-pressure steam injection model assuming a quasi-steady behavior and the presence of a liquid slug, and neglecting axial conduction in the dry air-saturated downstream region.

Constant-pressure injection experiments have been reported by Nilson and Montoya (1980), Tsuruta et al. (1988), and Hanamura and Kaviany (1995). Nilson and Montoya (1980) studied the injection of freon vapor into an initially dry sand pack. Tsuruta et al. (1988) and Hanamura and Kaviany (1995) investigated the injection of steam into a dry porous medium formed by packed glass beads. In both studies it was observed that if the condensate saturation is higher than the residual saturation, the superfluous condensate swept as a slug ahead of the steam front.

Constant-pressure steam injection and transient condensing flow in dry sand has, to the author's knowledge, never been reported. This situation is considered to be typical for the cleaning of the vadose zone of polluted subsoils. Accordingly, such experiments have been performed and the results are presented in this paper.

Contributed by the Heat Transfer Division for publication in the JOURNAL OF HEAT TRANSFER. Manuscript received by the Heat Transfer Division June 1995; revision received December 1995. Keywords: Condensation, Moving Boundaries, Porous Media. Associate Technical Editor: R. Viskanta.

Theory

In this section the analysis of Brouwers and Li (1994), concerning the one-dimensional longitudinal and unsteady propagation of the steam front, is recapitulated. The homogeneous and isotropic porous medium was considered to have a constant thickness and to be confined by impermeable and adiabatic top and bottom layers. The process studied involved the displacement of air by dry steam, which partly condenses to heat up the porous medium and initial groundwater.

Throughout their paper, it is assumed that the water saturation S_l is smaller than irreducible (residual or connate) water saturation S_{lr}, so that this liquid water is immobile. This water saturation consists of two parts, that is, the initial water saturation S_{l0}, which is zero, and the formed condensation water saturation S_{lc}. Thus it is assumed that

$$S_l = S_{lc} + S_{l0} < S_{lr} \tag{1}$$

It is noted that the assumption (1) is applicable because S_{lr} can amount to 20-25 percent (Buchlin and Stubos, 1991). Assumption (1) will be verified at the end of this section and in the experimental part of this paper.

The steam is injected at $x = 0$ at constant pressure. The steam flows through the unsaturated matrix to the condensation front (Fig. 1), the position of the front designated by $X_0(t)$, where the ambient pressure P_0 is attained.

There the condensation exists until the porous medium and the groundwater are heated up to the saturation temperature of the steam. It is assumed that the vapor, condensate, and matrix behind and in the front are in thermodynamic equilibrium, since the intraparticle thermal resistance and resistance from fluids to particles are both small.

The pressure drop between injection point and condensation front (typically 0.1 bar) is much smaller than the absolute pressure in the porous medium (ambient pressure), so that T_{sat} may be regarded as a constant. Hence, behind the steam front ($0 \leq x \leq X_0$), the temperature of the porous medium, water and steam, equals T_{sat}. Furthermore, a one-dimensional representation of the process was imposed by assuming the process to be uniform perpendicular to the direction of flow.

Based on an overall mass balance of water (steam and condensate), Darcy's law, and an energy balance at the steam front, the front position was obtained as

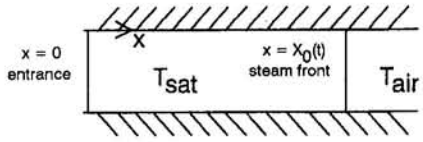

Fig. 1 Steam front position

$$X_0 = \sqrt{a_2}\lambda\sqrt{t} \tag{2}$$

where λ follows from

$$\sqrt{\pi}y \operatorname{erfc}(\lambda y)e^{\lambda^2 y^2} = \lambda \tag{3}$$

with

$$y = \left[\frac{a_2}{4a_1}\right]^{1/2} \equiv \left[\frac{\kappa H_{lat}(P_{in} - P_0)\kappa_{rv}}{2\overline{k}_s(T_{sat} - T_0)\nu_v}\right]^{1/2} \tag{4}$$

and

$$a_1 = \frac{\overline{k}_s}{\overline{\rho_s c}_{ps}} \tag{5}$$

and

$$a_2 = \frac{2\kappa_{rv}H_{lat}(P_{in} - P_0)\kappa}{\overline{\rho_s c}_{ps}(T_{sat} - T_0)\nu_v} \tag{6}$$

and erfc (x), the complementary error function, defined as:

$$\operatorname{erfc}(x) = 1 - \operatorname{erf}(x) = 1 - \frac{2}{\sqrt{\pi}}\int_{\eta=0}^{x} \exp(-\eta^2)d\eta \tag{7}$$

For a given y, which is determined by a_1 and a_2, λ can be determined as the root $\lambda(y)$ of Eq. (3). Subsequently, the steam-front position then follows from Eq. (2). Thus it is sufficient to know how $\lambda(y)$ changes versus y. The dimensionless group y is a measure for the latent heat transport by vapor flow divided by the heat conducted away ahead of the front.

Brouwers and Li (1994) computed $\lambda(y)$ numerically, the results of which are depicted in Fig. 2. Equation (4) reveals that the effect of condensed water in the porous medium on permeability was described with the concept of relative permeability.

The amount of condensed water in the porous medium was determined as:

$$S_{lc} = \frac{\overline{\rho_s c}_{ps}(T_{sat} - T_0)}{H_{lat}\phi\lambda^2\rho_l} \tag{8}$$

Equation (8) reveals that the amount of condensed steam does not depend on the position of the front. Hence, both the water saturation behind the front and the relative permeability of the steam are constant.

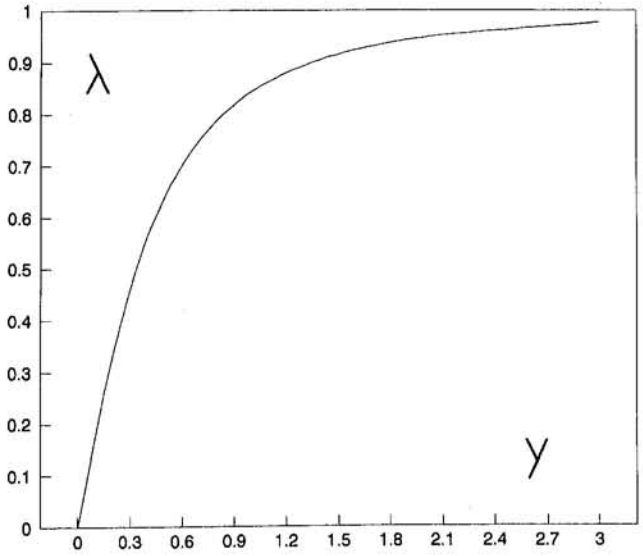

Fig. 2 Graphic representation of $\lambda(y)$

Experimental Results

One-dimensional steam injection experiments into an air-saturated dry sand pack were conducted for model comparison. Dry sand was chosen to avoid having the water saturation exceeding S_{ir}. Two pyrex glass tubes were used, one with a thin wall (tube I) and one with a thick wall (tube II); see Table 1. The length of the tubes (thickness of the packed bed) was about 1 m.

With each tube, two experiments were performed. The tubes were filled with dry quartz sand, because of the spherical grain size and nearly pure silica composition (≈99 percent). The particle size distribution of the sand is given in Table 2. From this distribution and the formula of Fair and Hatch (1933):

Table 1 Glass tubes used

Exp	Tube	D_i	D_o
1	I	50.0 mm	52.5 mm
2	I	50.0 mm	52.5 mm
3	II	51.0 mm	56.0 mm
4	II	51.0 mm	56.0 mm

Nomenclature

a_1 = thermal diffusivity, m^2s^{-1}
a_2 = parameter, Eq. (6), m^2s^{-1}
c_p = specific heat, $Jkg^{-1}K^{-1}$
D_i = inner diameter of the tube, m
D_o = outer diameter of the tube, m
d_p = mean particle size, m
H_{lat} = latent heat of condensation, Jkg^{-1}
k = thermal conductivity, $Wm^{-1}K^{-1}$
L = thickness of packed bed, m
n = power-law coefficient
P = pressure, Pa
S = saturation
T = temperature, K
t = time, s
u = superficial velocity, ms^{-1}
X_0 = position of steam front, m
x = coordinate, m
y = dimensionless group, Eq. (4)
β = parameter, Eq. (14)
η = dynamic viscosity, Pas
κ = absolute permeability, m^2
κ_r = relative permeability
λ = dimensionless parameter
ν = kinematic viscosity, m^2s^{-1}
ρ = density, kgm^{-3}
ϕ = porosity
ϕ = ωολθμε οφ ρατε< μ×σ−+

Subscripts

a = air
c = condensate
g = glass tube
in = injection
l = water
s = pertaining to sand and air
sat = saturation
v = vapor
0 = initial condition

Superscripts

¯ = mean

Table 2 Particle size distribution

Diameter, μm	Mass fraction, percent
>300	2.92
250–300	36.08
212–250	30.21
150–212	28.33
125–150	1.78
90–125	0.39
63–90	0.05
<63	0.00

$$d_p = 0.78\left(\sum \frac{w_i}{d_i}\right)^{-1} \tag{9}$$

an effective particle diameter $d_p = 0.228$ mm follows. In Eq. (9) w_i represents the mass fraction of particles between two sieves with diameter d_1 and d_2, and d_i the geometric mean of the two sieves, or $\sqrt{d_1 d_2}$.

After each experiment the sand was removed and the tube cleaned and dried. For each experiment, new and dried sand was used, so that an initial water saturation of zero was ensured. Both ends of the tube were sealed with removable nylon plates with inlet connections and mounted filter screens to prevent the passage of sand.

Before the steam injection experiments were run, the permeability of the dry sand bed was determined by measuring the pressure drop of air flow across the sand pack for various flow rates and pressure drops. The Reynolds number ranged from 1.2 to 2.2. The permeability was determined via

$$\kappa = \frac{4\eta_a P_{in} L \phi_{in}}{\pi D_i^2 (P_{in}^2 - P_0^2)}, \tag{10}$$

which takes into account the compressibility of the air. ϕ_{in} is the volume flow rate at the entrance of the column. The permeability of the packed beds ranged from 6.6×10^{-11} m^2 to 8.6×10^{-11} m^2 and the porosity from 43 to 45 percent; see Table 3. The porosity was determined by comparing the bulk density of the packed column and the density of the sand. In Table 4 the physical properties of the sand are tabulated. With the porosity and the effective particle diameter (see Eq. (9)), the permeability can also be computed with the Kozeny–Carman equation (Buchlin and Stubos, 1991):

$$\kappa = \frac{d_p^2 \phi^3}{181(1-\phi)^2} \tag{11}$$

In Table 3 the computed κ are also included. One can see the fair agreement between the κ values based on the air flow measurements and the κ values based on the particle size distribution and the Kozeny–Carman equation. In what follows the values obtained with the air flow measurements will be employed.

During the steam injection experiments, to prevent heat losses to the surroundings, approximately 20 mm of insulation was wrapped around the tube. A small stripe was uncovered to permit visual inspection and determination of the steam front. Immediately after the front, in the region passed by, by the front, this small stripe was closed with insulation as well. As soon as the steam front had attained the top of the tube, the steam injection was stopped.

In a low-pressure steam generator distilled water was evaporated, providing steam with a maximum absolute pressure of 4 bar. This steam was reduced in pressure, and premature condensation of the superheated steam in the supply channels (ID 0.25 in.) was prevented by electrical resistance heating.

Dry steam was injected with an absolute inlet pressure of 1.2 bar. With a thermometer the steam temperature at the entrance of the tube was measured, showing a slight and negligible superheat of the steam (of order 3°C).

The initial temperature T_0 of the sand pack was around 20°C. The ambient pressure P_0 was measured with a mercury barometer and ranged from 1.004 to 1.024 bar.

In Figs. 3 and 4 the experimentally observed position of the steam front is depicted against the elapsed time for the experiments with tube I and II, respectively. One can see that the position of the steam front by good approximation varies with the square root of time indeed for all experiments. This remark is in qualitative agreement with the theory; see Eq. (2). In the next section the measured results are compared quantitatively with theory.

The effective permeability of sand bed with condensate, $\kappa_{rv}\kappa$, was measured 24 hours after the experiment by measuring the pressure drop of air in the wet column at ambient temperature, yielding values of κ_{rv} ranging from 0.54 to 0.73 (Table 3). This procedure is acceptable as Piquemal (1994) concluded that air–water relative permeabilities at room temperature are in accordance indeed with steam–water relative permeabilities at elevated temperatures.

The amount of condensate in the tube was computed by measuring the increase in weight of the tube due to the condensation of water. From this information experimentally determined values of the water saturation were obtained, which are listed in Table 3.

The relative permeability and water saturation are generally related by:

$$\kappa_{rv} = (1 - S_l)^n \tag{12}$$

With κ_{rv} and S_l known ($S_l = S_{lc}$, since $S_{l0} = 0$), n can be computed with the help of Eq. (12), the result is included in Table 3. One can see that the magnitude of n is in the range found in the literature (Buchlin and Stubos, 1991; Falta et al., 1992). Note that $1 - S_l$ corresponds to S_v.

These measured water saturations are in fact averaged values within the tube. In order to investigate the homogeneity of the water saturation in the sand pack, and possible transport of water, a fifth experiment was executed with tube II. To create a larger amount of condensate, the sand was densely packed ($\phi = 0.41$) by intense vibrating and the tube was not insulated. During the experiment it was verified that the steam front is planar. The maximum distance between foremost and hindmost front position amounted to only a few mm.

After the experiment the average water saturation was determined in the same way as for experiments 1–4; see Table 5. In addition, after the tube cooled down, samples of the sand were taken at the bottom (where the injection takes place), the middle and the top of the tube. By drying these samples (105°C)

Table 3 Experimental data and computed κ, n, and S_{lc}

Exp	κ [m^2]	κ_{rv}	ϕ	S_{lc}	β	κ [m^2]	n	S_{lc}
	Experiments					Eq. (11)	Eq. (12)	Eq. (18)
1	7.4×10^{-11}	0.54	0.45	0.133	1.150	8.6×10^{-11}	4.24	0.126
2	6.6×10^{-11}	0.62	0.45	0.140	1.148	8.6×10^{-11}	3.12	0.128
3	8.6×10^{-11}	0.73	0.44	0.146	1.293	7.8×10^{-11}	2.04	0.149
4	6.7×10^{-11}	0.69	0.43	0.157	1.387	7.0×10^{-11}	2.17	0.156

Table 4 Properties of quartz sand, air, and glass tube

	Sand	Air	Glass
k, W/mK	8.8	0.0257	1.17
ρ, kg/m^3	2650	1180	2500
c_p, J/gK	1000	1007	840

and measuring the weight loss, the water saturation at these three locations is obtained. In Table 5 the results are summarized.

The values of Table 5 indicate that indeed the water saturation is higher than with experiments 1 and 4, due to greater heat loss. Furthermore, one can see that the water saturation is practically constant in the tube, confirming a prediction of the presented model. Table 5 also shows that, even for the large water saturation, no water has been transported as a slug ahead of the front. This contrasts with the experiments of Nilson and Montoya (1980), Tsuruta et al. (1988), and Hanamura and Kaviany (1995), who observed a liquid slug. Obviously, here the water saturation is still smaller than the irreducible saturation. This observation of S_{ir} being larger than 0.21 corresponds with values of S_{ir} found in the literature (Buchlin and Stubos, 1991). As water has not been swept for $S_l \approx 0.21$, it can be assumed that this was not the case either in experiments 1–4 where $S_l < 0.16$. This conclusion is confirmed by the observation during experiments 1 to 5 that no water was leaving the column at the exit. The immobile water phase formed a major assumption of the one-phase flow model of Brouwers and Li (1994).

In order to determine the temperature in the dry sand ahead of the front, two experiments have been performed with five equidistant thermocouples placed in the center of the sand pack. The measurements revealed that the dry sand is at ambient temperature up to the moment the steam front passes by. So, in the column a sharp temperature rise occurs at the steam front, implying negligible axial conduction ahead of the front.

Model Validation

In order to compare the theory with the experimental data, the properties appearing in a_1 and a_2 need be assessed. Both in a_1 and a_2 several physical properties appear. In a_2 also the effective permeability $\kappa_{rv}\kappa$ figures, which was obtained experimentally with the help of the air flow–pressure drop measurements 24 hours after the experiment, as explained in the previous section.

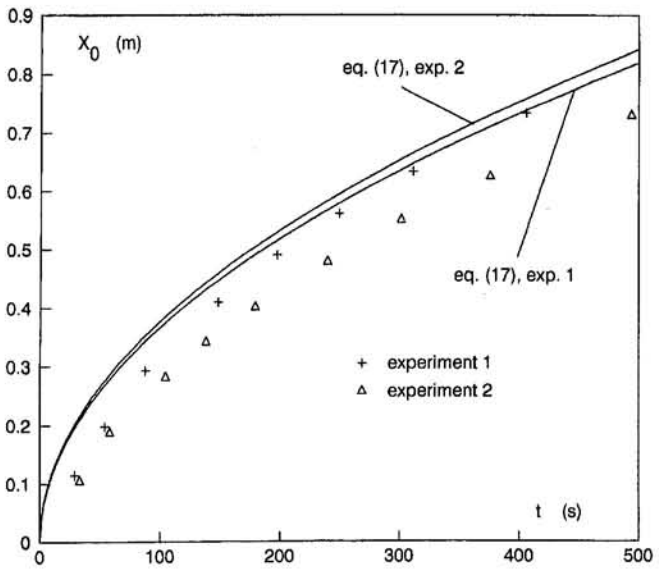

Fig. 3 The experimentally measured steam front position in tube I and the pertaining theoretical predictions

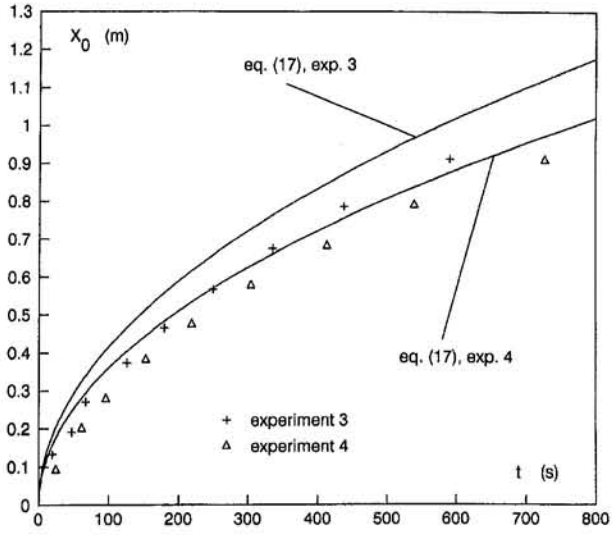

Fig. 4 The experimentally measured steam front position in tube II and the pertaining theoretical predictions

The physical properties appearing in a_1 were evaluated at P_0 and T_0 (ambient conditions), as these conditions prevail ahead of the front. The effective thermal conductivity $\overline{k}_s$ is computed with the model of Zehner and Schlünder (1970). This procedure yields values of $\overline{k}_s$ of 0.270 W/mK to 0.301 W/mK. The mean heat capacity $\overline{\rho_s c_{ps}}$ is obtained by adding the weighed contributions of sand and air. Both $\overline{k}_s$ and $\overline{\rho_s c_{ps}}$ depend on the porosity of the packed sand.

The properties appearing in a_2 were evaluated at the mean conditions between entrance and steam front, i.e., $(P_{in} + P_0)/2 (\approx 1.1$ bar) and T_{sat} (depends on P_0, $T_{sat} \approx 100°C$). The physical properties of the steam were taken from V.D.I. (1991).

With a_1 and a_2 known, y was computed to have a value ranging from 40 to 47. Subsequently, values of λ greater than 0.999 followed from Eq. (3). These values of λ, which are nearly unity, imply that all liberated latent heat at the front is available for heating up the sand pack, and that axial heat losses are negligible (Brouwers and Li, 1994). This result is in agreement with the measured temperature profile in the dry sand.

A first comparison of experimental data with theory showed that the progress of the front is slower than expected theoretically. This can be explained by the heat needed to heat up the walls of the glass tube and heat loss to the surroundings. This supposition is confirmed by the fact that the theoretical S_{lc}, following from Eq. (8), equals about 0.11. Table 3 reveals that after the experiment, depending on the used tube, $S_{lc} = 0.13$–0.16 is measured. This result implies that more steam has condensed than is needed for heating up the sand pack. One can also see that this effect is more pronounced for the thick-walled tube. Accordingly, a modification of the theory is presented to take account of the heating up of the glass tube.

Table 5 Measured average water saturation, and water saturation at three positions in the tube (experiment 5)

Tube	S_{lc}
Average	0.194
Bottom	0.219
Middle	0.189
Top	0.204

As has been said, $\lambda \approx 1$, implying that all liberated latent heat is used to heat up the sand and the glass tube at the front. An energy balance at the front yields:

$$\rho_v u_v H_{lat} = \overline{\rho_s c}_{ps} \beta (T_{sat} - T_0) \frac{dX_0}{dt} \tag{13}$$

In this equation the term β reckons with the heating up of the glass tube:

$$\beta = 1 + \frac{\rho_g c_{pg}}{\overline{\rho_s c}_{ps}} \left[\frac{D_o^2}{D_i^2} - 1 \right] \tag{14}$$

The steam flow to the front obeys Darcy's law:

$$\frac{X_0 u_v \eta_v}{\kappa_{rv} \kappa} = P_{in} - P_0 \tag{15}$$

Combining Eqs. (13) and (15), inserting Eq. (6), solving the differential equation, and applying the initial condition

$$X_0|_{t=0} = 0 \tag{16}$$

yields:

$$X_0 = \left(\frac{a_2 t}{\beta} \right)^{1/2} \tag{17}$$

The amount of condensed water in the porous medium can be obtained from an energy balance of liberated latent heat and heat required to heat up packed sand and tube wall, yielding:

$$S_{lc} = \frac{\overline{\rho_s c}_{ps} (T_{sat} - T_0) \beta}{H_{lat} \phi \rho_l} \tag{18}$$

Equations (17) and (18) are modifications of Eqs. (2) and (8), respectively, and account for the heating-up of the tube wall in case $\lambda = 1$. That is, $\lambda = 1$ when the thermal conductivity ahead of the front (or resistance to vapor flow) is negligibly small. In Table 3 β is given for both tubes, confirming that β is highest for the experiments with the thick-walled tube.

Note that axial conduction in the glass tube, as well as the sand bed, can be neglected. This can be verified by considering the poor thermal conductivity of the pyrex glass (Table 4).

Now it is possible to compare the theoretical prediction of the steam front position (Eq. (17)) with the experimental observations. In Fig. 3 the results of experiments 1 and 2 with tube I are presented with the applicable theoretical predictions. In Fig. 4 experiments 3 and 4 with tube II are summarized. The theoretical lines do not coincide as for each experiment ϕ, κ, κ_{rv}, etc. (and hence also a_2) have different values.

One can readily see that the theoretical predictions of the position of the steam front agree well, at least qualitatively, with the observed position. Particularly for the experiments with tube II, there is good agreement. The worst prediction of the steam front is found with experiment 2, and corresponds to the worst agreement between the predicted and measured amounts of condensate; see Table 3. A part of the discrepancy can be attributed to the inaccuracy of the measurements. The uncertainty analysis in the appendix reveals that the maximum relative error of the front position, dX_0/X_0, is 7.5 percent.

Conclusions

In this paper the constant-pressure steam injection into a dry and air-saturated porous medium has been investigated experimentally. To measure the vertical upward flow of the steam front, a test setup and two vertical glass tubes packed with quartz sand have been used.

A comparison of the experimental results reveal that the conduction ahead of the front can be neglected. Furthermore, the heating of the glass walls, on the other hand, has a substantial effect on the steam front position and amount of condensed water.

In order to account for this effect, a simple modification of the theory by Brouwers and Li (1994) is proposed. A comparison of the predicted steam front position and condensed water by this modified theory with the experimental result yields fairly good agreement.

Furthermore, it has been verified that the water saturation remains below the irreducible saturation and is homogeneously distributed in the sand pack. These features formed the basis of and were predicted by, respectively, the one-phase flow model of Brouwers and Li (1994).

Acknowledgments

The author is indebted to Messrs. A. F. B. Zijlstra and H. Menkehorst, who performed the experimental runs.

References

Brouwers, H. J. H., and Li, S., 1994, "An Analysis of Constant Pressure Steam Injection in an Unsaturated Porous Medium," *Proc. 10th Int. Heat Transfer Conf.*, G. F. Hewitt, ed., Brighton, Vol. 5, pp. 219–224.

Buchlin, J. M., and Stubos, A., 1991, "Phase Change Phenomena at Liquid Saturated Self Heated Particulate Beds," in: *Modelling and Applications of Transport Phenomena in Porous Media*, Chap. 3, J. Bear and J. M. Buchlin, eds., Kluwer Academic Publishers, Dordrecht.

Fair, G. M., and Hatch, L. P., 1933, "Fundamental Factors Governing Streamline Flow of Water Through Sand," *J. Am. Water Works*, Vol. 25, pp. 1551–1565.

Falta, R. W., Pruess, K., Javandel, I., and Witherspoon, P. A., 1992, "Numerical Modeling of Steam Injection for the Removal of Nonaqueous Phase Liquids From the Subsurface. 2. Code Validation and Application," *Water Resources Research*, Vol. 28, pp. 451–465.

Hanamura, K., and Kaviany, M., 1995, "Propagation of Condensation Front in Steam Injection Into Dry Porous Media," *Int. J. Heat Mass Transfer*, Vol. 38, pp. 1377–1386.

Holman, J. P., 1978, *Experimental Methods for Engineers*, 3rd ed., McGraw-Hill, New York.

Kline, S. J., and McClintock, F. A., 1953, "Describing Uncertainties in Single-Sample Experiments," *Mech. Eng.*, Vol. 75, Jan., pp. 3–8.

Mandl, G., and Volek, C. W., 1969, "Heat and Mass Transport in Steam-Drive Processes," *Soc. Pet. Eng. J.*, Mar., pp. 59–79.

Marx, J. W., and Langenheim, R. H., 1959, "Reservoir Heating by Hot Fluid Injection," *Trans. AIME*, Vol. 216, pp. 312–315.

Menegus, D. K., and Udell, K. S., 1985, "A Study of Steam Injection Into Water Saturated Capillary Porous Media," ASME HTD-Vol. 46, pp. 151–157.

Morrison, F. A., 1973, "Transient Multiphase Multicomponent Flow in Porous Media," *Int. J. Heat Mass Transfer*, Vol. 16, pp. 2331–2342.

Nilson, R. H., and Montoya, P. C., 1980, "Experiments on Transient Condensing Flow Through a Porous Medium," ASME JOURNAL OF HEAT TRANSFER, Vol. 102, pp. 489–494.

Piquemal, J., 1994, "Saturated Steam Relative Permeabilities of Unconsolidated Porous Media," *Transport in Porous Media*, Vol. 17, pp. 105–120.

Ramey, H. J., 1959, Discussion on the paper by Marx and Langenheim, *Trans. AIME*, Vol. 216, pp. 364–365.

Stewart, L. D., Basel, M. D., and Udell, K. S., 1989, "The Effect of Gravity on Steam Propagation in Porous Media," ASME HTD-Vol. 91, pp. 31–42.

Tsuruta, T., Narazaki, K., and Masuoka, T., 1988, "Transient Condensing Two-Phase Flow Through an Initially Subcooled Porous Medium," *JSME Int. J.*, Series II, Vol. 31, pp. 81–87.

V. D. I., 1991, *V. D. I. Wärmeatlas (6. Aufl.)*, V. D. I. Verlag GmbH, Düsseldorf [in German].

Zehner, P., and Schlünder, E. U., 1970, "Wärmeleitfähigkeit von Schüttungen bei mäßigen Temperaturen," *Chemie Ing. Techn.*, Vol. 42, pp. 933–941 [in German].

APPENDIX

Uncertainty Analysis

The uncertainty analysis presented here follows the procedures described by Kline and McClintock (1953) and Holman (1978). The primary experimental data, such as P_0, P_{in}, and T_0 are used to calculate the desired (dimensionless) quantities a_1, a_2, y, λ, and $X_0(t)$. The uncertainty in these calculated results is obtained by considering the uncertainties in the primary measurements and is discussed below.

The uncertainty in a calculated result I, which is a function of the independent variables $i_1, i_2, \ldots, i_n$, reads:

$$\left[\frac{dI}{I}\right]^2 = \left[\frac{\partial I}{\partial i_1}\frac{di_1}{I}\right]^2 + \left[\frac{\partial I}{\partial i_2}\frac{di_2}{I}\right]^2 + \ldots + \left[\frac{\partial I}{\partial i_n}\frac{di_n}{I}\right]^2 \tag{A.1}$$

where $di_1, di_2, \ldots, di_n$ represent the uncertainties in the quantities $i_1, i_2, \ldots, i_n$.

The uncertainty in a_2, denoted by da_2, depends on $d\kappa_{rv}\kappa$, $d\rho_s c_{ps}$, dP_0, dP_{in}, dT_{sat}, dT_0, dH_{lat}, and $d\nu_v$; see Eq. (6). The effective permeability of the wet sand $\kappa_{rv}\kappa$ is measured separately via flow and pressure drop measurements; see Eq. (10). Uncertainties in the physical properties, geometric properties, ambient pressure, and temperatures are much smaller than the uncertainty of the inlet pressure and gas flow, and are therefore neglected. Application of Eq. (A.1) to a_2 and $\kappa_{rv}\kappa$ produces:

$$\left[\frac{da_2}{a_2}\right]^2 = \left[\frac{dP_{in}}{P_{in} - P_0}\right]^2 + \left[\frac{d\kappa_{rv}\kappa}{\kappa_{rv}\kappa}\right]^2 \tag{A.2}$$

$$\left[\frac{d\kappa_{rv}\kappa}{\kappa_{rv}\kappa}\right]^2 = \left[\frac{P_{in}^2 + P_0^2}{P_{in}^2 - P_0^2}\right]^2 \left[\frac{dP_{in}}{P_{in}}\right]^2 + \left[\frac{d\phi_{in}}{\phi_{in}}\right]^2 \tag{A.3}$$

P_{in} and P_0 in Eq. (A.2) reflect the pressures during the steam front measurements (pressure drop amounts to 0.2 bar). P_{in} and P_0, appearing in Eq. (A.3), are the pressures during the air flow measurements, which took place 24 hours after the steam front measurement ($P_{in} - P_0$ is about 1.4 bar).

The inaccuracy in front position is mainly caused by the inaccuracy in a_2. Applying Eq. (A.1) to Eq. (2) yields:

$$\frac{dX_0}{X_0} = \frac{da_2}{2a_2} \tag{A.4}$$

With the help of Eqs. (A.2)-(A.4) the relative inaccuracy of the lines drawn in Figs. 3 and 4 can now be assessed. This uncertainty is much larger than the uncertainty in measured front position and time, which are depicted in both figures as discrete symbols.

The gas flow is measured with the aid of a rotameter with an inaccuracy $d\phi_{in}$ of 100 l/h, and the inlet pressure with a bourdon pressure gage with an inaccuracy dP_{in} of 0.02 bar. Hence, for the experimental data of Figs. 3 and 4 the maximum dX_0/X_0 amounts to 0.075.

A Pore-Network Study of Bubble Growth in Porous Media Driven by Heat Transfer

C. Satik[1]

Y. C. Yortsos

Petroleum Engineering Program
Department of Chemical Engineering,
University of Southern California,
Los Angeles CA 90089-1211

We present experimental and theoretical investigations of vapor phase growth in pore-network models of porous media. Visualization experiments of boiling of ethyl alcohol in horizontal etched-glass micromodels were conducted. The vapor phase was observed to grow into a disordered pattern following a sequence of pressurization and pore-filling steps. At sufficiently small cluster sizes, growth occurred "one pore at a time," leading to invasion percolation patterns. Single-bubble (cluster) growth was next simulated with a pore-network simulator that includes heat transfer (convection and conduction), and capillary and viscous forces, although not gravity. A boundary in the parameter space was delineated that separates patterns of growth dictated solely by capillarity (invasion percolation) from other patterns. The region of validity of invasion percolation was found to decrease as the supersaturation (heat flux), the capillary number, the thermal diffusivity, and the vapor cluster size increase. Implications to continuum models are discussed.

Introduction

Flows in porous media that involve liquid-to-gas phase change occur in many problems of interest. The phase change can be brought about by solute diffusion, where the supersaturation is supplied by pressure reduction (see Li and Yortsos, 1994, 1995a, b), or by heat conduction, where the phase growth is controlled by the rate of heat supply. The latter include problems in enhanced boiling heat transfer (Thome, 1990), flows in geothermal systems (Schubert and Straus, 1979; Straus and Schubert, 1981), heat pipes (Ogniewicz and Tien, 1979; Udell, 1983, 1985), and severe nuclear reactor accident scenarios (Dhir and Catton, 1977). In this paper we consider the second problem with particular emphasis on single-bubble growth.

As with other porous media processes, this problem can be studied at three different levels: (1) the single-pore level, where the emphasis is on the mechanics of gas-phase nucleation, film and corner flows, wetting phenomena, and the distribution of phases within single pores; (2) the pore-network level, where the emphasis is on the integration of events in an interacting ensemble of pores, where pore network topology is predominant; (3) the continuum level, where the emphasis is on the average behavior of the system in terms of variables such as heat fluxes, temperature, and saturation levels.

Most of past efforts have addressed the continuum level, where the pore-space dynamics are lumped into relative permeability and capillary pressure functions imported from the isothermal, immiscible displacement literature (Bau and Torrance, 1982; Udell, 1985; Stubos et al., 1993; see also Epstein, 1994). This approach has certain shortcomings: (1) In enhanced boiling experiments, the porous layers might not be extensive enough for the volume-averaging implicit in the continuum approach to be valid; (2) the relative permeability and capillary pressure functions are taken to be independent of the rates of heat transfer. This assumption may not be valid.

Experimental investigations also focused on macroscale quantities (Sondergeld and Turcotte, 1977; Straus and Schubert, 1981; Tung and Dhir, 1990). As in pool boiling (Thome, 1990), the relation between heat flux and applied superheat has been sought. Over porous surfaces the boiling curves are smoother than in typical pool boiling, while a substantial hysteresis exists in vaporization and condensation cycles (Afgan et al., 1985; Fukusako et al., 1986; Kovalev et al., 1987). Enhanced boiling data have been related to the mechanisms of pool boiling over smooth surfaces, but little effort has been devoted to analyzing the micromechanics in porous media. Thus, although fundamental to a variety of applications, the underlying mechanisms at the pore and pore-network levels are still poorly understood. The latter include the onset of nucleation, the configuration of vapor and liquid phases within single pores or networks of pores, the roles of heat transfer, capillarity, phase equilibria and superheat rates.

Contrary to growth in the bulk (Plesset and Prosperetti, 1977) or in effective media (Li and Yortsos, 1994; Epstein, 1994), the patterns of growth of the vapor phase in porous media are expected to be disordered and not compact. We expect a similarity with external *drainage* patterns (displacement of a *wetting* fluid by an externally injected *nonwetting* fluid). These depend on the viscosity ratio and the capillary number, $Ca = u\mu/\gamma$, where u is the injection velocity, μ is viscosity, and γ is the interfacial tension, as follows: At low Ca, where capillarity controls, the pattern obeys the well known *Invasion Percolation (IP)* (Wilkinson and Willemsen, 1983), where the interface advances by always occupying the perimeter pore throat with the smallest capillary barrier (the largest radius in the case of cylindrical throats). Given a pore network of specified sizes, therefore, this pattern is deterministic and can be readily identified. As viscous forces increase (larger Ca), the displacement pattern evolves toward the other limiting regime of *viscous fingering* (in the case of negligible viscosity of the injected phase), which can be described by *Diffusion-Limited-Aggregation (DLA)* (e.g., see Feder, 1988, and Lenormand, 1990). We expect similar patterns in the growth of a gas phase, with the important exception that the driving force here is the applied superheat, thus growth is *internally* rather than *externally* driven.

To model bubble growth at the pore network level, Kovalev et al. (1987) used the unrealistic model of a bundle of parallel capillaries, which differs little from a single-pore model. Parlar and Yortsos (1987) applied percolation theory to steam injec-

[1] Current address: Department of Petroleum Engineering, Stanford University, Stanford CA 94305-2220.

Contributed by the Heat Transfer Division for publication in the JOURNAL OF HEAT TRANSFER. Manuscript received by the Heat Transfer Division October 1994; revision received December 1995. Keywords: Boiling, Multiphase Flows, Porous Media. Associate Technical Editor: V. K. Dhir.

tion, while Styrikovich et al. (1990) used percolation scaling laws for boiling in porous media. Satik and Yortsos (1991) modeled slow (quasi-static) growth also using percolation theory, and included nucleation and phase behavior, but only limited aspects of heat transfer. All these studies were limited to very low superheats, where temperature gradients are sufficiently small for fluid distributions to change in a quasi-static fashion, as required by percolation theory. This assumption is likely to fail in many applications. In this paper, we describe the alternative of a pore-network simulation, the results of which can elucidate the relevant physics in the more general case.

Pore-network simulation has been quite successful in displacements in porous media (Lenormand et al., 1988). In the context of phase change, however, such models were only recently used (Li and Yortsos, 1995a) in a study of diffusion-driven bubble growth. The process of interest to this paper shares common mechanisms with the latter, although there are also important differences, e.g., the importance of heat conduction in the solid matrix, and the generally faster rates of growth (with consequences for convection, etc.) in the heat transfer-driven problem. These aspects are explored here. We present experimental and theoretical studies of heat transfer-driven bubble growth in porous media, with emphasis on the pore-network level. In this context, a "bubble" refers to a singly connected, vapor-occupied region in the porespace with irregular, in general, geometry, and will also be referred to as "cluster." The paper is organized as follows: First, we present experimental results from etched-glass micromodel experiments, which help us formulate rules for the development of the pore-network simulator. Subsequently, we describe pore-network simulation, based on which the sensitivity of the results to process parameters is analyzed. Finally, the boundary in the parameter space that delineates the validity of the various patterns, and notably of percolation, is described.

Experimental

Visualization studies in two-dimensional etched glass micromodels were conducted to identify the key mechanisms at the pore-network level during bubble growth. Experiments with glass micromodels have been successfully used in the past (see Buckley, 1990, for a review). The micromodels are fabricated by etching a desired pattern on a glass plate and fusing it with another glass plate to create a pore network. The pattern consists of a network of nodes (sites or pores) of variable size connected to neighboring nodes by links (bonds or throats) also of variable size. Various geometries and topologies can be constructed, with a typical network being square or triangular containing 100×200 pores. In our study, the patterns were square networks with pore sizes randomly distributed in the interval 600–1200 μm and throat sizes in the interval 100–600 μm. However, because of various uncertainties during the fabrication process (glass defects, etching, and fusion nonuniformities), the actual pore geometry of the glass micromodel was not identical to the etched pattern.

All boiling experiments were performed by keeping the micromodel horizontal. One end was kept at constant subcooled conditions, with provisions for liquid outflow from an outlet port, so as to maintain a constant outlet pressure. To induce boiling, the opposite side was subject to a heat flux. Heat losses were partly minimized by covering all sides of the micromodel with silicon rubber, except for the top surface, where a double-panel glass was used for visualization (see Satik, 1994, for details). A mixture of ethyl alcohol (boiling point of 78.5°C) and a coloring dye was used. The key steps in the experiment involved: (1) saturation of the micromodel with a deaerated mixture, and (2) visualizing the growth process after application of the side heat flux.

The process begins with the onset of a nucleation event. This is likely to proceed by a heterogeneous mechanism from pore surface irregularities (cracks, scratches, pits, etc.), containing pre-existing or trapped gases. Depending on various factors, a number of nucleation centers may exist. In our experiments, usually only one nucleation event occurred and the problem studied was one of single-bubble growth. Figure 1 shows consecutive snapshots of vapor phase growth in a single pore. The gas phase first forms somewhere on the pore walls. Then, it grows in a radially symmetric fashion while still within the pore body (Fig. 1(*a*)). As the converging part of the pore throat geometry is encountered, the interface starts deforming to conform with the capillary characteristics of the pore throats, although it keeps a locally spherical geometry (Fig. 1(*b*)). This step terminates when the pore body becomes completely filled, at which time invasion of a neighboring throat commences (Figs. 1(*c*) and 1(*d*)). This *pore-filling* step is one of the two key steps repeatedly observed during subsequent growth.

Following the pore-filling step, the vapor–liquid interface advances to occupy a neighboring pore provided that the capillary barrier of the connecting throat is exceeded, which is achieved by an increase in the pressure of the vapor. During this *pressurization* step, there is little flow, the vapor–liquid menisci remain in a stable configuration in the converging pore geometries (Fig. 1(*c*)), and there is an increase of the vapor pressure (and temperature). The step continues until the capillary barrier at the perimeter throat is exceeded, at which time the adjacent pore is invaded. In the terminology of drainage, this rapid event is known as a *rheon* (see Dullien, 1992). Depending on the parameter values, the simultaneous penetration of multiple pores is also possible. Following penetration, the vapor volume is redistributed among previously occupied and newly penetrated pore bodies, the interface accordingly ad-

Nomenclature

A_{ij} = cross-sectional area of the bond connecting adjacent sites i and j, L^2
a_{ik} = cross-sectional area of the bond connecting liquid site i with solid site k, L^2
Ca = capillary number
C_p = specific heat, $L^2T^{-2}K^{-1}$
d = heat transfer coupling parameter
G = flow conductance, L^2
Ja = Jakob number
k = thermal conductivity, $MLT^{-3}K^{-1}$
l = bond length, L
L_v = latent heat, L^2T^{-2}
M = molecular weight of water, $Mmole^{-1}$
n = number of moles
P = pressure, $ML^{-1}T^{-2}$
q = heat flux, MT^{-3}
Q = total net heat flow rate, ML^2T^{-3}
r = radius, L
R = gas constant, $L^2T^{-2}mole^{-1}K$
R^* = characteristic radius, L
R_g = radius of gyration, L
R_g^p = percolation boundary, L
t = time, T
T = temperature, K
u = velocity, LT^{-1}
V = volume, L^3
α = heat transfer coefficient, $MT^{-3}K^{-1}$
γ = surface tension, MT^{-2}
δ = boundary layer thickness, L
κ = k_S/k_L
μ = viscosity, $ML^{-1}T^{-1}$
ρ = density, ML^{-3}

Subscripts

b = bond
L = liquid
s = site
S = solid
V = vapor
0 = far-field

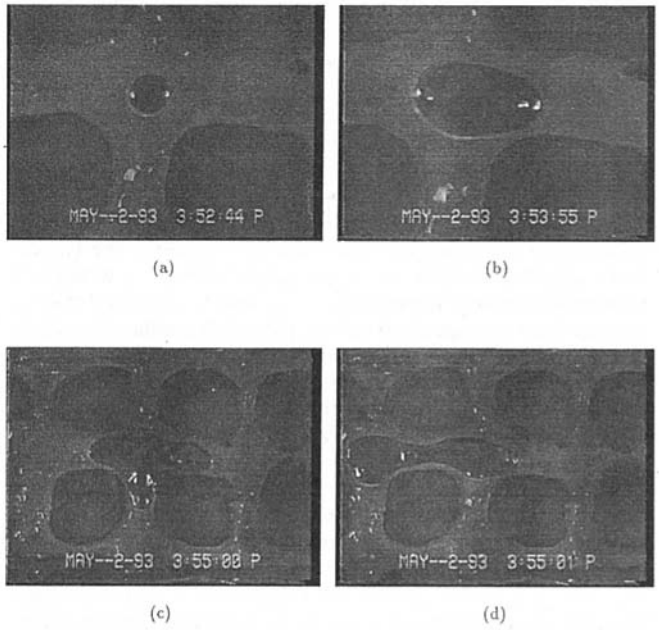

Fig. 1 Visualization of bubble growth in a single pore following a nucleation event: (*a*, *b*) pressurization step, (*c*, *d*) penetration step (rheon); vapor denoted by black

justing by a slight retreat of the menisci from all perimeter pore throats (Fig. 1(*d*)). Then, the previous pore-filling step begins until all newly penetrated pore bodies are completely filled by vapor. Pore-filling and pressurization steps are continuously repeated.

Figure 2 shows a typical macroscopic bubble growth pattern obtained in the experiments. Contrary to growth in the bulk, the patterns are quite disordered and not compact. They differ according to two modes of growth: One involves a "one-pore-at-a-time" advance, where following pressurization, there is penetration of a single pore throat. As discussed below, this occurs when viscous forces are sufficiently weak, so that variations in the liquid pressure at the perimeter sites are not sufficiently large for other pore throat barriers to be exceeded at the same time. Such patterns can be described by IP. The other mode involves the simultaneous penetration of multiple throats and occurs at sufficiently large cluster sizes or superheats, where viscous forces dominate. The limiting pattern in such cases is DLA, in which even adjacent pore throats can be simultaneously invaded. This pattern was not observed. In the experiments, the interface occasionally retreated rapidly as a result of possible condensation events induced by heat losses. This feature was also observed in related steam injection experiments and it was also attributed to heat losses (Kong et al., 1992).

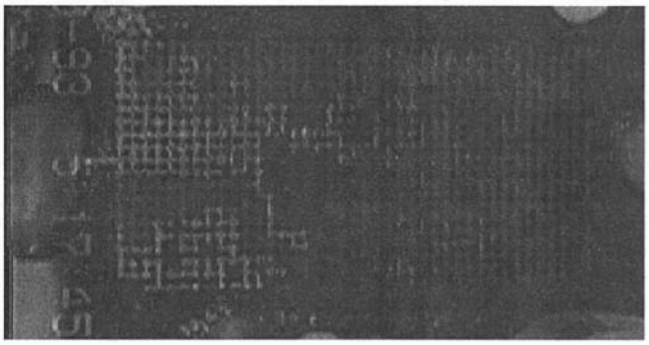

Fig. 2 Visualization of a vapor bubble ("cluster") in an etched-glass pore network; vapor denoted by white; the pattern is irregular and much different from a single bubble in the bulk

In the next section we discuss pore network models that simulate heat transfer-driven bubble growth in the porespace. These models incorporate the mechanisms identified in the visualizations described above.

Pore-Network Simulation

To simulate this process we used pore-network models (Lenormand et al., 1988; Blunt and King, 1991; Li and Yortsos, 1995b). Here, the pore space is modeled by a network composed of sites (pores) and bonds (throats) of various sizes randomly distributed, much like in the glass micromodels. For the problem of phase change in porous media, one additionally needs to discretize the solid. For this purpose, a square network of solid sites and bonds, complementary to that of the pore space, was constructed to account for heat capacity and heat conduction in the solid matrix, respectively. A schematic of the two lattices is shown in Fig. 3. The key elements of the algorithm are as follows:

1 Variables, such as pressure and temperature, are assigned to sites (pores or solid sites) only. They represent lumped variables, volume-averaged over the respective site volumes (much like a finite-differencing scheme). Vapor–liquid menisci reside in sites at the cluster perimeter, whose occupancy by vapor may be partial or complete, as determined from fluid flow and heat transfer.

2 Pore throats provide the capillary pressure barrier to the motion of the menisci and also control transport. A pore throat is invaded when the capillary pressure across the meniscus in that throat exceeds for the first time the capillary barrier

$$P_{Vi} - P_{Lj} = \gamma \mathcal{H}_{ij} \tag{1}$$

where i and j denote adjacent sites at the cluster perimeter and $\mathcal{H}$ is the throat mean curvature (equal to $2/r_{ij}$ for a cylindrical throat).

3 The pressure field is solved from mass and momentum balances. For a liquid-filled site not in the bubble perimeter, the continuity equation was discretized as follows:

$$\sum_j A_{ij} u_{i \to j} = 0 \tag{2}$$

where A_{ij} is the cross-sectional area connecting adjacent sites i and j and the summation is over all sites j (4 for square lattices).

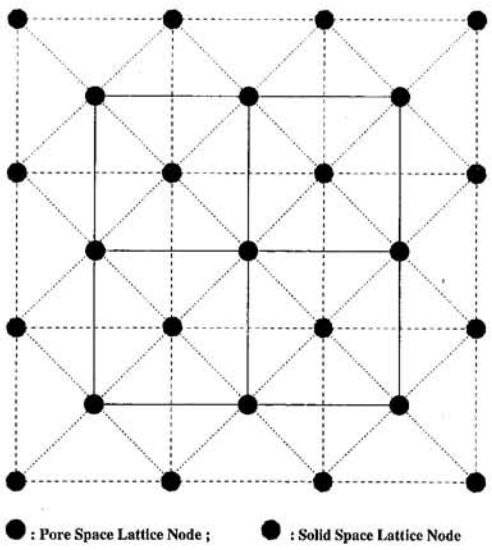

Fig. 3 Schematic of the square network used to approximate the pore space and the complementary network used to approximate the solid space; in each network, sites are denoted by circles, bonds by straight lines

For a liquid-filled site on the perimeter, Eq. (2) was modified to also account for vaporization, by adding a sink term as follows:

$$\sum_{j \neq k} A_{ij} u_{i \to j} + \frac{k_L \pi r_{ik}^2}{\rho_L L_v l} (T_L^i - T_V^k) = 0 \quad (3)$$

where the right-hand side denotes the heat transfer-driven phase change and k is the vapor-occupied site. Assuming creeping flow in the absence of gravity, the equation for the flow velocity from i to j is $u_{i \to j} = (G_{ij}/\mu)\,[(P_i - P_j)/l]$, where G_{ij} is the flow conductivity (in general a geometric parameter), l is the bond length, P is pressure, and pressure drops were assumed associated with throats only. For viscous (Poiseuille-type) flow in a capillary, $G_{ij} = r_{ij}^2/8$. A similar equation also applies for the vapor, although here we treated the vapor at constant pressure.

4 Heat transfer by conduction and convection in the liquid phase, and by conduction in the solid phase was simulated. Sufficiently fast heat transfer is assumed for the gas phase, so that its temperature is spatially uniform. In the liquid-occupied lattice, we assigned T_L to the sites of the porespace lattice and T_S to the sites of the solid lattice, and expressed the energy balance for site i as follows:

$$(\rho C_p)_L V_s^i \frac{\partial T_L^i}{\partial t} + \sum_j A_{ij}(u_{i \to j} T_L^i + q_{L,i \to j}) = -\alpha_{SL} \sum_k a_{ik}(T_L^i - T_S^k) \quad (4)$$

Here, the conductive flux is $q_{L,i \to j} = k_L(T_{L,i} - T_{L,j})/l$ for throats joining sites i and j. Solid-liquid coupling between site i and its neighboring solid site k is expressed through the last term in Eq. (4), where a_{ik} refers to the area between liquid site i and adjacent solid site k, and the heat transfer coefficient, α_{SL}, was taken as *constant*. The energy balance in the solid was discretized likewise, with conductive heat fluxes approximated by $q_{S,i \to j} = k_S(T_{S,i} - T_{S,j})/l_S$, where k_S is solid conductivity and l_S is a length scale of the solid "grain" (also assumed constant). Heat conduction in the solid occurs through the bonds of the solid lattice, which "bridge" adjacent solid grains (sites). Heat transfer at the vapor–solid interface was assumed much weaker than the solid–liquid coupling ($\alpha_{SV} \ll \alpha_{SL}$) and was neglected.

5 Only *one* nucleation center was activated (see Satik and Yortsos, 1991, and Li and Yortsos, 1995b, for the more general case). Local phase equilibria are assumed, so that the Clausius–Clapeyron equation $P_{Vi} = P_{vo}(T_V)$ applies, where P_{vo} is the saturation pressure.

6 The net molar influx to the cluster, $dn/dt = \dot{Q}/ML_v$, is calculated by evaluating the total net heat flow rate, $\dot{Q}$, which contains heat transfer at the vapor–solid interface and at all vapor–liquid perimeter sites. The rate dn/dt determines the changes in the pressure or volume of the cluster (bubble) via an equation of state (here taken to be the ideal gas law), $(d/dt)(P_V V/T_V) = R(dn/dt)$, where R is the ideal gas constant and V the cluster volume. Whether the bubble grows ($dV > 0$), and at which perimeter site (pore-filling step), or the interface remains fixed while the pressure increases ($dP_V > 0$) (pressurization step), depends on whether or not capillary condition (1) is satisfied at the perimeter. If none of the perimeter capillary barriers is reached, the interface remains stationary and the cluster pressure P_V increases at a constant volume. When Eq. (1) is satisfied for the first time a rheon occurs, invasion of the site adjacent to that throat begins, and the pore-filling step commences. During this step, we neglect the capillary pressure in the invaded sites. The liquid is then displaced from the invaded site(s), and both vapor volume and pressure (or temperature) can vary as determined from the heat transfer and fluid flow calculations. When the cluster is sufficiently large, multiple sites may be invaded (and filled) at the same time, in which case pore-filling in each pore is calculated incrementally in small time steps. The entire pressure and temperature fields are needed to determine pore throat penetration and pore-filling, and although pressure drops are not large, they must be computed to account for convection and viscous forces. Details can be found in Satik (1994).

7 The liquid phase may be trapped by the expanding gas cluster. In the numerical algorithm, the volume of the trapped liquid is taken as constant, since the ratio of liquid to vapor densities is large.

Expressed in dimensionless terms, the equations given above give rise to the following dimensionless numbers: the (modified) capillary number $Ca = (k_L l_{\mu L}/\rho_L C_{pL} r^2 \gamma)$ Ja, which expresses the relative importance of viscous to capillary effects, where r is an average bond radius; the Jakob number, Ja, which is a measure of the imposed superheat; the two dimensionless heat transfer coefficients, $d_{SL} = \alpha_{SL} l/k_S$ and $d_{SV} = \alpha_{SV} l/k_S$; and the ratio of thermal conductivities $\kappa = k_S/k_L$. This extends the conventional definition of the capillary number ($Ca = u\mu/\gamma$), by using a heat conduction-driven velocity ($u \sim (k_L l/\rho_L C_{pL} r^2)$ Ja). The expression for the Jakob number depends on the particular application. When the liquid in the far field is kept at a constant temperature and pressure (to be referred to in the following as Case 1), we have $\mathrm{Ja} = \rho_L C_{pL} \Delta T/\rho_V L_v$, where $\Delta T = T_0 - T_{vo}(P_0)$, and T_0 and $T_{vo}(P_0)$ denote far-field temperature and saturation temperature at the far-field pressure, respectively. When a constant heat flux is applied (Case 2), we have $\mathrm{Ja} = \rho_L C_{pL} l_q/\rho_V L_v k_l$, where q is the prescribed heat flux. The sensitivity of the process to these parameters was analyzed.

Results and Discussion

The pore network simulator was subsequently used to examine bubble growth in the two different cases. In the simulations, throat sizes were randomly assigned from a uniform distribution, while pore body sizes were kept constant. In the absence of better information, geometric parameters, such as the throat mean curvature, flow conductivity, etc., were approximated by their expressions in cylindrical geometries. Although certainly different from the glass micromodel values, these parameters are unlikely to affect the qualitative pattern characteristics (e.g., percolation, etc.), while this approximation does not detract from the value of the simulator. In Case 1, the pore space is initially filled with a superheated liquid at a uniform temperature, and far-field temperatures and pressures are prescribed. A square (or radially symmetric) lattice (31×31), all far-field boundaries of which are open to a constant (atmospheric) pressure, was used, with a single nucleation site at the center of the lattice. Typical parameter values were: $k_L = 0.6808$ W/m-K, $\mu_L = 2.4799 \times 10^{-4}$ N-s/m^2, $L_v = 2.2568 \times 10^6$ J/kg, $\gamma = 0.0584$ N/m, $C_{pS} = 8.3732 \times 10^2$ J/kg-K, $k_S = 6.808$ W/m-K, $d_{SL} = 1$, $d_{SV} = 0.01$, $l = 1320$ μm, $R_p^* = 450$ μm, and $R_s^* = 601$ μm. In Case 2, a heat flux is imposed on one side of a rectilinear domain, with no-heat flux boundary conditions imposed on all other boundaries. A constant pressure condition is applied on the opposite boundary, with no-flow conditions imposed on all other boundaries. The initial nucleation site is located at the center of the side where the heat flux is imposed.

Case 1. Fluid distributions at three different stages of bubble growth (and for times equal to 2.45, 2.89, and 7.42 seconds, respectively) are shown in Fig. 4 ($T_0 = 104.44$°C, $P_0 = 1.0133 \times 10^5$ N/m^2 for a superheat of 4.44°C). Corresponding Ja and Ca were 13.52 and 6.30×10^{-5}, respectively. In the figures, sites colored with white or black represent liquid-only or vapor-only occupancy, respectively, while gray denotes partial liquid occupancy. The solid lattice is also indicated in white. All throats are shown in black, regardless of their occupancy. At the completion of a nucleation, bubble growth begins. Heat transfer takes place toward the bubble, to drive the phase change. For the sizes and superheats of the particular simulation, the characteristic times of growth are quite small (of the order

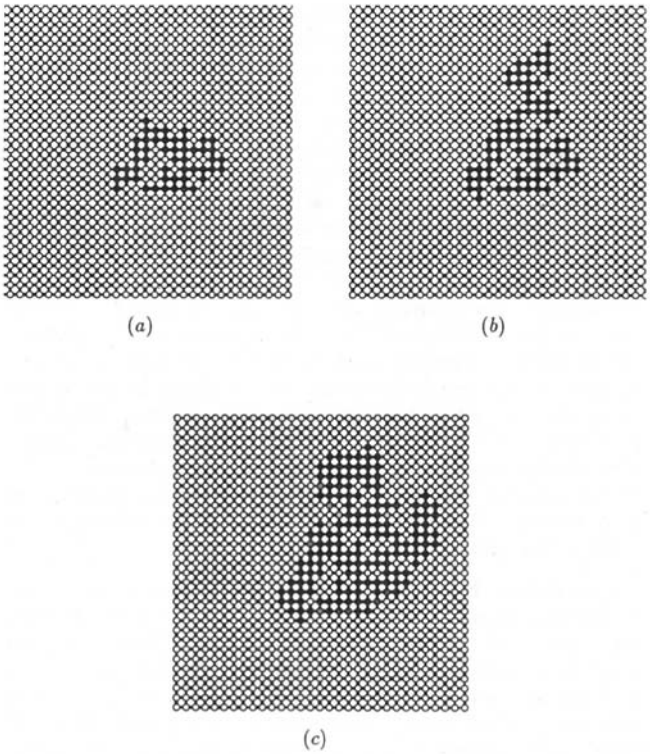

Fig. 4 Fluid distributions at three stages of bubble growth for Case 1 of a fixed far-field superheat

of a few seconds). Despite the fast growth, the patterns during the early part (Fig. 4(a, b)) are of the percolation (IP) type, during which penetration of the throat with the smallest barrier occurs at the end of each pressurization step. This pattern can be identified in advance by tracing the sequence of throats with the smallest barrier (largest radius) which are connected to the nucleation site. Thus, one can readily determine whether the pattern follows IP. As the cluster size increases, multiple pore penetration occurs, some of the pore bodies are partially liquid-occupied (note several perimeter sites in gray) and the corresponding pattern is no longer percolation (Fig. 4(c)).

Fluid temperature, fluid pressure, and solid temperature distributions corresponding to one of these patterns are shown in Fig. 5, where black or white denotes maximum or minimum values, respectively. Figure 5(a) shows that fluid temperatures are quite flat in the liquid-occupied pore space, except for a boundary layer near the bubble, where a temperature gradient develops. The boundary layer was found to increase with a decrease in the Jakob number (see below). The solid temperatures are rather uniform (Fig. 5(b)), due to the strong coupling with the liquid and the high thermal conductivity of the solid. Corresponding fluid pressure distributions are shown in Fig. 5(c). Pressure gradients develop at the growing site (here located at the top of the cluster) in the direction from the bubble to the boundaries, driving liquid outward.

The sensitivity to Ca was examined by independently varying three parameters, liquid viscosity, surface tension, and liquid conductivity, such that the capillary number varied in the same proportion in all cases. Figure 6 shows patterns at four different viscosities ($\mu_L = 2.4799 \times 10^{-5}$, 2.4799×10^{-4}, 2.4799×10^{-3}, and 2.4799×10^{-1} N-s/m^2) and at Ja = 13.52. Corresponding Ca values were 6.30×10^{-6}, 6.30×10^{-5}, 6.30×10^{-4}, and 6.30×10^{-2}, respectively. At low liquid viscosity, a percolation pattern is obtained (Fig. 6(a)). As μ_L increases, the pattern deviates from percolation (Fig. 6(b, c)), and eventually reaches a viscous fingering pattern (at $\mu_L = 2.4799 \times 10^{-1}$ N-s/m^2, Fig. 6(d)). A similar behavior was found for the effect of surface tension and for the effect of liquid conductivity (Satik, 1994). The latter controls the rate of heat conduction in the liquid, hence larger values in liquid conductivity lead to faster heat transfer rates and to an earlier departure from percolation. This behavior is consistent with the definition of the capillary number for phase change problems. Patterns corresponding to the same capillary number were found to be similar (if not identical), regardless of the particular parameter (viscosity, surface tension, or liquid conductivity) in the simulation, indicating that the dimensionless description given above accurately describes the growth process.

To examine the sensitivity to Ja, we independently varied the applied superheat and the latent heat. As the superheat increases, evaporation rates also increase, leading to faster growth and larger displacement rates. As a result, larger pressure drops are induced, which affect the competition between capillary and viscous forces. At sufficiently small superheats (small Ja, hence Ca), capillary forces dominate over viscous, provided that the cluster size is small, thus the growth pattern is of the percolation type. As the superheat increases, viscous forces become stronger and bubble growth patterns deviate from percolation. Similar results were also found for the effect of the latent heat (Satik, 1994), with smaller values of the latent heat leading to faster processes, larger viscous pressure drops, and an earlier departure from percolation. The sensitivity to the latent heat could be of importance at conditions of phase change near the critical point. These simulations show that an increase in Ja leads to an earlier departure from a percolation pattern. However, this is due not so much to an increase in convection, as it is due to the increase in Ca (compare with the definition of Ca). Larger Ja values do produce higher heat convection, which additionally contributes to a faster growth (see also below). However, at least for low Ja, the dominant effect is the dependence on the capillary number, as outlined above. The sensitivity to other parameters was also investigated (see Satik, 1994).

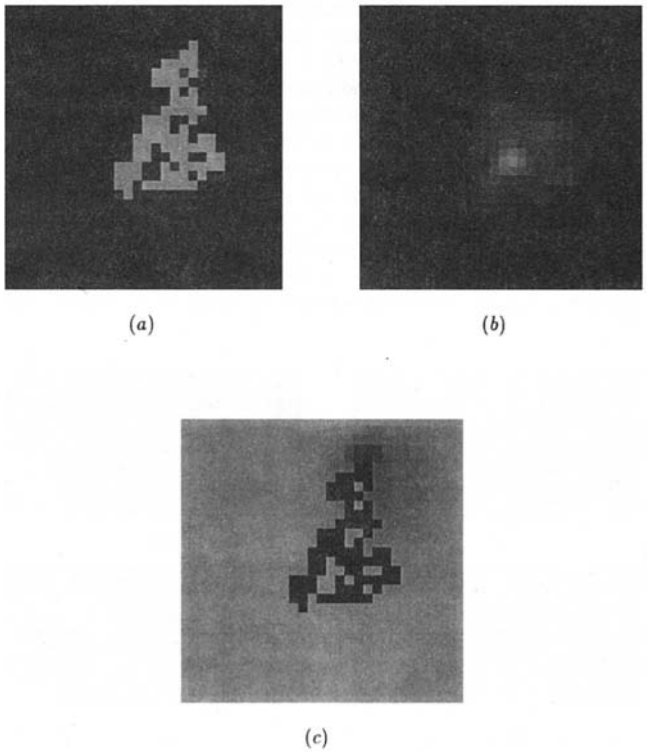

Fig. 5 Fluid temperature, solid temperature, and fluid pressure distributions for the pattern of Fig. 4(b); minimum and maximum values are (a) 100.02 and 104.51°C, (b) 104.37 and 104.44°C, and (c) 14.696 and 14.7041 psi, respectively

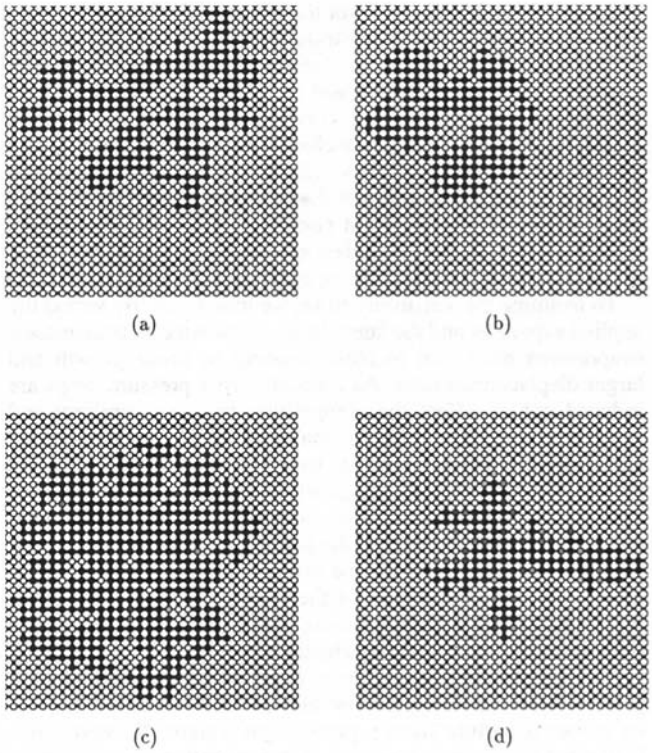

Fig. 6 Growth patterns at four different viscosities: (*a*) $\mu_L = 2.4799 \times 10^{-5}$ N-s/m^2, (*b*) $\mu_L = 2.4799 \times 10^{-4}$ N-s/m^2, (*c*) $\mu_L = 2.4799 \times 10^{-3}$ N-s/m^2, (*d*) $\mu_L = 2.4799 \times 10^{-1}$ N-s/m^2

Case 2. The second case involved application of a heat flux on the left-side of the lattice to simulate the experimental results. A rectilinear two-dimensional lattice (21×42) of the same bond and site distributions as in the previous case was used. Fluid distributions at two different stages of bubble growth for the previous typical parameters and $q = 9.4607 \times 10^4$ W/m^2 are shown in Fig. 7(a, b) ($T_0 = 100$°C, $P_0 = 1.0133 \times 10^5$ N/m^2). Corresponding Ja and Ca values were 558.5 and 2.602×10^{-4}, respectively. In both stages, fast growth was observed with several partially liquid-occupied pores at the perimeter, indicating regimes other than percolation. Although not identical, these numerical patterns are qualitatively similar to the experimental (Fig. 2). A detailed comparison is difficult, due to the uncertainty in the geometric parameters of the glass micromodel and the heat losses, which were not included in the simulations. Corresponding solid temperature and fluid temperature fields for one of the patterns are shown in Figs. 7(c, d), respectively. In Case 2, the applied heat flux is prescribed only on the solid, thus generating a temperature gradient in the solid (and, by extension, to the liquid). Contrary to the smooth temperature field in the solid, however, fluid temperature patterns are disordered due to convection and bubble growth (some of the nonuniformity shown in Fig. 7(c) may be also due to the restricted two-dimensional geometry and the trapped liquid). Fluid pressure fields are similar to Case 1.

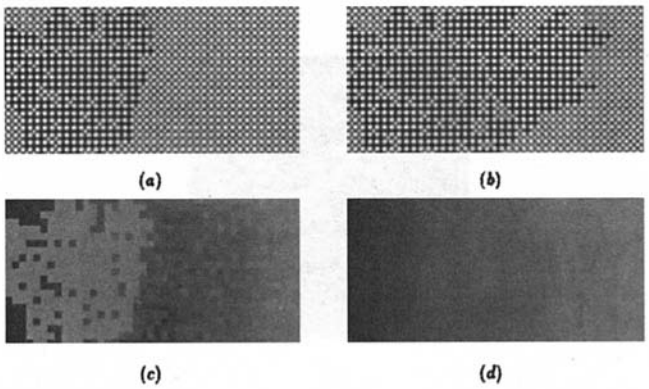

Fig. 7 (a, b) Fluid distributions at two stages of bubble growth for Case 2 of a fixed applied heat flux; (c, d) fluid temperature and solid temperature distributions for the pattern of (a); minimum and maximum values are (a) 99.78 and 107.77°C, (b) 100.07 and 108.29°C, respectively

The sensitivity of these results to the process parameters, notably Ja and Ca, was similar to the previous (see Satik, 1994 for details). For example, the effect of the heat flux, which enters in the definition of Ca, was such that when q is sufficiently small, the pattern is of the percolation type, while as q increases the pattern deviates from percolation and takes various configurations (which here are affected by the lattice size). We must point out that, consistently with the experiments, we have been unable to obtain DLA-type growth at the largest q value tested, and it is doubtful that this can be actually achieved in such problems. Identifying the particular pattern beyond percolation is the subject of current research.

Percolation Boundary. The previous results show that bubble growth patterns follow invasion percolation at relatively small values of Ca and cluster size. In this regime, pores are penetrated "one at a time," the largest available throat (that with the smallest barrier) always being penetrated first, with only one partially vapor-occupied pore during pore filling. At larger sizes, capillary numbers, or superheats, the vapor pressure is sufficiently large for multiple penetration, thus bubble growth patterns deviate from percolation.

To define this transition, we denote the dimensionless (scaled with l) cluster size at the limit of the validity of the percolation regime as the *percolation boundary*, R_g^p. Because of the disordered pattern, we use the radius of gyration of the cluster, $R_g^2 = (1/2N^2) \sum_{i,j} (r_i - r_j)^2$, to quantify bubble size. R_g denotes the root-mean-square radius of the vapor bubble measured from its center of gravity. Figure 8 plots R_g^p versus Ca for various parameters. The curves shown delineate two regimes, one at low values of capillary number and bubble size, described by IP, and another at larger values, the pattern of which is not strictly percolation. All data appear to be close to a single curve in a plot of R_g^p versus Ca (Fig. 8). This suggests that the percolation boundary is mostly a function of Ca. At the same time, this figure shows that the Jakob number does exert an additional indirect effect through the particular heat transfer mechanism (liquid convection and conduction).

To investigate this, we simulated processes where only conduction is considered in the liquid (*quasi-static* conditions) as well as processes where all heat transfer mechanisms (transient, convection, and conduction) were included. Qualitatively, the

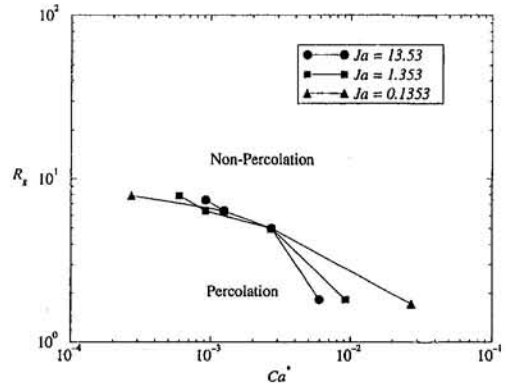

Fig. 8 Percolation boundary plotted versus Ca (both liquid viscosity and Ja were varied)

results are similar to Fig. 8, with the quasi-static results being similar to the case of low Ja and the results including convection being similar to those at higher Ja, namely with a smaller slope. Under quasi-static conditions, the size at the percolation boundary was found to be generally larger, suggesting that percolation patterns last for larger cluster sizes. In a recent study we proposed a scaling theory for the percolation boundary in problems controlled by quasi-static solute diffusion (Satik et al., 1995), where the following scaling was found for three dimensions:

$$R_g^p \sim Ca^{-\nu/(\nu+1)} \tag{5}$$

where the correlation length exponent ν is 0.88 (e.g., see Stauffer, 1985). A result involving logarithmic corrections was obtained for two dimensions. The theory predicts that the cluster size at the percolation boundary, R_g^p, decreases following a power-law (in three dimensions and with logarithmic corrections in two dimensions), as a diffusion-based capillary number increases. The simulations of Fig. 8 are in qualitative agreement with the theory. However, a quantitative agreement is difficult, in view of the fact that the theory is based on statistical physics arguments requiring large sizes, while the present computations are restricted to small sizes.

When convection is included, the deviation from percolation occurs earlier, as a result of faster heat transfer due to the thermal boundary layer becoming smaller. We illustrate this dependence in Fig. 9, which shows temperature profiles for two different values of Ja. In the quasi-static case (Fig. 9(a)), heat transfer occurs over a thick boundary layer, of a size comparable to the effective cluster radius, R_g. When convection increases (Fig. 9(b)), the thermal boundary layer decreases (and ultimately tends to a thickness equal to the pore spacing, which is the computational limit in our discrete approximations at large Ja). Temperature gradients become much larger than in the quasi-static case and lead to faster growth and corresponding stronger viscous effects. We expect that in addition to the indirect effect it exerts through Ca (and which is captured in the quasi-static limit by the power-law of Satik et al., 1995), Ja has also a direct heat transfer effect on the percolation boundary (see also Fig. 8). The scaling of the percolation boundary when convection dominates can be readily obtained (appendix).

Conclusions

In this paper, we have presented visualization experiments and pore network simulations of bubble growth driven by heat transfer. Visualization of boiling in a horizontal etched-glass micromodel was conducted. Bubble growth occurred by two steps (pore filling and pressurization), which were repeatedly followed. We identified two different modes of bubble growth, one in which perimeter throats are penetrated one at a time and patterns obey invasion percolation rules, and another in which multiple throat penetrations at the bubble perimeter are possible.

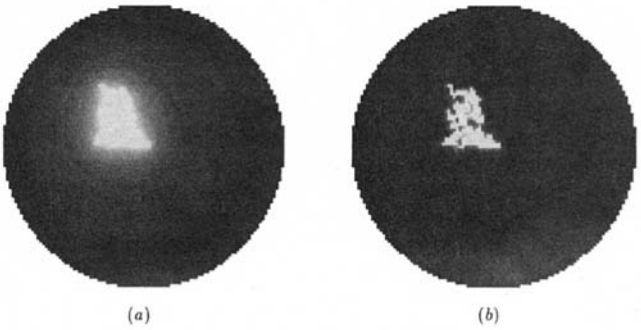

Fig. 9 Effect of Ja on the temperature profiles and the thermal boundary layer: (a) Ja = 0.051 (quasi-static case), (b) Ja = 5.1

A novel pore network simulator was next developed that accounts for heat conduction and convection in the liquid and heat conduction in the solid. Bubble growth under the application of a fixed far-field superheat or an applied heat flux was simulated. It was shown that at sufficiently small values of the cluster size or the capillary number, the growth patterns are of the percolation type, where capillary forces control. When a limiting size (denoted as the percolation boundary) is reached, the patterns deviate from percolation. This boundary was numerically determined and was shown to be mostly a function of the capillary number, Ca, and to a lesser extent of the Jakob number, Ja. These results are applicable in the absence of gravity or capillary instabilities, such as snap-offs.

The results imply that the use of a relative permeability formalism to describe the growth of a vapor phase, using concepts borrowed directly from the isothermal displacement literature, must be carefully examined. Percolation patterns can exist only for sufficiently small sizes or capillary numbers. The latter are modified versions of the more conventional definition, involving the rate of applied superheat, and they can be considerably larger in typical applications than the standard values of $O(10^{-6})$ taken in typical immiscible displacements. Questions of process scale-up, effects of finite sample size, and the merger of discrete and continuum approaches and the rate of heat transfer should be probed with the use of such an approach.

Acknowledgments

This work was partly supported by DOE contract No. DE-FG22-93BC14899, the contribution of which is gratefully acknowledged.

References

Afgan, N. H., Jovic, L. A., Kovalev, S. A., and Lenykov, V. A., 1985, "Boiling Heat Transfer From Surfaces With Porous Layers," *Int. J. Heat Mass Trans.*, Vol. 28, pp. 415–422.

Bau, H. H., and Torrance, K. E., 1982, "Boiling in Low-Permeability Porous Materials," *Int. J. Heat Mass Trans.*, Vol. 25, pp. 45–54.

Blunt, M., and King, P., 1991, "Relative Permeabilities From Two- and Three-Dimensional Pore-Scale Network Modelling," *Transport in Porous Media*, Vol. 6, pp. 407–433.

Buckley, J. S., 1990, *Interfacial Phenomena in Petroleum Recovery*, N. R. Morrow, ed., Marcel Dekker Inc., New York.

Dhir, V., and Catton, I., 1977, "Dryout Heat Fluxes for Inductively Heated Particulate Beds," ASME JOURNAL OF HEAT TRANSFER, Vol. 99, pp. 250–256.

Dullien, F. A. L., 1992, *Porous Media: Fluid Transport and Pore Structure*, Academic Press, New York.

Epstein, M., 1994, "Similarity Solution for Combined Hydrodynamic and Heat Transfer Controlled Bubble Growth in a Porous Medium," ASME JOURNAL OF HEAT TRANSFER, Vol. 116, pp. 516–518.

Feder, J., 1988, *Fractals*, Plenum Press, New York.

Fukusako, S., Komoriya, T., and Seki, N., 1986, "An Experimental Study of Transition and Film Boiling Heat Transfer in Liquid-Saturated Porous Bed." ASME JOURNAL OF HEAT TRANSFER, Vol. 108, pp. 117–124.

Kong, X., Haghighi, M., and Yortsos, Y. C., 1992, "Visualization of Steam Displacement of Heavy Oils in a Hele-Shaw Cell," *Fuel*, Vol. 71, pp. 1465–1471.

Kovalev, S. A., Solovyev, S. L., and Ovodkov, O. A., 1987, "Liquid Boiling on Porous Surfaces," *Heat Transfer—Sov. Res.*, Vol. 19, pp. 109–120.

Lenormand, R., Touboul, E., and Zarcone, C., 1988, "Numerical Models and Experiments on Immiscible Displacements in Porous Media," *J. Fluid Mech.*, Vol. 189, pp. 165–187.

Lenormand, R., 1990, "Liquids in Porous Media," *J. Phys.: Condens. Matter*, Vol. 2, pp. SA79–SA88.

Li, X., and Yortsos, Y. C., 1994, "Bubble Growth and Stability in an Effective Porous Medium," *Phys. Fluids*, Vol. 6, No. 5, pp. 1663–1676.

Li, X., and Yortsos, Y. C., 1995a, "Bubble Growth in Porous Media by Solute Diffusion," *Chem. Eng. Sci.*, Vol. 50, No. 8, pp. 1247–1271.

Li, X., and Yortsos, Y. C., 1995b, "Visualization and Simulation of Bubble Growth in Pore Networks," *AIChE J.*, Vol. 41, No. 2, pp. 214–222.

Ogniewicz, Y., and Tien, C. L., 1979, "Porous Heat Pipe," in: *Heat Transfer, Thermal Control and Heat Pipes*, W. B. Olstad, ed., Progress in Astronautics, Vol. 70, pp. 239–345.

Parlar, M., and Yortsos, Y. C., 1987, "Percolation Theory of Steam–Water Relative Permeability," SPE Paper No. 16969.

Plesset, M. S., and Prosperetti, A., 1977, "Bubble Dynamics and Cavitation," *Ann. Rev. Fluid Mech.*, Vol. 9, pp. 145–185.

Satik, C., and Yortsos, Y. C., 1991, "Percolation Models for Boiling and Bubble Growth in Porous Media at Low Superheats," presented at the 3rd Symposium on

Multiphase Transport in Porous Media, ASME Winter Annual Meeting, Atlanta, GA.

Satik, C., 1994, "Studies in Vapor-Liquid Flow in Porous Media," PhD thesis, University of Southern California, Los Angeles, CA.

Satik, C., Li, X., and Yortsos, Y. C., 1995, "Scaling of Single-Bubble Growth in a Porous Medium," *Phys. Rev. E,* Vol. 51, No. 4, pp. 3286–3295.

Schubert, G., and Straus, J. M., 1979, "Steam–Water Counterflow in Porous Media," *J. Geophysical Res.,* Vol. 84, pp. 1621–1679.

Sondergeld, C. H., and Turcotte, L., 1977, "An Experimental Study of Two Phase Convection in a Porous Medium With Application to Geological Problems," *J. Geophys. Res.,* Vol. 82, pp. 2045–2053.

Stauffer, D., 1985, *Introduction to Percolation Theory,* Taylor & Francis, Inc.

Straus, J. M., and Schubert, G., 1981, "One Dimensional Model of Vapor-Dominated Geothermal Systems," *J. Geophysical Res.,* Vol. 86, No. B10, pp. 9433–9438.

Stubos, A. K., Satik, C., and Yortsos, Y. C., 1993, "Effects of Capillary Heterogeneity on Vapor—Liquid Counterflow in Porous Media," *Int. J. Heat Mass Transfer,* Vol. 36, No. 4, pp. 967–976.

Styrikovich, M. A., Malysenko, S. P., and Andrianov, A. B., 1990, "Nonequilibrium Phase Transitions at Boiling on Surfaces With Porous Coating," *Proceedings of the 9th Int. Heat Transfer Conference,* Vol. 2, Jerusalem, Israel.

Thome, J. R., 1990, *Enhanced Boiling Heat Transfer,* Hemisphere Publishing Co.

Tung, V. X., and Dhir, V. K., 1990, "Experimental Study of Boiling Heat Transfer From a Sphere Embedded in a Liquid-Saturated Porous Medium," ASME JOURNAL OF HEAT TRANSFER, Vol. 112, pp. 736–743.

Udell, K. S., 1983, "Heat Transfer in Porous Media Heated From Above With Evaporation, Condensation, and Capillary Effects," ASME JOURNAL OF HEAT TRANSFER, Vol. 105, pp. 485–492.

Udell, K. S., 1985, "Heat Transfer in Porous Media Considering Phase Change and Capillarity—the Heat Pipe Effect," *Int. J. Heat Mass Trans.,* Vol. 28, pp. 485–495.

Wilkinson, D., and Willemsen, J. F., 1983, "Invasion Percolation: A New Form of Percolation Theory," *J. Phys. A,* Vol. 16, pp. 3365–3376.

APPENDIX

Consider a bubble growth process where convection dominates. If the boundary layer δ is sufficiently thin, the entire perimeter of the cluster participates in heat transfer, as opposed to the effective perimeter in the mean-field approximation of Satik et al. (1995) for the quasi-static case. From percolation theory (Stauffer, 1985; Feder, 1988), the number of perimeter sites N_p scales with size as $N_p \sim R_g^{D_h}$, where the hull exponent D_h equals 1.75 in two dimensions and 2.53 in three dimensions. Based on this, we can directly evaluate the heat transfer rate into the bubble, as $\dot{Q} \sim \pi N_p r^2 (k_L \Delta T/\delta)$. This expression can be used to estimate the average bubble growing velocity, hence the pressure field in the liquid. Satik et al. (1995) developed an expression for the flow field induced by a growing bubble. By substituting in their expression the heat flow rate obtained above, one obtains the following estimate for the typical viscous pressure drop in three-dimensional bubble growth

$$\Delta P_V \sim \frac{k_L \, \mathrm{Ja} \mu}{\rho_L C_{pL} \delta r} R_g^{D_h} \tag{A.1}$$

Clearly, the viscous pressure drop is an increasing function of Ja, k_L, and R_g and a decreasing function of δ, as expected. Using Eq. (A.1), we may now compare viscous and capillary forces and estimate the percolation boundary scaling, by proceeding as in Satik et al. (1995). We obtain the final result

$$R_g^p \sim \frac{\delta}{r} Ca^{-\nu/(1+\nu D_h)} \tag{A.2}$$

Comparison with Eq. (5) shows that in convection-dominated systems the percolation boundary size decreases faster with Ca than in diffusion-dominated systems (compare the slope $\nu/(1 + \nu D_h)$ with $\nu/(1 + \nu)$). Furthermore, convection-dominated problems would involve an additional effect of Ja, which in the theory given above enters indirectly through δ (the limit of which in the present approximation is l). We anticipate that as Ja increases, δ decreases, resulting into an effectively larger Ca, hence in a smaller percolation boundary. Both these observations are consistent with the simulation.

A Variable Heat Flux Model of Heat Transfer in Grinding With Boiling

T.-C. Jen

A. S. Lavine

Mechanical and Aerospace Engineering Department, University of California, Los Angeles, Los Angeles, CA 90095-1597

In grinding processes, the grinding fluid is used to suppress the temperature rise in the grinding zone. Under some circumstances, the grinding fluid may undergo film boiling in the grinding zone, causing the workpiece temperature to rise significantly. The onsets of nucleate boiling and film boiling in the grinding zone are investigated in the present study. A model of heat transfer in grinding was previously developed (Jen and Lavine, 1995), which predicts the temperatures and heat fluxes in the grinding zone. With some modification, this model is used here to predict the occurrence of film boiling of the grinding fluid. The dependence of the workpiece background temperature on the various grinding parameters is explored. The workpiece background temperature distribution along the grinding zone, and comparisons with experimental results, are presented.

Introduction

Thermal damage is one of the main process limitations in grinding. Grinding fluid is usually introduced to lubricate and remove heat from the grinding zone, and thereby reduce the workpiece temperature. However, the grinding fluid may undergo film boiling under some conditions. When this happens, the cooling effect of the grinding fluid diminishes, and a sudden increase in temperature results. The objective of this paper is to model boiling of the grinding fluid and explore how the workpiece temperature is affected.

The physical configuration and coordinate system for a typical grinding wheel and workpiece are shown in Fig. 1. The grinding zone is the region of length l and width b over which the wheel contacts the workpiece. Some typical grinding parameters are shown in Table 1. There are two basic types of grinding: conventional and creep feed grinding. The major distinguishing features of creep feed grinding are the larger depth of cut and the lower workpiece speed.

There has been a substantial amount of research concerning heat transfer in grinding. Snoeys et al. (1978) and Malkin (1984) give detailed literature reviews. Some particularly relevant papers are reviewed here. Ohishi and Furukawa (1985), Yasui and Tsukuda (1983), Shafto et al. (1975), and Powell and Howes (1978) showed experimentally that a sudden rise in workpiece surface temperature was observed when this temperature exceeded a critical value. Lavine and Jen (1991b) used an analytical model of heat transfer in grinding to predict the occurrence of film boiling of the grinding fluid, and to determine whether or not workpiece burn would subsequently occur. This model assumed an abrupt transition between no boiling and film boiling over the entire grinding zone, where film boiling is modeled as dry grinding. Jen and Lavine (1992a) modified this earlier model to allow film boiling over a portion of the grinding zone. However, as indicated by Jen and Lavine (1992b), this model is only valid when the grinding power input is uniformly distributed along the grinding zone. An improved general grinding model was developed (Jen and Lavine, 1995), which accounts for the variation of heat fluxes along the grinding zone, using Duhamel's Theorem. With appropriate modification, this improved model is used in this paper to account for film boiling with variable heat fluxes. The onsets of nucleate boiling and film boiling in the grinding zone are investigated. The dependence of the workpiece background temperature on the various grinding parameters is explored. The workpiece background temperature distribution along the grinding zone, and comparisons with experimental results, are presented.

Theoretical Analysis

When an individual grain moves along the workpiece, heat is generated due to friction and plastic deformation. A model was previously developed to describe how the generated heat is transferred to the workpiece, the grinding fluid, and the abrasive grain (Jen and Lavine, 1995; Lavine and Jen, 1991b). The basic approach is first to develop thermal models for each heat transfer path (i.e., workpiece, grain, and fluid) based on the assumption of uniform heat flux. Each of these separate models includes convection in the direction of motion and conduction in the direction perpendicular to the workpiece surface. One result is a relationship between heat flux, q'', and surface temperature rise, θ, for each heat transfer path, of the form $q'' = h\theta$. The function h will be called a local heat transfer coefficient. Then the "conjugate" heat transfer problem, with varying heat fluxes, is solved using Duhamel's Theorem. The only change in the present model is the treatment of boiling, which will be discussed in the next section.

Heat Transfer to Grinding Fluid. In analyzing the heat transfer from the workpiece to the fluid, it is helpful to recognize that the contact area between the workpiece and the grains is typically only a few percent of the total grinding zone area. Thus, over most of the grinding zone, the fluid comes into contact with the workpiece surface. There is assumed to be a heat flux q_f'' into the fluid from the workpiece surface. This heat flux will first be assumed uniform over the grinding zone, and will be modified later by using Duhamel's Theorem. The heat transfer between the fluid and the grain is neglected.

Assuming that the free-stream fluid velocity is equal to the wheel speed, the Reynolds number based on the grinding zone length (see Table 1) for water-based grinding fluid (kinematic viscosity $= 1.06 \times 10^{-6}$ m^2/s) is 3×10^4 and 3×10^5 for conventional and creep feed grinding, respectively. Based on these values, the flow is assumed to be laminar, although in creep feed grinding it may be in the low transitional range. It is further assumed that the grinding fluid fills the space around the abrasive grains to a depth greater than the thermal boundary

Contributed by the Heat Transfer Division for publication in the JOURNAL OF HEAT TRANSFER. Manuscript received by the Heat Transfer Division February 1995; revision received February 1996. Keywords: Boiling, Conduction, Materials Processing and Manufacturing Processes. Associate Technical Editor: R. Viskanta.

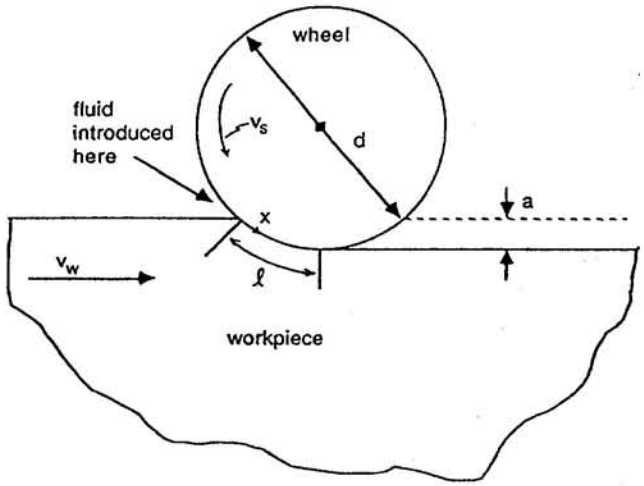

Fig. 1 Grinding geometry

thickness (which is estimated to be on the order of 10 μm to 100 μm), so that the fluid can be viewed as semi-infinite. The validity of this assumption depends on the details of the fluid application system, the applied flow rate, the porosity of the wheel, and other factors.

Jen (1993) considered two models for the fluid flow and corresponding heat transfer: Blasius boundary layer flow and slug flow (uniform velocity). Due to the better agreement with experimental results (Jen, 1993), only slug flow will be used in the present study. It may be that slug flow is a better approximation because the action of abrasive grains moving through the grinding zone periodically accelerates the fluid to the wheel velocity all the way to the workpiece surface, or because of local turbulence in the wake of the grains. The local heat transfer coefficient for slug flow can be written as follows (Lavine and Jen, 1991b):

$$h_f = \sqrt{\frac{\pi(k\rho c_p)_f v_s}{4x}} \tag{1}$$

This heat transfer coefficient result assumes that the fluid remains liquid. In reality, the fluid may boil under some conditions. This will now be discussed in detail.

Boiling. Jen and Lavine (1992a) presented a simple model as a first approximation to clarify the importance of nucleate and film boiling. In this approximation, two correlations were used (i.e., Bergles and Rohsenow, 1964; Rohsenow, 1952) to determine the nucleate boiling heat flux. It was found that the single-phase (liquid) forced convection heat flux is very large due to a very thin thermal boundary layer. In fact, the single-phase heat flux is typically at least an order of magnitude larger than the nucleate boiling heat flux. This reveals that the heat flux into the grinding fluid is nearly determined by the single-phase forced convection heat flux, provided that the grinding fluid remains predominantly liquid.

Table 1 Typical grinding conditions

(v_s = 30 m/s, d = 200 mm, A = 0.01, ℓ_g = 110 μm)

	v_w (mm/s)	a (mm)	$\ell = \sqrt{ad}$ (mm)
Conventional	100	0.005	1
Creep Feed	1	0.5	10

Ohishi and Furukawa (1985) and Yasui and Tsukuda (1983) experimentally showed that when the workpiece temperature reaches approximately 130°C for water-based grinding fluid and 300°C for oil, the workpiece temperature suddenly increases substantially. It has been hypothesized that this is associated with the transition from nucleate to film boiling of the grinding fluid. This hypothesis will now be considered in detail.

We begin by finding the needed wall superheat for the inception of nucleate boiling under typical grinding conditions. According to Hsu's criterion (Hsu, 1962), a cavity will activate when the liquid temperature at the top of a vapor bubble embryo is at least equal to the saturation temperature corresponding to the pressure in the bubble embryo. This criterion can be used to determine the required temperature at the top of the bubble embryo. It is also possible that gas may be entrapped inside the cavity. The effect of gas entrapment inside a cavity was considered by Wang and Dhir (1993b). The presence of gas in a cavity reduces the required superheat for a bubble to grow. From Wang and Dhir (1993b), the minimum superheat needed at the top of a bubble embryo for a bubble to grow on the workpiece surface in a cavity of diameter D_c is:

$$T_b - T_{\text{sat}} = \frac{4\sigma T_{\text{sat}}}{h_{fg}\rho_v D_c} K \tag{2}$$

Here, T_b is the fluid temperature at the top of the bubble and T_{sat} is the saturation temperature at the system pressure. For water, the properties are as follows:

Nomenclature

a = depth of cut
A = fractional grain/workpiece contact area
b = grinding zone depth
$C = \sqrt{(k\rho c_p)_f v_s/(k\rho c_p)_w v_w}$
c_p = specific heat
D_c = cavity diameter
d_s = wheel diameter
$f(\zeta)$ = function defined by Eq. (10)
h = heat transfer coefficient
k = thermal conductivity
K = nondimensional parameter defined by Eq. (3)
l = grinding zone length
l_g = width of individual grain heat source
p_o = system pressure
q'' = heat flux
R = radius of the bubble
R^+ = nondimensional radius of the bubble
T = temperature
T_b = temperature at top of bubble embryo
T_w = surface temperature in bubble analysis
t = time
t^+ = nondimensional time defined in Eq. (6)
v_s = wheel velocity
v_w = workpiece velocity
V_b = volume of the bubble embryo
V_c = volume of the cavity
x = distance from beginning of grinding zone
y = mole fraction of gases in the vapor/gas mixture
z = distance from workpiece surface
α = thermal diffusivity
γ = radius of curvature of the liquid-vapor interface
$\zeta = (\pi\alpha_g x/l_g^2 v_s)^{1/2}$
ρ = density
σ = surface tension

Subscripts

f = fluid
g = grain
grind = grinding power
l = liquid
s = surface (except in v_s)
sat = saturated condition
v = vapor
wb = workpiece background
wg = workpiece under grain

$$T_{sat} = 373.15 \text{ K}, \; h_{fg} = 2.257 \times 10^6 \text{ J/kg},$$

$$\sigma = 58.9 \times 10^{-3} \text{ N/m}, \quad \rho_v = 0.596 \text{ kg/m}^3$$

The parameter K, the nondimensional modified curvature (Wang and Dhir, 1993b), can be written as follows:

$$K = \frac{D_c}{2\gamma} - y \frac{p_o D_c}{4\sigma} \cdot \frac{V_c}{V_b} \tag{3}$$

where γ, y, p_o, V_c, and V_b are the radius of curvature of the liquid–vapor interface, the mole fraction of gases in the vapor/gas mixture in the bubble embryo, system pressure (1 atm here), the volume of the cavity and the volume of the bubble embryo. In the examples that follow, the volume of the cavity (V_c) is chosen to be equal to the volume of the bubble embryo (V_b), which corresponds to the metastable condition of the bubble embryo (Wang and Dhir, 1993b), and the radius of the bubble embryo is assumed to be equal to the cavity radius, that is, $2\gamma = D_c$.

Once the minimum superheat at the top of a bubble embryo is obtained, the required wall superheat to initiate nucleate boiling is of interest. Similar to Hsu (1962), a linear temperature profile is assumed, with the slope determined by the heat flux at the surface, $z = 0$, that is:

$$T = T_w - \frac{q_f'' z}{k_l} \tag{4}$$

The required wall superheat is then calculated as follows:

$$T_w - T_{sat} = (T_b - T_{sat}) + \frac{q_f'' D_c}{2k_l}$$

$$= \frac{4\sigma T_{sat}}{h_{fg} \rho_v D_c} \left(1 - y \frac{p_o D_c}{4\sigma}\right) + \frac{q_f'' D_c}{2k_l} \tag{5}$$

It will be assumed that $q_f'' = 10^7 \text{ W/m}^2$, based on the calculation results (see Figs. 3(b) and 4(b)), which show q_f'' varies from 10^7 to $4 \times 10^7 \text{ W/m}^2$. For water, $k_l = 0.68$ W/m-K. Now all values in Eq. (5) have been specified except for D_c and y.

Under realistic grinding conditions, the characteristic dimension of surface roughness may vary from less than 1 μm up to 8 μm (Vansevenant, 1987). We take the surface roughness as an estimate of the maximum cavity radius; thus D_c varies up to 16 μm. However, there may be cavities smaller than the measured surface roughness (Hsu and Graham, 1976). Differentiation of Eq. (5) shows that the minimum wall superheat occurs for $D_c = 3$ μm, approximately. Thus, if 3 μm diameter cavities exist, these will nucleate first. Evaluating Eq. (5) for $D_c = 3$ μm results in wall superheats to initiate bubble nucleation of 44°C, 30°C, and 16°C for $y = 0.0$, 0.5, and 1.0, respectively. These values are larger than the typical wall superheats to initiate nucleate boiling under pool boiling conditions. The reason is the very large heat flux, which causes a large temperature difference between the top of a bubble embryo and the wall. Note that, if there are no cavities of diameter 3 μm, only either smaller or larger cavities, the required wall superheat will be even larger.

It is worth noting that a broad range of results could be generated depending on the values of different parameters (e.g., D_c, V_b, y, and q_f'', etc.) which typically are not accurately known. Also, the studies of Hsu and Graham (1976) and Wang and Dhir (1993a, b) are for pool boiling, not for flow boiling. The examples shown here are intended to give a rough idea of the magnitude of the wall superheat.

Once the temperature reaches the required superheat, the bubbles start to grow from the cavity sites. We next investigate how quickly the bubbles might either grow to the height of the gap between the workpiece and wheel or merge with each other to blanket the workpiece surface. The latter case may be more likely due to the strong forced convection, which will tend to compress the bubbles near the workpiece surface.

For the case of bubbles filling the gap, Ohishi and Furukawa (1985) calculated the bubble growth time using an equation that is valid only for large growing time. They found that the growth time required to fill the gap between the workpiece and wheel is small in comparison to the total time for a point moving through the grinding zone *at the wheel velocity*. This is an odd criterion to use, because the bubble moves at the workpiece speed (as long as it remains attached to the nucleation site), not the wheel speed.

A more accurate solution, which is not limited to large time, and which accounts for the curvature effect of the bubble is as follows (Dhir, 1988):

$$R^+ = \tfrac{2}{3} [t^+ + 1]^{3/2} - \tfrac{2}{3} [(t^+)^{3/2} + 1] \tag{6}$$

where

$$R^+ = \hat{A} \frac{R}{B^2}, \quad t^+ = \frac{\hat{A}^2 t}{B^2}$$

$$\hat{A} = \left(\frac{\hat{b} \rho_v h_{fg} \Delta T_w}{\rho_l T_{sat}}\right)^{1/2}, \; B = \left(\frac{12}{\pi} \alpha_l\right)^{1/2} \frac{c_{pl} \rho_l \Delta T_w}{h_{fg} \rho_v}$$

where R is the radius of the bubble, $\hat{b}$ depends on the shape of the bubble (for a sphere, $\hat{b} = \frac{2}{3}$), and ΔT_w is the wall superheat relative to the saturation temperature. Note that large ΔT_w (as in this case) causes rapid bubble growth.

It has been shown experimentally for copper surfaces that the distance between cavities of diameter 3 μm is approximately 90 μm (Wang and Dhir, 1993a), and it will be assumed that this result applies to other metallic surfaces. The gap between the workpiece and wheel is of irregular geometry. The order of magnitude of the gap height is the distance by which grains protrude from the bond, which is roughly the grain dimension. This is typically larger than 90 μm (e.g., around 200 μm for aluminum oxide), so that bubbles will merge together before they fill the gap. Thus, when a bubble embryo grows to a diameter of 90 μm ($R = 45$ μm), the workpiece surface will be blanketed with vapor. As demonstrated earlier, a plausible wall superheat required to initiate bubble nucleation is 30°C. From Eq. (6), the bubble growth time for $R = 45$ μm is then approximately 0.0065 ms. For a cavity on the workpiece surface, the required time to pass through the grinding zone, traveling at the workpiece speed, varies from 10 ms (conventional grinding conditions) to 10^4 ms (creep feed grinding conditions) (see Table 1). Therefore, the bubble growth time is negligible in comparison to the time for a cavity to pass through the grinding zone. This result would hold regardless of the exact values chosen in the preceding analysis.

Thus, almost immediately after bubbles first nucleate, the bubbles would merge together. When this occurs, the vapor obstructs the liquid from reaching the surface, and greatly decreases the heat flux to the fluid. This is the phenomenon known as film boiling. Recall that experimental data (e.g., Ohishi and Furukawa, 1985; Yasui and Tsukuda, 1983) showed that a sharp temperature rise occurs when the workpiece temperature reaches about 100–130°C for a water-based grinding fluid, and 300°C for oil. The present analysis also supports these experimental observations (for water), since it shows that a wall superheat of 16–44°C is reasonable for bubble nucleation for water, and that very quickly after nucleation, conditions comparable to film boiling would occur. In agreement with experimental evidence and the present theoretical analysis, transition temperatures are taken as 130°C and 300°C for water-based grinding fluid and oil, respectively.

From the analyses presented above, three important conclusions can be made. First, due to the large single-phase (liquid) heat transfer coefficient of the grinding fluid, nucleate boiling

has a negligible effect on heat transfer. Second, the required wall temperature for nucleate boiling for water could potentially be around 130°C for a cavity size of 3 μm. Finally, the bubble growth time required to blanket the workpiece surface is much smaller than the time that a cavity stays in the grinding zone. Thus, the temperature at which nucleate boiling is initiated can also be taken as the temperature criterion for film boiling.

Based on these conclusions, film boiling will be handled in the following manner in our thermal model of grinding. The workpiece background temperature at the surface will be calculated as a function of distance along the grinding zone. Film boiling is assumed to occur when this temperature exceeds a critical value of 130°C for water-based grinding fluid and 300°C for oil. Note that these critical temperatures are applied to the workpiece background temperature at the surface (not the peak temperature under a grain) since this temperature is equal to the fluid temperature. When transition to film boiling occurs, the cooling effect of grinding fluid diminishes greatly. It is therefore reasonable to assume that the heat flux to the fluid is zero beyond this point (i.e., $h_f = 0$). Radiation heat transfer between the workpiece surface and the surroundings is also negligible: Using a workpiece temperature of 1100 K (high enough to cause workpiece burn) and surroundings at 300 K, and assuming black surfaces, the radiation heat flux is only 8×10^4 W/m^2, which is negligible compared to the grinding heat flux of order 10^7 W/m^2.

Coupling the Models. In Jen and Lavine (1995), Duhamel's Theorem was used to account for the actual variation of heat fluxes along the grinding zone. The models for the wheel, fluid, and workpiece were coupled by requiring that the surface temperatures match. Under the assumption of no transition to film boiling, an integral equation was derived that could be solved for $q''_{wb}(x)$, the heat flux remaining in the workpiece. Once this function is known, all surface temperatures and heat fluxes can be calculated.

In the present paper, the previous result is extended to the case in which there is transition to film boiling. In order to include this effect, another discontinuity must be accounted for in the formulation of Duhamel's Theorem. An integral equation can be derived for $q''_{wb}(x)$ beyond the transition point ($x = x_1$), in a manner similar to the result without transition from Jen and Lavine (1995). The resulting equations for $q''_{wb}(x)$ before and after transition are (see Jen, 1993, for a detailed derivation):

$$q''_{wb}(x) = \frac{A\bar{h}_{wg}}{1 + (1 - A)C}\left\{\int_0^x \left(\left[\frac{dq''_{\text{grind}}(\xi)}{d\xi} - \frac{1}{A}\frac{dq''_{wb}(\xi)}{d\xi}(1 + (1 - A)C)\right]\frac{1}{h_g(x - \xi)} - \frac{dq''_{wb}(\xi)}{d\xi}\frac{1}{h_{wb}(x - \xi)}\right)d\xi + \frac{q''_{\text{grind}}(0)}{h_g(x)}\right\} \quad x \le x_1 \quad (7)$$

$$q''_{wb}(x) = A\bar{h}_{wg}\left\{\int_0^x \left(\left[\frac{dq''_{\text{grind}}(\xi)}{d\xi} - \frac{1}{A}\frac{dq''_{wb}(\xi)}{d\xi}\right]\frac{1}{h_g(x - \xi)} - \frac{dq''_{wb}(\xi)}{d\xi}\frac{1}{h_{wb}(x - \xi)}\right)d\xi + \frac{q''_{\text{grind}}(0)}{h_g(x)} + \frac{\Delta q''_{wb}(x_1)}{h_{wb}(x - x_1)} - \frac{(1 - A)C}{A}\int_0^{x_1}\frac{dq''_{wb}(\xi)}{d\xi}\frac{1}{h_g(x - \xi)}d\xi\right\} \quad x \ge x_1 \quad (8)$$

where q''_{grind} is the total grinding power per unit area of actual wheel/workpiece contact, $\Delta q''_{wb}(x_1) = q''_{wb}(x_1^+) - q''_{wb}(x_1^-)$ and $C = \sqrt{(k\rho c_p)_s v_s/(k\rho c_p)_w v_w}$. Also in these equations, the heat transfer coefficients are given by:

$$h_{wb}(x) = \sqrt{\frac{\pi(k\rho c_p)_w v_w}{4x}}, \quad \bar{h}_{wg} = \frac{3}{4}\sqrt{\frac{\pi(k\rho c_p)_w v_s}{l_g}},$$

$$h_g = \sqrt{\frac{\pi(k\rho c_p)_g v_s}{4x}} f(\zeta) \quad (9)$$

where $\zeta(x) = (\pi\alpha_g x/l_g^2 v_s)^{1/2}$, and

$$f(\zeta) = \frac{2}{\pi^{1/2}}\frac{\zeta}{1 - \exp(\zeta^2)\,\text{erfc}\,(\zeta)} \quad (10)$$

Note that the uniform heat flux heat transfer coefficients given in Eq. (9) are used as building blocks in Duhamel's Theorem to yield the *correct* solution for the *variable* heat flux conjugate problem.

Numerical Procedure. The same numerical procedures are used as in Jen and Lavine (1995) with the slight modification that the discontinuity at the onset of film boiling is handled in the same way as at the origin. Grid convergence tests were reported in the earlier paper (Jen and Lavine, 1995). It was shown that 40,001 grid points are sufficient, and this number will be used throughout this study.

Table 2 Material properties

	steel	water	oil	Al_2O_3
k (W/m-K)	60.5	0.68	0.15	46
ρ (kg/m^3)	7854	1000	820	4000
c_p (J/kg-K)	434	4180	2000	770

Results and Discussion

The physical properties of the workpiece (plain carbon steel), grinding fluids (water or oil), and abrasive grains (Al_2O_3) are listed in Table 2. The grinding conditions, unless specifically stated, are the conditions listed in Table 1. The parameters A and l_g are not well known, and were estimated based on conversations with grinding wheel manufacturers and other experts. It has been shown by Kohli (1993) that a triangular grinding power input is more appropriate than a uniform distribution, and it is therefore used in this paper (unless otherwise stated). A triangular grinding power input is defined to have its maximum at $x = 0$, decreasing linearly to zero along the grinding zone. The average grinding powers used here are in the normal ranges of conventional and creep feed grinding conditions. The grinding power is treated as a known input parameter, even though in reality it is determined by the grinding conditions. Fortunately, in practice the grinding power can be measured easily either directly from the spindle power less the power required for idling, or indirectly using a force dynamometer. The ambient temperature is taken to be 25°C for water based grinding fluid and 40°C for oil (as explained in Lavine and Jen, 1991a).

Typical cases of grinding without film boiling were demonstrated by Jen and Lavine (1995), and will not be repeated here. The following sections will be used to demonstrate the effect of film boiling on the thermal behavior of the grinding process.

Comparison to Experimental Data. The theoretical predictions of maximum workpiece background temperature of the present model have been compared with experimental data, un-

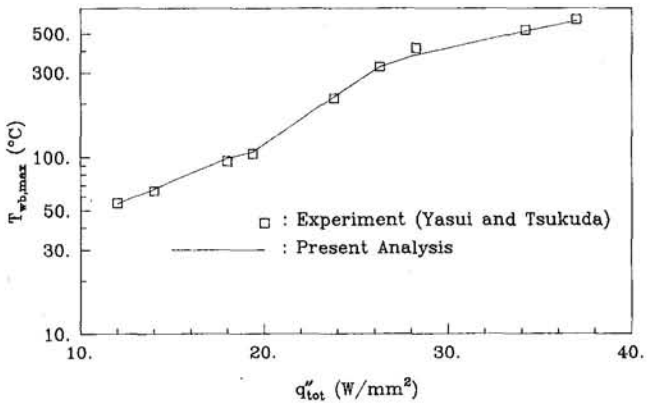

Fig. 2 Comparison to experimental data

der conditions for which no film boiling occurs (Jen and Lavine, 1995). The agreement is excellent under conventional grinding conditions, and is good under creep feed grinding conditions when oil is used as the grinding fluid. However, the agreement with experimental data becomes worse under creep feed grinding conditions when water-based grinding fluid is used (see Jen, 1993, for detailed discussions). Now, with appropriate handling of the film boiling condition, the present model will be compared to published experimental data for conventional grinding *with* film boiling, using aluminum oxide wheels with water-based grinding fluids.

The experimental data presented by Yasui and Tsukuda (1983) show a significant increase in maximum workpiece background temperature when that temperature exceeds around 100–130°C for water-based grinding fluid. The comparisons between these experimental data and the theoretical predictions of the present model for the maximum workpiece background temperature are presented in Fig. 2 as functions of the average grinding power per unit area. The grinding power is varied by changing the depth of cut. This is accounted for in the model. The experimental data are denoted by the square symbols. It can be seen that when the average grinding power (per unit area of the grinding zone), q''_{tot}, exceeds about 2×10^7 W/m^2, the workpiece background temperature increases significantly. By using the present model with the slug flow assumption, the predicted curve is in excellent agreement with the experimental data. Note that none of the parameters was chosen to fit the experimental data. Using Blasius boundary layer flow results in higher temperatures since the heat transfer coefficient of the fluid is smaller (not shown). Interested readers are referred to Jen (1993) for more discussion of Blasius flow.

Examples for Triangular Grinding Power Input

Conventional Grinding Conditions. One example will be given to demonstrate the temperature and heat flux distributions along the grinding zone with film boiling under conventional grinding conditions (see Table 1) with a water-based grinding fluid. The surface temperature distributions along the grinding zone are presented in Fig. 3(a). A triangular grinding power input with average grinding power input of 6×10^7 W/m^2 is used. The grain temperature increases rapidly near the beginning of the grinding zone, and reaches its maximum temperature of 809°C at $x = 0.18$ mm. It can be seen that film boiling occurs at $x = 0.4$ mm. It seems that the onset of film boiling does not change the grain temperature significantly. After the onset of film boiling, a small increase in grain temperature is observed, followed by a temperature decrease until the end of the grinding zone (due to the decreasing power input). A stronger effect of film boiling is observed for the workpiece background temperature ($T_{wb,s}$). The workpiece background temperature increases rapidly after the onset of film boiling, and reaches its maximum value of 241°C at $x = 0.7$ mm. This workpiece background temperature is well below the "workpiece burn" temperature (approximately 700–800°C, see Snoeys et al., 1978; Malkin, 1989). Therefore, no thermal damage is expected in this case. This result, namely that the increase in workpiece background temperature is significant when film boiling occurs, but not large enough to cause workpiece burn, is fairly typical of conventional grinding conditions (Lavine and Malkin, 1990). Later, larger workpiece background temperatures will be demonstrated for creep feed grinding conditions, in which "workpiece burn" does occur.

The heat flux distributions along the grinding zone are shown in Fig. 3(b). (The heat fluxes are multiplied by the fractional areas over which they apply.) Before film boiling occurs, about 30 percent of the heat that enters the workpiece (Aq''_{wg}) remains in the workpiece (q''_{wb}) and the other 70 percent of the heat is taken away by the grinding fluid ($(1 - A)q''_f$). Therefore, when film boiling occurs and q''_f goes to zero, q''_{wb} must increase strongly. Consequently, the workpiece background temperature ($T_{wb,s}$) increases significantly (see Fig. 3(a)). However, there is no significant change in q''_g when film boiling occurs, and therefore the increase in $T_{g,s}$ is small, as seen in Fig. 3(a).

Creep Feed Grinding Conditions. One example will be used to show the temperatures and heat flux distributions along the grinding zone under creep feed grinding conditions with film boiling, using water based grinding fluid. The grinding conditions are the typical creep feed conditions given in Table 1. The average grinding power input is set to be 1.5×10^7 W/m^2.

Figure 4(a) demonstrates the surface temperature distributions along the grinding zone when film boiling occurs. It can

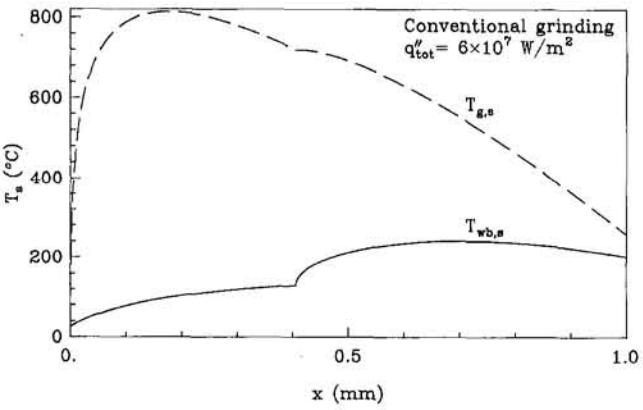

Fig. 3(a) Temperature distributions (triangular grinding power input, $q''_{tot} = 6 \times 10^7$ W/m^2, conventional grinding with water-based grinding fluid)

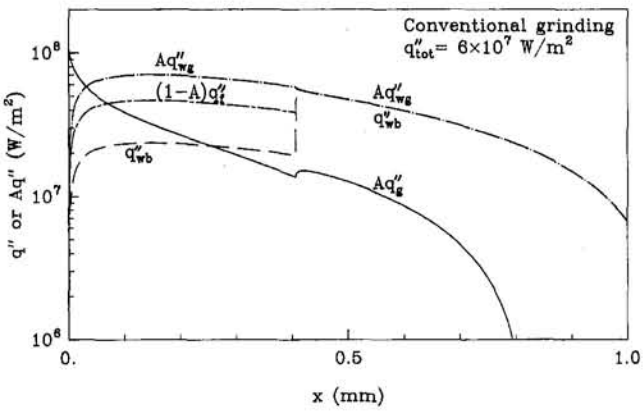

Fig. 3(b) Heat flux distributions (triangular grinding power input, $q''_{tot} = 6 \times 10^7$ W/m^2, conventional grinding with water-based grinding fluid)

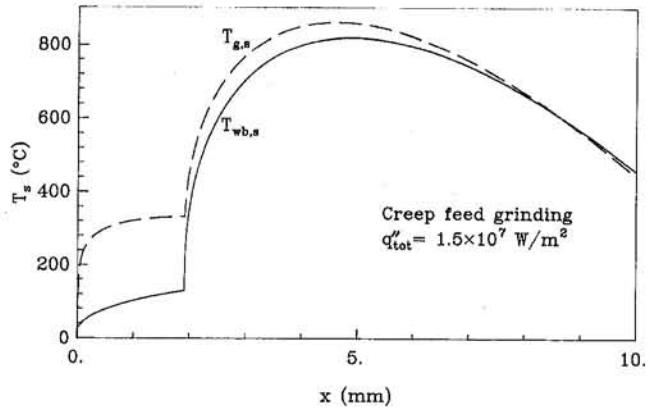

Fig. 4(*a*) Temperature distributions (triangular grinding power input, $q''_{tot} = 1.5 \times 10^7$ W/m^2, creep feed grinding with water-based grinding fluid)

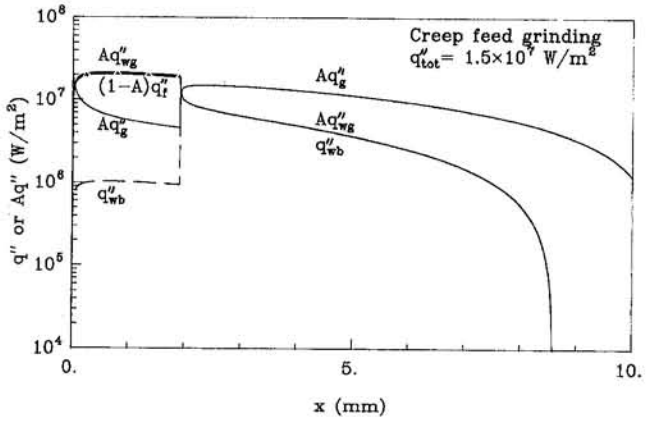

Fig. 4(*b*) Heat flux distributions (triangular grinding power input, $q''_{tot} = 1.5 \times 10^7$ W/m^2, creep feed grinding with water-based grinding fluid)

be seen that a very rapid increase in both $T_{g,s}$ and $T_{wb,s}$ is clearly observed when the workpiece background temperature exceeds the film boiling temperature. These temperature increases are much greater than under conventional grinding conditions (Fig. 3(*a*)). The maximum workpiece background temperature reaches about 785°C at about $x = 4.5$ mm. This elevated workpiece temperature is probably high enough to cause workpiece burn. It is also worth noting that the calculated workpiece background temperature distribution agrees qualitatively with the observations reported in a number of experimental studies (Ohishi and Furukawa, 1985; Yasui, 1984; and Snoeys et al., 1978), in which the workpiece temperature increases gradually, followed by a sharp increase in the workpiece temperature at the location where film boiling occurs, and decreases near the end of the grinding zone. Returning to Fig. 4(*a*), it can be seen that near the end of the grinding zone, $T_{wb,s}$ is larger than $T_{g,s}$. This indicates that the grains are cooler than the workpiece background surface temperature, so that when a grain passes over a point on the workpiece it will cool it. Therefore, negative heat fluxes for $q''_{wg}(x)$ and $q''_{wb}(x)$ are expected (this was also predicted by Guo and Malkin, 1995).

Figure 4(*b*) presents the heat flux distributions along the grinding zone for this case. Before film boiling occurs, $q''_{wg}(x)$ is larger than $q''_g(x)$ as for the conventional grinding case (see Fig. 3(*b*)). However, more heat is removed by the fluid for creep feed grinding conditions than for conventional grinding conditions. Before the onset of film boiling, about 7 percent of the heat that enters the workpiece (Aq''_{wg}) remains in the workpiece (q''_{wb}) and the rest of the heat (93 percent) is carried away by the grinding fluid ($(1 - A)q''_f$) (compared to 70 percent for the conventional grinding case demonstrated earlier). Consequently, when film boiling occurs and the cooling effect of the grinding fluid diminishes, not only the workpiece but the grain as well must remove the excess heat. The figure shows that *both* q''_g and q''_{wb} increase significantly at the onset of film boiling, in contrast to the conventional grinding case for which only q''_{wb} increased significantly. This explains why both $T_{wb,s}$ and $T_{g,s}$ increase at the onset of film boiling.

Workpiece Background Temperature. For the purpose of predicting thermal damage to the workpiece, the workpiece background temperature is of interest, not the peak temperature underneath a grain, as has been shown experimentally by Malkin (1974). Therefore, the remainder of this study will address the workpiece background temperature prediction, and its dependence on several of the parameters. In this section, the word "temperature" will be used to mean the "workpiece background temperature at the workpiece surface."

The Effect of Grinding Power Distribution. One example will be shown here to demonstrate the different profiles of workpiece background temperature when different shapes are used for the grinding power input. Note that only a case with film boiling is shown here. The interested readers are referred to Jen and Lavine (1995) for cases without film boiling. The grinding conditions are for conventional grinding with a water-based grinding fluid.

An example for which film boiling occurs under conventional grinding conditions is demonstrated in Fig. 5. The conditions are the same as for Fig. 3, except that the results for a triangular and a uniform power input are compared. In many earlier works (e.g., Des Ruisseaux and Zerkle, 1970; Malkin, 1974; Lavine and Jen, 1991a), a uniform grinding power input is assumed along the grinding zone. Recently, Kohli (1993) used a combined experimental and analytical approach to investigate the appropriate distribution of the grinding power input. His results reveal that a triangular heat flux input may be more appropriate. It can be seen from the figure that a distinct difference is observed between the two curves for the point where film boiling begins. For the triangular heat flux case, the transition point is located at $x = 0.4$ mm, in comparison to $x = 0.8$ mm for the uniform heat flux case. The maximum temperature for the case of triangular grinding power input is located at around $x = 0.7$ mm, and has a value of 265°C, which does not exceed the temperature required for workpiece burn. For the case of uniform grinding power input, the maximum temperature is almost the same (267°C), but is located at the end of the grinding zone. A further investigation by varying the grinding power inputs with uniform and triangular profiles shows that the peak temperatures are consistently almost the same, even though the transition point occurs earlier for triangular grinding power input. It is also important to note that if the peak temperature

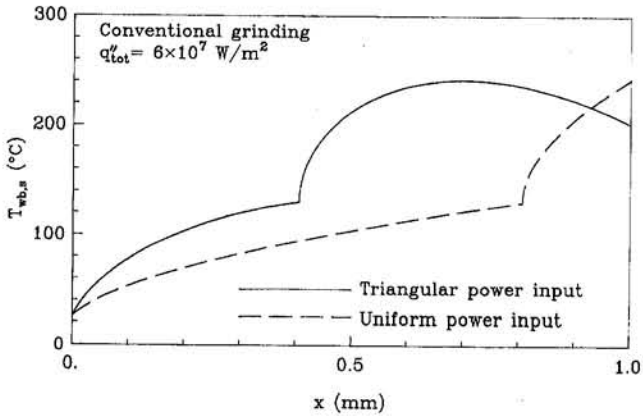

Fig. 5 Effect of grinding power input, conventional grinding, $q''_{tot} = 6 \times 10^7$ W/m^2, water-based grinding fluid

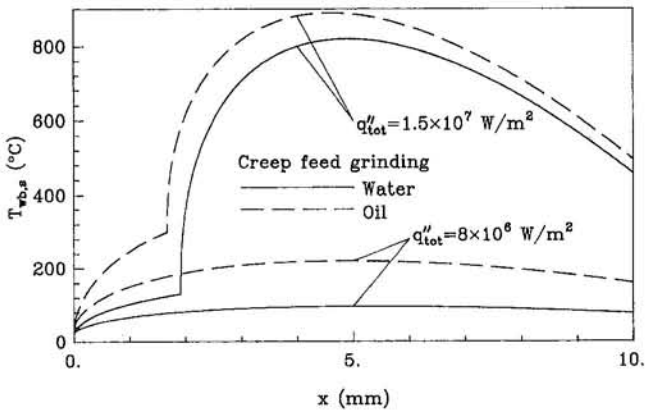

Fig. 6(*a*) Effect of grinding fluids (creep feed grinding)

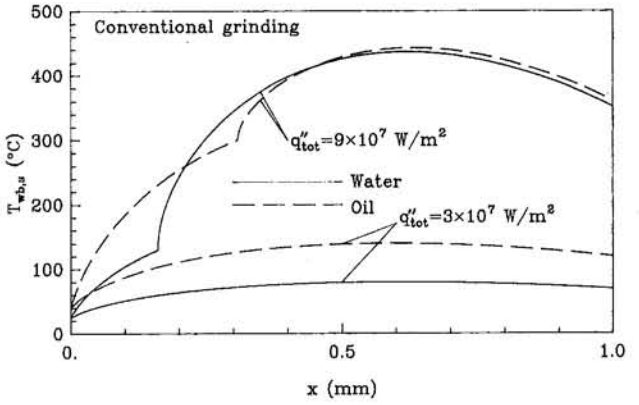

Fig. 6(*b*) Effect of grinding fluids (conventional grinding)

occurs at the end of the grinding zone, this temperature could possibly be reduced easily by injecting grinding fluid at the end of the grinding zone. For the case of triangular grinding power input, however, this will not significantly reduce the possibility of workpiece burn because the peak temperature is located in the middle portion of the grinding zone.

The Effect of Grinding Fluids. Two examples using two different grinding fluids (i.e., oil and water-based grinding fluids) for the cases of creep feed and conventional grinding conditions are shown in this section. The first example is for creep feed grinding conditions. A triangular grinding power input is used with two different average grinding power inputs as shown in the figure.

With an average grinding power input of 8×10^6 W/m^2, the temperature is higher when oil is used, as shown in Fig. 6(*a*). For oil, the maximum temperature is about two times larger than for water-based grinding fluid. This is not surprising because the heat transfer coefficient is smaller for oil due to its smaller thermal conductivity. When the average grinding power input increases to 1.5×10^7 W/m^2, both oil and water-based grinding fluids undergo film boiling. Recall that the film boiling temperature for oil is about 300°C, compared to 130°C for water-based grinding fluid. It can be seen that although the transition temperature for water based grinding fluid is smaller than for oil, transition occurs slightly further along the grinding zone for water-based grinding fluid. The workpiece temperature for both grinding fluids exceeds 800°C, so that workpiece burn would occur. However, the maximum temperature for oil is larger than for water-based grinding fluid. These results seem to suggest that water-based grinding fluid gives better performance under creep feed grinding conditions. Note that this may not be true under conventional grinding conditions, as will be demonstrated in the next example. It also should be recognized that, since oil is a better lubricant, the grinding power might be lower for oil than for water based grinding fluid, even though we have compared them on the basis of equal grinding power input.

The next example is for the case of conventional grinding conditions. A triangular grinding power input is used with two different average grinding power inputs as shown in the figure. Similar to the last example, the temperature is higher for oil at the lower grinding power input (3×10^7 W/m^2) when film boiling does not occur. However, in comparison to the last example a distinct difference is observed when film boiling occurs. It can be seen from Fig. 6(*b*) that the maximum temperatures in the grinding zone are almost the same for both oil and water-based grinding fluid. The higher boiling point of the oil almost exactly makes up for its lower heat transfer coefficient. Again, this comparison is on the basis of equal grinding power input. These results may partially explain why oil generally gives better performance for conventional grinding whereas water-based grinding fluid is usually used in creep feed grinding.

The Effect of Elastic Flattening. The length of the grinding zone is usually calculated by using the following equation (Des Ruisseaux and Zerkle, 1970):

$$l = \sqrt{ad_s} \tag{11}$$

where a is the depth of cut, and d_s the wheel diameter. However, as indicated by Snoeys et al. (1978), the elastic flattening of the wheel against the workpiece will increase the length of the grinding zone. As demonstrated in their paper, the actual length may be twice as long as the value calculated by using Eq. (11). This was also pointed out by Hahn in his comments on the paper presented by Des Ruisseaux and Zerkle (1970). If the grinding power is distributed over a longer length, the average grinding power will decrease. This is an issue in need of further investigation, since Guo and Malkin (1995) show that even with elastic flattening, the power dissipation is concentrated mainly in the theoretical grinding zone length. However, it will be assumed here that the grinding power is distributed over the entire actual grinding zone length.

Figure 7 demonstrates the effect of elastic flattening on the workpiece temperature by increasing the grinding zone length as much as a factor of two over the theoretical length of 1 mm. Conventional grinding conditions are used with a water-based grinding fluid. A triangular grinding power input is used. The solid line represents the original temperature curve, when the elastic flattening effect is neglected. It can be seen that film boiling occurs, and a maximum workpiece temperature of 250°C is observed. However, when the length of the grinding zone increases to 1.5 mm, the average grinding power decreases from 6×10^7 W/m^2 to 4×10^7 W/m^2. As a result, the film boiling effect disappears, and the workpiece temperature falls below 120°C. For the largest enlargement of the grinding zone length,

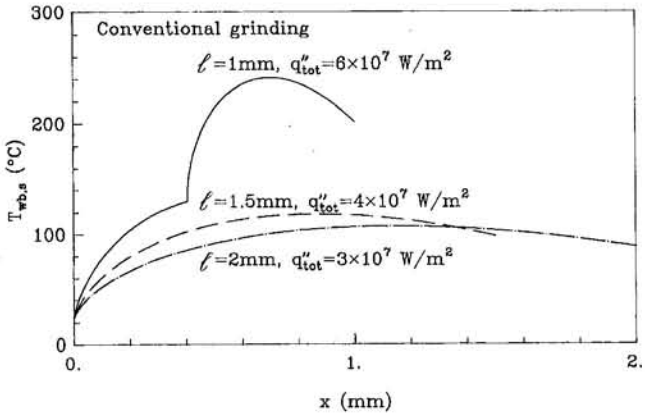

Fig. 7 Effect of elastic flattening

2.0 mm, the maximum workpiece temperature is lower than 110°C. Note that the average grinding power flux is 3×10^7 W/m^2 in this case. It is also interesting to note that the maximum temperature does not change significantly when the actual grinding zone length varies from 1.5 mm to 2.0 mm. An important conclusion can be made: As long as no film boiling occurs, the elastic flattening effect is not extremely important in determining the maximum temperature. However, this effect can be very significant if it makes the difference between film boiling occurring or not.

Conclusions

An improved model has been developed to predict the temperature and heat flux distributions along the grinding zone when film boiling occurs. By appropriate handling of the film boiling condition, this model successfully eliminates the abrupt transition as predicted in the earlier models (Lavine and Jen, 1991; Jen and Lavine, 1992a). Several major conclusions can be made as follows:

1 An analysis that accounts for the effect of gas entrapment in a cavity has been presented to estimate the required wall superheat to initiate the nucleate boiling of a bubble embryo. A broad range of wall superheats could be generated depending on the values of different parameters. For instance, for a cavity size of 3 μm with several parameters fixed, the required wall temperature to initiate nucleate boiling of water varies from 116°C to 144°C when the mole fraction of the entrapped gas varies from 1 to 0.

2 Once nucleate boiling begins, the bubble growth time required to blanket the workpiece surface is much smaller than the time that a cavity stays in the grinding zone. Thus, the workpiece temperature rises rapidly after the onset of nucleate boiling because the cooling effect of the grinding fluid diminishes in a very short time. This explains the experimentally observed temperature increase once the workpiece temperature reaches around 100–130°C for water based grinding fluid.

3 Accounting for the effect of film boiling, the predicted maximum temperatures are in excellent agreement with the experimental results presented by Yasui and Tsukuda (1983), when slug flow is used.

4 The workpiece temperature distributions along the grinding zone predicted by the present model agree qualitatively with experimental results (Ohishi and Furukawa, 1985; Yasui, 1984; Snoeys et al., 1978).

5 When film boiling occurs, the workpiece background temperature increase is greater under creep feed grinding conditions than under conventional grinding conditions.

6 In the example given, when film boiling occurs, the maximum workpiece temperature is larger for oil than for water-based grinding fluid under creep feed grinding conditions, whereas the maximum workpiece temperature is approximately the same under conventional grinding conditions.

7 The maximum temperatures are almost the same when two different grinding power input profiles, namely uniform and triangular grinding power inputs, are used even when film boiling occurs. The point of onset of film boiling is earlier for the triangular grinding power input than for the uniform grinding power input.

8 The effect of elastic flattening can be very significant if it makes the difference between film boiling occurring or not. However, this effect is not very important in determining the maximum temperature when there is no film boiling.

Acknowledgments

The support of the National Science Foundation, General Motors, and General Electric is gratefully acknowledged.

References

Bergles, A. E., and Rohsenow, W. M., 1964, "The Determination of Forced-Convection Surface-Boiling Heat Transfer," ASME JOURNAL OF HEAT TRANSFER, Vol. 86, pp. 365–372.

Des Ruisseaux, N. R., and Zerkle, R. D., 1970, "Thermal Analysis of the Grinding Process," ASME *Journal of Engineering for Industry,* Vol. 92, pp. 428–434.

Dhir, V. K., 1988, "Boiling and Condensation," 231C class notes, Mechanical, Aerospace, and Nuclear Engineering Department, University of California, Los Angeles.

Gardinier, C. F., 1988, "Physical Properties of Superabrasives," *Ceramic Bull.,* Vol. 67, pp. 1006–1009.

Guo, C., and Malkin, S., 1995, "Analysis of Energy Partition in Grinding," ASME *Journal of Engineering for Industry,* Vol. 117, pp. 55–61.

Hsu, Y. Y., 1962, "On the Size Range of Active Nucleation Cavities on a Heating Surface," ASME JOURNAL OF HEAT TRANSFER, Vol. 84, pp. 206–216.

Hsu, Y. Y., and Graham, R. W., 1976, *Transport Processes in Boiling and Two-Phase Systems,* McGraw-Hill, New York, pp. 35–36.

Jen, T. C., and Lavine, A. S., 1992a, "Thermal Aspects of Grinding: the Effect of Flow Boiling," in: *Transport Phenomena in Materials Processing and Manufacturing,* ASME HTD-Vol. 196, pp. 91–98.

Jen, T. C., and Lavine, A. S., 1992b, "Thermal Aspects of Grinding: An Improved Model of Heat Transfer to Workpiece, Wheel and Fluid," in: *Heat Transfer in Material Processing,* ASME HTD-Vol. 224, pp. 1–7.

Jen, T. C., 1993, "Thermal Aspects of Grinding: Heat Transfer to Workpiece, Wheel and Fluid," Ph.D. dissertation, Mechanical, Aerospace and Nuclear Engineering Department, University of California, Los Angeles.

Jen, T. C., and Lavine, A. S., 1995, "A Variable Heat Flux Model of Heat Transfer in Grinding: Model Development," ASME JOURNAL OF HEAT TRANSFER, Vol. 117, pp. 473–478.

Kohli, S., 1993, "Energy Partition for Grinding With Aluminum Oxide and Cubic Boron Nitride Abrasive Wheels," Master's Thesis, Department of Mechanical Engineering, University of Massachusetts.

Lavine, A. S., Malkin, S., and Jen, T. C., 1989, "Thermal Aspects of Grinding With CBN Wheels," *CIRP Annals,* Vol. 38, No. 1, pp. 557–560.

Lavine, A. S., and Malkin, S., 1990, "The Role of Cooling in Creep Feed Grinding," *Int. J. Adv. Manuf. Technol.,* Vol. 5, pp. 97–111.

Lavine, A. S., and Jen, T. C., 1991a, "Thermal Aspects of Grinding: Heat Transfer to Workpiece, Wheel, and Fluid," ASME JOURNAL OF HEAT TRANSFER, Vol. 113, pp. 296–303.

Lavine, A. S., and Jen, T. C., 1991b, "Coupled Heat Transfer to Workpiece, Wheel, and Fluid in Grinding, and the Occurrence of Workpiece Burn," *Int. J. Heat Mass Transfer,* Vol. 34, No. 4/5, pp. 983–992.

Malkin, S., 1974, "Thermal Aspects of Grinding. Part 2—Surface Temperatures and Workpiece Burn," ASME *Journal of Engineering for Industry,* Vol. 96, pp. 1184–1191.

Malkin, S., 1984, "Grinding of Metals: Theory and Application," *J. Applied Metalworking,* Vol. 3, No. 2, pp. 95–109.

Malkin, S., 1989, *Grinding Technology: Theory and Applications of Machining With Abrasives,* Chap. 6, Ellis Horward, Chichester/Wiley, New York.

Ohishi, S., and Furukawa, Y., 1985, "Analysis of Workpiece Temperature and Grinding Burn in Creep Feed Grinding," *Bulletin of JSME,* Vol. 28, No. 242, pp. 1775–1781.

Powell, J. W., and Howes, T. D., 1978, "A Study of the Heat Flux at Which Burn Occurs in Creep Feed Grinding," *Proc. 19th Machine Tool Design Research Conf.,* Manchester, United Kingdom, pp. 629–636.

Rohsenow, W. M., 1952, "A Method of Correlating Heat Transfer Data for Surface Boiling of Liquids," *Transactions of ASME,* Vol. 74, pp. 969–974.

Shafto, G. R., Howes, T. D., and Andrew, C., 1975, "Thermal Aspects of Creep Feed Grinding," *Proc. 16th Machine Tool Design Research Conf.,* Manchester, United Kingdom, pp. 31–37.

Snoeys, R., Maris, M., and Peters, J., 1978, "Thermally Induced Damage in Grinding," *CIRP Annals,* Vol. 27, No. 2, pp. 571–581.

Vansevenant, Ir.E., 1987, "A Subsurface Integrity Model in Grinding," Ph.D. Dissertation, University of Leuven, Belgium.

Wang, C. H., and Dhir, V. K., 1993a, "Effect of Surface Wettability on Active Nucleation Site Density During Pool Boiling of Water on a Vertical Surface," ASME JOURNAL OF HEAT TRANSFER, Vol. 115, pp. 659–669.

Wang, C. H., and Dhir, V. K., 1993b, "On the Gas Entrapment and Nucleation Site Density During Pool Boiling of Saturated Water," ASME JOURNAL OF HEAT TRANSFER, Vol. 115, pp. 670–679.

Wylie, C. R., and Barrett, L. C., 1982, *Advanced Engineering Mathematics,* McGraw-Hill, pp. 454–455.

Yasui, H., and Tsukuda, S., 1983, "Influence of Fluid Type on Wet Grinding Temperature," *Bull. Japan Soc. of Prec. Engg.,* Vol. 17, No. 2, pp. 133–134.

Yasui, H., 1984, "On Limiting Grinding Condition for Fluid Supply Effect," *Proc. 5th International Conference on Production Engineering,* Tokyo, pp. 58–63.

Transient Heating and Melting of Particles in Plasma Spray Coating Process

M. A. Jog
Mem. ASME

L. Huang

Department of Mechanical, Industrial, and Nuclear Engineering, University of Cincinnati, Cincinnati, OH 45221-0072.

In the plasma spray coating process, solid particles are injected into a plasma jet. The heat transfer from the plasma to the particles results in heating and melting of the particles. The molten particles impact on a surface forming a thin coat. In this paper, we investigate the heating and melting of a spherical particle injected into a thermal plasma. The transient temperature distribution in the particle interior is obtained simultaneously with the temperature and number density variations of the ions, electrons, and the neutrals as well as the electric potential variation in the plasma. Our analysis incorporates a model for the production and recombination of electrons and ions. The transport in the plasma is modeled by considering the main body of the plasma as charge neutral and a charge sheath in the vicinity of the particle surface. The heat flux to the particle is evaluated by taking into account all modes of heat transfer to the surface. The temporal variations of the particle temperature distribution are calculated. Results are compared with the available predictions made without taking into account the gas ionization to assess the importance of ionization and particle charging on the heat transport to the particle. For argon, for the particle materials considered in this study, the effect of gas ionization on the heat transport was found to be negligible for plasma temperatures below 6500 K.

I Introduction

A plasma-aided spray coating process is used to produce surface coatings with desired characteristics. In this process, particulate matter and an inert gas are injected into a plasma torch. An electric discharge provides energy to heat and partially ionize the gas. The injected particulate matter is heated and melted due to the heat transfer from the ionized gas. These molten droplets then impinge on a surface to be coated. The spreading of the droplets and the subsequent solidification forms a thin layer. The particle heating and melting play an important role in controlling the quality of the coating. In this paper we have analyzed the heating and melting of a spherical particle in a thermal plasma. Once a particle is introduced into an ionized gas, owing to the large difference in the mobilities of ions and electrons, initially more electrons impact on the particle than the ions. The particle becomes negatively charged with respect to the main body of the plasma such that the current of the ions and the current of electrons toward the particle are equal. Under these conditions, the electric potential at the particle surface with respect to the undisturbed plasma is known as the floating potential. A thin charge sheath is present in the vicinity of the particle surface. Chen and He (1986) analyzed the heat transport to a particle in a rarefied ionized gas. They showed that particle charging significantly increases the rate of heat transport to the particles in rarefied gases. Analytical expressions for the heat flux were derived by Gnedovets and Uglov (1992) in their study of nonspherical particles injected into rarefied plasmas. Although these studies show the importance of particle charging on the heat transport to the particle, their models are appropriate for solid particles in rarefied plasma and are not applicable under continuum conditions. A continuum model to predict the electron and ion flux to a spherical body in a weakly ionized gas was first reported by Cohen (1963) and Su and Lam (1963) in their analyses of electrostatic probes. Barad and Cohen (1974) extended the analysis to a moderately ionized plasma by accounting for both the charge-charge and the charge-neutral collisions. Measurements of heat flux to cylindrical probes in high intensity arcs have been reported by Meyer and Pfender (1973). They have also provided a simplified model to estimate the heat transport to cylindrical probes in highly ionized arcs. Their results indicate that the recombination of ion and electrons at the surface of the probe is an important mechanism of heat transport to the probes. In their model, Meyer and Pfender have considered a *collisionless* electric sheath close to the probe surface. We note that this limit is completely different from the continuum analysis presented in this paper. McAssey and Yeh (1970) calculated the heat transfer to electrostatic probes by accounting for the electron-ion recombination at the probe surface. However, they did not consider the variation of the electron and ion temperatures in their model. In a recent study we have presented a model to calculate transport in thermal plasmas including the variation of the electron and ion temperatures (Jog, 1995). Lee et al. (1985) and Chyou and Pfender (1989) have reviewed the experimental and computational studies on the behavior of particles in thermal plasma.

Bourdin et al. (1983) have analyzed the transient heating of spherical particle under plasma conditions without considering the effects due to ionization of the gas. They showed that for a stationary particle, the Nusselt number based on the particle diameter equals 2 if the integral average values of plasma thermal conductivities are used. The integral average value of the thermal conductivity is defined as

$$\bar{\chi} = \frac{1}{T_\infty - T_w} \int_{T_w}^{T_\infty} \chi(T)\, dT$$

It was found that for a particle immersed in a plasma, the instantaneous Nusselt number drops rapidly with time and attains its asymptotic value of 2.0 in less than 1 μs. They also showed that the heat transport to the particle by radiation is negligible compared to that by conduction for far-field plasma temperatures greater than 4000 K. They have reported the transient variation of the particle temperature for several particle

Contributed by the Heat Transfer Division for publication in the JOURNAL OF HEAT TRANSFER. Manuscript received by the Heat Transfer Division July 1995; revision received February 1996. Keywords: High-Temperature Phenomena, Materials Processing and Manufacturing Process, Numerical Methods. Associate Technical Editor: A. Lavine.

materials. We have compared our results with those of Bourdin et al. (1983) to ascertain the effect of gas ionization on the heat transfer to the particle. The comparison reveals that the effect of particle charging on the heat transport to the particle from an argon plasma is significant for far-field temperatures above 6500 K.

II Problem Formulation

Consider a spherical solid particle introduced in a quiescent plasma consisting of electrons, ions, and neutrals. The typical particle diameters used in DC plasma coating are 20–100 μm and the typical particle diameters used for RF plasma coating are 50–200 μm. The range of Reynolds number based on the particle diameter and the relative velocity between the plasma and the particle is Re < 30 (Boulos and Gauvin, 1974; Yoshida and Akashi, 1977; Bronet and Boulos, 1989). It is important to understand the effects of gas ionization on a stationary particle fully before making the model more complicated. Therefore, we have first considered a stationary particle in a plasma. Our results will be useful for particles moving with low Reynolds number Re < 10 in plasma spraying. The ionized gas is considered as collision dominated and the mean free path is the smallest length scale in the problem. Good collision coupling exists between the heavy species (ions and neutrals) and their temperatures are considered equal at any given location. For plasma spraying at atmospheric pressure, the Knudsen number is typically less than 10^{-2}. Hence, a continuum model adequately describes the process. In our model, the mean free path is smaller than the Debye length, which is smaller than the particle diameter. It can be seen from our results that the sharp change in plasma parameters in the vicinity of the particle surface occurs over a distance of about 5 μm. At atmospheric pressure, the mean free path is about 0.1 μm. The mean free path is at least an order of magnitude smaller than the distant over which large variations are present, thereby validating a continuum model.

The formulation is spherico-symmetric. It is convenient to use spherical coordinates with the origin of the coordinate system at the center of the particle as shown in Fig. 1. The background gas is considered homogeneous, stationary, and optically thin. The thermal conductivities of electrons, ions, and the neutrals are considered variable. Their variation with temperature is incorporated in this model. Beyond the initial short period of rapid transients, the heat transport to the particle surface may be regarded as quasi-steady. As the time scale for particle heating and melting ($\sim$1 ms) is much larger than the time scale for transport in the gaseous phase ($\sim$1 μs), the quasi-steady approach can provide accurate results (Lee et al., 1985). The

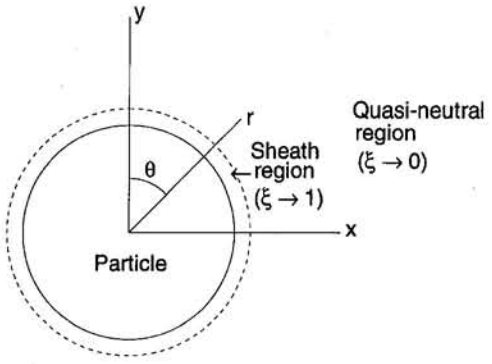

Fig. 1 Problem schematic

transport in the plasma is determined by the time-independent form of the governing equations, whereas the transport in the particle is considered fully transient. As the temperature distribution in the particle and the particle surface temperature changes with time, the corresponding solutions for the governing equations in the plasma phase are obtained for each time step. The time scale for particle charging is orders of magnitude smaller than that for particle heating and the particle can be considered at its floating potential at all times.

Under these assumptions, the governing continuum conservation equations with the Poisson equation for the self-consistent electric field can be written as (Jog et al., 1992):

$$\nabla \cdot \Gamma_e = P - R \tag{1}$$

$$\nabla \cdot \Gamma_i = P - R \tag{2}$$

$$\nabla \cdot q_e = -e\Gamma_e \cdot E \tag{3}$$

$$\nabla \cdot E = -\left(\frac{e}{\epsilon_0}\right)(N_e - N_i) \tag{4}$$

with

$$E = -\nabla V.$$

The electron and the ion fluxes are given by

$$\Gamma_e = -\frac{\mu_e}{e}\nabla(N_e k T_e) + \mu_e N_e \nabla V, \tag{5}$$

$$\Gamma_i = -\frac{\mu_i}{e}\nabla(N_i k T_i) - \mu_i N_i \nabla V \tag{6}$$

Nomenclature

c_p = specific heat at constant pressure
E = electric field
e = magnitude of electric charge on a single electron
g_i = statistical weight of ions
g_n = statistical weight of the ground state of neutrals
h = Planck's constant
k = Boltzmann constant
L = latent heat of melting
m_e = mass of an electron
N = number density
N_n = neutral number density
N_0 = far field electron and ion number density
n = nondimensional number density
P = production rate
q = heat flux
R = recombination rate
r_m = location of the melt front
r_p = particle radius
T = temperature
t = time
V = electric potential
V_i = ionization potential
$\hat{\alpha}$ = Townsend's first ionization coefficient
α_p = thermal diffusivity = $\chi_p/(\rho_p c_p)$
Γ_e, Γ_i = electron flux and ion flux, respectively
ϵ = λ_D/r_p
ϵ_0 = permittivity of free space
λ_D = Debye length
μ = mobility
ξ = inverse of nondimensional distance = r_p/r
ρ = density
χ = thermal conductivity

Subscripts

e = electron
i = ion
m = melt
n = neutral
s = solid
w = particle surface
∞ = far-field conditions

Superscript

$*$ = nondimensional quantities

The electron heat flux is given by

$$q_e = \frac{5}{2} kT_e\Gamma_e - \chi_e \nabla T_e \tag{7}$$

The particle heating is governed by the energy conservation equation:

$$\rho_p c_p \frac{\partial T_p}{\partial t} = \nabla \cdot (\chi_p \nabla T_p) \tag{8}$$

Once the particle surface reaches its melting temperature, the particle begins to melt from the surface inward. The movement of the melt front can be tracked by employing an energy balance at the melt front as

$$-\chi_m \left.\frac{\partial T_{p,m}}{\partial r}\right|_{r=r_m} = -\chi_s \left.\frac{\partial T_{p,s}}{\partial r}\right|_{r=r_m} + L\rho_p \frac{dr_m}{dt}, \tag{9}$$

and using the temperature continuity condition

$$\text{at } r = r_m, \quad T_p = T_m. \tag{10}$$

The particle is initially at a uniform temperature T_0.

$$\text{at } t = 0, \quad T_p(r, 0) = T_0 \tag{11}$$

At the particle center we employ the symmetry condition

$$\text{at } r = 0, \quad \frac{\partial T_p}{\partial r} = 0. \tag{12}$$

At the particle surface the electron and ion fluxes are equal, and the temperature continuity and the energy balance is employed. Due to a fast recombination process at the surface, ion and electron number densities are specified as very small values (Stahl and Su, 1971). Thus

$$\text{at } r = r_p\text{:} \quad \Gamma_e = \Gamma_i, \quad N_e = N_i = N_w, \tag{13}$$

$$T_p = T_e, \quad \text{and} \quad -\chi_p \frac{\partial T_p}{\partial r} = q_w.$$

Here q_w is the net heat flux from the plasma to the particle surface. The details of the calculation of q_w by accounting for all the modes of heat transport at the surface are provided later in this paper.

At $r = \infty$, the ion and electron densities and temperatures are specified. We consider a plasma at atmospheric pressure. Under this condition the difference between the electron and ion temperatures is small (Pfender, 1978) and thus at $r = \infty$, we consider $T_e = T_i = T_\infty$.

$$\text{at } r \to \infty, \quad N_e = N_i = N_0, \quad T_e = T_\infty \quad \text{and} \quad V = 0. \tag{14}$$

The rate of electron impact ionization is (Loeb, 1939)

$$P = \hat{\alpha}\mu_e E N_e.$$

where the Townsend's first ionization coefficient $\hat{\alpha}$ is given by $\hat{\alpha} = Ap \exp(-Bp/E)$. The coefficients A and B depend on the particular gas and p is pressure. The coefficient $\hat{\alpha}$ decreases exponentially with the electric field E. The electric field is expected to be low in the quasi-neutral region and the impact ionization will be essentially zero. The electron temperature is expected to be high in most of the domain and thermal ionization and three body recombination will govern the production and recombination of ions and electrons. The net production by thermal ionization and three body recombination is given by the Saha equations as (Mitchner and Kruger, 1973)

$$P - R = \gamma N_e \left[\frac{2g_i N_n}{g_n} \left(\frac{2\pi m_e kT_e}{h^2} \right)^{3/2} \exp\left(-\frac{eV_i}{kT_e} \right) - N_e N_i \right] \tag{15}$$

where $\gamma = 1.09 \times 10^{-20}\ T_e^{-9/2}\ m^6/\text{s}$ (Hinnov and Hirshberg, 1962).

III Mathematical Formulation for Transport in Plasma

The time is nondimensionalized by the diffusion time scale $t^* = t\alpha_p/r_p^2$. The distance is scaled by the particle radius $r^* = r/r_p$, the temperature is scaled by the far-field temperature $T^* = T/T_\infty$, the number density by the far-field electron number density $n_{e,i} = N_{e,i}/N_0$. The Debye length is given by $\lambda_D = (\epsilon_0 kT_\infty/(e^2 N_0))^{1/2}$. The ion and the electron flux, the heat flux, and the electric potential are nondimensionalized by $\Gamma^*_{e,i} = er_p/(\mu_{e,i} N_0 kT_\infty)\Gamma_{e,i}$, $q_e^* = q_e er_p/(\mu_e N_0 k^2 T_\infty^2)$, and $V^* = eV/(kT_\infty)$. We consider the limit $\lambda_D/r_p \ll 1$ and denote the small ratio of the Debye length to the particle radius as $\epsilon = \lambda_D/r_p$. A coordinate transformation ($\xi = 1/r^*$) is used to map the computational domain in the plasma ($r^* = 1 \to \infty$) onto a finite domain ($\xi = 0 \to 1$). The governing equations in the plasma are written in terms of the dimensionless variables as

$$\frac{d^2V^*}{d\xi^2} = \frac{\epsilon^2}{\xi^4}(n_e - n_i) \tag{16}$$

$$-\frac{d^2}{d\xi^2}(n_e T_e^*) + \frac{d}{d\xi}\left(n_e \frac{dV^*}{d\xi} \right) = \frac{1}{\xi^4} \frac{er_p^2}{\mu_e N_0 kT_\infty} (P - R) \tag{17}$$

$$-\frac{d^2}{d\xi^2}(n_i T_i^*) - \frac{d}{d\xi}\left(n_i \frac{dV^*}{d\xi} \right) = \frac{1}{\xi^4} \frac{er_p^2}{\mu_i N_0 kT_\infty} (P - R) \tag{18}$$

$$\frac{d}{d\xi}\left\{ T_e^* \left[-\frac{d(n_e T_e^*)}{d\xi} + n_e \frac{dV^*}{d\xi} \right] - \frac{2}{5} \frac{e\chi_e}{\mu_e N_0 k^2 T_\infty} \frac{dT_e^*}{d\xi} \right\} = \frac{2}{5}\left[n_e \left(\frac{dV^*}{d\xi} \right)^2 - \frac{d(n_e T_e^*)}{d\xi} \frac{dV^*}{d\xi} \right] \tag{19}$$

The boundary conditions at the particle surface are

$$n_e = n_i = n_w, \quad T_e^* = T_p^*, \quad \text{and} \quad \mu_e \Gamma_e^* = \mu_i \Gamma_i^*.$$

The remaining boundary conditions have to be obtained by matching the solutions to those in the quasi-neutral region as described later.

The above governing Eqs. (16)–(19) are valid in most of the computational domain. However, Eq. (16) has a singularity at $\xi = 0$. This corresponds to a region far away from the particle where the ion and the electron number densities and temperatures are high. Both terms on the right-hand side of Eq. (16) are several orders of magnitude larger than the left-hand side. The zeroth-order solution in this case is $n_e = n_i \equiv n$. This is the quasi-neutral region ($\xi \to 0$). Now consider Eqs. (17) and (18). The right-hand side of the equation shows a balance between two very large numbers compared to the left-hand side. Hence, the zeroth-order solution is the balance of thermal ionization and three body recombination, $P \approx R$. In the electron energy equation, in the distant quasi-neutral region, the most dominant term is the one due to conduction. With these simplifications the governing equations in the region near $\xi \to 0$ are:

$$n \frac{dV^*}{d\xi} = \frac{1}{\mu_e + \mu_i}\left(\mu_e \frac{d(nT_e^*)}{d\xi} - \mu_i \frac{d(nT_i^*)}{d\xi} \right) \tag{20}$$

$$n^2 = \frac{2g_i N_n}{g_n N_0^2} \left(\frac{2\pi m_e kT_\infty}{h^2} \right)^{3/2} T_e^{*3/2} \exp\left(-\frac{V_i^*}{T_e^*} \right) \tag{21}$$

$$0 = \frac{d}{d\xi}\left(\chi_e \frac{dT_e^*}{d\xi}\right) \tag{22}$$

The boundary conditions are

$$\xi \to 0, \quad n = 1, \quad T_e^* = 1, \quad \text{and} \quad V^* = 0.$$

As $\xi \to 1$ the variations of the electron temperature, number densities, and electric potential in the quasi-neutral region should match with the corresponding solutions in the sheath region. This matching provides the remaining boundary conditions.

IV Heat Transport to Particle Surface

The heat flux to the particle surface is determined by accounting for all modes of heat transport at the surface. The particle receives energy by conduction from neutrals, ions, and electrons, and also by recombination of ions and electrons at the particle surface. The temperature variation for a stationary background gas can be obtained by solving the energy equation

$$\frac{d}{d\xi}\left(\chi_n \frac{dT_n^*}{d\xi}\right) = 0 \tag{23}$$

with the appropriate boundary conditions as:

$$T_n^* = 1 \quad \text{at} \quad \xi = 0 \quad \text{and} \quad T_n^* = T_p^* \quad \text{at} \quad \xi = 1.$$

Good collision coupling exists between the ions and the neutrals, and their temperatures are considered equal at a given location. Therefore a numerical solution to Eq. (23) provides the neutral and the ion temperature variation in the computational domain ($\xi = 0 \to 1$). The conduction of heat from the neutral gas can be calculated as

$$q_n^* = \frac{e\chi_n}{\mu_e N_0 k^2 T_\infty} \frac{dT_n^*}{d\xi}\bigg|_{\xi=1} \tag{24}$$

At the particle surface, energy is deposited by recombination of ions and electrons as well as conduction from neutrals, ions and electrons. The total dimensionless heat flux to the particle surface from the plasma can be written as

$$q_w^* = q_n^* + q_e^* + q_i^* + q_r^*. \tag{25}$$

The heat fluxes are nondimensionalized by $q^* = qer_p/(\mu_e N_0 k^2 T_\infty^2)$.

q_r^* is the energy provided to the surface by the recombination of the ions and electrons equivalent to the ionization potential:

$$q_r^* = \Gamma^*|_{\xi=1} V_i^*. \tag{26}$$

q_e^* and q_i^* represent the thermal energy deposited by conduction by electrons and ions, respectively:

$$q_{e,i}^* = \frac{e\chi_{e,i}}{\mu_e N_0 k^2 T_\infty} \frac{dT_{e,i}^*}{d\xi}\bigg|_{\xi=1} \tag{27}$$

V Solution Procedure

The simultaneous solutions of the governing equations for the particle temperature and the transport in plasma are carried out by an iterative procedure. The transient particle temperature distribution is calculated by solution of Eq. (8) with appropriate boundary conditions using an implicit finite difference method. The diffusion terms are discretized by the central difference technique. The algebraic equations resulting from the discretization are solved by the tridiagonal algorithm. The heat transport from the plasma has to be calculated for each time step. Particle surface temperature from the previous time step is used as the first guess. Using this temperature value, the solutions of the governing equations in the plasma are obtained as described below. The solution in the plasma provide the heat flux to the particle. This value of the heat flux is used to solve for the particle temperature distribution and an improved value of the particle surface temperature is obtained. The procedure is continued until the change in the surface temperature is below a specified convergence limit (relative error < 0.001 percent). The calculations are then advanced to the next time step. Once the particle begins to melt, the energy equation is solved in the molten and the solid regions with the boundary conditions Eqs. (9) and (10).

The solutions in the plasma are obtained by solving appropriate governing equations in the quasi-neutral region and the sheath region. An iterative method is used to obtain uniformly valid matched solutions. Equations (20) – (22) are the governing equations for the quasi-neutral region ($\xi \to 0$) whereas Eqs. (16) – (19) are valid for the sheath region ($\xi \to 1$). The governing equations are discretized using a hybrid finite difference scheme. In this scheme, central differencing or upwind differencing method is used based on the relative magnitude of diffusion and drift terms (Patankar, 1980). The algebraic equations resulting from the discretization are solved by the tridiagonal algorithm. The governing equations in the quasi-neutral region are first solved in the entire domain. Then a grid point is chosen where the number densities are $O(\epsilon^{-2})$. The governing equations for the sheath region are then solved toward the particle. These solutions in the sheath region provide the inner boundary conditions to solve the governing equations in the quasi-neutral region. This iterative procedure is continued until the changes in all variables are below a specified convergence limit (relative error $< 10^{-6}$). Although the condition at the particle surface is that of ion and electron flux being equal, in the computational procedure a value for the potential at the particle surface is specified and it is iteratively changed so as to get the required flux condition at the particle surface. Due to the coupled and nonlinear nature of the equations, an underrelaxation method was used with the relaxation coefficient 0.9. The source terms in Eqs. (17) and (18) were linearized by the method outlined by Patankar (1980) to increase the diagonal dominance and obtain faster convergence. Computations were carried out on Ohio Supercomputer Center's Cray Y-MP. Each run took about 30 cpu minutes.

VI Results and Discussion

The results are obtained for particle radii of 50, 100, and 200 μm. This corresponds to the typical size of the particulate matter used in the plasma spray coating process. The background gas is argon plasma at atmospheric pressure. To make fruitful comparisons with Bourdin et al. (1983), three particle materials are considered, viz., alumina, nickel, and tungsten. For these particulate materials, the change in thermophysical properties is not very large. For example, for nickel, a temperature change from 800 K to 1500 K results in a variation in thermal conductivity from 67.6 W/m K to 76.2 W/m K, and the specific heat changes from 530 kJ/kg K to 616 kJ/kg K. In contrast, the variations in the thermal conductivities of electrons, ions, and neutrals in the plasma can be large (more than an order of magnitude). Therefore, we have considered constant thermophysical properties for particulate materials where as the variation of thermal conductivities of electrons, ions and neutrals with temperature is fully accounted for in our model. Also, the simplification of constant properties of particulates enables us to directly compare our results to those of Bourdin et al. (1983) and identify the effect of gas ionization.

The thermophysical properties used for the particulate materials are as follows. For alumina: $\rho = 4 \times 10^3$ kg/m^3, $c_p = 1.5$ kJ/kg K, $L = 10^6$ J/kg, and $\chi_p = 6.3$ W/m K. The melting

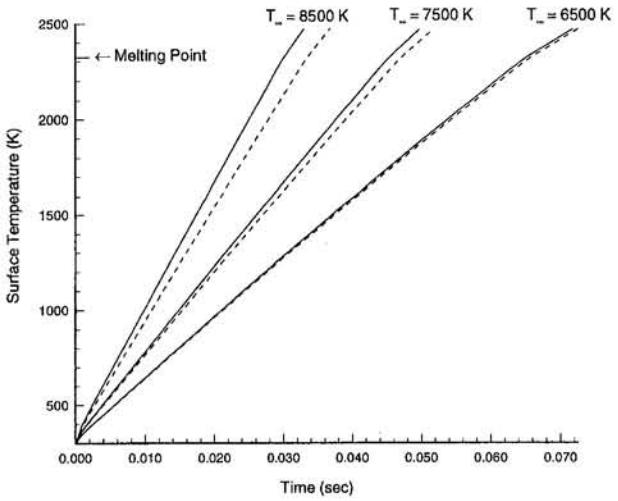

Fig. 2 Transient temperature variation for an alumina particle. Legend: solid lines—surface temperature, dashed lines—surface temperature solution without considering gas ionization, r_p = 100 μm, T_0 = 300 K.

temperature is 2323 K and the boiling temperature is 4000 K. For nickel: $\rho = 8.9 \times 10^3$ kg/m^3, $c_p = 541$ J/kg K, $L = 3 \times 10^5$ J/kg, and $\chi_p = 73.3$ W/m K. The melting temperature is 1727 K and the boiling temperature is 3005 K. For tungsten: $\rho = 1.935 \times 10^4$ kg/m^3, $c_p = 170$ J/kg K, $L = 1.9 \times 10^5$ J/kg, and $\chi_p = 110$ W/m K. The melting temperature is 3680 K and the boiling temperature is 6200 K. Other thermophysical properties were taken from Devoto (1973), Brown (1967), and Yoshida and Akashi (1977). The following data are used in our numerical computations: $\mu_e = 0.075$ m^2/Vs, $\mu_i = 6.25 \times 10^{-4}$ m^2/Vs, $n_w = 10^{-9}$, $g_i = 2$, $g_n = 2$, $V_i = 15.68$ V, $T_0 = 300$ K. The temperature dependence on thermal conductivities of electrons, ions, and neutrals is taken from the data provided by Devoto (1973).

The transient variation of the particle surface temperature is shown in Fig. 2 for alumina particles of 100 μm radius. The particle temperature variations are calculated until the particle is completely molten. In the surface temperature variations, the initial part corresponds to heating without a change of phase. The slope of the surface temperature variation changes as melting begins. The change in the slope of the surface temperature variation during particle melting depends on the thermal diffusivity of the particle material. For a particle material with high thermal diffusivity, the temperature variations in the molten part and the solid part will be small, i.e., while the particle is undergoing melting, the temperature throughout the particle will be close to the melting temperature. Such a behavior will result in a large change in slope of the temperature curve. In contrast, a particle material with very low thermal diffusivity (such as alumina) will have large temperature variations in the particle interior at all times, including the duration when the particle undergoes melting. Hence, in the case of alumina, the particle surface temperature continues to increase when the particle is undergoing melting. Therefore, the change in the slope of the temperature curve is expected to be small. The dotted lines show the surface temperature variations obtained without accounting for gas ionization (Bourdin et al., 1983). Their results have been recalculated and replotted on our coordinates. The difference between the two predictions is due to the inclusion of gas ionization and particle charging effects in our model. The predictions of time required for the complete melting of a particle can be compared to ascertain the effect of gas ionization. At low far-field temperature, the effect on heat transport to the particle due to particle charging is small (only about 1 percent). The effect of particle charging on the heat transport to the particle increases with an increase in the far field temperature. At $T_\infty = 8500$ K, the time required for complete melting of the particle calculated by our formulation is about 12 percent less than that predicted without taking into account the gas ionization. In the quasi-neutral region, as evident from Eq. (21), the electron and ion number densities are a direct function of electron temperature. As the far-field temperature is increased, the extent of the quasi-neutral region increases, the temperature gradients near the particle surface and the electron flux to the particle surface increase. Therefore, the heat flux to the particle surface due to recombination of electrons and ions increases as the far-field temperature is increased. Therefore, at higher far-field temperatures, the effect of particle charging on the heat transport to the particle surface is significant.

Figure 3 shows the temperature histories for 100 μm radius particles of different materials. The dotted lines indicate the surface temperature histories obtained without considering gas ionization. The thermal diffusivities of nickel and tungsten are an order of magnitude greater than that of alumina. Under the conditions considered here, the Biot number for alumina is about 0.03, whereas the Biot numbers for nickel and tungsten particles are less than 0.003. Therefore the temperature nonuniformities in alumina particles are significantly greater than those in the nickel and tungsten particles. The melting temperature of tungsten is considerably greater than that for alumina and nickel. It is seen from the transient temperature variations that the surface temperature is near or higher than the melting temperature for most of the particle residence time. This behavior agrees well with the surface temperature measurements carried out by Vardelle et al. (1988). The electron conductivity is a very strong function of temperature. The conductivity of ions also increases with temperature. Thus higher surface temperature for tungsten leads to an increase in the conduction heat flux to the surface from electrons and ions. Thus the effect of gas ionization is more pronounced for a tungsten particle than that for alumina and nickel. Figure 4 shows the surface temperature variations for three different particle sizes. Due to the large difference in the time required for melting among these particle sizes, it is convenient to plot the temperature variations on a log scale. In all these cases the far-field temperature and therefore the Debye length is the same. An increase in the particle radius results in a smaller value of the Debye ratio $\epsilon = \lambda_D / r_p$. The electron and ion flux is a function of the Debye ratio ϵ (Cohen, 1963; Su and Lam, 1963). This results in an increase in the electron and ion flux to the surface and the energy depos-

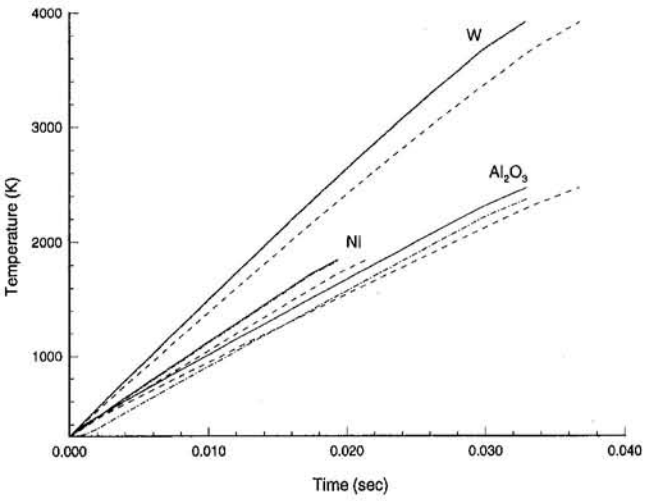

Fig. 3 Temperature variation for alumina, nickel, and tungsten particles. Legend: solid lines—surface temperature, – · – · – · – · – center temperature, dashed lines—surface temperature solution without considering gas ionization, r_p = 100 μm, T_∞ = 8500 K, and T_0 = 300 K.

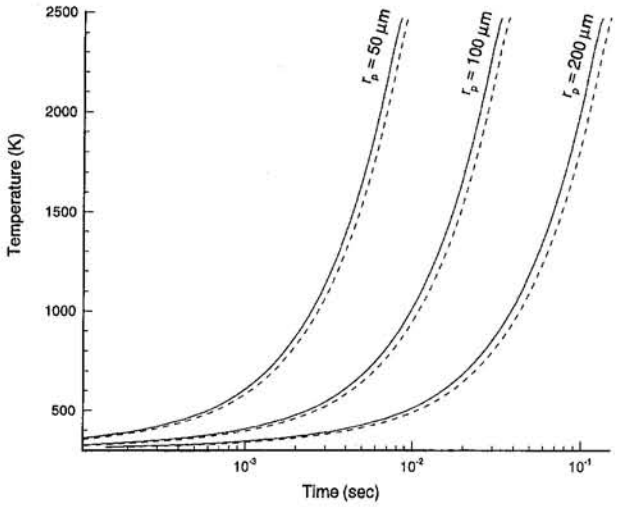

Fig. 4 Surface temperature variation for alumina particles of different sizes. Legend: solid lines—surface temperature, dashed lines—surface temperature solution without considering gas ionization, r_p = 100 μm, T_∞ = 8500 K, and T_0 = 300 K.

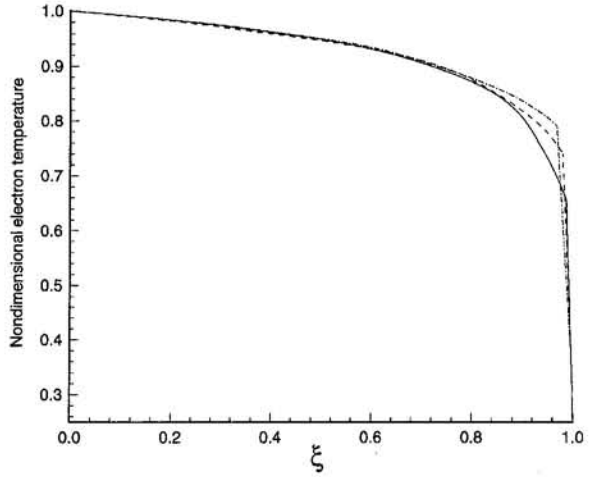

Fig. 6 Variation of the nondimensional electron temperature at t = 0.025 s. Legend: solid line—T_∞ = 8500 K, dashed line—T_∞ = 7500 K, – · – · – · – T_∞ = 6500 K. Alumina particle, r_p = 100 μm.

ited due to recombination. Hence the effect due to particle charging is more prominent for larger particles.

As the particle surface temperature changes, the corresponding solutions in the plasma are calculated for each time step. The behavior of the plasma can be analyzed by considering the spatial variations of the electron and ion temperatures and the electric potential at a fixed instant of time. The spatial variation of the dimensionless electric potential is shown in Fig. 5. These variations are obtained for an alumina particle immersed into a plasma. Three different values of the plasma temperature are considered. In all these cases, the results are plotted for a time of t = 0.025 seconds. The electric potential distribution shows a gradual variation away from the particle (in the quasi-neutral region $\xi \to 0$) with a sharp change in the vicinity of the particle surface (in the sheath region $\xi \to 1$). The electron and ion densities in the quasi-neutral region are a strong function of the electron temperature. Higher electron temperature results in higher electron and ion densities. Therefore, for a particle immersed in an ionized gas at higher temperature, the charge sheath becomes thinner and the electric potential variation becomes steeper. Figure 6 shows the dimensionless electron temperature variations for an alumina particle immersed in argon plasma for a time of t = 0.025 seconds. In the quasi-neutral region, the electron temperature variation is gradual. Large electron temperature gradients are present near the particle surface. This is due to the strong dependence of electron thermal conductivity on temperature. The electron temperature and hence the thermal conductivity in the quasi-neutral region is high. The electron temperature near the particle surface is low and the electron thermal conductivity is small. This results in high temperature gradients near the particle surface.

Direct measurements of heat transfer data for stationary particles in thermal plasma are not available in the published literature. Measurements of the particle surface temperatures have been reported for particles moving in a plasma jet (Fincke et al., 1990, 1993; Vardelle et al., 1988). The temperature of the plasma varies in the jet with location and therefore a direct comparison is not possible. Surface temperatures of alumina particles of diameters between 45 μm and 90 μm in a argon plasma jet have been measured by Vardelle et al. (1988). Our particle temperature predictions for alumina particles are in the same range as the measured temperatures. Considering the difference in the conditions of the experiments and our model, only a qualitative agreement is expected.

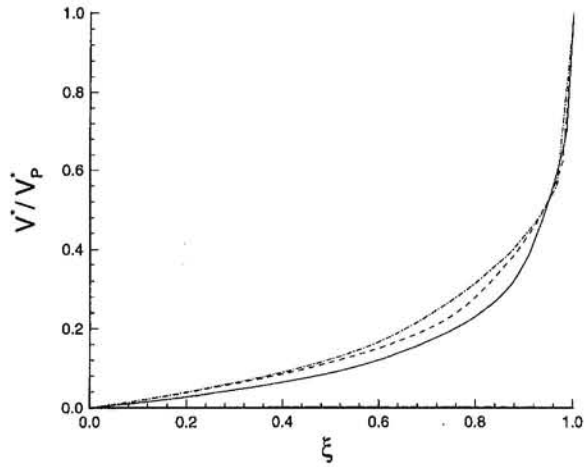

Fig. 5 Variation of dimensionless electric potential at t = 0.025 s. Legend: solid line—T_∞ = 8500 K, dashed line—T_∞ = 7500 K, – · – · – · – T_∞ = 6500 K. Alumina particle, r_p = 100 μm.

VII Conclusions

We have considered a spherical particle undergoing heating and melting in a thermal plasma. The transports in both the plasma and the particle have been simultaneously solved. Transient temperature distribution in the particle is determined. Results are obtained for particle sizes and materials typically used in plasma coating process. It is found that a thin charge sheath is present near the particle surface with steep gradients in electron and ion densities and temperatures. Most of the plasma is quasi-neutral with nearly equal ion and electron densities. Inclusion of the gas ionization shows an increase in heat transport compared to pure conduction. For the particle materials considered in this study, the effect of gas ionization and particle charging on the heat transport to the particle in an argon plasma is very small for far-field temperatures below 6500 K. The effects due to particle charging become significant at higher far field temperatures. At T_∞ = 8500 K, the time required for complete melting of a particle calculated using our formulation is about 12 percent less than that predicted without considering gas ionization. The effects due to particle charging become more pronounced with particle size and with an increase in the surface temperature.

Acknowledgments

The authors are grateful to the National Science Foundation for supporting this work under grant No. CTS-9409140. Computer time provided by the Ohio Supercomputer Center on OSC's Cray Y-MP under grant No. PES505-1 is thankfully acknowledged.

References

Barad, M. S., and Cohen, I. M., 1974, "Continuum Theory of Spherical Electrostatic Probes in a Stationary, Moderately Ionized Plasma," *Physics of Fluids,* Vol. 17, pp. 724–734.

Boulos, M. I., and Gauvin, W. H., 1974, "Powder Processing in a Plasma Jet: A Proposed Model," *Canadian Journal of Chemical Engineering,* Vol. 52, pp. 355–363.

Bourdin, E., Fauchais, P., and Boulos, M., 1983, "Transient Heat Conduction Under Plasma Conditions," *International Journal of Heat and Mass Transfer,* Vol. 26, pp. 567–582.

Bronet, M. S., and Boulos, M. I., 1989, "Particle Velocity Measurements in Induction Plasma Spraying," *Plasma Chemistry and Plasma Processing,* Vol. 9, pp. 343–353.

Brown, S. C., 1967, *Basic Data of Plasma Physics,* MIT Press, Cambridge, MA.

Chen, X., and He, P., 1986, "Heat Transfer From a Rarefied Plasma Flow to a Metallic or Nonmetallic Particle," *Plasma Chemistry and Plasma Processing,* Vol. 6, pp. 313–333.

Chyou, Y. P., and Pfender, E., 1989, "Behavior of Particulates in Thermal Plasma Flows," *Plasma Chemistry and Plasma Processing,* Vol. 9, pp. 45–71.

Cohen, I. M., 1963, "Asymptotic Theory of Spherical Electrostatic Probes in a Slightly Ionized, Collision-Dominated Gas," *Physics of Fluids,* Vol. 6, pp. 1492–1499.

Devoto, R. S., 1973, "Transport Coefficients of Ionized Argon," *Physics of Fluids,* Vol. 16, pp. 616–623.

Fincke, J. R., Swank, W. D., and Jeffery, C. L., 1990, "Simultaneous Measurements of Particle Size, Velocity and Temperature in Thermal Plasma," *IEEE Transactions on Plasma Science,* Vol. PS-18, pp. 948–957.

Fincke, J. R., Swank, W. D., and Haggard, D. C., 1993, "Plasma Spraying of Alumina: Plasma and Particle Flow Fields," *Plasma Chemistry and Plasma Processing,* Vol. 13, pp. 579–600.

Gnedovets, A. G., and Uglov, A. A., 1992, "Heat Transfer to Nonspherical Particles in a Rarefied Plasma Flow," *Plasma Chemistry and Plasma Processing,* Vol. 12, pp. 383–402.

Hinnov, E., and Hirshberg, J. G., 1962, "Electron-Ion Recombination in Dense Plasmas," *Physical Review,* Vol. 125, pp. 795–801.

Jog, M. A., Cohen, I. M., and Ayyaswamy, P. S., 1992, "Electrode Heating in a Wire-to-Plane Arc," *Physics of Fluids,* Vol. B4, pp. 465–472.

Jog, M. A., 1995, "Analysis of Heat Transfer to a Spherical Particle From Continuum Plasma," *Journal of Applied Physics,* Vol. 78, pp. 1424–1429.

Lee, Y. C., Chyou, Y. P., and Pfender, E., 1985, "Particle Dynamics and Particle Heat and Mass Transfer in Thermal Plasmas. Part II. Particle Heat and Mass Transfer in Thermal Plasmas," *Plasma Chemistry and Plasma Processing,* Vol. 5, pp. 391–414.

Loeb, L. B., 1939, *Fundamental Processes of Electrical Discharges in Gases,* Wiley, New York, Chap. 8.

McAssey, E. V., Jr., and Yeh, S., 1970, "Electron Heat Transfer in a Quiescent Nonequilibrium Plasma," ASME JOURNAL OF HEAT TRANSFER, Vol. 92, pp. 447–455.

Meyer, T. N., and Pfender, E., 1973, "Experimental and Analytical Aspects of Plasma Heat Transfer," *Wärme- und Stoffübertragung,* Vol. 6, pp. 25–31.

Mitchner, M., and Kruger, C. H., 1973, *Partially Ionized Gases,* Wiley, New York, p. 78.

Patankar, S. V., 1980, *Numerical Heat Transfer and Fluid Flow,* Hemisphere Publishing Co., Washington, DC.

Pfender, E., 1978, "Electric Arcs and Arc Gas Heaters," in: *Gaseous Electronics, Vol. 1 Electrical Discharges,* M. N. Hirsh and H. J. Oskam, eds., Academic Press, pp. 298–391.

Stahl, N., and Su, C. H., 1971, "Theory of Continuum Flush Probes," *Physics of Fluids,* Vol. 14, pp. 1366–1376.

Su, C. H., and Lam, S. H., 1963, "Continuum Theory of Spherical Electrostatic Probes," *Physics of Fluids,* Vol. 6, pp. 1479–1491.

Vardelle, M., Vardelle, A., Fauchais, P., and Boulos, M., 1988, "Particle Dynamics and Heat Transfer Under Plasma Conditions," *AIChE Journal,* Vol. 34, pp. 567–573.

Yoshida, T., and Akashi, K., 1977, "Particle Heating in a Radio-Frequency Plasma Torch," *Journal of Applied Physics,* Vol. 48, pp. 2252–2260.

Journal of Heat Transfer

Technical Notes

This section contains shorter technical papers. These shorter papers will be subjected to the same review process as that for full papers.

Thermal Conductivity of Graphite/Aluminum and Graphite/Copper Composites

M. A. Lambert[1] and L. S. Fletcher[2]

Nomenclature

f = fiber volume fraction
k = thermal conductivity, W/mK or Btu/hr-ft^2-°F

Subscripts

in = in-plane
long = longitudinal, i.e., parallel to axis of fiber
m = matrix (aluminum alloy 6063 or OFHC copper)
r = reinforcement (graphite fiber)
thru = through-plane
trans = transverse, i.e., transverse to axis of fiber

Introduction

Metal matrix composites (MMC's) may be tailored to provide greater strength, stiffness, and thermal conductivity, as well as lower density, than nonreinforced, or monolithic, metals. Specifically, continuous graphite fiber reinforced aluminum (Gr/Al) and copper (Gr/Cu) MMC's are being considered (Beasley, 1990) to replace monolithic aluminum and copper frames for military standard electronic modules (SEM's). Module frames provide structural support and serve as heat sinks for the attached electronics. High-conductivity graphite fibers increase the conductivity of MMC's in directions parallel to the fiber orientations.

Previous studies of the thermophysical properties of graphite and carbon fiber reinforced MMC's include: Kuniya et al. (1987), Ellis and McDanels (1991), Gordon et al. (1991), Reeves et al. (1991), Maass and Makwinski (1992), and Pfeiffer and Tallon (1992). Ellis and McDanels (1991) measured in-plane, k_{in}, and through-plane, k_{thru}, thermal conductivity and coefficient of thermal expansion of cross-plied and unidirectional Gr/Cu.

Experimental Program

The k_{in} and k_{thru} for Gr/Al and Gr/Cu were experimentally determined. The k_{thru} data for Gr/Al have been previously presented by Lambert and Fletcher (1994) and are included here for purposes of comparison and completeness. Three-fourths of the data, that is, k_{in} of Gr/Al, as well as k_{in} and k_{thru} for Gr/Cu were determined in the present investigation.

Both the Gr/Al and Gr/Cu contain Thornel P130 graphite pitch fibers (Amoco Corp.) in a balanced cross-ply (0–90 deg) orientation. This particular grade of graphite fiber is employed for its high longitudinal conductivity, $k_{r,long}$, of 1111 W/mK (642 Btu/hr-ft-°F), as reported by Montesano et al. (1992). The Gr/Al and Gr/Cu MMC's have fiber volumes of 42 and 43 percent, respectively. The aluminum matrix is alloy 6063, chosen for its high k, 218 W/mK (126 Btu/hr-ft-°F), in the annealed condition. Oxygen-free, high-conductivity (OFHC) copper with a k of 380 W/mK (220 Btu/hr-ft-°F) is the other matrix. Module frames are presently made from monolithic aluminum alloy 6101-T6 (k = 218 W/mK (126 Btu/hr-ft-°F)) and electrolytic tough pitch (ETP) copper (k = 387 W/mK (224 Btu/hr-ft-°F)). The k values for the various alloys were taken from the *ASM Metals Reference Book* (1983) and Touloukian and Ho (1972).

Fabrication of the composite panels began with lay-up of fiber bundles into a preform with the desired cross-ply orientation. In the case of the Gr/Al, a submicron thick, chemically vapor deposited, proprietary coating was applied to the fibers to increase wettability and prevent them from reacting with the aluminum matrix during casting. The preform was positioned in a precision machined steel mold that was coated with a boron nitride release agent to facilitate extraction of the composite panel after casting. The preform/mold assembly was charged with the required quantity of matrix material then placed in a pressure casting unit.

The pressure casting unit was evacuated, after which it was heated to melt the matrix, then pressurized with nitrogen to ensure full densification of the composite. The heaters were turned off and an active cold plate was brought in contact with the preform/mold assembly to cool it quickly. Three panels of each material were produced, measuring 7.62 × 7.62 cm (3.0 × 3.0 in.) with thicknesses of 0.254, 0.762, and 1.270 cm (0.1, 0.3, and 0.5 in., respectively). The MMC thermal test specimens were machined from the panels.

Lambert and Fletcher (1994) describe the experimental facility and methods for measuring k_{in} and k_{thru}. Uncertainties were computed according to the method of Kline and McClintock

[1] Assistant Professor, Department of Mechanical Engineering, San Jose State University, San Jose, CA 95192-0087; Mem. ASME.
[2] Thomas A. Dietz Professor, Department of Mechanical Engineering, Texas A&M University, College Station, TX 77840-3123; Fellow ASME.

Contributed by the Heat Transfer Division of THE AMERICAN SOCIETY OF MECHANICAL ENGINEERS. Manuscript received by the Heat Transfer Division January 1995; revision received December 1995. Keywords: Conduction, Electronic Equipment, Thermophysical Properties. Associate Technical Editor: K. Vafai.

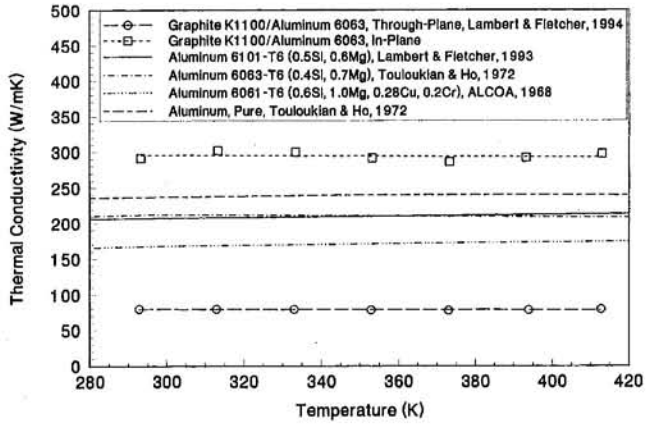

Fig. 1 In-plane and through-plane thermal conductivity versus temperature for graphite P130/aluminum 6063 with comparison to selected 6000 (Al–Mg–Si) series aluminum alloys and pure aluminum

(1953) as ±5.5 percent for k_{thru} and ±9.6 percent for k_{in} of the Gr/Al and Gr/Cu.

Results and Discussion

Figure 1 shows the k_{in} and k_{thru} of the Gr/Al compared to the k values of selected 6000 series (Al–Mg–Si) aluminum alloys and pure aluminum. The k_{in} and k_{thru} of the Gr/Al are 294 and 78 W/mK, respectively, which are 135 and 36 percent of the k, 218 W/mK (126 Btu/hr-ft-°F), of the currently used aluminum 6101-T6 SEM's. This is due to the high axial conductivity, $k_{r,\text{long}}$, (1111 W/mK), and apparently low transverse conductivity, $k_{r,\text{trans}}$, of the graphite fibers.

Figure 2 illustrates k_{in} and k_{thru} of the Gr/Cu compared to the k values of selected grades of copper. The k_{in} and k_{thru} of Gr/Al are 323 and 32.4 W/mK (187 and 18.7 Btu/hr-ft-°F), respectively, which are 83 and 8.4 percent of the k, 387 W/mK (224 Btu/hr-ft-°F), of the presently used electrolytic tough pitch (ETP) copper SEM's.

According to Clyne and Withers (1993) the k_{thru} for a long fiber reinforced composite is:

$$k_{\text{thru}} = k_m + \frac{k_m(k_{r,\text{trans}} - k_m)f}{k_m + (1-f)(k_{r,\text{trans}} - k_m)/2} \qquad (1)$$

However, although $k_{r,\text{long}}$ of the graphite fibers is very high (1111 W/mK), their $k_{r,\text{trans}}$ is probably quite small, judging from the small value of $k_{r,\text{trans}}$ (5.7 W/mK) reported by Touloukian and Ho (1972) for graphite in the direction perpendicular to the hexagonal planes, which are oriented parallel to the axis of the graphite fibers. Also, there is probably significant interfacial resistance between the fibers and matrix. Thus, the effective $k_{r,\text{trans}}$ of the graphite fibers is assumed to equal zero, for which k_{thru} reduces to:

$$k_{\text{thru}} = k_m\left(\frac{1-f}{1+f}\right) \qquad (2)$$

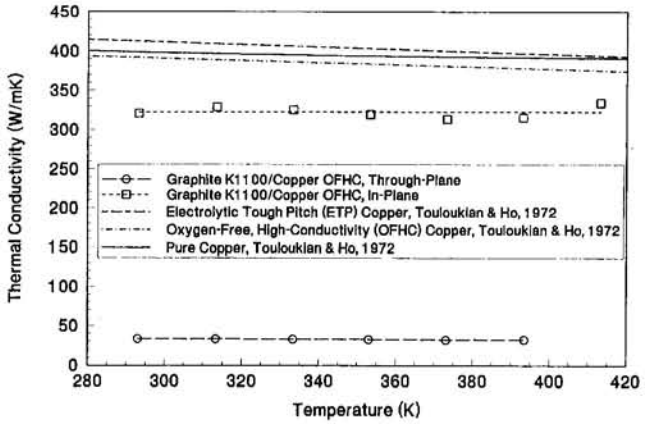

Fig. 2 In-plane and through-plane thermal conductivity versus temperature for graphite P130/copper OFHC with comparison to selected grades of copper

Table 1 Experimental and predicted values of k_{thru} and k_{in} for balanced cross-ply (0/90 deg) Gr/Al and Gr/Cu from the present study with a comparison to experimental results for unidirectional (0 deg) Gr/Cu with a range of fiber volume fractions by Ellis and McDanels (1991)

W/mK ↓	Present Study						Ellis & McDanels (1991)			
	Gr/Al 293 → 413 K 0°/90° f=.42			Gr/Cu 293 → 413 K 0°/90° f=.43			Gr/Cu 0° Experiment 373 K			
	Exp.	Pred.	Diff.	Exp.	Pred.	Diff.	f=.19	f=.35	f=.50	f=.67
k_{thru}	78	89	-12%	32.4	151	-79%	259	174	115	62
k_{in}	294	301	-2.3%	323	355	-9.0%	422	→		450

Because the Gr/Al and Gr/Cu are balanced cross-ply laminates, half the fibers (either the 0 or 90 deg plies) were oriented parallel to the direction of heat flux for in-plane tests. The remainder of the composite, including the other half of the fibers oriented perpendicular to the direction of heat flux, is assumed to exhibit k_{thru}. From the rule of mixtures:

$$k_{in} = k_{r,\text{long}}\left(\frac{f}{2}\right) + k_{\text{thru}}\left(1 - \frac{f}{2}\right) \qquad (3)$$

Substituting values for k_m, $k_{r,\text{trans}}$, $k_{r,\text{long}}$, and f yields the theoretical k_{thru} and k_{in} for Gr/Al and Gr/Cu, which are compared to the experimental values in Table 1.

Assuming $k_{r,\text{trans}}$ of the fibers is zero, k_{in} for Gr/Al is nearly equal to the theoretical value, while k_{thru} for Gr/Al is moderately less than the theoretical value. However, although the k_{in} for Gr/Cu is slightly less than its theoretical value, k_{thru} for Gr/Cu is only a fraction ($\approx\frac{1}{5}$) of its predicted value. Recall that the graphite fibers used in the Gr/Al were coated to improve wettability, thus allowing full densification. Conversely, the graphite fibers used in the Gr/Cu were not coated, and, hence, were not completely wetted by the copper matrix, causing porosity. It would appear that wetting agents are necessary to obtain the maximum possible k_{in} and k_{thru}.

Also included in Table 1 are experimental values of k_{in} and k_{thru} for unidirectional (0 deg) Gr/Cu for four fiber volume fractions obtained by Ellis and McDanels (1991). They employed P100 ultra-high-modulus (UHM) graphite pitch fibers (American Cyanamid Co.) in a pure copper matrix. Their reported k_{in} increases only slightly with increasing fiber volume fraction and is only marginally greater than the k of pure copper (401 W/mK (232 Btu/hr-ft^2-°F)). This suggests that $k_{r,\text{long}}$ of P100 graphite fibers is not considerably greater than the k of copper. If their experimental k_{thru} values for $f = 0.35$ and $f = 0.50$, 174 and 115 W/mK, respectively, are interpolated for $f = 0.43$ (the value of f for Gr/Cu in the present investigation), the result is 143 W/mK, which is only 5.3 percent less than the theoretical k_{thru} (151 W/mK) for Gr/Cu in the present study. Thus, it would appear that the effective $k_{r,\text{trans}}$ of P100 graphite fibers is also negligibly small, as is the effective $k_{r,\text{trans}}$ for P130 graphite fibers.

Acknowledgments

Support for this study was provided by Naval Surface Warfare Center Contract No. N00164-91-C-0043 and the Center for Space Power at Texas A&M University.

References

Aluminum Company of America (ALCOA), 1968, personal communication to L. S. Fletcher, Dec. 10.

ASM Metals Reference Book, 1983, American Society for Metals, Metals Park, Ohio.

Beasley, K. G., 1990, "Thermal Management of Electronics: Annual Status Report for Office of Naval Technology (ONT)," Naval Weapons Support Center (NWSC), Crane, IN, Report No. ESE-04409, Dec.

Clyne, T. W., and Withers, P. J., 1993, *An Introduction to Metal Matrix Composites*, Cambridge University Press, Cambridge, United Kingdom.

Ellis, D. L., and McDanels, D. L., 1991, "Thermal Conductivity and Thermal Expansion of Graphite Fiber/Copper Matrix Composites," presented at the Annual Meeting of the Metallurgical Society, New Orleans, LA, Feb. 17–21.

Gordon, F. H., and Clyne, T. W., 1991, "Transport Properties of Short Fibre SiC Reinforced Ti," in *Metal Matrix Composites—Processing, Microstructure, and Properties, 12th Ris0 International Symposium*, N. Hansen, D. Juul-Jensen, T. Leffers, H. Lilholt, T. Lorentzen, A. S. Pedersen, J. B. Pedersen, and B. Ralph, eds., Ris0 National Laboratory, pp. 361–366.

Kline, S. J., and McClintock, F. A., 1953, "Describing Uncertainties in Single-Sample Experiments," *Mechanical Engineering*, Vol. 75, No. 1, Jan., pp. 3–8.

Kuniya, K., Arakawa, T. K., and Chiba, A., 1987, "Thermal Conductivity, Electrical Conductivity, and Specific Heat of Copper-Carbon Fiber Composite," *Transactions of the Japanese Institute for Metals*, Vol. 28, pp. 819–826.

Lambert, M. A., and Fletcher, L. S., 1993, "The Experimental Thermal Contact Conductance of Vapor Deposited, Electroplated, and Flame Sprayed Silver Coatings," AIAA Paper No. 93-0846.

Lambert, M. A., and Fletcher, L. S., 1994, "Experimental Thermal Contact Conductance of Continuous Fiber Metal Matrix Composites," AIAA Paper No. 94-0122.

Maass, D., and Makwinski, M., 1992, "Pitch Fiber Composites as an Aluminum Replacement for High Performance Avionics Heatsinks," Advanced Composite Products, Inc., Report to Naval Surface Warfare Center (NSWC), Crane, IN.

Montesano, M. J., Wigand, J. T., and Roesch, J. C., 1992, "Demonstration of Advanced Pitch Fiber Composite Heat Sink With Enhanced Through Core Thermal Conductivity," ASME Paper No. 92-WA/EEP-31.

Pfeiffer, W., and Tallon, J., 1992, "High Conductivity Carbon-Carbon Composites for SEM-E Heat Sinks," SAMPE Electronics Conference, June.

Reeves, A. J., Taylor, R., and Clyne, T. W., 1991, "The Effect of Interfacial Reaction or Thermal Properties of Titanium Reinforced With Particulate SiC," *Materials Science and Engineering*, Vol. A141, pp. 129–138.

Touloukian, Y. S., and Ho, C. Y., eds., 1972, *Thermophysical Properties of Matter: Vol. 1, Thermal Conductivity of Metallic Solids; Vol. 2, Thermal Conductivity of Nonmetallic Solids*, Plenum Press, New York.

Conditionally Sampled Turbulent Prandtl Number in the Outer Region of a Turbulent Boundary Layer

D. E. Wroblewski[1]

Introduction

Much of the interest in turbulent Prandtl number models for boundary-layer flows has concentrated on the near-wall region, since predictions of wall heat transfer are most sensitive to near-wall transport. Reviews of turbulent Prandtl number data and modeling approaches were provided by Kays (1994), Reynolds (1975), Kestin and Richardson (1963), and Launder (1976). Despite the critical need for near-wall models, an understanding of the behavior of Pr_t in the outer region of the boundary layer may help to illuminate mechanisms of passive-scalar transport associated with large-scale mixing. This may be directly applicable to flows in which passive contaminants are introduced in the outer layer of boundary-layer flows, and indirectly relevant to transport processes in free-shear turbulent flows such as jets and wakes.

Studies of turbulent Prandtl number in air flow have been carried out by, among others, Kays (1994), Johnson (1959), Simpson et al. (1970), Subramanian and Antonia (1984), Gibson and Verriopoulos (1984), Blair and Bennett (1987), Wroblewski and Eibeck (1991), and Kim et al. (1992). These have shown Pr_t is generally between 0.8 and 1.2 for $y/\delta < 0.6$, with values between 0.86 to 0.9 often chosen for simulations in which Pr_t is assumed constant. A majority of the investigations also indicated a decrease in Pr_t for $y/\delta > 0.6$. Although this behavior is sometimes ignored due to experimental uncertainty, typically $Pr_t \pm 0.2$ or higher, the prevalence of this drop in recent experimental and numerical studies suggests otherwise.

The experimentally observed decrease in turbulent Prandtl number was matched using a combined diffusion-convection model for the Reynolds heat flux (Simpson et al., 1970). The heat-flux model included both gradient transport, due to small-scale eddy mixing, and convective transport, due to larger-scale eddy mixing, while momentum transport was modeled as gradient transport only:

$$-\overline{v\theta} = \epsilon_m \frac{\partial \overline{T}}{\partial y} - V_h\theta_h; \quad -\overline{uv} = \epsilon_m \frac{\partial \overline{U}}{\partial y};$$

$$\mathrm{Pr}_t = \frac{\overline{uv}\,\dfrac{\partial \overline{T}}{\partial y}}{\overline{v\theta}\,\dfrac{\partial \overline{U}}{\partial y}} = \frac{\epsilon_m}{\epsilon_m - V_h\theta_h/(\partial \overline{T}/\partial y)} \tag{1}$$

where V_h is a convection velocity, θ_h is some characteristic temperature scale, and the overbar denotes time averaging. Note that the diffusive component was assumed to be governed by the same diffusivity for both heat and momentum, ϵ_m. In applying this model, Simpson et al. (1970) assumed that θ_h was related to the mean temperature gradient through a mixing length, $\theta_h = l|\partial \overline{T}/\partial y|$, so that overall heat transport was still governed by gradient diffusion. According to Reynolds (1975), it is unlikely that bulk convection, occurring over large length scales, can be adequately represented by gradient diffusion. This paper describes an analysis involving the use of Eq. (1) (Simpson et al., 1970) to match experimental data, without retaining the mixing length approach for the convective transport component, $V_h\theta_h$. The objective of this effort was to further illuminate the roll of large-scale convective transport in the wake region of a boundary layer.

Conditional Sampling

In intermittent regions of the boundary layer, conventional time-mean quantities include contributions from the nonturbulent, free-stream flow, as well as the turbulent flow inside the boundary layer. Conditional sampling with zone averaging was employed to isolate the turbulent zone contributions. For example, the turbulent zone average (denoted by the tz subscript) for the temperature was found from

$$\overline{T}_{tz} = \frac{1}{\gamma t_p}\int_0^{t_p} T(t)I(t)dt \tag{2}$$

where t_p is a sampling period, $I(t) = 1$ in the turbulent zone and $I(t) = 0$ in the free stream, and γ is the time-mean value of $I(t)$. Turbulence quantities, such as the Reynolds stresses and heat fluxes, were determined based on the zone averages, e.g., $\theta_{tz}(t) = T(t) - \overline{T}_{tz}$.

The temperature signal was used to determine the intermittency, since, compared to the velocity signal, it presented a clearer indication of the turbulent/non-turbulent interface (Antonia and Browne, 1987). The resulting intermittency was used for conditional averaging the velocity as well as the temperature.

[1] Aerospace and Mechanical Engineering, Boston University, Boston, MA 02215.

Contributed by the Heat Transfer Division of THE AMERICAN SOCIETY OF MECHANICAL ENGINEERS. Manuscript received by the Heat Transfer Division March 1995; revision received November 1995. Keywords: Forced convection, Turbulence. Associate Technical Editor: B. W. Webb.

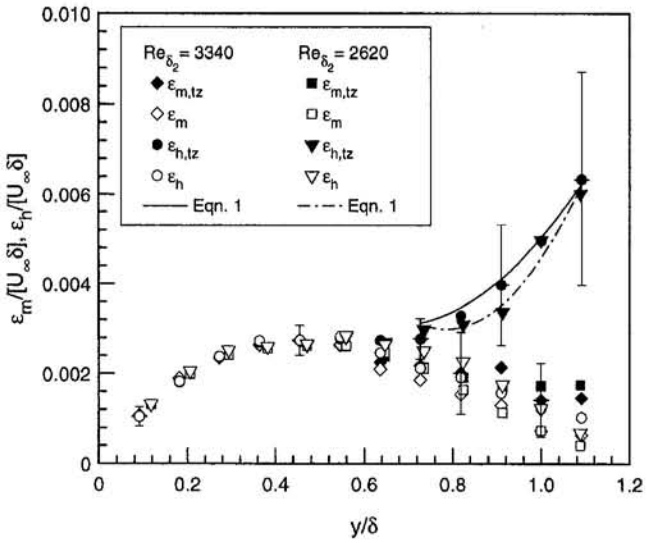

Fig. 1 Eddy diffusivity for heat, ϵ_h, and eddy viscosity, ϵ_m: conventional average (ϵ_h, ϵ_m) and turbulent-zone average ($\epsilon_{h,tz}$, $\epsilon_{m,tz}$). Error bars represent uncertainty (95 percent confidence). Lines are calculations based on Eq. (1).

A simple threshold level approach was employed here to determine the intermittency:

$$T(t) \le T_\infty + k_t; \quad I(t) = 0; \quad T(t) > T_\infty + k_t; \quad I(t) = 1 \quad (3)$$

where k_t is the threshold level and T_∞ is the free-stream temperature. The threshold level was set to twice the rms level of free-stream fluctuations, which were due to signal noise and not actual temperature fluctuations. Calculated values of $v\theta_{tz}$ showed some sensitivity to the choice of k_t, with variations of ±7 percent when k_t was varied over a range from one-half to twice the chosen level. This sensitivity, along with the smaller sensitivities calculated for $\overline{uv}_{tz}$, $\overline{T}_{tz}$, and $\overline{U}_{tz}$, were incorporated into the uncertainty analysis. A more detailed discussion of the conditional sampling, along with comparisons of the intermittency results with standard models, is provided by Wroblewski (1994).

Results

The experimental data considered here were obtained in the U.C. Berkeley Convective Boundary Layer Facility, featuring a constant area cross section (slight favorable pressure gradient) and a constant-heat-flux boundary condition. Details of the facility and instrumentation system can be found from Wroblewski and Eibeck (1991). Operating conditions and general features of the momentum and thermal boundary layers at the two streamwise locations studied were as follows: location, 1.89 and 2.65 m from the test section entrance; free-stream velocity, U_∞, 10.45 and 10.55 m/s; Reynolds numbers, Re_x, 1.29×10^6 and 1.81×10^6; momentum thickness Reynolds number, Re_{δ_2}, 2620 and 3340; 0.99 momentum-boundary-layer thickness, 3.4 and 4.4 cm; wall heat flux, 350 W/m^2, temperature difference between wall and free stream, 15.0 and 15.6°C.

Eddy diffusivity and eddy viscosity were calculated from simultaneous measurements of velocity and temperature, obtained with a triple-wire, heat-flux probe. The probe consisted of a standard X-wire, for two-component velocity measurements, with a constant-current cold wire, used to measure temperature, placed between the two X-wire sensors. To calculate $\epsilon_m = -\overline{uv}/(\partial\overline{U}/\partial y)$ from the measured experimental values, $\partial\overline{U}/\partial y$ was found from an equation of the form $\overline{U}/U_\infty = C(y/\delta)^n$, which was used to fit the measured data. A similar approach was used for ϵ_h, $\epsilon_{m,tz}$, and $\epsilon_{h,tz}$.

Conventional values of ϵ_m and ϵ_h exhibited peak levels near $y/\delta = 0.5$, and a drop toward zero as the outer edge of the boundary layer was approached (Fig. 1). Turbulent zone averages of the eddy viscosity approached an approximately constant level for $y/\delta > 0.7$. In contrast, $\epsilon_{h,tz}$ increased significantly in the intermittent region (Fig. 1). Values of $Pr_{t,tz}$ ($=\epsilon_{m,tz}/\epsilon_{h,tz}$) are lower than conventionally averaged Pr_t (Fig. 2), dropping to 0.15 at the boundary-layer edge. Antonia and Browne (1987) have observed similar trends in wakes, which is not surprising, since the outer region of the boundary layer is quite similar to boundary-free shear flows that are also governed by wakelike mechanisms, i.e., large eddies that scale on the overall turbulent-zone thickness.

In using Eq. (1) to fit the experimental heat-flux values, it was assumed that the convective component of the turbulent heat flux was uniform over a region that scaled on the size of the large eddies responsible for the transport; i.e., $V_h\theta_h$ should be constant in the intermittent region of the boundary layer.

A bulk convection velocity, based on the transport of temperature fluctuations, was used for V_h: $V_c = \overline{v\theta^2}/\overline{\theta^2}$, where $\overline{v\theta^2}$ is a triple velocity-temperature product. V_c is similar to a convection velocity defined by Bradshaw et al. (1967), based on transport of turbulent kinetic energy, and used for modeling triple products in second-order-closure turbulence models. Its use here as the characteristic convection velocity in a diffusion-convection model of heat transport follows the approach of Simpson et al. (1970), and is based on the premise that all scalar properties are transported by analogous mechanisms.

Figure 3 shows that conventionally averaged values of V_c continually increase throughout the boundary layer, similar to trends for V_c calculated using the kinetic energy (Bradshaw et al., 1967). In contrast, $V_{c,tz}$ is nearly constant for $y/\delta > 0.7$, providing some support to the premise that convective transport due to large-scale eddy motions is approximately constant across the intermittent region of the boundary layer. Based on the data in Fig. 3, average values for $y/\delta > 0.7$ are $V_{c,tz}/U_\infty = 0.011$ for $Re_{\delta_2} = 2620$ and $V_{c,tz}/U_\infty = 0.012$ for $Re_{\delta_2} = 3340$.

To determine a proper value of the temperature scale, Eq. (1) can be used along with measured values of $\epsilon_{h,tz}$, $\epsilon_{m,tz}$, $\partial\overline{T}_{tz}/\partial y$, and the average values of $V_{c,tz}$ given above, to find the value for θ_h that best fits the data. This analysis revealed $\theta_h/\Delta T_{tz} = 0.28$ for $Re_{\delta_2} = 2260$ and $\theta_h/\Delta T_{tz} = 0.29$ for $Re_{\delta_2} = 3340$, where $\Delta T_{tz} = \overline{T}_{tz}(y = \delta) - T_\infty$ is a temperature scale characteristic of the intermittent region ($\Delta T_{tz}/[T_w - T_\infty] =$

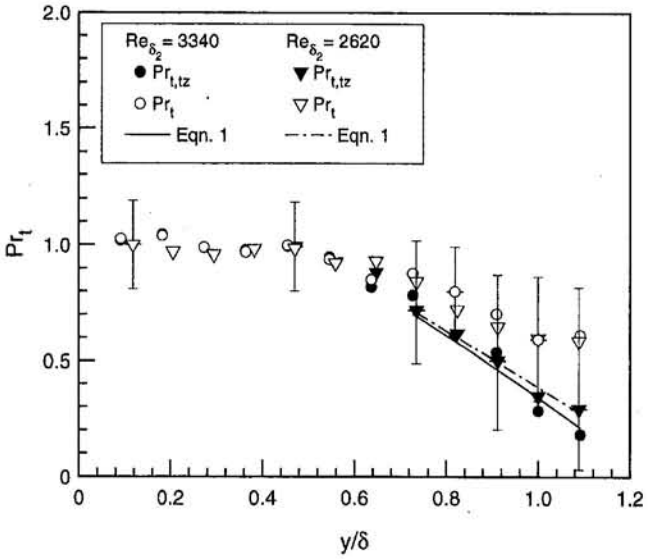

Fig. 2 Turbulent Prandtl number: conventional average (Pr_t) and turbulent-zone average ($Pr_{t,tz}$). Error bars represent uncertainty (95 percent confidence). Lines are calculations based on Eq. (1).

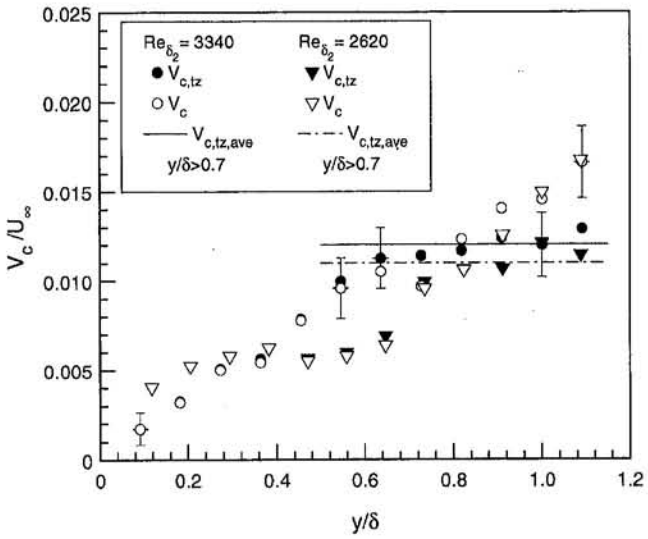

Fig. 3 Bulk convection velocity: conventional average (V_c) and turbulent-zone averages ($V_{c,tz}$). Error bars represent uncertainty (95 percent confidence). Lines are mean of turbulent-zone-average values for $y/\delta > 0.7$.

0.042 for $Re_{\delta_2} = 2260$ and 0.045 for $Re_{\delta_2} = 3340$). Using these values for θ_h, $\epsilon_{h,tz}$ and $Pr_{t,tz}$ were calculated from Eq. (1), with results compared to measurements in Figs. 1 and 2. Calculated values of $Pr_{t,tz}$ matched experimental values within ±0.04 (standard deviation = 0.03) for $y/\delta > 0.7$.

An inherent difficulty in measuring the turbulent Prandtl number is a high degree of uncertainty. Use of turbulent zone averaging tended to exacerbate the problem, since $\partial \overline{T}_{tz}/\partial y < \partial \overline{T}/\partial y$. Uncertainties, shown in each figure, were determined using the method described by Moffat (1988), and are discussed by Wroblewski and Eibeck (1991) for conventional values. For conditional averages, additional analysis was performed to determine the extent of propagation of uncertainties associated with the parameters in the equation used to fit the mean temperature and velocity, as well as sensitivities to the choice of threshold level. The uncertainties suggest that $Pr_{t,tz}$ may not decrease as strongly as indicated by the data (Fig. 2) and the fine detail provided by the diffusion-convection model may be unwarranted. The true test of the generality of the concepts discussed here will be confirmation with experimental data obtained in other facilities.

Conclusions

A composite model, with a diffusive and convective component, was used to analyze the turbulent zone-averaged eddy diffusivity and turbulent Prandtl number in a turbulent boundary layer. The hypothesis that the convective component was uniform across the outer region of the boundary layer ($y/\delta > 0.75$) was consistent with measured data.

Acknowledgments

The experimental data were obtained at the University of California, Berkeley, under grant No. DE-FG03-87ER 13780 from DOE Office of Basic Energy Sciences, and under the supervision of Professor Pamela Eibeck.

References

Antonia, R. A., and Browne, L. W. B., 1987, "Conventional and Conditional Prandtl Number in a Turbulent Wake," *Int. J. Heat Mass Transfer*, Vol. 30, pp. 2023–2030.

Blair, M. F., and Bennett, J. C., 1987, "Hot Wire Measurements of Velocity and Temperature Fluctuations in a Heated Turbulent Boundary Layer," *J. Phys. E.: Sci Instrum.*, Vol. 20, pp. 209–216.

Bradshaw, P., Ferriss, D. H., and Atwell, N. P., 1967, "Calculation of Boundary-Layer Development Using the Turbulent Energy Equation," *J. Fluid Mech.*, Vol. 28, pp. 593–616.

Gibson, M. M., and Verriopoulos, C. A., 1984, "Turbulent Boundary Layer on a Mildly Curved Surface: Part 2: Temperature Field Measurements," *Exp. Fluids*, Vol. 2, pp. 73–80.

Johnson, D. S., 1959, "Velocity and Temperature Fluctuation Measurements in a Turbulent Boundary Layer Downstream of a Stepwise Discontinuity in Wall Temperature," ASME *Journal of Applied Mechanics*, Vol. 26, pp. 325–336.

Kays, W. M., 1994, "Turbulent Prandtl Number—Where Are We?" ASME JOURNAL OF HEAT TRANSFER, Vol. 116, pp. 284–295.

Kestin, I. J., and Richardson, P. D., 1963, "Heat Transfer Across Turbulent, Incompressible Boundary Layers," *Int. J. Heat Mass Transfer*, Vol. 6, pp. 147–189.

Kim, J., Simon, T. W., and Russ, S. G., 1992, "Free Stream Turbulence and Concave Curvature Effects on Heated, Transitional Boundary Layers," ASME JOURNAL OF HEAT TRANSFER, Vol. 114, pp. 338–347.

Launder, B. E., 1976, "Heat and Mass Transport," in: *Turbulence*, P. Bradshaw, ed., Springer, Berlin.

Moffat, R. J., 1988, "Describing Uncertainty in Experimental Results," *Exp. Thermal Fluid Sci.*, Vol. 1, pp. 3–17.

Reynolds, A. J., 1975, "The Prediction of Turbulent Prandtl and Schmidt Numbers," *Int. J. Heat Mass Transfer*, Vol. 18, pp. 1055–1069.

Simpson, R. L., Whitten, D. G., and Moffat, R. J., 1970, "An Experimental Study of the Turbulent Prandtl Number of Air With Injection and Suction," *Int. J. Heat Mass Transfer*, Vol. 13, pp. 125–143.

Subramanian, C. S., and Antonia, R. A., 1984, "Effect of Reynolds Number on a Slightly Heated Boundary Layer," *Int. J. Heat Mass Transfer*, Vol. 24, pp. 1833–1846.

Townsend, A. A., 1976, *The Structure of Turbulent Shear Flow*, Cambridge University Press, Cambridge.

Wroblewski, D. E., and Eibeck, P. A., 1991, "A Frequency Response Compensation Technique for Cold Wires and Its Application to a Heat Flux Probe," *Experimental Thermal and Fluid Science*, Vol. 4, pp. 452–463.

Wroblewski, D. E., 1994, "Conventional and Conditional Eddy Diffusivity and Turbulent Prandtl Number in the Outer Region of a Turbulent Boundary Layer," *Fundamentals of Forced Convection Heat Transfer*, ASME HTD-Vol. 285.

The Conjugate Graetz Problem With Axial Conduction

X. Yin[1] and H. H. Bau[1]

Nomenclature

H, h = conduit's outer radius (half-width)
Hc = conduit's inner radius (half-width)
k = thermal conductivity
Q = heat flux
T = temperature
u = velocity profile
y = a coordinate perpendicular to the flow direction
z = axial coordinate
θ = nondimensional temperature

Subscripts

0 = entrance conditions
f = fluid
s = solid
w = wall

[1] Department of Mechanical Engineering and Applied Mechanics, University of Pennsylvania, Philadelphia, PA 19104-6315.

Contributed by the Heat Transfer Division of THE AMERICAN SOCIETY OF MECHANICAL ENGINEERS. Manuscript received by the Heat Transfer Division May 1995; revision received February 1996. Keywords: Conduction, Conjugate Heat Transfer. Associate Technical Editor: T. Bergman.

1 Introduction

The problem of heat transfer from fluids flowing in conduits (the Graetz problem) is of importance in many technological processes and has been studied extensively in studies dating back to Graetz (1885). The classical Graetz problem neglects axial conduction and considers forced convection heat transfer in a fluid flowing in conduits of various cross-sectional geometries subject to various peripheral boundary conditions imposed at the fluid's boundary. The pertinent literature is summarized in excellent compendiums by Shah and London (1978) and Shah and Bhatti (1987). Studies by Mori et al. (1974, 1976) and Guedes and Ozişik (1992) have taken into account axial conduction in the solid but not in the fluid.

Our study is motivated by recent investigations of heat transfer in microheat exchangers fabricated on silicon wafers (i.e., Weisberg et al., 1992; Yin and Bau, 1995). Flows in these microheat exchangers are characterized by small Peclet numbers, and the area of a solid's cross section perpendicular to the direction of such flows may be as large as or larger than the cross-sectional area available to the flow itself. Thus, axial conduction effects may be important in microheat exchangers. The objective of this paper is to assess the importance of axial heat conduction in both the solid and the liquid. To this end, we studied slug and Poiseuille flows between parallel plates and in circular cylinders. The energy equation was solved simultaneously in the fluid and the solid regions. Uniform temperature (case I) and uniform flux (case II) boundary conditions were imposed on the external solid surface. The equations were solved utilizing eigenfunction expansions. Various properties of the mathematical problem were proved by Yin (1995) but are not presented here.

2 The Mathematical Model

We consider velocity-wise, fully developed flow between two parallel, semi-infinite plates ($m = 0$) distance $2H_C$ apart as well as inside a semi-infinite, circular pipe ($m = 1$) of radius H_C. The solid wall thickness is $(H - H_c)$. Dimensional and nondimensional quantities are denoted, respectively, with upper and lower case letters. Two different velocity profiles, Poiseuille and uniform (slug), are considered:

$$u(y) = \begin{cases} 1 & \text{for slug flow} \\ (1 - y^2) & \text{for Poiseuille flow} \\ 0 & \end{cases} \begin{matrix} (0 < y < 1) \\ \\ (1 < y < h). \end{matrix} \quad (1)$$

The velocity is normalized with the center line speed, $U_{\max}$. y is the nondimensional coordinate normal to the direction of the flow. H_c is the length scale.

The energy equation,

$$u(y)\frac{\partial \theta_i}{\partial z} = \frac{1}{y^m}\frac{\partial}{\partial y}\left(y^m \frac{\partial \theta_i}{\partial y}\right) + \frac{1}{\mathrm{Pe}^2}\frac{\partial^2 \theta_i}{\partial z^2}, \quad (0 < y < h, 0 < z < \infty), \quad (2)$$

takes into account axial conduction in both the fluid and the solid. In the equation above, $\theta_i(y, z)$ is the nondimensional temperature; and the subscripts $i = f$ and $i = s$ refer, respectively, to the fluid and the solid. The nondimensional axial coordinate, z, is normalized with $H_c\mathrm{Pe}$. $\mathrm{Pe} = U_{\max}H_c/\alpha_f$ is the Peclet number and α_f is the fluid's thermal diffusivity. Although viscous dissipation was not included in Eq. (2), if so desired, the viscous dissipation's contribution to the temperature field can be separately computed and superposed on the results presented here.

Table 1 Case II—uniform flux boundary condition—expressions for $f(z)$ and $g_i(y)$

	Planar slug flow	Planar Poiseuille flow	Pipe slug flow	Pipe Poiseuille flow
$f(z)$	z	$\frac{3}{2}z$	$2hz$	$4hz$
$g_f(y)$	$\frac{1}{2}y^2 - \frac{1}{2} + \frac{k_f}{k_s}$	$\frac{3}{4}y^2 - \frac{1}{8}y^4 + \frac{k_f}{k_s} - \frac{5}{8}$	$\frac{h}{2}\left(y^2 - 1\right)$	$h\left(y^2 - \frac{1}{4}y^4\right) - \frac{3}{4}h$
$g_s(y)$	$\frac{k_f}{k_s}y$	$\frac{k_f}{k_s}y$	$\frac{k_f}{k_s}h\ell n(y)$	$\frac{k_f}{k_s}h\ell n(y)$

The thermal boundary and interfacial conditions are:

$$0 = \frac{\partial \theta_f(0, z)}{\partial y} = \theta_f(1, z) - \theta_s(1, z) = \frac{\partial \theta_f(1, z)}{\partial y} - \frac{k_s}{k_f}\frac{\partial \theta_s(1, z)}{\partial y} = \begin{cases} \theta_s(h, z) & \text{(case I)} \\ \dfrac{\partial \theta_s(h, z)}{\partial y} - \dfrac{k_f}{k_s} & \text{(case II).} \end{cases} \quad (3)$$

In case I, the nondimensional temperature is defined as $\theta_i = (T_i - T_w)/(T_r - T_w)$, where T_w is the dimensional temperature at $y = h$ and T_r is the maximum value of the entrance temperature at $z = 0$. Consequently, $0 < \theta_i < 1$. In case II, $\theta_i = k_f(T_i - T_r)/Q_wH_c$, where Q_w is the uniform flux at $y = h$. k_s and k_f denote, respectively, the thermal conductivities of the solid and the fluid. The temperature distribution at the channel's entrance is given by: $\theta_{f,s}(y, 0) = \theta_0(y)$.

We seek a solution of the form:

$$\theta_i(y, z) = \sum_{n=1}^{\infty} C_n\phi_{i,n}(y)\exp(-\lambda_n z) + f(z) + g_i(y) + C_0 \quad (4)$$

with $\lambda_n > 0$. In case I, $f(z) = g_i(y) = C_0 \equiv 0$. In case II, the corresponding values of $f(z)$ and $g_i(y)$ are specified in Table 1 and C_0 must be evaluated from initial conditions. Without loss of generality, we set $f(0) = 0$. Note that due to the negative exponents in Eq. (4), the series converges rapidly for $z > 0$.

We require that ϕ_n satisfy the eigenvalue problem:

$$\left\{\frac{1}{y^m}\frac{d}{dy}\left(y^m\frac{d}{dy}\right) + \lambda_n\left(u_i + \frac{\lambda_n}{\mathrm{Pe}^2}\right)\right\}\phi_{i,n} = 0. \quad (5)$$

The boundary and interfacial conditions are the homogeneous version of Eq. (3).

For $\mathrm{Pe} \to \infty$, Eq. (5) reduces to the classical Graetz problem (without axial conduction). For $\mathrm{Pe} < \infty$, Eq. (5) with the boundary conditions (3) is not a Sturm–Liouville problem since the eigenvalue (λ_n) appears nonlinearly. Yin (1995) showed that the eigenvalues λ_n are real, their magnitude is smaller than those of the corresponding eigenvalues in the classical Graetz problem, and λ_n are a minimum of a variational problem. We calculate the first few eigenpairs using the Prüfer transformation (Birkhoff and Rota, 1978) and a shooting technique.

Once the eigenfunctions were computed, the coefficients C_n are evaluated by satisfying the initial condition at $z = 0$. Unfortunately, the orthogonality conditions, which are satisfied by the eigenfunctions, cannot be used to calculate the coefficients C_n and C_0 in Eq. (4) since their use requires knowledge of *both* the temperature and heat-flux distributions at $z = 0$. This information is not usually available to us. Instead at $z = 0$, we required Eq. (4) to be satisfied in the sense of weighted residuals. We multiply Eq. (7) by weighing functions ($\chi_p(y)$) and

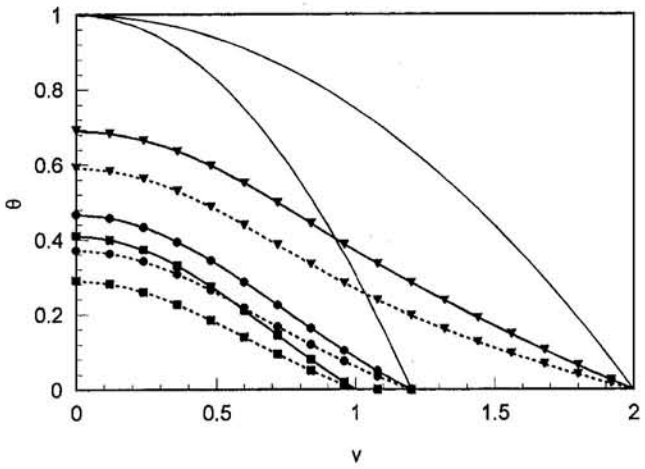

Fig. 1 The temperatures at $z = 0$ (the line without symbols) and 0.2 (the lines with symbols) are depicted as functions of y for pipe Poiseuille flow. Case I. $\{h, k_s/k_f\} = \{2, 1\}$ (triangles), $\{1.2, 243\}$ (squares), and $\{1.2, 1\}$ (circles). Pe = 5. Solid and dashed lines correspond, respectively, to cases when axial conduction is accounted for and those when it is neglected.

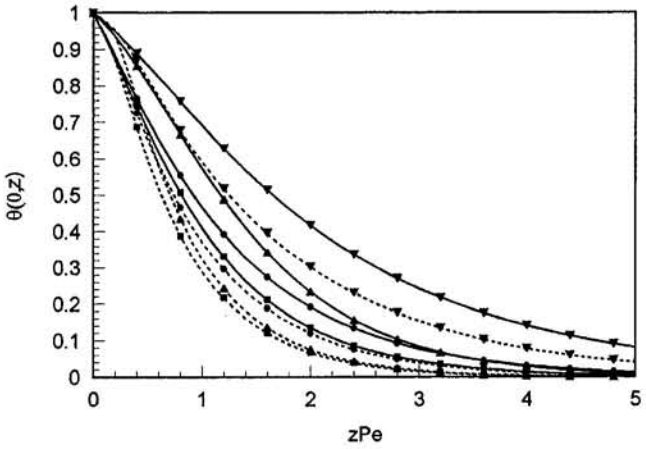

Fig. 2 The centerline temperature is depicted as a function of zPe for pipe Poiseuille flow. Case I. Pe = 5. Inverted triangles, upright triangles, circles, and squares, represent, respectively, $\{h, k_s/k_f\} = \{2, 1\}, \{2, 243\}, \{1.2, 1\}$, and $\{1.2, 243\}$. The solid and dashed lines correspond, respectively, to cases when axial conduction is accounted for and cases when it is neglected.

integrate over the domain $(0 < y < h)$ to obtain an infinite set of algebraic equations for the coefficients C_n:

$$B_p = \sum_{n=0}^{\infty} C_n G_{pn} \quad (0 \le p < \infty), \tag{6}$$

where $B_p = \int_0^h y^m(\theta_0(y) - g(y))\chi_p(y)dy$ and $G_{p,n} = \int_0^h \phi_n(y)\chi_p(y)y^m dy$. Typically, we choose $\chi_p(y) = \phi_p(y)$ for $p > 0$ and $\chi_0(y) = 1$; but these are not the only possible choices.

Next, we truncate the resulting infinite set of equations at $n = N$ and solve the truncated equations. The level of truncation is determined by requiring that $|(C_1^{(N+1)} - C_1^{(N)})/C_1^{(N)}| < \epsilon_1$ and $\int_0^h (\sum_1^N C_n\phi_n(y) + f(z) + g(y) + C_0 - \theta_0(y))^2 dy < \epsilon_1$, where typically $\epsilon_1 \sim 10^{-4}$.

For small z, the rate of convergence of the series (4) depends on the smoothness of the inlet temperature profile. Unrealistic, discontinuous profiles give rise to the Gibbs phenomenon and slow convergence. For smooth inlet temperature distributions such as $\theta_0(y) = \sin((\pi/2)(1 - y/h))$, a few terms $(N < 20)$ in the series are sufficient to satisfy the convergence criteria. As z increases, due to the rapid decay of exponential terms, only a very few terms are required to obtain an accurate description of the temperature field.

It is convenient to summarize the results in terms of the local Nusselt number at the outer surface:

$$\mathrm{Nu}_h(z) = \frac{-2k_s h^m \theta_s'(h, z)}{k_f(\theta_b(z) - \theta(h, z))} \tag{7}$$

The bulk temperature is:

$$\theta_b(z) = \frac{1}{\overline{u}A}\int_A u\theta(y, z)dA = B\int_0^1 \theta_f(y, z)u(y)y^m dy. \tag{8}$$

For planar slug and Poiseuille flows, $B = 1$ and $B = 3/2$, respectively. For slug and Poiseuille flows in circular pipes, $B = 2$ and $B = 4$, respectively.

In general, the Nusselt number $\mathrm{Nu}_h(z)$ depends on the initial conditions. Often one is interested in the fully developed Nusselt number, $\mathrm{Nu}_{h,\infty}$. For case I,

$$\mathrm{Nu}_{h,\infty} = \frac{2\lambda_1}{B}\left\{\frac{1 - \dfrac{\lambda_1^2}{\mathrm{Pe}^2}\dfrac{\overline{\phi_{s,1}}}{\phi_{s,1}'(1)}}{1 + \dfrac{\lambda_1^2}{\mathrm{Pe}^2}\dfrac{\overline{\phi_{f,1}}}{\phi_{f,1}'(1)}}\right\} > \frac{2\lambda_1}{B}, \tag{9}$$

where $\overline{\phi_{f,1}} = \int_0^1 y^m\phi_{f,1}(y)dy$ and $\overline{\phi_{s,1}} = \int_1^h y^m\phi_{s,1}(y)dy$. In the classical Graetz problem (without axial conduction), the inequality in Eq. (9) should be replaced with an equality. For case II, to the leading order, the large z values for the Nusselt number are identical to the same values in the absence of axial conduction.

When axial conduction is accounted for, the asymptotic Nusselt number is larger than when axial conduction is neglected. For large Peclet numbers and slug flow, perturbation theory shows that $\mathrm{Nu}^{\infty}_{h,\text{with axial conduction}} = \mathrm{Nu}^{\infty}_{h,\text{without axial conduction}} + \mathrm{Pe}^{-2}N_1$, where $N_1 > 0$ (Yin, 1995).

3 Results and Discussion

In this section, we present a sample of our results. Due to space limitations, results are given only for Poiseuille flow in circular conduits, for case I, and for solid–liquid conductivity ratios $k_s/k_f = 1$ and 243. The latter corresponds to water flow in a silicon conduit. In all the figures, we compared our results for the generalized, conjugate Graetz problem (solid lines) with results (dashed lines) obtained for the classical conjugate Graetz problem without axial conduction.

Figure 1 depicts the temperature profiles, $\theta(y, 0)$ (inlet, lines without symbols) and $\theta(y, 0.2)$ as functions of y for $\{h, k_s/k_f\} = \{1.2, 1\}$ (circles), $\{1.2, 243\}$ (squares), and $\{2, 1\}$ (triangles), Pe = 5. The thicker wall $(h = 2)$ introduces a higher thermal resistance between the fluid and the ambient than the thinner wall $(h = 1.2)$ does, thus resulting in higher

Table 2 Asymptotic values for the Nusselt numbers in circular pipe flow with Pe = 5

k_s/k_f	h	Nu	With axial conduction	Without axial conduction
1	1.2	Nu_h	2.9686	2.8397
	2	Nu_h	1.8621	1.6867
243	1.2	Nu_h	3.8567	3.6527
	2	Nu_h	7.0152	3.6412

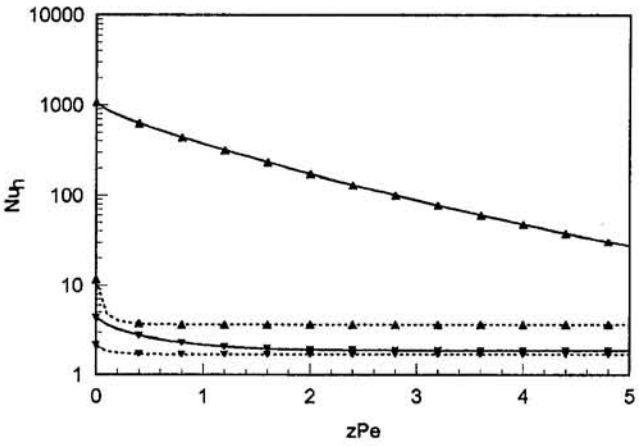

Fig. 3 The Nusselt number at the outer surface (Nu_h) is depicted as a function of zPe for pipe Poiseuille flow. $h = 2$, Pe = 5, $k_s/k_f = 243$ (upright triangles), and $k_s/k_f = 1$ (inverted triangles). Case I. The solid and dashed lines correspond, respectively, to cases when axial conduction is accounted for and cases when it is neglected.

temperatures in the fluid. In the case of $k_s/k_f = 243$, the solid's temperature is almost isothermal due to the solid's high thermal conductivity. Because of this conductivity, the solid offers less thermal resistance to heat losses from the fluid to the ambient, as reflected by the lower temperatures in the case of $k_s/k_f = 243$ than in the case of $k_s/k_f = 1$. A comparison of the solid and dashed lines indicates that at $z\text{Pe} = 1$, axial conduction plays a significant role, increasing the centerline temperature by more than 30 percent above the case without axial conduction ($h = 1.2$, $k_s/k_f = 243$).

Figure 2 depicts the centerline temperature $\theta(0, z)$ as a function of the axial coordinate $z\text{Pe}$ for Pe = 5, $h = 1.2$, $h = 2$, $k_s/k_f = 1$, and $k_s/k_f = 243$. The temperature decays most slowly (rapidly) for the case of $k_s/k_f = 1$, $h = 2$ ($k_s/k_f = 243$, $h = 1.2$) since this case offers the largest (smallest) thermal resistance between the fluid and the ambient. The effects of axial conduction diminish in importance as $z\text{Pe}$ increases.

Figure 3 depicts the Nusselt number at the outer surface, $Nu_h(z)$, as a function of the axial coordinate, $z\text{Pe}$, for Pe = 5, $h = 2$, and $k_s/k_f = 1$ (inverted triangles) and 243 (triangles). As z increases, the Nu numbers approach the asymptotic values we list in Table 2. When axial conduction is accounted for, the thermal development length is longer than when axial conduction is neglected. This is consistent with the eigenvalues of the generalized problem (with axial conduction) being smaller than the corresponding eigenvalues of the classical problem.

4 Conclusions

In this paper, we studied the generalized conjugate Graetz problem (with axial conduction). As expected, axial conduction plays an important role at the entrance region. As the distance from the entrance increases, the role of axial conduction diminishes. In the case of uniform temperature wall conditions, the asymptotic (large $z\text{Pe}$) Nusselt numbers accounting for axial conduction are consistently larger than those obtained neglecting axial conduction. The omission of axial conduction in the uniform temperature and heat flux cases leads, respectively, to under and overestimation of the temperature field in the entrance's vicinity. Omission of axial conduction also leads to an underestimation of the development length.

The analytic solutions produced in this paper are useful for obtaining fully developed Nusselt numbers and for verifying computer codes. For the latter purpose, it would be convenient to use initial conditions that are proportional to the first eigenfunction or a combination of a few eigenfunctions. When doing so, one obtains an exact, closed-form solution for the generalized Graetz problem.

Acknowledgments

The research reported in this paper has been supported, in part, by the National Science Foundation through grant No. CTS 90-12904.

References

Birkhoff, G., and Rota, G., 1978, *Ordinary Differential Equations,* Wiley, New York.

Graetz, L., 1885, "Uber die Warmeleitungsfähigkeit von Flussigkeiten (On the Thermal Conductivity of Liquids)," *Ann. Phys. Chem.,* Vol. 25, pp. 337–357.

Guedes, R. O. C., and Özişik, M. N., 1992, "Conjugated Turbulent Heat Transfer With Axial Conduction in Wall and Convection Boundary Conditions in a Parallel-Plate Channel," *Int. J. Heat and Fluid Flow,* Vol. 13, pp. 322–328.

Mori, S., Sakakibara, M., and Tanimoto, A., 1974, "Steady Heat Transfer to Laminar Flow in a Circular Tube With Conduction in the Tube Wall," *Heat Transfer—Jpn. Res.,* Vol. 3(2), pp. 37–46.

Mori, S., Shinke, T., Sakakibara, M., and Tanimoto, A., 1976, "Steady Heat Transfer to Laminar Flow Between Parallel Plates With Conduction in the Wall," *Heat Transfer—Jpn. Res.,* Vol. 5(4), pp. 17–25.

Shah, R. K., and London, A. L., 1978, *Laminar Flow Forced Convection in Ducts,* Academic Press, New York.

Shah, R. K., and Bhatti, M. S., 1987, "Laminar Convective Heat Transfer in Ducts," in *Handbook of Single-Phase Heat Convective Heat Transfer,* S. Kakac, R. K. Shah, and W. Aung, eds., Wiley, New York.

Weisberg, A., Bau, H. H., and Zemel, J., 1992, "Analysis of Microchannels for Integrated Cooling," *Int. J. Heat Mass Transfer,* Vol. 35, pp. 2465–2474.

Yin, X., and Bau, H. H., 1993, "Axial Conduction Effects on the Performance of Micro Heat Exchangers," ASME Paper No. 93-WA/HT-5.

Yin, X., 1995, "Micro Heat Exchangers," Ph.D. Thesis, University of Pennsylvania, Philadelphia.

Yin, X., and Bau, H. H., 1995, "Uniform Channel Microheat Exchangers," *Proceedings of the Symposium on Thermal Science and Engineering in Honor of Chancellor Chang-Lin Tien,* pp. 171–177.

Heat Transfer and Fluid Mechanics Measurements for the Endwall Boundary Layer Downstream of a Streamlined Strut

D. A. Tyszka[1] and D. E. Wroblewski[2,3]

Introduction

Past studies involving simplified strut–wall intersections fall into two categories: studies of "bluff-body" strut geometries and studies with streamlined struts. Past studies with bluff-body strut shapes (i.e., circular cylinders, tapered cylinders, prismatic bodies, etc.) have addressed endwall-boundary-layer fluid mechanics (Baker, 1979; Eibeck, 1990; Eibeck and Barland, 1993), endwall heat transfer (Fisher and Eibeck, 1990), or both fluid mechanics and heat transfer (Wroblewski and Eibeck, 1992; Pauley, 1993). Past studies involving streamlined strut shapes (i.e., NACA airfoils and airfoil-like bodies) have addressed only fluid mechanics without coverage of heat transfer

[1] Engineer, General Electric Aircraft Engines, Lynn, MA 01910.

[2] Assistant Professor, Dept. of Aerospace and Mechanical Engineering, Boston University, Boston, MA 02215.

[3] Mem. ASME.

Contributed by the Heat Transfer Division and presented at the International Mechanical Engineering Congress and Exposition, Chicago, Illinois, November 6–11, 1994. Manuscript received February 1995; revision received December 1995. Keywords: Forced Convection, Turbulence. Associate Technical Editor: T. W. Simon.

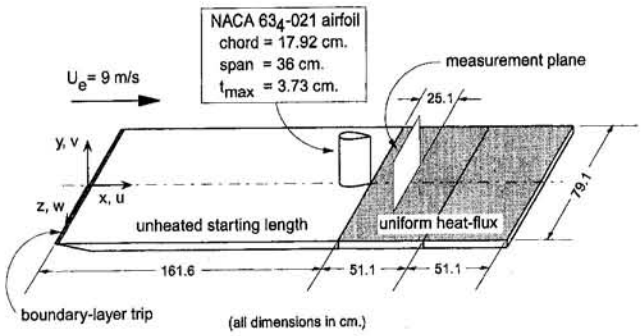

Fig. 1 Experimental setup

(Mehta, 1984; Rood, 1984; Merati et al., 1988). To the authors' knowledge, the current study is the first investigation of its kind to address both heat transfer and fluid mechanics for the endwall boundary layer downstream of a streamlined strut.

Two flow effects typically dominate near-wall flows downstream of strut–wall intersections: streamwise vorticity and the turbulent wake. Researchers in this field currently disagree on the relative importance of these two effects to endwall heat transfer. By investigating a strut geometry for which wake effects were minimized, but streamwise vorticity was still present, the current study attempted to address the question of which effect is more important to endwall heat transfer.

Experimental Method

The current study was conducted in the Boston University boundary layer wind tunnel using the experimental setup shown in Fig. 1. The test setup consisted of a flat-plate unheated starting length followed by a region of uniform heat flux (produced by a pair of electrical resistance heaters). A NACA 63$_4$-021 airfoil was mounted perpendicular to the plate and at zero incidence to the flow. The airfoil's trailing edge coincided with the start of heating while its plane of symmetry coincided with the plane $z = 0$.

For all tests in the current study, the wind tunnel free-stream velocity, U_e, was approximately 9 m/s, and Re_{chord} (Reynolds number based on airfoil chord and U_e) was approximately 10^5. For these flow conditions, r_0/δ (the ratio of strut leading-edge radius to flat-plate velocity-boundary-layer thickness at airfoil leading edge) was approximately 0.19. Per Rood (1984) and Mehta (1984), this condition should have produced a relatively weak, diffuse horseshoe vortex. Also, due to the streamlined shape of the airfoil, the wake region should have been relatively weak.

Five-hole directional pressure probe velocity-boundary-layer measurements, cold-wire anemometer thermal-boundary measurements, and endwall-heat-transfer measurements were taken across y–z planes located approximately 1.4 and 4.3 chord lengths downstream of the airfoil trailing edge. Due to space limitations, only the 1.4 chord results are presented in this article. Results for the 4.3 chord cases, as well as detailed descriptions of instrumentation, data acquisition systems, and data reduction methods used during this study are contained in the work by Tyszka and Wroblewski (1994). Estimated 95 percent confidence experimental uncertainties for the results presented in this article were calculated using the method described by Moffat (1988) and are reported in the captions of the appropriate figures.

Results and Discussion

Figures 2 and 3 present measurements of the velocity boundary layer. The vector plot of mean secondary velocity, $(v^2 + w^2)^{1/2}$, shown in Fig. 2 reveals the presence of *weak* organized vorticity whose sense and location are consistent with those of a horseshoe vortex leg located *some distance above the wall.* Contours of normalized mean streamwise velocity, u/U_e, shown in Fig. 3, reveal the narrow wake region, which appears as a symmetrically shaped local deficit in streamwise velocity centered at $z/t_{max} = 0$ and spanning a region approximately equal to the airfoil maximum thickness, t_{max}. Effects of the weak horseshoe vortex noted in Fig. 2 are visible in Fig. 3 near $z/t_{max} = \pm 0.5$ and $z/t_{max} = 2$, where normalized streamwise velocity contours are locally distorted. Near $z/t_{max} = \pm 0.5$, several contours in Fig. 3 dip toward the wall slightly. This local velocity-boundary-layer thinning is probably a result of the weak intervortex downflow visible in Fig. 2 near $z/t_{max} = 0$. Near $z/t_{max} = 2$, several contours in Fig. 3 move away from the wall slightly, locally thickening the velocity boundary layer. We note that $z/t_{max} = 2$ corresponds approximately to the location of a weak vortex-induced upflow in Fig. 2.

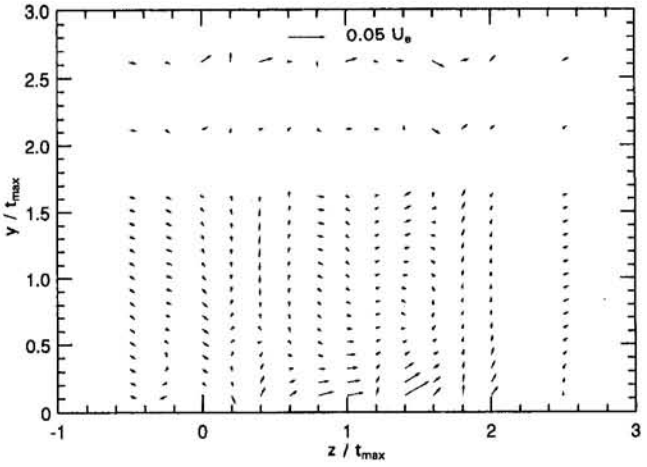

Fig. 2 Mean secondary velocity vectors, $vj + wk$ across 1.5 chord length downstream measurement plane. $Re_{chord} = 9.82 \times 10^4$. Uncertainty in v, $w = \pm 8.9$ percent U_e.

Figures 4 and 5 present measurements of the thermal boundary layer. From Fig. 4, which shows contours of normalized *mean* temperature, $(T_w - T)/(T_w - T_e)$ (note: T_w is spanwise average wall temperature, T is local mean air temperature, and T_e is free-stream air temperature), it is apparent that the thermal boundary layer is also distorted by the presence of the airfoil. The thermal boundary layer is locally thinned over $-1 < z/t_{max} < +1$ (which roughly coincides with the wake and intervortex downflow regions noted in the velocity-boundary-layer results),

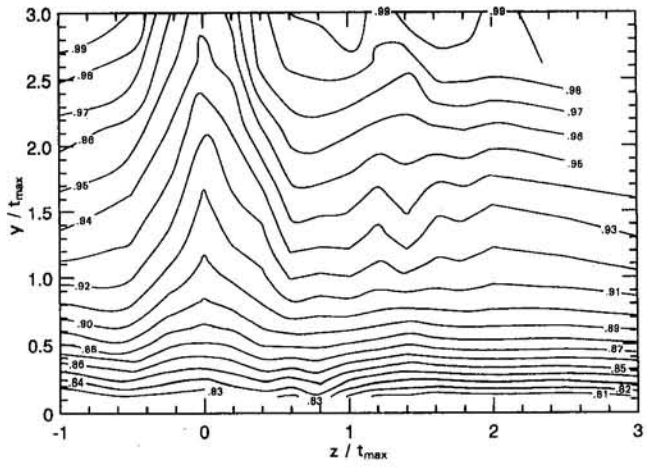

Fig. 3 Contours of normalized mean streamwise velocity, u/U_e across 1.5 chord length downstream measurement plane. $Re_{chord} = 9.82 \times 10^4$. Uncertainty in $u/U_e = \pm 0.059$.

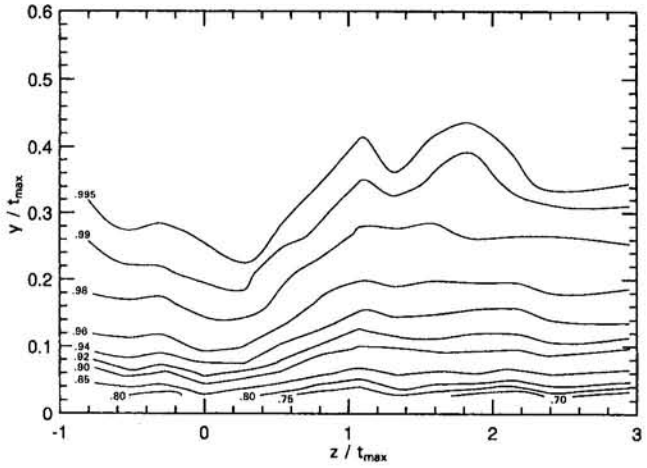

Fig. 4 Contours of normalized mean temperature, $(T_w - T)/(T_w - T_e)$ across 1.4 chord length downstream measurement plane. $Re_{chord} = 1.11 \times 10^5$.

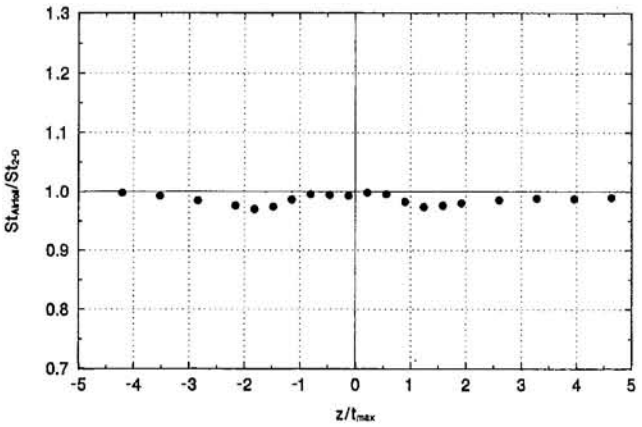

Fig. 6 Transverse variation of wall Stanton number ratio, $St_{Airfoil}/St_{2\text{-}D}$ across 1.4 chord length downstream measurement plane. $Re_{chord} = 1.11 \times 10^5$. Uncertainty in $St_{Airfoil}/St_{2\text{-}D} = \pm 0.076$.

and locally thickened over the region $+1 < z/t_{max} < +2.4$ (which roughly lines up with the horseshoe vortex-induced upflow visible in Fig. 2).

It should be emphasized that distortions of the velocity and thermal boundary layers noted in Figs. 3 and 4 are only present *far above the wall.* The *near-wall* structures of these boundary layers are not significantly different from those of simple flat-plate boundary layers. This finding has particular significance in interpretations of endwall-heat-transfer results.

Figure 5 shows localized distortions of normalized *fluctuating* temperature contours, $\theta'/(T_w - T_e)$, where θ' is the root-mean-square of the local air temperature fluctuations. If enhanced turbulent mixing in the near-wall wake was significant for the flow of interest, there should be a peak in the fluctuating temperature contours over $-0.5 < z/t_{max} < +0.5$. Since such a peak does not occur (in fact, there is a local trough in this region), wake-related effects are likely unimportant for the subject near-wall flow.

Figure 6 gives endwall-heat-transfer results as ratios of local wall Stanton numbers for cases with and without the airfoil. From Fig. 6, it is apparent that endwall heat transfer with the NACA 63_4-021 airfoil in place differs by no more than 3 percent from that of the corresponding flat-plate-only case. This result is somewhat surprising, since *significant* localized downstream endwall-heat-transfer enhancement has been observed by others for *bluff body* struts. The lack of significant enhancement in the current study is explained by two observations from the velocity and thermal boundary-layer results. First, boundary-layer distortions caused by the horseshoe vortex and wake only occur *far above the wall.* Second, the wake is weak and does not seem to influence turbulence levels significantly *near the wall.*

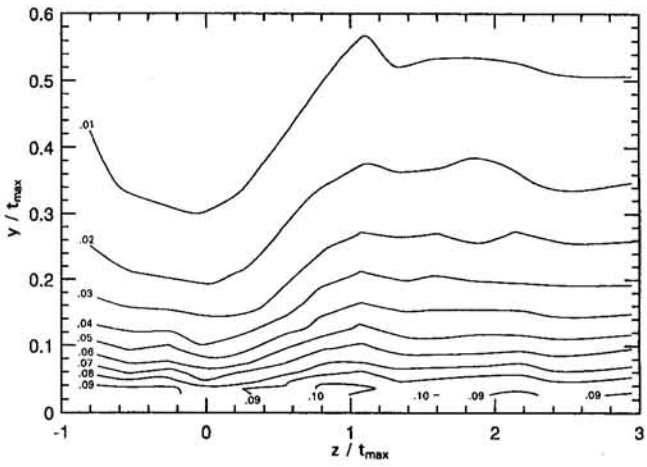

Fig. 5 Contours of normalized fluctuating temperature, $\theta'/(T_w - T_e)$ across 1.4 chord length downstream measurement plane. $Re_{chord} = 1.11 \times 10^5$.

Summary/Conclusions

Endwall heat transfer downstream of a simple strut–wall intersection featuring a NACA 63_4-021 airfoil is not significantly different from that of the corresponding flat-plate-only case. This lack of significant endwall-heat-transfer enhancement occurs in the presence of a weak horseshoe vortex and a weak wake, which both cause localized distortions of the velocity and thermal boundary layers in the *outer regions* of these layers, but *not near the wall.*

When considered with results from previous studies by others of bluff-body struts (Pauley, 1993; Wroblewski and Eibeck, 1992), the results of the current study suggest the existence of a previously undocumented trend relating absolute level of downstream endwall-heat-transfer augmentation to degree of strut streamlining. Blunt strut shapes (such as circular cylinders) produce the greatest endwall-heat-transfer enhancement. Moderately streamlined struts (such as tapered cylinders) produce less enhancement. Highly streamlined struts (i.e., airfoils) produce almost no enhancement. *Peak enhancement levels seem to drop as strut streamlining increases.*

It should be noted that for the progression of increasingly streamlined strut shapes given above, streamwise vorticity in one form or another is always present (in various strengths), but the turbulent wake region is continually diminishing in strength and extent. Thus, the results of the current study (when considered with findings from previous research by others) seem to suggest that the wake region (*not* the horseshoe vortex or other streamwise vorticity) is likely the primary factor responsible for endwall-heat-transfer augmentation downstream of strut–wall intersections.

As a footnote to this last conclusion it should be mentioned that the relative importance of wake and streamwise vorticity effects to endwall heat transfer is likely dependent not only on strut shape, but also on strut size and free-stream flow conditions. In fact, it is fully reasonable to expect that for any given strut shape, there may exist combinations of flow conditions and strut size for which the wake is *not* the dominant endwall heat transfer-controlling factor. Although exploration of this issue was beyond the scope of the present study, the authors nonetheless wish to point out that the conclusion stated in the preceding paragraph on the relative importance of wake versus

streamwise vorticity effects *may not* be universally applicable, but may instead only apply for certain strut sizes and flow regimes.

Acknowledgments

Sincere appreciation is expressed to Ms. Qi Xie for her contributions to this research, to the General Electric Company for its support of the first author during this research project, and to the National Science Foundation for its support of the second author under grant No. CTS-9211282.

References

Baker, C. J., 1979, "The Laminar Horseshoe Vortex," *J. Fluid Mech.*, Vol. 95, Pt. 2, pp. 347–368.

Eibeck, P. A., 1990, "An Experimental Study of the Flow Downstream of a Circular and Tapered Cylinder," ASME *Journal of Fluids Engineering*, Vol. 112, pp. 393–401.

Eibeck, P. A., and Barland, D. E., 1993, "Turbulent Mixing Behind Two-Dimensional and Finite Obstacles," *Turbulent Mixing*, ASME FED-Vol. 174, pp. 57–63.

Fisher, E. M., and Eibeck, P. A., 1990, "The Influence of a Horseshoe Vortex on Local Convective Heat Transfer," ASME JOURNAL OF HEAT TRANSFER, Vol. 112, pp. 329–335.

Mehta, R. D., 1984, "Effect of Wing Nose Shape on the Flow in a Wing/Body Junction," *Aeronautical Journal*, Vol. 88, No. 880, pp. 456–460.

Merati, P., McMahon, H. M., and Yoo, K. M., 1988, "Experimental Modeling of a Turbulent Flow in the Junction and Wake of an Appendage Flat Plate," presented at the AIAA/ASME/SIAM/APS 1st National Fluid Dynamics Congress, Cincinnati, OH, pp. 1255–1264.

Moffat, R. J., 1988, "Describing Uncertainty in Experimental Results," *Exp. Thermal Fluid Sci.*, Vol. 1, pp. 3–17.

Pauley, W. R., 1993, "The Fluid Mechanics and Heat Transfer Downstream of Struts Spanning a Low-Aspect-Ratio Channel," ASME Paper No. 93-HT-41.

Rood, E. P., 1984, "The Separate Spatial Extents of the Trailing Horseshoe Root Vortex Legs From a Wing and Plate Junction," Paper No. AIAA-84-1526.

Tyszka, D. A., and Wroblewski, D. E., 1994, "An Experimental Investigation of Heat Transfer and Fluid Mechanics in the Turbulent Endwall Junction Boundary Layer Downstream of a Truly Streamlined Body," *Fundamentals of Heat Transfer in Forced Convection*, ASME HTD-Vol. 285, pp. 25–32.

Wroblewski, D. E., and Eibeck, P. A., 1992, "Turbulent Heat Transport in a Boundary Layer Behind a Junction of a Streamlined Cylinder and a Wall," ASME JOURNAL OF HEAT TRANSFER, Vol. 114, pp. 840–849.

The LMTD Correction Factor for Single-Pass Crossflow Heat Exchangers With Both Fluids Unmixed

A. S. Tucker[1]

Introduction

The majority of undergraduate texts on heat transfer include a chapter on heat exchangers, almost always containing a section that explains the concept of the log mean temperature difference (LMTD) for simple parallel and counterflow heat exchangers, and the correction factor, F, which must be applied to the LMTD for other heat exchanger types.

Whenever that section of such a text includes a reproduction of the LMTD correction factor chart for single-pass crossflow heat exchangers with both fluids unmixed (see Fig. 1 and, for example, Holman (1992), Incropera and DeWitt (1990), Kreith and Bohn (1986), and White (1988)), it is highly probable that the text authors have unwittingly extended the propagation of small but discernible errors directly traceable to a paper by one of the most recognizable names in the early heat transfer literature, Wilhelm Nusselt. To illustrate by typical example the extent of the error: For such a crossflow heat exchanger with a capacity ratio of unity (i.e., the dimensionless temperature ratio $R = \Delta t_{hot}/\Delta t_{cold} = 1$) in which the change in the cold fluid temperature relative to the difference between the inlet temperatures of the two fluids is $P = \Delta t_{cold}/\Delta t_{in} = 0.6$, the error in the LMTD correction factor, F, read off the chart is 3 percent. At the extreme combination of low values of R and values for P approaching unity, the error is considerably greater: At $R = 0.2$ and $P = 0.975$ the error exceeds 10 percent.

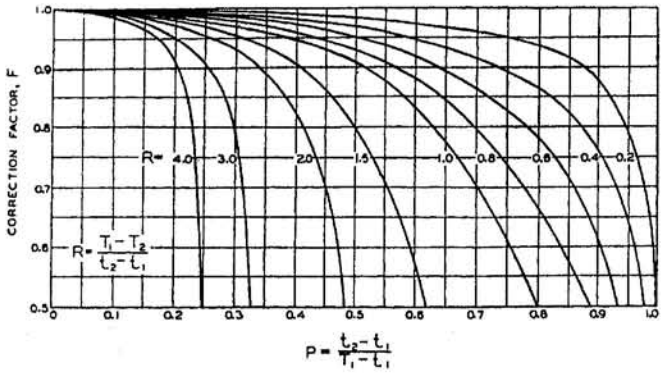

Fig. 1 The original LMTD correction factor chart for a single-pass crossflow heat exchanger in which both fluids are unmixed (from Bowman et al., 1940)

Background

The existence of these errors was discovered in the course of preparing a partial set of LMTD correction factor charts and effectiveness-NTU charts for inclusion in a student handout. Rather than copying the frequently reproduced figures, it was decided to generate them directly in a spreadsheet by making use of the well-established formulae readily available in the literature. This is a quite straightforward task for all but the case of a crossflow heat exchanger in which both fluids are unmixed. The two-dimensional temperature field for both fluids in this particular exchanger configuration requires a more complex analysis, which has been attempted by a number of authors. Notable among these, Nusselt published an analytical solution to the problem in 1911, the solution being in the form of a doubly infinite series, which was acknowledged to exhibit very slow convergence. Almost two decades later (1930), he produced an alternative solution, again in the form of an infinite series but more rapidly convergent than his earlier solution. This later paper of Nusselt included tabulated numerical values, derived from his series solution, which were utilized by Smith (1934) and have been reproduced in their original three significant figure form in at least one reasonably modern heat transfer text (Bayley et al., 1972).

The landmark paper that originated the most commonly used form of LMTD correction charts was that of Bowman et al. (1940) and, for the case of the crossflow heat exchanger with both fluids unmixed, these authors drew on the work of both Nusselt (1930) and Smith. It is this particular chart of Bowman et al. that most heat transfer texts present and acknowledge.

Subsequent to the LMTD analysis approach, the extensive work of Kays and London (1958) was published, presenting the often-used effectiveness-NTU (ϵ-NTU) charts, which overcame some shortcomings in the LMTD analysis procedure. To con-

[1] Department of Mechanical Engineering, University of Canterbury, Christchurch, New Zealand.

Contributed by the Heat Transfer Division of THE AMERICAN SOCIETY OF MECHANICAL ENGINEERS. Manuscript received by the Heat Transfer Division June 1995; revision received October 1995. Keywords: Heat Exchangers, Numerical Methods. Associate Technical Editor: T. J. Rabas.

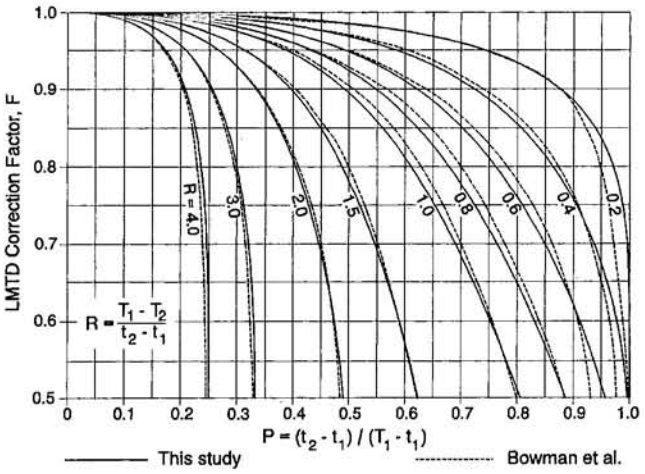

Fig. 2 A comparison between the correction factor curves of the present study and those of Fig. 1

struct the ϵ-NTU chart for the crossflow heat exchanger with both fluids unmixed also requires use of an analytical expression for the mean outlet temperatures of the fluids, and Kays and London used an even more rapidly convergent infinite series solution, this one being due to Mason (1955). This solution was also the one that had been utilized by Stevens et al. (1957) but, like Kays and London, their charts of heat exchanger performance were in terms of effectiveness rather than LMTD correction.

Roetzel and Nicole (1975) recognized the potential usefulness of explicit representations of LMTD correction factors in developing computerized packages for heat exchanger design. In obtaining suitable values for the coefficients to be inserted in their equation for the case of crossflow heat exchangers, they made use of the doubly infinite series solution of Nusselt (1930). As will be seen, it is significant that it was Nusselt's solution series that they used, rather than the subsequent tabulated numerical values that Nusselt presented in his paper.

Methodology

Because Mason's paper was immediately accessible, his solution was the one initially chosen for the present exercise of generating the LMTD correction chart from first principles. Thus an iterative solution procedure was set up within a spreadsheet to produce the desired chart, in the confident expectation that it would be indistinguishable from that published by Bowman et al.

Very briefly, the iterative scheme to generate the curve for a particular value of R proceeded as follows: For a particular value of P at which F was to be evaluated, a trial value for a (defined as the number of transfer units for the hot fluid) was assumed, and Mason's series summed to include sufficient terms that there was no change in the fifth significant figure. From that summed series, P was calculated and compared with the value for P at which the value for F was being sought. By simply iterating on a in increments that were suitably reduced as the final solution was approached, the solution was completed when the calculated value for P matched the desired value within an acceptable tolerance (0.00001, with P being in the range from 0 to 1). With each point on each curve being calculated independently of its neighboring points, there was no possibility of accumulating errors as P was incremented.

The end result of doing this for the same values of R as are plotted in Fig. 1 is shown in Fig. 2 (in which the curves from Fig. 1 have been superimposed as accurately as physically reading values off a chart allows). Clearly there are areas of the chart where there are small but significant discrepancies that were found to be insensitive to both retaining even more terms in the series (typically six were more than sufficient in the areas of noticeable discrepancy) and the error tolerance applied on P in the iteration procedure.

Discussion

Possible explanations for the discrepancies are: Nusselt's 1930 series solution is in error; Nusselt's numerical values derived from his series are in error; Bowman et al. made an error in implementing Nusselt's numerical values; Mason's solution is in error (which would, if true, result in consequential errors in Kays and London's ϵ-NTU chart); or the numerical iterative procedure being utilized was erroneous.

The third of these possible explanations can be quickly eliminated by comparing Nusselt's numerical results with the curve of Bowman et al. for the case of R being unity (implying a capacity ratio of unity): The agreement is very good, verifying that they had correctly interpreted his tabulated data. When Nusselt's series solution (rather than his table of numerical results) was subsequently encoded and summed within a spreadsheet by a procedure very similar to that described above, the resultant curves were indistinguishable from those obtained via the Mason solution and, as independent verification of the numerical procedure, matched extremely well with selected points from an ϵ-Ntu analysis.

For example, for the case $R = 1.0$ and $P = 0.6$, the iteration procedure outlined above (using either the Mason or the Nusselt series) results in a solution $F = 0.8113$ at which the number of transfer units Ntu = 1.8486 and the effectiveness $\epsilon = 0.6000$ (as it should if $P = 0.6$ at a capacity ratio of unity, as is implied by $R = 1.0$).

This effectiveness value also corresponds very well with the prediction of 0.6003 obtained from the empirical relationship

$$\epsilon \approx 1 - \exp\{[\exp(-\mathrm{NTU}^{0.78} r) - 1] \cdot \mathrm{NTU}^{0.22}/r\}$$

(where r represents the capacity ratio $C_{\min}/C_{\max} = R = 1$ in this particular case) which usually is accepted as an approximate representation of the ϵ-NTU relationship for an exchanger of this type (see, for example, Holman, 1992).

Furthermore, when $R = 1$ and $P = 0.6$ are substituted into the general approximate explicit equation for mean temperature difference developed by Roetzel and Nicole—based on Nusselt's solution but *not* on his tabulated values—the resulting value of $F = 0.8117$ is in almost exact agreement with the solution value of 0.8113 obtained here.

On the other hand, for the same values of $R = 1.0$ and $P = 0.6$, Nusselt's numerical value for F (reflected in Fig. 1) is 0.835 which, for the same Ntu value of 1.8486, corresponds to an incompatible value of 0.617 for the effectiveness.

The explanation for the discrepancies is therefore clear: The error lies in the numerical values presented by Nusselt and embraced by Bowman et al., not in the series solution he derived. Close examination of Nusselt's paper reveals three principal points at which the errors arose, and these are attributable to the severely limited calculator resources available in 1930.

First, it appears from the numbers presented that Nusselt retained only five terms in evaluating his series and, while this is of adequate accuracy over most of the domain of interest, the higher order terms do become significant under particular combinations of his initial input parameters. Second, for three of his five-term series summation calculations (out of a total of 20) there were not-insignificant outright numerical errors.

Finally, and probably most importantly, the subsequent calculation sequence adopted by Nusselt had the potential to introduce significant interpolation errors. From the original table of only 20 evaluated data points (many of which were inaccurate for either or both of the first two reasons above), Nusselt developed a three-dimensional surface over a square coordinate base,

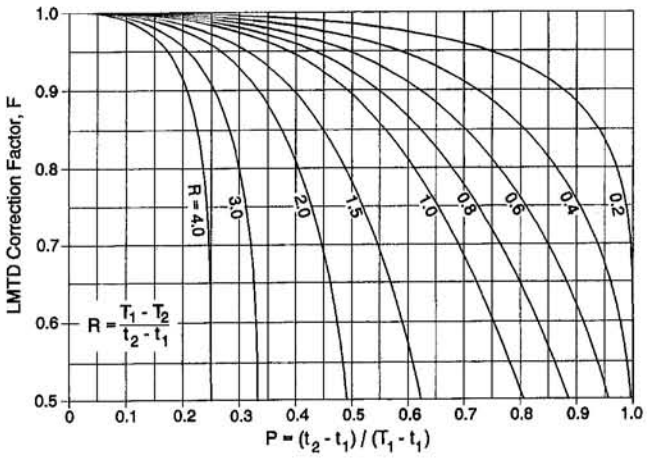

Fig. 3 The correct form of the LMTD correction factor chart for a single-pass crossflow heat exchanger in which both fluids are unmixed. (This figure repeats the corrected curves generated in this study and included in Fig. 2, with the erroneous curves of Bowman et al. removed so as to provide an uncluttered chart for other users.)

and this surface had pronounced curvature at two of its edges. By interpolating over this surface, he generated two subsequent tables each containing 100 points, the vast majority of which did not coincide with any of the comparatively sparse data points from which the surface had been constructed.

Consequently, Nusselt's final tables of values presented to three significant figures imply a calculation accuracy that is, in fact, quite unjustified. Indeed, were Nusselt to submit his paper to ASME JOURNAL OF HEAT TRANSFER under its current policy of requiring that papers containing numerical solutions have an assessment of numerical errors, it is probable that it would not be considered for review!

Conclusion

It must be acknowledged that in current heat exchanger design practice, rarely would use be made of LMTD correction factor charts such as the one discussed here. Normally it would be expected that LMTD correction factors, if used, would be represented by the appropriate equations incorporated into computer-based design packages. Alternatively, the need for an LMTD correction factor can be bypassed through the use of the ϵ-NTU method of analysis.

Nevertheless, and although generally they are not major in their magnitude, the errors revealed unexpectedly as a result of this work do illustrate that even a respected name in the heat transfer literature was not totally infallible, and that errors can easily propagate through the literature for decades; it is hoped that now there is no need for those errors to propagate further, particularly in undergraduate heat transfer texts where the LMTD correction factor charts are commonly presented. For this purpose, Fig. 3 has been prepared.

Finally, out of fairness to Nusselt and out of respect for his standing, it must be said that current computers enable us easily to undertake tasks that would not have been even contemplated a few decades ago. Had Nusselt attempted his task with access to the facilities now available to even the most humble of researchers, his published results almost certainly would have been accurate and unchallengeable.

References

Bayley, F. J., Owen, J. M., and Turner, A. B., 1972, *Heat Transfer,* Nelson, London.

Bowman, R. A., Mueller, A. C., and Nagle, W. M., 1940, "Mean Temperature Difference in Design," *Trans. ASME,* Vol. 62, pp. 283–294.

Holman, J. P., 1992, *Heat Transfer,* 7th ed., McGraw-Hill, New York.

Incropera, F. P., and DeWitt, D. P., 1990, *Fundamentals of Heat and Mass Transfer,* 3rd ed., Wiley, New York.

Kays, W. M., and London, A. L., 1958, *Compact Heat Exchangers,* McGraw-Hill, New York.

Kreith, F., and Bohn, M. S., 1986, *Principles of Heat Transfer,* 4th ed., Harper and Row, New York.

Mason, J. L., 1955, "Heat Transfer in Crossflow," *Proc. 2nd U.S. National Congress of Applied Mechanics,* ASME, New York, pp. 801–803.

Nusselt, W., 1911, "Der Wärmeübergang im Kreutzstrom," *Zeitschrift des Vereines deutscher Ingenieur,* Vol. 55, pp. 2021–2024.

Nusselt, W., 1930, "Eine neue Formel für den Wärmedurchgang im Kreuzstrom," *Technische Mechanik und Thermodynamik,* Vol. 1, pp. 417–422.

Roetzel, W., and Nicole, F. J. L., 1975, "Mean Temperature Difference for Heat Exchanger Design—A General Approximate Explicit Equation," ASME JOURNAL OF HEAT TRANSFER, Vol. 97, pp. 5–8.

Smith, D. M., 1934, "Mean Temperature-Difference in Cross Flow," *Engineering,* Vol. 138, pp. 479–481, 606–607.

Stevens, R. A., Fernandez, J., and Woolf, J. R., 1957, "Mean-Temperature Difference in One, Two, and Three-Pass Crossflow Heat Exchangers," *Trans. ASME,* Vol. 79, pp. 287–297.

White, F. M., 1988, *Heat and Mass Transfer,* Addison-Wesley, Reading, MA.

Optimum Design of Radiating Rectangular Plate Fin Array Extending From a Plane Wall

C. K. Krishnaprakas[1]

Nomenclature

A_p = profile area of fin array, m^2
b = fin spacing, m
$dF_{d\mu 1-d\mu 2}$ = elemental view factor from $d\mu_1$ to $d\mu_2$
h = height of fin array, m
J = radiosity, W/m^2
K = thermal conductivity of fin material, W/mK
l = length of fin, m
N = number of grid points along fin length
N_c = conduction-radiation number = $Kt/l^2\sigma T_b^3$
N_p = dimensionless profile area = A_p/w^2
N_w = dimensionless width = $\sigma T_b^3 w/K$
t = semithickness of fin, m
T = temperature of fin, K
T_b = temperature of base, K
w = width of fin = $b + 2t$, m
x = coordinate along the length of the fin
β = dimensionless radiosity = $J/\sigma T_b^4$
ϵ = emittance
θ = dimensionless temperture = T/T_b
μ = dimensionless coordinate length = x/l
σ = Stefan–Boltzmann constant = 5.67*E*-8 W/m^2K^4
ϕ = dimensionless rate of heat loss from fin and base

Introduction

Radiating fins are used in spacecraft and space vehicles for rejecting on-board waste heat to deep space. Since weight is at a premium, it is important to have minimum fin mass in these applications. Several investigators have analyzed the problem of minimization of fin mass in the past; however, there exist a

[1] Thermal Systems Group, ISRO Satellite Centre, Bangalore-560 017, India.

Contributed by the Heat Transfer Division of THE AMERICAN SOCIETY OF MECHANICAL ENGINEERS. Manuscript received by the Heat Transfer Division August 1994; revision received August 1995. Keywords: Numerical Methods, Radiation Interactions. Associate Technical Editor: M. F. Modest.

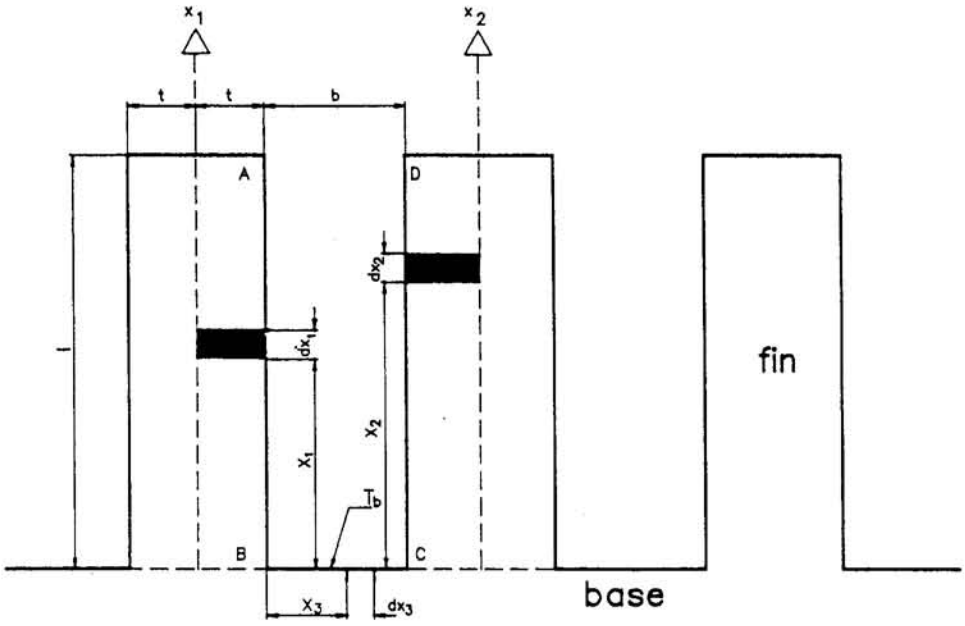

Fig. 1 Schematic of rectangular plate fin system

few works that discuss the optimum design of radiating fin array considering mutual interactions between the radiator elements.

Sparrow et al. (1961) presented the optimum design of radiatively interacting longitudinal fins without considering the fin-to-base mutual irradiation. Later Sparrow and Eckert (1962) emphasized the importance of mutual radiation interaction between fin and its base surface. Schnurr et al. (1976) employed a nonlinear optimization technique to determine the minimum weight design for straight and circular fins of rectangular and triangular profiles, protruding from a cylinder, considering fin-to-fin and fin-to-base radiation interactions. Chung and Zhang (1991a) determined the optimum shape and minimum mass of a thin fin accounting for fin-to-base interaction based on a variational calculus approach. Chung and Zhang (1991b) later extended their analysis to minimize the weight of a radiating straight fin array projecting from a cylindrical surface considering both fin-to-fin and fin-to-base interactions. The papers by Schnurr et al. and Chung and Zhang do not discuss the configuration of a straight rectangular plate fin array extending from a plane wall.

The purpose of the present analysis is to determine the minimum mass design of a straight rectangular fin array extending from a plane wall considering fin-to-fin and fin-to-base radiation interactions. Correlations in terms of dimensionless numbers are presented to facilitate an easy design, i.e., to select the optimum fin length, thickness, and spacing.

Mathematical Model

Figure 1 shows a schematic of the configuration considered for the present analysis. We make the following assumptions: (1) steady-state operation, (2) one-dimensional temperature distribution in the fin, (3) isothermal base surface, (4) gray-diffuse radiator surfaces, (5) absolute zero temperature of the environment, (6) no external heat load from the environment, and (7) the temperature and radiosity distribution with respect to length is the same in every fin, i.e., symmetry condition. The symmetry condition enables us to focus our attention only on a rectangular groove made up of half-thickness portions of two adjacent fins while analyzing the heat transfer mechanism in the fin array (see groove ABCD in Fig. 1). The governing equations for the heat transfer in the fin may be written in terms of dimensionless quantities as

$$d^2\theta(\mu_1)/d\mu_1^2 = (\epsilon/N_c)\left[\theta^4(\mu_1) - \int_{\mu_2=0}^{1} \beta(\mu_2)\,dF_{d\mu 1-d\mu 2} - \int_{\mu_3=0}^{b/l} \beta_3(\mu_3)\,dF_{d\mu 1-d\mu 3}\right] \quad (1)$$

subject to the boundary conditions

$$\theta = 1 \quad \text{at} \quad \mu_1 = 0 \quad (2a)$$

$$d\theta/d\mu_1 = -(\epsilon/N_c)(t/l)\theta^4(\mu_1) \quad \text{at} \quad \mu_1 = 1 \quad (2b)$$

and the dimensionless radiosities are given by

$$\beta(\mu_1) = \epsilon\theta^4(\mu_1) + (1-\epsilon)\int_{\mu_2=0}^{1} \beta(\mu_2)\,dF_{d\mu 1-d\mu 2} + (1-\epsilon)\int_{\mu_3=0}^{b/l} \beta_3(\mu_3)\,dF_{d\mu 1-d\mu 3} \quad (3)$$

$$\beta_3(\mu_3) = \epsilon + (1-\epsilon)\int_{\mu_1=0}^{1} \beta(\mu_1)\,dF_{d\mu 3-d\mu 1} + (1-\epsilon)\int_{\mu_2=0}^{1} \beta(\mu_2)\,dF_{d\mu 3-d\mu 2} \quad (4)$$

where the dimensionless temperature, radiosities, and lengths are defined by $\theta = T_1/T_b$, $\beta = J_1/\sigma T_b^4 = J_2/\sigma T_b^4$, $\beta_3 = J_3/\sigma T_b^4$, $\mu_1 = x_1/l$, $\mu_2 = x_2/l$, $\mu_3 = x_3/l$; the subscripts 1, 2, and 3 refer to fin 1, fin 2, and base surface, respectively. The subscript b also refers to the base surface.

Solution of Eqs. (1)–(4) yields the temperature and radiosity distributions along the length of the fin.

It is a common practice to express the effectiveness of a radiating fin as the ratio of the heat loss from the fin to that from a perfectly black isothermal fin of the same configuration (Sparrow and Cess, 1978; Özişik, 1973). However, the addition of fins, although enhancing the total radiating area, also reduces the direct radiative transfer from the base surface due to the view blockage of the base to the environment caused by the fins. Therefore, in order to determine the overall effect, which is of practical interest, we define a dimensionless heat loss quantity ϕ as the ratio of the actual heat loss from the fin and

base surfaces to that from a perfectly black unfinned surface with the same temperature. This may be written in terms of dimensionless quantities as

$$\phi = \left\{ 2 \int_{\mu_1=0}^{1} \left[\beta(\mu_1) - \int_{\mu_2=0}^{1} \beta(\mu_2) dF_{d\mu 1 - d\mu 2} - \int_{\mu_3=0}^{b/l} \beta_3(\mu_3) dF_{d\mu 1 - d\mu 3} \right] d\mu_1 + 2\epsilon(t/l)\theta^4_{\mu 1=1} + \int_{\mu_3=0}^{b/l} \left[\beta_3(\mu_3) - \int_{\mu_1=0}^{1} \beta(\mu_1) dF_{d\mu 3 - d\mu 1} - \int_{\mu_2=0}^{1} \beta(\mu_2) dF_{d\mu 3 - d\mu 2} \right] d\mu_3 \right\} \Big/ [b/l + 2t/l) \quad (5)$$

It is to be noted that this definition of ϕ is similar to the apparent emittance term (ϵ_a) defined to represent the emission characteristics of cavities with isothermal walls (Sparrow and Cess, 1978). From the definition of ϕ it is clear that finning is effective only when $\phi > \epsilon$.

Numerical Scheme

A numerical iterative scheme consisting of a finite difference technique and Nystrom technique (Delves and Mohamed, 1985) based on the Gauss–Legendre quadrature rule is employed to solve the governing coupled integro-differential and integral equations (Eqs. (1)–(4)). Convergence of the iterative scheme is enhanced by applying the Ng acceleration method (Auer, 1987).

Optimum Fin Design

From Eq. (5) we see that ϕ depends on four parameters: ϵ, N_c, b/l, and t/l, i.e., $\phi = \phi(\epsilon, N_c, b/l, t/l)$. For a given emittance ϵ, profile area, $A_p = 2tl$ and fin width, $w = b + 2t$, there is an optimum combination of the variables N_c, b/l, and t/l such that ϕ is maximum. We may state the constrained optimization problem mathematically as:

for given ϵ, N_p, and N_w,

$$\text{maximize } \phi(\epsilon, N_c, b/l, t/l) \quad (6)$$

$$\text{subject to } N_p = 2(t/l)/[(b/l + 2t/l)^2] \quad (6a)$$

$$N_w = (t/l)(b/l + 2t/l)/N_c \quad (6b)$$

$$\text{and } \phi > \epsilon \quad (6c)$$

where N_p and N_w are, respectively, the dimensionless profile area and width. N_w may also be thought of as a Biot number defined for radiation.

The constraints aid in transforming the multidimensional optimization problem into a univariate one and polynomial interpolation scheme may be used to solve it (Gill et al., 1981).

Results and Discussion

Figure 2 shows the maximum value of ϕ (ϕ_{max}) plotted as a function of N_p for different ϵ and N_w values. It is seen that as N_p increases ϕ_{max} increases and the rate of increase in ϕ_{max} decreases. $(t/l)_{opt}$ increases and $(b/l)_{opt}$ decreases as N_p is increased. $(N_c)_{opt}$ increases with N_p, indicating that higher conduction to radiation interaction is required for higher values of ϕ_{max}.

The optimum b/l and t/l may well be correlated by the following expressions:

$$(b/l)_{opt} = 3.18\phi_{max}^{-6.27}\epsilon^{3.05}N_w^{0.16} \quad (7)$$

$$(t/l)_{opt} = 5.11\phi_{max}^{12.41}\epsilon^{-1.79}N_w^{0.68} \quad (8)$$

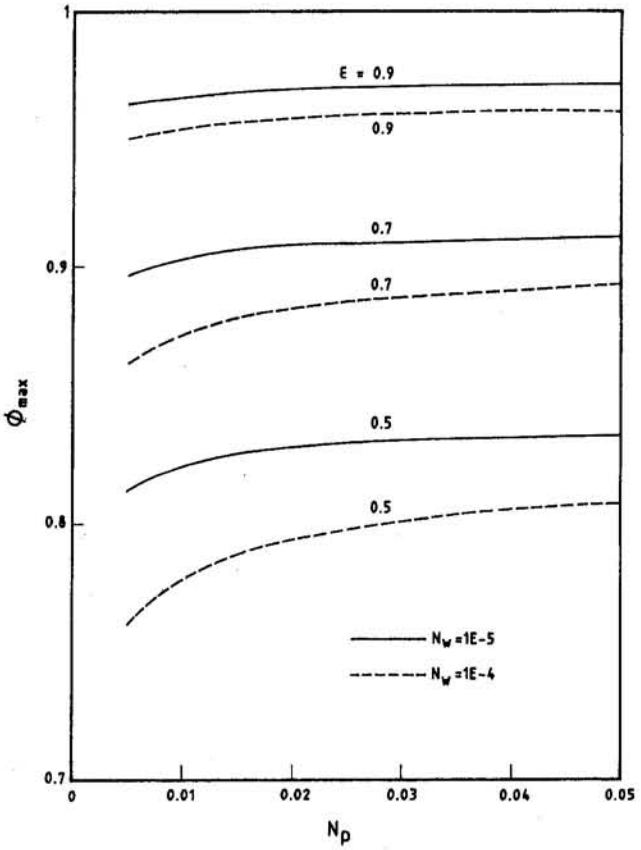

Fig. 2 $\phi_{max} = f(\epsilon, N_p, N_w)$

Validation of the numerical results was obtained by comparing the ϕ versus l/b graphs for $1/N_c = 0$ with the curves presented by Sparrow and Cess (1978) for the apparent emittance (ϵ_a) of rectangular groove cavities, since $\phi = \epsilon_a$ when $1/N_c = 0$ and terms containing t/l vanish in Eq. (5). Our results have been found to be indistinguishable, within the scale of the plots, from the curves presented by Sparrow and Cess.

Conclusions

Results are presented to obtain the optimum mass design of a straight rectangular plate fin array extending from a plane wall for emittance values in the range 0.5–0.9. Higher heat transfer rates are achieved at higher values of N_c and lower values of t/l, i.e., the best performance is achieved by short and thin fins. Apparently, the fin array extending from a plane wall is not very attractive if the heat transfer mode is radiation alone. For most radiative fins, the emittance is usually high, e.g., $\epsilon \geq 0.9$. As demonstrated by the top curve ($\epsilon = 0.9$) of Fig. 2, ϕ increases only to 0.97, i.e., the increase in heat transfer from unfinned condition to finned condition is only 7.8 percent. This indicates that the heat transfer enhancement by using the radiative fin array is limited.

Acknowledgments

The author wishes to thank D. R. Bhandari, Head, Thermal Design and Analysis Division, H. Narayanamurthy, Group Director, Thermal Systems Group and A. V. Patki, Deputy Director, ISRO Satellite Centre, for their support and encouragement in this work.

References

Auer, L., 1987, "Acceleration of Convergence," in: W. Kalkofen, ed., *Numerical Radiative Transfer*, Cambridge University Press, Cambridge, United Kingdom.

Chung, B. T. F., and Zhang, B. X., 1991a, "Minimum Mass Longitudinal Fins With Radiation Interaction at the Base," *Journal of the Franklin Institute,* Vol. 328, pp. 143–161.

Chung, B. T. F., and Zhang, B. X., 1991b, "Optimization of Radiating Fin Array Including Mutual Irradiations Between Radiator Elements," ASME JOURNAL OF HEAT TRANSFER, Vol. 113, pp. 814–822.

Delves, L. M., and Mohamed, J. L., 1985, *Computational Methods for Integral Equations,* Cambridge University Press, Cambridge, United Kingdom.

Gill, P. E., Murray, W., and Wright, M. H., 1981, *Practical Optimization,* Academic Press, Inc., London.

Özişik, M. N., 1973, *Radiative Transfer and Interactions With Conduction and Convection,* Wiley, New York.

Schnurr, N. M., Shapiro, A. B., and Townsend, M. A., 1976, "Optimization of Radiating Fin Arrays With Respect to Weight," ASME JOURNAL OF HEAT TRANSFER, Vol. 98, pp. 643–648.

Sparrow, E. M., Eckert, E. R. G., and Irvine, T. F., Jr., 1961, "The Effectiveness of Radiating Fins With Mutual Irradiation," *Journal of the Aerospace Sciences,* Vol. 28, pp. 763–772.

Sparrow, E. M., and Eckert, E. R. G., 1962, "Radiant Interaction Between Fin and Base Surfaces," ASME JOURNAL OF HEAT TRANSFER, Vol. 84, pp. 12–18.

Sparrow, E. M., and Cess, R. D., 1978, *Radiation Heat Transfer,* Augmented Edition, Hemisphere, Washington, DC.

Measurements of the Structure of Self-Preserving Round Buoyant Turbulent Plumes

Z. Dai[1] **and G. M. Faeth**[1]

Nomenclature

a = acceleration of gravity
B_o = source buoyancy flux
d = source diameter
f = mixture fraction
$F(r/(x - x_o))$ = scaled radial distribution of $\bar{f}$, Eq. (1)
Fr_o = source Froude number = $(4/\pi)^{1/4} l_M/d$
k_f, k_u = plume width coefficients based on $\bar{f}$ and $\bar{u}$
l_M = Morton length scale = $M_o^{3/4}/B_o^{1/2}$
M_o = source specific momentum flux
r = radial distance
u = streamwise velocity
$U(r/(x - x_o))$ = scaled radial distribution of $\bar{u}$, Eq. (2)
x = streamwise distance
ρ = density

Subscripts

c = centerline value
o = initial value or virtual origin location
∞ = ambient value

Superscripts

$(\bar{\ })$ = time-averaged mean value
$(\bar{\ })'$ = root-mean-squared fluctuating value

Introduction

Round buoyant turbulent plumes in still and unstratified environments are classical flows that are important for evaluating concepts and models of buoyancy/turbulence interactions. Fully developed buoyant turbulent plumes are of greatest interest because they have lost extraneous source disturbances and their structure is self-preserving, which simplifies both theory and the interpretation of measurements (Morton, 1959). These observations have prompted many studies of self-preserving buoyant turbulent plumes; see, for example, Dai et al. (1994, 1995a, b), Papanicolaou and List (1988), Papantoniou and List (1989), Shabbir and George (1992), and references cited therein. In contrast to most earlier studies, which were carried out nearer to the source, however, the recent measurements of Dai et al. (1994, 1995a, b) showed that self-preserving round buoyant turbulent plumes were narrower, and had larger mean mixture fractions and streamwise velocities near the axis, than previously thought. The objective of the present investigation was to extend earlier evaluations of these measurements, emphasizing potential problems due to flow confinement, to help insure that an artifact of the experiments was not responsible for these somewhat startling findings.

Consistent with most studies of round buoyant turbulent plumes, self-preserving plume properties will be defined for conditions where buoyant jets are used as plume sources and all scalar properties can be represented conveniently as functions of the mixture fraction. Reaching self-preserving conditions for buoyant jet sources requires that $(x - x_o)/d$ and $(x - x_o)/l_M \gg 1$, to insure that effects of both source disturbances and source momentum have been lost (Morton, 1959; List, 1982); then, self-preserving behavior implies that $f \ll 1$, that the buoyancy flux is conserved, and that $\bar{f}$ and $\bar{u}$ scale as follows:

$$\bar{f} a B_o^{-2/3} (x - x_o)^{5/3} \left| d(\ln \rho)/df \right|_{f \to 0} = F(r/(x - x_o)) \quad (1)$$

$$\bar{u}((x - x_o)/B_o)^{1/3} = U(r/(x - x_o)) \quad (2)$$

where $F(r/(x - x_o))$ and $U(r/(x - x_o))$ are universal functions that generally are approximated by Gaussian fits; in addition, various other flow statistics can be represented as universal functions of $r/(x - x_o)$ after normalizing mixture fraction and velocity properties by $\bar{f}_c$ and $\bar{u}_c$, respectively (Dai et al., 1994, 1995a, b).

The controversy concerning the properties of self-preserving round buoyant turbulent plumes involves both the conditions needed to observe them and their structure. In particular, most earlier measurements to establish the self-preserving structure of round buoyant turbulent plumes were limited to $(x - x_o)/d \leq 62$, which seems small for self-preserving behavior. For example, Panchapakesan and Lumley (1993) only observed self-preserving behavior for round nonbuoyant turbulent jets when $(x - x_o)/d \geq 70$, which is consistent with the observations of Dai et al. (1994, 1995a, b), that self-preserving behavior for round buoyant turbulent plumes required $(x - x_o)/d \geq 87$ and $(x - x_o)/l_M \geq 12$. In addition, Dai et al. (1994, 1995a) found that characteristic flow widths were up to 40 percent smaller, and $F(0)$ and $U(0)$ were up to 30 percent larger, than earlier results in the literature. Notably, this behavior is consistent with the development of plume structure toward self-preserving conditions for buoyant jet sources, where normalized flow widths progressively decrease, and $F(0)$ and $U(0)$ progressively increase, with increasing streamwise distance until the flow becomes self-preserving (Dai et al., 1994). Finally, the self-preserving plume properties of $\bar{f}$ observed by Dai et al. (1994) were in good agreement with measurements of Papantoniou and List (1989), which were carried out at comparable distances from the source.

Dai et al. (1994, 1995a, b) completed several typical checks of their measurements, including evaluating the measurements using the governing equations for mean quantities, establishing that the measurements satisfied conservation of buoyancy fluxes, and showing that the measurements were relatively independent of the rate of removal of plume gases from the test enclosure. Nevertheless, observing narrower self-preserving plumes than numerous earlier studies raises new concerns about

[1] Department of Aerospace Engineering, The University of Michigan, Ann Arbor, MI.

Contributed by the Heat Transfer Division of THE AMERICAN SOCIETY OF MECHANICAL ENGINEERS. Manuscript received by the Heat Transfer Division August 1995; revision received February 1996. Keywords: Natural Convection, Plumes, Turbulence. Associate Technical Editor: Y. Jaluria.

effects of removal rates of exhaust gases from the test enclosure because this flow places the plumes in a coflow, which would tend to make them narrower than truly unconfined self-preserving round buoyant turbulent plumes (see Shabbir and George (1992) for a detailed discussion of this and other potential error sources for measurements of buoyant turbulent plumes). Thus, in order to resolve these concerns about the measurements of Dai et al. (1994, 1995a, b), the objective of the present investigation was to quantify the effects of plume exhaust rates on their reported self-preserving distributions of $\bar{f}$, $\bar{u}$, $\bar{f}'$, and $\bar{u}'$.

Experimental Methods

Test Apparatus. Experimental methods were identical to those of Dai et al. (1994, 1995a, b) and will only be described briefly. Present considerations were limited to downward-flowing plumes from a source flow of sulfur hexafluoride in still air at atmospheric pressure and temperature, and involved laser-induced iodine fluorescence (LIF) to measure mixture fractions and laser velocimetry (LV) to measure streamwise velocities. The plumes were observed in a 3000 × 3000 × 3400 mm high plastic enclosure within a large high-bay test area, which had a screen across the top for air inflow, to compensate for the removal of air entrained by the plume. The plume flow was removed by 300-mm-dia ducts mounted on the floor at the four corners of the outer enclosure, with the exhaust flow controlled by a bypass/damper system. Probe measurements showed that exhaust flows through the four exhaust duct inlets were essentially the same, and provided measurements of exhaust flow rates (95 percent confidence) within 10 percent. The test plume was within a smaller enclosure (1100 × 1100 × 3200 mm high) with plastic screen walls; however, this enclosure had no effect on flow properties, i.e., measurements with and without these screens present were identical. The plume sources were mounted on the inner enclosure, which could be traversed to accommodate rigidly mounted instrumentation. The plume sources consisted of rigid plastic tubes with flow straighteners at the inlet and length-to-diameter ratios of 50:1. The source flows were seeded with iodine vapor for LIF measurements, while the ambient air was seeded with oil drops for LV measurements. Maximum mean mixture fractions in the self-preserving region were less than 6 percent; therefore, effects of concentration bias of LV measurements, because only the ambient air was seeded, were negligible.

Instrumentation. The LIF signal was produced by the fluorescence of iodine at the 514.5 nm line of an argon-ion laser, separating the LIF emission from light scattered at the laser line using a long-pass optical filter. The detector output was amplified and low-pass filtered to control alias signals to provide roughly four decades of power spectral densities in the present flow. Calibration showed that iodine seeding levels varied less than 1 percent, that the LIF signal varied linearly with laser power and iodine concentration, that reabsorption of the LIF emission was negligible, and that differential diffusion effects between the source gases and iodine were negligible (Dai et al., 1994). Finally, experimental uncertainties (95 percent confidence) were less than 5 and 10 percent for $\bar{f}$ and $\bar{f}'$ up to $r/(x - x_o) = 0.15$ but increased roughly inversely proportional to $\bar{f}$ at larger radial distances.

A dual-beam, frequency-shifted LV was used for velocity measurements, based on the 514.5 nm line of an argon-ion laser. The detector output was processed using a burst-counter signal processor with the low-pass-filtered analog output of the signal processor sampled at equal times to avoid problems of velocity bias, while directional bias and ambiguity were controlled by frequency shifting. The processor output was sampled at rates more than twice the break frequency of the low-pass filter to control alias signals. Effects of step noise contributed less than 3 percent to the determination of velocity fluctuations, while the

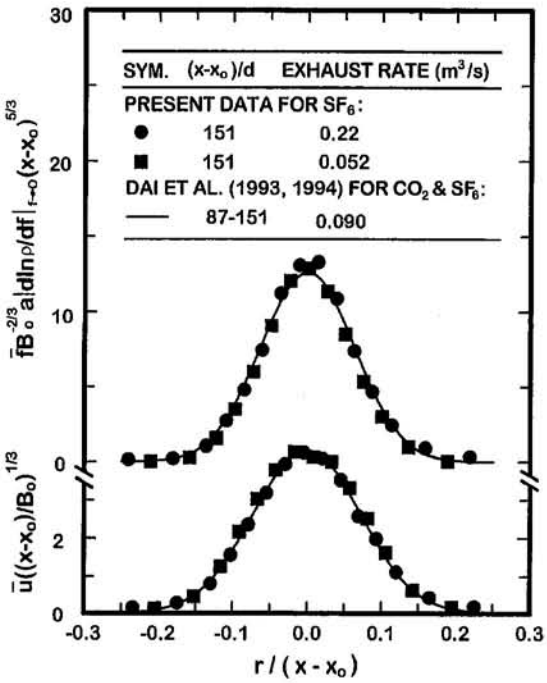

Fig. 1 Radial profiles of mean mixture fractions and streamwise velocities for self-preserving round buoyant turbulent plumes

measurements yielded roughly four decades of power spectral densities similar to the mixture fraction fluctuations (Dai et al., 1995a). Experimental uncertainties of $\bar{u}$ and $\bar{u}'$ were similar to $\bar{f}$ and $\bar{f}'$.

Test Conditions. Major parameters of the present measurements of SF_6 plumes were as follows: $d = 6.4$ mm, $u_o = 1890$ mm/s, $\rho_o/\rho_\infty = 5.06$, $\mathrm{Fr}_o = 3.75$, $l_M/d = 3.53$, and $x_o/d = 0.0$. The measuring station farthest from the source was at $(x - x_o)/d = 151$, while the edge of the plume is at roughly $r/(x - x_o) = 0.2$, which yields plume diameters and streamwise distances less than 360 and 900 mm. This implies that the maximum plume cross-sectional area is less than 1.2 percent of the enclosure cross-sectional area. Exhaust volume flow rates were roughly half, equal to, and twice the nominal flow rates used earlier, or 0.052, 0.090, and 0.22 m^3/s. Assuming uniform conditions over the cross section of the enclosure, these exhaust flows imply coflow velocities of roughly 6, 10, and 24 mm/s at the plane of the source exit, which are less than 1.3 percent of the source velocity.

Results and Discussion

Present measurements at the nominal exhaust flow rate agreed with Dai et al. (1994, 1995a, b) within experimental uncertainties; therefore, these results will be represented by their earlier correlations. Present measurements of $\bar{f}$ and $\bar{u}$ in the self-preserving region of buoyant turbulent plumes are plotted in Fig. 1 for the various flow rates according to the self-preserving scaling parameters of Eqs. (1) and (2). The present measurements were limited to $(x - x_o)/d = 151$ because this was the most critical condition with respect to potential coflow effects. The effect of varying plume exhaust rates, and thus coflow velocities, is seen to be negligible over the present range, with profiles of $\bar{f}$ and $\bar{u}$ for all coflow rates agreeing within experimental uncertainties. Thus, including the new measurements with the earlier results of Dai et al. (1994, 1995a, b) yields the same universal fitting parameters as before: $F(0) = 12.6$ and $k_f^2 = 125$, $U(0) = 4.3$ and $k_u^2 = 93$. The main effect of increased coflow velocities was evidence of a slight increase of streamwise velocity near the edge of the plume, which can be seen

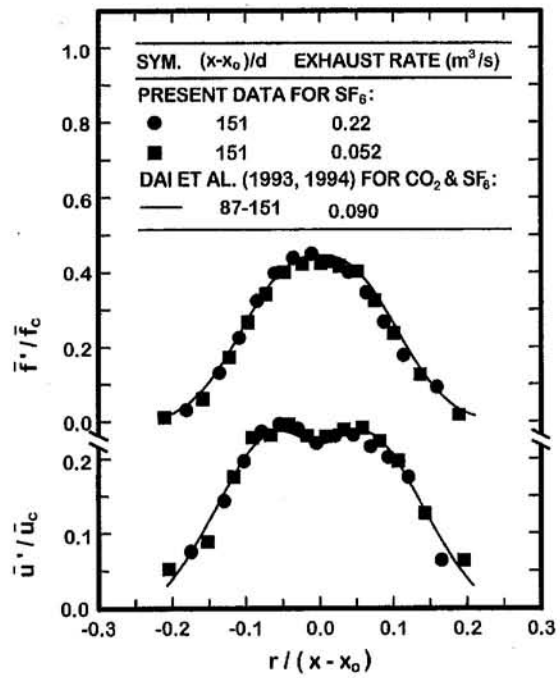

Fig. 2 Radial profiles of rms mixture fraction and streamwise velocity fluctuations for self-preserving round buoyant turbulent plumes

most clearly at the outmost points of $\bar{u}$ at an exhaust flow rate of 0.22 m^3/s.

Radial profiles of fluctuating mixture fractions and streamwise velocities are illustrated in Fig. 2 for the various exhaust flow rates. The values of $\bar{f}'$ and $\bar{u}'$ are plotted according to the self-preserving scaling observed by Dai et al. (1994, 1995a). Similar to the results for mean properties in Fig. 1, the fluctuating properties illustrated in Fig. 2 exhibit variations with exhaust rate within experimental uncertainties. Thus, present estimates of mixture fraction and streamwise velocity intensities at the axis are not changed significantly from the findings of Dai et al. (1994, 1995a), i.e., $(\bar{f}'/\bar{f})_c = 0.45$ and $(\bar{u}'/\bar{u})_c = 0.22$.

Taking the findings illustrated in Figs. 1 and 2 together, it appears that the measurements of flow properties within the self-preserving region of round buoyant turbulent plumes due to Dai et al. (1994, 1995a) were not affected by coflow caused by effects of confinement within their stated experimental uncertainties. Thus, the fact that the measured profiles of Dai et al. (1994, 1995a, b) are narrower, and have larger scaled mean values of mixture fractions and velocities near the axis, than previously thought, is due to additional flow development to reach truly self-preserving behavior compared to most earlier measurements, rather than due to an effect of coflow.

Acknowledgments

This research was sponsored by the United States Department of Commerce, National Institute of Standards and Technology, Grant Nos. 60NANB1D1175 and 60NANB4D1696, with H. R. Baum and K. C. Smyth of the Building and Fire Research Laboratories serving as Scientific Officers.

References

Dai, Z., Tseng, L.-K., and Faeth, G. M., 1994, "Structure of Round, Fully Developed, Buoyant Turbulent Plumes," ASME JOURNAL OF HEAT TRANSFER, Vol. 116, pp. 409–417.

Dai, Z., Tseng, L.-K., and Faeth, G. M., 1995a, "Velocity Statistics of Round, Fully Developed Buoyant Turbulent Plumes," ASME JOURNAL OF HEAT TRANSFER, Vol. 117, pp. 138–145.

Dai, Z., Tseng, L.-K., and Faeth, G. M., 1995b, "Velocity/Mixture-Fraction Statistics of Round, Self-Preserving Buoyant Turbulent Plumes," ASME JOURNAL OF HEAT TRANSFER, Vol. 117, pp. 918–926.

List, E. J., 1982, "Turbulent Jets and Plumes," *Ann. Rev. Fluid Mech.*, Vol. 14, pp. 189–212.

Morton, B. R., 1959, "Forced Plumes," *J. Fluid Mech.*, Vol. 5, pp. 151–163.

Panchapakesan, N. R., and Lumley, J. L., 1993, "Turbulence Measurements in Axisymmetric Jets of Air and Helium. Part. 1. Air Jet," *J. Fluid Mech.*, Vol. 246, pp. 197–223.

Papanicolaou, P. N., and List, E. J., 1988, "Investigation of Round Vertical Turbulent Buoyant Jets," *J. Fluid Mech.*, Vol. 195, pp. 341–391.

Papantoniou, D., and List, E. J., 1989, "Large Scale Structure in the Far Field of Buoyant Jets," *J. Fluid Mech.*, Vol. 209, pp. 151–190.

Rouse, H., Yih, C. S., and Humphreys, H. W., 1952, "Gravitational Convection From a Boundary Source," *Tellus*, Vol. 4, pp. 201–210.

Shabbir, A., and George, W. K., 1992, "Experiments on a Round Turbulent Buoyant Plume," NASA Technical Memorandum 105955.

A Calculation and Experimental Verification of the Infrared Transmission Coefficient of Straight Cylindrical Metal Tubes

P. Cavaleiro Miranda[1]

Introduction

An accurate figure for the infrared (IR) transmission coefficient of a stainless steel guide tube that transports ultra-cold neutrons (UCN) from a cryostat at 0.5 K to a room temperature apparatus is required in order to estimate the reduction in the heat load on the cryostat's UCN window achieved by cooling down the guide tube from 300 K to 77 K. The heat emitted by the cooled guide tube is negligible compared to the heat input from the room temperature apparatus, which behaves approximately like a blackbody at 300 K, and so the reduction in heat load is given by the transmission coefficient of the guide tube for 300 K blackbody radiation.

It was shown by Ohlmann et al. (1958) that the transmission of infrared (IR) radiation by cylindrical metal pipes decreases exponentially with length, for a monochromatic point source located on-axis and taking into account only rays making small grazing angles with the wall. In the case of an IR source covering the whole cross section of the tube and providing 2π steradians illumination a significant part of the emitted energy is carried by skew rays. As these rays undergo more reflections the attenuation will be significantly higher than that predicted by Ohlmann's formula.

Calculation of the IR Transmission Coefficient of a Straight Cylindrical Metal Pipe

In the case of 300 K blackbody radiation traveling in a vacuum and incident on stainless steel, the low-frequency limit expressions for the reflection coefficients apply. The coefficients for both polarizations, $\rho\perp$ and $\rho\parallel$, depend essentially on the wavelength λ, the cosine of the angle of incidence Φ, and the DC electrical conductivity k_e of the metal (e.g., Stratton, 1941). For one particular ray of unpolarized "light" traveling down the tube and making a total of N identical reflections, the fraction t of energy transmitted will be

[1] Institut Laue Langevin, 156X, 38042 Grenoble Cedex, France; present position and address: Assistant Professor, Departamento de Física, Faculdade de Ciências da Universidade de Lisboa, Campo Grande, 1700 Lisboa, Portugal.

Contributed by the Heat Transfer Division of THE AMERICAN SOCIETY OF MECHANICAL ENGINEERS. Manuscript received by the Heat Transfer Division November 1994; revision received October 1995. Keywords: Radiation. Associate Technical Editor: M. F. Modest.

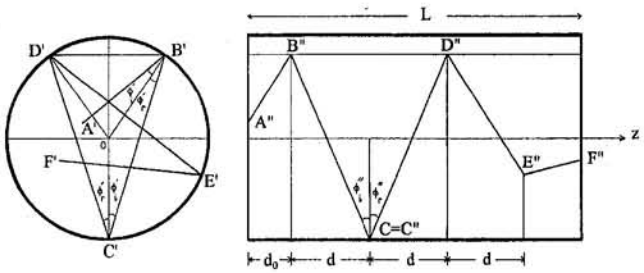

Fig. 1 Projections of the trajectory of a ray traveling down a cylindrical pipe by specular reflection. Capital letters denote reflection points in space, primed letters denote the projection of those points onto the *xy* plane, and double-primed letters the projection of the points onto a plane containing the *z* axis. Note that Φ_i'' is equal to Φ_r'' only in the longitudinal plane containing the reflection point.

$$t = \frac{\rho_\perp^N + \rho_\parallel^N}{2}. \tag{1}$$

Because parallel and perpendicular refer to the plane of incidence, which for a cylindrical tube takes up all possible angles around the z axis uniformly, any light entering the tube can be regarded as unpolarized as far as the overall transmission coefficient is concerned.

Due to the cylindrical symmetry of the geometry, a ray always strikes the wall at the same angle of incidence and covers a constant distance between bounces. Let d be this distance measured along the axis of the cylinder, the z axis, and d_0 the distance covered along z before the first bounce. N is then equal to the first integer greater than $(L - d_0)/d$. The constancy of d and Φ can be deduced from a drawing like the one shown in Fig. 1. The origin of the coordinate system is the center of the circle of radius R defined by the tube's entrance, r is the distance from the origin at which the ray crosses the entrance plane, θ is the angle that the projection of the ray onto this plane makes with $\mathbf{r}$, and α is the angle the trajectory makes with the z axis. By considering the projection of the trajectory onto the entrance plane, it can be shown that

$$d = 2\frac{\sqrt{R^2 - r^2\sin^2\theta}}{\tan\alpha},$$

$$d_0 = \frac{\sqrt{R^2 - r^2\sin^2\theta} - r\cos\theta}{\tan\alpha},$$

$$\cos\Phi = \frac{\sqrt{R^2 - r^2\sin^2\theta}}{R}\sin\alpha \tag{2}$$

It is assumed that emission is uniform over the area of the entrance disk and that its spectrum is that of a blackbody at temperature T. The transmission coefficient is then given by

$$t = \frac{\int\int\int\int t(r, \theta, \alpha, \lambda)w(r, \alpha, \lambda)drd\theta d\alpha d\lambda}{\int\int\int\int w(r, \alpha, \lambda)drd\theta d\alpha d\lambda} \tag{3}$$

where the weighting function $w(r, \alpha, \lambda) = r\sin 2\alpha\, E_b(\lambda, T)$ and where $E_b(\lambda, T)$ is the spectral emissive power of a blackbody (e.g., Incropera and DeWitt, 1981).

The guide tubes used in the experimental verification of these calculations have a radius $R = 3.35$ cm and are made out of 316 stainless steel, which has an electrical conductivity of about 2×10^6 S/m at 77 K and a relative permeability $\mu/\mu_0 \approx 1.01$ when austenized (Smithells, 1967; Meaden, 1965). The integration ranges were set to r: 0–3.15 cm, α: $0-\pi/2$, λ: 3–250 μm, and θ: $0-\pi$. The fact that the radiation source does not cover the whole of the entrance plane increases the transmission by approximately 1 percent.

Table 1 Theoretical and experimental IR transmission coefficients for 316 stainless steel guide tubes of various lengths (I.D. = 67 mm and $k_e = 2 \times 10^6$ S/m). The 63-mm-dia coaxial source of 300 K blackbody radiation is located at the entrance to the tube.

Theoretical		Experimental			
L (cm)	t (%)	L (cm)	t_A (%)	t_B (%)	t (%)
0.1	99.91±0.02	0.4±0.1	99.5±1.2	98.9±1.1	99.2±0.8
1	98.2±0.2	1.05±0.15	98.5±1.1	98.0±1.1	98.2±0.8
5	90.5±0.2	9.8±0.2	90.2±1.2	89.8±1.1	90.0±0.8
10	82.9±0.2	25.4±0.2	71.3±1.3	71.0±1.3	71.2±0.9
20	70.9±0.2	50.3±0.2	51.7±1.5	51.3±1.6	51.5±1.1
40	54.8±0.1	79.8±0.2	37.5±1.6	36.9±1.6	37.2±1.1
60	44.4±0.1	114.8±0.2	27.1±1.8	26.4±1.8	26.8±1.3
80	37.1±0.1				
100	31.77±0.05				
120	27.73±0.03				
200	18.32±0.01				
300	12.98±0.01				

The integral was evaluated numerically using a standard NAG Library routine (D01FCF) yielding the theoretical results listed in Table 1 and plotted in Fig. 2 as a solid curve.

Experimental Verification With UCN Guide Tubes

A length of honed and electropolished stainless steel tube is sealed at both ends by flanges through which the electrical and vacuum connections are made. Each flange carries on an insulating stem a concentric copper disk of radius r_0 uniformly heated and whose temperature is monitored by two thermistors and one Pt resistor. The disk surfaces facing each other are covered with a fine carborundum powder and painted black to increase their IR emissivity. The evacuated assembly is immersed in liquid nitrogen.

The experiment consists in measuring the electrical power P_e, which must be fed into each heater in order to keep the disks' temperature constant at $T = 300$ K as a function of the distance L between the disks, each of which is acting both as a source and a detector of IR radiation. When the disks are "zero" distance it is only necessary to dissipate a small amount of power P_0 in the heaters. When the disks are so far apart that one does not receive any heat from the other, a maximum amount of power $P_{max} = P_0 + P_s$ must be supplied to the heaters, where $P_s = \epsilon(\pi r_0^2)\sigma T^4$ and ϵ is the emissivity of the black surfaces. In order to keep the radiation and conduction losses P_0

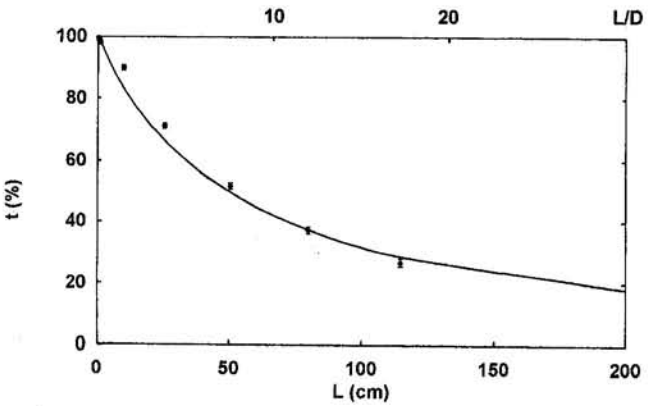

Fig. 2 The calculated (solid curve) and experimental values for the IR transmission of a 67 mm ID stainless steel tube, honed and electropolished, illuminated by a 63 mm diameter coaxial blackbody source at 300 K located at the tube's entrance.

constant throughout the experiment, the disks are permanently assembled on the flanges and the distance between the disks is varied by cutting the tube.

For each disk the value of P_{max} was measured by mounting the flange on a 77 K "cavity" and estimates of P_0, and hence $\epsilon = (P_{max} - P_0)/(\pi r_0^2 \sigma T^4)$, were obtained a posteriori by extrapolation of the $P_e(L)$ curve to $L = 0$.

The existence of a small annular spacing around the disks to prevent thermal contact causes the transmission to be underestimated as only a fraction γ of the transmitted power tP_s impinges on the other disk. An approximate expression for γ with the correct behavior as a function of L is

$$\gamma = \frac{F}{t} + \left(1 - \frac{F}{t}\right)\left(\frac{r_0}{R}\right)^2 \tag{4}$$

where F is the view or shape factor and is defined as the fraction of the radiation leaving one disk and intercepted directly by the other (cf. Incropera and DeWitt, for example). The theoretical transmission values were taken as estimates for the transmission t. The emission and absorption of radiation travelling in the tube by the shiny rear surface of the disks have been neglected.

Taking this correction into account as well as the multiple reflections due to the finite reflectivity $1 - \epsilon$ of the black surfaces, the expression relating the transmission coefficient $t(L)$ to the electric power $P_e(L)$ dissipated in a heater is

$$t(L) = \frac{P_{max} - P_e(L)}{\gamma(P_{max} - P_0 - (1 - \epsilon)[P_e(L) - P_0])} \tag{5}$$

The IR radiation emitted by the tube itself has not been taken into account in this analysis as it represents, at most, $(\frac{77}{300})^4 = 0.5$ percent of the heat input.

The measured values of $t(L)$ are compiled in Table 1. Each disk provides an independent measurement of the transmission, t_A and t_B, respectively, and so their average value t is calculated and plotted with error bars in Fig. 2. An experimental error is calculated for each power measurement $P_e(L)$, taking into account the uncertainty in measuring the voltage applied to the heater and the current flowing through it as well as the uncertainty in determining the average temperature of the disk. In the case of P_{max} there is also a small contribution from the uncertainty in the emissivity of the 77 K cavity, for P_0 a large contribution from the extrapolation procedure and for ϵ a small contribution from the uncertainty in disk area. The overall error calculated for each value of $t(L)$ is dominated by the uncertainties associated with P_0 and the average disk temperature.

The difference between the experimental points and the theoretical curve is significant but it is always less than 8 percent for lengths up to 1.2 m. It can be explained by the combination of the two following opposite tendencies, which were not taken into account in the calculation or in the analysis. The lower transmission observed at longer tube lengths can be attributed to diffuse reflection caused by surface roughness or waviness or to contamination of the surface with a lower reflectivity layer, such as water vapor. For the shorter lengths these effects are less noticeable and so nonideal properties of the emitters, namely forward-peaked emission of a soft spectrum, could contribute to a higher measured transmission. The crude correction implemented to account for the existence of small annuli around the disks will also tend to overestimate the transmission for guide lengths of less than three radii. The first tendency reflects the real properties of the tube's surface, whereas the second one is due to artifacts of this particular experimental method.

Conclusions

The analytical expression derived in this paper (Eq. (3)) yields good estimates for the IR transmission coefficient of straight metal pipes even when the source is large and close to or within the pipe. It was verified experimentally that a 1.5 m length of 67 mm ID stainless steel tube will attenuate by a factor of 5 the radiation emitted by a blackbody at 300 K placed at its entrance. A 90 deg bend in the tube is likely to provide another attenuation factor of 2 (Ohlmann et al., 1958) resulting in an overall reduction in the radiation heat load on the cryostat's window by a factor of 10.

References

Incropera, F. P., and DeWitt, D. P., 1981, *Fundamentals of Heat Transfer*, Wiley, New York.

Jewell, C. I., 1983, "The Interaction of Ultra-Cold Neutrons With Superfluid ^{4}He and a New Possible Super Thermal Ultra-Cold Neutron Source," Ph.D. thesis, University of Lancaster, United Kingdom.

Meaden, G. T., 1965, *Electrical Resistivity of Metals*, Heywood Books Ltd.

Ohlmann, R. C., Richards, P. L., and Tinkham, M., 1958, "Far Infrared Transmission Through Metal Pipes," *Journal of the Optical Society of America*, Vol. 48, pp. 531–533.

Smithells, C. J., 1967, *Metal Reference Book*, 4th ed., Butterworth, United Kingdom.

Stratton, J. A., 1941, *Electromagnetic Theory*, McGraw-Hill, New York.

Flow Boiling Heat Transfer Coefficients of R-134a in a Microfin Tube

A. Singh,[1] M. M. Ohadi,[2] and S. Dessiatoun[2]

Nomenclature

D = inside diameter of tube, mm
Fr_{lo} = Froude number with all flow as liquid = $G^2/(\rho_l g D)$
g = acceleration due to gravity, m/s^2
G = mass flux, kg/m^2·s
ρ_l = density of liquid refrigerant, kg/m^3

Introduction

This paper presents results of an experimental study for forced convection evaporative heat transfer coefficients of R-134a (a replacement for R-12), inside a horizontal microfin tube. Data are reported as a function of parametric values of mass flux, quality, and heat flux in the test section. Results include heat transfer coefficients for the low mass flux levels typically encountered in household refrigerators and certain small-scale commercial evaporators.

Previous work with microfin tubes and R-134a appears to be limited to a study by Eckels and Pate (1991). Because of the difference in experimental apparatus and the operating conditions it was not possible to provide a one-to-one comparison of the present study results with those of Eckels and Pate (1991). However, for selected points where the conditions were close to each other a satisfactory comparison was documented by Ohadi et al. (1994). In a recent study, Thors and Bogart (1994) report results for in-tube evaporation of R-22 with microfin

[1] ADC, Copeland Corporation, 1675 W. Campbell Road, Sidney, OH 45365.

[2] Heat Transfer Enhancement Laboratory, Center for Environmental Energy Engineering, Department of Mechanical Engineering, University of Maryland, College Park, MD 20742.

Contributed by the Heat Transfer Division of THE AMERICAN SOCIETY OF MECHANICAL ENGINEERS. Manuscript received by the Heat Transfer Division November 1994; revision received June 1995. Keywords: Boiling, Evaporation, Heat Exchangers. Associate Technical Editor: R. A. Nelson, Jr.

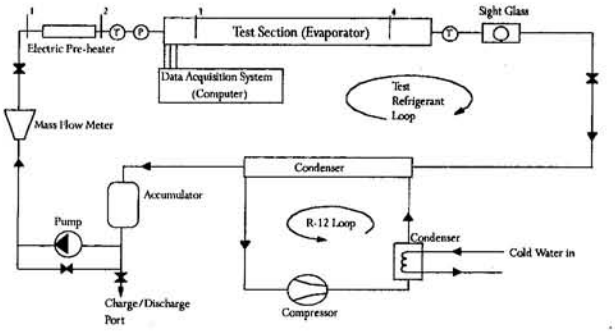

Fig. 1 Schematic of the experimental apparatus

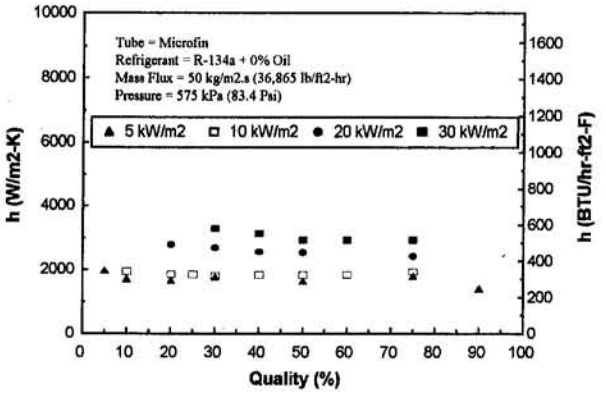

Fig. 3 Variation of heat transfer coefficient with quality at various heat flux levels

tubes. A comprehensive documentation of the literature on microfin tubes can be found from Schlager et al. (1987) and Eckels and Pate (1991).

Experimental Apparatus

The experimental test apparatus used in the present study is schematically shown in Fig. 1. As seen there, the setup consists of two distinct flow loops: (1) the test section refrigerant loop and (2) a condenser cooling loop utilizing R-12. The test section refrigerant loop includes a hermetic oil-free pump, a drier filter, a precision coriolis mass flowmeter, an electrical preheater, the test section, a condenser unit, and an accumulator. The refrigerant flow rate can be controlled by the pump in the range of 20 $kg/m^2 \cdot s$ to 200 $kg/m^2 \cdot s$ (liquid Reynolds number between 1200 and 12,000) and the quality at which the refrigerant enters the test section can be controlled by the electric preheater from subcooled to superheated condition. The test section is a horizontally mounted, microfin copper tube with 12.7 mm (0.5 in.) OD, 60 fins, and 18 deg helix angle. The nominal inside diameter of this tube is 11.78 mm (0.46 in.) with ridge height of 0.3 mm (0.012 in.).

The heat flux required for boiling the refrigerant is provided by an electrical heater wrapped around the test-section tube. The portion of the test section where electrical heating is applied is 495 mm (19.5 in.) long. The wall temperature measurements are done in the middle 305 mm (12 in.) portion of the test section (Fig. 2). All calculations for heat transfer coefficients are based on this test section length so as to minimize the effect of axial heat losses within the test section. The test section instrumentation allows operation up to 30 kW/m^2 of heat flux. The exit end of the test section has a sight glass of almost the same inside diameter as the test section in order to observe the flow patterns. Although the sight glass was not designed to reflect the details of the flow patterns, it served as a good qualitative guide to characterize the flow regimes. The wall temperatures are measured using copper-constantan thermocouples directly soldered on the outside of the tube. Temperatures are measured at four axial locations at equal intervals of 76 mm (3 in.). At each axial location, two thermocouples are placed circumferentially, one at the top and one at the bottom of the tube. The location of thermocouples and exact dimensions of the test section are indicated in Fig. 2. Details of the experimental setup and the procedure can be found from Ohadi et al. (1994).

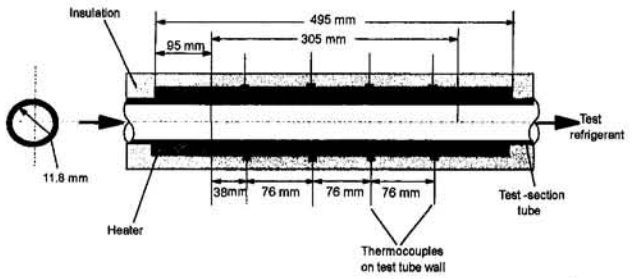

Fig. 2 Schematic of the test section

Results and Discussion

Calculation of the heat transfer coefficient h was based on the following defining equation:

$$h = \frac{Q}{A(T_w - T_{sat})} \tag{1}$$

in which T_w is the tube wall temperature, which is taken as the arithmetic mean of eight thermocouples installed on the test-section wall. Strictly speaking, T_w should be the average inner tube wall temperature. However, simple calculations justified the approximation of taking outside wall temperature as T_w. The temperature T_{sat} is the saturation temperature of the test refrigerant corresponding to the test section pressure. Since the test section was just 305 mm long, the pressure drop in this length in all flow regimes was found to be negligibly small and the test section pressure was assumed to be equal to the pressure at the inlet of the test section. A is the heat transfer area based on the nominal diameter of the test section tube.

The quality calculation for the refrigerant at different locations (see Fig. 1 for state points) in the test-section loop is done by utilizing appropriate energy balance equations. The quality after the preheater is calculated by using the following equations:

$$e_1 = f(T_1, P) \tag{2}$$

$$e_2 = e_1 + \frac{Q_{ph}}{m_r} \tag{3}$$

$$X_2 = f(P, e_2) \tag{4}$$

where e_1 and e_2 are the specific enthalpy of the refrigerant at the preheater inlet and exit, respectively. Having T_1 and P measured, the specific enthalpy can easily be obtained from the corresponding equation of state. Q_{ph} is the heat transferred to the refrigerant by the preheater and m_r is the mass flow rate of the refrigerant. It is assumed that the pressure drop across the preheater is negligible. The quality of the refrigerant at the test section entrance X_3 and exit X_4 can be obtained once the heat input to the test section Q_e is known. The average test-section quality X_{avg} is calculated by taking the arithmetic mean of X_3 and X_4. The maximum uncertainty in heat flux measurement is ±4.6 percent. The maximum uncertainty in heat transfer coefficient and quality is ±4.8 and ±4.7 percent, respectively.

Experiments were conducted at 575 kPa (83.4 psi) pressure. The saturation temperature corresponding to this pressure is

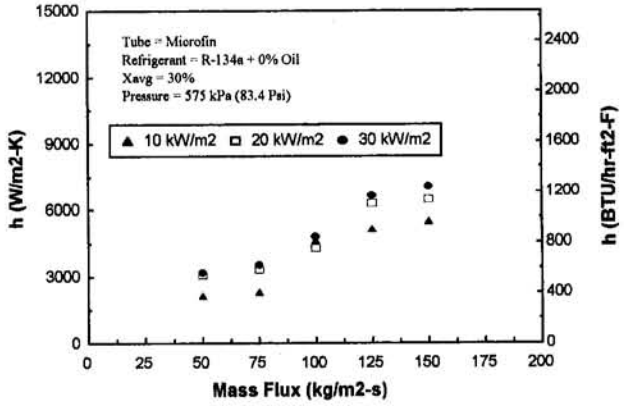

Fig. 4 Variation of heat transfer coefficient with mass flux at different heat flux levels

20.15°C (68.3°F). This operating condition was selected so that the heat losses to the surroundings were kept minimum. Figure 3 shows the variation of heat transfer coefficient with quality at various heat flux levels for a mass flux of 50 $kg/m^2 \cdot s$. At this relatively low mass flux, the sight glass downstream of the test section indicated the flow pattern was predominantly wavy–stratified. For such a regime the effect of quality on the heat transfer coefficient should be insignificant. This is because at low mass flow rates, the convective boiling is less dominant than the nucleate boiling and nucleate boiling does not appear to get suppressed even at higher qualities. From the figure it can also be observed that as the heat flux increases, the heat transfer coefficient increases due to the increase in nucleate boiling dynamics associated with a higher heat flux.

Figure 4 shows the variation of the heat transfer coefficient with mass flux at an average quality of 30 percent for different heat flux levels. As expected, with an increase in the mass flux heat transfer coefficient increases for the range of heat fluxes examined here. It is also seen that for a given mass flux, a higher heat flux results in a higher heat transfer coefficient. Note that for a mass flux larger than 100 $kg/m^2 \cdot s$, the heat transfer coefficient experiences a marked increase. This indicates the influence of stratification at low flow rates in horizontal tubes. The visual observation of the flow through the sight glass indicated that for mass fluxes less than 100 $kg/m^2 \cdot s$, the flow was predominantly stratified, but as the mass flux increased the flow became annular. The 100 $kg/m^2 \cdot s$ mass flux represents the transition value from stratified flow to annular for the microfin tube tested here and corresponds to *all flow liquid* Froude number (Fr_{lo}) of 0.058. This compares to Fr_{lo} of 0.04 value predicted by Shah (1982) and Kandlikar (1990) for horizontal smooth tubes. However, it has been described in a recent publication (Kattan et al., 1995) that the transition from stratified to unstratified flow may not depend solely on Fr_{lo}.

References

Eckels, S. J., and Pate, M. B., 1991, "Evaporation and Condensation of HCFC-134a and CFC-12 in a Smooth Tube and a Micro-fin Tube," *ASHRAE Transactions,* Vol. 97, Part 2, pp. 71–81.

Kandlikar, S. G., 1990, "A General Correlation for Saturated Two-Phase Flow Boiling Heat Transfer Inside Horizontal and Vertical Tubes," ASME JOURNAL OF HEAT TRANSFER, Vol. 112, pp. 219–228.

Kattan, N., Thome, J. R., and Favrat, D., 1995, "R-502 and Two Near-Azeotropic Alternatives—Part II: Two-Phase Flow Patterns," *ASHRAE Transactions,* Vol. 101, Pt. 1, in press.

Manwell, S. P., and Bergles, A. E., 1990, "Gas–Liquid Flow Patterns in Refrigerant–Oil Mixtures," *ASHRAE Transactions,* Vol. 96, Part 2, pp. 456–464.

Ohadi, M. M., Dessiatoun, S., Singh, A., Cheung, K., Salehi, M., and Blanford, M., 1994, "EHD-Enhanced Boiling/Condensation of Alternate Refrigerants," Quarterly Progress Report Nos. 4 & 5, DOE Grant No. DE-FG02-93CE23803.A000, Oct.

Schlager, L. M., Bergles, A. E., and Pate, M. B., 1987, "A Survey of Refrigerant Heat Transfer and Pressure Drop Emphasizing Oil Effects and In-Tube Augmentation," *ASHRAE Transactions,* Vol. 93, Part 1, pp. 392–416.

Shah, M. M., 1982, "Chart Correlation for Saturated Boiling Heat Transfer: Equations and Further Study," *ASHRAE Transactions,* Vol. 88, Part 1, pp. 185–196.

Thors, P., and Bogart, J., 1994, "In-Tube Evaporation of HCFC-22 With Enhanced Tubes," *J. of Enhanced Heat Transfer,* Vol. 1, No. 4, pp. 365–377.

Experimental Study of Electrohydrodynamically Augmented Condensation Heat Transfer on a Smooth and an Enhanced Tube

M. Wawzyniak[1] and J. Seyed-Yagoobi[1]

Introduction

The enhancement of condensation heat transfer is of crucial importance to many industries, including the HVAC, power, process, and aerospace industries. A variety of enhancement techniques have been researched and implemented to a limited range of industrial applications. These techniques are commonly referred to as passive and active means of condensation heat transfer enhancement.

The electrohydrodynamically (EHD) enhanced condenser is still considered a rather exotic candidate in the field. Nevertheless, the recent progress made indicates that this technique will find its way in the market place in the near future. With this active technique, the extraction of the performance restricting liquid from the condensation surface can be realized by nonuniform electric fields. The EHD enhancement of condensation heat transfer features several distinct advantages over conventional methods. Surface coating with nonwetting substances, for example Teflon or noble metals in steam condensers, is not applicable for refrigerants due to their low surface tension. Another important benefit is the possibility of varying the condensation heat transfer by simply changing the applied voltage. Furthermore, the EHD condenser contains no moving parts and the electric power input is negligible.

EHD enhancement of condensation heat transfer has been studied only over the past three decades. Velkoff and Miller (1965), Choi (1968), Didkovsky and Bologa (1981), Cooper and Allen (1984), Yabe et al. (1985), and Trommelmans and Berghmans (1986) are among a few others who investigated this topic.

The work conducted in the past dealt exclusively with the EHD enhancement of condensation heat transfer on smooth surfaces. However, a variety of enhanced tubes has been developed that can passively increase the condensation heat transfer coefficient by several hundred percent. This paper presents the results of an EHD-extraction phenomenon study to enhance condensation heat transfer using a smooth and an enhanced tube.

[1] Department of Mechanical Engineering, Texas A&M University, College Station, TX 77843-3123.

Contributed by the Heat Transfer Division of THE AMERICAN SOCIETY OF MECHANICAL ENGINEERS. Manuscript received by the Heat Transfer Division April 1995; revision received February 1996. Keywords: Augmentation and Enhancement, Condensation, Heat Exchangers. Associate Technical Editor: T. J. Rabas.

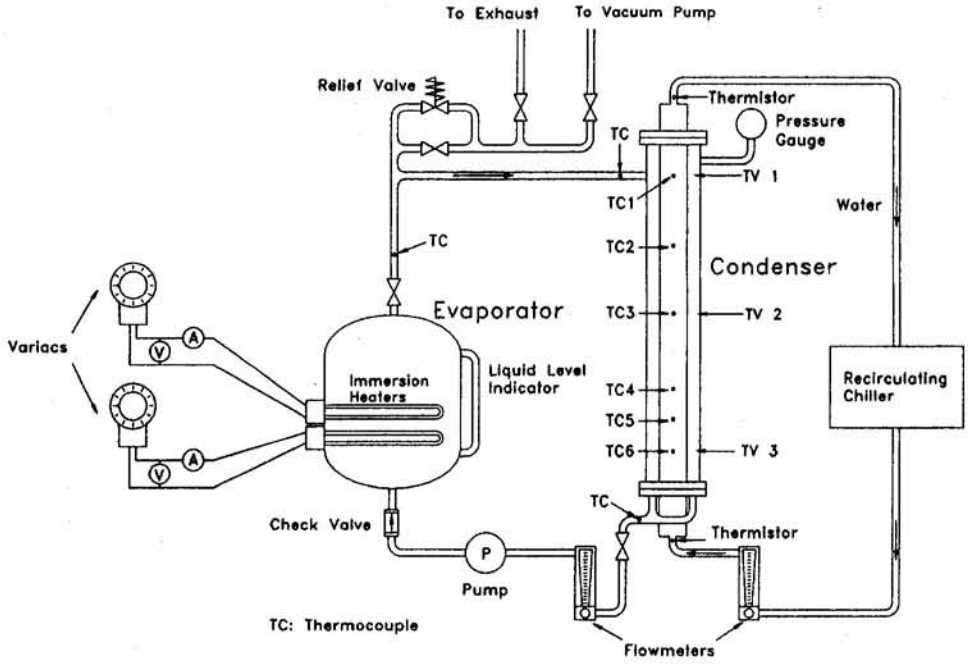

Fig. 1 Schematic of experimental apparatus

Experimental Setup

An experimental apparatus was designed and built to study the EHD enhanced condensation heat transfer in a vertical configuration. Details regarding the experimental setup can be found from Wawzyniak (1993). The main loop consists of an evaporator, the vertical condenser, a flow meter, and a pump as shown in Fig. 1. The acrylic shell of the condenser measures 1000 mm in length, 76.2 mm (3 in.) ID, and 88.9 mm ($3\frac{1}{2}$ in.) OD. Two 1 kW immersion heaters are utilized in the evaporator. To prevent heat losses, the entire main loop including evaporator and condenser is insulated with fiberglass. The cooling loop includes a recirculating chiller, a flow meter, and the condensation tube. The chiller is capable of removing 4.5 kW heat at a fluid temperature of 20°C. The condensation surface temperature is measured by 12 T-type (special limits of error) thermocouples. The thermocouples are soldered into the tube wall. The thermocouples are ground down to be flush with the condensation surface. The thermocouples are located at 100 mm, 300 mm, 500 mm, 700 mm, 800 mm, and 900 mm, respectively, measured from the top of the condenser. At each height, two thermocouples are arranged 180 deg apart around the circumference.

A 50 kV-5 mA DC power supply is employed to generate the required electric potential. The condenser tube, the rig containing the condenser, and the power supply are grounded through a common terminal board. Three acrylic spacers are employed to hold four brass rods (4.76 mm diameter, 915 mm long) over the condensation surface. The electrodes are soldered to these vertical rods and a high voltage cable is connected to these supporting rods.

Refrigerant-113 is used as working fluid. It was chosen because of its well-established properties (*ASHRAE Handbook, Fundamentals,* 1993) and because it is fairly easy to handle. It has a relatively high boiling point and is compatible with a wide array of common materials. However, R-113 is being phased out due to its high ozone depletion potential and global warming potential. Nevertheless, Sunada et al. (1991) showed that for EHD pseudo-dropwise condensation even better enhancement ratios can be reached when using R-123, an environmentally much friendlier substance. The EHD phenomena can be realized with most dielectric fluids, including various refrigerants. The two electric properties, conductivity and permittivity, of a working fluid are the most critical properties directly affecting the EHD phenomena. The electric conductivity and electric permittivity of pure working fluid in this study were measured at 6.5×10^{-12} S/m and 2.3×10^{-11} F/m, respectively, at atmospheric pressure and 21°C.

Prior to each test, the system was evacuated by means of a vacuum pump to remove the noncondensable gases. The tests were conducted at a constant vapor pressure slightly above atmospheric (106.80 kPa). A change in the heat transfer coefficient due to the EHD-extraction phenomenon results in a change of the system pressure, which is then compensated for by varying the heater input.

The electrode design utilized during this study follows the one suggested by Yabe et al. (1985). The electrodes are made from brass rods (2.38 mm diameter), which are cold rolled to obtain a rectangular cross section of 1.4 mm by 3 mm. This procedure results in a more effective electrode with rounded edges, thus minimizing the possibility of electric discharge. The extraction section, characterized by a constant electrode-tube gap of 1.6 mm and an angle of 5 deg with the horizontal direction, is set over one pitch (see Fig. 2). A total of eight electrodes is then built into the condenser to realize the extraction phenomenon at various locations. The electrodes are spaced evenly over the length of the supporting rods at a distance of 110 mm between them.

One smooth copper tube and one externally enhanced copper tube (Turbo CII®), both having an outer diameter of 19.05 mm, were tested. The enhanced tube is manufactured by a cold forming process followed by a serrating operation. Thus, closely packed fins with a rectangular cross section of approximately 0.3 mm × 0.5 mm and a length of 0.5 mm are created.

The method of Kline and McClintock (1953) was used to determine the uncertainty of the calculated average condensation heat transfer coefficients. For the smooth tube an uncertainty between 5.71 and 8.07 percent has to be considered. The higher heat fluxes encountered with the enhanced tube result in a smaller vapor-wall temperature difference and thus, an uncertainty in the condensation heat transfer coefficient ranging from 5.86 to 22.53 percent with an average value of 9.86 percent is found.

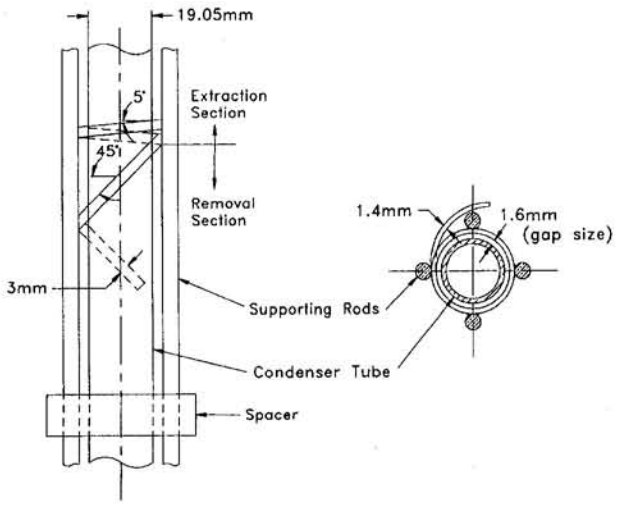

Fig. 2 Electrode design

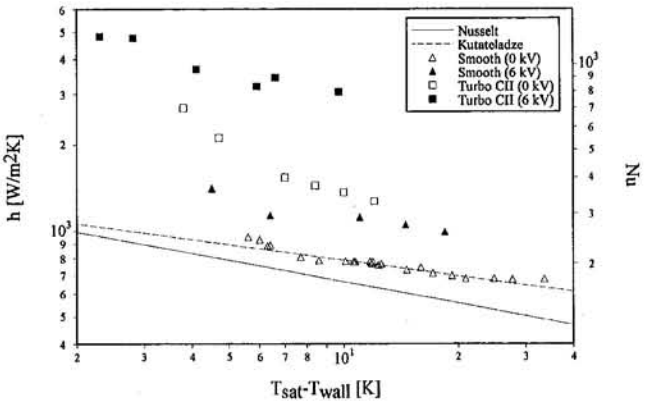

Fig. 3 Comparison of the condensation heat transfer coefficient as function of the temperature differences for tubes both with and without EHD

Results

The increase in the coolant temperature was less than 3°C over the entire length of the condenser for all cases. Hence, the heat flux can be assumed approximately uniform over the condenser tube surface. The local condensation heat transfer coefficient can then be determined by dividing the heat flux by the vapor-tube surface temperature difference at a given vertical location. The condenser tube surface temperature is obtained by averaging the two circumferential surface temperatures measured at one vertical location. The average condensation heat transfer coefficient can then be computed by integrating the local condensation heat transfer coefficients along the length of the condenser. The results are given in terms of the average condensation heat transfer coefficient and Nusselt number, which is defined based on the outside diameter of the condenser tube.

In this study, the film Reynolds number ranges from 200 to 1250, thus indicating that the condensation occurs in the wavy laminar regime. Tests were conducted with and without the electrode setup in place to investigate whether the electrode spacers might act as skirts stripping the liquid from the tube, thus causing an increase in the heat transfer coefficient. The results without EHD enhancement, with and without the electrode setup installed, were identical, indicating that the spacers have no impact on the results.

Initially, data were taken at voltages of 0, 4, and 6 kV. These values were selected because no significant enhancement was obtained below 4 kV, and for voltages exceeding 6 kV electric breakdown occurred. A comparison between the smooth and enhanced tube with and without EHD is given in Fig. 3. The data at 4 kV are not included in this figure for reasons of clarity. Without EHD, the condensation heat transfer coefficient of the Turbo CII® tube is 2.06 times higher than the heat transfer coefficient for the smooth tube at a temperature difference of 6°C. The enhancement ratio reduces to 1.75 for a temperature difference of 10°C. The condensation heat transfer coefficient realized by combining EHD and the Turbo CII® tube is approximately 4 times as high as for the smooth tube without EHD over the entire range of temperature difference. However, Fig. 3 also shows that for low temperature differences (<4°C) a relatively high enhancement can be achieved by employing the Turbo CII® alone. As the benefit of the Turbo CII® tube decreases with higher temperature differences, the importance of the EHD enhancement becomes apparent. For reasons of verification, the experimental data are compared to the Nusselt solution for laminar condensation (Incropera and De Witt, 1990) and a well-established correlation by Kutateladze (1963) for wavy laminar condensation. The experimental data without the EHD effect compare favorably to the Kutateladze correlation due to the condensate film flow regime.

The experimental data in terms of the film Reynolds number and heat flux are presented in Fig. 4. A correlation by Labuntsov (1957) for turbulent film condensation is included to illustrate the flow regime. From the figure, it can be deduced that the enhancement ratios for a given Reynolds number follow the same trend as for a given temperature difference, i.e., they decrease with higher Reynolds numbers for the smooth tube and increase for the Turbo CII® tube. By combining EHD and the Turbo CII® tube, a 6.1-fold enhancement is obtained over the tested range of film Reynolds number when the data for the smooth tube without EHD are used as the base case.

Figure 4 also emphasizes that with a Turbo CII® tube the EHD-extraction phenomenon is realized more effectively than with a smooth tube. The reason for this can be found in the tube surface geometry. The fins of the Turbo CII® tube create an electric field with high localized nonuniformities. The electric field created with a smooth surface, on the other hand, is relatively uniform directly at the tube surface. The body force density due to the electric field acting on the condensate is given as

$$\vec{f}_e = \rho_e \vec{E} - \frac{1}{2}\vec{E}^2 \nabla \epsilon + \frac{1}{2}\nabla\left[\vec{E}^2 \rho \left(\frac{\partial \epsilon}{\partial \rho}\right)\right],$$

where ρ_e, E, ϵ, and ρ are electric charge density, electric field

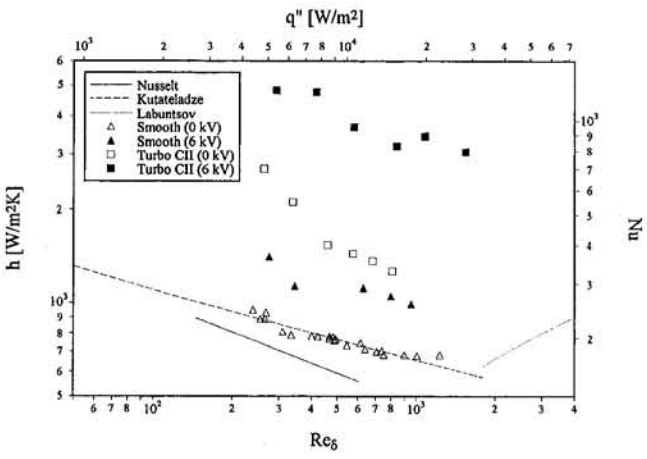

Fig. 4 Comparison of the condensation heat transfer coefficient versus film Reynolds number for tubes both with and without EHD

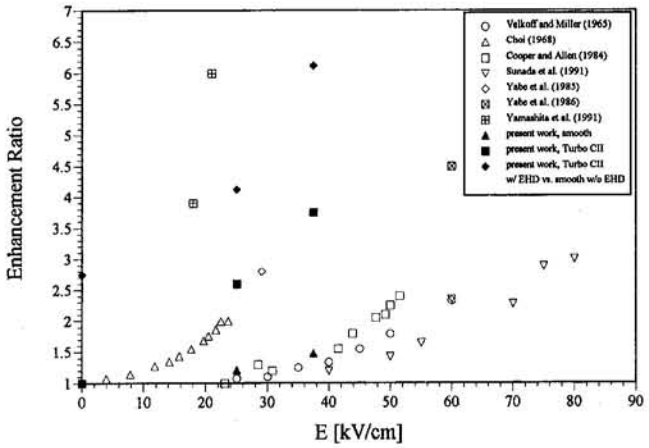

Fig. 5 Comparison to previous studies

strength, electric permittivity, and fluid density, respectively. Since no free charges are generated or introduced for the EHD-extraction phenomenon, the Coulomb force, which is the first term in the equation given above, is negligible. The second term, the dielectrophoretic force, describes the force due to spatial changes in the electric permittivity ϵ. Due to the drastic change of the electric permittivity across the liquid–vapor interface, this term in conjunction with the last term will play the major role for the discussed situation. The last term in this equation, called the electrostriction term, quantifies the force created due to the inhomogeneity of the electric field. For the electrode design at hand—a narrow electrode placed over a large surface—this term will be of importance regardless of the surface geometry. Using the Turbo CII® tube, however, additional nonuniformities in the electric field distribution are generated at the condensation surface, and thus the electrostriction force is increased. Furthermore, it is observed that the setup is less prone to electric discharge from the electrode when the Turbo CII® tube is utilized. Note that electric breakdown will always be initiated at the energized electrode. Since the electrode-tube gap is the same for the two tubes, the electric field distribution around the energized electrode remains nearly unchanged. Hence, the initiation of breakdown is not affected by the local geometry of the grounded tube.

Finally, Fig. 5 is included for the purpose of providing a general idea how this work compares to previous studies. It has to be pointed out that these studies involved various working fluids, different surfaces, and distinct testing procedures. The enhancement mechanism was the EHD-extraction phenomenon, except for Sunada et al. (1991), which dealt with EHD pseudo-dropwise condensation, and Yabe et al. (1986) and Yamashita et al. (1991), which studied the combination of the EHD extraction phenomenon and EHD pseudo-dropwise condensation. However, all previous studies were concerned with smooth condensation surfaces. Figure 5 gives the enhancement ratio (condensation heat transfer coefficient obtained with EHD over condensation heat transfer coefficient without EHD) as a function of the applied electric field strength. Maximum results at a given film Reynolds number are given from this study. The combination of the EHD extraction phenomenon and the Turbo CII® tube yields results that go far beyond that of previous studies based on the EHD extraction phenomenon using smooth tubes. Studies dealing with EHD pseudo-dropwise condensation using smooth tubes, however, produced enhancement ratios similar to those presented in this study. Nevertheless, it must be noted that the electrode designs necessary to initiate EHD pseudo-dropwise condensation can be expected to increase the pressure drop drastically across the condenser.

The electric current does not exceed 40 μA for all conditions considered in this study. Thus, the electric power amounts to less than 0.24 W, corresponding to less than 0.08 percent of the exchanged heat.

Acknowledgments

This work was supported by the NASA Johnson Space Center. The enhanced tube was provided by Wolverine Tube, Inc.

References

ASHRAE, 1993, *1993 ASHRAE Handbook: Fundamentals,* American Society of Heating, Refrigerating and Air-Conditioning Engineers, Inc., Atlanta, GA.

Choi, H. Y., 1968, "Electrohydrodynamic Condensation Heat Transfer," ASME JOURNAL OF HEAT TRANSFER, Vol. 90, pp. 98–102.

Cooper, P., and Allen, P. H. G., 1984, "The Potential of Electrically Enhanced Condensers," *Proc. 2nd International Symposium on the Large Scale Applications of Heat Pumps,* York, United Kingdom, Sept., pp. 295–309.

Didkovsky, A. B., and Bologa, M. K., 1981, "Vapour Film Condensation Heat Transfer and Hydrodynamics Under the Influence of an Electric Field," *International Journal of Heat and Mass Transfer,* Vol. 24, No. 5, pp. 811–819.

Incropera, F. P., and De Witt, D. P., 1990, *Fundamentals of Heat and Mass Transfer,* 3rd ed., Wiley, New York.

Kline, S. J., and McClintock, F. A., 1953, "Describing Uncertainties in Single-Sample Experiments," *Mechanical Engineering,* Vol. 75, Jan., pp. 3–8.

Kutateladze, S. S., 1963, *Fundamentals of Heat Transfer,* 2nd ed., Academic Press, New York.

Labuntsov, D. A., 1957, "Heat Transfer in Film Condensation of Pure Steam on Vertical Surfaces and Horizontal Tubes," *Teploenergetika,* Vol. 4, pp. 72.

Sunada, K., Yabe, A., Taketani, T., and Yoshizawa, Y., 1991, "Experimental Study of EHD Pseudo-Dropwise Condensation," *Proc. 3rd ASME/JSME Thermal Engineering Joint Conference,* Reno, NV. Mar.

Trommelmans, J., and Berghmans, J., 1986, "Influence of Electric Fields on Condensation Heat Transfer of Nonconducting Fluids on Horizontal Tubes," *Proc. 8th International Heat Transfer Conference,* Vol. 6, pp. 2969–2974.

Velkoff, H. R., and Miller, J. H., 1965, "Condensation of Vapor on a Vertical Plate With a Transverse Electrostatic Field," ASME JOURNAL OF HEAT TRANSFER, Vol. 87, pp. 197–201.

Wawzyniak, M., 1993, "Electrohydrodynamically Enhanced Condensation Heat Transfer," M. S. Thesis, Department of Mechanical Engineering, Texas A&M University, College Station, TX.

Yabe, A., Taketani, T., Kikuchi, K., Mori, Y., and Hijikata, K., 1985, "Augmentation of Condensation Heat Transfer Around Vertical Cooled Tubes Provided With Helical Wire Electrodes by Applying Nonuniform Electric Fields," *Proc. International Symposium on Heat Transfer,* Peking, China, Oct., pp. 812–819.

Yabe, A., Taketani, T., Kikuchi, K., and Maki, H., 1986, "Augmentation of Condensation Heat Transfer by Applying Electro-Hydro-Dynamic Pseudo-Dropwise Condensation," *Proc. 8th International Heat Transfer Conference,* Vol. 6, pp. 2957–2962.

Yamashita, K., Kumagai, M., Sekita, S., Yabe, A., Taketani, T., and Kikuchi, K., 1991, "Heat Transfer Characteristics on an EHD Condenser," *Proc. 3rd ASME/JSME Thermal Engineering Joint Conference,* Reno, NV, Mar., pp. 61–67.

Non-Darcy Effects in Natural Convection Heat Transfer in a Vertical Porous Annulus

V. Dharma Rao,[1,3] S. V. Naidu,[1,3] and P. K. Sarma[2,3]

Nomenclature

b = inertial resistance coefficient, m

C_m, C_f = specific heats of medium and fluid, respectively, J kg^{-1} K^{-1}

[1] Chemical Engineering Department.

[2] Mechanical Engineering Department.

[3] Andhra University, Visakhapatnam-530 003, India.

Contributed by the Heat Transfer Division of THE AMERICAN SOCIETY OF MECHANICAL ENGINEERS. Manuscript received by the Heat Transfer Division March 1995; revision received January 1996. Keywords: Enclosure Flows, Natural Convection, Porous Media. Associate Technical Editor: K. Vafai.

d = diameter of the solid bead, m
D = gap width of porous annulus = $\bar{r}_o - \bar{r}_i$, m
Da = Darcy number = K/D^2
g = acceleration due to gravity, m s^{-2} [$g^+ = gD^3/(\alpha_m^2\ \mathrm{Ra}^{*2})$]
h = heat transfer coefficient, W m^{-2} K^{-1}
k_m = effective thermal conductivity of porous medium, W m^{-1} K^{-1}
K = permeability of the porous medium, m^2
L = height of porous annulus, m
Nu_x, Nu_{av} = local and average Nusselt numbers ($\mathrm{Nu}_x = h_x D/k_m$)
P = normalized pressure = $\bar{P}D^2/(\rho_f \alpha_m^2\ \mathrm{Ra}^{*2})$
Pr_m = Prandtl number of the porous medium = ν_f/α_m
$\bar{r}_i$, $\bar{r}_o$ = inner and outer radii of the annulus, respectively, m
r = normalized space coordinate = $\bar{r}/D$
Ra* = modified Rayleigh number = $g\beta(\bar{T}_w - \bar{T}_a)KD/(\nu_f \alpha_m)$
t = normalized time = $\alpha_m \bar{t}\ \mathrm{Ra}^*/D^2$
T = normalized temperature = $(\bar{T} - \bar{T}_a)/(\bar{T}_w - \bar{T}_a)$
u = normalized velocity in x direction = $D\bar{u}/(\alpha_m\ \mathrm{Ra}^*)$
v = normalized velocity in r direction = $D\bar{v}/(\alpha_m\ \mathrm{Ra}^*)$
V = $\sqrt{u^2 + v^2}$
x = normalized space coordinate in vertical direction = $\bar{x}/D$
α_m = thermal diffusivity of porous medium = $k_m/(C_f \rho_f)$, m^2 s^{-1}
β = isobaric coefficient of thermal expansion of fluid, K^{-1}
ϵ = porosity
μ' = apparent viscosity; $\mu^* = (\mu'/\mu_f)$
ν = kinematic viscosity, m^2 s^{-1}
ρ_m, ρ_f = densities of porous medium and fluid respectively, kg m^{-3}
$(\rho C)^+$ = $\rho_m C_m/(\rho_f C_f)$
ϕ = b/D
ψ = normalized stream function = $\bar{\psi}/(D\alpha_m)$
ζ = normalized vorticity function = $\bar{\zeta}D^2/(\alpha_m\ \mathrm{Ra}^*)$

Subscripts

a = ambient
f = fluid
w = at the wall, i.e., at $\bar{r} = \bar{r}_i$

Introduction

The study of flow and heat transfer characteristics in porous media finds applications in varied fields such as geothermal operations, heat loss estimation in thermal insulation, packed beds used in chemical reactors, metal processing in a blast furnace, etc. The theoretical investigation of Minkowycz and Cheng (1976) illustrates the effect of permeability of the porous medium as characterized by Darcy's law. Boundary effects of the velocity profiles near the rigid wall were included in the analysis by some of the investigators (for example, Vafai and Tien, 1981). It has been observed that the boundary and inertia effects are more pronounced in high-permeability porous media. The problem of natural convection in a vertical porous annulus has been studied experimentally and theoretically by Prasad and Kulacki (1984, 1985) and Prasad et al. (1986) covering good range of Rayleigh numbers and aspect ratios. Their experimental data indicate effects of curvature and Prandtl number on temperature profiles and on Nusselt numbers. Another important parameter, the inertial (or, turbulent) resistance coefficient, originally used in theoretical studies on forced flow of fluids through packed beds (Choudhary et al., 1976), has found its application in studies in natural convection as well (Jonsson and Catton, 1987) at high Rayleigh numbers. Kaviany and Mittal (1987) conducted experiments to study the natural convection heat transfer from a vertical plate to polyurethane foam saturated with air.

It is felt from the studies of various authors cited above that there is a need for an analysis of the present problem considering a generalized model so as to obtain accurate results at both low and high Rayleigh numbers. Also, it is intended to present the effects of various parameters in the form of explicit expressions based on computer results.

Physical Model and Problem Formulation

The physical model considered is a vertical cylindrical annulus with inner radius $\bar{r}_i$, outer radius $\bar{r}_o$ and height L and filled with a saturated porous medium. The gap width is D, where $D = \bar{r}_o - \bar{r}_i$. The inner and outer vertical walls of the annulus are maintained at constant temperatures $\bar{T}_w$ and $\bar{T}_a$, respectively, where $\bar{T}_w > \bar{T}_a$. The adiabatic condition of heat flow is maintained at both the bottom and top boundaries at $\bar{x} = 0$ and at $\bar{x} = L$, respectively, for $\bar{r}_i \le \bar{r} \le \bar{r}_o$. The transport and heat transfer processes in the porous annulus are governed by the following normalized energy and momentum balance equations, with the use of Boussinesq approximation (Choudhary et al., 1976; Jonsson and Catton, 1987):

$$(\rho C)^+ \frac{\partial T}{\partial t} + u\frac{\partial T}{\partial x} + v\frac{\partial T}{\partial r} = \frac{1}{\mathrm{Ra}^*}\left\{\frac{1}{r}\frac{\partial}{\partial r}\left(r\frac{\partial T}{\partial r}\right) + \frac{\partial^2 T}{\partial x^2}\right\} \quad (1)$$

$$\frac{\partial u}{\partial t} + \frac{u}{\epsilon}\frac{\partial u}{\partial x} + \frac{v}{\epsilon}\frac{\partial u}{\partial r} = -\epsilon\frac{\partial P}{\partial x} - g^+ + \frac{\epsilon\ \mathrm{Pr}_m}{\mathrm{Da}\ \mathrm{Ra}^*}(T - u) - \frac{\epsilon\phi}{\mathrm{Da}}uV + \frac{\mu^*\epsilon\ \mathrm{Pr}_m}{\mathrm{Ra}^*}\left\{\frac{1}{r}\frac{\partial}{\partial r}\left(r\frac{\partial u}{\partial r}\right) + \frac{\partial^2 u}{\partial x^2}\right\} \quad (2)$$

$$\frac{\partial v}{\partial t} + \frac{u}{\epsilon}\frac{\partial v}{\partial x} + \frac{v}{\epsilon}\frac{\partial v}{\partial r} = -\epsilon\frac{\partial P}{\partial r} - \frac{\epsilon\ \mathrm{Pr}_m}{\mathrm{Da}\ \mathrm{Ra}^*}v - \frac{\epsilon\phi}{\mathrm{Da}}vV + \frac{\mu^*\epsilon\ \mathrm{Pr}_m}{\mathrm{Ra}^*}\left\{\frac{1}{r}\frac{\partial}{\partial r}\left(r\frac{\partial v}{\partial r}\right) + \frac{\partial^2 v}{\partial x^2}\right\} \quad (3)$$

Vorticity ζ in dimensionless form is defined as $\zeta = (\partial u/\partial r) - (\partial v/\partial x)$ and the momentum balance Eqs. (2) and (3) are combined to give the following equation in vorticity:

$$\frac{\partial \zeta}{\partial t} + \frac{u}{\epsilon}\frac{\partial \zeta}{\partial x} + \frac{v}{\epsilon}\frac{\partial \zeta}{\partial r} = \frac{\epsilon\ \mathrm{Pr}_m}{\mathrm{Da}\ \mathrm{Ra}^*}\left\{\frac{\partial T}{\partial r} - \left(1 + \frac{\mathrm{Da}}{r^2}\right)\zeta\right\} + \frac{\mu^*\epsilon\ \mathrm{Pr}_m}{\mathrm{Ra}^*}\left\{\frac{1}{r}\frac{\partial}{\partial r}\left(r\frac{\partial \zeta}{\partial r}\right) + \frac{\partial^2 \zeta}{\partial x^2} - \frac{1}{r^2}\frac{\partial v}{\partial x}\right\} - \frac{\epsilon\phi}{\mathrm{Da}}\left\{\left(V + \frac{u^2}{V}\right)\zeta + \frac{(u^2 - v^2)}{V}\frac{\partial v}{\partial x} + \frac{2uv}{V}\frac{\partial v}{\partial r} + \frac{uv^2}{rV}\right\} \quad (4)$$

The dimensionless stream function ψ is defined as shown below satisfying the equation of continuity:

$$ru = \frac{\partial \psi}{\partial r}; \quad rv = -\frac{\partial \psi}{\partial x} \quad (5)$$

Making use of Eq. (5), the following relation between ζ and ψ is obtained:

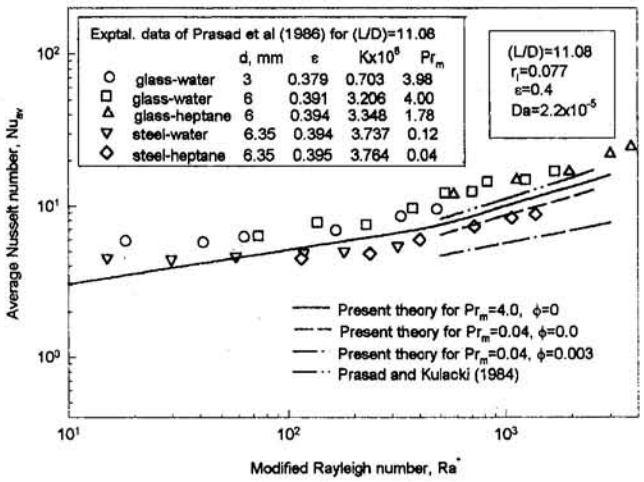

Fig. 1 Comparison of the present theory with the experimental data of Prasad et al. (1986) for the case of a long cylinder with (*L/D*) = 11.08

$$r\zeta = \frac{\partial^2\psi}{\partial r^2} - \frac{1}{r}\frac{\partial\psi}{\partial r} + \frac{\partial^2\psi}{\partial x^2} \tag{6}$$

Initial and boundary conditions in dimensionless form (conditions stipulated at various boundaries for the stream function ψ and vorticity ζ in dimensionless form are also included):

$$t = 0: \quad u = v = T = 0$$

$$\text{for} \quad 0 \le x \le (L/D) \quad \text{and for} \quad r_i \le r \le r_o$$

For $t > 0$ and for $0 \le x \le (L/D)$:

$$\text{At} \quad r = r_i: \quad u = v = \psi = 0 \quad \text{and} \quad T = 1;$$

$$\text{At} \quad r = r_o: \quad u = \frac{\partial\psi}{\partial r} = \zeta = T = 0$$

$$\text{At} \quad x = 0, \quad \frac{\partial T}{\partial x} = \psi = 0;$$

$$\text{At} \quad x = (L/D), \quad \frac{\partial\psi}{\partial x} = \frac{\partial T}{\partial x} = \zeta = 0 \ (\text{for } r_i < r < r_o) \tag{7}$$

In Eq. (7), the boundary condition at the upper boundary, $x = (L/D)$, is prescribed based on a discussion presented by Roache (1985) on boundary conditions for vorticity and stream functions.

The local heat transfer coefficient at the wall ($\bar{r} = \bar{r}_i$) is defined by the equation

$$-k_m \left.\frac{\partial\bar{T}}{\partial\bar{r}}\right|_{\bar{r}=\bar{r}_i} = h_x(\bar{T}_w - \bar{T}_a) \tag{8}$$

following which the local Nusselt number is obtained from the equation

$$-\left.\frac{\partial T}{\partial r}\right|_{\text{at } r=r_i} = \text{Nu}_x \tag{9}$$

Method of Solution

The unsteady-state energy and vorticity equations in dimensionless form (Eqs. (1) and (4)) are numerically solved by the Alternating Direction Implicit (ADI) method (Roache, 1985; Angirasa and Mahajan, 1993). This method gives the values of dimensionless temperature T and vorticity ζ at all grid points after each time step (Δt). Making use of the new values of ζ, the stream function ψ and the u and v velocities are obtained from Eqs. (6) and (5), respectively. The Successive Over Relaxation (SOR) method is used for the solution of Eq. (6). The solution procedure for successive time steps is continued until steady-state results are obtained. Local Nusselt numbers Nu_x are computed, making use of Eq. (9). Using these local values, an integrated average Nusselt number Nu_{av} is computed by Simpson's rule. The stability and consistency of the results are ascertained by subjecting the results to a grid-independence test and an iteration-convergence test in the cases of the ADI method and the successive overrelaxation method, respectively.

Results and Discussion

Results are obtained to study the effects of the parameters Ra*, (L/D) ratio, r_i, Pr_m, and Da on the velocity and temperature profiles and on Nusselt numbers. From the numerical results it is observed that the effect of Prandtl number Pr_m on Nusselt numbers is significant when $\text{Ra}^* > 100$ and $\text{Da} > 10^{-5}$. Further, the effect of the inertial (or turbulence) resistance parameter ϕ on Nusselt numbers is found to be significant at low Prandtl and high Darcy numbers. A comparison of the present theory is shown in Figs. 1 and 2 with the experimental data of Prasad et al. (1986), and Prasad and Kulacki (1985) for the cases of long and short cylinders, respectively. Numerical results are recast in the form of expressions for average Nusselt number as a function of various system parameters, by means of nonlinear regression analysis:

For $\phi = 0$ and for $\text{Ra}^* < 200$:

$$\text{Nu}_{av} = 1.2757\ \text{Ra}^{*0.226}\left(\frac{L}{D}\right)^{-0.279} \times \left(1 + \frac{1}{r_i}\right)^{0.382}\left(\frac{\epsilon}{\text{Pr}_m\ \text{Da}}\right)^{0.0014} \tag{10a}$$

For $\phi = 0$ and for $200 < \text{Ra}^* < 2500$:

$$\text{Nu}_{av} = 0.5685\ \text{Ra}^{*0.427}\left(\frac{L}{D}\right)^{-0.334} \times \left(1 + \frac{1}{r_i}\right)^{0.1366}\left(\frac{\epsilon}{\text{Pr}_m\ \text{Da}}\right)^{0.032} \tag{10b}$$

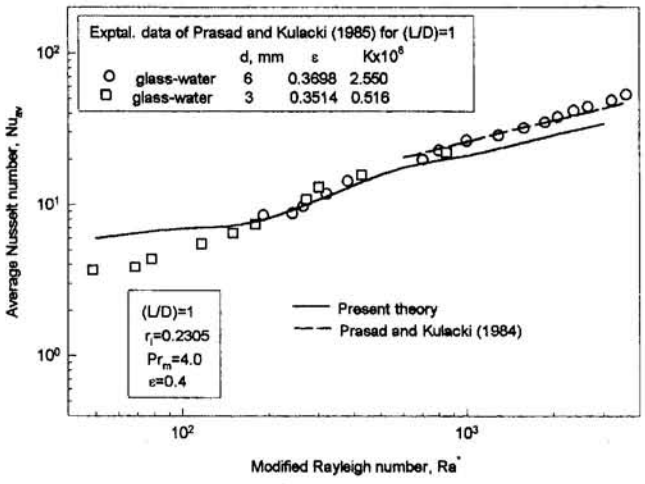

Fig. 2 Comparison of the present theory with the experimental data of Prasad and Kulacki (1985) for the case of a short cylinder with (*L/D*) = 1.0

For $\phi > 0$ and for $500 < \mathrm{Ra}^* < 2500$ and $\mathrm{Da} > 10^{-5}$:

$$\mathrm{Nu}_{av} = 1.013\ \mathrm{Ra}^{*0.276}\left(\frac{L}{D}\right)^{-0.368}\left(1+\frac{1}{r_i}\right)^{0.196} \times \left(\frac{\epsilon}{\mathrm{Pr}_m\,\mathrm{Da}}\right)^{0.082}\left(1+\frac{\epsilon\phi}{\mathrm{Da}}\right)^{-0.08} \quad (11)$$

These regression equations agree with the numerical results within a standard deviation of 6 percent for the following range of parameters: $1.0 \le (L/D) \le 15$; $0.07 \le r_i \le 40$; $0.04 \le \mathrm{Pr}_m \le 50$; and $4 \times 10^{-7} \le \mathrm{Da} \le 2 \times 10^{-4}$.

Acknowledgments

The authors thank Dr. Devarakonda Angirasa and Ms. D. S. Mary Sujatha for their help in connection with the ADI method, Prof. R. Krishna Murty for providing the computer facility, and AICTE, New Delhi, for the financial support.

References

Angirasa, D., and Mahajan, R. L., 1993, "Natural Convection From L-Shaped Corners With Adiabatic and Cold Isothermal Horizontal Walls," ASME JOURNAL OF HEAT TRANSFER, Vol. 115, pp. 149–157.

Choudhary, M., Proster, M., and Szekely, J., 1976, "On the Importance of Inertial Terms in the Modeling of Flow Maldistribution in Packed Beds," *AIChE Journal*, Vol. 22, pp. 600–603.

Jonsson, T., and Catton, I., 1987, "Prandtl Number Dependence of Natural Convection in Porous Media," ASME JOURNAL OF HEAT TRANSFER, Vol. 109, pp. 371–377.

Kaviany, M., and Mittal, M., 1987, "Natural Convection Heat Transfer From a Vertical Plate to High Permeability Porous Media: an Experimental and an Approximate Solution," *Int. J. Heat Mass Transfer*, Vol. 30, pp. 967–976.

Minkowycz, W. J., and Cheng, P., 1976, "Free Convection About a Vertical Cylinder Embedded in a Porous Medium," *Int. J. Heat Mass Transfer*, Vol. 19, pp. 805–813.

Prasad, V., and Kulacki, F. A., 1984, "Natural Convection in a Vertical Porous Annulus," *Int. J. Heat Mass Transfer*, Vol. 27, pp. 207–219.

Prasad, V., and Kulacki, F. A., 1985, "Natural Convection in Porous Media Bounded by Short Concentric Vertical Cylinders," ASME JOURNAL OF HEAT TRANSFER, Vol. 107, pp. 147–154.

Prasad, V., Kulacki, F. A., and Kulkarni, A. V., 1986, "Free Convection in a Vertical, Porous Annulus With Constant Heat Flux on the Inner Wall—Experimental Results," *Int. J. Heat Mass Transfer*, Vol. 29, pp. 713–722.

Roache, P. J., 1985, *Computational Fluid Dynamics*, Hermosa, Albuquerque, NM.

Vafai, K., and Tien, C. L., 1981, "Boundary and Inertia Effects on Flow and Heat Transfer in Porous Media," *Int. J. Heat Mass Transfer*, Vol. 24, pp. 195–203.

Laminar Forced Convection in the Entrance Region of a Semiporous Channel

T.-C. Jen[1]

Nomenclature

f_{pw} = friction factor at porous wall
f_{sw} = friction factor at solid wall
H = channel height
L = total channel length
n = direction normal to wall
Nu = Nusselt number
Pr = Prandtl number = ν/α
Re = inlet flow Reynolds number = $U_o H/\nu$
Re_m = mean flow Reynolds number = $U_m H/\nu$
Re_w = wall suction Reynolds number = $V_w H/\nu$
u, v = dimensionless velocity components
U_m = mean velocity at x
u_m = dimensionless mean velocity at x
V_w = wall suction velocity
x, y = dimensionless coordinates
x^+ = dimensionless axial coordinate = x/Re
θ = dimensionless temperature
θ_m = dimensionless bulk mean temperature

Introduction

The heat transfer and fluid flow in the entrance region of a semiporous channel is of importance in many engineering applications such as nuclear reactors, turbine engines, combustion chambers, solar collectors, and electrochemical systems. Detailed reviews of porous-walled-passage flow and heat transfer can be found in Raithby (1971), Rhee and Edwards (1981), and Jen (1994). Only papers closely related to the present study are reviewed here.

Rhee and Edwards (1981) presented the first study concerning heat transfer in the hydrodynamic and thermal entrance region of a semiporous channel. A tail-end-plate configuration was used and the parabolized governing equations were solved numerically. It is worth noting that their results are limited to the case where there is no flow reversal, and where the effects of axial diffusion and conduction are neglected. Soong and Hwang (1990) investigated the laminar mixed convection problem of a radially rotating semiporous channel. A closed-form solution for the fully developed regime was found. Accounting for the fluid flow in the porous wall, Abdel-Rahman et al. (1991) studied the heat transfer and fluid flow in the channel and duct with wall injection. They show that the effect of fluid flow in the porous wall may become significant when Darcy number is large. This effect will be neglected in the present study. Recently, Hwang et al. (1993) presented a three-dimensional numerical analysis in the entrance region of a square duct with injection or suction at one wall. However, because the parabolized equations were used, the results are limited to cases without flow reversal. Typically, wall transpiration cooling channels have low aspect ratios (where aspect ratio is defined as spacing divided by length) (e.g., Moskowitz and Lombardo (1971) and Raj (1983)). Thus, a two-dimensional analysis can be useful for understanding the convection mechanism of a semiporous channel.

A numerical analysis has been performed for the simultaneously developing laminar flow and temperature fields in the entrance region of a semiporous channel. Both constant wall temperature and constant wall heat flux thermal boundary conditions are considered. A vorticity–velocity method successfully developed for two-dimensional flow by Farouk and Fusegi (1986) is used for the present study. Note that this formulation can be extended directly to three-dimensional parabolic flow as shown by Chou and Hwang (1987) and Jen et al. (1992). The power law scheme (Patankar, 1980) is employed to solve the governing equations for the flow and temperature fields. Unlike previous studies (Rhee and Edwards, 1981; Hwang et al., 1993), the axial diffusion terms in the momentum equations and the axial conduction term of the energy equation have been retained. Jen (1994) has shown that a significant error can be introduced in the entrance region when these terms are neglected. Furthermore, instead of making the parabolic flow as-

[1] Mechanical and Aerospace Engineering Department, University of California, Los Angeles, Los Angeles, CA 90095-1597.

Contributed by the Heat Transfer Division and presented at the 6th AIAA/ASME Joint Thermophysics and Heat Transfer Conference, June 20–23, 1994. Manuscript received by the Heat Transfer Division June 1995; revision received February 1996. Keywords: Flow Separation, Forced Convection, Numerical Methods. Associate Technical Editor: R. Viskanta.

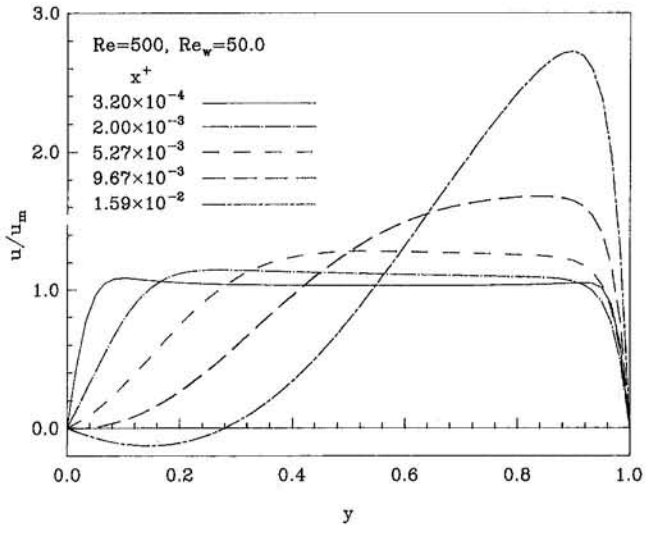

Fig. 1 Development of axial velocity profiles

sumption as in Rhee and Edwards (1981) and Hwang et al. (1993), fully elliptic governing equations are used here. This allows results to be obtained for regions with flow reversal. The effect of fluid flow in the porous wall is neglected here, even though this may become significant when Darcy number is large. A coordinate transformation technique is used to handle the boundary condition far downstream (see, Jen, 1994, for a detailed description). The effects of wall suction and heating are examined. The local friction factor and Nusselt number are presented as a function of axial position. It is seen that they are strongly affected by wall suction and heating. When wall suction is strong enough, flow reversals are observed. Comparisons with existing theoretical and experimental results are also presented.

Results and Discussion

Consider the steady, laminar, developing convection flow in a parallel channel with top wall suction, and solid bottom wall. A uniform inlet axial velocity and a constant inlet temperature are imposed at $x = 0$. Each channel wall is either under constant wall temperature or uniform wall heat flux conditions. The flow is assumed to be steady, constant-property, and incompressible. Viscous dissipation, compression work, and buoyancy are neglected. Details of the physical configuration, formulation, and numerical procedures used here can be found in Jen (1994), and will not be repeated here.

The computed results are first compared to theoretical results for the fully developed flow and heat transfer case with fully porous walls (i.e., both walls are porous). For a suction rate of $\mathrm{Re}_w = 2$ and $\mathrm{Pr} = 0.7$ fluid, $f\,\mathrm{Re}_m$ is found to be 24.87, and $\mathrm{Nu} = 4.8$ for the constant wall heat flux case. These are in excellent agreement with the data presented by Raithby (1971).

Because of the lack of experimental data in the developing region, the present numerical analysis has been compared with the only existing fully porous channel flow data (Raithby and Knudsen, 1974). With reference to Jen (1994), the agreement is seen to be excellent.

The present numerical analysis is also compared to theoretical results presented by Eckert et al. (1957) and Soong and Hwang (1990) for fully developed flow in semiporous channels. Again, with reference to Jen (1994), it is found that the agreement with the published theoretical results of Eckert et al. (1957) and Soong and Hwang (1990) are excellent for Re_w up to 6. For a larger suction rate, $\mathrm{Re}_w = 10$, the agreement is still reasonably good. Increasing the portion of the domain where there is suction and increasing the number of axial grid points change the results by an almost imperceptible amount. This suggests that the flow becomes fully developed very slowly. A measurable increase in computational domain size still does not yield a flow field that agrees with the analytical results for the fully developed case. This is in agreement with the results of Hwang et al. (1993), where it is shown that the flow is not quite fully developed at $\mathrm{Re}_w = 10$.

The present numerical analysis is compared to Rhee and Edwards (1981) where a marching technique was used for the simultaneously developing laminar convection in the entrance region. The velocity and temperature profiles for the constant wall temperature case of $\mathrm{Re}_w = 6.0$ (not shown) are in excellent agreement with their results except very near the inlet (i.e., $X/L = 0.02$). This is because the present analysis includes the effect of axial diffusion and axial conduction.

Profiles of the developing axial velocity, u/u_m, shown at different axial locations can be found in Jen (1994). Only one case, with flow reversal, is discussed here. For pure forced convection without suction, the axial velocity profile is symmetric about the $y = \frac{1}{2}$ plane. Wall suction has a clear effect on the velocity profiles. For $\mathrm{Re} = 500$, $\mathrm{Re}_w = 50$, the axial velocity profile, u/u_m, has been plotted on Fig. 1 for five axial locations starting from very near the entrance of the channel, $x^+ = 3.20 \times 10^{-4}$, to a location with flow reversal, $x^+ = 1.59 \times 10^{-2}$. It can be seen that the velocity profile is fairly uniform near the inlet. In the entrance region, the large flow resistance near the wall tends to accelerate the flow near the core region, the so-called "hydrodynamic center." Although the two curves nearest the inlet do not show significant distortion in the axial velocity profile, as the flow develops, the large suction rate distorts the axial velocity significantly. This is reflected by the increased top wall axial velocity gradient at the downstream axial location, $x^+ = 5.27 \times 10^{-3}$. In contrast to this, the velocity gradient near the solid wall is significantly decreased. At $x^+ = 9.67 \times 10^{-3}$, the velocity gradient near the solid wall approaches zero. For larger x^+, flow reversal occurs. Note that no fully developed region is observed in this case.

Figure 2 shows the local friction factor distribution at various axial locations for porous and solid walls. The parameters used in this figure are $\mathrm{Re} = 500$ and $\mathrm{Re}_w = 2$, 10, 20, and 50. It can be seen from Fig. 2 that $f_{pw}\mathrm{Re}_m$ increases with the suction rate. The suction effect at the porous wall results in a larger velocity gradient near the top wall (see Fig. 1). For the largest suction rate, $\mathrm{Re}_w = 50$, the porous wall friction factor increases signifi-

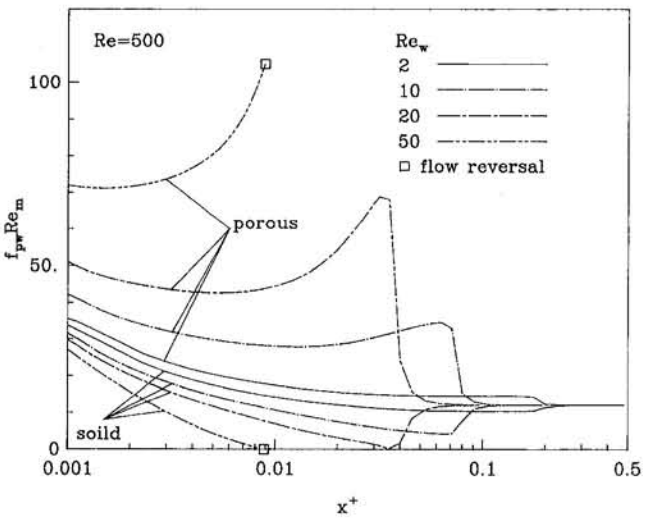

Fig. 2 Wall Reynolds number effects on friction factors along the axial direction

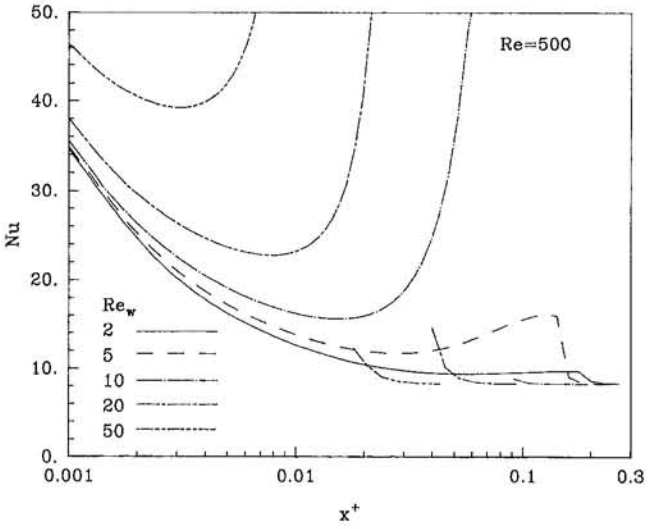

Fig. 3(*a*) constant wall heat flux case

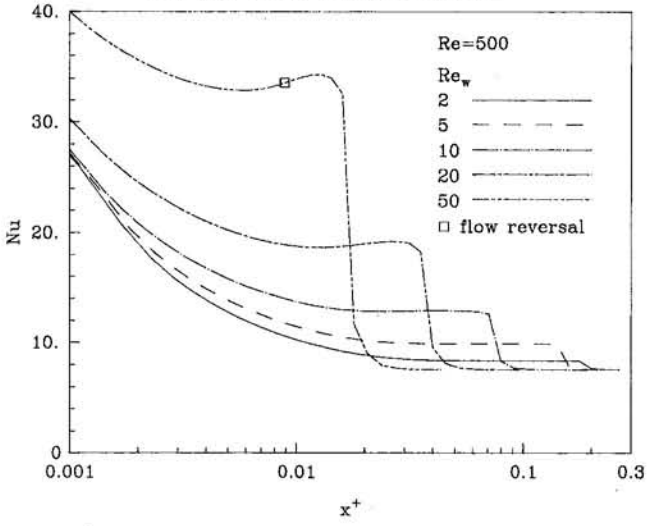

Fig. 3(*b*) constant wall temperature case

Fig. 3 Wall Reynolds number effects on Nusselt numbers along the axial direction

cantly, with flow reversal occurring at the bottom wall when $f_{pw}\mathrm{Re}_m$ reaches about 100. It can be seen that stronger suction rates at the porous wall cause the solid wall friction factor to decrease faster. Flow reversal occurs for the largest suction rate (i.e., $\mathrm{Re}_w = 50$) at $x^+ \simeq 0.008$, where the solid wall friction factor becomes zero. At low suction rates, as the mass flow in the axial location decreases along the channel, total fluid extraction will result at some axial position when mass flow goes to zero. In these cases (i.e., for Re_w from 2 to 10), no flow reversals are observed. However, for a larger suction rate, flow reversal will occur near the solid wall for the small axial velocity case due to the inability of the fluid to adjust for the large amount being extracted at the porous wall (Hwang et al., 1993). The flow reversal locations are seen to move upstream as the suction rate increases, in agreement with the results presented by Hwang et al. (1993).

The effect of Re_w on Nusselt numbers along the axial direction for Re = 500 and Pr = 0.7 in the entrance region for constant wall heat flux case is given in Fig. 3(*a*). As can be seen, heat transfer increases as the suction rate increases. The Nusselt number approaches infinity when the suction rate is greater or equal to 10. This is because the bulk mean temperature is equal to the porous wall temperature. Thus, the first term of the Nusselt number (defined as $(\partial\theta/\partial n)_{pw}1/(\theta_m - \theta_{pw})$) tends toward infinity (see Jen, 1994, for detailed discussion). A suction rate increase from 2 to 50 results in an increase in the heat transfer rate of more than 25 percent at $x^+ = 10^{-3}$. The effect is even larger farther downstream.

The effect of wall suction on the Nusselt numbers in the axial direction for the constant wall temperature case is demonstrated in Fig. 3(*b*). Similar to the constant wall heat flux case (i.e., Fig. 3(*a*)), the heat transfer rate increases as the suction rate increases. For a suction rate of $\mathrm{Re}_w = 50$, the increase in Nusselt number at $x^+ = 0.001$ is more than 50 percent, in comparison to the Nusselt number at $\mathrm{Re}_w = 2$. The amount of increase is larger further downstream. It is worth noting that for this case, the Nusselt number does not go toward ∞ because the bulk mean temperature of the fluid is always greater than the porous wall temperature.

Acknowledgments

The author would like to thank Dr. Stanley Chen for his assistance in proofreading this paper.

References

Abdel-Rahman, A. K., Suzuki, K., Hagiwara, Y., and Takaura, H., 1991, "Laminar Channel Flow With Fluid Injection Accounting for the Flow in the Porous Wall," *Proc. 28th National Heat Transfer Symposium of Japan,* pp. 406–408.

Chou, F. C., and Hwang, G. J., 1987, "Vorticity-Velocity Method for the Graetz Problem and the Effect of Natural Convection in a Horizontal Rectangular Channel With Uniform Wall Heat Flux," ASME JOURNAL OF HEAT TRANSFER, Vol. 109, pp. 704–710.

Eckert, E. R. G., Donoughe, P. L., and Moore, B. J., 1957, "Velocity and Friction of Laminar Viscous Boundary-Layer and Channel Flow Over Surfaces With Injection or Suction," NACA TN 4102.

Farouk, B., and Fusegi, T., 1986, "Predictions of Fluid and Heat Transfer Problems by the Vorticity-Velocity Formulation of the Navier–Stokes Equations," *J. Comp. Phys.,* Vol. 65, pp. 227–243.

Hwang, G. J., Cheng, Y. C., and Ng, M. L., 1993, "Developing Laminar Flow and Heat Transfer in a Square Duct With One-Walled Injection and Suction," *Int. J. Heat Mass Transfer,* Vol. 36, No. 9, pp. 2429–2440.

Jen, T. C., Lavine, A. S., and Hwang, G. J., 1992, "Simultaneously Developing Laminar Convection in Rotating Isothermal Square Channels," *Int. J. Heat Mass Transfer,* Vol. 35, No. 1, pp. 239–254.

Jen, T. C., 1994, "Simultaneously Developing Laminar Convection in the Entrance Region of a Semi-porous Channel," *Current Developments in Numerical Simulation of Flow and Heat Transfer,* ASME HTD-Vol. 275, pp. 111–122.

Moskowitz, S. L., and Lombardo, S., 1971, "2750 Deg F Engine Turbine Test of a Transpiration Air-Cooled Turbine," ASME *Journal of Engineering for Gas Turbines and Power,* Vol. 93, pp. 238–248.

Patankar, S. V., 1980, *Numerical Heat Transfer and Fluid Flow,* Hemisphere Publishing Co., pp. 96–100.

Raithby, G., 1971, "Laminar Heat Transfer in the Thermal Entrance Region of Circular Tubes and Two-Dimensional Rectangular Ducts With Wall Suction and Injection," *Int. J. Heat Mass Transfer,* Vol. 14, pp. 224–243.

Raithby, G. D., and Knudsen, D. C., 1974, "Hydrodynamic Development in a Duct With Suction and Blowing," *J. Appl. Mech.,* Vol. 41, pp. 896–902.

Raj, R., 1983, "Deposition Results of a Transpiration Air-Cooled Turbine Vane Cascade in a Contaminated Gas Stream," ASME *Journal of Engineering for Gas Turbines and Power,* Vol. 105, pp. 826–833.

Rhee, S. J., and Edwards, D. K., 1981, "Laminar Entrance Flow in a Flat Plate Duct With Asymmetric Suction and Heating," *Num. Heat Transfer,* Vol. 4, pp. 85–100.

Soong, C. Y., and Hwang, G. J., 1990, "Laminar Mixed Convection in a Radially Rotating Semiporous Channel," *Int. J. Heat Mass Transfer,* Vol. 33, No. 9, pp. 1805–1816.

A Perturbation Solution for a Nonthermal Equilibrium Fluid Flow Through a Three-Dimensional Sensible Heat Storage Packed Bed

A. V. Kuznetsov[1]

Nomenclature

a_{sf} = specific surface area common to solid and fluid phases, m^2/m^3
c_p = specific heat at constant pressure, J kg^{-1} K^{-1}
h_w = heat transfer coefficient at the porous bed walls, W m^{-2} K^{-1}
h_{sf} = fluid-to-particle heat transfer coefficient between solid and fluid phases, W m^{-2} K^{-1}
L_i = length of the packed bed (in x_i-direction), m
t = time, s
T = temperature, K
v = velocity of the fluid phase, m s^{-1}
x_1, x_2, x_3 = Cartesian coordinates, m
$\langle \ldots \rangle$ = local volume average
ϵ = porosity
λ = thermal conductivity, W m^{-1} K^{-1}
ξ_i = dimensionless coordinates
Θ = dimensionless temperature
$\Delta\Theta$ = dimensionless difference between temperatures of the solid and fluid phases
ρ = density, kg m^{-3}
τ = dimensionless time

Subscripts and Superscripts

eff = effective property
f = fluid phase
in = inlet
0 = initial
s = solid phase

1 Introduction

The investigation of a nonthermal equilibrium fluid flow through a porous packed bed is of permanent interest. This is because of the important applications of porous packed beds, such as the storage of heat energy. In recent works by Sözen and Vafai (1990), Vafai and Sözen (1990a, b), Sözen et al. (1991), and Amiri and Vafai (1994), a set of volume-averaged governing equations for nonthermal equilibrium, condensing, forced fluid flow through sensible and latent heat storage beds is presented and comprehensive numerical analyses of the phenomena are carried out. Analytical studies of the phenomena are presented by Amundson (1956a, b), Arpaci and Clark (1962), Hung and Nevins (1965), Jang and Lee (1974), Burch et al. (1976), Riaz (1977), and Spiga and Spiga (1981).

An investigation of a heating process of a semi-infinite packed bed based on the perturbation analysis of the full energy equations for the solid and fluid phases has been recently presented by Kuznetsov (1994). In the present analysis the considerably more complicated case of the three-dimensional porous packed bed is considered for the step response.

2 Physical Model and Governing Equations

A three-dimensional porous packed bed is filled with the incompressible fluid and is initially at a uniform temperature, T_0. The fluid flows in the x_1 direction; the peripheral walls ($x_2 = \pm L_2$, $x_3 = \pm L_3$) are heated by a fluid with a constant temperature, T_{in}. At the instant $t = 0$, fluid at a higher temperature, T_{in}, is suddenly allowed to flow through the packed bed. In establishing a model for analyzing this problem, the following assumptions and simplifications are employed: The fluid phase is incompressible and the mass flow rate at every cross section of the packed bed is constant; thermal, physical, and transport properties are constant; heat transfer is three dimensional and fluid flow is one dimensional; the dimensionless solid phase temperature differs from the fluid phase temperature by a small perturbation:

$$\Theta_s = \Theta_f + \delta\Delta\Theta \tag{1}$$

where δ is a dimensionless small parameter.

Following Sözen and Vafai (1990) and Vafai and Sözen (1990a, b), the effective thermal conductivity in both phases is assumed isotropic and constant.

Following the perturbation analysis presented by Kuznetsov (1994) it is easy to show that under this set of assumptions the dimensionless fluid phase temperature is governed by the following equation:

$$\frac{\partial\Theta_f}{\partial\tau} + \frac{\partial\Theta_f}{\partial\xi_1} = \sum_{i=1}^{3} \frac{\partial^2\Theta_f}{\partial\xi_i^2} + O(\delta) \tag{2}$$

and the dimensionless temperature difference between the solid and fluid phases is governed by the following equation:

$$\Delta\Theta = \frac{\partial\Theta_f}{\partial\tau} + \Lambda_1 \frac{\partial\Theta_f}{\partial\xi_1} - \Lambda_2 \sum_{i=1}^{3} \frac{\partial^2\Theta_f}{\partial\xi_i^2} \tag{3}$$

In Eqs. (1)–(3) the following dimensionless variables are utilized:

Temperature

$$\Theta = \frac{T_{in} - T}{T_{in} - T_0},$$

where T_{in} is the inlet temperature of the fluid phase and T_0 is the initial temperature of the packed bed,

Coordinates

$$\xi_i = \frac{\langle\rho_f\rangle^f (c_p)_f \langle v_f\rangle}{\lambda_{feff} + \lambda_{seff}} x_i,$$

Time

$$\tau = \frac{[\langle\rho_f\rangle^f (c_p)_f \langle v_f\rangle]^2}{[\epsilon\langle\rho_f\rangle^f (c_p)_f + (1-\epsilon)\langle\rho_s\rangle^s (c_p)_s](\lambda_{feff} + \lambda_{seff})} t,$$

and the dimensionless parameters

$$\Lambda_1 = \frac{\epsilon\langle\rho_f\rangle^f (c_p)_f + (1-\epsilon)\langle\rho_s\rangle^s (c_p)_s}{\epsilon\langle\rho_f\rangle^f (c_p)_f},$$

$$\Lambda_2 = \frac{\lambda_{feff}[\epsilon\langle\rho_f\rangle^f (c_p)_f + (1-\epsilon)\langle\rho_s\rangle^s (c_p)_s]}{\epsilon\langle\rho_f\rangle^f (c_p)_f [\lambda_{feff} + \lambda_{seff}]}, \quad \text{and}$$

$$\delta = \frac{1}{h_{sf} a_{sf}} \frac{\epsilon[\langle\rho_f\rangle^f (c_p)_f]^3 \langle v_f\rangle^2}{[\epsilon\langle\rho_f\rangle^f (c_p)_f + (1-\epsilon)\langle\rho_s\rangle^s (c_p)_s](\lambda_{feff} + \lambda_{seff})}$$

3 Solution and Analysis

For the function Θ_f, initial and boundary conditions discussed in the beginning of the previous section can be written in the following form:

[1] Mechanical Engineering Research Institute of Russian Academy of Sciences, Moscow, Russia; present address: Technical University of Vienna, Institute of Fluid Mechanics and Heat Transfer, Vienna, Austria.

Contributed by the Heat Transfer Division of THE AMERICAN SOCIETY OF MECHANICAL ENGINEERS. Manuscript received by the Heat Transfer Division July 1995; revision received February 1996. Keywords: Nonequilibrium Flows, Porous Media, Thermal Energy Storage. Associate Technical Editor: K. Vafai.

$$\Theta_f(\xi_1, \xi_2, \xi_3, 0) = 1 \tag{4}$$

$$\Theta_f(0, \xi_2, \xi_3, \tau) = 0, \frac{\partial \Theta_f}{\partial \xi_1}(R_1, \xi_2, \xi_3, \tau) = 0 \tag{5}$$

$$\frac{\partial \Theta_f}{\partial \xi_2}(\xi_1, \pm R_2, \xi_3, \tau) = \mp \alpha \Theta_f(\xi_1, \pm R_2, \xi_3, \tau), \tag{6}$$

$$\frac{\partial \Theta_f}{\partial \xi_3}(\xi_1, \xi_2, \pm R_3, \tau) = \mp \alpha \Theta_f(\xi_1, \xi_2, \pm R_3, \tau) \tag{7}$$

where

$$R_i = \langle \rho_f \rangle^f (c_p)_f \langle v_f \rangle L_i / (\lambda_{\text{feff}} + \lambda_{\text{reff}}) \ (i = 1, 2, 3) \quad \text{and}$$

$$\alpha = h_w / [\langle \rho_f \rangle^f (c_p)_f \langle v_f \rangle].$$

The zero temperature gradient at $\xi_1 = R_1$ (Eq. (5)) means that it is assumed that the temperature of the fluid does not change after the fluid leaves the packed bed and there is no temperature jump at the outlet boundary.

The solution of Eq. (2) with corresponding initial and boundary conditions (4)–(7) can be obtained as the product of the solutions of the pertinent one-dimensional problems:

$$\Theta_f(\xi_1, \xi_2, \xi_3, \tau) = \prod_{i=1}^{3} w_i(\xi_i, \tau) \tag{8}$$

The function $w_1(\xi_1, \tau)$ is the solution of the following equation:

$$\frac{\partial w_1}{\partial \tau} + \frac{\partial w_1}{\partial \xi_1} = \frac{\partial^2 w_1}{\partial \xi_1^2} \tag{9}$$

with its corresponding initial and boundary conditions

$$w_1(\xi_1, 0) = 1, \quad w_1(0, \tau) = 0, \quad \frac{\partial w_1}{\partial \xi_1}(R_1, \tau) = 0 \tag{10}$$

The functions $w_j(\xi_j, \tau)$ $(j = 2, 3)$ are the solutions of the following equations:

$$\frac{\partial w_j}{\partial \tau} = \frac{\partial^2 w_j}{\partial \xi_j^2} \tag{11}$$

with their corresponding initial and boundary conditions

$$w_j(\xi_j, 0) = 1, \quad \frac{\partial w_j}{\partial \xi_j}(0, \tau) = \alpha w_j,$$

$$\frac{\partial w_j}{\partial \xi_j}(R_j, \tau) = -\alpha w_j \tag{12}$$

The solution of the problem (9)–(10) is obtained using the classical Fourier method as

$$w_1 = \sum_{n=1}^{\infty} C_n \exp\left(\frac{\xi_1}{2}\right) \exp\left[-\left(\frac{1}{4} + b_n^2\right)\tau\right] \sin(b_n \xi_1) \tag{13}$$

where b_n are the positive solutions of the transcendental equation

$$\tan b_n R_1 = -2b_n \tag{14}$$

and the series coefficients in Eq. (15) are

$$C_n = \frac{\dfrac{b_n}{1/4 + b_n^2}}{\dfrac{R_1}{2} - \dfrac{\sin(2b_n R_1)}{4b_n}} \tag{15}$$

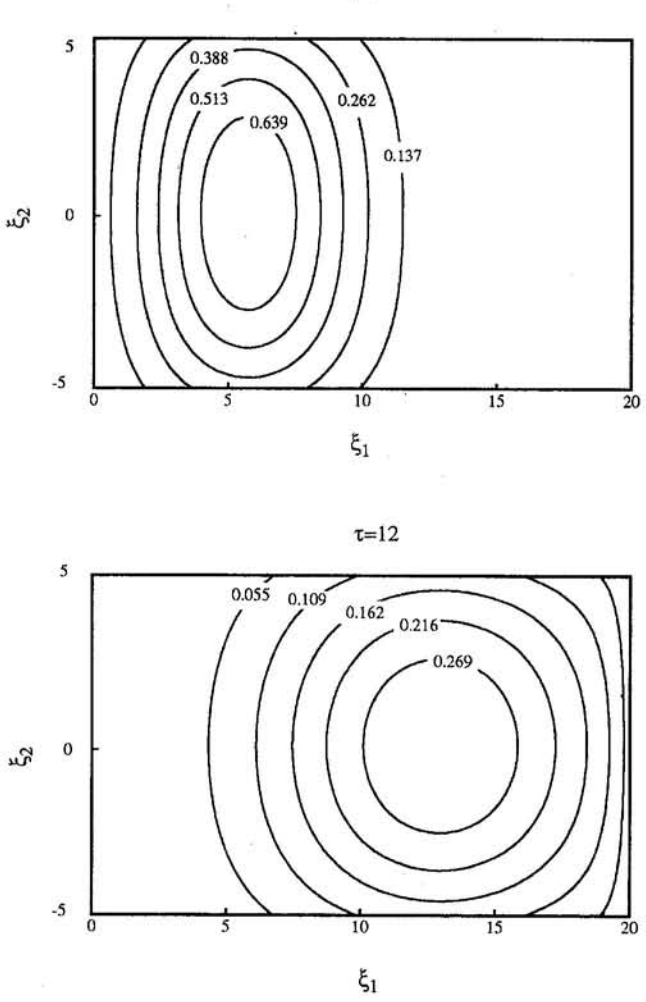

Fig. 1 Space distribution of dimensionless temperature difference, $\Delta\Theta$, for $\xi_3 = 0$

The solutions of the problems (11)–(12) are presented by Carslaw and Jaeger (1959) as:

$$w_j = \sum_{m=1}^{\infty} \frac{2\alpha \cos(\gamma_m \xi_j)}{[(\alpha^2 + \gamma_m^2)R_j + \alpha] \cos(\gamma_m R_j)} \exp[-\gamma_m^2 \tau] \tag{16}$$

where γ_m are the positive solutions of the transcendental equation

$$\gamma_m \tan \gamma_m R_j = \alpha \tag{17}$$

Finally, utilizing Eqs. (8), (13), and (16), the solution for the dimensionless fluid temperature Θ_f is

$$\Theta_f = \sum_{n,m,k=1}^{\infty} 4\alpha^2 C_n \exp\left[\frac{\xi_1}{2} - \left(\frac{1}{4} + b_n^2 + \gamma_m^2 + \gamma_k^2\right)\tau\right]$$

$$\times \frac{\sin(b_n \xi_1) \cos(\gamma_m \xi_2) \cos(\gamma_k \xi_3)}{[(\alpha^2 + \gamma_m^2)R_2 + \alpha][(\alpha^2 + \gamma_k^2)R_3 + \alpha] \cos(\gamma_m R_2) \cos(\gamma_k R_3)} \tag{18}$$

where the coefficients b_n, C_n, and $\gamma_{m,k}$ are determined by Eqs. (14), (15) and (17).

The dimensionless temperature difference between the solid and fluid phases can now be found from Eqs. (3) and (18) as

$$\Delta\Theta = \sum_{n,m,k=1}^{\infty} \frac{4\alpha^2 C_n \exp\left[\frac{\xi_1}{2} - \left(\frac{1}{4} + b_n^2 + \gamma_m^2 + \gamma_k^2\right)\tau\right] \cos(\gamma_m \xi_2) \cos(\gamma_k \xi_3)}{[(\alpha^2 + \gamma_m^2)R_2 + \alpha][(\alpha^2 + \gamma_k^2)R_3 + \alpha] \cos(\gamma_m R_2) \cos(\gamma_k R_3)} \times \left\{\left[-\frac{1}{4} + \frac{\Lambda_1}{2} - \frac{\Lambda_2}{4} + (\Lambda_2 - 1)(b_n^2 + \gamma_m^2 + \gamma_k^2)\right] \sin(b_n \xi_1) + (\Lambda_1 - \Lambda_2) b_n \cos(b_n \xi_1)\right\} \quad (19)$$

Figure 1 depicts the space distributions of the dimensionless temperature difference calculated utilizing Eq. (19) for $R_1 = 20$, $R_2 = 5$, $R_3 = 10$, $\alpha = 0.5$, $\Lambda_1 = 7$ and $\Lambda_2 = 1.4$. These values of Λ_1 and Λ_2 correspond to the following ratios of the thermophysical properties: $(c_p)_f\langle\rho_f\rangle^f = 0.5(c_p)_s\langle\rho_s\rangle^s$, $\lambda_{feff} = 0.25\lambda_{seff}$ and $\epsilon = 0.25$. This figure clearly shows that the temperature difference forms a thermocline. This thermocline has a local maximum. Analyzing the form of the thermocline for different moments of time, it can be seen that its local maximum moves downstream and its amplitude decreases as time increases.

4 Conclusions

The step response of a three-dimensional porous packed bed in nonthermal equilibrium is considered. The analytical solution for the problem is obtained by using the perturbation technique. It is shown that the temperature difference between the solid and fluid phases forms a thermocline. This thermocline has a local maximum and its amplitude decreases while the thermocline propagates downstream.

Acknowledgments

The author is grateful to the Ohio State University for a postdoctoral fellowship. The support provided by the AvHumboldt Foundation and by the Christian Doppler Laboratory for Continuous Solidification Processes is also gratefully acknowledged and appreciated.

References

Amiri, A., and Vafai, K., 1994, "Analysis of Dispersion Effects and Nonthermal Equilibrium, Non-Darcian, Variable Porosity Incompressible Flow Through Porous Media," *Int. J. Heat Mass Transfer,* Vol. 37, pp. 939–954.

Amundson, N. R., 1956a, "Solid–Fluid Interactions in Fixed and Moving Beds. Fixed Beds With Large Particles," *Industrial and Engineering Chemistry,* Vol. 48, pp. 26–35.

Amundson, N. R., 1956b, "Solid–Fluid Interactions in Fixed and Moving Beds. Fixed Beds With Small Particles," *Industrial and Engineering Chemistry,* Vol. 48, pp. 35–43.

Arpaci, V. S., and Clark, J. A., 1962, "Dynamic Response of Fluid and Wall Temperatures During Pressurized Discharge for Simultaneous Time-Dependent Inlet Gas Temperature, Ambient Temperature, and/or Ambient Heat Flux," *Advances in Cryogenic Engineering,* Vol. 7, pp. 419–432.

Burch, D. M., Allen, R. W., and Peavy, B. A., 1976, "Transient Temperature Distributions Within Porous Slabs Subjected to Sudden Transpiration Heating," ASME JOURNAL OF HEAT TRANSFER, Vol. 98, pp. 221–225.

Carslaw, H. S., and Jaeger, J. C., 1959, *Conduction of Heat in Solids,* Oxford University Press, United Kingdom.

Hung, F. T., and Nevins, R. G., 1965, "Unsteady-State Heat Transfer With a Flowing Fluid Through Porous Solids," ASME Paper No. 65-HT-10.

Jang, W. J., and Lee, C. P., 1974, "Dynamic Response of Solar Heat Storage Systems," ASME Paper No. 74-WA/HT-22.

Kuznetsov, A. V., 1994, "An Investigation of a Wave of Temperature Difference Between Solid and Fluid Phases in a Porous Packed Bed," *Int. J. Heat Mass Transfer,* Vol. 37, pp. 3030–3033.

Riaz, M., 1977, "Analytical Solutions for Single- and Two-Phase Models of Packed-Bed Thermal Storage Systems," ASME JOURNAL OF HEAT TRANSFER, Vol. 99, pp. 489–492.

Schumann, T. E. W., 1929, "Heat Transfer: Liquid Flowing Through a Porous Prism," *Journal of the Franklin Institute,* Vol. 208, pp. 405–416.

Sözen, M., and Vafai, K., 1990, "Analysis of the Non-thermal Equilibrium Condensing Flow of a Gas Through a Packed Bed," *Int. J. Heat Mass Transfer,* Vol. 33, pp. 1247–1261.

Sözen, M., Vafai, K., and Kennedy, L. A., 1991, "Thermal Charging and Discharging of Sensible and Latent Heat Storage Packed Beds," *J. Thermophysics,* Vol. 5, pp. 623–625.

Spiga, G., and Spiga, M., 1981, "A Rigorous Solution to a Heat Transfer Two Phase Model in Porous Media and Packed Beds," *Int. J. Heat Mass Transfer,* Vol. 24, pp. 355–364.

Vafai, K., and Sözen, M., 1990a, "Analysis of Energy and Momentum Transport for Fluid Flow Through a Porous Bed," ASME JOURNAL OF HEAT TRANSFER, Vol. 112, pp. 690–699.

Vafai, K., and Sözen, M., 1990b, "An Investigation of a Latent Heat Storage Porous Bed and Condensing Flow Through It," ASME JOURNAL OF HEAT TRANSFER, Vol. 112, pp. 1014–1022.

References

Aluminum Company of America (ALCOA), 1968, personal communication to L. S. Fletcher, Dec. 10.

ASM Metals Reference Book, 1983, American Society for Metals, Metals Park, Ohio.

Beasley, K. G., 1990, "Thermal Management of Electronics: Annual Status Report for Office of Naval Technology (ONT)," Naval Weapons Support Center (NWSC), Crane, IN, Report No. ESE-04409, Dec.

Clyne, T. W., and Withers, P. J., 1993, *An Introduction to Metal Matrix Composites*, Cambridge University Press, Cambridge, United Kingdom.

Ellis, D. L., and McDanels, D. L., 1991, "Thermal Conductivity and Thermal Expansion of Graphite Fiber/Copper Matrix Composites," presented at the Annual Meeting of the Metallurgical Society, New Orleans, LA, Feb. 17–21.

Gordon, F. H., and Clyne, T. W., 1991, "Transport Properties of Short Fibre SiC Reinforced Ti," in *Metal Matrix Composites—Processing, Microstructure, and Properties, 12th Ris0 International Symposium*, N. Hansen, D. Juul-Jensen, T. Leffers, H. Lilholt, T. Lorentzen, A. S. Pedersen, J. B. Pedersen, and B. Ralph, eds., Ris0 National Laboratory, pp. 361–366.

Kline, S. J., and McClintock, F. A., 1953, "Describing Uncertainties in Single-Sample Experiments," *Mechanical Engineering*, Vol. 75, No. 1, Jan., pp. 3–8.

Kuniya, K., Arakawa, T. K., and Chiba, A., 1987, "Thermal Conductivity, Electrical Conductivity, and Specific Heat of Copper-Carbon Fiber Composite," *Transactions of the Japanese Institute for Metals*, Vol. 28, pp. 819–826.

Lambert, M. A., and Fletcher, L. S., 1993, "The Experimental Thermal Contact Conductance of Vapor Deposited, Electroplated, and Flame Sprayed Silver Coatings," AIAA Paper No. 93-0846.

Lambert, M. A., and Fletcher, L. S., 1994, "Experimental Thermal Contact Conductance of Continuous Fiber Metal Matrix Composites," AIAA Paper No. 94-0122.

Maass, D., and Makwinski, M., 1992, "Pitch Fiber Composites as an Aluminum Replacement for High Performance Avionics Heatsinks," Advanced Composite Products, Inc., Report to Naval Surface Warfare Center (NSWC), Crane, IN.

Montesano, M. J., Wigand, J. T., and Roesch, J. C., 1992, "Demonstration of Advanced Pitch Fiber Composite Heat Sink With Enhanced Through Core Thermal Conductivity," ASME Paper No. 92-WA/EEP-31.

Pfeiffer, W., and Tallon, J., 1992, "High Conductivity Carbon-Carbon Composites for SEM-E Heat Sinks," SAMPE Electronics Conference, June.

Reeves, A. J., Taylor, R., and Clyne, T. W., 1991, "The Effect of Interfacial Reaction or Thermal Properties of Titanium Reinforced With Particulate SiC," *Materials Science and Engineering*, Vol. A141, pp. 129–138.

Touloukian, Y. S., and Ho, C. Y., eds., 1972, *Thermophysical Properties of Matter: Vol. 1, Thermal Conductivity of Metallic Solids; Vol. 2, Thermal Conductivity of Nonmetallic Solids*, Plenum Press, New York.

Conditionally Sampled Turbulent Prandtl Number in the Outer Region of a Turbulent Boundary Layer

D. E. Wroblewski[1]

Introduction

Much of the interest in turbulent Prandtl number models for boundary-layer flows has concentrated on the near-wall region, since predictions of wall heat transfer are most sensitive to near-wall transport. Reviews of turbulent Prandtl number data and modeling approaches were provided by Kays (1994), Reynolds (1975), Kestin and Richardson (1963), and Launder (1976). Despite the critical need for near-wall models, an understanding of the behavior of Pr_t in the outer region of the boundary layer may help to illuminate mechanisms of passive-scalar transport associated with large-scale mixing. This may be directly applicable to flows in which passive contaminants are introduced in the outer layer of boundary-layer flows, and indirectly relevant to transport processes in free-shear turbulent flows such as jets and wakes.

Studies of turbulent Prandtl number in air flow have been carried out by, among others, Kays (1994), Johnson (1959), Simpson et al. (1970), Subramanian and Antonia (1984), Gibson and Verriopoulos (1984), Blair and Bennett (1987), Wroblewski and Eibeck (1991), and Kim et al. (1992). These have shown Pr_t is generally between 0.8 and 1.2 for $y/\delta < 0.6$, with values between 0.86 to 0.9 often chosen for simulations in which Pr_t is assumed constant. A majority of the investigations also indicated a decrease in Pr_t for $y/\delta > 0.6$. Although this behavior is sometimes ignored due to experimental uncertainty, typically $Pr_t \pm 0.2$ or higher, the prevalence of this drop in recent experimental and numerical studies suggests otherwise.

The experimentally observed decrease in turbulent Prandtl number was matched using a combined diffusion-convection model for the Reynolds heat flux (Simpson et al., 1970). The heat-flux model included both gradient transport, due to small-scale eddy mixing, and convective transport, due to larger-scale eddy mixing, while momentum transport was modeled as gradient transport only:

$$-\overline{v\theta} = \epsilon_m \frac{\partial \overline{T}}{\partial y} - V_h\theta_h; \quad -\overline{uv} = \epsilon_m \frac{\partial \overline{U}}{\partial y};$$

$$\mathrm{Pr}_t = \frac{\overline{uv}\,\dfrac{\partial \overline{T}}{\partial y}}{\overline{v\theta}\,\dfrac{\partial \overline{U}}{\partial y}} = \frac{\epsilon_m}{\epsilon_m - V_h\theta_h/(\partial \overline{T}/\partial y)} \tag{1}$$

where V_h is a convection velocity, θ_h is some characteristic temperature scale, and the overbar denotes time averaging. Note that the diffusive component was assumed to be governed by the same diffusivity for both heat and momentum, ϵ_m. In applying this model, Simpson et al. (1970) assumed that θ_h was related to the mean temperature gradient through a mixing length, $\theta_h = l|\partial \overline{T}/\partial y|$, so that overall heat transport was still governed by gradient diffusion. According to Reynolds (1975), it is unlikely that bulk convection, occurring over large length scales, can be adequately represented by gradient diffusion. This paper describes an analysis involving the use of Eq. (1) (Simpson et al., 1970) to match experimental data, without retaining the mixing length approach for the convective transport component, $V_h\theta_h$. The objective of this effort was to further illuminate the roll of large-scale convective transport in the wake region of a boundary layer.

Conditional Sampling

In intermittent regions of the boundary layer, conventional time-mean quantities include contributions from the nonturbulent, free-stream flow, as well as the turbulent flow inside the boundary layer. Conditional sampling with zone averaging was employed to isolate the turbulent zone contributions. For example, the turbulent zone average (denoted by the tz subscript) for the temperature was found from

$$\overline{T}_{tz} = \frac{1}{\gamma t_p}\int_0^{t_p} T(t)I(t)dt \tag{2}$$

where t_p is a sampling period, $I(t) = 1$ in the turbulent zone and $I(t) = 0$ in the free stream, and γ is the time-mean value of $I(t)$. Turbulence quantities, such as the Reynolds stresses and heat fluxes, were determined based on the zone averages, e.g., $\theta_{tz}(t) = T(t) - \overline{T}_{tz}$.

The temperature signal was used to determine the intermittency, since, compared to the velocity signal, it presented a clearer indication of the turbulent/non-turbulent interface (Antonia and Browne, 1987). The resulting intermittency was used for conditional averaging the velocity as well as the temperature.

[1] Aerospace and Mechanical Engineering, Boston University, Boston, MA 02215.

Contributed by the Heat Transfer Division of THE AMERICAN SOCIETY OF MECHANICAL ENGINEERS. Manuscript received by the Heat Transfer Division March 1995; revision received November 1995. Keywords: Forced convection, Turbulence. Associate Technical Editor: B. W. Webb.

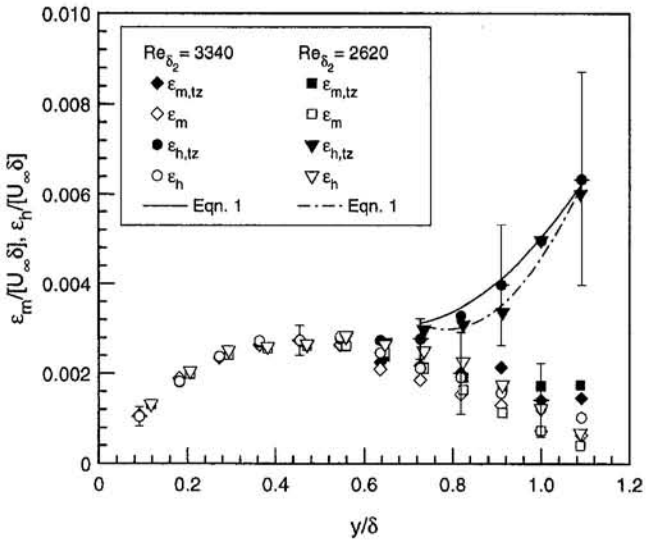

Fig. 1 Eddy diffusivity for heat, ϵ_h, and eddy viscosity, ϵ_m: conventional average (ϵ_h, ϵ_m) and turbulent-zone average ($\epsilon_{h,tz}$, $\epsilon_{m,tz}$). Error bars represent uncertainty (95 percent confidence). Lines are calculations based on Eq. (1).

A simple threshold level approach was employed here to determine the intermittency:

$$T(t) \le T_\infty + k_t; \quad I(t) = 0; \quad T(t) > T_\infty + k_t; \quad I(t) = 1 \quad (3)$$

where k_t is the threshold level and T_∞ is the free-stream temperature. The threshold level was set to twice the rms level of free-stream fluctuations, which were due to signal noise and not actual temperature fluctuations. Calculated values of $v\theta_{tz}$ showed some sensitivity to the choice of k_t, with variations of ±7 percent when k_t was varied over a range from one-half to twice the chosen level. This sensitivity, along with the smaller sensitivities calculated for $\overline{uv}_{tz}$, $\overline{T}_{tz}$, and $\overline{U}_{tz}$, were incorporated into the uncertainty analysis. A more detailed discussion of the conditional sampling, along with comparisons of the intermittency results with standard models, is provided by Wroblewski (1994).

Results

The experimental data considered here were obtained in the U.C. Berkeley Convective Boundary Layer Facility, featuring a constant area cross section (slight favorable pressure gradient) and a constant-heat-flux boundary condition. Details of the facility and instrumentation system can be found from Wroblewski and Eibeck (1991). Operating conditions and general features of the momentum and thermal boundary layers at the two streamwise locations studied were as follows: location, 1.89 and 2.65 m from the test section entrance; free-stream velocity, U_∞, 10.45 and 10.55 m/s; Reynolds numbers, Re_x, 1.29×10^6 and 1.81×10^6; momentum thickness Reynolds number, Re_{δ_2}, 2620 and 3340; 0.99 momentum-boundary-layer thickness, 3.4 and 4.4 cm; wall heat flux, 350 W/m^2, temperature difference between wall and free stream, 15.0 and 15.6°C.

Eddy diffusivity and eddy viscosity were calculated from simultaneous measurements of velocity and temperature, obtained with a triple-wire, heat-flux probe. The probe consisted of a standard X-wire, for two-component velocity measurements, with a constant-current cold wire, used to measure temperature, placed between the two X-wire sensors. To calculate $\epsilon_m = -\overline{uv}/(\partial\overline{U}/\partial y)$ from the measured experimental values, $\partial\overline{U}/\partial y$ was found from an equation of the form $\overline{U}/U_\infty = C(y/\delta)^n$, which was used to fit the measured data. A similar approach was used for ϵ_h, $\epsilon_{m,tz}$, and $\epsilon_{h,tz}$.

Conventional values of ϵ_m and ϵ_h exhibited peak levels near $y/\delta = 0.5$, and a drop toward zero as the outer edge of the boundary layer was approached (Fig. 1). Turbulent zone averages of the eddy viscosity approached an approximately constant level for $y/\delta > 0.7$. In contrast, $\epsilon_{h,tz}$ increased significantly in the intermittent region (Fig. 1). Values of $Pr_{t,tz}$ ($=\epsilon_{m,tz}/\epsilon_{h,tz}$) are lower than conventionally averaged Pr_t (Fig. 2), dropping to 0.15 at the boundary-layer edge. Antonia and Browne (1987) have observed similar trends in wakes, which is not surprising, since the outer region of the boundary layer is quite similar to boundary-free shear flows that are also governed by wakelike mechanisms, i.e., large eddies that scale on the overall turbulent-zone thickness.

In using Eq. (1) to fit the experimental heat-flux values, it was assumed that the convective component of the turbulent heat flux was uniform over a region that scaled on the size of the large eddies responsible for the transport; i.e., $V_h\theta_h$ should be constant in the intermittent region of the boundary layer.

A bulk convection velocity, based on the transport of temperature fluctuations, was used for V_h: $V_c = \overline{v\theta^2}/\overline{\theta^2}$, where $\overline{v\theta^2}$ is a triple velocity-temperature product. V_c is similar to a convection velocity defined by Bradshaw et al. (1967), based on transport of turbulent kinetic energy, and used for modeling triple products in second-order-closure turbulence models. Its use here as the characteristic convection velocity in a diffusion-convection model of heat transport follows the approach of Simpson et al. (1970), and is based on the premise that all scalar properties are transported by analogous mechanisms.

Figure 3 shows that conventionally averaged values of V_c continually increase throughout the boundary layer, similar to trends for V_c calculated using the kinetic energy (Bradshaw et al., 1967). In contrast, $V_{c,tz}$ is nearly constant for $y/\delta > 0.7$, providing some support to the premise that convective transport due to large-scale eddy motions is approximately constant across the intermittent region of the boundary layer. Based on the data in Fig. 3, average values for $y/\delta > 0.7$ are $V_{c,tz}/U_\infty = 0.011$ for $Re_{\delta_2} = 2620$ and $V_{c,tz}/U_\infty = 0.012$ for $Re_{\delta_2} = 3340$.

To determine a proper value of the temperature scale, Eq. (1) can be used along with measured values of $\epsilon_{h,tz}$, $\epsilon_{m,tz}$, $\partial\overline{T}_{tz}/\partial y$, and the average values of $V_{c,tz}$ given above, to find the value for θ_h that best fits the data. This analysis revealed $\theta_h/\Delta T_{tz} = 0.28$ for $Re_{\delta_2} = 2260$ and $\theta_h/\Delta T_{tz} = 0.29$ for $Re_{\delta_2} = 3340$, where $\Delta T_{tz} = \overline{T}_{tz}(y = \delta) - T_\infty$ is a temperature scale characteristic of the intermittent region ($\Delta T_{tz}/[T_w - T_\infty] =$

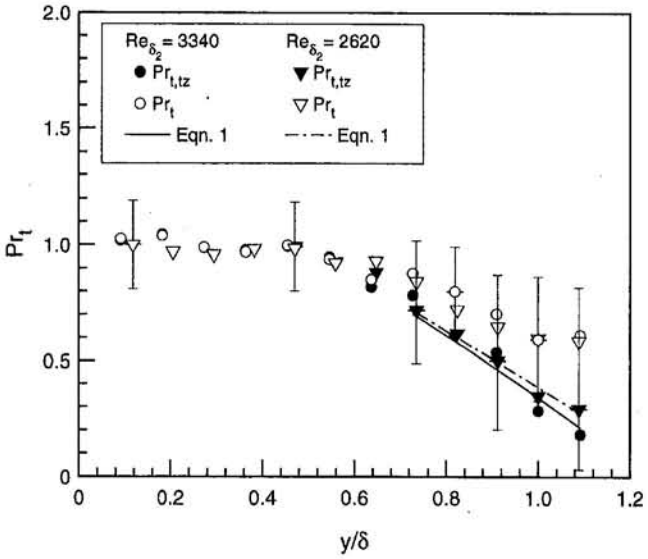

Fig. 2 Turbulent Prandtl number: conventional average (Pr_t) and turbulent-zone average ($Pr_{t,tz}$). Error bars represent uncertainty (95 percent confidence). Lines are calculations based on Eq. (1).

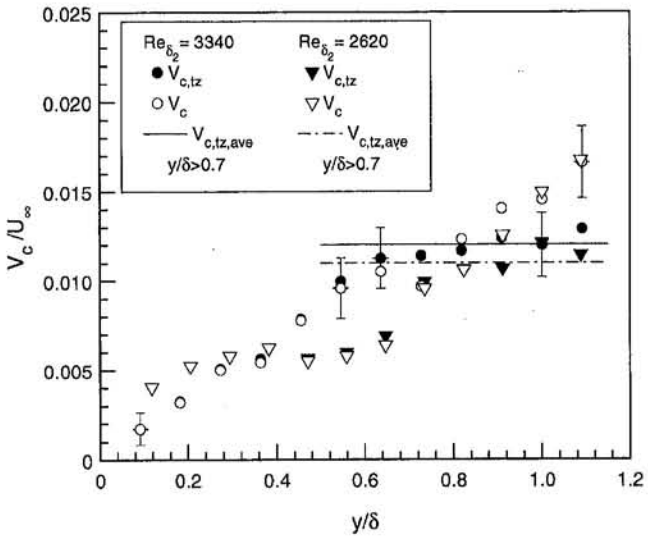

Fig. 3 Bulk convection velocity: conventional average (V_c) and turbulent-zone averages ($V_{c,tz}$). Error bars represent uncertainty (95 percent confidence). Lines are mean of turbulent-zone-average values for $y/\delta > 0.7$.

0.042 for $Re_{\delta_2} = 2260$ and 0.045 for $Re_{\delta_2} = 3340$). Using these values for θ_h, $\epsilon_{h,tz}$ and $Pr_{t,tz}$ were calculated from Eq. (1), with results compared to measurements in Figs. 1 and 2. Calculated values of $Pr_{t,tz}$ matched experimental values within ±0.04 (standard deviation = 0.03) for $y/\delta > 0.7$.

An inherent difficulty in measuring the turbulent Prandtl number is a high degree of uncertainty. Use of turbulent zone averaging tended to exacerbate the problem, since $\partial \overline{T}_{tz}/\partial y < \partial \overline{T}/\partial y$. Uncertainties, shown in each figure, were determined using the method described by Moffat (1988), and are discussed by Wroblewski and Eibeck (1991) for conventional values. For conditional averages, additional analysis was performed to determine the extent of propagation of uncertainties associated with the parameters in the equation used to fit the mean temperature and velocity, as well as sensitivities to the choice of threshold level. The uncertainties suggest that $Pr_{t,tz}$ may not decrease as strongly as indicated by the data (Fig. 2) and the fine detail provided by the diffusion-convection model may be unwarranted. The true test of the generality of the concepts discussed here will be confirmation with experimental data obtained in other facilities.

Conclusions

A composite model, with a diffusive and convective component, was used to analyze the turbulent zone-averaged eddy diffusivity and turbulent Prandtl number in a turbulent boundary layer. The hypothesis that the convective component was uniform across the outer region of the boundary layer ($y/\delta > 0.75$) was consistent with measured data.

Acknowledgments

The experimental data were obtained at the University of California, Berkeley, under grant No. DE-FG03-87ER 13780 from DOE Office of Basic Energy Sciences, and under the supervision of Professor Pamela Eibeck.

References

Antonia, R. A., and Browne, L. W. B., 1987, "Conventional and Conditional Prandtl Number in a Turbulent Wake," *Int. J. Heat Mass Transfer*, Vol. 30, pp. 2023–2030.

Blair, M. F., and Bennett, J. C., 1987, "Hot Wire Measurements of Velocity and Temperature Fluctuations in a Heated Turbulent Boundary Layer," *J. Phys. E.: Sci Instrum.*, Vol. 20, pp. 209–216.

Bradshaw, P., Ferriss, D. H., and Atwell, N. P., 1967, "Calculation of Boundary-Layer Development Using the Turbulent Energy Equation," *J. Fluid Mech.*, Vol. 28, pp. 593–616.

Gibson, M. M., and Verriopoulos, C. A., 1984, "Turbulent Boundary Layer on a Mildly Curved Surface: Part 2: Temperature Field Measurements," *Exp. Fluids*, Vol. 2, pp. 73–80.

Johnson, D. S., 1959, "Velocity and Temperature Fluctuation Measurements in a Turbulent Boundary Layer Downstream of a Stepwise Discontinuity in Wall Temperature," ASME *Journal of Applied Mechanics*, Vol. 26, pp. 325–336.

Kays, W. M., 1994, "Turbulent Prandtl Number—Where Are We?" ASME JOURNAL OF HEAT TRANSFER, Vol. 116, pp. 284–295.

Kestin, I. J., and Richardson, P. D., 1963, "Heat Transfer Across Turbulent, Incompressible Boundary Layers," *Int. J. Heat Mass Transfer*, Vol. 6, pp. 147–189.

Kim, J., Simon, T. W., and Russ, S. G., 1992, "Free Stream Turbulence and Concave Curvature Effects on Heated, Transitional Boundary Layers," ASME JOURNAL OF HEAT TRANSFER, Vol. 114, pp. 338–347.

Launder, B. E., 1976, "Heat and Mass Transport," in: *Turbulence*, P. Bradshaw, ed., Springer, Berlin.

Moffat, R. J., 1988, "Describing Uncertainty in Experimental Results," *Exp. Thermal Fluid Sci.*, Vol. 1, pp. 3–17.

Reynolds, A. J., 1975, "The Prediction of Turbulent Prandtl and Schmidt Numbers," *Int. J. Heat Mass Transfer*, Vol. 18, pp. 1055–1069.

Simpson, R. L., Whitten, D. G., and Moffat, R. J., 1970, "An Experimental Study of the Turbulent Prandtl Number of Air With Injection and Suction," *Int. J. Heat Mass Transfer*, Vol. 13, pp. 125–143.

Subramanian, C. S., and Antonia, R. A., 1984, "Effect of Reynolds Number on a Slightly Heated Boundary Layer," *Int. J. Heat Mass Transfer*, Vol. 24, pp. 1833–1846.

Townsend, A. A., 1976, *The Structure of Turbulent Shear Flow*, Cambridge University Press, Cambridge.

Wroblewski, D. E., and Eibeck, P. A., 1991, "A Frequency Response Compensation Technique for Cold Wires and Its Application to a Heat Flux Probe," *Experimental Thermal and Fluid Science*, Vol. 4, pp. 452–463.

Wroblewski, D. E., 1994, "Conventional and Conditional Eddy Diffusivity and Turbulent Prandtl Number in the Outer Region of a Turbulent Boundary Layer," *Fundamentals of Forced Convection Heat Transfer*, ASME HTD-Vol. 285.

The Conjugate Graetz Problem With Axial Conduction

X. Yin[1] and H. H. Bau[1]

Nomenclature

H, h = conduit's outer radius (half-width)
Hc = conduit's inner radius (half-width)
k = thermal conductivity
Q = heat flux
T = temperature
u = velocity profile
y = a coordinate perpendicular to the flow direction
z = axial coordinate
θ = nondimensional temperature

Subscripts

0 = entrance conditions
f = fluid
s = solid
w = wall

[1] Department of Mechanical Engineering and Applied Mechanics, University of Pennsylvania, Philadelphia, PA 19104-6315.

Contributed by the Heat Transfer Division of THE AMERICAN SOCIETY OF MECHANICAL ENGINEERS. Manuscript received by the Heat Transfer Division May 1995; revision received February 1996. Keywords: Conduction, Conjugate Heat Transfer. Associate Technical Editor: T. Bergman.

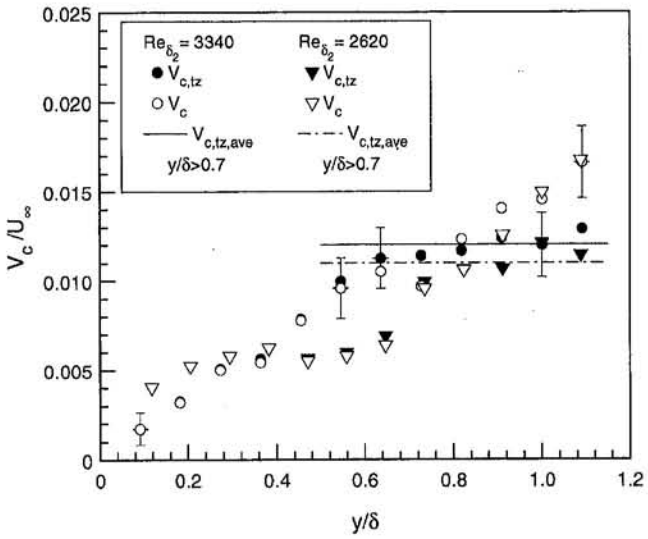

Fig. 3 Bulk convection velocity: conventional average (V_c) and turbulent-zone averages ($V_{c,tz}$). Error bars represent uncertainty (95 percent confidence). Lines are mean of turbulent-zone-average values for $y/\delta > 0.7$.

0.042 for $Re_{\delta_2} = 2260$ and 0.045 for $Re_{\delta_2} = 3340$). Using these values for θ_h, $\epsilon_{h,tz}$ and $Pr_{t,tz}$ were calculated from Eq. (1), with results compared to measurements in Figs. 1 and 2. Calculated values of $Pr_{t,tz}$ matched experimental values within ±0.04 (standard deviation = 0.03) for $y/\delta > 0.7$.

An inherent difficulty in measuring the turbulent Prandtl number is a high degree of uncertainty. Use of turbulent zone averaging tended to exacerbate the problem, since $\partial \overline{T}_{tz}/\partial y < \partial \overline{T}/\partial y$. Uncertainties, shown in each figure, were determined using the method described by Moffat (1988), and are discussed by Wroblewski and Eibeck (1991) for conventional values. For conditional averages, additional analysis was performed to determine the extent of propagation of uncertainties associated with the parameters in the equation used to fit the mean temperature and velocity, as well as sensitivities to the choice of threshold level. The uncertainties suggest that $Pr_{t,tz}$ may not decrease as strongly as indicated by the data (Fig. 2) and the fine detail provided by the diffusion-convection model may be unwarranted. The true test of the generality of the concepts discussed here will be confirmation with experimental data obtained in other facilities.

Conclusions

A composite model, with a diffusive and convective component, was used to analyze the turbulent zone-averaged eddy diffusivity and turbulent Prandtl number in a turbulent boundary layer. The hypothesis that the convective component was uniform across the outer region of the boundary layer ($y/\delta > 0.75$) was consistent with measured data.

Acknowledgments

The experimental data were obtained at the University of California, Berkeley, under grant No. DE-FG03-87ER 13780 from DOE Office of Basic Energy Sciences, and under the supervision of Professor Pamela Eibeck.

References

Antonia, R. A., and Browne, L. W. B., 1987, "Conventional and Conditional Prandtl Number in a Turbulent Wake," *Int. J. Heat Mass Transfer*, Vol. 30, pp. 2023–2030.

Blair, M. F., and Bennett, J. C., 1987, "Hot Wire Measurements of Velocity and Temperature Fluctuations in a Heated Turbulent Boundary Layer," *J. Phys. E.: Sci Instrum.*, Vol. 20, pp. 209–216.

Bradshaw, P., Ferriss, D. H., and Atwell, N. P., 1967, "Calculation of Boundary-Layer Development Using the Turbulent Energy Equation," *J. Fluid Mech.*, Vol. 28, pp. 593–616.

Gibson, M. M., and Verriopoulos, C. A., 1984, "Turbulent Boundary Layer on a Mildly Curved Surface: Part 2: Temperature Field Measurements," *Exp. Fluids*, Vol. 2, pp. 73–80.

Johnson, D. S., 1959, "Velocity and Temperature Fluctuation Measurements in a Turbulent Boundary Layer Downstream of a Stepwise Discontinuity in Wall Temperature," ASME *Journal of Applied Mechanics*, Vol. 26, pp. 325–336.

Kays, W. M., 1994, "Turbulent Prandtl Number—Where Are We?" ASME JOURNAL OF HEAT TRANSFER, Vol. 116, pp. 284–295.

Kestin, I. J., and Richardson, P. D., 1963, "Heat Transfer Across Turbulent, Incompressible Boundary Layers," *Int. J. Heat Mass Transfer*, Vol. 6, pp. 147–189.

Kim, J., Simon, T. W., and Russ, S. G., 1992, "Free Stream Turbulence and Concave Curvature Effects on Heated, Transitional Boundary Layers," ASME JOURNAL OF HEAT TRANSFER, Vol. 114, pp. 338–347.

Launder, B. E., 1976, "Heat and Mass Transport," in: *Turbulence*, P. Bradshaw, ed., Springer, Berlin.

Moffat, R. J., 1988, "Describing Uncertainty in Experimental Results," *Exp. Thermal Fluid Sci.*, Vol. 1, pp. 3–17.

Reynolds, A. J., 1975, "The Prediction of Turbulent Prandtl and Schmidt Numbers," *Int. J. Heat Mass Transfer*, Vol. 18, pp. 1055–1069.

Simpson, R. L., Whitten, D. G., and Moffat, R. J., 1970, "An Experimental Study of the Turbulent Prandtl Number of Air With Injection and Suction," *Int. J. Heat Mass Transfer*, Vol. 13, pp. 125–143.

Subramanian, C. S., and Antonia, R. A., 1984, "Effect of Reynolds Number on a Slightly Heated Boundary Layer," *Int. J. Heat Mass Transfer*, Vol. 24, pp. 1833–1846.

Townsend, A. A., 1976, *The Structure of Turbulent Shear Flow*, Cambridge University Press, Cambridge.

Wroblewski, D. E., and Eibeck, P. A., 1991, "A Frequency Response Compensation Technique for Cold Wires and Its Application to a Heat Flux Probe," *Experimental Thermal and Fluid Science*, Vol. 4, pp. 452–463.

Wroblewski, D. E., 1994, "Conventional and Conditional Eddy Diffusivity and Turbulent Prandtl Number in the Outer Region of a Turbulent Boundary Layer," *Fundamentals of Forced Convection Heat Transfer*, ASME HTD-Vol. 285.

The Conjugate Graetz Problem With Axial Conduction

X. Yin[1] and H. H. Bau[1]

Nomenclature

H, h = conduit's outer radius (half-width)
Hc = conduit's inner radius (half-width)
k = thermal conductivity
Q = heat flux
T = temperature
u = velocity profile
y = a coordinate perpendicular to the flow direction
z = axial coordinate
θ = nondimensional temperature

Subscripts

0 = entrance conditions
f = fluid
s = solid
w = wall

[1] Department of Mechanical Engineering and Applied Mechanics, University of Pennsylvania, Philadelphia, PA 19104-6315.

Contributed by the Heat Transfer Division of THE AMERICAN SOCIETY OF MECHANICAL ENGINEERS. Manuscript received by the Heat Transfer Division May 1995; revision received February 1996. Keywords: Conduction, Conjugate Heat Transfer. Associate Technical Editor: T. Bergman.

1 Introduction

The problem of heat transfer from fluids flowing in conduits (the Graetz problem) is of importance in many technological processes and has been studied extensively in studies dating back to Graetz (1885). The classical Graetz problem neglects axial conduction and considers forced convection heat transfer in a fluid flowing in conduits of various cross-sectional geometries subject to various peripheral boundary conditions imposed at the fluid's boundary. The pertinent literature is summarized in excellent compendiums by Shah and London (1978) and Shah and Bhatti (1987). Studies by Mori et al. (1974, 1976) and Guedes and Ozişik (1992) have taken into account axial conduction in the solid but not in the fluid.

Our study is motivated by recent investigations of heat transfer in microheat exchangers fabricated on silicon wafers (i.e., Weisberg et al., 1992; Yin and Bau, 1995). Flows in these microheat exchangers are characterized by small Peclet numbers, and the area of a solid's cross section perpendicular to the direction of such flows may be as large as or larger than the cross-sectional area available to the flow itself. Thus, axial conduction effects may be important in microheat exchangers. The objective of this paper is to assess the importance of axial heat conduction in both the solid and the liquid. To this end, we studied slug and Poiseuille flows between parallel plates and in circular cylinders. The energy equation was solved simultaneously in the fluid and the solid regions. Uniform temperature (case I) and uniform flux (case II) boundary conditions were imposed on the external solid surface. The equations were solved utilizing eigenfunction expansions. Various properties of the mathematical problem were proved by Yin (1995) but are not presented here.

2 The Mathematical Model

We consider velocity-wise, fully developed flow between two parallel, semi-infinite plates ($m = 0$) distance $2H_C$ apart as well as inside a semi-infinite, circular pipe ($m = 1$) of radius H_C. The solid wall thickness is $(H - H_c)$. Dimensional and nondimensional quantities are denoted, respectively, with upper and lower case letters. Two different velocity profiles, Poiseuille and uniform (slug), are considered:

$$u(y) = \begin{cases} 1 & \text{for slug flow} \\ (1 - y^2) & \text{for Poiseuille flow} \\ 0 & \end{cases} \begin{matrix} (0 < y < 1) \\ \\ (1 < y < h). \end{matrix} \quad (1)$$

The velocity is normalized with the center line speed, $U_{\max}$. y is the nondimensional coordinate normal to the direction of the flow. H_c is the length scale.

The energy equation,

$$u(y)\frac{\partial \theta_i}{\partial z} = \frac{1}{y^m}\frac{\partial}{\partial y}\left(y^m \frac{\partial \theta_i}{\partial y}\right) + \frac{1}{\mathrm{Pe}^2}\frac{\partial^2 \theta_i}{\partial z^2}, \quad (0 < y < h, 0 < z < \infty), \quad (2)$$

takes into account axial conduction in both the fluid and the solid. In the equation above, $\theta_i(y, z)$ is the nondimensional temperature; and the subscripts $i = f$ and $i = s$ refer, respectively, to the fluid and the solid. The nondimensional axial coordinate, z, is normalized with $H_c\mathrm{Pe}$. $\mathrm{Pe} = U_{\max}H_c/\alpha_f$ is the Peclet number and α_f is the fluid's thermal diffusivity. Although viscous dissipation was not included in Eq. (2), if so desired, the viscous dissipation's contribution to the temperature field can be separately computed and superposed on the results presented here.

Table 1 Case II—uniform flux boundary condition—expressions for $f(z)$ and $g_i(y)$

	Planar slug flow	Planar Poiseuille flow	Pipe slug flow	Pipe Poiseuille flow
$f(z)$	z	$\frac{3}{2}z$	$2hz$	$4hz$
$g_f(y)$	$\frac{1}{2}y^2 - \frac{1}{2} + \frac{k_f}{k_s}$	$\frac{3}{4}y^2 - \frac{1}{8}y^4 + \frac{k_f}{k_s} - \frac{5}{8}$	$\frac{h}{2}\left(y^2 - 1\right)$	$h\left(y^2 - \frac{1}{4}y^4\right) - \frac{3}{4}h$
$g_s(y)$	$\frac{k_f}{k_s}y$	$\frac{k_f}{k_s}y$	$\frac{k_f}{k_s}h\ell n(y)$	$\frac{k_f}{k_s}h\ell n(y)$

The thermal boundary and interfacial conditions are:

$$0 = \frac{\partial \theta_f(0, z)}{\partial y} = \theta_f(1, z) - \theta_s(1, z) = \frac{\partial \theta_f(1, z)}{\partial y} - \frac{k_s}{k_f}\frac{\partial \theta_s(1, z)}{\partial y} = \begin{cases} \theta_s(h, z) & \text{(case I)} \\ \dfrac{\partial \theta_s(h, z)}{\partial y} - \dfrac{k_f}{k_s} & \text{(case II).} \end{cases} \quad (3)$$

In case I, the nondimensional temperature is defined as $\theta_i = (T_i - T_w)/(T_r - T_w)$, where T_w is the dimensional temperature at $y = h$ and T_r is the maximum value of the entrance temperature at $z = 0$. Consequently, $0 < \theta_i < 1$. In case II, $\theta_i = k_f(T_i - T_r)/Q_wH_c$, where Q_w is the uniform flux at $y = h$. k_s and k_f denote, respectively, the thermal conductivities of the solid and the fluid. The temperature distribution at the channel's entrance is given by: $\theta_{f,s}(y, 0) = \theta_0(y)$.

We seek a solution of the form:

$$\theta_i(y, z) = \sum_{n=1}^{\infty} C_n\phi_{i,n}(y)\exp(-\lambda_n z) + f(z) + g_i(y) + C_0 \quad (4)$$

with $\lambda_n > 0$. In case I, $f(z) = g_i(y) = C_0 \equiv 0$. In case II, the corresponding values of $f(z)$ and $g_i(y)$ are specified in Table 1 and C_0 must be evaluated from initial conditions. Without loss of generality, we set $f(0) = 0$. Note that due to the negative exponents in Eq. (4), the series converges rapidly for $z > 0$.

We require that ϕ_n satisfy the eigenvalue problem:

$$\left\{\frac{1}{y^m}\frac{d}{dy}\left(y^m\frac{d}{dy}\right) + \lambda_n\left(u_i + \frac{\lambda_n}{\mathrm{Pe}^2}\right)\right\}\phi_{i,n} = 0. \quad (5)$$

The boundary and interfacial conditions are the homogeneous version of Eq. (3).

For $\mathrm{Pe} \to \infty$, Eq. (5) reduces to the classical Graetz problem (without axial conduction). For $\mathrm{Pe} < \infty$, Eq. (5) with the boundary conditions (3) is not a Sturm–Liouville problem since the eigenvalue (λ_n) appears nonlinearly. Yin (1995) showed that the eigenvalues λ_n are real, their magnitude is smaller than those of the corresponding eigenvalues in the classical Graetz problem, and λ_n are a minimum of a variational problem. We calculate the first few eigenpairs using the Prüfer transformation (Birkhoff and Rota, 1978) and a shooting technique.

Once the eigenfunctions were computed, the coefficients C_n are evaluated by satisfying the initial condition at $z = 0$. Unfortunately, the orthogonality conditions, which are satisfied by the eigenfunctions, cannot be used to calculate the coefficients C_n and C_0 in Eq. (4) since their use requires knowledge of *both* the temperature and heat-flux distributions at $z = 0$. This information is not usually available to us. Instead at $z = 0$, we required Eq. (4) to be satisfied in the sense of weighted residuals. We multiply Eq. (7) by weighing functions ($\chi_p(y)$) and

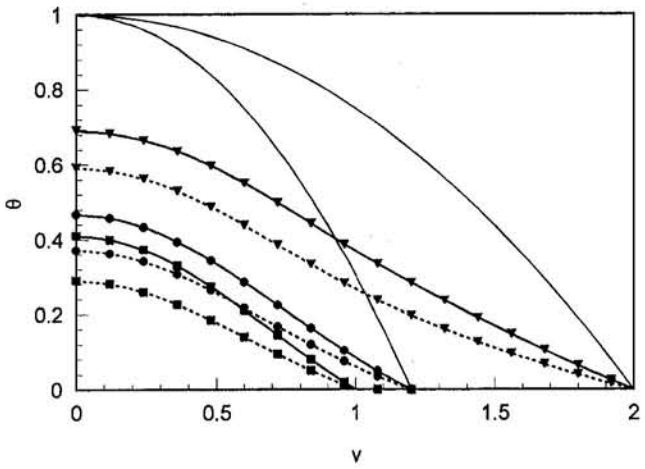

Fig. 1 The temperatures at $z = 0$ (the line without symbols) and 0.2 (the lines with symbols) are depicted as functions of y for pipe Poiseuille flow. Case I. $\{h, k_s/k_f\} = \{2, 1\}$ (triangles), $\{1.2, 243\}$ (squares), and $\{1.2, 1\}$ (circles). Pe = 5. Solid and dashed lines correspond, respectively, to cases when axial conduction is accounted for and those when it is neglected.

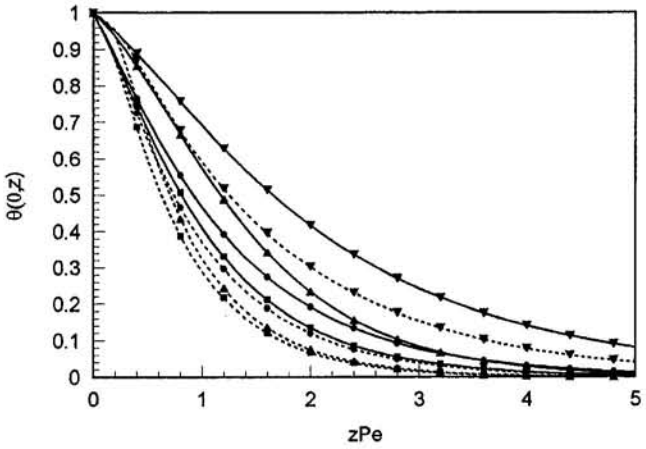

Fig. 2 The centerline temperature is depicted as a function of zPe for pipe Poiseuille flow. Case I. Pe = 5. Inverted triangles, upright triangles, circles, and squares, represent, respectively, $\{h, k_s/k_f\} = \{2, 1\}, \{2, 243\}, \{1.2, 1\}$, and $\{1.2, 243\}$. The solid and dashed lines correspond, respectively, to cases when axial conduction is accounted for and cases when it is neglected.

integrate over the domain $(0 < y < h)$ to obtain an infinite set of algebraic equations for the coefficients C_n:

$$B_p = \sum_{n=0}^{\infty} C_n G_{pn} \quad (0 \le p < \infty), \tag{6}$$

where $B_p = \int_0^h y^m(\theta_0(y) - g(y))\chi_p(y)dy$ and $G_{p,n} = \int_0^h \phi_n(y)\chi_p(y)y^m dy$. Typically, we choose $\chi_p(y) = \phi_p(y)$ for $p > 0$ and $\chi_0(y) = 1$; but these are not the only possible choices.

Next, we truncate the resulting infinite set of equations at $n = N$ and solve the truncated equations. The level of truncation is determined by requiring that $|(C_1^{(N+1)} - C_1^{(N)})/C_1^{(N)}| < \epsilon_1$ and $\int_0^h (\sum_1^N C_n\phi_n(y) + f(z) + g(y) + C_0 - \theta_0(y))^2 dy < \epsilon_1$, where typically $\epsilon_1 \sim 10^{-4}$.

For small z, the rate of convergence of the series (4) depends on the smoothness of the inlet temperature profile. Unrealistic, discontinuous profiles give rise to the Gibbs phenomenon and slow convergence. For smooth inlet temperature distributions such as $\theta_0(y) = \sin((\pi/2)(1 - y/h))$, a few terms $(N < 20)$ in the series are sufficient to satisfy the convergence criteria. As z increases, due to the rapid decay of exponential terms, only a very few terms are required to obtain an accurate description of the temperature field.

It is convenient to summarize the results in terms of the local Nusselt number at the outer surface:

$$\mathrm{Nu}_h(z) = \frac{-2k_s h^m \theta_s'(h, z)}{k_f(\theta_b(z) - \theta(h, z))} \tag{7}$$

The bulk temperature is:

$$\theta_b(z) = \frac{1}{\overline{u}A}\int_A u\theta(y, z)dA = B\int_0^1 \theta_f(y, z)u(y)y^m dy. \tag{8}$$

For planar slug and Poiseuille flows, $B = 1$ and $B = 3/2$, respectively. For slug and Poiseuille flows in circular pipes, $B = 2$ and $B = 4$, respectively.

In general, the Nusselt number $\mathrm{Nu}_h(z)$ depends on the initial conditions. Often one is interested in the fully developed Nusselt number, $\mathrm{Nu}_{h,\infty}$. For case I,

$$\mathrm{Nu}_{h,\infty} = \frac{2\lambda_1}{B}\left\{\frac{1 - \dfrac{\lambda_1^2}{\mathrm{Pe}^2}\dfrac{\overline{\phi_{s,1}}}{\phi_{s,1}'(1)}}{1 + \dfrac{\lambda_1^2}{\mathrm{Pe}^2}\dfrac{\overline{\phi_{f,1}}}{\phi_{f,1}'(1)}}\right\} > \frac{2\lambda_1}{B}, \tag{9}$$

where $\overline{\phi_{f,1}} = \int_0^1 y^m\phi_{f,1}(y)dy$ and $\overline{\phi_{s,1}} = \int_1^h y^m\phi_{s,1}(y)dy$. In the classical Graetz problem (without axial conduction), the inequality in Eq. (9) should be replaced with an equality. For case II, to the leading order, the large z values for the Nusselt number are identical to the same values in the absence of axial conduction.

When axial conduction is accounted for, the asymptotic Nusselt number is larger than when axial conduction is neglected. For large Peclet numbers and slug flow, perturbation theory shows that $\mathrm{Nu}^{\infty}_{h,\text{with axial conduction}} = \mathrm{Nu}^{\infty}_{h,\text{without axial conduction}} + \mathrm{Pe}^{-2}N_1$, where $N_1 > 0$ (Yin, 1995).

3 Results and Discussion

In this section, we present a sample of our results. Due to space limitations, results are given only for Poiseuille flow in circular conduits, for case I, and for solid–liquid conductivity ratios $k_s/k_f = 1$ and 243. The latter corresponds to water flow in a silicon conduit. In all the figures, we compared our results for the generalized, conjugate Graetz problem (solid lines) with results (dashed lines) obtained for the classical conjugate Graetz problem without axial conduction.

Figure 1 depicts the temperature profiles, $\theta(y, 0)$ (inlet, lines without symbols) and $\theta(y, 0.2)$ as functions of y for $\{h, k_s/k_f\} = \{1.2, 1\}$ (circles), $\{1.2, 243\}$ (squares), and $\{2, 1\}$ (triangles), Pe = 5. The thicker wall $(h = 2)$ introduces a higher thermal resistance between the fluid and the ambient than the thinner wall $(h = 1.2)$ does, thus resulting in higher

Table 2 Asymptotic values for the Nusselt numbers in circular pipe flow with Pe = 5

k_s/k_f	h	Nu	With axial conduction	Without axial conduction
1	1.2	Nu_h	2.9686	2.8397
	2	Nu_h	1.8621	1.6867
243	1.2	Nu_h	3.8567	3.6527
	2	Nu_h	7.0152	3.6412

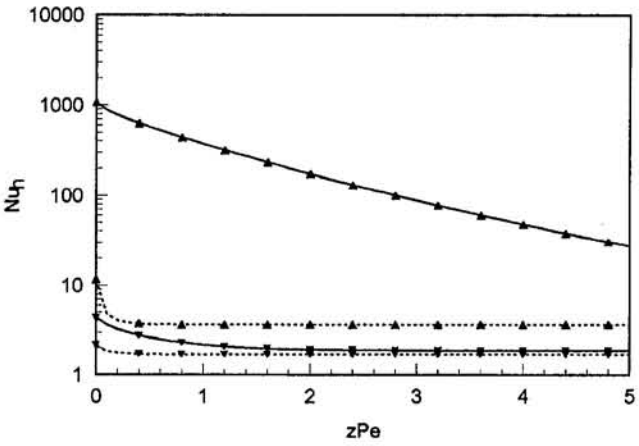

Fig. 3 The Nusselt number at the outer surface (Nu_h) is depicted as a function of zPe for pipe Poiseuille flow. $h = 2$, Pe = 5, $k_s/k_f = 243$ (upright triangles), and $k_s/k_f = 1$ (inverted triangles). Case I. The solid and dashed lines correspond, respectively, to cases when axial conduction is accounted for and cases when it is neglected.

temperatures in the fluid. In the case of $k_s/k_f = 243$, the solid's temperature is almost isothermal due to the solid's high thermal conductivity. Because of this conductivity, the solid offers less thermal resistance to heat losses from the fluid to the ambient, as reflected by the lower temperatures in the case of $k_s/k_f = 243$ than in the case of $k_s/k_f = 1$. A comparison of the solid and dashed lines indicates that at $z\text{Pe} = 1$, axial conduction plays a significant role, increasing the centerline temperature by more than 30 percent above the case without axial conduction ($h = 1.2$, $k_s/k_f = 243$).

Figure 2 depicts the centerline temperature $\theta(0, z)$ as a function of the axial coordinate $z\text{Pe}$ for Pe = 5, $h = 1.2$, $h = 2$, $k_s/k_f = 1$, and $k_s/k_f = 243$. The temperature decays most slowly (rapidly) for the case of $k_s/k_f = 1$, $h = 2$ ($k_s/k_f = 243$, $h = 1.2$) since this case offers the largest (smallest) thermal resistance between the fluid and the ambient. The effects of axial conduction diminish in importance as $z\text{Pe}$ increases.

Figure 3 depicts the Nusselt number at the outer surface, $Nu_h(z)$, as a function of the axial coordinate, $z\text{Pe}$, for Pe = 5, $h = 2$, and $k_s/k_f = 1$ (inverted triangles) and 243 (triangles). As z increases, the Nu numbers approach the asymptotic values we list in Table 2. When axial conduction is accounted for, the thermal development length is longer than when axial conduction is neglected. This is consistent with the eigenvalues of the generalized problem (with axial conduction) being smaller than the corresponding eigenvalues of the classical problem.

4 Conclusions

In this paper, we studied the generalized conjugate Graetz problem (with axial conduction). As expected, axial conduction plays an important role at the entrance region. As the distance from the entrance increases, the role of axial conduction diminishes. In the case of uniform temperature wall conditions, the asymptotic (large $z\text{Pe}$) Nusselt numbers accounting for axial conduction are consistently larger than those obtained neglecting axial conduction. The omission of axial conduction in the uniform temperature and heat flux cases leads, respectively, to under and overestimation of the temperature field in the entrance's vicinity. Omission of axial conduction also leads to an underestimation of the development length.

The analytic solutions produced in this paper are useful for obtaining fully developed Nusselt numbers and for verifying computer codes. For the latter purpose, it would be convenient to use initial conditions that are proportional to the first eigenfunction or a combination of a few eigenfunctions. When doing so, one obtains an exact, closed-form solution for the generalized Graetz problem.

Acknowledgments

The research reported in this paper has been supported, in part, by the National Science Foundation through grant No. CTS 90-12904.

References

Birkhoff, G., and Rota, G., 1978, *Ordinary Differential Equations,* Wiley, New York.

Graetz, L., 1885, "Uber die Warmeleitungsfähigkeit von Flussigkeiten (On the Thermal Conductivity of Liquids)," *Ann. Phys. Chem.,* Vol. 25, pp. 337–357.

Guedes, R. O. C., and Özişik, M. N., 1992, "Conjugated Turbulent Heat Transfer With Axial Conduction in Wall and Convection Boundary Conditions in a Parallel-Plate Channel," *Int. J. Heat and Fluid Flow,* Vol. 13, pp. 322–328.

Mori, S., Sakakibara, M., and Tanimoto, A., 1974, "Steady Heat Transfer to Laminar Flow in a Circular Tube With Conduction in the Tube Wall," *Heat Transfer—Jpn. Res.,* Vol. 3(2), pp. 37–46.

Mori, S., Shinke, T., Sakakibara, M., and Tanimoto, A., 1976, "Steady Heat Transfer to Laminar Flow Between Parallel Plates With Conduction in the Wall," *Heat Transfer—Jpn. Res.,* Vol. 5(4), pp. 17–25.

Shah, R. K., and London, A. L., 1978, *Laminar Flow Forced Convection in Ducts,* Academic Press, New York.

Shah, R. K., and Bhatti, M. S., 1987, "Laminar Convective Heat Transfer in Ducts," in *Handbook of Single-Phase Heat Convective Heat Transfer,* S. Kakac, R. K. Shah, and W. Aung, eds., Wiley, New York.

Weisberg, A., Bau, H. H., and Zemel, J., 1992, "Analysis of Microchannels for Integrated Cooling," *Int. J. Heat Mass Transfer,* Vol. 35, pp. 2465–2474.

Yin, X., and Bau, H. H., 1993, "Axial Conduction Effects on the Performance of Micro Heat Exchangers," ASME Paper No. 93-WA/HT-5.

Yin, X., 1995, "Micro Heat Exchangers," Ph.D. Thesis, University of Pennsylvania, Philadelphia.

Yin, X., and Bau, H. H., 1995, "Uniform Channel Microheat Exchangers," *Proceedings of the Symposium on Thermal Science and Engineering in Honor of Chancellor Chang-Lin Tien,* pp. 171–177.

Heat Transfer and Fluid Mechanics Measurements for the Endwall Boundary Layer Downstream of a Streamlined Strut

D. A. Tyszka[1] and D. E. Wroblewski[2,3]

Introduction

Past studies involving simplified strut–wall intersections fall into two categories: studies of "bluff-body" strut geometries and studies with streamlined struts. Past studies with bluff-body strut shapes (i.e., circular cylinders, tapered cylinders, prismatic bodies, etc.) have addressed endwall-boundary-layer fluid mechanics (Baker, 1979; Eibeck, 1990; Eibeck and Barland, 1993), endwall heat transfer (Fisher and Eibeck, 1990), or both fluid mechanics and heat transfer (Wroblewski and Eibeck, 1992; Pauley, 1993). Past studies involving streamlined strut shapes (i.e., NACA airfoils and airfoil-like bodies) have addressed only fluid mechanics without coverage of heat transfer

[1] Engineer, General Electric Aircraft Engines, Lynn, MA 01910.

[2] Assistant Professor, Dept. of Aerospace and Mechanical Engineering, Boston University, Boston, MA 02215.

[3] Mem. ASME.

Contributed by the Heat Transfer Division and presented at the International Mechanical Engineering Congress and Exposition, Chicago, Illinois, November 6–11, 1994. Manuscript received February 1995; revision received December 1995. Keywords: Forced Convection, Turbulence. Associate Technical Editor: T. W. Simon.

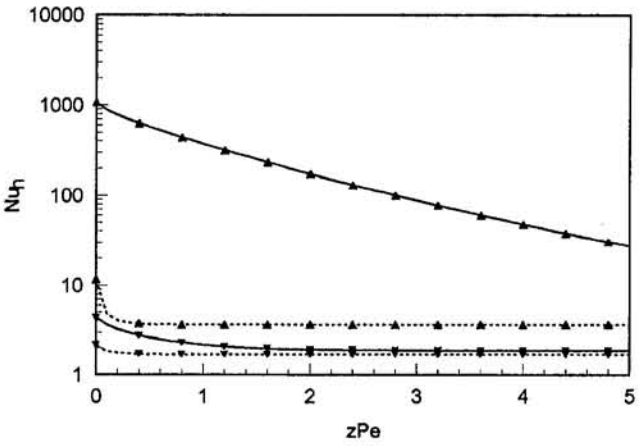

Fig. 3 The Nusselt number at the outer surface (Nu_h) is depicted as a function of zPe for pipe Poiseuille flow. $h = 2$, Pe = 5, $k_s/k_f = 243$ (upright triangles), and $k_s/k_f = 1$ (inverted triangles). Case I. The solid and dashed lines correspond, respectively, to cases when axial conduction is accounted for and cases when it is neglected.

temperatures in the fluid. In the case of $k_s/k_f = 243$, the solid's temperature is almost isothermal due to the solid's high thermal conductivity. Because of this conductivity, the solid offers less thermal resistance to heat losses from the fluid to the ambient, as reflected by the lower temperatures in the case of $k_s/k_f = 243$ than in the case of $k_s/k_f = 1$. A comparison of the solid and dashed lines indicates that at $z\text{Pe} = 1$, axial conduction plays a significant role, increasing the centerline temperature by more than 30 percent above the case without axial conduction ($h = 1.2$, $k_s/k_f = 243$).

Figure 2 depicts the centerline temperature $\theta(0, z)$ as a function of the axial coordinate $z\text{Pe}$ for Pe = 5, $h = 1.2$, $h = 2$, $k_s/k_f = 1$, and $k_s/k_f = 243$. The temperature decays most slowly (rapidly) for the case of $k_s/k_f = 1$, $h = 2$ ($k_s/k_f = 243$, $h = 1.2$) since this case offers the largest (smallest) thermal resistance between the fluid and the ambient. The effects of axial conduction diminish in importance as $z\text{Pe}$ increases.

Figure 3 depicts the Nusselt number at the outer surface, $Nu_h(z)$, as a function of the axial coordinate, $z\text{Pe}$, for Pe = 5, $h = 2$, and $k_s/k_f = 1$ (inverted triangles) and 243 (triangles). As z increases, the Nu numbers approach the asymptotic values we list in Table 2. When axial conduction is accounted for, the thermal development length is longer than when axial conduction is neglected. This is consistent with the eigenvalues of the generalized problem (with axial conduction) being smaller than the corresponding eigenvalues of the classical problem.

4 Conclusions

In this paper, we studied the generalized conjugate Graetz problem (with axial conduction). As expected, axial conduction plays an important role at the entrance region. As the distance from the entrance increases, the role of axial conduction diminishes. In the case of uniform temperature wall conditions, the asymptotic (large $z\text{Pe}$) Nusselt numbers accounting for axial conduction are consistently larger than those obtained neglecting axial conduction. The omission of axial conduction in the uniform temperature and heat flux cases leads, respectively, to under and overestimation of the temperature field in the entrance's vicinity. Omission of axial conduction also leads to an underestimation of the development length.

The analytic solutions produced in this paper are useful for obtaining fully developed Nusselt numbers and for verifying computer codes. For the latter purpose, it would be convenient to use initial conditions that are proportional to the first eigenfunction or a combination of a few eigenfunctions. When doing so, one obtains an exact, closed-form solution for the generalized Graetz problem.

Acknowledgments

The research reported in this paper has been supported, in part, by the National Science Foundation through grant No. CTS 90-12904.

References

Birkhoff, G., and Rota, G., 1978, *Ordinary Differential Equations,* Wiley, New York.

Graetz, L., 1885, "Uber die Warmeleitungsfähigkeit von Flussigkeiten (On the Thermal Conductivity of Liquids)," *Ann. Phys. Chem.,* Vol. 25, pp. 337–357.

Guedes, R. O. C., and Özişik, M. N., 1992, "Conjugated Turbulent Heat Transfer With Axial Conduction in Wall and Convection Boundary Conditions in a Parallel-Plate Channel," *Int. J. Heat and Fluid Flow,* Vol. 13, pp. 322–328.

Mori, S., Sakakibara, M., and Tanimoto, A., 1974, "Steady Heat Transfer to Laminar Flow in a Circular Tube With Conduction in the Tube Wall," *Heat Transfer—Jpn. Res.,* Vol. 3(2), pp. 37–46.

Mori, S., Shinke, T., Sakakibara, M., and Tanimoto, A., 1976, "Steady Heat Transfer to Laminar Flow Between Parallel Plates With Conduction in the Wall," *Heat Transfer—Jpn. Res.,* Vol. 5(4), pp. 17–25.

Shah, R. K., and London, A. L., 1978, *Laminar Flow Forced Convection in Ducts,* Academic Press, New York.

Shah, R. K., and Bhatti, M. S., 1987, "Laminar Convective Heat Transfer in Ducts," in *Handbook of Single-Phase Heat Convective Heat Transfer,* S. Kakac, R. K. Shah, and W. Aung, eds., Wiley, New York.

Weisberg, A., Bau, H. H., and Zemel, J., 1992, "Analysis of Microchannels for Integrated Cooling," *Int. J. Heat Mass Transfer,* Vol. 35, pp. 2465–2474.

Yin, X., and Bau, H. H., 1993, "Axial Conduction Effects on the Performance of Micro Heat Exchangers," ASME Paper No. 93-WA/HT-5.

Yin, X., 1995, "Micro Heat Exchangers," Ph.D. Thesis, University of Pennsylvania, Philadelphia.

Yin, X., and Bau, H. H., 1995, "Uniform Channel Microheat Exchangers," *Proceedings of the Symposium on Thermal Science and Engineering in Honor of Chancellor Chang-Lin Tien,* pp. 171–177.

Heat Transfer and Fluid Mechanics Measurements for the Endwall Boundary Layer Downstream of a Streamlined Strut

D. A. Tyszka[1] and D. E. Wroblewski[2,3]

Introduction

Past studies involving simplified strut–wall intersections fall into two categories: studies of "bluff-body" strut geometries and studies with streamlined struts. Past studies with bluff-body strut shapes (i.e., circular cylinders, tapered cylinders, prismatic bodies, etc.) have addressed endwall-boundary-layer fluid mechanics (Baker, 1979; Eibeck, 1990; Eibeck and Barland, 1993), endwall heat transfer (Fisher and Eibeck, 1990), or both fluid mechanics and heat transfer (Wroblewski and Eibeck, 1992; Pauley, 1993). Past studies involving streamlined strut shapes (i.e., NACA airfoils and airfoil-like bodies) have addressed only fluid mechanics without coverage of heat transfer

[1] Engineer, General Electric Aircraft Engines, Lynn, MA 01910.

[2] Assistant Professor, Dept. of Aerospace and Mechanical Engineering, Boston University, Boston, MA 02215.

[3] Mem. ASME.

Contributed by the Heat Transfer Division and presented at the International Mechanical Engineering Congress and Exposition, Chicago, Illinois, November 6–11, 1994. Manuscript received February 1995; revision received December 1995. Keywords: Forced Convection, Turbulence. Associate Technical Editor: T. W. Simon.

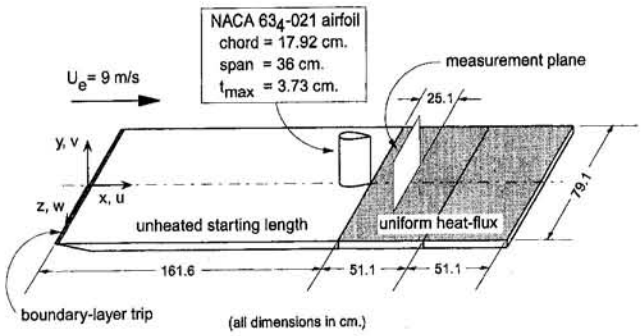

Fig. 1 Experimental setup

(Mehta, 1984; Rood, 1984; Merati et al., 1988). To the authors' knowledge, the current study is the first investigation of its kind to address both heat transfer and fluid mechanics for the endwall boundary layer downstream of a streamlined strut.

Two flow effects typically dominate near-wall flows downstream of strut–wall intersections: streamwise vorticity and the turbulent wake. Researchers in this field currently disagree on the relative importance of these two effects to endwall heat transfer. By investigating a strut geometry for which wake effects were minimized, but streamwise vorticity was still present, the current study attempted to address the question of which effect is more important to endwall heat transfer.

Experimental Method

The current study was conducted in the Boston University boundary layer wind tunnel using the experimental setup shown in Fig. 1. The test setup consisted of a flat-plate unheated starting length followed by a region of uniform heat flux (produced by a pair of electrical resistance heaters). A NACA 63$_4$-021 airfoil was mounted perpendicular to the plate and at zero incidence to the flow. The airfoil's trailing edge coincided with the start of heating while its plane of symmetry coincided with the plane $z = 0$.

For all tests in the current study, the wind tunnel free-stream velocity, U_e, was approximately 9 m/s, and Re_{chord} (Reynolds number based on airfoil chord and U_e) was approximately 10^5. For these flow conditions, r_0/δ (the ratio of strut leading-edge radius to flat-plate velocity-boundary-layer thickness at airfoil leading edge) was approximately 0.19. Per Rood (1984) and Mehta (1984), this condition should have produced a relatively weak, diffuse horseshoe vortex. Also, due to the streamlined shape of the airfoil, the wake region should have been relatively weak.

Five-hole directional pressure probe velocity-boundary-layer measurements, cold-wire anemometer thermal-boundary measurements, and endwall-heat-transfer measurements were taken across y–z planes located approximately 1.4 and 4.3 chord lengths downstream of the airfoil trailing edge. Due to space limitations, only the 1.4 chord results are presented in this article. Results for the 4.3 chord cases, as well as detailed descriptions of instrumentation, data acquisition systems, and data reduction methods used during this study are contained in the work by Tyszka and Wroblewski (1994). Estimated 95 percent confidence experimental uncertainties for the results presented in this article were calculated using the method described by Moffat (1988) and are reported in the captions of the appropriate figures.

Results and Discussion

Figures 2 and 3 present measurements of the velocity boundary layer. The vector plot of mean secondary velocity, $(v^2 + w^2)^{1/2}$, shown in Fig. 2 reveals the presence of *weak* organized vorticity whose sense and location are consistent with those of a horseshoe vortex leg located *some distance above the wall.* Contours of normalized mean streamwise velocity, u/U_e, shown in Fig. 3, reveal the narrow wake region, which appears as a symmetrically shaped local deficit in streamwise velocity centered at $z/t_{max} = 0$ and spanning a region approximately equal to the airfoil maximum thickness, t_{max}. Effects of the weak horseshoe vortex noted in Fig. 2 are visible in Fig. 3 near $z/t_{max} = \pm 0.5$ and $z/t_{max} = 2$, where normalized streamwise velocity contours are locally distorted. Near $z/t_{max} = \pm 0.5$, several contours in Fig. 3 dip toward the wall slightly. This local velocity-boundary-layer thinning is probably a result of the weak intervortex downflow visible in Fig. 2 near $z/t_{max} = 0$. Near $z/t_{max} = 2$, several contours in Fig. 3 move away from the wall slightly, locally thickening the velocity boundary layer. We note that $z/t_{max} = 2$ corresponds approximately to the location of a weak vortex-induced upflow in Fig. 2.

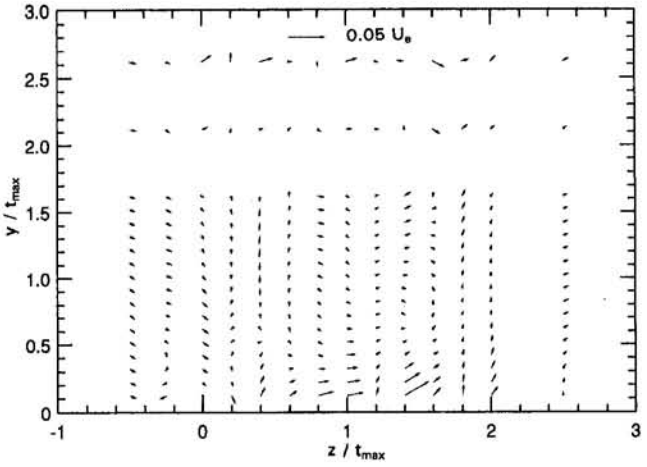

Fig. 2 Mean secondary velocity vectors, $vj + wk$ across 1.5 chord length downstream measurement plane. $Re_{chord} = 9.82 \times 10^4$. Uncertainty in v, $w = \pm 8.9$ percent U_e.

Figures 4 and 5 present measurements of the thermal boundary layer. From Fig. 4, which shows contours of normalized *mean* temperature, $(T_w - T)/(T_w - T_e)$ (note: T_w is spanwise average wall temperature, T is local mean air temperature, and T_e is free-stream air temperature), it is apparent that the thermal boundary layer is also distorted by the presence of the airfoil. The thermal boundary layer is locally thinned over $-1 < z/t_{max} < +1$ (which roughly coincides with the wake and intervortex downflow regions noted in the velocity-boundary-layer results),

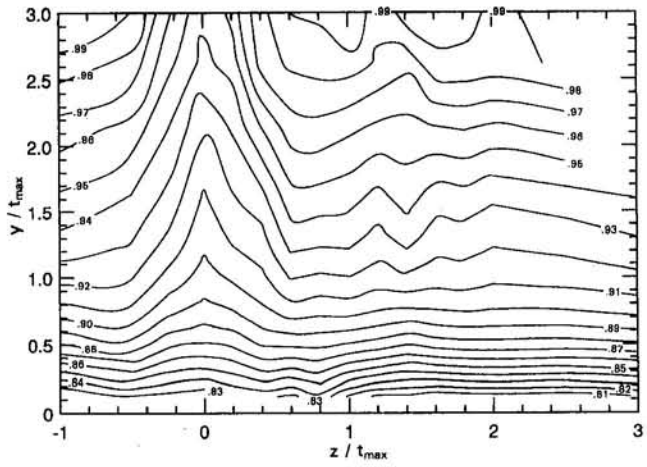

Fig. 3 Contours of normalized mean streamwise velocity, u/U_e across 1.5 chord length downstream measurement plane. $Re_{chord} = 9.82 \times 10^4$. Uncertainty in $u/U_e = \pm 0.059$.

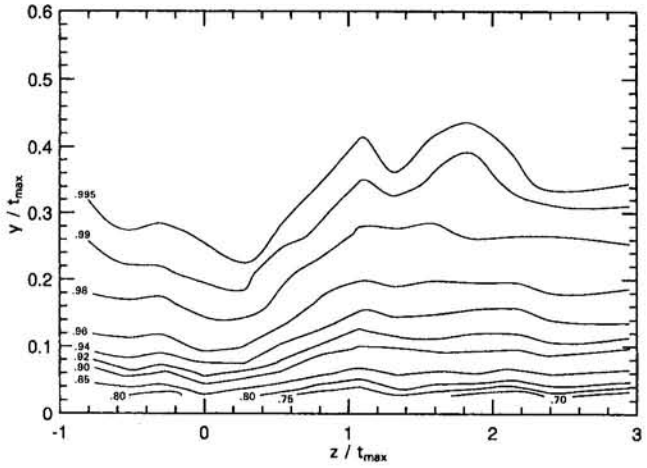

Fig. 4 Contours of normalized mean temperature, $(T_w - T)/(T_w - T_e)$ across 1.4 chord length downstream measurement plane. $Re_{chord} = 1.11 \times 10^5$.

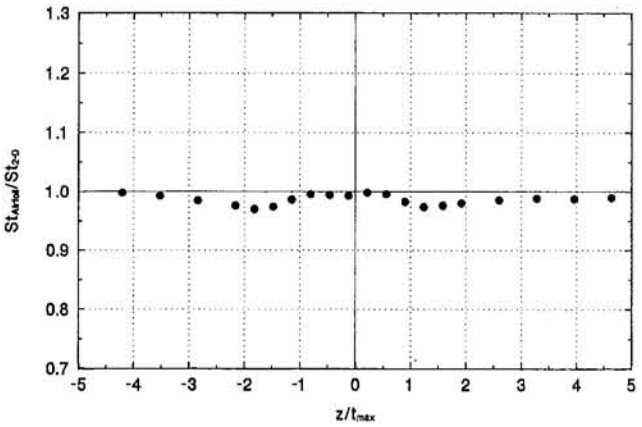

Fig. 6 Transverse variation of wall Stanton number ratio, $St_{Airfoil}/St_{2\text{-}D}$ across 1.4 chord length downstream measurement plane. $Re_{chord} = 1.11 \times 10^5$. Uncertainty in $St_{Airfoil}/St_{2\text{-}D} = \pm 0.076$.

and locally thickened over the region $+1 < z/t_{max} < +2.4$ (which roughly lines up with the horseshoe vortex-induced upflow visible in Fig. 2).

It should be emphasized that distortions of the velocity and thermal boundary layers noted in Figs. 3 and 4 are only present *far above the wall.* The *near-wall* structures of these boundary layers are not significantly different from those of simple flat-plate boundary layers. This finding has particular significance in interpretations of endwall-heat-transfer results.

Figure 5 shows localized distortions of normalized *fluctuating* temperature contours, $\theta'/(T_w - T_e)$, where θ' is the root-mean-square of the local air temperature fluctuations. If enhanced turbulent mixing in the near-wall wake was significant for the flow of interest, there should be a peak in the fluctuating temperature contours over $-0.5 < z/t_{max} < +0.5$. Since such a peak does not occur (in fact, there is a local trough in this region), wake-related effects are likely unimportant for the subject near-wall flow.

Figure 6 gives endwall-heat-transfer results as ratios of local wall Stanton numbers for cases with and without the airfoil. From Fig. 6, it is apparent that endwall heat transfer with the NACA 63_4-021 airfoil in place differs by no more than 3 percent from that of the corresponding flat-plate-only case. This result is somewhat surprising, since *significant* localized downstream endwall-heat-transfer enhancement has been observed by others for *bluff body* struts. The lack of significant enhancement in the current study is explained by two observations from the velocity and thermal boundary-layer results. First, boundary-layer distortions caused by the horseshoe vortex and wake only occur *far above the wall.* Second, the wake is weak and does not seem to influence turbulence levels significantly *near the wall.*

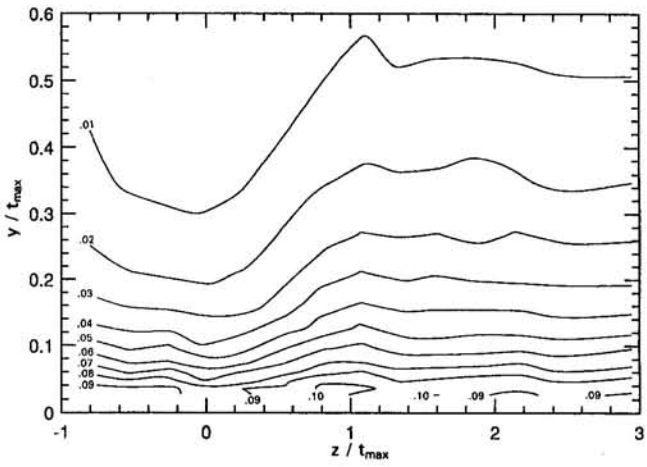

Fig. 5 Contours of normalized fluctuating temperature, $\theta'/(T_w - T_e)$ across 1.4 chord length downstream measurement plane. $Re_{chord} = 1.11 \times 10^5$.

Summary/Conclusions

Endwall heat transfer downstream of a simple strut–wall intersection featuring a NACA 63_4-021 airfoil is not significantly different from that of the corresponding flat-plate-only case. This lack of significant endwall-heat-transfer enhancement occurs in the presence of a weak horseshoe vortex and a weak wake, which both cause localized distortions of the velocity and thermal boundary layers in the *outer regions* of these layers, but *not near the wall.*

When considered with results from previous studies by others of bluff-body struts (Pauley, 1993; Wroblewski and Eibeck, 1992), the results of the current study suggest the existence of a previously undocumented trend relating absolute level of downstream endwall-heat-transfer augmentation to degree of strut streamlining. Blunt strut shapes (such as circular cylinders) produce the greatest endwall-heat-transfer enhancement. Moderately streamlined struts (such as tapered cylinders) produce less enhancement. Highly streamlined struts (i.e., airfoils) produce almost no enhancement. *Peak enhancement levels seem to drop as strut streamlining increases.*

It should be noted that for the progression of increasingly streamlined strut shapes given above, streamwise vorticity in one form or another is always present (in various strengths), but the turbulent wake region is continually diminishing in strength and extent. Thus, the results of the current study (when considered with findings from previous research by others) seem to suggest that the wake region (*not* the horseshoe vortex or other streamwise vorticity) is likely the primary factor responsible for endwall-heat-transfer augmentation downstream of strut–wall intersections.

As a footnote to this last conclusion it should be mentioned that the relative importance of wake and streamwise vorticity effects to endwall heat transfer is likely dependent not only on strut shape, but also on strut size and free-stream flow conditions. In fact, it is fully reasonable to expect that for any given strut shape, there may exist combinations of flow conditions and strut size for which the wake is *not* the dominant endwall heat transfer-controlling factor. Although exploration of this issue was beyond the scope of the present study, the authors nonetheless wish to point out that the conclusion stated in the preceding paragraph on the relative importance of wake versus

streamwise vorticity effects *may not* be universally applicable, but may instead only apply for certain strut sizes and flow regimes.

Acknowledgments

Sincere appreciation is expressed to Ms. Qi Xie for her contributions to this research, to the General Electric Company for its support of the first author during this research project, and to the National Science Foundation for its support of the second author under grant No. CTS-9211282.

References

Baker, C. J., 1979, "The Laminar Horseshoe Vortex," *J. Fluid Mech.*, Vol. 95, Pt. 2, pp. 347–368.

Eibeck, P. A., 1990, "An Experimental Study of the Flow Downstream of a Circular and Tapered Cylinder," ASME *Journal of Fluids Engineering*, Vol. 112, pp. 393–401.

Eibeck, P. A., and Barland, D. E., 1993, "Turbulent Mixing Behind Two-Dimensional and Finite Obstacles," *Turbulent Mixing*, ASME FED-Vol. 174, pp. 57–63.

Fisher, E. M., and Eibeck, P. A., 1990, "The Influence of a Horseshoe Vortex on Local Convective Heat Transfer," ASME JOURNAL OF HEAT TRANSFER, Vol. 112, pp. 329–335.

Mehta, R. D., 1984, "Effect of Wing Nose Shape on the Flow in a Wing/Body Junction," *Aeronautical Journal*, Vol. 88, No. 880, pp. 456–460.

Merati, P., McMahon, H. M., and Yoo, K. M., 1988, "Experimental Modeling of a Turbulent Flow in the Junction and Wake of an Appendage Flat Plate," presented at the AIAA/ASME/SIAM/APS 1st National Fluid Dynamics Congress, Cincinnati, OH, pp. 1255–1264.

Moffat, R. J., 1988, "Describing Uncertainty in Experimental Results," *Exp. Thermal Fluid Sci.*, Vol. 1, pp. 3–17.

Pauley, W. R., 1993, "The Fluid Mechanics and Heat Transfer Downstream of Struts Spanning a Low-Aspect-Ratio Channel," ASME Paper No. 93-HT-41.

Rood, E. P., 1984, "The Separate Spatial Extents of the Trailing Horseshoe Root Vortex Legs From a Wing and Plate Junction," Paper No. AIAA-84-1526.

Tyszka, D. A., and Wroblewski, D. E., 1994, "An Experimental Investigation of Heat Transfer and Fluid Mechanics in the Turbulent Endwall Junction Boundary Layer Downstream of a Truly Streamlined Body," *Fundamentals of Heat Transfer in Forced Convection*, ASME HTD-Vol. 285, pp. 25–32.

Wroblewski, D. E., and Eibeck, P. A., 1992, "Turbulent Heat Transport in a Boundary Layer Behind a Junction of a Streamlined Cylinder and a Wall," ASME JOURNAL OF HEAT TRANSFER, Vol. 114, pp. 840–849.

The LMTD Correction Factor for Single-Pass Crossflow Heat Exchangers With Both Fluids Unmixed

A. S. Tucker[1]

Introduction

The majority of undergraduate texts on heat transfer include a chapter on heat exchangers, almost always containing a section that explains the concept of the log mean temperature difference (LMTD) for simple parallel and counterflow heat exchangers, and the correction factor, F, which must be applied to the LMTD for other heat exchanger types.

Whenever that section of such a text includes a reproduction of the LMTD correction factor chart for single-pass crossflow heat exchangers with both fluids unmixed (see Fig. 1 and, for example, Holman (1992), Incropera and DeWitt (1990), Kreith and Bohn (1986), and White (1988)), it is highly probable that the text authors have unwittingly extended the propagation of small but discernible errors directly traceable to a paper by one of the most recognizable names in the early heat transfer literature, Wilhelm Nusselt. To illustrate by typical example the extent of the error: For such a crossflow heat exchanger with a capacity ratio of unity (i.e., the dimensionless temperature ratio $R = \Delta t_{hot}/\Delta t_{cold} = 1$) in which the change in the cold fluid temperature relative to the difference between the inlet temperatures of the two fluids is $P = \Delta t_{cold}/\Delta t_{in} = 0.6$, the error in the LMTD correction factor, F, read off the chart is 3 percent. At the extreme combination of low values of R and values for P approaching unity, the error is considerably greater: At $R = 0.2$ and $P = 0.975$ the error exceeds 10 percent.

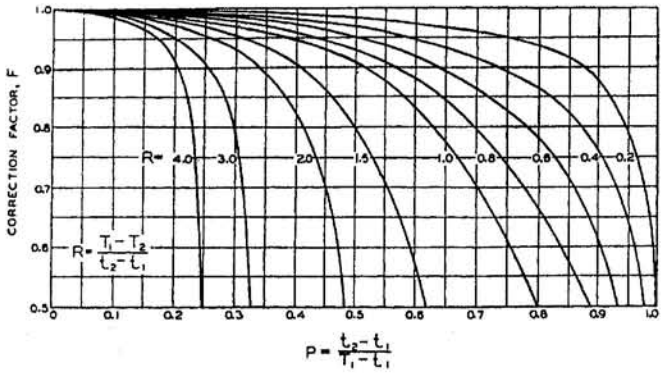

Fig. 1 The original LMTD correction factor chart for a single-pass crossflow heat exchanger in which both fluids are unmixed (from Bowman et al., 1940)

Background

The existence of these errors was discovered in the course of preparing a partial set of LMTD correction factor charts and effectiveness-NTU charts for inclusion in a student handout. Rather than copying the frequently reproduced figures, it was decided to generate them directly in a spreadsheet by making use of the well-established formulae readily available in the literature. This is a quite straightforward task for all but the case of a crossflow heat exchanger in which both fluids are unmixed. The two-dimensional temperature field for both fluids in this particular exchanger configuration requires a more complex analysis, which has been attempted by a number of authors. Notable among these, Nusselt published an analytical solution to the problem in 1911, the solution being in the form of a doubly infinite series, which was acknowledged to exhibit very slow convergence. Almost two decades later (1930), he produced an alternative solution, again in the form of an infinite series but more rapidly convergent than his earlier solution. This later paper of Nusselt included tabulated numerical values, derived from his series solution, which were utilized by Smith (1934) and have been reproduced in their original three significant figure form in at least one reasonably modern heat transfer text (Bayley et al., 1972).

The landmark paper that originated the most commonly used form of LMTD correction charts was that of Bowman et al. (1940) and, for the case of the crossflow heat exchanger with both fluids unmixed, these authors drew on the work of both Nusselt (1930) and Smith. It is this particular chart of Bowman et al. that most heat transfer texts present and acknowledge.

Subsequent to the LMTD analysis approach, the extensive work of Kays and London (1958) was published, presenting the often-used effectiveness-NTU (ϵ-NTU) charts, which overcame some shortcomings in the LMTD analysis procedure. To con-

[1] Department of Mechanical Engineering, University of Canterbury, Christchurch, New Zealand.

Contributed by the Heat Transfer Division of THE AMERICAN SOCIETY OF MECHANICAL ENGINEERS. Manuscript received by the Heat Transfer Division June 1995; revision received October 1995. Keywords: Heat Exchangers, Numerical Methods. Associate Technical Editor: T. J. Rabas.

streamwise vorticity effects *may not* be universally applicable, but may instead only apply for certain strut sizes and flow regimes.

Acknowledgments

Sincere appreciation is expressed to Ms. Qi Xie for her contributions to this research, to the General Electric Company for its support of the first author during this research project, and to the National Science Foundation for its support of the second author under grant No. CTS-9211282.

References

Baker, C. J., 1979, "The Laminar Horseshoe Vortex," *J. Fluid Mech.*, Vol. 95, Pt. 2, pp. 347–368.

Eibeck, P. A., 1990, "An Experimental Study of the Flow Downstream of a Circular and Tapered Cylinder," ASME *Journal of Fluids Engineering*, Vol. 112, pp. 393–401.

Eibeck, P. A., and Barland, D. E., 1993, "Turbulent Mixing Behind Two-Dimensional and Finite Obstacles," *Turbulent Mixing*, ASME FED-Vol. 174, pp. 57–63.

Fisher, E. M., and Eibeck, P. A., 1990, "The Influence of a Horseshoe Vortex on Local Convective Heat Transfer," ASME JOURNAL OF HEAT TRANSFER, Vol. 112, pp. 329–335.

Mehta, R. D., 1984, "Effect of Wing Nose Shape on the Flow in a Wing/Body Junction," *Aeronautical Journal*, Vol. 88, No. 880, pp. 456–460.

Merati, P., McMahon, H. M., and Yoo, K. M., 1988, "Experimental Modeling of a Turbulent Flow in the Junction and Wake of an Appendage Flat Plate," presented at the AIAA/ASME/SIAM/APS 1st National Fluid Dynamics Congress, Cincinnati, OH, pp. 1255–1264.

Moffat, R. J., 1988, "Describing Uncertainty in Experimental Results," *Exp. Thermal Fluid Sci.*, Vol. 1, pp. 3–17.

Pauley, W. R., 1993, "The Fluid Mechanics and Heat Transfer Downstream of Struts Spanning a Low-Aspect-Ratio Channel," ASME Paper No. 93-HT-41.

Rood, E. P., 1984, "The Separate Spatial Extents of the Trailing Horseshoe Root Vortex Legs From a Wing and Plate Junction," Paper No. AIAA-84-1526.

Tyszka, D. A., and Wroblewski, D. E., 1994, "An Experimental Investigation of Heat Transfer and Fluid Mechanics in the Turbulent Endwall Junction Boundary Layer Downstream of a Truly Streamlined Body," *Fundamentals of Heat Transfer in Forced Convection*, ASME HTD-Vol. 285, pp. 25–32.

Wroblewski, D. E., and Eibeck, P. A., 1992, "Turbulent Heat Transport in a Boundary Layer Behind a Junction of a Streamlined Cylinder and a Wall," ASME JOURNAL OF HEAT TRANSFER, Vol. 114, pp. 840–849.

The LMTD Correction Factor for Single-Pass Crossflow Heat Exchangers With Both Fluids Unmixed

A. S. Tucker[1]

Introduction

The majority of undergraduate texts on heat transfer include a chapter on heat exchangers, almost always containing a section that explains the concept of the log mean temperature difference (LMTD) for simple parallel and counterflow heat exchangers, and the correction factor, F, which must be applied to the LMTD for other heat exchanger types.

Whenever that section of such a text includes a reproduction of the LMTD correction factor chart for single-pass crossflow heat exchangers with both fluids unmixed (see Fig. 1 and, for example, Holman (1992), Incropera and DeWitt (1990), Kreith and Bohn (1986), and White (1988)), it is highly probable that the text authors have unwittingly extended the propagation of small but discernible errors directly traceable to a paper by one of the most recognizable names in the early heat transfer literature, Wilhelm Nusselt. To illustrate by typical example the extent of the error: For such a crossflow heat exchanger with a capacity ratio of unity (i.e., the dimensionless temperature ratio $R = \Delta t_{hot}/\Delta t_{cold} = 1$) in which the change in the cold fluid temperature relative to the difference between the inlet temperatures of the two fluids is $P = \Delta t_{cold}/\Delta t_{in} = 0.6$, the error in the LMTD correction factor, F, read off the chart is 3 percent. At the extreme combination of low values of R and values for P approaching unity, the error is considerably greater: At $R = 0.2$ and $P = 0.975$ the error exceeds 10 percent.

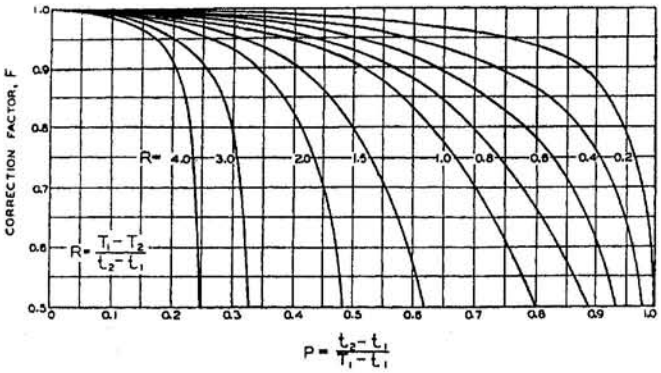

Fig. 1 The original LMTD correction factor chart for a single-pass crossflow heat exchanger in which both fluids are unmixed (from Bowman et al., 1940)

Background

The existence of these errors was discovered in the course of preparing a partial set of LMTD correction factor charts and effectiveness-NTU charts for inclusion in a student handout. Rather than copying the frequently reproduced figures, it was decided to generate them directly in a spreadsheet by making use of the well-established formulae readily available in the literature. This is a quite straightforward task for all but the case of a crossflow heat exchanger in which both fluids are unmixed. The two-dimensional temperature field for both fluids in this particular exchanger configuration requires a more complex analysis, which has been attempted by a number of authors. Notable among these, Nusselt published an analytical solution to the problem in 1911, the solution being in the form of a doubly infinite series, which was acknowledged to exhibit very slow convergence. Almost two decades later (1930), he produced an alternative solution, again in the form of an infinite series but more rapidly convergent than his earlier solution. This later paper of Nusselt included tabulated numerical values, derived from his series solution, which were utilized by Smith (1934) and have been reproduced in their original three significant figure form in at least one reasonably modern heat transfer text (Bayley et al., 1972).

The landmark paper that originated the most commonly used form of LMTD correction charts was that of Bowman et al. (1940) and, for the case of the crossflow heat exchanger with both fluids unmixed, these authors drew on the work of both Nusselt (1930) and Smith. It is this particular chart of Bowman et al. that most heat transfer texts present and acknowledge.

Subsequent to the LMTD analysis approach, the extensive work of Kays and London (1958) was published, presenting the often-used effectiveness-NTU (ϵ-NTU) charts, which overcame some shortcomings in the LMTD analysis procedure. To con-

[1] Department of Mechanical Engineering, University of Canterbury, Christchurch, New Zealand.

Contributed by the Heat Transfer Division of THE AMERICAN SOCIETY OF MECHANICAL ENGINEERS. Manuscript received by the Heat Transfer Division June 1995; revision received October 1995. Keywords: Heat Exchangers, Numerical Methods. Associate Technical Editor: T. J. Rabas.

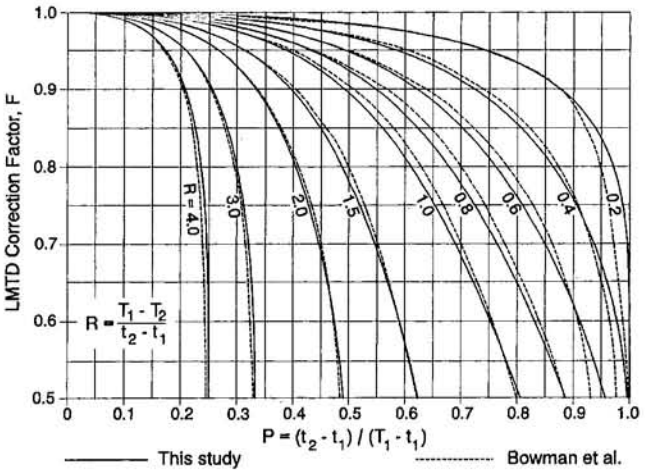

Fig. 2 A comparison between the correction factor curves of the present study and those of Fig. 1

struct the ϵ-NTU chart for the crossflow heat exchanger with both fluids unmixed also requires use of an analytical expression for the mean outlet temperatures of the fluids, and Kays and London used an even more rapidly convergent infinite series solution, this one being due to Mason (1955). This solution was also the one that had been utilized by Stevens et al. (1957) but, like Kays and London, their charts of heat exchanger performance were in terms of effectiveness rather than LMTD correction.

Roetzel and Nicole (1975) recognized the potential usefulness of explicit representations of LMTD correction factors in developing computerized packages for heat exchanger design. In obtaining suitable values for the coefficients to be inserted in their equation for the case of crossflow heat exchangers, they made use of the doubly infinite series solution of Nusselt (1930). As will be seen, it is significant that it was Nusselt's solution series that they used, rather than the subsequent tabulated numerical values that Nusselt presented in his paper.

Methodology

Because Mason's paper was immediately accessible, his solution was the one initially chosen for the present exercise of generating the LMTD correction chart from first principles. Thus an iterative solution procedure was set up within a spreadsheet to produce the desired chart, in the confident expectation that it would be indistinguishable from that published by Bowman et al.

Very briefly, the iterative scheme to generate the curve for a particular value of R proceeded as follows: For a particular value of P at which F was to be evaluated, a trial value for a (defined as the number of transfer units for the hot fluid) was assumed, and Mason's series summed to include sufficient terms that there was no change in the fifth significant figure. From that summed series, P was calculated and compared with the value for P at which the value for F was being sought. By simply iterating on a in increments that were suitably reduced as the final solution was approached, the solution was completed when the calculated value for P matched the desired value within an acceptable tolerance (0.00001, with P being in the range from 0 to 1). With each point on each curve being calculated independently of its neighboring points, there was no possibility of accumulating errors as P was incremented.

The end result of doing this for the same values of R as are plotted in Fig. 1 is shown in Fig. 2 (in which the curves from Fig. 1 have been superimposed as accurately as physically reading values off a chart allows). Clearly there are areas of the chart where there are small but significant discrepancies that were found to be insensitive to both retaining even more terms in the series (typically six were more than sufficient in the areas of noticeable discrepancy) and the error tolerance applied on P in the iteration procedure.

Discussion

Possible explanations for the discrepancies are: Nusselt's 1930 series solution is in error; Nusselt's numerical values derived from his series are in error; Bowman et al. made an error in implementing Nusselt's numerical values; Mason's solution is in error (which would, if true, result in consequential errors in Kays and London's ϵ-NTU chart); or the numerical iterative procedure being utilized was erroneous.

The third of these possible explanations can be quickly eliminated by comparing Nusselt's numerical results with the curve of Bowman et al. for the case of R being unity (implying a capacity ratio of unity): The agreement is very good, verifying that they had correctly interpreted his tabulated data. When Nusselt's series solution (rather than his table of numerical results) was subsequently encoded and summed within a spreadsheet by a procedure very similar to that described above, the resultant curves were indistinguishable from those obtained via the Mason solution and, as independent verification of the numerical procedure, matched extremely well with selected points from an ϵ-Ntu analysis.

For example, for the case $R = 1.0$ and $P = 0.6$, the iteration procedure outlined above (using either the Mason or the Nusselt series) results in a solution $F = 0.8113$ at which the number of transfer units Ntu = 1.8486 and the effectiveness $\epsilon = 0.6000$ (as it should if $P = 0.6$ at a capacity ratio of unity, as is implied by $R = 1.0$).

This effectiveness value also corresponds very well with the prediction of 0.6003 obtained from the empirical relationship

$$\epsilon \approx 1 - \exp\{[\exp(-\mathrm{NTU}^{0.78} r) - 1] \cdot \mathrm{NTU}^{0.22}/r\}$$

(where r represents the capacity ratio $C_{\min}/C_{\max} = R = 1$ in this particular case) which usually is accepted as an approximate representation of the ϵ-NTU relationship for an exchanger of this type (see, for example, Holman, 1992).

Furthermore, when $R = 1$ and $P = 0.6$ are substituted into the general approximate explicit equation for mean temperature difference developed by Roetzel and Nicole—based on Nusselt's solution but *not* on his tabulated values—the resulting value of $F = 0.8117$ is in almost exact agreement with the solution value of 0.8113 obtained here.

On the other hand, for the same values of $R = 1.0$ and $P = 0.6$, Nusselt's numerical value for F (reflected in Fig. 1) is 0.835 which, for the same Ntu value of 1.8486, corresponds to an incompatible value of 0.617 for the effectiveness.

The explanation for the discrepancies is therefore clear: The error lies in the numerical values presented by Nusselt and embraced by Bowman et al., not in the series solution he derived. Close examination of Nusselt's paper reveals three principal points at which the errors arose, and these are attributable to the severely limited calculator resources available in 1930.

First, it appears from the numbers presented that Nusselt retained only five terms in evaluating his series and, while this is of adequate accuracy over most of the domain of interest, the higher order terms do become significant under particular combinations of his initial input parameters. Second, for three of his five-term series summation calculations (out of a total of 20) there were not-insignificant outright numerical errors.

Finally, and probably most importantly, the subsequent calculation sequence adopted by Nusselt had the potential to introduce significant interpolation errors. From the original table of only 20 evaluated data points (many of which were inaccurate for either or both of the first two reasons above), Nusselt developed a three-dimensional surface over a square coordinate base,

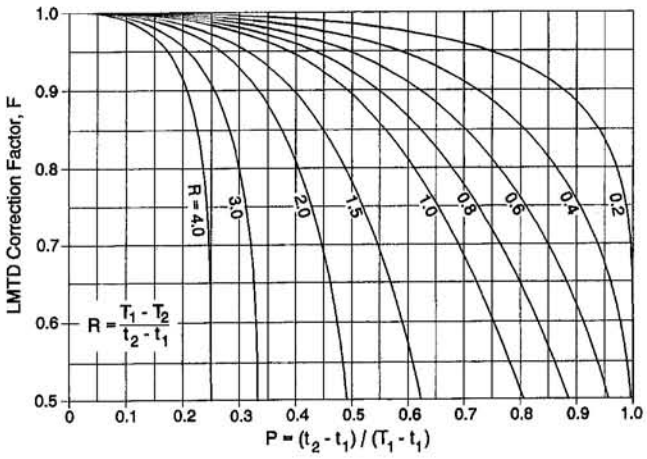

Fig. 3 The correct form of the LMTD correction factor chart for a single-pass crossflow heat exchanger in which both fluids are unmixed. (This figure repeats the corrected curves generated in this study and included in Fig. 2, with the erroneous curves of Bowman et al. removed so as to provide an uncluttered chart for other users.)

and this surface had pronounced curvature at two of its edges. By interpolating over this surface, he generated two subsequent tables each containing 100 points, the vast majority of which did not coincide with any of the comparatively sparse data points from which the surface had been constructed.

Consequently, Nusselt's final tables of values presented to three significant figures imply a calculation accuracy that is, in fact, quite unjustified. Indeed, were Nusselt to submit his paper to ASME JOURNAL OF HEAT TRANSFER under its current policy of requiring that papers containing numerical solutions have an assessment of numerical errors, it is probable that it would not be considered for review!

Conclusion

It must be acknowledged that in current heat exchanger design practice, rarely would use be made of LMTD correction factor charts such as the one discussed here. Normally it would be expected that LMTD correction factors, if used, would be represented by the appropriate equations incorporated into computer-based design packages. Alternatively, the need for an LMTD correction factor can be bypassed through the use of the ϵ-NTU method of analysis.

Nevertheless, and although generally they are not major in their magnitude, the errors revealed unexpectedly as a result of this work do illustrate that even a respected name in the heat transfer literature was not totally infallible, and that errors can easily propagate through the literature for decades; it is hoped that now there is no need for those errors to propagate further, particularly in undergraduate heat transfer texts where the LMTD correction factor charts are commonly presented. For this purpose, Fig. 3 has been prepared.

Finally, out of fairness to Nusselt and out of respect for his standing, it must be said that current computers enable us easily to undertake tasks that would not have been even contemplated a few decades ago. Had Nusselt attempted his task with access to the facilities now available to even the most humble of researchers, his published results almost certainly would have been accurate and unchallengeable.

References

Bayley, F. J., Owen, J. M., and Turner, A. B., 1972, *Heat Transfer,* Nelson, London.

Bowman, R. A., Mueller, A. C., and Nagle, W. M., 1940, "Mean Temperature Difference in Design," *Trans. ASME,* Vol. 62, pp. 283–294.

Holman, J. P., 1992, *Heat Transfer,* 7th ed., McGraw-Hill, New York.

Incropera, F. P., and DeWitt, D. P., 1990, *Fundamentals of Heat and Mass Transfer,* 3rd ed., Wiley, New York.

Kays, W. M., and London, A. L., 1958, *Compact Heat Exchangers,* McGraw-Hill, New York.

Kreith, F., and Bohn, M. S., 1986, *Principles of Heat Transfer,* 4th ed., Harper and Row, New York.

Mason, J. L., 1955, "Heat Transfer in Crossflow," *Proc. 2nd U.S. National Congress of Applied Mechanics,* ASME, New York, pp. 801–803.

Nusselt, W., 1911, "Der Wärmeübergang im Kreutzstrom," *Zeitschrift des Vereines deutscher Ingenieur,* Vol. 55, pp. 2021–2024.

Nusselt, W., 1930, "Eine neue Formel für den Wärmedurchgang im Kreuzstrom," *Technische Mechanik und Thermodynamik,* Vol. 1, pp. 417–422.

Roetzel, W., and Nicole, F. J. L., 1975, "Mean Temperature Difference for Heat Exchanger Design—A General Approximate Explicit Equation," ASME JOURNAL OF HEAT TRANSFER, Vol. 97, pp. 5–8.

Smith, D. M., 1934, "Mean Temperature-Difference in Cross Flow," *Engineering,* Vol. 138, pp. 479–481, 606–607.

Stevens, R. A., Fernandez, J., and Woolf, J. R., 1957, "Mean-Temperature Difference in One, Two, and Three-Pass Crossflow Heat Exchangers," *Trans. ASME,* Vol. 79, pp. 287–297.

White, F. M., 1988, *Heat and Mass Transfer,* Addison-Wesley, Reading, MA.

Optimum Design of Radiating Rectangular Plate Fin Array Extending From a Plane Wall

C. K. Krishnaprakas[1]

Nomenclature

A_p = profile area of fin array, m^2
b = fin spacing, m
$dF_{d\mu 1-d\mu 2}$ = elemental view factor from $d\mu_1$ to $d\mu_2$
h = height of fin array, m
J = radiosity, W/m^2
K = thermal conductivity of fin material, W/mK
l = length of fin, m
N = number of grid points along fin length
N_c = conduction-radiation number = $Kt/l^2\sigma T_b^3$
N_p = dimensionless profile area = A_p/w^2
N_w = dimensionless width = $\sigma T_b^3 w/K$
t = semithickness of fin, m
T = temperature of fin, K
T_b = temperature of base, K
w = width of fin = $b + 2t$, m
x = coordinate along the length of the fin
β = dimensionless radiosity = $J/\sigma T_b^4$
ϵ = emittance
θ = dimensionless temperture = T/T_b
μ = dimensionless coordinate length = x/l
σ = Stefan–Boltzmann constant = 5.67*E*-8 W/m^2K^4
ϕ = dimensionless rate of heat loss from fin and base

Introduction

Radiating fins are used in spacecraft and space vehicles for rejecting on-board waste heat to deep space. Since weight is at a premium, it is important to have minimum fin mass in these applications. Several investigators have analyzed the problem of minimization of fin mass in the past; however, there exist a

[1] Thermal Systems Group, ISRO Satellite Centre, Bangalore-560 017, India.

Contributed by the Heat Transfer Division of THE AMERICAN SOCIETY OF MECHANICAL ENGINEERS. Manuscript received by the Heat Transfer Division August 1994; revision received August 1995. Keywords: Numerical Methods, Radiation Interactions. Associate Technical Editor: M. F. Modest.

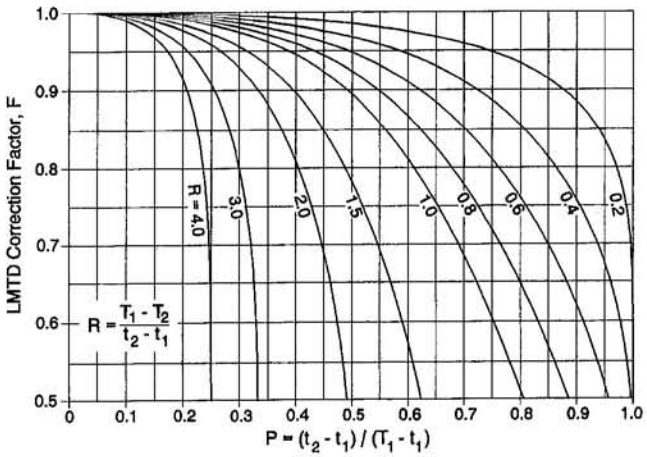

Fig. 3 The correct form of the LMTD correction factor chart for a single-pass crossflow heat exchanger in which both fluids are unmixed. (This figure repeats the corrected curves generated in this study and included in Fig. 2, with the erroneous curves of Bowman et al. removed so as to provide an uncluttered chart for other users.)

and this surface had pronounced curvature at two of its edges. By interpolating over this surface, he generated two subsequent tables each containing 100 points, the vast majority of which did not coincide with any of the comparatively sparse data points from which the surface had been constructed.

Consequently, Nusselt's final tables of values presented to three significant figures imply a calculation accuracy that is, in fact, quite unjustified. Indeed, were Nusselt to submit his paper to ASME JOURNAL OF HEAT TRANSFER under its current policy of requiring that papers containing numerical solutions have an assessment of numerical errors, it is probable that it would not be considered for review!

Conclusion

It must be acknowledged that in current heat exchanger design practice, rarely would use be made of LMTD correction factor charts such as the one discussed here. Normally it would be expected that LMTD correction factors, if used, would be represented by the appropriate equations incorporated into computer-based design packages. Alternatively, the need for an LMTD correction factor can be bypassed through the use of the ϵ-NTU method of analysis.

Nevertheless, and although generally they are not major in their magnitude, the errors revealed unexpectedly as a result of this work do illustrate that even a respected name in the heat transfer literature was not totally infallible, and that errors can easily propagate through the literature for decades; it is hoped that now there is no need for those errors to propagate further, particularly in undergraduate heat transfer texts where the LMTD correction factor charts are commonly presented. For this purpose, Fig. 3 has been prepared.

Finally, out of fairness to Nusselt and out of respect for his standing, it must be said that current computers enable us easily to undertake tasks that would not have been even contemplated a few decades ago. Had Nusselt attempted his task with access to the facilities now available to even the most humble of researchers, his published results almost certainly would have been accurate and unchallengeable.

References

Bayley, F. J., Owen, J. M., and Turner, A. B., 1972, *Heat Transfer,* Nelson, London.

Bowman, R. A., Mueller, A. C., and Nagle, W. M., 1940, "Mean Temperature Difference in Design," *Trans. ASME,* Vol. 62, pp. 283–294.

Holman, J. P., 1992, *Heat Transfer,* 7th ed., McGraw-Hill, New York.

Incropera, F. P., and DeWitt, D. P., 1990, *Fundamentals of Heat and Mass Transfer,* 3rd ed., Wiley, New York.

Kays, W. M., and London, A. L., 1958, *Compact Heat Exchangers,* McGraw-Hill, New York.

Kreith, F., and Bohn, M. S., 1986, *Principles of Heat Transfer,* 4th ed., Harper and Row, New York.

Mason, J. L., 1955, "Heat Transfer in Crossflow," *Proc. 2nd U.S. National Congress of Applied Mechanics,* ASME, New York, pp. 801–803.

Nusselt, W., 1911, "Der Wärmeübergang im Kreutzstrom," *Zeitschrift des Vereines deutscher Ingenieur,* Vol. 55, pp. 2021–2024.

Nusselt, W., 1930, "Eine neue Formel für den Wärmedurchgang im Kreuzstrom," *Technische Mechanik und Thermodynamik,* Vol. 1, pp. 417–422.

Roetzel, W., and Nicole, F. J. L., 1975, "Mean Temperature Difference for Heat Exchanger Design—A General Approximate Explicit Equation," ASME JOURNAL OF HEAT TRANSFER, Vol. 97, pp. 5–8.

Smith, D. M., 1934, "Mean Temperature-Difference in Cross Flow," *Engineering,* Vol. 138, pp. 479–481, 606–607.

Stevens, R. A., Fernandez, J., and Woolf, J. R., 1957, "Mean-Temperature Difference in One, Two, and Three-Pass Crossflow Heat Exchangers," *Trans. ASME,* Vol. 79, pp. 287–297.

White, F. M., 1988, *Heat and Mass Transfer,* Addison-Wesley, Reading, MA.

Optimum Design of Radiating Rectangular Plate Fin Array Extending From a Plane Wall

C. K. Krishnaprakas[1]

Nomenclature

A_p = profile area of fin array, m^2
b = fin spacing, m
$dF_{d\mu 1-d\mu 2}$ = elemental view factor from $d\mu_1$ to $d\mu_2$
h = height of fin array, m
J = radiosity, W/m^2
K = thermal conductivity of fin material, W/mK
l = length of fin, m
N = number of grid points along fin length
N_c = conduction-radiation number = $Kt/l^2\sigma T_b^3$
N_p = dimensionless profile area = A_p/w^2
N_w = dimensionless width = $\sigma T_b^3 w/K$
t = semithickness of fin, m
T = temperature of fin, K
T_b = temperature of base, K
w = width of fin = $b + 2t$, m
x = coordinate along the length of the fin
β = dimensionless radiosity = $J/\sigma T_b^4$
ϵ = emittance
θ = dimensionless temperture = T/T_b
μ = dimensionless coordinate length = x/l
σ = Stefan–Boltzmann constant = 5.67*E*-8 W/m^2K^4
ϕ = dimensionless rate of heat loss from fin and base

Introduction

Radiating fins are used in spacecraft and space vehicles for rejecting on-board waste heat to deep space. Since weight is at a premium, it is important to have minimum fin mass in these applications. Several investigators have analyzed the problem of minimization of fin mass in the past; however, there exist a

[1] Thermal Systems Group, ISRO Satellite Centre, Bangalore-560 017, India.

Contributed by the Heat Transfer Division of THE AMERICAN SOCIETY OF MECHANICAL ENGINEERS. Manuscript received by the Heat Transfer Division August 1994; revision received August 1995. Keywords: Numerical Methods, Radiation Interactions. Associate Technical Editor: M. F. Modest.

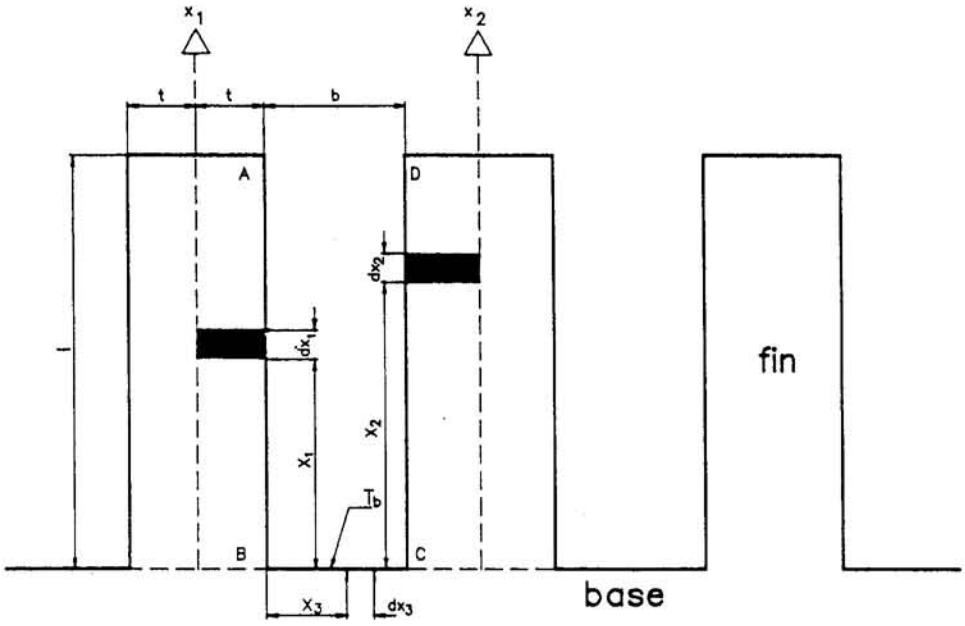

Fig. 1 Schematic of rectangular plate fin system

few works that discuss the optimum design of radiating fin array considering mutual interactions between the radiator elements.

Sparrow et al. (1961) presented the optimum design of radiatively interacting longitudinal fins without considering the fin-to-base mutual irradiation. Later Sparrow and Eckert (1962) emphasized the importance of mutual radiation interaction between fin and its base surface. Schnurr et al. (1976) employed a nonlinear optimization technique to determine the minimum weight design for straight and circular fins of rectangular and triangular profiles, protruding from a cylinder, considering fin-to-fin and fin-to-base radiation interactions. Chung and Zhang (1991a) determined the optimum shape and minimum mass of a thin fin accounting for fin-to-base interaction based on a variational calculus approach. Chung and Zhang (1991b) later extended their analysis to minimize the weight of a radiating straight fin array projecting from a cylindrical surface considering both fin-to-fin and fin-to-base interactions. The papers by Schnurr et al. and Chung and Zhang do not discuss the configuration of a straight rectangular plate fin array extending from a plane wall.

The purpose of the present analysis is to determine the minimum mass design of a straight rectangular fin array extending from a plane wall considering fin-to-fin and fin-to-base radiation interactions. Correlations in terms of dimensionless numbers are presented to facilitate an easy design, i.e., to select the optimum fin length, thickness, and spacing.

Mathematical Model

Figure 1 shows a schematic of the configuration considered for the present analysis. We make the following assumptions: (1) steady-state operation, (2) one-dimensional temperature distribution in the fin, (3) isothermal base surface, (4) gray-diffuse radiator surfaces, (5) absolute zero temperature of the environment, (6) no external heat load from the environment, and (7) the temperature and radiosity distribution with respect to length is the same in every fin, i.e., symmetry condition. The symmetry condition enables us to focus our attention only on a rectangular groove made up of half-thickness portions of two adjacent fins while analyzing the heat transfer mechanism in the fin array (see groove ABCD in Fig. 1). The governing equations for the heat transfer in the fin may be written in terms of dimensionless quantities as

$$d^2\theta(\mu_1)/d\mu_1^2 = (\epsilon/N_c)\left[\theta^4(\mu_1) - \int_{\mu_2=0}^{1} \beta(\mu_2)\,dF_{d\mu 1-d\mu 2} - \int_{\mu_3=0}^{b/l} \beta_3(\mu_3)\,dF_{d\mu 1-d\mu 3}\right] \quad (1)$$

subject to the boundary conditions

$$\theta = 1 \quad \text{at} \quad \mu_1 = 0 \quad (2a)$$

$$d\theta/d\mu_1 = -(\epsilon/N_c)(t/l)\theta^4(\mu_1) \quad \text{at} \quad \mu_1 = 1 \quad (2b)$$

and the dimensionless radiosities are given by

$$\beta(\mu_1) = \epsilon\theta^4(\mu_1) + (1-\epsilon)\int_{\mu_2=0}^{1} \beta(\mu_2)\,dF_{d\mu 1-d\mu 2} + (1-\epsilon)\int_{\mu_3=0}^{b/l} \beta_3(\mu_3)\,dF_{d\mu 1-d\mu 3} \quad (3)$$

$$\beta_3(\mu_3) = \epsilon + (1-\epsilon)\int_{\mu_1=0}^{1} \beta(\mu_1)\,dF_{d\mu 3-d\mu 1} + (1-\epsilon)\int_{\mu_2=0}^{1} \beta(\mu_2)\,dF_{d\mu 3-d\mu 2} \quad (4)$$

where the dimensionless temperature, radiosities, and lengths are defined by $\theta = T_1/T_b$, $\beta = J_1/\sigma T_b^4 = J_2/\sigma T_b^4$, $\beta_3 = J_3/\sigma T_b^4$, $\mu_1 = x_1/l$, $\mu_2 = x_2/l$, $\mu_3 = x_3/l$; the subscripts 1, 2, and 3 refer to fin 1, fin 2, and base surface, respectively. The subscript b also refers to the base surface.

Solution of Eqs. (1)–(4) yields the temperature and radiosity distributions along the length of the fin.

It is a common practice to express the effectiveness of a radiating fin as the ratio of the heat loss from the fin to that from a perfectly black isothermal fin of the same configuration (Sparrow and Cess, 1978; Özişik, 1973). However, the addition of fins, although enhancing the total radiating area, also reduces the direct radiative transfer from the base surface due to the view blockage of the base to the environment caused by the fins. Therefore, in order to determine the overall effect, which is of practical interest, we define a dimensionless heat loss quantity ϕ as the ratio of the actual heat loss from the fin and

base surfaces to that from a perfectly black unfinned surface with the same temperature. This may be written in terms of dimensionless quantities as

$$\phi = \left\{ 2 \int_{\mu_1=0}^{1} \left[\beta(\mu_1) - \int_{\mu_2=0}^{1} \beta(\mu_2) dF_{d\mu 1 - d\mu 2} - \int_{\mu_3=0}^{b/l} \beta_3(\mu_3) dF_{d\mu 1 - d\mu 3} \right] d\mu_1 + 2\epsilon(t/l)\theta^4_{\mu 1=1} + \int_{\mu_3=0}^{b/l} \left[\beta_3(\mu_3) - \int_{\mu_1=0}^{1} \beta(\mu_1) dF_{d\mu 3 - d\mu 1} - \int_{\mu_2=0}^{1} \beta(\mu_2) dF_{d\mu 3 - d\mu 2} \right] d\mu_3 \right\} \Big/ [b/l + 2t/l) \quad (5)$$

It is to be noted that this definition of ϕ is similar to the apparent emittance term (ϵ_a) defined to represent the emission characteristics of cavities with isothermal walls (Sparrow and Cess, 1978). From the definition of ϕ it is clear that finning is effective only when $\phi > \epsilon$.

Numerical Scheme

A numerical iterative scheme consisting of a finite difference technique and Nystrom technique (Delves and Mohamed, 1985) based on the Gauss–Legendre quadrature rule is employed to solve the governing coupled integro-differential and integral equations (Eqs. (1)–(4)). Convergence of the iterative scheme is enhanced by applying the Ng acceleration method (Auer, 1987).

Optimum Fin Design

From Eq. (5) we see that ϕ depends on four parameters: ϵ, N_c, b/l, and t/l, i.e., $\phi = \phi(\epsilon, N_c, b/l, t/l)$. For a given emittance ϵ, profile area, $A_p = 2tl$ and fin width, $w = b + 2t$, there is an optimum combination of the variables N_c, b/l, and t/l such that ϕ is maximum. We may state the constrained optimization problem mathematically as:

for given ϵ, N_p, and N_w,

$$\text{maximize } \phi(\epsilon, N_c, b/l, t/l) \quad (6)$$

$$\text{subject to } N_p = 2(t/l)/[(b/l + 2t/l)^2] \quad (6a)$$

$$N_w = (t/l)(b/l + 2t/l)/N_c \quad (6b)$$

$$\text{and } \phi > \epsilon \quad (6c)$$

where N_p and N_w are, respectively, the dimensionless profile area and width. N_w may also be thought of as a Biot number defined for radiation.

The constraints aid in transforming the multidimensional optimization problem into a univariate one and polynomial interpolation scheme may be used to solve it (Gill et al., 1981).

Results and Discussion

Figure 2 shows the maximum value of ϕ (ϕ_{max}) plotted as a function of N_p for different ϵ and N_w values. It is seen that as N_p increases ϕ_{max} increases and the rate of increase in ϕ_{max} decreases. $(t/l)_{opt}$ increases and $(b/l)_{opt}$ decreases as N_p is increased. $(N_c)_{opt}$ increases with N_p, indicating that higher conduction to radiation interaction is required for higher values of ϕ_{max}.

The optimum b/l and t/l may well be correlated by the following expressions:

$$(b/l)_{opt} = 3.18\phi_{max}^{-6.27}\epsilon^{3.05}N_w^{0.16} \quad (7)$$

$$(t/l)_{opt} = 5.11\phi_{max}^{12.41}\epsilon^{-1.79}N_w^{0.68} \quad (8)$$

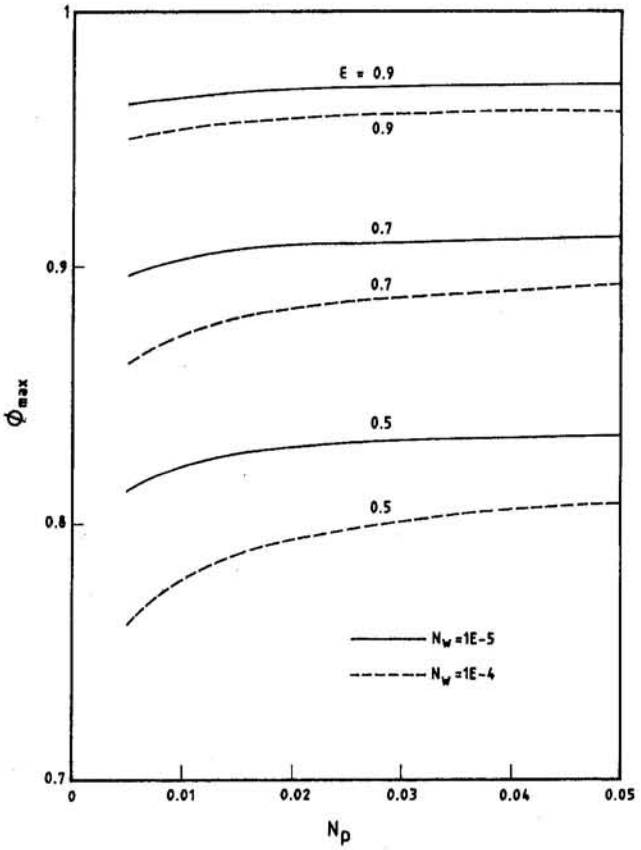

Fig. 2 $\phi_{max} = f(\epsilon, N_p, N_w)$

Validation of the numerical results was obtained by comparing the ϕ versus l/b graphs for $1/N_c = 0$ with the curves presented by Sparrow and Cess (1978) for the apparent emittance (ϵ_a) of rectangular groove cavities, since $\phi = \epsilon_a$ when $1/N_c = 0$ and terms containing t/l vanish in Eq. (5). Our results have been found to be indistinguishable, within the scale of the plots, from the curves presented by Sparrow and Cess.

Conclusions

Results are presented to obtain the optimum mass design of a straight rectangular plate fin array extending from a plane wall for emittance values in the range 0.5–0.9. Higher heat transfer rates are achieved at higher values of N_c and lower values of t/l, i.e., the best performance is achieved by short and thin fins. Apparently, the fin array extending from a plane wall is not very attractive if the heat transfer mode is radiation alone. For most radiative fins, the emittance is usually high, e.g., $\epsilon \geq 0.9$. As demonstrated by the top curve ($\epsilon = 0.9$) of Fig. 2, ϕ increases only to 0.97, i.e., the increase in heat transfer from unfinned condition to finned condition is only 7.8 percent. This indicates that the heat transfer enhancement by using the radiative fin array is limited.

Acknowledgments

The author wishes to thank D. R. Bhandari, Head, Thermal Design and Analysis Division, H. Narayanamurthy, Group Director, Thermal Systems Group and A. V. Patki, Deputy Director, ISRO Satellite Centre, for their support and encouragement in this work.

References

Auer, L., 1987, "Acceleration of Convergence," in: W. Kalkofen, ed., *Numerical Radiative Transfer*, Cambridge University Press, Cambridge, United Kingdom.

Chung, B. T. F., and Zhang, B. X., 1991a, "Minimum Mass Longitudinal Fins With Radiation Interaction at the Base," *Journal of the Franklin Institute,* Vol. 328, pp. 143–161.

Chung, B. T. F., and Zhang, B. X., 1991b, "Optimization of Radiating Fin Array Including Mutual Irradiations Between Radiator Elements," ASME JOURNAL OF HEAT TRANSFER, Vol. 113, pp. 814–822.

Delves, L. M., and Mohamed, J. L., 1985, *Computational Methods for Integral Equations,* Cambridge University Press, Cambridge, United Kingdom.

Gill, P. E., Murray, W., and Wright, M. H., 1981, *Practical Optimization,* Academic Press, Inc., London.

Özişik, M. N., 1973, *Radiative Transfer and Interactions With Conduction and Convection,* Wiley, New York.

Schnurr, N. M., Shapiro, A. B., and Townsend, M. A., 1976, "Optimization of Radiating Fin Arrays With Respect to Weight," ASME JOURNAL OF HEAT TRANSFER, Vol. 98, pp. 643–648.

Sparrow, E. M., Eckert, E. R. G., and Irvine, T. F., Jr., 1961, "The Effectiveness of Radiating Fins With Mutual Irradiation," *Journal of the Aerospace Sciences,* Vol. 28, pp. 763–772.

Sparrow, E. M., and Eckert, E. R. G., 1962, "Radiant Interaction Between Fin and Base Surfaces," ASME JOURNAL OF HEAT TRANSFER, Vol. 84, pp. 12–18.

Sparrow, E. M., and Cess, R. D., 1978, *Radiation Heat Transfer,* Augmented Edition, Hemisphere, Washington, DC.

Measurements of the Structure of Self-Preserving Round Buoyant Turbulent Plumes

Z. Dai[1] **and G. M. Faeth**[1]

Nomenclature

a = acceleration of gravity
B_o = source buoyancy flux
d = source diameter
f = mixture fraction
$F(r/(x - x_o))$ = scaled radial distribution of $\bar{f}$, Eq. (1)
Fr_o = source Froude number = $(4/\pi)^{1/4} l_M/d$
k_f, k_u = plume width coefficients based on $\bar{f}$ and $\bar{u}$
l_M = Morton length scale = $M_o^{3/4}/B_o^{1/2}$
M_o = source specific momentum flux
r = radial distance
u = streamwise velocity
$U(r/(x - x_o))$ = scaled radial distribution of $\bar{u}$, Eq. (2)
x = streamwise distance
ρ = density

Subscripts

c = centerline value
o = initial value or virtual origin location
∞ = ambient value

Superscripts

$(\bar{\ })$ = time-averaged mean value
$(\bar{\ })'$ = root-mean-squared fluctuating value

Introduction

Round buoyant turbulent plumes in still and unstratified environments are classical flows that are important for evaluating concepts and models of buoyancy/turbulence interactions. Fully developed buoyant turbulent plumes are of greatest interest because they have lost extraneous source disturbances and their structure is self-preserving, which simplifies both theory and the interpretation of measurements (Morton, 1959). These observations have prompted many studies of self-preserving buoyant turbulent plumes; see, for example, Dai et al. (1994, 1995a, b), Papanicolaou and List (1988), Papantoniou and List (1989), Shabbir and George (1992), and references cited therein. In contrast to most earlier studies, which were carried out nearer to the source, however, the recent measurements of Dai et al. (1994, 1995a, b) showed that self-preserving round buoyant turbulent plumes were narrower, and had larger mean mixture fractions and streamwise velocities near the axis, than previously thought. The objective of the present investigation was to extend earlier evaluations of these measurements, emphasizing potential problems due to flow confinement, to help insure that an artifact of the experiments was not responsible for these somewhat startling findings.

Consistent with most studies of round buoyant turbulent plumes, self-preserving plume properties will be defined for conditions where buoyant jets are used as plume sources and all scalar properties can be represented conveniently as functions of the mixture fraction. Reaching self-preserving conditions for buoyant jet sources requires that $(x - x_o)/d$ and $(x - x_o)/l_M \gg 1$, to insure that effects of both source disturbances and source momentum have been lost (Morton, 1959; List, 1982); then, self-preserving behavior implies that $f \ll 1$, that the buoyancy flux is conserved, and that $\bar{f}$ and $\bar{u}$ scale as follows:

$$\bar{f} a B_o^{-2/3} (x - x_o)^{5/3} \left| d(\ln \rho)/df \right|_{f \to 0} = F(r/(x - x_o)) \quad (1)$$

$$\bar{u}((x - x_o)/B_o)^{1/3} = U(r/(x - x_o)) \quad (2)$$

where $F(r/(x - x_o))$ and $U(r/(x - x_o))$ are universal functions that generally are approximated by Gaussian fits; in addition, various other flow statistics can be represented as universal functions of $r/(x - x_o)$ after normalizing mixture fraction and velocity properties by $\bar{f}_c$ and $\bar{u}_c$, respectively (Dai et al., 1994, 1995a, b).

The controversy concerning the properties of self-preserving round buoyant turbulent plumes involves both the conditions needed to observe them and their structure. In particular, most earlier measurements to establish the self-preserving structure of round buoyant turbulent plumes were limited to $(x - x_o)/d \leq 62$, which seems small for self-preserving behavior. For example, Panchapakesan and Lumley (1993) only observed self-preserving behavior for round nonbuoyant turbulent jets when $(x - x_o)/d \geq 70$, which is consistent with the observations of Dai et al. (1994, 1995a, b), that self-preserving behavior for round buoyant turbulent plumes required $(x - x_o)/d \geq 87$ and $(x - x_o)/l_M \geq 12$. In addition, Dai et al. (1994, 1995a) found that characteristic flow widths were up to 40 percent smaller, and $F(0)$ and $U(0)$ were up to 30 percent larger, than earlier results in the literature. Notably, this behavior is consistent with the development of plume structure toward self-preserving conditions for buoyant jet sources, where normalized flow widths progressively decrease, and $F(0)$ and $U(0)$ progressively increase, with increasing streamwise distance until the flow becomes self-preserving (Dai et al., 1994). Finally, the self-preserving plume properties of $\bar{f}$ observed by Dai et al. (1994) were in good agreement with measurements of Papantoniou and List (1989), which were carried out at comparable distances from the source.

Dai et al. (1994, 1995a, b) completed several typical checks of their measurements, including evaluating the measurements using the governing equations for mean quantities, establishing that the measurements satisfied conservation of buoyancy fluxes, and showing that the measurements were relatively independent of the rate of removal of plume gases from the test enclosure. Nevertheless, observing narrower self-preserving plumes than numerous earlier studies raises new concerns about

[1] Department of Aerospace Engineering, The University of Michigan, Ann Arbor, MI.

Contributed by the Heat Transfer Division of THE AMERICAN SOCIETY OF MECHANICAL ENGINEERS. Manuscript received by the Heat Transfer Division August 1995; revision received February 1996. Keywords: Natural Convection, Plumes, Turbulence. Associate Technical Editor: Y. Jaluria.

Chung, B. T. F., and Zhang, B. X., 1991a, "Minimum Mass Longitudinal Fins With Radiation Interaction at the Base," *Journal of the Franklin Institute,* Vol. 328, pp. 143–161.

Chung, B. T. F., and Zhang, B. X., 1991b, "Optimization of Radiating Fin Array Including Mutual Irradiations Between Radiator Elements," ASME JOURNAL OF HEAT TRANSFER, Vol. 113, pp. 814–822.

Delves, L. M., and Mohamed, J. L., 1985, *Computational Methods for Integral Equations,* Cambridge University Press, Cambridge, United Kingdom.

Gill, P. E., Murray, W., and Wright, M. H., 1981, *Practical Optimization,* Academic Press, Inc., London.

Özişik, M. N., 1973, *Radiative Transfer and Interactions With Conduction and Convection,* Wiley, New York.

Schnurr, N. M., Shapiro, A. B., and Townsend, M. A., 1976, "Optimization of Radiating Fin Arrays With Respect to Weight," ASME JOURNAL OF HEAT TRANSFER, Vol. 98, pp. 643–648.

Sparrow, E. M., Eckert, E. R. G., and Irvine, T. F., Jr., 1961, "The Effectiveness of Radiating Fins With Mutual Irradiation," *Journal of the Aerospace Sciences,* Vol. 28, pp. 763–772.

Sparrow, E. M., and Eckert, E. R. G., 1962, "Radiant Interaction Between Fin and Base Surfaces," ASME JOURNAL OF HEAT TRANSFER, Vol. 84, pp. 12–18.

Sparrow, E. M., and Cess, R. D., 1978, *Radiation Heat Transfer,* Augmented Edition, Hemisphere, Washington, DC.

Measurements of the Structure of Self-Preserving Round Buoyant Turbulent Plumes

Z. Dai[1] **and G. M. Faeth**[1]

Nomenclature

a = acceleration of gravity
B_o = source buoyancy flux
d = source diameter
f = mixture fraction
$F(r/(x - x_o))$ = scaled radial distribution of $\bar{f}$, Eq. (1)
Fr_o = source Froude number = $(4/\pi)^{1/4} l_M/d$
k_f, k_u = plume width coefficients based on $\bar{f}$ and $\bar{u}$
l_M = Morton length scale = $M_o^{3/4}/B_o^{1/2}$
M_o = source specific momentum flux
r = radial distance
u = streamwise velocity
$U(r/(x - x_o))$ = scaled radial distribution of $\bar{u}$, Eq. (2)
x = streamwise distance
ρ = density

Subscripts

c = centerline value
o = initial value or virtual origin location
∞ = ambient value

Superscripts

$(\bar{\ })$ = time-averaged mean value
$(\bar{\ })'$ = root-mean-squared fluctuating value

Introduction

Round buoyant turbulent plumes in still and unstratified environments are classical flows that are important for evaluating concepts and models of buoyancy/turbulence interactions. Fully developed buoyant turbulent plumes are of greatest interest because they have lost extraneous source disturbances and their structure is self-preserving, which simplifies both theory and the interpretation of measurements (Morton, 1959). These observations have prompted many studies of self-preserving buoyant turbulent plumes; see, for example, Dai et al. (1994, 1995a, b), Papanicolaou and List (1988), Papantoniou and List (1989), Shabbir and George (1992), and references cited therein. In contrast to most earlier studies, which were carried out nearer to the source, however, the recent measurements of Dai et al. (1994, 1995a, b) showed that self-preserving round buoyant turbulent plumes were narrower, and had larger mean mixture fractions and streamwise velocities near the axis, than previously thought. The objective of the present investigation was to extend earlier evaluations of these measurements, emphasizing potential problems due to flow confinement, to help insure that an artifact of the experiments was not responsible for these somewhat startling findings.

Consistent with most studies of round buoyant turbulent plumes, self-preserving plume properties will be defined for conditions where buoyant jets are used as plume sources and all scalar properties can be represented conveniently as functions of the mixture fraction. Reaching self-preserving conditions for buoyant jet sources requires that $(x - x_o)/d$ and $(x - x_o)/l_M \gg 1$, to insure that effects of both source disturbances and source momentum have been lost (Morton, 1959; List, 1982); then, self-preserving behavior implies that $f \ll 1$, that the buoyancy flux is conserved, and that $\bar{f}$ and $\bar{u}$ scale as follows:

$$\bar{f} a B_o^{-2/3} (x - x_o)^{5/3} \left| d(\ln \rho)/df \right|_{f \to 0} = F(r/(x - x_o)) \quad (1)$$

$$\bar{u}((x - x_o)/B_o)^{1/3} = U(r/(x - x_o)) \quad (2)$$

where $F(r/(x - x_o))$ and $U(r/(x - x_o))$ are universal functions that generally are approximated by Gaussian fits; in addition, various other flow statistics can be represented as universal functions of $r/(x - x_o)$ after normalizing mixture fraction and velocity properties by $\bar{f}_c$ and $\bar{u}_c$, respectively (Dai et al., 1994, 1995a, b).

The controversy concerning the properties of self-preserving round buoyant turbulent plumes involves both the conditions needed to observe them and their structure. In particular, most earlier measurements to establish the self-preserving structure of round buoyant turbulent plumes were limited to $(x - x_o)/d \leq 62$, which seems small for self-preserving behavior. For example, Panchapakesan and Lumley (1993) only observed self-preserving behavior for round nonbuoyant turbulent jets when $(x - x_o)/d \geq 70$, which is consistent with the observations of Dai et al. (1994, 1995a, b), that self-preserving behavior for round buoyant turbulent plumes required $(x - x_o)/d \geq 87$ and $(x - x_o)/l_M \geq 12$. In addition, Dai et al. (1994, 1995a) found that characteristic flow widths were up to 40 percent smaller, and $F(0)$ and $U(0)$ were up to 30 percent larger, than earlier results in the literature. Notably, this behavior is consistent with the development of plume structure toward self-preserving conditions for buoyant jet sources, where normalized flow widths progressively decrease, and $F(0)$ and $U(0)$ progressively increase, with increasing streamwise distance until the flow becomes self-preserving (Dai et al., 1994). Finally, the self-preserving plume properties of $\bar{f}$ observed by Dai et al. (1994) were in good agreement with measurements of Papantoniou and List (1989), which were carried out at comparable distances from the source.

Dai et al. (1994, 1995a, b) completed several typical checks of their measurements, including evaluating the measurements using the governing equations for mean quantities, establishing that the measurements satisfied conservation of buoyancy fluxes, and showing that the measurements were relatively independent of the rate of removal of plume gases from the test enclosure. Nevertheless, observing narrower self-preserving plumes than numerous earlier studies raises new concerns about

[1] Department of Aerospace Engineering, The University of Michigan, Ann Arbor, MI.

Contributed by the Heat Transfer Division of THE AMERICAN SOCIETY OF MECHANICAL ENGINEERS. Manuscript received by the Heat Transfer Division August 1995; revision received February 1996. Keywords: Natural Convection, Plumes, Turbulence. Associate Technical Editor: Y. Jaluria.

effects of removal rates of exhaust gases from the test enclosure because this flow places the plumes in a coflow, which would tend to make them narrower than truly unconfined self-preserving round buoyant turbulent plumes (see Shabbir and George (1992) for a detailed discussion of this and other potential error sources for measurements of buoyant turbulent plumes). Thus, in order to resolve these concerns about the measurements of Dai et al. (1994, 1995a, b), the objective of the present investigation was to quantify the effects of plume exhaust rates on their reported self-preserving distributions of $\bar{f}$, $\bar{u}$, $\bar{f}'$, and $\bar{u}'$.

Experimental Methods

Test Apparatus. Experimental methods were identical to those of Dai et al. (1994, 1995a, b) and will only be described briefly. Present considerations were limited to downward-flowing plumes from a source flow of sulfur hexafluoride in still air at atmospheric pressure and temperature, and involved laser-induced iodine fluorescence (LIF) to measure mixture fractions and laser velocimetry (LV) to measure streamwise velocities. The plumes were observed in a 3000 × 3000 × 3400 mm high plastic enclosure within a large high-bay test area, which had a screen across the top for air inflow, to compensate for the removal of air entrained by the plume. The plume flow was removed by 300-mm-dia ducts mounted on the floor at the four corners of the outer enclosure, with the exhaust flow controlled by a bypass/damper system. Probe measurements showed that exhaust flows through the four exhaust duct inlets were essentially the same, and provided measurements of exhaust flow rates (95 percent confidence) within 10 percent. The test plume was within a smaller enclosure (1100 × 1100 × 3200 mm high) with plastic screen walls; however, this enclosure had no effect on flow properties, i.e., measurements with and without these screens present were identical. The plume sources were mounted on the inner enclosure, which could be traversed to accommodate rigidly mounted instrumentation. The plume sources consisted of rigid plastic tubes with flow straighteners at the inlet and length-to-diameter ratios of 50:1. The source flows were seeded with iodine vapor for LIF measurements, while the ambient air was seeded with oil drops for LV measurements. Maximum mean mixture fractions in the self-preserving region were less than 6 percent; therefore, effects of concentration bias of LV measurements, because only the ambient air was seeded, were negligible.

Instrumentation. The LIF signal was produced by the fluorescence of iodine at the 514.5 nm line of an argon-ion laser, separating the LIF emission from light scattered at the laser line using a long-pass optical filter. The detector output was amplified and low-pass filtered to control alias signals to provide roughly four decades of power spectral densities in the present flow. Calibration showed that iodine seeding levels varied less than 1 percent, that the LIF signal varied linearly with laser power and iodine concentration, that reabsorption of the LIF emission was negligible, and that differential diffusion effects between the source gases and iodine were negligible (Dai et al., 1994). Finally, experimental uncertainties (95 percent confidence) were less than 5 and 10 percent for $\bar{f}$ and $\bar{f}'$ up to $r/(x - x_o) = 0.15$ but increased roughly inversely proportional to $\bar{f}$ at larger radial distances.

A dual-beam, frequency-shifted LV was used for velocity measurements, based on the 514.5 nm line of an argon-ion laser. The detector output was processed using a burst-counter signal processor with the low-pass-filtered analog output of the signal processor sampled at equal times to avoid problems of velocity bias, while directional bias and ambiguity were controlled by frequency shifting. The processor output was sampled at rates more than twice the break frequency of the low-pass filter to control alias signals. Effects of step noise contributed less than 3 percent to the determination of velocity fluctuations, while the

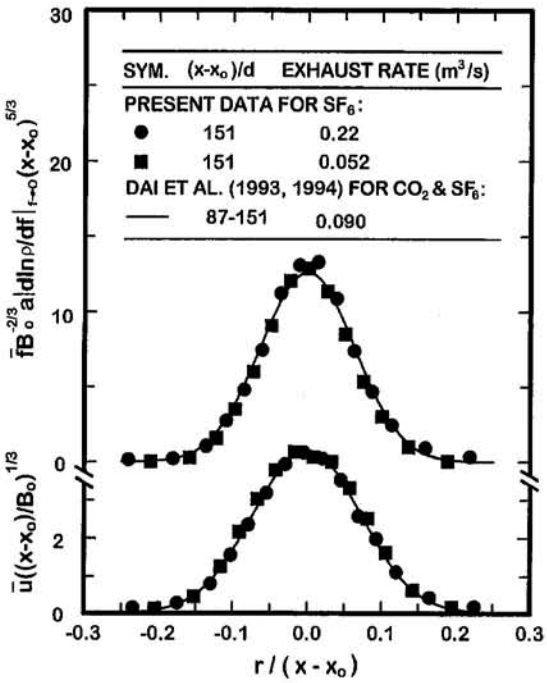

Fig. 1 Radial profiles of mean mixture fractions and streamwise velocities for self-preserving round buoyant turbulent plumes

measurements yielded roughly four decades of power spectral densities similar to the mixture fraction fluctuations (Dai et al., 1995a). Experimental uncertainties of $\bar{u}$ and $\bar{u}'$ were similar to $\bar{f}$ and $\bar{f}'$.

Test Conditions. Major parameters of the present measurements of SF_6 plumes were as follows: $d = 6.4$ mm, $u_o = 1890$ mm/s, $\rho_o/\rho_\infty = 5.06$, $\mathrm{Fr}_o = 3.75$, $l_M/d = 3.53$, and $x_o/d = 0.0$. The measuring station farthest from the source was at $(x - x_o)/d = 151$, while the edge of the plume is at roughly $r/(x - x_o) = 0.2$, which yields plume diameters and streamwise distances less than 360 and 900 mm. This implies that the maximum plume cross-sectional area is less than 1.2 percent of the enclosure cross-sectional area. Exhaust volume flow rates were roughly half, equal to, and twice the nominal flow rates used earlier, or 0.052, 0.090, and 0.22 m^3/s. Assuming uniform conditions over the cross section of the enclosure, these exhaust flows imply coflow velocities of roughly 6, 10, and 24 mm/s at the plane of the source exit, which are less than 1.3 percent of the source velocity.

Results and Discussion

Present measurements at the nominal exhaust flow rate agreed with Dai et al. (1994, 1995a, b) within experimental uncertainties; therefore, these results will be represented by their earlier correlations. Present measurements of $\bar{f}$ and $\bar{u}$ in the self-preserving region of buoyant turbulent plumes are plotted in Fig. 1 for the various flow rates according to the self-preserving scaling parameters of Eqs. (1) and (2). The present measurements were limited to $(x - x_o)/d = 151$ because this was the most critical condition with respect to potential coflow effects. The effect of varying plume exhaust rates, and thus coflow velocities, is seen to be negligible over the present range, with profiles of $\bar{f}$ and $\bar{u}$ for all coflow rates agreeing within experimental uncertainties. Thus, including the new measurements with the earlier results of Dai et al. (1994, 1995a, b) yields the same universal fitting parameters as before: $F(0) = 12.6$ and $k_f^2 = 125$, $U(0) = 4.3$ and $k_u^2 = 93$. The main effect of increased coflow velocities was evidence of a slight increase of streamwise velocity near the edge of the plume, which can be seen

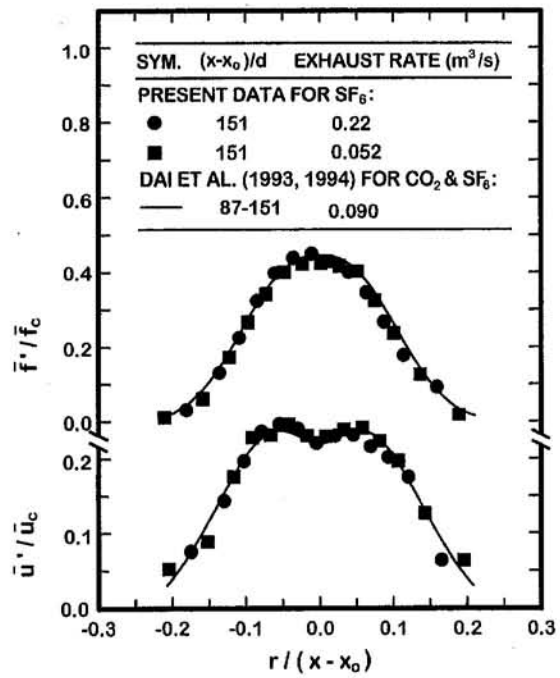

Fig. 2 Radial profiles of rms mixture fraction and streamwise velocity fluctuations for self-preserving round buoyant turbulent plumes

most clearly at the outmost points of $\bar{u}$ at an exhaust flow rate of 0.22 m^3/s.

Radial profiles of fluctuating mixture fractions and streamwise velocities are illustrated in Fig. 2 for the various exhaust flow rates. The values of $\bar{f}'$ and $\bar{u}'$ are plotted according to the self-preserving scaling observed by Dai et al. (1994, 1995a). Similar to the results for mean properties in Fig. 1, the fluctuating properties illustrated in Fig. 2 exhibit variations with exhaust rate within experimental uncertainties. Thus, present estimates of mixture fraction and streamwise velocity intensities at the axis are not changed significantly from the findings of Dai et al. (1994, 1995a), i.e., $(\bar{f}'/\bar{f})_c = 0.45$ and $(\bar{u}'/\bar{u})_c = 0.22$.

Taking the findings illustrated in Figs. 1 and 2 together, it appears that the measurements of flow properties within the self-preserving region of round buoyant turbulent plumes due to Dai et al. (1994, 1995a) were not affected by coflow caused by effects of confinement within their stated experimental uncertainties. Thus, the fact that the measured profiles of Dai et al. (1994, 1995a, b) are narrower, and have larger scaled mean values of mixture fractions and velocities near the axis, than previously thought, is due to additional flow development to reach truly self-preserving behavior compared to most earlier measurements, rather than due to an effect of coflow.

Acknowledgments

This research was sponsored by the United States Department of Commerce, National Institute of Standards and Technology, Grant Nos. 60NANB1D1175 and 60NANB4D1696, with H. R. Baum and K. C. Smyth of the Building and Fire Research Laboratories serving as Scientific Officers.

References

Dai, Z., Tseng, L.-K., and Faeth, G. M., 1994, "Structure of Round, Fully Developed, Buoyant Turbulent Plumes," ASME JOURNAL OF HEAT TRANSFER, Vol. 116, pp. 409–417.

Dai, Z., Tseng, L.-K., and Faeth, G. M., 1995a, "Velocity Statistics of Round, Fully Developed Buoyant Turbulent Plumes," ASME JOURNAL OF HEAT TRANSFER, Vol. 117, pp. 138–145.

Dai, Z., Tseng, L.-K., and Faeth, G. M., 1995b, "Velocity/Mixture-Fraction Statistics of Round, Self-Preserving Buoyant Turbulent Plumes," ASME JOURNAL OF HEAT TRANSFER, Vol. 117, pp. 918–926.

List, E. J., 1982, "Turbulent Jets and Plumes," *Ann. Rev. Fluid Mech.*, Vol. 14, pp. 189–212.

Morton, B. R., 1959, "Forced Plumes," *J. Fluid Mech.*, Vol. 5, pp. 151–163.

Panchapakesan, N. R., and Lumley, J. L., 1993, "Turbulence Measurements in Axisymmetric Jets of Air and Helium. Part. 1. Air Jet," *J. Fluid Mech.*, Vol. 246, pp. 197–223.

Papanicolaou, P. N., and List, E. J., 1988, "Investigation of Round Vertical Turbulent Buoyant Jets," *J. Fluid Mech.*, Vol. 195, pp. 341–391.

Papantoniou, D., and List, E. J., 1989, "Large Scale Structure in the Far Field of Buoyant Jets," *J. Fluid Mech.*, Vol. 209, pp. 151–190.

Rouse, H., Yih, C. S., and Humphreys, H. W., 1952, "Gravitational Convection From a Boundary Source," *Tellus*, Vol. 4, pp. 201–210.

Shabbir, A., and George, W. K., 1992, "Experiments on a Round Turbulent Buoyant Plume," NASA Technical Memorandum 105955.

A Calculation and Experimental Verification of the Infrared Transmission Coefficient of Straight Cylindrical Metal Tubes

P. Cavaleiro Miranda[1]

Introduction

An accurate figure for the infrared (IR) transmission coefficient of a stainless steel guide tube that transports ultra-cold neutrons (UCN) from a cryostat at 0.5 K to a room temperature apparatus is required in order to estimate the reduction in the heat load on the cryostat's UCN window achieved by cooling down the guide tube from 300 K to 77 K. The heat emitted by the cooled guide tube is negligible compared to the heat input from the room temperature apparatus, which behaves approximately like a blackbody at 300 K, and so the reduction in heat load is given by the transmission coefficient of the guide tube for 300 K blackbody radiation.

It was shown by Ohlmann et al. (1958) that the transmission of infrared (IR) radiation by cylindrical metal pipes decreases exponentially with length, for a monochromatic point source located on-axis and taking into account only rays making small grazing angles with the wall. In the case of an IR source covering the whole cross section of the tube and providing 2π steradians illumination a significant part of the emitted energy is carried by skew rays. As these rays undergo more reflections the attenuation will be significantly higher than that predicted by Ohlmann's formula.

Calculation of the IR Transmission Coefficient of a Straight Cylindrical Metal Pipe

In the case of 300 K blackbody radiation traveling in a vacuum and incident on stainless steel, the low-frequency limit expressions for the reflection coefficients apply. The coefficients for both polarizations, $\rho\perp$ and $\rho\parallel$, depend essentially on the wavelength λ, the cosine of the angle of incidence Φ, and the DC electrical conductivity k_e of the metal (e.g., Stratton, 1941). For one particular ray of unpolarized "light" traveling down the tube and making a total of N identical reflections, the fraction t of energy transmitted will be

[1] Institut Laue Langevin, 156X, 38042 Grenoble Cedex, France; present position and address: Assistant Professor, Departamento de Física, Faculdade de Ciências da Universidade de Lisboa, Campo Grande, 1700 Lisboa, Portugal.

Contributed by the Heat Transfer Division of THE AMERICAN SOCIETY OF MECHANICAL ENGINEERS. Manuscript received by the Heat Transfer Division November 1994; revision received October 1995. Keywords: Radiation. Associate Technical Editor: M. F. Modest.

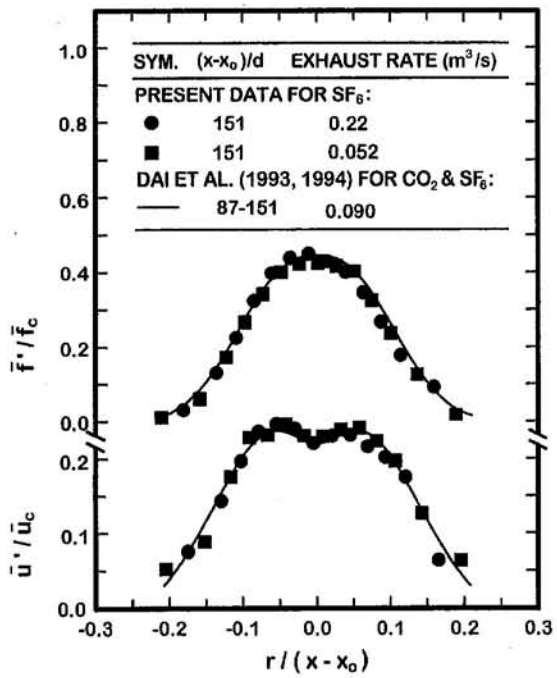

Fig. 2 Radial profiles of rms mixture fraction and streamwise velocity fluctuations for self-preserving round buoyant turbulent plumes

most clearly at the outmost points of $\bar{u}$ at an exhaust flow rate of 0.22 m^3/s.

Radial profiles of fluctuating mixture fractions and streamwise velocities are illustrated in Fig. 2 for the various exhaust flow rates. The values of $\bar{f}'$ and $\bar{u}'$ are plotted according to the self-preserving scaling observed by Dai et al. (1994, 1995a). Similar to the results for mean properties in Fig. 1, the fluctuating properties illustrated in Fig. 2 exhibit variations with exhaust rate within experimental uncertainties. Thus, present estimates of mixture fraction and streamwise velocity intensities at the axis are not changed significantly from the findings of Dai et al. (1994, 1995a), i.e., $(\bar{f}'/\bar{f})_c = 0.45$ and $(\bar{u}'/\bar{u})_c = 0.22$.

Taking the findings illustrated in Figs. 1 and 2 together, it appears that the measurements of flow properties within the self-preserving region of round buoyant turbulent plumes due to Dai et al. (1994, 1995a) were not affected by coflow caused by effects of confinement within their stated experimental uncertainties. Thus, the fact that the measured profiles of Dai et al. (1994, 1995a, b) are narrower, and have larger scaled mean values of mixture fractions and velocities near the axis, than previously thought, is due to additional flow development to reach truly self-preserving behavior compared to most earlier measurements, rather than due to an effect of coflow.

Acknowledgments

This research was sponsored by the United States Department of Commerce, National Institute of Standards and Technology, Grant Nos. 60NANB1D1175 and 60NANB4D1696, with H. R. Baum and K. C. Smyth of the Building and Fire Research Laboratories serving as Scientific Officers.

References

Dai, Z., Tseng, L.-K., and Faeth, G. M., 1994, "Structure of Round, Fully Developed, Buoyant Turbulent Plumes," ASME JOURNAL OF HEAT TRANSFER, Vol. 116, pp. 409–417.

Dai, Z., Tseng, L.-K., and Faeth, G. M., 1995a, "Velocity Statistics of Round, Fully Developed Buoyant Turbulent Plumes," ASME JOURNAL OF HEAT TRANSFER, Vol. 117, pp. 138–145.

Dai, Z., Tseng, L.-K., and Faeth, G. M., 1995b, "Velocity/Mixture-Fraction Statistics of Round, Self-Preserving Buoyant Turbulent Plumes," ASME JOURNAL OF HEAT TRANSFER, Vol. 117, pp. 918–926.

List, E. J., 1982, "Turbulent Jets and Plumes," *Ann. Rev. Fluid Mech.*, Vol. 14, pp. 189–212.

Morton, B. R., 1959, "Forced Plumes," *J. Fluid Mech.*, Vol. 5, pp. 151–163.

Panchapakesan, N. R., and Lumley, J. L., 1993, "Turbulence Measurements in Axisymmetric Jets of Air and Helium. Part. 1. Air Jet," *J. Fluid Mech.*, Vol. 246, pp. 197–223.

Papanicolaou, P. N., and List, E. J., 1988, "Investigation of Round Vertical Turbulent Buoyant Jets," *J. Fluid Mech.*, Vol. 195, pp. 341–391.

Papantoniou, D., and List, E. J., 1989, "Large Scale Structure in the Far Field of Buoyant Jets," *J. Fluid Mech.*, Vol. 209, pp. 151–190.

Rouse, H., Yih, C. S., and Humphreys, H. W., 1952, "Gravitational Convection From a Boundary Source," *Tellus*, Vol. 4, pp. 201–210.

Shabbir, A., and George, W. K., 1992, "Experiments on a Round Turbulent Buoyant Plume," NASA Technical Memorandum 105955.

A Calculation and Experimental Verification of the Infrared Transmission Coefficient of Straight Cylindrical Metal Tubes

P. Cavaleiro Miranda[1]

Introduction

An accurate figure for the infrared (IR) transmission coefficient of a stainless steel guide tube that transports ultra-cold neutrons (UCN) from a cryostat at 0.5 K to a room temperature apparatus is required in order to estimate the reduction in the heat load on the cryostat's UCN window achieved by cooling down the guide tube from 300 K to 77 K. The heat emitted by the cooled guide tube is negligible compared to the heat input from the room temperature apparatus, which behaves approximately like a blackbody at 300 K, and so the reduction in heat load is given by the transmission coefficient of the guide tube for 300 K blackbody radiation.

It was shown by Ohlmann et al. (1958) that the transmission of infrared (IR) radiation by cylindrical metal pipes decreases exponentially with length, for a monochromatic point source located on-axis and taking into account only rays making small grazing angles with the wall. In the case of an IR source covering the whole cross section of the tube and providing 2π steradians illumination a significant part of the emitted energy is carried by skew rays. As these rays undergo more reflections the attenuation will be significantly higher than that predicted by Ohlmann's formula.

Calculation of the IR Transmission Coefficient of a Straight Cylindrical Metal Pipe

In the case of 300 K blackbody radiation traveling in a vacuum and incident on stainless steel, the low-frequency limit expressions for the reflection coefficients apply. The coefficients for both polarizations, $\rho\perp$ and $\rho\parallel$, depend essentially on the wavelength λ, the cosine of the angle of incidence Φ, and the DC electrical conductivity k_e of the metal (e.g., Stratton, 1941). For one particular ray of unpolarized "light" traveling down the tube and making a total of N identical reflections, the fraction t of energy transmitted will be

[1] Institut Laue Langevin, 156X, 38042 Grenoble Cedex, France; present position and address: Assistant Professor, Departamento de Física, Faculdade de Ciências da Universidade de Lisboa, Campo Grande, 1700 Lisboa, Portugal.

Contributed by the Heat Transfer Division of THE AMERICAN SOCIETY OF MECHANICAL ENGINEERS. Manuscript received by the Heat Transfer Division November 1994; revision received October 1995. Keywords: Radiation. Associate Technical Editor: M. F. Modest.

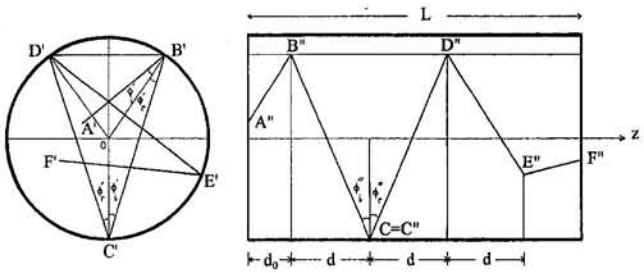

Fig. 1 Projections of the trajectory of a ray traveling down a cylindrical pipe by specular reflection. Capital letters denote reflection points in space, primed letters denote the projection of those points onto the *xy* plane, and double-primed letters the projection of the points onto a plane containing the *z* axis. Note that Φ_i'' is equal to Φ_r'' only in the longitudinal plane containing the reflection point.

$$t = \frac{\rho_\perp^N + \rho_\parallel^N}{2}. \tag{1}$$

Because parallel and perpendicular refer to the plane of incidence, which for a cylindrical tube takes up all possible angles around the z axis uniformly, any light entering the tube can be regarded as unpolarized as far as the overall transmission coefficient is concerned.

Due to the cylindrical symmetry of the geometry, a ray always strikes the wall at the same angle of incidence and covers a constant distance between bounces. Let d be this distance measured along the axis of the cylinder, the z axis, and d_0 the distance covered along z before the first bounce. N is then equal to the first integer greater than $(L - d_0)/d$. The constancy of d and Φ can be deduced from a drawing like the one shown in Fig. 1. The origin of the coordinate system is the center of the circle of radius R defined by the tube's entrance, r is the distance from the origin at which the ray crosses the entrance plane, θ is the angle that the projection of the ray onto this plane makes with $\mathbf{r}$, and α is the angle the trajectory makes with the z axis. By considering the projection of the trajectory onto the entrance plane, it can be shown that

$$d = 2\frac{\sqrt{R^2 - r^2\sin^2\theta}}{\tan\alpha},$$

$$d_0 = \frac{\sqrt{R^2 - r^2\sin^2\theta} - r\cos\theta}{\tan\alpha},$$

$$\cos\Phi = \frac{\sqrt{R^2 - r^2\sin^2\theta}}{R}\sin\alpha \tag{2}$$

It is assumed that emission is uniform over the area of the entrance disk and that its spectrum is that of a blackbody at temperature T. The transmission coefficient is then given by

$$t = \frac{\int\int\int\int t(r, \theta, \alpha, \lambda)w(r, \alpha, \lambda)drd\theta d\alpha d\lambda}{\int\int\int\int w(r, \alpha, \lambda)drd\theta d\alpha d\lambda} \tag{3}$$

where the weighting function $w(r, \alpha, \lambda) = r\sin 2\alpha\, E_b(\lambda, T)$ and where $E_b(\lambda, T)$ is the spectral emissive power of a blackbody (e.g., Incropera and DeWitt, 1981).

The guide tubes used in the experimental verification of these calculations have a radius $R = 3.35$ cm and are made out of 316 stainless steel, which has an electrical conductivity of about 2×10^6 S/m at 77 K and a relative permeability $\mu/\mu_0 \approx 1.01$ when austenized (Smithells, 1967; Meaden, 1965). The integration ranges were set to r: 0–3.15 cm, α: $0-\pi/2$, λ: 3–250 μm, and θ: $0-\pi$. The fact that the radiation source does not cover the whole of the entrance plane increases the transmission by approximately 1 percent.

Table 1 Theoretical and experimental IR transmission coefficients for 316 stainless steel guide tubes of various lengths (I.D. = 67 mm and $k_e = 2 \times 10^6$ S/m). The 63-mm-dia coaxial source of 300 K blackbody radiation is located at the entrance to the tube.

Theoretical		Experimental			
L (cm)	t (%)	L (cm)	t_A (%)	t_B (%)	t (%)
0.1	99.91±0.02	0.4±0.1	99.5±1.2	98.9±1.1	99.2±0.8
1	98.2±0.2	1.05±0.15	98.5±1.1	98.0±1.1	98.2±0.8
5	90.5±0.2	9.8±0.2	90.2±1.2	89.8±1.1	90.0±0.8
10	82.9±0.2	25.4±0.2	71.3±1.3	71.0±1.3	71.2±0.9
20	70.9±0.2	50.3±0.2	51.7±1.5	51.3±1.6	51.5±1.1
40	54.8±0.1	79.8±0.2	37.5±1.6	36.9±1.6	37.2±1.1
60	44.4±0.1	114.8±0.2	27.1±1.8	26.4±1.8	26.8±1.3
80	37.1±0.1				
100	31.77±0.05				
120	27.73±0.03				
200	18.32±0.01				
300	12.98±0.01				

The integral was evaluated numerically using a standard NAG Library routine (D01FCF) yielding the theoretical results listed in Table 1 and plotted in Fig. 2 as a solid curve.

Experimental Verification With UCN Guide Tubes

A length of honed and electropolished stainless steel tube is sealed at both ends by flanges through which the electrical and vacuum connections are made. Each flange carries on an insulating stem a concentric copper disk of radius r_0 uniformly heated and whose temperature is monitored by two thermistors and one Pt resistor. The disk surfaces facing each other are covered with a fine carborundum powder and painted black to increase their IR emissivity. The evacuated assembly is immersed in liquid nitrogen.

The experiment consists in measuring the electrical power P_e, which must be fed into each heater in order to keep the disks' temperature constant at $T = 300$ K as a function of the distance L between the disks, each of which is acting both as a source and a detector of IR radiation. When the disks are "zero" distance it is only necessary to dissipate a small amount of power P_0 in the heaters. When the disks are so far apart that one does not receive any heat from the other, a maximum amount of power $P_{max} = P_0 + P_s$ must be supplied to the heaters, where $P_s = \epsilon(\pi r_0^2)\sigma T^4$ and ϵ is the emissivity of the black surfaces. In order to keep the radiation and conduction losses P_0

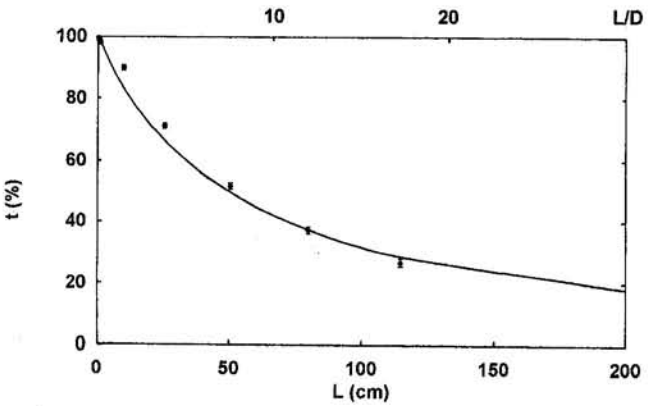

Fig. 2 The calculated (solid curve) and experimental values for the IR transmission of a 67 mm ID stainless steel tube, honed and electropolished, illuminated by a 63 mm diameter coaxial blackbody source at 300 K located at the tube's entrance.

constant throughout the experiment, the disks are permanently assembled on the flanges and the distance between the disks is varied by cutting the tube.

For each disk the value of P_{max} was measured by mounting the flange on a 77 K "cavity" and estimates of P_0, and hence $\epsilon = (P_{max} - P_0)/(\pi r_0^2 \sigma T^4)$, were obtained a posteriori by extrapolation of the $P_e(L)$ curve to $L = 0$.

The existence of a small annular spacing around the disks to prevent thermal contact causes the transmission to be underestimated as only a fraction γ of the transmitted power tP_s impinges on the other disk. An approximate expression for γ with the correct behavior as a function of L is

$$\gamma = \frac{F}{t} + \left(1 - \frac{F}{t}\right)\left(\frac{r_0}{R}\right)^2 \tag{4}$$

where F is the view or shape factor and is defined as the fraction of the radiation leaving one disk and intercepted directly by the other (cf. Incropera and DeWitt, for example). The theoretical transmission values were taken as estimates for the transmission t. The emission and absorption of radiation travelling in the tube by the shiny rear surface of the disks have been neglected.

Taking this correction into account as well as the multiple reflections due to the finite reflectivity $1 - \epsilon$ of the black surfaces, the expression relating the transmission coefficient $t(L)$ to the electric power $P_e(L)$ dissipated in a heater is

$$t(L) = \frac{P_{max} - P_e(L)}{\gamma(P_{max} - P_0 - (1 - \epsilon)[P_e(L) - P_0])} \tag{5}$$

The IR radiation emitted by the tube itself has not been taken into account in this analysis as it represents, at most, $(\frac{77}{300})^4 = 0.5$ percent of the heat input.

The measured values of $t(L)$ are compiled in Table 1. Each disk provides an independent measurement of the transmission, t_A and t_B, respectively, and so their average value t is calculated and plotted with error bars in Fig. 2. An experimental error is calculated for each power measurement $P_e(L)$, taking into account the uncertainty in measuring the voltage applied to the heater and the current flowing through it as well as the uncertainty in determining the average temperature of the disk. In the case of P_{max} there is also a small contribution from the uncertainty in the emissivity of the 77 K cavity, for P_0 a large contribution from the extrapolation procedure and for ϵ a small contribution from the uncertainty in disk area. The overall error calculated for each value of $t(L)$ is dominated by the uncertainties associated with P_0 and the average disk temperature.

The difference between the experimental points and the theoretical curve is significant but it is always less than 8 percent for lengths up to 1.2 m. It can be explained by the combination of the two following opposite tendencies, which were not taken into account in the calculation or in the analysis. The lower transmission observed at longer tube lengths can be attributed to diffuse reflection caused by surface roughness or waviness or to contamination of the surface with a lower reflectivity layer, such as water vapor. For the shorter lengths these effects are less noticeable and so nonideal properties of the emitters, namely forward-peaked emission of a soft spectrum, could contribute to a higher measured transmission. The crude correction implemented to account for the existence of small annuli around the disks will also tend to overestimate the transmission for guide lengths of less than three radii. The first tendency reflects the real properties of the tube's surface, whereas the second one is due to artifacts of this particular experimental method.

Conclusions

The analytical expression derived in this paper (Eq. (3)) yields good estimates for the IR transmission coefficient of straight metal pipes even when the source is large and close to or within the pipe. It was verified experimentally that a 1.5 m length of 67 mm ID stainless steel tube will attenuate by a factor of 5 the radiation emitted by a blackbody at 300 K placed at its entrance. A 90 deg bend in the tube is likely to provide another attenuation factor of 2 (Ohlmann et al., 1958) resulting in an overall reduction in the radiation heat load on the cryostat's window by a factor of 10.

References

Incropera, F. P., and DeWitt, D. P., 1981, *Fundamentals of Heat Transfer*, Wiley, New York.

Jewell, C. I., 1983, "The Interaction of Ultra-Cold Neutrons With Superfluid ^{4}He and a New Possible Super Thermal Ultra-Cold Neutron Source," Ph.D. thesis, University of Lancaster, United Kingdom.

Meaden, G. T., 1965, *Electrical Resistivity of Metals*, Heywood Books Ltd.

Ohlmann, R. C., Richards, P. L., and Tinkham, M., 1958, "Far Infrared Transmission Through Metal Pipes," *Journal of the Optical Society of America*, Vol. 48, pp. 531–533.

Smithells, C. J., 1967, *Metal Reference Book*, 4th ed., Butterworth, United Kingdom.

Stratton, J. A., 1941, *Electromagnetic Theory*, McGraw-Hill, New York.

Flow Boiling Heat Transfer Coefficients of R-134a in a Microfin Tube

A. Singh,[1] M. M. Ohadi,[2] and S. Dessiatoun[2]

Nomenclature

D = inside diameter of tube, mm
Fr_{lo} = Froude number with all flow as liquid = $G^2/(\rho_l g D)$
g = acceleration due to gravity, m/s^2
G = mass flux, kg/m^2·s
ρ_l = density of liquid refrigerant, kg/m^3

Introduction

This paper presents results of an experimental study for forced convection evaporative heat transfer coefficients of R-134a (a replacement for R-12), inside a horizontal microfin tube. Data are reported as a function of parametric values of mass flux, quality, and heat flux in the test section. Results include heat transfer coefficients for the low mass flux levels typically encountered in household refrigerators and certain small-scale commercial evaporators.

Previous work with microfin tubes and R-134a appears to be limited to a study by Eckels and Pate (1991). Because of the difference in experimental apparatus and the operating conditions it was not possible to provide a one-to-one comparison of the present study results with those of Eckels and Pate (1991). However, for selected points where the conditions were close to each other a satisfactory comparison was documented by Ohadi et al. (1994). In a recent study, Thors and Bogart (1994) report results for in-tube evaporation of R-22 with microfin

[1] ADC, Copeland Corporation, 1675 W. Campbell Road, Sidney, OH 45365.

[2] Heat Transfer Enhancement Laboratory, Center for Environmental Energy Engineering, Department of Mechanical Engineering, University of Maryland, College Park, MD 20742.

Contributed by the Heat Transfer Division of THE AMERICAN SOCIETY OF MECHANICAL ENGINEERS. Manuscript received by the Heat Transfer Division November 1994; revision received June 1995. Keywords: Boiling, Evaporation, Heat Exchangers. Associate Technical Editor: R. A. Nelson, Jr.

constant throughout the experiment, the disks are permanently assembled on the flanges and the distance between the disks is varied by cutting the tube.

For each disk the value of P_{max} was measured by mounting the flange on a 77 K "cavity" and estimates of P_0, and hence $\epsilon = (P_{max} - P_0)/(\pi r_0^2 \sigma T^4)$, were obtained a posteriori by extrapolation of the $P_e(L)$ curve to $L = 0$.

The existence of a small annular spacing around the disks to prevent thermal contact causes the transmission to be underestimated as only a fraction γ of the transmitted power tP_s impinges on the other disk. An approximate expression for γ with the correct behavior as a function of L is

$$\gamma = \frac{F}{t} + \left(1 - \frac{F}{t}\right)\left(\frac{r_0}{R}\right)^2 \tag{4}$$

where F is the view or shape factor and is defined as the fraction of the radiation leaving one disk and intercepted directly by the other (cf. Incropera and DeWitt, for example). The theoretical transmission values were taken as estimates for the transmission t. The emission and absorption of radiation travelling in the tube by the shiny rear surface of the disks have been neglected.

Taking this correction into account as well as the multiple reflections due to the finite reflectivity $1 - \epsilon$ of the black surfaces, the expression relating the transmission coefficient $t(L)$ to the electric power $P_e(L)$ dissipated in a heater is

$$t(L) = \frac{P_{max} - P_e(L)}{\gamma(P_{max} - P_0 - (1 - \epsilon)[P_e(L) - P_0])} \tag{5}$$

The IR radiation emitted by the tube itself has not been taken into account in this analysis as it represents, at most, $(\frac{77}{300})^4 = 0.5$ percent of the heat input.

The measured values of $t(L)$ are compiled in Table 1. Each disk provides an independent measurement of the transmission, t_A and t_B, respectively, and so their average value t is calculated and plotted with error bars in Fig. 2. An experimental error is calculated for each power measurement $P_e(L)$, taking into account the uncertainty in measuring the voltage applied to the heater and the current flowing through it as well as the uncertainty in determining the average temperature of the disk. In the case of P_{max} there is also a small contribution from the uncertainty in the emissivity of the 77 K cavity, for P_0 a large contribution from the extrapolation procedure and for ϵ a small contribution from the uncertainty in disk area. The overall error calculated for each value of $t(L)$ is dominated by the uncertainties associated with P_0 and the average disk temperature.

The difference between the experimental points and the theoretical curve is significant but it is always less than 8 percent for lengths up to 1.2 m. It can be explained by the combination of the two following opposite tendencies, which were not taken into account in the calculation or in the analysis. The lower transmission observed at longer tube lengths can be attributed to diffuse reflection caused by surface roughness or waviness or to contamination of the surface with a lower reflectivity layer, such as water vapor. For the shorter lengths these effects are less noticeable and so nonideal properties of the emitters, namely forward-peaked emission of a soft spectrum, could contribute to a higher measured transmission. The crude correction implemented to account for the existence of small annuli around the disks will also tend to overestimate the transmission for guide lengths of less than three radii. The first tendency reflects the real properties of the tube's surface, whereas the second one is due to artifacts of this particular experimental method.

Conclusions

The analytical expression derived in this paper (Eq. (3)) yields good estimates for the IR transmission coefficient of straight metal pipes even when the source is large and close to or within the pipe. It was verified experimentally that a 1.5 m length of 67 mm ID stainless steel tube will attenuate by a factor of 5 the radiation emitted by a blackbody at 300 K placed at its entrance. A 90 deg bend in the tube is likely to provide another attenuation factor of 2 (Ohlmann et al., 1958) resulting in an overall reduction in the radiation heat load on the cryostat's window by a factor of 10.

References

Incropera, F. P., and DeWitt, D. P., 1981, *Fundamentals of Heat Transfer*, Wiley, New York.

Jewell, C. I., 1983, "The Interaction of Ultra-Cold Neutrons With Superfluid ^{4}He and a New Possible Super Thermal Ultra-Cold Neutron Source," Ph.D. thesis, University of Lancaster, United Kingdom.

Meaden, G. T., 1965, *Electrical Resistivity of Metals*, Heywood Books Ltd.

Ohlmann, R. C., Richards, P. L., and Tinkham, M., 1958, "Far Infrared Transmission Through Metal Pipes," *Journal of the Optical Society of America*, Vol. 48, pp. 531–533.

Smithells, C. J., 1967, *Metal Reference Book*, 4th ed., Butterworth, United Kingdom.

Stratton, J. A., 1941, *Electromagnetic Theory*, McGraw-Hill, New York.

Flow Boiling Heat Transfer Coefficients of R-134a in a Microfin Tube

A. Singh,[1] M. M. Ohadi,[2] and S. Dessiatoun[2]

Nomenclature

- D = inside diameter of tube, mm
- Fr_{lo} = Froude number with all flow as liquid = $G^2/(\rho_l g D)$
- g = acceleration due to gravity, m/s^2
- G = mass flux, kg/m^2·s
- ρ_l = density of liquid refrigerant, kg/m^3

Introduction

This paper presents results of an experimental study for forced convection evaporative heat transfer coefficients of R-134a (a replacement for R-12), inside a horizontal microfin tube. Data are reported as a function of parametric values of mass flux, quality, and heat flux in the test section. Results include heat transfer coefficients for the low mass flux levels typically encountered in household refrigerators and certain small-scale commercial evaporators.

Previous work with microfin tubes and R-134a appears to be limited to a study by Eckels and Pate (1991). Because of the difference in experimental apparatus and the operating conditions it was not possible to provide a one-to-one comparison of the present study results with those of Eckels and Pate (1991). However, for selected points where the conditions were close to each other a satisfactory comparison was documented by Ohadi et al. (1994). In a recent study, Thors and Bogart (1994) report results for in-tube evaporation of R-22 with microfin

[1] ADC, Copeland Corporation, 1675 W. Campbell Road, Sidney, OH 45365.

[2] Heat Transfer Enhancement Laboratory, Center for Environmental Energy Engineering, Department of Mechanical Engineering, University of Maryland, College Park, MD 20742.

Contributed by the Heat Transfer Division of THE AMERICAN SOCIETY OF MECHANICAL ENGINEERS. Manuscript received by the Heat Transfer Division November 1994; revision received June 1995. Keywords: Boiling, Evaporation, Heat Exchangers. Associate Technical Editor: R. A. Nelson, Jr.

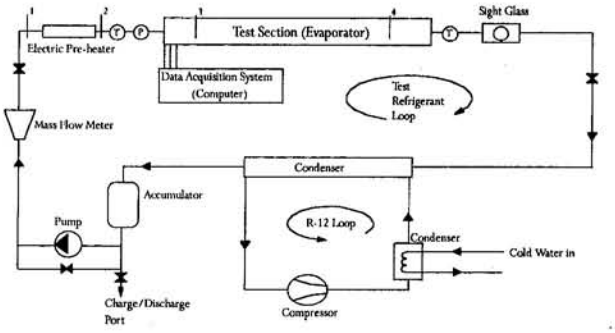

Fig. 1 Schematic of the experimental apparatus

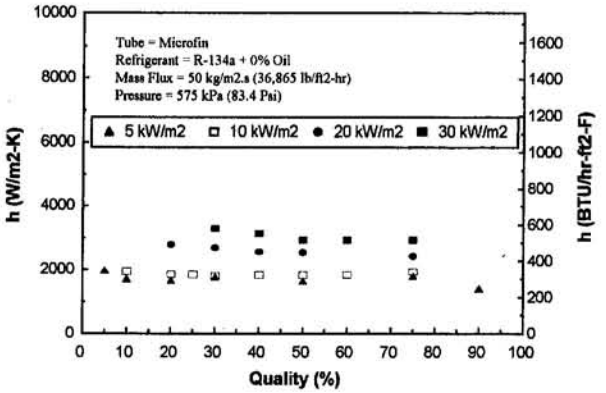

Fig. 3 Variation of heat transfer coefficient with quality at various heat flux levels

tubes. A comprehensive documentation of the literature on microfin tubes can be found from Schlager et al. (1987) and Eckels and Pate (1991).

Experimental Apparatus

The experimental test apparatus used in the present study is schematically shown in Fig. 1. As seen there, the setup consists of two distinct flow loops: (1) the test section refrigerant loop and (2) a condenser cooling loop utilizing R-12. The test section refrigerant loop includes a hermetic oil-free pump, a drier filter, a precision coriolis mass flowmeter, an electrical preheater, the test section, a condenser unit, and an accumulator. The refrigerant flow rate can be controlled by the pump in the range of 20 $kg/m^2 \cdot s$ to 200 $kg/m^2 \cdot s$ (liquid Reynolds number between 1200 and 12,000) and the quality at which the refrigerant enters the test section can be controlled by the electric preheater from subcooled to superheated condition. The test section is a horizontally mounted, microfin copper tube with 12.7 mm (0.5 in.) OD, 60 fins, and 18 deg helix angle. The nominal inside diameter of this tube is 11.78 mm (0.46 in.) with ridge height of 0.3 mm (0.012 in.).

The heat flux required for boiling the refrigerant is provided by an electrical heater wrapped around the test-section tube. The portion of the test section where electrical heating is applied is 495 mm (19.5 in.) long. The wall temperature measurements are done in the middle 305 mm (12 in.) portion of the test section (Fig. 2). All calculations for heat transfer coefficients are based on this test section length so as to minimize the effect of axial heat losses within the test section. The test section instrumentation allows operation up to 30 kW/m^2 of heat flux. The exit end of the test section has a sight glass of almost the same inside diameter as the test section in order to observe the flow patterns. Although the sight glass was not designed to reflect the details of the flow patterns, it served as a good qualitative guide to characterize the flow regimes. The wall temperatures are measured using copper-constantan thermocouples directly soldered on the outside of the tube. Temperatures are measured at four axial locations at equal intervals of 76 mm (3 in.). At each axial location, two thermocouples are placed circumferentially, one at the top and one at the bottom of the tube. The location of thermocouples and exact dimensions of the test section are indicated in Fig. 2. Details of the experimental setup and the procedure can be found from Ohadi et al. (1994).

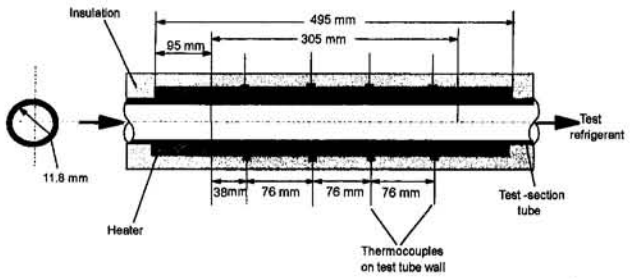

Fig. 2 Schematic of the test section

Results and Discussion

Calculation of the heat transfer coefficient h was based on the following defining equation:

$$h = \frac{Q}{A(T_w - T_{sat})} \tag{1}$$

in which T_w is the tube wall temperature, which is taken as the arithmetic mean of eight thermocouples installed on the test-section wall. Strictly speaking, T_w should be the average inner tube wall temperature. However, simple calculations justified the approximation of taking outside wall temperature as T_w. The temperature T_{sat} is the saturation temperature of the test refrigerant corresponding to the test section pressure. Since the test section was just 305 mm long, the pressure drop in this length in all flow regimes was found to be negligibly small and the test section pressure was assumed to be equal to the pressure at the inlet of the test section. A is the heat transfer area based on the nominal diameter of the test section tube.

The quality calculation for the refrigerant at different locations (see Fig. 1 for state points) in the test-section loop is done by utilizing appropriate energy balance equations. The quality after the preheater is calculated by using the following equations:

$$e_1 = f(T_1, P) \tag{2}$$

$$e_2 = e_1 + \frac{Q_{ph}}{m_r} \tag{3}$$

$$X_2 = f(P, e_2) \tag{4}$$

where e_1 and e_2 are the specific enthalpy of the refrigerant at the preheater inlet and exit, respectively. Having T_1 and P measured, the specific enthalpy can easily be obtained from the corresponding equation of state. Q_{ph} is the heat transferred to the refrigerant by the preheater and m_r is the mass flow rate of the refrigerant. It is assumed that the pressure drop across the preheater is negligible. The quality of the refrigerant at the test section entrance X_3 and exit X_4 can be obtained once the heat input to the test section Q_e is known. The average test-section quality X_{avg} is calculated by taking the arithmetic mean of X_3 and X_4. The maximum uncertainty in heat flux measurement is ±4.6 percent. The maximum uncertainty in heat transfer coefficient and quality is ±4.8 and ±4.7 percent, respectively.

Experiments were conducted at 575 kPa (83.4 psi) pressure. The saturation temperature corresponding to this pressure is

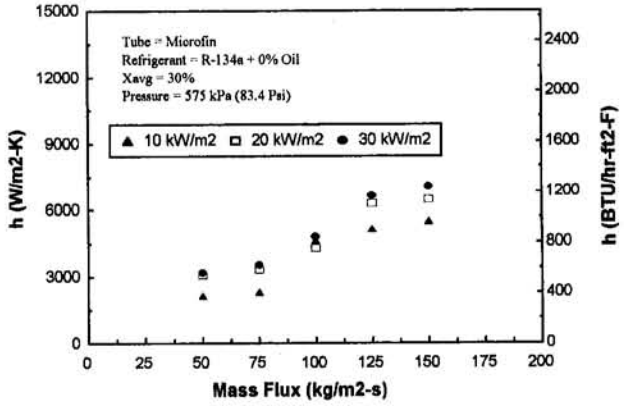

Fig. 4 Variation of heat transfer coefficient with mass flux at different heat flux levels

20.15°C (68.3°F). This operating condition was selected so that the heat losses to the surroundings were kept minimum. Figure 3 shows the variation of heat transfer coefficient with quality at various heat flux levels for a mass flux of 50 $kg/m^2 \cdot s$. At this relatively low mass flux, the sight glass downstream of the test section indicated the flow pattern was predominantly wavy–stratified. For such a regime the effect of quality on the heat transfer coefficient should be insignificant. This is because at low mass flow rates, the convective boiling is less dominant than the nucleate boiling and nucleate boiling does not appear to get suppressed even at higher qualities. From the figure it can also be observed that as the heat flux increases, the heat transfer coefficient increases due to the increase in nucleate boiling dynamics associated with a higher heat flux.

Figure 4 shows the variation of the heat transfer coefficient with mass flux at an average quality of 30 percent for different heat flux levels. As expected, with an increase in the mass flux heat transfer coefficient increases for the range of heat fluxes examined here. It is also seen that for a given mass flux, a higher heat flux results in a higher heat transfer coefficient. Note that for a mass flux larger than 100 $kg/m^2 \cdot s$, the heat transfer coefficient experiences a marked increase. This indicates the influence of stratification at low flow rates in horizontal tubes. The visual observation of the flow through the sight glass indicated that for mass fluxes less than 100 $kg/m^2 \cdot s$, the flow was predominantly stratified, but as the mass flux increased the flow became annular. The 100 $kg/m^2 \cdot s$ mass flux represents the transition value from stratified flow to annular for the microfin tube tested here and corresponds to *all flow liquid* Froude number (Fr_{lo}) of 0.058. This compares to Fr_{lo} of 0.04 value predicted by Shah (1982) and Kandlikar (1990) for horizontal smooth tubes. However, it has been described in a recent publication (Kattan et al., 1995) that the transition from stratified to unstratified flow may not depend solely on Fr_{lo}.

References

Eckels, S. J., and Pate, M. B., 1991, "Evaporation and Condensation of HCFC-134a and CFC-12 in a Smooth Tube and a Micro-fin Tube," *ASHRAE Transactions,* Vol. 97, Part 2, pp. 71–81.

Kandlikar, S. G., 1990, "A General Correlation for Saturated Two-Phase Flow Boiling Heat Transfer Inside Horizontal and Vertical Tubes," ASME JOURNAL OF HEAT TRANSFER, Vol. 112, pp. 219–228.

Kattan, N., Thome, J. R., and Favrat, D., 1995, "R-502 and Two Near-Azeotropic Alternatives—Part II: Two-Phase Flow Patterns," *ASHRAE Transactions,* Vol. 101, Pt. 1, in press.

Manwell, S. P., and Bergles, A. E., 1990, "Gas–Liquid Flow Patterns in Refrigerant–Oil Mixtures," *ASHRAE Transactions,* Vol. 96, Part 2, pp. 456–464.

Ohadi, M. M., Dessiatoun, S., Singh, A., Cheung, K., Salehi, M., and Blanford, M., 1994, "EHD-Enhanced Boiling/Condensation of Alternate Refrigerants," Quarterly Progress Report Nos. 4 & 5, DOE Grant No. DE-FG02-93CE23803.A000, Oct.

Schlager, L. M., Bergles, A. E., and Pate, M. B., 1987, "A Survey of Refrigerant Heat Transfer and Pressure Drop Emphasizing Oil Effects and In-Tube Augmentation," *ASHRAE Transactions,* Vol. 93, Part 1, pp. 392–416.

Shah, M. M., 1982, "Chart Correlation for Saturated Boiling Heat Transfer: Equations and Further Study," *ASHRAE Transactions,* Vol. 88, Part 1, pp. 185–196.

Thors, P., and Bogart, J., 1994, "In-Tube Evaporation of HCFC-22 With Enhanced Tubes," *J. of Enhanced Heat Transfer,* Vol. 1, No. 4, pp. 365–377.

Experimental Study of Electrohydrodynamically Augmented Condensation Heat Transfer on a Smooth and an Enhanced Tube

M. Wawzyniak[1] and J. Seyed-Yagoobi[1]

Introduction

The enhancement of condensation heat transfer is of crucial importance to many industries, including the HVAC, power, process, and aerospace industries. A variety of enhancement techniques have been researched and implemented to a limited range of industrial applications. These techniques are commonly referred to as passive and active means of condensation heat transfer enhancement.

The electrohydrodynamically (EHD) enhanced condenser is still considered a rather exotic candidate in the field. Nevertheless, the recent progress made indicates that this technique will find its way in the market place in the near future. With this active technique, the extraction of the performance restricting liquid from the condensation surface can be realized by nonuniform electric fields. The EHD enhancement of condensation heat transfer features several distinct advantages over conventional methods. Surface coating with nonwetting substances, for example Teflon or noble metals in steam condensers, is not applicable for refrigerants due to their low surface tension. Another important benefit is the possibility of varying the condensation heat transfer by simply changing the applied voltage. Furthermore, the EHD condenser contains no moving parts and the electric power input is negligible.

EHD enhancement of condensation heat transfer has been studied only over the past three decades. Velkoff and Miller (1965), Choi (1968), Didkovsky and Bologa (1981), Cooper and Allen (1984), Yabe et al. (1985), and Trommelmans and Berghmans (1986) are among a few others who investigated this topic.

The work conducted in the past dealt exclusively with the EHD enhancement of condensation heat transfer on smooth surfaces. However, a variety of enhanced tubes has been developed that can passively increase the condensation heat transfer coefficient by several hundred percent. This paper presents the results of an EHD-extraction phenomenon study to enhance condensation heat transfer using a smooth and an enhanced tube.

[1] Department of Mechanical Engineering, Texas A&M University, College Station, TX 77843-3123.

Contributed by the Heat Transfer Division of THE AMERICAN SOCIETY OF MECHANICAL ENGINEERS. Manuscript received by the Heat Transfer Division April 1995; revision received February 1996. Keywords: Augmentation and Enhancement, Condensation, Heat Exchangers. Associate Technical Editor: T. J. Rabas.

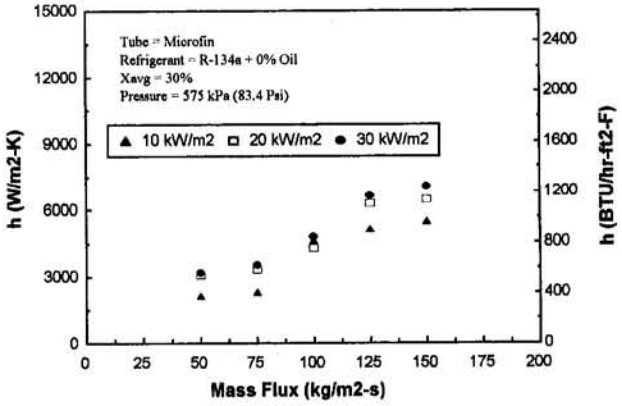

Fig. 4 Variation of heat transfer coefficient with mass flux at different heat flux levels

20.15°C (68.3°F). This operating condition was selected so that the heat losses to the surroundings were kept minimum. Figure 3 shows the variation of heat transfer coefficient with quality at various heat flux levels for a mass flux of 50 $kg/m^2 \cdot s$. At this relatively low mass flux, the sight glass downstream of the test section indicated the flow pattern was predominantly wavy–stratified. For such a regime the effect of quality on the heat transfer coefficient should be insignificant. This is because at low mass flow rates, the convective boiling is less dominant than the nucleate boiling and nucleate boiling does not appear to get suppressed even at higher qualities. From the figure it can also be observed that as the heat flux increases, the heat transfer coefficient increases due to the increase in nucleate boiling dynamics associated with a higher heat flux.

Figure 4 shows the variation of the heat transfer coefficient with mass flux at an average quality of 30 percent for different heat flux levels. As expected, with an increase in the mass flux heat transfer coefficient increases for the range of heat fluxes examined here. It is also seen that for a given mass flux, a higher heat flux results in a higher heat transfer coefficient. Note that for a mass flux larger than 100 $kg/m^2 \cdot s$, the heat transfer coefficient experiences a marked increase. This indicates the influence of stratification at low flow rates in horizontal tubes. The visual observation of the flow through the sight glass indicated that for mass fluxes less than 100 $kg/m^2 \cdot s$, the flow was predominantly stratified, but as the mass flux increased the flow became annular. The 100 $kg/m^2 \cdot s$ mass flux represents the transition value from stratified flow to annular for the microfin tube tested here and corresponds to *all flow liquid* Froude number (Fr_{lo}) of 0.058. This compares to Fr_{lo} of 0.04 value predicted by Shah (1982) and Kandlikar (1990) for horizontal smooth tubes. However, it has been described in a recent publication (Kattan et al., 1995) that the transition from stratified to unstratified flow may not depend solely on Fr_{lo}.

References

Eckels, S. J., and Pate, M. B., 1991, "Evaporation and Condensation of HCFC-134a and CFC-12 in a Smooth Tube and a Micro-fin Tube," *ASHRAE Transactions,* Vol. 97, Part 2, pp. 71–81.

Kandlikar, S. G., 1990, "A General Correlation for Saturated Two-Phase Flow Boiling Heat Transfer Inside Horizontal and Vertical Tubes," ASME JOURNAL OF HEAT TRANSFER, Vol. 112, pp. 219–228.

Kattan, N., Thome, J. R., and Favrat, D., 1995, "R-502 and Two Near-Azeotropic Alternatives—Part II: Two-Phase Flow Patterns," *ASHRAE Transactions,* Vol. 101, Pt. 1, in press.

Manwell, S. P., and Bergles, A. E., 1990, "Gas–Liquid Flow Patterns in Refrigerant–Oil Mixtures," *ASHRAE Transactions,* Vol. 96, Part 2, pp. 456–464.

Ohadi, M. M., Dessiatoun, S., Singh, A., Cheung, K., Salehi, M., and Blanford, M., 1994, "EHD-Enhanced Boiling/Condensation of Alternate Refrigerants," Quarterly Progress Report Nos. 4 & 5, DOE Grant No. DE-FG02-93CE23803.A000, Oct.

Schlager, L. M., Bergles, A. E., and Pate, M. B., 1987, "A Survey of Refrigerant Heat Transfer and Pressure Drop Emphasizing Oil Effects and In-Tube Augmentation," *ASHRAE Transactions,* Vol. 93, Part 1, pp. 392–416.

Shah, M. M., 1982, "Chart Correlation for Saturated Boiling Heat Transfer: Equations and Further Study," *ASHRAE Transactions,* Vol. 88, Part 1, pp. 185–196.

Thors, P., and Bogart, J., 1994, "In-Tube Evaporation of HCFC-22 With Enhanced Tubes," *J. of Enhanced Heat Transfer,* Vol. 1, No. 4, pp. 365–377.

Experimental Study of Electrohydrodynamically Augmented Condensation Heat Transfer on a Smooth and an Enhanced Tube

M. Wawzyniak[1] and J. Seyed-Yagoobi[1]

Introduction

The enhancement of condensation heat transfer is of crucial importance to many industries, including the HVAC, power, process, and aerospace industries. A variety of enhancement techniques have been researched and implemented to a limited range of industrial applications. These techniques are commonly referred to as passive and active means of condensation heat transfer enhancement.

The electrohydrodynamically (EHD) enhanced condenser is still considered a rather exotic candidate in the field. Nevertheless, the recent progress made indicates that this technique will find its way in the market place in the near future. With this active technique, the extraction of the performance restricting liquid from the condensation surface can be realized by nonuniform electric fields. The EHD enhancement of condensation heat transfer features several distinct advantages over conventional methods. Surface coating with nonwetting substances, for example Teflon or noble metals in steam condensers, is not applicable for refrigerants due to their low surface tension. Another important benefit is the possibility of varying the condensation heat transfer by simply changing the applied voltage. Furthermore, the EHD condenser contains no moving parts and the electric power input is negligible.

EHD enhancement of condensation heat transfer has been studied only over the past three decades. Velkoff and Miller (1965), Choi (1968), Didkovsky and Bologa (1981), Cooper and Allen (1984), Yabe et al. (1985), and Trommelmans and Berghmans (1986) are among a few others who investigated this topic.

The work conducted in the past dealt exclusively with the EHD enhancement of condensation heat transfer on smooth surfaces. However, a variety of enhanced tubes has been developed that can passively increase the condensation heat transfer coefficient by several hundred percent. This paper presents the results of an EHD-extraction phenomenon study to enhance condensation heat transfer using a smooth and an enhanced tube.

[1] Department of Mechanical Engineering, Texas A&M University, College Station, TX 77843-3123.

Contributed by the Heat Transfer Division of THE AMERICAN SOCIETY OF MECHANICAL ENGINEERS. Manuscript received by the Heat Transfer Division April 1995; revision received February 1996. Keywords: Augmentation and Enhancement, Condensation, Heat Exchangers. Associate Technical Editor: T. J. Rabas.

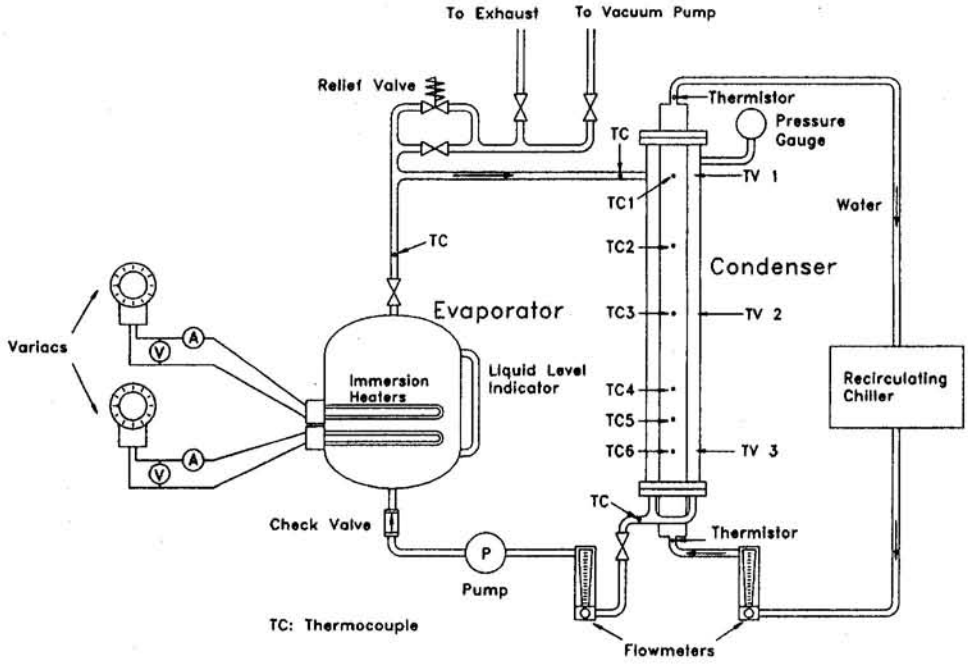

Fig. 1 Schematic of experimental apparatus

Experimental Setup

An experimental apparatus was designed and built to study the EHD enhanced condensation heat transfer in a vertical configuration. Details regarding the experimental setup can be found from Wawzyniak (1993). The main loop consists of an evaporator, the vertical condenser, a flow meter, and a pump as shown in Fig. 1. The acrylic shell of the condenser measures 1000 mm in length, 76.2 mm (3 in.) ID, and 88.9 mm ($3\frac{1}{2}$ in.) OD. Two 1 kW immersion heaters are utilized in the evaporator. To prevent heat losses, the entire main loop including evaporator and condenser is insulated with fiberglass. The cooling loop includes a recirculating chiller, a flow meter, and the condensation tube. The chiller is capable of removing 4.5 kW heat at a fluid temperature of 20°C. The condensation surface temperature is measured by 12 T-type (special limits of error) thermocouples. The thermocouples are soldered into the tube wall. The thermocouples are ground down to be flush with the condensation surface. The thermocouples are located at 100 mm, 300 mm, 500 mm, 700 mm, 800 mm, and 900 mm, respectively, measured from the top of the condenser. At each height, two thermocouples are arranged 180 deg apart around the circumference.

A 50 kV-5 mA DC power supply is employed to generate the required electric potential. The condenser tube, the rig containing the condenser, and the power supply are grounded through a common terminal board. Three acrylic spacers are employed to hold four brass rods (4.76 mm diameter, 915 mm long) over the condensation surface. The electrodes are soldered to these vertical rods and a high voltage cable is connected to these supporting rods.

Refrigerant-113 is used as working fluid. It was chosen because of its well-established properties (*ASHRAE Handbook, Fundamentals,* 1993) and because it is fairly easy to handle. It has a relatively high boiling point and is compatible with a wide array of common materials. However, R-113 is being phased out due to its high ozone depletion potential and global warming potential. Nevertheless, Sunada et al. (1991) showed that for EHD pseudo-dropwise condensation even better enhancement ratios can be reached when using R-123, an environmentally much friendlier substance. The EHD phenomena can be realized with most dielectric fluids, including various refrigerants. The two electric properties, conductivity and permittivity, of a working fluid are the most critical properties directly affecting the EHD phenomena. The electric conductivity and electric permittivity of pure working fluid in this study were measured at 6.5×10^{-12} S/m and 2.3×10^{-11} F/m, respectively, at atmospheric pressure and 21°C.

Prior to each test, the system was evacuated by means of a vacuum pump to remove the noncondensable gases. The tests were conducted at a constant vapor pressure slightly above atmospheric (106.80 kPa). A change in the heat transfer coefficient due to the EHD-extraction phenomenon results in a change of the system pressure, which is then compensated for by varying the heater input.

The electrode design utilized during this study follows the one suggested by Yabe et al. (1985). The electrodes are made from brass rods (2.38 mm diameter), which are cold rolled to obtain a rectangular cross section of 1.4 mm by 3 mm. This procedure results in a more effective electrode with rounded edges, thus minimizing the possibility of electric discharge. The extraction section, characterized by a constant electrode-tube gap of 1.6 mm and an angle of 5 deg with the horizontal direction, is set over one pitch (see Fig. 2). A total of eight electrodes is then built into the condenser to realize the extraction phenomenon at various locations. The electrodes are spaced evenly over the length of the supporting rods at a distance of 110 mm between them.

One smooth copper tube and one externally enhanced copper tube (Turbo CII®), both having an outer diameter of 19.05 mm, were tested. The enhanced tube is manufactured by a cold forming process followed by a serrating operation. Thus, closely packed fins with a rectangular cross section of approximately 0.3 mm × 0.5 mm and a length of 0.5 mm are created.

The method of Kline and McClintock (1953) was used to determine the uncertainty of the calculated average condensation heat transfer coefficients. For the smooth tube an uncertainty between 5.71 and 8.07 percent has to be considered. The higher heat fluxes encountered with the enhanced tube result in a smaller vapor-wall temperature difference and thus, an uncertainty in the condensation heat transfer coefficient ranging from 5.86 to 22.53 percent with an average value of 9.86 percent is found.

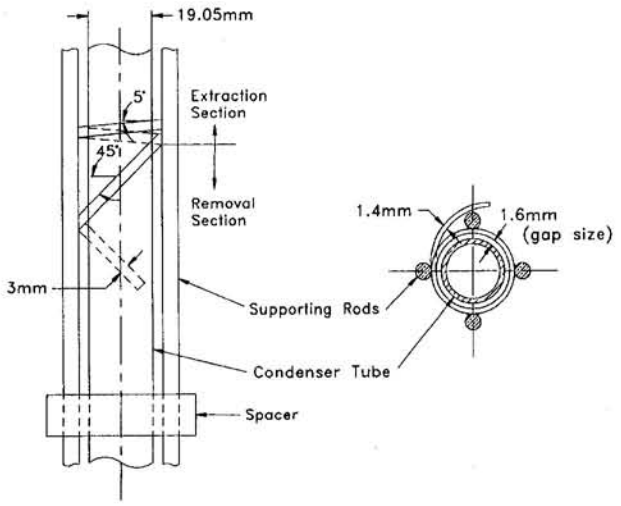

Fig. 2 Electrode design

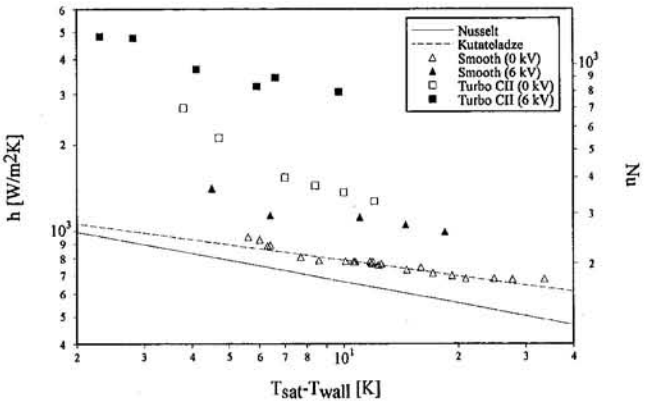

Fig. 3 Comparison of the condensation heat transfer coefficient as function of the temperature differences for tubes both with and without EHD

Results

The increase in the coolant temperature was less than 3°C over the entire length of the condenser for all cases. Hence, the heat flux can be assumed approximately uniform over the condenser tube surface. The local condensation heat transfer coefficient can then be determined by dividing the heat flux by the vapor-tube surface temperature difference at a given vertical location. The condenser tube surface temperature is obtained by averaging the two circumferential surface temperatures measured at one vertical location. The average condensation heat transfer coefficient can then be computed by integrating the local condensation heat transfer coefficients along the length of the condenser. The results are given in terms of the average condensation heat transfer coefficient and Nusselt number, which is defined based on the outside diameter of the condenser tube.

In this study, the film Reynolds number ranges from 200 to 1250, thus indicating that the condensation occurs in the wavy laminar regime. Tests were conducted with and without the electrode setup in place to investigate whether the electrode spacers might act as skirts stripping the liquid from the tube, thus causing an increase in the heat transfer coefficient. The results without EHD enhancement, with and without the electrode setup installed, were identical, indicating that the spacers have no impact on the results.

Initially, data were taken at voltages of 0, 4, and 6 kV. These values were selected because no significant enhancement was obtained below 4 kV, and for voltages exceeding 6 kV electric breakdown occurred. A comparison between the smooth and enhanced tube with and without EHD is given in Fig. 3. The data at 4 kV are not included in this figure for reasons of clarity. Without EHD, the condensation heat transfer coefficient of the Turbo CII® tube is 2.06 times higher than the heat transfer coefficient for the smooth tube at a temperature difference of 6°C. The enhancement ratio reduces to 1.75 for a temperature difference of 10°C. The condensation heat transfer coefficient realized by combining EHD and the Turbo CII® tube is approximately 4 times as high as for the smooth tube without EHD over the entire range of temperature difference. However, Fig. 3 also shows that for low temperature differences (<4°C) a relatively high enhancement can be achieved by employing the Turbo CII® alone. As the benefit of the Turbo CII® tube decreases with higher temperature differences, the importance of the EHD enhancement becomes apparent. For reasons of verification, the experimental data are compared to the Nusselt solution for laminar condensation (Incropera and De Witt, 1990) and a well-established correlation by Kutateladze (1963) for wavy laminar condensation. The experimental data without the EHD effect compare favorably to the Kutateladze correlation due to the condensate film flow regime.

The experimental data in terms of the film Reynolds number and heat flux are presented in Fig. 4. A correlation by Labuntsov (1957) for turbulent film condensation is included to illustrate the flow regime. From the figure, it can be deduced that the enhancement ratios for a given Reynolds number follow the same trend as for a given temperature difference, i.e., they decrease with higher Reynolds numbers for the smooth tube and increase for the Turbo CII® tube. By combining EHD and the Turbo CII® tube, a 6.1-fold enhancement is obtained over the tested range of film Reynolds number when the data for the smooth tube without EHD are used as the base case.

Figure 4 also emphasizes that with a Turbo CII® tube the EHD-extraction phenomenon is realized more effectively than with a smooth tube. The reason for this can be found in the tube surface geometry. The fins of the Turbo CII® tube create an electric field with high localized nonuniformities. The electric field created with a smooth surface, on the other hand, is relatively uniform directly at the tube surface. The body force density due to the electric field acting on the condensate is given as

$$\vec{f}_e = \rho_e \vec{E} - \frac{1}{2}\vec{E}^2 \nabla \epsilon + \frac{1}{2}\nabla\left[\vec{E}^2 \rho \left(\frac{\partial \epsilon}{\partial \rho}\right)\right],$$

where ρ_e, E, ϵ, and ρ are electric charge density, electric field

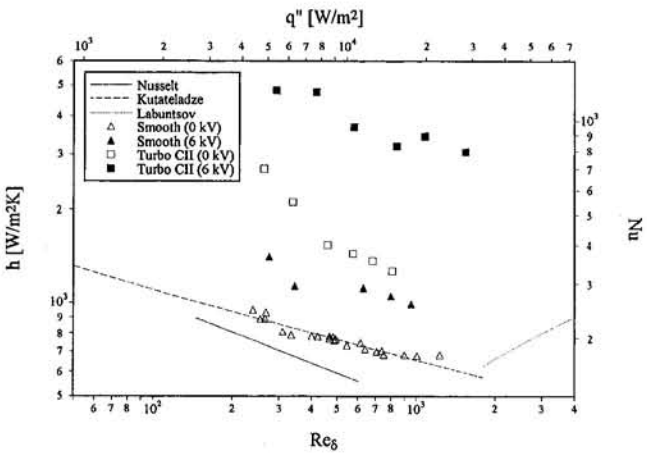

Fig. 4 Comparison of the condensation heat transfer coefficient versus film Reynolds number for tubes both with and without EHD

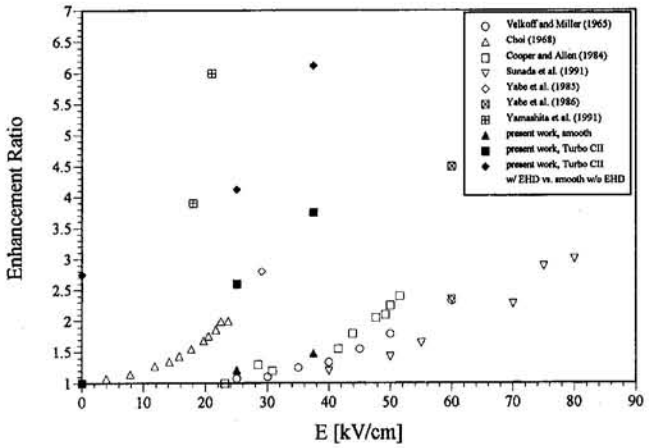

Fig. 5 Comparison to previous studies

strength, electric permittivity, and fluid density, respectively. Since no free charges are generated or introduced for the EHD-extraction phenomenon, the Coulomb force, which is the first term in the equation given above, is negligible. The second term, the dielectrophoretic force, describes the force due to spatial changes in the electric permittivity ϵ. Due to the drastic change of the electric permittivity across the liquid–vapor interface, this term in conjunction with the last term will play the major role for the discussed situation. The last term in this equation, called the electrostriction term, quantifies the force created due to the inhomogeneity of the electric field. For the electrode design at hand—a narrow electrode placed over a large surface—this term will be of importance regardless of the surface geometry. Using the Turbo CII® tube, however, additional nonuniformities in the electric field distribution are generated at the condensation surface, and thus the electrostriction force is increased. Furthermore, it is observed that the setup is less prone to electric discharge from the electrode when the Turbo CII® tube is utilized. Note that electric breakdown will always be initiated at the energized electrode. Since the electrode-tube gap is the same for the two tubes, the electric field distribution around the energized electrode remains nearly unchanged. Hence, the initiation of breakdown is not affected by the local geometry of the grounded tube.

Finally, Fig. 5 is included for the purpose of providing a general idea how this work compares to previous studies. It has to be pointed out that these studies involved various working fluids, different surfaces, and distinct testing procedures. The enhancement mechanism was the EHD-extraction phenomenon, except for Sunada et al. (1991), which dealt with EHD pseudo-dropwise condensation, and Yabe et al. (1986) and Yamashita et al. (1991), which studied the combination of the EHD extraction phenomenon and EHD pseudo-dropwise condensation. However, all previous studies were concerned with smooth condensation surfaces. Figure 5 gives the enhancement ratio (condensation heat transfer coefficient obtained with EHD over condensation heat transfer coefficient without EHD) as a function of the applied electric field strength. Maximum results at a given film Reynolds number are given from this study. The combination of the EHD extraction phenomenon and the Turbo CII® tube yields results that go far beyond that of previous studies based on the EHD extraction phenomenon using smooth tubes. Studies dealing with EHD pseudo-dropwise condensation using smooth tubes, however, produced enhancement ratios similar to those presented in this study. Nevertheless, it must be noted that the electrode designs necessary to initiate EHD pseudo-dropwise condensation can be expected to increase the pressure drop drastically across the condenser.

The electric current does not exceed 40 μA for all conditions considered in this study. Thus, the electric power amounts to less than 0.24 W, corresponding to less than 0.08 percent of the exchanged heat.

Acknowledgments

This work was supported by the NASA Johnson Space Center. The enhanced tube was provided by Wolverine Tube, Inc.

References

ASHRAE, 1993, *1993 ASHRAE Handbook: Fundamentals,* American Society of Heating, Refrigerating and Air-Conditioning Engineers, Inc., Atlanta, GA.

Choi, H. Y., 1968, "Electrohydrodynamic Condensation Heat Transfer," ASME JOURNAL OF HEAT TRANSFER, Vol. 90, pp. 98–102.

Cooper, P., and Allen, P. H. G., 1984, "The Potential of Electrically Enhanced Condensers," *Proc. 2nd International Symposium on the Large Scale Applications of Heat Pumps,* York, United Kingdom, Sept., pp. 295–309.

Didkovsky, A. B., and Bologa, M. K., 1981, "Vapour Film Condensation Heat Transfer and Hydrodynamics Under the Influence of an Electric Field," *International Journal of Heat and Mass Transfer,* Vol. 24, No. 5, pp. 811–819.

Incropera, F. P., and De Witt, D. P., 1990, *Fundamentals of Heat and Mass Transfer,* 3rd ed., Wiley, New York.

Kline, S. J., and McClintock, F. A., 1953, "Describing Uncertainties in Single-Sample Experiments," *Mechanical Engineering,* Vol. 75, Jan., pp. 3–8.

Kutateladze, S. S., 1963, *Fundamentals of Heat Transfer,* 2nd ed., Academic Press, New York.

Labuntsov, D. A., 1957, "Heat Transfer in Film Condensation of Pure Steam on Vertical Surfaces and Horizontal Tubes," *Teploenergetika,* Vol. 4, pp. 72.

Sunada, K., Yabe, A., Taketani, T., and Yoshizawa, Y., 1991, "Experimental Study of EHD Pseudo-Dropwise Condensation," *Proc. 3rd ASME/JSME Thermal Engineering Joint Conference,* Reno, NV. Mar.

Trommelmans, J., and Berghmans, J., 1986, "Influence of Electric Fields on Condensation Heat Transfer of Nonconducting Fluids on Horizontal Tubes," *Proc. 8th International Heat Transfer Conference,* Vol. 6, pp. 2969–2974.

Velkoff, H. R., and Miller, J. H., 1965, "Condensation of Vapor on a Vertical Plate With a Transverse Electrostatic Field," ASME JOURNAL OF HEAT TRANSFER, Vol. 87, pp. 197–201.

Wawzyniak, M., 1993, "Electrohydrodynamically Enhanced Condensation Heat Transfer," M. S. Thesis, Department of Mechanical Engineering, Texas A&M University, College Station, TX.

Yabe, A., Taketani, T., Kikuchi, K., Mori, Y., and Hijikata, K., 1985, "Augmentation of Condensation Heat Transfer Around Vertical Cooled Tubes Provided With Helical Wire Electrodes by Applying Nonuniform Electric Fields," *Proc. International Symposium on Heat Transfer,* Peking, China, Oct., pp. 812–819.

Yabe, A., Taketani, T., Kikuchi, K., and Maki, H., 1986, "Augmentation of Condensation Heat Transfer by Applying Electro-Hydro-Dynamic Pseudo-Dropwise Condensation," *Proc. 8th International Heat Transfer Conference,* Vol. 6, pp. 2957–2962.

Yamashita, K., Kumagai, M., Sekita, S., Yabe, A., Taketani, T., and Kikuchi, K., 1991, "Heat Transfer Characteristics on an EHD Condenser," *Proc. 3rd ASME/JSME Thermal Engineering Joint Conference,* Reno, NV, Mar., pp. 61–67.

Non-Darcy Effects in Natural Convection Heat Transfer in a Vertical Porous Annulus

V. Dharma Rao,[1,3] S. V. Naidu,[1,3] and P. K. Sarma[2,3]

Nomenclature

b = inertial resistance coefficient, m

C_m, C_f = specific heats of medium and fluid, respectively, J kg^{-1} K^{-1}

[1] Chemical Engineering Department.

[2] Mechanical Engineering Department.

[3] Andhra University, Visakhapatnam-530 003, India.

Contributed by the Heat Transfer Division of THE AMERICAN SOCIETY OF MECHANICAL ENGINEERS. Manuscript received by the Heat Transfer Division March 1995; revision received January 1996. Keywords: Enclosure Flows, Natural Convection, Porous Media. Associate Technical Editor: K. Vafai.

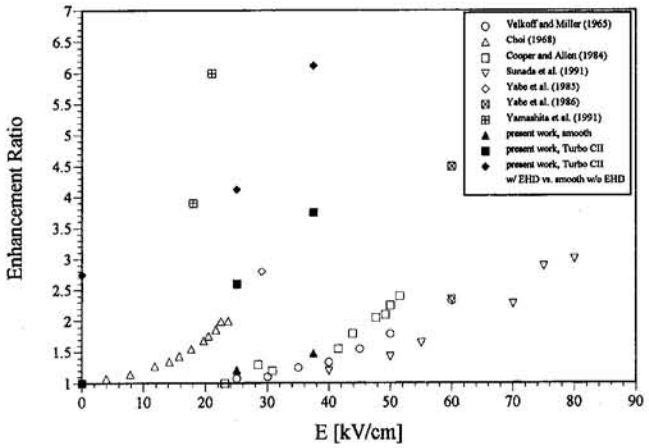

Fig. 5 Comparison to previous studies

strength, electric permittivity, and fluid density, respectively. Since no free charges are generated or introduced for the EHD-extraction phenomenon, the Coulomb force, which is the first term in the equation given above, is negligible. The second term, the dielectrophoretic force, describes the force due to spatial changes in the electric permittivity ϵ. Due to the drastic change of the electric permittivity across the liquid–vapor interface, this term in conjunction with the last term will play the major role for the discussed situation. The last term in this equation, called the electrostriction term, quantifies the force created due to the inhomogeneity of the electric field. For the electrode design at hand—a narrow electrode placed over a large surface—this term will be of importance regardless of the surface geometry. Using the Turbo CII® tube, however, additional nonuniformities in the electric field distribution are generated at the condensation surface, and thus the electrostriction force is increased. Furthermore, it is observed that the setup is less prone to electric discharge from the electrode when the Turbo CII® tube is utilized. Note that electric breakdown will always be initiated at the energized electrode. Since the electrode-tube gap is the same for the two tubes, the electric field distribution around the energized electrode remains nearly unchanged. Hence, the initiation of breakdown is not affected by the local geometry of the grounded tube.

Finally, Fig. 5 is included for the purpose of providing a general idea how this work compares to previous studies. It has to be pointed out that these studies involved various working fluids, different surfaces, and distinct testing procedures. The enhancement mechanism was the EHD-extraction phenomenon, except for Sunada et al. (1991), which dealt with EHD pseudo-dropwise condensation, and Yabe et al. (1986) and Yamashita et al. (1991), which studied the combination of the EHD extraction phenomenon and EHD pseudo-dropwise condensation. However, all previous studies were concerned with smooth condensation surfaces. Figure 5 gives the enhancement ratio (condensation heat transfer coefficient obtained with EHD over condensation heat transfer coefficient without EHD) as a function of the applied electric field strength. Maximum results at a given film Reynolds number are given from this study. The combination of the EHD extraction phenomenon and the Turbo CII® tube yields results that go far beyond that of previous studies based on the EHD extraction phenomenon using smooth tubes. Studies dealing with EHD pseudo-dropwise condensation using smooth tubes, however, produced enhancement ratios similar to those presented in this study. Nevertheless, it must be noted that the electrode designs necessary to initiate EHD pseudo-dropwise condensation can be expected to increase the pressure drop drastically across the condenser.

The electric current does not exceed 40 μA for all conditions considered in this study. Thus, the electric power amounts to less than 0.24 W, corresponding to less than 0.08 percent of the exchanged heat.

Acknowledgments

This work was supported by the NASA Johnson Space Center. The enhanced tube was provided by Wolverine Tube, Inc.

References

ASHRAE, 1993, *1993 ASHRAE Handbook: Fundamentals,* American Society of Heating, Refrigerating and Air-Conditioning Engineers, Inc., Atlanta, GA.

Choi, H. Y., 1968, "Electrohydrodynamic Condensation Heat Transfer," ASME JOURNAL OF HEAT TRANSFER, Vol. 90, pp. 98–102.

Cooper, P., and Allen, P. H. G., 1984, "The Potential of Electrically Enhanced Condensers," *Proc. 2nd International Symposium on the Large Scale Applications of Heat Pumps,* York, United Kingdom, Sept., pp. 295–309.

Didkovsky, A. B., and Bologa, M. K., 1981, "Vapour Film Condensation Heat Transfer and Hydrodynamics Under the Influence of an Electric Field," *International Journal of Heat and Mass Transfer,* Vol. 24, No. 5, pp. 811–819.

Incropera, F. P., and De Witt, D. P., 1990, *Fundamentals of Heat and Mass Transfer,* 3rd ed., Wiley, New York.

Kline, S. J., and McClintock, F. A., 1953, "Describing Uncertainties in Single-Sample Experiments," *Mechanical Engineering,* Vol. 75, Jan., pp. 3–8.

Kutateladze, S. S., 1963, *Fundamentals of Heat Transfer,* 2nd ed., Academic Press, New York.

Labuntsov, D. A., 1957, "Heat Transfer in Film Condensation of Pure Steam on Vertical Surfaces and Horizontal Tubes," *Teploenergetika,* Vol. 4, pp. 72.

Sunada, K., Yabe, A., Taketani, T., and Yoshizawa, Y., 1991, "Experimental Study of EHD Pseudo-Dropwise Condensation," *Proc. 3rd ASME/JSME Thermal Engineering Joint Conference,* Reno, NV. Mar.

Trommelmans, J., and Berghmans, J., 1986, "Influence of Electric Fields on Condensation Heat Transfer of Nonconducting Fluids on Horizontal Tubes," *Proc. 8th International Heat Transfer Conference,* Vol. 6, pp. 2969–2974.

Velkoff, H. R., and Miller, J. H., 1965, "Condensation of Vapor on a Vertical Plate With a Transverse Electrostatic Field," ASME JOURNAL OF HEAT TRANSFER, Vol. 87, pp. 197–201.

Wawzyniak, M., 1993, "Electrohydrodynamically Enhanced Condensation Heat Transfer," M. S. Thesis, Department of Mechanical Engineering, Texas A&M University, College Station, TX.

Yabe, A., Taketani, T., Kikuchi, K., Mori, Y., and Hijikata, K., 1985, "Augmentation of Condensation Heat Transfer Around Vertical Cooled Tubes Provided With Helical Wire Electrodes by Applying Nonuniform Electric Fields," *Proc. International Symposium on Heat Transfer,* Peking, China, Oct., pp. 812–819.

Yabe, A., Taketani, T., Kikuchi, K., and Maki, H., 1986, "Augmentation of Condensation Heat Transfer by Applying Electro-Hydro-Dynamic Pseudo-Dropwise Condensation," *Proc. 8th International Heat Transfer Conference,* Vol. 6, pp. 2957–2962.

Yamashita, K., Kumagai, M., Sekita, S., Yabe, A., Taketani, T., and Kikuchi, K., 1991, "Heat Transfer Characteristics on an EHD Condenser," *Proc. 3rd ASME/JSME Thermal Engineering Joint Conference,* Reno, NV, Mar., pp. 61–67.

Non-Darcy Effects in Natural Convection Heat Transfer in a Vertical Porous Annulus

V. Dharma Rao,[1,3] S. V. Naidu,[1,3] and P. K. Sarma[2,3]

Nomenclature

b = inertial resistance coefficient, m

C_m, C_f = specific heats of medium and fluid, respectively, J kg^{-1} K^{-1}

[1] Chemical Engineering Department.

[2] Mechanical Engineering Department.

[3] Andhra University, Visakhapatnam-530 003, India.

Contributed by the Heat Transfer Division of THE AMERICAN SOCIETY OF MECHANICAL ENGINEERS. Manuscript received by the Heat Transfer Division March 1995; revision received January 1996. Keywords: Enclosure Flows, Natural Convection, Porous Media. Associate Technical Editor: K. Vafai.

d = diameter of the solid bead, m
D = gap width of porous annulus = $\bar{r}_o - \bar{r}_i$, m
Da = Darcy number = K/D^2
g = acceleration due to gravity, m s^{-2} [$g^+ = gD^3/(\alpha_m^2\ \mathrm{Ra}^{*2})$]
h = heat transfer coefficient, W m^{-2} K^{-1}
k_m = effective thermal conductivity of porous medium, W m^{-1} K^{-1}
K = permeability of the porous medium, m^2
L = height of porous annulus, m
Nu_x, Nu_{av} = local and average Nusselt numbers ($\mathrm{Nu}_x = h_x D/k_m$)
P = normalized pressure = $\bar{P}D^2/(\rho_f \alpha_m^2\ \mathrm{Ra}^{*2})$
Pr_m = Prandtl number of the porous medium = ν_f/α_m
$\bar{r}_i$, $\bar{r}_o$ = inner and outer radii of the annulus, respectively, m
r = normalized space coordinate = $\bar{r}/D$
Ra* = modified Rayleigh number = $g\beta(\bar{T}_w - \bar{T}_a)KD/(\nu_f \alpha_m)$
t = normalized time = $\alpha_m \bar{t}\ \mathrm{Ra}^*/D^2$
T = normalized temperature = $(\bar{T} - \bar{T}_a)/(\bar{T}_w - \bar{T}_a)$
u = normalized velocity in x direction = $D\bar{u}/(\alpha_m\ \mathrm{Ra}^*)$
v = normalized velocity in r direction = $D\bar{v}/(\alpha_m\ \mathrm{Ra}^*)$
V = $\sqrt{u^2 + v^2}$
x = normalized space coordinate in vertical direction = $\bar{x}/D$
α_m = thermal diffusivity of porous medium = $k_m/(C_f \rho_f)$, m^2 s^{-1}
β = isobaric coefficient of thermal expansion of fluid, K^{-1}
ϵ = porosity
μ' = apparent viscosity; $\mu^* = (\mu'/\mu_f)$
ν = kinematic viscosity, m^2 s^{-1}
ρ_m, ρ_f = densities of porous medium and fluid respectively, kg m^{-3}
$(\rho C)^+$ = $\rho_m C_m/(\rho_f C_f)$
ϕ = b/D
ψ = normalized stream function = $\bar{\psi}/(D\alpha_m)$
ζ = normalized vorticity function = $\bar{\zeta}D^2/(\alpha_m\ \mathrm{Ra}^*)$

Subscripts

a = ambient
f = fluid
w = at the wall, i.e., at $\bar{r} = \bar{r}_i$

Introduction

The study of flow and heat transfer characteristics in porous media finds applications in varied fields such as geothermal operations, heat loss estimation in thermal insulation, packed beds used in chemical reactors, metal processing in a blast furnace, etc. The theoretical investigation of Minkowycz and Cheng (1976) illustrates the effect of permeability of the porous medium as characterized by Darcy's law. Boundary effects of the velocity profiles near the rigid wall were included in the analysis by some of the investigators (for example, Vafai and Tien, 1981). It has been observed that the boundary and inertia effects are more pronounced in high-permeability porous media. The problem of natural convection in a vertical porous annulus has been studied experimentally and theoretically by Prasad and Kulacki (1984, 1985) and Prasad et al. (1986) covering good range of Rayleigh numbers and aspect ratios. Their experimental data indicate effects of curvature and Prandtl number on temperature profiles and on Nusselt numbers. Another important parameter, the inertial (or, turbulent) resistance coefficient, originally used in theoretical studies on forced flow of fluids through packed beds (Choudhary et al., 1976), has found its application in studies in natural convection as well (Jonsson and Catton, 1987) at high Rayleigh numbers. Kaviany and Mittal (1987) conducted experiments to study the natural convection heat transfer from a vertical plate to polyurethane foam saturated with air.

It is felt from the studies of various authors cited above that there is a need for an analysis of the present problem considering a generalized model so as to obtain accurate results at both low and high Rayleigh numbers. Also, it is intended to present the effects of various parameters in the form of explicit expressions based on computer results.

Physical Model and Problem Formulation

The physical model considered is a vertical cylindrical annulus with inner radius $\bar{r}_i$, outer radius $\bar{r}_o$ and height L and filled with a saturated porous medium. The gap width is D, where $D = \bar{r}_o - \bar{r}_i$. The inner and outer vertical walls of the annulus are maintained at constant temperatures $\bar{T}_w$ and $\bar{T}_a$, respectively, where $\bar{T}_w > \bar{T}_a$. The adiabatic condition of heat flow is maintained at both the bottom and top boundaries at $\bar{x} = 0$ and at $\bar{x} = L$, respectively, for $\bar{r}_i \le \bar{r} \le \bar{r}_o$. The transport and heat transfer processes in the porous annulus are governed by the following normalized energy and momentum balance equations, with the use of Boussinesq approximation (Choudhary et al., 1976; Jonsson and Catton, 1987):

$$(\rho C)^+ \frac{\partial T}{\partial t} + u\frac{\partial T}{\partial x} + v\frac{\partial T}{\partial r} = \frac{1}{\mathrm{Ra}^*}\left\{\frac{1}{r}\frac{\partial}{\partial r}\left(r\frac{\partial T}{\partial r}\right) + \frac{\partial^2 T}{\partial x^2}\right\} \quad (1)$$

$$\frac{\partial u}{\partial t} + \frac{u}{\epsilon}\frac{\partial u}{\partial x} + \frac{v}{\epsilon}\frac{\partial u}{\partial r} = -\epsilon\frac{\partial P}{\partial x} - g^+ + \frac{\epsilon\ \mathrm{Pr}_m}{\mathrm{Da}\ \mathrm{Ra}^*}(T - u) - \frac{\epsilon\phi}{\mathrm{Da}}uV + \frac{\mu^*\epsilon\ \mathrm{Pr}_m}{\mathrm{Ra}^*}\left\{\frac{1}{r}\frac{\partial}{\partial r}\left(r\frac{\partial u}{\partial r}\right) + \frac{\partial^2 u}{\partial x^2}\right\} \quad (2)$$

$$\frac{\partial v}{\partial t} + \frac{u}{\epsilon}\frac{\partial v}{\partial x} + \frac{v}{\epsilon}\frac{\partial v}{\partial r} = -\epsilon\frac{\partial P}{\partial r} - \frac{\epsilon\ \mathrm{Pr}_m}{\mathrm{Da}\ \mathrm{Ra}^*}v - \frac{\epsilon\phi}{\mathrm{Da}}vV + \frac{\mu^*\epsilon\ \mathrm{Pr}_m}{\mathrm{Ra}^*}\left\{\frac{1}{r}\frac{\partial}{\partial r}\left(r\frac{\partial v}{\partial r}\right) + \frac{\partial^2 v}{\partial x^2}\right\} \quad (3)$$

Vorticity ζ in dimensionless form is defined as $\zeta = (\partial u/\partial r) - (\partial v/\partial x)$ and the momentum balance Eqs. (2) and (3) are combined to give the following equation in vorticity:

$$\frac{\partial \zeta}{\partial t} + \frac{u}{\epsilon}\frac{\partial \zeta}{\partial x} + \frac{v}{\epsilon}\frac{\partial \zeta}{\partial r} = \frac{\epsilon\ \mathrm{Pr}_m}{\mathrm{Da}\ \mathrm{Ra}^*}\left\{\frac{\partial T}{\partial r} - \left(1 + \frac{\mathrm{Da}}{r^2}\right)\zeta\right\} + \frac{\mu^*\epsilon\ \mathrm{Pr}_m}{\mathrm{Ra}^*}\left\{\frac{1}{r}\frac{\partial}{\partial r}\left(r\frac{\partial \zeta}{\partial r}\right) + \frac{\partial^2 \zeta}{\partial x^2} - \frac{1}{r^2}\frac{\partial v}{\partial x}\right\} - \frac{\epsilon\phi}{\mathrm{Da}}\left\{\left(V + \frac{u^2}{V}\right)\zeta + \frac{(u^2 - v^2)}{V}\frac{\partial v}{\partial x} + \frac{2uv}{V}\frac{\partial v}{\partial r} + \frac{uv^2}{rV}\right\} \quad (4)$$

The dimensionless stream function ψ is defined as shown below satisfying the equation of continuity:

$$ru = \frac{\partial \psi}{\partial r}; \quad rv = -\frac{\partial \psi}{\partial x} \quad (5)$$

Making use of Eq. (5), the following relation between ζ and ψ is obtained:

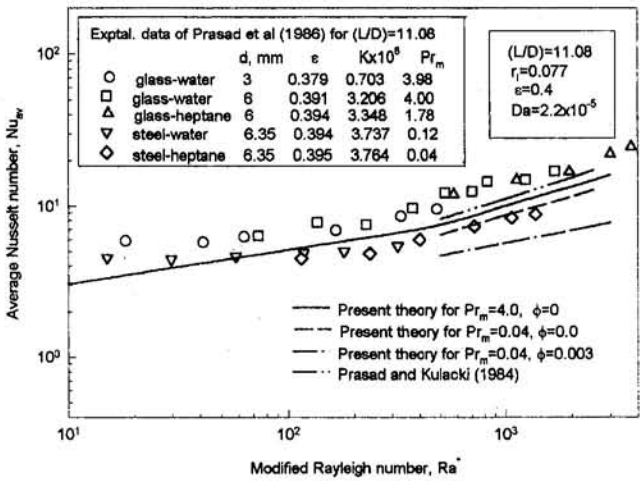

Fig. 1 Comparison of the present theory with the experimental data of Prasad et al. (1986) for the case of a long cylinder with (*L/D*) = 11.08

$$r\zeta = \frac{\partial^2\psi}{\partial r^2} - \frac{1}{r}\frac{\partial\psi}{\partial r} + \frac{\partial^2\psi}{\partial x^2} \tag{6}$$

Initial and boundary conditions in dimensionless form (conditions stipulated at various boundaries for the stream function ψ and vorticity ζ in dimensionless form are also included):

$$t = 0: \quad u = v = T = 0$$

$$\text{for} \quad 0 \le x \le (L/D) \quad \text{and for} \quad r_i \le r \le r_o$$

For $t > 0$ and for $0 \le x \le (L/D)$:

$$\text{At} \quad r = r_i: \quad u = v = \psi = 0 \quad \text{and} \quad T = 1;$$

$$\text{At} \quad r = r_o: \quad u = \frac{\partial\psi}{\partial r} = \zeta = T = 0$$

$$\text{At} \quad x = 0, \quad \frac{\partial T}{\partial x} = \psi = 0;$$

$$\text{At} \quad x = (L/D), \quad \frac{\partial\psi}{\partial x} = \frac{\partial T}{\partial x} = \zeta = 0 \ (\text{for } r_i < r < r_o) \tag{7}$$

In Eq. (7), the boundary condition at the upper boundary, $x = (L/D)$, is prescribed based on a discussion presented by Roache (1985) on boundary conditions for vorticity and stream functions.

The local heat transfer coefficient at the wall ($\bar{r} = \bar{r}_i$) is defined by the equation

$$-k_m \left.\frac{\partial\bar{T}}{\partial\bar{r}}\right|_{\bar{r}=\bar{r}_i} = h_x(\bar{T}_w - \bar{T}_a) \tag{8}$$

following which the local Nusselt number is obtained from the equation

$$-\left.\frac{\partial T}{\partial r}\right|_{\text{at } r=r_i} = \text{Nu}_x \tag{9}$$

Method of Solution

The unsteady-state energy and vorticity equations in dimensionless form (Eqs. (1) and (4)) are numerically solved by the Alternating Direction Implicit (ADI) method (Roache, 1985; Angirasa and Mahajan, 1993). This method gives the values of dimensionless temperature T and vorticity ζ at all grid points after each time step (Δt). Making use of the new values of ζ, the stream function ψ and the u and v velocities are obtained from Eqs. (6) and (5), respectively. The Successive Over Relaxation (SOR) method is used for the solution of Eq. (6). The solution procedure for successive time steps is continued until steady-state results are obtained. Local Nusselt numbers Nu_x are computed, making use of Eq. (9). Using these local values, an integrated average Nusselt number Nu_{av} is computed by Simpson's rule. The stability and consistency of the results are ascertained by subjecting the results to a grid-independence test and an iteration-convergence test in the cases of the ADI method and the successive overrelaxation method, respectively.

Results and Discussion

Results are obtained to study the effects of the parameters Ra*, (L/D) ratio, r_i, Pr_m, and Da on the velocity and temperature profiles and on Nusselt numbers. From the numerical results it is observed that the effect of Prandtl number Pr_m on Nusselt numbers is significant when $\text{Ra}^* > 100$ and $\text{Da} > 10^{-5}$. Further, the effect of the inertial (or turbulence) resistance parameter ϕ on Nusselt numbers is found to be significant at low Prandtl and high Darcy numbers. A comparison of the present theory is shown in Figs. 1 and 2 with the experimental data of Prasad et al. (1986), and Prasad and Kulacki (1985) for the cases of long and short cylinders, respectively. Numerical results are recast in the form of expressions for average Nusselt number as a function of various system parameters, by means of nonlinear regression analysis:

For $\phi = 0$ and for $\text{Ra}^* < 200$:

$$\text{Nu}_{av} = 1.2757\ \text{Ra}^{*0.226}\left(\frac{L}{D}\right)^{-0.279} \times \left(1 + \frac{1}{r_i}\right)^{0.382}\left(\frac{\epsilon}{\text{Pr}_m\ \text{Da}}\right)^{0.0014} \tag{10a}$$

For $\phi = 0$ and for $200 < \text{Ra}^* < 2500$:

$$\text{Nu}_{av} = 0.5685\ \text{Ra}^{*0.427}\left(\frac{L}{D}\right)^{-0.334} \times \left(1 + \frac{1}{r_i}\right)^{0.1366}\left(\frac{\epsilon}{\text{Pr}_m\ \text{Da}}\right)^{0.032} \tag{10b}$$

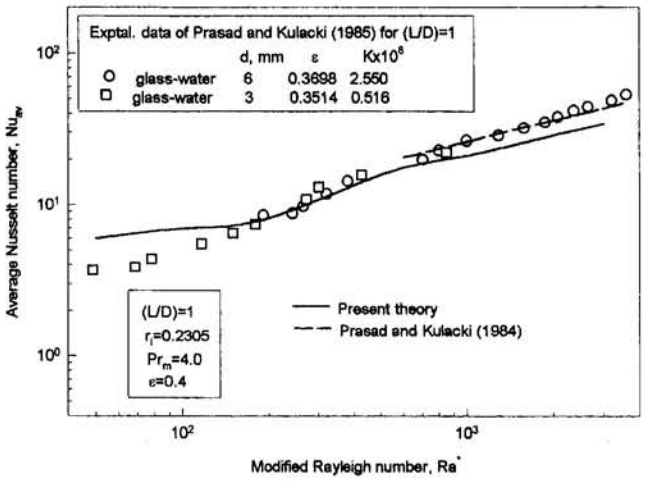

Fig. 2 Comparison of the present theory with the experimental data of Prasad and Kulacki (1985) for the case of a short cylinder with (*L/D*) = 1.0

For $\phi > 0$ and for $500 < \mathrm{Ra}^* < 2500$ and $\mathrm{Da} > 10^{-5}$:

$$\mathrm{Nu}_{av} = 1.013\ \mathrm{Ra}^{*0.276}\left(\frac{L}{D}\right)^{-0.368}\left(1+\frac{1}{r_i}\right)^{0.196} \times \left(\frac{\epsilon}{\mathrm{Pr}_m\,\mathrm{Da}}\right)^{0.082}\left(1+\frac{\epsilon\phi}{\mathrm{Da}}\right)^{-0.08} \quad (11)$$

These regression equations agree with the numerical results within a standard deviation of 6 percent for the following range of parameters: $1.0 \le (L/D) \le 15$; $0.07 \le r_i \le 40$; $0.04 \le \mathrm{Pr}_m \le 50$; and $4 \times 10^{-7} \le \mathrm{Da} \le 2 \times 10^{-4}$.

Acknowledgments

The authors thank Dr. Devarakonda Angirasa and Ms. D. S. Mary Sujatha for their help in connection with the ADI method, Prof. R. Krishna Murty for providing the computer facility, and AICTE, New Delhi, for the financial support.

References

Angirasa, D., and Mahajan, R. L., 1993, "Natural Convection From L-Shaped Corners With Adiabatic and Cold Isothermal Horizontal Walls," ASME JOURNAL OF HEAT TRANSFER, Vol. 115, pp. 149–157.

Choudhary, M., Proster, M., and Szekely, J., 1976, "On the Importance of Inertial Terms in the Modeling of Flow Maldistribution in Packed Beds," *AIChE Journal*, Vol. 22, pp. 600–603.

Jonsson, T., and Catton, I., 1987, "Prandtl Number Dependence of Natural Convection in Porous Media," ASME JOURNAL OF HEAT TRANSFER, Vol. 109, pp. 371–377.

Kaviany, M., and Mittal, M., 1987, "Natural Convection Heat Transfer From a Vertical Plate to High Permeability Porous Media: an Experimental and an Approximate Solution," *Int. J. Heat Mass Transfer*, Vol. 30, pp. 967–976.

Minkowycz, W. J., and Cheng, P., 1976, "Free Convection About a Vertical Cylinder Embedded in a Porous Medium," *Int. J. Heat Mass Transfer*, Vol. 19, pp. 805–813.

Prasad, V., and Kulacki, F. A., 1984, "Natural Convection in a Vertical Porous Annulus," *Int. J. Heat Mass Transfer*, Vol. 27, pp. 207–219.

Prasad, V., and Kulacki, F. A., 1985, "Natural Convection in Porous Media Bounded by Short Concentric Vertical Cylinders," ASME JOURNAL OF HEAT TRANSFER, Vol. 107, pp. 147–154.

Prasad, V., Kulacki, F. A., and Kulkarni, A. V., 1986, "Free Convection in a Vertical, Porous Annulus With Constant Heat Flux on the Inner Wall—Experimental Results," *Int. J. Heat Mass Transfer*, Vol. 29, pp. 713–722.

Roache, P. J., 1985, *Computational Fluid Dynamics*, Hermosa, Albuquerque, NM.

Vafai, K., and Tien, C. L., 1981, "Boundary and Inertia Effects on Flow and Heat Transfer in Porous Media," *Int. J. Heat Mass Transfer*, Vol. 24, pp. 195–203.

Laminar Forced Convection in the Entrance Region of a Semiporous Channel

T.-C. Jen[1]

Nomenclature

f_{pw} = friction factor at porous wall
f_{sw} = friction factor at solid wall
H = channel height
L = total channel length
n = direction normal to wall
Nu = Nusselt number
Pr = Prandtl number = ν/α
Re = inlet flow Reynolds number = $U_o H/\nu$
Re_m = mean flow Reynolds number = $U_m H/\nu$
Re_w = wall suction Reynolds number = $V_w H/\nu$
u, v = dimensionless velocity components
U_m = mean velocity at x
u_m = dimensionless mean velocity at x
V_w = wall suction velocity
x, y = dimensionless coordinates
x^+ = dimensionless axial coordinate = x/Re
θ = dimensionless temperature
θ_m = dimensionless bulk mean temperature

Introduction

The heat transfer and fluid flow in the entrance region of a semiporous channel is of importance in many engineering applications such as nuclear reactors, turbine engines, combustion chambers, solar collectors, and electrochemical systems. Detailed reviews of porous-walled-passage flow and heat transfer can be found in Raithby (1971), Rhee and Edwards (1981), and Jen (1994). Only papers closely related to the present study are reviewed here.

Rhee and Edwards (1981) presented the first study concerning heat transfer in the hydrodynamic and thermal entrance region of a semiporous channel. A tail-end-plate configuration was used and the parabolized governing equations were solved numerically. It is worth noting that their results are limited to the case where there is no flow reversal, and where the effects of axial diffusion and conduction are neglected. Soong and Hwang (1990) investigated the laminar mixed convection problem of a radially rotating semiporous channel. A closed-form solution for the fully developed regime was found. Accounting for the fluid flow in the porous wall, Abdel-Rahman et al. (1991) studied the heat transfer and fluid flow in the channel and duct with wall injection. They show that the effect of fluid flow in the porous wall may become significant when Darcy number is large. This effect will be neglected in the present study. Recently, Hwang et al. (1993) presented a three-dimensional numerical analysis in the entrance region of a square duct with injection or suction at one wall. However, because the parabolized equations were used, the results are limited to cases without flow reversal. Typically, wall transpiration cooling channels have low aspect ratios (where aspect ratio is defined as spacing divided by length) (e.g., Moskowitz and Lombardo (1971) and Raj (1983)). Thus, a two-dimensional analysis can be useful for understanding the convection mechanism of a semiporous channel.

A numerical analysis has been performed for the simultaneously developing laminar flow and temperature fields in the entrance region of a semiporous channel. Both constant wall temperature and constant wall heat flux thermal boundary conditions are considered. A vorticity–velocity method successfully developed for two-dimensional flow by Farouk and Fusegi (1986) is used for the present study. Note that this formulation can be extended directly to three-dimensional parabolic flow as shown by Chou and Hwang (1987) and Jen et al. (1992). The power law scheme (Patankar, 1980) is employed to solve the governing equations for the flow and temperature fields. Unlike previous studies (Rhee and Edwards, 1981; Hwang et al., 1993), the axial diffusion terms in the momentum equations and the axial conduction term of the energy equation have been retained. Jen (1994) has shown that a significant error can be introduced in the entrance region when these terms are neglected. Furthermore, instead of making the parabolic flow as-

[1] Mechanical and Aerospace Engineering Department, University of California, Los Angeles, Los Angeles, CA 90095-1597.

Contributed by the Heat Transfer Division and presented at the 6th AIAA/ASME Joint Thermophysics and Heat Transfer Conference, June 20–23, 1994. Manuscript received by the Heat Transfer Division June 1995; revision received February 1996. Keywords: Flow Separation, Forced Convection, Numerical Methods. Associate Technical Editor: R. Viskanta.

For $\phi > 0$ and for $500 < \mathrm{Ra}^* < 2500$ and $\mathrm{Da} > 10^{-5}$:

$$\mathrm{Nu}_{av} = 1.013\ \mathrm{Ra}^{*0.276}\left(\frac{L}{D}\right)^{-0.368}\left(1+\frac{1}{r_i}\right)^{0.196} \times \left(\frac{\epsilon}{\mathrm{Pr}_m\,\mathrm{Da}}\right)^{0.082}\left(1+\frac{\epsilon\phi}{\mathrm{Da}}\right)^{-0.08} \quad (11)$$

These regression equations agree with the numerical results within a standard deviation of 6 percent for the following range of parameters: $1.0 \le (L/D) \le 15$; $0.07 \le r_i \le 40$; $0.04 \le \mathrm{Pr}_m \le 50$; and $4 \times 10^{-7} \le \mathrm{Da} \le 2 \times 10^{-4}$.

Acknowledgments

The authors thank Dr. Devarakonda Angirasa and Ms. D. S. Mary Sujatha for their help in connection with the ADI method, Prof. R. Krishna Murty for providing the computer facility, and AICTE, New Delhi, for the financial support.

References

Angirasa, D., and Mahajan, R. L., 1993, "Natural Convection From L-Shaped Corners With Adiabatic and Cold Isothermal Horizontal Walls," ASME JOURNAL OF HEAT TRANSFER, Vol. 115, pp. 149–157.

Choudhary, M., Proster, M., and Szekely, J., 1976, "On the Importance of Inertial Terms in the Modeling of Flow Maldistribution in Packed Beds," *AIChE Journal,* Vol. 22, pp. 600–603.

Jonsson, T., and Catton, I., 1987, "Prandtl Number Dependence of Natural Convection in Porous Media," ASME JOURNAL OF HEAT TRANSFER, Vol. 109, pp. 371–377.

Kaviany, M., and Mittal, M., 1987, "Natural Convection Heat Transfer From a Vertical Plate to High Permeability Porous Media: an Experimental and an Approximate Solution," *Int. J. Heat Mass Transfer,* Vol. 30, pp. 967–976.

Minkowycz, W. J., and Cheng, P., 1976, "Free Convection About a Vertical Cylinder Embedded in a Porous Medium," *Int. J. Heat Mass Transfer,* Vol. 19, pp. 805–813.

Prasad, V., and Kulacki, F. A., 1984, "Natural Convection in a Vertical Porous Annulus," *Int. J. Heat Mass Transfer,* Vol. 27, pp. 207–219.

Prasad, V., and Kulacki, F. A., 1985, "Natural Convection in Porous Media Bounded by Short Concentric Vertical Cylinders," ASME JOURNAL OF HEAT TRANSFER, Vol. 107, pp. 147–154.

Prasad, V., Kulacki, F. A., and Kulkarni, A. V., 1986, "Free Convection in a Vertical, Porous Annulus With Constant Heat Flux on the Inner Wall—Experimental Results," *Int. J. Heat Mass Transfer,* Vol. 29, pp. 713–722.

Roache, P. J., 1985, *Computational Fluid Dynamics,* Hermosa, Albuquerque, NM.

Vafai, K., and Tien, C. L., 1981, "Boundary and Inertia Effects on Flow and Heat Transfer in Porous Media," *Int. J. Heat Mass Transfer,* Vol. 24, pp. 195–203.

Laminar Forced Convection in the Entrance Region of a Semiporous Channel

T.-C. Jen[1]

Nomenclature

f_{pw} = friction factor at porous wall
f_{sw} = friction factor at solid wall
H = channel height
L = total channel length
n = direction normal to wall
Nu = Nusselt number
Pr = Prandtl number = ν/α
Re = inlet flow Reynolds number = $U_o H/\nu$
Re_m = mean flow Reynolds number = $U_m H/\nu$
Re_w = wall suction Reynolds number = $V_w H/\nu$
u, v = dimensionless velocity components
U_m = mean velocity at x
u_m = dimensionless mean velocity at x
V_w = wall suction velocity
x, y = dimensionless coordinates
x^+ = dimensionless axial coordinate = x/Re
θ = dimensionless temperature
θ_m = dimensionless bulk mean temperature

Introduction

The heat transfer and fluid flow in the entrance region of a semiporous channel is of importance in many engineering applications such as nuclear reactors, turbine engines, combustion chambers, solar collectors, and electrochemical systems. Detailed reviews of porous-walled-passage flow and heat transfer can be found in Raithby (1971), Rhee and Edwards (1981), and Jen (1994). Only papers closely related to the present study are reviewed here.

Rhee and Edwards (1981) presented the first study concerning heat transfer in the hydrodynamic and thermal entrance region of a semiporous channel. A tail-end-plate configuration was used and the parabolized governing equations were solved numerically. It is worth noting that their results are limited to the case where there is no flow reversal, and where the effects of axial diffusion and conduction are neglected. Soong and Hwang (1990) investigated the laminar mixed convection problem of a radially rotating semiporous channel. A closed-form solution for the fully developed regime was found. Accounting for the fluid flow in the porous wall, Abdel-Rahman et al. (1991) studied the heat transfer and fluid flow in the channel and duct with wall injection. They show that the effect of fluid flow in the porous wall may become significant when Darcy number is large. This effect will be neglected in the present study. Recently, Hwang et al. (1993) presented a three-dimensional numerical analysis in the entrance region of a square duct with injection or suction at one wall. However, because the parabolized equations were used, the results are limited to cases without flow reversal. Typically, wall transpiration cooling channels have low aspect ratios (where aspect ratio is defined as spacing divided by length) (e.g., Moskowitz and Lombardo (1971) and Raj (1983)). Thus, a two-dimensional analysis can be useful for understanding the convection mechanism of a semiporous channel.

A numerical analysis has been performed for the simultaneously developing laminar flow and temperature fields in the entrance region of a semiporous channel. Both constant wall temperature and constant wall heat flux thermal boundary conditions are considered. A vorticity–velocity method successfully developed for two-dimensional flow by Farouk and Fusegi (1986) is used for the present study. Note that this formulation can be extended directly to three-dimensional parabolic flow as shown by Chou and Hwang (1987) and Jen et al. (1992). The power law scheme (Patankar, 1980) is employed to solve the governing equations for the flow and temperature fields. Unlike previous studies (Rhee and Edwards, 1981; Hwang et al., 1993), the axial diffusion terms in the momentum equations and the axial conduction term of the energy equation have been retained. Jen (1994) has shown that a significant error can be introduced in the entrance region when these terms are neglected. Furthermore, instead of making the parabolic flow as-

[1] Mechanical and Aerospace Engineering Department, University of California, Los Angeles, Los Angeles, CA 90095-1597.

Contributed by the Heat Transfer Division and presented at the 6th AIAA/ASME Joint Thermophysics and Heat Transfer Conference, June 20–23, 1994. Manuscript received by the Heat Transfer Division June 1995; revision received February 1996. Keywords: Flow Separation, Forced Convection, Numerical Methods. Associate Technical Editor: R. Viskanta.

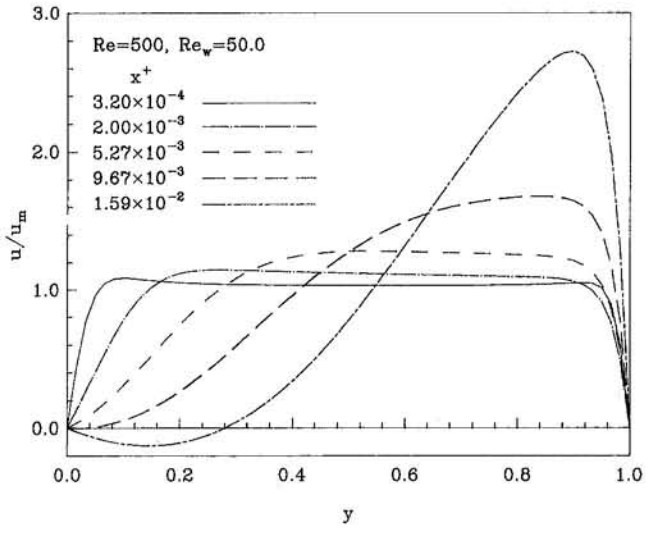

Fig. 1 Development of axial velocity profiles

sumption as in Rhee and Edwards (1981) and Hwang et al. (1993), fully elliptic governing equations are used here. This allows results to be obtained for regions with flow reversal. The effect of fluid flow in the porous wall is neglected here, even though this may become significant when Darcy number is large. A coordinate transformation technique is used to handle the boundary condition far downstream (see, Jen, 1994, for a detailed description). The effects of wall suction and heating are examined. The local friction factor and Nusselt number are presented as a function of axial position. It is seen that they are strongly affected by wall suction and heating. When wall suction is strong enough, flow reversals are observed. Comparisons with existing theoretical and experimental results are also presented.

Results and Discussion

Consider the steady, laminar, developing convection flow in a parallel channel with top wall suction, and solid bottom wall. A uniform inlet axial velocity and a constant inlet temperature are imposed at $x = 0$. Each channel wall is either under constant wall temperature or uniform wall heat flux conditions. The flow is assumed to be steady, constant-property, and incompressible. Viscous dissipation, compression work, and buoyancy are neglected. Details of the physical configuration, formulation, and numerical procedures used here can be found in Jen (1994), and will not be repeated here.

The computed results are first compared to theoretical results for the fully developed flow and heat transfer case with fully porous walls (i.e., both walls are porous). For a suction rate of $\mathrm{Re}_w = 2$ and $\mathrm{Pr} = 0.7$ fluid, $f\,\mathrm{Re}_m$ is found to be 24.87, and $\mathrm{Nu} = 4.8$ for the constant wall heat flux case. These are in excellent agreement with the data presented by Raithby (1971).

Because of the lack of experimental data in the developing region, the present numerical analysis has been compared with the only existing fully porous channel flow data (Raithby and Knudsen, 1974). With reference to Jen (1994), the agreement is seen to be excellent.

The present numerical analysis is also compared to theoretical results presented by Eckert et al. (1957) and Soong and Hwang (1990) for fully developed flow in semiporous channels. Again, with reference to Jen (1994), it is found that the agreement with the published theoretical results of Eckert et al. (1957) and Soong and Hwang (1990) are excellent for Re_w up to 6. For a larger suction rate, $\mathrm{Re}_w = 10$, the agreement is still reasonably good. Increasing the portion of the domain where there is suction and increasing the number of axial grid points change the results by an almost imperceptible amount. This suggests that the flow becomes fully developed very slowly. A measurable increase in computational domain size still does not yield a flow field that agrees with the analytical results for the fully developed case. This is in agreement with the results of Hwang et al. (1993), where it is shown that the flow is not quite fully developed at $\mathrm{Re}_w = 10$.

The present numerical analysis is compared to Rhee and Edwards (1981) where a marching technique was used for the simultaneously developing laminar convection in the entrance region. The velocity and temperature profiles for the constant wall temperature case of $\mathrm{Re}_w = 6.0$ (not shown) are in excellent agreement with their results except very near the inlet (i.e., $X/L = 0.02$). This is because the present analysis includes the effect of axial diffusion and axial conduction.

Profiles of the developing axial velocity, u/u_m, shown at different axial locations can be found in Jen (1994). Only one case, with flow reversal, is discussed here. For pure forced convection without suction, the axial velocity profile is symmetric about the $y = \frac{1}{2}$ plane. Wall suction has a clear effect on the velocity profiles. For $\mathrm{Re} = 500$, $\mathrm{Re}_w = 50$, the axial velocity profile, u/u_m, has been plotted on Fig. 1 for five axial locations starting from very near the entrance of the channel, $x^+ = 3.20 \times 10^{-4}$, to a location with flow reversal, $x^+ = 1.59 \times 10^{-2}$. It can be seen that the velocity profile is fairly uniform near the inlet. In the entrance region, the large flow resistance near the wall tends to accelerate the flow near the core region, the so-called "hydrodynamic center." Although the two curves nearest the inlet do not show significant distortion in the axial velocity profile, as the flow develops, the large suction rate distorts the axial velocity significantly. This is reflected by the increased top wall axial velocity gradient at the downstream axial location, $x^+ = 5.27 \times 10^{-3}$. In contrast to this, the velocity gradient near the solid wall is significantly decreased. At $x^+ = 9.67 \times 10^{-3}$, the velocity gradient near the solid wall approaches zero. For larger x^+, flow reversal occurs. Note that no fully developed region is observed in this case.

Figure 2 shows the local friction factor distribution at various axial locations for porous and solid walls. The parameters used in this figure are $\mathrm{Re} = 500$ and $\mathrm{Re}_w = 2$, 10, 20, and 50. It can be seen from Fig. 2 that $f_{pw}\mathrm{Re}_m$ increases with the suction rate. The suction effect at the porous wall results in a larger velocity gradient near the top wall (see Fig. 1). For the largest suction rate, $\mathrm{Re}_w = 50$, the porous wall friction factor increases signifi-

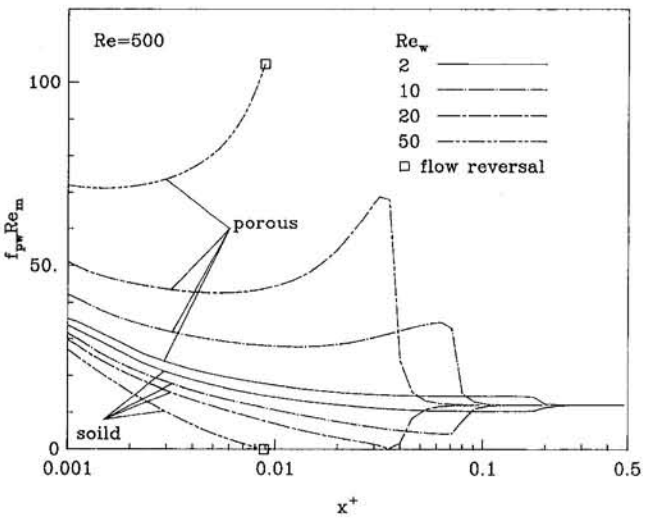

Fig. 2 Wall Reynolds number effects on friction factors along the axial direction

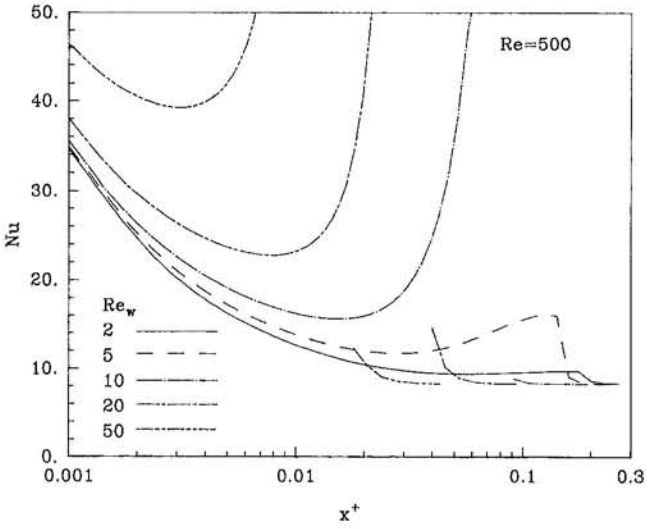

Fig. 3(*a*) constant wall heat flux case

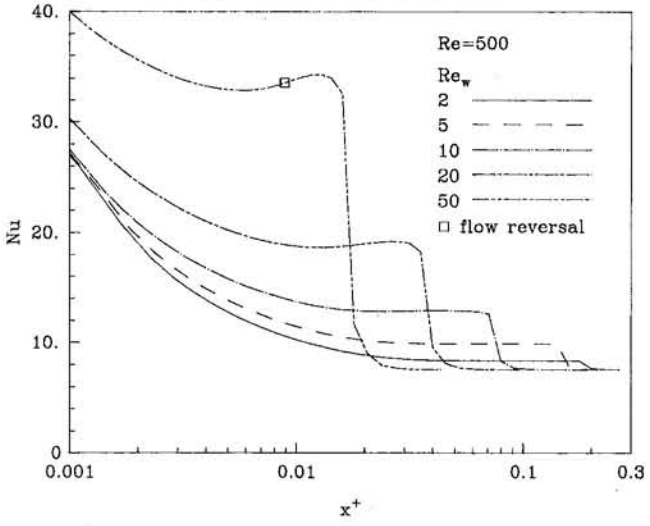

Fig. 3(*b*) constant wall temperature case

Fig. 3 Wall Reynolds number effects on Nusselt numbers along the axial direction

cantly, with flow reversal occurring at the bottom wall when $f_{pw}\mathrm{Re}_m$ reaches about 100. It can be seen that stronger suction rates at the porous wall cause the solid wall friction factor to decrease faster. Flow reversal occurs for the largest suction rate (i.e., $\mathrm{Re}_w = 50$) at $x^+ \simeq 0.008$, where the solid wall friction factor becomes zero. At low suction rates, as the mass flow in the axial location decreases along the channel, total fluid extraction will result at some axial position when mass flow goes to zero. In these cases (i.e., for Re_w from 2 to 10), no flow reversals are observed. However, for a larger suction rate, flow reversal will occur near the solid wall for the small axial velocity case due to the inability of the fluid to adjust for the large amount being extracted at the porous wall (Hwang et al., 1993). The flow reversal locations are seen to move upstream as the suction rate increases, in agreement with the results presented by Hwang et al. (1993).

The effect of Re_w on Nusselt numbers along the axial direction for Re = 500 and Pr = 0.7 in the entrance region for constant wall heat flux case is given in Fig. 3(*a*). As can be seen, heat transfer increases as the suction rate increases. The Nusselt number approaches infinity when the suction rate is greater or equal to 10. This is because the bulk mean temperature is equal to the porous wall temperature. Thus, the first term of the Nusselt number (defined as $(\partial\theta/\partial n)_{pw}1/(\theta_m - \theta_{pw})$) tends toward infinity (see Jen, 1994, for detailed discussion). A suction rate increase from 2 to 50 results in an increase in the heat transfer rate of more than 25 percent at $x^+ = 10^{-3}$. The effect is even larger farther downstream.

The effect of wall suction on the Nusselt numbers in the axial direction for the constant wall temperature case is demonstrated in Fig. 3(*b*). Similar to the constant wall heat flux case (i.e., Fig. 3(*a*)), the heat transfer rate increases as the suction rate increases. For a suction rate of $\mathrm{Re}_w = 50$, the increase in Nusselt number at $x^+ = 0.001$ is more than 50 percent, in comparison to the Nusselt number at $\mathrm{Re}_w = 2$. The amount of increase is larger further downstream. It is worth noting that for this case, the Nusselt number does not go toward ∞ because the bulk mean temperature of the fluid is always greater than the porous wall temperature.

Acknowledgments

The author would like to thank Dr. Stanley Chen for his assistance in proofreading this paper.

References

Abdel-Rahman, A. K., Suzuki, K., Hagiwara, Y., and Takaura, H., 1991, "Laminar Channel Flow With Fluid Injection Accounting for the Flow in the Porous Wall," *Proc. 28th National Heat Transfer Symposium of Japan,* pp. 406–408.

Chou, F. C., and Hwang, G. J., 1987, "Vorticity-Velocity Method for the Graetz Problem and the Effect of Natural Convection in a Horizontal Rectangular Channel With Uniform Wall Heat Flux," ASME JOURNAL OF HEAT TRANSFER, Vol. 109, pp. 704–710.

Eckert, E. R. G., Donoughe, P. L., and Moore, B. J., 1957, "Velocity and Friction of Laminar Viscous Boundary-Layer and Channel Flow Over Surfaces With Injection or Suction," NACA TN 4102.

Farouk, B., and Fusegi, T., 1986, "Predictions of Fluid and Heat Transfer Problems by the Vorticity-Velocity Formulation of the Navier–Stokes Equations," *J. Comp. Phys.,* Vol. 65, pp. 227–243.

Hwang, G. J., Cheng, Y. C., and Ng, M. L., 1993, "Developing Laminar Flow and Heat Transfer in a Square Duct With One-Walled Injection and Suction," *Int. J. Heat Mass Transfer,* Vol. 36, No. 9, pp. 2429–2440.

Jen, T. C., Lavine, A. S., and Hwang, G. J., 1992, "Simultaneously Developing Laminar Convection in Rotating Isothermal Square Channels," *Int. J. Heat Mass Transfer,* Vol. 35, No. 1, pp. 239–254.

Jen, T. C., 1994, "Simultaneously Developing Laminar Convection in the Entrance Region of a Semi-porous Channel," *Current Developments in Numerical Simulation of Flow and Heat Transfer,* ASME HTD-Vol. 275, pp. 111–122.

Moskowitz, S. L., and Lombardo, S., 1971, "2750 Deg F Engine Turbine Test of a Transpiration Air-Cooled Turbine," ASME *Journal of Engineering for Gas Turbines and Power,* Vol. 93, pp. 238–248.

Patankar, S. V., 1980, *Numerical Heat Transfer and Fluid Flow,* Hemisphere Publishing Co., pp. 96–100.

Raithby, G., 1971, "Laminar Heat Transfer in the Thermal Entrance Region of Circular Tubes and Two-Dimensional Rectangular Ducts With Wall Suction and Injection," *Int. J. Heat Mass Transfer,* Vol. 14, pp. 224–243.

Raithby, G. D., and Knudsen, D. C., 1974, "Hydrodynamic Development in a Duct With Suction and Blowing," *J. Appl. Mech.,* Vol. 41, pp. 896–902.

Raj, R., 1983, "Deposition Results of a Transpiration Air-Cooled Turbine Vane Cascade in a Contaminated Gas Stream," ASME *Journal of Engineering for Gas Turbines and Power,* Vol. 105, pp. 826–833.

Rhee, S. J., and Edwards, D. K., 1981, "Laminar Entrance Flow in a Flat Plate Duct With Asymmetric Suction and Heating," *Num. Heat Transfer,* Vol. 4, pp. 85–100.

Soong, C. Y., and Hwang, G. J., 1990, "Laminar Mixed Convection in a Radially Rotating Semiporous Channel," *Int. J. Heat Mass Transfer,* Vol. 33, No. 9, pp. 1805–1816.

A Perturbation Solution for a Nonthermal Equilibrium Fluid Flow Through a Three-Dimensional Sensible Heat Storage Packed Bed

A. V. Kuznetsov [1]

Nomenclature

a_{sf} = specific surface area common to solid and fluid phases, m^2/m^3
c_p = specific heat at constant pressure, J kg^{-1} K^{-1}
h_w = heat transfer coefficient at the porous bed walls, W m^{-2} K^{-1}
h_{sf} = fluid-to-particle heat transfer coefficient between solid and fluid phases, W m^{-2} K^{-1}
L_i = length of the packed bed (in x_i-direction), m
t = time, s
T = temperature, K
v = velocity of the fluid phase, m s^{-1}
x_1, x_2, x_3 = Cartesian coordinates, m
$\langle \ldots \rangle$ = local volume average
ϵ = porosity
λ = thermal conductivity, W m^{-1} K^{-1}
ξ_i = dimensionless coordinates
Θ = dimensionless temperature
$\Delta\Theta$ = dimensionless difference between temperatures of the solid and fluid phases
ρ = density, kg m^{-3}
τ = dimensionless time

Subscripts and Superscripts

eff = effective property
f = fluid phase
in = inlet
0 = initial
s = solid phase

1 Introduction

The investigation of a nonthermal equilibrium fluid flow through a porous packed bed is of permanent interest. This is because of the important applications of porous packed beds, such as the storage of heat energy. In recent works by Sözen and Vafai (1990), Vafai and Sözen (1990a, b), Sözen et al. (1991), and Amiri and Vafai (1994), a set of volume-averaged governing equations for nonthermal equilibrium, condensing, forced fluid flow through sensible and latent heat storage beds is presented and comprehensive numerical analyses of the phenomena are carried out. Analytical studies of the phenomena are presented by Amundson (1956a, b), Arpaci and Clark (1962), Hung and Nevins (1965), Jang and Lee (1974), Burch et al. (1976), Riaz (1977), and Spiga and Spiga (1981).

An investigation of a heating process of a semi-infinite packed bed based on the perturbation analysis of the full energy equations for the solid and fluid phases has been recently presented by Kuznetsov (1994). In the present analysis the considerably more complicated case of the three-dimensional porous packed bed is considered for the step response.

2 Physical Model and Governing Equations

A three-dimensional porous packed bed is filled with the incompressible fluid and is initially at a uniform temperature, T_0. The fluid flows in the x_1 direction; the peripheral walls ($x_2 = \pm L_2$, $x_3 = \pm L_3$) are heated by a fluid with a constant temperature, T_{in}. At the instant $t = 0$, fluid at a higher temperature, T_{in}, is suddenly allowed to flow through the packed bed. In establishing a model for analyzing this problem, the following assumptions and simplifications are employed: The fluid phase is incompressible and the mass flow rate at every cross section of the packed bed is constant; thermal, physical, and transport properties are constant; heat transfer is three dimensional and fluid flow is one dimensional; the dimensionless solid phase temperature differs from the fluid phase temperature by a small perturbation:

$$\Theta_s = \Theta_f + \delta\Delta\Theta \tag{1}$$

where δ is a dimensionless small parameter.

Following Sözen and Vafai (1990) and Vafai and Sözen (1990a, b), the effective thermal conductivity in both phases is assumed isotropic and constant.

Following the perturbation analysis presented by Kuznetsov (1994) it is easy to show that under this set of assumptions the dimensionless fluid phase temperature is governed by the following equation:

$$\frac{\partial\Theta_f}{\partial\tau} + \frac{\partial\Theta_f}{\partial\xi_1} = \sum_{i=1}^{3} \frac{\partial^2\Theta_f}{\partial\xi_i^2} + O(\delta) \tag{2}$$

and the dimensionless temperature difference between the solid and fluid phases is governed by the following equation:

$$\Delta\Theta = \frac{\partial\Theta_f}{\partial\tau} + \Lambda_1 \frac{\partial\Theta_f}{\partial\xi_1} - \Lambda_2 \sum_{i=1}^{3} \frac{\partial^2\Theta_f}{\partial\xi_i^2} \tag{3}$$

In Eqs. (1)–(3) the following dimensionless variables are utilized:

Temperature

$$\Theta = \frac{T_{in} - T}{T_{in} - T_0},$$

where T_{in} is the inlet temperature of the fluid phase and T_0 is the initial temperature of the packed bed,

Coordinates

$$\xi_i = \frac{\langle\rho_f\rangle^f (c_p)_f \langle v_f\rangle}{\lambda_{feff} + \lambda_{seff}} x_i,$$

Time

$$\tau = \frac{[\langle\rho_f\rangle^f (c_p)_f \langle v_f\rangle]^2}{[\epsilon\langle\rho_f\rangle^f (c_p)_f + (1-\epsilon)\langle\rho_s\rangle^s (c_p)_s](\lambda_{feff} + \lambda_{seff})} t,$$

and the dimensionless parameters

$$\Lambda_1 = \frac{\epsilon\langle\rho_f\rangle^f (c_p)_f + (1-\epsilon)\langle\rho_s\rangle^s (c_p)_s}{\epsilon\langle\rho_f\rangle^f (c_p)_f},$$

$$\Lambda_2 = \frac{\lambda_{feff}[\epsilon\langle\rho_f\rangle^f (c_p)_f + (1-\epsilon)\langle\rho_s\rangle^s (c_p)_s]}{\epsilon\langle\rho_f\rangle^f (c_p)_f [\lambda_{feff} + \lambda_{seff}]}, \quad \text{and}$$

$$\delta = \frac{1}{h_{sf} a_{sf}} \frac{\epsilon[\langle\rho_f\rangle^f (c_p)_f]^3 \langle v_f\rangle^2}{[\epsilon\langle\rho_f\rangle^f (c_p)_f + (1-\epsilon)\langle\rho_s\rangle^s (c_p)_s](\lambda_{feff} + \lambda_{seff})}$$

3 Solution and Analysis

For the function Θ_f, initial and boundary conditions discussed in the beginning of the previous section can be written in the following form:

[1] Mechanical Engineering Research Institute of Russian Academy of Sciences, Moscow, Russia; present address: Technical University of Vienna, Institute of Fluid Mechanics and Heat Transfer, Vienna, Austria.

Contributed by the Heat Transfer Division of THE AMERICAN SOCIETY OF MECHANICAL ENGINEERS. Manuscript received by the Heat Transfer Division July 1995; revision received February 1996. Keywords: Nonequilibrium Flows, Porous Media, Thermal Energy Storage. Associate Technical Editor: K. Vafai.

$$\Theta_f(\xi_1, \xi_2, \xi_3, 0) = 1 \tag{4}$$

$$\Theta_f(0, \xi_2, \xi_3, \tau) = 0, \frac{\partial \Theta_f}{\partial \xi_1}(R_1, \xi_2, \xi_3, \tau) = 0 \tag{5}$$

$$\frac{\partial \Theta_f}{\partial \xi_2}(\xi_1, \pm R_2, \xi_3, \tau) = \mp \alpha \Theta_f(\xi_1, \pm R_2, \xi_3, \tau), \tag{6}$$

$$\frac{\partial \Theta_f}{\partial \xi_3}(\xi_1, \xi_2, \pm R_3, \tau) = \mp \alpha \Theta_f(\xi_1, \xi_2, \pm R_3, \tau) \tag{7}$$

where

$$R_i = \langle \rho_f \rangle^f (c_p)_f \langle v_f \rangle L_i / (\lambda_{\text{feff}} + \lambda_{\text{reff}}) \ (i = 1, 2, 3) \quad \text{and}$$

$$\alpha = h_w / [\langle \rho_f \rangle^f (c_p)_f \langle v_f \rangle].$$

The zero temperature gradient at $\xi_1 = R_1$ (Eq. (5)) means that it is assumed that the temperature of the fluid does not change after the fluid leaves the packed bed and there is no temperature jump at the outlet boundary.

The solution of Eq. (2) with corresponding initial and boundary conditions (4)–(7) can be obtained as the product of the solutions of the pertinent one-dimensional problems:

$$\Theta_f(\xi_1, \xi_2, \xi_3, \tau) = \prod_{i=1}^{3} w_i(\xi_i, \tau) \tag{8}$$

The function $w_1(\xi_1, \tau)$ is the solution of the following equation:

$$\frac{\partial w_1}{\partial \tau} + \frac{\partial w_1}{\partial \xi_1} = \frac{\partial^2 w_1}{\partial \xi_1^2} \tag{9}$$

with its corresponding initial and boundary conditions

$$w_1(\xi_1, 0) = 1, \quad w_1(0, \tau) = 0, \quad \frac{\partial w_1}{\partial \xi_1}(R_1, \tau) = 0 \tag{10}$$

The functions $w_j(\xi_j, \tau)$ $(j = 2, 3)$ are the solutions of the following equations:

$$\frac{\partial w_j}{\partial \tau} = \frac{\partial^2 w_j}{\partial \xi_j^2} \tag{11}$$

with their corresponding initial and boundary conditions

$$w_j(\xi_j, 0) = 1, \quad \frac{\partial w_j}{\partial \xi_j}(0, \tau) = \alpha w_j,$$

$$\frac{\partial w_j}{\partial \xi_j}(R_j, \tau) = -\alpha w_j \tag{12}$$

The solution of the problem (9)–(10) is obtained using the classical Fourier method as

$$w_1 = \sum_{n=1}^{\infty} C_n \exp\left(\frac{\xi_1}{2}\right) \exp\left[-\left(\frac{1}{4} + b_n^2\right)\tau\right] \sin(b_n \xi_1) \tag{13}$$

where b_n are the positive solutions of the transcendental equation

$$\tan b_n R_1 = -2b_n \tag{14}$$

and the series coefficients in Eq. (15) are

$$C_n = \frac{\dfrac{b_n}{1/4 + b_n^2}}{\dfrac{R_1}{2} - \dfrac{\sin(2b_n R_1)}{4b_n}} \tag{15}$$

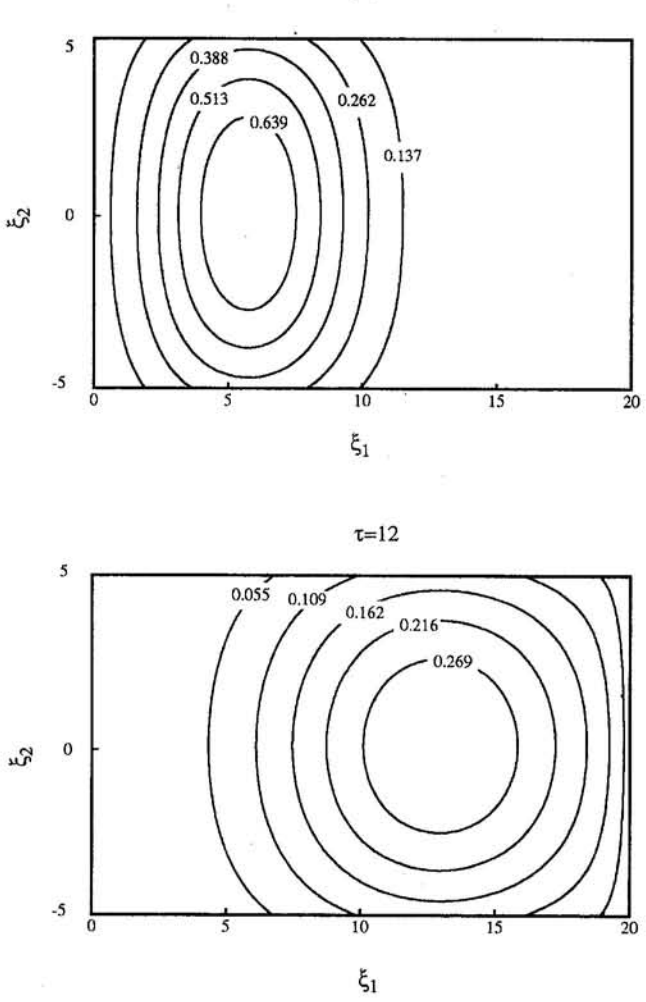

Fig. 1 Space distribution of dimensionless temperature difference, $\Delta\Theta$, for $\xi_3 = 0$

The solutions of the problems (11)–(12) are presented by Carslaw and Jaeger (1959) as:

$$w_j = \sum_{m=1}^{\infty} \frac{2\alpha \cos(\gamma_m \xi_j)}{[(\alpha^2 + \gamma_m^2)R_j + \alpha] \cos(\gamma_m R_j)} \exp[-\gamma_m^2 \tau] \tag{16}$$

where γ_m are the positive solutions of the transcendental equation

$$\gamma_m \tan \gamma_m R_j = \alpha \tag{17}$$

Finally, utilizing Eqs. (8), (13), and (16), the solution for the dimensionless fluid temperature Θ_f is

$$\Theta_f = \sum_{n,m,k=1}^{\infty} 4\alpha^2 C_n \exp\left[\frac{\xi_1}{2} - \left(\frac{1}{4} + b_n^2 + \gamma_m^2 + \gamma_k^2\right)\tau\right]$$

$$\times \frac{\sin(b_n \xi_1) \cos(\gamma_m \xi_2) \cos(\gamma_k \xi_3)}{[(\alpha^2 + \gamma_m^2)R_2 + \alpha][(\alpha^2 + \gamma_k^2)R_3 + \alpha] \cos(\gamma_m R_2) \cos(\gamma_k R_3)} \tag{18}$$

where the coefficients b_n, C_n, and $\gamma_{m,k}$ are determined by Eqs. (14), (15) and (17).

The dimensionless temperature difference between the solid and fluid phases can now be found from Eqs. (3) and (18) as

$$\Delta\Theta = \sum_{n,m,k=1}^{\infty} \frac{4\alpha^2 C_n \exp\left[\frac{\xi_1}{2} - \left(\frac{1}{4} + b_n^2 + \gamma_m^2 + \gamma_k^2\right)\tau\right] \cos(\gamma_m \xi_2) \cos(\gamma_k \xi_3)}{[(\alpha^2 + \gamma_m^2)R_2 + \alpha][(\alpha^2 + \gamma_k^2)R_3 + \alpha] \cos(\gamma_m R_2) \cos(\gamma_k R_3)} \times \left\{\left[-\frac{1}{4} + \frac{\Lambda_1}{2} - \frac{\Lambda_2}{4} + (\Lambda_2 - 1)(b_n^2 + \gamma_m^2 + \gamma_k^2)\right] \sin(b_n \xi_1) + (\Lambda_1 - \Lambda_2) b_n \cos(b_n \xi_1)\right\} \quad (19)$$

Figure 1 depicts the space distributions of the dimensionless temperature difference calculated utilizing Eq. (19) for $R_1 = 20$, $R_2 = 5$, $R_3 = 10$, $\alpha = 0.5$, $\Lambda_1 = 7$ and $\Lambda_2 = 1.4$. These values of Λ_1 and Λ_2 correspond to the following ratios of the thermophysical properties: $(c_p)_f\langle\rho_f\rangle^f = 0.5(c_p)_s\langle\rho_s\rangle^s$, $\lambda_{feff} = 0.25\lambda_{seff}$ and $\epsilon = 0.25$. This figure clearly shows that the temperature difference forms a thermocline. This thermocline has a local maximum. Analyzing the form of the thermocline for different moments of time, it can be seen that its local maximum moves downstream and its amplitude decreases as time increases.

4 Conclusions

The step response of a three-dimensional porous packed bed in nonthermal equilibrium is considered. The analytical solution for the problem is obtained by using the perturbation technique. It is shown that the temperature difference between the solid and fluid phases forms a thermocline. This thermocline has a local maximum and its amplitude decreases while the thermocline propagates downstream.

Acknowledgments

The author is grateful to the Ohio State University for a postdoctoral fellowship. The support provided by the AvHumboldt Foundation and by the Christian Doppler Laboratory for Continuous Solidification Processes is also gratefully acknowledged and appreciated.

References

Amiri, A., and Vafai, K., 1994, "Analysis of Dispersion Effects and Nonthermal Equilibrium, Non-Darcian, Variable Porosity Incompressible Flow Through Porous Media," *Int. J. Heat Mass Transfer,* Vol. 37, pp. 939–954.

Amundson, N. R., 1956a, "Solid–Fluid Interactions in Fixed and Moving Beds. Fixed Beds With Large Particles," *Industrial and Engineering Chemistry,* Vol. 48, pp. 26–35.

Amundson, N. R., 1956b, "Solid–Fluid Interactions in Fixed and Moving Beds. Fixed Beds With Small Particles," *Industrial and Engineering Chemistry,* Vol. 48, pp. 35–43.

Arpaci, V. S., and Clark, J. A., 1962, "Dynamic Response of Fluid and Wall Temperatures During Pressurized Discharge for Simultaneous Time-Dependent Inlet Gas Temperature, Ambient Temperature, and/or Ambient Heat Flux," *Advances in Cryogenic Engineering,* Vol. 7, pp. 419–432.

Burch, D. M., Allen, R. W., and Peavy, B. A., 1976, "Transient Temperature Distributions Within Porous Slabs Subjected to Sudden Transpiration Heating," ASME JOURNAL OF HEAT TRANSFER, Vol. 98, pp. 221–225.

Carslaw, H. S., and Jaeger, J. C., 1959, *Conduction of Heat in Solids,* Oxford University Press, United Kingdom.

Hung, F. T., and Nevins, R. G., 1965, "Unsteady-State Heat Transfer With a Flowing Fluid Through Porous Solids," ASME Paper No. 65-HT-10.

Jang, W. J., and Lee, C. P., 1974, "Dynamic Response of Solar Heat Storage Systems," ASME Paper No. 74-WA/HT-22.

Kuznetsov, A. V., 1994, "An Investigation of a Wave of Temperature Difference Between Solid and Fluid Phases in a Porous Packed Bed," *Int. J. Heat Mass Transfer,* Vol. 37, pp. 3030–3033.

Riaz, M., 1977, "Analytical Solutions for Single- and Two-Phase Models of Packed-Bed Thermal Storage Systems," ASME JOURNAL OF HEAT TRANSFER, Vol. 99, pp. 489–492.

Schumann, T. E. W., 1929, "Heat Transfer: Liquid Flowing Through a Porous Prism," *Journal of the Franklin Institute,* Vol. 208, pp. 405–416.

Sözen, M., and Vafai, K., 1990, "Analysis of the Non-thermal Equilibrium Condensing Flow of a Gas Through a Packed Bed," *Int. J. Heat Mass Transfer,* Vol. 33, pp. 1247–1261.

Sözen, M., Vafai, K., and Kennedy, L. A., 1991, "Thermal Charging and Discharging of Sensible and Latent Heat Storage Packed Beds," *J. Thermophysics,* Vol. 5, pp. 623–625.

Spiga, G., and Spiga, M., 1981, "A Rigorous Solution to a Heat Transfer Two Phase Model in Porous Media and Packed Beds," *Int. J. Heat Mass Transfer,* Vol. 24, pp. 355–364.

Vafai, K., and Sözen, M., 1990a, "Analysis of Energy and Momentum Transport for Fluid Flow Through a Porous Bed," ASME JOURNAL OF HEAT TRANSFER, Vol. 112, pp. 690–699.

Vafai, K., and Sözen, M., 1990b, "An Investigation of a Latent Heat Storage Porous Bed and Condensing Flow Through It," ASME JOURNAL OF HEAT TRANSFER, Vol. 112, pp. 1014–1022.

Journal of Heat Transfer

Discussion

Non-Quasi-Steady Analysis of Heat Conduction From a Moving Heat Source[1]

S. M. Zubair[2,4] and M. A. Chaudhry.[3,4] The author has attempted an important problem of a moving heat source, which has applications to many physical problems of engineering sciences. It should, however, be noted that the transformation used in Eq. (4) of the paper is not correct. The correct transformation, as referenced by Carslaw and Jaeger (1959) should be

$$\theta(x, \tau) = \phi(x, \tau) \exp(-am^2\tau). \quad (1)$$

The transformation and thus the temperature formulation resulting from the moving heat source with constant power as given in Eq. (6) of the paper appears to be incorrect. The correct formulation in the notation of the paper is

$$\theta(X, \tau) = \frac{q_c}{\rho C_p (\pi a)^{1/2}} \exp\left(-\frac{UX}{2a} - am^2\tau\right) \times \int_{1/\sqrt{\tau}}^{\infty} \exp\left[-\frac{X^2}{4a}\eta^2 - \frac{U^2}{4a}\eta^{-2}\right]\eta^{-2}d\eta. \quad (2)$$

On substituting,

$$\xi = \frac{X^2}{4a}\eta^2 \quad \text{and} \quad \frac{d\xi}{\xi} = 2\frac{d\eta}{\eta},$$

leading to

$$\theta(X, \tau) = \frac{q_c X}{4\pi^{1/2}k} \exp\left(-\frac{UX}{2a} - am^2\tau\right) \times \int_{X^2/4a\tau}^{\infty} \exp\left[-\xi - \left(\frac{U^2}{4a}\right)\left(\frac{X^2}{4a}\right)\xi^{-1}\right]\xi^{-3/2}d\xi, \quad (3)$$

which can be expressed in terms of generalized incomplete gamma functions recently described by Chaudhry and Zubair (1994, 1995) as

$$\theta(X, \tau) = \frac{q_c X}{4\pi^{1/2}k} \exp\left(-\frac{UX}{2a} - am^2\tau\right) \times \Gamma\left(-\frac{1}{2}, \frac{X^2}{4a\tau}; \left(\frac{UX}{4a}\right)^2\right). \quad (4)$$

[1] By H. J. Zhang, published in the August 1990 issue of the ASME JOURNAL OF HEAT TRANSFER, Vol. 112, pp. 777–779.

[2] Mechanical Engineering Department.
[3] Mathematical Sciences Department.
[4] King Fahd University of Petroleum and Minerals, Dhahran 31261, Saudi Arabia.

The quasi-steady temperature solution for the case when the rod is insulated ($h = 0$, $m^2 = 0$), can be written as

$$\theta_1 = \frac{q_c X}{4\pi^{1/2}k} \exp\left(-\frac{UX}{2a}\right) \Gamma\left(-\frac{1}{2}, 0; \left(\frac{UX}{4a}\right)^2\right). \quad (5)$$

This can be simplified to give

$$\theta_1 = \frac{q_c a}{kU}\frac{X}{|X|} \exp\left[-0.5\frac{U}{a}(X + |X|)\right], \quad (6)$$

which coincides with Eq. (10*b*) of the paper if $X > 0$.

In addition, it is important to emphasize that the use of generalized incomplete gamma functions can facilitate finding exact analytical solutions of several time-dependent moving heat source problems (Chaudhry and Zubair, 1993; Zubair and Chaudhry, 1996).

References

Chaudhry, M. A., and Zubair, S. M., 1993, "Analytic Study of Temperature Solutions Due to Gamma-Type Moving Point-Heat Sources," *International Journal of Heat and Mass Transfer,* Vol. 36, No. 6, pp. 1633–1639.

Chaudhry, M. A., and Zubair, S. M., 1994, "Generalized Incomplete Gamma Functions With Applications," *Journal of Computational and Applied Mathematics,* Vol. 55, No. 1, pp. 99–124.

Chaudhry, M. A., and Zubair, S. M., 1995, "On the Decomposition of Generalized Incomplete Gamma Functions With Applications to Fourier Transforms," *Journal of Computational and Applied Mathematics,* Vol. 59, No. 3, pp. 253–284.

Zubair, S. M., and Chaudhry, M. A., 1996, "Temperature Solutions Due to Time-Dependent Moving-Line-Heat Sources," *Wärme- und Stoffübertragung,* in press.

Author's Closure

The discussion by Zubair and Chaudhry emphasizes the great importance of heat conduction from a moving heat source and the value of the generalized incomplete gamma function to some moving heat source problems. The special attention to this important problem is gratifying.

It should, however, be pointed out that the mistake noted by Zubair and Chaudhry in the transformation used in Eq. (4) of my paper is merely an erratum and was found by me some time ago. In fact, Eq. (5) of my paper can be derived from Eq. (4) only when the correct transformation, $\theta(x, \tau) = \phi(x, \tau) \exp(-am^2\tau)$, is used as is proved in my previous paper (Zhang, 1986). In the paper, there is also an erratum, i.e., "a finite medium" in the last paragraph of the introduction, and the correct description should be "an infinite medium."

Next, the formulation (2) of the discussion appears to be incorrect. When the heat source method is chosen to solve heat conduction from a moving heat source, the transformation mentioned above should be applied to all the instantaneous plane heat source at different time τ' rather than applied only once on the resulting $\phi(x, \tau)$ at time τ (Zhang, 1992). As shown